

Technical Editor
ARTHER J. WENNERSTROM
Associate Editors
Air Pollution Control
S. R. OREM
Diesel and Gas Engine Power
W. R. TABER, Jr.
Gas Turbine
H.C. EATOCK
Power
N. T. NEFF
Advanced Energy Systems
R. SHANKLIN
Fuels
H. A. GRABOWSKI
Nuclear Engineering
B. R. SHELTON

**BOARD ON
COMMUNICATIONS**
Chairman and Vice-President
MICHAEL J. RABINS

Members-at-Large
W. BEGELL
W. G. GOTTENBERG
D. KOENIG
M. KUTZ
F. LANDIS
J. W. LOCKE
J. E. ORTLOFF
C. PHILLIPS
H.C. REEDER
K. REID

President, **FRANK M. SCOTT**
Executive Director,
PAUL ALLMENDINGER
Treasurer, **ROBERT A. BENNETT**

PUBLISHING STAFF
Mng. Dir., Publ., **J. J. FREY**
Dep. Mng. Dir., Pub.,
JOS. SANSONE
Managing Editor,
CORNELIA MONAHAN
Production Editor,
JACK RUMMEL
Editorial Production Asst.,
BETH DARCHI

The Journal of Engineering for Power (ISSN 0022-025) is published quarterly for \$72 per year by The American Society of Mechanical Engineers, 345 East 47th Street, New York, NY 10017. Second class postage paid at New York, NY and additional mailing offices. POSTMASTER: Send address change to The Journal of Engineering for Power, c/o THE AMERICAN SOCIETY OF MECHANICAL ENGINEERS, P.O. Box 3199, Grand Central Station, New York, NY 10163.

CHANGES OF ADDRESS must be received at Society headquarters seven weeks before they are to be effective. Please send old label and new address.

PRICES: To members, \$36.00, annually; to nonmembers, \$72.00. Single copies, \$24.00 each. Add \$6.00 for postage to countries outside the United States and Canada.

STATEMENT from By-Laws. The Society shall not be responsible for statements or opinions advanced in papers or ... printed in its publications (B 7.1, para. 3).

COPYRIGHT © 1983 by the American Society of Mechanical Engineers. Reprints from this publication may be made on condition that full credit be given the TRANSACTIONS OF THE ASME - JOURNAL OF ENGINEERING FOR POWER, and the author, and date of publication be stated.

INDEXED by the Engineering Index, Inc.

TECHNICAL PAPERS

- 403 A Theory for Boundary Layer Growth on the Blades of a Radial Impeller Including Endwall Influence (82-GT-90)
H. Ekerol and J. W. Raily
- 412 Manufacturing Methods for Erosion-Resistant Ceramic Nozzles for Small Gas Turbines (82-GT-160)
J. P. Arnold, W. McGovern, A. D. Russell, and J. C. Napier
- 417 Transonic Compressor Development for Large Industrial Gas Turbines (82-GT-219)
B. Becker, M. Kwasniewski, and O. von Schwerdtner
- 422 A Three-Dimensional Turbulent Flow Analysis Method for the Rotating Channels of a Centrifugal Turbomachine (82-GT-221)
D. A. Fraser, J. H. G. Howard, and W. C. Lennox
- 430 Effect of Using Emulsions of High Nitrogen Containing Fuels and Water in a Gas Turbine Combustor on NO_x and Other Emissions (82-GT-224)
P. P. Singh, P. R. Mulik, and A. Cohn
- 438 The Gas Turbine Heat Exchanger in the Fluidized Bed Combustor (82-GT-225)
C. F. Holt, A. A. Boiarski, and H. E. Carlton
- 446 Materials Selection for Metallic Heat Exchangers in Advanced Coal-Fired Heaters (82-GT-226)
I. G. Wright and A. J. Minchener
- 452 A Theoretical Investigation of Transonic Flows in Radial Compressor Diffusers (82-GT-227)
H. O. Jeske and I. Teipel
- 457 Effect of Impeller-Extended Shrouds on Centrifugal Compressor Performance as a Function of Specific Speed (82-GT-228)
L. Sapiro
- 466 The Design and Testing of Air-Cooled Blading for an Industrial Gas Turbine (82-GT-229)
J. M. Hannis and M. K. D. Smith
- 474 The Calculation of Deviation Angle in Axial-Flow Compressor Cascades (82-GT-230)
L. C. Wang, R. Hetherington, and A. Goulas
- 480 Transient Vibration of High-Speed, Lightweight Rotors Due to Sudden Imbalance (82-GT-231)
M. Sakata, T. Aiba, and H. Ohnabe
- 487 Optimal Design of Squeeze Film Supports for Flexible Rotors (82-GT-232)
M. D. Rabinowitz and E. J. Hahn
- 495 Experimental Evaluation of Squeeze Film Supported Flexible Rotors (82-GT-233)
M. D. Rabinowitz and E. J. Hahn
- 504 Unconditionally Stable Calculation of Transonic Potential Flow Through Cascades Using an Adaptive Mesh for Shock Capture (82-GT-238)
J. R. Caspar
- 514 An Improved Time-Marching Method for Turbomachinery Flow Calculation (82-GT-239)
J. D. Denton
- 525 The Control of Engine Vibration Using Squeeze Film Dampers (82-GT-241)
R. Holmes
- 530 The Elliptic Solution of the Secondary Flow Problem (82-GT-242)
S. Abdallah and A. Hamed
- 536 A Quasi-Three-Dimensional Finite Element Solution for Steady Compressible Flow Through Turbomachines (82-GT-261)
A. S. Ucer, I. Yegen, and T. Durmaz
- 543 Eigensolution Reanalysis of Rotor Dynamic Systems by the Generalized Receptance Method (82-GT-262)
A. B. Palazzolo, Bo Ping Wang, and W. D. Pilkey
- 551 Closed-Form, Steady-State Solution for the Unbalance Response of a Rigid Rotor in Squeeze Film Damper (82-GT-263)
D. L. Taylor and B. R. K. Kumar
- 560 The Effect of Journal Misalignment on the Oil-Film Forces Generated in a Squeeze Film Damper (82-GT-285)
R. A. Cookson, X. A. Feng, and S. S. Kossa

(Contents Continued on pg. 411)

(Contents Continued)

- 565 **Unsteady Aerodynamics and Gapwise Periodicity of Oscillating Cascaded Airfoils** (82-GT-286)
F. O. Carta
- 575 **Aerodynamic Damping Measurements in a Transonic Compressor** (82-GT-287)
E. F. Crawley
- 585 **In-Plane Inertial Coupling in Tuned and Severely Mistuned Bladed Disks** (82-GT-288)
E. F. Crawley
- 591 **An Improved Method for Calculating Critical Speeds and Rotordynamic Stability of Turbomachinery** (82-GT-294)
B. T. Murphy and J. M. Vance
- 596 **Comparison of Two- and Three-Dimensional Flow Computations With Laser Anemometer Measurements in a Transonic Compressor Rotor** (82-GT-302)
R. V. Chima and A. J. Strazisar
- 606 **Nonlinear Analysis of Rotor-Bearing Systems Using Component Mode Synthesis** (82-GT-303)
H. D. Nelson, W. L. Meacham, D. P. Fleming, and A. F. Kascak
- 615 **The Effect of Temperature Ratios on the Film Cooling Process** (82-GT-305)
P. J. Loftus and T. V. Jones
- 621 **RACER Conceptual Design** (83-GT-50)
J. T. Halkola, A. H. Campbell, and D. Jung
- 627 **Investigation of F/A-18A Engine Throttle Usage and Parameteric Sensitivities** (83-GT-64)
C. L. Hall, R. W. Hathaway, and S. M. Cote
- 635 **The Feasibility of Water Injection into the Turbine Coolant to Permit Gas Turbine Contingency Power for Helicopter Application** (83-GT-66)
G. J. Van Fossen
- 643 **Inertia Effects on the Dynamics of a Disk Levitated by Incompressible Laminar Fluid Flow** (83-GT-149)
D. K. Warinner and J. T. Pearson
- 654 **Vectoring Exhaust Systems for STOL Tactical Aircraft** (83-GT-212)
R. F. Tape, W. R. Hartill, Lt. S. Curry, and T. J. Jones
- 663 **F-14 Aircraft and Propulsion Control Integration Evaluation** (83-GT-234)
W. J. Davies, C. A. Hoelzer, and R. W. Vizzini
- 669 **LMFBR Operational and Experimental In-Core, Local-Fault Experience, Primarily With Oxide Fuel Elements** (80-C2/NE-21)
D. K. Warinner
- 679 **The LMFBR Fuel Design Environment for Endurance Testing, Primarily of Oxide Fuel Elements With Local Faults** (80-C2/NE-25)
D. K. Warinner
- 690 **Design Concept and Development of a Heavy-Duty Truck Diesel Engine for Better Fuel Economy** (82-DGEP-3)
A. Kobayashi, M. Ozawa, M. Noda, and K. Kikuchi
- 697 **Some Aspects of Constant Pressure Turbocharged Marine Diesel Engines of Medium and Low Speed** (82-DGEP-4)
T. Azuma, T. Yura, and Y. Tokunaga

ANNOUNCEMENTS

- 416 **Change of address form for subscribers**
- 437 **Mandatory excess-page charges**
- 712 **Information for authors**

A Theory for Boundary Layer Growth on the Blades of a Radial Impeller Including Endwall Influence

H. Ekerol
Research Fellow.

J. W. Raily
Professor.
Mem ASME

Department of Mechanical Engineering,
University of Birmingham,
Birmingham B15 2IT, England

Experimental data on the wall shear stress of a turbulent boundary layer on the suction side of a blade in a two-dimensional radial impeller is compared with the predictions of a theory which takes account of rotation and curvature effects as well as the three-dimensional influence of the endwall boundary layers. The latter influence is assumed to arise mainly from mainstream distortion due to secondary flows created by the endwall boundary layers, and it appears as an extra term in the momentum integral equation of the blade boundary layer which has allowance, also for the Coriolis effect; an appropriate form of the Head entrainment equation is derived to obtain a solution and a comparison made. A comparison of the above theory with the Patankar-Spalding prediction method, modified to include the effects of Coriolis (including mixing length modification, MLM), is also made.

Introduction

A great deal of the structure of two-dimensional cascade aerodynamics is erected on the assumption that boundary layer flows over the suction and pressure surface may be treated as if they were exactly two-dimensional. Further, the curvature (convex or concave) of these surfaces has usually been ignored so that much of existing two-dimensional boundary layer theory has been used directly in cascade analysis. It has been felt that the presence of blade surface rotation is a factor that ought to be allowed for but in the majority of cases the boundary layers are then firmly three-dimensional (if they were not so already) so that there has been little incentive to include Coriolis effects, which may well be lost in the presence of existing three-dimensionality.

A considerable amount of experimental work on Coriolis effects (apart from the work discussed below) has been carried out by a number of investigators, much of which has been summarized by Sharma [1] and Johnston and Eide [2]. In the latter work, data from the measurements of Moore [3], carried out on a rotating channel, is referred to and the mechanism of flow stabilization on the suction or "trailing" face of the channel is described. In those tests, however, it is possible that three-dimensional (secondary flow) effects arising from the low aspect ratio (unity) might have had the major influence on the observed boundary layer behavior. In the later work of Koyama et al. [4], experiments on a rotating duct having an aspect ratio of 7 were carried out and strong evidence of two-dimensional Coriolis effects were exhibited

revealing suppression of turbulence on the suction side of the duct and evidence of changes in the von Karman constant (reduced on the suction side, increased on the pressure side). These changes were especially significant for the large rotation numbers.

It was with a view to understanding Coriolis effects in developing boundary layers on rotating surfaces that a program of investigation on a rotating nominally two-dimensional impeller was initiated, Singh [5], Sharma (loc. cit.) Sharma and Raily [6]. In that work, a 6-bladed impeller, radial in the meridional plane, was studied in order to investigate Coriolis effects. In a later investigation a 24-blade impeller was employed in order to eliminate curvature effects. Referring to Fig. 1 the direction of the Coriolis force is clear as it applies to suction and pressure surfaces. In the case of the first impeller, much stress was laid upon the importance of attached flow; hence, the blades were designed so as to have a modest degree of diffusion, especially on the suction side (or "trailing" face, Fig. 1) of the blades. The first experiments

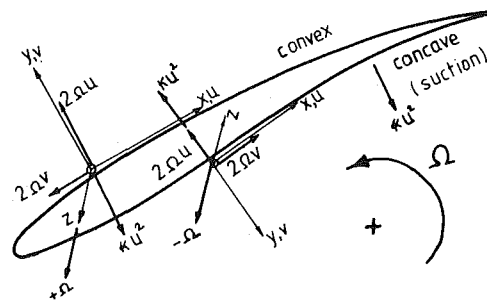


Fig. 1 Boundary layer coordinate system

Contributed by the Gas Turbine Division of THE AMERICAN SOCIETY OF MECHANICAL ENGINEERS and presented at the 27th International Gas Turbine Conference and Exhibit, London, England, April 18-22, 1982. Manuscript received at ASME Headquarters December 7, 1981. Paper No. 82-GT-90.

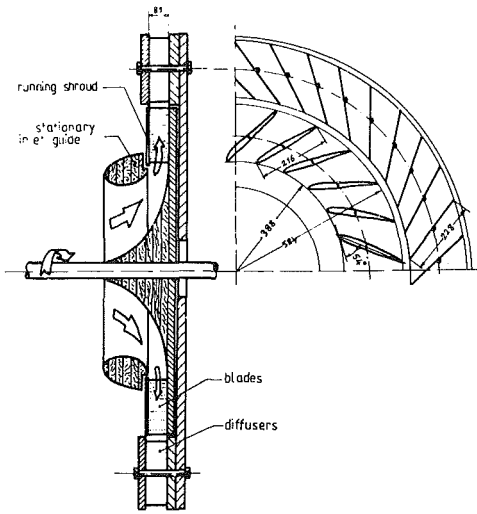


Fig. 2 Experimental machine

were aimed at measuring, directly, the surface shear stress, using thin hot-films (DISA TYPE 55R47) bonded to the surfaces of the impeller blades and surfaces. Two-dimensional computation of shear stress were carried out in order to obtain comparison with the measurements [1]; the results indicated that even the most liberal allowances for Coriolis effects failed to produce agreement between theory and measurement. One of the disadvantages in the first experimental arrangement (the 6-blade impeller which was the subject of the comparison) arose out of the fact that surface curvature and Coriolis forces were simultaneously present and, furthermore, tended to have mutually opposing effects. In a two-dimensional turbulent boundary layer, the momentum equations along and normal to the surface may be written in the form

$$u \frac{\partial u}{\partial x} + v \frac{\partial u}{\partial y} - 2\Omega v = -\frac{1}{\rho} \frac{\partial p^*}{\partial x} + \frac{\partial}{\partial y} \left(\nu \frac{\partial u}{\partial y} - u'v' \right) \quad (1)$$

$$\frac{\partial}{\partial y} (\bar{v}'^2) + 2\Omega u \pm \kappa u^2 = -\frac{1}{\rho} \frac{\partial p^*}{\partial y} \quad (2)$$

where κ is the surface curvature and Ω the angular velocity of frame rotation. If the third term on the left of equation (1) is

ignored, then equation (2) implies that the effects of rotation and curvature, seen as influencing the pressure difference across the layer, are mutually opposing when (see Fig. 1) the "leading" face has convex curvature and the "trailing face" concave curvature.

A further influence on turbulent boundary layers arising from Coriolis and curvature effects may be introduced on the basis of the Stratford-Bradshaw mixing length model [1] which implies that, if the previous mixing length is l_0 , that is, for flow over flat plates in nonrotating systems, then the modified mixing length is given by

$$l = l_0(1 + \beta_\Omega Ri_\Omega + \beta_\kappa Ri_\kappa) \quad (3)$$

where Ri_Ω , Ri_κ are Richardson numbers defined by

$$Ri_\Omega = 2\Omega / \left(\frac{\partial u}{\partial y} \right) \quad (4)$$

$$Ri_\kappa = 2(u/\kappa) / \left(\frac{\partial u}{\partial y} \right) \quad (5)$$

Values of the proportionately constants suggested on the basis of other experiments were, β_Ω equal to 7.0 for trailing face and 4.0 for leading face, with β_κ equal to 4.0 for concave surfaces and 7.0 for convex surfaces. As mentioned above, the computations based on this procedure failed to account for the modified surface shear stresses except on the basis of extremely large values of β_Ω . Furthermore, the fact that the signs of Ω and of κ (see Fig. 1) were such that over the last one-third of the suction surface of the blade the second and third terms on the right of equation (3) were in opposition tended to destroy the accuracy of the comparison.

The second set of blades were designed to have nearly flat trailing (i.e., suction) faces. In order to limit the adverse velocity gradients on this surface, the blade number was increased to 24. The resulting blade layout is shown in Fig. 2, and experiments relate to the suction surface.

Additional experimental information from the 24-blade impeller obtained by means of a constant temperature hot-wire anemometer mounted on the blade, was obtained by Ekerol [7]. This hot-wire anemometer is shown diagrammatically in Fig. 3, from which it was possible to obtain velocity profiles in the boundary layer along the center-plane of the blade. Confirmation of the configuration of the mainstream flow near the center-plane, namely that the streamlines of this flow lay substantially in that plane, was also obtained by Ekerol using a photographic technique.

Nomenclature

b = blade half-span, m
 b_n = binormal direction
 C_f = coefficient of skin friction
 F_r, F_ϕ, F_z = blade forces in r, ϕ, z directions, N/m³
 H = boundary layer shape factor
 \bar{H} = entrainment shape factor
 h_1, h_2, h_3 = metric coefficients in ξ, η, ζ directions
 I = pressure term (rothalpy), m²/s²
 k = parameter in secondary flow analysis,
 $k = \sqrt{12}/s'$
 l = mixing length, m

N = number of blades in the impeller
 n = power in the velocity profile
 p = pressure, N/m²
 p^* = reduced pressure, N/m²
 R_0 = rotation number
 R_n = radius of curvature of streamline, m
 Re_θ = Reynolds number based on momentum thickness
 Ri_Ω = Richardson number for rotation
 Ri_κ = Richardson number for surface curvature
 r, ϕ, z = cylindrical-polar coordinates

s, n, z = coordinates for secondary flow
 s' = local blade spacing, m
 U_1 = free-stream velocity along the centerline of the blade, m/s
 U, V = radial and peripheral components of pitch averaged flow, m/s
 u, v, w = endwall boundary layer velocities in r, ϕ, z directions, m/s, respectively, and blade boundary layer velocities in streamline coordinate system (ξ, η, ζ).
 u_s, v_n = secondary flow

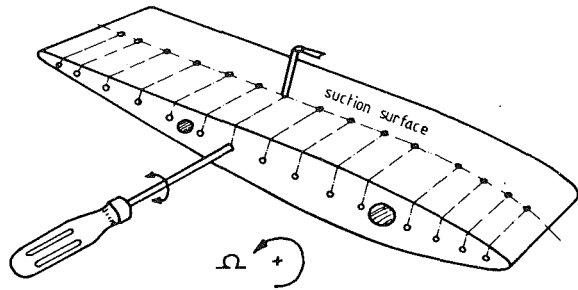


Fig. 3 Hot-wire anemometer mounted on blade

These photographs (taken using a short duration flash) show the position of a number of short threads attached to the suction surface during running. While there are some difficulties in the interpretation of these photographs (due to the action of centrifugal force) they do show clearly that the streamline down the center of the blade surface is almost coplanar with the center-plane and, further, that there is evidence of slight convergence of the flow towards that center-plane. A diagram shown in Fig. 4, drawn from the photographs shows this effect clearly. There is thus some justification in using two-dimensional theory but at the same time the implication is clear that three-dimensional effects may be important.

Only the experimental evidence from the 24-blade impeller has been considered in this work: firstly, because of the absence on these blades of suction-side curvature and, secondly, because of the boundary layer traverse information which has been obtained pertaining to the velocity profile relative to the blade.

Theoretical two-dimensional boundary layer analysis has been based upon the use of the numerical method due to Sharma [1] based on the Patankar-Spalding procedure but which incorporates modifications of the equations to include the extra terms (in equations (1) and (2)) which take account of the Coriolis force. In addition, the hypothesis on which the effective viscosity is determined, in particular, the mixing length hypothesis, has been modified in the manner of equation (3) to take account of the effect of Coriolis force on the turbulent shear stress. Calculations (see below) have been carried out to determine the wall shear stress corresponding to the velocity distribution measured at a particular mass flow

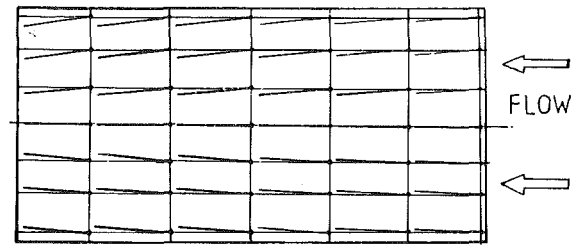


Fig. 4 Flow pattern as revealed by cotton threads; plane view of suction side

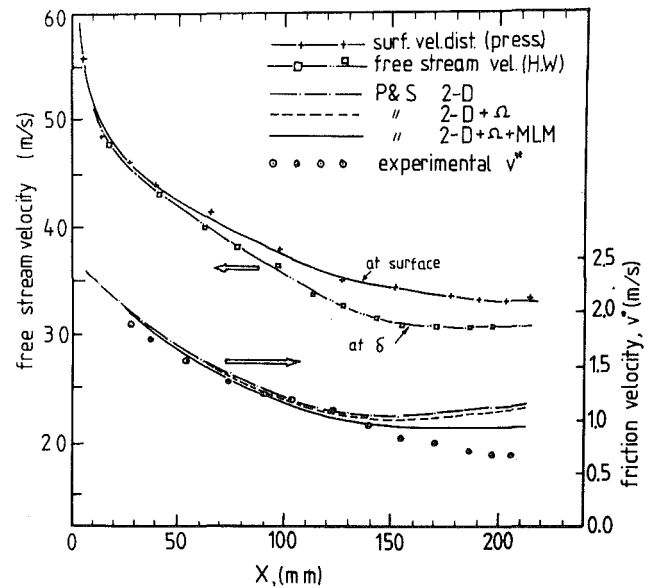


Fig. 5 Surface and free-stream velocity distributions and comparison of two-dimensional P & S calculations with experimental v^*

through the 24-blade impeller. The mainstream velocity distribution is available both from pressure and from hot-wire traverse data at the edge of the boundary layer and the results are plotted in Fig. 5. The computed shear stress is plotted on the same figure for three two-dimensional cases as follows:

Nomenclature (cont.)

velocities in stream wise and normal directions, m/s
 V^* = friction velocity, m/s
 v, w = secondary flow velocities, m/s
 x, y, z = Cartesian coordinate system
 α = direction of average streamline to the radial direction
 β = streamline direction w.r.t. blade centerline, angle between tangent to the blade camber and peripheral direction
 θ = momentum thickness, m

ϕ = polar angle, mass flow coefficient
 δ = boundary layer thickness, m
 δ^* = displacement thickness, m
 ν = kinematic viscosity, m^2/s
 κ = surface curvature m^{-1}
 ϵ = crossflow wall angle
 Ω = angular velocity of the impeller, s^{-1}
 ω = streamwise vorticity, s^{-1}
 τ = shear, stress, N/m^2
 ρ = density of air kg/m^3
 ξ, η, ζ = streamline coordinate system
 χ = dimensionless distance normal to endwall, $2/\delta e$

Subscripts

b = refers to the blade-centerline
 e = refers to endwall
 m = mean value
 s = streamwise direction
 t = refers to the trailing face
 l = refers to the leading face
 w = wall values
 Ω = rotation
 κ = curvature
 ∞ = free-stream value

Superscripts

' = derivative, fluctuating quantity
 $-$ = Cartesian component

- (i) without any effect of rotation
- (ii) with the inclusion of the Coriolis terms but without shear stress modification
- (iii) with both Coriolis terms and shear stress modifications

The results were obtained from the Patankar-Spalding computer program as modified by Sharma [1]. The experimental shear stress results which were obtained by the abovementioned hot-film technique, are also shown on the same figure.

It is clear from this figure that even by the use of both the Coriolis terms and shear stress modification, the trend of the experimental values, especially for the larger boundary layer thicknesses mean the trailing edge, is significantly below the predicted results.

As a consequence of this fact and the photographic evidence, the hypothesis is put forward that the observed low level of wall stress is the consequence of the influence of the endwall boundary layer upon the central plane blade boundary layer. The major part of the theoretical presentation below is concerned with predicting the influence of the endwalls on the boundary layer growth and skin friction along the center-plane of the impeller blades. Thereafter a comparison with experiments is made.

Influence of the Endwall Boundary Layer Upon the Blade

The Thin Boundary Layer Model. In a previous work [8], a simple model for the influence of the endwall boundary layer upon the blade boundary layer for the type of geometry depicted in Fig. 2 was discussed. In that model, which may be termed the "thin boundary layer" model, the rigorous condition that the boundary layer would be so thin that no effect was manifested on the mainstream flow was maintained. Under this circumstance it was assumed that there would be a "law of connection" for the endwall layer and the blade layer along the lines of Moore's "corner-flow" model [3]. Thus, mass conservation would apply to the crossflow from the endwall to the blade surface (and vice-versa) and, in addition, longitudinal momentum would also have to be conserved. The treatment of the problem along these lines was carried out rigorously in the aforementioned work [8], and the deduction was made that the thin boundary layer hypothesis led to a contradiction which was only resolvable by allowing distortion of the mainstream flow over the blade surface to occur.

That mathematical treatment, starting from the assumption of zero free-stream distortion, shows that, over the blade suction surface (for the geometry under discussion) no three-dimensionality may appear, this being an exact statement in one restricted case and approximately true in all other cases. The physical implications are that the endwall boundary layer fluid may not pass into (or out of) the blade boundary layer, thus forcing a boundary condition, for the endwall layer, of the collateral flow where the endwall meets the blade. The crossflow within the endwall layer represents a streamwise vorticity, and it is therefore likely that such a boundary condition would not be realistic. It is thus more likely that crossflow in the endwall boundary layer will give rise to an overall distortion of the mainstream. Indeed this situation has been studied by, for example, Majumdar and Spalding [9] using the "partially-parabolic treatment of the full equations of motion in which the entire cross section, normal to the nominal mainstream direction, shares in this crossflow.

The 'Distorted Mainstream' Treatment. The growth of the endwall boundary layer may be considered, in the first place, as an axisymmetric flow taking place over the endwalls

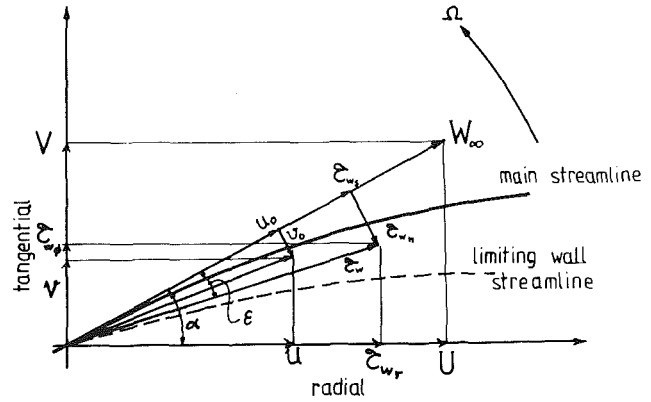


Fig. 6 Endwall boundary layer parameters

(the backplate, for example, Fig. 2) in which the peripheral pressure gradient due to the pressures on suction and pressure side of the blades is considered to be uniformly distributed around the flow; this is equivalent to the replacement of the blades by the use of a force field, F_ϕ , given by

$$(p_l - p_t)\delta r = F_\phi r \delta r (\phi_l - \phi_t) \quad (6)$$

The resulting endwall boundary layer flow violates the boundary conditions (as mentioned above) inasmuch as the calculated crossflow has a component normal to the blade surface. To avoid this difficulty, only the boundary layer thickness, δ_e , is retained and at each increment of radius the crossflow is recalculated in the form of a streamwise vorticity (i.e., the component of absolute vorticity pointing along the direction of the relative velocity vector at the edge of the endwall boundary layer). This strip of streamwise vorticity gives rise, at each radius, to a secondary flow field which must be contained in accordance with the boundary conditions, depicted in Fig. 6, due to the blades. The center-plane of the impeller, at height $z=b$, becomes a plane-of-symmetry and the problem is to calculate the blade surface flow field along the blade center-plane due to the action of the secondary flow, (which has now become the agency whereby the mainstream distortion takes place). A second distortion at the center-plane arises due to the displacement thickness of the endwall layer (the so-called "squeeze effect"). The two effects are considered separately. Before proceeding with this treatment of the blade boundary layer, calculation of the magnitude of the endwall boundary layer thickness must be completed.

Simplified Treatment of the Endwall Layer. As already pointed out, a simple model of the endwall layer is used which bears a close resemblance to previous treatments of the annulus wall layer in an axial compressor except that the rotation vector, now normal to the endwall, Fig. 6, gives rise to important terms absent from the axial compressor case. Adopting the simplification of blade force in an axisymmetric flow, the equations of motion in the radial, r , peripheral, ϕ , and axial (i.e., normal to the endwall) direction, z , become

$$u \frac{\partial u}{\partial r} + w \frac{\partial u}{\partial z} - \frac{v^2}{r} - 2\Omega v - \Omega^2 r = \frac{F_r}{\rho} - \frac{1}{\rho} \frac{\partial p}{\partial r} + \frac{1}{\rho} \frac{\partial \tau_r}{\partial z} \quad (7)$$

$$u \frac{\partial v}{\partial r} + w \frac{\partial v}{\partial z} + \frac{uv}{r} + 2\Omega v = \frac{F_\phi}{\rho} - \frac{1}{\rho} \frac{\partial \tau_\phi}{\partial z} \quad (8)$$

$$u \frac{\partial w}{\partial r} + w \frac{\partial w}{\partial z} = -\frac{F_z}{\rho} - \frac{1}{\rho} \frac{\partial \phi}{\partial z} \quad (9)$$

where F_r , F_ϕ , F_z are the components of the "blade force." The equation of continuity is also necessary, viz.,

$$\frac{1}{r} \frac{\partial}{\partial r} (ru) + \frac{\partial w}{\partial z} = 0 \quad (10)$$

Making the common assumption that, since the layer is thin, the blade forces (arising from the peripheral pressure gradient) do not change, then, the boundary layer equations may be shown to be given by

$$u \frac{\partial u}{\partial r} - UU' + w \frac{\partial u}{\partial z} - \frac{u^2 - V^2}{r} - 2\Omega(u - V) = \frac{1}{\rho} \frac{\partial \tau_r}{\partial z} \quad (11)$$

$$u \frac{\partial v}{\partial r} - UV' + w \frac{\partial v}{\partial z} - \frac{uv - UV}{r} + 2\Omega(u - U) = \frac{1}{\rho} \frac{\partial \tau_\phi}{\partial z} \quad (12)$$

the primes implying differentiation with respect to radius.

These equations reduce to a pair of ordinary differential equations upon integration with respect to z , from 0 to δ ; they are

$$\frac{d}{dr} (U^2 \theta_r) + \delta_r^* U U' + \frac{1}{r} (U^2 \theta_r - V^2 \theta_\phi) - \delta_\phi^* V \left(\frac{V}{r} + 2\Omega \right) = \frac{\tau_{wr}}{\rho} \quad (13)$$

$$\frac{d}{dr} (V^2 \theta_\phi) + \delta_r^* U \left(V + \frac{V}{r} + 2\Omega \right) + \frac{2}{r} V^2 \theta_{\phi r} = \frac{\tau_{w\phi}}{\rho} \quad (14)$$

in which the various thicknesses are defined as follows

$$U^2 \theta_r = \int_0^\delta u(U-u) dz, \quad V^2 \theta_\phi = \int_0^\delta v(V-v) dz,$$

$$V^2 \theta_{\phi r} = \int_0^\delta v(U-u) dz,$$

$$U \delta_r^* = \int_0^\delta (U-u) dz, \quad V \delta_\phi^* = \int_0^\delta (V-v) dz$$

It is possible to solve these equations by the introduction of an appropriate wall model, such as, for example, the Prandtl-Mager law

$$u_0/W_\infty = \chi^{1/n} \quad (15a)$$

$$v_0/W_\infty = \epsilon \chi^{1/2} (1-\chi)^2 \quad (15b)$$

where ϵ is the "wall angle" (the inclination to the free-stream vector \mathbf{W}_∞). If we regard n as unknown, an auxiliary equation is necessary, and, in particular the Head entrainment equation may be used in the manner suggested by Cumpsty and Head [10]. The system of equations has been solved by Sharma and Raily [11] and, including entrainment, by Ekerol. The form of the entrainment equation used was based upon the assumption that the two-dimensional form may be retained. In the context of the coordinate system we are here concerned with, the equation of continuity, equation (11), may be integrated over the interval $z=0$ to δ and an appropriate equation derived. More simply, we may state that the entrainment rate for an axially symmetric flow over a radial plane is given, per unit of width around an arc of sectorial extent, $\Delta\phi$ by

$$\frac{1}{r\Delta\phi} \frac{d}{dr} [r\Delta\phi U(\delta - \delta_r^*)] = UF(\bar{H})/\cos\alpha \quad (16)$$

to cosine being necessary to associate the entrainment function, $F(\bar{H})$, with the total velocity outside the boundary layer. We may then use the Head entrainment function unchanged from its two-dimensional origins. The association of \bar{H} , the

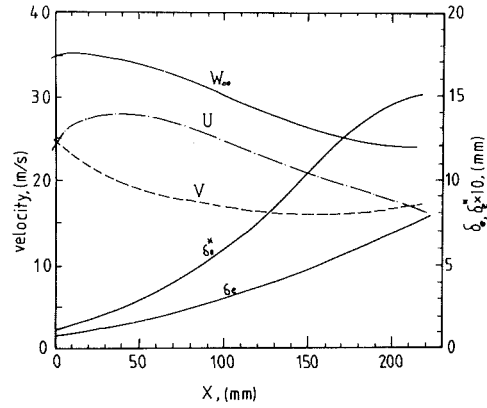


Fig. 7 Components of pitch-averaged main flow and results of end-wall boundary layer calculations

form factor, and the power law exponent of the main streamwise profile is then as follows

$$\bar{H} = (\delta - \delta_s^*)/\theta_s = n + 2 \quad (17)$$

where the suffix, s , refers to the main streamwise profile. Equations (13), (14), and (16) together with (15 a,b) and (17) are sufficient to obtain a solution for δ and n , after an assumption is made about the total shear stress. In line with previous work we assume that

$$\tau_w/\rho W_\infty^2 = 0.123 \times 10^{-0.678H} \times \text{Re}_\theta^{-0.268} \quad (18)$$

which is the Ludwig-Tillmann relation. To obtain the solution in a given case, the free-stream velocity must be specified in magnitude and direction and since the equations were devised on the basis of a pitchwise averaging of the equations of motion, (which introduced the forces, F_r and F_ϕ), these latter must now be related to the pressure distribution around the blades which, in the context of an experiment, is a measurable quantity. It is fairly straightforward procedure to obtain smooth curves for the pressure distribution around the blades and to calculate, for each increment of radius, the tangential blade force component and from it, the mean tangential velocity. Actually a considerable amount of theoretical extrapolation (from the measured pressures) had to be carried out around the nose and potential flow programs were of assistance here, exact specification of leading edge profile shape being necessary. The averaged radial velocity then followed using the continuity condition, and in Fig. 7 resulting distributions of absolute and relative whirl velocity as well as radial velocity corresponding to the blade pressure distribution of Fig. 5 are shown.

Integration was commenced (in the relative frame of reference) by assuming that at a distance 25 mm ahead of the leading edges of the impeller blades the thickness, δ , had a small value, 1.5 mm, while the wall angle, ϵ , was 0.07. The relative flow angle was computed from the known radial velocity and the knowledge that absolute whirl was initially zero. The output of this calculation, namely, δ_e and δ_e^* , is needed in the next phase of the calculation, as described in the above section, to determine the growth of streamwise vorticity. The radial distribution of these quantities is plotted in Fig. 7.

Secondary Flow Treatment of the Endwall Boundary Layer. The foregoing prediction of the endwall boundary layer growth is to be used only as the source of two quantities, namely, δ_e and δ_e^* , while the values of wall angle, ϵ , are to be disregarded. The flow in the endwall boundary layer over a step length, $\delta r = r^{(n+1)} - r^{(n)}$ is to be regarded as inviscid, consisting of a streamwise vorticity, $\omega_s^{(n)}$ at entry to represent the crossflow and a "normal" vorticity representing the gradient of the main-streamwise velocity component. The

calculation of the former in terms of the latter is more complicated in a relative flow system than it is in a stationary system where streamwise vorticity is simply proportional to stream deflection. A formula for streamwise vorticity in a relative system was first given by Smith [12] but, in the present case, it is more convenient to use the formula due to Johnson [13], namely,

$$\frac{\partial}{\partial s} \left(\frac{\omega_s}{W} \right) = (2/\rho W^2) \left[\frac{1}{R_n} \frac{\partial I}{\partial b_n} + \frac{\Omega}{W} \frac{\partial I}{\partial z} \right] = \frac{2}{W} \left[\frac{1}{R_n} + \frac{\Omega}{W} \right] \frac{\partial W}{\partial z} \quad (19)$$

where b_n , the binormal and z , have the directions shown in Fig. 6, and I is the rothalpy for frictionless flow, $p/\rho + W^2/2 - \Omega^2 r^2/2$, W being total relative velocity. Assuming a linear profile for the main streamwise velocity, u_s , then here

$$\frac{\partial W}{\partial z} = \frac{\partial U_s}{\partial z} = W_e(1-f)/\delta_e \quad (20)$$

which implies a slip velocity, fW_e , on the wall. The value of f would follow from a knowledge of the form factor, H ; thus a value of 0.4 corresponds to a form factor of 5/3. Over a given step length equation (19) is integrated and $\omega_{s2}^{(n)}$ calculated at the end of the step. However, since δ_e has meanwhile increased, use is made of the divergence theorem to calculate ω_s at the start of the next interval, which gives, disregarding the radius change

$$\omega_{s1}^{(n+1)} = \omega_{s2}^{(n)} \delta_e(r)/\delta_e(r+\delta r) \quad (21)$$

and the procedure is repeated. Thus the boundary layer theory has been used only to calculate δ_e at each point (later δ_e^* will also be needed). It is now possible to calculate the large-scale crossflow due to this streamwise vorticity.

The linear profile used in equation (20) may seem to be a drastic simplification; however, the values of f were seen to have not a large influence on the final outcome.

The picture presented by the combination of two blade surfaces and two endwalls, Fig. 8, allows the application of the simplified calculation of secondary flow, Horlock [14], in which the aspect ratio of the passage, normal to the mean flow, is $2b/s'$, the smaller dimension being the blade span, $2b$. In the now appropriate system of coordinates (Fig. 8), streamwise vorticity, absolute and relative, is given by

$$\omega_s = \frac{\partial w}{\partial n} - \frac{\partial v}{\partial z} \quad (22)$$

in which

$$\omega = [\omega_s(z)/s'](n-n_m) \quad (23)$$

$$v = [v_s(z)/2s'] [s'^2/4 - (n-n_m)^2] \quad (24)$$

The solution due to Horlock, is applicable provided the form

$$\omega_s = B \frac{\partial u_s}{\partial z} \quad (25)$$

may be retained. This is permissible since there has been maintained a constant value (with z) of the above gradient of u_s ; thus a single value of ω_s emerges for each streamwise location. In the basic situation discussed by Horlock, B is $2 \times$ deflection, but in the present case it is found after vorticity has been calculated from equations (19) and (21). The appearance of f twice reveals why the fairly arbitrary assumption of the linear profile in equation (20) is permissible. The underlying assumption in this use of secondary flow theory is that the velocity gradients of the mainstream flow in the streamwise direction are effectively small compared with the

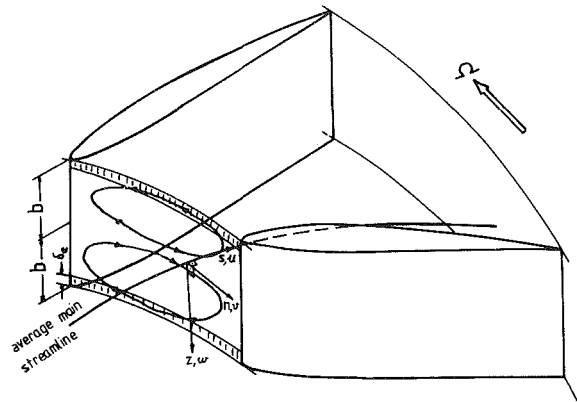


Fig. 8 Secondary flow pattern and coordinate system

gradients over the surface which is normal to that direction, namely, that

$$\frac{\partial u_s}{\partial s} \ll \frac{\partial w}{\partial z}, \frac{\partial v}{\partial n}$$

so that the secondary flow is established at each value of s . It is next necessary to find the mean value of the velocity, v , which is parallel to the endwall and normal to the blade surface. Thus, using equation (24)

$$v_m = \frac{1}{s'} \int_{-s'/2}^{+s'/2} v dz = \frac{u_s}{12} \quad (26)$$

The Horlock procedure replaces equation (22) with an averaged value obtained from equations (23) and (24), which together with the use of the equation of continuity (also averaged) yields the equation

$$\frac{d^2 v_m}{dz^2} - \frac{12v}{s'^2} = -B \frac{d^2 u_s}{dz^2} \quad (27)$$

the solution to which is

$$v_m = -\frac{6BW_\infty}{ks'^2} \left[\frac{I_1(\delta_e) + I_2(\delta_e)}{1 - e^{-2ks_1}} \right] \left[e^{-kz} + e^{k(z-2s_1)} \right] \quad (28)$$

and in which W_∞ is the total (relative) velocity outside of the endwall layer with $k = \sqrt{12}/s'$ and $s_1 = b - \delta_e^*$. Also

$$I_1(\delta_e) = \int_0^{\delta_e} (1 - u_s/W_\infty) e^{kz} dz,$$

$$I_2(\delta_e) = \int_0^{\delta_e} (1 - u_s/W_\infty) e^{-kz} dz$$

$$s' = [(2\pi r/N) - t/\sin\beta](U/W_\infty)$$

The gradient of the spanwise velocity, w , along the blade surface, is the quantity required from this analysis. In the present geometry, it may be shown that, at the center plane

$$\left(\frac{\partial w}{\partial z} \right)_{z=b} = -41.569 \left(\frac{W_\infty \delta_e^*}{s'^2} \right) B \left[\frac{e^{-3.464(s_1/s')}}{1 - e^{-6.928(s_1/s')}} \right] \quad (29)$$

provided $k\delta_e$ is small (which is true, as the numerical calculations show).

Influence of Secondary Flow on the Blade Boundary Layer. A development of the three-dimensional boundary layer equations applicable to the rotating blade surface in terms of a general orthogonal curvilinear coordinate system has been carried out by Ekerol [7]. For the purposes of the present comparison, by taking advantage of the symmetry conditions in the radial plane at midspan, a much simplified equation may be obtained. The deduction of the general equation is lengthy and reference should be made to the work above quoted. At the center-plane the momentum integral

equation in the x -direction (along the blade, at the center-plane) is

$$\begin{aligned} & \frac{\partial}{\partial \xi} (\theta_{\xi\xi}) + \frac{1}{U_1} \frac{\partial U_1}{\partial \xi} (2\theta_{\xi\xi} + \delta_{\xi}^*) \\ & + \frac{1}{h_3} \frac{\partial}{\partial \zeta} (\theta_{\xi\zeta}) + \frac{1}{h_3} \theta_{\xi\xi} \left(\frac{\partial \beta}{\partial \zeta} \right) = \frac{\zeta \omega_{\xi}}{\rho U_1^2} \\ & + R_0 \left[\frac{1}{U_1} \left(\frac{\partial U_1}{\partial \xi} \right) (\delta - \delta_{\xi}^*) + \frac{\partial}{\partial \xi} (\delta - \delta_{\xi}^*) \right. \\ & \left. + \frac{1}{h_3 \delta} \frac{\partial}{\partial \zeta} \int_0^{\delta} \int_0^{\eta} \frac{\omega}{U_1} d\eta d\eta + \frac{1}{h_3 \delta} \frac{\partial \beta}{\partial \zeta} \int_0^{\delta} \int_0^{\eta} \frac{u}{U_1} d\eta d\eta \right] \quad (30) \end{aligned}$$

where ξ is a coordinate measured along the free-stream vector direction; see Fig. 9 for the system of coordinates, ξ, η, ζ , in which ξ and ζ form an orthogonal network covering the blade surface. R_0 is the rotation number here defined as $2 \Omega \delta / U_1$. Further simplification of this equation is achieved following the use of the substitution made by Pierce [15], namely

$$\begin{aligned} U_1 &= \bar{U} \\ u &\simeq \bar{u} + \beta \bar{w} \\ w &\simeq \bar{w} - \beta \bar{u} \end{aligned} \quad (31)$$

provided β is small near the center-plane; the bar indicates the Cartesian components of the vector. Making use of these relationships the last two terms on the left-hand side reduce to a single term, noting that $dz = h_3 d\zeta$ and $d\xi$ is dx along the center-plane as follows

$$\begin{aligned} & \frac{\partial}{\partial z} (\theta_{\xi\xi}) + \theta_{\xi\xi} \left(\frac{\partial \beta}{\partial z} \right) \\ &= \frac{\partial}{\partial z} \left(\int_0^{\delta} \left(\frac{\omega}{U_1} \right) \left(1 - \frac{u}{U_1} \right) dy \right) + \theta_{xx} \left(\frac{\partial \beta}{\partial z} \right) \\ &= \frac{\partial}{\partial z} \left(\int_0^{\delta} \left(\frac{\bar{u}}{\bar{U}} \right) \left(1 - \frac{\bar{u}}{\bar{U}} \right) dy \right) = \frac{\partial}{\partial z} (\theta_{xz}) \end{aligned} \quad (32)$$

using equations (31) and noting that β is zero on the center-plane. If the flow is assumed to be locally collateral around the center-plane, z equal zero, then this term reduces to $\theta_{xx} (\partial \beta / \partial x)$, since $\partial \theta_{xx} / \partial z$ is zero at the center-plane. The terms multiplied by R_0 on the right-hand side may be treated similarly so that, along the center-plane, the momentum integral equation reduces to

$$\begin{aligned} & \frac{\partial \theta}{\partial x} + \frac{\theta}{U_1} \left(\frac{\partial U_1}{\partial x} \right) (2 + H) + \theta \left(\frac{\partial \beta}{\partial z} \right) \\ &= \frac{C_f}{2} + R_0 \left[\frac{1}{U_1} \left(\frac{\partial U_1}{\partial x} \right) (\delta - \delta^*) + \frac{\partial}{\partial x} (\delta - \delta^*) \right] \end{aligned} \quad (33)$$

The entrainment equation in the ξ, ζ set is given by

$$\begin{aligned} & \frac{\partial}{\partial \xi} (\delta - \delta_{\xi}^*) - \frac{1}{h_3} \frac{\partial}{\partial \zeta} (\delta_{\zeta}^*) = F(\bar{H}) \\ & - (\delta - \delta_{\xi}^*) \left(\frac{1}{U_1} \left(\frac{\partial U_1}{\partial \xi} \right) + \left(\frac{\partial \beta}{\partial \zeta} \right) \right) \end{aligned} \quad (34)$$

and this, Cartesian form at the center-plane, becomes

$$\frac{\partial}{\partial x} (\delta - \delta^*) + (\delta - \delta^*) \left(\frac{1}{U_1} \frac{\partial U_1}{\partial x} + 2 \frac{\partial \beta}{\partial z} \right) = F(\bar{H}) \quad (35)$$

where $F(\bar{H})$ is the usual Head entrainment function, Head and Patel [16]. The need for an extra term in the momentum equation related to three-dimensional effects was also appreciated by Dunham [17]. In that case, the linear cascade, $R_0 = 0$, and the term he used depended only on the "squeeze"

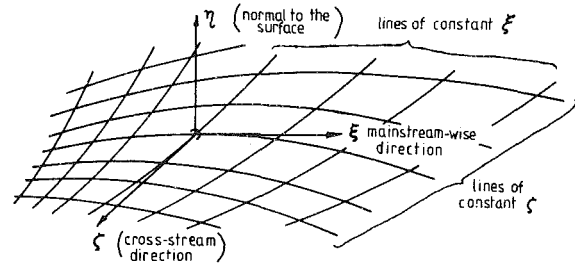


Fig. 9 Streamline coordinate system

effect, the secondary flow effect being ignored, (see equations (40) and (41) below).

Equations (33) and (35), upon the substitution of the empirical Head entrainment function [7], may be solved together and the momentum thickness and skin friction (in the form of v^* , the friction velocity, using equation (18)) obtained for the experimental blade surface velocity distribution obtained, in turn, from the measurements of blade surface pressure. The lateral gradient of β is easily related to the lateral gradient of free-stream velocity obtained from the secondary flow solution, namely, equation (29), and the "squeeze" effect of the endwall displacement.

The two effects on the above lateral gradient may be considered separately. Thus if the "convergence" of the free-stream at the endwall (due to the growing displacement thickness there) is considered and if it is assumed that that effect is uniformly spread across the span, $2b$, then

$$\left(\frac{\partial \beta}{\partial z} \right)_{\text{disp}} = - \frac{1}{b} \left(\frac{d\delta_e^*}{dx} \right) \quad (36)$$

On the account of the secondary flow there is also the contribution

$$\left(\frac{\partial \beta}{\partial z} \right)_{\text{sec}} = \frac{1}{U_1} \left(\frac{\partial \omega_{\text{sec}}}{\partial z} \right) \quad (37)$$

which follows from equation (29). The resulting value of the gradient is obtained by addition. The final pair of simultaneous equations for θ and \bar{H} , the Head entrainment form factor, are

$$\begin{aligned} & (1 - R_0 \bar{H}) \left(\frac{d\theta}{dx} \right) - R_0 \theta \left(\frac{d\bar{H}}{dx} \right) \\ &= \frac{C_f}{2} + [R_0 \bar{H} - (2 + H)] \left(\frac{\theta}{U_1} \right) \left(\frac{dU_1}{dx} \right) - \theta \left(\frac{\partial \beta}{\partial z} \right)_b \end{aligned} \quad (38)$$

$$\bar{H} \left(\frac{d\theta}{dx} \right) + \theta \left(\frac{d\bar{H}}{dx} \right) = F(\bar{H}) - \bar{H}\theta$$

$$\left[\frac{1}{U_1} \left(\frac{dU_1}{dx} \right) + 2 \left(\frac{\partial \beta}{\partial z} \right)_b \right] \quad (39)$$

where $F(\bar{H})$ is the empirical entrainment function, and R_0 is the rotation number, $2\Omega\delta/U_1$. These two equations have been solved numerically by Ekerol [7], and the solutions are presented in Figs. 10, 11.

Comparison with Experiment. Before obtaining the full solution of equations (38) and (39), it is valuable to compare the two-dimensional solutions of these with the predictions of the Patankar-Spalding (P-S) equations, modified for rotation, and discussed in Section 1. Thus putting the last term in each of equations (38) and (39) equal to zero, the two sets of equations may be applied to the same data. The result, in terms of v^* , is shown in Fig. 9 from which it is evident that the P-S method gives rather better results in the initial growth region. The influence of rotation (without mixing length modification) is similar for each prediction and is

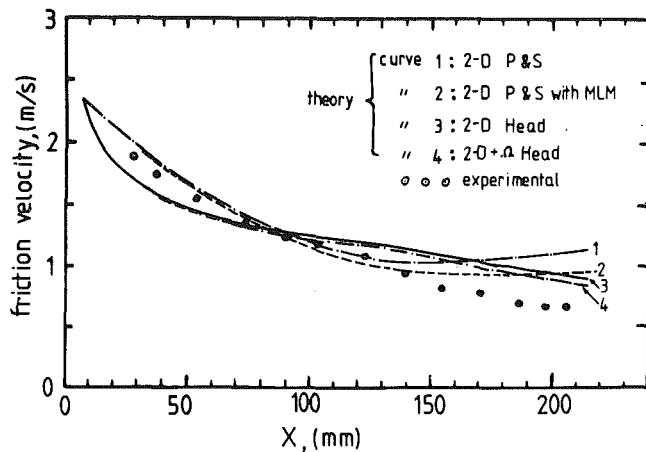


Fig. 10 Comparison of two-dimensional head method with P & S calculations with and without MLM

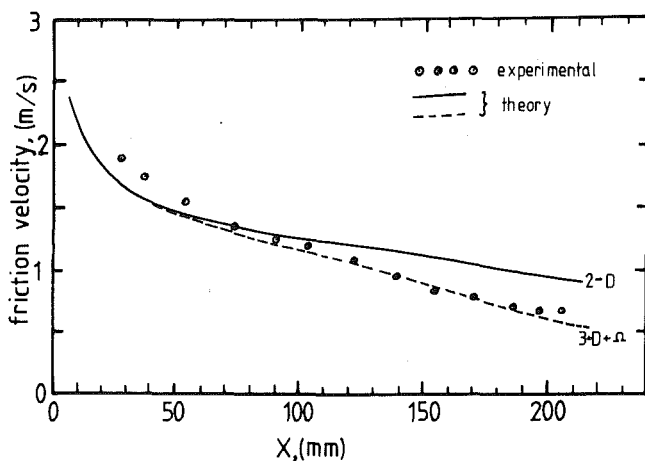


Fig. 11 Comparison of present three-dimensional theory with experiment

rather small; it has not been plotted in the P-S case. It is reasonable, therefore, to argue that the effect of mixing length modification, MLM, (were it possible to introduce it into the Head method) would be as plotted in Fig. 5. Assuming the same reduction of v^* due to MLM is allowed to the results from the Head method, it is possible to make an overall comparison of the combined influence of three-dimensionality as well as of MLM. The result is shown in Fig. 10 from which it may be concluded that the combined effect causes too large a reduction in the effective v^* . Without MLM, the three-dimensional correction applied to the modified Head method accounts satisfactorily for the observed trend. All the prediction methods were started from the same initial condition located about $3\frac{1}{2}$ percent aft of the blade leading edge. The initial velocity profile for the Patankar-Spalding solution along with the boundary layer thickness was chosen to match the experimental slightly extrapolated value of skin friction at this point. Up to this point, from the forward stagnation position a laminar layer was assumed. The calculations using the momentum-integral-entrainment equations (38) and (39) were initiated using the same skin-friction and a form-factor of 1.4, the momentum thickness being consistent with equation (18). The relatively poor performance of the latter in the earlier part of the blade surface must be put down to the limitations of the entrainment method as used.

The experimental values of V^* referred to above were all obtained by the hot-film method which has been described by

X , mm	94.5	112.8	126.5
V^* (m/s) hot film	1.235	1.174	1.036
$L&T$	1.323	1.256	1.116
Clauser		1.250	
θ , mm, traverse	0.64	0.73	1.28
theory	0.61	0.79	0.98
H , traverse	1.86	1.72	1.68
theory	1.83	1.81	1.80

Sharma [1]. However, in a number of cases it was possible to compare these measurements with the results of "log-law" plotting obtained from the hot-wire traverses obtained by Ekerol [7] and also by the use of the Ludwig-Tillman equation.

Results were obtained at three chordwise stations along the suction (or "trailing") face and given in Table 1 below corresponding to 600 rpm of the rotor. " $L+T$ " refers to the Ludwig-Tillman equation (19), while "Clauser" refers to the log-law plotting of velocity, u , versus $\log y$ to give the slope, V^* , using 0.4 for the von Karman constant. At all other locations, values of V^* were obtained by the hot-film method. Values of momentum thickness, for use in equation (18) were obtained also from the hot-wire traverse of the boundary layer and these are shown in Table 1 along with the theoretical predictions of θ . Also shown are the experimental and predicted values of shape factor, H , but the degree of variation shown does not afford a critical test amongst the various theoretical predictions of these quantities.

In assuming the velocity profiles it is necessary to allow for the fact that the free-stream velocity is not a unique quantity since the potential flow outside the boundary layer has an apparent vorticity (-2Ω) viewed from the relative frame. Approximately, we may write, for the suction side

$$W(y) = W_0 - 2\Omega y$$

where W_0 would be the wall velocity with a zero thickness boundary layer and y is distance from the wall. The actual boundary layer profiles were all corrected using this equation.

Conclusions

A method for the prediction of blade boundary layer growth in the presence of slight three-dimensionality and of rotation and/or blade curvature has been presented. With allowance for the former and with zero curvature and with rotation numbers in the range 0.03 to 0.1, good agreement with measured surface skin friction is obtained provided mixing length modification is ignored. When the latter influence is also included, the theory tends to overestimate the amount of reduction of skin friction, the predicted value being as low as 60 percent of the observed value near the trailing edge.

Acknowledgments

The Authors are indebted to the University of Birmingham for the provision of facilities and Science and Engineering Research Council for support.

References

- 1 Sharma, O. P., "Coriolis and Curvature Effects in the Boundary Layers of Centrifugal Impellers," Ph.D. thesis, University of Birmingham, 1975.
- 2 Johnston, J. P., and Eide, S. A., "Turbulent Boundary Layers on Centrifugal Compressor Blades: Prediction of the Effects of Surface Curvature and Rotation," ASME *Journal of Fluids Engineering*, Vol. 98, Series I, 1976, pp. 374-381.
- 3 Moore, J., "A Wake and an Eddy in a Rotating, Radial Flow Passage, Part 1: Experimental Investigation; Part 2: Flow Model," ASME *JOURNAL OF ENGINEERING FOR POWER*, Vol. 95, No. 3, Jul. 1975, pp. 205-337.
- 4 Koyama, H., et al., "Stabilizing and Destabilising Effects of Coriolis

Force on Two-Dimensional Laminar and Turbulent Boundary Layers," ASME JOURNAL OF ENGINEERING FOR POWER, Vol. 101, Jan. 1979, pp. 23-31.

5 Singh, G., "Boundary Layer Investigations in a Rotating Radial Flow Cascade," Ph.D thesis, University of Birmingham, 1970.

6 Sharma, O. P., and Raily, J. W., "Coriolis and Curvature Effects on the Skin-Friction in Two-Dimensional Transitional Boundary Layers," *Euromech*, Vol. 72, University of Salford, Mar. 1976.

7 Ekerol, H., "Effect of End-Wall Boundary Layers on the Flow in a Two-Dimensional Radial Impeller," Ph.D thesis, University of Birmingham, 1978.

8 Ekerol, H., and Raily, J. W., "The Three-Dimensional Boundary Layer on a Rotating Flat Plate as Influenced by the Containing End-Walls," *International Journal of Heat and Fluid Flow*, Vol. 2, No. 1, pp. 35-40.

9 Majumdar, A. K., and Spalding, D. B., "A Numerical Investigation of Three-Dimensional Flows in a Rotating Duct by a Partially Parabolic Procedure," Aero. Res. Council, ARC 37189.

10 Cumpsty, N. A., and Head, M. R., "The Calculation of Three-Dimensional Turbulent Boundary Layers, Part 1: Flow over the Rear of an Infinite Swept Wing," *Aero. Quart.*, Vol. 18, 1967.

11 Sharma, O. P., and Raily, J. W., "Coriolis, Curvature and End Wall Effects on the Blade Boundary Layer in a Two-Dimensional Radial Impeller," Research Report 158, University of Birmingham, (presented at the Israel Conference of Mechanical Engineering, Haifa, 1977).

12 Smith, A. G., "On the Generation of the Streamwise Component of Vorticity for Flows in Rotating Passages," *Aero. Quart.* Vol. 7 and 8, pp. 374.

13 Johnson, M. W., "Secondary Flow in Rotating Bends," ASME JOURNAL OF ENGINEERING FOR POWER, Vol. 100, No. 3, Oct. 1978, pp. 553-560.

14 Horlock, J. H., "Cross Flows in Bounded Three-Dimensional Turbulent Boundary Layers," *J. Mech. Eng. Sci.*, Vol. 15, pp. 274-284.

15 Pierce, F. J., "The Turbulent Flow at the Plane-of-Symmetry of a Collateral Three-Dimensional Boundary Layer," ASME, *Journal of Basic Engineering*, Vol. 86, pp. 227-233.

16 Head, M. R., "Entrainment in the Turbulent Boundary Layer," *Aero. Res. Council. Arc.*, R & M 3152.

17 Dunham, J., "The Effect of Axial Velocity Ratio on Turbomachine Blade Boundary Layers," *Nat. Gas. Turb. Est., Aero. Res. Council. ARC* 33229.

J. P. Arnold

W. McGovern

U.S. Army Mobility Equipment Research
and Development Command,
Fort Belvoir, Va.

A. D. Russell

J. C. Napier

Solar Turbines Incorporated,
San Diego, Calif.

Manufacturing Methods for Erosion-Resistant Ceramic Nozzles for Small Gas Turbines

Ceramic vanes significantly improve erosion resistance of small gas turbines. Methods of economically manufacturing ceramic vanes and associated metal shrouds were developed. Nozzle performance was verified for corrosion, thermal shock, and erosion. Detailed cost studies have shown a ceramic vane nozzle can be built for 150 percent of the cost of a metal vane nozzle. Production tooling has been ordered and engine qualification is planned.

Introduction

Recent emphasis on the development of silicon based ceramics for use in the severe environment of gas turbine engines has provided the incentive to consider ceramic materials for engines used in military application to obtain the benefit of improved erosion and corrosion resistance. The Gemini engine shown in Fig. 1 has been developed as a simple cycle radial gas turbine engine to provide 10 kW continuous electrical power for various military needs. The engine has been designed for long life (6000 hrs minimum before overhaul) with low maintenance requirements. Its multipurpose uses may frequently include operation in dusty or corrosive environments on a variety of fuels which can be detrimental to performance, increase maintenance, and shorten life of the engine. Research and development has been initiated to consider the optimum use of ceramic materials throughout the engine to increase power output, improve thermal efficiency, extend life, and decrease dependence on strategic metals.

Promising near term uses of ceramic materials appear to exist in engine applications for wear and corrosion resistance where thermal and mechanical stresses are moderate in comparison to ultimate usage objectives for these materials. Near-term cost premiums for ceramic components may be offset by decreases in life cycle costs if significant improvements can be realized in reliability, life, and maintenance. Use of ceramic materials in a conservatively loaded mode will contribute to the technology of materials fabrication, quality control, and engineering design so that more advanced highly loaded applications may be realized in the future. This paper deals with the rationale for selecting the turbine nozzle as the component for the initial utilization of ceramic materials and the research, design, and testing to achieve operational success.

Background

Experience in field operation has shown that nozzle vanes in the Gemini radial turbine engine are the most vulnerable

portion of the engine to degradation in extended service. Nozzle vane deterioration, particularly in the form of erosion, can severely reduce performance, as shown in Fig 2. There appear to be two principal sources of this degradation. The first results from the ingestion of dust particles when high loading conditions do not allow practical removal of all particles with filters or other air cleaning devices at the engine compressor inlet. (Figure 3 shows severe nozzle section erosion in a radial turbine similar to the Gemini after only 68 hrs operation in a highly laden dust environment.) The second source of degradation relates to the uniquely small size of the engine and multifuel capability. The use of heavy fuels (e.g., Diesel #2) over long periods of operation can result in carbon particle buildup in the small scale Gemini combustor. These carbon particles eventually break off and can result in highly erosive conditions downstream at the nozzle. In affected engines, teardown experience has shown nozzle vane trailing edges to suffer damage in the form of erosion and/or sulfidation (due to high sulfur in Diesel #2) before other hot components of the engine, including the turbine wheel. (This is due to particle trajectory mechanics in a radial turbine to be discussed later.)

Operation of the 10 kW with heavy fuels in a hot dusty, desert environment is not uncommon and, as a result of the above factors, imposes severe requirements on vane materials.

Certain ceramics offer properties which meet all of the above needs for a vane material, i.e., high erosion resistance, stable to corrosive/sulfidizing environments and temperature capability well in excess of requirements cited here. Ceramics show the promise of meeting the material needs of this application which includes a specified engine TBO interval of 6000 to 10,000 hrs regardless of severity of operating environment or fuels to be used during this period. Additional incentive for use of ceramic materials in this turbine, or any turbine, is the noncriticality of ceramic material supply which has become an increasingly important problem recently for superalloys, especially those containing cobalt.

All of the benefits given here for ceramics translate into incentives for ceramics application because of improved total life cycle costs, which include costs of maintenance, component replacement, fuel, fuel logistics, and secondary costs of unscheduled shutdowns.

Contributed by the Gas Turbine Division of THE AMERICAN SOCIETY OF MECHANICAL ENGINEERS and presented at the 27th International Gas Turbine Conference and Exhibit, London, England, April 18-22, 1982. Manuscript received at ASME Headquarters December 14, 1981. Paper No. 82-GT-160.

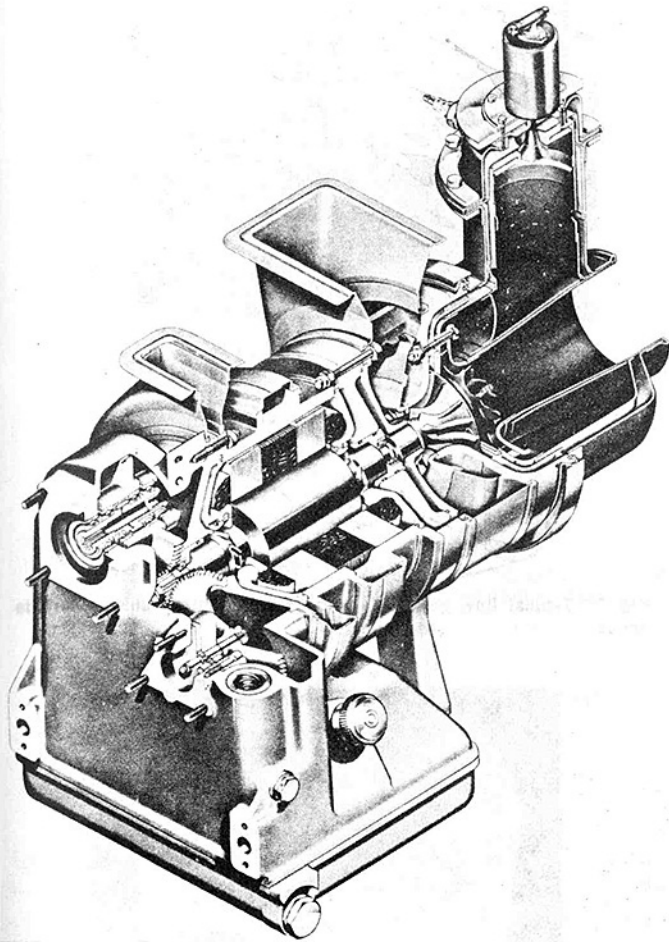


Fig. 1 Gemini radial turbine

Technical feasibility of replacing metal nozzle vanes with ceramics to improve erosion resistance was demonstrated in research and development programs at Solar Turbines International (now Solar Turbines Incorporated) under U.S. Army sponsorship [1]. This work involved replacement of the trailing edges of the nozzle vanes with ceramic inserts trapped loosely in recesses as shown in Fig. 4. Figure 5 is a nozzle aft shroud with vanes in place.

With the success of this effort, the Army is now involved in a program to demonstrate a cost-effective method of manufacturing ceramic vane nozzles, as well as further demonstrating reliability and improved engine lifetimes.

Initially in this program, erosion testing was done on various ceramic materials to determine the most effective ceramics for this application. As a result of those tests, shown in Fig. 6, the candidate materials were selected. Four materials—hot pressed silicon nitride, sintered silicon nitride, siliconized silicon carbide, and alpha-sintered silicon carbide were selected. Four different vendors provided vanes and test bars using different manufacturing methods and to provide cost estimates for quantity production of the vanes.

Manufacturers provided vanes made by the following processes:

Vendor A—Hot Pressed Silicon Nitride. These vanes are made by hot pressing a billet of silicon nitride to a partial net shape, cutting bars with vane shape from the billet, grinding, and slicing individual vanes out of the bars. Edge and corner radii were created by a tumbling process.

Vendor B—Sintered Silicon Nitride. These vanes were made by injection molding, and then firing the “green” vanes to sinter the material.

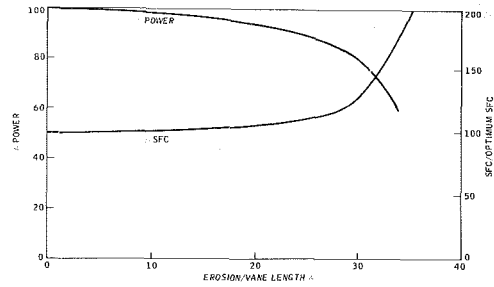


Fig. 2 Relative performance loss with nozzle vane erosion in a small radial gas turbine (references [1] and [2])

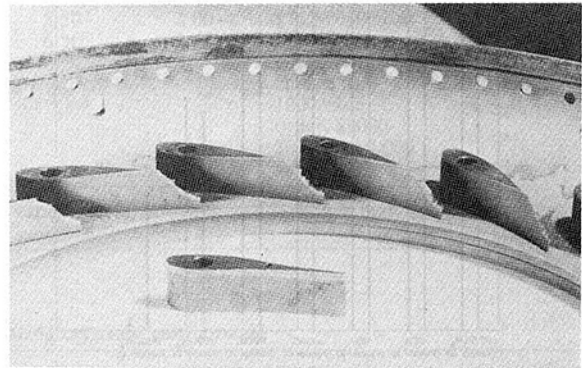


Fig. 3 Typical turbine nozzle vanes after 68 hrs of Vietnam dust erosion

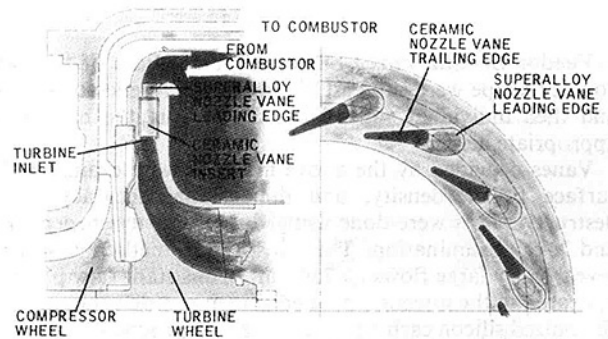


Fig. 4 Ceramic nozzle vane in 10-kW turboalternator

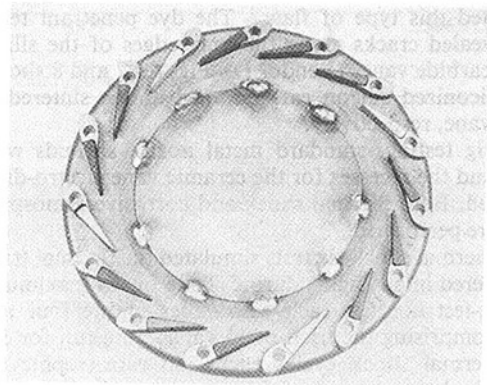


Fig. 5 Nozzle aft shroud with ceramic vane inserts (modified for rig tests)

Vendor C—Alpha-Sintered Silicon Carbide. These vanes were originally to be made by individually cold pressing vanes, then firing. This method did not work (vanes were successfully pressed, but cracked upon firing), so they were individually slip cast instead, then fired.

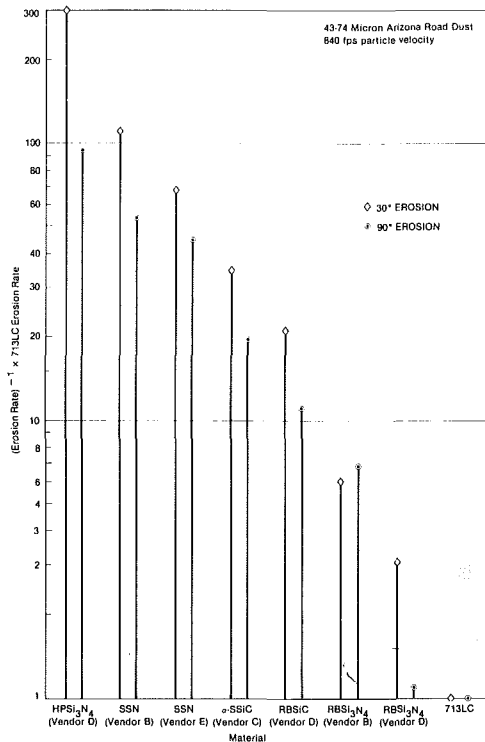


Fig. 6 Erosion advantages of ceramics over 713 LC superalloy (volumetric)

Vendor D—Siliconized Silicon Carbide. Bars of the vane contour shape were slip cast, fired in the presence of silicon, and then individual vanes were sliced from the bar to the appropriate height.

Vaness provided by the above methods were examined for surface finish, density, and dimensional accuracy. Non-destructive tests were done using fluorescent dye penetration and X-ray examination. These inspection methods can only reveal fairly large flaws (>250 μm). Consistent flaw patterns appeared in the injection molded silicon nitride vanes and the siliconized silicon carbide vanes. The first production batch of injection molded sintered silicon nitride vanes showed frequent large internal voids with radiography and gate flaws with dye penetrant. A second production batch reduced or eliminated this type of flaw.¹ The dye penetrant technique also revealed cracks along the long edges of the siliconized silicon carbide vanes (Vendor D). Figures 7 and 8 show flaws in a siliconized silicon carbide vane and a sintered silicon nitride vane, respectively.

For rig testing, standard metal nozzle shrouds were obtained and the recesses for the ceramic vane electro-discharge machined. Both thermal shock and corrosive atmosphere rig tests were performed.

The thermal shock rig tests simulated the thermal transients encountered in an engine during flame-out at maximum TIT. Two rig-test nozzles, each with vanes of the four material types, comprising the total of 15 vanes were run for 500 and 1000 thermal shock cycles each. No catastrophic failures occurred, although some of the ceramic vanes with preexisting flaws found by NDE lost some surface material.

A 100 hr corrosive atmosphere rig test was performed with 30 ppm sea salt solution injected upstream to one of the nozzles. This concentration was selected in an attempt to "accelerate" the test but proved to be too high, causing molten salt buildup on vane surfaces and choking of the

¹The sintered silicon nitride material produced in 1978 has been superseded by an improved molded and sintered silicon nitride.

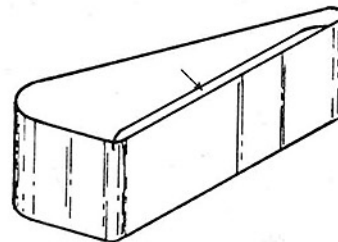
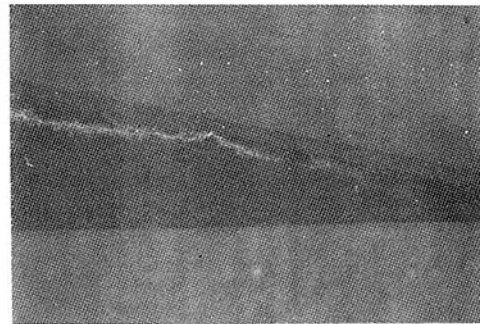


Fig. 7 Typical flaw pattern in slip cast siliconized silicon carbide vanes



Fig. 8 Processing defects in batch #1 injection molded sintered Si₃N₄ vane (magnification, 14 ×)

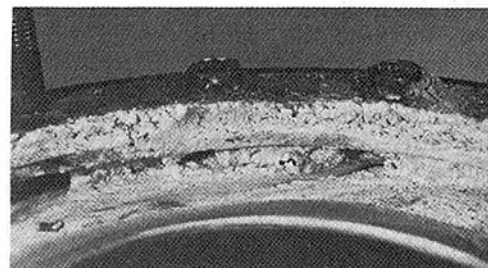


Fig. 9 Corrosion test nozzle showing areas of heavy salt product build-up

nozzle throat as shown in Fig. 9. Vanes under the coating were subjected to an unrealistic reducing atmosphere and some of the silicon carbide vanes from both vendor C and Vendor D

Table 1 Ceramic vane estimated production costs (1981 dollars—100 percent yield assumed and inspection cost not included)

Vendor	Material	Process	Cost Estimate		Nonamortized Costs
			1000 Vanes	10,000 Vanes	
A	HPSi ₃ N ₄	Press to near net shape, slice & grind	13.36	13.36	Tooling costs amortized in quote
B	Sintered Si ₃ N ₄	Injection mold then fire	28.80	23.00	\$13,355 tooling cost
C	Sintered SiC	Slip cast, then fire	9.76/ 12.78*	8.36/ 10.86*	Tooling costs amortized in quote
D	Siliconized SiC	Slip cast bar, fire and slice	5.50– 6.50	2.00– 2.40	\$750-1000 non-recurring engineering charge for 1000 vane order. \$2000-3000 for 10,000 vane order.

*Difference is for different vane designs. Lower cost is for vanes with larger trailing edge radius; higher is quote for vanes with the smaller trailing edge radius.

Table 2 Cost summary for fabricating ceramic vane nozzle

Current (1980) invoice cost of MAR-M421 castings	\$293				
Current estimated dollar cost of machining, plating, assembly, brazing, and final machining standard nozzle (quantities > 50 nozzles)	\$350				
Subtotal	\$643				
Additional manhour cost added to assembly process (\$25/Hour)	\$ 25				
	1	2	3	4	5
Manufacturing method for ceramic vane recesses	Original limited quantity	Multiple copper tungsten EDM bars no rear shroud change	Same as 2 but modified bear shroud	Multiple punch throw away copper electrodes no rear shroud casting changes	Same as 4 but modify rear shroud
Man-hour cost for manufacturing recesses (\$25/Hour)	\$ 408	\$113	\$108	\$ 91.5	\$ 85.5
Cost of ceramic vanes	HPSi ₃ N ₄ \$120 × 15	HPSi ₃ N ₄ (Vendor A) \$13.40 × 15 = \$201			
Total estimated cost of ceramic vane nozzle	\$2,876	\$982	\$977	\$961	\$965
	Project Goal 150% × 643 = \$964				

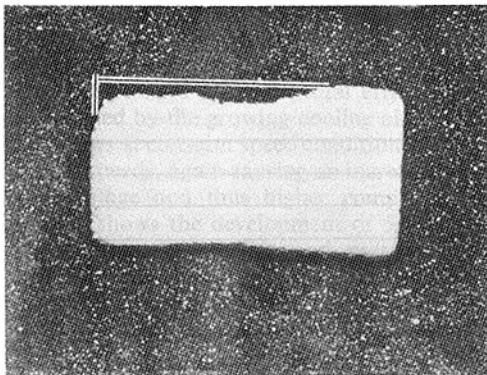


Fig. 10 Siliconized SiC vane cross section after hot corrosion nozzle rig test (original vane shape indicated by white line): magnification, 10 ×

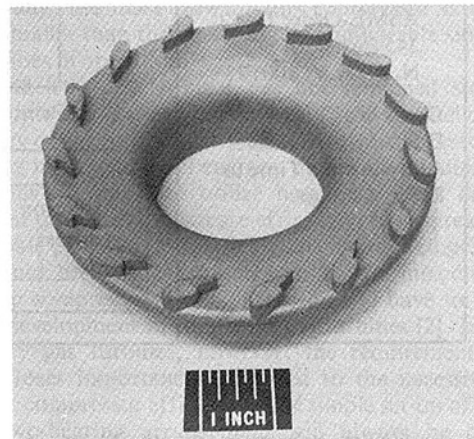


Fig. 11 New rear shroud casting (RSK 230861)

showed corrosive attack, such as shown in Fig. 10 and discussed in references [2] and [3].

Cost estimates for quantity production of vanes as provided by vendors is shown in Table 1 and generally were very encouraging. All were near or below cost goals for the program.

Redesign of the existing all metal nozzle is necessary to minimize additional machining steps to provide recesses for the ceramic vanes. Changes in the casting to eliminate metal trailing edges and use of special tooling to 'gang' EDM recesses provided the cost estimates shown in Table 2. Note that these cost estimates are close to or under the goal of a ceramic vane nozzle no more than 50 percent more expensive than a standard nozzle.

Work is currently in progress to provide the ceramic vanes, tooling, and production experience necessary to further prove cost and performance goals.

Two vendors (A and D) from the first efforts were selected to produce tooling suitable for mass production of vanes as well as produce vanes utilizing this tooling. Three lots of vanes and test bars have been procured from each vendor for lot-to-lot comparisons and for future rig and engine testing.

Redesigned nozzle castings (Fig. 11) and tooling have been procured, and an initial production run of six nozzles is on hand. EDM tooling for machining of the nozzles has been acquired (Fig. 12) and manufacturer of ceramic vane nozzles is underway. Cost estimates for vanes, nozzle castings, and nozzle machining work now in progress will provide firm data for the future quantity nozzle production costs.

Engine tests to qualify the nozzle and to provide information suitable for a production quality assurance program are planned for the future.

Conclusions

Cost reductions for ceramics in gas turbine applications are

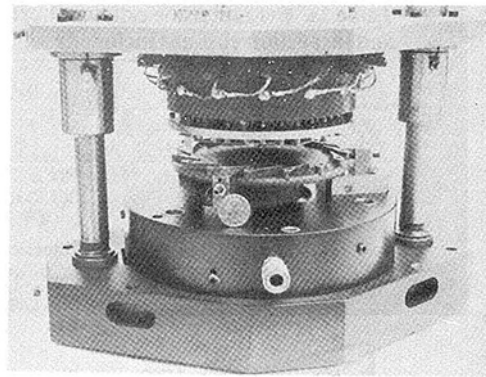


Fig. 12 EDM tooling for gang machining of vane recesses

necessary if the advantage of these materials are to be realized. Program estimates have shown that costs of ceramic components could be successfully reduced to very competitive levels. Work is now in progress to provide for the economic manufacture of the erosion resistant nozzle and to prove its performance in rig and engine tests. Estimates to date have shown that costs of the ceramic components of this nozzle meet program goals.

References

- 1 Napier, J. C., Metcalfe, A. G., and Duffy, T. E., "Application of Ceramic Nozzles to 10kW Engine," Final Report, Solar Contract No. DAAK02-75-C-0138, Dec. 1978.
- 2 Tressler, R. E., Meiser, M. D., and Yonushonia, T., "Molten Salt Corrosion of SiC and Si₃N₄ Ceramics," *Journal of the American Ceramic Society*, Vol. 59, 1976, pp. 278.
- 3 McKee, D. W., and Chatlerji, D., "Corrosion of Silicon Carbide in Gases and Alkaline Melts," *Journal of the American Ceramic Society*, Vol. 59, 1976, pp. 44.

Transonic Compressor Development for Large Industrial Gas Turbines

B. Becker

Subdivision Manager,
Gas Turbine Technology.

M. Kwasniewski

Project Engineer,
Gas Turbine Technology.

O. von Schwerdtner

Department Manager,
Flow Laboratory.

Kraftwerk Union AG,
Mülheim a. d. Ruhr,
West Germany

With increasing mass flow and constant rotational speed of the single shaft gas turbine, the diameters and tip speeds of compressor and turbine blading have to be enlarged. A significant further increase in mass flow can be achieved with transonic compressor stages, as they have been in service in aero gas turbines for many years. For industrial applications, weight and stage pressure ratio are not nearly as important as efficiency. Therefore, different design criteria had to be applied, which led to a moderate front stage pressure ratio of 1.5 with a rotor tip inlet Mach number of 1.37 and a high solidity blading. In order to simulate the first three stages of a 200-MW gas turbine, a test compressor scaled by 1:5.4 was built and tested. These measurements confirmed the aerodynamic performance in the design point very well. The compressor map showed a satisfactory part speed behavior. These results prove that the single-shaft industrial gas turbine still has a high development potential with respect to power increase. Additionally, with the higher pressure ratio, the cycle efficiency will be improved considerably.

Introduction

The gas turbine rating is to be considered directly proportional to the air mass flow taken in. The overall cost for more powerful gas turbines having the same speed increases as well, though at a smaller factor. In the plant there are generally several components, the costs of which change in a nearly proportional ways to the air amount (e.g., sound absorbers), while the costs for other parts to do not vary considerably (e.g., instruments and control). Thus, a mass flow increase naturally causes a reduction of the specific capital expense (expense per kw). The staff expenditure with respect to maintenance and operation activities is lower than in the case of two units of half the rating. Accordingly, as long as the rating of the individual gas turbine is small compared to the output of the power supply system as a whole, the higher rated unit constitutes the more economic solution. This has resulted in a continuous increase in the mass flow by all manufacturers.

The basis for high efficiency of gas turbines is a high pressure ratio. In the case of otherwise equivalent thermodynamic data, increasing turbine inlet temperatures generally have a positive effect on total efficiency, but this effect is extenuated by the growing cooling air requirements. Higher mass flows at constant speed conditions require higher circumferential speeds, again causing an increased conversion of energy per stage and thus higher compressor pressure ratios. Figure 1 shows the development of 50-Hz KWU gas turbine compressors. Mass flow and pressure ratio have grown regularly in the past. A report of the last development step, which resulted in nearly 500 kg/s mass flow and a

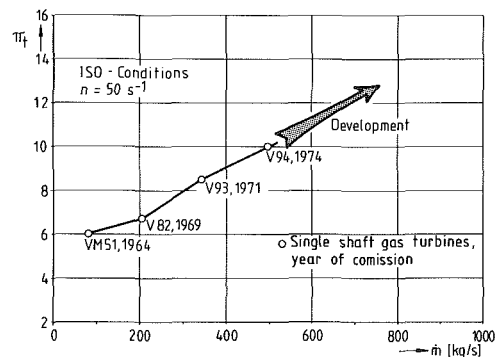


Fig. 1 Compressor development at KWU

pressure ratio of 10, was given at the 1978 ASME meeting [1]. Even today, the mass flow of this compressor is about 15 percent higher than the maximum of comparable single-shaft gas turbines in operation.

Nevertheless, development has not remained stationary. Especially with regard to continuously growing fuel costs, the efficiency of gas turbines, and thus the relevant pressure ratio, is gaining importance. Jet engines, having no possibilities due to reasons of weight to utilize heat exchangers and other combined processes to increase efficiency, have already made remarkable progress in this field. The average stage pressure ratio could be drastically increased by the introduction of transonic compressor stages. This way will have to be taken for the development of industrial gas turbines [2]. In case of stationary gas turbines, however, the requirement of low weights loses importance compared to the necessity of an adequate compressor efficiency. The simple set-up of a single-shaft, two-bearing arrangement will always be preferred under rough power plant operating conditions to a more

Contributed by the Gas Turbine Division of THE AMERICAN SOCIETY OF MECHANICAL ENGINEERS and presented at the 27th International Gas Turbine Conference and Exhibit, London, England, April 18-22, 1982. Manuscript received at ASME Headquarters, December 15, 1981. Paper No. 82-GT-219.

complicated multishaft arrangement with a number of bearings. Thus, due to these different boundary conditions, the solutions developed for jet engines cannot be applied to industrial gas turbines without certain modifications.

Principal Considerations Regarding the Front Compressor Stage Design

All the values stated in the following are given with reference to the ambient conditions (15 °C; 1.013 bar; no inlet pressure losses) specified in standard ISO 2314. Thus, total temperature and pressure extant before the compressor are defined. Furthermore, if the mass flow standardized in such a way is referenced to the circular cross section, A_o , defined by the maximum outer rotor diameter, compressors of different designs may be compared to each other (Fig. 2). The theoretical maximum mass flow per unit area would be achieved if the uniform axial flow velocity equaled the sound velocity ($Ma = 1$) and if there would be no hub ($\nu = 0$). With jet engines, the front faces of which must be as small as possible due to minimized external drag, about 80 percent of this maximum value can be reached. The industrial gas turbines developed up to now have considerably lower specific flows, as the design point entered for the V-94 unit shows. For the following reasons the new design objective is also below the range of typical jet engines:

1 The flight Mach numbers of today's big airplanes are at least as high as the axial inflow Mach number to the compressor. Therefore, the kinematic energy of the air is already present. With stationary gas turbines, however, the air must be accelerated in the inflow section first. This leads to an initial decrease in static pressure which has to be built up again in the compressor blading later. As these proceedings are accompanied by losses, lower velocities are used, especially as larger front faces do not have any great disadvantage.

2 The journal bearings of the relatively heavy industrial gas turbine rotors need quite a lot of space in the compressor hub as they must be supported rigidly and the bearing should be accessible without opening the outer casings. The shaft diameter in the bearing is determined by the allowable surface pressure in the oil film. This shaft diameter suffices for the required power transfer, thus preventing any additional disadvantages due to the request for a generator drive at the cold end. Figure 3 shows the design selected for the V-94 type, which will be utilized in a similar way with the even larger and thus heavier transonic compressor unit. Therefore, the hub-to-tip ratio cannot be further minimized.

The compressors of industrial gas turbines are usually provided with an inlet guide vane while jet engines often do not have one. This is due to the fact that in case of current flow rates and circumferential velocities of stationary units the Mach numbers could be kept subsonic by the proper use of an inlet guide vane. Accordingly, losses caused by compression shocks and shock-boundary layer-interaction could be avoided. The dotted arrows of Fig. 4 exhibit the relevant Mach number triangles of the front stage tip section of the V-94. Considerable Mach number increases cannot be prevented in the case of a mass flow raise to 770 kg/s because of the increasing circumferential velocity. A part from that, they are necessary to improve the stage pressure ratio. Therefore, one has to investigate primarily whether an inlet guide vane will still lead to efficiency improvements in this case. Obviously, the inlet Mach number of the rotor blades increases distinctively, and there will be higher shock losses without an inlet guide vane (compare Fig. 4 left and right). This disadvantage, however, is balanced by quite a number of positive factors in the case of no inlet guide vane:

- The losses of one blade row are eliminated.
- The absolute rotor inlet velocity is smaller at the same

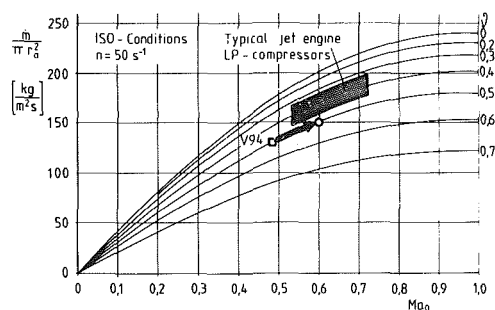


Fig. 2 Specific mass flow of compressor

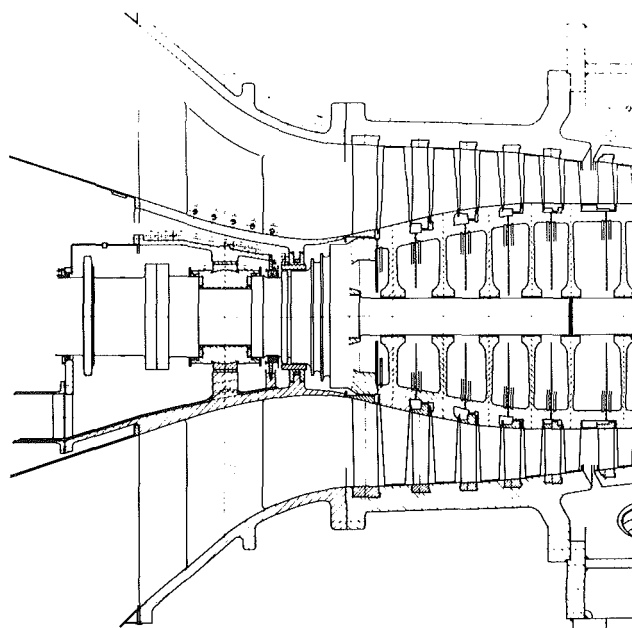


Fig. 3 Inlet cross section V-94

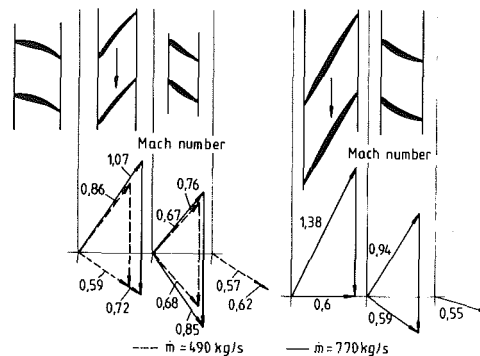


Fig. 4 Mach number triangles

axial velocity. Thus, the aforementioned losses by succeeding expansion and compression are minimized.

- With equal energy input, the turning in of the rotor blading is smaller, thus reducing the danger of separation due to cross-section enlargements downstream of the strong shock.

- The stator blades must absorb the stresses provoked by the gas bending moment. Therefore they are decisively thicker than the rotor blades optimized for transonic flows. Thus, it is advantageous to keep the stator inlet Mach number within the subcritical range, an objective which cannot be reached in the solution on the left.

- In order to gain favorable reaction numbers close to 0.55 and a fast reduction of the peak Mach numbers in the

following stages, the stator exit velocity vector won't be turned back to axial direction. Accordingly, there will be a smaller turning angle for the stator blading, with less deceleration, lower bending stresses, thinner profiles, and thus smaller losses.

When evaluating these effects, taking both types with equivalent mass flow and stage pressure ratio into consideration, the result showed definite advantages for the blading without inlet guide vane.

In the hub region, the circumferential velocity is considerably smaller and transonic Mach numbers can be avoided. Even with compressors having an inlet guide vane, the deviation from the axial flow direction is small here. Due to the lower circumferential velocity, however, it is difficult to apply as much energy as at the tip section.

$$\Delta h_t = u_2 c_{u2} - u_1 c_{u1}$$

As the circumferential component, c_{u1} , at rotor inlet is very small or equal to zero, energy input is essentially dependent on the conditions at rotor outlet. In the case of transonic rotor blading, the change in density is considerable, and, therefore, the blade height at the trailing edge is much smaller than at the leading edge. Therefore, the three passage designs shown in Fig. 5 differ distinctively.

On the left, typical flow triangles for the case of a constant inner diameter CID of the rotor are shown. Just in the center and on the right, it can be seen how these triangles and the resulting diffusion factors and the de Haller numbers vary if the mean diameter CMD or, as another extreme, the outer diameter COD remain constant. In this comparison the total enthalpy rise is constant, thus resulting in a smaller turning in the rotor blading with increasing u_2 . Obviously, an increase of the outlet diameter results in a reduction of the aerodynamic loading at the rotor hub section and of the inlet velocity of the stator c_2 . Both have a positive effect on the losses of the high turning thick rotor profiles at the hub.

Description of Transonic Profiles

The NACA-65 profiles used in subsonic blade rows are not appropriate for the rotor blading of the first and second compressor stage. In the transonic range from the critical Mach number up to about $Ma = 1.2$, DCA profiles (double circular arc) may be used expediently due to the fact that thickness and curvature are combined in such a way that the passage will not be blocked. In the outer half of the first rotor blade, the inlet Mach numbers are so high, however, that due to the considerable curvature near the leading edge of DCA-profiles, the Mach number is increased in front of the compression shock. Because of greatly increasing shock losses caused by higher Mach numbers, a straight or even slightly concave contour is more advantageous in this area. These profiles may be combined from several circular arcs (MCA).

Figure 6 shows the principle run of the MCA and DCA profile suction side curvature. The description of the profile by circular arcs has the advantage of simple geometrical parameters. However, the illustration in Fig. 6 also clearly indicates two disadvantages:

- The MCA profile exhibits a discontinuous increase in curvature, leading to a step function in the flow velocity. Such severe velocity gradients easily cause increased boundary-layer losses.
- The transition of the slightly curved MCA profile at the tip section to the strongly deflecting DCA profile near the hub contains distinctive difficulties for a geometrical description.

It was deduced from these considerations that it would be more practical to specify the second derivative of the contour instead of the profile itself. One can provide any profile shape

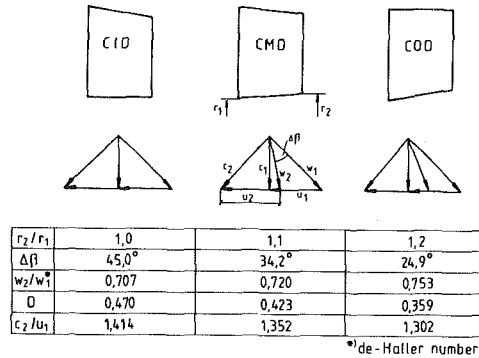


Fig. 5 Velocity triangles at different hub contours

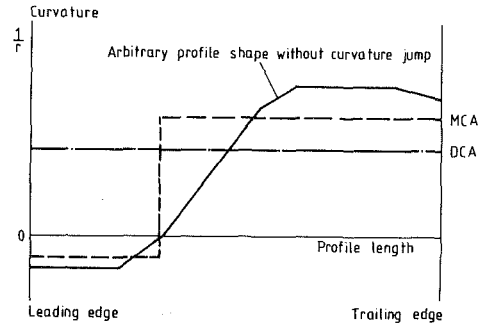


Fig. 6 Curvature of the suction side

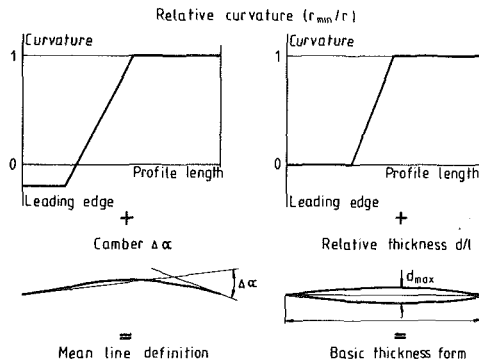


Fig. 7 Definition of transonic compressor profiles

and with this provision guarantee a step-free curvature, as the example shows. When developing this procedure, it became obvious that it would be more favourable to avoid a separate assumption of suction and pressure side contours and define the mean camber line and the basic thickness form as is the case with NACA-profiles. Figure 7 shows how a mean camber line suitable for the high transonic range may result from an assumption running from a negative to a positive curvature and a relevant camber angle.

The relative curvature distribution has to be integrated twice in order to get the mean line shape itself. The first integration of the curvature distribution results in a dimensionless value for $\Delta\alpha$. The integration constant can now be calculated according to the chosen turning angle from inlet to outlet. The second integration then gives the mean line with a prescribed profile length.

An arbitrary and rough modification of the continuous curvature distribution by the designer always results in a smooth mean line shape without altering the turning angle. Moving the curvature increase backwards or forwards results in a shift of the point of maximum camber.

A similar system is used for the thickness distribution. The

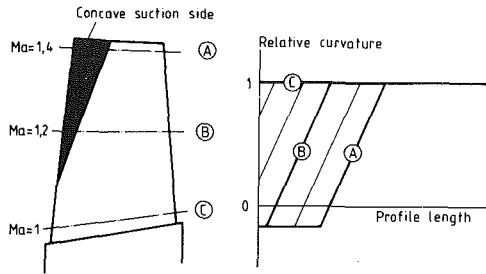


Fig. 8 Profile variation of blade height

designer normally wants to generate a profile with a given relative thickness. Therefore, the integration constant is calculated accordingly after the second integration. Zero curvature near the trailing edge results in wedge type profiles. Moving the curvature distribution shifts the point of maximum thickness to a desired position.

A systematic curvature variation, as shown in Fig. 8, will easily allow for the arrangement of various profiles at different radii. The shaded transonic portion at the profile suction side will taper off towards the hub until a pure DCA profile is finally achieved in section C. Turning angle and maximum profile thickness may be assumed arbitrarily as a function of blade height.

Two views of the rotor blade constructed in such a way can be seen in Fig. 9. It can be seen that the profiles are provided with relatively small turning angles compared to typical jet engine compressor blades. When designing, care was taken so that the cross-section increase behind the strong shock established by curvature and thickness would not lead to boundary-layer separation near the leading edge. Therefore, in order to achieve a high compressor efficiency, one abandoned the idea of bringing the pressure ratio to a maximum. The relatively long chord length compared to the blade height guarantees flutter-free operation and has a positive effect on the compressor stall line at partial speed. By selecting a curved hub contour, the cross section of the flow passage as well as the adaptation to the front and rear hub contour inclinations could be optimized.

Experimental Investigations

The four-stage compressor test rig described in [1] was rebuilt to a three-stage test compressor for these experiments. Figure 10 shows the rotor with the upper half of the stator blade carrier open. The circumferential speed is above the V-94 test compressor by 20 percent. The outer diameter is nearly the same but the rotational speed is increased, respectively. The scaling factor for the 50-Hz compressor amounts to 5.4. Due to the higher stage pressure ratios the rating of the new three-stage compressor is higher than that of the older four-stage design.

The following table gives a comparison of the main data of both compressors:

	Four-stage V-94	Three-stage transonic
Rotational speed (s^{-1})	231	271
First rotor:		
Tip speed (m/s)	341	408
Axial Mach number	0.56	0.59
Inlet radius ratio	0.52	0.51
Tip solidity	0.90	1.31
Average solidity	1.17	1.64
Aspect ratio	2.47	1.50
First stage:		
Pressure ratio	1.2	1.5

Figure 11 shows a cross section of the test rig that was

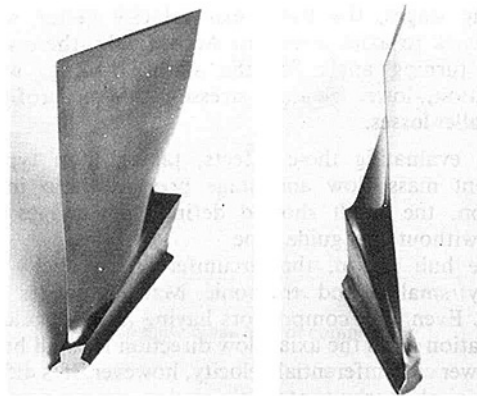


Fig. 9 Transonic compressor, first rotor blades

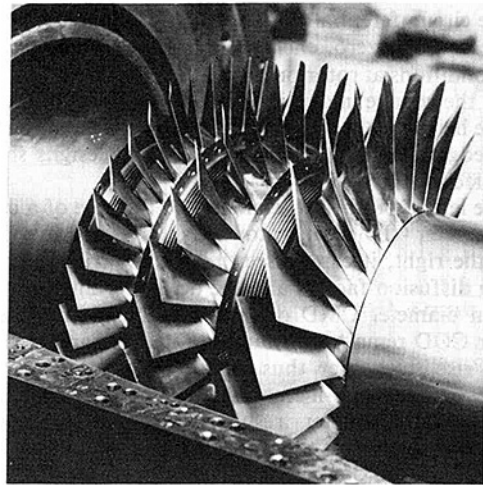


Fig. 10 Transonic compressor, rotor blading

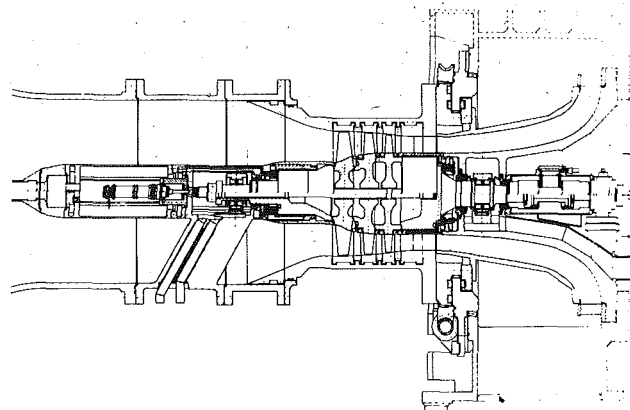


Fig. 11 Transonic compressor, cross section

operated with an axial inlet. Probe traversing installations at various axial positions allow for detailed measurements of the flow field. In order to determine blade vibrations, data from the rotating system were transferred by slip rings in the front hub section. As a new instrumentation, dynamic pressure transducers are arranged directly above the rotor blade tip in several axial positions in order to measure the position of the compression shocks. The compressor is operated with air in a closed circuit. It is quite interesting to compare the performance map of the three-stage transonic compressor (in Fig. 12) to the four-stage subsonic compressor of the V-94 (in Fig. 13). The flow rate has been given in the form of a reduced volume flow

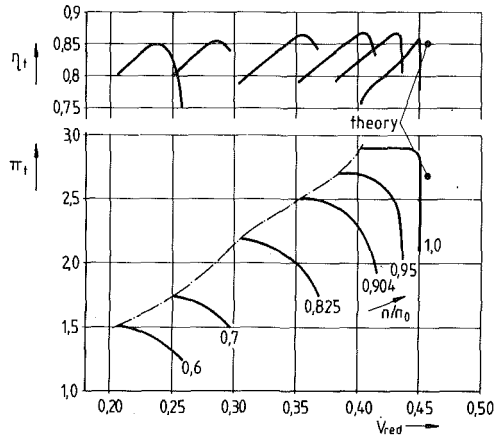


Fig. 12 Performance map of transonic compressor

$$\dot{V}_{red} = \frac{\dot{m}}{P_{t0} A_1} \sqrt{\frac{I_{t0} R}{k}}$$

This definition eliminates the influence of the inflow conditions (subscript $t0$). A_1 is the ring area at the inlet of the first rotor blade. Comparing at $n_{red} = 1$ shows that the flow rate per unit area has increased by about 6 percent at design speed. Despite the transonic flow which will usually react more sensitively to incidence angles than subsonic flow with NACA-65-profiles, the volume flow differential between choke and stall conditions has grown. This is essentially caused by the smaller pitchchord ratios. The maximum pressure ratio reached, increased from almost 2.5 to 2.9. This increase is greater than the growth of the design pressure ratio from 2.35 to 2.6, so that the stall margin of the operating line is improved. The mean stage pressure ratio has grown from 1.25 to 1.42. As expected, the efficiency at nominal speed is definitely lower due to considerable shock losses. On the other hand, the higher stage pressure ratio of the three first compressor stages alone results in a 40 percent improvement of the pressure ratio of the gas turbine at the same stage number. The increase in overall gas turbine efficiency thereby gained is remarkably higher than the losses caused by the decrease in compressor efficiency.

In order to determine the shock positions at the tip section of the first rotor blade row, measurements by dynamic pressure transducers were performed. The measuring diaphragms of 1.5 mm dia were mounted flush to the wall in the casing. Figure 14 shows two typical recorded signals. Together with a trigger signal generated by the blades the position of steep positive pressure gradients determined the locations of compression shock waves. Figure 15 shows the shock patterns at design speed and different pressure ratios. At open throttle the flow is supersonic throughout the blade channel. The bowed front shock wave is only slightly detached from the leading edge. With increasing pressure ratio a strong shock leading to subsonic velocity is moving into the blade channel from the rear. At design conditions this passage shock is still separated from the leading edge shock. Therefore, the inflowing velocity field remains unchanged, and the mass flow is constant. Near the surge line, the right part of the leading edge shock in converted to a strong normal shock wave, and the distance to the leading edge has increased. The flow field at the cascade inlet is modified by the left part of the detached leading edge shock, and the mass flow is reduced (compare Fig. 12).

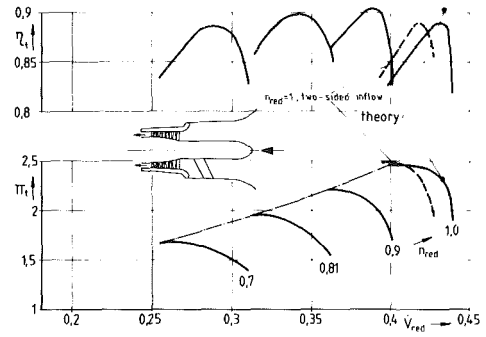


Fig. 13 Performance map V-94, axial inflow

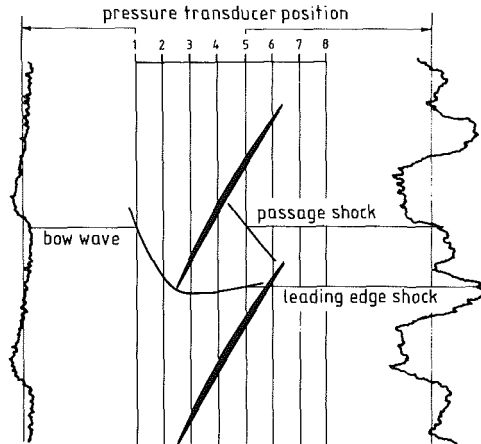


Fig. 14 Pressure transducer signals at design point

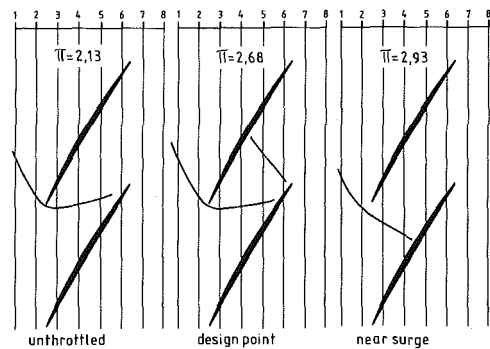


Fig. 15 Shock patterns at design speed

Strain-gage measurements in all stationary and rotating blade rows were taken in order to prove, that the dynamic stresses were well within tolerable levels and that flutter of the free standing transonic rotor blades could be avoided.

References

- 1 Becker, B., von Schwerdtner, O., Günther, J., "Investigations of an Axial Flow Compressor with Variable Reynolds Number and Inlet Casing Geometry," ASME 78-GT-185, London.
- 2 Maghon, H., "Die Entwicklung der einwilligen Gasturbine," VGB Kraftwerkstechnik 53, Heft 10, 1973, pp. 651-656.

D. A. Fraser
Lecturer,
Civil Engineering Department.

J. H. G. Howard
Professor,
Mechanical Engineering Department.

W. C. Lennox
Professor,
Civil Engineering Department.

University of Waterloo,
Waterloo, Ontario, Canada

A Three-Dimensional Turbulent Flow Analysis Method for the Rotating Channels of a Centrifugal Turbomachine

A three-dimensional turbulent flow analysis method is described based on transformations of the equations to follow an arbitrary curved passage center-line and allowing for passage area and aspect ratio variations. The numerical method is arranged to allow either parabolic or partially parabolic solution methods in the main passage direction. The method has been tested for radial turbomachine elements and comparisons are included with measured internal passage flows in a radial impeller.

Introduction

In a centrifugal impeller passage, the flow field is complex and subject to many influences. It is strongly influenced by viscous and turbulent shear forces and can be significantly three-dimensional in character. Passage curvature and Coriolis effects act both in the generation of the secondary flow field and in the modification of turbulent shear forces on the passage flow. The analysis of such a flow field has been the subject of considerable effort for some time.

Perhaps the most common form of analysis procedure presently in use employs a quasi-three-dimensional inviscid flow model. This presumes that, in the blade-to-blade plane, stream surfaces lie along surfaces of revolution. Thus, neither the three dimensionality nor the viscous nature of the flow is accounted for directly. Inviscid flow analyses for fully three-dimensional impeller flows were described by Bosman and Highton [1] and Denton and Singh [2]. A review of inviscid methods was carried out by Adler [3].

A method which introduced viscous terms was described by Dodge [4], based on separating the momentum and continuity equations into coupled elliptic and parabolic groups and iterating between equations.

One of the most promising approaches has been based on three-dimensional finite volume methods described by Patankar and Spalding [5] and Pratap and Spalding [6], where the solution in the principal flow direction was respectively parabolic and partially-parabolic. This approach retains the potential advantage of limited computer storage space and run times. A recent development of the method was reported in [7]. A powerful variation of it was developed by Moore and Moore [8] who used finely spaced grid points near the walls, together with a mixing length turbulence model.

The approach described here also owes its origin to [5] and is a generalization of the program described by Howard, Patankar and Bordyniuk [9] where flow in straight rotating

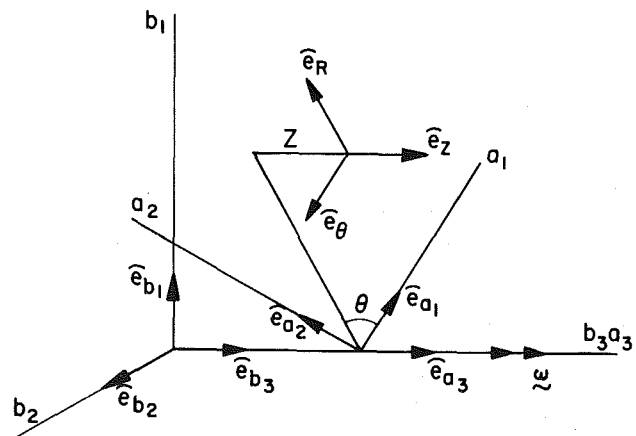


Fig. 1 Coordinate systems for a general impeller

ducts was analyzed using a two-equation turbulence model with Coriolis effects. The extension to channels with arbitrary curvature and variation of cross-sectional area is achieved by transforming the equations to a curvilinear form arranged to follow the passage centerline as a "spine." This defines the passage-wise direction in the computation, while the other two directions are defined on plane surfaces normal to the centerline. Since the passage walls will not, in general, be normal to the calculation cross-sections, further coordinate transformations have been required, thus allowing also for area and aspect ratio variations along the curved passage. One advantage in this approach lies in the maintenance of a dominant velocity direction in the computation. The numerical procedure was organized so that either parabolic or partially-parabolic solution methods could be employed in the direction along the channel.

A program using this method has been written for radial turbomachinery such as [10] where internal velocity measurements were reported. Preliminary comparisons between analysis and data are presented and discussed.

Contributed by the Gas Turbine Division of THE AMERICAN SOCIETY OF MECHANICAL ENGINEERS and presented at the 27th International Gas Turbine Conference and Exhibit, London, England, April 18-22, 1982. Manuscript received at ASME Headquarters December 15, 1981. Paper No. 82-GT-221.

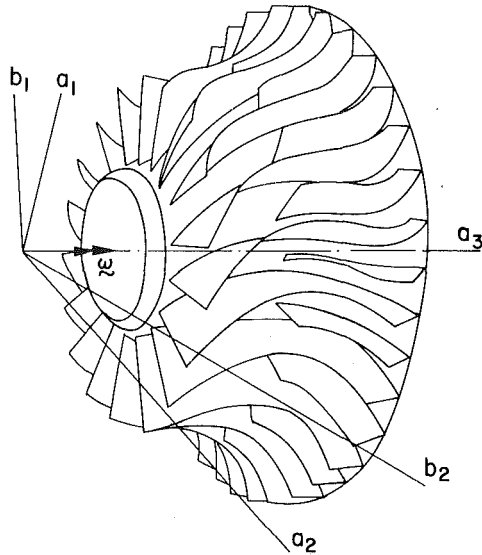


Fig. 2 A mixed flow impeller showing the a_i and b_i coordinate systems

Coordinate Systems

The necessary coordinate systems and unit vectors shown in Fig. 1 and Fig. 2 are defined below.

- b_i ($i = 1, 2, 3$) are orthogonal Cartesian coordinates fixed in inertial space.
- \hat{e}_{b_i} are unit vectors in the b_i directions.
- a_i ($i = 1, 2, 3$) are orthogonal Cartesian coordinates fixed to the impeller such that a_3 and b_3 are coincident with the impeller axis.
- \hat{e}_{a_i} are unit vectors in the a_i -directions.
- ω is the constant angular velocity of the impeller (a_i coordinate system) with respect to the inertial frame (b_i coordinate system).
- R, θ, Z are the cylindrical coordinate of a point referred to the impeller (a_i coordinate system).

Nomenclature

$\nabla = e_{a_i} \partial / \partial a_i$ = the gradient operator shown in the a_i system
 a_i = noninertial coordinate system fixed to impeller
 A_{12}, A_{13}, A_{23} = curvature-torsion parameters
 A_{xy}, A_{xz}, A_{yz} = A_{12}, A_{13}, A_{23} , respectively
 $a = \frac{1}{XY} \frac{\partial(XY)}{\partial Z}$ = normalized space rate of change of passage cross sectional area
 b_i = inertial coordinate system
 c_i = semipath coordinates
 $e_{a_i}, e_{b_i}, e_{c_i}$ = unit vectors in the a_i -, b_i -, c_i -directions, respectively
 G = time rate of production of k per unit volume of fluid
 G_B = value of G near a boundary
 G_C, C_{e1}, C_{e2}, C_C = turbulence parameters for the k and ϵ equations
 $k = \frac{\overline{v' \cdot v'}}{2}$ = the kinetic energy of turbulence per unit mass of fluid
 m = meridional plane
 $p = \bar{P} + P'$ = static pressure at a point

Fundamental Equations

The following are the fundamental equations including the $k \epsilon$ two-equation model of turbulence to be solved in the a_i frame. Reference is made to the Nomenclature for symbol definitions.

Continuity:
$$\nabla \cdot (\rho \mathbf{v}) = 0 \quad (1)$$

Momentum:
$$\nabla \cdot (\rho \mathbf{v} \mathbf{v}) = \nabla \cdot \underline{\underline{\tau}}_e + [-\nabla p - 2\rho(\omega \times \mathbf{v})] \quad (2)$$

Transport equation for the general quantity, ϕ :
$$\nabla \cdot (\rho \mathbf{v} \phi) = \nabla \cdot [\Gamma_{e,\phi} \nabla \phi] + S_\phi \quad (3)$$

Kinetic energy of turbulence:
$$\nabla \cdot (\rho \mathbf{v} k) = \nabla \cdot [\Gamma_{e,k} \nabla k] + S_k \quad (4)$$

$$S_k = G + G_c - \rho \epsilon$$

G is the rate of production of k per unit volume.

$$G = \frac{\mu_\tau}{2\mu_e^2} \underline{\underline{\tau}}_e \cdot \underline{\underline{\tau}}_e$$

remote from boundaries and equals G_B near a boundary and will be given later for a radial impeller (see equation (42)). G_c is a curvature and Coriolis parameter given by [9] for three models. It is written out fully for radial impeller (see equation (43)).

Dissipation rate:
$$\nabla \cdot (\rho \mathbf{v} \epsilon) = \nabla \cdot [\Gamma_{e,\epsilon} \nabla \epsilon] + S_\epsilon \quad (5)$$

$$S_\epsilon = \epsilon/k [C_{e1} G + G_c - C_{e2} (1 + C_c) \rho \epsilon]$$

$$C_{e1} = 1.44$$

and

$$C_{e2} = 1.92$$

from Launder and Spalding [11].

C_c is a curvature and Coriolis parameter given by [9] for three models. It is written out fully for radial impellers (see equation (47)).

$$P = \bar{P} + \frac{2}{3} \rho k - \frac{1}{2} \rho \omega^2 R^2 =$$

reduced effective pressure

\mathbf{q} = a vector shown in the a_i system, $q_i \hat{e}_{a_i}$

$\underline{\underline{q}}$ = a dyadic shown in the a_i system, $q_{ij} \hat{e}_{a_i} \hat{e}_{a_j}$

$\bar{\mathbf{q}}$ = the expansion of a time varying quantity into a time average and a fluctuating part whose time average is zero ($\bar{\mathbf{q}} + \mathbf{q}'$)

$$\underline{\underline{q}} : \underline{\underline{r}} = q_{ij} \hat{e}_{a_i} \hat{e}_{a_j} : r_{lm} \hat{e}_{a_l} \hat{e}_{a_m} = q_{ij} r_{lm} (\hat{e}_{a_i} \cdot \hat{e}_{a_l}) (\hat{e}_{a_j} \cdot \hat{e}_{a_m}) = q_{ij} r_{ij}$$

R, θ, Z = cylindrical coordinates referred to the a_i frame

\mathbf{r} = position vector of point P

S_ϕ, S_k, S_ϵ = general production (source) terms in the ϕ, k, ϵ equations, respectively

\hat{T} = unit tangent

\hat{T}_m = meridional unit vector

T^ϕ = a group of terms describing the diffusion of ϕ in the Z -direction

u, v, w = velocities in the x -, y -, z -directions, respectively

$$u_d = u - x \frac{\partial X}{\partial z} w = u \text{ "diffuser"}$$

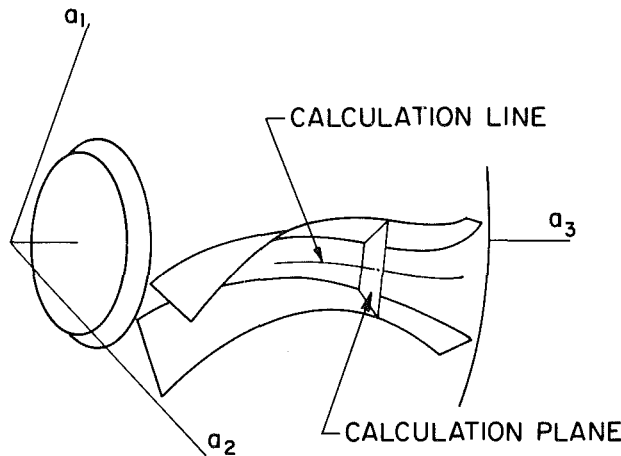


Fig. 3 A typical blade passage showing the calculation line and a calculation plane

The values of C_μ and C_p given in the Nomenclature are from Launder and Spalding [11].

Semipath Coordinates

A coordinate system is sought such that one of the principal directions will be tangent to a line called the calculation line. This line is chosen near the center of the blade passage and will closely follow the principal flow direction as shown in Fig. 3. The advantage of choosing such a system is that the equations and computer program will be invariant with respect to impeller geometry. The disadvantage is that the coordinate parameters must be calculated from input geometry, thus involving numerical differentiation and interpolation.

The Frenet Serret [12] path coordinates from differential geometry are the most general coordinates available but the fundamental equations become too awkward when transformed. The Frenet Serret coordinates are altered so that one

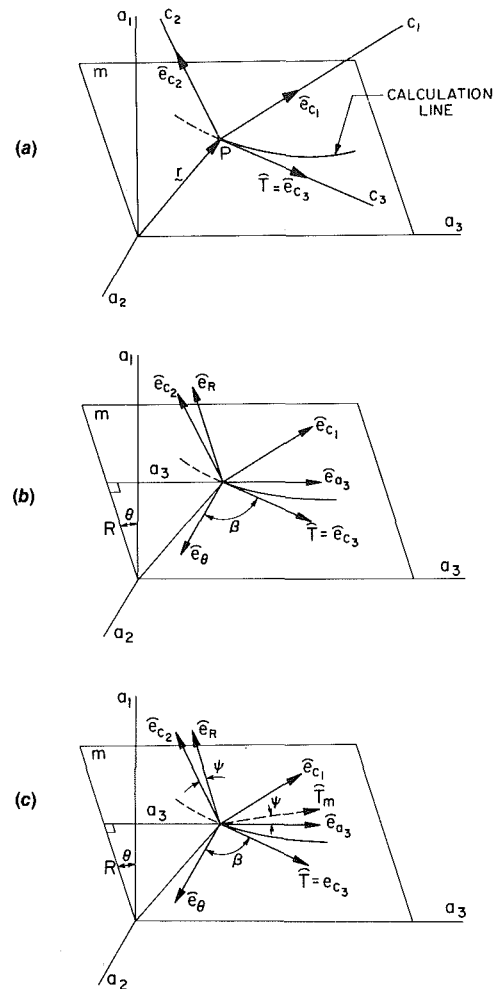


Fig. 4 Semipath coordinates—(a) the c_i frame; (b) the $r\theta a_3$ frame; (c) parameters β, ψ and unit vector \hat{T}_m

Nomenclature (cont.)

$\mathbf{v} = \bar{\mathbf{V}} + \mathbf{V}' = \mathbf{v} + \mathbf{v}'$ = where \mathbf{v} is the velocity of fluid seen by an observer fixed to the impeller (a_i coordinate system). For convenience $\bar{\mathbf{V}}$ is replaced by \mathbf{v} without a bar and \mathbf{V}' is replaced by \mathbf{v}'

v_1, v_2, v_3 = velocities in the C_1 -, C_2 -, C_3 -directions, respectively

$$v_d = v - y \frac{\partial Y}{\partial z} \quad w = v \text{ "diffuser"}$$

X, Y = dimensions of calculation plane

$$x = \frac{C_1}{X}; \quad y = \frac{C_2}{Y}; \quad z = C_3$$

$$\mathcal{X} = \frac{1}{X} \frac{\partial X}{\partial z}; \quad \mathcal{Y} = \frac{1}{Y} \frac{\partial Y}{\partial z}$$

α_C = space rate of change with respect to C_3 of the angular position of the C_i frame relative to the $R\theta a_3$ frame.

$\alpha_{R\theta a_3}$ = space rate of change with respect to C_3 of the angular position of the $R\theta a_3$ frame relative to the a_i frame.

β = angle between \hat{e}_ϕ and \hat{T}

$\Gamma_{e,\phi}$ = effective coefficient of diffusion for the general quantity, ϕ

$\Gamma_{e,k}$ = effective coefficient of diffusion for k, μ_e

$\Gamma_{e,\epsilon}$ = effective coefficient of diffusion for ϵ where $C_p = 1.3$

$$\left(\mu + \frac{\mu_t}{C_p} \right)$$

ϵ = the rate of dissipation of k per unit mass of fluid ($\nu \nabla \mathbf{v}' : \nabla \mathbf{v}'$)

ρ = fluid density

\mathcal{I}_e = effective internal shear stress of fluid, $\mu_e (\mathbf{v} \nabla + \nabla \mathbf{v})$

μ = absolute viscosity

μ_t = turbulent viscosity where $C_\mu = 0.09, C_\mu k^2 \rho / \epsilon$

μ_e = effective viscosity, $\mu + \mu_t$

$\nu = \frac{\mu}{\rho}$ kinematic viscosity

$$\bar{\phi} = \lim_{T \rightarrow \infty} \frac{1}{T} \int_{t_0}^{t_0+T} \phi(t) dt, \text{ the time}$$

average of the quantity ϕ .

It should be noted that $\bar{\phi} = \bar{\phi} + \bar{\phi}'$
 $= \bar{\phi} + \bar{\phi}' = \bar{\phi} + \bar{\phi}'$ making $\bar{\phi}' = 0$

ψ = angle between e_{a_3} and T_m

ω = constant angular speed of impeller

of the principal directions remains fixed in the meridional plane; thus suggesting the name "semipath" coordinates.

Let the semipath coordinates be c_i in the directions of the unit vectors \hat{e}_{c_i} as shown in Fig. 4(a). c_i 's are always referred to the a_i frame fixed to the impeller. c_3 is chosen tangent to the calculation line so that the principal tangent vector \hat{T} is identical to \hat{e}_{c_3} . c_2 must always lie in the meridional plane, m . c_1 has the direction dictated by the fact that c_i 's form a right-handed orthogonal system. \mathbf{r} is the position vector of point, P , on the calculation line.

In Fig. 4(b) the $R\theta Z$ (or $R\theta a_3$) frame is superimposed on the c_i system. \hat{e}_{a_3} and \hat{e}_R lie in the meridional plane, m . \hat{e}_θ is perpendicular to m as shown. β is the angle between \hat{e}_θ and \hat{T} and is a common parameter used in turbomachine analysis.

In Fig. 4(c) a meridional unit vector, \hat{T}_m , is shown. This is not the projection of \hat{T} on m but is obtained by rotating the c_i frame about c_2 until \hat{T} lies in m . The angle ψ separates \hat{e}_{a_3} and \hat{T}_m as well as \hat{e}_{c_2} and \hat{e}_R .

The fundamental equations are now written in c_i coordinates. Since ∇ operates on vector and dyadic quantities involving the unit vectors \hat{e}_{c_i} , it is necessary to calculate the quantities $(\partial \hat{e}_{c_i} / \partial c_j)_a$ where $()_a$ means that the derivative must be taken with respect to the a_i frame. Since the directions of \hat{e}_{c_i} only vary with respect to c_3 , the only nonzero quantities are $(d\hat{e}_{c_i} / dc_3)_a$ where the total derivative now replaces the partial derivative. Fraser [13] shows that these derivatives are given by

$$\left(\frac{d\hat{e}_{c_i}}{dc_3} \right)_a = \left[\left(\frac{d\hat{e}_{c_i}}{dc_3} \right)_c + (\alpha_c \cdot \mathbf{x} \hat{e}_{c_i}) \right] + (\alpha_{R\theta a_3} \cdot \mathbf{x} \hat{e}_{c_i}) \quad (6)$$

where $()_c$ means that the derivative is taken with respect to the c_i frame.

$$\alpha_c = -\frac{d\psi}{dc_3} \sin\beta \hat{e}_{c_1} + \frac{d\beta}{dc_3} \hat{e}_{c_2} + \frac{d\psi}{dc_3} \cos\beta \hat{e}_{c_3} \quad (7)$$

and is the space rate of change with respect to c_3 of the angular position of the c_i frame relative to the $R\theta a_3$ frame.

$$\alpha_{R\theta a_3} = \frac{\cos\psi}{R} \cos^2\beta \hat{e}_{c_1} - \frac{\sin\psi}{R} \cos\beta \hat{e}_{c_2} - \frac{\cos\psi}{R} \sin\beta \cos\beta \hat{e}_{c_3} \quad (8)$$

and is the space rate of change with respect to c_3 of the angular position of the $R\theta a_3$ frame relative to the a_i frame.

Dropping the subscript a in equation (6) with the understanding that quantities are referred to the a_i frame

$$\frac{d\hat{e}_{c_1}}{dc_3} = A_{12} \hat{e}_{c_2} + A_{13} \hat{e}_{c_3} \quad (9)$$

$$\frac{d\hat{e}_{c_2}}{dc_3} = -A_{12} \hat{e}_{c_1} + A_{23} \hat{e}_{c_3} \quad (10)$$

$$\frac{d\hat{e}_{c_3}}{dc_3} = -A_{13} \hat{e}_{c_1} - A_{23} \hat{e}_{c_2} \quad (11)$$

where:

$$A_{12} = \frac{d\psi}{dc_3} \cos\beta + \frac{\cos\psi}{R} \sin\beta \cos\beta \quad (12)$$

$$A_{13} = -\frac{d\beta}{dc_3} + \frac{\sin\psi}{R} \cos\beta \quad (13)$$

$$A_{23} = -\frac{d\psi}{dc_3} \sin\beta + \frac{\cos\psi}{R} \cos^2\beta \quad (14)$$

A_{12} , A_{13} , and A_{23} are called curvature-torsion parameters because they account for the curvature of the calculation line in the meridional plane, m , and for the torsion of the calculation line as m rotates with point P (see Fig. 4). It is emphasized that this rotation is not due to the impeller rotation since the a_i frame is fixed to the impeller, but is due

rather to the twisting of the blade passage about the impeller axis as c_3 increases. It is a space rather than a time rate of change of angular position of plane m and point P .

The fundamental equations are now written in semipath coordinates. v_1 , v_2 , v_3 are respectively the velocities in the c_1 -, c_2 -, c_3 -directions.

Continuity:

$$\frac{\partial(\rho v_1)}{\partial c_1} + \frac{\partial(\rho v_2)}{\partial c_2} + \frac{\partial(\rho v_3)}{\partial c_3} + \rho v_1 A_{13} + \rho v_2 A_{23} = 0 \quad (15)$$

Momentum:

$$\tau_{eij} = \mu_e$$

$$\left[\begin{array}{cc} \left(2 \frac{\partial v_1}{\partial c_1} \right) & \text{symmetric} \\ \left(\frac{\partial v_1}{\partial c_2} + \frac{\partial v_2}{\partial c_1} \right) & \left(2 \frac{\partial v_2}{\partial c_2} \right) \\ \left(\frac{\partial v_1}{\partial c_3} + \frac{\partial v_2}{\partial c_1} - v_2 A_{12} - v_3 A_{13} \right) & \left(\frac{\partial v_2}{\partial c_3} + \frac{\partial v_3}{\partial c_3} + v_1 A_{12} - v_3 A_{23} \right)^2 \left(\frac{\partial v_3}{\partial c_3} + v_1 A_{13} + v_2 A_{23} \right) \end{array} \right] \quad (16)$$

c_1 equation:

$$\begin{aligned} \frac{\partial}{\partial c_1} (\rho v_1 v_1) + \frac{\partial}{\partial c_2} (\rho v_2 v_1) + \frac{\partial}{\partial c_3} (\rho v_3 v_1) - \rho v_2 v_3 A_{12} \\ + \rho (v_1^2 - v_3^2) A_{13} + \rho v_1 v_2 A_{23} = \frac{\partial \tau_{e11}}{\partial c_1} + \frac{\partial \tau_{e12}}{\partial c_2} \\ + \frac{\partial \tau_{e13}}{\partial c_3} - \tau_{e23} A_{12} + (\tau_{e11} - \tau_{e33}) A_{13} + \tau_{e12} A_{23} \\ - \frac{\partial P}{\partial c_1} + 2\rho\omega (v_3 \sin\psi + v_2 \cos\psi \sin\beta) \end{aligned} \quad (17)$$

c_2 equation:

$$\begin{aligned} \frac{\partial}{\partial c_1} (\rho v_1 v_2) + \frac{\partial}{\partial c_2} (\rho v_2 v_2) + \frac{\partial}{\partial c_3} (\rho v_3 v_2) + \rho v_1 v_3 A_{12} \\ + \rho (v_2^2 - v_3^2) A_{23} + \rho v_1 v_2 A_{13} = \frac{\partial \tau_{e12}}{\partial c_1} + \frac{\partial \tau_{e22}}{\partial c_2} \\ + \frac{\partial \tau_{e23}}{\partial c_3} + \tau_{e13} A_{12} + (\tau_{e22} - \tau_{e33}) A_{23} + \tau_{e12} A_{13} \\ - \frac{\partial P}{\partial c_3} + 2\rho\omega \cos\psi (v_3 \cos\beta - v_1 \sin\beta) \end{aligned} \quad (18)$$

c_3 equation:

$$\begin{aligned} \frac{\partial}{\partial c_1} (\rho v_1 v_3) + \frac{\partial}{\partial c_2} (\rho v_2 v_3) + \frac{\partial}{\partial c_3} (\rho v_3 v_3) \\ + 2\rho v_1 v_3 A_{13} + 2\rho v_2 v_3 A_{23} = \frac{\partial \tau_{e13}}{\partial c_1} + \frac{\partial \tau_{e23}}{\partial c_2} \\ + \frac{\partial \tau_{e33}}{\partial c_3} + 2\tau_{e13} A_{13} + 2\tau_{e23} A_{23} \\ - \frac{\partial P}{\partial c_3} - 2\rho\omega (v_2 \cos\psi \cos\beta + v_1 \sin\psi) \end{aligned} \quad (19)$$

ϕ equation:

$$\begin{aligned} \frac{\partial}{\partial c_1} (\rho v_1 \phi) + \frac{\partial}{\partial c_2} (\rho v_2 \phi) + \frac{\partial}{\partial c_3} (\rho v_3 \phi) + \rho v_1 \phi A_{13} \\ + \rho v_2 \phi A_{23} = \frac{\partial}{\partial c_1} \left(\Gamma_{e,\phi} \frac{\partial \phi}{\partial c_1} \right) + \frac{\partial}{\partial c_2} \left(\Gamma_{e,\phi} \frac{\partial \phi}{\partial c_2} \right) \end{aligned}$$

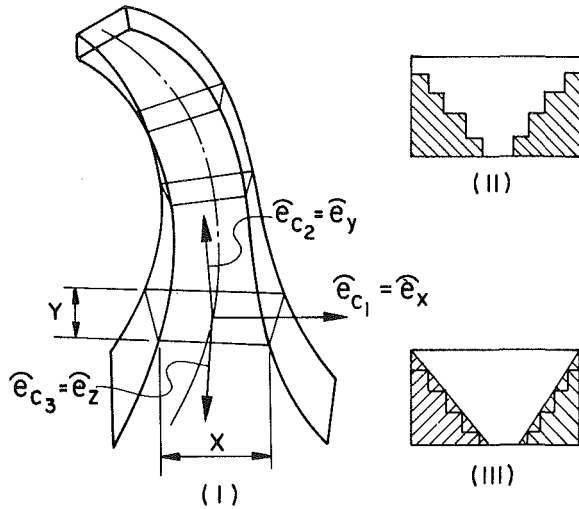


Fig. 5 Rectangular calculation planes—(i) dimensions of planes; (ii) fine grid approximation of a mixed flow impeller; (iii) coarse grid approximation with triangular elements

$$+ \frac{\partial}{\partial c_3} \left(\Gamma_{e,\phi} \frac{\partial \phi}{\partial c_3} \right) + \Gamma_{e,\phi} \frac{\partial \phi}{\partial c_1} A_{13} + \Gamma_{e,\phi} \frac{\partial \phi}{\partial c_2} A_{23} + S_\phi \quad (20)$$

Kinetic Energy of Turbulence. In (20), replace ϕ with k , $\Gamma_{e,\phi}$ with $\Gamma_{e,k}$ and S_ϕ with S_k . (21)

Dissipation Rate. In (20), replace ϕ with ϵ , $\Gamma_{e,\phi}$ with $\Gamma_{e,\epsilon}$ and S_ϕ with S_ϵ . (22)

Transformation for Rectangular Calculation Planes

Equations (15) to (22) are valid for any blade passage. However, because the c_i system is Cartesian then control volumes in the shape of parallelepipeds are most convenient since principal velocities will be perpendicular to control volume faces. Also rectangular calculation planes are recommended as shown in Fig. 5(i) because variation in passage width or height with respect to c_1 or c_2 make equations (15–22) unwieldy. This does not restrict the impeller geometry as much as it would seem on first consideration. The passage still has arbitrary curvature and torsion. Divergence is accounted for by allowing X and Y to vary with c_3 . Passages with nonrectangular cross sections such as the trapezoidal shape of the mixed flow impeller can be handled by Patankar's [14] method of setting the values of variables in the control volumes located within the solution domain. An alternative approach suitable for some cross sections in the axial and mixed flow regions of an impeller is to employ a further transformation from a rectangular cross section to a segment of an annulus. In the first method, an existing program is permitted to solve equations for the entire rectangular cross section but the variables in a specified region retain their fixed values. For a fine grid the shaded region of Fig. 5(ii) would have prescribed variable values. If a coarser grid is desirable, then triangular control volumes of Fig. 5(iii) would have to be developed.

$$\begin{aligned} \text{Let: } x &= \frac{c_1}{X}; \quad u = v_1 = \frac{dc_1}{dt} = X \frac{dx}{dt} \\ y &= \frac{c_2}{Y}; \quad v = v_2 = \frac{dc_2}{dt} = Y \frac{dy}{dt} \\ z &= c_3; \quad w = v_3 = \frac{dc_3}{dt} = \frac{dz}{dt} \\ A_{xy} &= A_{12}; \quad A_{xz} = A_{13}; \quad A_{yz} = A_{23} \end{aligned} \quad (23)$$

Therefore:

$$\begin{aligned} \frac{\partial}{\partial c_1} &= \frac{1}{X} \frac{\partial}{\partial x}; \quad \frac{\partial}{\partial c_2} = \frac{1}{Y} \frac{\partial}{\partial y} \\ \frac{\partial}{\partial c_3} &= -\frac{x}{X} \frac{\partial X}{\partial z} \frac{\partial}{\partial x} - \frac{y}{Y} \frac{\partial Y}{\partial z} \frac{\partial}{\partial y} + \frac{\partial}{\partial z} \end{aligned} \quad (24)$$

For convenience, only the ϕ equation is shown. The full set of transformed equations is given by Fraser [13].

$$\begin{aligned} \frac{1}{X} \frac{\partial}{\partial x} (\rho u_d \phi) + \frac{1}{Y} \frac{\partial}{\partial y} (\rho v_d \phi) + \frac{\partial}{\partial z} (\rho w \phi) \\ = \frac{1}{X^2} \frac{\partial}{\partial x} \left\{ \Gamma_{e,\phi} \frac{\partial \phi}{\partial x} \left[1 + x^2 \left(\frac{\partial X}{\partial z} \right)^2 \right] \right\} \\ + \frac{1}{Y^2} \frac{\partial}{\partial y} \left\{ \Gamma_{e,\phi} \frac{\partial \phi}{\partial y} \left[1 + y^2 \left(\frac{\partial Y}{\partial z} \right)^2 \right] \right\} \\ + \left(\frac{x}{X} \frac{y}{Y} \frac{\partial X}{\partial z} \frac{\partial Y}{\partial z} \right) \left[\frac{\partial}{\partial x} \left(\Gamma_{e,\phi} \frac{\partial \phi}{\partial y} \right) + \frac{\partial}{\partial y} \left(\Gamma_{e,\phi} \frac{\partial \phi}{\partial x} \right) \right] \\ + \frac{\Gamma_{e,\phi}}{X} \frac{\partial \phi}{\partial x} \left[A_{xz} - \frac{x}{X} \left(\frac{\partial X}{\partial z} \right)^2 \right] + \frac{\Gamma_{e,\phi}}{Y} \frac{\partial \phi}{\partial y} \left[A_{yz} - \frac{y}{Y} \left(\frac{\partial Y}{\partial z} \right)^2 \right] \\ + T^\phi + S_\phi + [S_\phi^1 - \rho(uAxz + vAyZ) - \rho w \omega] \phi \end{aligned} \quad (25)$$

where:

$$u_d = \left(u - x \frac{\partial X}{\partial z} w \right) = u \text{ "diffuser"} \quad (26)$$

u_d is so named because its behavior in the transformed equation (25) is analogous to the behavior of u in the original equation (20), and it accounts for the extra component $x(\partial X/\partial z)w$ describing the widening of the blade passage.

$$v_d = \left(v - y \frac{\partial Y}{\partial z} w \right) = v \text{ "diffuser"} \quad (27)$$

$$a = \frac{1}{XY} \frac{\partial(XY)}{\partial z} = \text{the normalized space rate of change of passage cross sectional area} \quad (28)$$

T^ϕ is a group of terms describing the diffusion of ϕ in the z -direction.

S_ϕ of equation (20) is linearized as follows:

$$S_\phi = S_\phi + S_\phi' \phi \quad (29)$$

S_ϕ includes all source terms not having ϕ as a factor.

S_ϕ' includes all source terms having ϕ as a factor.

The Coriolis terms in the transformed momentum equations are listed

$$\text{from (17) } 2\rho \omega (w \sin \psi + v \cos \psi \sin \beta) \quad (30)$$

$$\text{from (18) } 2\rho \omega \cos \psi (w \cos \beta - u \sin \beta) \quad (31)$$

$$\text{from (19) } -2\rho \omega (v \cos \psi \cos \beta + u \sin \psi) \quad (32)$$

Simplified Equations for Specific Application

The equations are now simplified further to test them on radial impellers. The following simplifications are given in order of decreasing generality.

Duct Flow. By adopting the common assumption of zero diffusion in the z -direction, parabolic or partially parabolic computation schemes are possible. Terms like T^ϕ are set to zero.

Limiting the Rate of Passage Divergence. For a passage whose rate of divergence is small enough to make the previous simplification valid, the following approximations are made

$$x \frac{\partial X}{\partial z} < 10^{-1}; \quad y \frac{\partial Y}{\partial z} < 10^{-1} \quad (33)$$

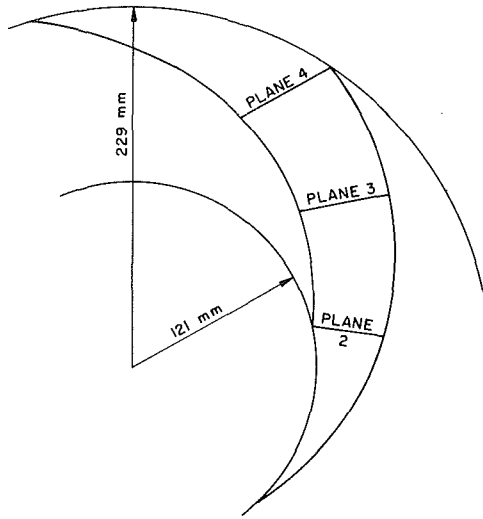


Fig. 6 Dimensions of the Kittmer radial impeller—showing measurement planes 2, 3 and 4

Radial impellers.

$$\psi = 90 \text{ deg} \\ A_{xy} = A_{yz} = 0 \quad (34)$$

$\frac{\partial Y}{\partial z} \ll \frac{\partial X}{\partial z}$ (if the hub to shroud distance is slowly varying)

Equations in Final Form for Solution. The equations for radial impellers are now given

Let

$$x = \frac{1}{X} \frac{\partial X}{\partial z}; \quad y = \frac{1}{Y} \frac{\partial Y}{\partial z} \quad (35)$$

Continuity:

$$\frac{1}{X} \frac{\partial}{\partial x} (\rho u_d) + \frac{1}{Y} \frac{\partial}{\partial y} (\rho v_d) \\ + \frac{\partial}{\partial z} (\rho w) + \rho w_a + \rho u A_{xz} = 0 \quad (36)$$

Momentum:

x-equation:

$$\frac{1}{X} \frac{\partial}{\partial x} (\rho u_d u) + \frac{1}{Y} \frac{\partial}{\partial y} (\rho v_d u) + \frac{\partial}{\partial z} (\rho w u) \\ = \frac{1}{X^2} \frac{\partial}{\partial x} \left[\mu_e \frac{\partial u}{\partial x} \right] + \frac{1}{Y^2} \frac{\partial}{\partial y} \left[\mu_e \frac{\partial u}{\partial y} \right] + \frac{\mu_e}{X} \frac{\partial u}{\partial x} A_{xz} \\ + \left\{ \frac{1}{X^2} \frac{\partial}{\partial x} \left[\mu_e \frac{\partial u}{\partial x} \right] + \frac{1}{XY} \frac{\partial}{\partial y} \left[\mu_e \frac{\partial v}{\partial x} \right] \right. \\ \left. - x \mathfrak{X} \frac{\partial}{\partial x} \left[\mu_e \left(\frac{1}{X} \frac{\partial w}{\partial x} - w A_{xz} \right) \right] \right. \\ \left. - y \mathfrak{Y} \frac{\partial}{\partial y} \left[\mu_e \left(\frac{1}{X} \frac{\partial w}{\partial x} - w A_{xz} \right) \right] \right. \\ \left. + A_{xz} \left[\mu_e \left(\frac{1}{X} \frac{\partial u}{\partial x} + 2x \mathfrak{X} \frac{\partial w}{\partial x} + 2y \mathfrak{Y} \frac{\partial w}{\partial y} \right) \right. \right. \\ \left. \left. + \rho w^2 \right] - \frac{1}{X} \frac{\partial P}{\partial x} + 2\rho \omega w \right\} - [\rho u A_{xz} + 2\mu_e A_{xz}^2 + \rho w_a] u \quad (37)$$

y-equation:

$$\frac{1}{X} \frac{\partial}{\partial x} (\rho u_d v) + \frac{1}{Y} \frac{\partial}{\partial y} (\rho v_d v) + \frac{\partial}{\partial z} (\rho w v)$$

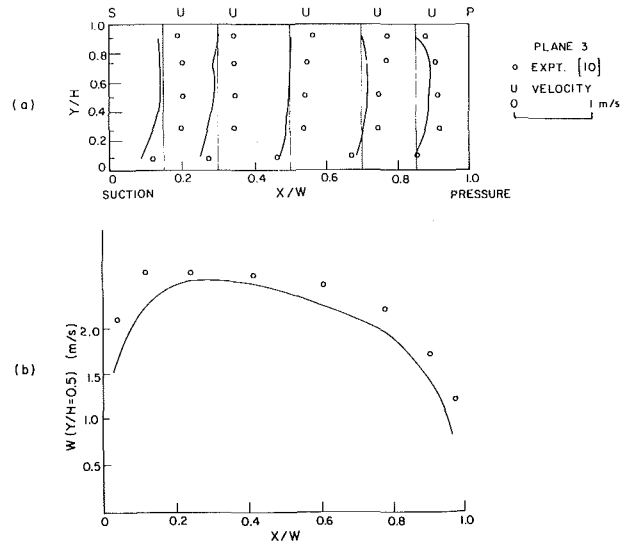


Fig. 7 Comparison of predictions with data by Howard and Kittmer [10] for midpoint observation plane 3. Solid lines indicate predictions: (a) cross-channel velocities (u); (b) mainstream velocity (w).

$$= \frac{1}{X^2} \frac{\partial}{\partial x} \left[\mu_e \frac{\partial v}{\partial x} \right] + \frac{1}{Y^2} \frac{\partial}{\partial y} \left[\mu_e \frac{\partial v}{\partial y} \right] + \frac{\mu_e}{X} \frac{\partial v}{\partial x} A_{xz} \\ + \left\{ \frac{1}{Y^2} \frac{\partial}{\partial y} \left[\mu_e \frac{\partial v}{\partial y} \right] + \frac{1}{XY} \frac{\partial}{\partial x} \left[\mu_e \frac{\partial u}{\partial y} \right] \right. \\ \left. - x \mathfrak{X} \frac{\partial}{\partial x} \left[\mu_e \left(\frac{1}{Y} \frac{\partial w}{\partial y} \right) \right] - y \mathfrak{Y} \frac{\partial}{\partial y} \left[\mu_e \left(\frac{1}{Y} \frac{\partial w}{\partial y} \right) \right] \right. \\ \left. + A_{xz} \left[\mu_e \left(\frac{1}{Y} \frac{\partial v}{\partial y} \right) \right] - \frac{1}{Y} \frac{\partial P}{\partial y} \right\} - [\rho u A_{xz} + \rho w_a] v \quad (38)$$

z-equation:

$$\frac{1}{X} \frac{\partial}{\partial x} (\rho u_d w) + \frac{1}{Y} \frac{\partial}{\partial y} (\rho v_d w) + \frac{\partial}{\partial z} (\rho w w) \\ = \frac{1}{X^2} \frac{\partial}{\partial x} \left[\mu_e \frac{\partial w}{\partial x} \right] + \frac{1}{Y^2} \frac{\partial}{\partial y} \left[\mu_e \frac{\partial w}{\partial y} \right] \\ + \frac{\mu_e}{X} \frac{\partial w}{\partial x} A_{xz} + \left\{ - \frac{1}{X} \frac{\partial}{\partial x} \left[\mu_e \left(x \mathfrak{X} \frac{\partial u}{\partial x} \right. \right. \right. \\ \left. \left. + y \mathfrak{Y} \frac{\partial u}{\partial y} - w A_{xz} \right) \right] - \frac{1}{Y} \frac{\partial}{\partial y} \left[\mu_e \left(x \mathfrak{X} \frac{\partial v}{\partial x} - y \mathfrak{Y} \frac{\partial v}{\partial y} \right) \right] \right. \\ \left. - 2\mu_e \left\{ x \mathfrak{X} \frac{\partial}{\partial x} (u A_{xz}) + y \mathfrak{Y} \frac{\partial}{\partial y} (u A_{xz}) \right\} \right. \\ \left. + \left[x \mathfrak{X} \frac{\partial}{\partial x} \left(\frac{\partial u}{\partial x} + \frac{\partial v}{\partial x} \right) + y \mathfrak{Y} \frac{\partial}{\partial y} \left(\frac{\partial u}{\partial y} + \frac{\partial v}{\partial y} \right) \right] A_{xz} \right\} \\ + x \mathfrak{X} \frac{\partial P}{\partial x} + y \mathfrak{Y} \frac{\partial P}{\partial y} - \frac{\partial P}{\partial z} - 2\omega u \rho \left. \right\} \\ - [2[\rho u A_{xz} + \mu_e A_{xz}^2] + \rho w_a] w \quad (39)$$

ϕ equation:

$$\frac{1}{X} \frac{\partial}{\partial x} (\rho u_d \phi) + \frac{1}{Y} \frac{\partial}{\partial y} (\rho v_d \phi) + \frac{\partial}{\partial z} (\rho w \phi) \\ = \frac{1}{X^2} \frac{\partial}{\partial x} \left[\Gamma_{e,\phi} \frac{\partial \phi}{\partial x} \right] + \frac{1}{Y^2} \frac{\partial}{\partial y} \left[\Gamma_{e,\phi} \frac{\partial \phi}{\partial y} \right] + \frac{\Gamma_{e,\phi}}{X} \frac{\partial \phi}{\partial x} A_{xz} \\ + S_\phi + [S'_\phi - \rho u A_{xz} - \rho w_a] \phi \quad (40)$$

Kinetic Energy of Turbulence. In (40), ϕ is replaced by k , $\Gamma_{e,\phi}$ with $\Gamma_{e,k}$, S_ϕ with S_k and S'_ϕ with S'_k

where

$$S_k = [G + G_c] \quad (41)$$

$$G = \begin{cases} \mu_t \left[2 \left(\frac{1}{X} \frac{\partial u}{\partial x} \right)^2 + 2 \left(\frac{1}{Y} \frac{\partial v}{\partial y} \right)^2 + 2 \left(-x \mathcal{X} \frac{\partial w}{\partial x} - y \mathcal{Y} \frac{\partial w}{\partial y} + u A_{xz} \right)^2 \right. \\ \left. + \left(\frac{1}{Y} \frac{\partial u}{\partial y} + \frac{1}{X} \frac{\partial v}{\partial x} \right)^2 + \left(\frac{1}{X} \frac{\partial w}{\partial x} - w A_{xz} \right)^2 + \left(\frac{1}{Y} \frac{\partial w}{\partial y} \right)^2 \right] \\ \text{remote from a boundary} \quad (42) \\ \left| \frac{\kappa C_\mu^{1/4} k \rho w}{\ln \left(\frac{C_E C_\mu^{1/4} k^{1/2} \rho X x}{\mu} \right)} \left(\frac{1}{X} \frac{\partial w}{\partial x} - w A_{xz} \right) \right| \text{near a blade} \\ \left| \frac{\kappa C_\mu^{1/4} k \rho w}{\ln \left(\frac{C_E C_\mu^{1/4} k^{1/2} \rho Y y}{\mu} \right)} \left(\frac{1}{Y} \frac{\partial w}{\partial y} \right) \right| \text{near the hub or shroud} \end{cases}$$

$K = .42$; $C_E = 8.8$ after Pratap [16].

$$G_c = \begin{cases} \frac{9}{2} \mu_t (2\omega - w A_{xz}) \frac{\partial w}{\partial x} & \text{Model 1} \\ 0 & \text{Model 2} \\ 0 & \text{Model 3} \end{cases} \quad (43)$$

adapted from Howard et al. [9]

$$S'_k = -\rho \frac{\epsilon}{k} \quad (44)$$

Dissipation Rate. In (40), ϕ is replaced by ϵ , $\Gamma_{e,\phi}$ with $\Gamma_{e,\epsilon}$, S_ϕ with S_ϵ and S'_ϕ with S'_ϵ ,

where

$$S_\epsilon = \frac{\epsilon}{k} [C_{\epsilon 1} G + G_c] \quad (45)$$

$$S'_\epsilon = \frac{1}{k} [-C_{\epsilon 2} (1 + C_c) \rho \epsilon] \quad (46)$$

$$C_c = \begin{cases} 0 & \text{Model 1} \\ 0.2 \left(\frac{k}{\epsilon} \right)^2 (2\omega - w A_{xz}) \left(\frac{\partial w}{\partial x} - 2\omega \right) & \text{Model 2} \\ 0.2 \left(\frac{k}{\epsilon} \right)^2 (2\omega - w A_{xz}) \left(\frac{\partial w}{\partial x} \right) & \text{Model 3} \end{cases} \quad (47)$$

adapted from Howard et al. [9]

Solution of the Equations

The equations were modeled using finite volumes after Patankar and Spalding [5] and further described by Patankar [14]. Certain of the curvature and expansion terms in equations (36-40) are absorbed in the evaluation of control volume surface integrals during the discretization process. A program was written by Fraser [13] to use the fully parabolic solution method for the first pass down the blade passage. The pressure was stored in a three-dimensional array. Then the partially parabolic method of Pratap and Spalding [6], further described by Pratap [16], was employed with the fully parabolic grid and established pressure field to complete several passes down the channel. The fully parabolic grid

differs from the grid usually used for partially parabolic calculations in that w is stored on the calculation plane instead of midway between planes. This makes it necessary to use a

forward difference for the streamwise pressure gradient in place of a central difference. The program was tested for laminar flow in a square duct and was successfully compared to the calculations of Briley [17]. It was also tested for turbulent flow in the rotating rectangular duct of Wagner [18] at 300 rpm and it gave results as close to the data as were calculations of Howard, Patankar and Bordinuk [9].

After the preceding tests the program was used to predict the flow in a backward curved radial impeller and the calculations were compared to the measurements of Howard and Kittmer [10]. The impeller is shown in Fig. 6. It has seven logarithmic spiral blades 3.2-mm thick at an angle of 22 deg from tangential which extend from an inner radius of 121 mm to an outer radius of 229 mm. The axial depth of the blades varies linearly from 23.4 mm at the inlet to 21.3 mm at the exit. The fluid used was water and the impeller was rotated at 140 rpm. The measured velocities at observation plane 2 were used as input. The measured velocities at observation plane 4 were used to generate a pressure distribution whose level was adjusted to the level of the pressure field generated by the fully parabolic solution on the first pass. The distribution

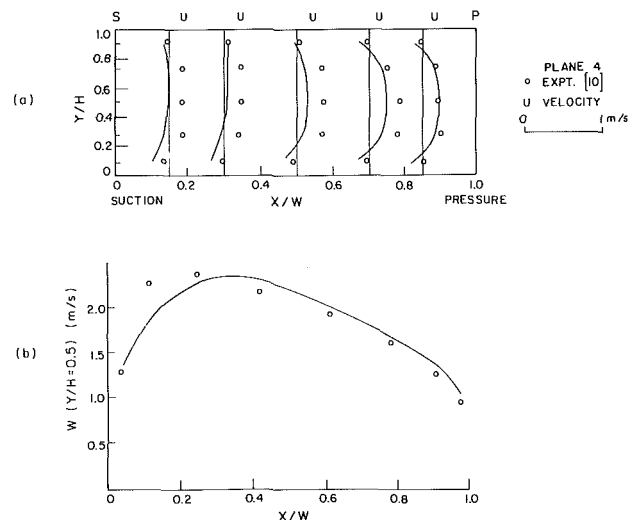


Fig. 8 Comparison of predictions with data by Howard and Kittmer [10] for downstream observation plane 4. Solid lines indicate predictions at a plane 9-mm upstream from plane 4: (a) cross-channel velocities (u); (b) mainstream velocity (w).

with the adjusted level was then used in the partially parabolic solution to impose downstream pressure on the upstream flow field. The predictions on observation plane 3 were then compared to measured values. The comparison is shown in Fig. 7.

Comparison with the data from Howard and Kittmer [10] presents certain difficulties. The measured cross-velocities were obtained from cylindrical hot-film probe measurements which assume a zero v -component of velocity. This and other sources of error adds a greater uncertainty to the u -component than to the w -component. For example, the uncertainty in the angle of the hot-film probe relative to the passage could result in a shift in u values of about 0.05 m/s. The input conditions for the analysis require P , u , v , and w at plane 2. The pressure gradient for this plane is based on the u -momentum equation (37) ignoring the effect of convection and diffusion of u . The starting velocity values consisted of measured distribution of the u - and w -components and an assumed zero v -component. The analysis provides adjustment of u , v , and pressure (and w for the partially parabolic mode) during the first calculation step. The pressure distribution on plane 4 is established on the same basis as at plane 2 and then remains fixed in distribution but not level with each pass. The comparison in Fig. 8 of measured and predicted velocities at plane 4 is useful since only the w -velocity component is effective in the simplified exit pressure distribution calculation.

At both planes 3 and 4, the discrepancy between measured and predicted cross-channel velocities is ascribed in part to the uncertainties in the experimental measurements, and also, for plane 4, to the approximate method employed in establishing the downstream pressure distribution. The u -velocity distribution at plane 3 was found to be insensitive to variations in the imposed pressure distributions at planes 2 and 4. The grid spacing has not been optimized but was chosen to facilitate comparisons and use of data for boundary values. Twenty-one calculation planes were used, including planes 2 and 4. A 10×9 grid was employed in the X - Y -plane, with the near-wall grid lines at 0.028 times the width from the blade walls, and 0.023 times the passage height from the hub and shroud surfaces. The predicted velocities are from the fourth pass of the partially parabolic calculation. In Fig. 8, the predictions are those for a calculation plane 9-mm upstream of plane 4, since the partially parabolic scheme does not calculate at the exit plane. The predictions do not include direct modification of turbulence by Coriolis and curvature, having G_c and C_c set to zero in equations (43) and (47). Small changes in u and w were observed when Model 1 turbulence modifications were introduced. A full investigation of turbulence models for this geometry has not been completed. The use of wall functions is another limitation. It might be overcome by finer grids near the wall and modified k and ϵ equations such as described by Lam and Bremhorst [19].

Conclusions

In order to analyze the flow in a curved rotating passage of a turbomachine, the basic flow equations have been transformed to follow a curved "spine" along the midpassage line. Further transformations allow for changes in the cross-section area and aspect ratio. A principal advantage of this approach lies in the maintenance of a dominant streamwise direction in the coordinate system. This assists in the ease of calculation of pressure gradient adjustments and reduces the problem of

false diffusion. Drawbacks of this approach include geometric limitations on cross-section shape. The calculation method for the flow field in the entry and exit regions of the bladed passage has not been treated here.

The numerical solution technique has employed the wall function method and allows for the inclusion of previously developed turbulence modification models. Both parabolic and partially parabolic solution methods are used on a common grid as part of the flow analysis procedure. The present program written to test the transformation system is limited to handling flow in radial machines. The comparison with measured data appears to be satisfactory for a preliminary test, taking into account the uncertainties in the experimental data.

References

- 1 Bosman, C., and Highton, J., "A Calculation Procedure for Three-Dimensional, Time-Dependent, Inviscid Compressible Flow Through Turbomachine Blades of any Geometry," *Journal of Mech. Eng. Sci.*, Vol. 21, Feb. 1979, pp. 39-49.
- 2 Denton, J. D., and Singh, U. K., "Time Marching Methods for Turbomachinery Flow Calculation," VKI Lecture Series 7, 1979; used by Sarathy, K. P., "Computation of Three-Dimensional Flow Fields through Rotating Blade Rows and Comparison with Experiment," ASME Paper No. 81-GT-121.
- 3 Adler, D., "Status of Centrifugal Impeller Internal Aerodynamics, Part I: Inviscid Flow Prediction Methods," *JOURNAL OF ENGINEERING FOR POWER*, 1980, pp. 728-737; "Part II: Experiments and Influence of Viscosity," *JOURNAL OF ENGINEERING FOR POWER*, 1980, pp. 738-746.
- 4 Dodge, P. R., "Numerical Method for Two-Dimensional and Three-Dimensional Viscous Flows," AIAA Paper No. 76-425, 1976.
- 5 Patankar, S. V., and Spalding, D. B., "A Calculation Procedure for Heat, Mass and Momentum Transfer in Three-Dimensional Parabolic Flows," *International Journal of Heat and Mass Transfer*, Vol. 15, 1972, pp. 1787-1806.
- 6 Pratap, V. S., and Spalding, D. B., "Fluid Flow and Heat Transfer in Three-Dimensional Duct Flows," *International Journal of Heat and Mass Transfer*, Vol. 19, 1976, pp. 1183-1188.
- 7 Malin, M. R., Rosten, H. I., and Tatchell, D. G., "Three-Dimensional Computations of Flows in Centrifugal Pumps and Compressors," *Performance Prediction of Centrifugal Pumps and Compressors*, ASME, New York, 1980, pp. 33-45.
- 8 Moore, J., and Moore, J. G., "Calculations of Three-Dimensional Viscous Flow and Wake Development in a Centrifugal Impeller," *JOURNAL OF ENGINEERING FOR POWER*, Vol. 103, Apr. 1981, pp. 367-372.
- 9 Howard, J. H. G., Patankar, S. V., and Bordyniuk, R. M., "Flow Prediction in Rotating Ducts Using Coriolis-Modified Turbulence Models," *ASME Journal of Fluids Engineering*, Vol. 102, December 1980, pp. 456-461.
- 10 Howard, J. H. G., and Kittmer, C. W., "Measured Passage Velocities in a Radial Impeller with Shrouded and Unshrouded Configurations," *JOURNAL OF ENGINEERING FOR POWER*, Vol. 97, Apr. 1975, pp. 207-213.
- 11 Launder, B. E., and Spalding, D. B., "The Numerical Computation of Turbulent Flows," *Computer Methods in Applied Mechanics and Engineering*, Vol. 3, 1974, pp. 269-289.
- 12 Spiegel, M. R., *Vector Analysis*, McGraw-Hill, 1959, pp. 37-38.
- 13 Fraser, D. A., "A Three-Dimensional Solution for Turbulent Flow in the Blade Passage of a Turbomachine Impeller," PhD thesis, Civil Engineering Dept., University of Waterloo, 1983.
- 14 Patankar, S. V., *Numerical Heat Transfer and Fluid Flow*, Hemisphere Publishing Co., New York, 1980.
- 15 Majumdar, A. K., Pratap, V. S., and Spalding, D. B., "Numerical Computation of Flow in Rotating Ducts," *ASME Journal of Fluids Engineering*, Vol. 99, No. 1, 1977, pp. 148-153.
- 16 Pratap, V. S., "Flow and Heat Transfer in Curved Ducts," PhD thesis, Faculty of Engineering, Imperial College, University of London, 1975.
- 17 Briley, W. R., "The Computation of Three-Dimensional Viscous Internal Flows," *Proceedings of the Third International Conference on Numerical Methods in Fluid Mechanics*, Vol. 2, July 1972, pp. 33-38.
- 18 Wagner, R. E., and Velkoff, H. R., "Measurement of Secondary Flows in a Rotating Duct," *JOURNAL OF ENGINEERING FOR POWER*, Vol. 94, 1972, pp. 261-270.
- 19 Lam, C. K. G., and Bremhorst, K., "A Modified Form of the k - ϵ Model for Predicting Wall Turbulence," *ASME Journal of Fluids Engineering*, Vol. 103, Sept. 1981, pp. 456-460.

Effect of Using Emulsions of High Nitrogen Containing Fuels and Water in a Gas Turbine Combustor on NO_x and Other Emissions

P. P. Singh
Mem. ASME

P. R. Mulik
Westinghouse Electric Corporation,
Pittsburgh, Pa. 15235

A. Cohn
Electric Power Research Institute,
Palo Alto, Calif.

A total of four combustion tests studying the response of various water/fuel emulsion rates on NO_x emissions have been conducted on: (a) Paraho shale oil, (b) H-Coal[®] (372x-522 K) distillate, (c) No. 2 oil doped with quinoline, (d) H-Coal[®] (505-616 K) distillate, utilizing a 0.14-m dia gas turbine can-type combustor at base-load conditions. Each test fuel run was preceded with a base-line fuel run with No. 2 distillate oil. The results indicate that the effectiveness of water injection to reduce NO_x decreased rapidly with an increase in the fuel-bound nitrogen (FBN) content of the test fuels. The smoke number, in general, decreased with increased water injection, while carbon monoxide and unburned hydrocarbons increased at high water/fuel flow rates.

Introduction

NO_x , which is formed by the combustion of fuels, such as coal-derived liquids (CDL) and shale-derived liquids (SDL) containing FBN, comes from two mechanisms. The first is the conversion of the FBN into "fuel NO_x " or FBN NO_x ; the second is the fixation of nitrogen in the combustion air to form "thermal NO_x " in the high-temperature flame as described by the Zeldovich mechanism [1]. As discussed by Vermes, Toof, and Cohn (2), the NO_x produced by these two mechanisms is not additive; the presence of fuel NO_x retards the formation of thermal NO_x . Furthermore, the formulation of NO_x from both mechanisms is influenced by the design of the combustor, especially the fuel/air ratios of the various regions in the combustor flame.

For fuels being burned today, NO_x emissions from combustion turbines are regulated by the United States Environmental Protection Agency (EPA) to 75 ppm by volume, corrected to 15 percent oxygen in the exhaust gases, with an additional allowance for turbine efficiencies. There is also a full allowance for conversion of FBN to fuel NO_x for fuels with FBN up to 0.1 percent with a partial allowance up to 0.25.

The thermal NO_x produced by commercial combustion turbines on essentially nitrogen-free conventional fuels is higher than the EPA allowance. It can be reduced to the EPA limit by injecting water into the flame, a system that works with No. 2 distillate oil, but this procedure incurs incremental installation and operating costs.

Under the sponsorship of the Electric Power Research Institute (EPRI), Westinghouse Electric Corporation has been involved in a program [3, 4] to determine the effectiveness of water injection for NO_x reduction with synthetic CDL and SDL fuels containing high FBN. Cold water was injected through the same ports in the fuel nozzle assembly that are used for atomizing air. These water injection tests were conducted at combustor inlet temperatures of 603 K (630°F) and outlet temperatures ranging from 1273 to 1373 K (1850 to 2000°F) with various water-to-fuel ratios up to a maximum of 1.2. Four fuels were tested, including SRC-II heavy distillate, Paraho shale oil, a 3-to-1 mixture of No. 2 oil to SRC-II middle distillate, and a light H-Coal[®] distillate. We found that water injection was not effective in controlling NO_x at base-load conditions in conventional combustors for fuels containing more than 0.2 percent FBN, and certainly 0.3 percent FBN.

In the current series of tests reported herein, the EPRI-sponsored water injection work was extended to include four additional tests with CDL and SDL fuels. Three of four fuels tested were identical to those in the previous study, the exception being SRC-II heavy distillate. It was replaced by No. 2 oil doped with quinoline. Test conditions and equipment utilized were comparable to the earlier tests with two principal exceptions. The first of these involved the temperature of the water used for injection, i.e., room temperature for the previous runs versus $\sim 180^\circ\text{F}$ in the current experiments. Secondly, the water and fuel were mixed to produce an emulsion prior to injection into the combustor. As in our previous work, a secondary objective was to ascertain the effect of water injection on other parameters, including combustion efficiency, CO, smoke, unburned hydrocarbons (UHC), and combustor wall temperature.

Contributed by the Gas Turbine Division of THE AMERICAN SOCIETY OF MECHANICAL ENGINEERS and presented at the 27th International Gas Turbine Conference and Exhibit, London, England, April 18-22, 1982. Manuscript received at ASME Headquarters December 15, 1981. Paper No. 82-GT-224.

Table 1 Analytical characterization of fuels tested

Synthetic fuel	Shale oil (Paraho)	H-coal (505–616 K)		H-coal (372–522 K)		No. 2 oil (Doped) ^c	
Physical and chemical properties							
Gravity, °API	30.0	18.4		30.0		36.3	
Pour point, K	308	<226		<226		<291(max)	
Flash point, K	366	336		297		330	
Gross heat of combustion, MJ/kg	45.04	42.36		43.55		45.70	
Kinematic viscosity, cs at 313K	14.45	2.56		1.12		1.9	
Kinematic viscosity, cs at 373K	3.15	0.99		0.62			
Conradson carbon residue, wt %	0.23	0.08		0.05		0.2(max)	
Aromaticity, % C _A	14	43		34			
Distillation, K at % (ASTM method)	(D2887) ^a	(D86)	(D-2887)	(D-86)	(D-2887)	(D-86)	(D86)
IBP	489	459	419	451	350	386	483
5	586	513	459	479	371	410	—
10	609	550	471	487	398	424	508
30	666	611	492	502	437	443	—
50	702	635	510	510	460	463	563
70	730	655	533	537	479	478	—
90	769	660 (at 84%) ^b	565	575	504	501	608
95	787	ND	581	597	514	516	—
EP	819	ND	635	607	561	536	638
Elemental analysis, wt %							
Hydrogen	12.80	10.03		11.38		13.2	
Sulfur	0.02	0.09		0.13		0.242	
Nitrogen	0.33	0.33		0.16		0.33	
Oxygen	0.33	1.2		1.4		nil	
Ash	0.01	<0.01		<0.01		<0.003	
Trace metals, ppm wt							
Titanium	<0.1	<0.1		<1.0		0.03	
Sodium	1.4	0.67		0.43		0.3	
Potassium	2.6	0.26		0.06		—	
Calcium	0.96	0.29		0.15		0.2	
Vanadium	0.12	0.1		0.9		0.07	
Lead	0.36	0.14		0.2		0.5	
Iron	6.7	3.7		0.7		2.0	
Phosphorus	<0.01	—		<0.2		0.3	

^aASTM procedure modified by decreasing rate to prevent foaming

^bSample decomposed (cracked)

^cSupplied by Exxon

Fuels Tested

The four fuels tested were:

- Paraho shale oil
- H-Coal[®] (372 to 522 K)
- H-Coal[®] (505 to 616 K)
- No. 2 oil doped with quinoline.

The Paraho shale oil was supplied by the Radian Corporation of Pasadena, Calif. and is the heavier fraction of highly hydrogenated distillate produced by the Paraho Company and upgraded by SOHIO. The H-Coal[®] fuel was obtained from the Hydrocarbon Research, Inc., Process Development Unit at Trenton, N.J. The No. 2 oil used for the baseline tests, as well as that doped with quinoline, was supplied by Exxon. Fuel analyses for the synthetic fuels, presented in Table 1, were performed by the Mobil Research and Development Corporation of Paulsboro, N.J. The analyses for No. 2 oil were obtained from two sources—Exxon and Westinghouse. In addition, fuel-bound nitrogen (FBN) determinations were made at the Westinghouse Research and Development Center on all the fuels in parallel with the water injection tests, to primarily assess the effect of storage on FBN. In the case of No. 2 oil doped with quinoline, the nitrogen determination varied somewhat in response to analysis in various versions of Kjeldahl method. A value of 0.33 wt percent, therefore, based on blending a known volume of quinoline with No. 2 oil, was used for the doped fuel. FBN contents (wt percent) were: 0.33 percent (0.27 percent) for the Paraho shale, 0.16 percent (0.16 percent) for the H-Coal[®] (505 to 616 K). The values shown in the parentheses represent

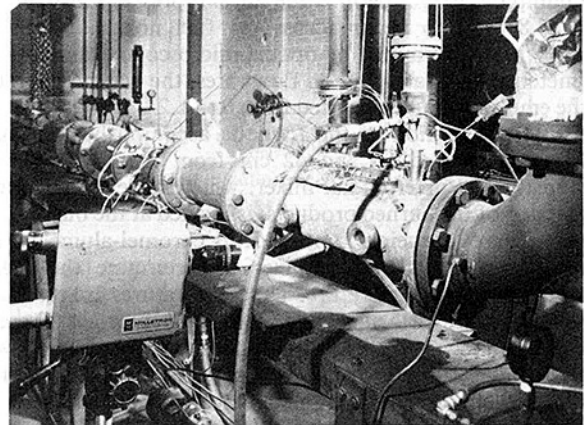


Fig. 1 Subscale test facility used

the Westinghouse determinations and were used for subsequent analyses in this paper. Note that the 0.33 percent value reported by Mobil for shale oil was from a sample shipped directly to the Westinghouse Combustion Turbine System Division at Concordville, Pa., and the Westinghouse Research and Development Center sample was a five-drum lot from the same refinery run by SOHIO but shipped directly to Pittsburgh. A small difference between the two, therefore, cannot be ruled out.

Experimental Program and Facilities

The test facility is shown in Fig. 1 and schematically in Fig.

2. Air is supplied by a Fuller rotary, sliding-vane air compressor, capable of generating 1.1 kg/s of air at 709 kPa (7 atm) pressure. Air supply pressure is controlled by a pneumatic bypass valve, and flow is measured by an air-flow-measuring nozzle located downstream of a pneumatically operated control valve. The air is passed through an indirectly fired heat exchanger and is preheated to a temperature of 590 K, which is representative of an actual Westinghouse gas turbine. For the water injection tests, an actual airflow of 0.68 kg/s was supplied to the test section that houses the combustor. The combustor itself is approximately 1/2 the diameter (0.14 m) of the Westinghouse commercial-scale combustor and is configured to resemble it for combustion purposes. The typical airflow split in this combustor is approximately 1/3 for primary zone combustion, 1/3 for cooling, and 1/3 for secondary quench. The full load fuel/air ratio is approximately 0.02. The total pressure drop is about 4 percent of the static pressure at full load conditions. It is equipped with six thermocouples to indicate wall temperatures.

An air-assist, pressure-atomizing fuel nozzle is used. The atomizing air assist is about 1 percent of the total airflow at a pressure ratio of 2.

The synthetic fuel is stored in a closed 200-L tank from which it is supplied to the combustor at 2430 kPa (24 atm) with a gear-type pump. No. 2 oil is supplied at the same pressure from a separate and larger supply tank equipped with a constant pressure fuel forwarding system. Provisions are incorporated into the fuel forwarding system that make it possible to transfer between the two fuels without interrupting test passage operation.

The water/fuel emulsifier assembly is shown in Fig. 3. Water and fuel at a high pressure (approximately 2100 kPa (21 atm)) are metered and passed through a mixing tube that converts this pressure drop to high shearing forces and creates an emulsion of water and oil. The mixing length of 46 cm was selected so that ~1050 kPa (10 atm) pressure drop through the mixing tube is obtained under full flow conditions. Operating under these conditions, i.e., 2100 kPa (21 atm) at the pump discharge, permits the normal pressure loss of 690 kPa (6.8 atm) to occur across the fuel nozzle. Emulsion stability was determined by optical microscope examination. By metering the water and oil flow rates, the water/fuel ratio in the emulsion could be varied from 0 to 1.2.

Visual observation of the flame is accomplished through sight ports located 15 and 42 cm from the dome of the combustor. An inverted hat mixer, which serves to complete the mixing of the burned products, is located at the burner exit plane. There are eight unshielded, chromel-alumel thermocouples located in the mixer to determine the mean combustor outlet temperature. The temperatures are recorded on a Leeds and Northrup Speedomax™ W recorder. There is also a gas analysis rake located in the mixer that extracts a representative sample of the combustion products. At the outlet of the test passage, a pneumatically operated butterfly valve is used to maintain a constant test pressure.

The exhaust gas sample is piped to the gas analysis panel through a heated line maintained at 670 K. Analyzers used for the various exhaust gas species were

Species	Analyzer
CO ₂	Beckman model 865 NDIR
CO	Beckman model 865 NDIR
UHC	Beckman model 108 FID
NO _x	TECO model 12A (chemiluminescent)
NO _x	Dynasciences model FS330 (wet cell)

Smoke was measured by a motor-driven RDC smoke-meter (made by Bacharach Instrument Co. of Pittsburgh) and conforming to ASTM D2156 standards. It was mounted

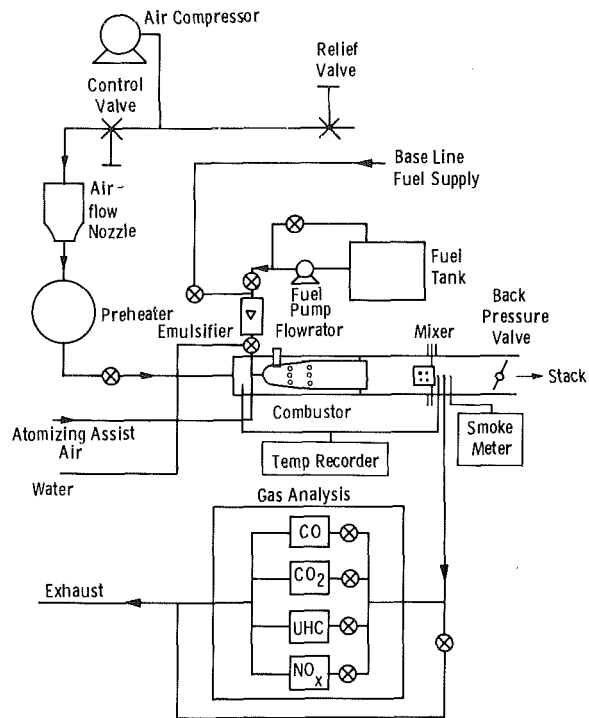


Fig. 2 Schematic of test facility

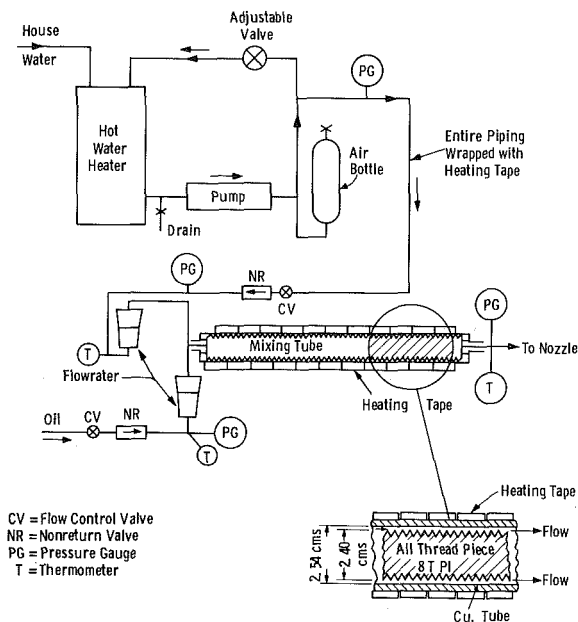


Fig. 3 Fuel water emulsifier system

adjacent to the test passage to avoid a long sampling line, thereby preserving the integrity of the sample.

The water injection tests were conducted at a nominal combustor outlet temperature of 1339 K and water/fuel mass ratios varying from 0.0 to 1.2. Baseline tests with No. 2 oil (dry and with water injection) were made immediately before the tests for each of the CDL and SDL fuels investigated. This procedure not only provided input on the performance of the system for a given test, i.e., by comparing the baseline data of the various tests, but also enabled direct comparisons to be made between a given CDL or SDL fuel and its baseline. Furthermore, these initial baseline tests with No. 2 oil, especially at low water injection rates, were used to check the

entire system for general agreement among the measured fuel/air ratio, the combustor temperature rise, and the CO₂ measurements. Only when the agreement was good did we proceed with the tests.

Test Results

The primary objective of these tests was to investigate the effect of water injection supplied as a fuel emulsion on NO_x from fuels with high FBN content. Also from these tests, the effect of FBN concentration and water injection rate on FBN conversion to NO_x could be determined. The secondary objective of these tests was to ascertain the effect of water injection on other emissions and combustion parameters, including wall temperature.

Testing was carried out essentially at gas turbine baseload conditions. Test parameters were as follows:

- Combustor inlet temperature – 590 K (600°F)
- Pressure – 405.3 kPa abs (4 atm abs)
- Relative humidity – 0
- Flow rate – 0.68 kg/s
- Combustor exit temperature – 1340 K (1950°F).

In carrying out the tests, we found differences, generally small, in the target and the actual operating conditions. NO_x corrections were made as follows

$$(NO_x)_{corr} = (NO_x)_{meas} \left[\text{EXP} \left(\frac{590 - T_{in}}{248} \right) \right] \left(\frac{4.00}{P_{in}} \right)^{1.5} \text{EXP}(19H)$$

where T_{in} is the inlet temperature in K, P_{in} is the pressure in atm, and H is the relative humidity of the inlet air to the test passage. This experimentally determined equation, based on previous work [5, 6], correlates well with NO_x experimental data derived from the test passage, with little divergence from the standard set of combustor inlet conditions in the absence of water injection. The validity of this equation under water injection was also found to be fairly good for low-FBN fuels. For high-RBN fuels, however, the validity has not been firmly established, but preliminary indications are favorable.

The practical difficulty of obtaining the respective CDL and SDL fuels with their FBN content removed precluded their use as the baseline fuels for determining thermal NO_x. The baseline tests were performed with No. 2 oil which, compared to the synthetic fuel, had almost negligible FBN. For a typical No. 2 oil with 0.008 wt percent FBN, approximately 4 ppm(v) NO_x would be generated at 1340 K if we assume complete conversion of FBN to NO_x. Under the same conditions, the thermal NO_x contribution would be approximately 110 ppm(v). On this basis we have assumed that the contribution of FBN to total NO_x is negligible for the baseline fuel. The substitution of No. 2 oil as the baseline fuel for FBN-free CDL and SDL fuels is much more significant.

The baseline-corrected NO_x emissions for all the subscale tests as a function of water/fuel mass for combustor exit temperatures in the range of 1310 to 1340 K (1900 to 1950°F) are shown in Fig. 4. In carrying out these tests, we noticed a much wider scatter than in our earlier tests, in which water was sprayed into the flame. Also shown on the figure as a dotted curve are the results obtained earlier [3] with water injection for very nearly identical conditions. The fact that most of the data lie below the dotted curve seems to say that the water-fuel emulsion form of water injection is much more efficient in reducing NO_x than is the system that sprays that water into the flame.

The effect of water injection on NO_x emissions with Paraho shale oil is shown in Fig. 5. The shale oil was heated to a temperature of 395 K. At this temperature its viscosity was

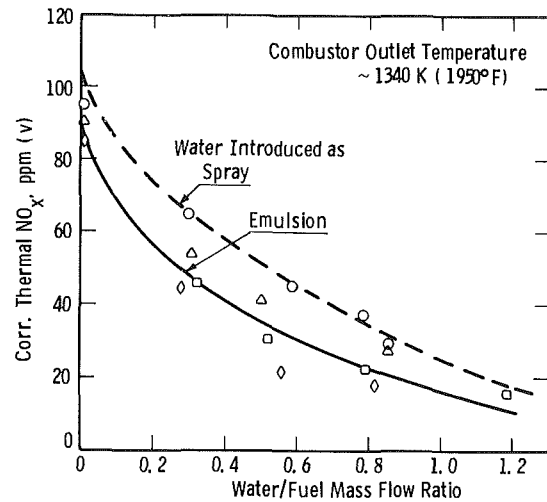


Fig. 4 Thermal NO_x emissions versus water/fuel ratio for No. 2 oil

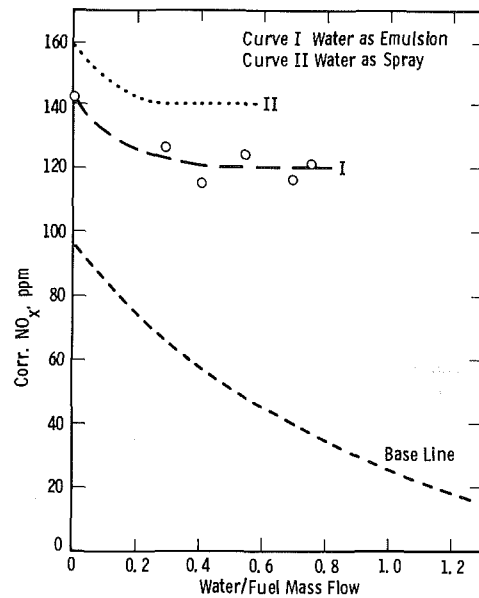


Fig. 5 Effect of water injection on NO_x emissions for Paraho shale

similar to that of No. 2 oil. The fuel forwarding system, therefore, as well as the emulsifying system, would suffer no serious difficulties from the high viscosity of the fuel. The water was heated to 355 K (180°F). These temperatures were maintained at the nozzle by wrapping the tubes with heating tape. The combustor exit temperature was maintained between 1310 and 1340 K (1900 and 1950°F). Curve I is for the present test, i.e., the water injection is in the form of an emulsion with fuel. Curve II is for earlier tests at almost identical conditions in which the water was sprayed into the flame. As pointed out before, the water supplied as an emulsion was more efficient in suppressing NO_x than when it was sprayed into the flame. At zero water injection rate, the corrected NO_x emission was 142 ppm compared with 160 ppm measured for the earlier system. Though this difference is small and various probable reasons can be ascribed to it, one important difference is the use of a much larger nozzle in the emulsion tests. This was required to handle the large combined flow of fuel and water. That the size of fuel droplets affects the thermal NO_x produced, as well as the FBN NO_x, is well known. The response of NO_x to water injection, however, is the same for both, i.e., a rapid drop of NO_x with

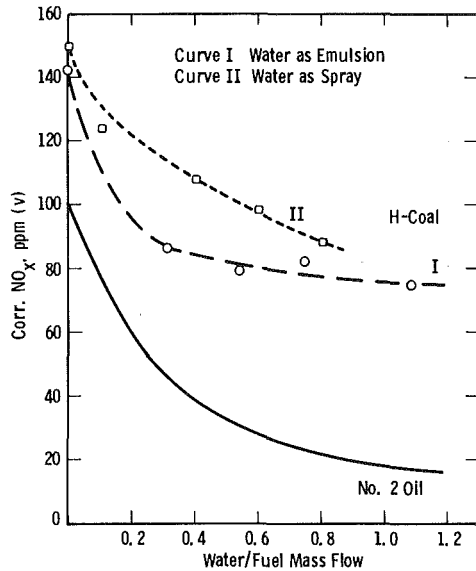


Fig. 6 Effect of water injection on NO_x emissions for H-Coal[®] (372 to 522 K)

water/fuel mass flow to about 0.4 and no change thereafter. At a water/fuel ratio of about 0.9, the flame became very unsteady and exhibited severe instability and high CO emissions.

The effect of water injection on NO_x emissions for H-Coal[®] (372 to 522 K) is shown in Fig. 6 as Curve I. The baseline curve with No. 2 oil is also shown for comparison. Curve II data from our earlier work is for the case when water was injected as a spray close to the fuel nozzle. Both curves show a similar trend, i.e., almost identical NO_x emissions at zero water injection rate, and a rapid drop of NO_x at low water/fuel ratios, with the emulsion form being much more effective. Curve I, however, tends to flatten out beyond a water/fuel ratio of 0.3, indicating that the suppression of thermal NO_x is about equal to the increased generation of FBN NO_x and resulting in no net change. That Curve II is higher than Curve I at the same corresponding water/fuel ratios and its slope is less (at the low water/fuel ratios) lead one to restate that the emulsion is much more effective than the spray in reducing NO_x .

The effect of water injection on NO_x emissions during H-Coal[®] (505 to 616 K) with a FBN content of 0.33 percent is shown in Fig. 7. Also included is the baseline curve for the corrected NO_x emissions. The response of NO_x to water injection of this fuel was similar to that in the earlier fuels, i.e., a rapid decrease in NO_x with small increases in water injection and leveling of NO_x reduction around a water/fuel mass flow of around 0.5. A small increase was observed in NO_x when the water/fuel ratio was increased further.

The effect of water injection on the doped No. 2 oil is shown in Fig. 8, along with the corresponding baseline data. The trend observed with this fuel was very similar to that observed with the other synthetic fuels.

In order to understand better the interaction of fuel FBN content and the effectiveness of water injection, we investigated the conversion of FBN to NO_x with water injection for the various fuels. Conversion of fuel nitrogen to NO_x is defined as follows:

$$x \left\{ \frac{\text{conc. of nitrogen in exh. NO}_x \text{ at a given water injection rate}}{\text{conc. of nitrogen in base-line exh. NO}_x \text{ interpolated to the set water injection rate}} \div (\text{mass of nitrogen in fuel}) \right\}$$

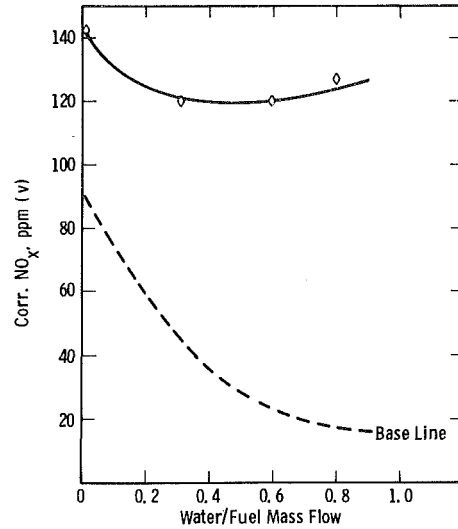


Fig. 7 Effect of water injection on NO_x emissions for H-Coal[®]

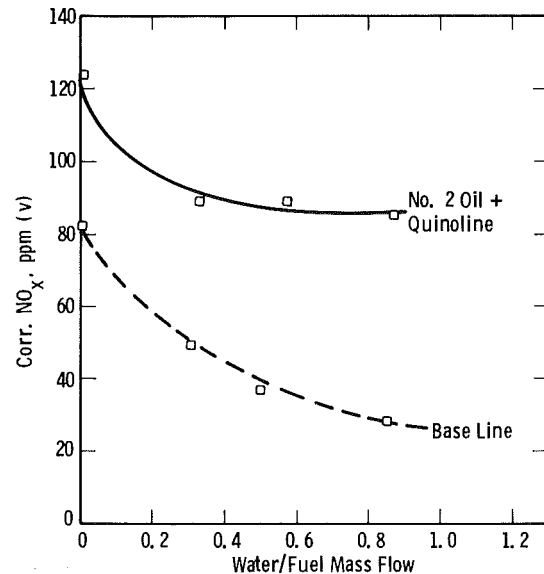


Fig. 8 Effect of water injection on NO_x emissions for No. 2 oil doped with quinoline

As was explained earlier, the practical difficulty of obtaining the respective CDL and SDL fuels with their FBN content removed forced the use of No. 2 oil as the baseline test fuel. Thus, the first term of the numerator is derived from CDL or SDL combustion and the second from No. 2 oil combustion. The constant takes into consideration the assumed molecular weight of the exhaust gas, the air/fuel ratio, and the mass of water injected. We evaluated the test data for the conversion of FBN to NO_x versus water injection based on the NO_x measured for the CDL or SDL fuel and the NO_x value corresponding to the baseline fuel for the same water/fuel ratio. We ignored small differences in fuel flow and hydrogen content, as well as in the exhaust gas molecular weight for the test fuel and the baseline fuel.

The conversion of FBN to NO_x with water injection is shown in Figs. 9-12 for the four fuels, respectively. The data are for a combustor operating at an inlet air temperature of 590 K at a pressure of 405.3 kPa (abs) and zero relative humidity, and with a combustor exit temperature of approximately 1340 K.

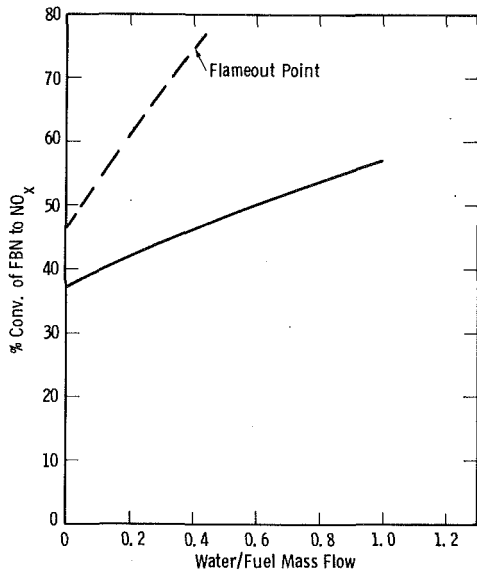


Fig. 9 Effect of Water Injection of FBN Conversion to NO_x for Paraho shale oil

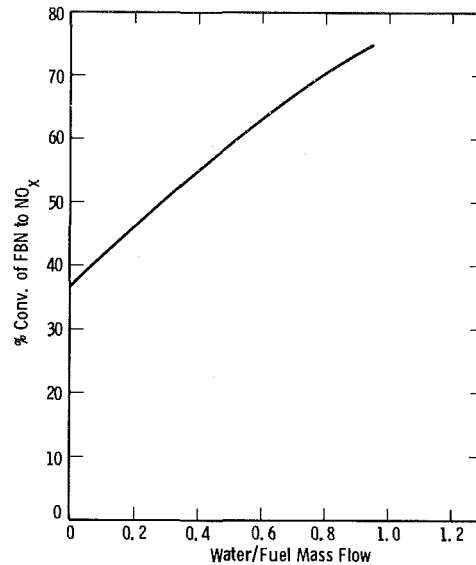


Fig. 11 Effect of Water Injection on FBN Conversion to NO_x for H-Coal[®] (505 to 616 K)

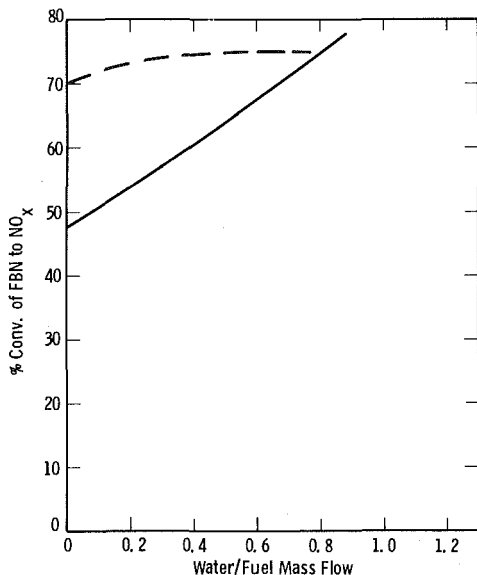


Fig. 10 Effect of Water Injection on FBN Conversion to NO_x for H-Coal[®] (372 to 522 K)

In all cases and in agreement with our previous work, the conversion of fuel nitrogen to NO_x increases with increasing water injection. Figure 9 illustrates the Paraho shale oil with a FBN content of 0.33 wt percent. The percent conversion was found to increase from 37 percent at the no water injection point to about 52 percent at a water/fuel mass flow rate of 1.0. The dotted curve in this figure is for an earlier test in which the water was sprayed into the flame rather than supplied as an emulsion. Also, in those tests a water/fuel mass flow rate of 0.4 could not be exceeded because of combustor flameout. It is obvious when the two curves are compared that water supplied as an emulsion is better able to suppress the conversion of FBN to NO_x at least as far as shale oil is concerned.

Figure 10 is for H-Coal[®] (372 to 522 K), which was the lowest FBN fuel tested. The solid curve is for the current series of tests in which the water was injected as a fuel emulsion. The dotted curve is for our previous tests, in which

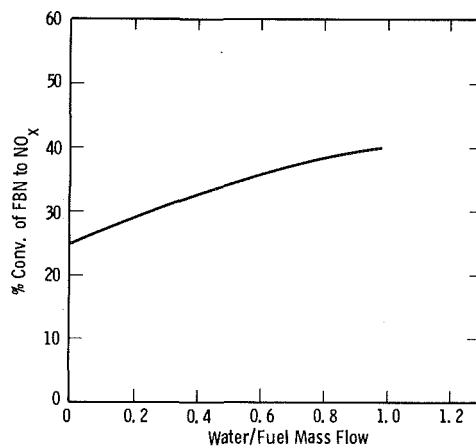


Fig. 12 Effect of water injection on FBN conversion to NO_x for doped no. 2 oil

the water was sprayed into the flame. It is obvious from these tests that supplying water as a fuel emulsion is much more effective in suppressing conversion of FBN to NO_x at low water/fuel mass flow rates. At high water/fuel mass flow rates, however, the reverse may be true.

Figure 11 is for H-Coal[®] (505 to 616 K) with a FBN content of 0.33 wt percent. This fuel has the same FBN as Paraho shale oil and the doped No. 2 oil. The conversion was found to increase from 37 percent at no water injection to about 75 percent at one-to-one water/fuel mass flow. For No. 2 oil doped with quinoline, the conversion to the same FBN content was much lower (Fig. 12), 25 percent at zero water injection to about 40 percent at one-to-one water/fuel mass flow rate.

The significance of these changes in the conversion of FBN to NO_x with water injection is too complex to be fully comprehended in a work as brief as this. This investigation is continuing and will, we hope, lead to knowledge of those factors that influence the conversion of FBN to NO_x in CDL and SLD fuels in the presence of water injection.

Smoke Emissions

Water injection as an emulsion with the fuel appeared to

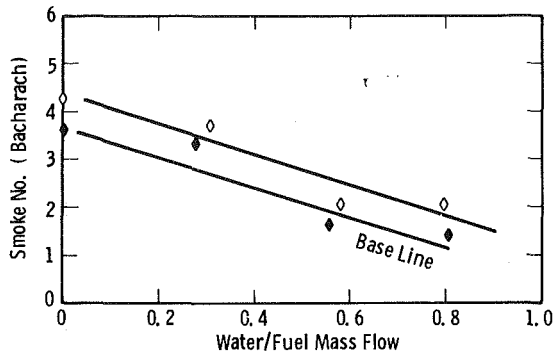


Fig. 13 Effect on water injection on smoke for H-Coal[®] (505 to 616 K)

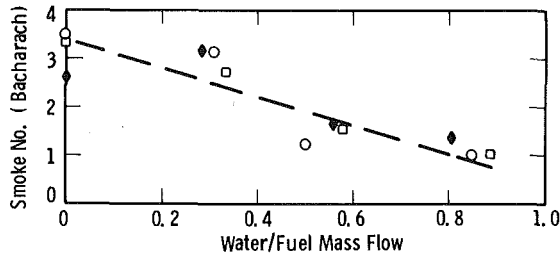


Fig. 14 Effect on water injection on smoke for the baseline fuel and doped no. 2 oil

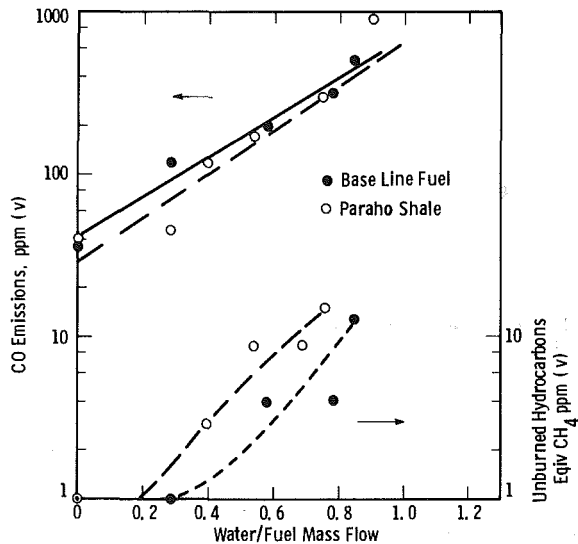


Fig. 15 Effect of water injection on CO and UHC emissions for Paraho shale oil

have a beneficial effect on smoke emissions. The use of emulsions has shown great promise in practical combustion systems in reducing smoke [7], presumably because of:

- Chemical kinetic effects, such as increased hydroxyl radical concentration and its high effectiveness in oxidizing soot precursor species
- Physical effects, such as the explosion of the droplets of water in fuel causing better atomization and improved mixing of the burning substances.

The smoke emission data obtained with H-Coal[®] (505 to 616 K) and the baseline fuel are shown in Fig. 13 as a function of water/fuel mass flow. H-Coal[®] tended to yield higher smoke than the baseline fuel by about half a Bacharach smoke

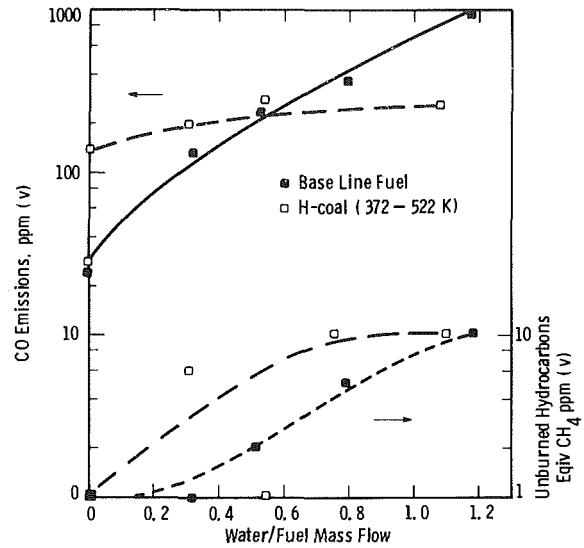


Fig. 16 Effect of water injection on CO and UHC emissions for H-Coal[®] (372 to 522 K)

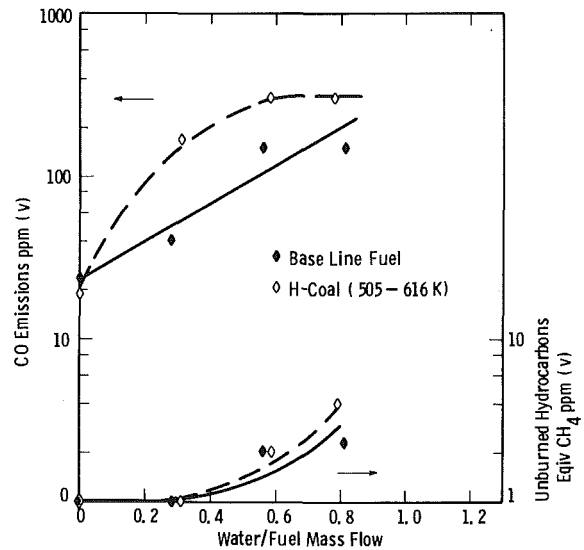


Fig. 17 Effect of water injection on CO and UHC emissions for H-Coal[®] (505 to 616 K)

number. Under dry conditions, the H-Coal[®] gave a smoke number of 4.2, and the baseline fuel 3.6. With increasing water injection, smoke decreased to about 1.8 for H-Coal[®] and 1.1 for No. 2 oil at a water/fuel mass flow of 0.8.

The smoke emission data for the doped and pure No. 2 oil shown in Fig. 14 showed almost identical values, indicating that the dropout quinoline did not affect smoke emissions. Smoke numbers close to 3.5 (Bacharach) were observed under dry conditions and found to decrease with water injection to about 1.0 at a water/fuel mass flow ratio of 0.9.

The results observed for Paraho shale oil and H-Coal[®] (372 to 522 K) showed a similar trend, i.e., a decreasing smoke number with an increasing water flow rate. The smoke readings for these tests, however, including the baseline fuel, were rather high, and, therefore, the absolute smoke numbers were suspect. The smoke emission data, therefore, are not presented for these fuels.

Carbon Monoxide and Unburned Hydrocarbon Emissions

The CO and UHC emissions in the exhaust of a well-

designed combustor represent that portion of the fuel that at some point in the combustor has been quenched sufficiently to inhibit combustion. This quenching results in CO and UHC emissions significantly higher than those based on equilibrium considerations. Injecting water increases this quenching effect and, thus, from a practical viewpoint, decreases combustion efficiency.

The effect of water injection on CO and UHC emissions for Paraho shale oil is shown in Fig. 15, along with that observed for the baseline fuel. The CO emissions are plotted on a log scale. Paraho shale oil was found to yield slightly lower CO emissions than the baseline fuel but slightly higher UHC emissions at the same corresponding water/fuel mass flows.

The CO emissions increase rather significantly at high water/fuel ratios, over an order of magnitude above the water/fuel range of 0 to about 0.9. The corresponding increase of UHC is about 1.5 orders of magnitude. At very high water flow rates, however, these increases become precipitous.

Figure 16 compares the CO and UHC emissions of H-Coal[®] (372 to 522 K) and the baseline fuel. Increased CO emissions occur at low water/fuel mass flow conditions. Beyond about 0.5 water/fuel mass flow, however, the measured CO for H-Coal[®] was less than that for the baseline fuel. UHC emissions remained consistently higher than H-Coal[®].

Figure 17 shows the CO and UHC emissions observed for H-Coal[®] (505 to 616 K) compared to the baseline fuel. CO and UHC emissions were consistently higher for H-Coal[®] than for the baseline fuel.

Conclusions

The results of this investigation carried out on a static combustor test rig demonstrate the degree of NO_x reduction possible with water injection of high-FBN synthetic fuels and the degree of conversion of the nitrogen in the fuel to NO_x. The conclusions are valid for the range of combustor conditions covered. No effort was made to optimize the water injection system, the fuel spray pattern, or the combustor air distribution. The combustor had a lean front-end reaction zone followed by a quick quench, i.e., a mode typical of a conventional combustor.

Water injection becomes extremely ineffective in inhibiting NO_x in fuels containing even moderate amounts of FBN.

The effectiveness of water in reducing NO_x with FBN fuels occurs only at low to moderate water flow rates and reduces NO_x only marginally. At high water flow rates NO_x emission is almost independent of water flow rate.

The conversion of fuel-bound nitrogen NO_x at zero water injection and baseload combustor exit temperature varies widely. It is as high as 47 percent for H-Coal[®] (372 to 522 K) with 0.16 percent FBN and as low as 25 percent for the doped No. 2 oil. For Paraho shale oil and H-Coal[®] (505 to 616 K) with 0.33 percent FBN, the conversion was approximately 37 percent. With increased water injection, conversion of FBN to NO_x rises.

Smoke emissions were lowered with water injection in the form of a water-in-oil emulsion.

The emissions of CO and UHC generally increased with water injection. This increase was small at relatively moderate water injection rates where most of the NO_x reduction occurred. At high water/fuel mass flow rates (>1), however, drastic increases in CO were observed.

Acknowledgments

This work was performed with the support of the Electric Power Research Institute Contract No. RP 1345-1. The authors wish to acknowledge the contributions of the following persons and thank them for their assistance:

R. M. Chamberlin
S. M. DeCorso
T. P. Sherlock
L. Paulukonis

References

- 1 Zeldovich, J., "The Oxidation of Nitrogen in Combustion and Explosions," *Acta Physicochimica U.R.S.S.*, Vol. 21, No. 4, 1946, p. 577.
- 2 Vermes, G., Toof, J. L., and Cohn, A., "The Modeling of NO_x Generation from Coal-Derived Liquids in Combustion Turbines," Paper 79-JPGC-GT-4, presented at the Joint ASME/IEEE/ASCE Power Generation Conference, Charlotte, N.C., Oct. 8-10, 1979.
- 3 Mulik, P. R., Singh, P. P., and Cohn A., "Effect of Water Injection for NO_x Reduction With Synthetic Liquid Fuels Containing High Fuel Bound Nitrogen in a Gas Turbine Combustor," ASME Paper No. 81-GT-51.
- 4 "Gas Turbine Combustor Performance on Synthetic Fuels," Vol. 1, prepared by Westinghouse Electric Corporation, EPRI, Contract RP 989-1, published July 24, 1980.
- 5 Marchionna, N. R., Diehl, L. A., and Trout, A. M., "Effect of Inlet Air Humidity, Temperature, Pressure, and Reference Mach Number on the Formation of Oxides of Nitrogen in a Gas Turbine Combustor," NASA TN D-7396, Oct. 1973.
- 6 Vermes, G., "A NO_x Correlation Method for Gas Turbine Combustors Based on NO_x Formation Assumptions," ASME Paper No. 74-WA/GT-10, 1974.
- 7 Dryer, F. L., "Water Addition to Practical Combustion Systems—Concept and Application," 16th International Symposium on Combustion at Cambridge, Mass.

The Gas Turbine Heat Exchanger in the Fluidized Bed Combustor

C. F. Holt

A. A. Boiarski

H. E. Carlton

Battelle-Columbus Laboratories,
Columbus, Ohio 43201

In a current research and development program a coal-fired atmospheric fluidized bed combustor is being designed to supply the heat to a closed cycle gas turbine cogeneration system. The major technical effort is directed towards the design of the in-bed heat exchanger, which is required to operate near bed temperature. This high temperature (850° C) exposes the heat exchanger tubes to potentially severe sulfidation. The corrosion behavior depends upon the intimate details of the bed environment and may be related to the occurrence of localized areas of low oxygen partial pressure and high sulfur partial pressure. This paper describes a series of measurements of oxygen partial pressure at various locations within a fluidized bed. The bed, containing densely packed heat exchanger tubes, was operated under various conditions to observe the effect of coal mixing and devolatilization on local oxygen activity. Substantial variations of oxygen partial pressure (below 10^{-14} atmospheres) were observed. It was noted that these locally severe variations could be substantially modified by changes in coal mixing (as through coal port design). The experiments with varying coal size suggest that rapid devolatilization is desirable and would reduce the extent of locally corrosive environments.

Introduction

The coal-fired, closed-cycle gas turbine (CCGT) cogeneration system promises the simultaneous generation of electrical power and useful process heat while using less coal than competing steam turbine based systems. The gas turbine working fluid is completely isolated from the products of coal combustion. In a current research and development program a coal fired atmospheric fluidized bed combustor is being designed to supply heat to such a system. This program has been described elsewhere [1]. The program is directed at fired heater concepts suitable for application to CCGT/cogeneration systems having 25 to 50 MWe output. The major technical development challenge is in the development of the in-bed primary heat exchanger. To supply working fluid temperatures to the turbine inlet of 1550°F (850°C), the heat exchanger is required to operate within 100° F (40°C) of the bed temperature. The objective is to design a system to utilize a high sulfur coal such as Illinois No. 6 (approximately 4 percent sulfur). In the presence of sulfur the metal heat exchanger tubes are subject to strong sulfidation attack.

The Heat Exchanger Environment. Fluidized bed combustion has been studied extensively by many investigators [2], and the basic operating principles are known even if they are not fully understood.

The dense bed regime in an AFB combustor consists of a mass of particles, usually a sulfur absorber such as limestone or dolomite, expanded by air flow from beneath. The bed also contains approximately 0.1 percent coal. The size of the

particles is 20 to 60 mesh (250 to 850 μ), and the fluidizing velocity ranges from 1.0 M/S to 2.5 M/S. Particle motion within the bed is complex, but in general, two distinct phases of motion prevail: (i) the bubble phase, which can be described as slugs of rising air characterized by low-density, high-velocity, particle flow; and (ii) the dense bed phase, characterized by high-density, low-velocity particle flow. Measurements in an AFB combustor at Battelle with a superficial gas velocity of 1.8 M/S showed that approximately 30 percent of the particles had velocities greater than the superficial gas velocity, 10 percent had velocities greater than twice the superficial velocity, and a few had velocities greater than four times the superficial gas velocity.

The corrosive character of the dense bed is more complex than it would at first appear. In spite of the inherent good mixing characteristics of fluidized beds, the oxygen partial pressure inside the bed is by no means uniform. In situ oxygen probe measurements made at Battelle (3) indicate that the partial pressure of oxygen in the bed could be as low as 10^{-14} atmospheres. The sulfur released from the burning coal has some residence time in the bed before it is captured by the sorbent, so a significant sulfur partial pressure is expected.

Previous corrosion experiments in various fluidized-bed coal combustors have indicated that some of the commercially available heat exchanger alloys can undergo very severe sulfidation attack within the in-bed environment [4-7]. This corrosive potential is much more severe for the Brayton cycle than for the Rankine cycle because of the elevated metal temperatures (850°C compared to temperatures below 538°C).

Observations of such corrosion behavior have not been systematic nor correlated to bed operating or design variables.

Contributed by the Gas Turbine Division of THE AMERICAN SOCIETY OF MECHANICAL ENGINEERS and presented at the 27th International Gas Turbine Conference and Exhibit, London, England, April 18-22, 1982. Manuscript received at ASME Headquarters December 15, 1981. Paper No. 82-GT-225.

It is of considerable interest to know whether the regions where low oxygen partial pressures occur within the bed correspond to the locations where sulfidation attack has been observed.

The average oxygen content of the in-bed FBC environment is approximately 3 volume percent which implies a relatively oxidizing environment (20 percent excess air). This relatively oxidizing environment might be expected to pose no exceptional corrosion threat to in-bed heat exchanger materials. However, data acquired with an in situ stabilized zirconia solid electrolyte probe in the Battelle 0.6M AFBC showed a substantial time dependent oscillation of the PO_2 .

Measurements were taken with an in-bed heat exchanger having tube size and spacing identical to that proposed for a full-scale primary heater of a 25 MWe CCGT cogeneration system. Figure 1, taken from [4], presents the PO_2 as a function of time at the center line of the bed for two positions. In the center of the bed about 58 cm above the coal feed port, sharp excursions of PO_2 to very low values from a baseline reading of approximately $10^{-1.5}$ atm occurred with a frequency of approximately 1 Hz indicating that the bed was well mixed in this location. At the bottom of the heat exchanger about 20 cm above the coal feed port, the PO_2 was found to oscillate between 10^{-1} and 10^{-14} atm. The time spent at each extreme depended on the exact location with respect to the entering coal stream.

The surprisingly low PO_2 readings at the bottom of the heat exchanger suggested that in the region of the coal feed port the heat exchanger tubes would be subjected to severe sulfidation.

As a result of these data, it was decided that a more extensive study to characterize the heat exchanger environment was warranted. Results from this study, reported below, had as its objective to discover what factors influenced the locally strong reducing zones and what effect operational or design changes might have on overall bed performance.

The Characterization Experiments

It seems reasonable to presume that the release of volatile matter can cause locally reducing conditions—especially above the coal feed port. The volatiles can account for as much as 50 percent of the coal heating value. Depending on relative devolatilization, mixing and particle residence times, fuel rich regions may exist, especially around the coal feed port or regions of poor fluidization.

It has been suggested that volatiles released from injected coal may rise through the bed in a plumelike path [8, 9]. If lateral mixing is not strong, then the dense volatiles plume may burn in a diffusion flame with the surrounding oxygen creating a zone of very low oxygen partial pressure. The geometry of the coal injector region and the turbulent bubbling motion interactions with the volatiles release would have a strong impact on the combustion environment. This could in turn have a strong influence on the corrosion behavior of immersed heat exchanger surface.

Since the distance from the coal feed port to the bottom bank of heat exchanger tubes may be critical in allowing sufficient mixing of the coal, to provide approximately the same distance as was intended for the full scale unit, this distance was increased from 20 cm to about 53 cm as shown in Fig. 2.

The 2-in-dia (5-cm) tubes entered the combustor and returned through the west wall. The mitre bends along the east wall allowed a gap of approximately 0.5 in. (1.3 cm) or less.

The Test Matrix. In the characterization test series as outlined in Table 1, conditions were chosen in an effort to demonstrate the effect of mixing and of devolatilization on the local reducing or oxidizing conditions. Test 1 represented the base condition and was also used during the earlier

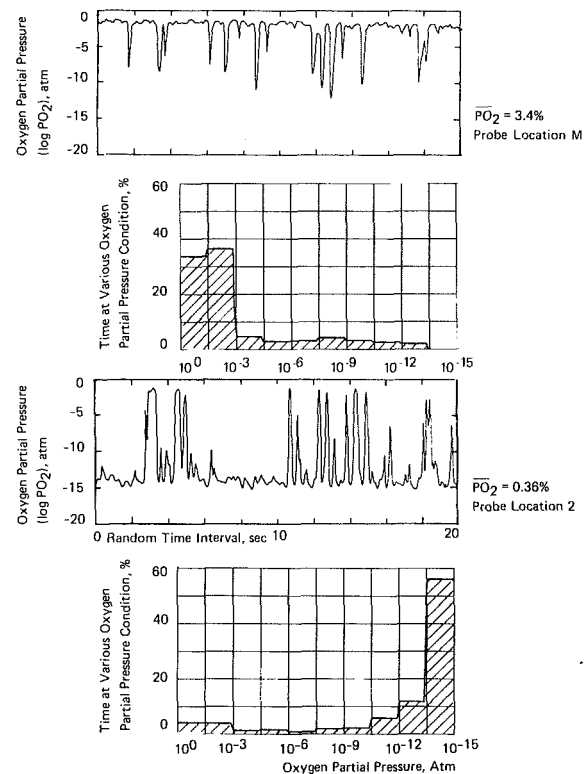


Fig. 1 Oxygen partial pressure versus time with corresponding histograms (from [1])

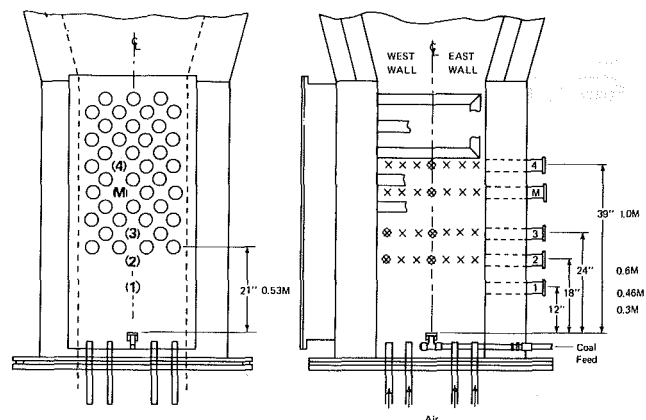


Fig. 2 (Locations within fluidized bed combustor where diagnostic data were measured (X = PO_2 data, \otimes = gas sampling data))

measurements described above. To examine the effect of mixing in the vicinity of the coal feed port, the percentage of total combustion of air used to convey the coal into the combustion zone was varied from a low of 5 percent to a high of 20 percent. Since a combustor containing a CCGT heater may be run at various conditions, a low superficial velocity case was included. Excess air was varied from a low of 10 percent to a high of 50 percent. The mixing of coal particles is also likely to be affected at least locally by the design of the coal feed port. Therefore, another coal port was installed and the above conditions were rerun. The two coal ports are shown in Figs. 3(a) and 3(b). The first port is simply a .063-m-dia plate fixed over the coal conveying pipe. The second port contains a 0.15-m-dia plate fixed over top of the coal conveying pipe. However, to enhance the mixing, the distributor plate bubble caps in the immediate vicinity of the coal port

Table 1 Test conditions during characterization experiments

Test no.	Port type	Description
1	A	Base conditions ^a
2	A	High conveying air (20%)
3	A	Low conveying air (5%)
4	A	High excess air (50%)
5	A	Low superficial gas velocity (3.5 FPS)
7	A	Coarse coal (-4 + 30 mesh)
8	A	Fine coal (-30 mesh)
9	A	Coke
10	A	Base conditions repeated
11	B	Base conditions
12	B	High conveying air (20%)
13	B	Low excess air (10%) high conveying air
14	B	High excess air (50%) high conveying air
15	B	Low superficial gas velocity (3.5 FPS)

^a Temperature = 1650°F (900°C)
 Superficial velocity = 6 FPS (1.8 M/S)
 Excess air = 20 percent
 Conveying air = 10 percent of total
 SO₂ in flue = 1.2 lb/mm Btu
 Bed depth = 58 in (1.47 m)
 Fuel: Illinois no. 6 coal
 Coal size: -8 mesh
 Limestone size: -8 + 20 mesh

Table 2

Coal	Size mesh	Particle diameter	Devolatilization time, s ^a
Illinois No. 6	-8	<2.5 mm	<7.1
	-30	<0.5 mm	<0.6
	-4 + 30	0.5 mm - 4.8 mm	0.6 - 22
Fluid coke	-8	<0.5 mm	0.6 - 22

^aFrom [8, 10]

were blocked off and all the air which would have passed through them was redirected through two tubes into a plenum chamber, the bottom acting as the splash plate against which entering coal was deflected. Holes in the periphery and in the bottom of the plenum help direct and disperse the coal particles.

In an attempt to vary the coal devolatilization time from less than 1 s to greater than 20 seconds, two additional coal sizes were used as shown in Table 2. The estimated devolatilization time which might be associated with these sizes is also indicated. In an effort to burn a material with little or no volatiles release, a fluid petroleum coke was included (Test No. 9).

Results

Four levels in the bed were probed and PO₂ data were acquired at seven radial positions for each bed level. Typical results are shown in Fig. 4 for the baseline conditions. Here the oxygen partial pressure fluctuations over a 20-s time interval are displayed at three radial locations and repeated for 3 levels in the bed (probe positions 2, 3, 4 marked on Fig. 2). For each 20-s display of data a histogram has been prepared to indicate the percent of time the PO₂ is registering a particular value. On the west wall of the combustor (position 3) the PO₂ values indicate very highly reducing conditions with a high percent of the time spent below 10⁻¹⁴ atmospheres. At the center of the bed almost 90 percent of the time the environment is above 10⁻² atmospheres. At the east wall we have a mixed condition with the local PO₂ spending nearly equal time below 10⁻¹⁴ atmospheres as above 10⁻³

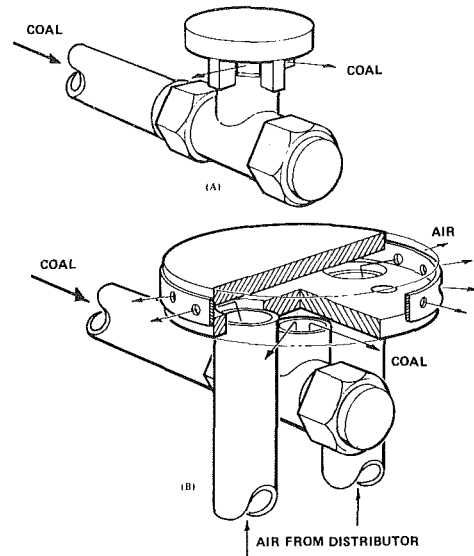


Fig. 3 Coal feed ports used (tests 1-10, port A; tests 11-15, port B)

atmospheres. The center line position seems to be very oxidizing and suggests a healthy condition for the heat exchanger tubes. The center line data taken at probe position 2 is in marked contrast to the data of Fig. 1. The only difference between these data is that the depth of bed beneath the heat exchanger tube bundle was increased from 0.23 to 0.53 m. The reducing zone originally observed at this location is not seen. Apparently the physical dimensions of the mixing zone beneath the tube bundle can change the local oxygen activity level substantially.

It would seem that any significant time spent under strongly reducing conditions may result in corrosion through sulfidation. It has not yet been established just what PO₂ is sufficient for serious degradation to take place. The relationship between low oxygen partial pressure, time, and the presence of sulfur is under study in the tests which have immediately followed these and have been reported in the references. The above test was run with coal feed port "A" (Fig. 3(a)).

Gas sampling was carried out only for the base test condition (mainly CO₂ and CO). The indication of reducing zones at the combustor walls near the bottom of the heat exchanger array was corroborated by gas sampling data as shown in Fig. 5. This data indicates that higher quantities of CO and CO₂ exist near the walls than at the combustor center line, but less oxygen is present in the wall region. A comparison was also made of oxygen gas sampling data to the time averaged output of the zirconia oxygen sensor. The results indicated that the trends in increasing and decreasing average oxygen content were identically shown by both. Throughout the test series the bed operated as a very efficient and well-behaved combustor. Table 3 gives a summary of combustion efficiency and calcium to sulfur mole ratio for sulfur emissions, about 1.5 lb/mm Btu (645 ng/J).

The terms oxidizing and reducing are relative. However, for purposes of this discussion we will define an "oxidizing" potential as PO₂ above 10⁻³ atmospheres and a reducing potential as that below 10⁻¹² atmospheres. These lines are drawn on the figures. Using these criteria, an oxidizing and reducing potential value can be chosen for each data set and plotted as a function of operating condition as shown in Fig. 6. Here the four radial positions probed, two below the heat exchanger and two within, are shown. The lowest position, No. 1, is 0.30 m above the coal feed port and 0.29 m below the heat exchanger tube bundle. Two sets of data are displayed,

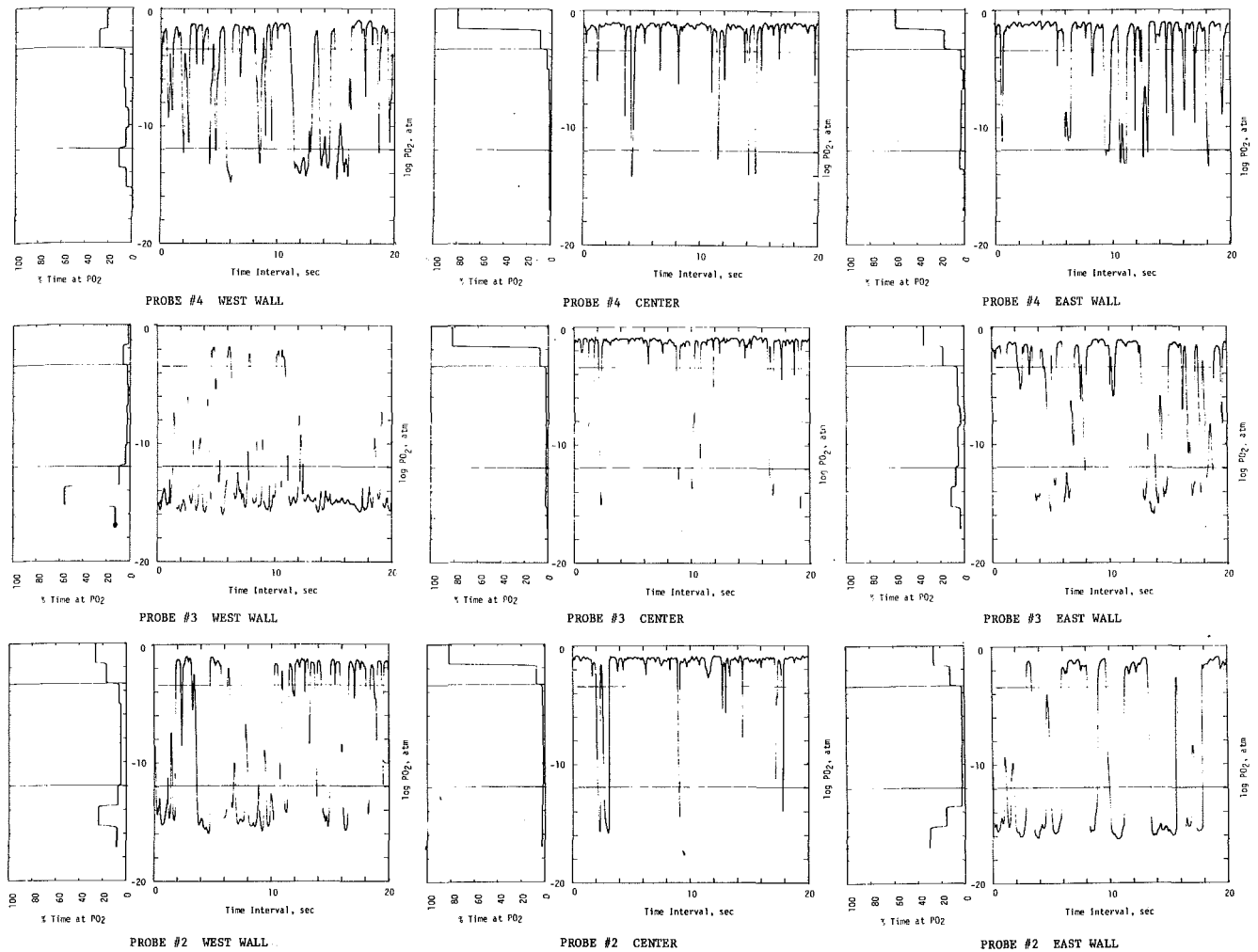


Fig. 4 Oxygen partial pressure versus time with corresponding histograms, base conditions test no. 10

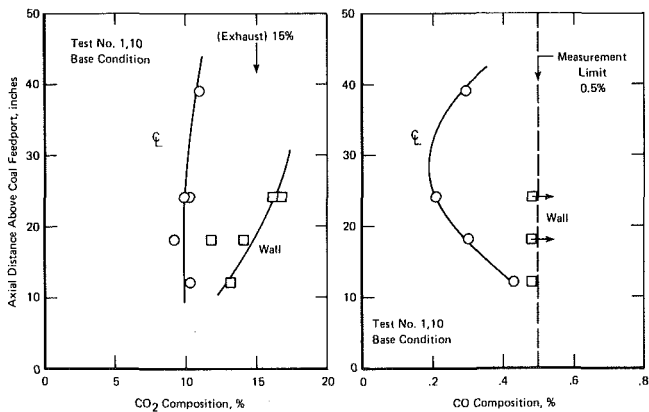


Fig. 5 Wall and Centerline CO, CO₂ concentrations as a function of axial location within the bed (gas sampling data)

which were taken several days apart and after substantial changes in operating conditions were made. The return to base conditions also meant a return to the same PO₂ distribution. The PO₂ measurements appear to be a reliable and repeatable diagnostic indicator of the bed environment.

The Role of Coal Mixing. The distribution of relative oxidizing and reducing conditions throughout the bed appears

Table 3 Run summary

Run no.	Bed temperature, °F	Combustion efficiency, percent	Ca/S ratio
1	1635	97.8	2.1
2	1640	98.8	3.7
3	1650	98.8	3.1
4	1640	99.0	3.5
5	1645	98.6	3.2
7	1640	97.4	2.7
8	1630	98.8	4.0
9	1695	85.7	—
10	1630	97.7	3.4
11	1650	97.8	3.0
12	1655	98.4	3.1
13	1650	97.9	3.2
14	1655	98.3	3.9
15	1650	99.1	3.4

to be the result of the mixing of the coal particles as influenced by the geometry of the bed and the heat exchanger. In this case, the wall region tends to be more reducing, suggesting several possible explanations. Perhaps there is a higher carbon content along the wall where there is likely to be net downward movement of the coal/char particles. In the center the moving coal particles might be expected to be moving generally upward more rapidly. The presence of horizontal heat exchanger tubes closely packed plays some

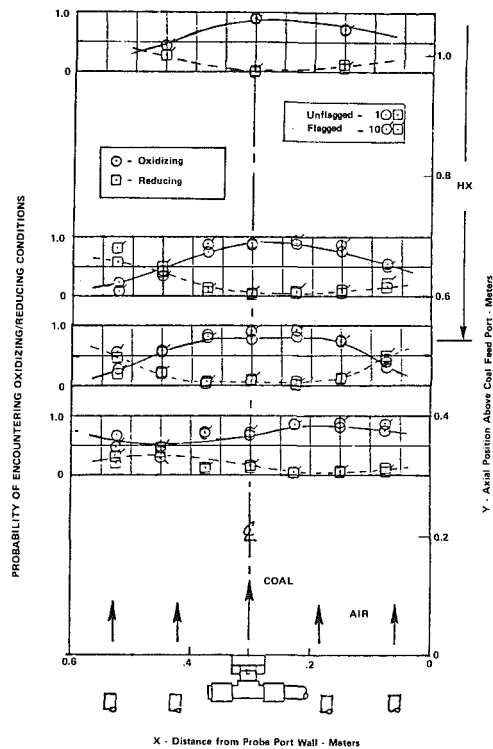


Fig. 6 Oxidizing/reducing potential as a function of in-bed position (test 1, 10 base condition)

role in moderating the mixing within the bed. The rising bubbles, characteristic of the fluidized bed in this operating range, are likely to be zones of highly oxidizing gas having originated at the distributor plate bubble caps. The number of bubbles rising in the center of this test bed is likely to be large compared to the "wall region" (a zone within 0.8 m to 0.15 m of the wall as suggested by the PO_2 data). Thus, the emulsion or dense phase near the wall should tend to be reducing or, at least on the average, less oxidizing than the center. This is only speculative since no measurement of bubble motion has yet been attempted. This, coupled with the fact that there has to be a net downward movement somewhere in every bed, makes the wall region the most likely to sustain locally low oxygen partial pressures. For larger beds, where "wall effects" may not exist in the vicinity of the coal port, there will be a net downward movement of solids at selected zones in the bed. These zones are likely to be determined by characteristics of the air distributor plate and, thus, by local fluidization conditions. If the reducing conditions are associated with such regions, then in larger beds they are likely to be more randomly located but have the same characteristics as those measured here near the wall. This is all speculation; however, as part of this current program, tests are to be conducted in larger fluidized beds with plan areas of 3.3 m^2 to examine such issues.

Changing to a high excess air (from 20 percent to 50 percent—Test No. 4) produces substantial changes in the PO_2 distribution as shown in Fig. 7. Conditions everywhere are improved—especially within the heat exchanger. The corrosion environment at the bottom of the heat exchanger may still be deleterious, as shown by the excursions to relatively low PO_2 values near the walls (nearly 40 percent of the time below 10^{-12} atm).

The Role of Coal Volatile Matter. It seems reasonable to presume that the release of volatile matter can cause locally reducing conditions, especially around the coal feed port. This situation has been discussed in the literature.

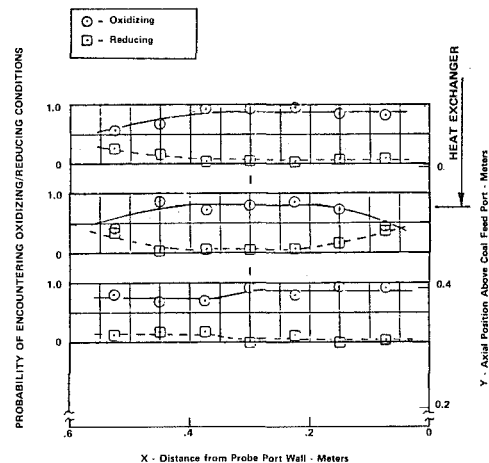


Fig. 7 Oxidizing/reducing potential as a function of in-bed position (test no. 4, 50 percent excess air)

To examine the influence of the released volatile matter, three coal sizes were run in addition to the base coal (Test Nos. 7, 8, and 9). Fine and coarse coal were chosen with the expectation that all other things being equal a reduction in coal size would cause a more rapid release of volatile matter, thus confining the reducing zones to the lower portion of the bed. Coke was chosen to represent a case where volatiles would be nearly absent. The results are shown in Figs. 8 and 9. Coke with less than 5 percent volatile matter showed little indication of significant reducing conditions anywhere in the bed where measurements were taken. Generally speaking, the fine coal resulted in conditions significantly less reducing than the base coal and the coarse coal size. The results suggest that the coal devolatilization process is a factor affecting the presence of the reducing zones and that coal size has an observable influence on coal devolatilization rate within a fluidized bed. This influence is felt throughout the bed, not just near the coal feed port.

The spatial variation of reducing potential for all four conditions is shown in Fig. 9. There is a definite effect of coal size on the local oxygen activity which could be attributed to both the effect of mixing due to coal size and devolatilization time. The one striking difference is the result with coke. Here the entire bed zone surveyed appears to be highly oxidizing. It is not a very reactive fuel which may have contributed to the high oxygen activity throughout the bed. In fact, the bed temperature had to be raised to 1700°F to reduce combustion in the freeboard. Approximately 5 percent of the coke did burn in the freeboard, and the overall combustion efficiency was only 85 percent (see Table 3). It is possible that an Illinois No. 6 coke might have produced different results because of its higher reactivity.

The mixing within the bed plays a significant role in the distribution of local oxygen activity. This was illustrated by the data when the ratio of coal-conveying air to fluidizing air was changed and when the coal feed port design was changed.

Using coal port "A," 5 percent, 10 percent, and 20 percent conveying air was used. The effect on the reducing potential is shown in Fig. 10. For this port design and test condition, a 10 percent conveying air setting provided overall the least reducing environment for the heat exchanger, using the reducing potential criteria defined earlier. This is not to say that corrosive conditions would not be present. Even with a very low reducing potential, excursions to fairly low PO_2 values are frequent. Figure 11 illustrates the influence coal port configuration can have on PO_2 distribution. By changing the design of the coal port and using some of the fluidizing air to help mix the coal, it was felt that some change in the

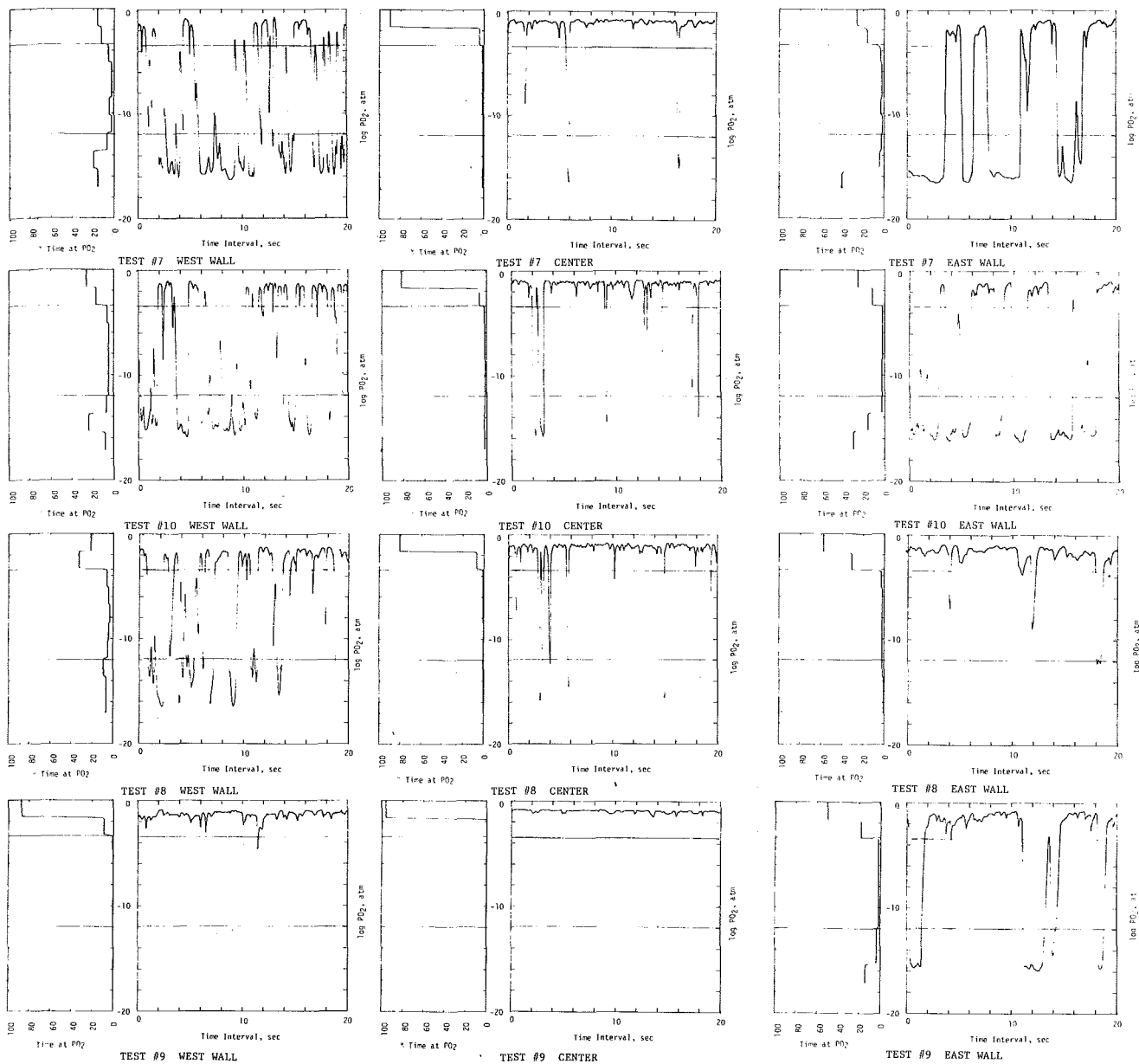


Fig. 8 Oxygen partial pressure versus time with corresponding histograms (tests no. 7, 8, 9, 10 at no. 2 probe position)

distribution of PO_2 could be made. At the locations where the change was most dramatic the additional mixing provided by this port with the radial air jets resulted in the lowest reducing potential distribution throughout the bed.

Reducing the superficial velocity from 1.8 to 1.0 M/S was shown to generally increase the oxidizing potential slightly throughout the bed but the differences were not enough to warrant any change in superficial velocity as a means of controlling reducing zones in the bed.

It should be noted that using coal port B at 20 percent conveying air and 20 percent excess air achieved equal or better results than with port A at 50 percent excess air at any conveying air percentage. This suggests that the fluid mechanics of coal port design deserves close attention when the local corrosion environment is of concern.

The oscillation of the PO_2 level over many orders of magnitude suggests substantial physical changes taking place locally. Due to the very low density of coal or char particles in the bed, it seems unlikely that the large fluctuations are the

result of probe proximity to a combusting particle unless there is a higher than normal concentration in the sampling region.

It may be that where oxidizing conditions occur they may be associated with the bubble phase and the sharp excursions to relatively low PO_2 values are the result of the passage of the bubble exposing the probe to an oxygen-deficient emulsion phase. Regions of low PO_2 may be the emulsion phase with either a higher than normal carbon loading and/or a region of poorly mixed volatile matter. The sharp excursions to high PO_2 values then come with the passage of a bubble.

Summary

A common misconception about fluidized bed combustors is that they consist of randomly mixed particles in an atmosphere that varies in composition only in the vertical dimension. However, certain kinds of reaction occur so fast that local effects are set up, while random motion of particles is inhibited by walls, heat transfer surfaces, and fuel feed devices.

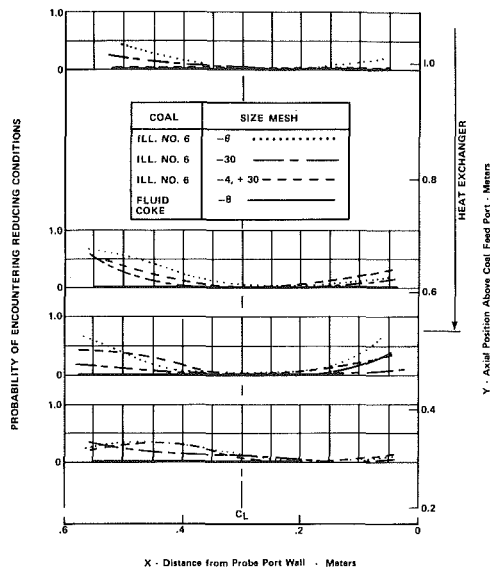


Fig. 9 Spatial variation of reducing potential as a function of various coal types (tests no. 7, 8, 9, 10 coal port A)

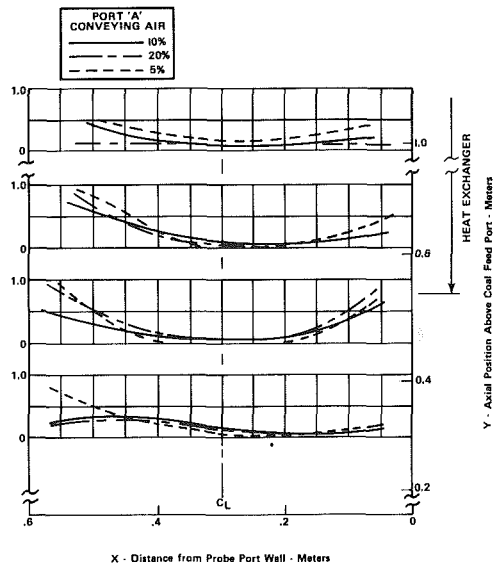


Fig. 10 Spatial variation of reducing potential as a function of coal conveying air (tests no. 1, 2, 3)

By means of in-bed measurements, we have been able to confirm that major variations in oxygen partial pressure exist, suggesting that significant variations in gas composition, fuel distribution, and particle movement exist from one position to another. These may have very deleterious effects on heat exchanger performance. Conversely, by studying in-bed conditions and by manipulating the design variables, it is possible to set up deliberate variations in local conditions which enhance heat exchanger performance and reduce actual or potential problems. Future designs of FBC will benefit from the use of controlled, rather than random, mixing behavior, based on well-planned experimentation.

The local variations in PO_2 can strongly affect the design of the CCGT heat exchanger, since the primary heater is the most technically challenging component in the system because of the difficulty with sulfidation attack.

The data obtained in this series of tests suggest that the design and operation of the coal feed port, inasmuch as it

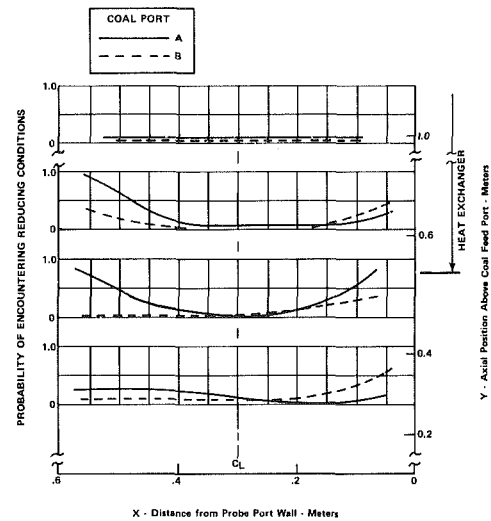


Fig. 11 Spatial variation of reducing potential as influenced by coal port design (at 20 percent conveying air)

influences the distribution of the coal, can produce a measurable change in the level and location of reducing conditions seen by the heat exchanger.

The experiments with varying coal size suggest (insofar as coal devolatilization is influenced by coal size) that rapid devolatilization is desirable. It is difficult to separate the influence of local volatiles release since a good model of the coal particle transport is not available. Therefore, the influence of carbon loading versus volatiles release cannot be separated—especially for the local zones at the bottom of the heat exchanger bundle. The results from burning petroleum coke (a very nonreactive, low volatile fuel) were not sufficient to draw definite conclusions. The coke did, however, produce almost a completely oxidizing environment throughout the heat exchanger.

In summary, it appears as though the local reducing environment measured by the oxygen probe can be significantly modified using parameters at the disposal of the designer. How they are used and to what extent modifications are necessary will depend on the outcome of the detailed corrosion exposure tests to be conducted in this unit. The PO_2 probe does offer a powerful diagnostic tool for the optimum design of a CCGT fired heater and for operational control of the combustor itself.

Acknowledgments

This program is part of a DOE Contract DE-AC01-80-ET15020 which is addressing the problems associated with coal-fired closed cycle gas turbine systems. Carey Kinney is the program monitor. The efforts described herein are part of a subcontract to Rockwell International, Rocketdyne Division, the prime contractor.

The authors would like to express their appreciation for the many helpful discussions with their colleagues I. Wright, D. Anson, A. E. Weller, and H. A. Arbib.

References

- 1 Campbell, J. Jr., Hastings, G. A., Holt, C. F., "Coal-Fired Heaters for CCGT Cogeneration Service," ASME Paper No. 81-GT-212, 1981.
- 2 *The Proceedings of the Sixth International Conference on Fluidized Bed Combustion*, Vol. 1-3, U.S. Department of Energy.
- 3 Boiarski, A., Nagarajan, V., Wright, I., and Carlton, H., "Oxygen Partial Pressure Measurements Inside a 0.6-m Fluidized-Bed Coal Combustor," paper submitted for publication to *Journal of Institute of Energy*.

4 Rogers, W. A., Page, A. J., and LaNauze, R. D., "The Corrosion Performance of Heat Exchanger Tube Alloys in Fluidized Combustion Systems," 6th European Corrosion Congress, London, 1977.

5 Minchener, A. J., et al., "Materials Problems in Fluidized-Bed Combustion Systems," Report No. EPRI CS-1853 on Project RP-979-1, 1981.

6 Rogers, E. A., et al., "Materials Problems in Fluidized-Bed Combustion Systems," Report No. EPRI CS-449 on Project RP-388-1, May 1980.

7 Godfrey, T. G., Cooper, R. H., Devan, J. H., and Drake, K. R., "Heat Exchanger Materials for Fluidized-Bed Coal Combustors," ASME Paper No. 79-GT-121, 1979.

8 Stubington, J. F., "The Role of Coal Volatiles in Fluidized-Bed Combustion," *Journal of the Institute of Energy*, 1980.

9 Bywater, R. J., "The Effects of Devolatilization Kinetics on the Injector Region of Fluidized Beds," The Aerospace Corporation, El Segundo, Calif.

10 Borghi, G., et al., "A Model of Coal Devolatilization and Combustion in Fluidized Beds," AICHE Annual Meeting, New York, Nov. 1979; supplemented by initial results of research in progress presented by R. R. Pattipati, (Chemical Engineering Department, West Virginia University, Morgantown, West Virginia), during lecture at Battelle-Columbus Laboratories.

APPENDIX A

Gas Sampling/Oxygen Activity Probe

The corrosive environment experienced by heat-exchanger tubes was examined using a special probe to measure oxygen activity and chemical makeup of in-bed gases. A schematic of this probe is shown in Fig. 12. The probe consisted of a water-cooled holder which was 5 cm in diameter and 2.1-m long. This geometry was chosen to simulate the presence of a single heat-exchanger tube within the in-bed heat-exchanger network. A thin-walled porous ceramic (i.e., alumina) cylinder with one closed end was used as a filter at the probe tip to remove solid particles while allowing in-bed gases to pass through. Inside the filter body was an oxygen sensing device (labeled PO₂ sensor in Fig. 12) and also a sampling tube

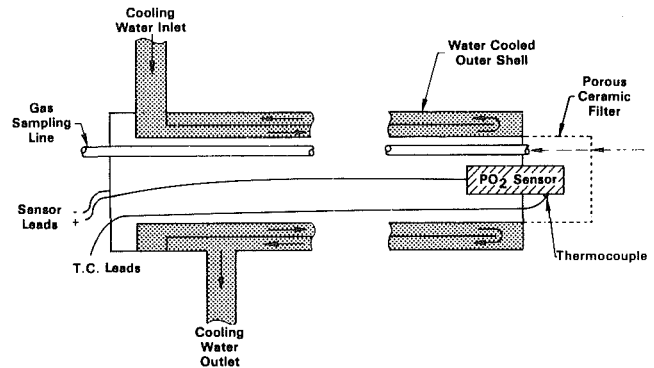


Fig. 12 The zirconia oxygen probe

which extracted some of the filtered in-bed gases for external analysis. The oxygen activity sensor was a platinum-zirconia/yttria-platinum cell that has been used in the field of chemistry for many years to monitor oxygen. A miniature version of this cell was developed by the automobile industry to monitor exhaust oxygen content, and a version of this cell was adapted for use in this study.

Oxygen partial pressure data were obtained with the porous alumina filter in place. The pressure differential across the filter was normally less than 3.45×10^4 pa/m². Even with the filter attached, large fluctuations in the PO₂ at frequencies near 1 Hz were easily noted using the oxygen sensor. The PO₂ sensor had a minimum response time of 0.01 s, allowing fluctuating oxygen partial pressure to be monitored. However, use of the porous alumina filter probably increased this value somewhat, so that the actual sensor/filter response time was approximately 0.1 s.

Materials Selection for Metallic Heat Exchangers in Advanced Coal-Fired Heaters

I. G. Wright

Battelle-Columbus Laboratories,
Columbus, Ohio 43201

A. J. Minchener

Coal Research Establishment,
Cheltenham, England

The application of advanced coal-fired heaters to heat the working fluid for a closed-cycle gas turbine provides some challenging problems for the selection of metallic heat exchanger materials. The requirements of a working fluid temperature of 1550°F (1116 K) at a pressure of 300–600 psig (2.07–4.14 MPa/m²) necessitate that the alloys used for the hottest part of the heat exchanger possess high-temperature strength in excess of that available in widely used alloys like alloy 800. The maximum-duty alloys must therefore be selected from a group of essentially nickel-base alloys for which there is scant information on long-term strength or corrosion resistance properties. The susceptibility to corrosion of a series of candidate heat exchanger alloys has been examined in a pilot plant size fluidized-bed combustor. The observed corrosion behavior confirmed that at certain locations in a fluidized-bed combustor nickel-base alloys are susceptible in varying degrees to rapid sulfidation attack, and must be protected by coating or cladding.

Introduction

Closed-cycle systems, in which a high-temperature fluid is used to drive a turbine to generate electricity, appear to offer an attractive prospect for high-efficiency, modular units which have little or no water requirement. A further advantage of such systems is that virtually all of the high-temperature compatibility problems are transferred to the heat exchanger, which could assume several different configurations and burn a range of fuels.

A particular design of high-temperature heat exchanger intended to burn coal to heat air to a temperature of 1550°F (1116 K) is the subject of a current combined combustion technology-materials-engineering study [1, 2]. The chosen maximum temperature yields a potential closed combined cycle system efficiency of 51 percent at a working fluid pressure of 600 psig (4.14 MPa/m²). More importantly, perhaps, it represents the maximum capability of practical metallic heat exchanger materials in terms of high-temperature strength. Assuming a maximum metal temperature of 1650°F (1172 K) calculated ASME Boiler Code-type strength requirements reveal a very limited choice of available alloys. In this study, alloy candidates for the top temperature duty, considering availability, fabricability, and cost are (in descending order of maximum allowable stress): Inconel 617, Inconel 618E, Nimonic 86, and Incoloy 800H. A heat exchanger construction is envisaged in which a minimum amount of one or two of these alloys is used in the outlet passes, and where the more conventional 300 series stainless steels and low-alloy steels are used as system temperature and pressure permit.

The coal-fired heat exchanger under consideration is a fluidized-bed combustor, using limestone as a sulfur sorbent. Experience in the use of metallic materials in this type of combustor is fairly sparse and is increasing at a slow rate, since only a few developmental units are in operation. Unfortunately, the materials compatibility studies linked to these units have been concerned with alloys required for steam-cycle duty [3], or for different air heater cycles which require less strength [4] than in the system of current interest. Results of direct interest, however, concern the widespread experience of rapid but sometimes unpredictable corrosion of nickel-rich alloys in the fireside environment of coal-fired, fluidized-bed combustion. Since the alloys of choice for the maximum temperature duty are unavoidably nickel-base, it is essential that their behavior in the fireside environment be understood so that decisions on strategies of location and protection can be properly made. The results described here represent one part of a materials compatibility study designed to support the materials selection decisions for this heat exchanger design.

Experimental

The alloys chosen for corrosion testing were four high-strength wrought alloys representing possible choices for very high temperature heat transfer tubing for advanced heat exchanger designs. The compositions are shown in Table 1.

Specimens 2 in. by 1.5 in. (51 mm by 38 mm) were cut from plate stock, and 0.25-in. (6.4-mm) holes drilled on 1.5-in. (38-mm) centers to allow for support in the fluidized-bed combustor. The cut edges were deburred, and an identifying code engraved on one face, but no machining was done on the major exposed surfaces, which were exposed in the mill-finished condition. The specimens were mounted on a refractory-lined door which comprises one wall of the

Contributed by the Gas Turbine Division of THE AMERICAN SOCIETY OF MECHANICAL ENGINEERS and presented at the 27th International Gas Turbine Conference and Exhibit, London, England, April 18–22, 1982, Manuscript received at ASME Headquarters December 15, 1981. Paper No. 82-GT-226.

Table 1 Alloy compositions

Alloy	Heat No.	C	P	S	Si	Mn	Ni	Fe	Co	Cr	Mo	Cu	Al	Ti	W	Ce
Inconel 617	XX19A7UK	.06	-	.001	.1	.01	55.4	.34	12.12	21.53	9.03	.02	1.11	-	-	-
Inconel 618E	-	.05	-	.005	.08	.04	55.5	14.97	-	22.78	-	.01	-	.32	6.24	-
Nimonic 86	UNJ 4360	.06	-	.004	.35	.48	65.0	1.76	.53	25.4	10.4	.11	.02	.05	-	.03
Incoloy 800	HH0229A	.06	-	.002	.21	.91	30.4	46.58	-	20.7	-	.44	.29	.41	-	-

Table 2 Summary of fluidized-bed operating conditions*

	Test No. 1	Test No. 2	Test No. 3
Fuel	Wellbeck (UK) coal (0.53% Cl, 1.6% S)	Illinois No. 5 coal (0.07% Cl, 2.9% S)	Char containing 2% volatiles (produced from Illinois No. 5)
Sulfur sorbent	None	Penrith limestone	Penrith limestone
Excess air level (%)	10-20	Substoichiometric	10-20
Ca:S Mole Ratio	0	3:1	3:1
Flue Gas Analysis (Vol.%)	O ₂ 2.6 CO - CO ₂ 16.0 SO ₂ 0.117 CH ₄ - H ₂ S -	O ₂ 0.1 CO 3.7 CO ₂ 17.0 SO ₂ 0.0357 CH ₄ 0.7 H ₂ S 0.0366	O ₂ 2.7 CO - CO ₂ 17.1 SO ₂ 0.046 CH ₄ - H ₂ S -

* In all runs, the fluidizing gas velocity was 3 ft/sec and the bed temperature was 1650 F.

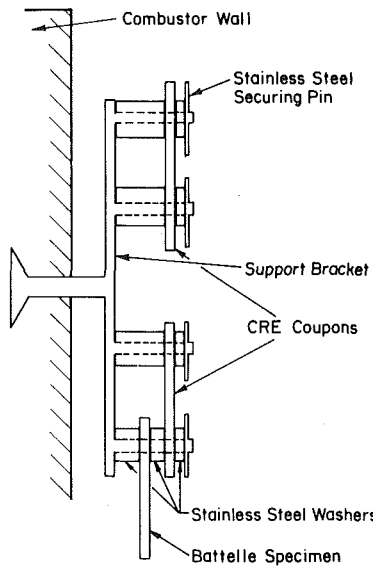


Fig. 1 Schematic diagram of specimen assembly

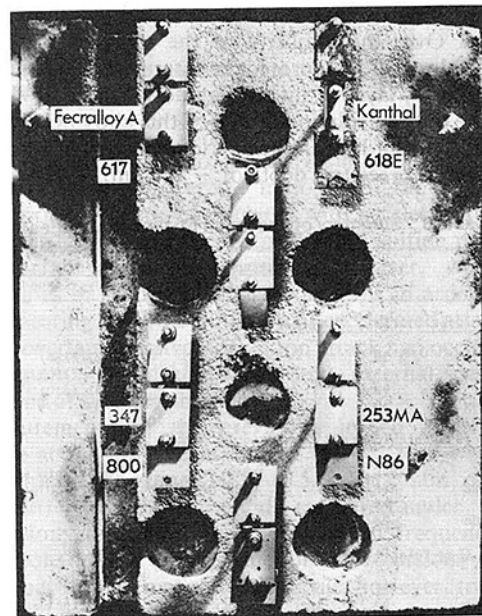


Fig. 2 Arrangement of specimens on combustor wall (after test no. 2)

fluidized-bed combustor. Figure 1 shows schematically the arrangement of the specimens, and their relationship to other test coupons, on the support bracket. A point worthy of note is that the specimens described here were all mounted with an area of overlap with test coupons from the main test program; these overlapping coupons were of alloys which have shown good resistance to corrosion in previous testing. The mounted specimens were located in the lower part of the tube bank, as can be judged from their positioning with respect to the holes in the door which accommodated the in-bed tubes in Fig. 2. The specimens of interest are labeled 617, 618E, 800, and N86; the lowest specimen being some 11 in. above the distributor plate. In test number 3, the location of specimens was slightly different, with Inconel 617 and 618E occupying the positions shown in Fig. 2 for Incoloy 800H and Nimonic 86, respectively; Nimonic 86 was in the overlapped position of the upper center mounting, while Inconel 800H was in the overlapped position of the lower center mounting, some six inches above the distributor plate.

The actual fluidized-bed combustor used was a 1-ft (0.3-m) square, atmospheric, fluidized-bed combustor at the Coal Research Establishment, near Cheltenham. The bed was run for a series of 250 hr (9×10^5 s) corrosion tests to investigate the effects of different operating conditions on candidate

alloys for in-bed heat exchangers [5], and the alloys described here were included in three of these runs. The conditions of operation during the three runs of interest are listed in Table 2.

In test number 1, a high chlorine coal was burned without a sulfur absorbent. Coals of this type have caused corrosion problems in pulverized-coal steam boilers in the United Kingdom, possibly because of the direct action of the chlorine or because high chlorine often implies a high level of alkali metal salts in the coal.

Test number 2 was run with a high sulfur coal and limestone, but under conditions of substoichiometric combustion air flow, in order to subject the corrosion coupons to the type of combustion conditions expected to be encountered near the coal feed ports, or near the walls in future commercial combustors. In this test, the fuel to air ratio was approximately twice that used in normal operation and 3 to 4 percent CO was measured in the flue gas stream.

The third test was run with a high-temperature char, produced by coking Illinois No. 5 coal at 1690°F (1194 K), and limestone. The use of this fuel was intended to minimize the emission of volatiles from the coal feed entering the

fluidized-bed combustor, so removing one possible source of the localized oxygen-deficient (and possibly sulfur-rich) conditions previously measured in this bed [6].

Results and Discussion

After removal from the fluidized-bed combustor at the end of a 250 hr (9×10^5 s) exposure, the specimens were visually examined, reweighed, and then sectioned for metallographic examination, along the longitudinal axis where pretest thickness measurements were made. The thickness of remaining metal at specific locations was measured from photographs made of the cross sections.

Test No. 1: High-Chlorine Coal, No Limestone. The specimens exhibited a very thin, uniform, orange-brown deposit after this test. The extent of material loss in this test, as measured by specimen thickness change, is presented in Table 3. The losses were very small except for a few locations on Nimonic 86. Examination of the cross sections shown in Fig. 3 confirm that all four alloys formed thin protective oxide scales, with localized breakdown observed only in the overlapped regions and on the free end of some of the specimens. Over the majority of the surface, Inconel 617 formed a thin, uniform, protective external oxide scale, and a thin ($10\text{--}20\ \mu\text{m}$) layer of internal oxide subscale, as shown in Fig. 3. The only sulfidation attack of this alloy occurred near the top attachment hole in the overlapped region; here sulfide penetration occurred to a depth of $\sim 150\ \mu\text{m}$.

Table 3 Summary of specimen thickness changes

Alloy	Thickness Loss ($\mu\text{m}/\text{Side}$)		
	Free End	Center	Overlapped End
Test No. 1 (High Cl Coal, No Sorbent)			
Inconel 617	38	36	27 (180) ^A
Inconel 618E	43	17	+4 (100)
Nimonic 86	98	79	61 (650)
Incoloy 800H	50	60	33
Test No. 2 (Substoichiometric Combustion)			
Inconel 617	>886	>880	>885 (Thin specimen)
Inconel 618E	582 (1433)	488 (956)	766 (1007)
Nimonic 86	+4	+4	885
Incoloy 800H	.28	0	372
Test No. 3 (Low-Volatility Char)			
Inconel 617	46	42	3 (292)
Inconel 618E	55	44	33 (461)
Nimonic 86	3	5	>883
Incoloy 800H	46	46	53

A: numbers in brackets indicate maximum loss including internal penetration.

Inconel 618E formed a thin, uniform, perfectly protective oxide over most of the exposed surface, except at the free end, and in the overlapped zone near the attachment hole and on the back face, where sulfidation occurred to about $100\ \mu\text{m}$. The behavior of Nimonic 86 was very similar to this, except that in the overlapped region around the hole and on the back face massive sulfidation attack produced large pools of internal sulfide and grain boundary penetration extending some $600\text{--}700\ \mu\text{m}$ into the alloy. At the free end, sulfides were present some $100\text{--}150\ \mu\text{m}$ beneath the outer scale. Incoloy 800H, on the other hand, exhibited completely protective behavior in this environment, though the oxide scale on the front face was thickened and nonuniform compared to that on the back face.

Clearly, little adverse effect is evident of the high-chlorine (high alkali metal content) coal on corrosive deposit formation or on the formation of adherent, protective oxide scales on the freely exposed surfaces of these alloys. In locations where deposits might accumulate by the action of the fluidized-bed, however, sulfidation attack was initiated. The susceptibility of Nimonic 86, in particular, to this attack is surprising.

Attempts to measure the prevailing oxygen partial pressure in the bed, through the top center port shown in Fig. 2, using a stabilized zirconia electro-chemical probe, were thwarted by rapid loss of the outer platinum electrode. Presumably, reaction occurred with the alkali chlorides or chlorine released from the coal. Previous measurements [5] under oxidizing conditions (using a sulfur sorbent) indicated a rapidly fluctuating oxygen partial pressure with a range of 10^{-13} to 4×10^{-8} atm., while the flue gas analysis indicated 3.4×10^{-2} atm. oxygen. At the lower central port (Fig. 2), previous readings ranged from 5×10^{-4} to 1×10^{-1} atm. oxygen.

Test No. 2: Substoichiometric Combustion. The surfaces of the specimens, except Inconel 617, after this run appeared light grey, and were quite smooth, with no obvious build up of deposit. During this test run, the specimen of Inconel 617 broke in half, separation occurring just below the bottom of the overlapping specimen. Visual examination of the remaining piece, and of the severed piece after recovery indicated very heavy corrosive attack. The surface of Inconel 618E exhibited gross attack with voluminous grey-appearing external scale at the top of the specimen, around the region of overlap, at the bottom of the specimen, and along the edges (see Fig. 2). The specimens of Nimonic 86 and Incoloy 800 were attacked only in very localized spots on the freely ex-

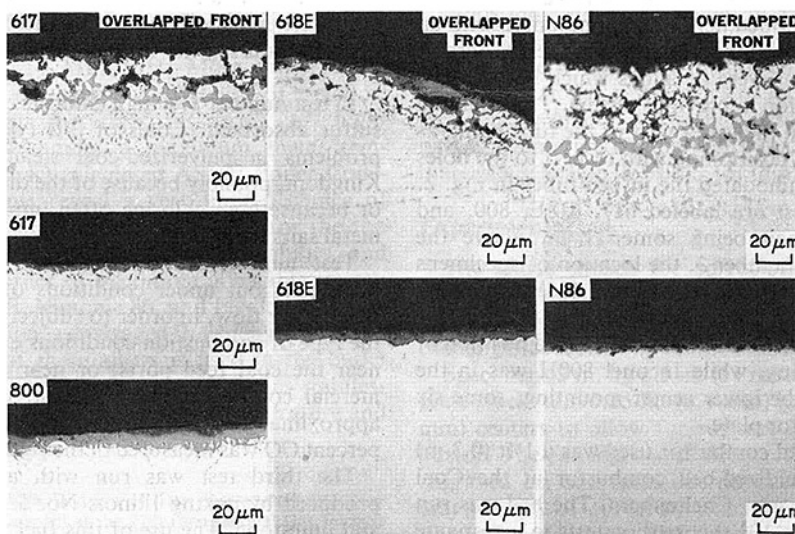


Fig. 3 Cross sections of alloys from test number 1

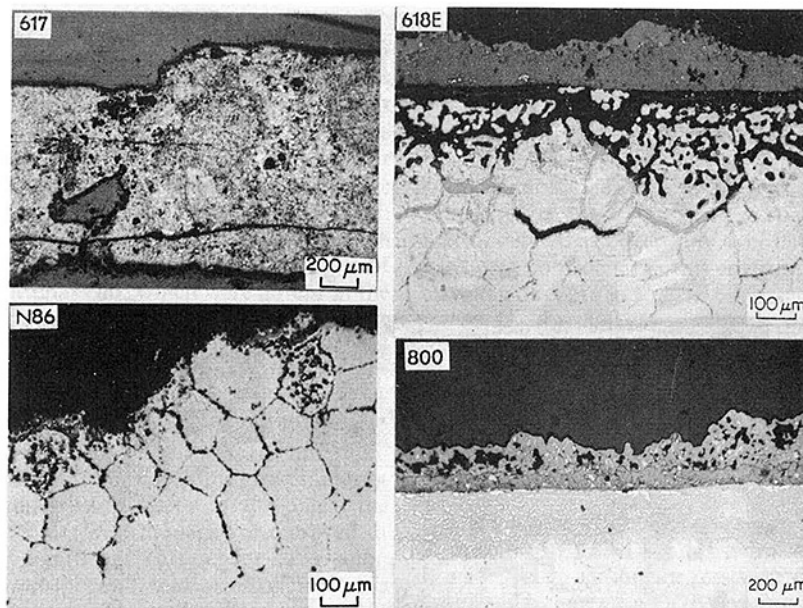


Fig. 4 Cross sections of the alloys from test number 2, showing corrosion morphologies in the overlapped areas

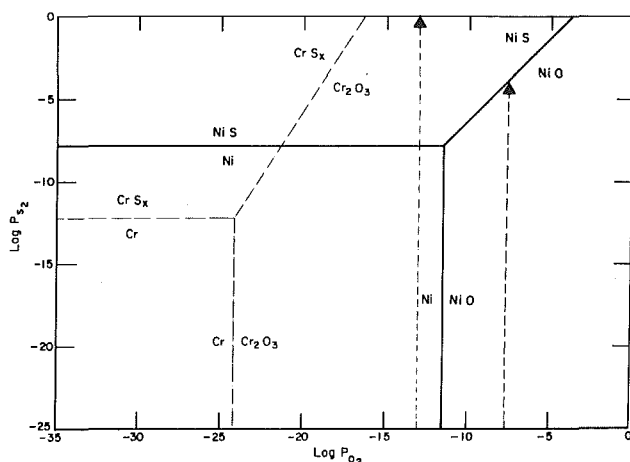


Fig. 5 Equilibrium thermodynamic diagram showing range of stability of phases in the Cr-O-S and Ni-O-S systems at 1650°F (1172 K).

posed surfaces, but were heavily corroded in the areas of overlap.

Cross sections of the alloys are presented in Fig. 4. The specimen of Inconel 617, which was only 0.15-in. (0.38-cm) thick initially (as indicated in Table 3), had been completely converted to an oxide/sulfide, with only isolated areas of metal remaining. The areas of Inconel 618E which were visibly attacked in fact exhibited extensive sulfidation. A thick (100–200 μm) external scale of mixed oxide/sulfide was formed in these areas, while sulfide penetration of alloy grain boundaries extended some 750 μm into the substrate. Large pools, apparently of chromium sulfide surrounded by nickel and iron essentially devoid of chromium, were also observed near the alloy/external scale interface, indicating the existence of intensely sulfidizing conditions in these locations.

Nimonic 86 formed a thin protective scale, with virtually no subsurface penetration, over most of its surface, as can be judged by the thickness change data in Table 3. In the overlapped end zones, however, very extensive corrosive loss had occurred. The external scale was missing, but pools of chromium-rich sulfide were observed in the surface of the remaining alloy, with further sulfide penetration extending down alloy grain boundaries a further 600 μm into the substrate.

The specimen of Incoloy 800H similarly exhibited quite protective behavior over the majority of the exposed face. Small, isolated blisters associated with accelerated oxidation and penetration of sulfur to form small sulfide pools at the near surface were also present, however, with sulfide precipitates in the alloy grain boundaries to a depth of 580 μm , indicating localized initiation of accelerated attack. In the area of overlap, massive sulfidation attack had occurred, with the formation of thick (200–400 μm), external scales, and a thick zone of sulfide subscale.

Measurements of the prevailing in-bed oxygen partial pressure at the upper central port in Fig. 2 showed a fairly steady value, in the range 10^{-13} to 5×10^{-12} atm. oxygen [7]. Major differences from the data measured under “normal” combustion conditions were the reduced frequency of the fluctuations and a great reduction in excursions to higher oxygen partial pressures. It is difficult, however, to reconcile the greatly increased severity of sulfidation attack of Inconel 617 and 618E specimens under the substoichiometric conditions with this observed change in frequency of fluctuation of the oxygen partial pressure, since the minimum achieved was similar in both tests.

As suggested by the superimposed phase stability diagrams for Cr-O-S and Ni-O-S shown in Fig. 5 [8, 9], the formation of chromium sulfide on the surface of an alloy is not possible in an oxygen-and sulfur-bearing gas mixture at 1650°F (1172 K), when the prevailing oxygen partial pressure is 10^{-12} to 10^{-13} atm. Only when the oxygen partial pressure is reduced below $\sim 10^{-16}$ atm. does this become possible at very high sulfur partial pressures; as the oxygen partial pressure is reduced further, the necessary sulfur partial pressure also falls. In practice, sufficiently low oxygen partial pressures exist beneath protective Cr_2O_3 scales, so that if sulfur can transport through these scales to create a sufficient partial pressure, chromium sulfide formation can occur in this location.

Nickel sulfide is thermodynamically less stable than chromium sulfide, and will, therefore, not form under equilibrium conditions in a Ni-Cr alloy unless the chromium activity is reduced to a very low level. Kinetically, however, nickel sulfide can form in areas of local chromium depletion in an alloy, providing a sufficient flux of sulfur to the alloy is maintained. Since nickel sulfide is molten at the temperature

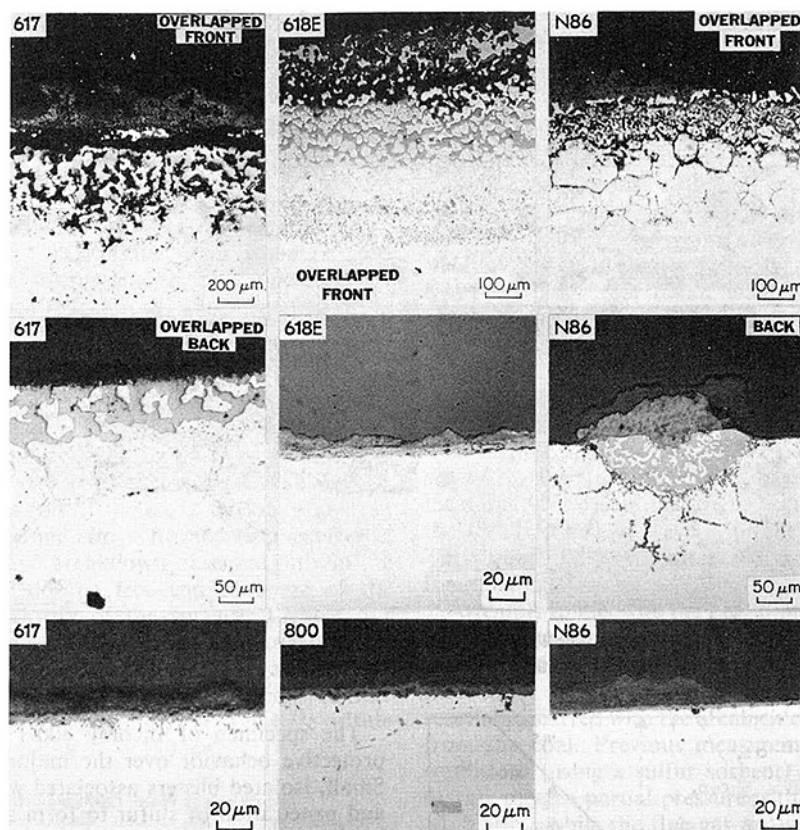


Fig. 6 Cross sections of the alloys from test number 3, showing variation of corrosion morphologies over the specimen surfaces

of interest, its presence ensures rapid degradation of the alloy. The NiO/NiS line in Fig. 5 indicates that NiS-formation is possible at oxygen partial pressures of 10^{-8} atm. and that the necessary sulfur partial pressure is reduced as the oxygen partial pressure is reduced down to $\sim 5 \times 10^{-11}$ atm., after which it remains constant. Since the mean oxygen partial pressure in test 2, and under "oxidizing" conditions, was $\sim 10^{-13}$ and $\sim 10^{-11}$ atm., respectively, the sulfur partial pressure required for nickel sulfide formation would have been expected to be similar in both cases.

Test No. 3: Combustion of Low-Volatility Char. The surface appearance of the specimens after this test was very similar to that after Test Number 1. The thickness change data, shown in Table 3, show that the three nickel-base alloys were heavily attacked in the overlapped areas, while the corrosion of Incoloy 800H in the same location was much less severe. Figure 6 illustrates the massive sulfidation/oxidation which occurred in the overlapped region on the front surface of Inconel 617. The corrosion penetration of the rear surface in the same location was less, but the extent of sulfidation was nevertheless quite massive. Almost all the freely exposed surface of this alloy exhibited protective behavior, with the formation of a thin, uniform oxide and a subscale of internal oxide; slight sulfidation occurred of the freely exposed end of the specimen.

The sulfidation attack of the front and rear surfaces of the overlapped zone of Inconel 618E was massive (see Fig. 6) with sulfide penetration to $\sim 300 \mu\text{m}$, and chromium depletion of the alloy extending a further $100 \mu\text{m}$. Slight sulfidation of the freely exposed end of this alloy was also observed. Over the rest of the free surface, perfectly protective behavior was exhibited, with the formation of a thin, uniform scale, with no subscale. The adherence of this scale appeared poor, however, since it detached in large pieces (still adhering to the bed-deposit) on handling.

Nimonic 86 was also grossly sulfidized on the front face in the overlapped region, while on the back face in the same location isolated pits of very heavy sulfidation occurred. The free end of the specimen was also slightly sulfidized. Over the rest of the free surface, a thin protective scale was evident, along with very localized pits associated with massive sulfidation.

Incoloy 800H formed an essentially protective oxide over its entire surface, except the line marking the start of the overlapped zone on the front face of the specimen. Here a few pits associated with localized sulfide formation and accelerated oxidation were formed.

The oxygen partial pressure at this location in the combustor was typical for 10–20 percent excess air combustion conditions, that is, rapidly oscillating between 10^{-13} and 10^{-8} atm.

Summary

The results of the corrosion tests described were intended to provide information on the susceptibility to corrosion attack of the four candidate heat exchanger alloys in the fireside environment of a coal-fired fluidized-bed combustor and cannot be used with any confidence to predict corrosion rates. It should also be noted that the combustion conditions used in these three tests were not normal operating conditions, but were designed to evaluate materials behavior in specific environments which might be encountered in some regimes of fluidized-bed operation.

All four alloys appeared susceptible to sulfidation related accelerated attack to some degree. In the two test runs which employed nominally oxidizing conditions of 10–20 percent excess air, the freely-exposed surfaces in general exhibited protective oxidation behavior. Sulfidation occurred in the areas where the specimens were overlapped with others, and at the upstream edge, areas where thick deposits of bed

material or erosion damage, respectively, might be expected. Whether these deposits were coal ash (test no. 1) or CaO/CaSO₄ (test no. 3) did not materially affect the susceptibility to sulfidation.

The combustion of char was intended to eliminate the plume of combusting volatiles, with its associated extremes of oxygen deficiency, expected to emanate from coal entering the bed. No noticeable differences occurred in the local oxygen partial pressure near the exposed specimens, however, though the free surface of one alloy, Nimonic 86, showed signs of localized sulfidation in the char run, which were absent in the coal run in test number 1.

In the substoichiometric run massive sulfidation attack was initiated on the free surfaces of Inconel 617 and 618E but, surprisingly, not on Nimonic 86 nor Incoloy 800H. While the local oxygen partial pressure near the specimens fluctuated less than under normal combustion conditions, the minimum levels were similar and, from a thermodynamic viewpoint, not low enough to initiate massive sulfidation attack unless the expected protective oxide scales were damaged or removed. It is difficult to envisage significant differences in erosion conditions arising between normal and substoichiometric combustion, unless the physical nature of the bed material is greatly changed. It is possible that under substoichiometric conditions, calcium sulfide may exist as a possibly transient species in a limestone bed. If this were included in the deposits formed on the alloy surfaces, it might constitute a local source of sulfur, or a possible reactant with the otherwise protective Cr₂O₃ scale.

Of the four alloys investigated, Inconel 800H with the lowest high-temperature strength capabilities, was the least attacked, although it was extensively sulfidized in the overlapped region in the substoichiometric run. The three nickel-base alloys were very susceptible to sulfidation in the overlapped regions under all three conditions examined. Substoichiometric combustion conditions led to comprehensive sulfidation of Inconel 617, and to massive localized sulfidation of Inconel 618E. Nimonic 86 appeared to be initiating catastrophic sulfidation conditions in the substoichiometric and char combustion runs, which suggests extreme sensitivity to the local environment, hence to location in the bed.

Conclusions

Conclusions which appear justified from this investigation are:

(i) The high-strength nickel-base alloys, Inconel 617 and 618E, are extremely susceptible to accelerated sulfidation attack at 1650°F (1172 K) in the bed of a fluidized-bed combustor where conditions of substoichiometric combustion are encountered. These alloys must be protected by a cladding or coating of oxidation/sulfidation-resistant alloy.

(ii) Nimonic 86 exhibited less susceptibility to sulfidation than the Inconels, but showed signs of initiating massive sulfide-related attack locally over its surface, and could not be used with confidence in this environment without a protective cladding or coating.

(iii) Incoloy 800 appeared to be fairly resistant when freely exposed but was sulfidized to a slight extent on leading edges.

(iv) All four alloys were susceptible to rapid sulfidation-related attack in occluded or stagnant locations, which are unavoidable in real systems.

Acknowledgments

The authors would like to express their appreciation to Dr. J. Stringer of EPRI for his permission to participate in the fluidized-bed combustor tests at CRE. The alloys were evaluated as part of a DOE program, Contract DE-AC01-80-ET15020, which is addressing the problems associated with coal-fired closed-cycle gas turbine systems; Carey Kinney is the program monitor.

References

- 1 Stambler, I., *Gas Turbine World*, Vol. 10, No. 2, 1980, p. 20.
- 2 Campbell, J., Hastings, G. A., and Holt, C. F., "Coal-Fired Heaters for CCGT Cogeneration Service," ASME Paper No. 81-GT-212, presented at the 26th International Gas Turbine Conference, Houston, 1981.
- 3 Rogers, W. A., Page, A. J., and LaNauze, R. D., "The Corrosion Performance of Heat Exchanger Tube Alloys in Fluidized Combustion Systems," 6th European Corrosion Congress, London, 1977.
- 4 Moskowitz, S., "Recent Developments in PFB Technology, 5th Annual Conference on Materials for Coal Conversion and Utilization, Gaithersburg, 1980.
- 5 Minchener, A. J., et al., "Materials Problems in Fluidized-Bed Combustion Systems," Report No. EPRI CS 1853 1981.
- 6 Cooke, M. J., Cutler, A. J. B., and Raask, E., *J. Inst. Fuel*, Vol. 45, No. 373, 1972, p. 153.
- 7 Lloyd, D., and Minchener, A. J., "Corrosion Within Coal-Fired Fluidized-Bed Combustion Systems," 6th Annual Conference on Materials for Coal Conversion and Utilization, Gaithersburg, 1981.
- 8 Gulbransen, E. A., and Jansson, S. A., "General Concepts of Oxidation and Sulfidation Reactions, A Thermochemical Approach," *High-Temperature Metallic Corrosion of Sulfur and Its Compounds*, edited by Z. A. Foroulis, The Electrochem. Soc., 1970.
- 9 Rapp, R. A., "High-Temperature Gaseous Corrosion of Metals in Mixed Environments," *Materials Problems and Research Opportunities in Coal Combustion*, NSF/OCR Workshop, Columbus, Ohio, 1974.

A Theoretical Investigation of Transonic Flows in Radial Compressor Diffusers

H. O. Jeske

Research Assistant.

I. Teipel

Professor.

Institute for Mechanics,
University of Hannover, West Germany

The transonic flow in a diffuser of a centrifugal compressor with high pressure ratio has been analyzed by a numerical procedure. The method consists of an inviscid calculation of the pressure field in the vaned diffuser and of a determination of the boundary layer flow along the blades. The diffuser has been equipped with curved vanes, and only the flow through one channel is considered. The two-dimensional pressure distribution has been calculated by a time-dependent finite difference scheme. The boundary layer flow has been determined by different integral methods with special attention concerning the shock-boundary-layer interaction. Finally, the numerical results are compared with experiments, and the agreement is satisfactory.

Introduction

Centrifugal compressors with high-pressure ratios per stage have been equipped in most cases with vaned diffusers. Because of the complicated flow field, it is not possible to obtain generally valid information for the optimal configuration. Nevertheless, during the last fifteen years advanced technology development of a compressor has reduced the number of stages by a considerable amount with even a better efficiency. One way to get such a performance is to increase the speed of the impeller.

At a certain limit the flow reaches the speed of sound at the impeller exit. In combination with vaned diffusers, shock waves may occur, and therefore the characteristic features of the flow field will be changed quite drastically. The shock waves interact with the boundary layer, which then will separate from the blades of the diffuser at a certain Mach number. A systematic increase of the efficiency and of the pressure ratio for a centrifugal compressor can be achieved if the influence of a change in geometry on the performance is completely understood. The theoretical investigation of the fluid flow in this connection is very complicated, because there may exist separation zones even at the design point which lead to a three-dimensional unsteady flow field for the entrance of the diffuser.

In this paper, a method for the calculation of the transonic flow in vaned diffuser including shock-boundary-layer interaction will be described. For one example, the pressure field and the boundary layer flow will be discussed. Comparisons with experimental results of a centrifugal compressor with an impeller speed of $n = 22000 \text{ min}^{-1}$ are made. Here the flow velocity at the entrance of the diffuser is supersonic. The pressure ratio at the impeller exit is so large that the cascade is not choked.

Analysis of the Pressure Field

For the calculation of the pressure field, only the inviscid flow has to be investigated. Because of the difficulties in connection with the transition from supersonic to subsonic regions, one has used an unsteady formulation of the fundamental equations. S. Gopalakrishnan and R. Bozzola [1] have applied this method for the computation of the transonic flow field in axial compressors. In order to include discontinuities, the differential equations in a conservative form have been considered for the finite difference procedure:

$$\frac{\partial U}{\partial t} + \frac{\partial F}{\partial r} + \frac{\partial G}{\partial \theta} + H = 0 \quad (1)$$

with the definitions

$$U = \begin{bmatrix} r\rho \\ \rho u_r \\ \rho u_\theta \\ r\rho(e + (u_r^2 + u_\theta^2)/2) \end{bmatrix} \quad F = \begin{bmatrix} r\rho u_r \\ \rho u_r^2 + p \\ \rho u_r u_\theta \\ (h + (u_r^2 + u_\theta^2)/2)r\rho u_r \end{bmatrix} \quad (2)$$

$$G = \begin{bmatrix} \rho u_\theta \\ \rho u_r u_\theta / r \\ (\rho u_\theta^2 + p) / r \\ \rho u_\theta (h + (u_r^2 + u_\theta^2)/2) \end{bmatrix} \quad H = \begin{bmatrix} 0 \\ \rho(u_r^2 - u_\theta^2) / r \\ 2\rho u_r u_\theta / r \\ 0 \end{bmatrix}$$

It can be seen that it is suitable to use a cylindrical system of coordinates for the description of the flow in the diffuser. The integration of equation (1) is carried out through a numerical method, first presented by MacCormack [2], which uses a predictor step and a corrector step:

Contributed by the Gas Turbine Division of THE AMERICAN SOCIETY OF MECHANICAL ENGINEERS and presented at the 27th International Gas Turbine Conference and Exhibit, London, England, April 18-22, 1982. Manuscript received at ASME Headquarters December 15, 1981. Paper No. 82-GT-227.

predictor step

$$U(\overline{n+1}, i, j) = U(n, i, j) - [F(n, i+1, j) - F(n, i, j)] \frac{\Delta t}{\Delta r} - [G(n, i, j+1) - G(n, i, j)] \frac{\Delta t}{\Delta \theta} - H(n, i, j) \cdot \Delta t \quad (3)$$

corrector step

$$U(n+1, i, j) = \left\{ U(n, i, j) + U(\overline{n+1}, i, j) - [F(\overline{n+1}, i, j) - F(\overline{n+1}, i-1, j)] \frac{\Delta t}{\Delta r} - [G(\overline{n+1}, i, j) - G(\overline{n+1}, i, j-1)] \frac{\Delta t}{\Delta \theta} \right\} / 2 - H(\overline{n+1}, i, j) \cdot \Delta t / A$$

The finite difference algorithm is stated to be of second-order accuracy. In the case, when $A=2$, consistency is guaranteed. The condition for Δt necessary for stability can be determined from an analysis of domains of both physical and mathematical dependence. Basically the step sizes Δr and $\Delta \theta$ are the important quantities. As a consequence, special problems concerning the fulfillment of the boundary conditions will arise. In order to avoid partly these difficulties, a transformation has been introduced, which will use a new coordinate system for mapping the complicated domain into a more regular one:

$$\vartheta = \frac{\theta - \theta_u(r)}{\theta_0(r) - \theta_u(r)} \quad (4)$$

The boundaries for the computational domain are formulated at first for the vaneless region. Here a periodic condition is achieved through the use of a row of exterior grid points at which the solution is equated to the solution at a row of interior points.

From the method of characteristics, one can see what kind of flow quantities at the entrance can be prescribed. In this example, the tangential velocity or in other words the rotating speed of the impeller is given. The flow in the exit region of the diffuser will be calculated by the difference scheme.

The flow angle is known at the blade surface. The contour of the blades is represented by a Spline-interpolation. Further details concerning some minor problems of evaluating correct surface points of grid system are outlined in [2].

The Boundary Layer Flow

For the calculation of the boundary layer flow one has to start from a stagnation point at the tip of a blade with laminar flow. Because of the high Reynolds number, the transition

point is found to be very near to the stagnation region. There a special approximation formula given by Cebeci and Smith [3] has been used to start the calculation of the turbulent boundary layer.

The turbulent boundary layer has been studied by three different methods. The first procedure is due to Stratford and Beavers [4], which gives an explicit representation of the most important boundary layer quantities. Direct formulas for the displacement thickness δ_1 and the momentum thickness δ_2 are obtained. The local skin friction coefficients c_f will be determined by the integrated form of the boundary layer equation.

As far as the separation criterion is concerned, no particular value for any boundary layer quantity will be used. A formula for the pressure coefficient prescribes the separation point.

The second method has been developed by Head [5] and by Green et al. [6]. It starts from the integrated form of the boundary layer equation. One has to add an equation for the boundary layer parameter \bar{H} and an entrainment equation. Having solved the system of differential equations one gets information about the boundary layer quantities. The condition for the separation point is the vanishing of the local skin friction coefficient.

The last procedure has been given by Nash and Macdonald [7]. The analysis starts again from the momentum equation in its integrated form. For the completeness of the whole system an empirical law for the local skin friction coefficient has been extended to the compressible case.

In order to carry out the calculation of the boundary layer flow the velocity at the outer edge has to be known. For the gradient of the velocity again a Spline-interpolation has been used with a sufficient accuracy. Accelerated flow is analyzed with these three different methods in order to get some information about the mathematical precision. It can be said that the first and the second procedure did not exhibit any differences within certain limits. The method published by Nash and Macdonald however showed some difficulties near the trailing edge of the blades. The displacement thickness is of particular interest because the blockage factor of the diffuser depends directly on δ_1 .

The Shock-Boundary-Layer Interaction

Interaction problems between shock waves and a turbulent boundary layer are very significant in transonic flows. It is essential to take them into account to obtain a good prediction of the performance of the diffuser. One of the main difficulties in the numerical evaluation of interaction effects is the modeling of the turbulence in a compressible flow. With a suitable turbulence model, the mean flow field may be calculated either by using interacting boundary layer approach or more directly by solving the full compressible Navier-Stokes equations.

Nomenclature

a = speed of sound, m/s	M_g = local Mach number	
c_f = local skin friction coefficient	\dot{m} = mass flux, kg/s	
e = internal energy, J/kg	n = rotating speed, min ⁻¹	x = coordinate along a blade, m
F = matrix, defined in equation (1)	p = pressure, bar	δ_1 = displacement thickness, mm
G = matrix, defined in equation (1)	p_R = stagnation pressure, bar	δ_2 = momentum thickness, mm
H = matrix, defined in equation (1)	Δr = radial step, m	ϑ = coordinate for the transformation of the angle
\bar{H} = shape factor of the boundary layer	r = radius, m	λ = diffuser radius ratio
h = enthalpy, J/kg	T_R = stagnation temperature, K	θ = coordinate of the angle
i = number for mesh points	Δt = time step, s	θ_0 = maximum coordinate of the angle
j = number for mesh points	t = time, s	θ_u = minimum coordinate of the angle
l = length of a blade, m	U = matrix, defined in equation (1)	ρ = density, kg/m ³
	u_r = radial velocity component, m/s	
	u_θ = tangential velocity component, m/s	

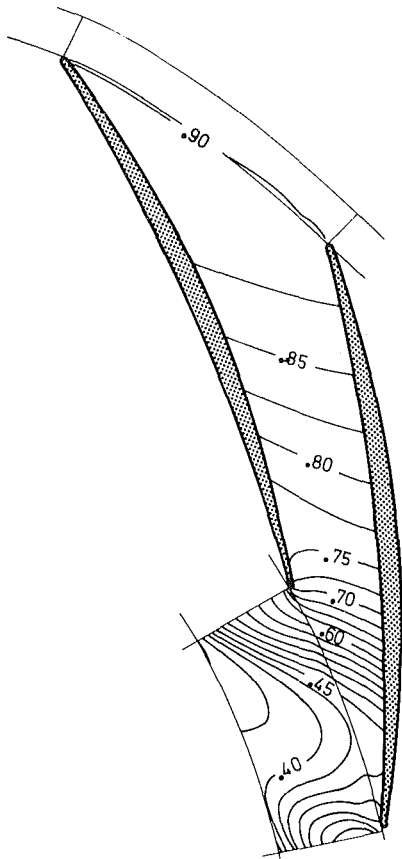


Fig. 1 Field of isobars

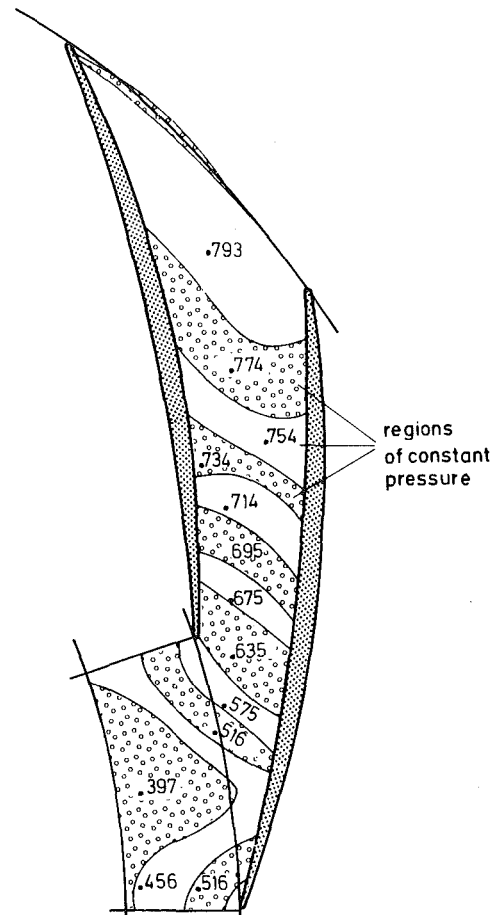


Fig. 2 Pressure field (measurements [8])

However, in many cases the computation becomes time-consuming. Therefore, it may be of great help for practical purposes to have a fast-working approximation, even if it is not very accurate in all details. An integral method will be used for the description of the whole flow field.

It can be shown that the entrainment method gives good results in comparison with measurements. But it is very important to use the correct pressure distribution. So one may face some difficulties, if applied the inviscid theory for the calculation of the outer flow.

The integral method by Stratford and Beavers presents some minor problems, because the values of the displacement thickness come out to be too large. Nevertheless this approach can be used to study the general behaviour of the boundary layer.

The model by Nash and Macdonald does not work, as at the beginning of the shock zone there is a breakdown of the whole calculation.

Results of the Pressure Distribution

Numerical results for a particular shape of a blade are presented in the following figures. In Fig. 1, pressure contours are shown for an impeller speed of $22,000 \text{ min}^{-1}$. The pressure is made dimensionless by using the stagnation pressure of the incoming flow. The major part of the pressure development appears in the region between the impeller exit and the entrance zone of the vaned diffuser. A shock wave is formed just before the flow reaches the section of minimum area. Here the isobars exhibit a steep gradient. At the end of the channel the pressure contours are more or less straight lines, such that it is possible to apply one-dimensional theory.

Experiments for the same diffuser have been performed at the Institute for Turbomachinery at the University of Hannover [8]. Figure 2 shows a plot of isobars, and the agreement

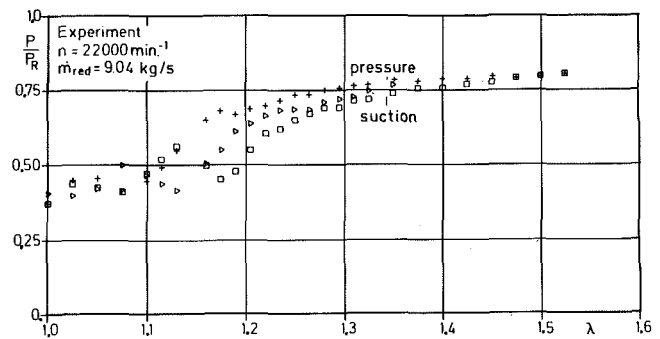


Fig. 3 Wall pressure (measurements [8])

between theory and measurements is encouraging. Again a rather steep pressure gradient occurs near the smallest cross section. In Fig. 3, the wall pressure for the suction and the pressure side has been presented as a function of the diffuser radius ratio λ . The crosses belong to the pressure side, the squares to the suction side, and the triangles to the mid-chord.

For comparison, the theoretical results for the wall pressure and the local Mach number have been shown in Fig. 4 and Fig. 5. The difference procedure (equation (3)) was applied with $A = 2$. The various values of ϑ refer again to the pressure side ($\vartheta = 1.0$), to the suction side ($\vartheta = 0$), and to the mid-chord ($\vartheta = 0.5$). Particularly from Fig. 5, one can see a rise of the Mach number on the suction side near $\lambda = 1.2$ and a decrease of M_g on pressure side.

As it was pointed out, it is very important to use the correct pressure distribution for the calculation of the shock-boundary-layer interaction. Otherwise the comparison with

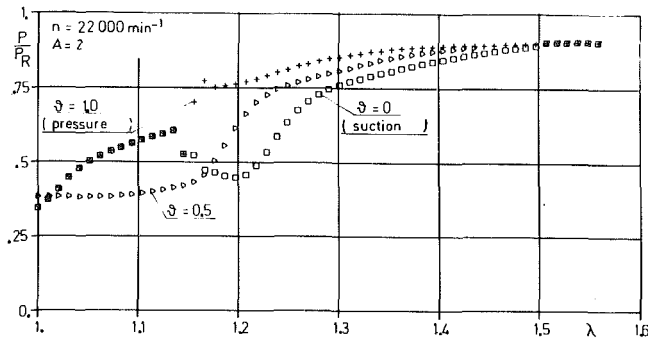


Fig. 4 Wall pressure (theory)

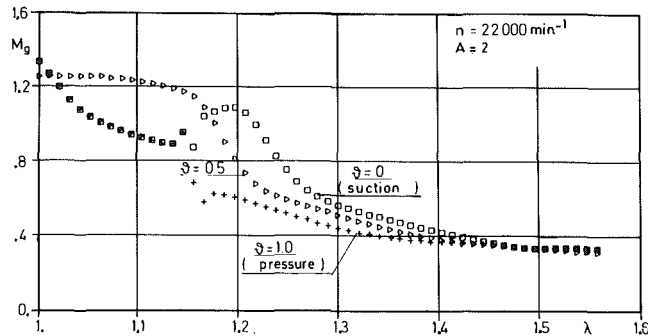


Fig. 5 Local Mach number (theory)

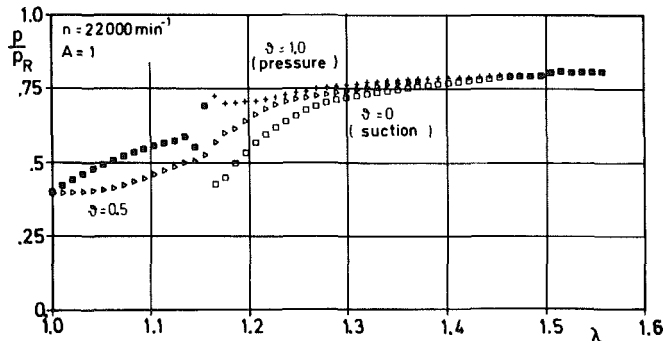


Fig. 6 Wall pressure (theory)

experiments is not good enough. In order to avoid these difficulties it has been shown in [2] that it is better to replace the factor A in the difference approach (equation (3)) by 1, even if the difference scheme is not consistent. Then the calculated loss of the total pressure is in the order of the measured value. The agreement of the pressure at the exit of the diffuser in comparison with experiments is better.

The new pressure distribution at the wall with $A = 1.0$ has been presented in Fig. 6. The important finding is now that p/p_R reaches 0.76 for large λ . This value has also been obtained by measurements (see Fig. 3). The pressure relation calculated by the correct theory yields 0.85, which is much too high in comparison with experiments. One has to include a larger entropy production because of the losses in the flow. In the following investigations for the boundary layer only the case with $A = 1.0$ will be applied.

As far as the separation is concerned no boundary layer method indicates a separation point on the pressure side. In Fig. 7, the momentum thickness δ_2 obtained by the three already mentioned procedures has been presented. The differences between these theories are small. Only the results of the model by Stratford and Beavers diverge at the end of the channel from the other approaches.

On the suction side separation will occur. The method

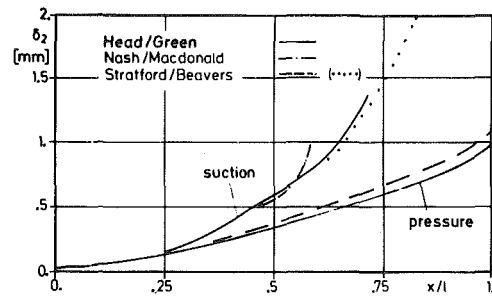


Fig. 7 The momentum thickness δ_2

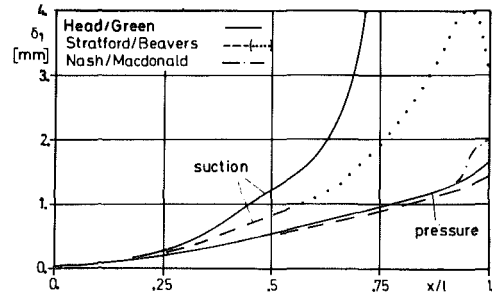


Fig. 8 The displacement thickness δ_1

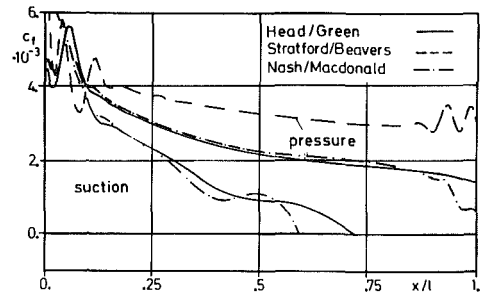


Fig. 9 Local skin friction coefficient c_f

developed by Nash and Macdonald reaches the point with $c_f = 0$ earlier than the entrainment method by Head and Green. The criterion by Stratford gives a separation point in between. The results of the model by Stratford and Beavers have been plotted in form of a dotted line after the separation point.

The solutions for the displacement thickness δ_1 are given in the next figure. On the pressure side in Fig. 8, again there is no significant difference between the values of the three methods. The model by Nash and Macdonald diverges at the trailing edge of the blades. For small values of x/l , the curve coincides with the results calculated by the entrainment method. Results given by Stratford and Beaver's procedure are slightly too small.

The suction side exhibits a rather wild development of δ_1 . The theory by Stratford and Beavers yields a separation point at $x/l \sim 0.6$. Further values are obtained, but they are probably without any meaning. For the results given by the method by Nash and Macdonald, there is again no difference with the entrainment theory.

Finally, the local wall skin friction coefficient has been shown in Fig. 9. In the entrance region of the diffuser a complicated evolution is obtained. Again for the pressure side, the c_f curves do not intersect with the abscissa. For the suction side, however, a separation point will appear at $x/l \sim 0.65$. Because of the large oscillations, the results obtained by the model of Stratford and Beavers have not been presented by Fig. 9.

The separation point predicted by the boundary layer

theory can be confirmed by the experimental data in Fig. 2. In the region about $p/p_B \sim 0.774$, the isobars at the wall change their curvature. It might be that this is an indication for separation. On the other hand it could also be justified that there will be a separation point at the pressure side. But no evidence for this effect can be seen from the theoretical results.

For this large impeller exit speed, no shock waves occur in the region behind the section of the smallest area. Therefore, the shock-boundary-layer interaction is not important for this case. But if one considers a point in the performance chart near the surge line a shock wave will appear in the channel of the diffuser. Here the shock-boundary-layer interaction will give an enormous effect [9].

Acknowledgments

The paper has been prepared in connection with the "Sonderforschungsbereich 61: Strömungsprobleme in der Energieumwandlung" at the University of Hannover in the Institute for Mechanics. The financial support of the Deutsche Forschungsgemeinschaft is gratefully acknowledged.

References

- 1 Gopalakrishnan, S. and Bozzola, R., "Computation of Shocked Flows in Compressor Cascades," ASME-Paper 72-GT-31, New York, 1972.
- 2 Jeske, H. O., "Die transsonische Strömung in beschauelten Diffusoren von Radialverdichtern," Ph.D. thesis, Hannover, 1980.
- 3 Cebeci, T. and Smith, A. M. O., *Analysis of Turbulent Boundary Layers*, Academic Press, New York, 1974.
- 4 Stratford, B. S. and Beavers, G. S., "The Calculation of the Compressible Turbulent Boundary Layer in an Arbitrary Pressure Gradient—a Correlation of Certain Previous Methods," ARC-RM 3207, Aeronautical Research Council, London, 1961.
- 5 Head, M. R., "Entrainment in the Turbulent Boundary Layer," ARC-RM-3152, Aeronautical Research Council, London, 1958.
- 6 Green, J. E., Weeks, D. J., and Brooman, J. W. F., "Prediction of Turbulent Boundary Layers and Wakes in Compressible Flow by a Lag-Entrainment Method," ARC-RM-3791, Aeronautical Research Council, London, 1973.
- 7 Nash, J. F. and Macdonald, A. G. J., "A Turbulent Skin-Friction Law for Use at Subsonic and Transonic Speeds," ARC-CP-948, Aeronautical Research Council, London, 1967.
- 8 Bammert, K., Jansen, M., Knapp, P., and Wittekind, W., "Strömungsuntersuchungen an beschauelten Diffusoren," *Konstruktion*, Vol. 28, 1976, pp. 313–319.
- 9 Jeske, H. O., and Teipel, I., "Die Strömung in Diffusoren für Radialverdichter an der Schluckgrenze," *Forschung auf dem Ingenieurwesen*, Vol. 47, No. 6, 1981, pp. 181–189.

Effect of Impeller-Extended Shrouds on Centrifugal Compressor Performance as a Function of Specific Speed

L. Sapiro

Senior Technical Consultant,
Solar Turbines Incorporated,
San Diego, Calif. 92138

Centrifugal compressors for gas compression applications usually employ low-pressure ratio, backward-swept impellers with vaneless diffusers. To increase the compressor flow range and speed, impeller blades are occasionally trimmed, resulting in an extended shroud configuration. The effect of extended front and back impeller shrouds on the performance of centrifugal compressors with vaneless diffusers, and the variation of this effect as a function of specific speed, is thus of concern and is the subject of this paper. An investigation was carried out on two backward-swept shrouded impellers of common blade tip and inducer hub diameters, but different inducer tip diameters (corresponding to low and high specific speeds), with the front and back shrouds extending 20 percent above the blade's outside diameter.

Introduction

In order to cover a wide range of flows and heads, centrifugal compressor families for gas compression applications normally contain several types of stages having common impeller tip diameters corresponding to a variety of specific speed values. This is shown in Fig. 1.

The performance range of a compressor family, as shown in Fig. 2, is basically defined by the impeller tip diameter, the minimum and maximum specific speed impeller types (thus the minimum and maximum inlet flow coefficients), the maximum number of stages, and the maximum rotational speed.

The minimum pressure ratio that can be handled by a compressor family, and which corresponds to a single stage, is determined by the minimum efficient speed of the driver. However, as a result of the "fan" law, lower speeds reduce the performance range, displacing the optimum efficiency to lower flows, as shown in Fig. 3.

The reduction of maximum flow is particularly significant for applications requiring high flows at very low pressure ratios.

Furthermore, there are cases in which the required compressor staging for a given application requires the use of very low speed and, consequently, an inefficient driver speed with higher required power.

One widely used method of avoiding this performance range limitation is trimming the impeller blades. In that case, the impeller has to rotate at a higher rpm to produce the same head.

The use of trimmed impellers in multistage compressors optimizes the matching between driver efficient speed and single stage compressor required speed, and covers higher flows. In many cases, it allows a better interstage matching by requiring more stages for the same speeds.

Also, there are applications with very few stages, for example two stages, which require exceeding the maximum allowable speed dictated by stress, rotor-dynamics, and Mach number considerations. In these cases, the addition of one more stage reduces the required speed to an inefficient low value for the driver. Trimming the higher number of stages optimizes the selection.

Some applications use series/parallel compressors which have casing with two identical compartments separated by a valve allowing a series or parallel mode of operation between two groups of stages. In these applications, the need for an even number of total stages requires a choice, for example, of four trimmed impellers rather than three standard ones (thus, two stages per compartment).

Normally, impeller trimming is limited to 15 percent of the original blade tip diameter to maintain a minimum radial portion of the impeller above the shroud diameter of the high specific speed types where the blade mean length is critical and to prevent excessive distortion of the flow profile at the impeller tip.

Trimming increases the specific speed of the given impeller; therefore, when applied to low specific speed wheels, it displaces their specific speed value closer to the optimum one, while on high specific speed types, it moves them further away into regions of even higher specific speed and lower efficiency.

In multistage compressor families, where the stages are

Contributed by the Gas Turbine Division of THE AMERICAN SOCIETY OF MECHANICAL ENGINEERS and presented at the 27th International Gas Turbine Conference and Exhibit, London, England, April 18-22, 1982. Manuscript received at ASME Headquarters December 15, 1981. Paper No. 82-GT-228.

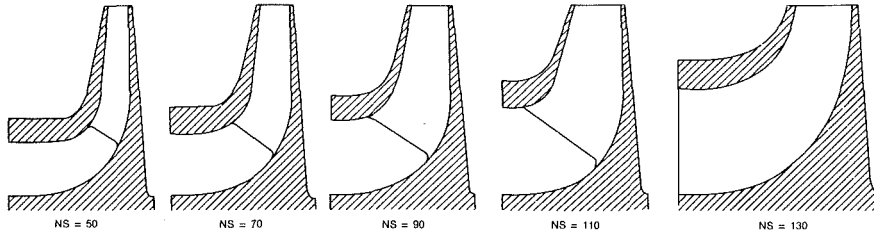


Fig. 1 Typical impeller types of a centrifugal compressor family

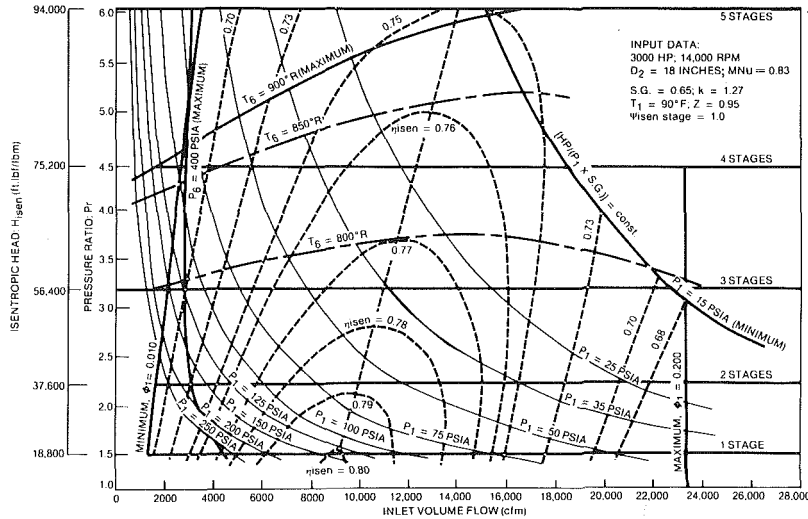


Fig. 2 Limitations of a typical dimensional performance map for a multistage compressor family

Nomenclature

b = axial width (in.)
 C_p = specific heat at constant pressure (0.2430 Btu/lb°R for ambient air)
 D = diameter (in.)
 g = gravitational acceleration (32.17 ft/s²)
 H = head (ft lbf/lbm)
 k = specific heat ratio (1.395 for ambient air)
MNU = machine Mach number
 n = number of blades
 N = rotational speed (rpm)
NS = specific speed [rpm × (CFS)^{1/2} / (ft·lbf/lbm)^{3/4}]
 p = static pressure (psia)
 P = total pressure (psia)
 Pr = pressure ratio
 q = work factor = half of actual head coefficient
SG = specific gravity (1.0 for air)
 T = total temperature (°R)
 U = impeller blade tangential velocity (ft/s)
 w = rotor maximum axial width (in.)
 Z = compressibility factor (1.00 for ambient air)
 β = impeller blade angle (deg), from axial at inlet and from radial at outlet
 Φ_1 = inlet flow coefficient
 Ψ_{isen} = isentropic head coefficient
 η_{isen} = isentropic efficiency

Subscripts

0 = Venturi
1 = compressor inlet
2 = impeller tip

3* = static tap position, slightly downstream of impeller disk tip
3 = inlet of parallel vaneless diffuser
4 = outlet of parallel vaneless diffuser
5 = exit guide vanes leading edge
6 = compressor outlet
av = average
blade = impeller blade
disk = impeller disk
isen = isentropic
s = inducer shroud or tip
h = inducer hub

Formulas

$$H_{isen} = 53.35 \times Z_{av} \times k \times T_1 \times [(P_6/P_1)^{\frac{k-1}{k}} - 1] / SG / (k-1)$$

$$MNU = U_2 / \sqrt{53.35g \times k \times Z_1 \times T_1 / SG}$$

$$NS = N \times Q_1 \sqrt{(CFS) / (H_{isen})^{0.75}}$$

$$q = J \times C_p \times (T_2 - T_1) \times g / U_2^2 = \psi_{isen} / 2\eta_{stage}$$

$$\Phi_1 = 144Q_1 / 60 / (\pi \times D_2^2 / 4) / U_2 = (700.3 / D_2^3) \times Q_1 / N$$

$$\psi_{isen} = H_{isen} / (U_2^2 / 2g) = (1838.3 / D_2^2)^2 \times H_{isen} / N^2$$

$$\eta_{stage} = [(P_6/P_1)^{\frac{k-1}{k}} - 1] \times T_1 / (T_2 - T_1)$$

$$\eta_{1-3^*} = [p_{3^*} / P_1]^{\frac{k-1}{k}} - 1 \times T_1 / (T_2 - T_1)$$

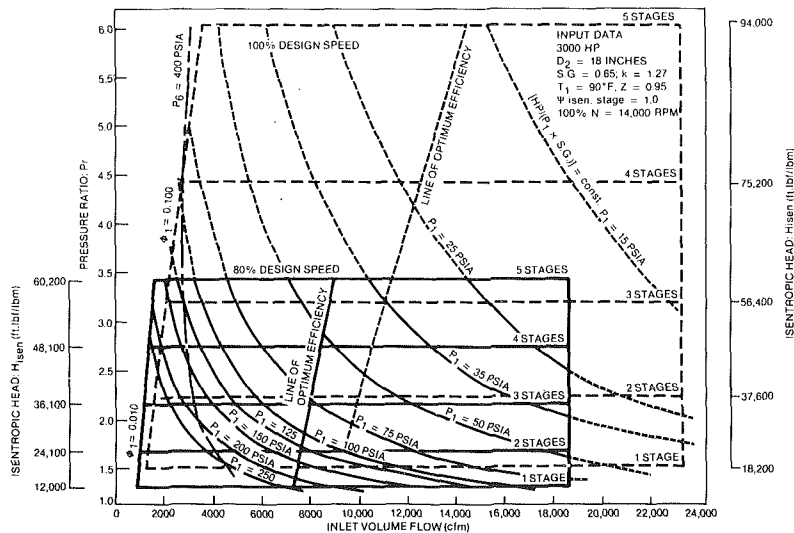


Fig. 3 Typical compressor flow and head coverage at 80 percent versus 100 percent speed

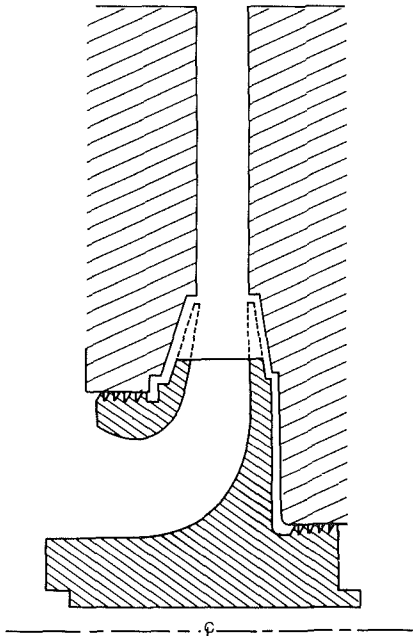


Fig. 4 Trimmed impeller blades with and without extended shrouds

interchangeable, the trimmed impellers cannot be suitably aligned with the standard stationary housings forming the radial diffuser unless the impeller disks remain unchanged; otherwise the flow leaving the impeller at the reduced diameter would impinge on the sides of the vaneless diffuser inner diameter (Fig. 4). Thus, the trimmed impellers of multistage compressor families resemble impellers with extended shrouds.

Impellers of Extended Shrouds

To support compressor staging selection with cropped impeller tips, and as part of a general centrifugal compressor development program, an investigation was conducted at the author's company in 1972 to determine the effect of maintaining the original shrouds on trimmed impellers rather than machining them to the blade's outside diameter.

Initial studies had predicted different effects of extended shrouds on performance as a function of specific speed; therefore, a test program was conducted on two single stages

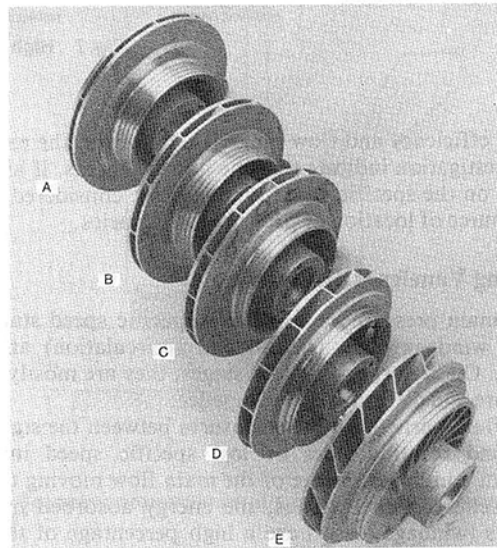


Fig. 5 Impellers of a 7-in. dia Solar compressor family

of a centrifugal compressor family of 7.0-in. backward-swept impellers with vaneless diffusers. The stages identified as "B" and "D," corresponded to low and high specific speed wheels, respectively, (NS of 56 and 105), and were selected from the family shown in Fig. 5.

Each of the two impellers, with a common hub diameter of 2.5 in., had the blade tip diameter reduced to 5.83 in. while maintaining the front and back shrouds at the original 7.0-in. dia. After testing each of the two types of stages with those impellers of extended shrouds, the disks were machined to 5.83 in. (Fig. 6 and 7), and the tests were repeated.

It should be noted that the final configurations became 5.83-in. dia impellers, similar to the original ones with a 7.0-in. dia, but of higher specific speed type (NS of 93 and 153, for "B" and "D," respectively, versus corresponding original values of about 56 and 105). Thus, the test program, when considered from a different point of view, investigated the effect of impeller extended shrouds on compressor performance.

Impeller extended shrouds, as a special type of rotating vaneless diffuser, periodically receive analytical and experimental attention in the hope of improving overall com-

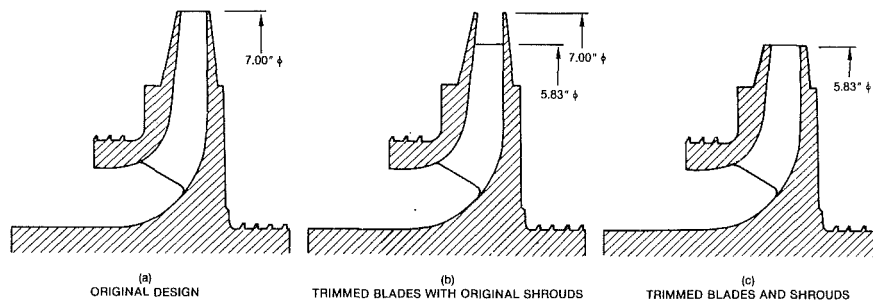


Fig. 6 Low specific speed, type "B" impeller

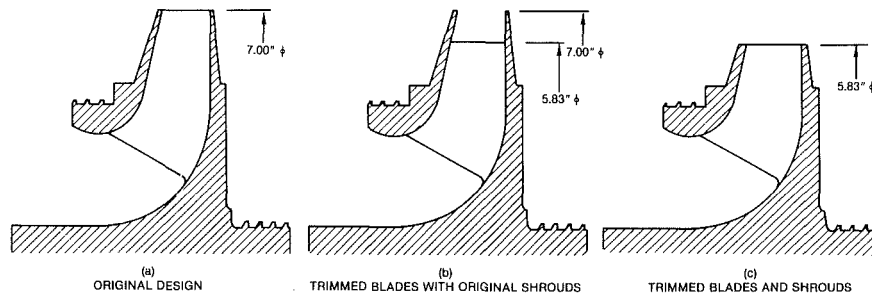


Fig. 7 High specific speed, type "D" impeller

pressor efficiency and flow range [1]. However, the results of this investigation indicate that the improvements, if any, will depend on the specific speed type of stage considered, as the main source of location of pressure losses varies.

Rotating Vaneless Diffusers

The main pressure losses of low specific speed stages are due to windage (disk friction and recirculation) and skin friction. On high specific speed stages, they are mostly due to curvature and diffusion in the impeller.

The fluid particles in the enclosures between the stationary walls and rotating sides of low specific speed impellers represent a high percentage of the main flow moving through the impeller channels. Thus, the energy absorbed by those particles (windage losses) are a high percentage of the total pressure losses.

The highly tangential angles of the flow leaving the low specific speed impellers produce long logarithmic path lengths. This, combined with the low hydraulic radius of the corresponding vaneless diffusers, produces high skin friction losses. In addition, the low-energy boundary layers developing on the diffuser walls, combined with the flat angles, tend to produce flow instabilities which may trigger surge.

One method of reducing the shear losses on the vaneless diffuser sidewalls, with probable improved efficiency and flow range of low-to-medium specific speed stages, is the use of a rotating diffuser.

If the vaneless diffuser sidewalls are stationary, the dynamic head and the logarithmic path length of the flow causing the shear losses are functions of the magnitude and direction of the absolute velocity leaving the impeller.

On the other hand, if the vaneless diffuser sidewalls are rotating, the dynamic head and the path length of the flow causing the shear losses are a function of the magnitude and direction of the relative velocity in the diffuser, which is much smaller and more radial than the absolute velocity. As a result of the reduced friction and the lower tangential flow direction, the tendency for backflow should be much smaller.

However, the gaps between the outside walls of the rotating diffuser and the diaphragms are a source of disk friction and

recirculation losses, similar to the ones at the impeller disk sides, which may nullify the advantages described previously.

Rotating vaneless diffusers have also been considered for use on compressors with vaneless diffusers. The use of a rotating vaneless diffuser between the impeller and the vaneless diffuser improves compressor efficiency [2]. The better flow profile and lower Mach number reaching the diffuser vane leading edge tend to increase the incidence tolerance and, as a result, the flow range, especially at high pressure ratios.

The rotating vaneless diffuser may be driven by the shear of the flow coming out of the impeller channels, thus being a "free" rotating diffuser which may accomplish reductions of up to 20 percent in vaneless diffuser losses [2], or may be driven at a certain fixed speed, thus being a "forced" rotating diffuser [3].

One particular type of "forced" rotating diffuser, where its rotational speed equals that of the impeller, is created by extending the impeller disks beyond the blades. However, tests [1] have shown that when such shroud extension reaches 25 percent of the backward-swept impeller blade diameter, there is no improvement but, rather, deterioration of performance.

This particular type of "forced" rotating vaneless diffuser (impeller with extended shrouds), having shrouds extending 20 percent above the impeller blade diameter, is the subject of this paper.

Stage Description

The two single stages investigated consisted of interchangeable impellers of equal axial length, and hub and tip diameters, but different shroud diameters for low and high specific speed types. These were preceded by radial inlet guide vanes of zero prewhirl, followed by a radial vaneless diffuser whose axial width could be adjusted to match the impeller. The vaneless diffuser was followed by a 90-deg, radial-to-axial bend and a row of 42 exit guide vanes to remove the swirl and to reduce the dynamic pressure before dumping into the exit collector.

These two impellers, originally designed for a blade diameter of 7.0 in., were trimmed to 5.83 in. Despite this 20 percent reduction, the disks maintained the original diameter.

Table 1 Stage geometric features

Symbol	Units	"B" Stage	"D" Stage
NS	---	93	153
$D_{2 \text{ blade}}$	in.	5.83	5.83
$D_{2 \text{ disks}}$	in.	5.83/7.00	5.83/7.00
D_{1h}	in.	2.50	2.50
D_{1s}	in.	3.75	4.40
D_{3^*}	in.	7.50	7.50
D_3	in.	8.24	8.24
D_4	in.	13.00	13.00
$b_{2 \text{ blade}}$	in.	0.336	0.624
$b_{2 \text{ disks}}$	in.	0.336/0.275	0.624/0.500
b_{3^*}	in.	0.380	0.626
$b_3 = b_4$	in.	0.250	0.455
w	in.	2.60	2.60
β_1 (from axial)	deg	71.5	60.00
β_2 (from radial)	deg	54.0	43.0
n	blades	12	14

Subsequently, the disks were machined to 5.83 in., thus creating conventional impellers of higher specific speed than the original design intent (Fig. 6 and 7).

The geometrical features of both types of stages, with impeller blades trimmed to 5.83 in. before and after trimming the 7.00-in. impeller disks to 5.83 in., are included in Table 1 and its corresponding nomenclature in Fig. 8. Figure 9 shows the "D" impeller in its three different configurations.

Test Rig Description

The housing, containing one of the two stages previously described, was connected upstream to a radial muff and downstream to an exit collector.

The rig was driven by a 200-hp electric d-c motor through a speed-increasing gear. Air was drawn from a filter room above the test cell through a bellmouth Venturi into an inlet muff. It was exhausted from the cell through the existing duct work, and the exhaust back pressure was regulated by 6-in. and 2-in. remote-controlled butterfly valves installed in parallel to provide a coarse and fine control.

The entire rig was heavily insulated to reduce heat transfer from or to the rig. Figure 10 shows the installation prior to adding the insulation.

Test Description

The first tests were conducted on the two types of stages with impellers of 5.83-in. blade dia and extended shrouds of 7.0-in. dia. This is shown in Fig. 6(b) and 7(b).

Each of the stages was tested in ambient air at speeds of 18,000, 22,000, and 26,000 rpm (machine Mach numbers of 0.49, 0.60, and 0.70, respectively). Sufficient time was allowed before recording data to stabilize the discharge temperature within half a degree Fahrenheit.

After completing the first phase of the test program, the impeller shrouds were machined down to the blade's outside diameter (Fig. 6(c) and 7(c)), new casing diaphragms were installed to match the vaneless diffusers to the new rotors, and the tests were repeated.

Test Data Acquisition

The air was metered through a bellmouth Venturi. The Venturi sizes were 2 and 3 in., respectively, for each of the two types of stages.

The discharge temperature was measured at four circumferential positions of the exit collector. The inlet temperature was measured at three positions of the transition duct upstream of the inlet muff. The temperature probes were type 104 platinum resistance detectors, using a Rosemount linear bridge system.

Temperature measurements were taken at the manometer

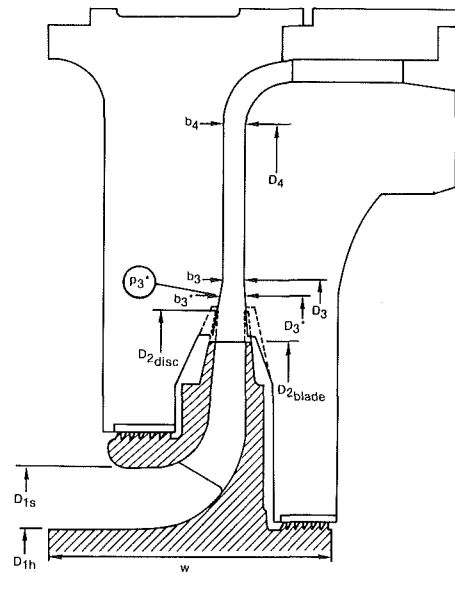


Fig. 8 Geometric nomenclature of a compressor stage with trimmed impeller

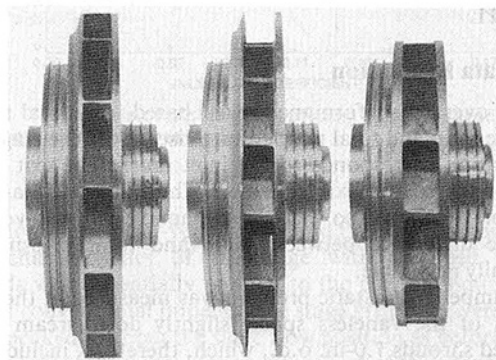


Fig. 9 "D" impeller in its three different configurations

bank (to permit correction for fluid specific gravity when converting to pressure) and at the inlet to the Venturi.

The discharge pressure was measured at three circumferential positions of the exit collector, using static taps. The inlet pressure was measured at three positions of the transition duct between inlet pipe and inlet muff, using static taps.

The static pressure at the vaneless space, slightly downstream of the original impeller tip (7-in. diameter) was

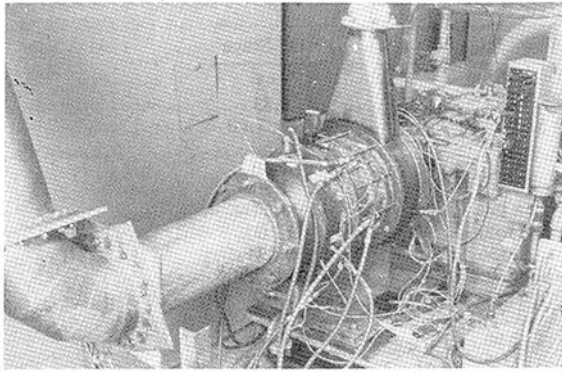


Fig. 10 Test rig for trimmed impellers

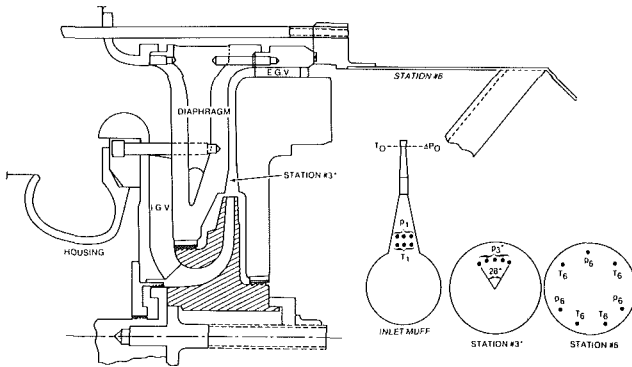


Fig. 11 Test instrumentation

measured at five circumferential positions covering a circular sector of 28 deg at a diameter of 7.5 in. on the front face.

Test rig and drive motor speeds were sensed by magnetic pickups and displayed on an electronic counter. All air pressures were indicated on water manometers using an ambient reference tube. Oil flow, oil temperature, and rig vibration were monitored as indicators of mechanical performance of the rig.

Sketches of test rig and instrumentation location are shown in Fig. 11.

Test Data Evaluation

The overall performance was based on total-to-total pressure ratio and total temperature rise across the stage. The inlet station corresponds to the inlet muff. The exit station corresponds to the exit collector. The inlet muff and exit collector were sized so that the dynamic head was very low and the difference between static and total pressure was essentially negligible.

The impeller tip static pressure was measured at the initial portion of the vaneless space, slightly downstream of the extended shrouds 7.0-in. o.d., which, therefore, includes part of the vaneless space losses.

Isentropic head and efficiencies were calculated from pressure and temperature measurements using isentropic relations. The inlet flow volume was calculated from Venturi temperature and differential pressure and converted to inlet muff conditions. The values of flow and head were non-dimensionalized and plotted as inlet flow coefficient and isentropic head coefficient, respectively.

The uncertainty of flow, head, and efficiency calculations, due to maximum differences of 0.2 in. of water in the bank of manometers and 0.6°C in temperature readings, is ±0.5, ±0.3, and ±1.6 percent, respectively.

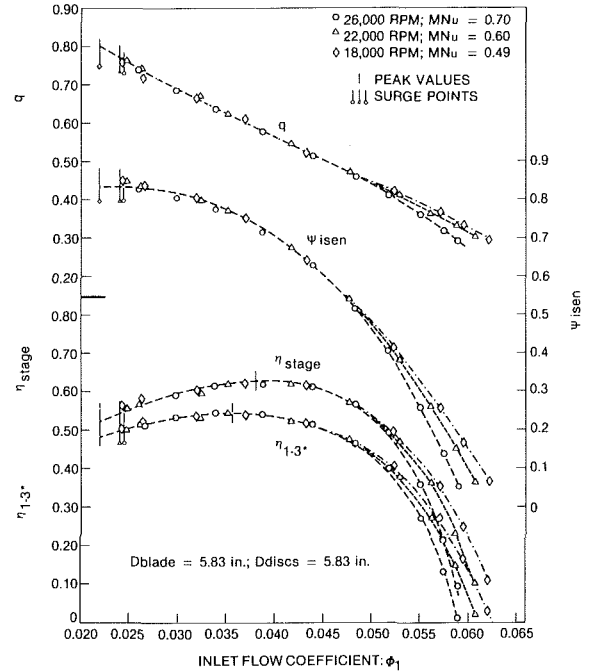


Fig. 12 Test results of lower-than-optimum specific speed impeller, "B" stage, without impeller extended shrouds

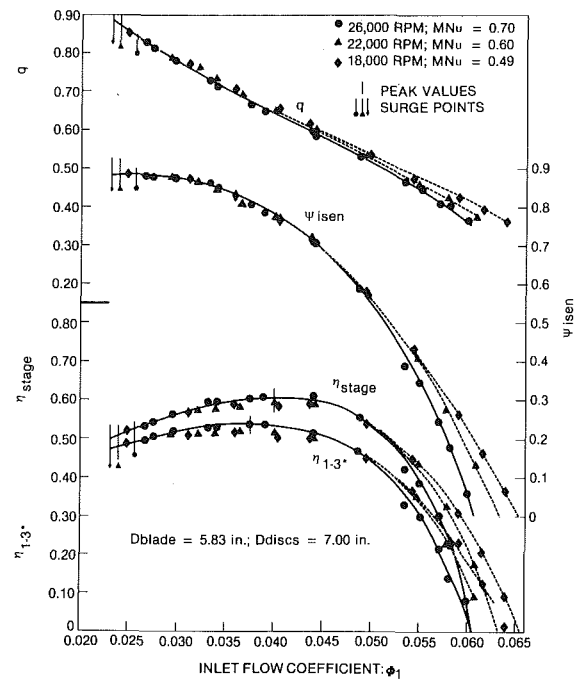


Fig. 13 Test results of lower-than-optimum specific speed impeller, "B" stage, with impeller extended shrouds

Test Results

Specific Speed of 93 ("B" Stage). The "B" stage characteristics, with cropped (same diameter as the blades) and extended impeller shrouds, are shown in Figs. 12 and 13, respectively, for three rotational speeds (18,000, 22,000, and 26,000 rpm). Figure 14 shows the performance comparison of both configurations for 26,000 rpm (machine Mach number of 0.70).

As a result of the 20 percent shroud extension, the peak head increased by about 7 percent. At the point of peak stage efficiency, which reduced by about 3.5 percent, the head

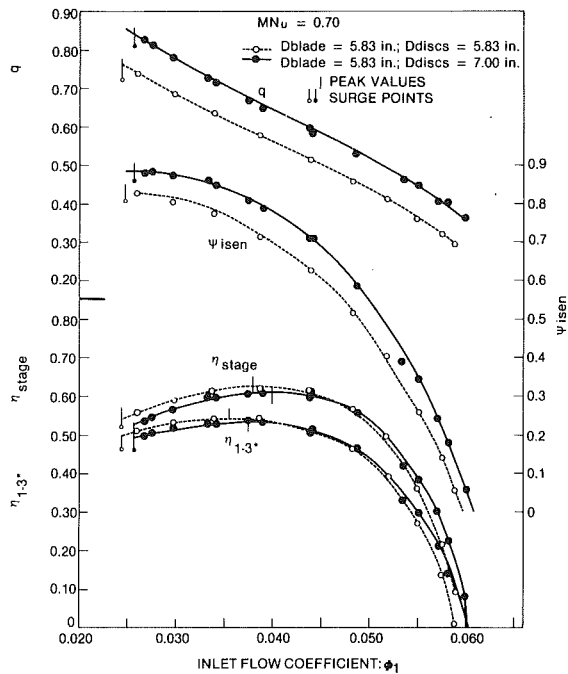


Fig. 14 Comparative test results: lower-than-optimum specific speed impeller, "B" stage, with and without impeller extended shrouds

increased by about 10.5 percent, and the work factor increased by about 14.5 percent.

The maximum flow increased by about 2 percent, while the surge was detected earlier at a 6 percent higher flow. However, the point of maximum pressure rise or maximum head, which is a more conservative measure of the limit of stable operation for high pressure level operations, was the same as before and coincident with the new surge point.

The head-versus-flow and the work factor-versus-flow characteristics of the stage with extended impeller shrouds were essentially parallel to their corresponding curves for the conventional impeller. However, the stage efficiency-versus-flow curve crossed over its corresponding curve before reaching its peak, thus showing a 3.5 percent reduction in its peak value. This peak value occurred at a higher flow than in the conventional stage.

The pseudo-impeller isentropic efficiency is based on static pressure measured slightly downstream of the impeller tip. Efficiency of the configuration with extended shrouds exhibited smaller differences with the corresponding curve of the conventional configuration, but the same crossover, which occurred closer to the point of peak efficiency. That peak value reduced by about 1 percent.

Specific Speed of 153 ("D" Stage). The "D" stage characteristics, with cropped (same diameter as the blades) and extended impeller shrouds, are shown in Fig. 15 and 16, respectively, for three rotational speeds (18,000, 22,000, and 26,000 rpm). Figure 17 shows the performance comparison of both configurations for 26,000 rpm (machine Mach number of 0.70).

As a result of the 20 percent shroud extension, the peak head increased by about 5.5 percent. At the point of peak stage efficiency, which increased by about 3.0 percent, the head increased by about 9.5 percent, and the work factor increased by about 6.3 percent.

The maximum flow increased by about 3 percent, while the surge was detected at a 5 percent lower flow. However, the flow position for maximum pressure rise was the same as before, occurring at much higher flow than the audible surge indication, which had a similar position for both configurations.

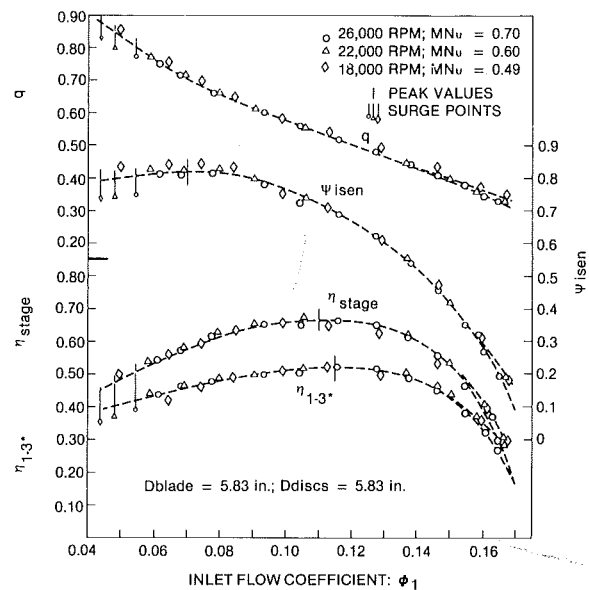


Fig. 15 Test results of higher-than-optimum specific speed impeller, "D" stage, without impeller extended shrouds

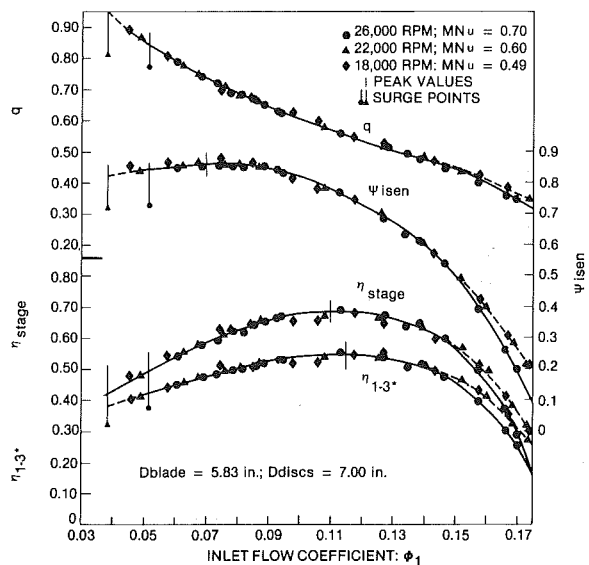


Fig. 16 Test results of higher-than-optimum specific speed impeller, "D" stage, with impeller extended shrouds

Although the head-versus-flow and the work factor-versus-flow characteristics of the stage with extended impeller shrouds were essentially parallel to the corresponding curves for the conventional impeller, the stage efficiency-versus-flow curve peaked at about the same flow position as before, with a 3 percent improvement. On the last third of the speed line, up to surge, the two efficiency curves were coincident.

The pseudo-impeller isentropic efficiency of the configuration with extended shrouds showed a characteristic essentially parallel to the corresponding curve of the conventional impeller, with about 4.4 percent improvement in its peak value.

Table 2 summarizes the test results of the two specific speed impeller types.

Figure 18 shows the trend of percentage change in stage efficiency, due to the impeller extended shrouds, as a function of specific speed, based on the two specific speed impeller types.

Discussion of Test Results

Specific Speed of 93 ("B" Stage). The extended shrouds, as expected, increased the head produced by the impeller blades. This is the result of the additional pumping action of the disks. This effect was higher than on the high specific speed impeller due to the smaller distance between disks.

The peak pseudo-impeller efficiency reduced about 1 percent, since the increase in work factor was slightly higher than the increase in head through the impeller. This indicates that the increase in disk friction and recirculation losses, due to the additional disk surfaces at increased diameter, had a higher effect than the increase in head.

The peak stage efficiency reduced by about 3.5 percent. This higher reduction in stage efficiency than in impeller efficiency (3.5 percent versus 1 percent) indicates that the friction losses in the reduced vaneless space were higher than in the conventional one. It is postulated that the centrifugal effect of the extended disk surfaces made the flow angle near the walls of the vaneless diffuser more tangential. This increased the flowpath length on that region, despite a shorter radial distance. Therefore, the vaneless space losses increased. Since the disk friction, recirculation, and vaneless space losses were higher towards surge, the peak efficiency occurred at a higher flow than in the conventional stage.

The extended shrouds apparently made the impeller more sensitive to the positive slope of the head-flow characteristic. Thus, the point at which the first indication of instability was detected occurred at a higher flow, coinciding with the point of maximum pressure rise. They caused no discernable change in the flow position of the point of maximum pressure rise. However, the maximum flow increased 2 percent.

In summary, since the main source of losses in a lower-than-optimum specific speed stage are the windage and vaneless space losses, the net effect of the extended shrouds on stage efficiency, despite an increase in head, is detrimental, and no discernable effect on surge margin (to the point of maximum pressure rise) is observed.

Specific Speed of 154 ("D" Stage). The extended shrouds, as expected, increased the head produced by the impeller blades. However, the effect was smaller than on the low specific speed wheel because the disks are more separated and the pumping influence on the flow main core is smaller.

The peak pseudo-impeller efficiency improved about 4.4 percent, still occurring at about the same flow position as in the conventional stage and showing that the increase in disk friction and recirculation losses, due to the additional disk surfaces at increased diameter, had a smaller effect than the increased head.

The peak stage efficiency increased by about 3 percent, still occurring at about the same flow position as in the con-

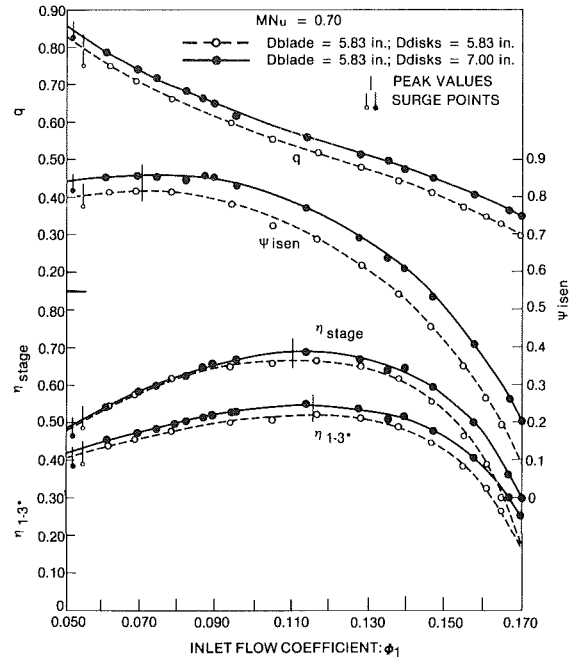


Fig. 17 Comparative test results: higher-than-optimum specific speed impeller, "D" stage, with and without impeller extended shrouds

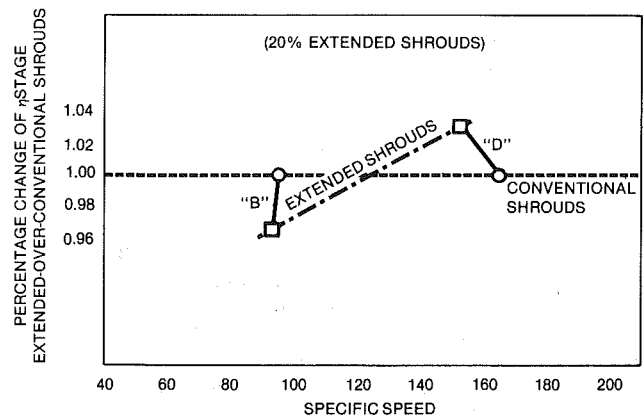


Fig. 18 General trend of the effect of impeller extended shrouds on stage efficiency as a function of specific speed

ventional stage. This slightly lower improvement in stage efficiency than in impeller efficiency (1.4 percent difference), which is within the band of uncertainty of the measurements, could be due simply to that band. Another possibility is that the friction losses in the outer portion of the vaneless space,

Table 2 Effect of extended shrouds test results

Stage type	Lower-than-optimum specific speed impeller "B"	Higher-than-optimum specific speed impeller "D"
Peak head	7% increase	5.5% increase
Head at peak efficiency	10.5% increase	9.5% increase
Work factor	14.5% increase	6.3% increase
Peak pseudo-impeller isentropic efficiency	1% reduction	4.4% increase
Peak stage isentropic efficiency	3.5% reduction	3.0% increase
Maximum flow	2% increase	3% increase
Surge flow	6% higher	5% lower
Flow at maximum pressure rise	same	same

between the static pressure tap and the diffuser exit, were slightly higher than in the conventional one. It is possible that the centrifugal effect of the extended disk surfaces, although smaller than in a low specific speed impeller, made the flow angle near the walls of the vaneless diffuser more tangential, thus increasing the flowpath length in that region, despite a shorter radial distance. Therefore, the vaneless space losses could have increased. However, since the vaneless space losses in a high specific speed stage are a low percentage of the total losses, its overall effect should be negligible.

The extended shrouds did not cause any discernable change in the flow position of the point of maximum pressure rise, which occurred at a much higher flow than the detection of surge. However, the maximum flow increased by about 3 percent.

In summary, the main losses in a higher-than-optimum specific speed stage are due to curvature and diffusion in the impeller, rather than windage and vaneless space skin friction. Therefore, the net effect of the extended shrouds, which increased the head with a negligible penalty in windage and vaneless space losses, has been an increase in stage efficiency. No effect on surge margin, to the point of maximum pressure rise, is observed.

It should be noted that the wheels used for this test program were originally designed for an impeller blade diameter of 7 in. and had much lower specific speed values. Therefore, when trimmed to 5.83 in. (20 percent reduction) and tested, they had lower aerodynamic loading. The use of extended shrouds on an optimum specific speed wheel, with high

loading, should produce higher losses, reducing, to some extent, the benefit in efficiency observed in this test.

Conclusion

These tests indicate that the use of impeller-extended shrouds for the purpose of improving the efficiency of centrifugal compressor stages of low pressure ratio, backward-swept impellers, with vaneless diffusers, will only benefit, and to a small extent, high specific speed stages. It will, however, be detrimental to low specific speed stages. The flow range in the region of acceptable efficiencies, and the surge position, are not influenced by extended shrouds.

It is possible that high pressure ratio compressors, with vaned diffusers, where the inlet conditions to the vaned diffuser throat are critical, could benefit more substantially from the impeller extended shrouds. A better flow profile and lower Mach number reaching the diffuser vanes could increase the incidence tolerance and, as a consequence, the flow range.

References

- 1 Northern Research and Engineering Corporation, "Improvements in Surge Margin and Diffuser Performance: Design, Test and Analysis Report for Task IV Stage Configurations '50 Degree Backslope Shrouded Impeller Series'," Report No. 1230-4, Mar. 1976.
- 2 Rodgers, C., and Mnew, H., "Experiments With a Model Free Rotating Vaneless Diffuser," ASME JOURNAL OF ENGINEERING FOR POWER, Vol. 97, No. 2, Apr. 1975, p. 231.
- 3 Balje, O. E., *Turbomachines—A Guide to Design, Selection and Theory*, John Wiley and Sons, New York, 1981.

J. M. Hannis
Principal Design Engineer.

M. K. D. Smith
Development Engineer.

Ruston Gas Turbines Ltd.,
Lincoln LN2 5DJ England

The Design and Testing of Air-Cooled Blading for an Industrial Gas Turbine

The design and testing of a cooled high-pressure turbine stage to provide advance information for the Ruston Tornado 6MW industrial gas turbine is described. The cooled stage was designed to replace an existing uncooled stage in a current Ruston gas turbine to allow development testing under actual engine conditions. The instrumentation techniques used on the development engine, including infrared pyrometry, are discussed and results of the tests covering nozzle vane and rotor blade cooling under steady-state and transient conditions and engine performance are presented and compared with the design predictions.

Introduction

Design studies for a new industrial gas turbine indicated that to achieve a significant improvement in fuel consumption over current engines, it would be necessary to increase both engine pressure ratio and turbine entry temperature. To achieve a thermal efficiency of over 30 percent a turbine entry temperature of 1000°C would be required and, together with a hot blading life requirement of 40,000 hrs, the necessity for cooling both the first stage nozzle vanes and rotor blades was indicated.

This new gas turbine has now entered production as the Ruston Tornado [1], and the purpose of this paper is to describe the design and development work that was carried out to provide advance information and design confidence in the cooled blading used in this engine.

The first major decision to be made was whether cooled turbine blading would be evaluated in a static cascade rig or in an engine. The latter solution was adopted despite being a longer and costlier route, and the decision was made to incorporate cooled turbine blading in a Ruston TB engine for the following reasons:

(a) The Ruston TB was capable of being uprated to 1000°C turbine entry temperature for development running, and the turbine blading physical size and aerodynamics were similar to the new engine design

(b) Only in a real engine environment can the important effects of combustor temperature distribution and turbulence and rotational effects be assessed.

(c) By treating the design and manufacture of the cooled blading as if it were for a production engine, valuable advance manufacturing experience and realistic data on tolerances could be gained.

(d) A direct comparison between uncooled and cooled engine performance could be made to assess the additional losses due to the turbine blade cooling.

This cooled blade demonstrator engine (CBDE) was extensively instrumented with thermocouples and pressure taps to measure turbine mainstream gas and cooling air conditions, thermocouples to record nozzle vane temperatures, and a traversing infrared pyrometer to measure rotor blade temperatures. An extensive development test program to verify the cooled blade design and to record its performance over a wide range of conditions was undertaken.

The results of this program form the subject matter of this paper which is divided into three sections covering design, instrumentation, and test results and analysis.

1 Design

1.1 General Considerations. The Ruston TB gas turbine is a 2-shaft machine [2] currently rated at 3.6 MW. A cooled turbine stage was designed to replace the uncooled first turbine stage of this engine, the minimum number of changes to the basic engine design needed to incorporate the cooled blading being made. The design objectives of the exercise were to achieve the same design life for the cooled blades at a T.E.T. of 1000°C as the uncooled blading and particularly on the nozzle vanes to achieve a significant reduction in the blade metal temperatures for improved corrosion resistance.

Operating the CBDE at 1000°C T.E.T. would produce a power output of 4.5 MW compared with 3.6 MW of the current uncooled engine. The turbine shafting was capable of absorbing the additional torque without modification.

The existing combustion chambers and burners were considered capable of operating at the increased temperature levels with minor modifications; however, the existing four-piece cast turbine inlet duct assembly would need re-designing to incorporate cooled blading and avoid thermal cracking. The turbine disks and the uncooled second stage turbine blading presented no problems in operating unmodified at the increased rating.

1.2 Turbine Cooling Air System. The first stage nozzle vane is of hollow shell design with a sheet metal insert tube (Fig. 1). Compressor discharge air is supplied to the inner

Contributed by the Gas Turbine Division of THE AMERICAN SOCIETY OF MECHANICAL ENGINEERS and presented at the 27th International Gas Turbine Conference and Exhibit, London, England, April 18-22, 1982. Manuscript received at ASME Headquarters December 15, 1981. Paper No. 82-GT-229.

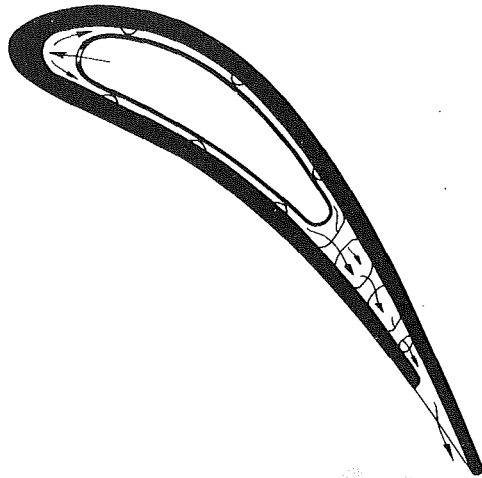


Fig. 1 Cooled nozzle vane, cross section

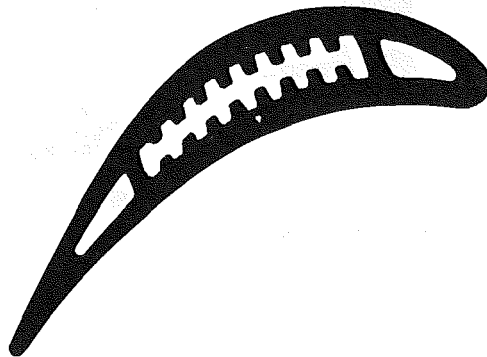
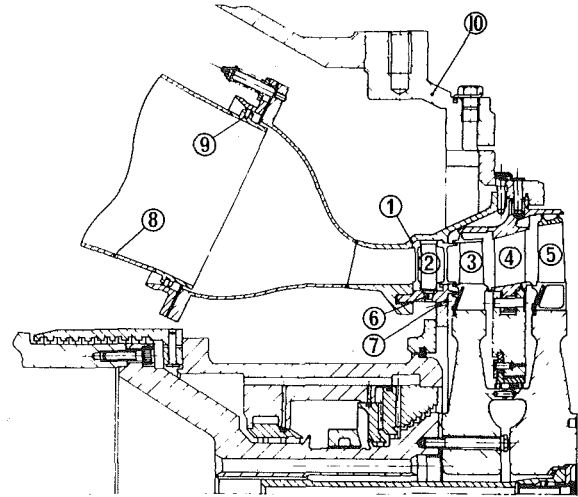


Fig. 2 Cooled rotor blade, cross section

diameter of the vane and flows through holes in the insert tube to provide impingement cooling of the vane leading edge. The cooling air then flows in a chordwise direction between the insert and the vane walls to convectively cool the vane walls. Pedestals between the vane walls enhance the convective cooling downstream of the insert and the air finally discharges through slots on the pressure surface of the vane to film cool the trailing edge.

To supply air to the first-stage rotor blades, compressor discharge air is expanded across a row of preswirl nozzles to provide a reduction in relative cooling air temperature to the blade. The rotor blade cooling is accomplished by a single pass of cooling air through three radial passages, the center passage having longitudinal ribs (Fig. 2). Orifices in a rotor tip cap control the cooling flow distribution between the three passages. The use of trailing edge film cooling in the highly stressed rotor blade was avoided. A double interlocking rim seal is provided at the rotor blade root, and the preswirl nozzles supply additional air above that required by the rotor blades to pack this seal and prevent hot gas ingress. No additional disk cooling air to the front face of the first disk was provided.

1.3 Turbine Mechanical Construction. The general arrangement of the HP turbine is shown in Fig. 3. A one piece turbine inlet duct provided the housing for the nozzle vanes which were thereby relieved of carrying mechanical loads. This inlet duct was a Shaw process investment casting in AIS1309 austenitic stainless with four Nimonic 75 sheet metal ducts welded to it. The nozzle vanes were located in the inlet duct by an inner support ring which also contained the air feed holes to the vanes and the preswirl nozzles for the rotor



- | | |
|------------------------|-----------------------------|
| 1. TURBINE INLET DUCT | 6. AIR FEED TO NOZZLE VANES |
| 2. COOLED NOZZLE VANE | 7. PRE-SWIRL NOZZLES |
| 3. COOLED ROTOR BLADE | 8. FLAME TUBE |
| 4. STAGE 2 NOZZLE VANE | 9. PISTON RING SEAL |
| 5. STAGE 2 ROTOR BLADE | 10. TURBINE OUTER CASING |

Fig. 3 CBDE compressor turbine

Table 1 CBDE design point performance

T.E.T.	1000°C
Inlet mass flow	22.0 kg/s
Pressure ratio	7.8
Compressor speed	11,400 rev/min
Exhaust temp.	556°C
Output power	4515 KW
Thermal efficiency	25.6%

blades. Due to the altered thermal expansion characteristics of this design, piston ring seals were fitted between the inlet duct and the combustor flame tubes.

The nozzle vanes themselves were individual investment castings in IN 939 alloy, selected for its excellent corrosion resistance. The insert tubes were in Nimonic 75 brazed to the vane at the inner platform. A seal plate at the outer platform to eliminate leakage was fitted.

The rotor blades were investment castings in IN 738LC alloy chosen for its combination of creep strength and corrosion resistance. The tip cap was again in Nimonic 75 attached by brazing. The rotor blade was shrouded and the internal coring of the cooling passages only allowed a single radial tip seal as opposed to two on the uncooled blade, accordingly an additional axial tip seal was provided at the blade L.E.

1.4 Turbine Aerodynamics. The turbine annulus, velocity triangles, and vortex distributions for the cooled turbine were maintained similar to the uncooled turbine; however, changes in blade profiles were required to incorporate blade cooling. The existing uncooled vane profile featured a long slender trailing edge and a profile redesign was necessary to incorporate the internal cooling passages. A blade to blade flow analysis by the streamline curvature method indicated that a considerable increase in pitch/chord ratio was practicable allowing the number of vanes to be reduced to 52 from 64 with a consequent benefit in reduced cooling air consumption. The new profile incorporated an increased radius L.E. to reduce the stagnation point heat transfer.

The rotor blade profile was little changed from the uncooled design, the number of blades was maintained at 85 to allow the use of the same disk; however, the pressure surface

Table 2

Coolant inlet temp (°C)	282	252
Coolant mass flow (%)	2.0	1.6
Blade material	IN 939	IN 738 LC
	at hottest vane	at critical section
Peak gas temperature (°C)	1072	927
Mean metal temperature (°C)	790	780
Mean cooling effectiveness	0.35	0.22
Creep life (hrs)	> 10 ⁵	60,000
Thermal fatigue life cycles	> 10 ⁵	4 × 10 ⁴

The cooling effectiveness is defined as $\frac{T_{\text{gas}} - T_{\text{blade}}}{T_{\text{gas}} - T_{\text{coolant inlet}}}$

was modified to increase trailing edge thickness and wedge angle for improved trailing edge cooling.

1.5 Engine Performance Prediction. The predicted performance of the CBDE at full load is summarized in Table 1. Due to the increased rating, causing the compressor to operate in a region of reduced efficiency, only a small increase in thermal efficiency over the uncooled engine is predicted.

1.6 Cooled Blading Design.

1.6.1 External Heat Transfer. For the computed profile velocity distributions, an analysis of the external heat transfer distribution by a momentum integral method [3] was carried out. In laminar flow regions the influence of mainstream turbulence on heat transfer levels was estimated [4]. The resulting heat transfer levels were compared with empirical correlations of gas to blade heat transfer levels [5].

1.6.2 Coolant Heat Transfer. Correlations from the open literature for impingement flow [6], pipe flow [7], and flow over longitudinal ribs [8] and pedestals [9, 10] were used to determine the internal convective heat transfer.

1.6.3 Combustor Traverse. Based on results from earlier tests on this combustion system, the traverse targets were set as follows:

OTDF = 10 percent. RTDF = 3½ percent @ 30 percent span
where the overall temperature distribution factor

$$\text{OTDF} = \frac{\text{Peak gas temp} - \text{Mean gas temp}}{\text{Combustor temp. rise}}$$

and is applied to nozzle vanes, and the radial temperature distribution factor

$$\text{RTDF} = \frac{\text{Circumferential mean gas temp} - \text{mean gas temp}}{\text{combustor temp. rise}}$$

The circumferential mean gas temperature is the circumferential average of the temperature distribution at a given radius.

1.6.4 Coolant Passage Design. Initial cooling passage optimization was carried out using a simple one-dimensional heat transfer model. This was followed by a two-dimensional finite element thermal analysis to give the detailed chordwise temperature distributions across the blade sections at the full load design point and for transient conditions. The aim of the optimization was to minimize the chordwise temperature gradient and in the case of the rotor blade to match the cooling to the radial gas temperature and centrifugal stress distributions.

Air flow tests on models were carried out to determine discharge coefficients for the orifices controlling the coolant flows to ensure that the blades would pass the required amount of cooling air.

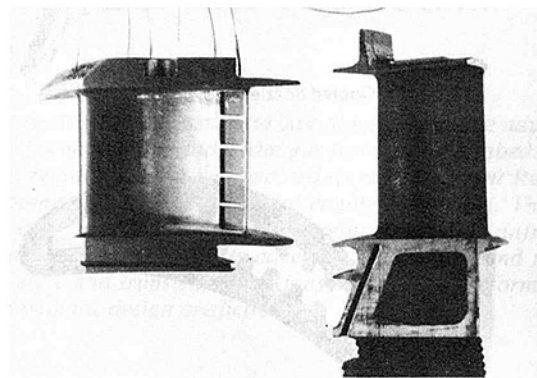


Fig. 4 NGV and rotor blade (showing NGV thermocouples)

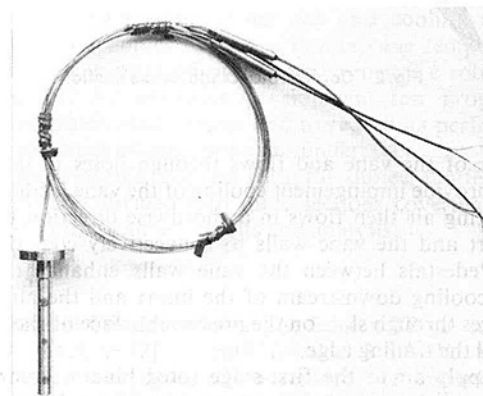


Fig. 5 T.E.T. probe

1.6.5 Blade Life Prediction. The thermal stress distributions due to the chordwise temperature gradients at both design point and for transient conditions were computed. The low mechanical stresses on the nozzle vane were such that no creep life limitation would exist. In the case of the rotor blade, allowance was made for the loss of material properties known to occur in thin sections of conventionally cast alloys. Initial creep life calculations used an empirical factor to account for the effect of the thermal stress distribution superimposed on the centrifugal mechanical stress. Subsequent computations to determine the creep relaxation of the thermal stress and the accumulation of creep damage within the blade section, indicated that the former approach was conservative. The determination of the thermal stress distributions under transient conditions indicated that the maximum strain range occurred at the leading edge for both nozzle vane and rotor blade. The cyclic fatigue life was assessed using a modified Goodman diagram and the Law of Universal Slopes [11].

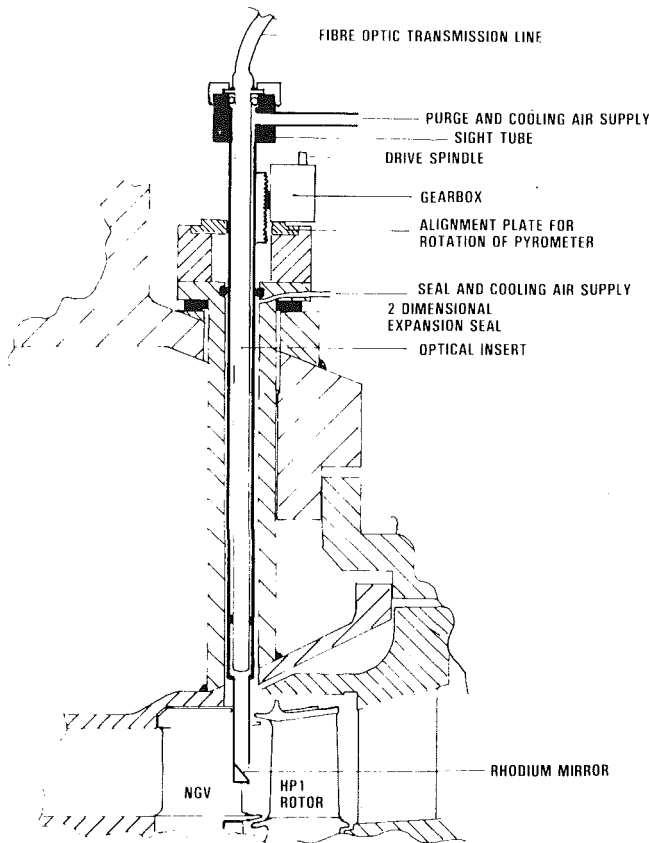


Fig. 6 Pyrometer installation (refer also to Fig. 3)

1.6.6 Predicted Cooled Blade Performance. The predicted temperature levels and life for the cooled nozzle vane and rotor blade are summarized in Table 2.

Instrumentation

The CBDE, having four symmetrically placed combustors, had stator instrumentation which was concentrated on one quadrant of the H.P. turbine, fed by a single combustor. The mechanical design of the test engine made the instrumentation installation difficult, and, consequently, well-proven mechanically simple techniques were used where possible. The installation was such that the turbine could be stripped for examination without destroying the instrumentation.

2.1 Turbine Entry Temperature (T.E.T.). The T.E.T. probes were placed about one chord length upstream of the NGV leading edge and were of a simple robust construction, with a small cross section to minimize flow disturbance. They were comprised of thin walled cylinders with three thermocouple junctions embedded in the wall, facing upstream (see Fig. 5). The high stagnation point heat transfer from the gas to the thermocouple bead reduced the effect of radiation and conduction errors to a level where only a small radiation correction was required, and local gas passage wall temperatures were measured for this purpose. Five probes were used in the "instrumented quadrant" and two in each of the other quadrants were used to assess non uniformity of gas temperature between combustors.

2.2 Nozzle Guide Vane (NGV) Metal Temperature. Six instrumented NGVs were fitted downstream of the T.E.T. probes in the instrumented quadrant. On each of these, wall temperatures were measured by means of six 0.5-mm grounded junction sheathed thermocouples embedded into the wall with Metco 443 Ni/cr/Aluminite plasma spray (see Figs. 4 and 12). To investigate the influence of the ther-

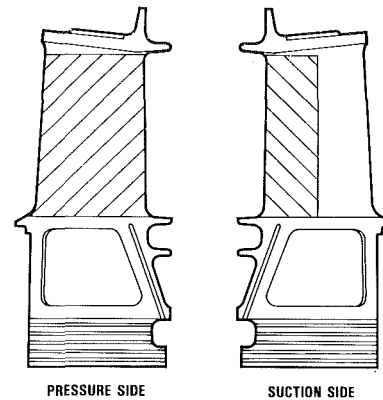


Fig. 7 H.P.1. rotor blade pyrometer coverage

mocouple on the local heat transfer and wall temperature distribution a finite element heat transfer analysis was performed on sections of blade wall with thermocouples present, thus enabling appropriate corrections to be made.

Thermocouple life was influenced by the local wall temperature during running, the hottest leading edge thermocouples having a life of about 5 hrs, other cooler positions surviving up to 25 hrs at design conditions. This phenomenon appeared to be a feature of the installation technique as the same type of thermocouples were used in the T.E.T. probes of which very few had failed, even though they ran 200°C hotter than those in the NGV.

2.3 Rotor Blade Metal Temperature. An infrared pyrometer was used to measure the rotor blade surface temperature. The installation in Fig. 6 enabled radial traversing and rotation of the line of view to give coverage of each blade in accordance with Fig. 7. A single pulse per revolution was used to synchronise the pyrometer output to a datum blade, enabling a full temperature analysis of each blade individually.

The results were displayed on an oscilloscope and recorded photographically, showing the local deviation of metal temperature from the indicated mean temperature. Elaborate signal processing was not found to be necessary as, by careful positioning and shielding of the pyrometer within the environment, the main sources of errors were avoided. Notably, the frequency of carbon spiking was sufficiently low (around 5 Hz compared with [12]) that it failed to register on the photographs which used an exposure of about $\frac{1}{8}$ s.

Also the presence of reflected radiation from objects hotter than the target can give rise to variations of the surface's "effective emissivity" (a combination of the true surface emissivity and the increase in that value which would account for the reflected radiation from the environment [13]). For this installation the predicted temperature gradients within the rotor blade, and the temperature levels of adjacent hot gas path components (including NGVs) were such that errors due to this effect were of the order of ± 5 °C and were consequently neglected.

The pyrometer's target on the blade surface was the projection of a 2-mm spot perpendicular to the direction of viewing. For sections of blade surface at an angle to the viewing direction the area under inspection is increased, but the radiation intensity in the direction of viewing is reduced. To a first approximation the resultant radiation intensity is independent of angle up to about 60 deg. This was confirmed experimentally during calibration tests of the unit prior to application to the engine. Also during normal use on the engine, some areas of the blade were covered at differing angles, by up to 45 deg, and agreement of the measurements was within a few degrees.

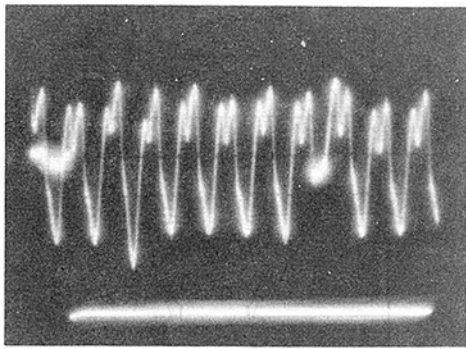


Fig. 8 Sample pyrometer output trace showing 10 blades note reduction in cooling on 8th blade

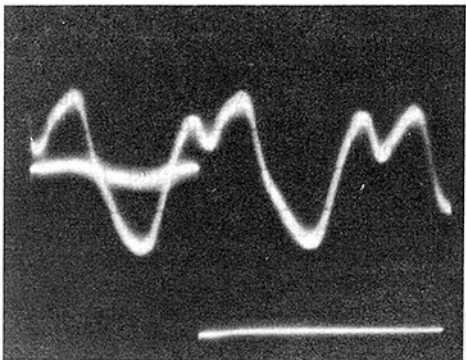


Fig. 9 Sample pyrometer output trace showing 2 blades for detailed analysis

Another effect of the target size is a “smearing” of sharp temperature gradients. The pyrometer measures the average radiation intensity of the target, thus, if there is a steep gradient across the target, the unit measures an average temperature, weighted substantially towards the maximum value as a result of the quasi-exponential response of the pyrometer system. This tends to reduce the sharp temperature gradients around the trailing edge particularly, but a theoretical correction can be applied with reasonable confidence.

Calibrations were performed both optically, using an oven as a radiation source of known temperature and emissivity, for the whole pyrometer system, and electronically, using a DC offset signal generator, to check the frequency response and accuracy of the signal processing unit. The accuracy on calibration was found to be within the quoted accuracy of the calibration equipment.

The uncorrected accuracy of the measurements is of the order of $\pm 15^\circ\text{C}$. However, the accuracy is a function of position on the blade surface and the uncertainty in local reading can, with simple two dimensional radiation and smearing corrections, be reduced to the order of $\pm 5^\circ\text{C}$.

A typical oscilloscope trace showing ten blades is reproduced in Fig. 8. A reduced trailing edge orifice flow area (by approx. 30%) was present in blade 8, and the resultant increase in surface temperature around the trailing edge passage is shown clearly in the figure. A typical trace showing detailed temperature distribution for 2 blades is shown in Fig. 9. Similar traces at different viewing angles and radial positions, enabled the full surface temperature distribution of the rotor blades to be built up.

2.4 Other Instrumentation and Data Handling. In addition to the standard development engine performance instrumentation, the only other equipment fitted was for

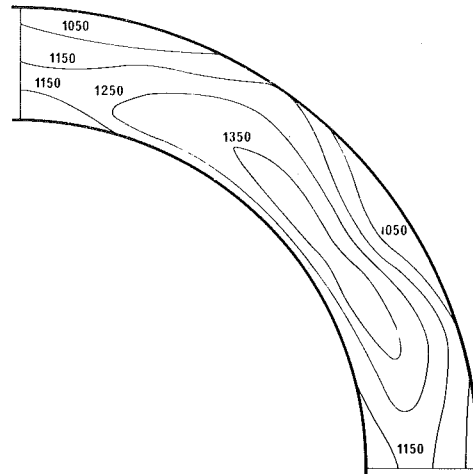


Fig. 10 T.E.T. distribution for one quadrant: isotherms labeled in K

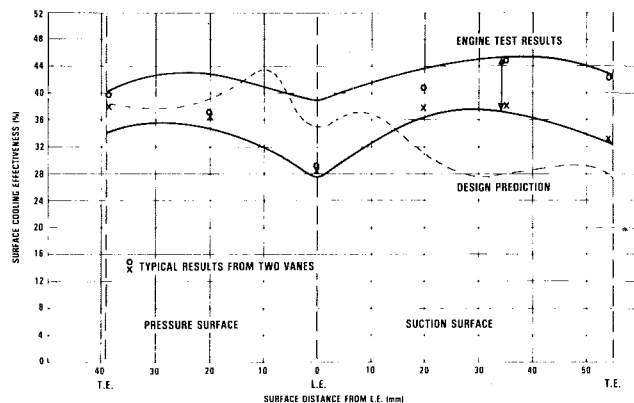


Fig. 11 Nozzle guide vane test results

measuring blade coolant inlet temperatures and inlet and exit pressures, from which, in conjunction with blade flow calibrations at room temperature, the coolant mass flows could be estimated.

Data acquisition was performed by two 60-channel data loggers and analysis of the results was performed “off line” by a PDP11/34 mini computer. For transient testing, selected readings were monitored by fibre optic ultra-violet recorders.

3 Testing: Results and Discussion

The following tests formed the basis of the work:

- Steady-state investigation of NGV cooling performance and engine performance at design and several off design conditions
- Rapid transient testing of NGVs using changing loads on an alternator to cause changes in fuel flow approximating to step functions
- Steady-state detailed analysis of Rotor Blade cooling performance at design and off design conditions

3.1 Mechanical Integrity. The use of thermal paints on turbine stator components and disks revealed no problem areas. In particular, the first stage turbine disk temperatures were no higher than those on the current uncooled engine despite the increased rating. No evidence of thermal cracking or of seal rubs was revealed on strip down.

3.2 Coolant Conditions. The coolant temperatures and pressures were generally in accordance with design predic-

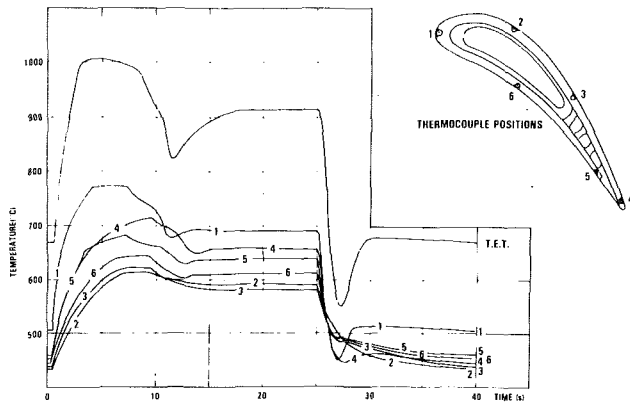


Fig. 12 N.G.V. wall temperature response to T.E.T. transients

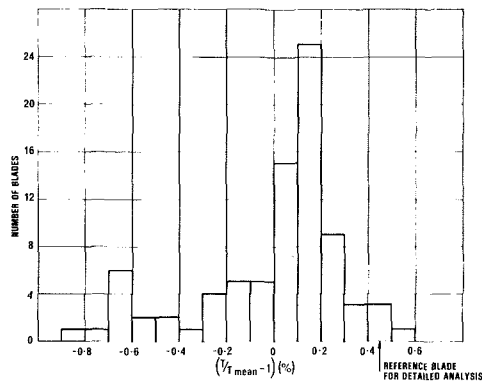


Fig. 13 Statistical distribution of rotor blade mean temperature

tions. Coolant inlet temperatures were slightly higher than expected, indicating a greater heat addition due to the proximity of combustors and hot turbine components than had been allowed for. The calculated coolant flows in the engine were in the range of 2.0–2.4 percent for the nozzle vanes and 1.45 to 1.7 percent for the rotor blades, compared to the design values of 2.0 percent and 1.6 percent, respectively, given in Table 1.

3.3 Combustor Temperature Traverse. Figure 10 shows the isothermals of Turbine Entry Temperature for one quadrant of the HP turbine at full load. It shows clearly the bias of the hotter regions towards the inner radius, with a peak of the radial temperature distribution at about 30 percent annulus span. This governs the critical span position on the rotor blade.

The inward bias of the radial temperature traverse had been expected for this combustor operating at uprated conditions, and while undesirable for a production engine, it was acceptable for development testing. The area averaged mean of the measured temperatures correlated well with T.E.T. values calculated by fuel addition and by heat balance. The temperature distribution factors derived from the measurements were OTDF = 13 percent RTDF = 5.5 percent at 30 percent span.

3.4 Nozzle Guide Vanes. The results obtained in this test agreed with the predictions on overall average metal temperature although the local metal temperature distribution varied. There was a large amount of scatter from vane to vane, both in average level and local distribution, and this is summarized by Fig. 11, which shows local cooling effectiveness versus position in the vane, for the design case, and the envelope of the measured local values.

Because of the short life of the embedded thermocouples, it

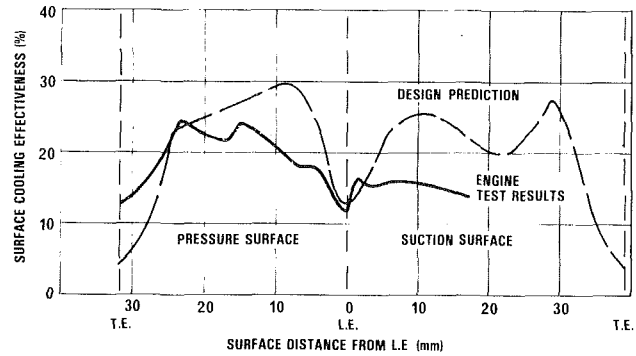


Fig. 14 H.P.1. rotor blade test results

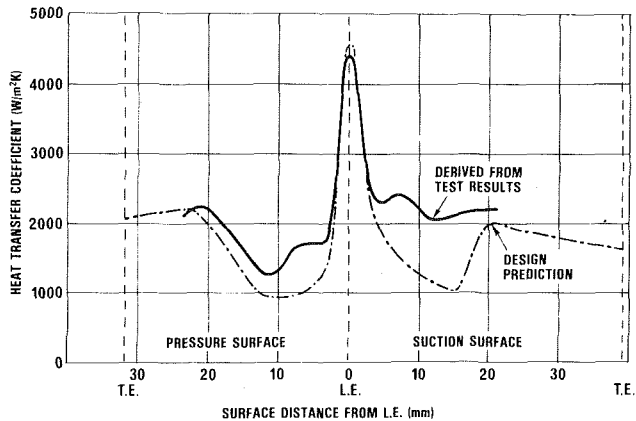


Fig. 15 H.P.1. rotor blade - external heat transfer

has not been possible to establish the repeatability of the results for some areas of the NGVs. Further testing is planned with new instrumentation, but from the results it appears that the pressure side temperatures agree reasonably well with design, the leading edge is hotter than predicted, but the suction side and trailing edge are significantly cooler.

The scatter observed in the results is greater than could be explained by cooling variations between vanes, and is believed to be due to both variations in the gas temperature distribution between the measurement plane and the NGVs, and local variations of velocity and turbulence in the highly disturbed combustor exit flow affecting NGV external heat transfer. The wakes due to the upstream T.E.T. probes, where they fall onto the NGVs, and secondary flows may also have a significant effect.

In general the results are acceptable, with the hottest point on the hottest vane being of the order of 850°C which is significantly less than the nominal turbine entry temperature of the current uncooled Ruston TB 5000 engine.

3.5 Nozzle Guide Vanes - Rapid Transient. The time response of the NGV wall temperatures to large rapid changes of T.E.T. was measured for various conditions of load acceptance and shedding when driving an alternator.

Figure 12 shows the case of a change from low engine load to high load and return to low load. From the results the leading edge was clearly the fastest to respond, followed by the trailing edge regions on both sides of the blade. Also the pressure side tends to respond faster than the suction side.

While no detailed analysis of transient stress and strain under test conditions has yet been undertaken, comparison with design predictions on the basis of the maximum metal temperature difference between hottest and coldest areas of the vane during the transient indicated good agreement during

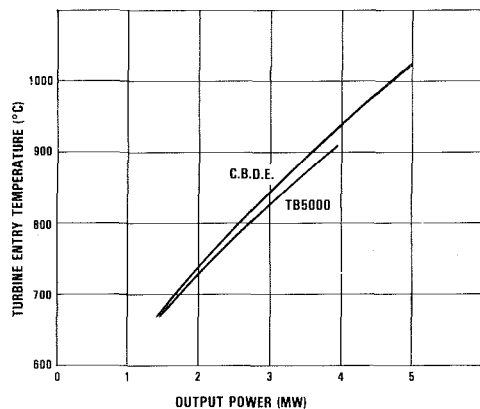


Fig. 16 Engine performance

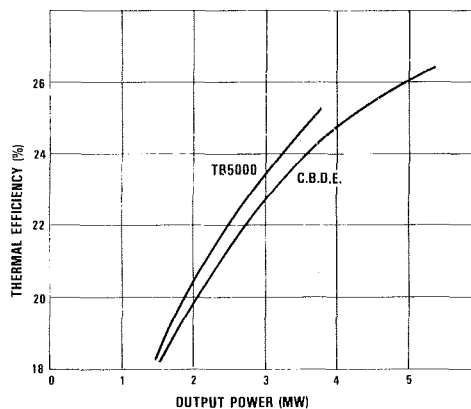


Fig. 17 Engine performance

load acceptance and smaller temperature gradients than predicted on load shed. Thermal fatigue life therefore should not be worse than predicted.

3.6 Rotor Blade Steady State. The results from this part of the testing are considered in two parts: (i) mean and statistical cooling performance; (ii) local cooling performance of individual blades.

(i) The mean blade surface temperature indicated by the pyrometer at the critical section was higher than the design value at 810°C. A major contribution to this was made by a worse radial temperature distribution giving + 5½ percent RTDF at the critical section which corresponds to + 11°C on relative gas temperature.

Statistically the distribution of the blade metal surface temperatures was as shown in Fig. 13. The range of mean surface temperature between hottest and coldest blades is 18°C and the distribution is distorted giving fewer blades above the peak of the distribution than below.

(ii) For the detailed local cooling performance analysis one of the hottest blades (Fig. 13) was selected for detailed analysis, so that creep life assessment could be made on the basis of the "worst case" as naturally one failed blade will cause full turbine failure.

Figure 14 shows the surface cooling effectiveness distribution for this blade as measured compared with that of the design prediction. The average measured value is lower than design and the distribution is different in shape. Notably, the leading edge agrees very well and the temperature gradient in the trailing edge section is less steep (desirable for fatigue life). The main regions of disagreement are on both sides of the blade leading edge for about one half of the chord, where the cooling effectiveness values are appreciably lower than design.

To gain a further insight into the reasons for this, the measured surface temperatures and coolant inlet temperatures were used to derive the gas to blade heat transfer coefficient for the rotor blade. This required the internal coolant heat transfer coefficient to be known and for the simple internal geometry featured on this blade, significant deviations in the coolant heat transfer coefficients from design predictions (section 1.6.2) were considered unlikely. Therefore, the use of design values, corrected for the calculated coolant flow of this blade, was considered adequate.

The resulting distribution compared with the design prediction is shown in Fig. 15, and it is apparent that the predicted areas of lower heat transfer coefficient associated with laminar boundary layers over the front half of the suction surface and at the start of the pressure surface do not appear to exist in the engine. The assumption of turbulent flow over both surfaces would have given a better prediction of the external heat transfer levels.

Table 3 CBDE design point performance as tested

T.E.T.	1000°C
Inlet mass flow	23.5 kg/s
Pressure ratio	8.1
Compressor speed	11,200 rpm
Exhaust temperature	562°C
Output power	4700 KW
Thermal efficiency	26%

Obviously the most important consideration on the rotor blade is whether the required creep life has been achieved. For the "worst case" blade with a measured surface temperature distribution as represented in Fig. 14 the mean metal temperature at the critical section is estimated at 805°C which is 25°C hotter than the predicted design temperature. However the temperature gradients and thermal stress within the blade section are significantly less than predicted and together with the design safety factors incorporated, the calculated creep life on the "worst blade" at measured engine full load conditions meets the design requirement of 40,000 hrs of life.

3.7 Engine Performance. The CBDE performance is summarized by Fig. 16, which shows T.E.T. versus output power for both cooled and uncooled running, and Fig. 17, which shows the thermal efficiency versus power in the same manner. The output power at 1000°C T.E.T. is slightly higher than predicted, as is the thermal efficiency at 26 percent. This shows a significant improvement over the uncooled performance at 3.6 MW even though the fall in compressor efficiency of 2 percent between 3.6 MW and 4.5 MW was greater than expected. The measured full load performance is summarized in Table 3.

Conclusions

A cooled first turbine stage for an industrial gas turbine has been designed and tested in a development engine instrumented to measure the performance of the cooled blades.

The instrumentation techniques used proved satisfactory although the life of the thermocouples used to measure nozzle vane temperature was rather short and improved techniques are to be investigated. The optical pyrometer measurement of rotor blade temperature proved to be very successful and it is intended that production Ruston Tornado engines will have provision for fitting an optical pyrometer as a diagnostic tool.

The results obtained indicated that the nozzle vane metal temperatures were generally, as predicted but the rotor blade temperatures, somewhat higher than predicted; however, the required hot blading design life would still be achieved. The performance of the engine was better than predicted both as regards power output and thermal efficiency.

The development test program described has formed a sound basis for future applications of cooled blading and had given a valuable insight into the problems likely to be en-

countered. In particular, this has allowed the cooled blading used in the Ruston Tornado engine to be designed with a high degree of confidence.

For future cooled blade development the authors' company has commissioned a high-pressure rig facility for testing combustors or static cascades of cooled blades at full engine temperature and pressure or at scaled conditions. The initial series of tests on this facility will be to test both nozzle vanes and rotor blades to obtain a correlation between their performance in the rig as compared to their performance in the engine. The development of improved turbine blade cooling configurations may then be undertaken on this new facility with a high degree of confidence as to their performance in the engine.

Acknowledgments

The authors wish to thank Ruston Gas Turbines Limited for permission to publish this paper and also their colleagues both at Ruston Gas Turbines and at GEC Gas Turbines Limited for their help and co-operation in the work described in the paper.

References

1 Wood, G. R., "The Ruston Tornado: A 6-MW Gas Turbine for Industrial Application," ASME Paper No. 81-GT-171, 1981.

2 Tyler, J. R., "A 3-MW Two-Shaft Industrial Gas Turbine Ruston TB 4000," GEC *Journal of Science and Technology*, No. 1, 1975, pp. 9-15.

3 Seyb, N. J., "A Simplified and Practical Method of determining the External Heat Transfer Coefficients around a Turbine Blade," Aeronautical Research Council Report No. 29398, 1967.

4 Brown, A., and Burton, R. C., "The Effects of Free Stream Turbulence and Velocity Distribution on Heat Transfer to Curved Surfaces," ASME Paper No. 77-GT-48, 1977.

5 Halls, G. A., "Air Cooling of Engine Blades and Vanes," *Aircraft Engineering*, Aug. 1967, pp. 4-14.

6 Chupp, R. E., et al., "Evaluation of Internal Heat Transfer Coefficients for Impingement Cooled Turbine Airfoils," *Journal of Aircraft*, Vol. 16, No. 3, May-June 1969, pp. 203-208.

7 McAdams, W. H., *Heat Transmission*, 3d ed., McGraw Hill, New York, 1954, pp. 202-251.

8 Stachiewicz, J. E., "Effect of Variation of Local Heat Transfer Coefficients on Fin Performance," ASME Paper No. 68-HT-20, 1968.

9 Theoclitus, G., "Heat Transfer and Flow Friction Characteristics of Nine Pin-Fin Surfaces," ASME *Journal of Heat Transfer*, Vol. 80, No. 4, Nov. 1966, pp. 385-390.

10 Faulkner, F. E., "Analytical Investigation of Chord Size and Cooling Methods on Turbine Blade Cooling Requirements," NASA.CR-120882, Aug. 1971, Appen dix D, pp. 189-194.

11 Manson, S. S., and Halford, G., "A Method of Predicting High Temperature Low-Cycle Fatigue Behaviour of Materials," *Proceedings International Conference on Thermal and High Strain Fatigue*, Metals and Metallurgy Trust, London, 1967, pp. 154-170.

12 Douglas, J., "High-Speed Turbine Blade Pyrometry in Extreme Environments," *Measurement Methods in Rotating Components of Turbomachinery*, ASME, 1980, pp. 335-343.

13 Barber, R., "A Radiation Pyrometer Designed for In-Flight Measurement of Turbine Blade Temperatures," SAE 690432, 1969.

The Calculation of Deviation Angle in Axial-Flow Compressor Cascades

L. C. Wang

Lecturer,
Nanking Aeronautic Institute,
Nanking, China

R. Hetherington

Professor.

A. Goulas

Senior Research Fellow,
Cranfield Institute of Technology,
Cranfield, England

The deviation angles of axial flow compressor cascades have been predicted by solving the Reynolds averaged fully turbulent Navier-Stokes equations. A finite element method has been used. To close the problem an algebraic eddy viscosity turbulent model has been chosen. The introduction of the idea of vorticity to the governing equation enables the establishment of a relation between the entropy and the vorticity fields, and the vorticity transport differential equation in the stream function-vorticity method is replaced by a differential operation. A series of calculations have been carried out to examine the influence of cascade geometry on the deviation angle. Very good agreement has been obtained for small angles of incidence with the correlations produced by NASA and using Carter's rule. Good agreement has also been shown for the variation of deviation angle with the angle of incidence with the experimental data of Felix and Emery, as well as for the distribution of the pressure coefficient along the blade axial chord.

Introduction

The estimation of the deviation angle of cascades, which is defined as the difference between the outlet flow angle and the blade mean camber line angle at the trailing edge over their operating range, is of great importance in axial-flow turbomachinery both in design and analysis calculation. Incorrect prediction of these flow angles will lead to the wrong estimation of energy transfer and consequently to mismatching.

Although Wu's general theory of three-dimensional flow [1] has been widely used in turbomachinery design and analysis, no completely satisfactory method for the prediction of flow in axial-flow compressor cascades is available even for the simpler case of design-point operation. In the past the search for better deviation angle prediction methods was confined mainly to correlations of experimental data [2]. Several factors of a cascade, such as camber, thickness, solidity, blade setting angle, incidence angle, inlet Mach number, Reynolds number, etc., influence the deviation angle, made it almost impossible to take all those effects into account when deriving correlation. A calculation therefore of the deviation angle would be highly desirable.

In the field of turbomachinery, while most numerical analysis methods were confined to inviscid flows [3, 4, 5], there is now a tendency towards solving the Reynolds averaged Navier-Stokes equations. Goulas and Baker [6, 7], have made a successful effort to extend the matrix through flow analysis to cover turbulent and viscous flow by solving the streamwise equation of motion to obtain a suitable entropy field derived from the stresses. A finite difference scheme was adopted to solve the resulting differential

equations. The method was applied to the flow in a centrifugal compressor impeller.

Khalil and others eliminated the pressure terms and obtained a vorticity transport differential equation [8] by cross differentiation of the meridian momentum equation and the tangential momentum equation. Using appropriate boundary conditions, they solved the vorticity transport equation to get the vorticity distribution. The stream function could then be calculated by solving numerically a Poisson type equation.

The present paper aims at providing a new blade-to-blade calculation method which is capable of dealing with subsonic fully turbulent flow. Unlike the traditional stream function-vorticity method, only one second-order differential equation is solved, and the other vorticity transport differential equation is replaced by a differential operation.

A finite element method is used as it is considered to be more convenient for handling curved boundaries like those in cascades.

A thin-layer approximation and the algebraic turbulence model produced by Baldwin and Lomax [9] has been chosen to close the Reynolds averaged Navier-Stokes equations.

Calculated deviation angles are compared with the experimental data, deviations obtained using Carter's rule and the NASA correlation, and fairly good agreement is shown. Pressure coefficient distribution is also given to show some aspects of the calculation method. The geometrical data of the cascades used for the calculation and the experimental results of deviation angles are taken from references [10] and [11].

Governing Equations

The three-dimensional momentum equation in turbomachines can be expressed as:

$$-\bar{W} \times (\nabla \times \bar{C}) = -\nabla I + T \nabla S + \bar{F} \quad (1)$$

The three component equations are as follows:

Contributed by the Gas Turbine Division of THE AMERICAN SOCIETY OF MECHANICAL ENGINEERS and presented at the 27th International Gas Turbine Conference and Exhibit, London, England, April 18-22, 1982. Manuscript received at ASME Headquarters December 15, 1981. Paper No. 82-GT-230.

$$\begin{aligned}
& -\frac{W_\theta}{r} \left(\frac{\partial(C_\theta r)}{\partial r} - \frac{\partial W_r}{\partial \theta} \right) + W_z \left(\frac{\partial W_r}{\partial z} - \frac{\partial W_z}{\partial r} \right) \\
& = -\frac{\partial I}{\partial r} + T \frac{\partial S}{\partial r} + f_r \\
& -W_z \left(\frac{1}{r} \frac{\partial W_z}{\partial \theta} - \frac{\partial W_\theta}{\partial z} \right) + \frac{W_r}{r} \left(\frac{\partial(C_\theta r)}{\partial r} - \frac{\partial W_r}{\partial \theta} \right) = -\frac{\partial I}{r \partial \theta} \\
& + T \frac{\partial S}{r \partial \theta} + f_\theta \\
& -W_r \left(\frac{\partial W_r}{\partial z} - \frac{\partial W_z}{\partial r} \right) + W_\theta \left(\frac{1}{r} \frac{\partial W_z}{\partial \theta} - \frac{\partial W_\theta}{\partial z} \right) = -\frac{\partial I}{\partial z} \\
& + T \frac{\partial S}{\partial z} + f_z \quad (2)
\end{aligned}$$

However, these three equations are not independent of the energy equation, so two of the above three (s and \bar{N} components) momentum equations and the energy equation are used here [12].

$$\bar{W} \cdot (-\bar{W}_X (\nabla \times \bar{C})) = \bar{W} \cdot (-\nabla I + T \nabla S + \bar{F}) \quad (3)$$

$$\bar{N} \cdot (-\bar{W}_X (\nabla \times \bar{C})) = \bar{N} \cdot (-\nabla I + T \nabla S + \bar{F}) \quad (4)$$

$$\frac{DI}{Dt} = 0 \quad (5)$$

From equations (3) and (5) we can obtain

$$\bar{W} \cdot T \nabla S = \bar{W} \cdot \bar{F} \quad (6)$$

which is the equation used later to evaluate the entropy field.

According to the definition of \bar{n}

$$\bar{N} = \bar{n} \times \bar{W} \quad (7)$$

Substituting equation (7) and (2) into (4), noticing that

$$\frac{\partial}{\partial m} = \frac{\partial}{\partial r} \sin \alpha + \frac{\partial}{\partial z} \cos \alpha \quad (8)$$

and after some rearrangement the momentum equation becomes

$$\begin{aligned}
\frac{\partial W_m}{\gamma \partial \theta} - \frac{\partial W_\theta}{\partial m} = & -\frac{T}{W^2} \left(W_m \frac{\partial S}{r \partial \theta} - W_\theta \frac{\partial S}{\partial m} \right) \\
& + \left(\frac{W_\theta}{r} + 2\omega \right) \sin \alpha \quad (9)
\end{aligned}$$

By introducing a stream function, ψ , equation (9) becomes

$$\begin{aligned}
\frac{\partial^2 \psi}{\partial m^2} + \frac{\partial^2 \psi}{r^2 \partial^2 \theta} = & \frac{1}{\rho B} \left(\frac{\partial(B\rho)}{\partial m} \frac{\partial \psi}{\partial m} + \frac{\partial(B\rho)}{r \partial \theta} \frac{\partial \psi}{r \partial \theta} \right) - \\
& - \frac{B\rho T}{W^2} \left(W_m \frac{\partial S}{r \partial \theta} - W_\theta \frac{\partial S}{\partial m} \right) + B\rho \left(\frac{W_\theta}{r} + 2\omega \right) \sin \alpha \quad (10)
\end{aligned}$$

for a S1 axisymmetric stream surface.

The turbulence model proposed by Baldwin and Lomax [9] is a two-layer algebraic eddy viscosity model in which μ_t is given as

$$\mu_t = \begin{cases} (\mu_t)_{\text{inner}} & y < y_{\text{crossover}} \\ (\mu_t)_{\text{outer}} & y > y_{\text{crossover}} \end{cases} \quad (11)$$

where y is the normal distance from the wall and $y_{\text{crossover}}$ is the smallest value of y at which values from the inner and outer formulae are equal.

The Prandtl-Van Driest formulation is used in the inner region

$$(\mu_t)_{\text{inner}} = \rho l^2 |\Omega| \quad (12)$$

where $l = K_1 y [1 - \exp(-y^+ / A^+)]$

$$y^+ = \frac{\rho_w u_T y}{\mu_w}$$

For the outer region

$$(\mu_t)_{\text{outer}} = K_2 C_{CP} \rho F_{\text{WAKE}} F_{\text{KLEB}}(y) \quad (13)$$

where K_2 is the Clauser constant, C_{CP} is an additional constant, and

Nomenclature

B = thickness of a S1 stream surface	S = entropy	y^+ = law-of-the-wall coordinate
\bar{C} = absolute velocity vector	s = streamwise direction along the S1 stream surface	z = axial direction of z coordinate
C_θ = absolute velocity component in θ direction	T = static temperature	X/C = fractional axial chord length of the blade
C_p = pressure coefficient	T^* = total temperature	α = angle between m and z direction
\bar{F} = dissipative force	T_l = pitch of the cascade	β = flow direction
f_r = dissipative force component in r direction	\bar{n} = a normal to the S1 stream surface	γ = blade setting angle of the cascade
f_θ = dissipative force component in θ direction	\bar{N} = a direction perpendicular to both s and n direction	ϕ = camber of the blade
f_z = dissipative force component in z direction	N_i = shape function of the finite element	ω = rotational angle speed of the cascade
G = total mass flow	U_T = friction velocity, $\sqrt{\tau_w / \rho_w}$	ψ = stream function
I = rothalpy	\bar{W} = relative velocity vector	ρ = density of the fluid
i = incidence angle	W_m = relative velocity component in m direction	σ = solidity of the cascade
K = stiffness matrix	W_θ = relative velocity component in θ direction	Ω = vorticity
K_c = ratio of specific heats	W_z = relative velocity component in z direction	θ = θ coordinate
m = length of meridian line (Fig. 1)	W_r = relative velocity component in r direction	δ = deviation angle of the cascade
P^* = total pressure	y = coordinate normal to solid surface	τ_{ij} = stress tensor
r = r coordinate		
R = gas constant		

Subscripts

1 = inlet
2 = outlet
w = on the wall

$$F_{\text{WAKE}} = \left\{ \begin{array}{l} \text{or} \\ C_{WK} y_{\text{MAX}} u_{\text{DIF}}^2 / F_{\text{MAX}} \end{array} \right\} \text{the smaller}$$

The quantities y_{MAX} and F_{MAX} are determined from the function

$$F(y) = y |\Omega| [1 - \exp(-y^+ / A^+)]$$

The quantity F_{MAX} is the maximum value of $F(y)$ that occurs in a profile and y_{MAX} is the value of y at which it occurs. The function $F_{\text{KLEB}}(y)$ is the Klebanoff intermittency factor given by

$$F_{\text{KLEB}}(y) = \left[1 + 5.5 \left(\frac{C_{\text{KLEB}} y}{y_{\text{MAX}}} \right)^6 \right]^{-1}$$

The quantity U_{DIF} is the difference between maximum and minimum total velocity in the profile (i.e., at a fixed station).

$$U_{\text{DIF}} = (\sqrt{u^2 + v^2 + w^2})_{\text{MAX}} - (\sqrt{u^2 + v^2 + w^2})_{\text{MIN}}$$

The second term in U_{DIF} is taken to be zero (except in wakes). The constants required in the calculations are given as:

$$\begin{aligned} A^+ &= 26 \\ C_{\text{CP}} &= 1.6 \\ C_{\text{KLEB}} &= 0.3 \\ C_{\text{WK}} &= 0.25 \\ K_1 &= 0.4 \\ K_2 &= 0.0168 \\ P_r &= 0.72 \\ P_{r1} &= 0.9 \\ C_{\text{MUTM}} &= 14.0 \end{aligned}$$

The advantage of the above algebraic model is that it does not require beforehand the knowledge of the edge of the boundary layer.

The dissipative force is a force opposing the velocity vector and was first introduced by Bosman and Marsh [12]. Goulas and Baker [17] have shown that the dissipative force can be expressed as

$$\bar{F} = - \frac{1}{\rho} (\nabla \cdot \tau) \quad (14)$$

where τ is the stress tensor.

The stress tensor can be obtained from

$$\tau_{ij} = \mu_t \frac{\partial W_i}{\partial x_j} \quad (15)$$

In an iterative scheme the velocity distribution is assumed to be known so the velocity gradients can be calculated. With the effective viscosity known through equations (11-13), the stress tensor can be obtained from equation (15), and finally the dissipative force can be calculated using equation (14).

Boundary Conditions

The boundary conditions for viscous flow are different from those used for solving inviscid flows, and it is the handling of those boundaries that present the main problem. The present method is based on a theorem which states that: "The motion of a fluid that occupies a limited, simply connected region is determinate when the value of the vorticity is known at all points in the region and the values of the normal velocity (or tangent velocity) are known at all points of the region's boundary" [15]. Although either normal velocity or tangent velocity is sufficient for the unique determination of the differential equation, the use of both conditions in a numerical procedure is legitimate provided that the two conditions are compatible with each other.

Using, then, equation (9), a relation for the vorticity can be produced as:

$$\begin{aligned} \Omega &= \frac{\partial W_m}{r \partial \theta} - \frac{\partial W_\theta}{\partial m} \\ &= - \frac{T}{W^2} \left(W_m \frac{\partial S}{r \partial \theta} - W_\theta \frac{\partial S}{\partial m} \right) + \left(\frac{W_\theta}{r} + 2\omega \right) \sin \alpha \quad (16a) \end{aligned}$$

As matter of fact, if we define \bar{n} direction component of the vorticity as Ω_n , then it is not difficult to obtain

$$\Omega = \Omega_n + \frac{W_\theta}{r} \sin \alpha \quad (16b)$$

and the governing equation then becomes

$$\frac{\partial^2 \psi}{\partial m^2} + \frac{\partial^2 \psi}{r^2 \partial \theta^2} = \frac{1}{\rho B} \left(\frac{\partial(\rho B)}{\partial m} \frac{\partial \psi}{\partial m} + \frac{\partial(\rho B)}{r \partial \theta} \frac{\partial \psi}{r \partial \theta} \right) + B \rho \Omega \quad (17)$$

With vorticity known at each point in the region and with the appropriate boundary conditions, the stream function can easily be obtained by solving differential equation (17). An estimate of vorticity can be obtained by solving equation (16a) everywhere in the field, except on the solid boundaries, where, because of the velocity being zero, equation (16a) is meaningless. Instead, the non-slip condition is used to determine vorticity on the solid boundaries where ψ is also constant.

For the upstream condition, the stream function distribution is assumed to be linear and the direction of the flow uniform, so that

$$\frac{\partial \psi}{\partial m} = \frac{G}{T_1} \tan \beta_1 \quad (18)$$

where G is the total mass flow, and T_1 is the pitch of the cascade. β_1 is the inlet flow angle measured between the inlet flow and the m direction. Since the inlet flow is assumed to be uniform, the value of vorticity at the inlet has to be

$$\Omega_1 = - \left(\frac{\partial W_\theta}{\partial m} \right)_1 \quad (19)$$

The periodicity condition is applied in the same way as in the inviscid flows, that is, the stream function values between corresponding points along the boundaries differ by G .

For the downstream boundary condition, the stream function distribution is linear, and the direction of outlet flow constant. As a result

$$\frac{\partial \psi}{\partial m} = \frac{G}{T_1} \cot \beta_2 \quad (20)$$

where β_2 refers to the outlet flow angle measured between the outlet flow and $(-\theta)$ directions.

The vorticity at the outlet will be

$$\Omega_2 = - \left(\frac{\partial W_\theta}{\partial m} \right)_2 \quad (21)$$

Of course, on solid boundaries the Dirichlet condition must be applied.

The Finite Element Approach and Calculation Procedure

A weighted residual process (Galerkin) is chosen for the finite element approach.

The stream function is interpolated in each element according to

$$\psi = \sum_{i=1}^n N_i \psi_i \quad (22)$$

where N_i is shape function, and ψ_i is the value of stream function at the node i of a finite element. For an S1 stream surface this leads to

$$[K]\{\psi\} = \{f\} + \{g\} \quad (23)$$

where

$$k_{ij} = \iint_{\Sigma} \left[\frac{\partial N_i}{\partial m} \frac{\partial N_j}{\partial m} + \frac{\partial N_i}{r\partial\theta} \frac{\partial N_j}{r\partial\theta} \right] d\Sigma \quad (24)$$

and

$$f_i = \iint_{\Sigma} N_i \left[\frac{1}{\rho B} \left(\frac{\partial(B\rho)}{\partial m} \frac{\partial\psi}{\partial m} + \frac{\partial(\rho B)}{r\partial\theta} \frac{\partial\psi}{r\partial\theta} \right) + \rho B \Omega \right] d\Sigma \quad (25)$$

$$g_i = \iint_{\Gamma_0} \frac{\partial\psi}{\partial m} N_i ds \quad (26)$$

Σ represents the finite element domain, Γ_0 represents the Neumann condition boundary, and $\partial\psi/\partial m$ refers to the outward derivative along the Neumann condition boundary. Two-dimensional integration is performed by a 2×2 Gauss points integration.

This system of equations (23) is nonlinear since the density ρ depends on the unknown value of ψ . An iterative procedure is therefore required. For a given distribution of the stream function the density can be calculated from the following equations

$$\rho = \frac{P^*}{RT^*} \left[1 - \frac{Kc-1}{2} \frac{W^2}{KcRT^*} \right]^{1/(Kc-1)}$$

$$W^2 = \left(\frac{1}{\rho B} \frac{\partial\psi}{\partial m} \right)^2 + \left(\frac{1}{\rho Br} \frac{\partial\psi}{\partial\theta} \right)^2$$

where P^* and T^* are the total pressure and total temperature at the point, respectively, R is the gas constant, and Kc is the ratio of specific heats. The procedure of solution is given briefly as follows:

The first step for the solution is to assume an initial distribution of the stream function, ψ , so the two components of the velocity vector can be calculated.

The second step is to calculate the resulting stresses. With velocity known at every point, eddy viscosity can be estimated by equations (11-13), and then the stresses and the dissipative force can be calculated using equations (14) and (15).

The third step is to integrate equation (6) along a stream line assuming that the expression $\bar{W} \cdot \bar{F} / TW$ is constant along a stream line between two consecutive θ lines. This integration yields an entropy field in accordance with the velocity field assumed. Equation (16) then is used to evaluate vorticity, Ω , except on the boundary element where the no-slip condition is applied to determine the necessary vorticity in a way similar to that applied in references [13] and [14].

Finally with the velocity, vorticity, and density known, the right hand side of equation (17) can be calculated and a banded matrix set up and solved.

The resulting distribution of ψ has to be compared with the initial one. The procedure is repeated until a convergence criterion defined as

$$\left| \frac{\psi_{\text{new}} - \psi_{\text{old}}}{\psi_{\text{old}}} \right| < \text{eps}$$

is satisfied at each point.

At this stage it must be underlined that the outlet flow angle, β_2 , which is required to determine the deviation angle is a boundary condition of the problem. So a criterion which is unique and physically reasonable has to be chosen to confine β_2 . For an inviscid flow calculation, the Kutta condition can be chosen as such a criterion. But in the present case the application of Kutta condition is impossible because velocities along solid boundaries including the trailing edge of the blades are always zero. Equality, therefore, of the static pressure is required for the two points closest to either side of the trailing edge.

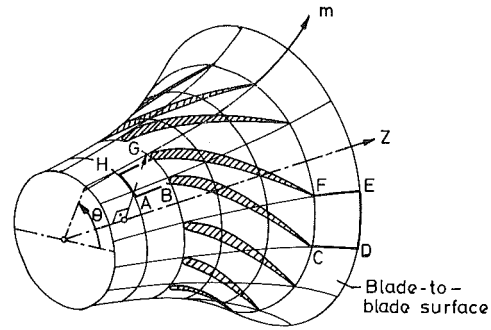


Fig. 1 Blade-to-blade surface of revolution showing $m - \theta$ coordinates.

The computation procedure indicated above for the calculation of ψ has to be repeated with a different β_2 until the condition of equal pressures at either side of the trailing edge is satisfied.

Results of Calculations and Discussions

To verify the present method, calculations have been carried out for the 10C4/30C50 blade cascades with blade section coordinates and other geometrical data taken from reference [10]. The camber of the blade section is $\phi = 30$ deg.

For computations at the trailing edge the pressure and suction lines were extended downstream to form a sharp edge.

As was indicated before, the deviation angle is the difference between outlet flow angle and the blade mean line angle at the trailing edge. Obviously, the flow deviation is an expression of the guidance capacity of the passage formed by adjacent blades. Hence, it is expected that the cascade geometry (blade setting angle, solidity, etc.) and incidence angle will be the principally influencing factors involved.

Since published experimental data for the deviation angle of cascades differ from each other even when the experimental conditions are nearly the same, it was preferred to make comparisons with correlations which are derived from experimental results rather than to compare with individual experimental values. Mainly, there are two correlations, one is the well-known Carter's rule and another one is the NASA correlation [16].

There is a relationship between the incidence angle, i , the blade setting angle, γ , the inlet flow angle, β_1 , and the camber, ϕ , of the cascade:

$$\gamma = \beta_1 - i - \phi/2$$

Because ϕ is fixed for a given blade, only two of those are independently changeable, for example, when i is fixed, then γ can be changed only by varying β_1 .

Figure 2 shows the influence of γ on deviation angle δ for $i = 0.0$ and solidity $\sigma = 1.0$ (achieved by changing the inlet flow angle β_1). Solid line 1 represents Carter's rule and solid line 2 the NASA correlations. The data marked with asterisks are the calculated values. The calculated deviation angles agree well with the NASA correlation within ± 0.5 deg. The maximum discrepancy from Carter's rule is 2.0 deg, which is considered fairly satisfactory.

The variation of the deviation angle δ with the solidity of the cascades σ for various blade setting angle γ and a given incidence angle i ($i = 0.0$) is indicated in Figs. 3 to Fig. 5. Again the solid line 1 refers to $\delta \propto 1/\sqrt{\sigma}$ variation (Carter's rule variation), and the solid line 2 is evaluated from the NASA correlations.

For the case of $\gamma = 14.7$ deg, the calculated values shown with asterisks coincide with the $1/\sqrt{\sigma}$ curve. For the case of $\gamma = 46.2$ deg, the calculated values are closer to the NASA correlation, and within ± 1 deg which is fairly good. For the middle one $\gamma = 22.7$ deg, the deviation angles predicted using

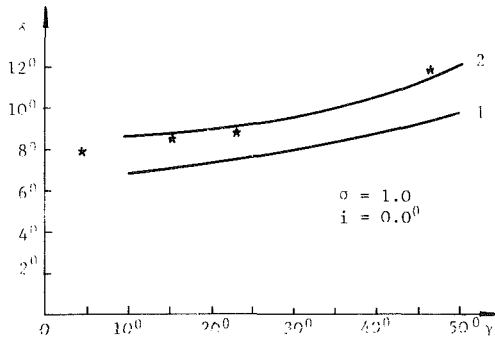


Fig. 2 The variation of deviation angles δ with blade setting angle of the cascade γ for incidence angle being zero and solidity of cascade being 1.0: 1—Carter's rule; 2—NASA correlation; *—calculated values of deviation angles

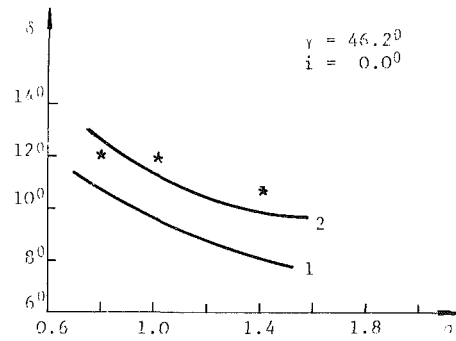


Fig. 5 Deviation angle δ against solidity of the cascade σ for blade setting angle $\gamma = 46.2$ deg and incidence angle $i = 0.0$ deg: 1—Carter's rule; 2—NASA correlation; *—calculated values of deviation angles

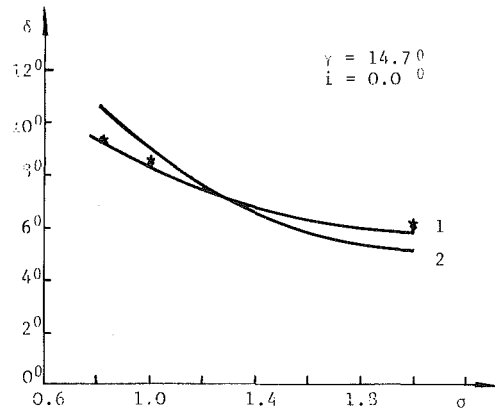


Fig. 3 Deviation angle δ against solidity of the cascade σ for blade setting angle $\gamma = 14.7$ deg and incidence angle $i = 0.0$ deg: 1—Carter's rule; 2—NASA correlation; *—calculated value of deviation angles

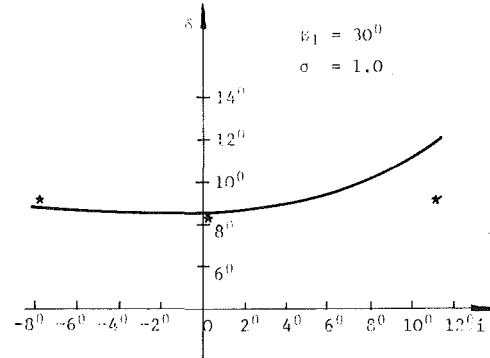


Fig. 6 Variation of the deviation angle δ with the incidence i for solidity of the cascade $\sigma = 1.0$ and inlet flow angle $\beta_1 = 30$ deg

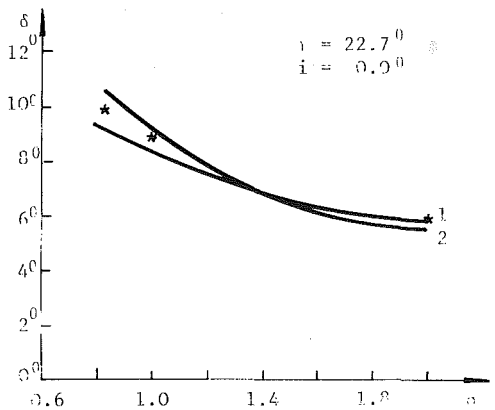


Fig. 4 Deviation angle δ against solidity of the cascade σ for blade setting angle $\gamma = 22.7$ deg and incidence angle $i = 0.0$ deg: 1—Carter's rule; 2—NASA correlation; *—calculated deviation angle

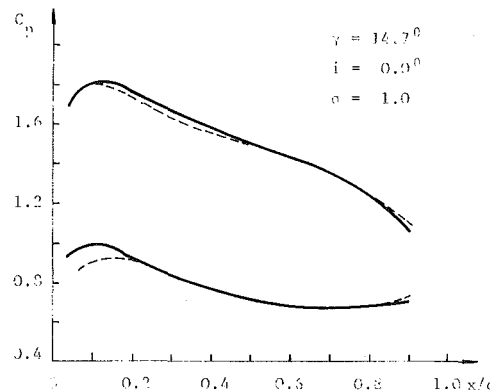


Fig. 7 Comparison of the calculated pressure coefficient with the measured value from [10]; solid line—experimental; dashed line—calculated

NASA correlation, Carter's variation, and the calculated results are all very close.

Figure 6 shows the variation of the deviation angle δ with the incidence angle i for $\sigma = 1$ and $\beta_1 = 30$ deg. In this case the change in incidence angle i is obtained by varying the blade setting angle γ . The solid line shows the experimental data obtained from [10]. Very good agreement is shown for small incidence angles.

For a large angle of incidence, 12 deg, the deviation is underestimated by about 3 deg.

Figure 7 shows a comparison between the calculated pressure coefficient and the one measured by Felix and Emery [10], for $\gamma = 14.7$ deg, zero incidence, and $\sigma = 1$.

Very good agreement is shown everywhere except near the

pressure side of the leading edge. The discrepancy at the leading edge is due to a combination of the rather coarse grid used for the calculation and the high curvature at the leading edge.

For a typical cascade calculation the total node number is 191, and the tolerance of convergence is 0.01. The limited number of grid points was due to the use of a mini-computer, GEC 4070, to carry out the calculations. The predicted total pressure recovery factor is 0.996.

Conclusion

A numerical method to predict the deviation angle for cascades has been developed. It is based on the solution of the flow field as a blade-to-blade surface using finite elements. The flow is considered to be subsonic and fully turbulent. A thin boundary layer approximation and an algebraic turbulence model has been used to close the Reynolds averaged

Navier-Stokes equations. The non-slip condition has been utilized to determine the boundary values of the vorticity. For the rest of the flow field the vorticity is calculated from a transport equation, the right hand side of which includes entropy gradients accounting for the losses.

The entropy field itself has been calculated through a first order partial differential equation, the right hand of which is a function of the dissipative force which is also a function of the stress gradients.

A series of calculations have been carried out to examine the influence of cascade geometry on deviation angle. Very good agreement has been obtained for small angles of incidence with the correlations produced by NASA and the values obtained by using Carter's rule. Good agreement has also been shown for the variation of deviation angle with angles of incidence with the experimental data of Felix et al. [10], as well as for the distribution of the pressure coefficient along the blade axial chord.

Acknowledgments

The authors would like to thank Professor N. Laws, Dr. D. Deeves, Mr. R. J. Goult, and Mr. G. J. Liu for helpful discussion.

References

- 1 Wu, C. H., "A General Theory of Three-Dimensional Flow in Subsonic and Supersonic Turbomachines of Axial, Radial and Mixed-Flow Types," NACA TN 2604, 1952.
- 2 Carter, A. D. S. and Hughes, H. P., "A Theoretical Investigation into the Effect of Profile Shape on the Performance of Aerofoils in Cascades," ARC, R&M 2384, Mar. 1946.
- 3 Hirsch, C. H. and Warzee, G., "A Finite Element Method for the

Axisymmetric Flow Computation in a Turbomachine," *International Journal for Numerical Methods in Engineering*, Vol. 10, No. 1, Jan. 1976, pp. 93-113.

4 Hirsch, C. H. and Warzee, G., "An Integrated Quasi-3D Finite Element Calculation Program for Turbomachinery Flows," *ASME JOURNAL OF ENGINEERING FOR POWER*, Vol. 101, No. 1, Jan. 1979.

5 Baskharone, E. and Hamed, A., "A New Approach in Cascade Flow Analysis Using the Finite Element Method," *AIAA Journal*, Vol. 19, No. 1, Jan. 1981, pp. 68-71.

6 Goulas, A. and Baker, R. C., "Flow in Centrifugal Compressor Impellers: A Hub-to-Shroud Solution," *The Journal of Mechanical Engineering Science*, Vol. 22, No. 1, Feb. 1980, pp. 1-8.

7 Goulas, A., "A Blade-to-Blade Solution of the Flow in a Centrifugal Compressor Impeller with Splitters," *ASME JOURNAL OF ENGINEERING FOR POWER*, Vol. 102, No. 3, July 1980, pp. 632-637.

8 Khalil, I., Tabakoff, W., and Hamed, A., "Viscous Flow Analysis in Mixed Flow Rotors," *ASME JOURNAL OF ENGINEERING FOR POWER*, Vol. 102, No. 1, Jan. 1980, pp. 193-201.

9 Baldwin, B. S. and Lomax, H., "Thin Layer Approximation and Algebraic Model for Separated Turbulent Flows," *AIAA Paper No. 78-257*, 1978.

10 Felix, A. R. and Emery, J. C., "A Comparison of Typical National Gas Turbine Establishment and NACA Axial-Flow Compressor Blade Sections in Cascade at Low Speed," *NACA TN 3937*, 1957.

11 Miller, M. J., "Estimation of Deviation Angle for Axial-Flow Compressor Blade Section Using Inviscid Flow Solution," *NASA TN D-7549*, 1974.

12 Bosman, C. and Marsh, H., "An Improved Method for Calculating the Flow in Turbomachines, Including a Consistent Loss Model," *Journal of Mechanical Engineering Science*, Vol. 16, No. 1, 1974, pp. 25-31.

13 Campion-Renson, A., "On the Stream Function-Vorticity Finite Element Solution of Navier Stokes Equations," *International Journal for Numerical Methods in Engineering*, Vol. 12, No. 12, Dec. 1978, pp. 1809-1818.

14 Gouri, D., Bonadventure, K. F., and Claude, B., "A $\psi - \omega$ Finite Element Formulation for the Navier-Stokes Equations," *International Journal for Numerical Methods in Engineering*, Vol. 17, No. 2, Feb. 1981, pp. 199-212.

15 Wu, J. C. and Gulcat, U., "Separate Treatment of Attached and Detached Flow Regions in General Viscous Flows," *AIAA Journal*, Vol. 19, No. 1, Jan. 1981, pp. 20-27.

16 "Aerodynamic Design of Axial-Flow Compressors," *NASA SP-36*, 1965.

17 Goulas, A. and Baker, R. C., "Through-flow Analysis of Viscous and Turbulent Flows," *ARC CP 1382*, 1978.

M. Sakata
Professor.

T. Aiba
Graduate Student.

Department of Physical Engineering,
Tokyo Institute of Technology,
Ookayama, Meguro-ku, Tokyo, Japan

H. Ohnabe
Chief Research Engineer,
Aero-Engine and Space Operations,
Ishikawajima-Harima Heavy
Industries Co., Ltd.
Mukodaicho, Tanashi, Tokyo, Japan
Mem. ASME

Transient Vibration of High-Speed, Lightweight Rotors Due to Sudden Imbalance

In the field of rotor dynamics, increased attention is being given to the transient response analysis of the rotor, since the effects of impact loading and vibrations of the rotor arising from blade loss can be studied by a time transient solution of the rotor system. As recent trends in rotating machinery have been directed towards lightweight, high-speed flexible rotors, the effect of flexibility on transient response analysis is becoming of increasing importance. In the present paper, a transient vibration analysis is carried out on a flexible-disk/flexible-shaft system or rigid-disk flexible-shaft system subjected to a sudden imbalance that is assumed to represent the effect of blade loss. To solve the basic equation governing a rotating flexible disk the Galerkin's method is used, and the equation of motion of the rotor system is numerically solved by employing the Runge-Kutta-Gill's method. Experiments were conducted on a model rotor having a blade loss simulator; the shaft vibrations were also measured. The validity of the analytical results was demonstrated by comparison with the experimental results.

Introduction

In the field of rotor dynamics, especially concerned with jet engines, the transient response analysis of a rotating system in the event of blade loss is becoming of increasing importance, since the effects of impact loading and vibration of rotor can only be studied by a time transient solution of the rotor system. The transient response of rotor-bearing system was studied by Kirk and Gunter [1] and analyses using a model for dual-rotor jet engine system were studied by Childs [2, 3] and Dennis, Eriksson, and Seitelman [4]. In these reports, analyses are carried out by assuming rigid disks fixed to flexible shafts and flexible bearing supports. Recent trends in rotating machinery have been directed towards lightweight, high-speed flexible rotors, and the effect of disk flexibility on the transient response is becoming of increasing importance also. A number of studies have been reported on the steady-state vibration of rotating systems constituted of flexible disks and shafts [5-9]. However, to the authors' knowledge, little has been studied so far on the transient vibration of a flexible-disk/flexible-shaft system arising from blade loss.

In the present paper, the equation of motion necessary to calculate the transient response is derived and a vibration analysis is carried out of a system consisting of a flexible disk fastened to a flexible shaft with a rigid boss. The effect of blade loss is represented by a sudden increase of imbalance or eccentricity of the rotor that is expressed by two types of time functions. In order to solve the basic equation governing a rotating flexible disk, the Galerkin method is used, and the equation of motion of the rotor system is numerically solved

by using the Runge-Kutta-Gill method. Although the effects of bearing flexibility and damping are very important in blade loss problems, a rigid bearing support is considered in the present study in order to pinpoint the effect of disk flexibility on the transient response.

Experiments were conducted using a model rotor having a blade loss simulator and the shaft vibrations arising from a sudden increase of imbalance were measured. The experimental results were compared with the analytical results.

Analysis

Basic Equation Governing Deformation of Rotating Flexible Disk. The coordinate systems adopted for analyzing the motion of the rotating shaft-disk system are shown in Fig. 1. The coordinate $O-XYZ$ constitutes the laboratory system, with the Z -axis being vertical and coinciding with the center line through bearings, and $S-xyz$ is the moving coordinates fixed to the boss-disk system, with origin S being the geometric center of the boss-disk system. The z -axis coincides with the tangent of the center line of the deformed shaft at S , the x -axis coincides with the direction of the segment SG , where G is the mass center of the boss-disk system and the distance $SG(=\delta)$ is the "eccentricity." The orientation of the moving coordinate system $S-xyz$ is defined by the Euler angle set θ, ϕ, ψ as illustrated in the figure. The displacement of the shaft, S , is represented by the cylindrical coordinate (δ, ζ) , where S is assumed to remain in the XY -plane since small deflection will be considered in the present paper. Hence, the rotating angle of the disk is given by $\alpha \doteq \phi + \psi$.

An element in the disk is located by r, η coordinate, and the lateral deflection is denoted by $U_z(r, \eta, t)$. The equation of motion is written as [10]

Contributed by the Gas Turbine Division of THE AMERICAN SOCIETY OF MECHANICAL ENGINEERS and presented at the 27th International Gas Turbine Conference and Exhibit, London, England, April 18-22, 1982. Manuscript received at ASME Headquarters December 15, 1981. Paper No. 82-GT-231.

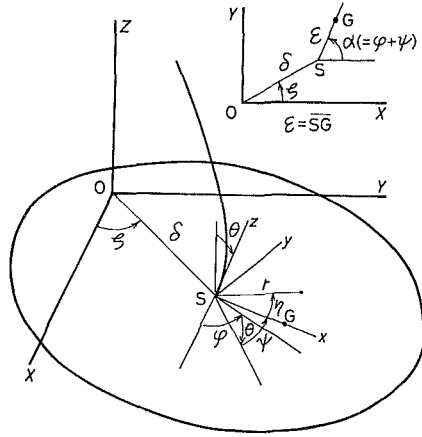


Fig. 1 Schematic representation of rotating disk-shaft system and coordinate system

$$\frac{1}{r} \frac{\partial}{\partial r} \left[r(\sigma_R)_c \frac{\partial U_z}{\partial r} \right] + \frac{1}{r} \frac{\partial}{\partial \eta} \left[(\sigma_T)_c \frac{1}{r} \frac{\partial U_z}{\partial \eta} \right] - \frac{D_s}{2h} \left(\frac{\partial^2}{\partial r^2} + \frac{1}{r} \frac{\partial}{\partial r} + \frac{1}{r^2} \frac{\partial^2}{\partial \eta^2} \right)^2 U_z - \rho A_z = 0 \quad (1)$$

where A_z is the acceleration; $(\sigma_R)_c$ and $(\sigma_T)_c$ are respectively, the radial and tangential component of the in-plane stresses due to the spin-induced centrifugal force-field; ρ , $2h$, and D_s , the density, thickness, and flexural rigidity, respectively, of the disk.

The in-plane stresses determined from the applicable conditions at the inner and outer disk boundaries, i.e., $U_r = 0$ at $r = b$ and $(\sigma_R)_c = 0$ at $r = a$, are represented as

$$(\sigma_R)_c = \frac{\rho \omega^2}{8} \left\{ a^2 R - \frac{a^4}{r^2} S - (3 + \nu) r^2 \right\}$$

$$(\sigma_T)_c = \frac{\rho \omega^2}{8} \left\{ a^2 R + \frac{a^4}{r^2} S - (1 + 3\nu) r^2 \right\} \quad (2)$$

where ω is the spin-angular velocity, ν the Poisson's ratio, and

$$R = \frac{(1 + \nu) \{ 3 + \nu + (1 - \nu) \beta^4 \}}{1 + \nu + (1 - \nu) \beta^2}$$

$$S = \frac{(1 - \nu) \{ (1 + \nu) \beta^4 - (3 + \nu) \beta^2 \}}{1 + \nu + (1 - \nu) \beta^2} \quad (3)$$

where $\beta = b/a$ is the boss/disk diameter ratio.

After some calculation and neglect of small terms, the acceleration is represented as

$$A_z = \ddot{U}_z - r \{ X_1 \cos \eta + X_2 \sin \eta \} + \frac{C_2}{\rho} \dot{U}_z \quad (4)$$

where C_2 is the damping coefficient of disk and

$$X_1 = (\ddot{\theta} + \theta \dot{\phi}^2 + 2\theta \dot{\phi} \dot{\psi}) \cos \psi + (\theta \ddot{\phi} - 2\dot{\theta} \dot{\psi}) \sin \psi$$

$$X_2 = -(\ddot{\theta} + \theta \dot{\phi}^2 + 2\theta \dot{\phi} \dot{\psi}) \sin \psi + (\theta \ddot{\phi} - 2\dot{\theta} \dot{\psi}) \cos \psi \quad (5)$$

It is extremely difficult to obtain the exact solution of equation (1) after substitution of equation (4). Hence, we resort to the Galerkin method and use the admissible function of the form

$$U_z(r/a, \eta, t) = U_z(\chi, \eta, t) = aW(\chi) \{ T_1(t) \cos \eta + T_2(t) \sin \eta \} \quad (6)$$

where $T_1(t)$ and $T_2(t)$ are arbitrary functions of time t and

$$W(\chi) = \chi^5 + A\chi + B\chi^3 + C\chi^{-1} + D\chi \ln \chi \quad (7)$$

is a function of the dimensionless variable $\chi = r/a$, where

$$A = \frac{(1 - \nu) \beta^8 - 3(1 + 3\nu) \beta^4 + 16(2 + \nu) \beta^2 - 6(3 + \nu)}{3 + \nu + (1 - \nu) \beta^4} + 12(-\ln \beta)$$

Nomenclature

a = inner radius of disk, m	disk-shaft interaction moments, Nm	(δ, ζ) = polar coordinate of shaft deflection
A_z = transverse acceleration of disk, m/s ²	M_r = bending moment of disk, Nm/m	ϵ = mass eccentricity of disk, m
b = outer radius of disk, m	M_{rt} = torsional moment of disk, Nm/m	(θ, ϕ, ψ) = Euler angles, rad
C_1, C_2 = damping coefficients of shaft and disk Ns/m, Ns/m ⁴ , respectively	q_r = shear force of disk, N/m	ν = Poisson's ratio
D_s = flexural rigidity of disk, Nm/rad	(r, η) = polar coordinate system fixed to disk	ρ = mass density of disk, kg/m ³
h = half thickness of disk, m	t = time, s	$(\sigma_R)_c, (\sigma_T)_c$ = radial and tangential components of in-plane stresses in disk, Pa
I_x, I_z = x, z components of moment of inertia of boss, kgm ²	t_0 = rise time, s	χ = dimensionless radius, (r/a)
k_1, k_2, k_3 = spring constants of shaft, N/m, N/rad, Nm/rad, respectively	U_z = transverse displacement of disk, m	ω = rotor spin velocity, rad/s
m = mass of boss and disk, kg	W = approximate solution for Galerkin's method	
M_{q1}, M_{q2} = x, y components of disk-shaft interaction moments, Nm	x, y, z = coordinate system fixed to disk, m	Subscripts
M_{qX}, M_{qY} = X, Y components of	X, Y, Z = coordinate system fixed to space, m	r = radial direction
	X_g, Y_g = X, Y coordinates of mass center, m	t = tangential direction
	α = rotor spin angle, rad	X, Y = X, Y -direction
	β = boss/disk diameter ratio, (b/a)	z = z direction
		0 = initial condition
		Superscript
		\wedge = maximum value

$$B = \frac{-8(2+\nu) - 2(1-\nu)\beta^2(3+\beta^4)}{3+\nu+(1-\nu)\beta^4}$$

$$C = \frac{-8(2+\nu)\beta^4 + 2(3+\nu)\beta^2(3+\beta^4)}{3+\nu+(1-\nu)\beta^4}$$

$$D = 12 \quad (8)$$

It is noted that the spatial part of the admissible function has been chosen as the solution for deflection of the disk that is subjected to the distributed load $p = r\cos\eta$ or $r\sin\eta$, as shown in Fig. 2. This satisfied the boundary condition, which is that the boss is absolutely rigid and the outer boundary of the disk is free from forces and bending moments [11]

$$U_z = 0, \quad \frac{\partial U_z}{\partial r} = 0, \quad \text{at } r = b$$

$$\left. \begin{aligned} \frac{\partial^2 U_z}{\partial r^2} + \nu \left(\frac{1}{r} \frac{\partial U_z}{\partial r} + \frac{1}{r^2} \frac{\partial^2 U_z}{\partial \eta^2} \right) &= 0 \\ \frac{\partial}{\partial r} \left(\frac{\partial^2}{\partial r^2} + \frac{1}{r} \frac{\partial}{\partial r} + \frac{1}{r^2} \frac{\partial^2}{\partial \eta^2} \right) U_z & \\ + (1-\nu) \frac{1}{r^2} \frac{\partial^2}{\partial \eta^2} \left\{ r \frac{\partial}{\partial r} \left(\frac{U_z}{r} \right) \right\} &= 0 \end{aligned} \right\} \text{at } r = a \quad (9)$$

Rewriting equation (1) in terms of the dimensionless variable, χ , denoting the resulting operator by $L(U_z)$, and applying the Galerkin method, we obtain the following equations involving the time functions $T_n(t)$, ($n = 1, 2$)

$$\int_0^{2\pi} \int_{\beta}^1 L[aW(\chi) \{T_1(t)\cos\eta + T_2(t)\sin\eta\}] W(\chi) \begin{pmatrix} \cos\eta \\ \sin\eta \end{pmatrix} \chi d\chi d\eta = 0 \quad (10)$$

Upon calculation and rearrangement, we have

$$\rho(I_6 + AI_2 + BI_4 + CI_0 + DG) \left(\ddot{T}_n + \frac{C_2}{\rho} \dot{T}_n \right) - \left[\frac{\rho\omega^2}{8} \{ -8(13+4\nu)I_6 - 4(2A-2BR+4S+3D+\nu D)I_2 + 2(-2BS+RD+2C+2\nu C)I_0 + 4(6R-11B-3\nu B)I_4 - 4CSI_{-4} - 8DG \} - 96 \frac{D_s}{ha^4} I_2 \right] T_n = \rho I_2 X_n \quad (n=1,2) \quad (11)$$

where I_m and G are respectively represented as

$$I_m = \int_{\beta}^1 \chi^m (\chi^5 + A\chi + B\chi^3 + C\chi^{-1} + D\chi \ln\chi) d\chi$$

$$G = \int_{\beta}^1 \chi^2 \ln\chi (\chi^5 + A\chi + B\chi^3 + C\chi^{-1} + D\chi \ln\chi) d\chi \quad (12)$$

The bending moment, M_r , torsional moment, M_{rt} , and shear force, q_r , are respectively given by

$$M_r = -\frac{D_s}{a^2} \left[\frac{\partial^2 U_z}{\partial \chi^2} + \nu \left(\frac{1}{\chi} \frac{\partial U_z}{\partial \chi} + \frac{1}{\chi^2} \frac{\partial^2 U_z}{\partial \eta^2} \right) \right]$$

$$M_{rt} = \frac{(1-\nu)}{a^2} D_s \left(\frac{1}{\chi} \frac{\partial^2 U_z}{\partial \chi \partial \eta} - \frac{1}{\chi^2} \frac{\partial U_z}{\partial \eta} \right)$$

$$q_r = -\frac{D_s}{a^3} \frac{\partial}{\partial \chi} \left(\frac{\partial^2 U_z}{\partial \chi^2} + \frac{1}{\chi} \frac{\partial U_z}{\partial \chi} + \frac{1}{\chi^2} \frac{\partial^2 U_z}{\partial \eta^2} \right) \quad (13)$$

The x, y components of the resultant bending moment acting on the boss from the disk are respectively represented in the form

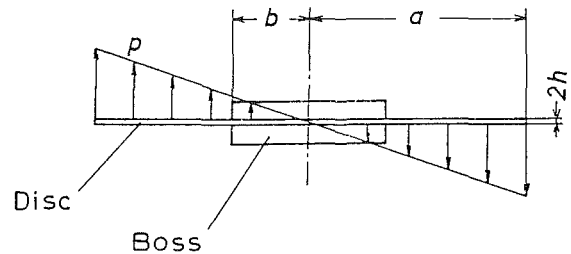


Fig. 2 Stationary disk subjected to the distributed load $p = r\cos\eta$ or $r\sin\eta$, chosen to determine the admissible mode function

$$M_{q1} = \left[-\int_0^{2\pi} M_r r \sin\eta d\eta + \int_0^{2\pi} M_{rt} r \cos\eta d\eta + \int_0^{2\pi} q_r r^2 \sin\eta d\eta \right]_{r=b}$$

$$M_{q2} = \left[\int_0^{2\pi} M_r r \cos\eta d\eta + \int_0^{2\pi} M_{rt} r \sin\eta d\eta - \int_0^{2\pi} q_r r^2 \cos\eta d\eta \right]_{r=b} \quad (14)$$

which, upon calculation, leads to

$$M_{q1} = -QT_2(t), \quad M_{q2} = QT_1(t), \quad Q = (48\beta^4 - 4D)\pi D_s \quad (15)$$

Similarly, the X, Y components of the resultant bending moment are given by

$$M_{qX} = M_{q1} \cos\alpha - M_{q2} \sin\alpha$$

$$M_{qY} = M_{q1} \sin\alpha + M_{q2} \cos\alpha \quad (16)$$

Equation of Motion of Shaft-Disk System. Having thus determined the components of the resultant bending moment acting to the boss from the disk, we can obtain the equation of motion of the boss-shaft system

$$m\ddot{X}_g + C_1\dot{X}_g + k_1X_g - k_2\theta_X = \epsilon k_1 \cos\alpha$$

$$m\ddot{Y}_g + C_1\dot{Y}_g + k_1Y_g - k_2\theta_Y = \epsilon k_1 \sin\alpha$$

$$I_x\ddot{\theta}_X + I_z(\dot{\alpha}\theta_Y + \ddot{\alpha}\theta_Y) - k_2X_g + k_3\theta_X = -\epsilon k_2 \cos\alpha + M_{qY}$$

$$I_x\ddot{\theta}_Y + I_z(\dot{\alpha}\theta_X + \ddot{\alpha}\theta_X) - k_2Y_g + k_3\theta_Y = -\epsilon k_2 \sin\alpha - M_{qX}$$

where (17)

$$\theta_X = \theta \cos\phi, \quad \theta_Y = \theta \sin\phi \quad (18)$$

and where, further, X_g and Y_g are the coordinates of the mass center, G ; m the total mass of boss and disk; C_1 the damping coefficient; I_x and I_z , respectively, the moment of inertia of the boss with respect to the diameter, and axis of the boss; k_1, k_2 , and k_3 the spring constants of the shaft. By using the following relation

$$X_g = \delta \cos\zeta + \epsilon \cos\alpha \quad Y_g = \delta \sin\zeta + \epsilon \sin\alpha \quad (19)$$

the equation of motion is written in the cylindrical coordinates as

$$\ddot{\delta} = \delta \dot{\zeta}^2 + \epsilon \dot{\alpha}^2 \cos(\alpha - \zeta) + 2\dot{\epsilon} \dot{\alpha} \sin(\alpha - \zeta) - \ddot{\epsilon} \cos(\alpha - \zeta) + \epsilon \ddot{\alpha} \sin(\alpha - \zeta) - \frac{C_1}{m} \{ \dot{\delta} - \epsilon \dot{\alpha} \sin(\alpha - \zeta) + \dot{\epsilon} \cos(\alpha - \zeta) \} - \frac{k_1}{m} \delta + \frac{k_2}{m} \theta \cos(\phi - \zeta)$$

$$\ddot{\zeta} = \frac{1}{\delta} \left[-2\dot{\delta} \dot{\zeta} + \epsilon \dot{\alpha}^2 \sin(\alpha - \zeta) - 2\dot{\epsilon} \dot{\alpha} \cos(\alpha - \zeta) - \ddot{\epsilon} \sin(\alpha - \zeta) - \epsilon \ddot{\alpha} \cos(\alpha - \zeta) \right]$$

$$\begin{aligned}
& -\frac{C_1}{m} \{ \delta \dot{\zeta} + \epsilon \dot{\alpha} \cos(\alpha - \zeta) + \dot{\epsilon} \sin(\alpha - \zeta) \} \\
& + \frac{k_2}{m} \theta \sin(\phi - \zeta) \Big] \\
\ddot{\theta} = & \theta \dot{\phi}^2 - \frac{I_z}{I_x} \theta \dot{\alpha} \dot{\phi} - \frac{k_3}{I_x} \theta + \frac{k_2}{I_x} \delta \cos(\zeta - \phi) \\
& + \frac{M_{q1}}{I_x} \sin(\alpha - \phi) + \frac{M_{q2}}{I_x} \cos(\alpha - \phi) \\
\ddot{\phi} = & \frac{1}{\theta} \left[-2\dot{\theta} \dot{\phi} + \frac{I_z}{I_x} (\dot{\alpha} \theta + \dot{\alpha} \dot{\theta}) + \frac{k_2}{I_x} \delta \sin(\zeta - \phi) \right. \\
& \left. - \frac{M_{q1}}{I_x} \cos(\alpha - \phi) + \frac{M_{q2}}{I_x} \sin(\alpha - \phi) \right] \quad (20)
\end{aligned}$$

where the eccentricity ϵ is assumed to be a function of time.

Steady-State Whirling. The steady-state whirl due to a constant rotor imbalance, i.e., $\epsilon = \epsilon_0 = \text{constant}$, is first considered. The following relations hold for the steady-state whirling

$$\begin{aligned}
\alpha &= \omega t + \alpha_0, \quad \zeta = \omega t + \zeta_0, \quad \phi = \omega t + \phi_0 \\
\ddot{\theta} = \dot{\theta} = 0, \quad \ddot{\phi} = \dot{\phi} = 0, \quad \delta = \hat{\delta}, \quad \epsilon = \epsilon_0 \quad (21)
\end{aligned}$$

where ω denotes the spin speed of rotor and coincides with the angular frequency of whirling in the steady state; α_0 , ζ_0 , and ϕ_0 are constants that are determined from the appropriate initial condition; $\hat{\delta}$ and $\hat{\theta}$ are the amplitude and deflection angle of the steady whirling. The acceleration of the disk determined from equation (4) is written as

$$\begin{aligned}
A_z = & \frac{\partial^2 U_z}{\partial t^2} - r \hat{\theta} \omega^2 \{ \cos(\phi_0 - \alpha_0) \cos \eta \\
& + \sin(\phi_0 - \alpha_0) \sin \eta \} + \frac{C_2}{\rho} \frac{\partial U_z}{\partial t} \quad (22)
\end{aligned}$$

and equation (5) is written as

$$X_1 = \hat{\theta} \omega^2 \cos(\phi_0 - \alpha_0), \quad X_2 = \hat{\theta} \omega^2 \sin(\phi_0 - \alpha_0) \quad (23)$$

Equation (11) leads to

$$T_1 = \frac{\hat{\theta} \omega^2 \cos(\phi_0 - \alpha_0)}{d_1 - d_2 \omega^2}, \quad T_2 = \frac{\hat{\theta} \omega^2 \sin(\phi_0 - \alpha_0)}{d_1 - d_2 \omega^2} \quad (24)$$

where

$$\begin{aligned}
d_1 &= \frac{96D_s}{h\rho a^4} \\
d_2 &= \frac{1}{8I_2} [-8(13+4\nu)I_6 - 4(2A-2BR+4S+3D+\nu D)I_2 \\
& + 2(-2BS+RD+2C+2\nu C)I_0 + 4(6R-11B-3\nu B)I_4 \\
& - 4CSI_{-4} - 8DG] \quad (25)
\end{aligned}$$

Substituting equations (21) and (15) together with equation (24) into equation (20), we have the solution for the steady-whirling as

$$\begin{aligned}
\hat{\delta} &= \epsilon_0 f_3 \cdot \sqrt{\frac{f_4^2 + f_5^2}{f_1^2 + f_2^2}} \quad \hat{\theta} = \epsilon_0 \cdot \sqrt{\frac{f_4^2 + f_5^2}{f_1^2 + f_2^2}} \\
\zeta_0 &= \alpha_0 + \tan^{-1} \left(\frac{f_1 f_4 - f_2 f_5}{f_1 f_5 + f_2 f_4} \right) \\
\phi_0 &= \zeta_0 \quad (26)
\end{aligned}$$

where

$$f_1 = f_3(k_1 - m\omega^2) - k_2, \quad f_2 = C_1 \omega f_3$$

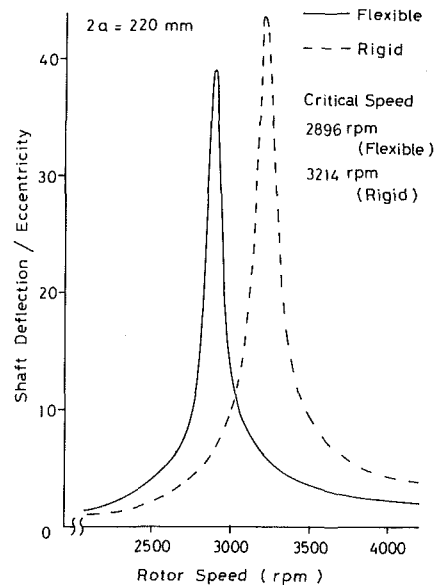


Fig. 3 Deflection versus rotating speed of shaft with flexible or rigid disk

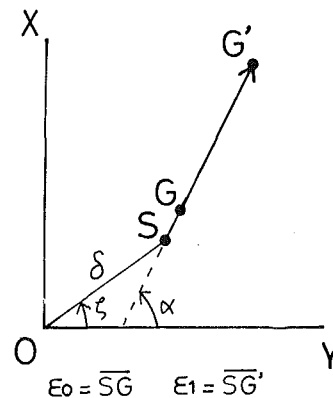


Fig. 4 Sudden increase of imbalance (G: initial location of mass center, G': final location of mass center)

$$\begin{aligned}
f_3 &= \frac{1}{k_2} \left\{ k_3 - (I_x - I_z) \omega^2 - \frac{Q \omega^2}{d_1 - d_2 \omega^2} \right\} \quad (27) \\
f_4 &= -C_1 \omega \\
f_5 &= m \omega^2
\end{aligned}$$

In the case of rigid disk, I_x and I_z have to be modified to include the moment of inertia of the disk and the relations $M_{q1} = M_{q2} = 0$ have to be substituted in equation (20).

A computation has been performed on the model rotor that will be used in the experimental phase of the present investigation. The shaft deflection/eccentricity versus rotor spin speed is shown in Fig. 3, where it is apparent that the analysis with a flexible disk results in a prediction of lower critical speed and smaller peak amplitude in the response curve than that with a rigid disk of the same mass and configuration as the flexible disk. It is noted that the damping coefficient of the shaft was determined from the wave forms of damped free transverse vibration of the stationary rotor used in the experiment.

Transient Vibration Due to Sudden Increase of Imbalance (Eccentricity). Blade loss is simulated by a sudden increase of imbalance or eccentricity. Consider a flexible-disk/flexible-shaft system that has an initial eccentricity $\epsilon_0 = SG$ and is rotating with angular velocity ω as shown in Fig 4, and assume that the imbalance suddenly increases with the location of mass center moving to G' ($SG' = \epsilon_1$). Since the resultant

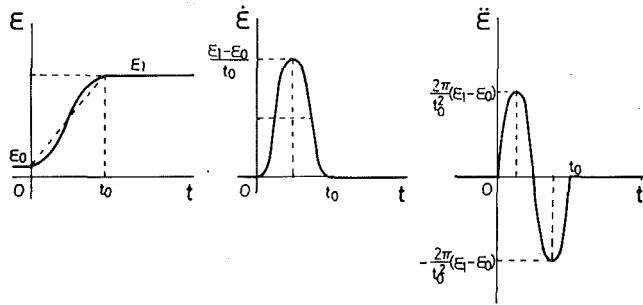


Fig. 5 Time variation of imbalance with cycloidal front step-type function

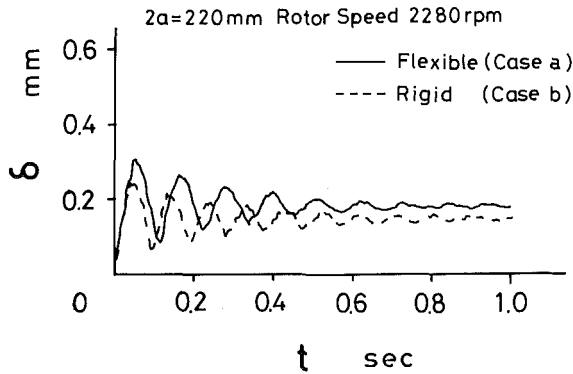


Fig. 6(a) Unit step increase

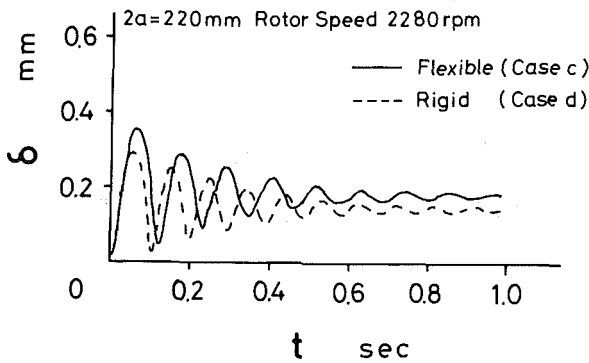


Fig. 6(b) Cycloidal front step-type increase

Fig. 6 Time variation of whirl envelope following sudden increase of eccentricity at subcritical speed ($t_0 = 0.019$ s)

eccentricity, ϵ_1 , after blade loss is thought to be much larger than the initial eccentricity, ϵ_0 , three points (S, G, G') are assumed to be on the same line. Two types of eccentricity increase are considered in this paper:

(i) Unit step function

$$\epsilon(t) = \epsilon_0 + (\epsilon_1 - \epsilon_0)u(t), \quad \dot{\epsilon}(t) = 0, \quad \ddot{\epsilon}(t) = 0 \quad (28)$$

In most of rotor dynamics, the effects of $\dot{\epsilon}(t)$ and $\ddot{\epsilon}(t)$ are not considered, so that $\dot{\epsilon}(t) = 0$ and $\ddot{\epsilon}(t) = 0$ are assumed here.

(ii) Cycloidal front step-type function

$$\epsilon(t) = \begin{cases} \epsilon_0, & t < 0 \\ \epsilon_0 + (\epsilon_1 - \epsilon_0) \left\{ \frac{t}{t_0} - \frac{1}{2\pi} \sin \frac{2\pi t}{t_0} \right\}, & 0 \leq t \leq t_0 \\ \epsilon_1, & t > t_0 \end{cases} \quad (29)$$

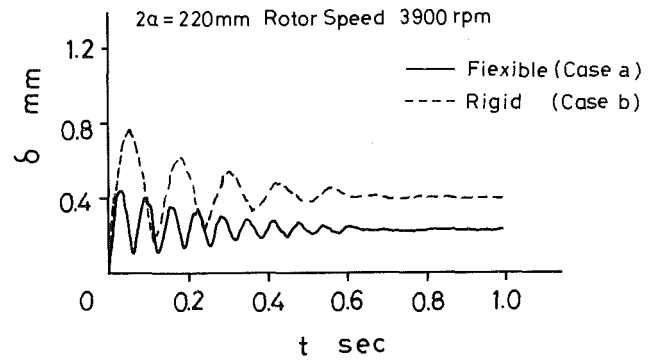


Fig. 7(a) Unit step increase

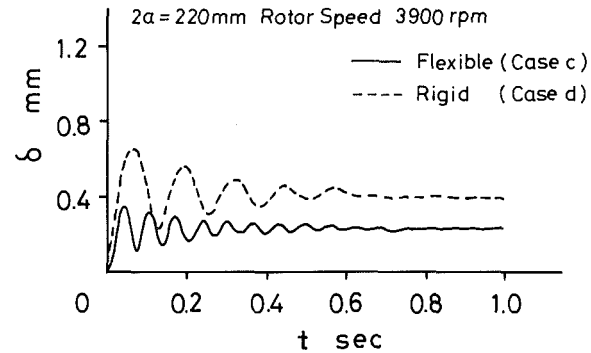


Fig. 7(b) Cycloidal front step-type increase

Fig. 7 Time variation of whirl envelope following sudden increase of eccentricity at supercritical speed ($t_0 = 0.011$ s)

where t_0 is the rise time. The time derivatives of eccentricity function are given by

$$\left. \begin{aligned} \dot{\epsilon}(t) &= \frac{\epsilon_1 - \epsilon_0}{t_0} \left(1 - \cos \frac{2\pi t}{t_0} \right) \\ \ddot{\epsilon}(t) &= \frac{2\pi}{t_0^2} (\epsilon_1 - \epsilon_0) \sin \frac{2\pi t}{t_0} \end{aligned} \right\} 0 \leq t \leq t_0 \quad (30)$$

The time variation of cycloidal front step-type function and its time derivatives are shown in Fig. 5.

Vibrations due to sudden increase of eccentricity $\epsilon(t)$ are analyzed numerically by means of the Runge-Kutta-Gill method, with 10,000 integration steps at a step size of 0.0001 s. Computations are carried out on four cases:

- Rotor with a flexible disk subjected to unit step input
- Rotor with a rigid disk subjected to unit step input
- Rotor with a flexible disk subjected to cycloidal front step-type input
- Rotor with a rigid disk subjected to cycloidal front step-type input.

Computations have been performed on the model rotor that will be used in the experiment described later. The time variations of whirl envelope following sudden increase of eccentricity at subcritical speed are shown in Figs. 6(a) and 6(b), while those at supercritical speed are shown in Figs. 7(a) and 7(b). The following tendency is observed in these figures:

For subcritical blade loss, the maximum amplitude increases with disk flexibility, and the analysis with cycloidal front step-type increase of imbalance predicts larger peak values in the response curves than that with unit step increase does. For supercritical blade loss, both of the above tendencies are reversed.

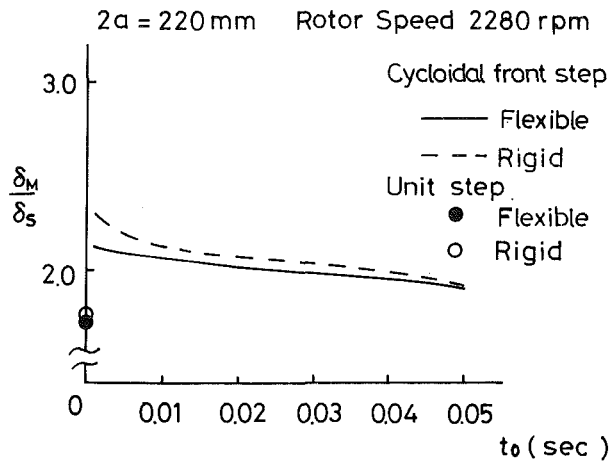


Fig. 8(a) Subcritical blade loss

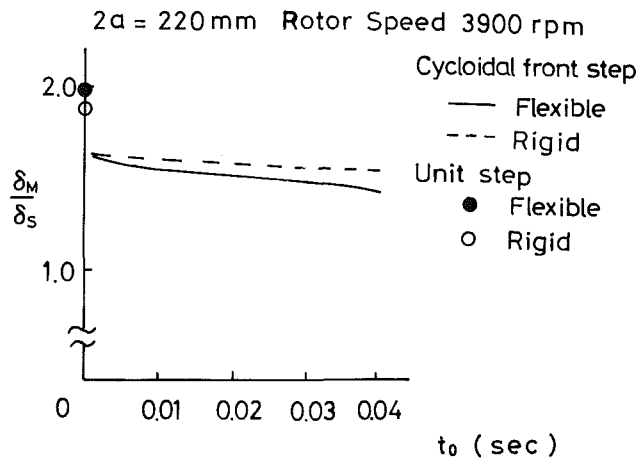


Fig. 8(b) Supercritical blade loss

Fig. 8 Maximum shaft deflection versus rise time of cycloidal front step-type increase of eccentricity

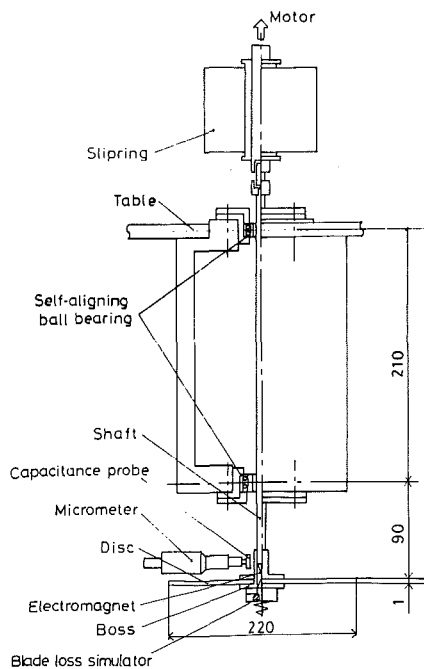


Fig. 9 General arrangement of experimental apparatus

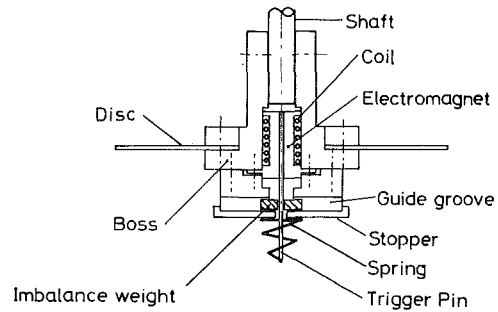


Fig. 10(a) Initial state

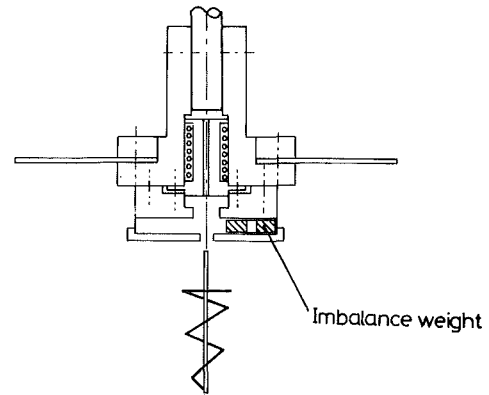


Fig. 10(b) Final state

Fig. 10 Schematic representation of blade loss or imbalance increase simulator

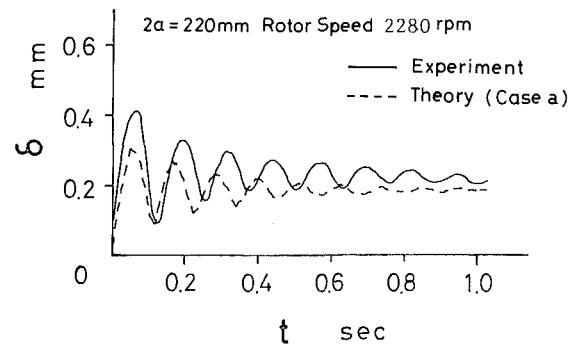


Fig. 11(a) Flexible disk

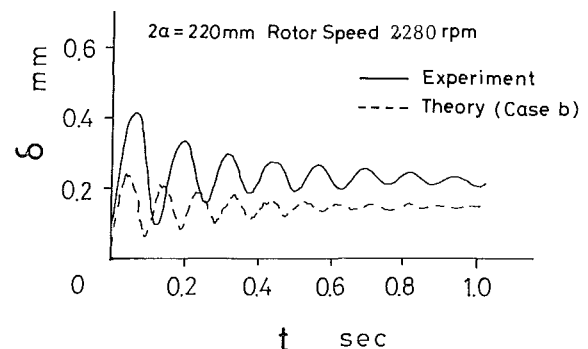


Fig. 11(b) Rigid disk

Fig. 11 Comparison of theory with the experiment of time variation of whirl envelope (unit step imbalance increase at subcritical speed)

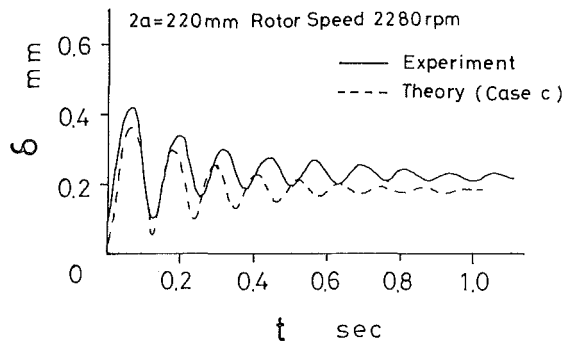


Fig. 12(a) Flexible disk

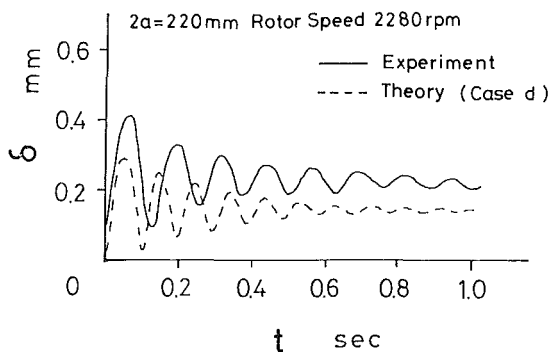


Fig. 12(b) Rigid disk

Fig. 12 Comparison of theory with the experiment of time variation of whirl envelope (cycloidal front step-type imbalance increase at subcritical speed, $t_0 = 0.019$ s)

Figures 8(a) and 8(b) show the maximum shaft deflection/stationary deflection versus rise time, t_0 , of cycloidal front step-type increase of imbalance in subcritical and supercritical blade loss, respectively. Maximum deflections in the case of unit step imbalance increase are also indicated in the figures.

Experimental

The general arrangement of the experimental apparatus is shown in Fig. 9. To eliminate the effects of gravity, the rotating shaft was supported vertically with a couple of self-aligning type ball bearings. The diameter of the shaft was 7.0 mm and a boss of aluminum alloy (diameter $2b = 40$ mm) and a flexible disk of brass (diameter $2a = 220$ mm and thickness $2h = 1.0$ mm) were attached to the end of the shaft. The rotor system was driven by an electric motor with a flexible coupling. A capacity-type probe was used to measure the shaft deflection. A blade loss simulator was mounted on the boss as shown in Fig. 9. It consists of an imbalance weight, a trigger pin, a spring, and an electromagnet, as shown in Fig. 10(a). The trigger pin is released by means of the spring that is triggered by force of the electromagnet. The imbalance weight moves along a guide groove by centrifugal force and is arrested by a stopper as shown in Fig. 10(b). The rise time, t_0 , was measured by an electric circuit which was shunted when the imbalance weight contacted with the stopper.

The experimental results are shown in Figs. 11 and 12. It is observed that the analysis, taking account of disk flexibility and assuming the increase of imbalance with a cycloidal front step-type, is in good agreement with the experimental results (Fig. 12(a)). It is noted that the predicted responses are lower than the measured although both curves are similar in character. This may be attributable to normal measurement errors, the initial distortion of the shaft and disk, and the discrepancy between the assumed and real forms of eccentricity function $\epsilon(t)$.

Concluding Remark

The transient vibration of a flexible-disk/shaft-system following blade loss is investigated both theoretically and experimentally. Although the effects of bearing stiffness and damping are very important on the transient response after blade loss, a rigid bearing support is considered in the present study in order to pinpoint the effect of disk flexibility. The following conclusions may be drawn from the present study:

- (i) Disk flexibility has to be considered to analyze the transient response following blade loss.
- (ii) For subcritical blade loss or sudden increase of imbalance, the maximum amplitude increases with disk flexibility, and the analysis with cycloidal front step-type imbalance increase predicts larger peak values in the response curves than that with unit step imbalance increase.
- (iii) For supercritical blade loss, both of the above tendencies are reversed.
- (iv) The theoretical prediction with a cycloidal front step-type imbalance increase is in good agreement with the experimental results.

References

- 1 Kirk, R. G., and Gunter, E. J., "Transient Response of Rotor-Bearing Systems," *ASME Journal of Engineering for Industry*, Vol. 96, No. 2, May 1974, pp. 682-693.
- 2 Childs, D. W., "A Modal Transient Rotordynamic Model for Dual-Rotor Jet Engine Systems," *ASME Journal of Engineering for Industry*, Vol. 98, No. 3, Aug. 1976, pp. 876-882.
- 3 Childs, D. W., and Bates III, J. B., "Residual-Flexibility Corrections for Transient Modal Rotordynamic Models," *ASME Journal of Mechanical Design*, Vol. 100, No. 2, Apr. 1978, pp. 251-256.
- 4 Dennis, A. J., Eriksson, R. H., and Seitelman, L. H., "Transient Response Analysis of Damped Rotor Systems by the Normal Mode Method," *ASME Paper No. 75-GT-58*, 1975.
- 5 Dopkin, J. A., and Shoup, T. E., "Rotor Resonant Speed Reduction Caused by Flexibility of Disks," *ASME Journal of Engineering for Industry*, Vol. 96, No. 4, Nov. 1974, pp. 1328-1333.
- 6 Chivens, D. R., and Nelson, H. D., "The Natural Frequencies and Critical Speeds of a Rotating, Flexible Shaft-Disk System," *ASME Journal of Engineering for Industry*, Vol. 97, No. 3, Aug. 1975, pp. 881-886.
- 7 Red, W. E., "Examination of the Response of a Flexible Circular Rotor Subjected to Specified Gyroscopic Rates," *ASME Journal of Engineering for Industry*, Vol. 96, No. 4, Nov. 1974, pp. 1296-1306.
- 8 Klompas, N., "Significance of Disk Flexing in Viscous-Damped Jet Engine Dynamics," *ASME Journal of Engineering for Power*, Vol. 100, No. 3, Oct. 1978, pp. 647-654.
- 9 Chen, L., and Dugundji, J., "Investigation of the Vibration Characteristics of Shrouded Bladed Disk Rotor Stages," *Journal of Aircraft*, Vol. 17, No. 7, July 1980, pp. 479-486.
- 10 Hirschberg, M. H., and Mendelson, A., *NACA Technical Note No. 4218*, 1958.
- 11 Timoshenko, S., and Woinowsky-Krieger, S., *Theory of Plate and Shells*, 2nd ed., McGraw-Hill 1959, p. 282.

M. D. Rabinowitz

Design Engineer,
Hawker DeHavilland Australia,
Lidcombe, New South Wales, Australia

E. J. Hahn

Senior Lecturer,
University of New South Wales,
Kensington, New South Wales, Australia
Mem. ASME

Optimal Design of Squeeze Film Supports for Flexible Rotors

Assuming central preloading, operation below the second bending critical speed, and full film lubrication, this paper presents a theoretical model which allows one, with minimum computation, to design squeeze film damped rotors under conditions of high unbalance loading. Closed form expressions are derived for the maximum vibration amplitudes pertaining to optimally damped conditions. The resulting vibration amplitude and transmissibility data of design interest are presented for a wide range of practical operating conditions on a single chart. It can be seen that for a given rotor, the lighter the bearing the more easily one can satisfy design constraints relating to allowable rotor vibration levels and lubricant supply pressure requirements. The data presented are shown to be applicable to a wide variety of rotors, and a recommended procedure for optimal design is outlined.

Introduction

In recent years, sophisticated computer programs have been developed for analyzing bearing systems. Reference [1] summarizes the capability of such programs to evaluate the effect of damped flexible supports on critical speed location, on unbalance response, and on stability. Linear theory techniques are used in most of these programs, and linear support damping and stiffness coefficients are needed as input. For those squeeze film dampers where the journal center rotates in a circular orbit about the bearing center (e.g., vertical rotors or centrally preloaded rotors), these linear coefficients have been evaluated both theoretically [2-4] and experimentally [5-9]. However, owing to their nonlinearity, apart from small unbalance loading situations, a knowledge of their value is of use more for stability rather than unbalance response investigations.

The unbalance response of even the simplest flexibly supported rotor, the so-called Jeffcott rotor, is already dependent on a daunting array of system parameters, making parametric response studies tedious and difficult to present in a form useful for design [10]. Actually, since the flexibly supported symmetric flexible rotor has two degrees of freedom, a logical design strategy has been to utilize the tuning capabilities of such systems as originally reported in [11] and later extended to flexibly supported Jeffcott rotors [12] and in particular, to squeeze film supported flexible rotors [13, 14].

More recently, an approach for optimally damping rotors at any critical speed has been proposed [15] and tested [16]. These methods implicitly assume constant support stiffness and damping, and for squeeze film supports, would appear to be restricted to small unbalance loadings. An alternative approach to support design has been suggested in [17], though it is not clear how easily this method can be simply extended to cater for nonlinear support forces.

However, unbalance loading, while small initially, can

increase markedly in service owing to corrosion, blade failure, and thermal effects. Since the stiffness and the damping of squeeze film bearings can be highly nonlinear, the unbalance response of a system using them can be markedly dependent on rotor unbalance and can result in bistable operation characterized by high unbalance transmissibilities and extremely high rotor amplitudes.

The design information in [10] does cater for large unbalance loading but owing to the nonlinearity of the system and the large number of parameters affecting the system response, the data are for discrete parameter values only, requiring interpolation for optimal system design. It is the aim of this paper to show how, by making use of frequency response intersection points pertaining to two degree-of-freedom systems, but also present in response data for nonlinear squeeze film supports [10], the design optimization process can be significantly simplified. Indeed, it will be shown that over a wide range of practical conditions, it is feasible to present relevant design data on a single design chart.

Theoretical Model

Figure 1 depicts schematically a flexible rotor running in a rolling element bearing, whose outer race forms the nonrotating journal of a centrally preloaded squeeze film damper support. The following assumptions, justified in [18], pertain to the analysis: (a) the rotor is symmetric; (b) part of the mass may be lumped at the rotor center with the remainder at the bearing stations; (c) gyroscopic effects are negligible; (d) excitation forces due to rolling element bearings are negligible; (e) the Reynolds equation for constant lubricant properties is applicable; (f) the short bearing approximation is valid; (g) the pressures at the ends of the bearings are either atmospheric or sufficiently above atmospheric to ensure full film lubrication; (h) only positive pressures contribute to the fluid film forces; (i) the rotor is centrally preloaded with constant radial support stiffness; (j) all unbalance in the rotor may be concentrated in the lumped mass at the rotor midspan; (k) operation is sufficiently below

Contributed by the Gas Turbine Division of THE AMERICAN SOCIETY OF MECHANICAL ENGINEERS and presented at the 27th International Gas Turbine Conference and Exhibit, London, England, April 18-22, 1982. Manuscript received at ASME Headquarters December 15, 1981. Paper No. 82-GT-232.

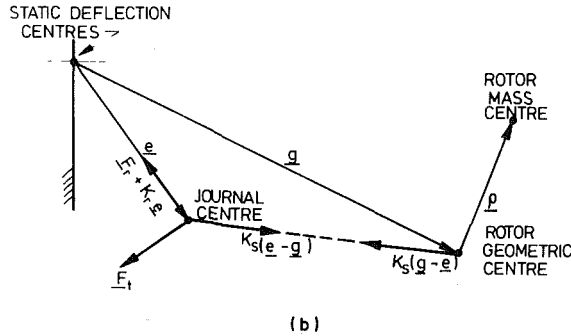
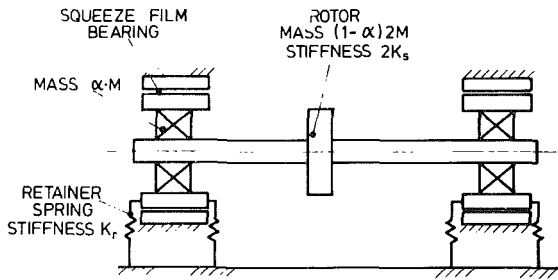


Fig. 1(a) Schematic diagram of squeeze film mounted single-disk flexible rotor; (b) vectorial representation of displacements and forces

the second bending pin-pin critical speed to enable its effect to be ignored; (l) any damping or flexibility in the rolling element bearings may be ignored.

Referring to Fig. 1, the equation of motion for the mass αM lumped at each bearing station is given by

$$\alpha M \ddot{\mathbf{e}} + C_1 \dot{\mathbf{e}} + K_s (\mathbf{e} - \mathbf{g}) + K_1 \mathbf{e} = 0, \quad (1)$$

where C_1 and K_1 are equivalent damping and stiffness coefficients respectively.

Similarly, for the mass $2(1 - \alpha)M$ lumped at the rotor midspan, the equation of motion is given by

$$(1 - \alpha)M(\ddot{\mathbf{g}} + \ddot{\rho}) + K_s (\mathbf{g} - \mathbf{e}) = 0. \quad (2)$$

Assuming that steady-state conditions have been reached, with the rotor and journal centers describing synchronous circular orbits about the static deflection line, equations (1) and (2) may be nondimensionalized and solved for the journal orbit radius, ϵ , the rotor orbit radius, G , and the unbalance transmissibility, T , as explained in [10]. An alternative derivation which leads to expressions for ϵ , G , and T in a form more suited to this paper, is given in Appendix A, where it is shown that

$$\epsilon = \frac{Ua^2}{\{[K_2 f^2 (1 - a^2) + a^2 (\alpha a^2 - 1)]^2 + C_2^2 a^2 f^2 (1 - a^2)^2\}^{1/2}}, \quad (3)$$

$$G = \frac{Ua^2}{(1 - \alpha) |1 - a^2|} \left\{ \frac{\left[K_2 - \alpha \frac{a^2}{f^2} + \frac{1 - \alpha}{f^2} \right]^2 + C_2^2 a^2 / f^2}{\left[K_2 + \frac{a^2}{f^2} \left(\frac{\alpha a^2 - 1}{1 - a^2} \right) \right]^2 + C_2^2 a^2 / f^2} \right\} \quad (4)$$

$$T = \frac{1}{|1 - a^2|} \left\{ \frac{K_2^2 f^2 / a^2 + C_2^2}{\left[K_2 f / a + \frac{a(\alpha a^2 - 1)}{f(1 - a^2)} \right]^2 + C_2^2} \right\}^{1/2} \quad (5)$$

In general, both the nondimensional stiffness coefficient, K_2 , and the nondimensional damping coefficient, C_2 , are themselves functions of the journal orbit radius, ϵ , and the bearing parameter, B . Hence, given the relevant system parameters, viz: the unbalance parameter, U , the mass ratio, α , the speed parameter, a , the frequency ratio, f , and the bearing parameter, B , equation (3) can be solved iteratively for ϵ , whereupon the corresponding solutions for the rotor orbit radius, G , and the transmissibility, T , follow. Since equation (3) is nonlinear, more than one solution for ϵ in the acceptable range $0 < \epsilon < 1$ may result, depending on the actual

Nomenclature

a = speed parameter, ω / ω_c
 $a_1 - a_6$ = unique speeds, defined in Table 1
 B = bearing parameter,
 $\frac{\mu R}{2M\omega_r} (L/C)^3$
 C = radial clearance of bearing
 C_1 = equivalent damping coefficient, $F_r / (\omega e)$
 C_2 = nondimensional damping coefficient, $C_1 / (M\omega_r)$
 e = journal eccentricity
 f = frequency ratio = ω_r / ω_c
 F_r, F_t = fluid film force on journal in radial and transverse directions,
 $\frac{\mu R L^3 \omega}{C^2} g_{r,t}$
 g = displacement of rotor geometric center with respect to static deflection
 $g_r = \frac{2e^2}{(1 - \epsilon^2)^2}$ or 0 for unpressurized or pressurized bearings

$g_t = \frac{\pi \epsilon}{2(1 - \epsilon^2)^{3/2}}$ or $\frac{\pi \epsilon}{(1 - \epsilon^2)^{3/2}}$
for unpressurized or pressurized bearings
 G = nondimensional rotor orbit radius at midspan, g/C
 G_R = nondimensional rotor orbit radius at midspan of a rigidly supported rotor assuming a damping ratio of 0.02
 K_r = retainer spring stiffness per bearing station
 $2K_s$ = rotor stiffness
 K_1 = equivalent stiffness coefficient, $K_r + F_r/e$
 K_2 = nondimensional stiffness coefficient, $K_1 / (M\omega_r^2) = K_1 / K_r$
 L = axial width of bearing
 $2M$ = rotor mass
 p = minimum supply pressure for full film
 P = pressure parameter, $pLR / (K_s C)$
 R = journal radius

T = transmissibility,
 $\frac{\sqrt{(F_r + K_r e)^2 + F_t^2}}{(1 - \alpha) M \omega^2 \rho}$
 T_R = transmissibility of a rigidly supported rotor
 U = unbalance parameter, $(1 - \alpha) \rho / C$
 α = mass ratio, equals fraction of the total mass lumped at the bearing
 ϵ = nondimensional journal orbit radius (eccentricity ratio), e/C
 μ = absolute viscosity of lubricant at the mean lubricant temperature
 ρ = unbalance eccentricity
 ω = rotor speed
 ω_c = first pin-pin critical speed of rotor,
 $\sqrt{\frac{K_s}{(1 - \alpha) M}}$
 ω_r = natural frequency of retainer spring with respect to rotor mass, $\sqrt{K_r / M}$

values of the system parameters. Equilibrium solutions for equations (3), (4), and (5) over a wide range of the system parameters have been presented in [4, 10] where the stability of these solutions has also been investigated. Note that in the case of pressurized supports (i.e., sufficiently high lubricant pressure to ensure a continuous lubricant film throughout the bearing), the fluid film force has no radial component, i.e., $F_r = 0$, so that $K_2 = 1$.

Figure 2 (Fig. 5(b) in [10]) shows the rotor amplitude ratio, G/U , frequency responses for a range of bearing parameter, B , and unbalance parameter, U , for pressurized mounts, mass ratio $\alpha = 0.25$ and frequency ratios $f = 0.2$ and 0.5 . As may be seen from Fig. 2 and from Figs. 2 to 7 in [10] for pressurized bearing mounts, for $0 \leq \alpha \leq 0.5$ and for $0.1 \leq f \leq 0.5$, unique points exist on the frequency response plots where all the rotor amplitude ratio frequency response curves intersect.

Also, it may be seen from Figs. 3 to 11 in [4] and Figs. 8 to 10 in [10], that similar unique points exist for the journal amplitude ratio ϵ/U frequency response plots for un-

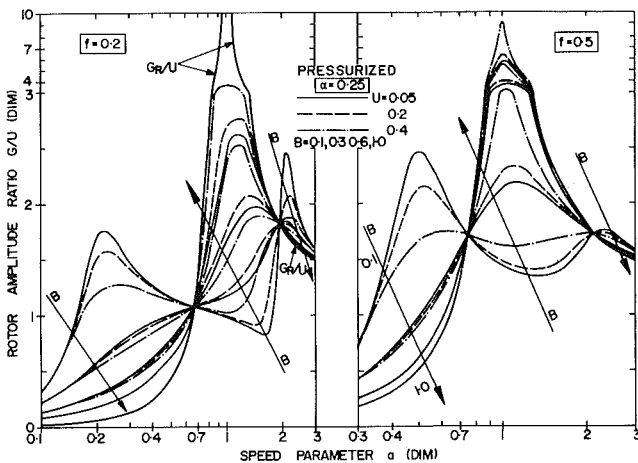


Fig. 2 Amplitude ratio frequency responses for range of B and U : pressurized mount, $\alpha = 0.25$, $f = 0.2$ and 0.5 (from [10])

pressurized mounts and for the transmissibility frequency response plots. These points are for a wide range of bearing parameter of $0.1 \leq B \leq 1$ and unbalance parameter $0.05 \leq U \leq 0.40$. At the unique speeds defining these points, the system response is independent of the bearing parameter, B , and so is independent of the support damping and in some cases, of the support stiffness.

As is shown in Appendix B, equations (3-5) yield six such unique speeds, viz: a_1 to a_6 . These speeds tend to depend on the mass ratio, α , and the frequency ratio f and are summarized in Table 1, together with the corresponding constant response expressions and an indication as to whether the results are applicable to unpressurized in addition to pressurized bearing supports.

Tuned Systems. For linear stiffness and damping, the existence of the unique speeds, a_1 and a_2 , has been long documented for two degree-of-freedom systems [11]. For pressurized bearing supports, where the support stiffness is linear, even though the damping is not, one can apply a similar approach to [19] to minimize rotor amplitudes. Thus, for systems operating at a speed above both unique speeds it may be possible to minimize the maximum rotor amplitude ratio, G/U_{\max} , encountered in attaining the operating speed by suitable choice of the frequency ratio, f , and the damping, C_2 . Such a system constitutes an optimally damped system.

Regardless of the damping C_2 , G/U_{\max} can never be less than the larger of G/U_1 and G/U_2 . Now since $a_1 < 1$ and $a_2 > 1$ (see Appendix B), G/U_1 increases as a_1 increases, and G/U_2 decreases as a_2 increases. Further, since both a_1 and a_2 increase as f increases (see Appendix B), G/U_{\max} will be minimal for that value of f for which

$$G/U_1 = G/U_2 \quad (6)$$

Substituting for a_1 and a_2 into equation (6) one obtains

$$f = \sqrt{\alpha} \quad (7)$$

Such a choice of f defines a tuned system, whereupon

$$G/U_{\max} \geq G/U_1 = G/U_2 = \left[\frac{1 + \alpha}{(1 - \alpha)^2} \right]^{1/2} \quad (8)$$

and

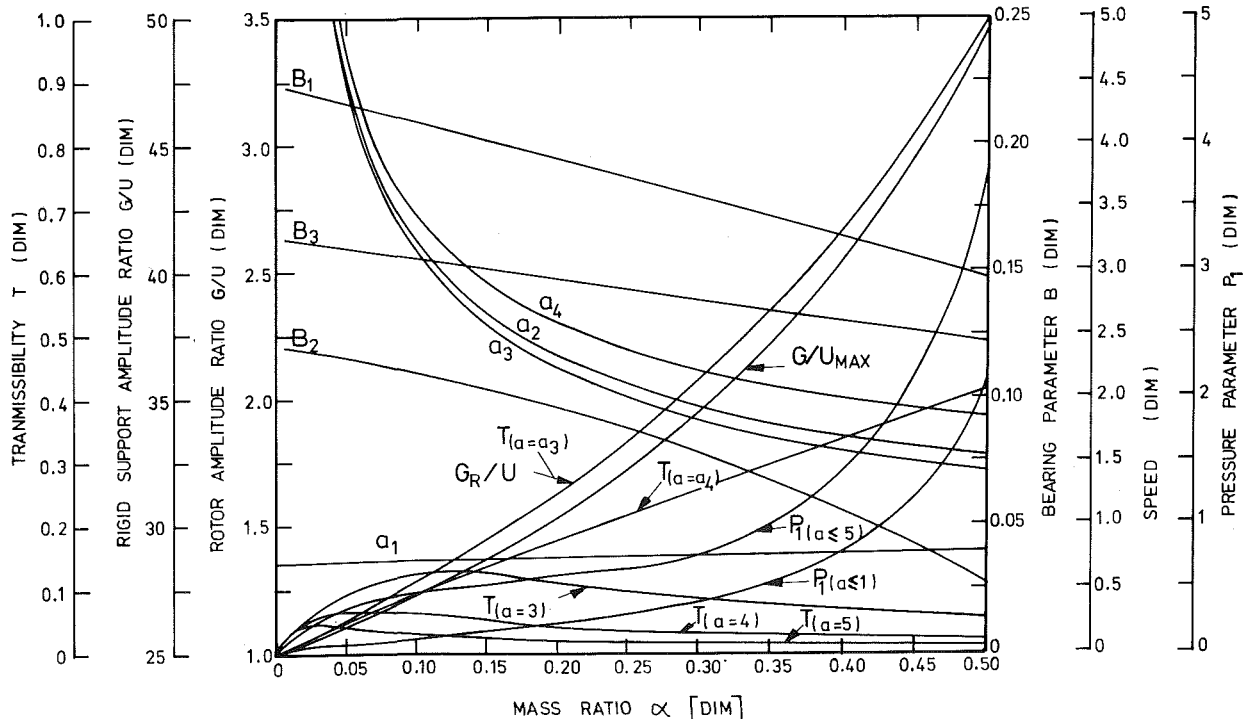


Fig. 3 Optimized design chart for pressurized mount

Table 1 Speed and response at the unique points

	Unique speeds	responses	unpressurized ?
G/U	$a_{1,2} = \left\{ \frac{f^2 + 1}{2\alpha} \mp \left[\left(\frac{f^2 + 1}{2\alpha} \right)^2 - \frac{f^2}{\alpha} - \frac{1 - \alpha}{2\alpha} \right]^{1/2} \right\}^{1/2}$	$G/U_{1,2} = \frac{a_{1,2}^2}{(1 - \alpha) 1 - a_{1,2}^2 }$	Only if $U \leq 0.05$
T	$a_3 = \alpha^{-1/2}$ $a_{4,5} = \left\{ \frac{1 + 2f^2}{2\alpha} \pm \left[\left(\frac{1 + 2f^2}{2\alpha} \right)^2 - \frac{2f^2}{\alpha} \right]^{1/2} \right\}^{1/2}$	$T_3 = \frac{\alpha}{1 - \alpha}$ $T_{4,5} = \frac{1}{ a_{4,5}^2 - 1 }$	Yes Only if $U \leq 0.05$
ϵ	$a_6 = 1$	$\epsilon_6 = \frac{U}{1 - \alpha} = \frac{\rho}{C}$	Yes

$$K_r = \frac{\alpha}{1 - \alpha} K_s \quad (9)$$

Though these results are valid for pressurized bearing systems regardless of unbalance loading, they may also be applied to unpressurized systems provided the unbalance load is sufficiently small. The results are in agreement with [12], which investigates a similar rotor bearing system but assumes linear stiffness and damping supports.

As an illustration of the above, one can see in Fig. 2 for $\alpha = 0.25$ and $f = 0.5$ (i.e., a tuned system) that $G/U_1 = G/U_2 = 1.72$. However, G/U_{\max} is generally much greater than 1.72, being apparently dependent on the value of the unbalance parameter U and bearing parameter B . Note that the curve for $U = 0.4$ and $B = 0.1$ suggests that G/U_{\max} can be lowered significantly to approach 1.72 by appropriately selecting B for a given unbalance; and that the appropriate value of B is that which satisfies the requirement that at a_1 and a_2

$$\frac{\partial(G/U)}{\partial a} = 0 \quad (10)$$

This approach, originally suggested in [11], has been used successfully in [12, 19] for linear systems where analytical expressions for the optimal damping were obtained. Unfortunately, no such expressions are available for nonlinear damping, and equation (10) needs to be satisfied numerically. Should appropriate damping be available to satisfy equation (10) at a_1 and a_2 , one has an optimally damped system, in that G/U_{\max} has been minimized to equal G/U_1 or G/U_2 .

Optimized Design Chart

Scope of Design Chart. The paramount design considerations in flexibly supported rotor bearing systems are that for the likely rotor unbalance: (i) the unbalance transmissibility at operating speed be low to achieve maximum bearing life and to minimize vibrations and stresses in the support structure, and (ii) the maximum rotor amplitude in attaining the operating speed be minimal to enable tight blade tip clearances to be maintained. The optimized design chart in Fig. 3 is presented to enable preloaded squeeze film dampers to be utilized as flexible supports to ensure minimum rotor vibration amplitudes. The design chart covers a wide range of operating conditions, viz: a mass ratio $\alpha \leq 0.5$, for an unbalance parameter $U \leq 0.4$ and a speed parameter $a \leq 5$. The chart assumes in addition to the assumptions pertaining to the theoretical model, that the bearings are pressurized and the rotor bearing system is tuned. It provides design information on (i) how to ensure that optimal damping can be assured over the speed range, (ii) what the corresponding unbalance transmissibility frequency response will be, (iii) what supply pressures are needed to ensure pressurization, (iv) what the maximum rotor amplitude ratio will be, and (v) what the

maximum amplitude ratio would be in the absence of flexible damped supports (assuming a damping ratio for the rotor of 0.02).

Optimal Damping. As noted in the foregoing section for tuned systems, a low value of G/U_{\max} requires careful consideration of the support damping C_2 which, for squeeze film supports, depends in a complicated manner on the bearing parameter, B , the unbalance parameter, U , the mass ratio, α , and the speed parameter, a . In no sense can a constant C_2 be maintained while coming up to operating speed. To further complicate matters, the value of U is not strictly defined, as significant deterioration in the level of unbalance over the life of the machine is a definite possibility. Also, without some form of lubricant temperature control, it is often impossible to properly fix the bearing parameter, B , which, by virtue of its dependence on the lubricant viscosity, is markedly temperature-dependent.

In view of this, the design strategy proposed here is to admit of possible variations in U and to utilize the temperature dependency of B to ensure that G/U_{\max} is minimized. A perusal of the rotor amplitude frequency responses for pressurized bearings in [10] shows that in all cases presented there, G/U decreases as B decreases and as U decreases in the speed range $a_1 < a < a_2$. For $a < a_1$ or $a > a_2$, this pattern is reversed. Hence, minimum G/U may be assured by maintaining a sufficiently low bearing parameter while running between the unique speeds, i.e., for $a_1 < a < a_2$, and by increasing the bearing parameter above prescribed limits for $a \leq a_1$ and for $a \geq a_2$. The result is given in Fig. 3, wherein B_1 and B_3 are the minimum bearing parameters recommended for the speed ranges $a < a_1$ and $a > a_2$, respectively (obtained by satisfying equation (9) for an assumed unbalance parameter $U = 0.05$), and B_2 is the maximum bearing parameter for the speed range $a_1 \leq a \leq a_2$ (obtained by ensuring that for $U = 0.4$, the maximum value of G/U in the speed range $a_1 \leq a \leq a_2$ is less than G/U_1 or G/U_2). Also shown are the unique speeds a_1 and a_2 which determine the switch from B_1 to B_2 and from B_2 to B_3 .

Hence, provided B_1 , B_2 , and B_3 are practically realizable, G/U_{\max} will be minimal for all unbalance parameters $U \leq 0.4$ (noting that for $U \leq 0.05$, the system behaves almost linearly in that G/U tends to be independent of U). Though the strategy has the apparent disadvantage that lubricant temperature control has to be provided while running up to or down from the operating speed, it is expected that some form of temperature control would normally be advisable to control B anyway; and by specifying B_1 , B_2 , and B_3 as limiting values of B , rather than actual values to be attained, the lubricant temperature control would be simple.

Also shown in Fig. 3 are the maximum rotor amplitudes G/U_{\max} , should the optimized damping strategy be adhered to, and the corresponding rigid support maximum amplitude

ratio g_R/U . It can be seen that reductions in amplitude ratio by factors of 14 or more are possible for mass ratio $\alpha \leq 0.5$.

Unbalance Transmissibilities. Five transmissibility values are shown for speeds in the range $\sqrt{2} \leq a \leq 5$. In addition to the transmissibilities T_3 and T_4 at the unique speeds a_3 and a_4 , the transmissibilities at $a = 3$, $a = 4$, and $a = 5$ are also included. These last three transmissibilities were also found to be insensitive to variation in U for $0.05 \leq U \leq 0.4$. The unique speed, a_5 , falls outside the speed range of interest, so T_5 is not included. The transmissibility, T , at the unique speed $a_6 = 1$, i.e., at the rotor pin-pin critical speed, is unbalance and damping dependent and is best calculated from

$$T = \frac{\sqrt{(K_r e)^2 + F_i^2}}{UMC\omega^2} = \frac{\sqrt{\alpha}}{1-\alpha} \left\{ \alpha + \frac{(2\pi B)^2}{[1-(\rho/C)^2]^3} \right\}^{1/2} \quad (11)$$

where $e = \rho$. These six values of transmissibility over the speed range $1 \leq a \leq 5$ should be adequate to approximate the transmissibility frequency response and thereby, to determine the unbalance transmissibility at operating speed. As an aid, the unique speeds a_3 and a_4 are also given in Fig. 3.

Supply Pressure. Implicit to the applicability of the design chart is that the bearing be pressurized. Should the bearing be pressurized at both ends, the minimum required pressure parameter, P , is given by [21]

$$P = \frac{48 Ba f [2(1 + 24\epsilon^2)^{1/2} - 8\epsilon^2 - 2]^{1/2}}{(1-\alpha)[5 - (1 + 24\epsilon^2)^{1/2}]^3} \quad (12)$$

One end pressurization would require four times this value of P .

One can see from equation (12) that for a tuned system, P is a function of B , α , a , and ϵ (which in turn is also a function of U). Hence, assuming an unbalance parameter $U = 0.4$ and a speed range $0 < a \leq 5$, P was computed for all values of α in the range $0 < \alpha \leq 0.5$ utilizing the appropriate bearing parameters in Fig. 3. The corresponding values of the journal eccentricity ratio ϵ may be obtained from the solution of equation (3). The resultant values of P are given in Fig. 3.

Regardless of pressurization, bistable operation is not predicted to occur above the first pin-pin critical speed. Thus, should it be desired to remove pressurization once $a > 1$, the required pressure parameter, P , which assumed a speed range up to $a = 5$, is unduly conservative. Hence, the required pressure parameter, P , for the more limited speed range of $0 < a \leq 1$ has been similarly evaluated and is also given in Fig. 3. Note that in such a case, once pressurization has been removed, the information obtainable from Fig. 3 becomes approximate only. Further, whereas the pressurized system is always stable, the stability of the unpressurized system is not globally guaranteed and needs to be investigated [4].

Applicability

Mass Ratio Considerations. As may be seen from Fig. 3, the lower the mass ratio, α , the lower the maximum amplitude, G/U_{\max} , the transmissibility, T , the required pressure parameter, P , and the bearing parameter ratio, B_2/B_1 . The

smaller the B_2/B_1 ratio, the smaller the required variation of the lubricant temperature for optimal damping and hence the shorter the delay in heating or cooling the lubricant while coming up to or down from the operating speed.

For heavy rotors, say $M > 20$ kg, it is reasonable to assume that a low mass ratio is attainable. In this case, the unique speed a_2 may be designed to occur outside the operating speed range, and there will be only one intersection point of the amplitude ratio G/U curves. In such a case, it may be beneficial to forgo a tuned system and select a frequency ratio for which $f < \sqrt{\alpha}$ to obtain a further reduction in the unique speed, a_1 , and hence, in the amplitude ratio, G/U_1 . In such cases, G/U_{\max} and a_1 may be obtained from Table 1, but Fig. 3 is no longer applicable, and the appropriate bearing parameters B_1 and B_2 to ensure optimal damping, the corresponding pressure parameter, P , and the transmissibility, T , would have to be evaluated from the nonlinear model.

For light rotors, mass ratios as high as $\alpha = 0.5$ are possible. For such a high α , relatively high transmissibility is predicted at the unique speed a_3 , and furthermore, as may be seen from Table 1, this transmissibility cannot be reduced by removing pressurization, being independent of pressurization. Since, at a_3 , the transmissibility of the squeeze film damper is predicted to be the same as that of the rigidly supported rotor [10], operation in the vicinity of this speed should be avoided by a careful selection of α .

Lubricant Viscosity and Supply Pressure Considerations. Basic conditions for the design to be practical are that: (a) the supply pressure required to ensure full film is not excessive; (b) the lubricant is an available Newtonian fluid.

The evaluation of the supply pressure and viscosity requirements necessitates knowledge of the rotor bearing system. The following approach is based on data taken from [22] for nine rotors. It is assumed that $U = 0.4$ and $L/R \approx 0.25$. $L = 10^{-2}$ m is assumed for the lighter rotors ($(1-\alpha)M \leq 20.5$ kg), whereas $L = 2 \times 10^{-2}$ is assumed for the heavier rotors ($(1-\alpha)M \geq 239$ kg). The supply pressure for two ends pressurization is then

$$p = \frac{K_c CP}{LR} = \frac{(1-\alpha)M\omega_c^2}{400L} P \quad (13)$$

and the lubricant viscosity is given by

$$\mu = \frac{2\sqrt{\alpha}M\omega_c BC^3}{RL^3} = 5 \times 10^{-7} \frac{\sqrt{\alpha}M\omega_c B}{L} \quad (14)$$

Due to lack of information in [22], αM values are assumed as shown in Table 2. Assuming an optimally damped system, one can obtain the required limiting values for P , B_1 , and B_2 from Fig. 3 and calculate the corresponding supply pressure, p , and viscosity, μ_1 , and μ_2 , requirements using equations (13) and (14). The results are summarized in Table 2 where it can be seen that the highest pressure, $p = 1.31$ MPa, is required for Case 8. This supply pressure does not appear to be excessive. The lubricants for all these cases are commercially available [23]. Cases 1 to 9 represent a wide variety

Table 2 Estimated lubricant supply pressure and viscosity requirements for nine cases discussed in [22], $U = 0.4$

Case	From [22] $(1-\alpha)M$ [kg]	ω_c [rad/s]	Estimated αM [kg]	α	p [MPa]	μ_1 Pa s $\times 10^{-3}$	μ_2 Pa s $\times 10^{-3}$
1	2.7	1257	0.45	0.14	0.53	14.1	7.0
2	9.1	943	0.9	0.09	0.89	29.7	15.6
3	318	388	1.4	0.004	0.12	43.1	23.5
4	295	388	1.4	0.005	0.17	44.7	24.4
5	239	848	1.4	0.006	0.75	86.8	47.4
6	20.5	785	1.4	0.06	1.20	45.3	24.2
7	0.91	1256	0.37	0.29	0.36	9.4	4.2
8	0.45	3142	0.27	0.38	1.31	11.6	4.4
9	255	293	1.4	0.005	0.08	29.2	15.9

of rotor bearing configurations, and, hence, it is concluded that the design information is practical for a wide range of applications.

Unpressurized Supports. Table 1 shows that at the first bending critical speed, $e = \rho$ is predicted regardless of pressurization. Similarly, the unique speed, a_3 , for the intersection of transmissibility curves is independent of pressurization. Further, it may be seen from Figs. 2(a) to 7(a) in [10] that for unpressurized bearing mounts and $U = 0.05$, a good approximation to the unique intersection points is obtained in the rotor amplitude and transmissibility frequency responses. Hence, it is reasonable to presume that the theoretical treatment presented here may be used for an optimal design of an unpressurized rotor bearing system, for which an unbalance greater than $\rho = 0.05C/(1 - \alpha)$ is unlikely to occur.

Thus, for $U \leq 0.05$, all the unique speeds and responses for pressurized systems, as summarized in Table 1, are applicable to unpressurized systems. The optimized design chart of Fig. 3 is also applicable except for the bearing parameter data for optimal damping for which further investigation is needed. However, the bearing parameter data may be approximated from Figs. 2(a) to 7(a) in [10] and from Fig. 2.12 in [18]. These are summarized in Table 3, which should be used in conjunction with Fig. 3 to evaluate the optimal supports design.

Comparison between Table 3 and Fig. 3 shows that the bearing parameters needed for optimal unpressurized supports are invariably higher than those required for the pressurized ones. The higher bearing parameter is needed to increase the damping reserve of the unpressurized mounts and to ensure stable operation [4].

For unpressurized rotor bearing systems operating with higher unbalance loading, higher eccentricity ratios and, consequently, larger radial film force components are expected in the vicinity of the intersection points. Hence, the approximation $K_2 \approx 1$ is no longer valid, Fig. 3 is not applicable, and detailed design charts should be used for the selection of design parameters [4, 10].

Design Procedure

This procedure for the design of squeeze film damped supports is for the usual case where the designer has no control over the rotor dimensions or the operating speed, a . However, one can find the rotor stiffness, K_s , the pin-pin critical speed, ω_c , and the mass of the rotor lumped at the center span using a procedure such as outlined in [13, 15]. Next, the following steps are suggested:

- 1 Assess the maximum unbalance eccentricity likely to be encountered, ρ .
- 2 Select radial clearance $C > \rho$.
- 3 Select bearing mean radius $100 C \leq R \leq 1000 C$, noting that as small an α as practicable is desirable
- 4 Select bearing land width $L \leq R/2$
- 5 Select rolling element bearing and estimate the mass ratio, α , avoiding $\alpha = 1/a^2$ if possible, when α is large

Table 3 Bearing parameter design data for unbalance parameter $U = 0.05$, unpressurized mount and mass ratios, $\alpha = 0.0$, $\alpha = 0.25$, and $\alpha = 0.5$

Mass ratio, α	Bearing parameter, B
0	$B \geq 0.6$
0.25	$B_1 > 0.3$
	$B_2 < 0.3$
	$B_2 > 0.3$
0.5	$B \approx 0.3$

6 Calculate the retainer spring stiffness, K_r , from equation (9)

7 Read the limiting bearing parameters, B_1 , B_2 , and B_3 , from Fig. 3

8 Calculate the oil viscosity from $\mu = 2BM\omega_c C^3 / (RL^2)$

9 Read the pressure parameter, P , from Fig. 3 and calculate the supply pressure required for two end pressurization form $p = K_s CP / (LR)$. For one end pressurization, use four times this pressure

10 Calculate the transmissibility $T(a = 1)$ from equation (11) and read from Fig. 3 $T_3(a = a_3)$, $T_4(a = a_4)$, $T(a = 3)$, $T(a = 4)$, and $T(a = 5)$. Using these transmissibilities plot a transmissibility versus speed curve and estimate the transmissibility at the operating speed.

11 Check expected life of selected rolling element bearing. If unsatisfactory, reselect bearing and return to Step 5.

Design Example

As an illustration of the suggested design procedure, consider the problem of providing a squeeze film damper support for Case 8 in [22]. The rotor mass $2(1 - \alpha)M$ is given as 0.90 kg, the first pin-pin critical speed, ω_c , as 3142 rad/s and the operating speed, a , as 2.0. It is desired to use an optimally damped support.

1 Assess that at worst $\rho = 0.045$ mm

2 Select $C = 0.10$ mm

3 Select $R = 20$ mm

4 Select $L = 8$ mm

5 Select a ball bearing with 28-mm o.d., 12-mm bore dia and 8-mm land width, with mass of 0.02 kg. Using a 6-mm thick sleeve integral with a squirrel cage type retainer spring, an additional 0.075 kg mass is lumped at the bearing station. For an assumed symmetric rotor, half the rotor mass is 0.45 kg, of which 1/6 is assumed to comprise the shaft portion (0.075 kg) and 1/3 of this shaft portion is assumed to be lumped at the bearing station (0.025 kg). Hence, the mass ratio, α , is estimated as $(0.02 + 0.075 + 0.025) / (0.45 + 0.075 + 0.02) = 0.22$. The unique speed $a_3 = 1/\sqrt{\alpha} = 2.1$. This is in the vicinity of the operating speed so that the transmissibility, T , will be around 0.3 regardless of pressurization. Should it be desired to reduce α , a ball bearing with 22-mm o.d., 8-mm bore dia and 7-mm land would have a mass of 0.012 kg and a squirrel cage type retainer spring with 30-mm o.d. and with an estimated mass of 0.035 kg could be selected, giving $\alpha = 0.14$ and $U = 0.39$. From Fig. 3, $a_1 = 0.73$, $a_2 = 2.76$, $a_3 = 2.67$, and $a_4 = 2.99$.

Note that in this case $a_2 = 2.76$ falls outside the speed range, simplifying bearing parameter control.

6 The retainer spring stiffness, K_r , is given by equation (9) as 6.9×10^5 N/m.

7 From Fig. 3, require that $B_1 \geq 0.205$ and $B_2 \leq 0.105$.

8 The values of B require lubricant viscosities of $\mu \geq 0.046$ Pa s for $a \leq 0.73$ and $\mu \leq 0.024$ Pa s for $a \geq 0.73$.

9 From Fig. 3, assuming two ends pressurization, $P \approx 0.55$ so that $p = 2.0$ MPa. Should pressurization be removed beyond the pin-pin critical speed, the supply pressure needed for pressurization up to the critical speed would be obtained as $P \approx 0.15$ or $p \approx 0.57$ MPa. Being an optimally damped system, from Fig. 3 $G/U_{\max} = 1.34$ so the maximum rotor amplitude would be $g_{\max} = 0.052$ mm, representing a 95 percent reduction in the maximum rotor amplitude of a rigidly supported rotor of damping ratio 0.02 for which $G_R/U = 26.5$.

10 From equation (11), $T(a=1)$ is 0.44. From Fig. 3 $T_3 = 0.16$, $T_4 = 0.13$, $T(a=3) = 0.13$, $T(a=4) = 0.065$. $T(a=5)$ is not needed for interpolation. Using these values, the transmissibility at operating speed is obtained by interpolation as $T = 0.24$, resulting in a transmitted force amplitude of 182.5 N under the worst unbalance condition.

11 Under this worst unbalance condition, the selected ball bearing would have a life of approximately 210 hrs. Whether this is satisfactory depends on the actual operating requirements. A further reduction in the transmitted force at operating speed would actually result if $\mu < 0.024$ Pa s ($B_2 < 0.105$) at the operating speed. Had the original support selection with $\alpha = 0.22$ been adhered to, there would have resulted a 19 percent increase in the maximum rotor amplitude and a 22 percent increase in the transmitted force, indicating the desirability of avoiding operation in the vicinity of the unique speed, a_3 , even for relatively low values of mass ratio, α .

For the design recommended here, depending on the operating temperature, a variety of lubricants would be available, and the required temperature change upon passage through the unique speed a_2 , while running up to or down from operating speed, is typically around 20°C.

Conclusions

1 A theoretical model has been presented, allowing for fast design of optimally damped pressurized rotor bearing systems.

2 All necessary design data for such optimally damped systems are presented on a single chart for a wide range of mass ratio and for a relatively high level of unbalance parameter.

3 The data presented are practical for a wide variety of rotors operating under the second bending critical speed. In particular, the design is not constrained in many practical applications by the lubricant supply pressure and viscosity.

4 In conjunction with additional bearing parameter data, the design chart may also be used for the design of optimally damped unpressurized support systems for low unbalance.

5 For operation outside the parameter ranges for which the design chart is intended, the analytical model allows for the desired design data to be obtained.

6 The smaller the mass ratio the lower the rotor amplitude and the supply pressure needed. However, the lower limit of the mass ratio may be dictated by rotor mass, and depending on the operating speed, by transmissibility considerations.

References

1 Rieger, N. F., "A Comprehensive Guide to Computer Programs for Analyzing Rotor Systems," *Machine Design*, Jan. 1976, pp. 89-95.

2 McGrew, J. M., Discussion, *ASME Journal of Lubrication Technology*, Vol. 92, No. 1, 1970, pp. 69-72.

3 White, D. C., "The Dynamics of a Rigid Rotor Supported on Squeeze Film Bearings," *Vibrations in Rotating Systems Conference*, I. Mech. E., 1972, pp. 213-219.

4 Rabinowitz, M. D., and Hahn, E. J., "Stability of Squeeze Film Damper Supported Flexible Rotors," *ASME JOURNAL OF ENGINEERING FOR POWER*, Vol. 99, No. 4, 1977, pp. 545-557.

5 Williams, R. J., and Holmes, R., "Determination of the Linear Characteristics of Squeeze Films," *Proc. I. Mech. E. Tribology Convention*, Paper No. C81/71, 1971, pp. 135-141.

6 Thomsen, K. K., and Andersen, H., "Experimental Investigation of a Simple Squeeze Film Damper," *ASME JOURNAL OF ENGINEERING FOR INDUSTRY*, Vol. 96, No. 2, 1974, pp. 427-430.

7 Tonnesen, J. T., "Further Experiments on Squeeze Film Bearings," Research Report No. FR11, Technical University of Denmark, 1975.

8 Tonnesen, J. T., "Experimental Squeeze Bearing Orbit Studies," *Conference on the Stability and Dynamic Response of Rotors with Squeeze Film Bearings*, US Army Research Office, Charlottesville, 1979.

9 Cunningham, R. E., "Steady-State Unbalance Response of a Three Disk Flexible Rotor on Flexible Damped Supports," *Trans. ASME Journal of Mechanical Design*, Vol. 100, No. 3, 1978, pp. 563-573.

10 Rabinowitz, M. D., and Hahn, E. J., "Steady-State Performance of Squeeze Film Damper Supported Flexible Rotors," *ASME JOURNAL OF ENGINEERING FOR POWER*, Vol. 99, No. 4, 1977, pp. 552-558.

11 Den Hartog, J. P., *Mechanical Vibrations*, 4th ed., McGraw-Hill, New York, 1956.

12 Kirk, R. G., and Gunter, E. J., "The Effect of Support Flexibility and Damping on the Synchronous Response of a Single Mass Flexible Rotor," *ASME Journal of Engineering for Industry*, Vol. 94, No. 1, 1972, pp. 221-232.

13 Cunningham, R. E., Fleming, D. P., and Gunter, E. J., "Design of a Squeeze Film Damper for a Multi-Mass Flexible Rotor," *ASME Journal of Engineering for Industry*, Vol. 98, No. 1, 1976, pp. 1383-1389.

14 Gunter, E. J., Barrett, L. E., and Allaire, P. E., "Design of Nonlinear Squeeze-Film Dampers for Aircraft Engines," *ASME Journal of Lubrication Technology*, Vol. 99, No. 1, 1977, pp. 57-64.

15 Barrett, L. E., Gunter, E. J., and Allaire, P. E., "Optimum Bearing and Support Damping for Unbalance Response and Stability of Rotating Machinery," *ASME JOURNAL OF ENGINEERING FOR POWER*, Vol. 100, No. 1, 1978, pp. 89-94.

16 Hibner, D. H., Bhat, S. T., and Buono, D. F., "Optimum Friction Damping of a Flexible Rotor," *ASME Paper No. 81-GT-156*, 5 pp.

17 Pilkey, W. D., Wang, B. P., and Vannoy, D., "Efficient Optimal Design of Suspension Systems for Rotating Shafts," *ASME Journal of Engineering for Industry*, Vol. 98, No. 3, 1976, pp. 1026-1029.

18 Rabinowitz, M. D., "Squeeze Film Damper Supports for Flexible Rotors," Ph.D. thesis, University of New South Wales, Kensington, 1979.

19 Brock, J. E., "A Note on the Damped Vibration Absorber," *ASME Journal of Applied Mechanics*, Vol. 68, No. 4, 1946, p. A-284.

20 Wood, H. T., "Nonlinear Vibration Damping Functions for Fluid Film Bearings," *SAE Transactions*, Vol. 76, No. 670061, 1967, pp. 494-506.

21 Simandiri, S., and Hahn, E. J., "Effect of Pressurization on the Vibration Isolation Capability of Squeeze Film Bearings," *ASME Journal of Engineering for Industry*, Vol. 98, No. 1, 1976, pp. 109-117.

22 Malanoski, S. B., "Case Histories in Which Subsynchronous or Synchronous Vibration Amplitudes have been Minimized After Employing Custom Designed Damper Bearings," *Conference on the Stability and Dynamic Response of Rotors with Squeeze Film Bearings*, US Army Research Office, Charlottesville, May 1979.

23 *Shell Lubricants Product Data Guide*, The Shell Company of Australia Ltd., Melbourne, 1977.

APPENDIX A

Under steady-state conditions, with the rotor geometric and mass centers, and the journal center describing synchronous circular orbits about the static deflection line in Fig. 1, one can write

$$\mathbf{e} = \mathbf{e} \exp(i\omega t) \quad (\text{A1})$$

whereupon

$$\dot{\mathbf{e}} = i\omega \mathbf{e} \quad (\text{A2})$$

and

$$\ddot{\mathbf{e}} = -\omega^2 \mathbf{e} \quad (\text{A3})$$

Similar expressions pertain to $\bar{\mathbf{g}}$ and $\bar{\mathbf{p}}$ so that equations (1) and (2) may be written as

$$-K_s \mathbf{g} + (K_s + K_1 - \alpha M \omega^2 + iC_1 \omega) \mathbf{e} = 0 \quad (\text{A4})$$

$$[K_s - (1 - \alpha) \omega^2 M] \mathbf{g} - K_s \mathbf{e} = (1 - \alpha) M \omega^2 \boldsymbol{\rho} \quad (\text{A5})$$

Elimination of \mathbf{g} from equations (A4) and (A5) gives

$$\mathbf{e} = \frac{(1 - \alpha) M \omega^2 K_s \boldsymbol{\rho}}{\alpha(1 - \alpha) M^2 \omega^4 - (1 - \alpha) M K_1 \omega^2 - M K_s \omega^2 + K_1 K_s - i(1 - \alpha) M C_1 \omega^2} \quad (\text{A6})$$

From this equation the magnitude of \mathbf{e} may be easily obtained, and upon appropriate nondimensionalization, one obtains equation (3) for ϵ .

Similarly, one can eliminate \mathbf{e} from equations (A4) and (A5) to yield equation (4) for G . Finally, substitution for e in the expression for transmissibility and nondimensionalizing yields, after some algebraic manipulation, equation (5) for T .

APPENDIX B

Rotor Amplitude Ratio

From equation (4) G/U is independent of the support damping when

$$\left[K_2 - \alpha \frac{a^2}{f^2} + \frac{1-\alpha}{f^2} \right]^2 = \left[K_2 + \frac{a^2}{f^2} \left(\frac{\alpha a^2 - 1}{1-a^2} \right) \right]^2 \quad (\text{B1})$$

Note that since $0 \leq \alpha < 1$, and f is assumed to be nonzero, this condition cannot be satisfied at $a = 1$. Nor can it be satisfied if K_2 is not constant except for $\alpha = 1$. However, for pressurized bearing supports, i.e., with $K_2 = 1$, equation (B1) is satisfied at the two speeds, a_1 and a_2 , where

$$a_{1,2} = \left\{ \frac{f^2 + 1}{2\alpha} \mp \left[\left(\frac{f^2 + 1}{2\alpha} \right)^2 - \frac{f^2}{\alpha} - \frac{1-\alpha}{2\alpha} \right]^{1/2} \right\}^{1/2} \quad (\text{B2})$$

The corresponding constant rotor amplitude ratios at these speeds are then given by

$$G/U_{1,2} = \frac{a_{1,2}^2}{(1-\alpha)|1-a_{1,2}^2|} \quad (\text{B3})$$

Equations (B2) and (B3) may also be used to predict the unique points for unpressurized bearing supports provided the unbalance parameter is sufficiently small so that $K_2 \approx 1$.

It may be noted that for all $0 \leq \alpha < 1$, equation (B2) requires that a_1 and a_2 be on either side of the pin-pin critical speed, i.e., that $a_1 < 1$ and $a_2 > 1$. Thus, $a_1 > 1$ would require that

$$1 < \frac{f^2 + 1}{2\alpha} - \left[\left(\frac{f^2 + 1}{2\alpha} \right)^2 - \frac{f^2}{\alpha} - \frac{1-\alpha}{2\alpha} \right]^{1/2} \quad (\text{B4})$$

This inequality can only be satisfied if $\alpha > 1$. Similarly, it may be shown that $a_2 < 1$ requires $\alpha > 1$. Hence, G/U_1 increases as a_1 increases and G/U_2 increases as a_2 decreases. Further, a rearrangement of equation (B2) yields

$$f^2 = \frac{\alpha a_{1,2}^4 - a_{1,2}^2 + (1-\alpha)/2}{a_{1,2}^2 - 1} \quad (\text{B5})$$

Differentiation of equation (B5) with respect to $a_{1,2}$ gives

$$2f \frac{df}{da_{1,2}} = 2\alpha a_{1,2} + \frac{a_{1,2}(1-\alpha)}{(1-a_{1,2}^2)^2} \quad (\text{B6})$$

Hence, for $0 \leq \alpha \leq 1$, $df/da_{1,2} > 0$ so that both a_1 and a_2 increase as f increases.

Unbalance Transmissibility

From equation (5) it can be seen that T is independent of the support stiffness and damping whenever

$$\frac{\alpha a^2 - 1}{1-a^2} = 0 \quad (\text{B7})$$

Equation (B7) is satisfied at the unique speed, a_3 , given by

$$a_3 = 1/\sqrt{\alpha} \quad (\text{B8})$$

and the corresponding constant transmissibility is given by

$$T_3 = \frac{\alpha}{1-\alpha} \quad (\text{B9})$$

For pressurized bearings, T will also be independent of support damping at the two speeds, a_4 and a_5 , where

$$a_{4,5} = \left\{ \frac{1+2f^2}{2\alpha} \pm \left[\left(\frac{1+2f^2}{2\alpha} \right)^2 - \frac{2f^2}{\alpha} \right]^{1/2} \right\}^{1/2} \quad (\text{B10})$$

The corresponding constant transmissibilities at these speeds are then given by

$$T_{4,5} = \frac{1}{|a_{4,5}^2 - 1|} \quad (\text{B11})$$

Again, equations (B10) and (B11) may also be used to predict unique points for unpressurized bearings provided the unbalance parameter is sufficiently small so that $K_2 \approx 1$.

Journal Amplitude Ratio

From equation (3), ϵ/U is independent of the support stiffness and damping when $a = 1$; i.e., the pin-pin critical speed corresponds to the unique speed a_6 . The corresponding constant journal amplitude ratio is then given by

$$\epsilon/U_6 = \frac{1}{1-\alpha} \quad (\text{B12})$$

Note that this implies that at the pin-pin critical speed, $e = \rho$, i.e., that the journal eccentricity must equal the mass eccentricity, as had already been noted in [20]. Physically, this means that squeeze film dampers necessarily lock up once the mass eccentricity equals or exceeds the bearing radial clearance.

Experimental Evaluation of Squeeze Film Supported Flexible Rotors

M. D. Rabinowitz

Design Engineer,
Hawker De Havilland Australia,
Lidcombe, New South Wales, Australia

E. J. Hahn

Senior Lecturer,
University of New South Wales,
Kensington, New South Wales, Australia
Mem. ASME

This paper describes the experimental investigations which were conducted to verify existing theoretical vibration amplitude predictions for centrally preloaded, squeeze film supported flexible rotors. The influence of measurement errors and operating condition uncertainties are quantified. The agreement between theory and experiment was excellent, and it is shown that any discrepancy can be explained in terms of errors in determining the mean lubricant viscosity and the orbit magnitudes. Hence, for the range of parameters investigated, the theoretical model and predictions therefrom are validated.

Introduction

Squeeze film dampers (see Fig. 1) have been the subject of numerous experimental investigations in recent years. Extensive work has been done to examine experimentally the fluid film behavior. In some of these investigations, test rigs were constructed where the squeeze film damper was constrained to move in circular orbits by means of an eccentric journal sleeve, exciter, etc., and in most of these cases, the pressure distribution or the fluid film forces were found to be in good agreement with theoretical predictions [1-4]. These experiments served to verify the theoretical hydrodynamic model for calculating fluid film forces under synchronous circular orbit type equilibrium conditions. In other experiments, rigid rotors supported by concentric squeeze film dampers were constructed and excited by dynamic unbalance loadings [5-9]. The results reported were not in such good agreement with theory, and in most cases steady-state circular orbits were not evident. However, the jump to or from an undesirable operation mode was reported to occur as predicted [5, 6].

Quantitative experimental data on journal eccentricity frequency response have been obtained for speeds at which the rotor may be regarded as rigid [10]. These results are in excellent agreement with theoretical predictions. However, very few experimental data are available in the literature at speeds in the vicinity of the rotor critical speed. Hence, experimental investigation to test the theoretical results previously reported by the authors [11-13] was felt to be necessary.

As the system behavior is predicted to depend strongly and in a nonlinear fashion on the bearing geometry, with radial clearances typically of the order of 0.1 mm, a carefully designed high-precision experimental rig was considered mandatory. This paper describes the experimental rig used,

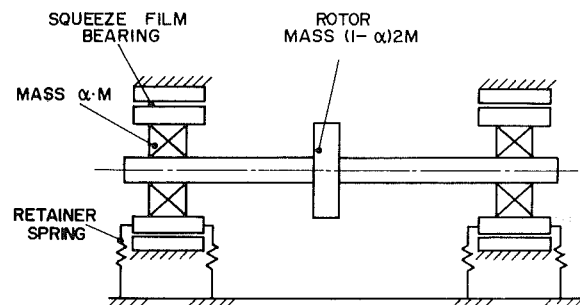


Fig. 1 Squeeze film mounted single-disk flexible rotor

the procedure adopted, and the results obtained. It is a summary and discussion of work comprising part of [14].

Description of the Experimental Rig

Rig Design. The following simplifying assumptions, pertinent to the experimental rig design, were made in obtaining the theoretical design data for the squeeze film supported flexible rotor: (a) the rotor is symmetric; (b) part of the mass may be lumped at the rotor center with the remainder at the bearing stations; (c) gyroscopic effects are negligible; (d) excitation forces due to rolling element bearings are negligible; (e) the rotor is centrally preloaded with symmetric radial stiffness.

The extent to which assumptions (a-c) are justified would depend on the precision of the experimental rotor bearing system and would involve high manufacturing costs if a two-bearing symmetric flexible rotor system were designed. Satisfaction of assumption (d) presumes that rolling element bearing tolerances are such as to maintain negligible clearances. However, as the lubricant heats up, the outer ring of the antifriction bearing would be expected to reach significantly different temperatures to its inner ring. It is important that any resulting differential expansion avoids

Contributed by the Gas Turbine Division of THE AMERICAN SOCIETY OF MECHANICAL ENGINEERS and presented at the 27th International Gas Turbine Conference and Exhibit, London, England, April 18-22, 1982. Manuscript received at ASME Headquarters December 15, 1981. Paper No. 82-GT-233.

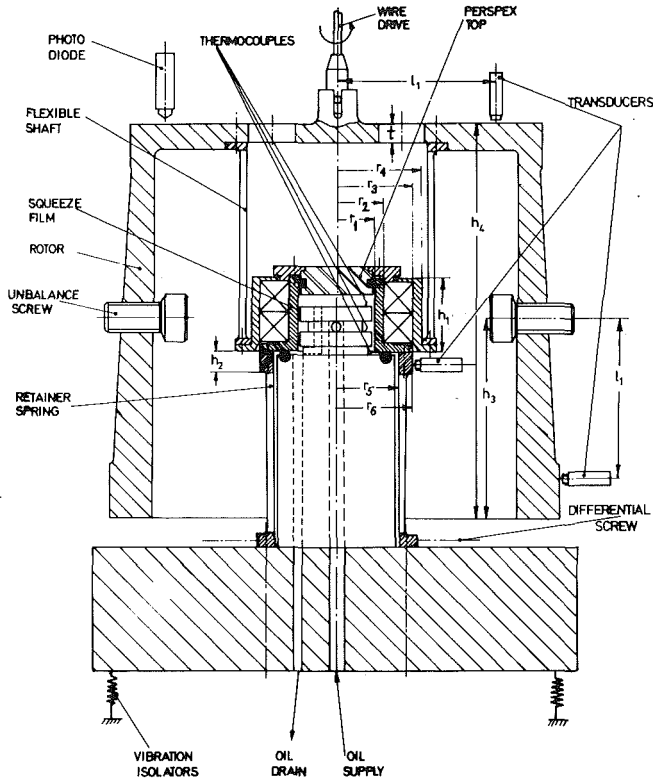


Fig. 2 Rotor bearing general assembly

undesirable clearance between the rolling elements and the rings.

The concept of an overhung rotor supported in an "internal" squeeze film bearing was decided upon. As can be seen from Fig. 2, it is similar to the rigid rotor rig arrangement of White [5, 6] in that the housing is the moving member. The system consists of a stationary shaft which forms one squeeze film bearing surface and a rotor supported in a light squirrel cage acting as a flexible shaft. This in turn is mounted on the outer race of a pair of high-precision rolling element bearings which are axially preloaded in back-to-back mounting. The inner races of these bearings are assembled integral with the squeeze film bearing housing. This is supported on a squirrel cage type retainer spring which is fixed to the base plate. Thus, satisfaction of assumptions (a), (b), (d), and (e) did not introduce major manufacturing difficulties.

The wire-drive-type flexible coupling reduces drive excitation to acceptable levels, and the rotor is mounted vertically to simplify centralization (by differential screws) and to avoid the need for a transverse preload. Such a preload would decrease the allowable dynamic load on the squirrel cages. Lubricant is supplied through a central bore in the

Table 1 Rig dimensions and relevant design values

Retainer spring (lower squirrel cage)	
ω_r	27.85 Hz
no. of bars	6
bar length	85 mm
bar width	4.23 mm
maximum predicted stress	121 MPa
Bearing (refer to Fig. 2)	
r_1	20 mm
r_2	25 mm
r_3	40 mm
r_4	46 mm
r_5	32 mm
r_6	41 mm
h_1	42 mm
h_2	16 mm
Rotor (refer to Fig. 2)	
i.d.	195 mm
o.d. min.	213 mm
o.d. max.	237 mm
h_3	108 mm
h_4	210 mm
t	10 mm
rotor mass	20.1 kg
maximum predicted stress	$129 \times \omega^2$ Pa
Flexible shaft (upper squirrel cage)	
ω_c	55.7 Hz
no. of bars	24
bar length	100 mm
bar width	4.65 mm
deflection	0.4 mm
corresponding stress	167 MPa
Wire drive	
torque transmitted	10 Nm
wire diameter	5.27 mm
length	400 mm
first critical speed	152 Hz
whirl force at this speed	0.25 N
corresponding unbalance force for $U=0.05$	181 N
speed at which ratio of rotor inertia "force" to wire drive retaining force exceeds 50	9.7 Hz

stationary shaft and feeds via four inlet holes into a circumferential groove. It is drained through outlet holes in the stationary shaft, with a needle valve controlling the outflow and, hence, the outlet pressure. The squeeze film bearing is sealed by O-rings, positioned to prevent them from themselves acting as squeeze film bearings. Rotor unbalance can be adjusted by means of unbalance screws of known weight and pitch. The upper oil outlet is visible through the transparent "perspex" top.

To ensure safe operation, acceptable stress levels are required in the rotor and the squirrel cages under operating conditions pertaining to the theoretical system frequency response data. To avoid the introduction of moments to the

Nomenclature

a = speed parameter, ω/ω_c	$2K_s$ = rotor stiffness	μ = absolute viscosity of lubricant at the mean lubricant temperature
B = bearing parameter, $\mu RL^3/(2M\omega_c C^3)$	L = axial width of bearing	ρ = unbalance eccentricity
C = radial clearance of bearing	$2M$ = rotor bearing system mass	ω = rotor speed
e = journal eccentricity	R = radius of journal	ω_c = first pin-pin critical speed of rotor, $\sqrt{K_s/[(1-\alpha)M]}$
f = frequency ratio, ω_r/ω_c	U = unbalance parameter, $(1-\alpha)\rho/C$	ω_r = natural frequency of retainer spring with respect to rotor mass, $\sqrt{K_r/M}$
g = rotor excursion amplitude at midspan with respect to static deflection line	α = mass ratio, equals fraction of the total mass lumped at the bearings	
G = nondimensional rotor amplitude at midspan, g/C	ϵ = eccentricity ratio, e/C	
K_r = retainer spring stiffness per bearing station	ζ = damping ratio at bearing centre due to O-ring	

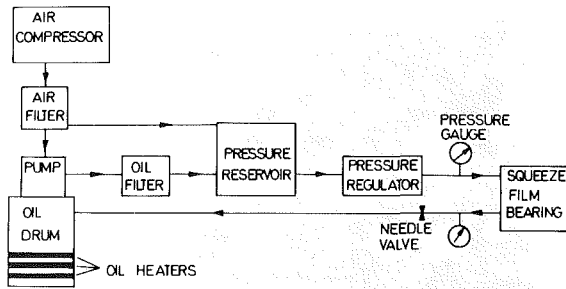


Fig. 3 Schematic of the lubrication system

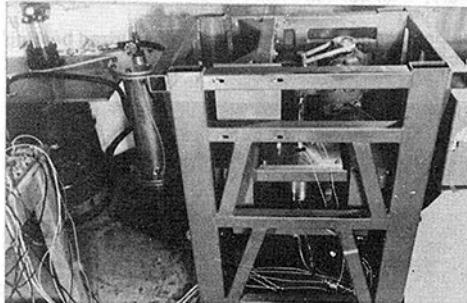


Fig. 4 Flexible rotor rig assembly

squeeze film bearing, the rotor and the base plate centers of mass are designed to coincide with the center of the bearing circumferential groove. The rotor spin moment of inertia has to be equal to its moment of inertia about a horizontal axis through its center of mass, to avoid introduction of bending moments by possible gyroscopic precession, thereby satisfying assumption (c). High lubricant supply pressures were considered unsafe, and low pressures could be vulnerable to substantial fluctuations.

These considerations imposed constraints on the design which were not easy to satisfy, as the design analyses depend in a complicated manner on the unbalance parameter, U , the bearing parameter, B , the frequency ratio, f , the mass ratio, α , and the speed parameter, a . Several possible rig configurations which covered the relevant range of these parameters were conceived and are summarized in [14]. Of these, only the second configuration, corresponding to $\alpha = 0.08$ and $f = 0.5$, was actually constructed.

Table 1 summarizes the design information pertaining to this configuration, and Fig. 2 shows schematically the general assembly. Important features of the design and the determination of its dimensions are discussed in [14]. Figure 3 shows the schematic diagram of the lubrication system. A low-pressure pump was selected to deliver oil to the squeeze film bearing via a $14\text{-}\mu\text{m}$ porous filter, an oil pressure regulating reservoir, and a pressure regulator. Pressurized air in the reservoir served to regulate the supply pressure and minimize pressure fluctuations. Either one or both ends of the squeeze film bearing could be pressurized using the downstream needle valve. The lubricant was isolated from the surroundings to avoid contamination by dust. Using an oil equivalent to ISO 680, a temperature range of $21\text{--}62^\circ\text{C}$, with nominal viscosities of $4000\text{ mm}^2/\text{s}$ and $200\text{ mm}^2/\text{s}$, respectively, enabled B to be varied in the range $0.05 \leq B \leq 1$. Drum heaters allowed for temperature control.

Figure 4 shows the fully assembled rig. The cylinder to the left of the vertical frame is part of the lubrication system. In Fig. 5 the rig is only partly assembled. One can see from left to right, the rotor, the wire drive, the driven pulley, the "flexible" shaft, and the motor with driving pulley. Figure 6 shows the squeeze film bearing and the retainer spring subassembly.

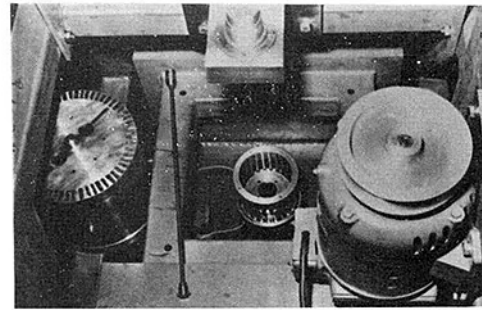


Fig. 5 Bearing assembly and system components

The rotor bearing system is isolated from the motor and the drive unit by mounting the rotor on a heavy base plate resting on vibration isolators. The centers of mass of the base plate, of the rotor, and the squeeze film bearing are all at the level of the vibration isolators. These were chosen to provide the rotor base plate assembly with a resonance of 4.5 Hz in both the horizontal and vertical directions and with a rocking mode resonance of 9 Hz . The motor and the drive unit in turn are mounted on the solid steel frame onto which the vibration isolators are bolted.

Instrumentation. The mean lubricant temperature was determined by taking the arithmetic average of the lubricant inlet and outlet temperatures. Three stations were assigned for temperature measurements, viz., the circumferential groove and the lubricant outlet end of each land. Temperatures were measured by two thermocouples positioned diametrically opposite at each station in the oil and recorded on a temperature recorder.

Journal and rotor deflections were measured by six non-contacting inductance transducers. Three pairs of probes were mounted in x - y configurations, one pair to measure journal displacement and two pairs to measure rotor radial displacement and tilt, enabling detection and subsequent correction for possible gyroscopic motions, to give the true rotor center orbit. The transducer output signals were displayed on two dual beam oscilloscopes. Two pressure gauges were positioned as shown in Fig. 3. The rotor angular velocity was measured by a photo diode cell.

Test Procedure

Commissioning of Experimental Rig. Prior to the running of the actual tests, the oscilloscopes and displacement transducers were calibrated. The kinematic viscosity-temperature characteristic of the oil was determined using a reverse flow viscometer. System components were weighed to give a rotor mass $2M = 23.35\text{ kg}$ and a mass ratio $\alpha = 0.079$. The natural frequencies, ω_c and ω_r , were measured to be 52.10 Hz and 33.86 Hz , respectively, giving $f = 0.650$. For the dry assembly, the damping ratio due to the O-ring was found to vary from 0.02 to 0.08 , being temperature dependent. Hence, a value of 0.05 was assumed. All base plate resonances were found to be below 10 Hz . The bearing was centralized using the inductance transducers and locked in position. The rotor was balanced statically and dynamically and found to have a residual unbalance less than 25 g mm (corresponding to an unbalance parameter $U \leq 0.01$). Full details of the commissioning procedure are outlined in [14].

Frequency Response Experiments. The frequency response of the system was investigated experimentally for unbalance parameter values of $U = 0.07, 0.15, 0.20, 0.25, 0.30,$ and 0.40 over as wide a range of the bearing parameter, B , as practical, i.e., $0.05 < B < 0.8$, for both pressurized and

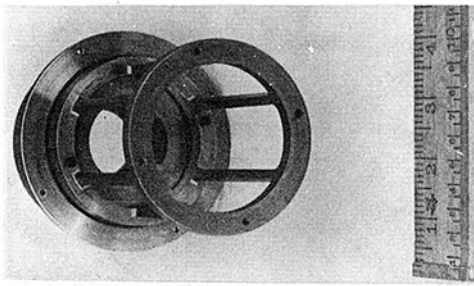


Fig. 6 Squeeze film bearing and retainer spring subassembly

unpressurized conditions. For pressurization, the lubricant supply pressure was kept at more than 1.2 times the theoretical pressure required to obtain a 2π film [13]. After heating the oil (often for several hours) lubricant flow had to be maintained for over half an hour before steady-state temperatures were obtained. Oil flow was regulated by adjusting the outlet needle valve. In some unpressurized bearing tests, small inlet pressures (≤ 0.007 MPa) were used to ensure some oil flow. To avoid supply pressure fluctuations, the oil reservoir was filled before every test and pressurized with compressed air. System response was observed in the frequency range 10-80 Hz at intervals of 5 Hz. Once the system was accelerated or decelerated to the speed of interest, this speed was maintained until the temperature stabilized. Readings of frequency, journal displacement, rotor deflection, inlet temperature, outlet temperature, inlet pressure, and outlet pressure were noted. During pressurized runs, the pressure was often increased during operation at some particular speed to check whether the journal orbit would remain unchanged as predicted by theory.

Pressurization Experiments. These tests were conducted to investigate the theoretical prediction for the extent of pressurization needed to obtain a full film. The system was accelerated to an operating speed in the range of $30 < \omega < 50$ Hz, where, theoretically, a substantial reduction in the journal displacement due to pressurization was expected. Once the temperature stabilized, the pressure was gradually changed and the journal displacement, the inlet and outlet temperatures, and the operating speed (which was reasonably constant) were recorded for each supply pressure level. The pressurization experiments were performed for unbalance parameter values $U=0.15, 0.25, 0.30$, and for bearing parameters in the range $0.1 < B < 0.4$.

Stability Experiments and Bistable Operation. Some of the frequency response tests were under conditions which would theoretically result in bistable operation with undesirable operation modes. The undesirable operation mode was to be avoided since the theoretically predicted rotor displacement of $g > 2C$ would, if attained in practice, overstress the rotor squirrel cage. For unbalance parameter $U=0.40$, bistable operation is predicted. Since jump down from the high to the low orbit is most unlikely in practice, the unpressurized system was run up to 43 Hz, where the rotor deflection, g , already exceeded 0.4 mm. From Hz to 60 Hz, the bearing was fully pressurized resulting in a reduction in the rotor displacement g . At 60 Hz, passage through resonance had been well and truly attained so pressurization was then removed and the system was further accelerated to 80 Hz.

Orbit stability was investigated by knocking the rotor or the base plate during operation. Although the theoretical stability analysis assumed small perturbations, no effort was made to keep the disturbance low, and perturbation peaks resulting in $\Delta e = 0.3C$, as observed on the oscilloscope, were induced.

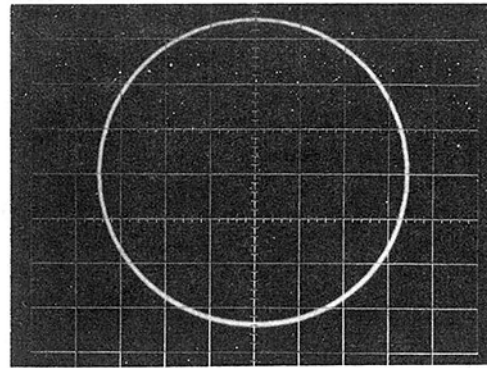


Fig. 7 Typical journal orbit photograph: pressurized bearing, $U = 0.20$, $\omega = 52$ Hz; scale: $12.7 \mu\text{m}$ per major division

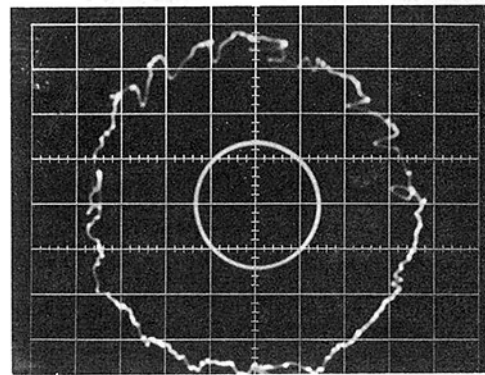


Fig. 8 Typical rotor and journal orbit photograph: unpressurized bearing, $U = 0.20$, $\omega = 33$ Hz; scale, $25.4 \mu\text{m}$ per major division

General Observations. The whole series of tests are fully recorded in [14]. In all cases, the journal and rotor orbits were circular. Typical examples are shown in Figs. 7 and 8. Unfortunately, the rotor surface used for observing the rotor displacements coincided with that used for clamping the rotor on the balancing machine and was thereby damaged. The adverse results of this can be clearly seen in Fig. 8. Nevertheless, with the orbits being very stable at all operating speeds, the gradual changes in the rotor orbit radius could be conveniently followed and recorded.

In all cases the orbit assumed its stable value within seconds, with the "circular orbit" changing progressively in the process. At low frequencies, i.e., below 3 Hz, the journal orbit appeared as a stationary point regardless of the unbalance. Steady speed could be maintained for long periods of time, with the period accurate to ± 0.0001 s (e.g., corresponding to an accuracy of ± 0.008 Hz at 80 Hz). The temperature readings of each thermocouple in a thermocouple pair were identical to the naked eye. When the oil flow through the bearings was restricted, both the inlet and outlet temperatures increased, with the upper outlet temperatures increasing the most and the inlet temperatures increasing the least. For example, in the absence of oil flow for an unpressurized bearing with $U=0.25$, after approximately 30 min of testing while running up in speed, the average outlet temperature increased by 18°C and the average inlet temperature increased by 15°C . On running down, further increases of 2.5°C and 4°C , respectively, were recorded, presumably resulting in a more reliable determination of the bearing parameter (which depends on the mean lubricant viscosity).

A sudden increase in the rotor and the journal orbits occurred occasionally when the oil outlet needle valve was closed and neither the rotor deflection nor the journal displacement stabilized. This phenomenon occurred shortly after the empty

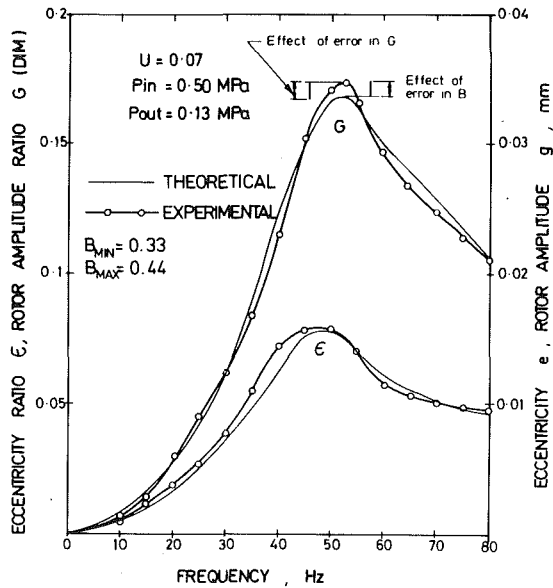


Fig. 9 Journal and rotor amplitude frequency responses for $U = 0.07$, pressurized mounts

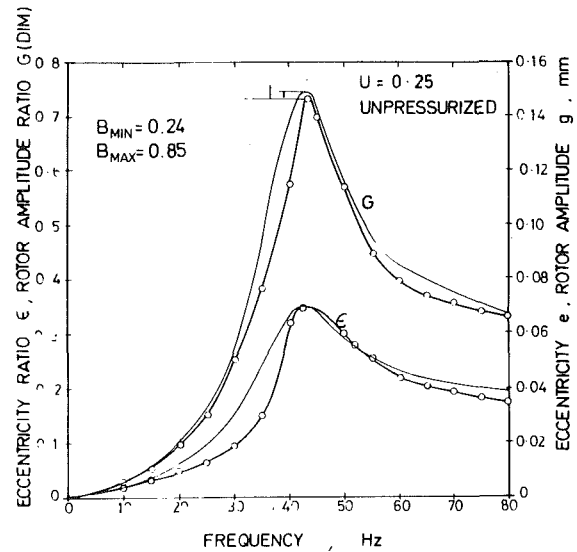


Fig. 11 Journal and rotor amplitude frequency responses for $U = 0.25$, unpressurized mounts

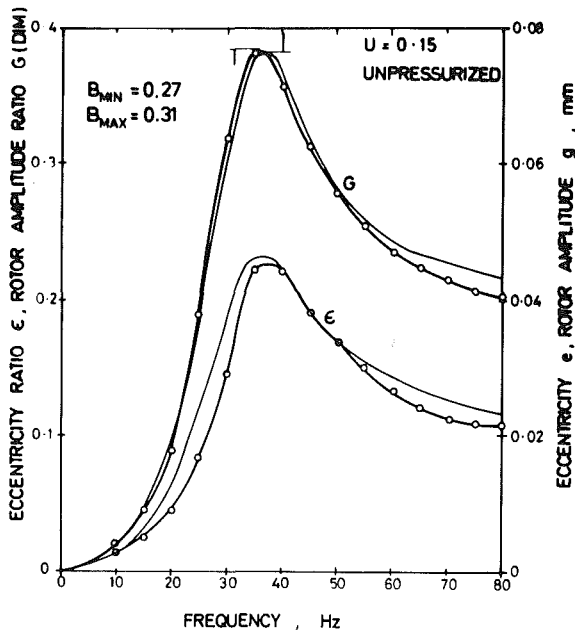


Fig. 10 Journal and rotor amplitude frequency responses for $U = 0.15$, unpressurized mounts

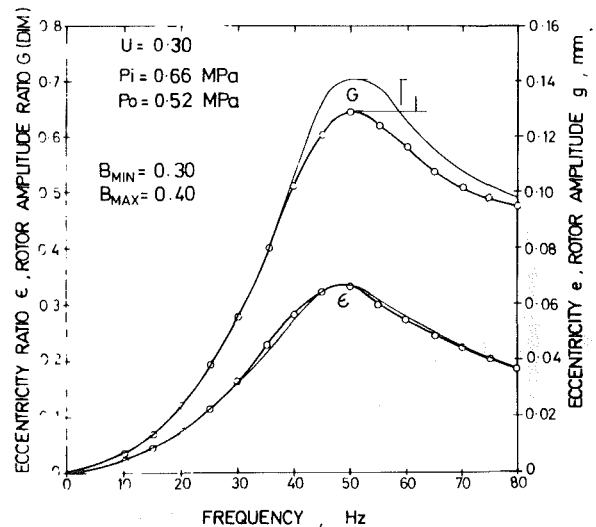


Fig. 12 Journal and rotor amplitude frequency responses for $U = 0.30$, pressurized mounts

oil reservoir was refilled. It was ascribed to the possibility of air bubbles being entrained in the oil film. On stopping the rotor and allowing a relatively slow lubricant flow, air bubbles of diameters up to 2 mm were indeed observed at the outlet station through the "perspex" top. No difficulties were encountered in keeping the supply pressure constant throughout an experiment, and no pressure fluctuations were observed. Upon closing the outlet needle valve, the same reading was obtained from the inlet and the outlet pressure gauges. An increase in the supply pressure during the frequency response tests for pressurized bearings did not influence the system behavior. However, until such fully pressurized (2π film) conditions had been reached, variations in the lubricant supply pressure did influence the system behavior.

With unpressurized bearings and with $U = 0.30$, a jump up was unintentionally encountered at $\omega \approx 46$ Hz. It was

presumed that the jump was initiated by the entrainment of air. It could also have been due to oil starvation. The journal and the rotor displacements quickly built up and disappeared from the oscilloscope screens, at which point $e > 0.86C$ and $g > 2.15C$. Orbit stabilization was not awaited and the power was cut off immediately. A decrease in the orbit followed instantly, suggesting that the jump speed was very close to the operating speed. Upon stopping the system, the air bubbles were again observed. Hence, great care was subsequently exercised to minimize the entrainment of air bubbles or the likelihood of oil starvation by slightly increasing the supply pressure.

With $U = 0.40$, the system could not operate in the range $43 \text{ Hz} < \omega < 52 \text{ Hz}$, with unpressurized oil supply as the rotor orbit not allowed to exceed $g = 2.3C$. No bistable operation was observed with the unpressurized oil supply, and $U = 0.40$, once $\omega \geq 60 \text{ Hz}$. With pressurized oil supply, however, operation throughout the speed range was quite safe.

During the frequency response and pressurization tests, the system was frequently excited but no jump or instability occurred. In all cases the system returned to its equilibrium orbits within five cycles or less. The return to the equilibrium

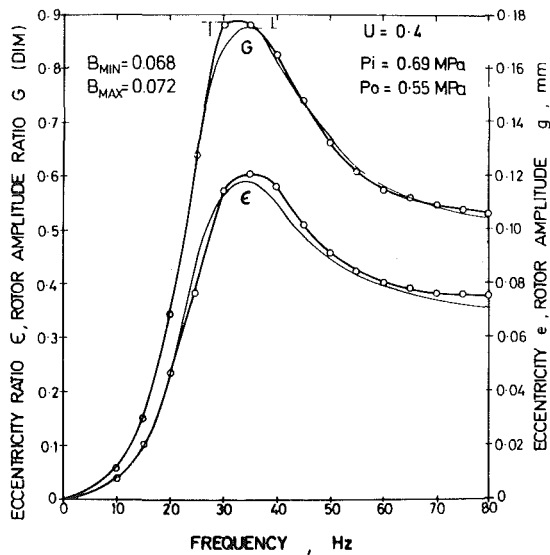


Fig. 13 Journal and rotor amplitude frequency responses for $U = 0.40$, pressurized mounts

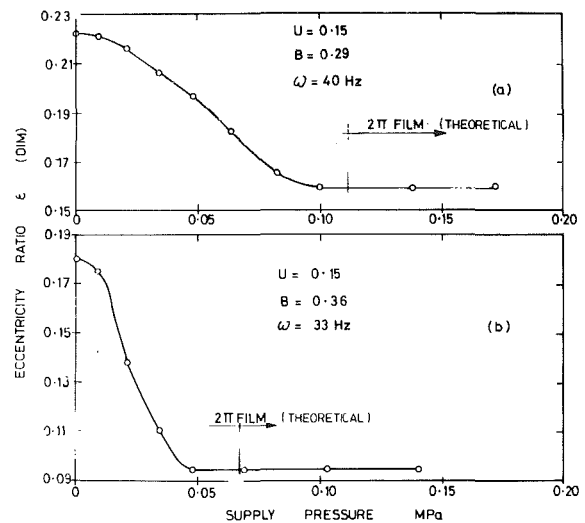


Fig. 15 Journal eccentricity ratio response to gradual change of supply pressure for (a) $U = 0.15$, $B = 0.29$, $\omega = 40$ Hz, and for (b) $U = 0.15$, $B = 0.31$, and $\omega = 33$ Hz

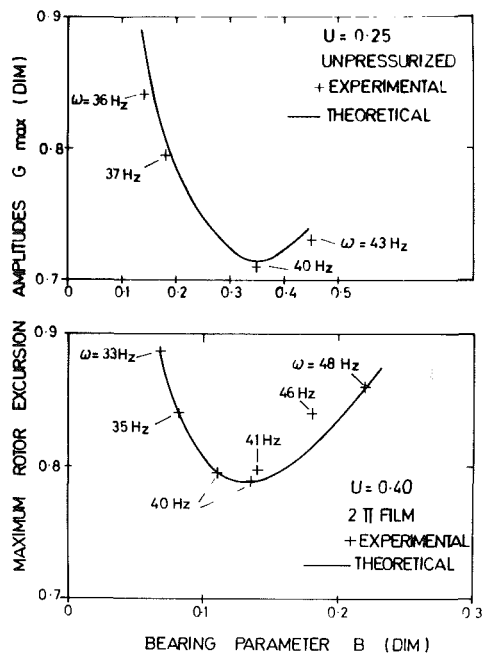


Fig. 14 Maximum rotor amplitudes versus bearing parameter for $U = 0.25$, unpessurized mounts; and $U = 0.40$, pressurized mounts

orbits was faster when the lubricant temperature was low and when the bearings were pressurized.

Results and Discussion

Test Results. The results for all tests are fully documented in [14]. Typical test results are included here for the purposes of discussion. Figures 9–13 and Figs. 17 and 18 show the rotor amplitude and the journal eccentricity frequency responses over a speed range of 0–80 Hz. The corresponding theoretical predictions based on the experimental operating conditions are also plotted. The system response to variation in the lubricant supply pressure is illustrated in Figs. 15 and 16. The theoretical pressure for 2π film was calculated from the experimental operating conditions and the corresponding theoretical journal eccentricity for full film lubrication.

Frequency Response Tests. The frequency response data

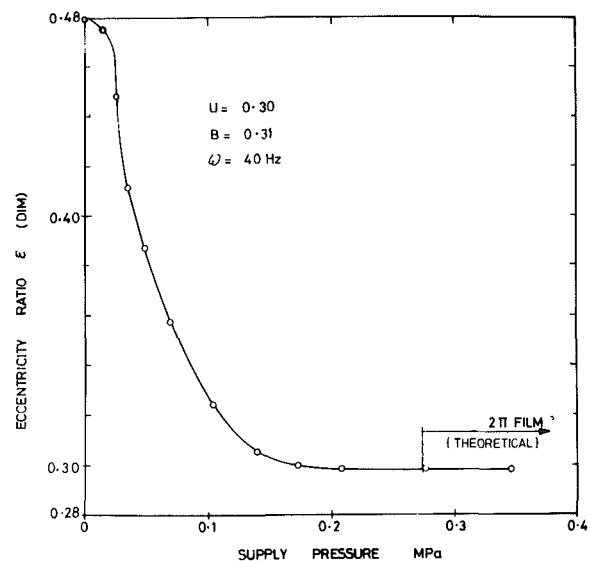


Fig. 16 Journal eccentricity ratio response to gradual change of supply pressure for $U = 0.30$, $B = 0.31$, and $\omega = 40$ Hz

for the journal and the rotor orbit radii were for values of unbalance parameter ranging from $U = 0.07$ to $U = 0.40$, with the bearing parameter ranging from $B = 0.068$ to $B = 0.85$. As can be seen from Figs. 9 to 13, the agreement between the experimental results and the theoretical predictions is good. As documented in [14], discrepancies never exceeded 9 percent and 7.5 percent for the maximum rotor and journal amplitudes, respectively. The average ratio, expressed as a percentage, between the experimental and the theoretical maximum rotor amplitude was 99.3 percent with a standard deviation of 3.6 percent, whereas the corresponding ratio for the journal displacement was 99.9 percent with a standard deviation of 2.6 percent. This strongly suggests that discrepancies between the theoretical prediction and experimental results may be entirely explained by measurement errors in e , g , and ω , and uncertainties in the assumed values of the independent parameters α , f , B , U , and ζ used to obtain the theoretical predictions.

The error in ω has already been noted above to be at most 0.01 percent and may be ignored. The error in determining α was estimated to be ± 4 percent. Its influence on the system response may be shown to be negligible compared to the effect

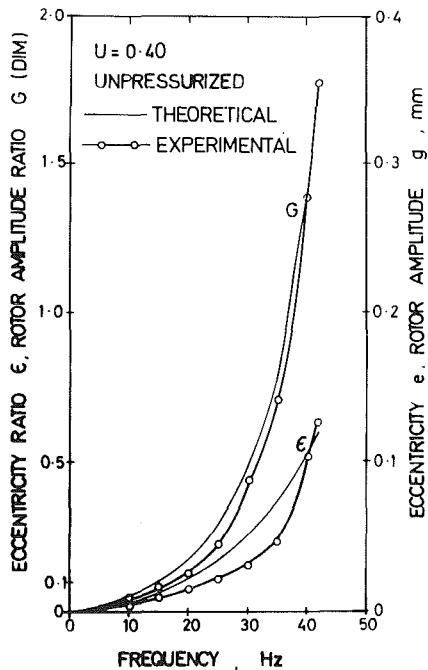


Fig. 17 Journal and rotor amplitude frequency responses for $U=0.40$, unpressurized mounts

of other errors [14]. Measurement errors in the journal and rotor orbit radii were estimated to be at worst ± 2 and ± 5 percent, respectively, corresponding to reading errors of at worst ± 1 mm and ± 2 mm, respectively, in the orbit radii. The influence of this measurement error on G is illustrated in Fig. 9 and shown in Figs. 10 to 13.

For operation at the rotor critical speed (i.e., $\omega=52.1$ Hz), theory predicts that the journal eccentricity ratio $\epsilon=U/(1-\alpha)$ [15], i.e., it is totally independent of the support characteristics B , f , and ζ . Hence, if this prediction is valid, one would expect that at this unique speed experimental errors in determining ϵ are solely due to observation errors in e and errors in determining U or α , and there should be superior agreement between predicted and experimental values of ϵ . Indeed, in no case did the discrepancy exceed 3.5 percent and the average ratio percentage between the experimental, and the theoretical eccentricity was 100.38 percent with a standard deviation of 1.10 percent. Such a relatively small error can be adequately explained by errors in e and U . Hence, it is concluded that the theoretical prediction $\epsilon=U/(1-\alpha)$ is valid.

Further, using this relationship, one can show that the original estimate for the residual unbalance is also valid, i.e., the residual unbalance parameter $U \approx 0.01$. The actual error in U depends also on the position of the residual unbalance. As shown in [14], the errors in U ranged from 0.01 percent for $U=0.30$ to 0.78 percent for $U=0.07$, and are seen to be small compared to observation errors in g and e and, as will be shown below, to possible errors in B , ζ , and f once operation is away from the critical speed.

Theory also predicts that under pressurized conditions there is a unique speed below the rotor critical speed where the rotor amplitude ratio G/U is independent of the support characteristics B and ζ . This unique speed is given by [14]

$$a = \left\{ \frac{f^2 + 1}{2\alpha} - \left[\left(\frac{f^2 + 1}{2\alpha} \right)^2 - \frac{f^2}{\alpha} - \frac{1 - \alpha}{2\alpha} \right]^{1/2} \right\}^{1/2} \quad (1)$$

with the constant value of G/U being given by

$$G/U = \frac{a^2}{(1 - \alpha)(1 - a^2)} \quad (2)$$

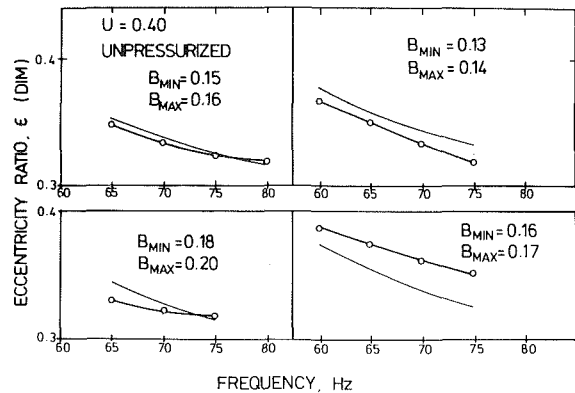


Fig. 18 Journal amplitude frequency responses for $U=0.40$, unpressurized mounts

Hence, if this prediction is valid, one would again expect superior agreement between predicted and experimental values of G/U . Theoretically, using the experimentally determined values of $f=0.650$ and $\alpha=0.079$, equations (1) and (2) predict a constant value for G/U of 1.96 at the unique speed $a=0.80$. Experimentally, investigation of all the pressurized rotor amplitude frequency response results confirmed that below the critical speed, G/U was reasonably constant at 1.96 over the speed range $41.6 \text{ Hz} < \omega < 42.0 \text{ Hz}$. Least scatter occurred at $\omega=41.9$ Hz, corresponding to $a=0.804$, where G/U had a mean value of 1.958 with a standard deviation of 0.0548 and varied over the range $1.85 < G/U < 2.05$. This scatter in G/U of ± 5 percent is adequately explained by errors in measuring g and evaluating U . Hence, it is concluded that the theoretical prediction of a unique speed as given by equation (1), at which G/U is independent of the support characteristics B and ζ and has a constant value as given by equations (1) and (2), is valid. Further, from equations (1) and (2) one can see that this constant, G/U , is dependent only on the system parameters f and α . Accepting the estimated value of $\alpha=0.079 \pm 0.003$ and using the just obtained constant value of $G/U=1.958$, one obtains a value for $f=0.649 \pm 0.25$ percent, which agrees well with the previously measured value of $f=0.650$. The influence on the system response of such an error in f may be shown to be negligible compared to the effect of other errors [14].

The error in B was caused mainly by uncertainty of the mean lubricant temperature, which was assumed to be the average of the inlet temperature, t_i , and the outlet temperature, t_o . The reading error due to scale limitation was 0.25°C . Hence, total error in the mean lubricant temperature was assumed to be

$$\Delta t = \pm [0.25(t_o - t_i) + 0.25]^\circ\text{C} \quad (3)$$

The corresponding possible variation in the theoretically predicted maximum rotor amplitude G is also illustrated in Fig. 9 and shown in Figs. 10 to 13. The effect of temperature variations on the lubricant density was not considered in determining the absolute viscosity. This error varies linearly with the temperature difference from the temperature datum at which the density was measured ($\approx 28^\circ\text{C}$) and would be ≤ 2 percent, (≈ 2 percent at the maximum operating temperature recorded of 65°C). Hence, the bands of uncertainty due to error in B , as shown in Figs. 9 to 13, are conservatively small.

In all tests the experimental results were always within the bands ascribed to these maximum errors in B and G [14]. Hence, there was no attempt to investigate further the additional influence of errors in ζ , errors which are rather hard to estimate.

It may therefore be concluded that for the frequency response tests, the agreement between theoretical predictions

and experimental results was very good, and that all discrepancies may be attributed to experimental error and uncertainty, particularly to measurement errors in ϵ and G and uncertainty in the evaluation of B and possibly ζ . No significant difference in agreement between theory and experiment was noted either with pressurization or with direction of rotor acceleration. Hence, it may be concluded that the approximate cavitation boundary conditions assumed for unpressurized bearings were adequate.

Optimal Damping. In all tests, the maximum rotor excursion amplitudes were encountered between the two natural frequencies, i.e., at $33.8 \text{ Hz} \leq \omega \leq 52.1 \text{ Hz}$. Figure 14 shows the relationship between the maximum rotor excursions, the speed, ω , at which they occurred, and the bearing parameter, B , using $U=0.25$ for unpressurized bearings and $U=0.40$ for pressurized bearings. In both these cases, the lowest maximum amplitudes were obtained at $\omega \approx 40 \text{ Hz}$ in agreement with theoretical predictions regarding the existence of optimal damping. Thus, for unpressurized bearing supports with $U=0.25$, optimal system damping was attained as predicted [14] at $0.2 < B < 0.6$. Similarly, for pressurized bearings with $U=0.40$, optimal system damping was attained at $0.08 < B < 0.2$ [14]. Lightly damped systems (low values of B) resonated in the vicinity of the retainer spring natural frequency; heavily damped systems (high values of B) resonated in the vicinity of the first pin-pin critical speed.

Equations (1) and (2) predict that for pressurized bearing supports, all G/U curves intersect at $\omega=41.8 \text{ Hz}$, where the amplitude ratio $G_{\max} = 1.96 U$. Thus, theoretically $G = 1.96 U$ is the lowest rotor excursion amplitude peak that can be obtained for this system. Although higher amplitude peaks are expected for unpressurized bearing supported rotors, the trends should be similar.

Figure 14 shows that optimal damping was obtained for pressurized bearings (for $U=0.40$) with $B \approx 0.14$, giving $(G/U)_{\max} = 1.965$; for unpressurized bearings (for $U=0.25$), it was obtained with $B \approx 0.35$, giving $(G/U)_{\max} = 2.8$. Note that a reasonable latitude is allowed in the actual value of B without affecting G/U_{\max} significantly. Such optimal damping is possible in practice, by controlling the lubricant operating temperature. Further, pressurization can reduce G/U_{\max} significantly from its unpressurized value.

Pressurization Data. Figures 15 and 16 show the journal orbit response to a gradual change of lubricant supply pressure for unbalance parameters $U=0.15$ and 0.30 , for bearing parameter $0.29 \leq B \leq 0.36$, and for speed $33 \text{ Hz} \leq \omega \leq 40 \text{ Hz}$. The theoretically predicted supply pressure required to obtain full film lubrication for the operating conditions indicated is also shown. In all these tests, steady temperature conditions were achieved prior to the test so that the error in B is likely to be constant throughout the test. It is the variations in ϵ that are of major interest in these tests. Since the error in reading e is expected to be constant, the error in evaluating the changes in e may be regarded as negligible.

The pressure was measured by the inlet and outlet pressure gauges, and identical pressure readings were always obtained. The error in the pressure due to scale limitation is 0.007 MPa . In all cases the pressure required theoretically for full film lubrication is greater, by more than 0.007 MPa , than the pressure above which the journal orbit remained constant.

Hence, it is concluded that the theoretical pressures for full film lubrication are indeed sufficient to achieve full film performance, insofar as no further changes in the journal orbit eccentricity were obtained once these theoretical pressures were exceeded.

Bistable Operation. Theory predicts bearing lock up

($\epsilon \rightarrow 1$) and very high rotor amplitudes, as $a \rightarrow 1$ if the unpressurized system is operating at the undesirable operation mode with $U > 0.2$. The system was often purposely excited throughout the speed range and jump up to the undesirable orbit never took place, indicating either that the excitation was inadequate or that the theoretical prediction was incorrect. However, the accidental apparent jump up which occurred with $U=0.30$ indicated that the former supposition is likely, for although no excitation was purposely provided, it is possible that entrained air in the oil film assisted in the orbit build up [5, 6]. The risk of entrained air bubbles can be minimized by maintaining oil flow. This accident proved convincingly that this operation mode should indeed be avoided. The jump occurred towards the completion of the experiments, and owing to its dangerous nature, no further attempt to excite the unpressurized system was made. For the unpressurized bearing, with $U=0.40$ and $B < 0.6$, bistable operation at the undesirable large amplitude mode is predicted in accelerating to $a=1$. The system is predicted to exhibit an ever increasing orbit with increase in speed until the critical speed. This trend is shown in Fig. 17, where orbit build up was allowed to a maximum of $g=0.38 \text{ mm}$. The theoretical curves show the undesirable operation mode. In no case could the critical speed be safely reached. Figure 18 shows unpressurized bearing frequency response curves for $U=0.40$ for operation above the rotor critical speed. No bistable operation was encountered. This is consistent with theory which predicts that bistable operation virtually disappears even for unpressurized bearing supports above the rotor critical speed.

Upon pressurization, no bistable operation is predicted, nor was any encountered, and as demonstrated on Fig. 13, with $U=0.40$, a passage through the rotor critical speed is possible. As noted earlier, the supply pressure needed to ensure full film lubrication was found to be in good agreement with theory.

System Stability. In all tests, steady-state synchronous circular orbit conditions were obtained regardless of external excitations. Although the theoretical system stability investigation assumed small perturbations about the equilibrium orbits, large perturbations were applied in the tests. The relatively fast decay of the transients, i.e., 1 to 5 cycles with the faster decay occurring for large B and for pressurized bearings, confirmed the predictions of the theoretical analysis. Actually, the theory does predict instability under certain operating conditions for journal orbits in the vicinity of $\epsilon=1.0$. However, such orbits were too large to allow for investigation with the present apparatus.

The Validity of the Theoretical Model. In addition to assumptions (a) to (e) already noted under Rig Design, the theoretical model for predicting the behavior of squeeze film damper supported flexible rotors assumed: (f) the Reynolds equation for constant lubricant properties is applicable; (g) the short bearing approximation is valid; (h) the pressures at the ends of the bearing are either atmospheric or sufficiently above atmospheric to ensure full film lubrication; (i) only positive pressures contribute to the fluid film forces; (j) all unbalance in the rotor may be concentrated in the lumped mass at the rotor midspan; (k) the rotor is torsionally rigid; (l) the rotor rotates at constant speed in spite of possible input torque fluctuations; (m) steady-state conditions have been reached with the journal center, the rotor geometric center, and the rotor mass center, all describing circular orbits about the bearing axis.

Assumptions (e) to (j) are now justified in view of the very good agreement between theoretical and experimental results for the particular rotor and squeeze film bearing geometry

and for the range of operating conditions tested. Stable synchronous circular rotor and journal orbits were observed throughout the experiments and constant speed could be maintained for long periods of time without noticeable speed fluctuations, justifying assumptions (k) to (m).

Hence, it is reasonable to conclude that over the range of parameters investigated, all the assumptions utilized in developing the hydrodynamic theoretical model were fully justified and so the model, and consequently its predictions, are valid. Although no extensive scaling tests were performed (i.e., no attempt was made to utilize totally different bearings and stiffnesses which nevertheless provided the same non-dimensional parameters), the bearing and rotor dimensions were chosen at random, the only constraint being to ensure safe and satisfactory operation over the wide range of parameters which were theoretically of interest. Nor is it likely that the assumptions of the theoretical model would be any less justified, except for extrapolating the predictions to ever higher operating speeds. Further investigations on the effect of ever increasing operating speeds is warranted, for cavitation behavior in the case of unpressurized bearings could alter markedly above some operating speed. Also, for both pressurized and unpressurized bearings, laminar flow and neglect of fluid inertia effects is assumed throughout (inherent in the Reynolds equation), assumptions which are less likely to be valid as the operating speed increases.

Conclusions

1 Over a wide range of speed, unbalance, oil viscosity, and degree of pressurization, the agreement between theoretical and experimental rotor and journal vibration amplitudes was very good. All discrepancies may be attributed to experimental error and uncertainty, particularly to measurement errors in the journal and rotor orbits and uncertainty in evaluating the mean lubricant viscosity.

2 As predicted theoretically, unique speeds existed at which either the journal vibration amplitudes or the rotor vibration amplitudes were independent of support characteristics.

3 As predicted, optimal damping is possible by controlling the lubricant temperature to minimize the maximum rotor vibration amplitude. Nor does the control need to be precise to achieve close to optimal performance.

4 The predicted pressurization to achieve 2π film was found to achieve 2π film conditions.

5 All predicted bistable and stability behavior was validated for both unpressurized and pressurized bearings, with the exception of unpressurized bearings with high unbalance ($U \approx 0.4$) in the vicinity of the pin-pin critical speed (which operating condition exceeded the safety limit of the test rig).

6 Over the range of parameters investigated, the assumed theoretical hydrodynamic model for the squeeze film bearing is valid, and consequently, the theoretical predictions on the behavior of squeeze film supported flexible rotors are valid. This conclusion is likely to hold beyond the parameter range actually tested, though the extrapolation of predictions to higher operating speeds warrants further investigation.

Acknowledgments

This work was carried out with the support of the Australian Research Grants Committee.

References

- 1 Jones, M. G., "An Experimental Investigation of Squeeze Film Hydrodynamics," NGTE Report No. 320, Jan. 1973.
- 2 Williams, R. J., and Holmes, R., "Determination of the Linear Characteristics of Squeeze Films," Paper No. C81/71, *Tribology Convention*, I. Mech. E., pp. 135-141.
- 3 Feder, E., Bansal, P. N., and Blanco, A., "Investigation of Squeeze Film Damper Forces Produced by Circular Centred Orbits," *ASME JOURNAL OF ENGINEERING FOR POWER*, Vol. 100, No. 1, 1978, pp. 15-21.
- 4 Marmol, R. A., and Vance, J. M., "Squeeze Film Damper Characteristics for Gas Turbine Engines," *ASME Journal of Mechanical Design*, Vol. 100, No. 1, 1978, pp. 139-146.
- 5 White, D. C., "Squeeze Film Journal Bearings," Ph.D. thesis, University of Cambridge, 1970.
- 6 White, D. C., "The Dynamics of a Rigid Rotor Supported on Squeeze Film Bearings," *Vibrations in Rotating Systems Conference*, I. Mech. E., 1972, pp. 213-229.
- 7 Hibner, D. H., Kirk, R. G., and Buona, D. F., "Analytical and Experimental Investigation of the Stability of Intershaft Squeeze Film Dampers, Part I: Demonstration of Instability," *ASME JOURNAL OF ENGINEERING FOR POWER*, Vol. 100, No. 1, 1977, pp. 47-52.
- 8 Tonnesen, J., "Further Experiments on Squeeze Film Bearings," Research Report No. FR11, Technical University of Denmark, 1975.
- 9 Tonnesen, J., and Lund, J. W., "Some Experiments on Instability of Rotors Supported in Fluid Film Bearings," *ASME Journal of Mechanical Design*, Vol. 100, No. 1, 1978, pp. 147-155.
- 10 Simandiri, S., and Hahn, E. J., "Experimental Evaluation of the Predicted Behaviour of Squeeze-Film-Bearing-Supported Rigid Rotors," *Journal of Mechanical Engineering Science*, I. Mech. E., Vol. 21, No. 6, 1979, pp. 439-457.
- 11 Rabinowitz, M. D., and Hahn, E. J., "Squeeze Film Bearing Supports for Flexible Rotors," *Proceedings of 4th World Congress on the Theory of Machines and Mechanisms*, Newcastle-upon-Tyne, England, 1975, pp. 575-580.
- 12 Rabinowitz, M. D., and Hahn, E. J., "Steady-State Performance of Squeeze Film Damper Supported Flexible Rotors," *ASME JOURNAL OF ENGINEERING FOR POWER*, Vol. 99, No. 4, 1977, pp. 552-558.
- 13 Rabinowitz, M. D., and Hahn, E. J., "Stability of Squeeze Film Damper Supported Flexible Rotors," *ASME JOURNAL OF ENGINEERING FOR POWER*, Vol. 99, No. 4, 1977, pp. 545-551.
- 14 Rabinowitz, M. D., "Squeeze Film Damper Supports for Flexible Rotors," Ph.D. thesis, University of New South Wales, Kensington, 1979.
- 15 Wood, H. J., "Nonlinear Vibration Damping Functions for Fluid Film Bearings," *SAE Transactions*, Vol. 76, No. 670061, 1967, pp. 494-506.

Unconditionally Stable Calculation of Transonic Potential Flow Through Cascades Using an Adaptive Mesh for Shock Capture

J. R. Caspar

United Technologies Research Center,
East Hartford, Conn. 06108

This paper describes an unconditionally stable procedure for calculating practical transonic potential flows through two-dimensional cascades. The full potential equation is cast in conservation form and approximated in physical space with centered control area techniques. Discrete analogs of nonphysical weak solutions are eliminated by the introduction of artificial viscosity in supersonic regions using artificial compressibility in which the density is evaluated a certain distance upstream from where it is to be applied. An explicit treatment of the density causes standard iterative procedures to diverge, except on relatively coarse meshes on which shocks are poorly captured. Instead, the insight of a model problem analysis is used to treat the density partially and implicitly.

Introduction

In the design of axial compressor and turbine airfoils, the objective is to define the contour that will most effectively provide the desired lift while maintaining desired boundary layer characteristics and high incidence tolerance. Thus, analytically designed airfoils, which can be tailored for a particular application, are superior to series airfoils. For analytic design, it is imperative that an accurate flow analysis be employed. Since the flow analysis will be used iteratively, the design process will be expedited if the flow analysis is computationally efficient. For this reason, the basic analytic tool for design is usually a two-dimensional potential flow solver. That the three-dimensional flows in question can often be accurately represented by such an analysis, i.e., that the flows are reasonably inviscid and irrotational and that radial effects can be modeled using quasi-three-dimensional techniques, is demonstrated in [1, 2], where good agreement is demonstrated between the analysis of [3] and measurements taken in compressor and turbine rows over a wide range of conditions.

In recent years, turbomachines have been designed with higher stage loadings than previously to permit fewer stages and lighter machines [4]. As a consequence, a region of transonic flow near some part of the blade in a compressor or turbine row is common even though the inlet and exit flow may be subsonic. Such a transonic flow field presents a formidable challenge to a potential flow procedure because of the change in type of the differential equation from elliptic in the subsonic regions to hyperbolic in the supersonic regions. The problem is essentially a boundary value problem, but an

attempt to calculate a flow with a large supersonic region using elliptic boundary value techniques is foredoomed to failure since the hyperbolic boundary value problem is ill-posed. Caspar, Hobbs and Davis [3] demonstrated that supersonic flow can be accurately calculated using centered differences (i.e., elliptic) techniques provided the calculation grid does not get too fine or the local Mach numbers too high. These restrictions effectively limit the application of centered difference approximations to shock free flows since the mesh cannot be made fine enough to capture a shock. The *symptom* of trouble when centered differences are used on too fine a mesh to calculate transonic flow is nonconvergence of the iterative procedure employed. Time can be wasted attempting to correct the iterative procedure unless it is realized that the *cause* is the emergence of nonphysical discrete solutions which prevent the iterative procedure from locating the physical discrete solution. This was demonstrated for a model problem by Caspar [5] who showed that the discrete equation has a unique solution for subsonic flow and even into the transonic regime but that as the local Mach number increases, multiple solutions ultimately emerge. The Mach number level at which nonuniqueness occurs is mesh dependent being closer and closer to sonic as the mesh is refined. This dovetailed with the transonic experience of the centered difference approach of [3]. The nonphysical discrete solutions may be thought of as approximations to nonphysical weak solutions [6] or as effects of the loss of well-posedness of the hyperbolic boundary value problem.

While the inviscid model of potential theory may be adequate for subsonic flow, it is deficient in supersonic flow where viscosity is needed to select the physical solution and reject the nonphysical solutions. In an attempt to make the mathematical approximation better model the physics and to account for the proper domain of dependence, Murman and

Contributed by the Gas Turbine Division of THE AMERICAN SOCIETY OF MECHANICAL ENGINEERS and presented at the 27th International Gas Turbine Conference and Exhibit, London, England, April 18-22, 1982. Manuscript received at ASME Headquarters December 18, 1981. Paper No. 82-GT-238.

Cole [7] introduced special backward or “upwind” differencing in supersonic regions. There was a small disturbance analysis of transonic flow past an isolated airfoil so that the calculation grid was aligned with the flow. Jameson [8] generalized this concept to apply to the full potential equation in nonconservative form, and his rotated difference scheme is now generally used for nonconservative transonic flow calculations. If these upwind difference schemes are interpreted in terms of centered differences, it is seen that they effectively introduce a third-order term which acts as an artificial viscosity (AV) [8]. Ives and Liutermoza [9] employed the rotated difference scheme in their nonconservative analysis of cascade flows.

For the conservative formulation of the potential equation, in which the density appears explicitly, AV is commonly introduced by evaluating the density at a certain distance upstream of the point at which it is to be applied [10–12]. This approach, called “artificial compressibility” (AC) or “artificial density” has been applied for cascade flows by a number of authors [13–16]. The treatment has been somewhat arbitrary both in the amount of AC used (how far upstream should the density be applied?) and in the definition of an appropriate iterative procedure: as a mesh is refined in supersonic regions, particularly near a shock, convergence may fail unless appropriate convergence parameters are suitably modified.

The purpose of this paper is to remove some of the ad hoc nature of AC use with conservative flow calculations by addressing (if not answering in full) the following questions: (i) What is the role of AC (or AV in general)? (ii) How much AC is needed? (iii) Why is convergence often difficult even with AC? (iv) How can convergence be made more reliable even for high Mach numbers and dense meshes?

In [5], which serves as a guide for the present work, the effect of artificial viscosity is shown to be the elimination of nonphysical discrete solutions leaving a (locally) unique discrete solution approximating the physical solution. However, the use of AV has little effect on the usual iterative procedures for the conservative formulation so that non-convergence still occurs for transonic flows if local Mach numbers get too high or if the mesh is made too dense. This is because, for conservative formulations, it is common to use some form of a “Taylor” iteration [17] in which the potential is calculated assuming the density is known and then the density is updated in terms of the new potential values. This explicit treatment of the density introduces a Mach number square scaling term to the eigenvalues of the asymptotic error matrix. This ensures nonconvergence if the local Mach number is too high or the local mesh too dense in supersonic regions. An artificial time (AT) term applied explicitly was suggested in [12] to enhance iterative stability. The model problem of [5] indicates that such strategy will indeed improve stability but not make it unconditional because of the explicit treatment of the density. Unconditional stability can only be obtained if the density is treated partially implicitly. This can be achieved with an appropriate *implicit* use of AT.

In this paper, the questions raised above are explored using the conservative “control area” procedure of [3] modified in supersonic regions to include the artificial compressibility form of artificial viscosity. Implicit AT is used to obtain stable Taylor and Taylor/SLOR iterations even with high Mach numbers and dense meshes. Mesh density is tested on an adaptive mesh which automatically and smoothly refines itself near a shock to provide sharp definition of the shock.

The Control Area Approximation

Consider isentropic irrotational flow in a two dimensional cascade passage. The velocity can be given in terms of a potential function by

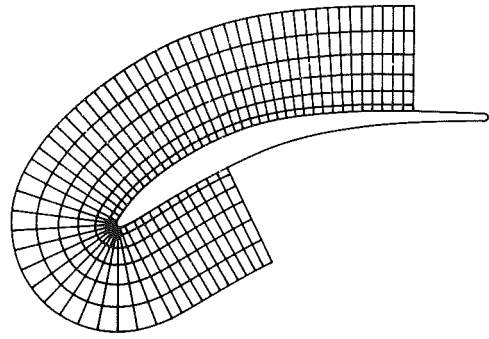


Fig. 1 61 x 6 local mesh

$$\phi_x = \hat{u}/V_1 \equiv u, \phi_y = \hat{v}/V_1 \equiv v \quad (1)$$

where \hat{u} and \hat{v} are the x and y components of the velocity, V is the speed with the subscript “1” indicating conditions at the inlet plane, and ϕ is the potential which must be determined. Given any finite control area enclosed by a piecewise smooth, simply connected curve, D , ϕ must satisfy the mass balance

$$\int_D r \phi_n ds = 0 \quad (2)$$

where r is the modified isentropic density ratio

$$r = \frac{H}{H_1} \frac{\rho}{\rho_0} = \frac{H}{H_1} (1 - \delta |\nabla \phi|^2)^{\frac{1}{\gamma-1}} \equiv \frac{H}{H_1} R(|\nabla \phi|^2) \quad (3)$$

Here H/H_1 measures relative stream tube contraction to give a quasi-three-dimensional aspect to the analysis, ρ is the density with the subscript “0” indicating stagnation conditions, γ is the specific heat ratio, and the constant δ is given in terms of the Mach number, M , at the inlet plane by

$$\delta = \frac{\gamma-1}{2} M_1^2 / \left(1 + \frac{\gamma-1}{2} M_1^2\right) \quad (4)$$

To simplify matters, H/H_1 will be set to 1 in the analysis. However, this is not the case in the sample calculations.

Using Green’s theorem, equation (2) can be expressed

$$\int_{\bar{D}} \int \nabla \cdot (r \nabla \phi) dA = 0 \quad (5)$$

where \bar{D} is the region enclosed by D . Since D is quite arbitrary, the integrand must be identically zero so that

$$\nabla \cdot (r \nabla \phi) = 0 \quad (6)$$

must hold. After eliminating r using equation (3) (with $H/H_1 = 1$) equation (6) becomes

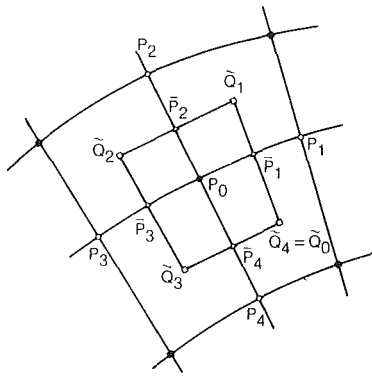
$$(a^2 - u^2) \phi_{xx} + (a^2 - v^2) \phi_{yy} - 2uv \phi_{xy} = 0 \quad (7)$$

where

$$a^2 = \frac{\gamma-1}{2\delta} - \frac{\gamma-1}{2} (u^2 + v^2) \quad (8)$$

is the square of the sound speed normalized by V_1 . Equation (6) directly represents mass continuity while equation (7) does not. Thus the former is termed the “conservative” form of the potential equation while the latter is called the “non-conservative” form. Except near shocks, the two forms are equivalent. However, across a shock the conservative form must be used to model mass conservation correctly and obtain the proper jump condition [11].

For the most part, the flow through a cascade scales with blade chord and can be accurately determined on a relatively coarse mesh. However, near a blunt leading edge or near a shock where the scale of the flow is much smaller, a much finer mesh is needed to produce the same accuracy. In [3], the large-scale effects are calculated on a skewed “global” mesh (not shown) and the small-scale effects due to a blunt leading



• CENTER MESH POINT
 ○ NEIGHBORING MESH POINT
 □ CELL CENTERS
 ▲ NEIGHBOR LINE MID POINTS
 ■ CORNER NEIGHBORS

Fig. 2 Local mesh polygon

edge are calculated on an orthogonal, body-fitted "local" mesh such as the one shown in Fig. 1. Properly, iteration between global and local calculations should be performed. However, in practice this has not been found necessary and so the local calculation is used as a one-step correction to the global calculation. No special techniques are used in supersonic regions so that shocks cannot be captured even on the local mesh. In this paper, the modifications needed to allow shock capturing on the local mesh are discussed.

The control area approximation is applied in physical space with no mapping procedures required even with nonrectangular geometry. The meshes are triangulated as described in [3] thus associating each mesh point, P_0 , with certain "neighboring" mesh points, P_m . The perpendicular bisectors of the line segments joining P_0 to its neighbors are constructed to form a "mesh polygon," D , about P_0 . On the skewed global mesh, the mesh polygons are usually hexagons, but on the orthogonal local mesh they are the quadrilaterals indicated in Fig. 2. The cell center and neighbor line midpoints are labeled \tilde{Q}_m and \tilde{P}_m , respectively. Quantities at the m th neighbor, cell center, or midpoint are subscripted with m , and, in addition, quantities at cell centers or midpoints carry the symbols " \sim " and " $-$ ", respectively. The mesh polygons fill space with no overlap so that if equation (2) is approximated for each polygon, continuity will be satisfied both locally and globally. The control area approximation to equation (2) takes the form

$$0 = \int_D r \phi_n ds \approx \sum_m \tilde{r}_m \frac{\phi_m - \phi_0}{|P_m - P_0|} |\tilde{Q}_m - \tilde{Q}_{m-1}|$$

$$\equiv \sum_m \tau_m \tilde{r}_m (\phi_m - \phi_0) \quad (9)$$

In [3], \tilde{r}_m is approximated by

$$\tilde{r}_m = (r_m + r_0)/2 \quad (10)$$

This requires the approximation of $\nabla \phi$ at the neighbors which causes equation (9) to involve values of ϕ on five mesh lines in each direction—three directly and the other two through the density terms. Equation (9) can be made more compact¹ (in that it involves fewer points) by replacing equation (10) with

$$\tilde{r}_m = (\tilde{r}_{m-1} + \tilde{r}_m)/2 \quad (11)$$

¹The author is indebted to Jerry South and Mohamed Hafez for suggesting this formulation.

The required approximation to $\nabla \phi$ at the cell center is then given in local circumferential (w), normal (z) coordinates by

$$\tilde{\phi}_w = \frac{1}{2} \left[\frac{\hat{\phi}_1 - \hat{\phi}_4}{|\tilde{P}_1 - \tilde{P}_4|} + \frac{\hat{\phi}_2 - \hat{\phi}_3}{|\tilde{P}_2 - \tilde{P}_3|} \right]$$

$$\tilde{\phi}_z = \frac{1}{2} \left[\frac{\hat{\phi}_3 - \hat{\phi}_4}{|\tilde{P}_3 - \tilde{P}_4|} + \frac{\hat{\phi}_2 - \hat{\phi}_1}{|\tilde{P}_2 - \tilde{P}_1|} \right] \quad (12)$$

Here $\phi_k = \phi(P_k)$, and the P_k are the cell corners as indicated in Fig. 3. The approximations of equations (10, 11) will be called "neighbor averaged" and "cell center averaged," respectively. These approximations produce similar results in subsonic flow, but in supersonic flow the cell center averaged approximation produces more sharply defined shocks as discussed below. In subsonic regions, values of \tilde{r}_m or r_m , as needed, are obtained with equation (3). In supersonic regions, equation (3) is modified as shown below.

Local Uniqueness and Convergence of the Taylor Iteration

The nonlinear compressible potential equation must be linearized in some fashion in order to be solved. For the conservative form, this is commonly done by assuming the density is known (from the previous iteration). Such an iteration has been called a Taylor iteration [17]. The non-conservative form leads to the fundamentally different linearization in which the sound speed and flow speed terms are taken as known.

The full Taylor iteration applied to equation (9) is

$$\sum_m \tau_m \tilde{r}_m (\Delta \phi_m^{n+1} - \Delta \phi_0^{n+1}) = - \sum_m \tau_m \tilde{r}_m (\phi_m^n - \phi_0^n) \quad (13)$$

where $\Delta \phi_m$ is the iterative difference

$$\Delta \phi^{n+1} = \phi^{n+1} - \phi^n \quad (14)$$

Calculating in terms of $\Delta \phi^{n+1}$ instead of directly in terms of ϕ^{n+1} minimizes the effect of roundoff and is always recommended. Here n is the iteration index. Note that the entire field is updated at once so that for incompressible flow, convergence is immediate. Although in [3] the full Taylor iteration is applied, it is commonly coupled with a linear inner iterative procedure such as SLOR. In any case, the iteration implicitly defines a one-step iterative procedure of the form

$$\Phi^{n+1} = h(\Phi^n) \quad (15)$$

where Φ is a vector of ϕ values at the mesh points.

Local uniqueness of the physical solution, Φ^* , to equation (9) and convergence of the iteration of equation (15) to Φ^* depends on the eigenvalues of the asymptotic error matrix $h'(\Phi^*)$ [5]: if none is equal to 1, the solution is locally unique; and if all are less than 1 in absolute value, convergence, at least locally, is guaranteed. For the model problem² of [5], involving uniform flow at Mach number, M , the eigenvalues of $h'(\Phi^*)$ for the Taylor or Taylor/SLOR iterations (without transonic modification) all have the form $\lambda = M^2 \alpha$ where the α values depend only on the geometry of the mesh. This follows from the explicit treatment of the density. Now because of the centered difference approximations, the α values are real, satisfying $0 \leq \alpha < 1$. Furthermore, the maximum α value moves closer to unity as the mesh is refined. Thus, convergence is achieved for subsonic flow and even into the transonic regime, but divergence is guaranteed if M^2 is too high or the mesh too dense. For cell-centered density averaging, the maximum α value is closer to unity than it is

²The model problem of [5], which considered only the neighbor averaged approximation, has been extended to include the cell centered approximation. The extended model problem study will be published later.

for neighbor-averaging. Thus convergence can be achieved on a tighter mesh or to a higher Mach number with neighbor averaging than with cell-centered averaging. Since the α values are positive, as M^2 increases various λ values pass through 1. Thus, local uniqueness does not hold and multiple solutions emerge. These two problems – nonuniqueness of solution and nonconvergence of the Taylor iteration – must be addressed. The problems have distinct causes: nonuniqueness follows from the use of centered difference approximations in supersonic regions and nonconvergence follows from the explicit treatment of the density common with a conservative treatment of the potential equation.

Artificial Compressibility

Artificial viscosity, e.g., that introduced through upwind differencing in nonconservative methods and artificial compressibility in conservative methods, is employed to address the nonuniqueness problem. Following [12], AV is introduced by replacing the density at a point by the density a certain distance upstream along a streamline. The distance increases as M increases above 1. Specifically,

$$r = R - \chi\mu\Delta R \quad (16)$$

where R is the isentropic density ratio value given in equation (3), χ is an input coefficient of AC, μ increases with M by

$$\mu = \max\left(0, 1 - \frac{1}{M^2}\right) \quad (17)$$

and ΔR is a small difference of R along the streamline. Now, since ϕ is tangent to the streamline, we may take

$$\Delta R = \nabla R \cdot \nabla \phi \Delta s / |\nabla \phi| \quad (18)$$

where Δs is a measure of the local mesh spacing and ∇R is approximated at cell centers by backward differences in the w - and z -directions.

For the model problem of [5], where the density is neighbor-averaged, the use of AC for any $\chi > 0$ causes the nonzero eigenvalues of $h'(\Phi^*)$ to become complex so that none can ever equal 1. This guarantees that the physical solution is always unique – at least locally. With cell-centered averaging one eigenvalue may remain positive even after the application of AC. To ensure that it can never be 1 as M increases, and hence to ensure that Φ^* is locally unique, it is necessary to take $\chi > 1/2$. Whether this is a quirk of the model problem or a fundamental limitation is not known, but computational experience suggests the latter.

The AC parameter, χ , must be chosen. Although the primary function of AV is to ensure uniqueness of the physical solution, some authors use it to enhance stability [13] since higher levels of AV drive the discrete system further from the multiple solution situation. However, increasing χ to enhance iterative stability should be done with care since the discrete solution is affected by the choice of χ : in particular the shock location can be shifted. Thus χ should be chosen as small as possible consistent with stability [16].

Increased levels of AV are also used to prevent a sharp Mach number rise or “peak” just before a shock [18]. Such nonphysical peaks, which are accentuated by small mesh spacing, are common to solutions obtained with shock capturing techniques. They are analogous to the “Gibbs phenomenon” always obtained when a discontinuous function is approximated by Fourier series [19].

Besides elevating AV globally by increasing χ , several ad hoc techniques for increasing AV only locally have been reported. In [20], AV is added in the subsonic region immediately downstream of the shock and in [16], AV is increased in supersonic regions where the Mach number is decreasing along a streamline as might be the case immediately before a shock. This latter approach was im-

plemented in the present analysis by replacing equation (17) with

$$\mu = \max\left(0, 1 - \frac{1}{M^2}, 1 - \frac{1}{M^2 - \theta\Delta M^2}\right) \quad (19)$$

where ΔM^2 is the upstream difference of M^2 along a streamline approximately one mesh spacing. It is defined as ΔR is in equation (18). Equation (19) gives the same results as equation (17) except where M^2 is decreasing so varying θ has a more local effect than varying χ . Because of the nonalgebraic form of equation (19), solutions obtained with it are not necessarily unique. Indeed peaky solutions were obtained if the initial approximation was peaky and peak free solutions otherwise (provided θ was large enough). A value of θ too large was found to smear the shock or to give it an excessively rounded peak. Shock fitting techniques such as that reported in [13] are more rational ways of treating shocks but are more difficult to apply.

Experience indicates that stable iterative procedures can be defined (see below) with $\chi = 1$, $\theta = 0$ even with high Mach numbers and dense meshes. Since the AC term in equation (16) scales with mesh size, the AV will become vanishingly small as the mesh is refined, and so, as Lax [6] suggests, the physical mesh solutions should be obtainable in the limit of zero mesh size. However, in practice, severe “Gibbs peaks” arise and get worse as the mesh is refined. These can be eliminated by increasing AV globally or locally but the required AV level seems to be mesh dependent so that it is not clear that AV will become vanishingly small as the mesh is refined.

Convergence of the Taylor Iteration

Assuming the model problem results carry over to problems of interest, the use of the AC form of AV produces a discrete system of equations for which the physical solution is unique, at least locally. However, convergence of the Taylor iteration is not assured because of the continued explicit treatment of the density.

In [13], underrelaxation of the potential is suggested to improve convergence. However, underrelaxation cannot possibly succeed unless all eigenvalues of the asymptotic error matrix have real part less than 1. Model problem considerations indicate that this requires a relatively coarse mesh or a high level of AC. Furthermore, as the local Mach number increases, the relaxation factor must be made smaller and smaller causing slow convergence.

In [12], it is suggested that after ϕ^n has been calculated and while \tilde{r}^n is being calculated, the isentropic term in equation (16) be evaluated using

$$R = R(|\nabla \phi|^2 + \epsilon\mu\phi_t) \quad (20)$$

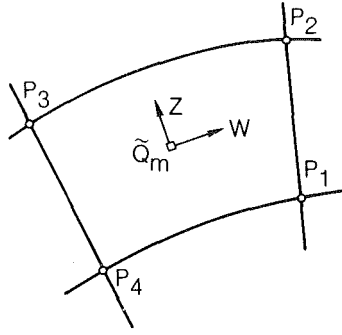
where ϕ_t is the artificial time term

$$\phi_t = \frac{\phi^n - \phi^{n-1}}{\Delta t} = \frac{\Delta\phi^n}{\Delta t} \quad (21)$$

ϵ is an input coefficient of AT, and Δt is an artificial time step. At convergence, $\phi_t = 0$ so that the solution is not altered. The model problem of [5] suggests that Δt scale with the geometric mesh spacing so we take $\Delta t = \Delta s$.

Since ϕ_t is known when \tilde{r}^n is being calculated, this use of artificial time is explicit. Model problem considerations suggest that this use of explicit AT will help force convergence on coarse meshes, but that the continued explicit treatment of the density will not permit convergence on finer meshes, particularly those needed to capture shocks. This has been verified in the present analysis.

Reference [5] suggests redefining equation (20) with an implicit AT term



□ CELL CENTER
○ CORRESPONDING MESH POINT NEIGHBORS

Fig. 3 Cell center and corresponding mesh point neighbors

$$\phi_t = \frac{\phi^{n+1} - \phi^n}{\Delta t} = \frac{\Delta\phi^{n+1}}{\Delta t} \quad (22)$$

This causes equation (13) to become implicit, but it is easily linearized by taking one Newton step from ϕ^n . Thus if $\Delta\phi_m$ is neighbor averaged, the Taylor iteration with implicit AT becomes

$$\begin{aligned} & \sum_m \tau_m \bar{r}_m^n (\Delta\phi_m^{n+1} - \Delta\phi_0^{n+1}) \\ & + \sum_m \tau_m (\phi_m^n - \phi_0^n) \bar{\zeta}_m^n (\Delta\phi_m^{n+1} + \Delta\phi_0^{n+1}) \\ & = - \sum_m \tau_m \bar{r}_m^n (\phi_m^n - \phi_0^n) \end{aligned} \quad (23)$$

where

$$\bar{\zeta} = \frac{\epsilon\mu}{2\Delta s} R'(|\nabla\phi|^2) \quad (24)$$

Since $R'(|\Delta\phi|^2)$ scales with M^2 [5], the coefficients of the implicit terms in equation (23) now scale with M^2 . This serves to counteract the M^2 scaling of the explicit terms so that, for the model problem at least, unconditional stability can be achieved by proper choice of ϵ independent of Mach number level and mesh density. Numerical experiments indicate this is true for practical problems also.

Alternative Iterative Procedures

Grouping mesh points along normal mesh lines, the linear system obtained by applying equation (23) at the mesh points has a block tridiagonal structure which can be conveniently solved directly using a block version of the familiar Thomas algorithm [21]. The calculation time per iteration scales with N , the number of normal mesh lines and with a cubic polynomial of K , the number of circumferential mesh lines. The number of iterations required to satisfy a reasonable convergence criterion is small for low compressibility flows since the explicitly treated density is relatively unimportant. Indeed, convergence is immediate for incompressible flow. However, as the Mach number level rises and the density becomes more important, convergence slows.

In contrast, convergence of the Taylor/SLOR iteration, in which the full Taylor system is only partially solved by relaxing on lines, is dominated by geometric aspects for subsonic flow so that convergence does not slow until near sonic flow is encountered. Since calculation times per iteration scale only with NK , one might expect – as the model

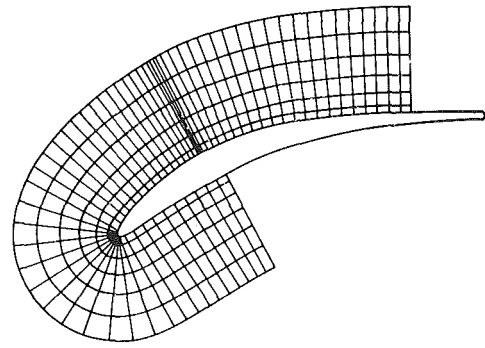


Fig. 4 61 x 6 local mesh with attraction at shock

problem suggests – that the Taylor iteration is more efficient than the Taylor/SLOR iteration at lower Mach numbers but that the opposite is true at higher Mach numbers. Numerical considerations discussed below bear this out. Of course, the division between “lower” and “higher” Mach numbers depends on several aspects including mesh size – particularly in the normal direction, relaxation factor, etc.

Since iterative difficulties arise with the Taylor iteration in transonic flow because of the explicit treatment of the density, it makes sense to consider a fully implicit treatment of the density (instead of the partially implicit AT treatment). Such is accorded by Newton’s procedure which can be written formally as

$$\begin{aligned} & \sum_m \tau_m \bar{r}_m^n (\Delta\phi_m^{n+1} - \Delta\phi_0^{n+1}) + \sum_m \tau_m (\phi_m^n - \phi_0^n) \Delta\bar{r}_m^{n+1} \\ & = - \sum_m \tau_m \bar{r}_m^n (\phi_m^n - \phi_0^n) \end{aligned} \quad (25)$$

where $\Delta\bar{r}_m$ must be expressed in terms of iterative differences of ϕ . This is similar to equation (23) but provides a more complete treatment of the density nonlinearity. With cell centered averaging of the density and without the AC modifications (subsonic flow), the Newton system has the same block tridiagonal structure as the Taylor system except that the corner neighbors indicated in Fig. 2 are involved. Calculations times per iteration should be about the same as for the Taylor iteration but convergence should be much more rapid. In transonic flow, with the AC term used, an extra normal line in the upstream direction is involved. This should cause only a slight increase in calculation time per iteration for the solution of the Newton system, but definition of the Newton coefficients becomes rather more complicated. In this analysis, Newton’s method has been implemented only for subsonic flow where its advantages are evident as discussed below.

Other iterative techniques, such as the approximate factorization procedures [22], can be considered. In each it must be taken into account that, for transonic flow, the density cannot be treated completely explicitly as is common with the conservative form of the potential equation. Otherwise convergence will fail on tight meshes needed to approximate shocks. This does not necessarily apply to nonconservative procedures because of the different linearization employed.

The Adaptive Calculation Mesh. Shock position can be predicted to no greater accuracy than the mesh spacing near the shock. Mesh refinement to better capture a shock can be wasteful if done over too large a region and futile if done over too small a region. Furthermore, if not done smoothly, loss of accuracy will occur at the refinement interface. The local mesh used in this analysis can be smoothly refined near one or more points on the airfoil called “attraction points.” The

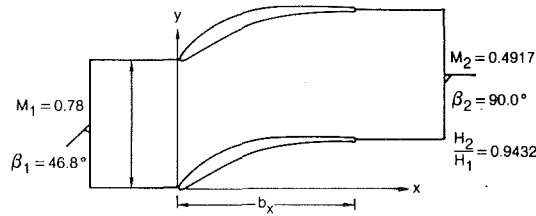


Fig. 5 NAVAIR Cascade, $\pi/b_x = 0.7266$

refinement is done in such a way that the total number of mesh points is not increased and mesh spacing away from the attraction points is not significantly changed. An attraction point can be defined a-priori, or it can be located automatically at the point where the flow on the airfoil passes from supersonic to subsonic during a previous analysis. The "previous analysis" can be on the global mesh or on a previous local mesh and need not be fully converged. In this way the local mesh can adapt itself to provide refinement in the immediate neighborhood of a shock. An example of a mesh with an attraction point is shown in Fig. 4.

The mesh is defined using exponential stretching. Suppose the interval $S_1 \leq x \leq S_2$ is to be discretized with $N+1$ points (N intervals): $S_1 = x_0 < x_1 < \dots < x_N = S_2$ in such a way that mesh density is greater near S_1 than near S_2 , but the change in mesh spacing size is smooth. This is accomplished simply by defining

$$x_i = S_1 + (w_i)^\beta (S_2 - S_1), w_i = \frac{i}{N} \quad (26)$$

and taking $\beta > 1$. The mesh density near S_1 increases as β_1 increases. We say S_1 is an attraction point and that the mesh is defined with *simple stretching*.

Alternatively, mesh attraction may be desired at interior points. Suppose the interval $S_1 \leq x \leq S_k$ is to be discretized with attraction at $S_1 < S_2 < \dots < S_k$. Let I_k be the mesh index of S_k and define mesh points between S_k and S_{k+1} by

$$x_i = (1 - w_i)[S_k + (w_i)^{\beta_k} (S_{k+1} - S_k)] + w_i[S_{k+1} - (1 - w_i)^{\beta_{k+1}} (S_{k+1} - S_k)] \quad (27)$$

where

$$w_i = \frac{i - I_k}{I_{k+1} - I_k} \quad (28)$$

If $\beta_k > 1$, S_k is an attraction point of the mesh which is said to be defined with *compound stretching*.

If the I_k and β_k are specified, the change in mesh size will not be smooth across the S_k . Thus let the β_k be specified and determine the I_k so that the mesh spacings on both sides of S_k are approximately equal. To this end, require

$$(S_k - S_{k-1}) / (I_k - I_{k-1})^{\beta_k} = (S_{k+1} - S_k) / (I_{k+1} - I_k)^{\beta_k} \quad (29)$$

This results in the recursion formula

$$I_{k+1} - I_k = \lambda_k (I_2 - I_1) \quad (30)$$

where

$$\lambda_k = \left(\frac{S_{k+1} - S_k}{S_k - S_{k-1}} \right)^{1/\beta_k} \lambda_{k-1}, \lambda_1 = 1 \quad (31)$$

Thus, with the total number of mesh intervals, N , specified, the number of mesh intervals between the first two attraction points must satisfy

$$N = (I_2 - I_1) \sum_k \lambda_k \quad (32)$$

Now $I_1 = 0$ so equations (30-32) can be used to define the I_k . Since the values of the I_k are probably not integral, they are

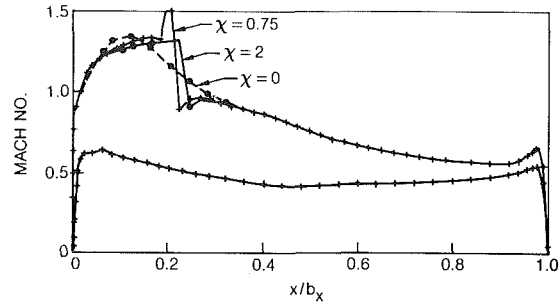


Fig. 6 Effects of artificial compressibility, $M_1 = 0.78$

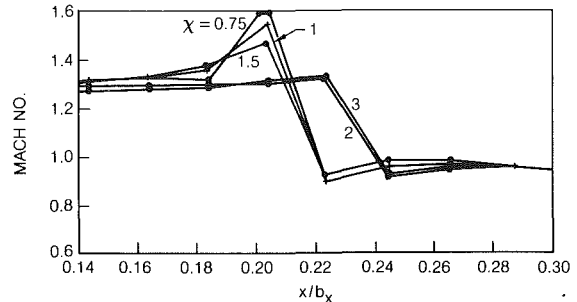


Fig. 7 Effects of artificial compressibility - shock detail, $M_1 = 0.78$

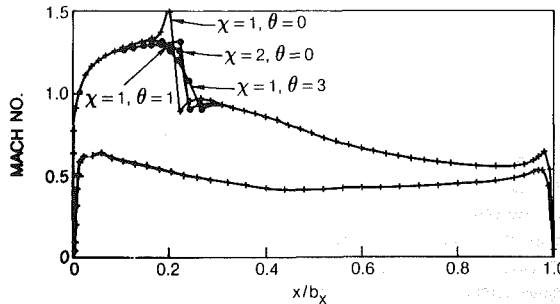


Fig. 8 Effects of local artificial compressibility, $M_1 = 0.78$

given the nearest integer value. The β_k can then be adjusted using equation (29)

$$\beta_k = \ln \left(\frac{S_{k+1} - S_k}{S_k - S_{k-1}} \right) / \ln \left(\frac{I_{k+1} - I_k}{I_k - I_{k-1}} \right) \quad (33)$$

The local mesh used in this analysis is defined using simple stretching in the normal direction with attraction at the airfoil. If capture of a shock or some other feature such as leading edge overspeed is desired, compound stretching is used in the circumferential direction with the attraction point at a shock automatically located. For the local mesh of Fig. 4, both attraction exponents were set to 1.5.

Sample Calculations

The results of a number of sample calculations are discussed first to indicate how the numerical solution is affected by modifications in the approximating model involving the AC parameters, mesh refinement, and density averaging; then to test various iterative strategies such as varying the AT parameter and employing SLOR or Newton; and finally to compare computed results with hodograph solutions.

For the first two categories sample calculations are presented for the cascade of NAVAIR airfoils [23] shown in Fig. 5 where geometric and aerodynamic conditions are indicated. The analyses indicate there is a supersonic region adjacent to the upper surface of the airfoil from near the leading edge to around quarter-chord, where it is terminated

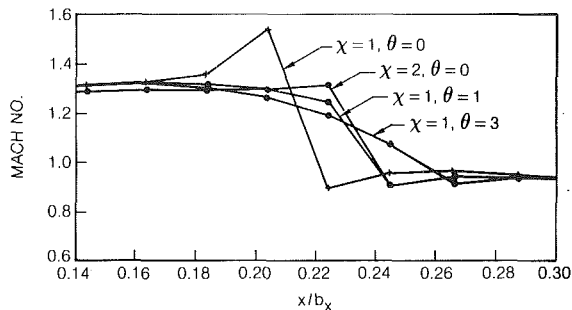


Fig. 9 Effects of local artificial compressibility—shock plots, $M_1 = 0.78$

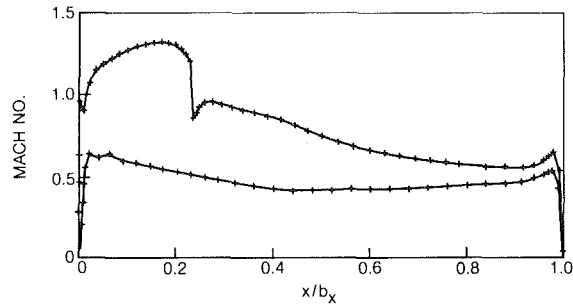


Fig. 11 Effect of mesh attraction at shock, $M_1 = 0.78$, $\chi = 1.0$, $\theta = 3.0$

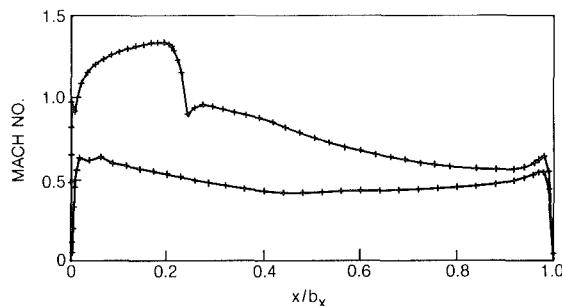


Fig. 10 Effect of mesh attraction slightly upstream of shock, $M_1 = 0.78$, $\chi = 1.0$, $\theta = 3.0$

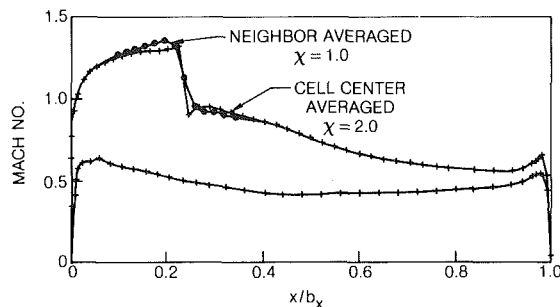


Fig. 12 Comparison of cell-centered averaged and neighbor averaged results, $M_1 = 0.78$

by a shock. An analysis was first performed on a global mesh with axial spacing of 4 percent using the neighbor averaged procedure of [3] with no AC. The mesh spacing was coarse enough to allow convergence in the supersonic region, but the shock was completely smeared. Local analyses with AC were then performed on meshes such as the "uniform" mesh of Fig. 1 or the "shock attraction" mesh of Fig. 4. A number of figures are presented showing the effects of artificial compressibility, mesh refinement, etc. In each case the Mach number distribution is plotted against axial chord normalized so that axial chord is 1. Some plots, called "airfoil plots" show the Mach number distribution over the entire airfoil while others called "shock plots" show the distribution only near the shock. In each case the number of normal mesh lines was about 61, but the mesh line locations were shifted when attraction was used. The number of circumferential mesh lines (excluding the outer boundary) was usually 6, since no significant differences were observed when 11 were used.

Effect of AC. The effects of adding AC to the potential model are shown in the airfoil plot of Fig. 6 and the shock plot of Fig. 7, which present results obtained on the uniform local mesh. The curve labeled " $\chi = 0$ " was obtained on the global mesh with no AC employed. It differs from the local results only near the supersonic region. For $\chi = .5$, no (local) solution could be obtained. This is not surprising since the model problem suggests χ should be chosen greater than .5. For χ increasing from .75 to 1.5 similar solutions were obtained which differed only in that the Gibbs peak dropped progressively from about $M = 1.62$ to about $M = 1.53$. For χ increasing from 2.0 to 3.0 similar solutions were again obtained; these however, differ from those with lower values of χ in three aspects: no Gibbs peak is present; the shock location is shifted downstream one mesh spacing, which is about 2 percent of axial chord; and the Mach number distribution is lowered slightly through most of the supersonic region. For each (positive) value of χ shown, the shock is not smeared being located between exactly two mesh points, and an isentropic expansion singularity [24, 25] with its Mach number contour slope discontinuity, is present downstream of the shock.

Effects of Local AC. The effects of increasing AC locally by increasing θ are shown in the airfoil plot of Fig. 8 and the shock plot of Fig. 9. With χ fixed at 1.0, $\theta = 1$ produces a peaky solution (as seen before); $\theta = 1$ produces a peakless solution with a rounded top (without a rounded top, local AC would have no effect) and a well defined shock between two points; and $\theta = 3$ completely rounds the shock so that it is smeared out. Indeed the only hint of a shock in this last case is the isentropic expansion behind the shock. Comparing the $\chi = 2$, $\theta = 0$ solution (global AC) and the $\chi = 1$, $\theta = 1$ solution (local AC) to the $\chi = 1$, $\theta = 0$ solution (nominal), we see that increasing local AC shifts the shock to the same location as increasing global AC does. However, the local AC solution does not differ from the nominal solution ahead of the shock as the global AC solution does.

Effect of Mesh Attractions at the Shock. In Figs. 10 and 11 is shown the effect of mesh attraction on the solutions. The nominal ($\chi = 1$, $\theta = 0$) solution on the uniform mesh of Figs. 7-9 was used to locate a shock ($M = 1$) located at .2205 of axial chord. A local mesh with attraction at this point was defined and used to produce the ($\chi = 1$, $\theta = 3$) solution of Fig. 10. It was evident that the attraction was not right on the shock so the latest solution was used to relocate the shock at .2371 of axial chord (a shift of .0166). The ($\chi = 1$, $\theta = 3$) solution on a mesh with attraction at this last point is shown in Fig. 11. The mesh attraction point seems better located now, and the mesh points defining the shock are about .6 percent of axial chord apart. This definition is obtained without needlessly refining the mesh elsewhere. The rounded top of the Mach number profile seems to be caused by the use of local AC. A value of θ which would eliminate the Gibbs peak but not cause such a rounded top was not found. It should be noted that values of θ less than 3.0 produced peaky solutions on this last mesh, but a value of 3.0 produced a smeared solution on the locally coarser "uniform" mesh. Thus the appropriate value of θ seems to be mesh size dependent.

Comparison of Cell-Centered Averaging and Neighbor Averaging. In Fig. 12, results of cell-centered averaging

Table 1 Convergence as ϵ is varied ($M_1 = .78$)

AT type mesh type	Implicit uniform	Implicit attraction	Explicit coarse
χ	1.0	1.0	1.0
θ	0	3.0	0.0
ϵ	N	N	N
0.	<i>a</i>	<i>a</i>	<i>a</i>
1.0	<i>a</i>		
3.0	58		31
5.0	45	63	<i>a</i>
10.0	40	46	
15.0	39		
20.0	48	67	
30.0	66		
40.0	81		

^adivergence occurred

Table 2 Comparison of calculation times for various procedures

Subsonic case $M_1 = .6$

Mesh	61×6			61×11		
	N	CPU	Ratio	N	CPU	Ratio
Taylor	6	2.49	1.0	6	8.02	1.0
SLOR/ $\omega = 1.5$	61	9.41	3.78	57	14.83	1.85
Newton	3	1.46	.59	3	4.42	.55

Transonic case $M_1 = .78$, $\chi = 1.0$, $\theta = 0$, $\epsilon = 15.0$

Mesh	61×6			61×11		
	N	CPU	Ratio	N	CPU	Ratio
Taylor	39	17.25	1.0	38	52.67	1.0
SLOR/ $\omega = 1.0$	80	14.64	.85	76	23.61	.45
SLOR/ $\omega = 1.5$	67	12.28	.71	67	20.88	.40

(CCA) and neighbor averaging (NA) are compared on the uniform mesh. While a χ value of 1.0 was sufficient to eliminate the Gibbs peak for the NA analysis, a value of 2.0 was needed for the CCA analysis. This is not surprising since the model problem indicates that less AV is needed to stabilize the NA analysis than to stabilize the CCA analysis. It is readily apparent that the CCA analysis predicts a sharper shock than the NA analysis with the former always placing the shock between two mesh points (one interval) and the latter generally smearing it over four mesh points. It is also apparent that the CCA analysis is better able than the NA analysis to predict the expansion singularity immediately downstream of the shock.

The Choice of ϵ . An iterative procedure whose stability depends on the proper but difficult choice of some iterative parameter is not practical. The model problem analysis indicates that with explicit AT convergence can be achieved only on coarse meshes and then only for ϵ in a certain "window," but that with implicit AT the convergence window extends without upper bound and with a lower bound that can be chosen independent of mesh density or Mach number level. Evidence that these results hold for practical problems is presented in the Table 1 where implicit and explicit AT are considered for three meshes—the uniform mesh, a coarse mesh with 1/3 the circumferential mesh density, and a mesh with attraction at the shock. In the table, N is the number of steps required before the maximum change in ϕ during the step falls below 10^{-5} .

With implicit AT, convergence is speeded by increasing ϵ until an optimal value—between 10.0 and 15.0 on both uniform and attraction meshes—is reached; convergence is then slowed as ϵ is further increased but is not halted even for large values of ϵ . With explicit AT, convergence could be obtained only on the coarse mesh and then only for ϵ near 3.0.

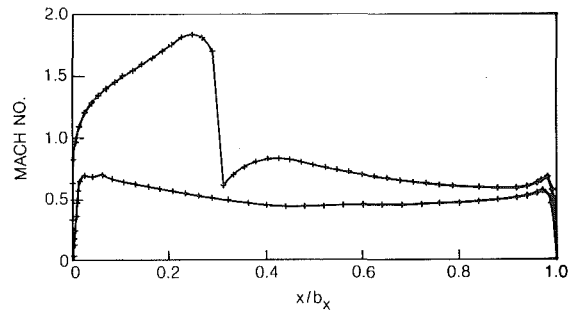


Fig. 13 High mach number solution, $M_1 = 0.9$, $M_2 = 0.518$, $\chi = 1.0$, $\theta = 1.0$

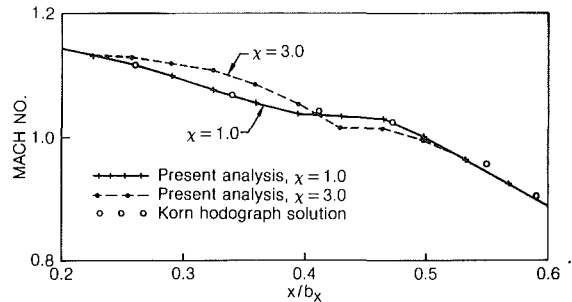


Fig. 14 Comparison of present analysis surface Mach numbers with Korn hodograph solution near sonic point

As predicted by the model problem, convergence slows as mesh density increases.

That ϵ may be chosen independently of Mach number for flows that can reasonably be considered isentropic is indicated by the converged solution of Fig. 13 for which the inlet Mach number of $M_1 = .9$ causes a maximum Mach number near 1.85 to occur. Convergence was achieved with $\epsilon = 15$, the optimal value for $M_1 = .78$ on the uniform mesh, in 100 steps—up from 39 for the $M_1 = .78$ case. A better value of ϵ for the $M_1 = .9$ case may exist, but slowing of the iteration as Mach number level increases is predicted by the Model Problem and should be expected. The AC parameters, $\chi = 1.0$, $\theta = 1.0$ seem appropriate for this case indicating—as model problem considerations predict—that the required amount of AC does not depend on Mach number levels.

Comparison of Taylor, Taylor/SLOR and Newton Iterations. Convergence of the Taylor and Taylor/SLOR iterations is compared on two meshes—with 6 and 11 circumferential mesh lines, respectively—for the $M_1 = .78$ case and also for a subsonic case ($M_1 = .6$, maximum Mach number $\approx .87$). The Newton iteration is also considered for the subsonic case. Results are shown in Table 2 where N is the number of iterations required to satisfy the convergence criterion mentioned above, CPU is the calculation time on a UNIVAC 1100/81 measured in SUP seconds, and RATIO is the ratio of calculation time to that required by the Taylor iteration. For the transonic case AC ($\chi = 1.0$) and implicit AT ($\epsilon = 15.0$) were employed.

As predicted by the model problem, the Taylor iteration is superior to the Taylor/SLOR iteration for the subsonic case but inferior for the transonic case. In both cases, as expected, the performance of Taylor/SLOR relative to Taylor is enhanced as the number of points in the normal direction is increased, and it is apparent that Taylor/SLOR would be preferred even for subsonic flow if the number of points in the normal direction were somewhat larger. Perhaps surprising is the superiority of overrelaxed Taylor/SLOR to unrelaxed Taylor/SLOR for the transonic case, a situation predicted by the model problem. This seems contrary to the findings of [8]

in which overrelaxation was found undesirable for transonic flow. However, the analysis of [8] was in terms of the non-conservative potential equation with the different linearization mentioned above so that no contradiction in fact occurs.

The performance of the Taylor/SLOR procedure could be improved even more if advanced techniques such as multigrid [26] were used. Nevertheless, if the subsonic Newton rate of convergence can be maintained for transonic flow, the Newton iteration would seem to be the most efficient on moderately sized (in the normal direction) meshes.

Comparison with Shock-Free Hodograph Solution. Results of the present analysis have not yet been compared with experimental or other analysis for a flow with a shock, but results have been compared for several transonic shock-free cases. In [3], computed results of the neighbor-averaged global analysis with no AC were compared with analytic hodograph solutions for transonic, shock-free cases of Korn [27] and Hobson [28]. Despite the absence of AC in the supersonic region, fully converged solutions, which agreed almost identically with the inviscid hodograph solutions, were obtained. For each of these cases, the calculation mesh was fine enough to provide high accuracy but coarse enough to ensure uniqueness of the discrete solution and convergence of the Taylor iteration. Such a fortuitous mesh density "window" cannot be counted on. Indeed, with cell-centered averaging discrete solution nonuniqueness occurs on much coarser meshes than with neighbor averaging. Thus AC (or some form of AV) is needed even for inviscid, shock-free transonic flows to produce a reliably accurate and stable procedure.

Since viscosity is not present in the hodograph solutions of Korn and Hobson, the effect of AC on the calculated solutions can be gauged by comparing them with the hodograph solutions. The Korn case was computed with the present analysis using cell-centered averaging on a mesh only slightly more dense than that used in the neighbor averaged global analysis. Because of the greater intolerance of the CCA procedure to centered differencing (compared to the NA procedure) AC was needed to obtain convergence. The computed solution with $\chi = 1.0$ agreed almost identically with the Korn hodograph solution over the entire airfoil, but the computed solution with $\chi = 3.0$ showed significant differences in the supersonic region. The comparisons of the computed surface Mach number profiles with that of the hodograph solution near the downstream sonic point are shown in Fig. 14. The computed profile with $\chi = 1.0$ tracks the hodograph solution almost perfectly even to the definition of the slight "table" near 40 percent of axial chord. In contrast the computed profile with $\chi = 3.0$ differs significantly from the hodograph profile with recompression being shifted downstream. Evidently a low level of AC produces a negligible effect on an inviscid solution but a higher level of AC produces a definite effect.

For the Hobson case (now shown), the geometry and hodograph solution are symmetric fore to aft. Results of the hodograph solution and computed solution with $\chi = 1.0$ again agreed very well although there was a very slight asymmetry in the computed solution caused by the upwinding influence of the AC. Initial calculations for this case yielded a Mach number profile which tracked that of the hodograph solution fairly well but which was quite rough in the supersonic region. The problem was tracked to a nonsmooth airfoil curvature which was not visible to the eye. A smooth Mach number profile was obtained after the airfoil was redefined with smoother curvature.

Concluding Remarks

A procedure is presented for calculating transonic potential

flow through cascades. Large-scale effects are obtained on a global mesh and small-scale effects such as a shock or leading edge detail are captured on a local mesh which can be adaptively and smoothly refined near points of interest. The conservative form of the potential equation is approximated with the control area technique in physical space without the use of mapping.

This work answers in part the questions raised in the introduction. (i) The role of AC (or AV in general) is to eliminate nonphysical discrete solutions to the potential equation. AC should not be used to enhance convergence. (ii) A nominal value of $\chi = 1.0$ seems appropriate except on dense meshes. Lower values, e.g., $\chi \leq 0.5$, seem insufficient to allow stable calculations. Larger values, e.g., $\chi > 2.0$, seem to have a significant effect on computed results including a shift of the recompression region (whether with shock or not) downstream. On finer meshes used to capture shocks, increased AC levels may be needed to eliminate the Gibbs peak before the shock, but the shock may be shifted downstream. Better shock treatments are needed. (iii) Convergence may fail even with the use of AC because of the explicit treatment of the density in Taylor-type iterations commonly used with conservative procedures. (iv) Convergence can be made stable even with high Mach numbers on dense meshes by a suitable partially implicit treatment of the density. The treatment suggested here involves an artificial time parameter which can be set independent of Mach number level and mesh density to obtain unconditional stability.

Acknowledgments

I wish to thank the Commercial Products Division of the Pratt & Whitney Aircraft Group of United Technologies Corporation for its strong and continued support of this work. I also wish to thank Mohamed Hafez for his interest and suggestions during many fruitful conversations.

References

- 1 Dring, R. P., Joslyn, H. D., and Hardin, L. W., "An Investigation of Axial Compressor Rotor Aerodynamics," *ASME JOURNAL OF ENGINEERING FOR POWER*, Vol. 104, Jan. 1982, pp. 84-96.
- 2 Dring, R. P., Joslyn, H. D., Hardin, L. W., and Wagner, J. H., "Turbine Rotor-Stator Interaction," *ASME JOURNAL OF ENGINEERING FOR POWER*, Vol. 104, Oct. 1982, pp. 729-942.
- 3 Caspar, J. R., Hobbs, D. E., and Davis, R. L., "Calculation of Two-Dimensional Potential Cascade Flow Using Finite Area Methods," *AIAA Journal*, Vol. 18, Jan. 1980, pp. 103-109.
- 4 Dring, R. P., and Heiser, W. H., "Turbine Aerodynamics," *The Aerothermodynamics of Aircraft Gas Turbine Engines*, edited by G. C. Oates, AFAPL-TR-78-52.
- 5 Caspar, J. R., "A Model Problem Study of Transonic Potential Flow Procedures," Paper 80-0337, AIAA 18th Aerospace Sciences Meeting, Pasadena, Calif., Jan. 1980.
- 6 Lax, P. D., "Weak Solution of Nonlinear Hyperbolic Equations and Their Numerical Computation," *Communications on Pure and Applied Mathematics*, Vol. 7, 1954, pp. 159-193.
- 7 Murman, E. M., and Cole, J. D., "Calculations of Plane Steady Transonic Flows," *AIAA Journal*, Vol. 9, No. 1, Jan. 1971, pp. 114-121.
- 8 Jameson, A., "Iterative Solution of Transonic Flows Over Airfoils and Wings, Including Flows at Mach 1," *Communications on Pure and Applied Mathematics*, Vol. 27, 1974, pp. 283-309.
- 9 Ives, D. C., and Liuteromoza, J. F., "Second-Order Accurate Calculation of Transonic Flow Over Turbomachinery Cascades," *AIAA Journal*, Vol. 17, Aug. 1979, pp. 870-876.
- 10 Eberle, A., "Eine Methode Finiter Elemente zur Berechnung der Transsonischen Potential-Stromung um Profile," MBB Bericht UEE 1352(0), 1977.
- 11 Jameson, A., "Transonic Potential Flow Calculations Using Conservation Form," *Proceedings of the AIAA Second Computational Fluid Dynamics Conference*, Hartford, Conn., June 1975, pp. 148-161.
- 12 Hafez, M. M., South, J. C., and Murman, E. M., "Artificial Compressibility Methods for Numerical Solution of Transonic Full Potential Equation," *AIAA Journal*, Vol. 17, Aug. 1979, pp. 838-844.
- 13 Ecer, A., and Akay, H. V., "Investigation of Transonic Flow in a Cascade Using an Adaptive Mesh," AIAA 13th Fluid & Plasma Dynamics Conference, Snowmass, Colo., July 14-16, 1980.

14 Deconinck, H., and Hirsch, C., "Finite Element Methods for Transonic Blade-to-Blade Calculation in Turbomachines," ASME Paper No. 81-GT-5, International Gas Turbine Conference, Houston, Texas, March 1981.

15 Farrell, C., and Adamczyk, J., "Full Potential Solution of Transonic Quasi-three-dimensional Flow Through A Cascade Using Artificial Compressibility," ASME Paper No. 81-GT-70, International Gas Turbine Conference, Houston, Texas, March 1981.

16 Habashi, W. G., and Hafez, M. M., "Finite Element Methods for Transonic Cascade Flows," AIAA Paper No. 81-1472, AIAA/SAE/ASME 17th Joint Propulsion Conference, Colorado Springs, Colo., July 27-29, 1981.

17 Shen, S-P., "Transonic Aerodynamic Computations with Finite Element Method," in *Finite Elements in Fluids*, Vol. 3, edited by R. H., Gallagher, John Wiley and Sons, 1978.

18 Notes on Numerical Fluid Mechanics, *GAMM Workshop on Numerical Methods for the Computation of Inviscid Transonic Flows with Shock Waves*, edited by A. Rizzi and H. Viviand, Vieweg & Sohn, 1980.

19 Franklin, P., *Fourier Methods*, McGraw-Hill, New York, 1949, pp. 70-71.

20 Jameson, A., "Acceleration of Transonic Potential Flow Calculations on Arbitrary Meshes by the Multiple Grid Method," *Proceedings of AIAA Computational Fluid Dynamics Conference*, Williamsburg, VA, July 23-25, 1979, pp. 122-146.

21 Varga, R. S., *Matrix Iterative Analysis*, Prentice-Hall, Englewood Cliffs, 1962, p. 196.

22 Ballhaus, W. F., Jameson, A., and Albert J., "Implicit Approximate-Factorization Schemes for Steady Transonic Flow Problems," *AIAA Journal*, Vol. 16, June 1978, pp. 573-579.

23 Stephens, H. E. and Hobbs, D. E., "Design and Performance Evaluation of Supercritical Airfoils for Axial Flow Compressors," Report FR11455, Naval Air Systems Command, June 1979.

24 Oswatitsch, K., and Zierep, J., "Das Problem des Senkrechten Stosses an einer Gekrummten Wand," *ZAMM* 40, 1960, p. 143.

25 Inger, G. R., "Transonic Shock-Turbulent Boundary Layer Interaction and Incipient Separation on Curved Surfaces," AIAA 14th Fluid and Plasma Dynamics Conference, June 23-25, 1981, Palo Alto, Calif.

26 Brandt, A., "Multi-Level Adaptive Solutions to Boundary Value Problems," *Mathematics of Computation*, Vol. 31, No. 138, Apr. 1977, pp. 333-390.

27 Korn, D. G., "Numerical Design of Transonic Cascades," Courant Institute of Mathematical Sciences, ERDA Mathematics and Computing Laboratory, Report No. CDD-3077-72, Jan. 1975.

28 Hobson, D. G., "Shock-Free Transonic Flow in Turbomachinery Cascades," University of Cambridge, Department of Engineering Report CUED/A Turbo/TR65, 1974.

An Improved Time-Marching Method for Turbomachinery Flow Calculation

J. D. Denton

Whittle Laboratory,
Cambridge University Engineering
Department,
Cambridge CB3 0EL,
England

Time-marching solutions of the Euler equations are now very widely used for calculation of flow through turbomachinery blade rows. All methods suffer from the disadvantages of shock smearing, lack of entropy conservation, and comparatively long run times. A new method is described which reduces all these problems. The method is based on the author's opposed difference scheme, but this is applied to a new grid consisting of quadrilateral elements which do not overlap and have nodes only at their corners. The use of a non-overlapping grid reduces finite differencing errors and gives complete freedom to vary the size of the elements. Both these factors help to improve entropy conservation. Considerable savings in run time (by a factor of about 3) are obtained by using a simple multigrid method whereby the solution is advanced simultaneously on a coarse and on a fine grid. The resulting method is simpler, faster, and more accurate than its predecessor.

Introduction

Time-dependent solutions of the Euler equations are now widely used for the analysis of the flow through turbomachine blade rows. Their main attraction is the ability to compute mixed subsonic-supersonic flows with automatic capturing of shock waves. Solutions of the potential flow equation have also recently been extended to compute transonic shocked flow (e.g., Farrell and Adamczyk [1]). Although these can be computationally much more efficient than solutions of the Euler equations, the limitation to potential flow rules them out for applications where strong shock waves can occur. Solving the Euler equations is also the most common way of computing fully three-dimensional flow in turbomachinery, even for subsonic flow, since it is not generally possible to assume irrotational flow.

The equations may be solved in either finite difference or finite volume form. In the former (e.g., Veuillot [2], Gliebe [3]), it is usual to transform the computational domain into a uniform rectangular grid and to express the derivatives of the flow variables in terms of values at the nodes of this grid. Specialized numerical techniques (e.g., McCormack or Lax-Wendroff schemes) are needed to ensure stability of the integration of the equations through time until a steady state is reached. In the finite volume form of the method (e.g., McDonald [4], Denton [5]) the equations are regarded as equations for the conservation of mass, energy, and momentum applied to a set of interlocking control volumes formed by a grid in the physical plane. When solved in this way it is easier to ensure conservation of mass and momentum

than in the differential approach but similar numerical schemes are necessary to ensure stability.

The argument as to whether finite difference or finite volume schemes are preferable is not resolved and both types are still used. The author's (not unbiased) view is that the finite volume approach is superior because of its simplicity and its automatic conservation of mass and momentum and also because of the better physical understanding of the flow development which is obtained from working in a physical grid. The latter is an important consideration for design engineers who are not usually specialists in numerical analysis.

The author's opposed-difference scheme for solving the Euler equations in finite volume form has been widely used since its publication in 1975 [5]. The basic philosophy of this method is to take a very simple and fast first-order scheme and progressively add on a second- or higher-order correction as the calculation converges. The resulting method appears to have advantages of speed and simplicity over alternative second-order schemes, and it is also extremely "robust." Because of these factors it is the only method which has been widely used for three-dimensional solutions of the Euler equations through blade rows (e.g., Denton and Singh [6], Kopper [7], Sarathy [8], Barber [9], and Singh [19]). The same basic algorithm has been used for flow in the meridional plane by Spurr [10], for unsteady flow by Mitchell [11] and for wet steam flow by Bakhtar et al. [12]. As a result a great deal of user experience has been accumulated (e.g., Bryce and Litchfield [13]). The general experience is that satisfactory accuracy can be obtained for most turbine blades although Singh [14] shows that in some cases the inviscid solutions is improved by the iterative addition of a boundary layer calculation. For compressor blades, however, Calvert and

Contributed by the Gas Turbine Division of THE AMERICAN SOCIETY OF MECHANICAL ENGINEERS and presented at the 27th International Gas Turbine Conference and Exhibit, London, England, April 18-22, 1982. Manuscript received at ASME Headquarters December 18, 1981. Paper No. 82-GT-239.

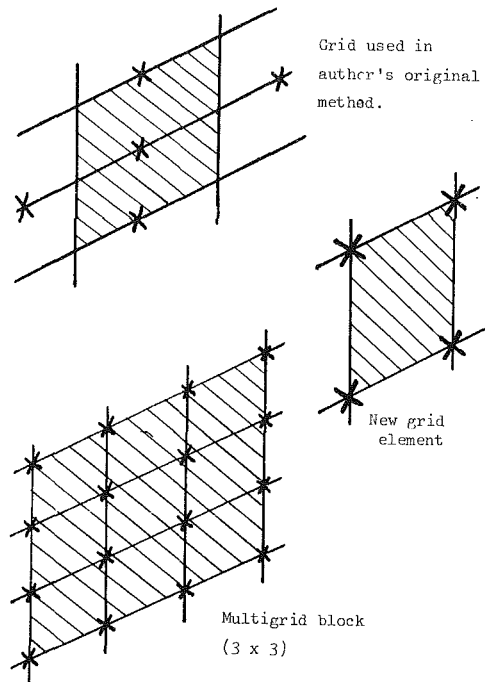


Fig. 1 Grid systems

Herbert [15] show that satisfactory accuracy cannot usually be achieved without the addition of boundary layer displacement to the inviscid calculation.

As a result of this experience several defects of the basic scheme have come to light. They arise mainly from the use of high-order correction factors which, although ideal for smoothly varying flows, can cause problems at points of discontinuity such as stagnation points and shock waves. The method also becomes unstable when the streamwise component of velocity is negative (i.e., for backflow) and so is unable to deal accurately with the leading edge flow on blades where the stagnation point lies on the pressure surface.

It is well known that for steady inviscid flow along a streamline, the streamwise momentum equation, the energy conservation equation, and the entropy conservation equation are not independent. Any two of these equations together imply the third equation. Hence, if two of the equations are satisfied in finite difference form the third equation will also only be satisfied in finite difference form with inevitably some numerical errors. When solving the Euler equations, it is usual to solve the momentum equations, and the energy equation, and hence entropy will not be conserved exactly. Similarly, if the momentum equation is solved and isentropic flow assumed (e.g., McDonald [4]), then the stagnation enthalpy will not be conserved. Since both stagnation enthalpy and entropy are associated with a particular element of

mass, errors in either will be convected downstream from their source and will influence the whole of the downstream flow. Finite differencing errors are particularly likely to occur in the very rapid changes in flow around a leading edge and these will then influence the flow on the whole blade surface. Hence, it is essential that accurate differencing schemes and sufficient grid points are used around the leading edge. At highly loaded leading edges it was found that the author's scheme could produce changes of entropy (stagnation pressure) which had an adverse effect on the blade surface velocities, particularly on the pressure surface. This is thought to be a (unpublicized) characteristic of all time-marching methods.

The method described in this paper has been developed to try to minimize these difficulties, whilst retaining the advantages of speed and simplicity of the original scheme.

Equations

The two-dimensional Euler equations may be written as conservation equations for a control volume, ΔV , over a time step, Δt , to give

$$\text{Continuity} \quad \Delta \rho = \Sigma_n (\rho \mathbf{V} \cdot d\mathbf{A}) \Delta t / \Delta V \quad (1)$$

$$x\text{-momentum} \quad \Delta (\rho V_x) = \Sigma_n (P dA_x + \rho V_x \mathbf{V} \cdot d\mathbf{A}) \Delta t / \Delta V \quad (2)$$

$$y\text{-momentum} \quad \Delta (\rho V_y) = \Sigma_n (P dA_y + \rho V_y \mathbf{V} \cdot d\mathbf{A}) \Delta t / \Delta V \quad (3)$$

$$\text{Energy} \quad \Delta (\rho E) = \Sigma_n (\rho H \mathbf{V} \cdot d\mathbf{A}) \Delta t / \Delta V \quad (4)$$

where $d\mathbf{A}$ is a vector representing the area of the face of the element in the direction of the inwards normal to the face, and the summations are over the n faces of the element. These equations must be solved in conjunction with the perfect gas relationships.

$$H = C_p T + \frac{1}{2} V^2$$

$$E = C_v T + \frac{1}{2} V^2 \quad (5)$$

$$P = \rho R T$$

In two-dimensional flow it is usual to replace the energy equation by the assumption $H = \text{constant}$. This assumption is not correct for an unsteady flow so the true time dependence of the solution is lost. However, in a steady adiabatic flow with H constant at inlet H is everywhere constant, and so a correct steady-state solution can be obtained without the need to solve the energy equation. A similar condition of constant rothalpy ($H - \Omega r V_\theta$) can be used in quasi-three-dimensional flow through rotating blade rows, but in fully three-dimensional flow it is generally necessary to solve the energy equation.

Grid

The finite volume elements used for the new scheme are

Nomenclature

A = area vector of face of element
 C = sonic velocity
 CFP = correction factor on pressure
 CFRO = correction factor on density
 C_p = specific heat capacity at constant pressure
 C_v = specific heat capacity at constant volume
 E = specific internal energy

f = downwinding factor for pressure or density
 H = specific stagnation enthalpy
 I = streamwise grid point number
 Δl = length of element controlling stability
 P = static pressure
 R = gas constant, $C_p - C_v$
 RF = relaxation factor
 T = static temperature

Δt = time step
 \mathbf{V} = velocity vector
 ΔV = volume of element
 α = distribution function for density
 ρ = static density
Subscripts
 $\left. \begin{matrix} x \\ y \\ z \end{matrix} \right\}$ = in coordinate directions
 0 = stagnation conditions
 * = at sonic condition

formed by the same pitchwise lines and quasi-streamlines as were used for the original method (Fig. 1.) However, instead of having a node at the center of each element, nodes are now located at each of the four corners. The fluxes of mass momentum and energy through each face are then found using averages of the flow properties stored at the ends of that face. These fluxes may then be used in the RHS of equations (1-3) to obtain the changes in ρ , ρV_x , and ρV_y for the element in time, Δt .

The question now arises as to how these changes should be distributed between the four corners of the element. It is important to realize that this distribution only affects the stability and time dependence of the method, but not the steady solution. As long as a steady solution is obtained, the sum of the fluxes of each conserved variable over the faces of each element will be zero, and hence the conservation equations satisfied, irrespective of how the changes were distributed. The manner of distribution must therefore be chosen to satisfy stability considerations rather than accuracy. The latter is only limited by the accuracy with which the flux across a face can be estimated from an average of the flow properties at its ends.

Differencing Schemes

A variety of stable distribution schemes have been discovered for this grid. The exact analogy of the opposed-difference scheme is to send the changes of all flow quantities to the two downstream corners of the element and then to let the average pressure calculated on the downstream face act on the upstream face when solving the axial momentum equation (equation (2)). Like the basic opposed-difference scheme, this method is only of first-order accuracy unless it is corrected, using a lagged correction factor to correct the downwind pressure to a value close to the true one, i.e., the pressure, $P_{A,I}$, acting on face I (Fig. 1) is taken as

$$P_{A,I} = P_{I+1} + CFP_I \quad (6)$$

where after every time step (or every few steps)

$$CFP_{I, \text{NEW}} = (1 - RF) CFP_{I, \text{OLD}} + RF(P_I - P_{I+1}) \quad (7)$$

RF is a relaxation factor whose value is typically 0.05. In the steady-state, equations (6) and (7) become

$$P_{A,I} = P_I \quad (8)$$

This scheme will be referred to as scheme A, it has exactly the same stability mechanism as the original opposed difference scheme [5], but is simpler because correction factors are only needed for pressure and because the correction factors are not based upon interpolation but on the difference between pressures stored at two nodes.

A second scheme (scheme B) was discovered as the result of trying to eliminate the use of correction factors completely. In scheme A, as in the opposed difference scheme, only pressure moves upwind; however, at low Mach numbers pressure is very closely tied to density so a scheme whereby the changes of density were sent to the upstream corners of the element was tried, the changes in ρV_x and ρV_y still being sent to the downstream corners. This scheme proved stable, without any correction factors or damping, at low Mach numbers but instability was found to develop at Mach numbers around unity and above. Despite this limitation, scheme B was found to have one important advantage; it remained stable for negative values of streamwise velocity and permitted solutions with a stagnation point on the pressure surface and reverse flow around the leading edge. No theoretical explanation of this tolerance of reverse flow has been found but a physical explanation must be related to the fact that mass can now be transported upstream by the upwinding of density. By using an upwinded density to obtain velocity from ρV , it was

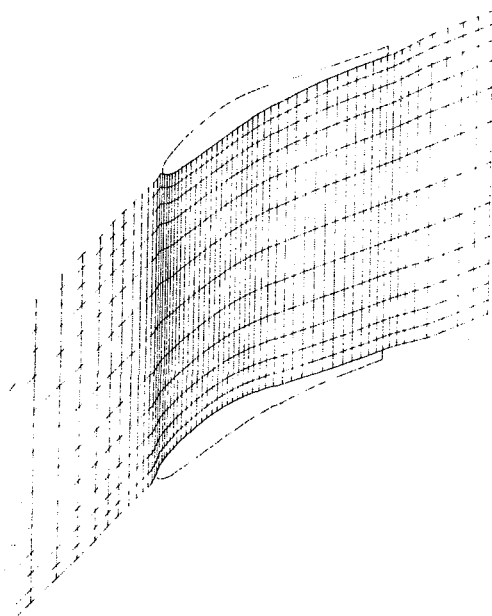


Fig. 2 Computational mesh

possible to stabilize this scheme for all cases where the axial Mach number was subsonic (hence covering most turbomachinery applications), but this loss of generality removes one of the main attractions of time marching methods.

A third scheme, (scheme C) was discovered whilst trying to combine the advantages of schemes A and B. As in scheme A, changes in all variables are sent to the downstream corners of the element but the pressure at any point is now calculated from the density at the next downstream point plus a correction factor, i.e.,

$$P_I = (\rho_{I+1} + CFRO_I) R T_I \quad (9)$$

where after every time step (or few steps)

$$CFRO_{I, \text{NEW}} = (1 - RF) CFRO_{I, \text{OLD}} + RF(\rho_I - \rho_{I+1})$$

so that in the steady state

$$P_I = \rho_I R T_I \quad (10)$$

This scheme was found to have good shock capturing properties. It was stable for all Mach numbers (with an appropriate time step) but would not permit reversed flow.

Further attempts to develop a single scheme which would permit both reverse flow and supersonic flow were not successful, so a linear combination of schemes B and C was adopted for the final program. The density change obtained for each element is distributed between upstream and downstream corners of the element according to

$$\begin{aligned} \Delta \rho_u &= \alpha \Delta \rho \\ \Delta \rho_D &= (1 - \alpha) \Delta \rho \end{aligned} \quad (11)$$

where α is a function of Mach number such that $\alpha \rightarrow 1$ as $M \rightarrow 0$ and $\alpha \rightarrow 0$ as $M \rightarrow \infty$. The precise form of $\alpha(M)$ is not critical as regards either the stability or the steady-state solution. A variation which is discontinuous at $M = 1$, i.e.,

$$\alpha = 1 \text{ for } M < 1$$

$$\alpha = 0 \text{ for } M \geq 1$$

gives very good shock fitting in one-dimensional flow, but the discontinuity caused problems in two-dimensional flow. Because temperature is a variable already calculated in the program, α is more conveniently expressed as a function of T than of M , and a linear variation of the form

$$\alpha = 0.5 \left(1 + \frac{T - T^*}{T_0 - T^*} \right)$$

$$\alpha \geq 0 \quad (12)$$

was chosen.

Having chosen the distribution of density change in this way, the pressure is calculated as an average, weighted with respect to α , of the pressures from schemes B and C; i.e.,

$$P_1 = RT_I (\alpha \rho_I + (1 - \alpha) (\rho_{I+1} + \text{CFRO}_I)) \quad (13)$$

The distribution function, α , does not affect the steady-state solution in any way and is merely a device to ensure stability of the scheme at both high and low Mach numbers and with reverse flow. As such, it is similar but not exactly analogous to the rotated difference schemes used for potential flow calculations. The difference arises because the latter introduce numerical damping which the distribution function does not.

With the pressure calculated in this way, all fluxes and pressure forces on the faces of the elements are, in the steady state, obtained from central difference formulae, using values stored at the corners of the elements. As a result the solution is second order in space for smoothly varying flows but does not have enough numerical damping to capture shocks without overshoots and undershoots being produced. It is known that numerical schemes need an artificial viscosity term proportional to the square of the first derivative of the flow properties in order to model the natural dissipative processes in a shock wave. Hence such a term was explicitly introduced into the equations in the form of an artificial pressure proportional to the square of the density gradient in the streamwise direction.

Equation (13) is thereby modified to become

$$P_I = RT_I (\alpha \rho_I + (1 - \alpha) (\rho_{I+1} + \text{CFRO}_I) + (\rho_{I+1} - \rho_I) (\rho_{I+1} - \rho_{I-1}) / \rho_I) \quad (14)$$

The last term is negligible for smoothly varying flows.

The scheme has been described so far as if it were applied to a one-dimensional flow. In practice a grid such as that shown in Fig. 2 is used for a blade-blade calculation. The flow variables at each node are then updated by half the change calculated for the element below and half that from the one above the node, with the distribution function α being evaluated as an average value for each element. As shown in Fig. 2, the scheme allows complete flexibility in choosing the spacing of the elements in both the pitchwise and axial directions and as such is an improvement on the original method where nonuniform spacing, although possible, caused significant complication. It is also apparent that when a steady state is reached the conservation equations are satisfied for each individual element. In the original scheme the elements overlapped in the pitchwise direction and so, for the same number of grid points, were of twice the pitchwise extent. Hence finite differencing in the pitchwise direction is considerably more accurate on the new grid.

Cusps, which were used at the leading and trailing edges of a blade in the original method, are not strictly necessary with the new grid. However, a cusped trailing edge is felt to be a better approximation to the real viscous flow than is a blunt trailing edge and so is usually used. At a leading edge a large number of grid points are necessary to resolve the flow accurately and a cusp is a useful means of minimizing the number used when details of the leading edge flow are not required.

Stability

As with all explicit time marching methods, the theoretical maximum stable time step is determined by the CFL condition, i.e.,

$$\Delta t < \frac{\Delta l}{C + V}$$

where Δl is usually the streamwise distance between the upstream and downstream faces of an element.

In practice the stability is found to depend more on the axial Mach number than on the absolute one and the less restrictive condition

$$\Delta t < \frac{\Delta x}{C + V_x}$$

can usually be used. For grids which are very closely spaced in the pitchwise direction the spacing perpendicular to the streamwise lines may become the limit on stability.

As pointed out in [6], it is not necessary to take the same physical time step for each element or even for each equation to obtain the correct steady state solution. Equations (1-4) show that as long as the conservation equations are satisfied for every element, the solution is independent of the magnitude of Δt . Hence, the maximum stable time step can be chosen for each individual element to obtain the fastest convergence to the steady state. This spatial variation of time step permits typically about 30 percent reduction in computer time but means that the transients of the calculation have no physical significance.

This ability to use variable time steps leads to a very powerful but simple means of controlling stability. If the local time step is made inversely proportional to the local rate of change of the property, then incipient instability will immediately (i.e., for the current property in the current time loop) reduce the time step, and hence the actual change produced in the element concerned. This technique is analogous to negative feedback and means that local instabilities do not grow and cause failure of the calculation. As a result the time step does not need to be reduced below the value which is stable for the converged solution in order to cope with large amplitude initial transients. Typically, a 25 percent reduction in the number of time steps to convergence can be obtained in this way.

Boundary Conditions

The conditions applied at the inlet and outlet flow boundaries are the same as in most other time marching methods. At the outflow boundary the static pressure is specified and held constant which is physically correct as long as the axial Mach number is subsonic. At the inflow boundary, the relative stagnation temperature and stagnation pressure are specified together with either the relative flow direction or the relative whirl velocity (V_y). The latter condition must be used if the relative inflow Mach number is supersonic and the calculation will then automatically satisfy the unique incidence condition.

The periodicity condition on the bounding streamwise lines upstream and downstream of the blade row is easily satisfied by first treating points on these lines as interior points and then equating values at corresponding points on the two boundaries. This periodicity applied immediately downstream of the trailing edge is found to be sufficient to very closely satisfy the Kutta condition at the trailing edge and no explicit Kutta condition need be applied.

The boundary conditions on the blade surfaces are the most difficult to satisfy accurately and usually a first-order boundary condition (e.g., assuming the second derivative in the y -direction to be zero on the surface) has to be applied. At first sight it would appear that with the new grid no special condition, other than zero flow through the surface, is needed. The boundary nodes can be updated by the changes calculated for the elements adjacent to the boundary, and the only difference between them and internal points is that the latter receive changes from two adjacent elements and the

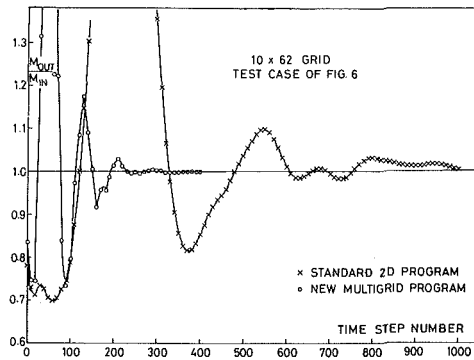


Fig. 3 Convergence

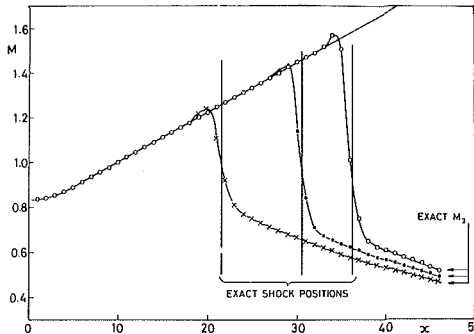
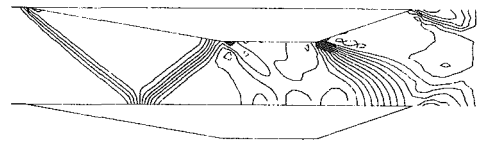


Fig. 4 Shocks in a one-dimensional nozzle

former from only one. However, this treatment ignores the fact that if there are n streamwise lines within the blade row then there are only $n-1$ elements. Hence, the number of equations is less than the number of unknowns, and this leads to a condition whereby the sum of the changes between the initial guess and final solution on even numbered nodes is related to the sum of the changes on odd numbered nodes. The final solution is therefore not independent of the initial guess. As a simple illustration of this effect, consider a case with only three nodes across the pitch. For each variable the change of the center node must equal the average of the changes on the two boundary nodes. Hence, if the initial guess was a linear variation across the pitch, the final solution must also be linear. With more quasi-streamlines the dependence on the initial guess becomes much weaker but remains an undesirable constraint upon that solution. The solution may be made unique by applying a boundary condition on one surface, e.g., by obtaining all flow properties on the pressure surface by extrapolation (not necessarily linear) from the interior points. However, a better method is to remove the dependence on the initial guess by a slight smoothing of the flow properties across the pitch. By providing a link between changes on odd and even points, the smoothing relaxes the condition that changes on them must be related and replaces it by a condition that the pitchwise variation must be in some sense smooth. The mathematical implications of the smoothing have not yet been understood but the treatment works well and is very simple to apply. In practice the smoothing factor is dropped to near zero as convergence is approached.

A further refinement is possible for points on the blade surfaces when the upstream flow can be assumed isentropic. As mentioned previously, the streamwise momentum equation can then be replaced by the equations for conservation of enthalpy and entropy. Hence, if the flow direction is known, as it is on the blade surfaces, and if the flow from the inlet to some point on the blade surface can be



Static pressure contours

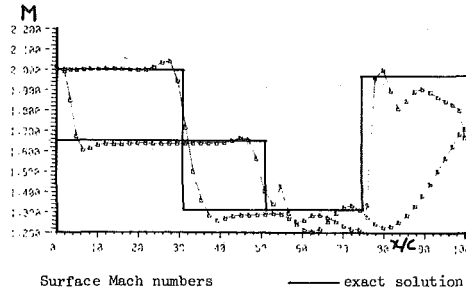


Fig. 5 Supersonic flow through a cascade of wedges

assumed reversible and adiabatic (i.e., H and S constant) the density computed at that point can be used to obtain the flow velocity via

$$T = T_0 (\rho / \rho_0)^{\gamma-1}$$

$$V = \sqrt{2 C_p (T_0 - T)} \quad (15)$$

Hence, the surface velocity can be found without using the streamwise momentum equation and so without its inevitable finite differencing errors. The assumptions used on the blade surface then become exactly the same as those used in potential flow methods, i.e., only the continuity equation is solved in finite volume form and constant enthalpy and entropy are assumed. This treatment is particularly valuable around a heavily loaded but shock-free leading edge where finite differencing errors are large and the associated entropy changes can influence the whole of the downstream flow. It may be applied over the whole surface if the blade is known to be shock-free or to have only weak shocks.

Multigrid Analysis

The method described so far is marginally faster than the original method (1.2×10^{-4} s/point/timestep cf 1.3×10^{-4} s) because of the simpler boundary conditions and fewer correction factors and because the rate of convergence is similar. Very large savings in computer time have been obtained for potential flow methods using the so-called multigrid method (e.g., Jameson [16]). The basic philosophy of this approach is to allow information regarding the overall flow pattern to propagate rapidly on a coarse grid whilst fine detail is resolved on one or more finer grids. Changes in potential on the coarse grid are interpolated into the finer grid. This philosophy is applicable in principle to solutions of the Euler equations but to the author's knowledge has not been previously used.

A course grid may be considered as being formed by combining a group of elements into a block (Fig. 1) of say 3×3 elements. This block may then be treated as a single large element and the conservation equations applied to it exactly as for basic elements. However, the CFL condition applied to the block shows that much larger stable timesteps can be taken for the block, e.g., for a 3×3 block 3 times the timestep can be used. The changes of flow properties for the block can be found either from summing the fluxes around its faces or, more easily, by summing the changes already calculated for the elements within it. Each element within the block is then updated by its own individual change, plus the

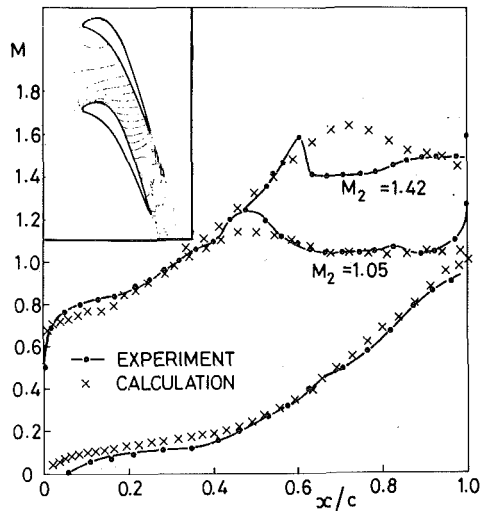


Fig. 6 VKI rotor blade-surface Mach numbers

(much larger) change for the block. Since the changes involve velocity and density it is not necessary to interpolate the block changes onto the fine grid as it is when dealing with the velocity potential which has to be subsequently differentiated. It is also apparent that the stability mechanism of the fine grid (i.e., opposed differencing) carries over unchanged to the course grid so no special techniques are needed to ensure convergence.

The multigrid method described above is very easy to program and involves little extra computer work per time step. With two levels of grid, block sizes of 3×3 elements appear about optimal and hence permit timesteps which are effectively 3 times as large as for the fine grid alone. Figure 3 compares the rate of convergence of the multigrid and single grid methods for the test case of Fig. 6. Mass balance is a suitable measure of convergence since it is found that the momentum balances converge at about the same rate. The convergence of the multigrid method is typically about four times faster than a single grid and uses about one-third the amount of computer time.

No difficulties have been encountered in using the multigrid method on a large number of test cases. In general the maximum stable timestep is slightly less than for a single grid and it is preferable to have an integral number of blocks across the pitch (e.g., 9 elements can be formed into three three-sided blocks). The method is equally applicable to the original grid and has been implemented on this in three-dimensional calculations. It should be possible to obtain further savings in computer time by using more than two levels of grid but preliminary attempts to use three levels have so far given no improvement. In principle, the multigrid approach should be applicable to other numerical schemes for solving the Euler equations the main requirement being that the stability mechanism for the fine grid carries over into the coarse grid.

Examples of Application

The method has been programmed for two-dimensional and quasi-three-dimensional blade to blade flow, the later permitting changes of stream tube thickness and radius. Because of the lack of exact solutions and of experimental data for quasi-three-dimensional flow, all the examples given here are for two-dimensional flow.

Figure 4 shows computed Mach number distributions in a one-dimensional nozzle designed to produce a linear variation of Mach number with distance for isentropic flow. Solutions are shown for three different back pressures all of which

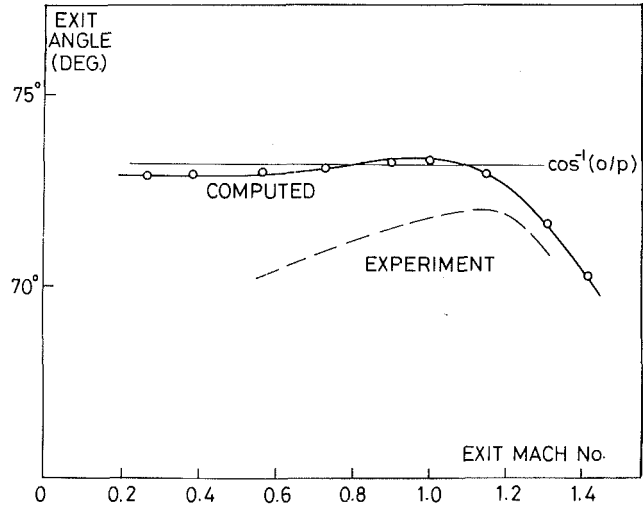


Fig. 7 Exit flow angle from VKI rotor blade

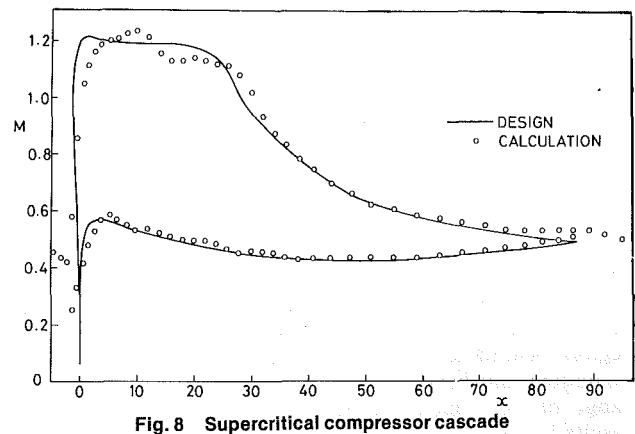


Fig. 8 Supercritical compressor cascade

produce shocked flow. In all cases the shock position and exit Mach number (hence stagnation pressure loss) are predicted almost exactly. The shock is smeared over three to four grid points in all cases with negligible overshoot or undershoot. The ability to capture a wide range of shock strengths with equal smearing indicates that the correct form of artificial viscosity (equation (14)) has been used.

To illustrate the shock capturing ability of the method for oblique shocks, Fig. 5 shows the solution for a cascade of wedges with inlet Mach number 2.0 and completely supersonic flow. The leading edge shock should be exactly cancelled at the upstream corner giving a uniform flow between the two parallel surfaces and an expansion off the downstream corner. The computed results show a sharp leading edge shock which is more highly smeared on reflection and probably as a result of this does not meet the adjacent blade exactly at the corner. Consequently, cancellation is not complete, and a weak expansion penetrates into what should be the region of uniform flow. The periodicity condition is applied downstream of the trailing edge and an interesting result is the prediction of two oblique shock waves, typical of those formed at the trailing edge of a turbine blade with supersonic exit flow. A 13×64 point grid was used for this example, and the CPU time was 50 s on an IBM 370-165.

Figure 6 shows a comparison with experimental measurements on a transonic turbine blade tested by Sieverding and McDonald at VKI, results from which are given in [17]. The results are compared at exit Mach numbers of 1.05 and 1.42. With this type of blade the trailing edge shock from one blade reflects off the suction surface of the

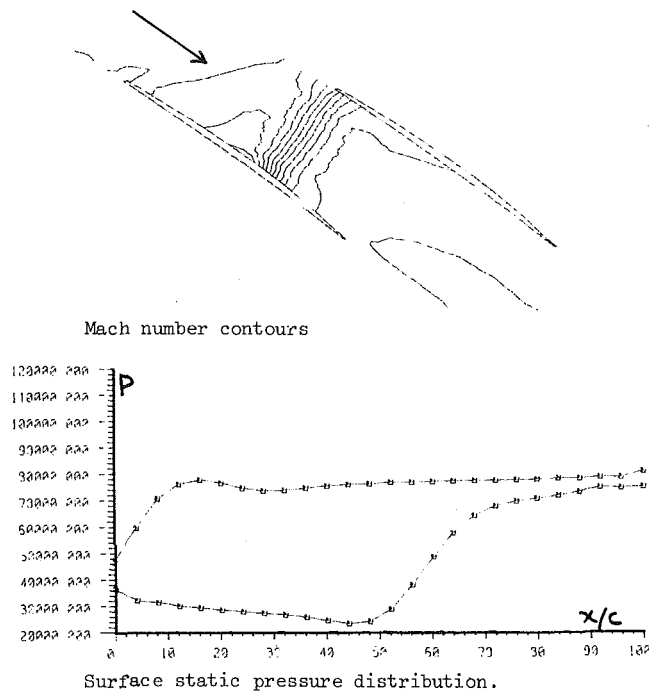


Fig. 9 Transonic fan blade

adjacent blade, and accurate results cannot be obtained unless this shock system is modelled correctly. Despite using a comparatively coarse grid, a trailing edge shock system was discernible in the solution, although (as shown by Fig. 6) this was smeared by the time it reached the suction surface. Better results have recently been obtained by modeling the base flow region behind the trailing edge. Figure 7 compares the computed and measured exit angles from this blade over a range of exit Mach numbers. The trend of the computed results is correct and the discrepancy of order 2 deg is in the direction expected from viscous effects. This solution took 48 s CPU time for a 10×62 point grid.

Figure 8 compares the computed and exact design solutions for the Bauer, Garabedian and Korn (reference 18) shock free supercritical compressor blade (Fig. 2). This blade has a highly loaded leading edge which initially caused significant loss of stagnation pressure on the surface streamlines. This was prevented by use of the isentropic surface boundary condition which lead to the good agreement shown in the figure. For this case 65 s CPU time were needed on a 13×60 point grid.

Perhaps the most important practical application of time marching methods is the calculation of flow through supersonic fan blades where the strong shocks present make all other methods inapplicable. The flow through such blades is strongly influenced by viscous effects, particularly downstream of the shock, so comparison of inviscid calculations with test data is not realistic. Figure 9 illustrates the ability of the method to compute such flows for a typical fan blade with an inlet Mach number of 1.4 and a strong shock attached at the leading edge. The shock is much cleaner than would be obtained from the original method despite the use of a fairly coarse 10×50 point grid. CPU time for this solution was 29 s.

Discussion and Conclusions

Many more test cases than those presented here have been calculated with the new method, and there is no doubt that the method is faster and more accurate than its predecessor. The improved accuracy comes about mainly because interpolation is no longer needed to evaluate the correction factors. Such

interpolations can increase accuracy for a smooth flow but experience is that they cause problems at shock waves and at leading edges. The isentropic surface boundary condition is an important aid to improving accuracy at highly loaded leading edges. The only non-second-order term in the new method is the numerical damping which is under the direct control of the user and which has negligible effect except at shock waves. Hence it seems likely that accuracy can only be further improved by using more complex higher order schemes or by using more grid points.

For two-dimensional calculations, the number of grid points is unlikely to be limited by computer storage and the main limitation is likely to be the consequent increase in CPU time. Use of the multigrid method allows more grid points to be used for the same CPU time (about twice as many) and so permits substantially greater accuracy for the same cost. With the present method a large modern computer could obtain solutions for a grid of 5000 or more points in few minutes CPU time. Such a large number of points should permit very detailed resolution if the flows around highly loaded leading edges and around supersonic trailing edges, which are the main problem areas with previous calculations. It is considered that the multigrid method has potential to provide further increases in speed by the use of more levels of grid, and this deserves further investigation.

The new grid geometry can be easily extended to three-dimensional flows, and work on this is proceeding. However, difficulty has been found in solving the energy equation (as is necessary in three-dimensions) using schemes B and C, and so it may be necessary to use scheme A, which does not permit reverse flow, for three-dimensional calculations.

Acknowledgments

The original idea of using a grid with nodes only at the corners of the elements was obtained from Dr. R. Ni of Pratt and Whitney Aircraft.

The wedge case test of Fig. 5 was provided by Brown Boveri & Co., Baden, Switzerland.

References

- Farrell, C., and Adamczyk, J., "Full Potential Solution of Transonic Quasi-Three-Dimensional Flow Through a Cascade Using Artificial Compressibility," ASME Paper No. 81-GT-70, 1981.
- Gopalakrishnan, S., and Bozzola, R., "A Numerical Technique for Calculation of Transonic Flows in Turbomachinery," ASME Paper No. 71-GT-42, 1971.
- Veuillot, J. P., "Calculation of Quasi-Three-Dimensional Flow in a Turbomachine Blade Row," ASME Paper No. 76-GT-56, 1976.
- McDonald, P. W., "The Computation of Transonic Flow Through Two-Dimensional Gas Turbine Cascades," ASME Paper No. 71-GT-89, 1971.
- Denton, J. D., "A Time Marching Method for Two- and Three-Dimensional Blade to Blade Flow," ARC R. & M. 3775, 1975.
- Denton, J. D., and Singh, U. K., "Time Marching Methods for Turbomachinery Flow Calculation," VKI Lecture Series on Transonic Flows for Turbomachinery, 1979.
- Kopper, F., Milano, R., and Vanco, M., "An Experimental Investigation of Endwall Profiling in a Turbine Vane Cascade," *AIAA Journal*, Vol. 19, No. 8, 1981.
- Sarathy, K. P., "Computation of Three-Dimensional Flow Fields Through Rotating Blade Rows and Comparison with Experiment," ASME Paper No. 81-GT-121, 1981.
- Barber, T. J., "Analysis of Shearing Internal Flows," AIAA Paper 81-0005, 1981.
- Spurr, A., "The Prediction of Three-Dimensional Transonic Flow in Turbomachinery Using a Combined Throughflow and Blade-to-Blade Time Marching Method," *International Journal Heat and Fluid Flow*, Dec. 1980.
- Mitchell, N., "A Time Marching Method for Unsteady Two-Dimensional Flow in a Blade Passage," *International Journal Heat and Fluid Flow*, 2, 4, 1980.
- Bakhtar, F., and Tochai, M., "An Investigation of Two-Dimensional Flows of Nucleating and Wet Steam by the Time-Marching Method," *International Journal Heat and Fluid Flow*, 2, 1, 1980.
- Bryce, J. D., and Litchfield, M., "Experience of the Denton Blade-Blade Time Marching Programs," NGTE Note 1050, Oct. 1976.
- Singh, U. K., "Computation of Transonic Flow in Cascade with Shock and Boundary Layer Interaction," *Proceedings First International Conference Num. Meth. in Laminar and Turbulent Flow*, Swansea, July 1978.

15 Calvert, W. J., and Herbert, M. V., "An Inviscid-Viscous Interaction Method to Predict the Blade-Blade Performance of Axial Compressors," NGTE Memo 80012, Feb. 1980.

16 Jameson, A., "Acceleration of Transonic Potential Flow Calculations on Arbitrary Meshes by the Multiple Grid Method," AIAA Paper No. 79-1458. 1979.

17 Sieverding, C., "Base Pressure in Supersonic Flow," VKI Lecture Series on Transonic Flows in Turbomachinery, 1976.

18 Bauer, F., Garabedian, P., Korn, D., and Jameson, A., "Supercritical Wing Sections II," *Lecture Notes in Economics and Mathematical Systems*, Vol. 108, Springer Verlag, 1975.

19 Singh, U. K., "A Computation and Comparison With Measurements of Transonic Flow in an Axial Compressor Stage With Shock and Boundary Layer Interaction," ASME Paper No. 81-Gr/GT-5, 1981.

Table 1 Supersonic compressor shock structure features

- 1 Wave angles approximate maximum deflection
- 2 Suction surface pressures near the leading edge are below 80% of upstream
- 3 Shock discontinuities are substantially below expectation
- 4 Pressure surface pressures in supersonic passages respond to back pressure
- 5 Passage and downstream shocks disappear at supersonic pressure levels

15 Calvert, W. J., and Herbert, M. V., "An Inviscid-Viscous Interaction Method to Predict the Blade-Blade Performance of Axial Compressors," NGTE Memo 80012, Feb. 1980.

16 Jameson, A., "Acceleration of Transonic Potential Flow Calculations on Arbitrary Meshes by the Multiple Grid Method," AIAA Paper No. 79-1458, 1979.

17 Sieverding, C., "Base Pressure in Supersonic Flow," VKI Lecture Series on Transonic Flows in Turbomachinery, 1976.

18 Bauer, F., Garabedian, P., Korn, D., and Jameson, A., "Supercritical Wing Sections II," *Lecture Notes in Economics and Mathematical Systems*, Vol. 108, Springer Verlag, 1975.

19 Singh, U. K., "A Computation and Comparison With Measurements of Transonic Flow in an Axial Compressor Stage With Shock and Boundary Layer Interaction," ASME Paper No. 81-Gr/GT-5, 1981.

DISCUSSION

David C. Prince, Jr.¹

A great deal of my professional effort over the last ten years has been spent searching for the theoretical pattern behind experimental data from supersonic compressor rotors. It is always my hope that papers like this one will contribute to that search.

Table 1 is reproduced from [20]. It attempts to summarize observations on compressor experiments over the past ten years. At least two elements of Table 1 seem especially germane to the subject of this paper. The fourth element pertains to observations about pressure surface pressures which respond to back pressure variations. This statement could be paraphrased bluntly: "Supersonic compressor flows violate (or circumvent) the 'Rule of Forbidden Signals.'" On the other hand, I have not seen any way in which a two-dimensional cascade analysis, for either compressor or turbine cascades, can contradict the Rule of Forbidden Signals and still satisfy the Equations of Motion. Furthermore, experimental evidence on the role of Forbidden Signals in two-dimensional cascades seem to be rather scarce. Figure 10 is a composite of figures found in [21]. For low back pressures, the Rule of Forbidden Signals seems to be operating to about 55 percent chord on the suction surface, to about 35 percent chord on the pressure surface. (Sonic pressure level is at $C_p \approx 0.5$.) The large trailing edge camber of this cascade is responsible for an extended subsonic zone at all back pressures, which makes it less than satisfactory for studying Forbidden Signals. At higher back pressures than those reproduced for Figure 10, the passage shock apparently moves forward to the passage inlet, leaving fully subsonic passage flow, but the signal propagation upstream of the leading edge continues to be "Forbidden." I suggest, therefore, that validation of any cascade analysis procedure must demonstrate that the procedures respect Forbidden Signals in two dimensions and circumvent Forbidden Signals in three dimensions. It is not appropriate to try to validate a two-dimensional analysis by using three-dimensional data that have been shown to violate Forbidden Signals. It should be observed that these violations of forbidden signals often occur in the pressure surface leading edge region, where boundary layer phenomenon are not likely to have much influence.

York and Woodard [23] showed that their two-dimensional analysis did give a good representation of the experimental flow through a two-dimensional supersonic compressor cascade. They do not mention any reliance on viscous flow effects to help them establish a good comparison. Their

¹ Consulting Engineer, General Electric Company, Aircraft Engine Group, Cincinnati, Ohio 45215

Table 1 Supersonic compressor shock structure features

- 1 Wave angles approximate maximum deflection
- 2 Suction surface pressures near the leading edge are below 80% of upstream
- 3 Shock discontinuities are substantially below expectation
- 4 Pressure surface pressures in supersonic passages respond to back pressure
- 5 Passage and downstream shocks disappear at supersonic pressure levels

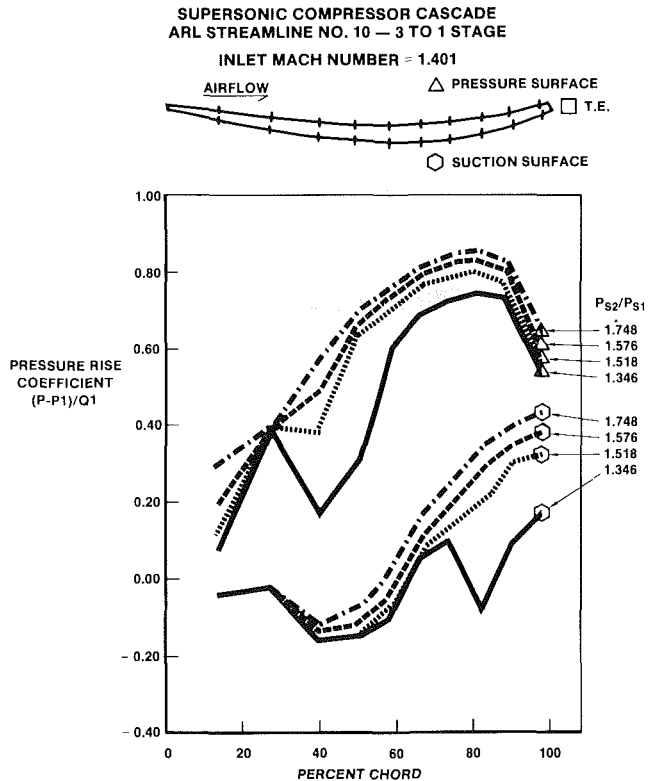


Fig. 10 The Rule of Forbidden Signals in compressor cascades – two-dimensional cascade

configuration, however, does not have a severe adverse pressure gradient on the suction surface, so that the boundary layer growth should not distort the effective shape very much. Figure 11 is reproduced from [23]. Part (a) of the figure shows the calculation of the curved leading edge shock propagating upstream and its weakening by interaction with expansion around the leading edge until it becomes asymptotic to the Mach direction. Part (b) of Fig. 11 shows the calculated shock overlaid on a Schlieren photograph of the experiment. The agreement is extremely good. Part (b) of Fig. 11 also shows that the experimental leading edge shock inside the cascade passage is substantially more oblique than the axial direction. This wave direction is typical of two-dimensional analytical predictions. Part (c) of Fig. 11 shows that the suction surface pressure gradient predicted analytically for the concave surface has experimental confirmation.

The fifth element in Table 1 could be paraphrased, "Apparent Mach numbers for supersonic compressor rotor cascades are substantially lower than the nominal Mach numbers." In my recollection, I first proposed this concept publicly in [22]. At that time, however, neither the quantity nor the quality of the experimental data justified any

Table 2 Basic questions for transonic flow analysis

- 1 Is "continuity" really being satisfied?
- 2 Does the calculation grid generate a built-in bias against some supersonic wave propagation?
- 3 Is "momentum balance" really being satisfied?

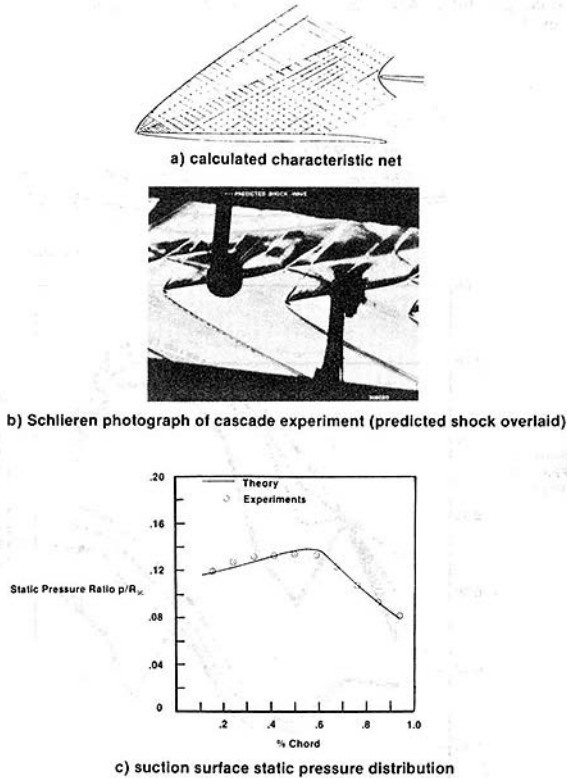


Fig. 11 Two-dimensional compressor cascades—comparison of theory with experiment

significant effort at incorporating the concepts in a theory. More evidence along this line has been accumulating; some of it was explored in [20]. Observations on leading edge wave angles summarized in the first element of Table 1 also suggest low apparent Mach numbers.

The author and his associates have had an opportunity to consider their acceptance of the ideas expressed in Table 1. References [8] and [19], at least, present applications of the author's methods to the rotor for which extensive experimental measurements were made at DFVLR [24–26]. I have prepared Fig. 12 from those references. I interpret the change in pressure surface Mach number from wide-open throttle to maximum efficiency as an example of "circumvention of forbidden signals" in the supersonic regime and the change in the Mach number contours across the passage exit as an example of shock disappearance at supersonic Mach numbers, i.e., as a case of substantially reduced apparent Mach number. I hope the author will share his experience on these observations.

An examination of the results in the paper, and in some of the reference papers, suggests some additional questions (Table 2) on which I would appreciate additional discussion.

Concerning satisfaction of continuity, Sarathy [8] attempted to analyze the flow through a compressor rotor, using the methods of [5], and to compare that analysis with

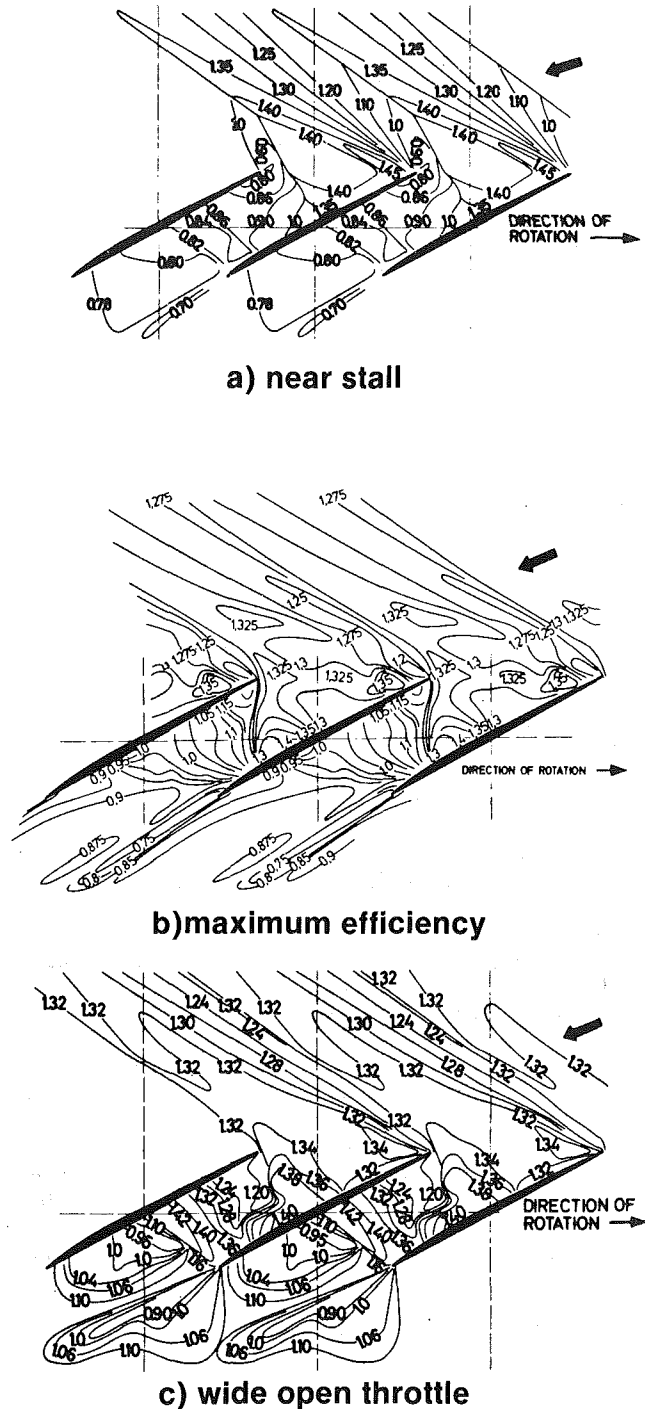


Fig. 12 The Rule of Forbidden Signals in compressor cascades—compressor rotor

experiment. The analysis predicted a flow level 4 percent below the experiment. Since the analysis presumably disregarded shock loss and boundary layer thicknesses at a choked area, it might more reasonably have been expected to predict a flow higher than experiment by 1-2 percent. The question, then, is: Does the present author assume that the solution of his equations automatically conserves mass, or has he incorporated positive procedures for evaluating his success at conserving mass across the surfaces of his finite volumes and/or from grid plane to grid plane in the streamwise direction in his calculation method? If he has such positive procedures built in, what standards does he set for success?

An error of 0.2 percent in flow conservation in the neighborhood of a choked area could, of course, easily allow the velocity estimate to be in error by 5 percent. My organization has experience with a derivative version of [5], in which the flow summations from grid plane to grid plane are erratic over a range of a percent or so. Apparently, mass conservation should not be taken for granted.

Figure 6 is an example of a situation where satisfaction of the momentum balance (question 3 of Table 2) may be questionable, possibly because a highly skewed calculation grid generates a bias against signal propagation in the appropriate wave direction. The locus of Mach number discontinuities originating at the trailing edge appears to lie at 22 deg from the flow direction. One may imagine a control volume generated by superposing a wedge on a uniform flow parallel to the pressure surface near the trailing edge, with the wedge centerline parallel to the downstream flow direction. The flow over the wedge would include a shock at a wave angle somewhat larger than the 45 deg Mach angle for the 1.42 downstream Mach number, which is consistent with the experimental distribution shown on Fig. 6. If the calculation grid is indeed highly skewed, with grid lines parallel to the trailing edge plane and intersecting grid lines approximating the highly staggered streamlines, one may imagine that the calculation attempts to represent pressure signal propagation across the short diagonals of the grid by propagation downstream along the parallels and upstream along the "streamlines." According to the Equations of Motion, upstream propagation is "Forbidden" and could well be rejected, or at least attenuated. This effect would account for the apparent wave angles of Fig. 6.

In a recent paper [30], I propose the concept of "Prince's MOC Rule"

$$\frac{\Delta p}{P} = 3\Delta\theta \quad (16)$$

relating the surface pressure distribution to the surface angle (in radians) in wave-of-one-family situations over a Mach number range from 1.2 to 1.8, (possibly from 1.0 to 2.0). Applying this rule to the cascade of Fig. 6 and assuming the suction surface curves through a 5 deg arc downstream of the passage exit, the Mach number after the shock would be estimated at 1.33 and the Mach number near the trailing edge would be estimated at 1.51. These estimates seem to give a reasonable approximation to the experimental trend of Fig. 6.

The highly staggered calculation grids used in [8] and [27, 28] for compressor cascades, and [29] for a turbine cascade also seem to have suppressed pressure signal propagation in a characteristic direction across a short diagonal.

The application of question 3 of Table 2 to Fig. 6 has been discussed above. The excellent agreement between the calculated Mach numbers of Fig. 5 and the exact solution constitutes as affirmative answer to the question for that case. I believe the question should be considered quite pertinent for Fig. 9. It is surprising to see a normal shock across the cascade passage near its inlet without substantial standoff and spillage. The experimental data of Fig. 12, for example, show a strong upstream shock when the passage shock is normal, near stall, and substantial upstream strength when the passage shock is attached and oblique. If Fig. 9 is drawn to scale, the upstream vector is approximately correct for "unique incidence" to the suction surface, but is at a 3 deg angle of attack to the suction surface leading edge, enough so that a well-defined upstream shock should show in the figure.

I hope the author will provide assurance that he is respecting and circumventing "Forbidden Signals" under appropriate circumstances, and that his success at conserving mass and momentum is being monitored aggressively.

References

- 20 Prince, D. C., Jr. "Three-Dimensional Shock Structures for Transonic/Supersonic Compressor Rotors," *AIAA Journal of Aircraft*, Jan. 1980, pp. 28-37.
- 21 Holtman, R. L., Huffman, G. D., McClure, R. B., and Sinnet, G. T., "Test of Supersonic Compressor Cascade," U.S. Air Force Aeronautical Research Laboratory Contractor Report ARL 72-0170, Vol. 1, Dec. 1972.
- 22 Prince, D. C., Jr., "Some Flow Pattern Features in Supersonic Compressor Cascades" presentation to University of Tennessee Space Institute Short Course on Air Breathing Engines, Oct. 1975.
- 23 York, R. E., and Woodard, H. S., "Supersonic Cascades—An Analysis of the Entrance Region Flow Field Containing Detached Shock Waves," *ASME JOURNAL OF ENGINEERING FOR POWER*, Apr. 1976, pp. 247-257.
- 24 McDonald, P. W., Bolt, C. R., Dunker, R. J., and Weyer, H. B., "A Comparison Between Measured and Computed Flow Fields in a Transonic Compressor Rotor," *ASME JOURNAL OF ENGINEERING FOR POWER*, Oct. 1980, pp. 883-891.
- 25 Weyer, H. B., and Dunker, R., "Dual Beam Laser Anemometry Study of the Flow Field in a Transonic Compressor" AGARD-CP-214, 1977.
- 26 Schodl, R., "A Laser-Two Focus (L2F) Velocimeter for Automatic Flow Vector Measurements in the Rotating Components of Turbomachines," *ASME Journal of Fluid Engineering*, 1980.
- 27 Gopalakrishnan, S., and Bozzola, R., "Computation of Shocked Flows in Compressor Cascades," *ASME Paper No. 72-GT-31*, Mar. 1972.
- 28 Erdos, J., Aizner, E., and Kalben, P., "Computation of Steady and Periodic Two-Dimensional Non-Linear Transonic Flow in Fan and Compressor Stages" *Transonic Flow Problems in Turbomachinery*, edited by T. C. Adamson and M. F. Platzer, MICH-16-PU, Feb. 1976, pp. 95-111.
- 29 Studerus, C. J., "Aerodynamic Effects of Surface Cooling-Flow Injection on Turbine Transonic Flow Fields," *AIAA Paper No. 79-0048*, Jan. 1979.
- 30 Prince, D. C., Jr. "The Method of Characteristics for Supersonic Flow Analysis—a Fresh Perspective," *AIAA Paper No. 82-0996*, June 1982.

Author's Closure

Mr. Prince's contribution is relevant, not only to this paper but to much of the work published in the field of flow computation in turbomachinery, and would be best answered by an open discussion at a specialized meeting on this subject. I am not an expert on transonic fan aerodynamics and so am not qualified to answer some of Mr. Prince's more detailed queries. However, I will try to answer the questions which are specific to my paper and to make some comments on the more general points.

The question of conservation of mass, momentum, and (in three-dimensions) energy by numerical methods is a longstanding issue. The advantage of finite volume methods is that they can easily be made to fully conserve these quantities. In the present scheme all fluxes are evaluated by assuming that quantities vary linearly between adjacent grid nodes, and the only nonconservative term is the slight smoothing which is discussed in the section on boundary conditions. If the same finite difference approximation is used to check the balance of mass, momentum, etc., then, if it were not for this smoothing, the balance would be *exact*. In practice, the smoothing can be kept so low that the overall mass balance is usually within 0.1 percent on convergence (see Fig. 3) and the momentum imbalances are only slightly larger.

The same findings apply to the three-dimensional method, and whilst it is agreed that Sarathy's result, showing a computed mass flow less than the measured flow, must be in error it seems to the author that the most probable source of the error is an incorrect allowance (if any) for the untwist of the blades under rotation.

The accuracy of flux conservation does not, unfortunately, imply that the computed velocities, pressures, etc., are of similar accuracy. The assumption of a linear variation between grid nodes is clearly not exact and introduces an error whose magnitude depends on the grid spacing and on the second derivative of the flow quantities. In particular, for shocked flows, no finite difference approximation which does not explicitly account for shock discontinuities can be accurate and characteristics methods, when they can be used, are clearly more satisfactory. The only way of overcoming this limitation is to use very fine grids, and [31] shows that

very complex shock structures can be accurately resolved by the present method when sufficient grid points are used. It is accepted that the results presented in Figs. 6 and 9 did not use sufficient points to obtain good predictions. For the compressor blade, Fig. 9, an extremely coarse grid was used, and the shock is smeared over a large part of the chord. The results presented by Calvert [32] show how much better results can be obtained from the same method. The turbine blade, Fig. 6, presents a much more difficult problem. Here the shock structure originates from a very small region at the base of the trailing edge and influences a large part of the flow. There is little hope of obtaining a good prediction of the overall flow unless the trailing edge region is first computed accurately. Since viscous effects are important in this region this cannot be achieved by an inviscid method, although it should be possible to build a trailing edge model involving empirical correlations into the inviscid calculation. Even so, an extremely fine grid would be needed.

In a finite difference (or volume) method there are no "forbidden directions," information is passed between all grid points but the equations being solved ensure that signals decay rapidly in the upstream direction when the local flow is supersonic. Hence, shocks are not captured as discontinuities but are smeared over several grid points. A highly skewed grid, as used by the author for staggered cascades, undoubtedly causes signals to decay at different rates in different directions. In particular, a shock lying perpendicular to the long diagonal of an element will be smeared over a much greater spatial extent than one perpendicular to the short diagonal. Hence, although the grid does not generate a bias against propagation in some directions it does introduce larger errors for some waves than for others. There is no doubt that a more nearly orthogonal grid could give better results from the same number of points, but the author's philosophy is that a simple fast scheme with many grid points is preferable to a slower, more complex scheme which achieves the same accuracy with fewer points.

On the more general point of the apparent violation of the laws of motion by supersonic compressor flows, there appear to me to be two possible explanations, namely, viscous effects and three dimensional effects.

In an *inviscid* two-dimensional cascade flow with a sonic

line crossing from the blade suction to pressure surface, conditions upstream of the sonic line cannot change in response to changes in downstream conditions. In a *real* cascade flow, conditions can only change via the propagation of signals through the subsonic flow in the blade and endwall boundary layers. It is well known that endwall boundary layer blockage (axial velocity-density ratio) plays a major part in compressor cascade tests, and it would not surprise me if this was significantly affected upstream of the inviscid sonic line by changes in exit pressure. This is a possible explanation for the results shown in Fig. 10.

The real three-dimensional flow in a fan is much more complex than that in a cascade and I suspect that two-dimensional cascade tests and calculations can be very misleading. In most fans the blades are not choked over the whole height, i.e., a continuous sonic surface does not extend from hub to tip and from pressure surface to suction surface. In particular, the root section may be completely subsonic. In this case, there is no barrier to the upstream propagation of changes in downstream pressure. Such changes can be transmitted through regions of subsonic flow and can influence the flow upstream of the fan (e.g., change the mass flow rate). In particular the effective stream tube thickness of the supersonic parts of the flow, and even the "unique" incidence angle can be changed. This is the likely explanation for the results shown in Fig. 12.

Such effects are predictable by fully three-dimensional calculation methods but will be missed by quasi-three-dimensional methods unless the stream tube thickness is allowed to change with change in exit conditions. In many cases, both viscous effects and three-dimensional effects will be operative and accurate predictions await the development of a fully three-dimensional viscous calculation method.

Additional References

31 Bryanston-Cross, P. J., and Denton, J. D., "Comparison of Interferometric Measurements and Computed Flow around a Wedge Profile in the Transonic Region," ASME Paper No. 82-GT-258.

32 Calvert, W. J., "An Inviscid-Viscous Interaction Treatment to Predict the Blade-to-Blade Performance of Axial Compressors With Leading Edge Normal Shock Waves," ASME Paper No. 82-GT-135.

The Control of Engine Vibration Using Squeeze Film Dampers

R. Holmes

University of Sussex,
School of Engineering and Applied Sciences
Falmer, Brighton,
Sussex BN1 9QT, England

This paper describes the following roles of a squeeze-film damper when used in gas turbine applications as a means of reducing vibration and transmitted force due to unbalance: (a) as an element in parallel with a soft spring in a vibration isolator; and (b) as an element in series with the stiffness of the engine pedestal. The effects of cavitation on performance are elucidated, and the dangers of jump phenomena and subsynchronous response are discussed. Experimental work is described in which both roles of the squeeze-film damper are investigated and the results are compared with theoretical predictions.

Introduction

A squeeze film is an annulus of oil supplied between the outer race of a rolling-element bearing (or the bush of a sleeve bearing) and its housing. It is used as a multidirectional damping element for the control of engine vibrations. Such a squeeze film is often placed in parallel with a soft flexible element to comprise a vibration isolator. By this means the natural frequencies of the engine are artificially reduced so that they may be traversed well before the normal operating speeds are reached. The purpose of the damper in this application is to reduce to acceptable levels the amplitudes of vibration and transmitted force due to unbalance as these low natural frequencies are traversed. Figure 1 shows such an arrangement in the Rover automotive gas turbine engine. The squeeze-film isolator can be seen supporting the compressor on the right of the photograph.

A squeeze-film damper is also often used on its own between a bearing and its housing, in which case no attempt is made to reduce the natural frequencies of the system – only to reduce vibration while running through the already-existing

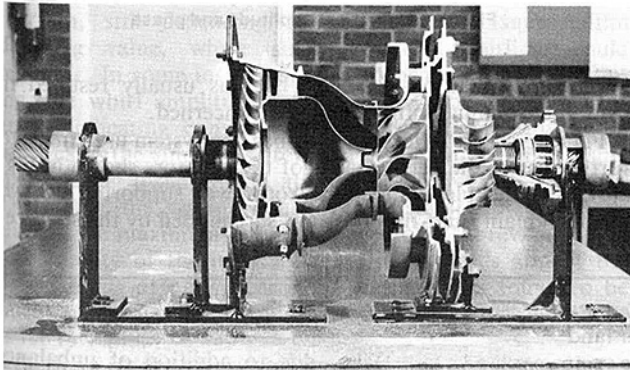


Fig. 1 Rover gas turbine

Contributed by the Gas Turbine Division of THE AMERICAN SOCIETY OF MECHANICAL ENGINEERS and presented at the 27th International Gas Turbine Conference and Exhibit, London, England, April 18–22, 1982, Manuscript received at ASME Headquarters December 18, 1981. Paper No. 82-GT-241.

natural frequencies. Rotation of the inner member of the squeeze-film damper is in this case prevented by antirotation pins or dogs. However, the damper now becomes part of a series structure of rotor, damper, and housing flexibility, and under these conditions the required degree of damping must be carefully considered. For example, excessive damping can offer little benefit, since the damper then operates almost as a rigid link. Likewise, deficient damping can allow large vibrations to occur between the rotor and its bearing housings, even though the rotor vibration itself may be kept to reasonable limits.

This paper describes investigations into the performance of squeeze-film dampers when used in parallel and in series with flexible structures in turbomachinery applications.

The Squeeze-Film Damper as a Parallel Element of a Vibration Isolator

The purpose of the squeeze-film damper in this application is to reduce the amplitude of vibration and of transmitted force to the engine frame due to rotor unbalance as the rotor is run through the artificially low natural frequencies of the system (ensured by the soft spring element) toward the normal operating speed. Most analyses, e.g., [1], assume that concentric vibration orbits exist when the rotor is running, due to preloading in the spring element or because the dynamic loading is large compared to the static loading, as may well be the case in the vicinity of a system natural frequency.

The squeeze film is, however, a nonlinear damper, and the designer must guard against two classical disadvantages of such damping, namely, jump phenomena and subsynchronous response. The former can arise in situations where cavitation occurs in the squeeze film [1]. Owing to the nonlinearity of the squeeze film, the graph of forced response versus force frequency can be distorted to such an extent that large vibrations (and hence transmitted forces) can be maintained for an extended speed range during run-up before jumping down to an acceptably low level. Indeed a “jump-up” with continuing increase in rotor speed can also be

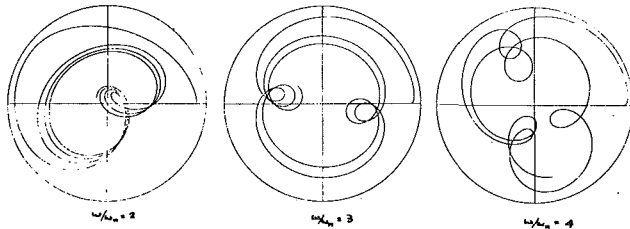


Fig. 2 Subsynchronous response: $A = 0.03$; $u/c = 0.25$

predicted under certain circumstances, and evidence of this has been recorded experimentally [2].

Subsynchronous response has also been recorded in systems employing squeeze-film isolators [3] and may be predicted whether or not cavitation is assumed to occur in the squeeze film. Figure 2 shows numerically predicted responses for a rigid rotor in uncavitated squeeze-film isolators which are centrally preloaded and in which the damping is fairly light. In this figure, A is a measure of the damping in the system, u/c is the ratio of rotor mass eccentricity to squeeze-film radial clearance, and ω/ω_n is the frequency ratio. Strong subsynchronous responses are suggested at running speeds of twice, three times, and four times the lowest (bounce) natural frequency, ω_n .

One design of squeeze-film isolator [3] is illustrated in cross section in Fig. 3(a). It consists of a mild steel bearing housing, A, and a cast iron damper bush, B, surrounding a journal, C. The bush is suspended concentrically in the squeeze-film clearance, D, by means of two horizontal springs and one vertical spring, E, made up of Watveare Belleville washers stacked in series along steel guide rods and preloaded for compression. The rods are connected to the bush via loose joints. The lubricating oil enters the circumferential groove, F, at point, G. Some of the oil continues through the oil hole in the damper bush to the circumferential oil grooves, H, of the journal bearing. The isolator stiffness can be varied by altering the suspension springing, and centering of the damper bushes in the squeeze-film clearance is carried out by means of the spring preloading nuts, M, compressing the Belleville washer stacks.

Agreement between theoretical predictions and experimental findings is fairly good for such uncavitated squeeze-film isolators, as polar graphs of vibration amplitude and phase (Fig. 3(b)) show. This figure relates to a rigid rotor centered in each squeeze-film annulus by preloading the flexible elements. Such agreement enables numerical results for uncavitated squeeze films to be accepted with a certain amount of confidence. If cavitation can take place, however, uncertainties as to its likely extent for a given dynamic loading and supply pressure made predictions difficult. Figure 4 shows the adverse effect on concentric vibration amplitude and on transmissibility, T , of cavitation which extends, say, over half the annulus of the squeeze film. Thus, if there is any likelihood of cavitation existing, extra caution will be required in rotor balancing and the oil-supply pressure should be made as high as possible to reduce the amount of cavitation. In spite of these reservations the use of squeeze-film isolators in

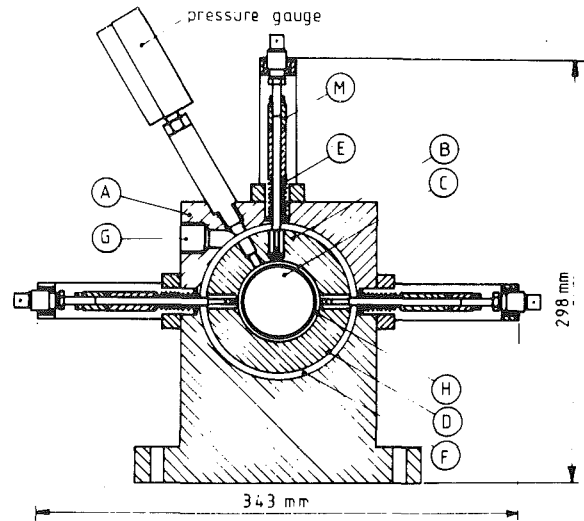


Fig. 3(a) Squeeze-film isolator

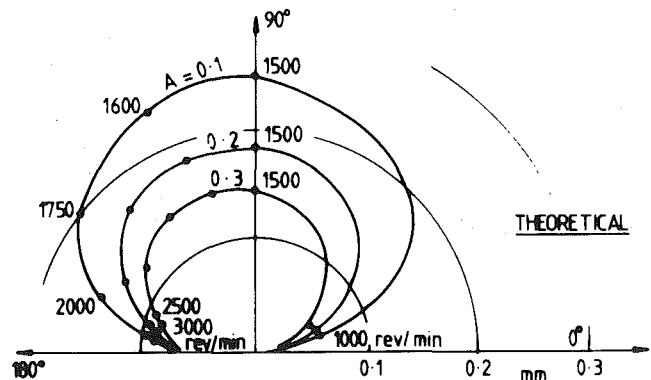
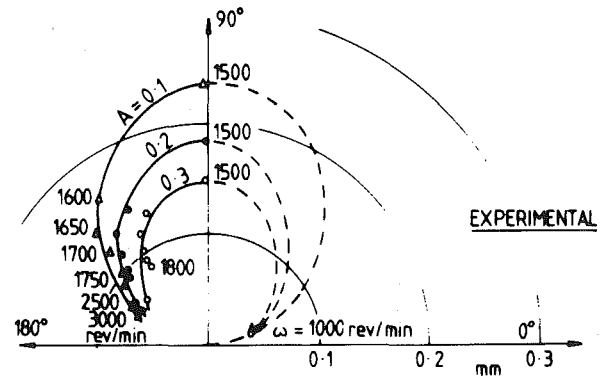


Fig. 3(b) Vibration amplitude and phase

practical installations [1, 3, 4, 5] has usually resulted in smoother running of the equipment concerned.

Figure 5 shows a flexible rotor-bearing system used in [3] to further assess the performance of the isolators shown in Fig. 3(a). The flexible symmetrical rotor was supported by two identical plain fluid-film bearings surrounded by the squeeze-

Nomenclature

$A = \pi\eta R(1/c)^3/\sqrt{km}$	$P =$ static load per land	
$c =$ radial clearance of squeeze film	$P_c =$ rotating force vector per land	due to addition of unbalance mass or loss of mass
$e =$ eccentricity of journal in bearing	$Q = P/mc\omega^2$	
$k =$ stiffness of retainer spring or of housing per land	$Q_c = P_c/mc\omega^2 = u/c$	$\beta = \eta R^3/mc^3\omega$
$l =$ squeeze-film land length	$R =$ journal radius	$\epsilon =$ dynamic eccentricity ratio (e/c)
$m =$ rotor mass per land	$T =$ transmissibility	$\eta =$ oil viscosity
	$u =$ displacement of rotor center of mass from geometric center	$\omega =$ frequency of dynamic load
		$\omega_n = \sqrt{k/m}$

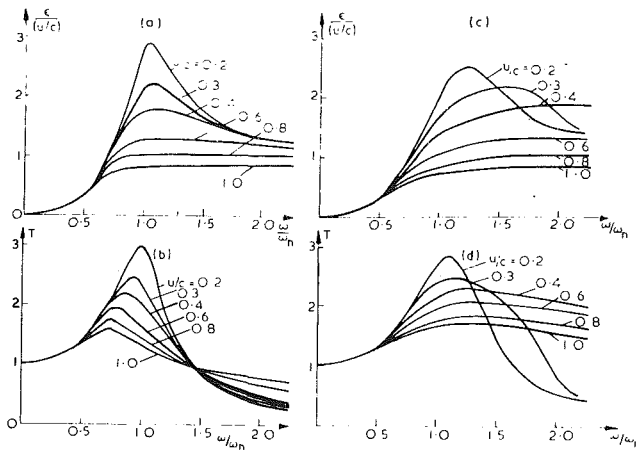


Fig. 4 $\epsilon/(u/c)$ and transmissibility, $v\omega/\omega_n$, for $A=0.2$: (a) and (b), full film; (c) and (d), half-film

film isolators. The fluid-film bearings were each supplied with oil to a central circumferential groove, and disks D1, D2, and D3 were positioned so as to allow easy unbalance excitation of the two lowest shaft bending modes by the attachment of unbalance masses at their peripheries. Journals J1 and J2 were fixed at each end of the shaft and were supported by the squeeze-film isolators S1 and S2.

Both the experimental results and the numerical predictions showed a continuous reduction of the maximum shaft displacement amplitude at both the first and second critical speeds for increasing support damping (up to about 10^4 Ns/m) with an increase in displacement for further increase in damping. This illustrates that an optimization procedure is in general necessary before specifying the necessary damping, if plain fluid-film bearings are present.

Well-defined instability threshold speeds, due to the fluid-film bearings, were observed for large values of squeeze-film damping, while for low values (below 5×10^3 Ns/m) the system was stable and well damped in the entire operating speed range 0–4000 rev/min. However, in the damping range $6.10^3 \times 3.10^4$ Ns/m, steady subsynchronous whirling commenced at a rotational speed in the region of 1740–2250 rev/min, that is, between twice and three times the first critical speed, with the exact onset speed depending on the damping value. The subsynchronous whirl amplitude would increase with speed up to about 2400 rev/min, that is, up to about three times the first critical speed, whereafter the subsynchronous whirl component amplitude would decrease rapidly and vanish at about 2400–2740 rev/min. The response would then remain synchronous up to about 2870–3230 rev/min, still depending on the particular squeeze-film damping value, where subsynchronous whirling would reappear. In some instances, again depending on the damping, the whirl amplitudes at this speed would continue to grow, indicating conventional system instability, while in other cases the amplitude grew to a maximum with increasing speed and disappeared at about 3690–3800 rev/min. Thereafter, the system would remain stable up to and including the maximum operating speed of 4000 rev/min. The repeatability of the instability threshold speeds and of the onset speeds of nonsynchronous whirling was found to be fair. On average, both could be reproduced to within about ± 100 rev/min.

With an increase in oil temperature, that is, a reduction in squeeze-film viscosity, it was possible to eliminate the second subsynchronous whirl region and a further temperature increase would result in the disappearance of the first whirl region also, making the system inherently stable by not allowing the journal bearing oil films to exert their full influence. However, the system remained very sensitive to

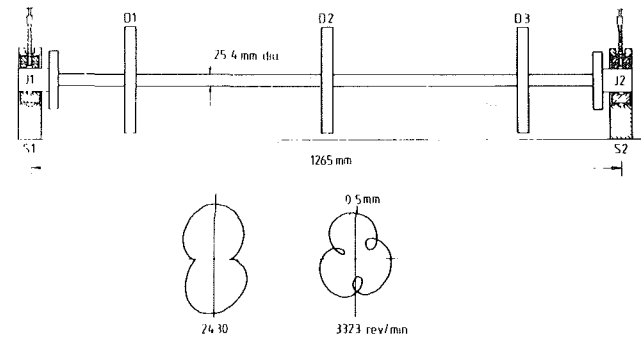


Fig. 5 Flexible rotor on squeeze-film isolators

random transient excitation, such as tapping of the foundation with a rubber hammer, particularly near the first whirl region, and generally appeared to be very lightly damped at all speeds above twice the first critical speed. Variations in oil supply pressure had relatively little influence and the subsynchronous whirling exhibited a hysteresis effect in persisting over a wider speed range once initiated.

Figure 5 shows examples of the subsynchronous whirl orbits in the two whirl regions. The steady-state double and triple loops indicate whirl speeds of exactly 1/3 and 1/4 of the respective rotational speeds. Only at speeds of 2430 and 3323 rev/min (corresponding to roughly three times and four times the first critical speed) were the orbits stationary. Subsynchronous whirling was never found to reappear as a result of reduction in the bearing support damping from about 1×10^4 Ns/m down to the minimum value of about 200 Ns/m.

Since the flexible element of a squeeze-film isolator is usually quite soft it may not always be possible to assume circular concentric orbits of vibration of the rotor center when subjected to unbalance forces. If, however, any vibrations may be assumed to have amplitudes less than about 1/3 of the radial clearance (a reasonable assumption in many practical situations) then linear damping coefficients [6, 7] may be assigned to the squeeze film and used in the linear analysis of rotor-bearing systems. For any larger vibrations, quasi-linear (amplitude dependent) coefficients may be specified [6] and again used in linear analyses, albeit in an iterative fashion.

The Squeeze-Film Damper as a Series Element in a Bearing Housing

In this application there is no attempt by the designer to reduce to lower values the natural frequencies of the overall system, as the rotor often runs supercritically anyway (that is, well above its two rigid-body bounce modes in the case of many aeroengines). The purpose of the squeeze film is simply to introduce damping so that the rotor can safely negotiate those bounce modes and operate smoothly at a higher speed. However, the amount of damping can be quite critical. If it is too little, excessive movement will take place within the squeeze-film annulus, if too great the damper will act like a rigid link, making its presence superfluous. Now, a squeeze-film damper is in effect a journal bearing in which the inner member does *not* rotate. Hence, it is not possible to assign to it any linear stiffness coefficients which might allow the oil film to take any gravity or other static load, since such coefficients are directly dependent on journal speed. Any lift emanates instead from nonlinear effects. For certain operating conditions, such as in the regions of critical speeds, where any static load is small compared to the dynamic load, circular concentric orbits could possibly be assumed [8], with the result that quasi-linear, amplitude-dependent coefficients could be used. Linear analyses could thus be carried out to obtain the vibration orbits in an iterative fashion. Transmitted forces could then be computed.

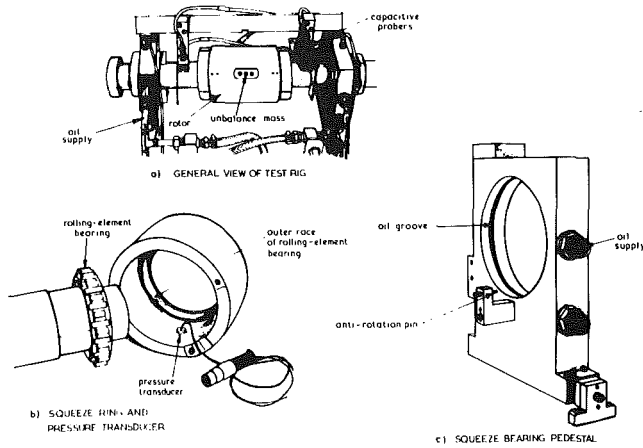


Fig. 6 Experimental rotor and damper

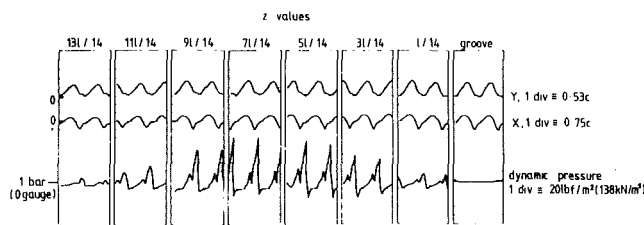


Fig. 7(a) Measured squeeze-film pressures

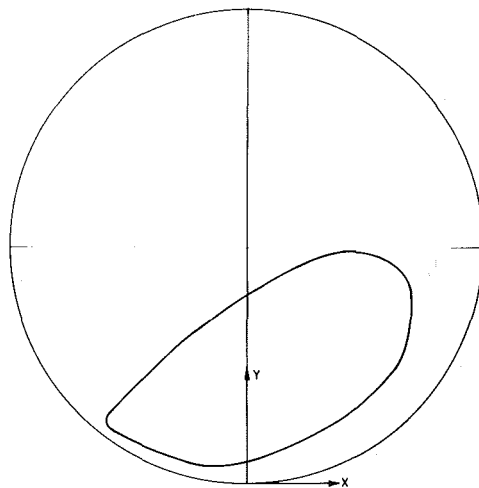


Fig. 7(b) Measured orbit of vibration

For cases where the static load is not small, a nonlinear analysis is called for. This requires a specification of the effect of cavitation which has a profound influence on both the static and the dynamic load-carrying capacity. For example, an uncavitated film may be shown to lead to the complete elimination of load-carrying capacity.

In order to investigate closely the performance of the squeeze-film damper in this kind of application, an experimental rigid rotor (Fig. 6(a)) was designed and built to simulate a small gas turbine running at speeds up to 4000 rev/min in rolling-element bearings mounted in squeeze rings (Fig. 6(b), which in turn were slipped into rigid housings, the annular gaps constituting the squeeze-film dampers. These dampers were provided with a central circumferential groove (Fig. 6(c) and supplied with oil at a pressure of about 2 lbf/in² (13.8 kN/m²). Each land on either side of the groove was of diameter 127 mm and length 10.9 mm, giving a gravity load per land of 10 lbf/in² (69 kN/m²). The radial clearance of each squeeze-film was 0.2082 mm. The purpose of the test rig was to study the orbits of vibration resulting from various degrees of mass unbalance, and a set of nondimensional

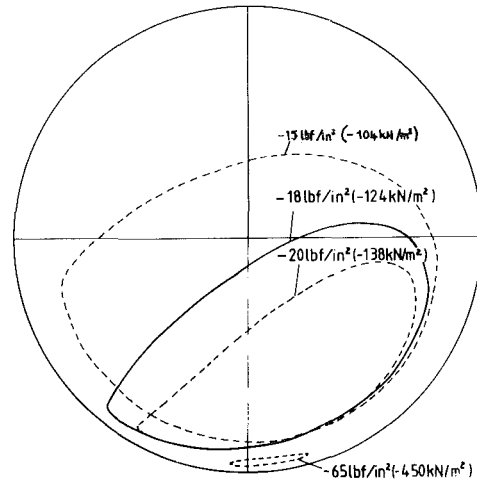


Fig. 8 Predicted orbits of vibration

groups was defined which governed the performance of the dampers. These groups are the nondimensional static load, the nondimensional dynamic load, and the nondimensional viscosity and are, respectively,

$$Q = P/mc\omega^2$$

$$Q_c = P_c/mc\omega^2 = u/c$$

and

$$\beta = \eta R I^3 / m\omega c^3$$

For values of these parameters of 0.68, 1.31, and 0.12, respectively, the resulting pressures measured by a pressure transducer (Fig. 6(b)), at various axial points along the base of the damper are shown in Fig. 7(a). The corresponding measured orbit of unbalance vibration is shown in Fig. 7(b).

An interesting feature of these pressure recordings is the presence of "tension spikes" in the negative pressure regions, followed by recovery to zero absolute pressure. Tensile stresses in oil have been investigated by workers (e.g., [9]) in the field of conventional journal bearings and in squeeze films trapped between flat plates [10].

With a view to obtaining reliable predictions of vibration orbits, the so-called short-bearing approximation was employed to obtain the full pressure distribution in axial and circumferential directions in the squeeze film. This pressure distribution was then curtailed at a prescribed negative value and integrated to obtain the squeeze film forces. These forces were used in a solution of the dynamical equations to obtain the orbits of vibration.

Figure 8 shows the predicted orbit of vibration of the rotor center. The negative pressure limit set was -18 lbf/in^2 (-124 kN/m^2), as obtained from the experimental recordings and used as an average value to account for the presence of the tension spike. As a result, the predicted orbit resembles fairly closely the experimental orbit of Fig. 7(b), particularly in size, disposition, and general height above the base of the clearance circle. This agreement is typical of the many results compared.

The effect of employing different negative pressures in the computations is indicated by the dashed orbits in Fig. 8. In some aeroengine applications the supply pressure can be as high as 50 lbf/in^2 gauge (345 kN/m^2), and the negative hydrodynamic pressure can thus be about -65 lbf/in^2 (-450 kN/m^2) before absolute zero pressure, and hence cavitation, take place in the film, with the resulting orbit shown in Fig. 8.

A further item of interest is the way in which the force transmitted to the engine frame varies throughout one rotor revolution. The transmitted force is the result of the film forces, and may be easily computed. Large vibration orbits

and orbits which feature a pronounced tail should be avoided in practice. In the former, the centrifugal force, and hence the transmitted force, become appreciable, while in the latter the rapid decelerations and accelerations in the vicinity of the tail may lead to sudden large changes in the force transmitted to the engine frame.

Recommendations for Future Research

There is a strong need to represent the parameters of a squeeze-film under noncentric whirling conditions in some sort of quasi-linear fashion for inclusion in programs for the solution of linear, multi degree-of-freedom, rotor-bearing systems.

One method of attack might be as follows. Assume that vibration takes place in the clearance circle of a squeeze-film damper about some mean eccentricity ratio, ϵ_0 . The experience of journal-bearing operation indicates that damping coefficients can be assigned to the squeeze film provided that vibration amplitudes are not more than about 1/3 of the radial clearance. Since the mean eccentricity ratio depends on the value of the nondimensional dynamic force, Q_c , these damping coefficients would also be dependent on dynamic force. Then, following the analogy of a conventional journal bearing, the specification of local stiffness coefficients is called for. Such stiffness coefficients would account for the lift generated by a squeeze film, and being nonlinear, would again depend on the value of the dynamic load causing the vibration. They could perhaps be found from measurements of amplitude and average phase relative to unbalance along mutually perpendicular axes. For given values of β and Q , a tabulation could thus be made of such coefficients against dynamic force for use in linear multidegree-of-freedom programs. Such an empirical procedure might offer a means of assessing the performance of complex machinery employing squeeze-film dampers.

Conclusions

The purpose of this paper has been to elucidate the roles of the squeeze-film damper when used with a parallel flexible element and in series with a bearing housing in turbomachinery applications. Since the damping endowed to the system by this means is strongly nonlinear, such effects as the jump phenomenon and subharmonic response should be guarded against.

The role of cavitation bubbles and of subatmospheric and

negative squeeze-film pressures on the performance of such dampers is very important and should be appreciated at the design stage.

Finally there is a need to be able to represent a squeeze film in terms of quasi-linear stiffness and damping coefficients so that standard linear programs can be used to analyze the performance of multidegree-of-freedom, rotor-bearing systems. In the regions of the system criticals, where vibration orbits are likely to be large and fairly concentric, the task is not too difficult. For other regions, a possible method of attack has been suggested.

Acknowledgments

The author acknowledges with thanks the financial support given for the work described in this paper by the Science and Engineering Research Council, London, and by the Ministry of Defence, London. Thanks are also due to the Council of the Institution of Mechanical Engineers for permission to publish extracts from one of their papers and to British Leyland Ltd. for permission to publish Fig. 1.

References

- 1 Gunter, E. J., Barrett, L. E., and Allaire, P. E., "Design of Nonlinear Squeeze-Film Dampers for Aircraft Engines," *ASME Journal of Lubrication Technology*, Vol. 99, No. 1 Jan. 1977, pp. 57.
- 2 Simandiri, S., and Hahn, E. J., "Experimental Evaluation of the Predicted Behaviour of Squeeze-Film-Bearing-Supported Rigid Rotors," *Journal of Mechanical Engineering Science*, Vol. 21, No. 6, 1979, pp. 439-451.
- 3 Nikolajsen, J. L., and Holmes, R., "Investigation of Squeeze-Film Isolators for the Vibration Control of a Flexible Rotor," *Journal of Mechanical Engineering Science*, 1979.
- 4 Glienicke, J., and Stanski, U., "External Bearing Damping—a Means of Preventing Dangerous Shaft Vibrations in Gas Turbines and Exhaust Turbochargers," *CIMAC Conference*, Barcelona, Jan. 1975, pp. 287-311.
- 5 Gunter, E. J., Barrett, L. E., and Allaire, P. E., "Stabilization of Turbomachinery with Squeeze-Film Dampers—Theory and Applications," Paper No. C233/76, *Proceedings of Inst. Mech. Engrs. Conference on Vibrations in Rotating Machinery*, Cambridge, 1976.
- 6 Holmes, R., "The Damping Characteristics of Vibration Isolators Used in Gas Turbines," *Journal of Mechanical Engineering Science*, Vol. 19, No. 6, 1977, pp. 271-277.
- 7 Tonnesen, J., "Experimental Parametric Study of a Squeeze-Film Bearing," *ASME Journal of Lubrication Technology*, Apr. 1976, pp. 206-213.
- 8 White, D. C., "Squeeze-film journal bearings," Ph.D thesis, Cambridge, 1970.
- 9 Dyer, D., and Reason, B. R., "A Study of Tensile Stresses in a Journal-Bearing Oil Film," *Journal of Mechanical Engineering Science*, Vol. 18, No. 1, Feb. 1976, pp. 46-52.
- 10 Kuroda, S. A., and Hori, Y., "An Experimental Study of Cavitation," *Journal of Japan Soc. Lub. Engrs*, June 1978.

The Elliptic Solution of the Secondary Flow Problem

S. Abdallah

Research Associate,
Applied Research Laboratory,
Pennsylvania State University,
State College, Pa. 16802

A. Hamed

Professor,
Department of Aerospace Engineering and
Applied Mechanics,
University of Cincinnati,
Cincinnati, Ohio 45221
Mem. ASME

This paper presents the elliptic solution of the inviscid incompressible secondary flow in curved passages. The three-dimensional flow field is synthesized between 3 sets of orthogonal nonstream surfaces. The two-dimensional flow field on each set of surfaces is considered to be resulting from a source/sink distribution. The distribution and strength of these sources are dependent on the variation in the flow properties normal to the surfaces. The dependent variables in this formulation are the velocity components, the total pressure, and the main flow vorticity component. The governing equations in terms of these dependent variables are solved on each family of surfaces using the streamlike function formulation. A new mechanism is implemented to exchange information between the solutions on the three family surfaces, resulting into a unique solution. In addition, the boundary conditions for the resulting systems of equations are carefully chosen to insure the existence and uniqueness of the solution. The numerical results obtained for the rotational inviscid flow in a curved duct are discussed and compared with the available experimental data.

Introduction

Three-dimensional flow calculations in turbomachines constitute a complex mathematical problem. The fact that the three velocity components change greatly in passing through a turbomachine limits the two-dimensional approximations to a few special cases. A major contribution in this field is Wu's general theory [1], for the inviscid flow calculations. In this theory the flow field is determined from two-dimensional solutions, which are obtained on two intersecting families of stream filaments with variable thickness. The governing equations are satisfied on the mean surfaces of these stream filaments, which are referred to as the S_1 (blade-to-blade) and the S_2 (meridional) surfaces. The correct solution of one family of surfaces requires some data from the other and, consequently, an iterative process between the solutions on these two families of surfaces is involved. Many investigators have applied Wu's theory to obtain solution on the S_1 or S_2 surfaces. Two techniques have been used in these studies; namely, the matrix method and the streamline curvature method.

Marsh [2], Katsanis [3, 4], Smith [5], Bosman and El-Shaarawi [6], and Biniaris [7], used the matrix method to obtain solutions on the S_1 and S_2 surfaces. Katsanis developed computer programs for a meridional solution [3] and also for solution on a blade-to-blade surface of revolution [4] with a tube thickness proportional to the blade height. In [5] and [6], a representative mass averaged S_2 stream surface is used, and the S_1 surfaces are generated by rotating the streamlines in the S_2 surface about the axis of revolution.

The streamline curvature method has been used by

Wilkinson [8] to obtain blade-to-blade solutions. The same method, has also been used by Novak and Hearsby [9] and by Katsanis [10, 11] to obtain meridional and blade-to-blade solutions. The assumptions and approximations used for the stream surface shape and stream filament thickness distribution in the S_1 and S_2 solution using this method are mainly similar to those discussed previously in connection with the matrix method.

Several problems are encountered in computing a synthesized three-dimensional turbomachine flow field from the solutions on the S_1 and S_2 surfaces. These problems are related to the exchanged information between the two solutions, concerning the stream surface shape and the stream filament thickness. Novak and Hearsby [9] pointed out that the S_2 filament thickness, as calculated from the blade-to-blade solution, is not constant upstream and downstream of the blade row. This is in contradiction with the requirement that the flow must be treated as axisymmetric in these regions. They also discussed the effect of the lean of the S_2 mean stream surface extending upstream and downstream of the blades, where the net angular momentum changes must be zero. Stuart and Hetherington [12] tried to use a technique similar to Wu's in their solution for rotational flow in a 90-deg bend, by synthesizing the three-dimensional flow field through the iterations between two-dimensional solutions. They were unable to reach convergence in the iterative numerical solution and had to abandon this approach. They speculated that the information conveyed between the two solutions was not sufficient to produce convergence.

The assumption that the S_1 stream surface is a body of revolution was common in all applications of Wu's theory in turbomachines [2-12]. This assumption is valid if the flow is irrotational. In general, the S_1 surface is twisted and skewed due to the presence of the secondary velocities. These

Contributed by the Gas Turbine Division of THE AMERICAN SOCIETY OF MECHANICAL ENGINEERS and presented at the 27th International Gas Turbine Conference and Exhibit, London, England, April 18-22, 1982. Manuscript received at ASME Headquarters December 18, 1981. Paper No. 82-GT-242.

transverse velocities exist due to the streamwise vorticity which is generated by the turning of a nonuniform flow with a vorticity component in the curvature plane [13, 14]. The nonuniformities of inlet velocities in turbomachines are associated with the hub and the tip boundary layers. Stream surface warpage pose additional mathematical difficulties in the solution of the rotational flow. Fagan [15] could not obtain a solution for highly rotational flow in curved ducts using Wu's approach. He resolved the problems encountered when the stream surfaces warpage approaches 90 deg through using a corkscrew coordinate system that operates at a specified angular rate.

In reference [16], Abdallah and Hamed developed an effective method for the solution of three-dimensional rotational flow in curved ducts, in which the throughflow velocity and vorticity components were computed using a marching technique in the main flow direction. This led to a very efficient numerical solution whose results compared favorably with the experimental data for duct flows. However, because of the marching technique used in computing the through flow velocity, the influence of the downstream conditions on the flow characteristics is not modeled. This effect, although not significant in duct flow, may be quite important in turbomachinery applications. Barber and Langston [17] contrasted the blade row and duct flow problems and discussed the importance of the elliptic solution to the flow in blade rows.

This investigation represents an elliptic solution for the internal nonviscous incompressible rotational flow in curved passages. The streamlike function method, which was developed by the authors [18] for the efficient numerical solution of the continuity and rotationality equations is implemented in the present problem formulation. The dependent variables in this formulation are the three streamlike functions, the total pressure, and the throughflow vorticity component. The equations of motion are satisfied on three arbitrary sets of orthogonal surfaces. On these surfaces, two-dimensional Poisson equations are derived, for the streamlike functions, with source terms representing the flow three-dimensionality. The source terms are dependent upon the variation of the flow properties in the direction normal to these surfaces. Because of the dependency of the solution on each set of surfaces on the solutions for the remaining two sets of surfaces, an iterative process is involved in the solution. The three flow velocity components are determined by the source terms and the three streamlike function derivatives. The total pressure and through flow vorticity are computed from Bernoulli and Helmholtz equations, respectively.

The initial and boundary conditions for a closed system of equations are carefully chosen to insure the existence and uniqueness of the solution. The no-flux condition at the solid boundaries leads to Dirichlet boundary conditions for the

streamlike functions. Downstream, the derivatives of the flow properties in the throughflow direction is set to zero. A Poisson type equation with Neumann boundary conditions is derived and solved for the static pressure at the inlet plane, which is then used together with the inlet velocity profile to determine the inlet total pressure profile.

Numerical results are obtained for the case of rotational flow in a curved duct with rectangular cross sections. The results are discussed and compared with the experimental data.

Mathematical Formulation

For simplicity and to be able to compare with existing experimental results in ducts [19], the cylindrical polar coordinates are used in the following presentation. The basic equations for nonviscous incompressible flow are expressed in terms of the three velocity components, the total pressure and the throughflow vorticity components as follows:

Conservation of mass

$$\frac{1}{r} \frac{\partial}{\partial r} (ru) + \frac{1}{r} \frac{\partial v}{\partial \theta} + \frac{\partial w}{\partial z} = 0 \quad (1)$$

Conservation of momentum in r -direction

$$v \left[\frac{\partial v}{\partial r} + \frac{v}{r} - \frac{1}{r} \frac{\partial u}{\partial \theta} \right] - w\xi = \frac{\partial P}{\partial r} \quad (2)$$

Conservation of momentum in z -direction

$$u\xi - v \left[\frac{1}{r} \frac{\partial w}{\partial \theta} - \frac{\partial v}{\partial z} \right] = \frac{\partial P}{\partial z} \quad (3)$$

where P is the total pressure divided by the density, and (u, v, w) are the three velocity components in (r, θ, z) -directions. The throughflow vorticity component, ξ , can be written in terms of the cross velocities, u and w , as follows

$$\xi = \frac{\partial u}{\partial z} - \frac{\partial w}{\partial r} \quad (4)$$

Bernoulli's Equation.

Bernoulli's equation is used instead of the momentum equation in the θ -direction.

$$u \frac{\partial P}{\partial r} + \frac{v}{r} \frac{\partial P}{\partial \theta} + w \frac{\partial P}{\partial z} = 0. \quad (5)$$

Helmholtz Equation.

$$u \frac{\partial \xi}{\partial r} + \frac{v}{r} \frac{\partial \xi}{\partial \theta} + w \frac{\partial \xi}{\partial z} = \eta \frac{\partial v}{\partial r} + \frac{\xi}{r} \frac{\partial v}{\partial \theta} + \zeta \frac{\partial v}{\partial z} + \frac{1}{r} (u\xi - v\eta) \quad (6)$$

Nomenclature

A = duct cross-sectional area
 C = contour enclosing A
 dC = incremental distance along C
 n = outward normal to the contour, C
 P = total pressure divided by the density
 P_s = inlet static pressure divided by the density
 (r, θ, z) = cylindrical polar coordinates

r_1, z_1 = arbitrary integration reference points on the r - and z -coordinates, respectively
 S_1, S_2 = blade-to-blade and meridional stream surfaces, respectively
 (u, v, w) = velocity components in (r, θ, z) directions, respectively
 χ = streamlike function
 ξ = main flow vorticity

component in θ -direction
 $(\Delta r, \Delta \theta, \Delta z)$ = space increments in (r, θ, z) directions

Subscripts

h = horizontal surfaces
 I = inlet conditions
 v = vertical surfaces
 c = cross-sectional surfaces

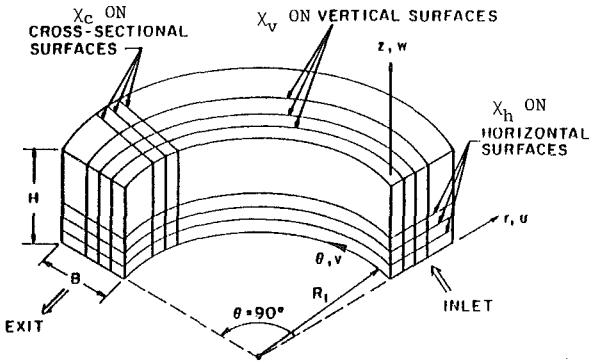


Fig. 1 Schematic of the curved duct showing the three sets of orthogonal surfaces and the corresponding streamlike functions

where

$$\eta = \frac{1}{r} \frac{\partial w}{\partial \theta} - \frac{\partial v}{\partial z}$$

and

$$\zeta = \frac{\partial v}{\partial r} + \frac{v}{r} - \frac{1}{r} \frac{\partial w}{\partial \theta}$$

The governing equations (1-4) are satisfied on three families of orthogonal surfaces, c , h and v , as shown in Fig. 1. The combined elliptic solutions on these surfaces provide the three velocity components, u , v and w , whereas the hyperbolic equations (5) and (6) are solved for P and ξ , respectively.

The streamlike function formulation, developed by the authors [18] is utilized in the present problem for the purpose of obtaining an economical numerical solution to equations (1-4). Three separate streamlike functions, χ_h , χ_v , and χ_c , are defined for the three sets of orthogonal surfaces shown in Fig. 1, to identically satisfy the principle of conservation of mass, given by equation (1).

The streamlike function, χ_h , is defined on the horizontal surfaces as follows

$$\frac{1}{r} \frac{\partial \chi_h}{\partial \theta} = u_h + \frac{1}{r} \int_{r_1}^r r \frac{\partial w_v}{\partial z} dr \quad (7a)$$

$$\frac{\partial \chi_h}{\partial r} = -v_h \quad (7b)$$

where r_1 is the radial coordinate of an arbitrary integration reference surface, and the subscripts h and v refer to the solutions on the horizontal and vertical surfaces, respectively.

The streamlike function, χ_v , is defined on the vertical surface as follows

$$\frac{1}{r} \frac{\partial \chi_v}{\partial \theta} = -w_v - \int_{z_1}^z \frac{1}{r} \frac{\partial}{\partial r} (ru_h) dz \quad (8a)$$

$$\frac{\partial \chi_v}{\partial z} = v_v \quad (8b)$$

where z_1 is the axial coordinate of an arbitrary integration reference surface.

The streamlike function, χ_c , is defined on the cross planes as follows

$$\frac{\partial \chi_c}{\partial z} = -u_c + \frac{1}{r} \int_{r_1}^r r \frac{\partial w_v}{\partial z} dr \quad (9a)$$

$$\frac{\partial \chi_c}{\partial r} + \frac{\chi_c}{r} = w_c - \int_{z_1}^z \frac{1}{r} \frac{\partial}{\partial r} (ru_h) dz \quad (9b)$$

where the subscript, c , refers to the solution on the cross-sectional surfaces.

The governing equations for these stream functions are obtained by substituting equations (7a,b) into equation (2),

equations (8a,b) into equation (3) and equations (8a,b) into equation (4), leading to the following equations

$$\begin{aligned} \frac{\partial^2 \chi_h}{\partial r^2} + \frac{1}{r} \frac{\partial \chi_h}{\partial r} + \frac{1}{r^2} \frac{\partial^2 \chi_h}{\partial \theta^2} \\ = - \left[w\xi + \frac{\partial P}{\partial r} \right] / v + \frac{1}{r} \frac{\partial}{\partial \theta} \int_{r_1}^r r \frac{\partial w_v}{\partial z} dr \\ + \left[\frac{\partial v_v}{\partial r} + \frac{v_v}{r} - \frac{1}{r} \frac{\partial u_c}{\partial \theta} \right] \end{aligned} \quad (10)$$

$$\begin{aligned} \frac{\partial^2 \chi_v}{\partial z^2} + \frac{1}{r^2} \frac{\partial^2 \chi_v}{\partial \theta^2} \\ = - \left[u\xi - \frac{\partial P}{\partial z} \right] / v - \frac{1}{r} \frac{\partial}{\partial \theta} \int_{z_1}^z \frac{1}{r} \frac{\partial}{\partial r} (ru_h) dz \\ + \left[\frac{1}{r} \frac{\partial w_c}{\partial \theta} - \frac{\partial v_h}{\partial z} \right] \end{aligned} \quad (11)$$

$$\begin{aligned} \frac{\partial^2 \chi_c}{\partial r^2} + \frac{1}{r} \frac{\partial \chi_c}{\partial r} - \frac{\chi_c}{r^2} + \frac{\partial^2 \chi_c}{\partial z^2} \\ = - \xi + \frac{1}{r} \frac{\partial}{\partial z} \int_{r_1}^r r \frac{\partial w_v}{\partial z} dr \\ - \frac{\partial}{\partial r} \int_{z_1}^z \frac{1}{r} \frac{\partial}{\partial r} (ru_h) dz + \left[\frac{\partial u_h}{\partial z} - \frac{\partial w_v}{\partial r} \right] \end{aligned} \quad (12)$$

The elliptic equations (10), (11), and (12) are solved on the horizontal, vertical, and cross-sectional surfaces for χ_h , χ_v and χ_c , respectively. The solution on one set of surfaces is influenced by the solutions on the other two sets of surfaces through the source terms. Consequently, an iterative process between the three families of surfaces is involved. The three-dimensional solution is obtained by adding the computed velocity components in each of the solutions as follows

$$u = u_h + u_c \quad (13a)$$

$$v = v_h + v_v \quad (13b)$$

$$w = w_v + w_c \quad (13c)$$

It can be easily shown that the velocity components as determined by equation (13) represent a unique solution.

Boundary Conditions. The inlet conditions for ξ and P are given by

$$\xi = 0 \quad (14)$$

$$P = P_s + \frac{1}{2} v_i^2 \quad (15)$$

where P_s is the inlet static pressure divided by the density. The static pressure distribution at the duct inlet cross section is computed from the numerical solution of the following equation

$$\frac{\partial^2 P_s}{\partial r^2} + \frac{1}{r} \frac{\partial P_s}{\partial r} + \frac{\partial^2 P_s}{\partial z^2} = \sigma \quad (16)$$

where

$$\begin{aligned} \sigma = \frac{\partial}{\partial r} \left[- \frac{v}{r} \frac{\partial u}{\partial \theta} + \frac{v^2}{r} \right] - \frac{\partial}{\partial z} \left[\frac{v}{r} \frac{\partial w}{\partial \theta} \right] \\ + \frac{1}{r} \left(\frac{v^2}{r} - \frac{v}{r} \frac{\partial u}{\partial \theta} \right) \end{aligned}$$

With the following boundary conditions

$$\frac{\partial P_s}{\partial r} = \frac{v^2}{r} \quad \text{at} \quad r = R_i, R_o \quad (17a)$$

$$\frac{\partial P_s}{\partial z} = 0 \quad \text{at } z=0, H \quad (17b)$$

The existence and uniqueness of the solution to equation (16), with the boundary conditions (17a) and (17b), requires the satisfaction of the following condition

$$\iint_A \sigma r dr dz = \int_C r \frac{\partial P_s}{\partial n} dC \quad (18)$$

where A is the duct inlet cross-sectional area, n is the outward normal to the contour, C , enclosing the area, A , and dC is the incremental distance along C . The derivation of Poisson's equation (16) is based on satisfying the continuity equation at the inlet plane, and its solution is unique within an arbitrary constant.

In addition, Bernoulli and Helmholtz equations take the following forms at the duct boundaries

$$\frac{v}{r} \frac{\partial P}{\partial \theta} + w \frac{\partial P}{\partial z} = 0 \quad \text{at } r=R_i, R_o, \quad (19a)$$

$$u \frac{\partial P}{\partial r} + \frac{v}{r} \frac{\partial P}{\partial \theta} = 0 \quad \text{at } z=0, H \quad (19b)$$

$$\begin{aligned} \frac{v}{r} \frac{\partial \xi}{\partial \theta} + w \frac{\partial \xi}{\partial z} &= \frac{1}{r} \frac{\partial w}{\partial \theta} \frac{\partial v}{\partial r} + \frac{\xi}{r} \frac{\partial v}{\partial \theta} + \frac{v}{r} \frac{\partial v}{\partial z} \\ &- \frac{1}{r} v \left[\frac{1}{r} \frac{\partial w}{\partial \theta} - \frac{\partial v}{\partial z} \right] \quad \text{at } r=R_i, R_o \end{aligned} \quad (20a)$$

and

$$\begin{aligned} u \frac{\partial \xi}{\partial r} + \frac{v}{r} \frac{\partial \xi}{\partial \theta} &= \frac{\xi}{r} \frac{\partial v}{\partial \theta} - \frac{1}{r} \frac{\partial u}{\partial \theta} \frac{\partial v}{\partial z} + \frac{1}{r} \left[u\xi + 2v \frac{\partial v}{\partial z} \right] \\ &\quad \text{at } z=0, H \end{aligned} \quad (20b)$$

The corner values for P and ξ are calculated using a stable extrapolation process, similar to the method used in [16].

The Boundary Conditions for the Streamlike Functions.

The following inlet and exit flow conditions for the flow velocities as well as the no-flux condition at the duct boundaries, are used to determine the boundary conditions for the three streamlike functions

At inlet

$$u=0 \quad (21a)$$

$$v=v_I \quad (21b)$$

$$w=0 \quad (21c)$$

At $r=R_i, R_o$

$$u=0 \quad (22)$$

At $z=0, H$

$$w=0 \quad (23)$$

At exit

$$\frac{1}{r} \frac{\partial u}{\partial \theta} = 0 \quad (24a)$$

$$\frac{1}{r} \frac{\partial w}{\partial \theta} = 0 \quad (24b)$$

$$\frac{1}{r} \frac{\partial v}{\partial \theta} = 0 \quad (24c)$$

In addition, the following condition is used to uniquely determine χ_h, χ_c , and χ_v :

$$\frac{\partial \chi_v}{\partial r} + \frac{\chi_v}{r} + \frac{1}{r} \frac{\partial \chi_c}{\partial \theta} + \frac{\partial \chi_h}{\partial z} = 0 \quad (25)$$

Equations (21-25) are used together with equations (7-9)

and equations (13), to obtain the following boundary conditions for χ_v, χ_c , and χ_h . The integration reference surfaces for the integrals in equations (7-9) are chosen here to be represented by $r_1 = R_i$ and $z_1 = 0$, respectively.

At inlet

$$\chi_v = 0 \quad (26a)$$

$$\chi_h = - \int_{R_i}^r v_I dr \quad (26b)$$

$$\frac{1}{r} \frac{\partial \chi_c}{\partial \theta} = \frac{\partial}{\partial z} \int_{R_i}^r v_I dr \quad (26c)$$

At $r=R_i$

$$\chi_h = 0 \quad (27a)$$

$$\chi_c = 0 \quad (27b)$$

$$\frac{\partial \chi_v}{\partial r} + \frac{\chi_v}{r} = 0 \quad (27c)$$

At $r=R_o$

$$\chi_h = - \int_{R_i}^{R_o} v_I dr \quad (28a)$$

$$\chi_c = 0 \quad (28b)$$

$$\frac{\partial \chi_v}{\partial r} + \frac{\chi_v}{r} = \frac{\partial}{\partial z} \int_{R_i}^{R_o} v_I dr \quad (28c)$$

At $z=0, H$

$$\chi_v = 0 \quad (29a)$$

$$\chi_c = 0 \quad (29b)$$

$$\frac{\partial \chi_h}{\partial z} = 0 \quad (29c)$$

At exit

$$\frac{1}{r} \frac{\partial \chi_h}{\partial \theta} = 0 \quad (30a)$$

$$\frac{1}{r} \frac{\partial \chi_c}{\partial \theta} = 0 \quad (30b)$$

$$\frac{1}{r} \frac{\partial \chi_v}{\partial \theta} = 0 \quad (30c)$$

The governing equations (5), (6), (10), (11) and (12) with the conditions given by equations (14), (15), and (26-30) form a closed system which is solved for the variables $\chi_h, \chi_c, \chi_v, \xi$, and P .

Results and Discussions

The results of the computations of the secondary flow in curved ducts caused by total pressure inlet distortion are presented. The iterative solution procedure is based on the use of successive over relaxation method for the solution of the three streamlike function equations, and Lax's [20] marching scheme for the total pressure and through flow vorticity equations. The results are presented and compared with the experimental measurements of Joy [19] for the flow in a curved duct with constant curvature and rectangular cross section. Joy [19] obtained flow measurements in a curved rectangular duct of 0.125×0.25 -m (5×10 -in.) cross section, 0.375 -m (15-in.) mean radius, and 90 deg turning angle. A large velocity gradient was produced in the experiment using screens placed before the curved portion of the duct, which resulted in a nearly symmetrical velocity profile at inlet to the bend. The velocity contours in the lower half of the duct are shown in Fig. 2. The computations were carried out in the lower half of the duct to take advantage of the symmetry. The

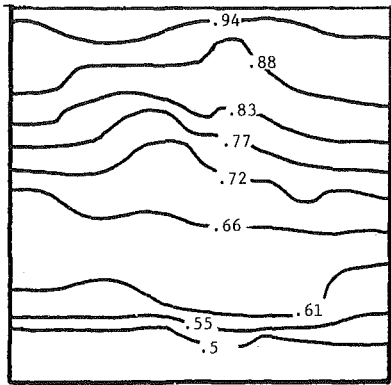
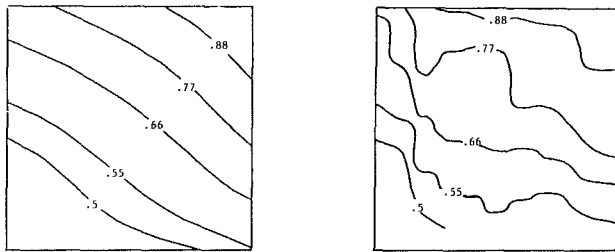


Fig. 2 Inlet velocity profile, experimental data, [19]

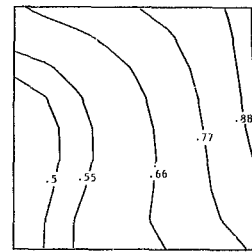


(a) Computed results

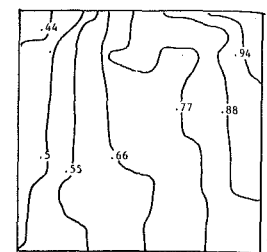
(b) Experimental data [19]

Fig. 3 Velocity contours at $\theta = 30$ deg

results of the computations are compared with Joy's flow measurements at 30, 60, and 90 deg turning angles. The magnitudes of the flow velocities in Figs. 2-5 are normalized with respect to the maximum inlet velocity. It can be seen from these figures that the computed results are in good agreement with the experimental measurements at the 30 and 90 deg turning angles. There is a lack of agreement however with the experimental results at the 60 deg turning angle inner wall near the duct centerline. Other investigators [12, 15] comparing with the same experimental results speculated viscous boundary layer separation there and attributed the lack of agreement to it. The analysis otherwise predicts the measured contour rotation caused by the secondary flow development. The computed static pressure contours at 0, 30, 60 and 90 deg turning angles are presented in Figs. 6. These contours show that the static pressure is not constant over the cross sections even at zero duct turning angle. The static pressure gradient in the radial direction is necessary to balance the centrifugal forces. Joy [19] did not obtain static pressure measurements that could be compared with the present results; however, static pressure contours similar to those of Fig. 6a, were measured by Brunn [20] in a curved duct at zero turning angles. The effect of the secondary flow development on the pressure distribution is demonstrated in these figures by the variation in the shape of the contours with the duct turning angle. The computations were carried out using a uniform ($9 \times 9 \times 31$) grid in the r -, z -, and θ -directions, respectively. The convergence of the iterative procedure was very fast, as shown in Fig. 7, which presents the average of the absolute value of the error in the calculation of u_h , the through velocity component from the χ_h solution. The exchange of information from the solutions on the vertical and cross-sectional surfaces to this surface does not start until the second iteration, which leads to maximum error that consequently decreases very rapidly. The solution was obtained using double precision with 50 outer iterations and 120 iterations in the solution of the differential equations for χ_o , χ_h , and χ_c on all 49 surfaces and required 4.5 min on AM-DAHL 370. The authors have not attempted to optimize the

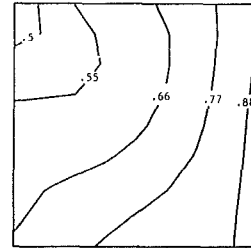


(a) Computed results

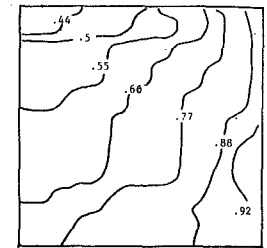


(b) Experimental data [19]

Fig. 4 Velocity contours at $\theta = 60$ deg

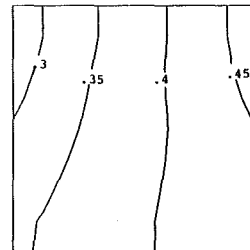


(a) Computed results

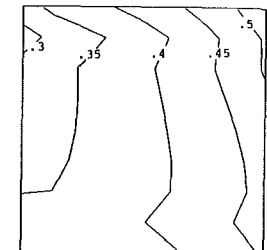


(b) Experimental data [19]

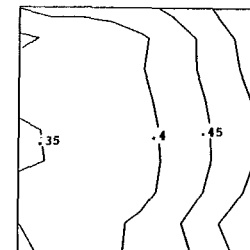
Fig. 5 Velocity contours at $\theta = 90$ deg



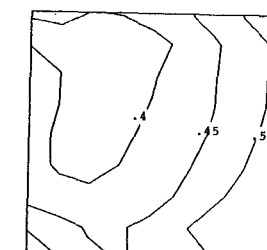
$\theta = 0$



$\theta = 30^\circ$



$\theta = 60^\circ$



$\theta = 90^\circ$

Fig. 6 Static pressure coefficient contours at $\theta = 0, 30, 60$ and 90 deg

CPU time through changing the number of iterations in the solution of Poisson's equations with the outer iteration cycles, or to reduce the CPU time through the use of noniterative methods [21, 22] in the code. At present, direct Poisson solvers codes are being studied for incorporation into the numerical solution. This is expected to lead to considerable CPU time savings when it is combined with the streamlike function formulation and its corresponding Dirichlet boundary conditions.

Conclusions

It can be concluded that the present analysis can predict the inviscid secondary flow development caused by inlet total pressure distortion and the results of the computations compare with the experimental measurements. Through the elliptic solution, the influence of the downstream conditions

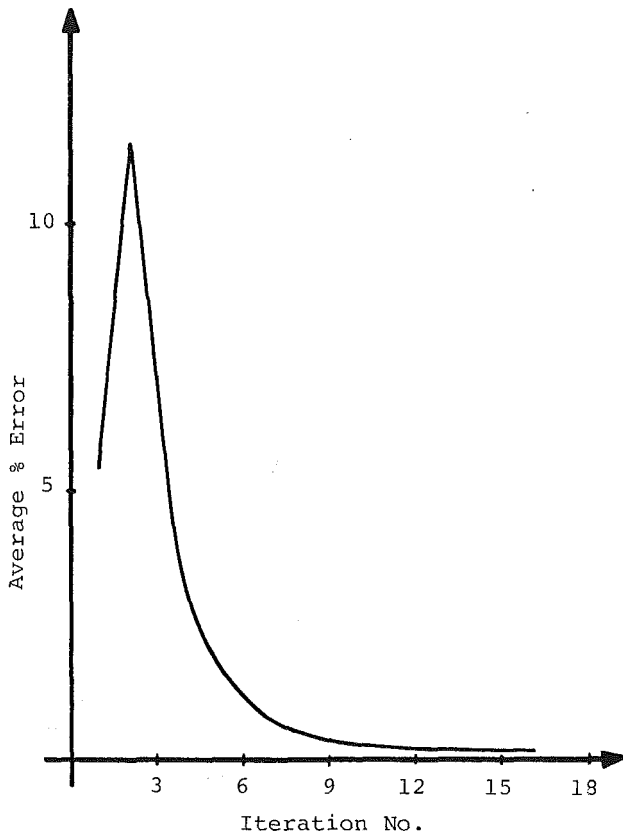


Fig. 7 Typical error variation for u_h solutions

on the flow is included. The solution is very efficient due to the use of the streamlike function in the formulation. In addition, convergence is very fast because of the interaction mechanism between the three solutions on the three sets of orthogonal surfaces.

Acknowledgment

This research was sponsored by the U.S. Air Force Office of Scientific Research under contract No. 80-0242.

References

- 1 Wu, C. H., "A General Theory of Three Dimensional Flow in Subsonic and Supersonic Turbomachines of Axial, Radial and Mixed-Flow Types," NACA TN-2604, 1952.
- 2 Marsh, H., "A Digital Computer Program for the Through Flow Fluid

Mechanics in an Arbitrary Turbomachine Using a Matrix Method," Aero. Research Council R&M 3509, 1968.

- 3 Katsanis, T., "Revised Fortran Program for Calculating Velocities and Streamlines on the Hub-Shroud Midchannel Stream Surface of an Axial-, Radial- or Mixed-Flow Turbomachine or Annular Duct. I: User's Manual," NASA TND-8430, July 1977.

- 4 Katsanis, T., "Computer Program for Calculating Velocities and Streamlines on a Blade-to-Blade Stream Surface of a Turbo-machine," NASA TND-4525, 1968.

- 5 Smith, D. J. L., "Computer Solutions of Wu's Equations for Compressible Flow Through Turbomachines," NASA SP-304, Fluid Mechanics Acoustics and Design of Turbomachinery, Part I, pp. 43-74, 1974.

- 6 Bosman, C., and El-Shaarawi, M. A. I., "Quasi-Three-Dimensional Numerical Solution of Flow in Turbomachines," ASME Paper No. 76-FE-23, 1976.

- 7 Biniaris, S., "The Calculation of the Quasi-Three-Dimensional Flow in an Axial Gas Turbine," ASME, JOURNAL OF ENGINEERING FOR POWER, Apr. 1975, pp. 283-294.

- 8 Wilkinson, D. H., "Calculation of Blade-to-Blade Flow in Turbomachines by Streamline Curvature," Aeronautical Research Council R&M No. 3704, 1972.

- 9 Novak, R. A., and Hearshy, R. M., "A Nearly Three-Dimensional Intra-blade Computing System for Turbomachinery," ASME, *Journal of Fluids Engineering*, Mar. 1977, pp. 154-166.

- 10 Katsanis, T., "Fortran Program for Calculating Transonic Velocities on a Blade-to-Blade Stream Surface of a Turbomachine," NASA TND-5427, Sept. 1969.

- 11 Katsanis, T., "Use of Arbitrary Quasi-Orthogonals for Calculating Flow Distribution in the Meridional Plane of a Turbomachine," NASA TND-2809, May 1965.

- 12 Stuart, A. R., and Hetherington, R., "The Solution of the Three Variable Duct Flow Equations," *Fluid Mechanics, Acoustics and Design of Turbomachinery*, pt. I, NASA SP-304, 1974, pp. 135-153.

- 13 Hawthorne, W. R., "Secondary Circulation in Fluid Flow," *Proc. Roy. Soc. A*, Vol. 206, 1951, p. 374.

- 14 Squire, H. B., and Winter, K. G., "The Secondary Flow in a Cascade of Airfoils in a Nonuniform Stream," *Journal of Aeronautical Sciences*, Vol. 18, 1951, pp. 247-274.

- 15 Fagan, J. R., "Three-Dimensional Subsonic Duct Flow Analysis," Detroit Diesel Allison, Division of General Motors Corp., EDR7451, 1972.

- 16 Abdallah, S., and Hamed, A., "Inviscid Solution for the Secondary Flow in Curved Ducts," *AIAA Journal*, Vol. 19, Aug. 1981, pp. 993-999.

- 17 Barber, T., and Langston, L. S., "Three-Dimensional Modelling of Cascade Flow," AIAA Paper 79-0047, 1979.

- 18 Hamed, A., and Abdallah, S., "Streamlike Function: A New Concept in Flow Problems Formulation," *Journal of Aircraft*, Vol. 16, No. 12, Dec. 1979, pp. 801-802.

- 19 Joy, W., "Experimental Investigation of Shear Flow in Rectangular Bends," M.S. thesis, Massachusetts Institute of Technology, 1950.

- 20 Lax, P. D., "Weak Solutions of Nonlinear Hyperbolic Equations and Their Numerical Computation," *Communications on Pure and Applied Mathematics*, Vol. 7, 1954, pp. 159-193.

- 21 Brunn, H. H., "An Experimental Investigation of Secondary Flow Losses in Bends with Rectangular Cross Sections," CUED/A-Turbo/TR 95, University of Cambridge, Department of Engineering, 1979.

- 22 Dorr, F. W., "The Direct Solution of the Discrete Poisson Equation on Rectangle," *SIAM Review*, Vol. 12, No. 2, Mar. 1970, pp. 248-263.

- 23 Sweet, R. A., "A Cyclic Reduction Algorithm for Solving Block Tridiagonal Systems of Arbitrary Dimension," *SIAM Journal on Numerical Analysis*, Vol. 14, No. 4, Sept. 1977, pp. 706-720.

A Quasi-Three-Dimensional Finite Element Solution for Steady Compressible Flow Through Turbomachines

A. S. Ücer
Professor.

İ. Yeğen
Instructor.

T. Durmaz
Formerly Research Assistant.
Mechanical Engineering Department,
Middle East Technical University,
Ankara, Turkey

A quasi-three-dimensional solution method is presented for subsonic flows through turbomachines of arbitrary geometry. Principal equations are based on Wu's formulation of flow on blade-to-blade and hub-to-shroud surfaces, modified such that the same hub-to-shroud principal equation is used for all types of stream surfaces. Blade-to-blade surfaces are assumed to be surfaces of revolution. A stream function is used as the field variable. The problem is solved by finite element method. An iterative solution is used to find the quasi-three-dimensional solution. Solutions at hub, tip, and midheight blade-to-blade surfaces are used to construct a mean hub-to-shroud surface and vice versa, until convergence is obtained. Results indicate that the developed technique is satisfactory for predicting the flow through turbomachine blades.

Introduction

In recent years, there has been much computational work on turbomachine internal flows aimed at obtaining three-dimensional solutions. The main interest is to describe the flow pattern in the rotating and stationary highly twisted blade passages of arbitrary shape. This problem was first investigated by Wu [1], where the quasi-three-dimensional flow is obtained by a succession of two-dimensional calculations. The interaction between the blade-to-blade surfaces and the hub-to-shroud surfaces can be of any complexity. Clearly, the solution is always iterative and rapidity of convergence depends on how the interaction between the surfaces is handled. The two solutions have almost always been developed separately. The hub-to-shroud solutions were used for through flow analysis by artificially prescribed surfaces and blade-to-blade solutions served for cascade analysis and design.

An early attempt to approach the three-dimensional solution was made by Katsanis [2]. The method of solution was based on an equation for the velocity gradient along arbitrary quasi-orthogonals. The quasi-three-dimensional solution was obtained by using a single solution for hub-to-shroud mean surface followed by solutions on hub, mean, and tip blade-to-blade surfaces. Later finite difference stream function solutions have also been obtained for hub-to-shroud and blade-to-blade flows by T. Katsanis and W. McNally [3, 4]. Novak and Hearsey [5] applied Novak's streamline curvature method for the solution on blade-to-blade axisymmetric surfaces. They calculated the flow on the blade-to-blade surfaces at three locations and used the resulting in-

formation for the hub-to-shroud solution and concluded that these two steps were enough for an accurate quasi-three-dimensional solution. Bosman and El-Shaarawi [6] proposed a similar quasi-three-dimensional solution using a stream function as the field variable. Their equations were solved by a matrix method. They chose a hub-to-shroud surface generated by defining blade-to-blade, mass-averaged streamlines.

Hirsh and Warzee [7] replaced the hub-to-shroud calculation by the calculation of the flow in the true meridional plane based on the solution of the exact pitch-averaged equations. These equations contain terms which represent the contributions from nonaxisymmetry of the flow. They used a finite element method for the solution. The quasi-three-dimensional interaction is made through the interaction terms in the through flow equation. Their blade-to-blade surfaces were also assumed axisymmetric. Y. Krimerman and D. Adler [8] used the finite element method in solving Wu's original equations. They started with a temporary hub-to-shroud surface defined parallel to the mean surface of the blades with exit directions adjusted to the flow directions at the inlet and outlet. The iterative interaction is started with axisymmetric blade-to-blade and hub-to-shroud surfaces and continued with nonaxisymmetric ones.

In this work the hub-to-shroud stream surface is described with the single equation of Bosman and Marsh [9]. This brings simplicity and uniformity to the hub-to-shroud solutions of different geometries. The blade-to-blade solution is similar to [7] and [8]. Unlike [7], for two-dimensional axisymmetric hub-to-shroud solution the geometry of the surface is obtained by taking it parallel to the mean surface of the blades. This allows to take into account the curvatures of the hub-to-shroud surface in all directions. The throughflow

Contributed by the Gas Turbine Division of THE AMERICAN SOCIETY OF MECHANICAL ENGINEERS and presented at the 27th International Gas Turbine Conference and Exhibit, London, England, April 18-22, 1982. Manuscript received at ASME Headquarters December 22, 1981. Paper No. 82-GT-261.

calculations are performed on such surfaces using the loss and deviation correlations for performance prediction. The quasi-three-dimensional solution is started with the blade-to-blade solutions on the hub, midspan, and the tip at the blades. The geometry of the hub-to-shroud surface and its thickness distribution is obtained at the midstreamline of blade-to-blade solutions. The hub-to-shroud solution is then used to determine the new blade-to-blade surfaces of revolution. The calculation is continued until convergence is reached. In the present quasi-three-dimensional solution the blade-to-blade surfaces of revolutions are obtained by rotating the streamlines around the axis, unlike [7] where the surfaces are located along the finite element boundaries in the meridional plane.

With regard to the numerical technique, the present solution differs entirely from techniques used in [2-6]. The method is similar to the one used in [7]; however, it differs considerably from the solution given by Krimerman and Adler [8], which uses triangular elements. Here, isoparametric elements are used which are more efficient and capable of describing the complicated geometries in a better way. Reference [8] also uses a different technique in locating the upstream and downstream boundaries in which the boundary is moved away from the blades during the iterations until no further change is observed in the flow field.

Since details of the blade-to-blade solution of this work is given elsewhere [10], the throughflow solution and quasi-three-dimensional solution are described in more detail here.

Theoretical Background

The two stream surfaces that have been proposed by C. H. Wu [1], and illustrated in Fig. 1, are used for obtaining the three-dimensional solution. The hub-to-shroud stream surface may be of any shape. Losses may be introduced along the streamlines. The blade-to-blade surface is assumed to be a surface of revolution. A properly defined stream function is used as the field variable in each of the principal equations of the flow on either stream surface.

Hub-to-Shroud Stream Surface. The principal equation on the hub-to-shroud stream surface is obtained in the N -direction shown in Fig. 1, which is normal to \mathbf{W} and tangent to the stream surface, \mathbf{W} being the relative velocity. This allows all types of meridional geometries to be handled by the same equation [9]. The flow is assumed adiabatic but irreversible. The problem may be formulated by using the continuity equation, equation of motion in N -direction, an entropy change (loss model), a geometrical condition, the energy equation, and equation of state.

The resulting principal equation may be formulated in the following form

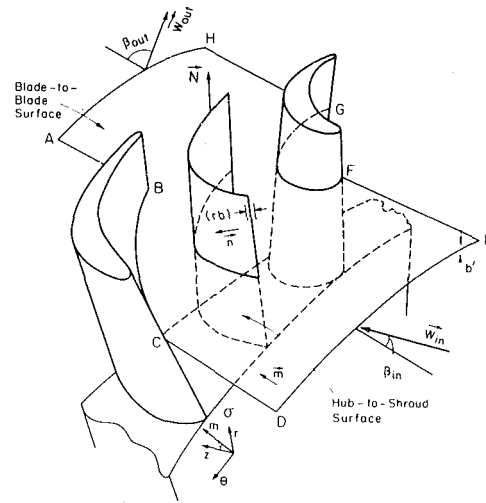


Fig. 1 Solution surfaces

$$\frac{\partial}{\partial r} \left(\frac{1}{\rho r b} \frac{\partial \psi}{\partial r} \right) + \frac{\partial}{\partial z} \left(\frac{1}{\rho r b} \frac{\partial \psi}{\partial z} \right) = \frac{1}{\dot{m}} \left[\frac{\rho r b}{\dot{m}} \frac{\partial I}{\partial \psi} - \frac{T}{w^2} \frac{\partial s}{\partial r} (W_z - W_\theta \tan \mu) + \frac{T}{w^2} \frac{\partial s}{\partial z} (W_r - W_\theta \tan \lambda) + \frac{1}{r} \frac{\partial}{\partial r} (r V_\theta) \tan \mu - \frac{1}{r} \frac{\partial}{\partial z} (r V_\theta) \tan \lambda \right] \quad (1)$$

$\tan \lambda$ and $\tan \mu$ in equation (1) describe the geometry of the stream surface and are defined by

$$\tan \mu = \frac{n_z}{n_\theta}, \quad \tan \lambda = \frac{n_r}{n_\theta} \quad (2)$$

where n_r , n_θ , n_z are the components of the unit normal to the stream surface. The nondimensional stream function, ψ , defined by the relations

$$\dot{m} \frac{\partial \psi}{\partial r} = \rho b r W_z, \quad \dot{m} \frac{\partial \psi}{\partial z} = -\rho b r W_r \quad (3)$$

satisfies the continuity equation along the prescribed stream surface, b , being a factor proportional to the angular thickness of the stream sheet, and, \dot{m} , being the mass flow rate through the stream sheet.

For flow through a stator the relative velocity \mathbf{W} is replaced by the absolute velocity \mathbf{V} .

In adiabatic flow rothalpy, $I = H - \omega(rV_\theta)$, remains constant along a relative streamline through a rotor. Similarly total enthalpy, H , remains constant along an absolute

Nomenclature

b = stream channel thickness of hub-to-shroud surface, rad
 b' = stream channel thickness of blade-to-blade surface, m
 F = load vector
 H = stagnation enthalpy, J/kg
 h = enthalpy, J/kg
 I = rothalpy, J/kg
 K = coefficient matrix
 m = meridional coordinate
 \dot{m} = mass flow rate, kg/s
 N = direction perpendicular to \mathbf{W} and tangent to hub-to-shroud surface

N_i = shape functions
 \mathbf{n} = unit normal vector
 n = number of nodal points in an element
 Q = right-hand side of principal equations
 r = radial coordinate
 S = blade pitch, rad
 S_2 = natural (Neumann) boundary
 s = entropy, J/kgK
 \mathbf{V} = absolute velocity, m/s
 \mathbf{W} = relative velocity, m/s
 w_i = weighting function

β = flow angle in blade-to-blade solution
 ϵ_{\max} = convergence criterion
 Λ = relaxation factor
 λ, μ = angles defining hub-to-shroud surface geometry
 ρ = density, kg/m³
 θ = tangential coordinate
 ψ = stream function
 $\tilde{\psi}$ = approximate solution for ψ
 $\bar{\omega}$ = angular velocity, rad/s
 ζ, ν = arbitrary orthogonal coordinates

streamline in a stator. Any variation of I with ψ represents a rotational inlet flow. The variation of entropy, s , in the radial and axial directions is obtained from the empirical loss models.

For a swirling flow in a duct the flow is assumed completely axisymmetric. The flow is not forced into any stream sheet by the blades and the equations describing the motion become

$$\frac{\partial}{\partial r} \left(\frac{1}{\rho r} \frac{\partial \psi}{\partial r} \right) + \frac{\partial}{\partial z} \left(\frac{1}{\rho r} \frac{\partial \psi}{\partial z} \right) = \frac{1}{\dot{m}} \left\{ \frac{\rho r}{\dot{m}} \frac{\partial H}{\partial \psi} + \frac{T}{W_m^2} \left(V_r \frac{\partial s}{\partial z} - V_z \frac{\partial s}{\partial r} \right) - \frac{V_\theta}{r V_m^2} \left[V_z \frac{\partial}{\partial r} (r V_\theta) - V_r \frac{\partial}{\partial z} (r V_\theta) \right] \right\}; \quad (4)$$

$$\dot{m} \frac{\partial \psi}{\partial r} = \rho r V_z, \quad \dot{m} \frac{\partial \psi}{\partial z} = \rho r V_r, \quad (5)$$

In a duct flow, both rV_θ and H remain constant along a streamline.

For subsonic flows, equations (1) and (4) are elliptic and the boundary conditions must be specified along all the boundaries in order to obtain a solution. Along the hub and tip boundaries where the stream function is specified, Dirichlet type of boundary conditions are applied. At the far upstream and far downstream boundaries of the bladelike surface, the flow may be assumed to be parallel. Taking these boundaries normal to the through flow velocity, Neumann type of boundary conditions are reduced to $\partial\psi/\partial n = 0$, where n is the direction normal to the boundary. At the far upstream boundary either the stream function is specified at the nodes or $\partial\psi/\partial n$ is set to zero. For the downstream boundary, $\partial\psi/\partial n = 0$ always. Any whirl component at the upstream is introduced as the velocity vector is calculated during the iterative solution.

Blade-to-Blade Stream Surface. The blade-to-blade stream surface is assumed to be a surface of revolution. The flow is assumed to be steady with respect to the blades and isentropic. The principal equation is obtained in m, θ coordinate system as

$$\frac{\partial}{\partial \theta} \left(\frac{1}{\rho r^2 b'} \frac{\partial \psi}{\partial \theta} \right) + \frac{\partial}{\partial m} \left(\frac{1}{\rho b'} \frac{\partial \psi}{\partial m} \right) = \frac{\sin \sigma}{\dot{m}} \left(\frac{W_\theta}{r} + 2\omega \right) \quad (6)$$

where m is the meridional coordinate, σ is the angle between z and m directions, and ψ is defined as

$$\dot{m} \frac{\partial \psi}{\partial \theta} = \rho b' r W_m, \quad \dot{m} \frac{\partial \psi}{\partial m} = -\rho b' W_\theta \quad (7)$$

b' is the thickness of the stream sheet normal to θ - and m -directions.

The boundary conditions of the flow on the blade-to-blade surface are of three types. Along the blade surfaces FG and CB shown in Fig. 1, Dirichlet conditions are applied, since the stream function is known. At the upstream and downstream boundaries, DE and AH, the flow is assumed to be uniform and the flow direction is assumed to be known. Therefore, the Neumann conditions are applied as

$$\frac{\partial \psi}{\partial n} \Big|_{DE} = \frac{\tan \beta_{in}}{S r_{in}}, \quad \frac{\partial \psi}{\partial n} \Big|_{AH} = \frac{\tan \beta_{out}}{S r_{out}} \quad (8)$$

where S is the blade pitch in radians. Subscripts "in" and "out" indicate the upstream and downstream boundaries of the solution domain, respectively.

Along the boundaries AB and GH, as well as along CD and FE, a periodic boundary condition which may be expressed as

$$\psi(\theta + S, m) - \psi(\theta, m) = 1.0 \quad (9)$$

is applied.

Method of Solution

Equations (1), (4), and (6) have the following form

$$\frac{\partial}{\partial \xi} \left(K \frac{\partial \psi}{\partial \xi} \right) + \frac{\partial}{\partial \nu} \left(K' \frac{\partial \psi}{\partial \nu} \right) = Q(\xi, \nu, \psi) \quad (10)$$

Equation (10) is nonlinear since K, K' , and Q are dependent on ψ . The equation may be linearized if K, K' , and Q are assumed to be known. The equation is in a quasi-harmonic form, since K and K' vary over the solution domain. An iterative solution of equation (10) is possible in which the distribution of K, K' and the right-hand side of equation (10) are calculated using the known field variable distribution from the previous step of iteration.

Galerkin's weighted residual method is used in order to get the finite element equations. The method does not require a variational statement. The weighted residual formulation of equation (10) over a finite element may be expressed as

$$\int \int_{\Omega^e} \left[\frac{\partial}{\partial \xi} \left(K \frac{\partial \tilde{\psi}}{\partial \xi} \right) + \frac{\partial}{\partial \nu} \left(K' \frac{\partial \tilde{\psi}}{\partial \nu} \right) - Q \right] w_i d\Omega + \int_{S_2^e} \left(q - K \frac{\partial \tilde{\psi}}{\partial \xi} n_\xi - K' \frac{\partial \tilde{\psi}}{\partial \nu} n_\nu \right) w_i dS = 0 \quad (11)$$

$\tilde{\psi}$ is the approximate solution satisfying the integral relationship (11), and w_i is the arbitrary weighting function. Ω^e is the solution domain and S_2^e represents the boundaries where Neumann boundary condition

$$q - K \frac{\partial \psi}{\partial \xi} n_\xi - K' \frac{\partial \psi}{\partial \nu} n_\nu = 0 \quad (12)$$

is applied.

For an element of n nodes the approximate solution is expressed as

$$\tilde{\psi} = \sum_{i=1}^n N_i \psi_i \quad (13)$$

in terms of n nodal values ψ_i and interpolation functions N_i .

Substituting equation (13) in equation (11), and noting that in Galerkin's formulation weighting functions are the same as the interpolation functions, the following system of equations is obtained at the element level

$$\int \int_{\Omega^e} \left[K \frac{\partial \{N\}}{\partial \xi} \frac{\partial \{N\}^T}{\partial \xi} + K' \frac{\partial \{N\}}{\partial \nu} \frac{\partial \{N\}^T}{\partial \nu} \right] d\Omega \{ \psi \} = - \int \int_{\Omega^e} Q \{N\} d\Omega + \int_{S_2^e} \{N\} q dS \quad (14)$$

where the derivatives of the field variable are evaluated as

$$\frac{\partial \tilde{\psi}}{\partial \xi} = \sum_{i=1}^n \frac{\partial N_i}{\partial \xi} \psi_i, \quad \frac{\partial \tilde{\psi}}{\partial \nu} = \sum_{i=1}^n \frac{\partial N_i}{\partial \nu} \psi_i \quad (15)$$

Eight-node, isoparametric, quadrilateral elements are used in this work. Having curved boundaries, these elements have proved to be very efficient in representing complicated boundaries of the solution domain, such as hub, tip, and blade walls. These elements satisfy the requirement of continuity of the field variable at the element interfaces. Use of isoparametric elements requires mapping of the parent square elements into the curved sided real elements using the interpolation functions N_i also as the mapping functions. Biquadratic functions are used for the interpolation functions. Since no closed form integration is possible, a two-dimensional, two-point Gaussian Quadrature method was used to evaluate the integrals in equation (14).

After the assemblage, the boundary conditions are applied in the usual way. The resulting system of equations, which is applicable to the whole solution domain, may be written as

$$[K] \{ \psi \} = \{ F \} \quad (16)$$

The system of equations is essentially nonlinear since $[K]$ and $\{F\}$ show dependence on the field variable ψ . Therefore,

an iterative solution is necessary. For the first iteration $[K]$ is calculated on the assumption that the density is uniform and equal to the inlet density, and the term Q in equation (10) is assumed to be zero. The results are used to calculate $[K]$ and $\{F\}$ of the next step. Thus, a numerical scheme with variable coefficient matrix $[K]$ is used. The solution of equation (16) is performed using the Gauss elimination method.

It was observed that no relaxation factor is required for the blade-to-blade solutions. The convergence is checked using the stream function values of the consecutive iteration steps. The maximum relative change ϵ_{\max} , which is

$$\epsilon_{\max} = \text{Max} \frac{\psi_{n+1} - \psi_n}{\psi_{n+1}} \quad (17)$$

is kept below 0.005 for all blade-to-blade calculations. The solutions converged in two or three iterations for low-speed flows and in three or four iterations for high-speed flows.

For the solution of hub-to-shroud flow, underrelaxation was required. The relaxation factor is introduced, through

$$\psi_{n+1} = \psi_n + \Lambda[\psi'_{n+1} - \psi_n] \quad (18)$$

where ψ'_{n+1} is the solution of equation (16) obtained at iteration $n+1$, while ψ_{n+1} is used to start the next iteration. The best value of the underrelaxation factor shows dependence on the Mach number level of the flow, as well as the geometry of the problem. An example of the effect of relaxation factor is seen in Fig. 2. The maximum absolute Mach number recorded in this flow was 0.89. The underrelaxation factor $\Lambda = 0.15$ has given the best convergence behavior by reducing ϵ_{\max} to 0.001 in 17 iterations. Figure 3 shows the effect of compressibility on the rate of convergence. At low Mach numbers fluctuations of ϵ_{\max} disappear and the solution converges quickly.

Both blade-to-blade, and hub-to-shroud solutions were compared with the existing analytical solutions. A comparison of the blade-to-blade finite element solution with the analytical solution for Gostelow's cascade is given in an earlier paper [10]. It was observed that a finer grid at the leading edge yields considerably more accurate prediction of the flow in this region. Blade-to-blade compressible flow solutions were also compared with the experimental results in the same paper. Hub-to-shroud solution was compared with Batchelor's converging duct solution with Swirl [11]. The discrepancy between the two solutions is within 0.2 percent for the tangential velocity at all points. Number of nodal points was 194, and the convergence was achieved in two iterations with $\epsilon_{\max} = 0.001$.

Through Flow Results with Losses

The hub-to-shroud program is used for solving the throughflow problem of two different axial flow turbines.

The losses are introduced into the solution through the entropy variation terms in the principal equations and the density determination process for the next iteration.

Craig and Cox loss correlations [12] were used for performance prediction. Profile, secondary, and annulus losses were included in the calculation. The losses were introduced into the flow as entropy increase through the stator and rotor blades along the streamlines. Entropy is assumed to be constant along the streamlines in duct regions. Profile and secondary losses were calculated at hub, mid-, and tip sections of the blades and interpolated linearly in radial direction. Annulus loss is evaluated using average exit velocity and kept constant over the blade length. It is assumed that entropy is uniform at the entry to the machine and entropy increase is linearly distributed in the flow direction.

Ainley-Mathieson deviation correlation [13] is used to find the deviation angles. Flow deviations in the rotor and stator blade rows were distributed linearly to the nodes in the axial

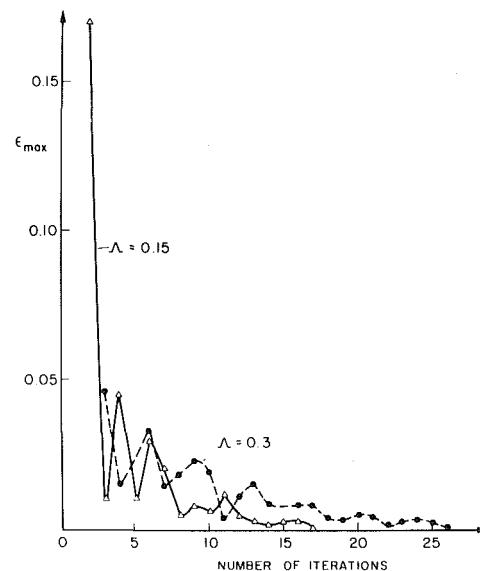


Fig. 2 Influence of relaxation factor on convergence

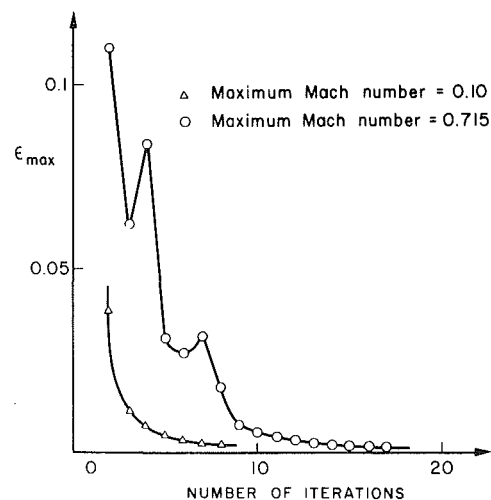


Fig. 3 Influence of Mach number on convergence

direction. The thickness of the stream sheet was calculated on the assumption that the blade blockage is uniform in the θ -direction. Thus, the geometry of the stream sheet was defined for the through flow solution.

The density at any point is determined using the condition that the rothalpy I is constant along a streamline through rotor blades. Total enthalpy is constant along a streamline through the stator blades and through a duct. These conditions, together with the velocity field calculated on the basis of the stream function definition, make it possible to calculate the temperature field. Calculations of the velocities at this stage are performed with the density values from the previous iterative solution. From the entropy distribution discussed above, the entropy-enthalpy diagram is constructed, and the state of the fluid at any point within the flow field is determined. No inner iteration using the new values of density is used. Convergence of density distribution is obtained together with the convergence of stream function distribution.

A low-speed axial flow turbine without any flare is used to test the low-speed capability of the solution method. The mass flow through the turbine is 20.1 kg/s, running at 525 rev/min with inlet stagnation pressure and temperature being 101.3

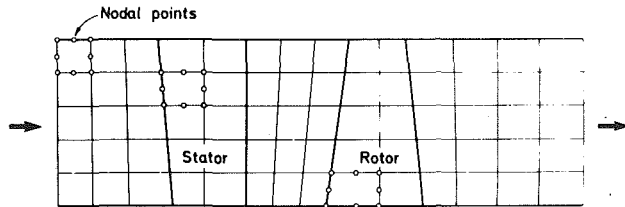


Fig. 4 Cambridge turbine geometry and finite element distribution

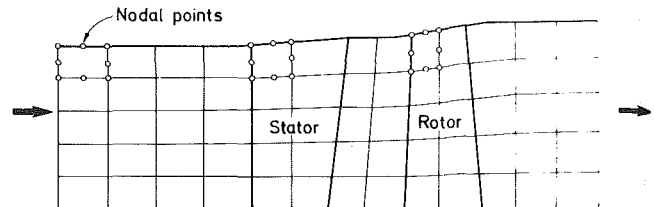


Fig. 7 Hannover turbine geometry and typical finite element distribution

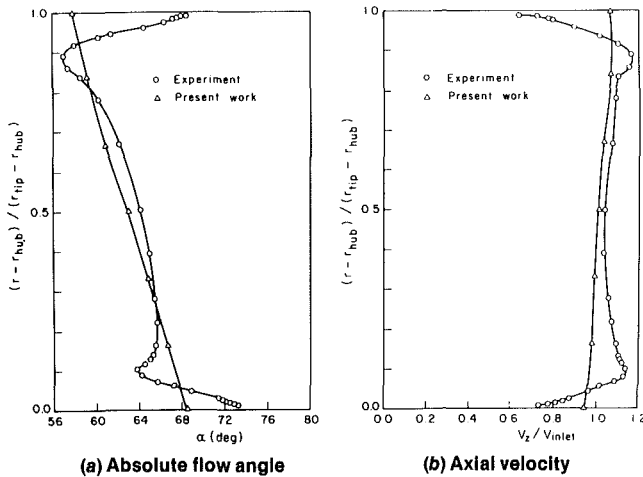


Fig. 5 Flow conditions downstream of Cambridge turbine nozzle

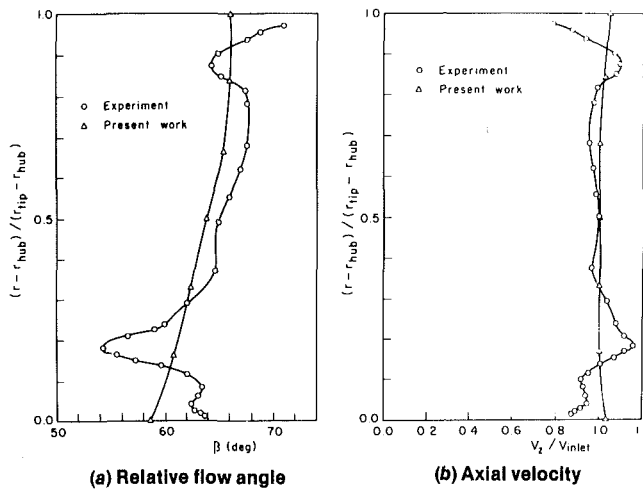


Fig. 6 Flow conditions downstream of Cambridge turbine rotor

kPa/m² and 293 K, respectively. Further details of the turbine may be found in [14]. The solution domain with a typical element distribution of the low-speed turbine is shown in Fig. 4. A grid refinement study has been performed. It is established that using seven elements in the radial direction gives very good results, but comparable results can be obtained also with five elements. It is also established that the solution changes only slightly with the number of elements used in the blade chord direction. However, in order to get more information, two elements are used to describe the blade row.

Variation of the fluid angle and the axial velocity after the nozzle blade row are compared with experimental results in Fig. 5. The results obtained after the rotor blade row are given in Fig. 6. Deviations from the experimental results at the hub

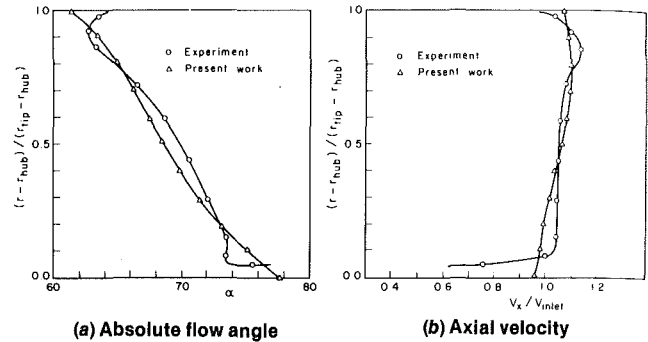


Fig. 8 Flow conditions downstream of Hannover turbine nozzle

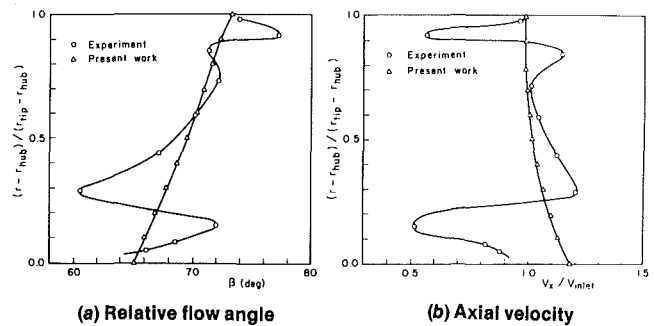


Fig. 9 Flow conditions downstream of Hannover turbine rotor

and tip boundaries are due to the endwall boundary layers and strong secondary flow effects in these regions. In all these calculations six elements are used in the radial direction. The predicted integrated total to total design point efficiency is 92.9 percent compared to the measured efficiency of 93.8 percent.

The geometry and typical element distribution of the second test turbine referred as Hannover turbine [12] is shown in Fig. 7. Near to its design condition, the turbine runs at 7500 rpm. The flow through is 7.8 kg/s, and upstream stagnation pressure and temperature are 125.4 Bar and 358 K, respectively. The calculated fluid angle and axial velocity distribution at the nozzle exit are shown in Fig. 8 in comparison with the experimental results. Corresponding results for the rotor exit are given in Fig. 9. The computed total to total stage efficiency was 93.3 percent whereas the measured efficiency was 90.5 percent. The discrepancy may be attributed to the correlations used which exclude complicated viscous three-dimensional flow phenomena through the flow passages of the highly twisted blades rows.

Quasi-Three-Dimensional Solution

In this solution, isentropic flow was assumed to exist both on blade-to-blade surface of revolution and on hub-to-shroud

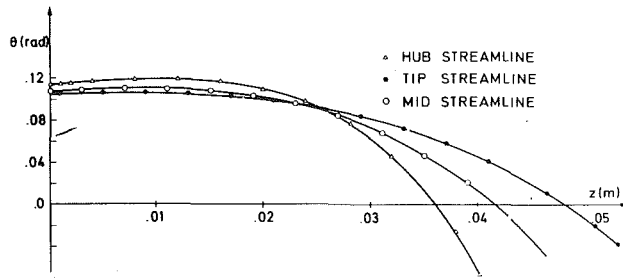


Fig. 10 Geometry of streamlines ($\psi = 1.5$) obtained from blade to blade solutions

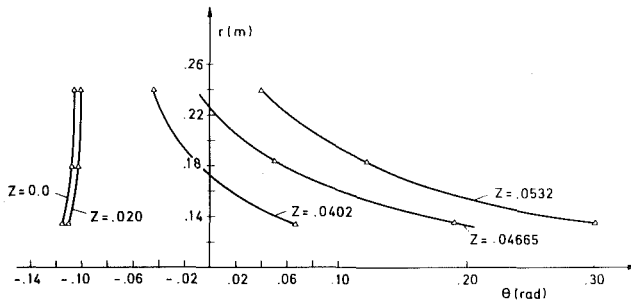


Fig. 11 Intersection of hub to shroud stream surface with Z-planes

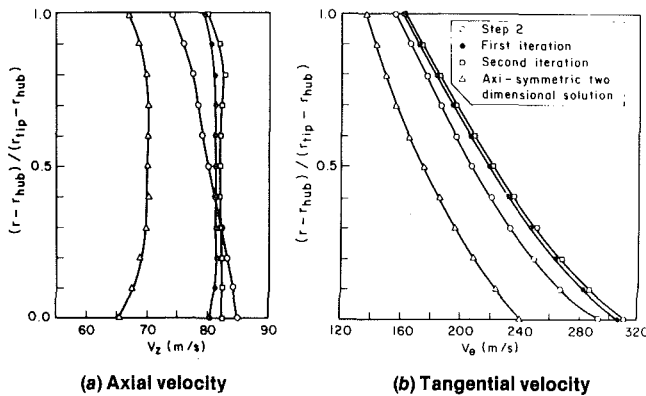


Fig. 12 Flow conditions downstream of the blade row predicted at various stages of iteration

surface. The solution of the flow only through the nozzle blades of the turbine of Fig. 7 was performed.

It is well known that the results obtained from blade-to-blade solutions should be used to construct hub-to-shroud surfaces and vice versa. The steps of the three-dimensional interaction algorithm are explained below.

Step 1. Blade-to-blade principal equation is solved using constant stream sheet thickness. Three blade-to-blade surfaces of revolution are taken: namely, at the hub, midsection, and tip of the blades. The outlet angle, β_{out} , (downstream boundary condition) of the blade-to-blade flow (see Fig. 1) is determined using a surface pressure extrapolation technique. At the condition when the pressure distribution on suction and pressure surfaces extrapolated linearly from 85 percent cord meet at the trailing edge, the corresponding outlet angle value is regarded as correct angle which satisfies the Kutta condition. It was observed that the geometry of the mid-streamline ($\psi = 1.5$) is not sensitive to small changes of the outlet flow angle near its correct value.

Step 2. The distribution of the λ and μ angles defined by equations (2) are calculated using the geometries of the

streamlines $\psi = 1.5$ obtained from the three blade-to-blade solutions. Figure 10 shows the geometries of the $\psi = 1.5$ streamlines of the three blade-to-blade surfaces. The figure is used to calculate the flow angle μ . Figure 11 shows the intersections of the hub-to-shroud surface with constant Z-planes which are used to determine the lean angle λ .

The conservation of mass through a stream tube formed by the intersection of a blade-to-blade stream sheet and a hub-to-shroud stream sheet may be written as

$$\rho W_m r b b' = \rho_1 W_{m1} r_1 b_1 b_1' \quad (19)$$

where the subscript 1 denotes the inlet conditions. Variation of b along the stream tube may be calculated as

$$b = \frac{\rho_1}{\rho} \frac{W_{m1}}{W_m} \frac{r_1}{r} \frac{b_1'}{b'} b_1 \quad (20)$$

The inlet width, b , of the stream tube in the tangential direction is taken as $2\pi/\text{number of blades}$. It can be shown that not the actual values but the relative variations of b and b' over the solution domains are important. Having defined the hub-to-shroud stream sheet, the hub-to-shroud solution is performed. The solution gives the streamline pattern on the meridional plane with the variation of fluid properties in the radial and axial directions.

Step 3. Three streamlines, namely $\psi = 1.1, 1.5$, and 1.9 are chosen for the construction of the blade-to-blade stream surfaces. The stream surfaces are constructed by rotating aforementioned streamlines around the axis of rotation. Variation of the stream sheet thickness b' (m) is calculated using the continuity equation (19) for the meridional flow. The inlet angle β_{in} and the outlet angle β_{out} necessary for the blade-to-blade solution are taken as the fluid angles computed at the upstream and downstream boundaries of the constructed blade-to-blade surface of revolution. The blade-to-blade solutions are then performed on the three stream surfaces considered.

It is now possible to go back to the step 2 and obtain a new hub-to-shroud solution. Iteration between steps 2 and 3 are continued until the results of two successive hub-to-shroud solutions are found to be close enough.

Figure 12 shows the changes in the distributions of the tangential and axial velocities at the exit of the blade row through various stages of iteration. It is clearly seen that the difference between the last two iterations is small, which shows a converging trend. It is established that any further iteration does not improve the results much and gives approximately the same axial and tangential velocity distributions of the second iteration. The results are also compared with the axisymmetric, two-dimensional isentropic solution in Fig. 12. The difference between the two-dimensional and the three dimensional solutions is significant.

Concluding Remarks

A set of computer programs for calculating the flow through turbomachines is presented in this paper. The solution method used in the development of these codes is a finite element technique. The principal equations are solved in their quasi-harmonic form. The convergence behavior of the solutions were found to be very successful. The blade-to-blade program converged almost always in two to three iterations without any relaxation factor. The hub-to-shroud program also has good convergence properties when a relaxation factor between 0.1 and 0.3 is used, the best value of the relaxation factor depending on the geometry and the Mach number level.

It is found that the three-dimensional solution converges rather rapidly to a definite distribution of properties in the blade passage. In the three-dimensional solution the skewed hub-to-shroud stream surface is represented in all details.

However, blade-to-blade surfaces are assumed to be surfaces of revolution which implies that their skewed orientations due to the secondary flows is ignored.

It is established that the loss and deviation correlations used here give good performance prediction with the present solution technique. With regard to the computing time, the blade-to-blade program takes in the order of 1 min on an IBM 370/145 computer when the computation is performed on 100 elements. The hub-to-shroud computations take approximately 3 min for obtaining a convergent solution at low speeds using 72 elements.

Acknowledgments

The members of the Working Group 12 of AGARD PEP and the investigators who had made available their geometrical and experimental data to the Group are gratefully acknowledged. This work is partially supported by the Turkish Scientific and Technical Research Council.

References

- 1 Wu, C. H., "A General Theory of Three Dimensional Flow in Subsonic and Supersonic Turbomachines of Axial, Radial and Mixed Flow Types," U.S. NACA-TN-2604, 1952.
- 2 Katsanis, T., "Use of Arbitrary Quasi-Orthogonals for Calculating Flow Distribution in a Turbomachine," ASME JOURNAL OF ENGINEERING FOR POWER, Vol. 88, No. 2, 1966, pp. 197-202.

3 Katsanis, T., and McNally, W. D., "Fortran Program for Calculating Velocities and Streamlines on the Hub-Shroud Mid-Channel Flow Surface of an Axial or Mixed-Flow Turbomachine," NASA-TN-D-7344, 1974.

4 Katsanis, T., and McNally, W. D., "Revised Fortran Program for Calculating Velocities and Streamlines on a Blade-to-Blade Stream Surface of a Turbomachine," NASA-TN-4525, 1968.

5 Novak, R. A., and Hearsey, R. M., "A Nearly Three-Dimensional In-trablade Computing System for Turbomachinery, Part I and Part II," ASME Paper 76-Fe-19 and 76-Fe-20, 1976.

6 Bosman, C., and El-Shaarawi, M. A. I., "Quasi-Three-Dimensional Numerical Solution of Flow in Turbomachines," ASME Paper 76-Fe-23, 1976.

7 Hirsch, Ch., and Warzee, G., "An Integrated Quasi-3D Finite Element Calculation Program for Turbomachinery Flows," ASME Paper 78-GT-56, 1978.

8 Krimerman, Y., and Adler, D., "The Complete Three-Dimensional Calculation of the Compressible Flow Field in Turbo Impellers," *Journal Mechanical Engineering Science*, Vol. 20, No. 3, 1978, pp. 149-158.

9 Bosman, C., and Marsh, H., "An Improved Method for Calculating the Flow in Turbo-Machines, Including a Consistent Loss Model," *Journal Mechanical Engineering Science*, Vol. 16, No. 1, 1974, pp. 25-31.

10 Üçer, A. S., Yeğen, İ., and Çetinkaya, T., "A Finite Element Solution of Compressible Flow Through Cascades of Turbomachines," *Proceedings of the Second International Conference on Numerical Methods in Laminar and Turbulent Flow*, Venice, July 1981, pp. 789-800.

11 Batchelor, G. K., *An Introduction to Fluid Dynamics*, Cambridge University Press, London, 1967.

12 Craig, H. R. M., and Cox, H. J. A., "Performance Estimation of Axial Flow Turbines," *Proceedings of the Institution of Mechanical Engineers 1970-71*, Vol. 185 32/71, pp. 407-424.

13 Ainley, D. G., and Mathieson, G. C. R., "A Method for Performance Estimation for Axial Flow Turbines," N. G. T. E. Report R.111, 1952.

14 Through Flow Calculations in Turbomachines, NATO-AGARD PEP W. G. 12 Report (AR 175), 1981.

A. B. Palazzolo

Southwest Research Institute,
San Antonio, Texas 78284

Bo Ping Wang

Associate Research Professor.

W. D. Pilkey

Professor.

Department of Mechanical and Aerospace
Engineering,
University of Virginia,
Charlottesville, Va.

Eigensolution Reanalysis of Rotor Dynamic Systems by the Generalized Receptance Method¹

A method is presented for efficiently calculating the damped natural frequencies of complex rotor bearings systems. The procedure is applicable to the repeated reanalysis of rotor systems during the search for an optimal design. The generalized receptances used in the method are calculated with a series of formulas that improves the convergence characteristics when only an incomplete set of modes is available. A nonsynchronous gyroscopic rotor example is examined to illustrate the reanalysis procedure.

1 Introduction

The computation cost of solving for the complex eigenvalues of large rotor dynamic-finite element models may be very high. This is certainly the case when (i) adjusting design parameters to obtain an optimal design, (ii) determining an instability onset condition due to aerodynamic, fluid film bearing or seal cross coupling forces, or (iii) in matching an analytic model with test data. These three objectives usually require many separate analyses, where only a small portion of the total system is altered per analysis. The capability to accurately and efficiently re-solve the free vibration problem for modified rotor-bearing systems may therefore be very important. This paper presents a receptance method for the approximate reanalysis of locally modified rotor models.

Since the excellent paper by Lund [1] much research has been devoted to damped critical speed calculation for flexible rotors, utilizing transfer matrices. Several papers [2, 3] have treated this same problem with finite element or direct stiffness approaches. Unlike the transfer matrix method, the finite element method is not restricted to line-type structural geometries. Specific examples of non-line type rotor bearing systems are (i) a high-speed centrifugal compressor rotor including impeller disk flexibility, and (ii) the rotating assembly of a large turbine-generator set with bearing supports and foundation of arbitrary geometries. The reanalysis approach presented here is directly applicable to general, linear, finite element rotor models.

Lund's recent paper [4] on the sensitivity of critical rotor speeds utilized a first-order eigenvalue-vector perturbation technique. His analysis treats the reanalysis and synthesis of undamped, synchronous gyroscopic rotor bearing systems. Similar perturbation approaches have been proposed by Fox [5], Gupta [6], Crandall [7], and Meirovitch [8]. In contrast, the non-perturbation approach presented in this paper may

incorporate original system modifications of arbitrary magnitude. All modifications are also treated simultaneously. This eliminates the error propagation that occurs in the successive modification method proposed by Hallquist, Pomazal, and Synder [9, 10]. The assumed modes, or Rayleigh Ritz approach, [11] restricts the modified rotor's eigenvectors to the subspace spanned by the eigenvectors of the original rotor model. The resulting condensed set of equations in the modal or generalized coordinates may form a complex matrix-quadratic eigenvalue problem. To avoid this formulation, which may be difficult to solve, the method presented here directly evaluates a form of the modified system's characteristic equation. The method presented extends previous approaches by incorporating the skew symmetric gyroscopic matrix and nonsymmetric damping and stiffness matrices encountered in rotor bearing system analyses.

The order of the modified system is reduced due to the sparsity of the local modifications. This condensation enhances the computational efficiency of the eigenvalue solution procedure. The order of the modified rotor-bearing system, after condensation, equals the number of degrees of freedom directly affected by the modifications.

The generalized receptances in the modified zones of the original system are used in the condensed system solution. These receptances are computed with a formula [12, 13] which combines both spectral and property matrix contributions from the unmodified rotor-bearing system. Receptances are typically computed by using only the eigensolutions (spectral) of the original rotor bearing system. By also utilizing original system property matrix expressions, the accuracy of the receptances, and consequently of the modified system eigenvalues, is shown to increase substantially. The efficiency and accuracy of the method presented is examined by analyzing the 40 deg of freedom, nonsynchronous, gyroscopic rotor model shown in Fig. 1.

2 Reanalysis Formulation

The formation of a base or original analytic system model

¹This work was supported by the U.S. Army Research Office, Research Triangle Park, North Carolina.

Contributed by the Gas Turbine Division of THE AMERICAN SOCIETY OF MECHANICAL ENGINEERS and presented at the 27th International Gas Turbine Conference and Exhibit, London, England, April 18-22, 1982. Manuscript received at ASME Headquarters December 22, 1981. Paper No. 82-GT-262.

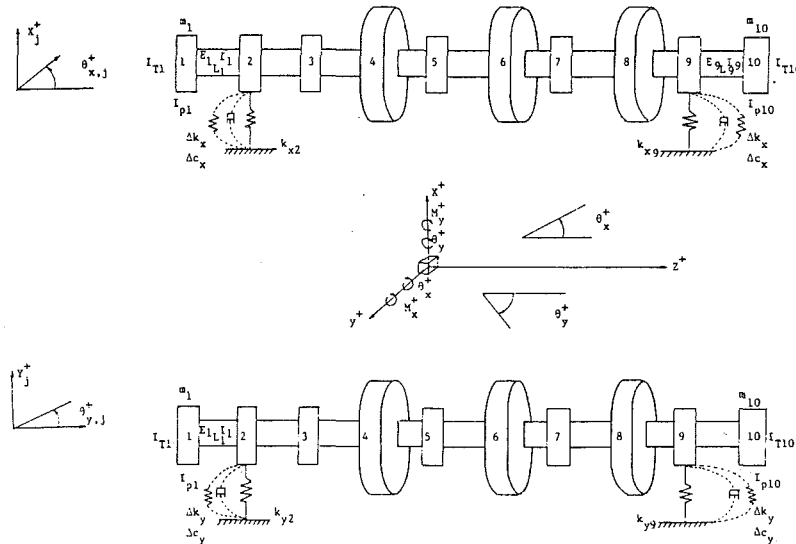


Fig. 1 Rotor model used for eigensolution reanalysis and eigenvalue design examples

is usually made during the initial stage of the design process. This model may undergo many modifications during the course of the design in order to match results with test data or to obtain a final design with desired stress or displacement levels. The free vibration problem for the original system model is represented by the quadratic eigenvalue problem

$$(\alpha_i^2 \mathbf{M} + \alpha_i \mathbf{C} + \mathbf{K}) \Delta_i = \mathbf{0} \quad (N \times 1) \quad (1)$$

and the left eigenvector problem is

$$(\alpha_i^2 \mathbf{M}^T + \alpha_i \mathbf{C}^T + \mathbf{K}^T) \delta_i \quad (N \times 1) \quad (2)$$

where α_i , Δ_i and δ_i are the i th eigenvalue, right eigenvector, and left eigenvector, respectively. In rotor-bearing analyses the right (Δ_i) and left (δ_i) eigenvectors are usually not equal since gyroscopic, internal friction and seal and bearing forces [11, 14] destroy the symmetry of the \mathbf{K} and \mathbf{C} matrices.

Modifications to the original design result from altering a selected set of design parameters. These typically include geometric or material properties such as element thicknesses, elastic moduli, shear factors or bearing, seal and Alford [15] coefficients. These parameters are contained in the vector

Nomenclature

- a_{2L} = a bilinear form - mode normalization constant for the L th original rotor bearing system mode
- \mathbf{C} = original system damping matrix
- $\Delta \mathbf{C}$ = damping modification matrix
- \mathbf{d} = vector design parameters
- d_i = i th design parameter
- \mathbf{e}_i = a vector of zeroes except a 1 in row i
- \mathbf{F} = a generalized receptance matrix
- \mathbf{F} = condensed form of \mathbf{F} containing receptances from the modified zones
- F_{ij} = ij element of \mathbf{F}
- $g(\lambda)$ = a form of the modified system's characteristic equation
- j_l = non-null row (or column) numbers for \mathbf{S} , $i = 1, 2, \dots, p$
- \mathbf{J} = $p \times 1$ vector of j_i
- \mathbf{K} = original system stiffness matrix
- $\Delta \mathbf{K}$ = stiffness modification matrix
- \mathbf{K}_i^{-1} = i th row of \mathbf{K}^{-1}
- \mathbf{K}_j^1 = j th column of \mathbf{K}^{-1}
- $(\mathbf{K}^1)_{ij}$ = ij element of \mathbf{K}^{-1}
- L = number of mode pairs (eigensolution and complex conjugate eigensolution) utilized to evaluate F_{ij}
- \mathbf{M} = original system inertia matrix
- $\Delta \mathbf{M}$ = inertia modification matrix
- N = total number of degrees of freedom in the original or modified rotor bearing models
- p = number of degrees of freedom directly affected by structural modifications
- q = number of selected design parameters
- R = generalized receptance higher mode factor
- \mathbf{S} = effective modification matrix

- α_i = i th eigenvalue of the original system
- δ_i = i th left eigenvector of the original system
- δ_{j1} = j th component of δ_1
- λ_n = n th eigenvalue of the modified system
- Δ_i = i th right eigenvector of the original system
- Δ_{i1} = i th component of Δ_1
- \mathbf{v}_n = generalized coordinate vector for τ_n transformation
- ξ_n = generalized coordinate vector for ψ_n transformation
- τ_n = n th left eigenvector of the modified system
- ψ_n = n th right eigenvector of the modified system

Symbols

- T = matrix-vector transpose
- Δ = change in a quantity
- π = series product designator

$$(\mathbf{A}) \begin{pmatrix} 1_1 & 1_2 & \dots & 1_s \\ m_1 & m_2 & \dots & m_r \end{pmatrix} = \begin{pmatrix} A_{1_1 m_1} & A_{1_1 m_2} & \dots & A_{1_1 m_r} \\ A_{1_2 m_1} & A_{1_2 m_2} & \dots & A_{1_2 m_r} \\ \vdots & \vdots & \ddots & \vdots \\ A_{1_s m_1} & A_{1_s m_2} & \dots & A_{1_s m_r} \end{pmatrix} \quad (s \times r)$$

where A_{ij} is the ij element of matrix \mathbf{A}
 $(x) (1_1 \ 1_2 \ \dots \ 1_s) = (x_{1_1} \ x_{1_2} \ \dots \ x_{1_s})^T \quad (s \times 1)$
 where x_i is the i th element of vector \mathbf{x}
 $\hat{\ } =$ condensed matrix-vector quantity
 $i =$ imaginary unit, $\sqrt{-1}$

$$\mathbf{d} = (d_1 \ d_2 \ \dots \ d_q)^T \quad (q \times 1) \quad (3)$$

The free vibration problem for the modified system becomes

$$(\lambda_n^2 (\mathbf{M} + \Delta\mathbf{M}) + \lambda_n (\mathbf{C} + \Delta\mathbf{C}) + (\mathbf{K} + \Delta\mathbf{K}))\psi_n = \mathbf{0} \quad (N \times 1) \quad (4)$$

and the left eigenvector problem is

$$(\lambda_n^2 (\mathbf{M}^T + \Delta\mathbf{M}^T) + \lambda_n (\mathbf{C}^T + \Delta\mathbf{C}^T) + (\mathbf{K}^T + \Delta\mathbf{K}^T))\tau_n = \mathbf{0} \quad (5)$$

where

$$\Delta M_{ij} = \Delta M_{ij}(\Delta \mathbf{d}), \quad \Delta C_{ij} = \Delta C_{ij}(\Delta \mathbf{d}), \quad \Delta K_{ij} = \Delta K_{ij}(\Delta \mathbf{d}) \quad (6)$$

An effective modification matrix may then be defined as

$$\mathbf{S}(\lambda) = \lambda^2 \Delta \mathbf{M} + \lambda \Delta \mathbf{C} + \Delta \mathbf{K} \quad (7)$$

The design parameters are assumed to physically affect only scattered, local portions of the system. Consequently the matrix \mathbf{S} is very sparse. This sparsity is quantified through the integer set

$$\mathbf{J} = (j_1 \ j_2 \ \dots \ j_p)^T \quad (p \times 1) \quad (8)$$

$p < N$

where j_i are the non-null row (or column) numbers of \mathbf{S} . Note that \mathbf{S} may then be expressed using the Boolean matrix

$$\mathbf{b} = [\mathbf{e}_{j_1} \ \mathbf{e}_{j_2} \ \dots \ \mathbf{e}_{j_p}] \quad (N \times p) \quad (9)$$

as

$$\mathbf{S} = \mathbf{b} \hat{\mathbf{S}} \mathbf{b}^T \quad (10)$$

where

$$\hat{\mathbf{S}} = \lambda^2 (\Delta \mathbf{M} \begin{bmatrix} j_1 & j_2 & \dots & j_p \\ j_1 & j_2 & \dots & j_p \end{bmatrix} + \lambda (\Delta \mathbf{C}) \begin{bmatrix} j_1 & j_2 & \dots & j_p \\ j_1 & j_2 & \dots & j_p \end{bmatrix} + (\Delta \mathbf{K}) \begin{bmatrix} j_1 & j_2 & \dots & j_p \\ j_1 & j_2 & \dots & j_p \end{bmatrix}) \quad (11)$$

The generalized receptance matrix of the original system is defined by

$$\mathbf{F}(\lambda) = (\lambda^2 \mathbf{M} + \lambda \mathbf{C} + \mathbf{K})^{-1} \quad (N \times N) \quad (12)$$

which exists for

$$\lambda \neq \alpha_i, \quad i = 1, 2, \dots, 2N \quad (13)$$

Matrix \mathbf{F} is a generalization of the common form of the receptance (dynamic flexibility influence coefficient) matrix appearing in the literature [16], i.e.,

$$\mathbf{G}(\omega) = (-\omega^2 \mathbf{M} + i\omega \mathbf{C} + \mathbf{K})^{-1} = \mathbf{F}(i\omega) \quad (14)$$

where ω is the frequency of sinusoidal vibration. Substitute the change of basis

$$\psi_n = \mathbf{F}(\lambda_n) \times \xi_n(\lambda_n) \quad (15)$$

$$\tau_n = \mathbf{F}^T(\lambda_n) \underline{\nu}_n(\lambda_n) \quad (16)$$

into equations (4) and (5). This yields

$$(\mathbf{I}_n + \mathbf{S}(\lambda_n) \mathbf{F}(\lambda_n)) \xi_n = \mathbf{0} \quad (N \times 1) \quad (17)$$

$$(\mathbf{I}_n + \mathbf{S}^T(\lambda_n) \mathbf{F}^T(\lambda_n)) \underline{\nu}_n = \mathbf{0} \quad (N \times 1) \quad (18)$$

By the definition (8), it immediately follows that

$$\xi_{kn} = 0, \quad k \notin (j_1 \ j_2 \ \dots \ j_p) \quad (19)$$

and

$$\xi_{j_r n} + \tilde{\mathbf{S}}_{j_r} \bar{\mathbf{F}} \bar{\xi}_n = 0, \quad r \in (1, 2, \dots, p) \quad (20)$$

where

$$\tilde{\mathbf{S}}_{j_r} = (\mathbf{S}) \begin{bmatrix} j_r \\ 1 \ 2 \ \dots \ N \end{bmatrix} \quad (N \times N) \quad (21)$$

$$\bar{\mathbf{F}} = (\mathbf{F}) \begin{bmatrix} 1 & 2 & \dots & N \\ j_1 & j_2 & \dots & j_p \end{bmatrix} \quad (N \times p) \quad (22)$$

$$\bar{\xi}_n = (\xi_n) (j_1 \ j_2 \ \dots \ j_p) \quad (p \times 1) \quad (23)$$

By again employing the sparsity of \mathbf{S} , equation (20) condenses to

$$(\mathbf{I}_p + \hat{\mathbf{S}}(\lambda_n) \hat{\mathbf{F}}(\lambda_n)) \bar{\xi}_n = \mathbf{0} \quad (p \times 1) \quad (24)$$

where

$$\hat{\mathbf{F}} = (\mathbf{F}) \begin{bmatrix} j_1 & j_2 & \dots & j_p \\ j_1 & j_2 & \dots & j_p \end{bmatrix} \quad (p \times p) \quad (25)$$

Equation (24), accompanied by

$$\psi_n = \bar{\mathbf{F}}(\lambda_n) \bar{\xi}_n \quad (N \times 1) \quad (26)$$

represents the final condensed form of the quadratic eigenvalue problem (equation (4)) for the modified system. The modified system's left eigenvector can be shown to be calculable from

$$(\mathbf{I}_p + \hat{\mathbf{S}}^T(\lambda_n) \hat{\mathbf{F}}^T(\lambda_n)) \underline{\nu}_n = \mathbf{0} \quad (p \times 1) \quad (27)$$

and

$$\tau_n^T = \underline{\nu}_n^T \bar{\mathbf{F}}(\lambda_n) \quad (1 \times N) \quad (28)$$

$$\bar{\mathbf{F}} = (\mathbf{F}) \begin{bmatrix} j_1 & j_2 & \dots & j_p \\ 1 & 2 & \dots & N \end{bmatrix} \quad (p \times N) \quad (29)$$

The rank of the coefficient matrix in equation (24) must be less than p for a nontrivial null space to exist, this requires that

$$g(\lambda_n) = \det(\mathbf{I}_p + \hat{\mathbf{S}}(\lambda_n) \hat{\mathbf{F}}(\lambda_n)) = 0 \quad (30)$$

The zeroes of $g(\lambda_n)$ are the eigenvalues (complex natural frequencies) of the modified system. Muller's approach [17] provides an excellent method for extracting the zeroes of equation (30). This approach does not require $\partial g / \partial \lambda$, and $g(\lambda)$ is easily computed using Gauss elimination. Numerical experiments have shown that convergence to zeroes occurs more reliably and rapidly if the auxiliary function

$$r(\lambda_n) = g(\lambda_n) \prod_{k=1}^{2l} (\lambda_n - \alpha_k) \quad (31)$$

is used instead of $g(\lambda)$ in Muller's method. These same results also show that convergence occurs on the average with approximately eight iterations per eigenvalue. After obtaining an eigenvalue by the aforementioned iterative search the corresponding left and right eigenvectors may be computed by (i) solving equations (24, 26) and (27, 28), (ii) by direct solution of the $N-1$ order systems formed by setting $\psi_{in} = \tau_{in} = 1.0$ (for some j) in equations (4) and (5), or by (iii) inverse iteration [18] on the N th order systems of equations (4) and (5).

The scalar λ_n is the n th complex natural frequency

$$\lambda_n = S_n + i\omega_n$$

of the modified rotor bearing system, where S_n indicates the decay rate and ω_n the oscillatory frequency of the n th mode. The $(N \times 1)$ vector ψ_n is the n th complex mode shape of the modified rotor-bearing system. These modes are in general twisted space curves due to the presence of discrete damping or cross coupled bearing coefficients at bearing and seal locations.

3 Receptance Computation

The iterative solution of equation (3) requires reevaluation

Table 1 Original rotor model data (see Fig. 1)

$\omega = 1200.0 \text{ rad/sec} = 11,459.16 \text{ rpm (spin rate)}$
 $D_j = 5.0 \text{ in.}, L_j = 12.0 \text{ in.}, E_j = 30.0 \times 10^6 \text{ lb/in}^2$
 $I_j = (\pi D_j^4)/64 = 30.68 \text{ in}^4$
 $K_{x2} = K_{y2} = K_{x9} = K_{y9} = 150,000.0 \text{ lb. in}$
 $\rho = 0.283/386 = 7.3316 \times 10^{-4} \text{ lbs}^2 \text{ in}^{-4}$
 $m_1 = m_{10} = A_j L_j \rho/2 = 0.08635 \text{ lbs}^2 \text{ in}^{-1}$
 $m_2 = m_3 = \dots = m_9 = 0.1727 \text{ lbs}^2 \text{ in}^{-1}$
 $I_{p1} = I_{p10} = m_1 D_1^2/8 = 0.2698 \text{ lb. in. s}^2$
 $I_{p2} = I_{p3} = \dots = I_{p9} = 0.5396 \text{ lb. in. s}^2$
 $I_{T1} = I_{T10} = m_1 (D_1^2/16 + L_1^2/12) = 1.1711 \text{ lb. in. s}^2$
 $I_{T2} = \dots = I_{T9} = 2.3422 \text{ lb. in. s}^2$
 Attached Disc Properties:
 $L_D = 0.50 \text{ in.}, D_D = 22.0 \text{ in.}$
 $m_D = 0.13935 \text{ lb. s}^2 \text{ in}^{-1}$
 $I_{pD} = 8.4306 \text{ lb. s}^2 \text{ in.}$
 $I_{TD} = 4.218 \text{ lb s}^2 \text{ in.}$
 Natural frequencies (Ω_i):
 $\Omega_1 = 240.65 \text{ rad/sec}, \Omega_2 = 253.25$
 $\Omega_3 = 526.92, \Omega_4 = 548.70, \Omega_5 = 645.74$
 $\Omega_6 = 683.76, \Omega_7 = 1040.9, \Omega_8 = 1118.2$
 $\Omega_9 = 1906.3, \Omega_{10} = 2025.5$
 Mode Normalization Constants (a_{2j}):
 $a_{21} = 160990.0 \text{ lb. s. in}^{-1}, a_{22} = 79934.0$
 $a_{23} = 2056.6, a_{24} = 1779.8, a_{25} = 802.51$
 $a_{26} = 784.86, a_{27} = 1946.3, a_{28} = 2252.6$
 $a_{29} = 6351.8, a_{2,10} = 8178.2$

of the submatrix $F(\lambda)$ for each eigenvalue guess λ . By equation (12), a direct approach necessitates the triangular factorization of

$$\lambda^2 \mathbf{M} + \lambda \mathbf{C} + \mathbf{K} \quad (N \times N) \quad (32)$$

and the forward and back substitution for the p right-hand sides

$$\mathbf{e}_{j_1}, \mathbf{e}_{j_2}, \dots, \mathbf{e}_{j_p} \quad (33)$$

at each guess of λ . It becomes clear that this approach to evaluating $\hat{\mathbf{F}}$ is even less efficient than solving [19]

$$f(\lambda) = \det(\lambda^2 [\mathbf{M} + \Delta \mathbf{M}] + \lambda [\mathbf{C} + \Delta \mathbf{C}] + [\mathbf{K} + \Delta \mathbf{K}]) = 0 \quad (34)$$

by Muller's method directly, using Gauss elimination to calculate \mathbf{f} . An alternative approach which allows for the computation of individual elements of $\mathbf{F}(\lambda)$ is to utilize its spectral representation [18]:

$$F_{ij}(\lambda) \cong \sum_{l=1}^{2L} \frac{\Lambda_{il} \delta_{jl}}{a_{2l}(\lambda - \alpha_l)} \quad (35)$$

where

$$a_{2l} = \delta_l^T (2\alpha_l \mathbf{M} + \mathbf{C}) \Delta_l \quad (36)$$

Equation (35) becomes exact when $L=N$, for instance, where all $2N$ original system modes are used.

Complex rotor-bearing systems which include flexible impeller wheels or foundations may be represented by hundreds or even thousands of independent degrees of freedom. Consequently the calculated eigensystem is incomplete, typically with

$$0.1 \leq L/N \leq 0.3 \quad (37)$$

For this reason, the accuracy of the elements of $\hat{\mathbf{F}}(\lambda)$ may not be sufficient to obtain reliable modified system eigenvalues. Considering both efficiency and accuracy, it is important to (i) obtain individual elements of $\mathbf{F}(\lambda)$ and (ii), if possible,

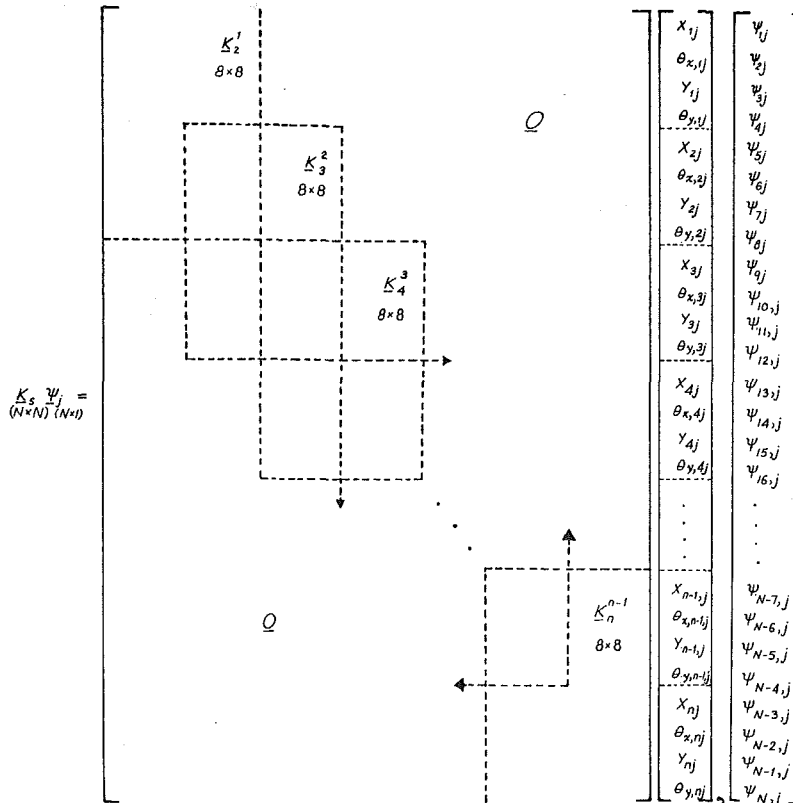


Fig. 2 K_s : symmetric shaft stiffness matrix $bw = 6, K_{sij} = 0 \text{ } |i - j| \geq 6$

improve the accuracy of these elements as calculated by an incomplete spectral representation.

The derivation of a hybrid spectral-property matrix representation for the generalized receptance matrix is included in references [12, 13]. This representation attenuates the higher mode contributions to the receptance elements and thereby provides increased accuracy when only the lower order modes of the unmodified system are available. This approach is analogous to the residual flexibility method which has previously appeared in the rotor dynamics literature [20]. The hybrid representation is rewritten here for higher mode factor values of $R=1, 2, 3$

$R=1$

$$F_{ij}(\lambda) \equiv (\mathbf{K}^{-1})_{ij} + \lambda \sum_{l=1}^{2L} \frac{\Lambda_{il} \delta_{jl}}{a_{2l} \alpha_l (\lambda - \alpha_l)} \quad (38)$$

$R=2$

$$F_{ij}(\lambda) \equiv (\mathbf{K}^{-1})_{ij} - \lambda \tilde{\mathbf{K}}_i^{-1} \mathbf{C} \mathbf{K}_j^{-1} + \lambda^2 \sum_{l=1}^{2L} \frac{\Lambda_{il} \delta_{jl}}{a_{2l} \alpha_l^2 (\lambda - \alpha_l)} \quad (39)$$

$R=3$

$$F_{ij}(\lambda) \equiv (\mathbf{K}^{-1})_{ij} - \lambda \tilde{\mathbf{K}}_i^{-1} \mathbf{C} \mathbf{K}_j^{-1} - \lambda^2 \{ \tilde{\mathbf{K}}_i^{-1} \mathbf{M} \mathbf{K}_j^{-1} - \tilde{\mathbf{K}}_i^{-1} \mathbf{C} \mathbf{K}^{-1} \mathbf{C} \mathbf{K}_j^{-1} \} + \lambda^3 \sum_{l=1}^{2L} \frac{\Lambda_{il} \delta_{jl}}{a_{2l} \alpha_l^3 (\lambda - \alpha_l)} \quad (40)$$

Although these formulas appear to involve a substantial amount of numerical computation, it should be noted that (i) only the submatrix $\tilde{\mathbf{F}}$ in equation (25) need be computed during each eigenvalue iteration, (ii) $N \times N$ matrix products are not required in equation (40) since a scalar results, and (iii) property matrix expressions such as

$$\tilde{\mathbf{K}}_i^{-1} \mathbf{M} \mathbf{K}_j^{-1}, \tilde{\mathbf{K}}_i^{-1} \mathbf{C} \mathbf{K}_j^{-1}$$

etc., need be calculated and stored only once for all values of λ . Equations (38, 39, 40) are valid only when $\alpha_l \neq 0$, and provide exact results if $L=N$.

4 Numerical Example

The reanalysis procedure is applied here to a ten-station, 40-degree-of-freedom, nonsynchronous gyroscopic rotor model. Although for simplicity, the application is restricted to a line type structure the procedure is generally applicable to any structural geometry, discretized by the finite element

vibration problem is mathematically described by the following quadratic eigenvalue problem

$$\{ \lambda_j^2 \mathbf{M} + \lambda_j \mathbf{C}_G + \mathbf{K}_s + \mathbf{K}_B \} \psi_j = \mathbf{0}, (40 \times 1) \quad (41)$$

where

$$\mathbf{K} = \mathbf{K}_s + \mathbf{K}_B$$

\mathbf{M} : a 40×40 block diagonal inertia matrix with j th block

$$\mathbf{M}_j = \begin{bmatrix} m_j & 0 & 0 & 0 \\ 0 & I_{Tj} & 0 & 0 \\ 0 & 0 & m_j & 0 \\ 0 & 0 & 0 & I_{Tj} \end{bmatrix} \quad (42)$$

$\mathbf{C} = \mathbf{C}_G$: a 40×40 block diagonal gyroscopic (coriolis) matrix with j th block

$$\mathbf{C}_{Gj} = \begin{bmatrix} 0 & 0 & 0 & 0 \\ 0 & 0 & 0 & \omega I_{pj} \\ 0 & 0 & 0 & 0 \\ 0 & -\omega I_{pj} & 0 & 0 \end{bmatrix} \quad (43)$$

\mathbf{K}_B : a 40×40 block diagonal bearing stiffness matrix with j th block

$$\mathbf{K}_{Bj} = \begin{bmatrix} K_{xj} & 0 & 0 & 0 \\ 0 & K_j & 0 & 0 \\ 0 & 0 & K_{yj} & 0 \\ 0 & 0 & 0 & K_j \end{bmatrix} \quad (44)$$

The terms m_j , I_{Tj} , and I_{pj} are lumped inertias composed of contributions from adjoining shaft segments and external disks attached at the respective mass stations. The rotor model numerical data is listed in Table 1. The shaft stiffness matrix, system displacement vector, and mode shape vector for a general n -disk configuration are shown in Fig. 2. The element stiffness matrix for the beam segment connecting mass stations j and $j+1$ is

$$\mathbf{K}_{j+1}^j = \frac{E_j I_j}{L_j^3} \begin{bmatrix} 12 & 6L_j & 0 & 0 & -12 & 6L_j & 0 & 0 \\ 6L_j & 4L_j^2 & 0 & 0 & -6L_j & 2L_j^2 & 0 & 0 \\ 0 & 0 & 12 & 6L_j & 0 & 0 & -12 & 6L_j \\ 0 & 0 & 6L_j & 4L_j^2 & 0 & 0 & -6L_j & 2L_j^2 \\ -12 & -6L_j & 0 & 0 & 12 & -6L_j & 0 & 0 \\ 6L_j & 2L_j^2 & 0 & 0 & -6L_j & 4L_j^2 & 0 & 0 \\ 0 & 0 & -12 & -6L_j & 0 & 0 & 12 & -6L_j \\ 0 & 0 & 6L_j & 2L_j^2 & 0 & 0 & -6L_j & 4L_j^2 \end{bmatrix} \quad (45)$$

method. The example rotor model is illustrated in Fig. 1. This model possesses a geometry similar to that of a centrifugal compressor in a chemical process application. The free

A common step in many rotor-bearing system analysis is to increment the bearing stiffness and damping coefficients and observe the change in the response characteristics. The logic

$$\hat{F}(\lambda) = \begin{bmatrix} K'_{5,5} & K'_{5,7} & K'_{5,33} & K'_{5,35} \\ K'_{7,5} & K'_{7,7} & K'_{7,33} & K'_{7,35} \\ K'_{33,5} & K'_{33,7} & K'_{33,33} & K'_{33,35} \\ K'_{35,5} & K'_{35,7} & K'_{35,33} & K'_{35,35} \end{bmatrix}$$

$$-\lambda \cdot \begin{bmatrix} (K'_{5,5})^T \\ (K'_{7,5})^T \\ (K'_{33,5})^T \\ (K'_{35,5})^T \end{bmatrix} \begin{bmatrix} C \\ M \\ C \\ C \end{bmatrix} \begin{bmatrix} K'_{5,5} & K'_{7,5} & K'_{33,5} & K'_{35,5} \\ K'_{5,7} & K'_{7,7} & K'_{33,7} & K'_{35,7} \\ K'_{5,33} & K'_{7,33} & K'_{33,33} & K'_{35,33} \\ K'_{5,35} & K'_{7,35} & K'_{33,35} & K'_{35,35} \end{bmatrix}$$

$$+\lambda^2 \cdot \begin{bmatrix} (K'_{5,5})^T \\ (K'_{7,5})^T \\ (K'_{33,5})^T \\ (K'_{35,5})^T \end{bmatrix} \begin{bmatrix} C \\ C \\ C \\ C \end{bmatrix} \begin{bmatrix} K'_{5,5} & K'_{7,5} & K'_{33,5} & K'_{35,5} \\ K'_{5,7} & K'_{7,7} & K'_{33,7} & K'_{35,7} \\ K'_{5,33} & K'_{7,33} & K'_{33,33} & K'_{35,33} \\ K'_{5,35} & K'_{7,35} & K'_{33,35} & K'_{35,35} \end{bmatrix}$$

$$+\lambda^3 \cdot \begin{bmatrix} \Delta_{5,5} & \Delta_{5,7} & \Delta_{5,33} & \Delta_{5,35} \\ \Delta_{7,5} & \Delta_{7,7} & \Delta_{7,33} & \Delta_{7,35} \\ \Delta_{33,5} & \Delta_{33,7} & \Delta_{33,33} & \Delta_{33,35} \\ \Delta_{35,5} & \Delta_{35,7} & \Delta_{35,33} & \Delta_{35,35} \end{bmatrix}$$

Fig. 3 The condensed generalized receptance calculation utilizing $R = 3$

behind this procedure may be based on the uncertainties in the bearing coefficient calculation involving for instance, bearing clearances, lubrication oil temperature, and preloads due to shaft misalignment, gear forces, and other nongravity-related forces. For this reason, the design parameter change vector for the example was chosen as

$$\Delta d = (\Delta K_x \ \Delta K_y \ \Delta C_x \ \Delta C_y)^T \quad (46)$$

$q = 4$

Clearly only the stiffness (K) and damping (C) matrices are affected by the modifications of the original system in equation (46). By inspection, the modification sparsity-integer set of equation (8) becomes

$$J = (j_1 \ j_2 \ j_3 \ j_4)^T = (5 \ 7 \ 33 \ 35)^T \quad (47)$$

$p = 4$

Equation (11) yields

$$\hat{S}(\lambda) = \begin{bmatrix} S_1(\lambda) & 0 & 0 & 0 \\ 0 & S_2(\lambda) & 0 & 0 \\ 0 & 0 & S_1(\lambda) & 0 \\ 0 & 0 & 0 & S_2(\lambda) \end{bmatrix} \quad (48)$$

where

$$S_1(\lambda) = \lambda \Delta C_x + \Delta K_x, \quad S_2(\lambda) = \lambda \Delta C_y + \Delta K_y \quad (49)$$

The condensed generalized receptance matrix of equation (25) becomes

$$\hat{F}(\lambda) = F \begin{bmatrix} 5 & 7 & 33 & 35 \\ 5 & 7 & 33 & 35 \end{bmatrix} \quad (4 \times 4) \quad (50)$$

Substitution of equations (48) and (50) into (30) leads to a form of the modified system's characteristic equation

Table 2 Initially gyroscopic rotor example. Design parameter change vector Δd (percent change from initial value where indicated)

Case	ΔK_x = Δd_1 lb/in.	ΔK_y = Δd_2 lb/in.	ΔC_x = Δd_3 lb.s./in.	ΔC_y = Δd_4 lb.s./in.
0	0.0 (0.0%)	0.0 (0.0%)	0.0	0.0
1	-100000.0 (-66.67%)	-75000.0 (-50.0%)	50.0	100.0
2	50000.0 (33.33%)	50000.0 (33.33%)	0.0	0.0
3	50000.0 (33.33%)	75000.0 (50.0%)	100.0	75.0
4	150000.0 (100.0%)	150000.0 (100.0%)	0.0	0.0
5	150000.0 (100.0%)	300000.0 (200.0%)	100.0	200.0
6	500000.0 (333.3%)	400000.0 (266.7%)	600.0	300.0
7	500000.0 (333.3%)	600000.0 (400%)	0.0	0.0
8	1000000.0 (666.7%)	500000.0 (333.3%)	1000.0	500.0

$$g(\lambda) = 0$$

$$= \det \begin{bmatrix} 1 + S_1 F_{55} & S_1 F_{57} & S_1 F_{5,33} & S_1 F_{5,35} \\ S_2 F_{75} & 1 + S_2 F_{77} & S_2 F_{7,33} & S_2 F_{7,35} \\ S_1 F_{33,5} & S_1 F_{33,7} & 1 + S_1 F_{33,33} & S_1 F_{33,35} \\ S_2 F_{35,5} & S_2 F_{35,7} & S_2 F_{35,33} & 1 + S_2 F_{35,35} \end{bmatrix} \quad (51)$$

During the iterative search for the zeros of $g(\lambda)$ (eigenvalues of the modified rotor bearing system), the elements of $F(\lambda)$ are computed with equations ((35), $R=0$) and ((38,39,40) $R=1,2,3$). These formulas may be simplified since the initial system is gyroscopic which implies

$$\delta_j = \tilde{\Lambda}_j, \quad \alpha_j = i\Omega_j, \quad a_{2j} = ia_j$$

where Ω_j and a_j are real scalars. The most efficient way to use equations (38, 39, 40) is to compute and store the property matrix contributions, separate from the spectral contributions. This is illustrated in Fig. 3 for the $R=3$ case. The first four 4×4 matrices in this figure are computed only once, for all values of λ . The spectral contributions are contained in the fifth 4×4 matrix, where

$$\Delta_{mm} = \sum_{l=1}^{L=10} \frac{\tilde{\Lambda}_{ml} \tilde{\Lambda}_{nl}}{(ia_l)(i\Omega_l)^3(\lambda - i\Omega_l)} + \sum_{l=1}^{L=10} \frac{\tilde{\Lambda}_{ml} \tilde{\Lambda}_{nl}}{(-ia_l)(-i\Omega_l)^3(\lambda + i\Omega_l)} \quad (52)$$

Note that although 40 original system modes exist in the example, only 10 are employed for the evaluation of the required receptances. This is within the typical interval of equation (37), i.e., $L/N=0.25$. For this reason the receptance values (F_{ij}) placed into equation (51) are only approximate. This emphasizes the importance of equations (38, 39, 40), which improve the accuracy of F_{ij} , for a fixed number of lower modes, as compared with a pure spectral representation (35).

Table 3 Initially gyroscopic rotor example. Eigenvalue accuracy comparison (real and imaginary part errors are shown) Case 8

EISPACK λ	R = 0 % Error	R = 1 % Error	R = 2 % Error	R = 3 % Error
-1.423 +i269.75	2.43691 0.12478	0.01110 0.00052	0.00861 0.00040	-0.00006 -0.00000
-1.960 +i292.53	2.42392 0.16534	0.00675 0.00042	0.01021 0.00061	0.00001 0.00000
-20.75 +i992.02	-10.05340 0.24599	-0.80983 0.02147	-0.74807 0.01975	-0.08661 0.00257
-24.77 +i1068.8	-11.94321 0.28023	-0.89410 0.02264	-0.98852 0.02493	-0.06551 0.00184
-437.3 +i1082.5	7.94283 -2.46447	0.16704 -0.37863	0.15659 -0.37969	-0.06619 -0.04027
-497.4 +i1136.1	6.06882 -2.43204	0.07815 -0.31096	0.07723 -0.31115	-0.05031 -0.02660
-993.71 +i1335.9	-0.21036 -12.11582	-3.17362 -0.72249	-3.16176 -0.72805	-0.36809 0.54731
-1136.4 +i1409.1	-3.88906 -14.09573	-4.33528 -0.96395	-4.33711 -0.96356	-0.62471 1.04633
-37.59 +i1884.8	-19.24200 -0.07412	-3.84475 -0.01983	-3.80527 -0.01917	-0.83167 -0.00382
-49.05 +i2003.1	-14.48791 -0.16824	-2.87997 -0.03442	-2.95558 -0.03612	-0.67794 -0.00755

Table 4 Initially gyroscopic rotor example. Maximum eigenvalue error (percent). Modes arranged in ascending order according to imaginary parts^a

Case	Mode No.	R = 0 real imaginary	Mode No.	R = 1 real imaginary	Mode No.	R = 2 real imaginary	Mode No.	R = 3 real imaginary
1	1 3	-3.2357 1.2760	10 3	-0.40802 0.0102	10 3	-0.4189 0.0098	10 10	-0.0952 -0.00011
2	1 3	0.0000 0.0746	- 3	0.0000 0.0023	- 4	0.0000 0.0020	- 3	0.0000 0.0001
3	4 4	1.6395 0.0707	10 3	0.1922 -0.0029	10 3	0.1978 -0.0026	10 10	0.0448 -0.00028
4	- 3	0.0000 0.41937	- 3	0.0000 0.0181	- 4	0.0000 0.01630	- 3	0.0000 0.0012
5	7 5	8.6299 1.0809	9 5	0.8826 0.0409	10 5	0.87235 0.04143	10 7	0.1994 -0.0034
6	4 8	16.187 -4.3599	6 5	-1.3788 -0.4286	6 5	-1.5015 -0.4264	9 4	-0.2013 -0.0197
7	- 8	0.0000 2.5574	- 8	0.0000 0.2817	- 8	0.0000 0.28382	- 8	0.0000 0.0401
8	9 8	-19.242 -14.096	8 8	-4.3353 -0.9640	8 8	-4.3371 -0.9636	9 8	-0.83167 1.0463

^a This table is read in the following fashion: For case 1: R = 0, the maximum error in the real part of an eigenvalue is -3.23 percent occurring in mode 1, the maximum error in the imaginary part of an eigenvalue is 1.276 percent occurring in mode 3, etc. The symbol (-) indicates that all of the eigenvalues for the case are pure imaginary.

Eigenvalue reanalysis is performed on the rotor-bearing model for the eight parameter change sets in Table 2. These cases include bearing stiffness changes from -67. to +667.percent of the original system values and bearing damping values ranging from 50.to 1000.lb.s in⁻¹. The

property matrix terms in Fig. 3 may be used for all eight cases without reevaluation. The zeroes of $g(\lambda)$ are obtained iteratively with Muller's method. For each eigenvalue guess (λ) , (i) the effective modification terms S_1 and S_2 in equation (49) are evaluated, (ii) F in equation (50) is evaluated employing computation schemes similar to Fig. 3, and (iii) $g(\lambda)$ is evaluated with Gauss elimination in equation (51).

To provide a benchmark for efficiency and accuracy of the reanalysis approach, the popular eigenvalue solver EISPACK [21] was utilized in producing "exact" modified system eigenvalues. The first-order system, $2N$ formulation shown in Appendix A is implemented to form a single input matrix for EISPACK. This matrix is inserted into the "real general matrix—all eigenvalues and selected eigenvectors" option, i.e.,

CALL BALANC, ELMHES, HQR, INVIT, ELMLBAK, BALBAK

The matrix is reduced to upper Hessenberg form with stabilized elementary similarity transformations. The eigenvalues of the similar upper Hessenberg matrix are obtained by the QR algorithm.

The accuracy of approximate eigenvalues, calculated utilizing the reanalysis theory with higher mode factors of $R=0,1,2,3$, is compared in Tables 3 and 4. Table 3 shows the lowest (as listed by $\text{Im}(\lambda)$) ten eigenvalues for the rotor-bearing model including modification case 8 (Table 2). The percent errors substantially decrease as the higher mode factor (R) increases, especially when comparing the $R=3$ results to the pure spectral representation ($R=0$). For each of the eight modification cases, Table 4 lists the maximum percent error in the ten lowest eigenvalues. This error analysis also exhibits a large increase in approximate eigenvalue accuracy as R is increased. An astonishing result is that considering all eight modification cases the maximum eigenvalue error for the $R=3$ approach is only 1.046 percent. This error occurs in the imaginary part of eigenvalue 8, in case 8. Percent error is defined in these tables by: percent Error = (Reanalysis - EISPACK) \times 100/EISPACK.

An efficiency comparison for this example showed that the reanalysis computation cost is between only 30 and 40 percent of the EISPACK cost. This percentage will considerably decrease for more complex rotor-bearing models since the EISPACK computation time increases approximately as the cube of the system order (N).

Some additional observations for this particular example are listed as follows.

1 The undamped modification cases (2, 4, and 7 in Table 2) show the smallest eigenvalue errors.

2 The accuracy of approximate eigenvalues, obtained with the reanalysis procedure, may be improved by increasing the number (L) or original system modes or by increasing the higher mode factor (R), in the computation of F .

3 A noticeable change in accuracy between the $R=1$ and $R=2$ results did not occur. This may not be true in general, particularly if the elements of C are large, as seen from equations (39) and (40).

4 The example was a 10 percent modification, i.e., $p/N=0.10$.

5 Muller's root solving method generally located complex zeroes in an order of increasing magnitude.

5 Discussion and Conclusions

A systematic procedure for the eigenvalue reanalysis of rotor-bearing systems has been presented. This method is applicable to general, nonlinear type structural geometries, modeled with finite element theory. The efficiency of the reanalysis procedure increases with the total number of analyses made. This point emphasizes the utility of the

method as a part of various iterative, optimization schemes. Since the order of the condensed modified system depends only on the number (p) of degrees of freedom directly affected by the modifications, the efficiency of the reanalysis procedure should increase as the ration p/N decreases.

It is tacitly assumed that the original rotor bearing system does not possess repeated eigenvalues, or eigenvalues that are invariant during the modification. Due to the lack of ideal symmetry characteristics both of these conditions are usually satisfied in actual rotor bearing system models.

The zeroes of the form of the modified system's characteristics equation (30) may be extracted by Newton Raphson iteration (NR), as well as Muller's method. When the modified system's eigenvalues are complex the NR approach requires a complex initial guess for an eigenvalue. The initial guesses may be arbitrarily chosen, or selected by utilizing a generalized Rayleigh quotient [12]. The latter procedure usually reduces the number of iterations required to achieve convergence.

The stiffness matrix (\mathbf{K}) for the original rotor model must be nonsingular to apply for $R = 1, 2, 3, \dots$ hybrid receptance formulas. The development of analogous formulas for unconstrained structures is an area for future research.

References

- 1 Lund, J. W., "Stability and Damped Critical Speeds of a Flexible Rotor in Fluid Film Bearings," *ASME Journal of Engineering for Industry*, May 1974, pp. 509-517.
- 2 Ruhl, R. L., "A Finite Element Model for Distributed Parameter Turborotor Systems," *ASME Journal of Engineering for Industry*, Feb. 1972, pp. 126-132.
- 3 Nelson, H. D., and McVaugh, "The Dynamics of Rotor Bearing Systems Using Finite Elements," *ASME Journal of Engineering for Industry*, May 1976, pp. 593-599.
- 4 Lund, J. W., "Sensitivity of the Critical Speeds of a Rotor to Changes in the Design," *ASME Journal of Mechanical Design*, Jan. 1980, pp. 115-121.
- 5 Fox, R. L., and Kapoor, M. P., "Rates of Change of Eigenvalues and Eigenvectors," *AIAA Journal*, Vol. 6, No. 12, 1968, pp. 2426-29.
- 6 Gupta, K. K., "Eigenproblem Solution of Damped Structural Systems," *Inter. Journal for Num. Meth. in Engr.*, Vol. 8, 1974, pp. 877-911.
- 7 Crandall, S. H., and McCally, R. B., Jr., "Matrix Methods of Analysis," *Shock and Vibration Handbook*, ch. 28, 2d ed., McGraw-Hill, 1976.
- 8 Meirovitch L., and Ryland, G., "Response of Slightly Damped Gyroscopic Systems," *Journal of Sound and Vibration*, Vol. 67, No. 1, 1979, pp. 1-19.
- 9 Pomazal, R. J., "Local Modifications of Damped Linear Systems," *AIAA Journal*, Vol. 9, No. 11, 1971, pp. 2216-2221.
- 10 Hallquist, J. O., "An Efficient Method for Determining the Effects of Mass Modifications in Damped Systems," *Journal of Sound and Vibration*, Vol. 44, No. 3, 1976, pp. 449-459.
- 11 Gunter, E. J., Choy, K. C., and Allaire, P. E., "Modal Analysis of

Turborotors Using Planar Modes Theory," *Journal of the Franklin Institute*, Vol. 305, No. 4, 1978, pp. 221-243.

12 Palazzolo, A. B., Vibrations of Locally Modified Mechanical and Structural Systems, Ph.D. dissertation, University of Virginia, January, 1981.

13 Palazzolo, A., Wang, B. P., and Pilkey, W., "An Improved Receptance Formulation for General Second Degree Square Lambda Matrices," submitted for publication to the *Inter. Journal of Num. Methods in Engr.*

14 Li, D. F., and Gunter, E. J., "Component Mode Synthesis of Large Rotor Systems," RLES Report No. UVA/464761/MAE80/166, University of Virginia Report, May 1980.

15 Alford, J. S., "Protecting Turbomachinery from Self Excited Rotor Whirl," *ASME Journal of Engineering for Power*, Oct. 1965, pp. 333-344.

16 Done, G. T. S., and Hughes, A. D., "The Response of a Vibrating Structure as a Function of Structural Parameters," *Journal of Sound and Vibration*, 38 (2), 1975, pp. 255-266.

17 Atkinson, K. E., *An Introduction to Numerical Analysis*, 1st ed., John Wiley and Sons, New York, 1978.

18 Lancaster, P., *Lambda Matrices and Vibrating Systems*, 1st ed., Pergamon Press, Toronto, 1966.

19 Tarnove, I., "Determination of Eigenvalues of Matrices Having Polynomial Elements," *J. Soc. Indust. Appl. Math.*, Vol. 6, No. 2, June, 1958, pp. 163-171.

20 Childs, D. W., and Bates, J. B., III, "Residual Flexibility Corrections for Transient Modal Rotordynamic Models," *ASME Journal of Mechanical Design*, Vol. 100, 1978, pp. 251-256.

21 Forsythe, G. E., Malcom, M. A., and Moler, C. B., *Computer Methods for Mathematical Computations*, 1st ed., Prentice Hall, 1977.

APPENDIX A

Exact Solution Procedure

The formulation of the eigenvalue problem for solution by EISPACK is outlined below. In general a quadratic eigenvalue problem is defined by

$$(\lambda^2 \mathbf{M} + \lambda \mathbf{C} + \mathbf{K})\psi = \mathbf{0} \quad N \times 1 \quad (\text{A1})$$

or

$$\lambda \begin{bmatrix} \mathbf{0} & \mathbf{M} \\ \mathbf{M} & \mathbf{C} \end{bmatrix} \begin{bmatrix} \lambda\psi \\ \psi \end{bmatrix} + \begin{bmatrix} -\mathbf{M} & \mathbf{0} \\ \mathbf{0} & \mathbf{K} \end{bmatrix} \begin{bmatrix} \lambda\psi \\ \psi \end{bmatrix} = \begin{bmatrix} \mathbf{0} \\ - \\ \mathbf{0} \end{bmatrix} \quad 2N \times 1 \quad (\text{A2})$$

Equation (A2) may be expressed as

$$\lambda \begin{bmatrix} \lambda\psi \\ \psi \end{bmatrix} = \begin{bmatrix} -\mathbf{M}^{-1}\mathbf{C} & -\mathbf{M}^{-1}\mathbf{K} \\ \mathbf{I}_N & \mathbf{0} \end{bmatrix} \begin{bmatrix} \lambda\psi \\ \psi \end{bmatrix} \quad (\text{A3})$$

The $2N \times 2N$ matrix in equation (A3) is the input matrix to the eigenvalue solver EISPACK.

Closed-Form, Steady-State Solution for the Unbalance Response of a Rigid Rotor in Squeeze Film Damper

D. L. Taylor

Assistant Professor,
Sibley School of Mechanical
and Aerospace Engineering,
Cornell University,
Ithaca, N.Y. 14853

B. R. K. Kumar

Engineer,
AiResearch Manufacturing Company,
Phoenix, Ariz.

This paper considers the steady-state response due to unbalance of a planar rigid rotor carried in a short squeeze film damper with linear centering spring. The damper fluid forces are determined from the short bearing, cavitating (π film) solution of Reynold's equation. Assuming a circular centered orbit, a change of coordinates yields equations whose steady-state response are constant eccentricity and phase angle. Focusing on this steady-state solution results in reducing the problem to solutions of two simultaneous algebraic equations. A method for finding the closed-form solution is presented. The system is nondimensionalized, yielding response in terms of an unbalance parameter, a damper parameter, and a speed parameter. Several families of eccentricity-speed curves are presented. Additionally, transmissibility and power consumption solutions are present.

Introduction

Design trends in turbomachinery have led to increased need for complete dynamic analyses. Controlled support compliance in the form of squeeze film dampers can limit rotor excursion and attenuate transmitted forces. A concise and comprehensive coverage of the state-of-the-art is contained in [1], to which the reader is referred for discussions of many aspects of the problem of design, testing, and implementation of squeeze film dampers.

The dynamics of the system are well understood and the differential equations governing the motion due to rotating imbalance are well documented [2, 3, 4].

Furthermore, experimental results [5] have shown that the damper is largely self centering, and that a cavitating film assumption is more valid than the uncavitating film assumption. Other extensive experimental activities have been reported also [6].

Analytically, a common procedure to obtain steady-state response has been either time step integration [2, 3] or some iterative algorithm [7]. There are disadvantages to these methods: (a) only stable solutions can be found, limiting an intuitive understanding of the structure of the dynamic response; (b) in regions of multiple-valued response, finding all possible solutions involves tedious trial and error; (c) false convergence is a serious drawback to time step integration [3]; (d) the particular algorithm and convergence criteria used in the iterative approach determines the accuracy and credibility of the results.

These drawbacks are circumvented by a closed-form

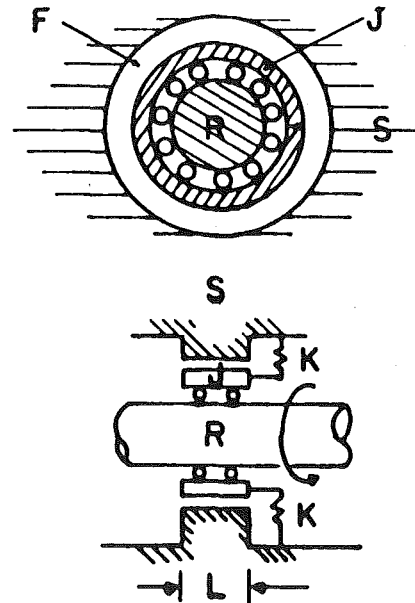


Fig. 1 Details of physical system

solution. Such a solution is possible for the case of circular centered synchronous procession of the squeeze film journal in the damper cavity. This is accepted as the normal response of the system to imbalance excitation and is supported both by time-step integration [2, 3] and experimental evidence [5, 6].

Based on more extensive investigation [8], attention in this paper will focus on the π film (cavitating) short (open-ended) squeeze film damper. The former assumption yields an ef-

Contributed by the Gas Turbine Division of THE AMERICAN SOCIETY OF MECHANICAL ENGINEERS and presented at the 27th International Gas Turbine Conference and Exhibit, London, England, April 18-22, 1982. Manuscript received at ASME Headquarters December 22, 1981. Paper No. 82-GT-263.

fective radial stiffness which is extremely hardening, leading to jump-drop phenomenon. The latter assumption is purely for convenience in calculating pressure distributions. The common Reynold's equation solution is developed and used to determine fluid forces.

The system will be nondimensionalized such that three parameters, λ, δ, Ω , will describe the system. The whirl orbit, ϵ_c , will be determined and then, later, transmissibility TR and power consumption P will be presented. A key step in the closed form solution is inversion of the problem to actually determine $\Omega = \Omega(\epsilon_c, \lambda, \delta)$ rather than $\epsilon_c = \epsilon_c(\lambda, r, \Omega)$.

Analytical Model

The results developed apply to the classical Jeffcott rotor carried on a single-journal, squeeze film damper with a linear centering spring (Fig. 1). The centering spring is assumed adjusted to offset any gravitational load. Alternatively, the axis of rotation is vertical, resulting in no gravitational loading.

The kinematic variables are defined as shown in Fig. 2. The geometric center of the displaced journal is located by polar coordinates e and ϕ . Two unit vectors, \underline{n}_e and \underline{n}_ϕ are oriented as shown along and perpendicular to the eccentricity vector \underline{e} . Two fixed unit vectors, \underline{n}_x and \underline{n}_y , serve as an inertial reference frame.

The velocity vector of the center of the journal is \underline{V} . The mass center of the rotor is offset from the geometric center of the journal a distance d . A line connecting the rotor mass center and journal geometric center is oriented relative to the inertial reference frame by the angle ψ , and the rotor rotation speed $\omega = d\psi/dt$ is assumed constant. The rotor mass is denoted by m , and the radial centering spring shown in Fig. 1 has stiffness k .

The fluid forces acting on the journal are described by two resolute in the \underline{n}_e and \underline{n}_ϕ directions, F_e and F_ϕ , respectively.

The derivation of the equations for the fluid forces has been previously presented [3, 9, 10, 12]. The basic procedure is to determine a pressure distribution over the entire journal and then integrate to obtain net force. The pressure distribution has been found from the Ocvirk (short bearing) solution to Reynolds equations. This is applicable to an open damper. The π film assumption has been used in that negative pressures predicted by the solution to Reynolds equation have not been included in the integral for net force. This is a common approximation for the cavitation phenomenon.

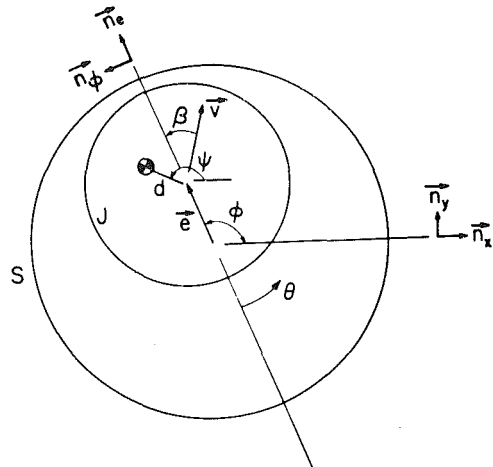


Fig. 2 Kinematic variables

The bearing forces ultimately require the evaluation of the definite integrals, $J_3^{02}, J_3^{11}, J_3^{20}$, where

$$J_n^m = \int_{\theta_1}^{\theta_1 + \pi} \frac{\sin^m \theta \cos^n \theta}{(1 + \epsilon \cos \theta)^n} d\theta \quad (1)$$

The limits of integration are for the region of positive film pressure

$$\theta_1 = \pi - \beta - \frac{\pi}{2} \quad (2)$$

where β and θ are measured as shown in Fig. 2. The governing differential equations of motion can be presented in non-dimensional form, as

$$\begin{aligned} \epsilon'' &= -\lambda[\epsilon' J_3^{02} + \epsilon(\Omega - \gamma') J_3^{11}] \\ &\quad - \epsilon + \epsilon(\Omega - \gamma')^2 + \delta \Omega^2 \cos \gamma \\ \gamma' &= \frac{1}{\epsilon} \{ \lambda[\epsilon' J_3^{11} + \epsilon(\Omega - \gamma') J_3^{20}] \\ &\quad + 2\epsilon'(\Omega - \gamma') - \delta \Omega^2 \sin \gamma \} \end{aligned} \quad (3)$$

where

$$\begin{aligned} \epsilon &= e/C, \text{ nondimensional eccentricity} \\ \Omega &= \omega/\sqrt{k/m}, \text{ nondimensional speed} \\ \delta &= d/C, \text{ nondimensional unbalance} \\ (\cdot)' &= d/dT \\ T' &= t\omega_n, \text{ nondimensional time} \end{aligned}$$

and

Nomenclature

C = Radial clearance between journal and sleeve, m
 d = Displacement of rotor center of mass from the geometric axis (i.e. unbalance), m
 e = eccentricity of journal, m
 F_e, F_ϕ = fluid film force resolute, N
 F_{TR} = force transmitted to support structure, N
 F_D = dynamic driving force magnitude, N
 f_e, f_ϕ = nondimensional fluid film force resolute, l
 J_n^m = definite bearing integral, l
 k = radial stiffness of centering spring, N/m
 L = length of journal, m
 m = mass of rotor, kg
 $\underline{n}_e, \underline{n}_\phi$ = unit vectors rotating with \underline{e} , l
 $\underline{n}_x, \underline{n}_y$ = unit vectors fixed to inertial reference, l

p = nondimensional power dissipated in damper, l
 \hat{P} = power dissipated in damper, KW
 R = radius of journal, m
 T = nondimensional time, s
 t = time, l
 TR = transmissibility, l
 \underline{V} = velocity of journal center, m/s
 β = angle measured from \underline{V} to \underline{e} , l
 γ = phase angle measured from \underline{e} to \underline{d} , l
 δ = nondimensional unbalance, l
 ϵ = nondimensional eccentricity, l

θ = angular coordinate of journal surface, l
 λ = nondimensional damper parameter, l
 μ = dynamic viscosity of damper fluid, N·s/m²
 ϕ = angle measured from \underline{n}_x to \underline{e} , l
 ψ = angle measured from \underline{n}_x to \underline{d} , l
 Ω = nondimensional rotor speed, l
 ω = rotor speed, l/s
 ω_n = natural frequency of damper system, l/s
 (\cdot) = operator d/dt , l/s
 $(\cdot)'$ = operator d/dT , l
 $(\cdot)_c$ = circular synchronous whirl, l

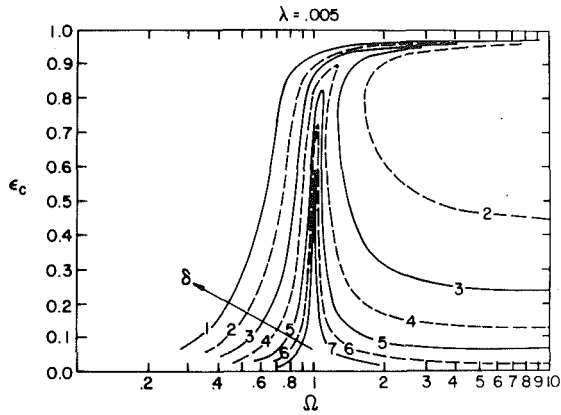


Fig. 3 Orbit speed response as a function of imbalance

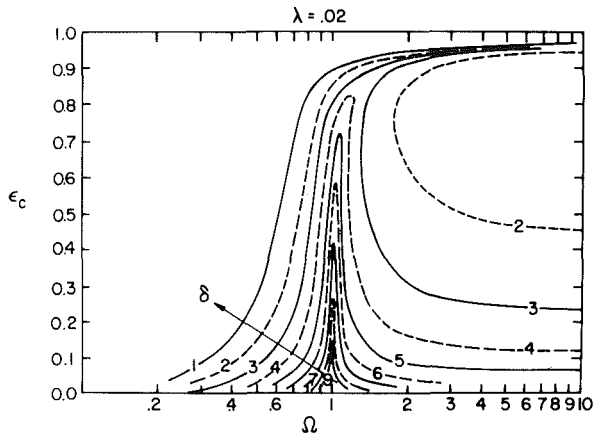


Fig. 4 Orbit speed response as a function of imbalance

$$\lambda = \frac{\mu L^3 R}{C^3 \sqrt{km}} \quad (4)$$

Characteristics of the damper appear only in the term λ , a nondimensional constant previously identified for squeeze film damper [4, 11].

Steady-State Response

Experiments and numerical integration of equation (4) have shown that centered circular orbits are the steady-state response. This motivates a change of coordinates. Four-state variables are required to describe the system. Two possibilities are Cartesian coordinates (x, \dot{x}, y, \dot{y}) and inertial polar coordinates $(e, \dot{e}, \phi, \dot{\phi})$. The best choice is polar coordinates which rotate synchronized with the rotor unbalance vector d in Fig. 2. In this reference frame, the centered circular orbit is a fixed point with position ϵ and phase γ relative to the unbalance vector direction. In this coordinate system, the steady-state equations can be written as

$$\begin{aligned} -\lambda(\epsilon_c \Omega J_3^1 |c) - \epsilon_c + \epsilon_c \Omega^2 + \delta \Omega^2 \cos \gamma_c &= 0 \\ 1/\epsilon_c \{ \lambda \epsilon_c \Omega J_3^0 |c - \delta \Omega^2 \sin \gamma_c \} &= 0 \end{aligned} \quad (5)$$

where ϵ_c, γ_c are the steady-state circular synchronous whirl values. Equation (5) is viewed as giving ϵ_c, γ_c as functions of Ω, δ and damper parameter λ . Rearranging:

$$\begin{aligned} \cos \gamma_c &= \frac{\epsilon_c}{\delta} \left(\frac{\lambda}{\Omega} J_3^1 |c + \frac{1}{\Omega^2} - 1 \right) \\ \sin \gamma_c &= \frac{\epsilon_c}{\delta} \left(\frac{\lambda}{\Omega} J_3^0 |c \right) \end{aligned} \quad (6)$$

The reader should note that integrals $J_3^1 |c$ and $J_3^0 |c$ are special forms of equation (1), evaluated for the centered circular orbit.

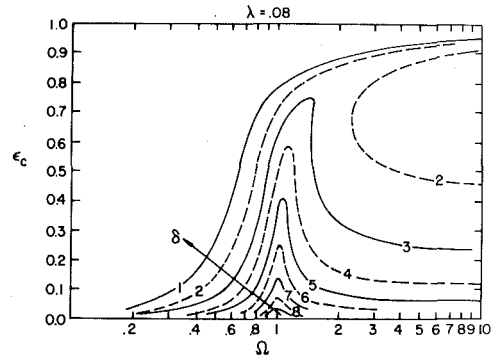


Fig. 5 Orbit speed response as a function of imbalance

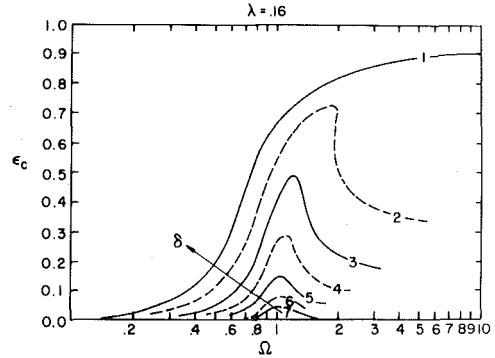


Fig. 6 Orbit speed response as a function of imbalance

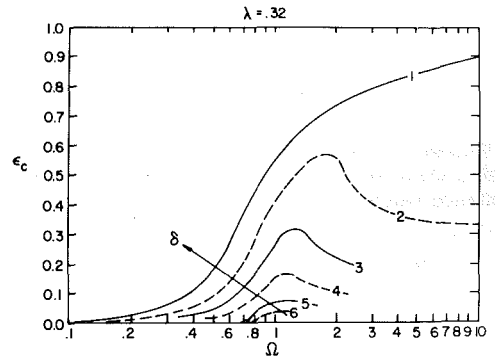


Fig. 7 Orbit speed response as a function of imbalance

$$\begin{aligned} J_3^1 |c &= \frac{2\epsilon_c}{(1-\epsilon_c^2)^2} \\ J_3^0 |c &= \frac{\pi}{2(1-\epsilon_c^2)^{3/2}} \end{aligned} \quad (7)$$

The presence of the term, ϵ_c , in equations (7) prevents the seemingly obvious nondimensionalization of ϵ_c/δ in equation (6). Elimination of γ_c from equation (6) yields a single equation for (ϵ_c, Ω) which can be written as a quartic in Ω .

$$\begin{aligned} \left(1 - \frac{\delta^2}{\epsilon_c^2} \right) \Omega^4 + \left(-2\lambda J_3^1 |c \right) \Omega^3 + \left\{ \lambda^2 \left(J_3^1 |c \right)^2 \right. \\ \left. + J_3^0 |c \right\} \Omega^2 + (2\lambda J_3^1 |c) \Omega + 1 = 0 \end{aligned} \quad (8)$$

To solve equation (8) for Ω , a value of ϵ_c is assumed, the coefficients of the quartic evaluated, and the quartic is then solved for Ω . A noniterative, closed-form routine is used to solve for all roots of the quartic in equation (8). Spurious values of Ω can be discarded because Ω by definition is positive and real. However, a single value of ϵ_c may correspond to 0, 1, or 2 valid speeds Ω . The solution pair (ϵ_c, Ω) is then used to find λ_c from

$$\gamma_c = \sin^{-1} \left(\frac{\epsilon_c}{\delta} \cdot \frac{\lambda}{\Omega} J_3^{20} \right) \quad (9)$$

Thus the solution $(\epsilon_c, \gamma_c, \Omega)$ is found. Although calculated as $\Omega = \Omega(\epsilon_c)$, for $0 < \epsilon < 1$, the data base was stored and plotted as $\epsilon_c = \epsilon(\Omega)$, $\delta = \delta(\Omega)$. In addition, the solutions $(\epsilon_c, \gamma_c, \Omega)$ were used to evaluate transmissibility and power consumption.

A family of curves of ϵ_c, γ_c versus Ω can be plotted for a particular damper (λ) for a range of excitations (δ). Figures 3-7 present such data, with an arrow designating the travel for increasing levels of imbalance. The legend for all figures is

1	$\delta = .849$
2	$\delta = .447$
3	$\delta = .235$
4	$\delta = .123$
5	$\delta = .065$
6	$\delta = .034$
7	$\delta = .018$
8	$\delta = .010$
9	$\delta = .005$

A family of response curves for constant δ and varying λ was prepared but did not communicate the results as well. A single family of phase angle plots has been included in Fig. 8.

The reader will remember that the system is basically a damped single degree of freedom system with strong hardening stiffness and damping. For low values of λ and δ , the system behaves like a lightly damped system, and the resonance peak for ϵ_c versus Ω occurs very nearly at $\Omega = 1$, and the phase angle shifts from 0 to π very sharply at $\Omega = 1$. (Here it is to be noted that γ is defined as being measured from \mathbf{d} to \mathbf{e} , and not from \mathbf{e} to \mathbf{d} , which accounts for the positive values of the phase angle.) The low frequency asymptote of ϵ_c is zero, and the high frequency asymptote is δ , which agrees with linear 1 D.O.F. theory.

Striking nonlinearity manifests itself, however, at larger values of δ , even for the smallest values of λ . This is because the resonance value of ϵ_c approaches unity, and the stiffness

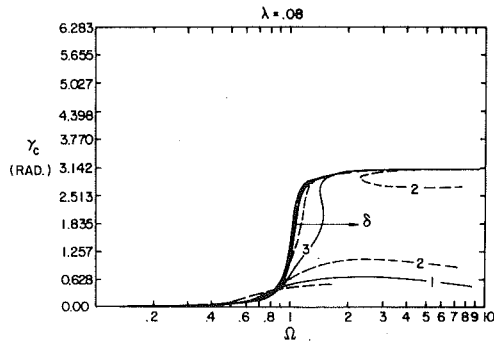


Fig. 8 Orbit phase response as a function of imbalance

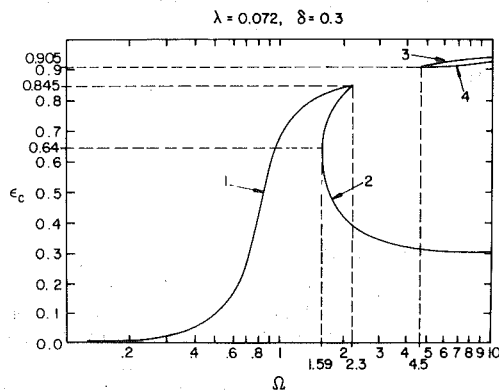


Fig. 9 Generic shape for orbit speed response curve

of the fluid film tends to infinity. The ϵ_c curves bend over to the right (i.e., the direction of increasing Ω) in the classic fashion of a hardening 1 D.O.F. system response. For sufficiently large values of δ , the ϵ_c versus Ω curve is not only multiple valued but also not connected, i.e., there is no jump-drop between the high frequency high response and low response. A typical curve ($\lambda = .072, \delta = .3$) is shown in Fig. 9. Close inspection shows a disconnected branch of the ϵ_c curve at high speeds, with large values of ϵ_c . This upper right branch of the operating locus was found in each of the previous figures but cannot be seen in detail. This disconnected branch is also present for low values of δ but is usually outside the frequency range $\Omega < 10$. For increasing values of δ , the "nose" of the resonance curve rises and tilts right. Simultaneously, the "nose" of upper branch moves left. For sufficiently large values of δ , the curves meet, and there is no drop to the underside of either. The implications of this high-speed, large-amplitude, steady-state solution have not been fully considered. However, studies have shown the upper side of the branch (labeled 3 in Fig. 9) is stable and the lower side of the branch (labeled 4 in Fig. 9) is unstable.

Transmissibility and Power Dissipation

A subject of utmost interest to the designer is the attenuation of dynamic forces by the squeeze film damper, and, to a lesser degree, the power dissipated in the damper fluid. An important function of the squeeze film damper is the attenuation of dynamic forces transmitted to the bearing support structure as the rotor is accelerated through the critical speed. However, an ill-designed damper can cause havoc if it has a transmissibility of much greater than unity in the operating speed range. The question of power dissipation is of importance is designing cooling systems for the damper fluid and in starter motor power requirement calculations.

The basic definition of the transmissibility of an isolation system is the ratio of the transmitted force to the driving harmonic force. The resultant of the force transmitted

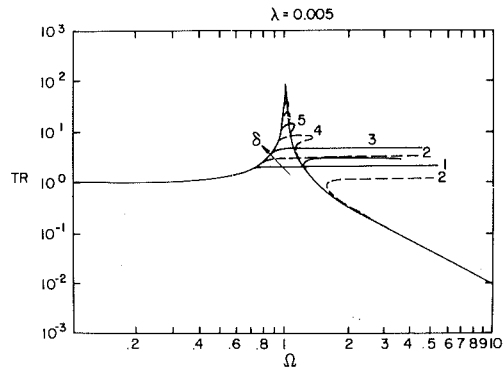


Fig. 10 Transmissibility speed curve as a function of imbalance

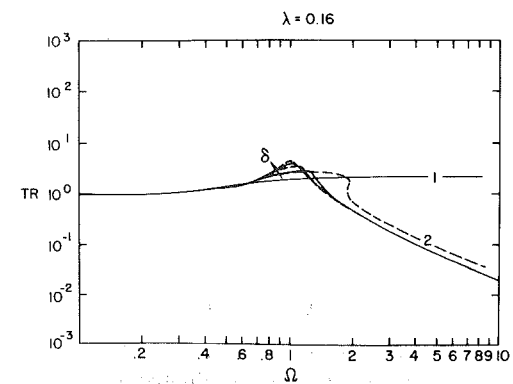


Fig. 11 Transmissibility speed curve as a function of imbalance

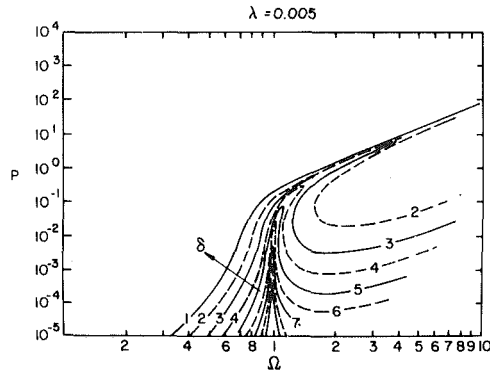


Fig. 12 Power consumption speed curve as a function of imbalance

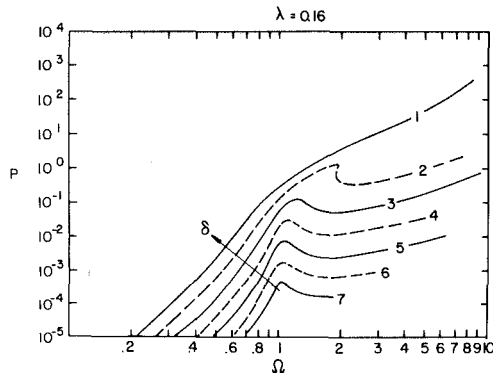


Fig. 13 Power consumption speed curve as a function of imbalance

through the squeeze film damper is the reaction force opposing the vectorial sum of the radial resolute F_e and tangential resolute F_ϕ of the fluid film forces and the force transmitted through the radial centering spring. Denoting this resultant reaction by F_{TR} , it is given by:

$$F_{TR} = -F_e |c n_e - F_\phi |c n_\phi + k e_c n_e \quad (10)$$

Substituting for the fluid forces and factoring already defined terms

$$F_{TR} = kC[(\lambda \Omega \epsilon_c J_3^1 |c) n_e + (\lambda \Omega \epsilon_c J_3^0 |c) n_\phi + \epsilon_c n_e] \quad (11)$$

The driving harmonic force is the imbalance force, the magnitude of which is:

$$F_D = m d \omega^2 \quad (12)$$

or in the nondimensionalized variables

$$F_D = kC \cdot \delta \Omega^2 \quad (13)$$

Thus, the transmissibility TR is given by:

$$TR = \frac{|F_{TR}|}{F_D} = \frac{\epsilon_c [(\lambda \Omega J_3^1 |c + 1)^2 + (\lambda \Omega J_3^0 |c)^2]^{1/2}}{\delta \Omega^2} \quad (14)$$

The transmissibility TR can be plotted in much the same fashion as the eccentricity ϵ_c versus Ω for families of varying δ for various values of λ (Figs. 10 and 11). The variation of TR is so great in the germane Ω - λ - δ range, it is necessary to use a log-log plot.

The plots of TR versus Ω exhibit the classical resonance and roll-off for small values of δ . The low-speed asymptote is 1 and the high-speed asymptote is $1/\Omega^2$. The effect of increasing δ is to reduce the peak of TR near $\Omega = 1$. This shows that the squeeze film damper becomes more effective in force attenuation as δ increases. However for very large values of δ (often referred to as an overloaded damper), the TR high speed roll-off does not occur until well beyond the limits of the graphs. The reduction of the maximum value of TR with increasing δ is dramatic at low values of λ and less marked at high values of λ . However, the maximum value of TR is well

below 10 for large values of λ , as compared to 100 for small values of λ . A review of several figures similar to Fig. 10 leads to the well-known conclusion that the best way to minimize TR is to have a large λ and a very small δ . In physical terms, this implies that the clearance C be large relative to the imbalance d , along with a very viscous damper fluid (large μ), large damper journal radius, R , and length, L , and a weak centering spring (small k). However, such a combination of large λ and small δ leads to excessive whirl radii ϵ_c , which will reduce the aerodynamic efficiency, due to the increased blading-casing clearance required. Thus, in optimizing the damper design, one must employ a performance index that includes both TR as well as ϵ_c , as both of these quantities are to be minimized. Myopic minimization of either could lead to unsatisfactory overall performance.

In circular, synchronous whirl, the only force doing work is the tangential fluid force resolute F_ϕ . Thus, the dimensional power dissipated \hat{P} is given by:

$$\hat{P} = F_\phi \cdot e_c \omega \quad (15)$$

or

$$\hat{P} = kC^2 \omega_n (\lambda \Omega^2 \epsilon_c^2 J_3^0 |c) \quad (16)$$

Defining a reference force $\hat{F} = kC$ and a reference speed $\hat{V} = \omega_n C$, one can nondimensionalize the dissipated power as:

$$P = \frac{\hat{P}}{\hat{F}\hat{V}} = \lambda \Omega^2 \epsilon_c^2 J_3^0 |c \quad (17)$$

The nondimensional power, P , is shown for families of varying δ for two values of λ in Figs. 12 and 13. The wide variation in magnitude of P necessitates the use of a logarithmic scale.

The dissipated power is very sensitive to increases in δ . The undesirability of a response locus that does not drop down to a small ϵ_c at large Ω is very evident here. The power dissipation is proportional to both the square of ϵ and Ω , and ϵ_c also appears in the denominator of $J_3^0 |c$. A large ϵ_c at large Ω raises the power requirements of the damper to astronomical levels.

Physically, the interpretation of power dissipation sensitivity to δ is linked to start-up power requirements of the turbomachine. Often, when the turbomachine is shut down after a period of operation, the phenomenon known as thermal-bow dramatically increases the imbalance, i.e., δ . When the machine is to be restarted, this increased δ causes a greatly increased P . Other effects of thermal-bow are also very significant, such as seal-rubs, etc., when considering the increased power requirement. When compounded, these effects so severely drain the power input to the rotor by the start-up system that often the rotor cannot be accelerated past its critical speed and the machine cannot be started.

Also, the solutions presented aid the designer in estimating the power dissipated as heat in the damper, and the extra cooling capacity required to support the squeeze film damper, in addition to the bearing lubrication cooling requirements.

Summary

An exact analytical solution to the steady-state system of nonlinear equations is developed assuming circular synchronous whirl. The simplification of the system equations into an algebraic quartic form permitted rapid, easy, and guaranteed solution for the equilibrium position. This steady-state analysis removes the uncertainty associated with steady-state results obtained by numerical integration methods (caused by numerical inaccuracies, uncertainty of asymptotic behavior, and limited number of initial conditions used). For instance, the disconnected upper branch of the ϵ_c versus Ω curves (for $\lambda = 0.072$, $\delta = 0.3$, for example) was not revealed by simulation in a previous study [3], because it required a narrow range of initial conditions to be achieved.

The parameters describing the system were reduced from seven or more dimensional parameters to three non-dimensional parameters (λ, δ, Ω). The reduction to a few manageable constants permits a better understanding of how the performance varies with design changes. The figures presented are intended to facilitate such insight. They are not primarily intended for direct use by a designer. Rather, the conclusion of the paper is that a steady-state solution can be rather easily obtained for any particular set of conditions. A designer can therefore generate his own set of response curves for any particular specific variable of interest.

Several questions not addressed in this paper have been dealt with in detail in previous work [8]. In combination with that work, all aspects of the design process have been considered, transient simulation, nonlinear, steady-state response, and stability of steady-state response.

Continuing efforts are aimed at an analysis of the nonlinear stability of the solutions. This is particularly interesting because a stable, asynchronous, noncircular, steady-state orbit seems to exist for a wide range of parameters. Other efforts are addressed at (a) effects of external, unidirectional forces such as gravity, (b) optimization with competing objectives, and (c) multi-degree-of-freedom systems with multiple dampers.

References

- 1 *Proceedings of the Conference on the Stability and Dynamic Response of Rotors with Squeeze-Film Bearings*, May 8-10, 1979, U.S. Army Research Office, Research Triangle Park, North Carolina.
- 2 Gunter, E. J., Barrett, L. E., and Allaire, P. E., "Design of Nonlinear Squeeze Film Dampers for Aircraft Engines," *Journal of Lubrication Technology*, Vol. 99, No. 1, Jan. 1977, pp. 57-64.
- 3 Taylor, D. L. and Kumar, B. R. K., "Nonlinear Response of Squeeze Film Dampers," *ASME Journal of Lubrication Technology*, Jan. 1980, Vol. 102, pp. 51-58.
- 4 Mohan, S. and Hahn, E. J., "Design of Squeeze Film Damper Supports for Rigid Rotors," *ASME Journal of Engineering for Industry*, Aug. 1974, pp. 976-982.
- 5 Pan, C. H. T. and Tonneson, Jr., "Eccentric Operation of the Squeeze Film Damper," *ASME Journal of Lubrication Technology*, Vol. 100, No. 2, July 1978, pp. 369-378.
- 6 Sharma, R. K. and Botman, M., "An Experimental Study of the Steady State Response of Oil-Film Dampers," *ASME Journal of Mechanical Design*, Vol. 100, No. 2, Apr. 1978, pp. 216-221.
- 7 Greenhill, L. M., and Nelson, H. D., "Iterative Determination of Squeeze Film Damper Eccentricity for Flexible Rotor Systems," ASME Paper No. 81-DET-87.
- 8 Kumar, B. R. K., *Nonlinear Dynamics of the Squeeze Film Damper*, M. S. thesis, Cornell University, 1980.
- 9 Childs, D., Moes, H., and van Leeuwen, H., "Journal Bearing Impedance Description for Rotor-dynamic Applications," ASME Paper No. 76-Lub-24, *ASME Journal of Lubrication Technology*, Apr. 1977.
- 10 Booker, J. F., "Dynamically Loaded Journal Bearings: Numerical Application of the Mobility Method," *ASME Journal of Lubrication Technology*, July 1971, pp. 168-176.
- 11 White, D. C., "The Dynamics of a Rigid Rotor Supported on Squeeze Film Bearings," *Proceedings of the Conference of Vibrations in Rotating Systems*, Institute of Mechanical Engineers, London, Feb. 14-15, 1972, pp. 213-229.
- 12 Booker, J. F., "A Table of the Journal-Bearing Integral," *Journal of Basic Engineering*, June 1965, pp. 533-535.

The parameters describing the system were reduced from seven or more dimensional parameters to three non-dimensional parameters (λ, δ, Ω). The reduction to a few manageable constants permits a better understanding of how the performance varies with design changes. The figures presented are intended to facilitate such insight. They are not primarily intended for direct use by a designer. Rather, the conclusion of the paper is that a steady-state solution can be rather easily obtained for any particular set of conditions. A designer can therefore generate his own set of response curves for any particular specific variable of interest.

Several questions not addressed in this paper have been dealt with in detail in previous work [8]. In combination with that work, all aspects of the design process have been considered, transient simulation, nonlinear, steady-state response, and stability of steady-state response.

Continuing efforts are aimed at an analysis of the nonlinear stability of the solutions. This is particularly interesting because a stable, asynchronous, noncircular, steady-state orbit seems to exist for a wide range of parameters. Other efforts are addressed at (a) effects of external, unidirectional forces such as gravity, (b) optimization with competing objectives, and (c) multi-degree-of-freedom systems with multiple dampers.

References

- 1 *Proceedings of the Conference on the Stability and Dynamic Response of Rotors with Squeeze-Film Bearings*, May 8-10, 1979, U.S. Army Research Office, Research Triangle Park, North Carolina.
- 2 Gunter, E. J., Barrett, L. E., and Allaire, P. E., "Design of Nonlinear Squeeze Film Dampers for Aircraft Engines," *Journal of Lubrication Technology*, Vol. 99, No. 1, Jan. 1977, pp. 57-64.
- 3 Taylor, D. L. and Kumar, B. R. K., "Nonlinear Response of Squeeze Film Dampers," *ASME Journal of Lubrication Technology*, Jan. 1980, Vol. 102, pp. 51-58.
- 4 Mohan, S. and Hahn, E. J., "Design of Squeeze Film Damper Supports for Rigid Rotors," *ASME Journal of Engineering for Industry*, Aug. 1974, pp. 976-982.
- 5 Pan, C. H. T. and Tonneson, Jr., "Eccentric Operation of the Squeeze Film Damper," *ASME Journal of Lubrication Technology*, Vol. 100, No. 2, July 1978, pp. 369-378.
- 6 Sharma, R. K. and Botman, M., "An Experimental Study of the Steady State Response of Oil-Film Dampers," *ASME Journal of Mechanical Design*, Vol. 100, No. 2, Apr. 1978, pp. 216-221.
- 7 Greenhill, L. M., and Nelson, H. D., "Iterative Determination of Squeeze Film Damper Eccentricity for Flexible Rotor Systems," ASME Paper No. 81-DET-87.
- 8 Kumar, B. R. K., *Nonlinear Dynamics of the Squeeze Film Damper*, M. S. thesis, Cornell University, 1980.
- 9 Childs, D., Moes, H., and van Leeuwen, H., "Journal Bearing Impedance Description for Rotor-dynamic Applications," ASME Paper No. 76-Lub-24, *ASME Journal of Lubrication Technology*, Apr. 1977.
- 10 Booker, J. F., "Dynamically Loaded Journal Bearings: Numerical Application of the Mobility Method," *ASME Journal of Lubrication Technology*, July 1971, pp. 168-176.
- 11 White, D. C., "The Dynamics of a Rigid Rotor Supported on Squeeze Film Bearings," *Proceedings of the Conference of Vibrations in Rotating Systems*, Institute of Mechanical Engineers, London, Feb. 14-15, 1972, pp. 213-229.
- 12 Booker, J. F., "A Table of the Journal-Bearing Integral," *Journal of Basic Engineering*, June 1965, pp. 533-535.

DISCUSSION

E. J. Hahn¹

The major portion of this paper deals with the determination of the steady-state unbalance response of centrally preloaded symmetric rigid rotors in squeeze film dampers, and it is instructive to note the relevance of previous in-

vestigations in this area. Though circular orbit solutions had been utilized even earlier [11], documentation for centrally preloaded situations appeared around 1974, as evidenced by [4], wherein the desirability of assuming synchronous circular steady-state solutions, leading to equations (6), rather than arriving at such solutions via the full transient solution of the equations of motion (3) (whether such transient solutions be via hybrid or digital computer solution procedures) was demonstrated. The regions of bistable operation were more extensively investigated and extended to include supply pressure effects in [13]. For the assumed pressure distributions in this paper corresponding to the special case of zero supply pressure parameter P in [13], the conditions for bistable operation are summarized in Fig. 14, where the nondimensional parameters Ω/ω , U , and B refer to Ω , δ , and $\lambda/2$ in the notation of this paper. Thus, Fig. 14 predicts jump up at nondimensional speeds of 2.3 and 4.5 for unbalance parameter $\delta=0.3$ and bearing parameter $\lambda=0.072$, in agreement with Fig. 9 of this paper. To avoid ambiguity, jump up or jump down refers to whether there is a (theoretically) possible orbit increase or decrease, should one enter a bistable operating speed range from a monostable operating speed range. Whether such a jump to the alternative stable solution is likely to occur is, of course, another question. That the complicated bistable operating regimes predicted in Fig. 14 are practically realizable was verified in [14] and is illustrated in Figs. 15 and 16. Figure 15 shows a typical frequency response test, corresponding to $\delta=0.372$ and $\lambda=0.240$, used to obtain the jump speeds p , q , and r necessary for Fig. 16. Considering the sensitivity of the predicted jump speeds to the unbalance parameter, U , the agreement between theory and experiment was surprisingly good.

With regard to the stability of these steady-state circular orbit solutions, it is noted by the authors that studies (in [8]?) have shown that branch 3 in Fig. 9 is stable and branch 4 is unstable. According to stability investigations in [15, 16], whenever three such synchronous orbit solutions were obtained, the in-between orbit solution was unstable. Thus, not only is branch 4 in Fig. 9 predicted to be unstable, but also that portion or branch 2 in Fig. 9 for which $\epsilon_c > 0.64$. Of particular interest is the comment of the authors regarding the apparent possibility of stable, asynchronous, noncircular, steady-state orbit solutions for a wide range of parameters. This discussor is somewhat sceptical of such solutions, for, as noted in the discussion to [17], such so-called nonsynchronous steady-state solutions can result from numerical inaccuracy in the case of very lightly damped circular orbit solutions. Further comments by the authors on such behaviour would be appreciated.

While it is agreed that the circular orbit steady-state solution approach is generally preferable to the transient solution approach, and hence has, circumstances permitting, been generally preferred, even for more complex rotor bearing systems [7], the authors appear to somewhat overstate the case for the solution procedure used. One of the advantages of transient solution approaches has surely been that *only* stable solutions can be found. Indeed, it is one of the disadvantages of the steady-state solution approach that the solutions obtained, in many instances, provide no indication at all as to whether they are stable; and one has to resort to transient solutions, linear stability analysis, or experimental evidence, to determine stability. Also, it is not clear how a noniterative solution procedure would have fared in the analysis of the more complex systems in [7].

Regarding solution procedures for synchronous circular orbit steady-state solutions, one is ultimately confronted with a nonlinear equation in the orbit radius in terms of the relevant system parameters; i.e., in the notation used in this paper, this involves the solution of equation (8) for ϵ_c in terms

¹Senior Lecturer, The University of New South Wales, Kensington, NSW, 2033, Australia

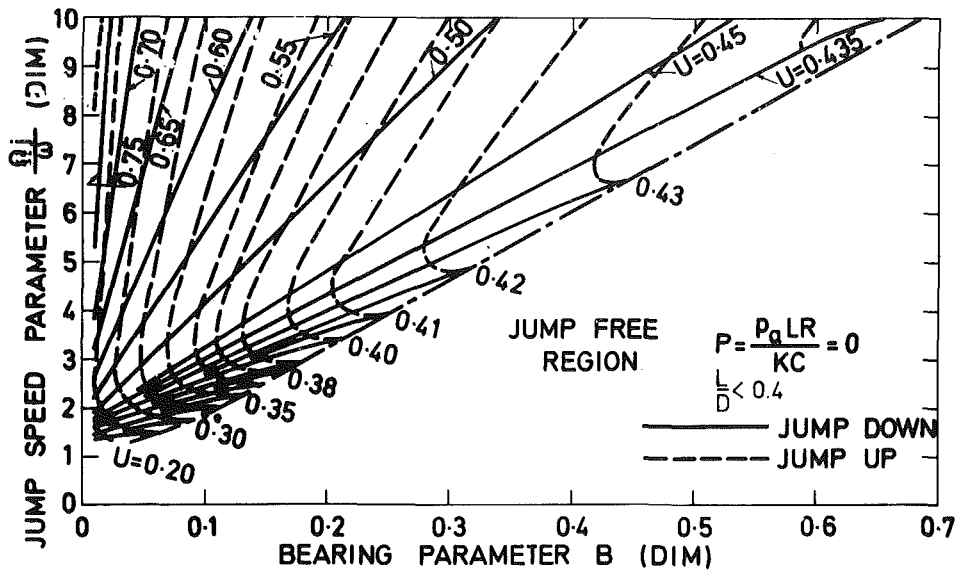


Fig. 14 Variation of jump speed with bearing parameter and unbalance parameter for unpressurized bearings (Fig. 4 of [13])

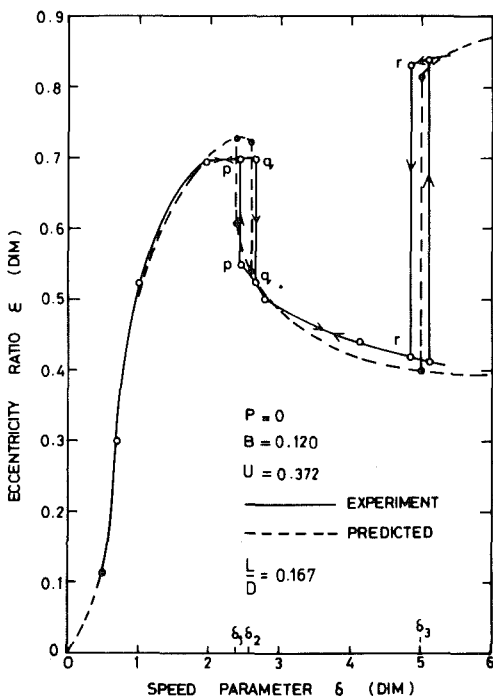


Fig. 15 Multiequilibrium frequency response of eccentricity ratio (Fig. 11 of [14])

of the three parameters Ω , λ , and δ . There are a variety of ways of solving equation (8) for physically meaningful values of ϵ_c (i.e., for $0 < \epsilon_c < 1$). Whether one adopts an iterative procedure, e.g., a simple search procedure, to find the value(s) of ϵ_c for some given values of Ω , λ , and δ (and this is the ultimate goal), or one avoids iteration by assuming values for the dependent parameter, ϵ_c , and for only two of the three system parameters Ω , λ and δ , and then solving for the third system parameter directly, is generally dictated by the amount of effort needed to achieve the required end results. Noniterative procedures, as adopted by the authors, solve equation (8) by an inverse-type approach. To obtain the actual value(s) of ϵ_c for, say, some specified Ω_0 , λ_0 , and δ_0 requires successive solutions of equation (8) for Ω over a sufficient range of ϵ_c values to ensure that all values of ϵ_c

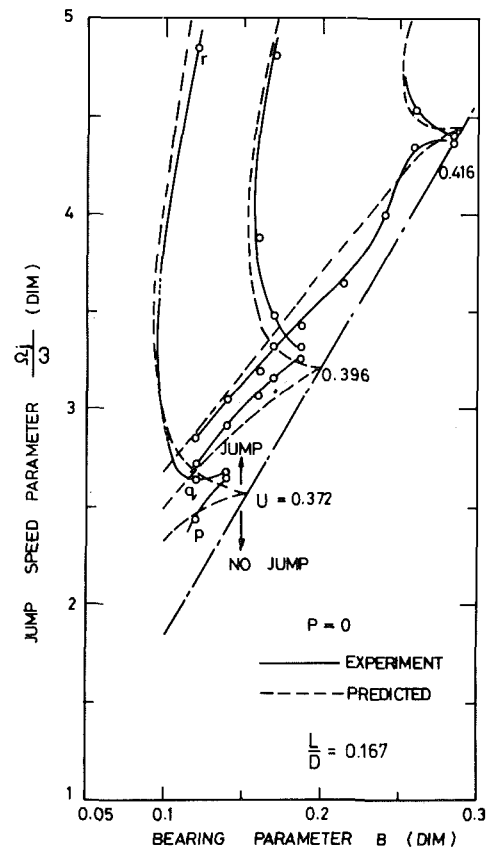


Fig. 16 Variation of jump speed with bearing and unbalance parameter for unpressurized bearings (Fig. 12 of [14])

likely to result in $\Omega \approx \Omega_0$, have been covered. The final values of ϵ_c at Ω_0 then need to be determined by interpolation (e.g., by graphing). Thus, if one is merely seeking the ϵ_c values corresponding to a single set of parameters Ω_0 , λ_0 , and δ_0 , such a noniterative procedure, which involves finding solutions over a range of Ω , is generally more time consuming than an iterative approach. On the other hand, if one is seeking to present solutions for ϵ_c over a range of the system parameters, the noniterative approach would generally be

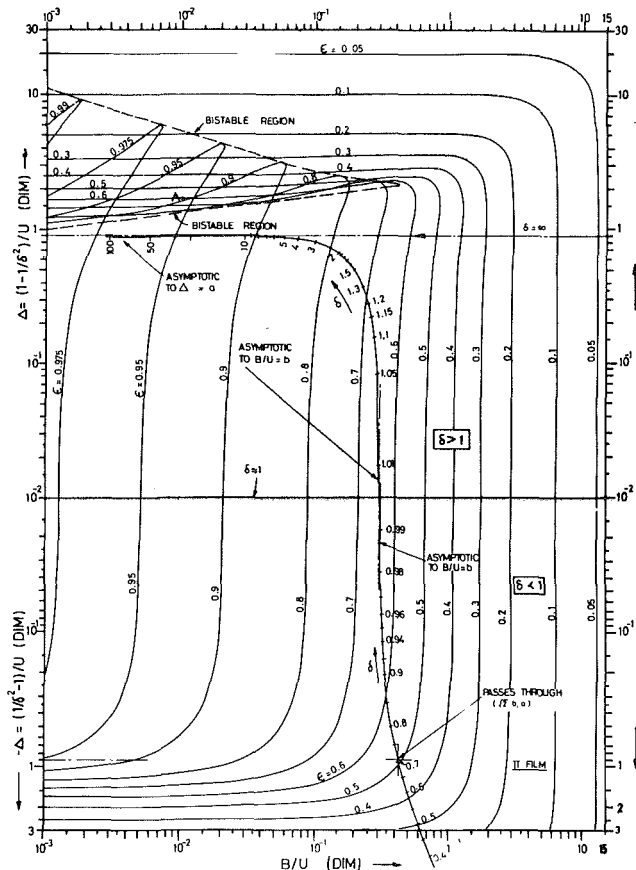


Fig. 17 Equilibrium orbit eccentricity data for unpressurized squeeze film supported rotors (Fig. 2 of [19] or [20])

preferable. In any case, it is felt misleading to refer to such noniterative numerical solution procedures as "closed form," a term which implies that an analytical expression is available for the dependent variable, ϵ_c , in terms of the system parameters Ω , λ , and δ .

Equation (8) of the paper corresponds to equation (13) in [18] or equation (6) in [19, 20] viz.,

$$(g_r B/U)^2 + (g_r B/U - \epsilon \Delta)^2 = 1 \quad (18)$$

where

$$\Delta = (1 - 1/\delta^2)/U \quad (19)$$

in the notation of [18-20].

In the notation of this paper, g_r corresponds to $\epsilon_c J_3^{20} |c_c$, g_r to $\epsilon_c J_3^{11} |c_c$, δ to Ω , U to δ , B to λ/Ω , and ϵ to ϵ_c . Equation (18) shows that in fact only two systems parameters, viz., B/U and Δ (or $\lambda/(\Omega\delta)$ and $(1 - 1/\Omega^2)/\delta$ in the notation used by the authors) are sufficient to uniquely determine the steady-state orbit radius ϵ_c . Hence, by solving equation (18) either using an iterative or noniterative procedure, it is possible to display all possible equilibrium solutions for the orbit radius, ϵ_c , on a single diagram. For reasons already discussed above, equation (18), being a quadratic in the parameter B/U , was solved for B/U directly over a physically meaningful range of ϵ_c and Δ , as shown in Fig. 17. Frequency response curves such as Figs. 3-7 and Fig. 9 of this paper may be all obtained from Fig. 17 by following the operating line, the positioning of which is explained in [19] or [20]. Once the ϵ_c solution has been obtained, corresponding transmissibility and phase angle values may be obtained as explained in [18-20], or in this paper. Unfortunately, it was not found possible to portray transmissibility data as conveniently. Figure 17 illustrates the

point made in the paper about the disappearance of bistable operation for sufficiently large unbalance. Thus, once Δ in Fig. 17 is less than unity, bistable operation is not possible. This is not, however, a recommended operating condition, since such low values of Δ , resulting from values of unbalance parameter in excess of unity, always result in transmissibilities in excess of 1, as explained in [19, 20]

Additional References

- 13 Simandiri, S., and Hahn, E. J., "Effect of Pressurization on the Vibration Isolation Capability of Squeeze Film Bearings," *ASME Journal of Engineering for Industry*, Vol. 98, No. 1, 1976, pp. 109-117.
- 14 Simandiri, S., and Hahn, E. J., "Experimental Evaluation of the Predicted Behavior of Squeeze-Film-Bearing-Supported Rigid Rotors," *Journal of Mechanical Engineering Science*, IME, Vol. 21, No. 6, 1979, pp. 439-451.
- 15 Simandiri, S., "A Study of Squeeze Film Bearings", Ph.D. thesis, University of New South Wales, 1978.
- 16 Rabinowitz, M. D., and Hahn, E. J., "Stability of Squeeze Film Damper Supported Flexible Rotors", *ASME JOURNAL OF ENGINEERING FOR POWER*, Vol. 99, No. 4, 1977, pp. 545-551.
- 17 Holmes, R., "The Control of Rotor Vibrations Using Squeeze Film Damper," *Proceedings of the Conference on the Stability and Dynamic Response of Rotors with Squeeze Film Bearings*, US Army Research Office, Charlottesville, Va., May 1979, pp. 53-72.
- 18 Hahn, E. J., "Stability and Unbalance Response of Centrally Preloaded Rigid Rotors Mounted in Journal and Squeeze Film Bearings," *ASME Journal of Lubrication Technology*, Vol. 101, No. 2, 1979, pp. 120-127.
- 19 Hahn, E. J., "Unbalance Behaviour of Squeeze Film Supported Rigid Rotors," *Proceedings of the Conference on the Stability and Dynamic Response of Rotors with Squeeze Film Bearings*, US Army Research Office, Charlottesville, Va., May 1979, pp. 176-188.
- 20 Hahn, E. J., "Squeeze Film Bearings as Vibration Isolators for Unbalanced Rigid Rotors," *ASLE Transactions*, Vol. 24, No. 2, 1981, pp. 239-246.

Authors' Closure

The authors are certain that readers will appreciate the additional references provided (also cited in [1, 8]). In response to the discussion, it seems appropriate to review why this approach was chosen. The basic goal is to determine the overall structure of the dynamic response of this well-known system. An associated problem is how much to distill (for presentation) the response of a four-state system with three physically meaningful parameters. To this end, a single graph is not as meaningful as a family of curves in understanding why multiple responses may or may not occur in one or more speed ranges. It would have been even better to present a series of phase plane plots at various speeds in place of each figure such as Fig. 3, but space is prohibitive. The interested reader is referred to [8].

The value of knowing the overall structure can be shown in that the stable, high-speed, high- ϵ response (branch 3,4 in Fig. 9) was deduced from purely structural reasoning prior to any confirmation of its existence. Given the goal of a total response characterization, it becomes clear that both stable and unstable responses must be known to understand the overall topology, of the system. (A stable point cannot simply become unstable or split into two but must follow well-known bifurcation laws.)

The desire for overall topology of all possible solutions drives the analysis to closed form. The determination of the governing algebraic equations is one step closer than the governing O.D.E. The further reduction from nonlinear to polynomial form assures that all fixed points are known (vital for topology), independent of how they are actually determined.

Based on discussions after this paper was written, it is clear that curve 4 in Fig. 9 must be unstable. However, this is not for the seemingly obvious reasoning that 2 and 3 are stable. The reader is cautioned that this is a four-state system and so many familiar phase plane rules do not hold. Rather, curve 4 must be unstable because a parameter variation in λ will cause

the two "noses" of the curve to meet and merge, and the stability characteristics before and after must be consistent. The stability of each branch has been determined in [8].

Although the discussion documents a jump at higher speeds (δ_3 in Fig. 15), the authors have no analytical basis for initiation of the jump, unlike the inevitability of the lower speed jump/drops shown during speed scans. The smaller response is stable and should be maintained unless greatly disturbed. It is a purely subjective conclusion of the authors that the larger response is less stable in a global sense and so should not dominate except for a particular range of initial conditions.

The existence or nonexistence of jump drop regions as seen from Fig. 17 can be confusing. The authors have found Fig. 17 easier to understand in light of Figs. 3-7. For instance, every damper, for any particular unbalance, has one (and possibly two) speed ranges for which multivalued response is possible. Thus, even larger values of unbalance lead to multivalued response (contrary to the discussion). Consider

curve 2 in Fig. 5. The lower half of the disconnected branch is stable, although during a speed scan a "drop" will not occur without external disturbance. In terms of Fig. 17, the bistable region monotonically expands with decreasing B/U , and thus any operating line will eventually intersect it at sufficiently high speed.

As noted, the nonsynchronous, high-speed, high-eccentricity orbits are mentioned in [13, 1], and the accompanying discussion submitted by the first author of this paper. It is true that the high-speed responses are very lightly damped [8], but this appears as a beat phenomenon of slowly decaying transient vibrations at the natural frequency superimposed on the forced response at the running speed. The nonsynchronous response (precessing loops) is numerically stable under changes in integration step size. The authors are currently trying to determine topologically if such a response is a valid response. Until then, any comments are welcomed as to how to determine if the "simulation response" is a valid "physical response."

The Effect of Journal Misalignment on the Oil-Film Forces Generated in a Squeeze Film Damper

R. A. Cookson

Head of Applied Mechanics,
School of Mechanical Engineering,
Cranfield Institute of Technology,
Bedford MK43 0AL,

X. H. Feng

Head of Vibration and Strength
Analytical Research Group,
Aero-Gas Turbine Research Institute,
Chinese Aeronautical Establishment,
Peking, China

S. S. Kossa

Lecturer,
Military Technical College,
Cairo, Egypt

Squeeze film damper performance is usually assessed on the assumption that the axis of the journal is parallel to that of the bearing housing. For many practical cases, for example that of the overhung fan shaft in an aero gas turbine, these two elements are unlikely to be parallel, even when self-aligning bearings are used. In this theoretical study an attempt has been made to evaluate the effect of misalignment on the magnitude of the oil-film forces produced in a squeeze film damper bearing, and to this end a computational procedure has been established. From the results reported in this paper, it has been clearly shown that the effect of misalignment in a two-land, squeeze film damper can lead to a significant increase in the transmission of unbalance force through the oil film. As an example, data from a previously reported investigation into the performance of a simple two-bearing model with a single centrally supported disk have been used in a typical calculation. The results from this computation indicated that the oil-film forces generated, could have been several times greater than those calculated on the assumption that the journal and bearing housing were parallel. Unfortunately, there do not appear to be any clear guidelines to lay down to the designers of squeeze film dampers at this moment, in relation to journal misalignment. In general, the effect of misalignment is strongest when the ratio of land-length to radial clearance is greatest, when large unbalance is being accommodated, and when the orbit size is large. In our own analytical studies, the effect of misalignment is allowed for whenever the angle of misalignment is greater than 0.0005 radians.

Introduction

Many modern rotating machines, in particular gas turbines, are fitted with squeeze film damper bearings in order that vibratory forces produced by the rotor are attenuated as they pass into the surrounding structure. By the very nature of the device these forces are transmitted through the fluid-film (squeeze film) which supports the orbiting journal. Hence, it is obvious that an accurate assessment of the fluid-film (usually oil) forces is required if an efficient, squeeze film damper design is to be achieved.

For normal, squeeze film damper design, a two-land geometry is adopted, and since the L/D ratio for these lands is small, it is usual to employ the so-called "short bearing" approximation when calculating the oil-film forces produced in the device. The short-bearing approximation arises naturally from the well-known Reynolds' equation for a plane slider bearing which in turn was derived from the Navier-Stokes equation for incompressible fluids [1]. Reference [2] has reduced this equation to the short journal condition in

detail but only for the case where the journal is parallel with the bearing housing.

In practice, it is unlikely that the slope of the journal, as it passes through the squeeze film damper, will correspond with that of the bearing housing, even when self-aligning rolling contact bearings are employed. Such misalignment will naturally change the fluid-film pressure distribution and consequently the resultant fluid-film force. It is possible that the misalignment existing (on occasion) in a simple, symmetric (two-bearing, midspan disk) system, as was employed for example in the research described in [3] and [4], could affect the load carrying characteristics of the squeeze-film dampers. For the asymmetric configuration often employed in gas turbines, where a heavy rotor (e.g., fan disk) is overhung beyond one of the bearings, it is obvious that the degree of misalignment could be significantly greater.

Dubois et al. [5, 6] have previously investigated the effect of misalignment in journal bearings and have produced photographic evidence that the oil-film pressure profile was sensitive to axial and twisting misaligning couples. Hence, it was decided to investigate the effect of misalignment on the fluid-film forces produced in a squeeze film damper, and to incorporate this analysis into a current study of the rotor-dynamic behaviour of an overhung disk/shaft system which is fitted with squeeze film dampers and flexible supports.

Contributed by the Gas Turbine Division of THE AMERICAN SOCIETY OF MECHANICAL ENGINEERS and presented at the 27th International Gas Turbine Conference and Exhibit, London, England, April 18-22, 1982. Manuscript received at ASME Headquarters December 22, 1981. Paper No. 82-GT-285.

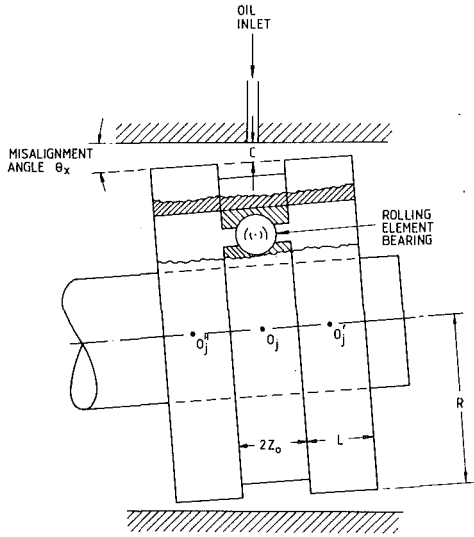


Fig. 1 Misaligned squeeze film damper

Analytical Model

The model employed assumes that there are two lands of similar length, radius, and radial clearance within the squeeze-film damper and that they are separated by an annular groove which is positioned at the bearing midspan (see Fig. 1).

If the axes of the journal (shaft) and the housing do not coincide, then the coordinates of the journal centerline, for different values of the z' coordinate, can be expressed as follows (see Fig. 2):

$$x = x_0 + \theta_x z' \quad \dots \dots \dots (1)$$

$$y = y_0 + \theta_y z' \quad \dots \dots \dots (2)$$

where

$$x_0 = x_{ji} - x_{Bi} \quad \dots \dots \dots (3)$$

$$y_0 = y_{ji} - y_{Bi} \quad \dots \dots \dots (4)$$

and are the coordinates of the journal centerline at its midspan for the i^{th} bearing.

o_j , o_j'' and o_j' are the centroids of the journal, the right-hand land, and the left-hand land, respectively (see Fig. 1). θ , θ' and θ'' are the angles, measured circumferentially, from the line passing through o_j and o_b in the plane of the center of the journal, from the line passing through o_j' and o_b in the plane of the center of the right-hand land, and from the line passing through o_j'' and o_b in the plane of the center of the left-hand land (see Fig. 2).

If the oil film thickness, h , at any axial coordinate z is expressed as a function of θ and z , it will be necessary to modify θ' and θ'' in the following manner:

$$\text{for the right-hand land} \quad \theta' = \theta - |\Delta\theta'| \quad \dots \dots \dots (5)$$

$$\text{for the left-hand land} \quad \theta'' = \theta + |\Delta\theta''| \quad \dots \dots \dots (6)$$

Consequently,

$$h(\theta, z) = c + \sqrt{(x_0 + \theta_x z)^2 + (y_0 + \theta_y z)^2} \cos(\theta - \Delta\theta) \quad (7)$$

Where

$$\Delta\theta = \tan^{-1} \left(\frac{y_0 + \theta_y z}{x_0 + \theta_x z} \right) - \tan^{-1} \left(\frac{y_0}{x_0} \right) \quad \dots (8)$$

It should be noticed that for some cases $\Delta\theta$ is not necessarily a small quantity.

The generalised Reynolds equation, derived from the flat plate model, can be expressed as follows:

$$\begin{aligned} \frac{\partial}{\partial x} \left[\frac{\rho}{\mu} \frac{\partial p}{\partial x} h^3 \right] + \frac{\partial}{\partial z} \left[\frac{\rho}{\mu} \frac{\partial p}{\partial z} h^3 \right] &= 12\rho(V_2 - V_4) + 12h \frac{\partial \rho}{\partial t} \\ + 6 \frac{\partial}{\partial x} \left[\rho h(U_1 + U_2) \right] + 6 \frac{\partial}{\partial z} \left[\rho h(W_1 + W_2) \right] \\ - 12\rho \left[U_2 \frac{\partial h}{\partial x} + W_2 \frac{\partial h}{\partial z} \right] &\dots \dots (9) \end{aligned}$$

Substituting (7) into (9) and treating the result in a manner similar to that used by [2], the oil-film pressure $p(\theta, z)$ can be expressed in the following form:

$$\begin{aligned} \frac{\partial^2 p}{\partial z^2} + \frac{3}{h} \left[\left(\frac{\theta_x(x_0 + \theta_x z) + \theta_y(y_0 + \theta_y z)}{\sqrt{(x_0 + \theta_x z)^2 + (y_0 + \theta_y z)^2}} \right) \cos(\theta - \Delta\theta) \right. \\ \left. + \left(\frac{\theta_y(x_0 + \theta_x z) - \theta_x(y_0 + \theta_y z)}{\sqrt{(x_0 + \theta_x z)^2 + (y_0 + \theta_y z)^2}} \right) \sin(\theta - \Delta\theta) \right] \frac{\partial p}{\partial z} \\ = \left[\left\{ \frac{-(y_0 + \theta_y z)(\dot{x}_0 + \dot{\theta}_x z) + (x_0 + \theta_x z)(\dot{y}_0 + \dot{\theta}_y z)}{\sqrt{(x_0 + \theta_x z)^2 + (y_0 + \theta_y z)^2}} \right\} \sin(\theta - \Delta\theta) \right. \\ \left. + \left\{ \frac{(x_0 + \theta_x z)(\dot{x}_0 + \dot{\theta}_x z) + (y_0 + \theta_y z)(\dot{y}_0 + \dot{\theta}_y z)}{\sqrt{(x_0 + \theta_x z)^2 + (y_0 + \theta_y z)^2}} \right\} \cos(\theta - \Delta\theta) \right] \frac{12\mu}{h^3} \dots \dots (10) \end{aligned}$$

Hence, the oil-pressure distribution can be obtained from (10) by means of the finite difference technique.

Analysis

For the purpose of calculating the oil-film pressure distribution, and the resulting oil-film forces from the Simpson integration procedure, each land is divided into 72 circumferential and 20 axial divisions. The pressure is determined at the center of each of the resulting rectangular

Nomenclature

- c = radial clearance of squeeze-film damper
- F_x, F_y = oil-film force components in the x and y directions
- F = resultant oil-film force
- h = oil-film thickness
- L = squeeze-film damper land length
- m = journal mass
- p = oil-film pressure
- R = bearing radius
- U = circumferential component of velocity

- V = radial component of velocity
- W = axial component of velocity
- x, y, z = Cartesian coordinate system
- θ = angle measured from line of centers
- μ = absolute viscosity of oil
- ρ = density of oil
- ϕ = attitude angle
- ω = angular speed

Subscripts

- B = bearing
- j = journal
- L = left-hand land
- R = right-hand land
- 0 = midspan or zero slope

Superscripts

- ($'$) = right-land
- ($''$) = left-land
- (\bullet) = d/dt

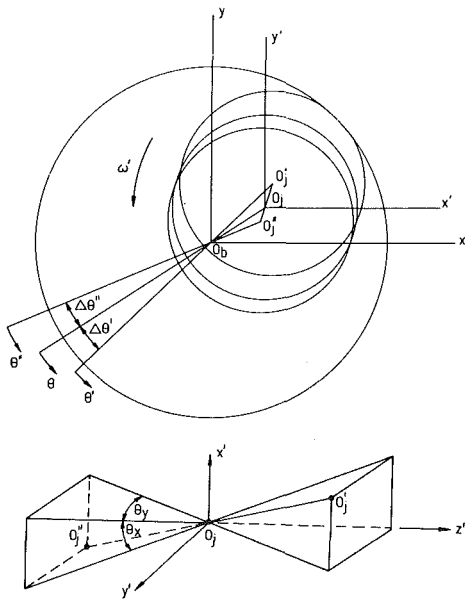


Fig. 2 Coordinate systems

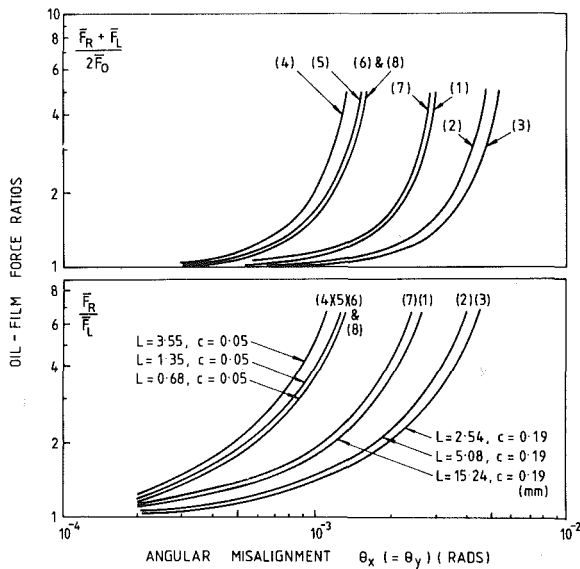


Fig. 3 Effect of land-length and clearance on the oil-film ratios in a misaligned squeeze film damper

elements, and is assumed to act uniformly over the entire area of the element. This finite difference technique has been written as a Fortran IV computer program and checked for accuracy against the full theoretical solution of [7] for a case with no misalignment. This comparison indicated that the 72×20 finite-difference mesh gave results which were very accurate and more than adequate for the present investigation.

For the above computer program the following input data are required: (a) squeeze film damper radial clearance, c ; (b) land length, L ; (c) bearing radius, R ; (d) bearing mass, m ; (e) absolute viscosity of oil, μ ; (f) first pin-pin critical speed of rotor, ω_c ; (g) oil supply pressure, p_0 ; (h) oil leakage pressure p_n ; (i) half-width of oil supply groove z_0 ; (j) x_0 and y_0 , coordinates of the journal centerline θ_x and θ_y , in the x_0z and y_0z planes, respectively; linear velocities, \dot{x}_0 , \dot{y}_0 of journal at its midspan; (k) angular velocities of journal centerline, $\dot{\theta}_x$ and $\dot{\theta}_y$, in x_0z and y_0z planes, respectively.

From the above computer program the following results are available, if required (i) distribution of oil-film thickness over land annular surface; (ii) distribution of oil-film

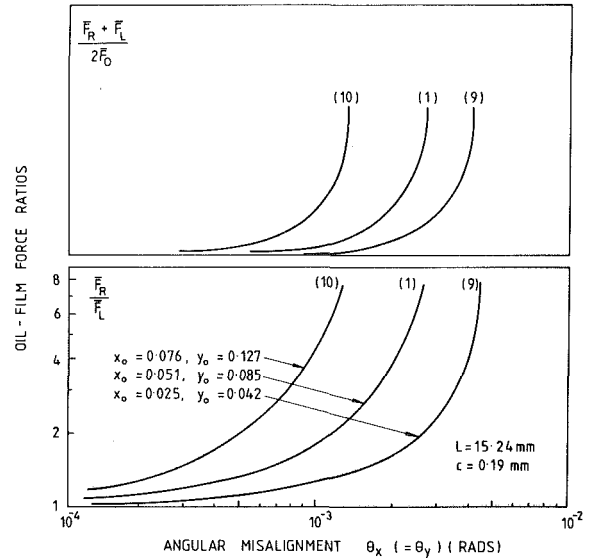


Fig. 4 Effect of bearing coordinates on the oil-film force ratios in a misaligned squeeze film damper

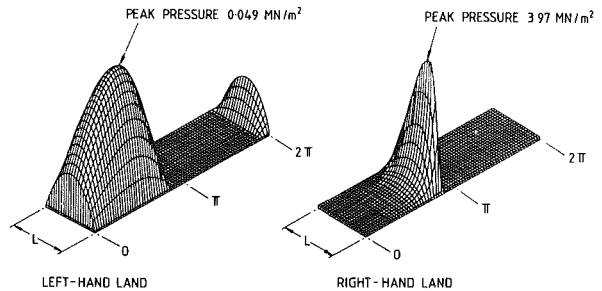


Fig. 5 Oil-film profiles in a misaligned two-land squeeze film damper (case No. 4 with $\theta_x = \theta_y = 0.00138$ rads)

hydrodynamic pressure over land annular surface; (iii) variation in the z (axial) direction of the x and y components of the oil-film resultant force; (iv) total x and y components of the oil-film resultant force; (v) nondimensional total oil-film resultant forces.

$$\bar{F}_x(\text{non-dimens.}) = \frac{F_x(\text{absolute})}{mc\omega_c^2}$$

$$\bar{F}_y(\text{non-dimens.}) = \frac{F_y(\text{absolute})}{mc\omega_c^2}$$

$$\bar{F}(\text{non-dimens.}) = \sqrt{\bar{F}_x^2 + \bar{F}_y^2}$$

The finite difference program also provides (vi) information on the influence of misalignment in the following form:

$$\frac{\bar{F}}{\bar{F}_0}$$

which is the ratio of the total oil-film resultant force with misalignment to that without misalignment (slope=0) for otherwise similar conditions

$$\frac{\bar{F}_R}{\bar{F}_L}$$

which is the ratio of the total oil-film resultant force acting on the right-hand land in a misaligned bearing to that acting on the left-hand land

$$\frac{\bar{F}_R + \bar{F}_L}{2\bar{F}_0}$$

which is the ratio of the sum of the oil-film resultant forces acting on the right-hand and left-hand land in a misaligned bearing to twice that acting on a single land in a bearing without misalignment

Also the computer program can provide (vii) a three-dimensional representation of the oil-film pressure profile around a land annular surface.

If the data fed into the finite difference program are unreasonable and lead (say) to an oil-film thickness which is < 0 , the computation is terminated.

Results

In order to determine the effect of misalignment on the oil-film forces and the relative importance of individual parameters, any reasonable damper parameters could be utilized in the finite difference program described above. However, for the sake of realism, the parameters employed in this investigation have been taken from (or are close to) the results given in [3].

The basic data employed in [3] are as follows:

Land-length, L	= 15.24, 5.08, 2.54 mm
Radial clearance, c	= 0.19, 0.10, 0.05 mm
Bearing radius, R	= 50.8 mm
Mass of bearing journal, m	= 3.98 kg.
Half groove width, z_0	= 8.58 mm
First critical speed of rotor, ω_c	= 759 rad/s
Absolute viscosity of oil, μ	= 2.36×10^{-2} Ns/m ²

Substituting these values into the dynamic equations of [8], realistic values of the bearing coordinates x_0 and y_0 , and the linear velocities \dot{x}_0 and \dot{y}_0 , were obtained. Other similar parametric values were then adopted and the table shown below compiled.

In order to eliminate one variable, $\dot{\theta}_x = \dot{\theta}_y$ was assumed to be constant (say zero) for the oil-film calculations which involved the parameters in the table below. This assumption was only true at one point on the journal orbit, but $\dot{\theta}_x = \dot{\theta}_y$ is always small. Not reported here for reasons of space, a further part to this investigation indicated that the influence of $\dot{\theta}_x$ and $\dot{\theta}_y$ (and \dot{x}_0 and \dot{y}_0) on the oil-film pressure distributions was small.

Using the parameters contained in the table below in the finite-difference solution to equation (10), values of $(\bar{F}_R + \bar{F}_L)/2\bar{F}_0$ and \bar{F}_R/\bar{F}_L were plotted for values of the misalignment angle θ_x . These curves are shown in Fig. 3. Similarly, because it was thought that the journal coordinates (which, of course, are not independent variables) would also have a strong influence on the nonsymmetric distribution and magnitude of the oil-film forces in a two-land, squeeze film damper, a further set of curves for constant L and c , and varying x_0 and y_0 , are shown in Fig. 4.

A typical representation of the oil-film pressure profile over the two lands in a misaligned squeeze film damper, is given in Fig. 5. This is for case No. 4 in the table where $L = 3.55$ mm, $c = 0.05$ mm, and the misalignment angle $\theta_x = \theta_y = 0.00138$ rads.

Discussion

From Fig. 3, it can be seen that the ratios $(\bar{F}_R + \bar{F}_L)/2\bar{F}_0$ and \bar{F}_R/\bar{F}_L increase most rapidly with the misalignment angle θ_x when the land-lengths are longest. That is, for cases 1, 2, and 3 where the clearance $c = 0.19$ mm, the most rapid increase in the oil-film force ratios is found when $L = 15.24$ mm. Similarly, for cases 4, 5 and 6 where $c = 0.05$ mm, $L = 3.55$ mm produces the most significant increase of the oil-film force ratios with the misalignment angle. This trend is surely to be expected, since for some specific radial clearance, oil-films produced by the longer lands will be most seriously influenced by the proximity of the bearing housing, until finally contact will be made between the edge of the journal and the housing.

For case 7, all of the parameters, except the bearing radius, were doubled (as compared with case 6), and the resulting oil-film forces were also found to increase by a factor of two. Hence, for this case the influence of the misalignment was much reduced. For case 8, all of the parameters, including the bearing radius, were again doubled and the misalignment influence was seen to remain the same as for that in case 6.

From Fig. 4, it can be seen that the influence of misalignment is most strongly felt when the journal coordinates are greatest, that is, when the centroid of the journal is furthest from the center of the clearance circle. Again, this is intuitively reasonable since the influence of the oil-film is nonlinear and will consequently be much stronger as the journal approaches the bearing housing.

As typical examples of the level of increase in the oil-film forces which can be created in a misaligned squeeze-film damper, three reasonably typical conditions have been taken from [3]. Reference [3] is based upon a simple, two-bearing, flexible shaft system with a single disk supported midway between the two, squeeze-film damper bearings. In general, conditions in [3] were expressed in terms of nondimensional parameters as follows. Bearing parameter $B = \mu RL^3/m_L \omega_c c^3$, gravity parameter $W = g/\omega_c^2 c$, frequency parameter $\Omega = \omega/\omega_c$, and mass parameter $\alpha =$ ratio of mass lumped at bearing to that lumped at the central disk.

The appropriate parametric values have been quoted in connection with the following examples, but absolute values of the salient dimensions have also been given. In each case, the slope of the shaft at each bearing θ_x has been calculated for the critical speed conditions quoted.

Example 1 $B = 0.5$, $W = 0.4$, $\alpha = 0.1$, $\Omega = 1.0$ $L = 1.24$ mm, $c = 0.037$ mm, $R = 50.8$ mm $\theta_x = \theta_y = 0.000183$ rads

$$\frac{\bar{F}_R + \bar{F}_L}{2\bar{F}_0} = 1.61$$

Example 2 $B = 0.2$, $W = 0.4$, $\alpha = 0.4$, $\Omega = 1.0$ $L = 1.24$ mm, $c = 0.037$ mm, $R = 50.8$ mm $\theta_x = \theta_y = 0.000259$ rads

$$\frac{\bar{F}_R + \bar{F}_L}{2\bar{F}_0} = 2.68$$

Case No.	Land length L (mm)	Radial clearance c (mm)	Bearing radius R (mm)	Journal centroid coordinates (mm)		Journal centroid linear velocities (mm/s)	
				x_0	y_0	\dot{x}_0	\dot{y}_0
1	15.24	0.19	50.8	0.051	0.085	2.679	-3.271
2	5.08	0.19	50.8	0.051	0.085	2.679	-3.271
3	2.54	0.19	50.8	0.051	0.085	2.679	-3.271
4	3.55	0.05	50.8	0.014	0.023	0.715	-0.872
5	1.35	0.05	50.8	0.014	0.023	0.715	-0.872
6	0.68	0.05	50.8	0.014	0.023	0.715	-0.872
7	1.36	0.10	50.8	0.028	0.046	1.430	-1.744
8	1.36	0.10	101.6	0.028	0.046	1.430	-1.744
9	15.24	0.19	50.8	0.028	0.046	2.679	-3.271
10	15.24	0.19	50.8	0.076	0.127	2.679	-3.271

Example 3 $B = 0.2$, $\bar{W} = 0.4$, $\alpha = 0.8$, $\Omega = 1.0$ $L = 1.24$ mm, $c = 0.037$ mm, $R = 50.8$ mm $\theta_x = \theta_y = 0.000329$ rads

$$\frac{\bar{F}_R + \bar{F}_L}{2\bar{F}_0} = 5.24$$

The three examples given above are for squeeze film damper configurations which are known to be less efficient in attenuating the transmitted unbalance forces than those which go to make up Fig. 3. However, it is clear from these sample calculations that misalignment can lead to significant increase in the transmitted force in a two-land, squeeze film damper. In practice, some of the misalignment could be taken up by means of self-aligning bearing but it is likely that the influence of misalignment will still be appreciable.

Conclusions

From the above work, it can be seen that the effect of misalignment in a two-land, squeeze film damper can lead to a significant increase in the transmission of unbalance force through the oil-film. For many situations, the effect will be tolerable but whenever the L/c ratio is large (equivalent to a high value of the bearing parameter B), the level of unbalance is large, or the bearing orbit is large, misalignment is likely to lead to an appreciable increase in the oil-film forces.

Unfortunately, at this stage there would appear to be no clear-cut indication (say in the form of a dimensionless parameter) of the range of operating conditions wherein allowance for misalignment should be made, except perhaps to say that a squeeze film damper, which is designed to minimise the transmitted forces, will also minimise the effect

of misalignment. However, for the theoretical studies currently being carried out at Cranfield into the effectiveness of uncentralised squeeze film dampers supporting an overhung (fan) disk and noncentral (turbine) disk, a threshold slope of $\theta_x = \theta_y = 0.0005$ radians has been adopted. Beyond this level, the oil-film forces required in the system dynamic analysis are calculated by means of the technique described in this report.

References

- 1 Pinkus, O., and Sternlicht, B., *Theory of Hydrodynamic Lubrication*, McGraw-Hill, New York, 1961.
- 2 Kirk, R. G., and Gunter, E. J., "Transient Journal Bearing Analysis," NASA Report CR-1549, 1970.
- 3 Kossa, S. S., "Theoretical and Experimental Investigation of Squeeze-film Damper Bearings Supporting Flexible Rotors without a Centralising Spring," Ph.D. Thesis, Cranfield Institute of Technology, 1980.
- 4 Cookson, R. A., and Kossa, S. S., "The Vibration Inhibiting Properties of Uncentralised Squeeze-film Damper Bearings Supporting a Flexible Rotor," ASME JOURNAL OF ENGINEERING FOR POWER, Vol. 103, No. 4, Oct. 1981, pp. 781-787.
- 5 Dubois, G. B., Ockvirk, F. W., and Wehe, R. L., "Experimental Investigation of Misaligning Couples and Eccentricity at the Ends of Misaligned Plain Bearings," NACA Report TN-3352, 1955.
- 6 Dubois, G. B., Mabie, H. H., and Ockvirk, F. W., "Experimental Investigation of Oil-film Pressure Distribution for Misaligned Plain Bearings," NACA Report TN-2507, 1951.
- 7 Barrett, L. E., and Gunter, E. J., "Steady-State and Transient Analysis of a Squeeze-film Damper Bearing for Rotor Stability," NASA Report CR-2548, 1975.
- 8 Cookson, R. A., and Feng, X-H., "The Effectiveness of Uncentralised Squeeze-film Damper Bearings Supporting an Overhung Flexible Rotor-Theoretical Study," *Applied Mechanics Report AM 71*, School of Mechanical Engineering, Cranfield Institute of Technology, 1981.

Unsteady Aerodynamics and Gapwise Periodicity of Oscillating Cascaded Airfoils¹

F. O. Carta

United Technologies Research Center,
East Hartford, Conn. 06108
Mem. ASME

Tests were conducted on a linear cascade of airfoils oscillating in pitch to measure the unsteady pressure response on selected blades along the leading edge plane of the cascade and over the chord of the center blade. The pressure data were reduced to Fourier coefficient form for direct comparison and were also processed to yield integrated loads and, particularly, the aerodynamic damping coefficient. In addition, results from two unsteady theories for cascaded blades with nonzero thickness and camber were compared with the experimental measurements. The three primary results that emerged from this investigation were: (a) from the leading edge plane blade data, the cascade was judged to be periodic in unsteady flow over the range of parameters tested, (b) as before, the interblade phase angle was found to be the single most important parameter affecting the stability of the oscillating cascade blades, and (c) the real blade theory and the experiment were in excellent agreement for the several cases chosen for comparison.

Introduction

The use of linear cascades to investigate phenomena related to turbomachinery blades has always been predicated on the ability of the rectilinear cascade to model blades in an annular array. To this end, steady-state experiments have customarily been devised with sufficient flow and geometric control to provide a uniform, or periodic, flow behavior over as much of the cascade center (i.e., the measurement region) as possible. Although this is desirable in dynamic testing as well, unsteady periodicity is not, as a rule, verified in such tests. Virtually all of the unsteady cascade experiments reported on in the open literature generate data on one or two blades near the center of the cascade with no additional measurements away from the cascade center.

Several test programs have been undertaken in the United Technologies Research Center (UTRC) Oscillating Cascade Wind Tunnel (OCWT) to measure the unsteady loads on the center blade of an 11-blade cascade oscillating in pitch [1-4]. These tests, which have investigated the effects of varying frequency, interblade phase angle, and incidence angle, have indicated a strong cascading effect, influenced largely by changes in interblade phase angle, on blade response. All tests previously conducted in the OCWT have been at the (relatively) large amplitude of $\bar{\alpha} = 2$ deg, and the mean camber line incidence angle has been representative of modest to high loading ($\alpha_{MCL} \geq 6$ deg). Furthermore, all

measurements have been made only on the center blade of the cascade, with no opportunity to verify dynamic periodicity.

The research program just completed had a threefold objective, addressing the three limitations of previous experimental programs. The specific major tasks undertaken in this experiment and reported on herein were:

- 1 To examine the gapwise periodicity of the steady and unsteady blade loads under a variety of conditions
- 2 To determine the effect of a smaller pitching amplitude on the unsteady response
- 3 To examine the effects of steady loading on the unsteady response by performing these tests at both low and modest incidence angles

In addition, comparisons with two advanced unsteady theories for thick, cambered airfoils were made.

Instrumentation

The OCWT, its blades, and the air supply system have been described previously in [1-4], and a detailed summary of the experiment and all its equipment is given in [5]. Hence, this section will focus on those aspects of instrumentation which are particularly relevant to the measurement of unsteady periodicity.

As in previous tests, the center airfoil (blade no. 6) of the eleven blade cascade was extensively instrumented to provide measurements of several flow parameters. Ten miniature high response pressure transducers were placed on each surface of the airfoil to obtain measurements of unsteady static pressures. Coincident in chord position with each high-response orifice is a pneumatic static pressure tap to provide a zero frequency reference for each unsteady pressure. The specific chordwise locations, from 1.2 to 91 percent, were

¹This research was supported by NASA Lewis Research Center under Contract NAS3-22018. Permission to present this material is gratefully acknowledged.

Contributed by the Gas Turbine Division of THE AMERICAN SOCIETY OF MECHANICAL ENGINEERS and presented at the 27th International Gas Turbine Conference and Exhibit, London, England, April 18-22, 1982. Manuscript received at ASME Headquarters December 22, 1981. Paper No. 82-GT-286.

arranged in a Gaussian array to yield maximum accuracy in the numerical integration of the resulting pressure distributions [6]. The same arrangement of pressure orifices was used on the pressure surface.

Five other blades were also instrumented with miniature transducers. The blades are located in the cascade as shown in the schematic diagram in Fig. 1. Blade no. 6 is the fully instrumented center blade. Partial instrumentation was placed on blades no. 3, 4, 5, 7, and 9. Locations, in chord fraction, $\chi = x/c$, of all transducer orifices are listed for all blades in Table 1.

Test Program and Data Acquisition

Test Plan. A total of 96 test conditions were run. These were comprised of all possible combinations of two mean camber line incidence angles ($\alpha_{MCL} = 2 \text{ deg}, 6 \text{ deg}$), two pitching amplitudes ($\bar{\alpha} = 0.5, 2 \text{ deg}$), three frequencies ($f = 9.2, 15.5, 19.2 \text{ Hz}$, and, for a constant velocity of 61 m/s, or 200 ft/s, this was equivalent to reduced frequencies $k = c\beta/2V = \pi cf/V = .072, .122, .151$), and eight interblade phase angles ($\sigma = 0 \text{ deg}, \pm 45 \text{ deg}, \pm 90 \text{ deg}, \pm 135 \text{ deg}, 180 \text{ deg}$).

Steady Data Acquisition and Reduction. Prior to the unsteady test sequences run at each mean camber line incidence angle, detailed steady-state tests were run. This was done to validate and document steady-state cascade periodicity over both leading and trailing edge cascade planes, and to obtain steady-state surface pressure measurements over the blade chord for subsequent use in comparisons with steady and unsteady theory. In addition, downstream flowfield measurements were taken that yielded cascade static pressure rise, flow turning, and blade loss.

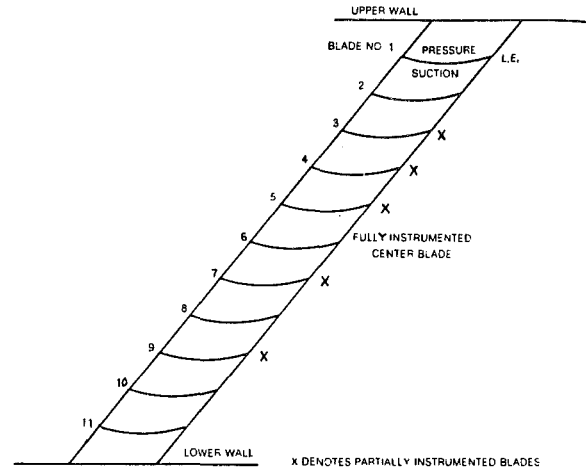


Fig. 1 Schematic of cascade showing instrumented blades

An initial cross tunnel total pressure survey was taken upstream of the blade row to ensure that the exit flow from the inlet honeycomb was undistorted and parallel to the desired flow direction. With the exception of the sidewall boundary layer, which was removed ahead of the cascade leading edge plane, the upstream core flow was found to have a uniform total pressure distribution with a nominal deviation from the mean of less than $\pm 5 \text{ mm H}_2\text{O}$ ($\pm 0.2 \text{ in H}_2\text{O}$). This is equivalent to a velocity deviation of approximately 1 percent relative to the free stream. A further indication of flow uniformity is shown in Fig. 2, in which the steady velocity profiles upstream and downstream of the cascade are shown. These values were calculated from a single total pressure measurement upstream of the blade row and two

Nomenclature

C_M = moment coefficient per unit amplitude, positive nose up, equation (A7)
 C_p = unsteady pressure coefficient per unit amplitude, equation (A1)
 C_W = work coefficient, equation (A8)
 c = airfoil chord, m, equation (B1)
 ΔC_p = unsteady pressure difference coefficient per unit amplitude, equation (A5)
 f = frequency, Hz
 k = reduced frequency, = $c\omega/2V$, equation (B1), or harmonic integer, equation (A14)
 M = Mach number, equation (B1)
 n = blade number, equation (A14)
 p = pressure, newton/m², equation (A1)
 q = dynamic pressure, newton/m², equation (A1)
 t = time, sec, equation (A1)

V = velocity, m/s
 x = chordwise blade coordinate, positive aft, m
 Z_p = total pressure loss coefficient, Fig. 4
 α = pitching angle, positive nose up, deg, equation (A3)
 $\bar{\alpha}$ = pitching amplitude, deg, equation (A1)
 β_1^* = mean camber line stagger angle, equation (B1)
 θ = response phase angle relative to motion, deg or radian, equation (A14)
 $\Delta\theta$ = flow turning angle, deg, Fig. 4
 ν = integer, equation (B1)
 Ξ = aerodynamic damping parameter, equation (A11)
 ρ = air density, newton s²/m⁴
 σ = interblade phase angle, positive for forward travelling wave, deg or radian, equation (A14)

τ = slant gap, m, equation (B1)
 ϕ_M = moment phase angle, deg or radian
 ϕ_p = pressure phase angle, deg or radian, equation (A4)
 χ = dimensionless distance along chord, positive aft, equation (A1)
 χ_p = pivot axis location, equation (A7)
 ω = frequency of oscillation, rad/s, equation (A2)

Subscripts, Superscripts, and Special Symbols

()_I = imaginary part, equation (A2)
()_L = lower or pressure surface, equation (A5)
()_R = real part, equation (A2)
()_U = upper or suction surface, equation (A5)
()ⁿ = blade n , equation (A14)
()⁻ = amplitude, equation (A2)
 $\text{Re}\{ \}$ = real part of { }, equation (A8)

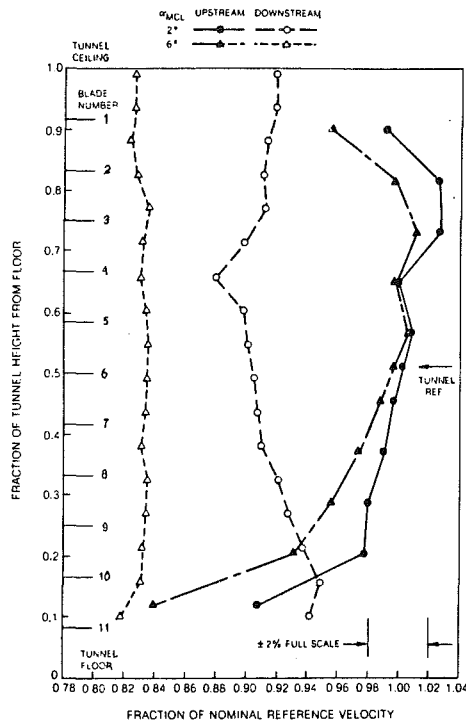


Fig. 2 Steady-state velocity profiles

arrays of sidewall static pressures measured along lines parallel to the plane of the cascade, approximately one blade chord upstream and downstream of the leading and trailing edge planes. In this figure, the vertical locations of all 11 blades and the upper and lower tunnel boundaries are also included along the ordinate.

With the assumption of a uniform total pressure field, the upstream velocity distributions in Fig. 2 are seen to be uniform to within ± 2 percent relative to the nominal velocity over the central measurement region (i.e., blades 3 through 9). The upstream velocity decreases near floor and ceiling are inferred from local sidewall static pressure increases. Downstream velocities show even greater uniformity. The small deviation in velocity between blades 4 and 5 (at .65 tunnel height) is a local sidewall phenomenon caused by the wake of the upstream wedge probe, and did not affect measurements at center span.

Steady-state chordwise pressure distributions for the two incidence angles tested are presented in Fig. 3. There is a marked contrast in pressure distribution between $\alpha_{MCL} = 2$ deg and 6 deg. It is obvious that $\alpha_{MCL} = 2$ deg represents a low load condition. The selection of $\alpha_{MCL} = 6$ deg satisfied two requirements: (i) to provide data on a modestly loaded but unstalled cascade (based on the unstalled behavior of the steady chordwise pressure distribution and other evidence cited below), and (ii) to examine the unsteady periodic behavior of a load condition run previously [4] over a wide range of parameters.

As in [4], several other steady-state parameters were measured. Cascade pressure rise was obtained from the downstream wall static pressure change and is indicated by the tic marks and the numerical values at the trailing edge of each plot in Fig. 3. In addition, flow turning through the cascade, $\Delta\theta$, was measured using the upstream and downstream wedge probes, and total pressure loss coefficient, Z_p , was measured at center span using a 20-tube total pressure rake downstream of the blade row. Values for all three parameters are plotted as circled points in Fig. 4 and are compared with the earlier results of [4], which are plotted as triangular points. The consistency of the detailed agreement at $\alpha_{MCL} = 6$ deg confirms the repeatability of the experiment. In addition, this

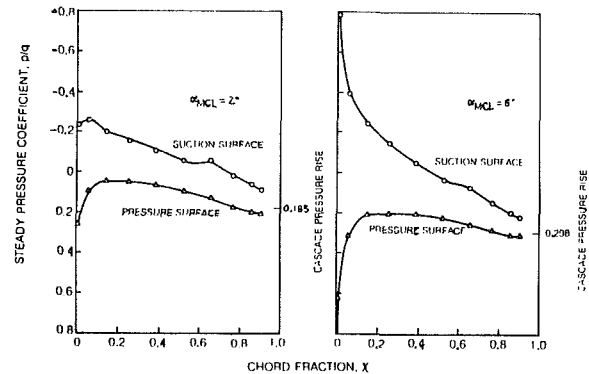


Fig. 3 Steady-state chordwise pressure distributions

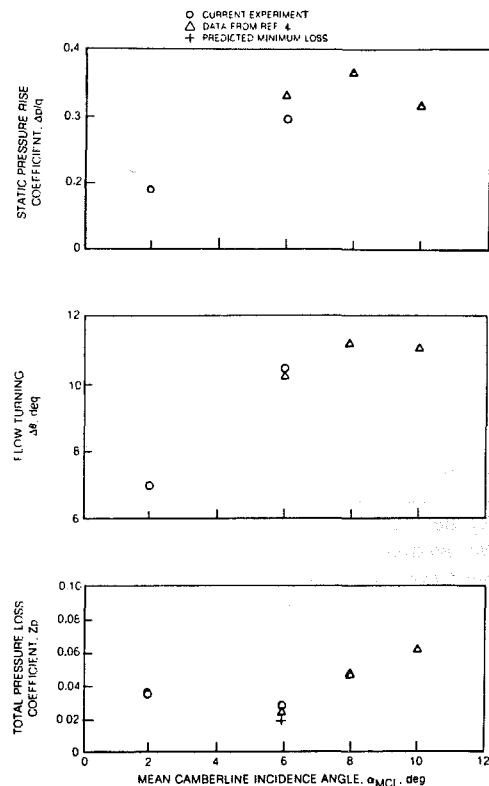


Fig. 4 Steady-state performance parameters

figure shows overall trend agreement for both experiments, from $\alpha_{MCL} = 2$ deg to 10 deg. Finally, the predicted minimum loss of $Z_p = 0.02$ at $\alpha_{MCL} = 6$ deg (cf. [4]) is strongly confirmed by both experiments.

Unsteady Data Acquisition and Initial Reduction. Unsteady blade pressures and blade angular displacement were obtained as time varying voltages which were acquired and recorded in digital form for subsequent off-line processing. The acquisition rate for all unsteady data was set at 1000 samples/s.

Unsteady data for each pressure channel were normalized with respect to the wind tunnel free-stream dynamic pressure and the blade pitching amplitude. Thus, in all subsequent discussions, the unsteady pressure coefficient is defined by

$$C_p(x, t) = \frac{p(x, t)}{q\bar{\alpha}} \quad (1)$$

where p and q have the same dimensions, and where $q = 0.5 \rho V^2$ is the dynamic pressure. Data for each channel were Fourier analyzed, primarily to provide first, second, and third harmonic results for ease in analysis, but also to provide a

Table 1 Transducer orifice locations (fraction of chord)

Blade Number	Values of X	
	Suction Surface	Pressure Surface
6	.0120	.0120
	.0622	.0622
	.1478	.1478
	.2612	.2612
	.3924	.3924
	.5297	.5297
	.6608	.6608
	.7742	.7742
3,5,7,9	.0120	.0120
	.0622	
4	.0050	
	.0120	
	.0350	
	.0622	

compact means of data storage for subsequent use. These data have been completely tabulated in a data report [7]. All results are harmonically referenced to the blade pitching motion.

Unsteady Results

Analysis. Many of the analytical techniques used in reducing data or preparing the reduced data for examination have been used before [1-4], and a full derivation would not normally be warranted. However, in view of the extended analyses needed for periodicity evaluation, the relevant equations have been collected in Appendix A.

All of the results described in the ensuing sections have been operated on by the analyses of Appendix A. With few exceptions, these descriptions cover only the major observed trends in the reduced data—a complete and detailed description of the results produced during the course of this investigation is clearly beyond the scope of the present document.

Gapwise Periodicity. The use of cascade data to represent turbomachinery behavior has always been predicated on the blade-to-blade periodicity of the cascade. In the past, steady-state periodicity was routinely checked and, in most cases, required as part of the data acceptance procedure. This is not the case with unsteady periodicity, for several reasons. For example, increased numbers of high response transducers on more than one blade, and correspondingly increased numbers of signal conditioning and data acquisition channels, produce significantly more data and represent considerably more cost than conventional unsteady tests. Nevertheless, such a test has been a recognized need for several years.

It is believed that the current experiment is the first systematic and detailed examination of unsteady periodicity in an oscillating cascade. As noted earlier, high response instrumentation has been confined to the leading edge regions of five blades grouped in the central region of the cascade and placed on both sides of the fully instrumented center blade (see Table 1). In the discussion that follows, reference will be made to the two suction surface locations as .012U and .062U, and to the pressure surface location as .012L.

Of the twelve possible combinations of incidence angle, pitching amplitude, and reduced frequency, only four will be discussed in detail. A survey of all results has shown that the

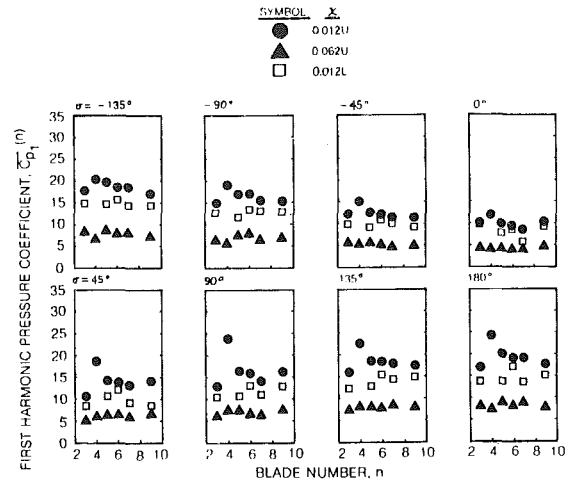


Fig. 5 Gapwise pressure amplitude for $\alpha=2 \text{ deg} \pm 0.5 \text{ deg}$ and $k=0.151$

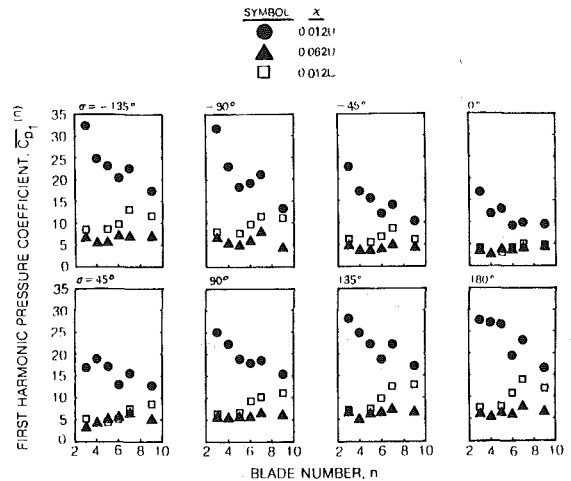


Fig. 6 Gapwise pressure amplitude for $\alpha=6 \text{ deg} \pm 0.5 \text{ deg}$ and $k=0.151$

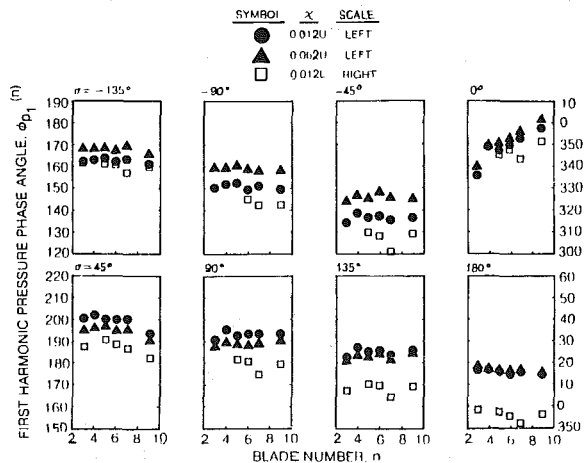


Fig. 7 Gapwise pressure phase angle for $\alpha=2 \text{ deg} \pm 2 \text{ deg}$ and $k=0.151$

data vary only superficially with reduced frequency (for the range tested) and only the $k = 0.151$ conditions have been selected for display. Figures 5 and 6 contain gapwise distributions of pressure amplitudes for $2 \pm .5$ and $6 \pm .5$ deg, and Figs. 7 and 8 contain gapwise distributions of pressure phase angles for 2 ± 2 and 6 ± 2 deg. Each figure has results for all interblade phase angles, and within each panel the two suction surface measurements are depicted by

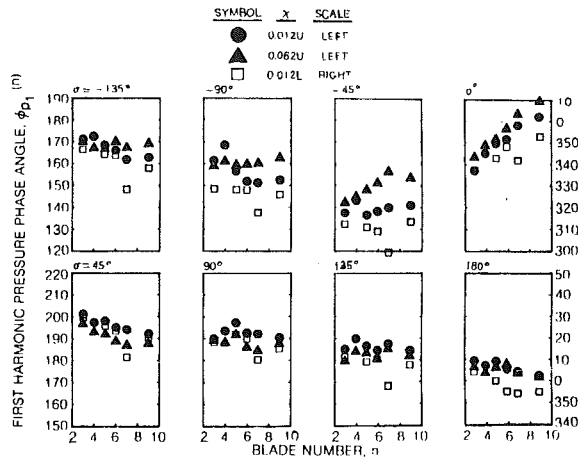


Fig. 8 Gapwise pressure phase angle for $\alpha = 6 \text{ deg} \pm 2 \text{ deg}$ and $k = 0.151$

solid symbols (circle for .012U and triangle for .062U) and the pressure surface measurement by the open square (for .012L). In each case only the first harmonic component is plotted.

Figure 5 shows the gapwise pressure amplitudes for $2 \pm .5 \text{ deg}$ to be relatively level for all three chordwise stations. This is particularly true for .062U and .012L. For the suction surface leading edge station (.012U), the measured results are generally level, but some deviation is evident at blade 4. No significant departures from these results are observed at the two lower frequencies (see [7]). In general, these results show the cascade to be acceptably periodic in pressure amplitude response at $\alpha_{MCL} = 2 \text{ deg}$.

The situation is somewhat altered for $\alpha_{MCL} = 6 \text{ deg}$ in Fig. 6. Here the second suction surface station (.062U) is still level, indicating good periodicity, and the pressure surface station (.012L) is generally level with only mild deviations from completely periodic behavior. However, at .012U there are strong gapwise gradients. This would suggest a significant loss in leading edge periodicity at $\alpha_{MCL} = 6 \text{ deg}$, but a recovery to periodic behavior within 5 percent of the chord aft of the leading edge. Once again, little change is evident for the other two reduced frequencies. It is probable that this reduced periodicity near the leading edge is associated with the increase in cascade loading. However, note that in both Figs. 5 and 6, local periodicity at the center of the cascade is still generally preserved; i.e., even in the presence of the overall gapwise gradient in Fig. 6, the response of blades 5, 6, and 7 is nearly level.

Figure 7 contains plots of the gapwise distribution of first harmonic pressure phase angle measured at each of the three blade stations for $2 \pm 2 \text{ deg}$. (Note that .012U and .062U are referred to the left scale and .012L to the right scale.) The phase angle for any blade is referenced to its own motion by the procedure derived in Appendix A. Thus, once again a flat distribution signifies good periodicity. With the exception of the results for $\sigma = 0 \text{ deg}$, the distributions are essentially flat. The gapwise phase gradient for $\sigma = 0 \text{ deg}$ may be associated with the so-called acoustical resonance phenomenon which occurs near $\sigma = 0 \text{ deg}$ for the test conditions of this experiment. This is discussed briefly in Appendix B. When these data are compared with data for the two lower frequencies (see [7]), it is found that there is virtually no change for $2 \pm 2 \text{ deg}$ at all frequencies. There is also little change for $2 \pm .5 \text{ deg}$ at $k = .122$, but there is an increase in the scatter for $k = .072$.

Similar trends are observed for $6 \pm 2 \text{ deg}$ in Fig. 8, with strong gapwise gradients for $\sigma = 0 \text{ deg}$, and a generally level behavior elsewhere. As before, recourse to the data in [7] shows that the scatter tends to increase at the lower

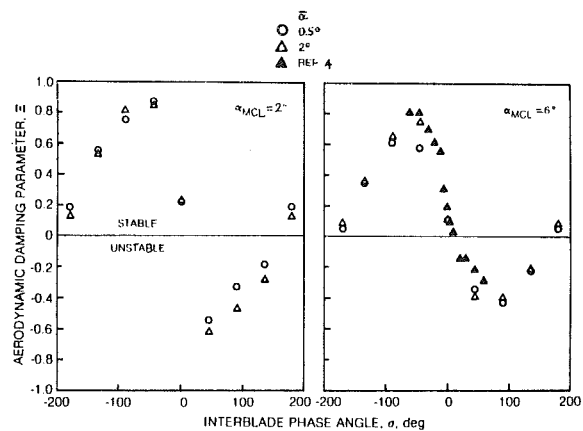


Fig. 9 Effect of pitching amplitude on aerodynamic damping parameter for $k = 0.122$

frequencies at $\pm .5 \text{ deg}$, with less tendency to do so at $\pm 2 \text{ deg}$.

Overall, this experiment has shown that the cascade blade response in its present configuration is periodic at the lowest load condition ($\alpha_{MCL} = 2 \text{ deg}$) for most parameter values tested but has a gapwise gradient in phase angle at $\sigma = 0 \text{ deg}$. Further, there is a significant gapwise gradient in magnitude at the airfoil leading edge over a wide range of σ at the modest load condition ($\alpha_{MCL} = 6 \text{ deg}$), but over the three center blades and within 5 percent of the chord aft of the leading edge the amplitude response is again periodic. Phase periodicity for $\alpha_{MCL} = 6 \text{ deg}$ is comparable to that for the low load condition. Thus, for these two load conditions the measured data satisfy the periodicity condition over most of the operating ranges and over most of the blade leading edge region, lending credence to the belief that the unsteady data obtained in this experiment are valid data. This belief is considerably strengthened below when the data are compared with theory.

Aerodynamic Damping and Stability. The most direct, global parameter that can be obtained from the unsteady pressure distributions over the entire blade chord is the aerodynamic damping parameter, Ξ . This is shown in Appendix A to be equal and opposite to the quadrature (or out of phase) component of the pitching moment coefficient per unit amplitude, and represents a measure of system stability in single degree of freedom torsional flutter (i.e., a system is stable if $\Xi > 0$). It has been measured and reported on many times for the current cascade model [1-4] and certain of these past results are available for comparison with those of the current test.

The aerodynamic damping parameter values plotted in Fig. 9 are typical of all values measured. Here Ξ is plotted versus σ , and the left and right panels represent $\alpha_{MCL} = 2$ and 6 deg , with amplitudes of $\bar{\alpha} = 0.5$ or 2 deg denoted within each panel by open circles or triangles, respectively. In addition, data from [4] for $\alpha = 6 \pm 2 \text{ deg}$, represented by solid triangles, are included in the right hand panel of this figure.

It is seen that damping increases with σ over the ranges $45 < \sigma < 180$ and $-180 < \sigma < -45 \text{ deg}$, and decreases sharply for $-45 < \sigma < 45 \text{ deg}$. The crossover from stable to unstable damping with increasing σ occurs at $\sigma > 0$, and from unstable to stable damping at $\sigma < 180 \text{ deg}$. (Note that $\sigma = +180 \text{ deg}$ and $\sigma = -180 \text{ deg}$ are actually the same point, and that damping trends over σ through this common point are continuous.) No significant trends with amplitude are discernible, although the effects of amplitude appear to be smaller for $\alpha_{MCL} = 6 \text{ deg}$ (right panel) than for $\alpha_{MCL} = 2 \text{ deg}$.

The agreement between current and previous [4] damping

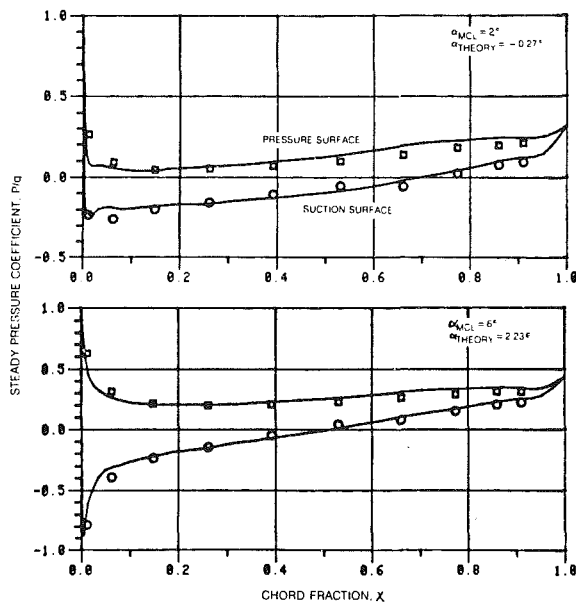


Fig. 10 Steady-state matching of potential flow theory and experiment

data for $\alpha = 6 \pm 2$ deg (open and closed triangular symbols, respectively, in right hand panel) is very good. Not only are trends strongly corroborated, but close agreement between damping measurements at common values of σ is seen to exist, confirming the ability of the OCWT to provide self-consistent, repeatable data from tests run at different times.

Comparison With Theory. Selected cases from these experimental results were chosen for comparison with the unsteady theory of Verdon and Caspar [8] for a blade having nonzero thickness and camber, operating in a subsonic, compressible flow. The basis of this theory is the unsteady perturbation of the potential function about the steady-state condition. Hence, it was necessary as an initial step to match the steady theory to the measured steady-state pressures. This is the only adjustment made to produce agreement between theory and experiment.

Comparisons were made at both incidence angles tested, but were restricted to a single value of $k = 0.122$. At $\alpha_{MCL} = 2$ deg the data and theory were compared at all eight values of interblade phase angle, and at $\alpha_{MCL} = 6$ deg only the data at $\sigma = -45$ and -135 deg were compared with theory. The initial steady potential flow was adjusted to the data for best fit at $\alpha_{THEORY} = -0.27$ and 2.23 deg, corresponding to $\alpha_{MCL} = 2$ and 6 deg, respectively. Plots showing the matched steady-state agreement for these two cases are presented in Fig. 10, in which the experimental distributions are the same as in Fig. 3. These and the following unsteady distributions have been inverted to conform to the computer-generated plots from the theory. It is seen that, within the scope of the present study, which was largely exploratory, a good match between steady theory and experiment has been achieved. It is not unusual for incidence angle discrepancies to occur between theory and experiment in making such a match because (i) the experimental cascade is finite in extent while the theory represents an infinite cascade, and (ii) no provision was made for adjusting the results for downstream diffusion associated with the presence of sidewalls and their growing boundary layers. These and other factors could have been refined for a better match in flow geometry, but such an effort would have been contrary to the needs of the present study.

In Fig. 11, the real and imaginary parts (circles and squares) of the measured unsteady pressure difference coefficient for $\alpha = 2 \pm .5$ deg are compared with the Verdon/Caspar "real

blade" theory (solid lines) and the flat-plate version of this theory (dashed lines) at all values of σ at which data were taken. For three values of interblade phase angle, $\sigma = -135$, -45 , and 135 deg, the agreement of the data with the Verdon/Caspar real blade theory is significantly better than with flat-plate theory, and without exception the agreement with Verdon/Caspar theory is excellent. At this incidence angle no distinction can be made between the data for the two separate amplitudes since they too are in nearly perfect agreement, and of course, the normalized theoretical values for the two amplitudes are identical.

In Fig. 12 the Verdon/Caspar theory and experiment for $\alpha_{MCL} = 6$ deg are compared at $\sigma = -135$ and -45 deg in the left and right panels, respectively. Here the experimental distributions have measurable differences at their leading edges, so the upper and lower panels are for $\alpha = 0.5$ and 2 deg. As before, the real blade theory is independent of amplitude and is the same for upper and lower panels at each σ . Furthermore, the flat-plate theory is independent of incidence so the plots in Fig. 12 are identical to those in Fig. 11 for $\sigma = -135$, -45 deg. Once again the agreement between real blade theory and the measured results is excellent, and this more complete theory is shown to be superior to the flat-plate theory.²

In addition to this comparison of data with the subsonic real blade analysis of Verdon/Caspar, theoretical predictions for this profile were also made by Atassi, based on the incompressible real blade analysis described in [9]. Four values of interblade phase angle, $\sigma = \pm 45$ and ± 135 deg, were chosen for comparison, and the results are shown in Fig. 13. Once again, the real and imaginary parts of the measured unsteady pressure difference coefficient for $\alpha = 2 \pm .5$ deg are denoted by circles and squares, the Verdon/Caspar prediction is denoted by the solid curves, and the dashed lines are now the Atassi prediction. With the exception of a slight overprediction by Atassi near the leading edge, and the small trailing edge deviation of the Verdon/Caspar theory (discussed earlier), both analyses are in excellent agreement with each other, and with the measured data.

It is recognized that within the scope of this study, only a small sample of the measured data could be compared with theory. Nevertheless, two major facts emerge clearly: (i) both real blade theories are consistently in excellent agreement with the measured unsteady results, and (ii) the flat-plate theory is shown to be useful in supplying trend information, but in many cases is inadequate to predict the details of unsteady loading.

Additional Comparisons. The observed changes in pressure levels with σ in Figs. 5 and 6 and in pressure phase angle with σ in Figs. 7 and 8 suggest a systematic variation with σ that is borne out in Fig. 14. The data points are taken from the 2 ± 2 deg, $k = .151$ case at $\chi = .012U$ and clearly show a symmetric pressure amplitude and skew-symmetric phase angle behavior relative to either $\sigma = 0$ or 180 deg. These results are typical, and a spot check of the data in [5, 7] shows a consistent pattern emerging for virtually all other cases.

Also displayed in Fig. 14 are solid lines denoted as "fitted theory." An oscillating aperture analysis has been performed in [10] in which the two sides of a two-dimensional opening

²It should be noted that, although the steady pressure distributions are sensitive to incidence angle (see Fig. 10), a cursory examination of Figs. 11 and 12 for $\sigma = -135$ and -45 deg shows very little difference in unsteady theoretical pressure distribution for the two incidence angles. This apparent insensitivity of the unsteady theory to modest loading changes is also implied by the additional theoretical comparison from the Atassi analysis [9] in which no steady incidence angle adjustment was applied. Finally, the small deviation in the real part of the Verdon/Caspar theory near the trailing edge appears to be caused by the difficulty of accurately capturing the singular behavior in unsteady pressure at a sharp trailing edge with a finite difference approximation.

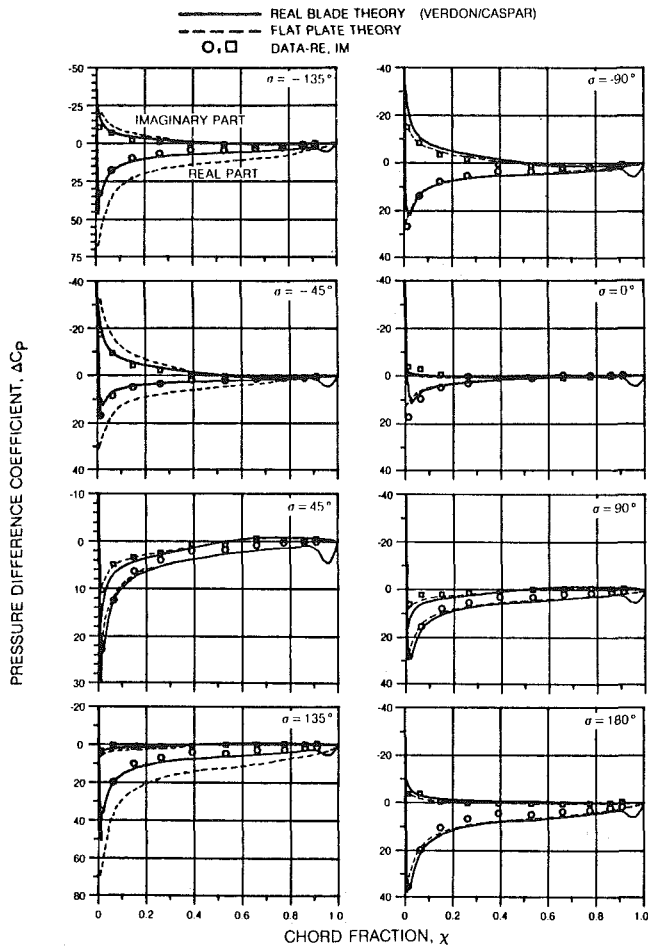


Fig. 11 Comparison of theory and experiment for $\alpha = 2 \pm 0.5$ deg and $k = 0.122$

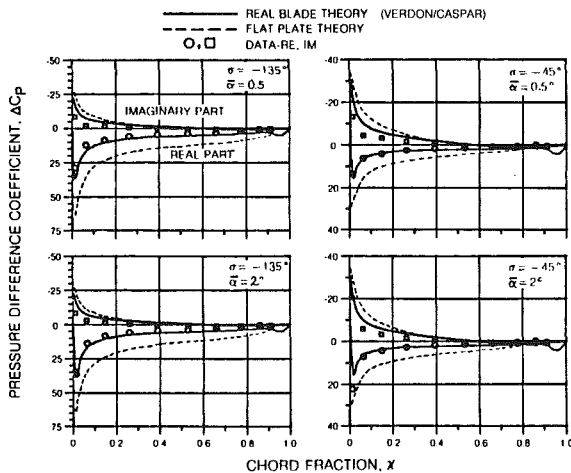


Fig. 12 Comparison of theory and experiment for $\alpha_{MCL} = 6$ deg and $k = 0.122$

oscillate sinusoidally with a phase shift, σ , between their motions, in the presence of a fluid stream. A velocity perturbation analysis is performed from which a perturbation pressure field can be inferred, having the form $\bar{C}_p = A + B\sqrt{2} - 2\cos\sigma$. A and B are free constants by virtue of the lack of specificity in this simplified formulation. This theory is fitted to the experimental data by evaluating A and B such that the curve passes through the measured values at $\sigma = 0$ and 180 deg. The resulting excellent agreement between fitted theory and measured data leads to the obvious conclusion that the

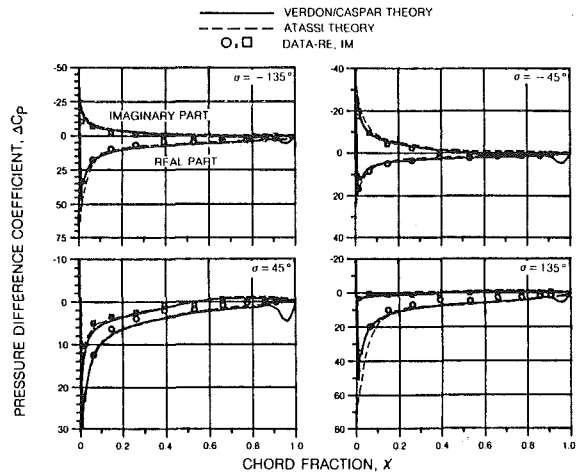


Fig. 13 Comparison of two theories with experiment for $\alpha = 2 \pm 0.5$ deg and $k = 0.122$

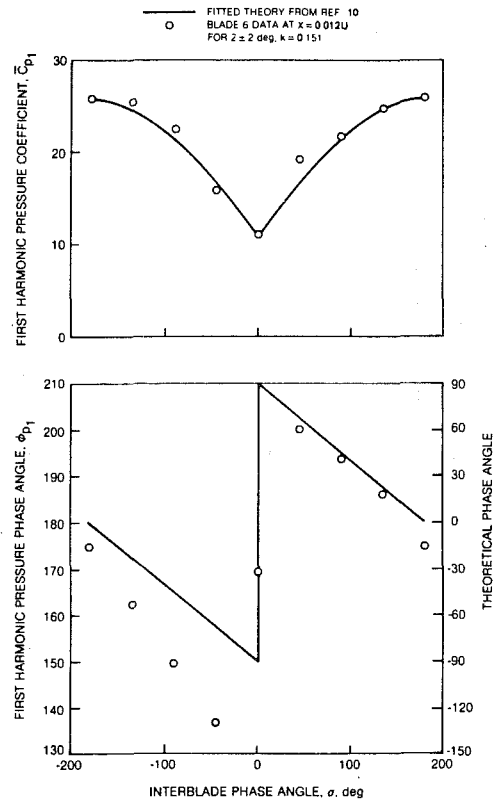


Fig. 14 Comparison of blade data with simple fitted theory

observed σ -variations in the measured data are directly related to the geometric constraints of the inlet aperture. Several comparable examples of this type of two-point fitted agreement are included in [10].

The phase "agreement" shown in the lower panel of Fig. 14 is necessarily contrived, primarily to allow both measured and theoretical results to coexist on the same plot. The data are referred to the left ordinate and the theory to the right ordinate, and because this is phase information, dependent on the ratio of real and imaginary quantities, no free constants exist. Nevertheless, both phase variations have the same continuous and (nearly) linear behavior across $\sigma = \pm 180$ deg and both exhibit a strong positive jump at $\sigma = 0$ deg. Again there is strong evidence that unsteady aperture geometry is an important factor in real blade response.

Further corroboration of this type of behavior is seen in the results of an unsteady turbine cascade experiment described in

[11] and elaborated on in [12]. This experiment was conducted on a cascade configuration that is significantly different from the subject of this report: turbine blades, 20 percent thick, with 112 deg turning at an inlet Mach number of 0.52, versus compressor blades, 6 percent thick, with 10 deg turning, at an inlet Mach number of 0.18. The pressure amplitude, plotted versus σ in Fig. 17 of [11] for an aft station on the blade, or in Fig. 44 of [12] for a forward station on the blade, has substantially the same form as the result in the upper panel of Fig. 14. In addition, the phase angle behavior in Fig. 18 of [11] or in Figs. 52–54 of [12] is similar to the result in the lower panel of Fig. 14. Here the comparison is more difficult to make by virtue of differences in several of the defining parameters of the turbine and compressor cascades. Nevertheless, the general pattern of agreement between these two sets of data is further evidence of a strong geometric interaction controlling the leading edge aerodynamics.

Conclusions and Observations

Preliminary Remarks. This investigation is the latest in a series of tests of oscillating blades in cascade conducted at UTRC. While the previous tests focused separately on individual phenomena such as aerodynamic damping or surface pressure response, the current test has concentrated on several items, making it one of the most comprehensive and self-consistent unsteady aerodynamic cascade experiments known to date. Specifically, it is believed that this experiment has examined, in detail, unsteady cascade periodicity for the first time. In addition, it has confirmed the previous tentative results for aerodynamic damping, has shown self-consistency and agreement in overall cascade performance, has provided verification of two “real blade” unsteady aerodynamic theories, and has produced a large body of unsteady aerodynamic data for future study.

It is recognized that data generated in this and in previous OCWT tests are at values of reduced frequency and Mach number that are lower than the values typically encountered in turbomachines. Nevertheless, the ability of these data to verify the real blade theory of [8] is of paramount importance in that the credibility of the theory in the region of low k and M is now firmly established. Although further verification of theory over a wider range of parameters is desirable, the turbomachinery designer is now in a position to introduce the theory into the aeroelastic design system with some confidence.

In this section are listed a set of conclusions reached and observations made in this paper. They are segregated below in two groups, comprising the primary and secondary findings of the experiment. Within each group they are enumerated in the approximate order of their appearance in the text. A more extensive list, based on the complete study, is contained in [5].

Primary Findings.

1 In general, for the two load conditions tested, the measured data satisfy the periodicity condition over most of the operating ranges and over most of the blade leading edge region. Specific observations follow below:

(a) The cascade is periodic in pressure amplitude response at all measuring stations at $\alpha_{MCL} = 2$ deg.

(b) Pressure amplitude periodicity deteriorates somewhat at $\alpha_{MCL} = 6$ deg at the leading edge station, but returns to periodic behavior within 5 percent of the chord aft of the leading edge.

(c) Pressure phase angle is periodic at all measured conditions, with the exception of $\sigma = 0$ deg, where a strong gapwise gradient is observed. This is believed to be associated with a cascade acoustical resonance condition.

2 In confirmation of the results of previous tests, in-

terblade phase angle, σ , is still the most important parameter affecting the stability of oscillating cascaded airfoils.

3 In comparing the measured chordwise pressure distribution with two unsteady theories for a thick, cambered, cascaded airfoil, the agreement was consistently excellent for both incidence angles tested.

4 The same comparison with flat-plate theory showed similar trends but, in general, was only in fair agreement when judged relative to the “real blade” theory.

Secondary Findings.

5 Steady-state measurements of cascade pressure rise, flow turning, and total pressure loss are in agreement with previous tests and with predicted minimum loss.

6 For the parameter ranges tested, no significant damping trends with amplitude are discernible.

7 Agreement between current and previously measured aerodynamic damping data for $\alpha = 6 \pm 2$ deg is very good.

8 A comparison of the leading edge pressure magnitude variation with σ and a two-point “fitted theory” for an oscillating aperture shows excellent agreement. This agreement suggests that the observed σ -variations in the measured data are directly related to the geometric constraints of the inlet aperture.

9 A similar comparison of measured and predicted phase angle variation with σ leads to the same conclusion.

10 This suggested dependence on inlet geometry is further corroborated by a qualitative comparison with results from a turbine experiment cited in the text.

Acknowledgment

Any large and complicated experimental program such as this one draws on the talents of many people, and a general acknowledgment of the special efforts of the UTRC staff who assisted in this program should be made. Particular thanks are extended to the author’s colleagues, Drs. Arthur O. St. Hilaire and Larry W. Hardin who were direct contributors to the experiment, instrumentation, and data reduction algorithms, to Drs. Joseph M. Verdon and Joseph R. Caspar who provided the real blade theory which agreed so well with the data, to Mr. Kenneth L. Dauphinais who created the data reduction software, to Mr. Paul R. Hamel who helped set up and run the test program, and to Ms. Janette L. Sniffin who prepared and assembled the graphics that ultimately told the story. In addition, the author is indebted to Prof. Hafiz Atassi of Notre Dame University for generously providing additional theoretical results from his real blade analysis which also agreed with the data.

References

- Carta, F. O., and St. Hilaire, A. O., “An Experimental Study on the Aerodynamic Response of a Subsonic Cascade Oscillating Near Stall,” Project SQUID Technical Report UTRC-2-PU, July 1976.
- Arnoldi, R. A., Carta, F. O., Ni, R. H., Dalton, W. N., and St. Hilaire, A. O., “Analytical and Experimental Study of Subsonic Stalled Flutter,” AFOSR-TR-77-0854, July 1977.
- Carta, F. O., and St. Hilaire, A. O., “Experimentally Determined Stability Parameters of a Subsonic Cascade Oscillating Near Stall,” ASME JOURNAL OF ENGINEERING FOR POWER, Vol. 100, Jan. 1978, pp. 111–120.
- Carta, F. O., and St. Hilaire, A. O., “Effect of Interblade Phase Angle and Incidence Angle on Cascade Pitching Stability,” ASME JOURNAL OF ENGINEERING FOR POWER, Vol. 102, No. 2, Apr. 1980, pp. 391–396.
- Carta, F. O., “An Experimental Investigation of Gapwise Periodicity and Unsteady Aerodynamic Response in an Oscillating Cascade: I, Experimental and Theoretical Results,” NASA CR 3513, June 1982.
- Davis, E. L., Jr., “The Measurement of Unsteady Pressures in Wind Tunnels,” AGARD Report 169, Mar. 1958.
- Carta, F. O., “An Experimental Investigation of Gapwise Periodicity and Unsteady Aerodynamic Response in an Oscillating Cascade: II, Data Report,” NASA CR 165457, Dec. 1981.
- Verdon, J. M., and Caspar, J. R., “Subsonic Flow Past an Oscillating Cascade with Finite Mean Flow Deflection,” AIAA Journal, Vol. 18, No. 5, May 1980, pp. 540–548.

9 Atassi, H., and Akai, T. J., "Aerodynamic and Aeroelastic Characteristics of Oscillating Loaded Cascades at Low Mach Number," ASME JOURNAL OF ENGINEERING FOR POWER, Vol. 102, No. 2, Apr. 1980, pp. 344-351.

10 St. Hilaire, A. O., "An Analysis of the Inlet Plane Aerodynamics of an Oscillating Subsonic Cascade: An Evaluation of Experimental Data," United Technologies Research Center Report R81-914838, prepared for the U.S. Navy, Office of Naval Research under Contract N00014-79-C-0772, (AD-A096077), Feb. 1981.

11 Rothrock, M. D., Jay, R. L., and Riffel, R. E., "Time-Variant Aerodynamics of High-Turning Blade Elements," Paper No. 81-GT-123, presented at the ASME Gas Turbine Conference, Houston, Texas, March 1981.

12 Jay, R. L., Rothrock, M. D., Riffel, R. E., and Sinnet, G. T., "Time-Variant Aerodynamics for Torsional Motion of Large-Turning Airfoils," Detroit Diesel Allison Report EDR 10192, prepared for the Department of the Navy, Naval Air Systems Command, under Contract N00019-79-C-0087, Jan. 1980.

13 Carta, F. O., "Aeroelasticity and Unsteady Aerodynamics," ch. 22 in the *Aerothermodynamics of Aircraft Gas Turbine Engines*, edited by G. C. Oates, U.S. Air Force Report AFAPL TR 78-52, July 1978.

APPENDIX A

Derivation of Relevant Equations

For convenience this Appendix is devoted to the derivations of the major equations used in the text. Although these equations represent standard concepts and most have been derived elsewhere, there is sufficient subtlety in their definitions and use to warrant their collection in this Appendix. It should be noted that all unsteady aerodynamic loads have an implicit normalization with respect to the pitching amplitude, $\bar{\alpha}$, in accordance with the definition of unsteady pressure coefficient from equation (1)

$$C_p(\chi, t) = \frac{p(\chi, t)}{q\bar{\alpha}} \quad (A1)$$

If blade 6 (the center reference blade) is the only one under consideration, no distinctive notation will be used, and the pressure coefficient in equation (A1) can be expressed in either complex exponential form or in component form as

$$C_p(\chi, t) = \bar{C}_p(\chi)e^{i(\omega t + \phi_p(\chi))} \\ = (C_{pR}(\chi) + iC_{pI}(\chi))e^{i\omega t} \quad (A2)$$

(If however, any other of the n -blades are being considered, a superscript notation denoting the specific blade will be employed. This will be demonstrated later.) The subscripts R and I denote the so-called real and imaginary components of C_p , but physically can be interpreted as the components of the pressure response that are in phase and out of phase with respect to the motion

$$\alpha(t) = \bar{\alpha}e^{i\omega t} \quad (A3)$$

In terms of the amplitude and phase angle

$$\bar{C}_p(\chi) = \sqrt{C_{pR}^2(\chi) + C_{pI}^2(\chi)} \quad (A4) \\ \phi_p(\chi) = \tan^{-1}(C_{pI}(\chi)/C_{pR}(\chi))$$

where $\phi_p(\chi)$, as defined here, is positive for the pressure leading the motion. Similar relationships involving in and out of phase components and their amplitudes and phase angles will exist for all other quantities, but for brevity will not be repeated here.

The pressure difference, ΔC_p , will be obtained from the difference between the pressures on the upper (or suction) and lower (or pressure) surfaces, denoted by subscripts U and L . Thus,

$$\Delta C_p(\chi, t) \equiv -[C_{pU}(\chi, t) - C_{pL}(\chi, t)] \quad (A5)$$

It should be noted that only components, and not magnitudes or phase angles, can be differenced, or

$$\Delta C_p(\chi, t) = (\Delta C_{pR}(\chi) + i\Delta C_{pI}(\chi))e^{i\omega t} \quad (A6)$$

For a continuous distribution of the pressure over the entire blade surface the unsteady pitching moment coefficient per unit amplitude about the airfoil pivot axis at χ_p is given by

$$C_M(t) = \int_0^1 (\chi_p - \chi) \Delta C_p(\chi, t) d\chi \quad (A7)$$

(where the phase lead angle associated with \bar{C}_M is denoted by ϕ_M). However, in this experiment a discrete array of transducers was used, necessitating a numerical integration of the pressures. As in earlier OCWT experiments [1-4], a ten-point Gaussian quadrature was performed over the forward 91 percent of the chord, and a three-point interpolation through the data at $\chi = 0.86, 0.91$, and through $\Delta C_p(1.0) = 0.0$ at the trailing edge was used to complete the integration.

System stability is obtained from a computation of the work per cycle, and its conversion to an aerodynamic damping parameter. The general form of the work coefficient is given by

$$C_W = \oint \text{Re}\{\bar{\alpha} C_M(t)\} d\alpha_R \quad (A8)$$

(In this formula the previously normalized $C_M(t)$ is multiplied by the normalizing pitching amplitude, $\bar{\alpha}$, to express the work coefficient in its conventional form.) For a pure sinusoidal moment response,

$$\text{Re}\{\bar{\alpha} C_M(t)\} = \bar{\alpha} \text{Re}\{\bar{C}_M e^{i(\omega t + \phi_M)}\} \\ = \bar{\alpha} \bar{C}_M \cos(\omega t + \phi_M) \quad (A9)$$

and substitution of equations (A3) and (A9) into equation (A8) ultimately yields

$$C_W = \pi \bar{\alpha}^2 \bar{C}_M \sin \phi_M \quad (A10)$$

From [1-4], the aerodynamic damping parameter is defined by

$$\bar{Z} = -C_W / \pi \bar{\alpha}^2 \quad (A11)$$

and hence, from equation (10),

$$\bar{Z} = -\bar{C}_M \sin \phi_M = -C_{MI} \quad (A12)$$

(Note that this result differs in form from the results in [1-4] because the C_M in these equations is implicitly normalized with respect to $\bar{\alpha}$.)

In the more general case, the response will not be a pure sinusoid, but will contain higher harmonics as well. Accordingly, in the present experiment the time histories of all response functions were decomposed into their harmonics by conventional techniques. In the analysis of [5] it is shown that equation (A12) is the general form for a sinusoidal motion if \bar{C}_M , ϕ_M , and C_{MI} are replaced by their first harmonic components,

$$\bar{Z} = -\bar{C}_{M1} \sin \phi_{M1} = -C_{MI1} \quad (A13)$$

Finally, as noted in the main text of this paper, unsteady blade-to-blade periodicity along the cascade leading edge plane is best evaluated by examining the gapwise distribution of pressure coefficient (both amplitude and phase angle) for common transducer locations. Normally, a single chordwise location will be examined at any one time, so the functional dependence on χ will be dropped for notational simplicity. As shown in [5], if $\theta_k^{(n)}$ is the actual k th harmonic response phase angle measured on blade n relative to the motion of blade 6, then phase periodicity may be evaluated by computing

$$\phi_{p_k}^{(n)} = \theta_k^{(n)} - k(n-6)\sigma \quad (A14)$$

which represents the k th harmonic of the response phase angle of blade n relative to its own motion. The comparable pressure coefficient amplitude on blade n , $\bar{C}_{p_k}^{(n)}$, is obtained directly from the Fourier tabulations in [7].

APPENDIX B

Acoustical Resonance

The object of the material presented in this Appendix is to show that the acoustical resonance phenomenon is a plausible explanation for the gapwise phase gradient when $\sigma = 0$ deg. However, it is important to note that no proof that the phenomenon exists is claimed or implied.

The concept of acoustical resonance in a cascade has been discussed by many authors, mostly in the context of a singular behavior of the cascade solution in a compressible flow. A more physical approach was recently described in [13] in which the general formula

$$2\pi\nu \pm \sigma = \frac{2kM \tau/c}{\sqrt{1 - M^2 \sin^2 \beta_1^* \pm M \cos \beta_1^*}} \quad (\text{B1})$$

$\nu = 0, 1, 2, \dots$

is given. Here k is reduced frequency, M is Mach number, τ/c is gap/chord ratio, and β_1^* is stagger angle. This solution represents two possible modes: a forward wave with $\nu = 0$

and use of the upper sign, and a backward wave with $\nu = 1$ and the lower sign. Both of these modes are valid, and both are computed. The parameters used here are

$$M \cong .18$$

$$\tau/c = .75$$

$$\beta_1^* = 30 \text{ deg}$$

A straightforward computation for the three test values of k leads to the results given below.

	Forward wave		Backward wave	
	$\nu = 0$		$\nu = 1$	
k	$\sigma(\text{rad})$	$\sigma(\text{deg})$	$\sigma(\text{rad})$	$\sigma(\text{deg})$
.072	.023	1.3	6.266	-1.0
.122	.039	2.2	6.255	-1.6
.151	.049	2.8	6.248	-2.0

With these values nested so closely about $\sigma = 0$, it is obvious that the opportunity for resonance exists.

Aerodynamic Damping Measurements in a Transonic Compressor

E. F. Crawley

Boeing Assistant Professor,
Department of Aeronautics and Astronautics,
Massachusetts Institute of Technology,
Cambridge, Mass. 02139

A method has been developed and demonstrated for the direct measurement of aerodynamic damping in a transonic compressor. The method is based on the inverse solution of the structural dynamic equations of motion of the blade-disk system. The equations are solved inversely to determine the forces acting on the system. If the structural dynamic equations are transformed to multiblade or modal coordinates, the damping can be measured for blade-disk modes, and related to a reduced frequency and interblade phase angle. This method of damping determination was demonstrated using a specially instrumented version of the MIT Transonic Compressor run in the MIT Blowdown Compressor Test Facility. No regions of aeroelastic instability were found. In runs at the operating point, the rotor was aerodynamically excited by a controlled two-per-revolution, fixed, upstream disturbance. The disturbance was sharply terminated midway through the test. Analysis of the data in terms of multiblade modes led to a direct measurement of aerodynamic damping for three interblade phase angles. Comparison between experimental damping values and theoretical values calculated using a weak shock two dimensional analysis show reasonable agreement.

Introduction

It is of primary importance in the study of turbomachine aeroelasticity to develop techniques for the measurement of aerodynamic damping and eventually to gain an understanding of the physical processes which control that damping. It is the purpose of this investigation to develop techniques for the measurement of aerodynamic damping, and to make direct measurements of damping in a transonic rotor operating at a known point on its performance map.

Flutter boundaries can place limits on all sides of the performance map of the modern, lightweight transonic fan or compressor. Adamczyk [1] identifies five different stability boundaries, each of which is associated with a different unsteady fluid mechanical process. Within the boundaries, the stage is aeroelastically stable, but is susceptible to forced vibration. While the stability and forced vibration problems are usually formulated differently, Dugundji [2] has shown that given the aerodynamic damping coefficients in a proper form, the two problems can be analyzed in a unified systematic manner. Aerodynamic damping coefficients used in such an analysis might be based on either analytic or experimental results.

Experimental investigations of turbomachine aerodynamic damping fall into one of two distinctly different categories, cascade experiments and rotating rig tests. Cascade experiments are conducted in essentially two-dimensional linear (finite) or annular (infinite) cascades. The blades are externally driven with a uniform oscillatory motion and fixed

interblade phase angle. Blades can be driven in rotational mode, representing torsional flutter [3], or in a translational mode, as in bending flutter [4].

Rotating tests are performed by instrumenting a specially prepared stage and running it in the vicinity of one of its stability boundaries. Instrumentation usually consists of a large number of strain gauges mounted on the rotating assembly to monitor blade strain and displacement levels [5]. Rigs have also been run with miniature high frequency response pressure transducers mounted on the blades, so that unsteady on-blade pressure measurements could be made [6]. These tests identify the location of the stability boundaries of real stages and the influence changes in operating parameters, such as inlet temperature and pressure, as well as changes in blade design, have on these boundary locations. A further objective is to identify the modes of aeroelastic instability [7].

Each of the two experimental procedures, cascade and rotating rig tests, have their advantages and shortcomings. Cascade experiments performed under controlled conditions lend themselves to careful study of the influence that Mach number, reduced frequency, and interblade phase angle have on aerodynamic damping. Detailed measurement of energy input and blade unsteady pressure distribution made in two-dimensional cascades can be directly correlated with existing two-dimensional theory. The principle shortcoming of cascades is that they fail to model the essential three-dimensional nature of the flow in axial flow turbomachines, including such potentially important effects as strong radial variation in shock strength and subsequent boundary layer interaction, and distribution of total pressure rise and flow quantities due to work done on the fluid [8].

Contributed by the Gas Turbine Division of THE AMERICAN SOCIETY OF MECHANICAL ENGINEERS and presented at the 27th International Gas Turbine Conference and Exhibit, London, England, April 18-22, 1982, Manuscript received at ASME Headquarters December 22, 1981. Paper No. 82-GT-287.

Rotating rig tests model this complex three-dimensional nature of the flow, but do so under conditions which make the extraction of detailed quantitative information about aerodynamic damping difficult. Since the blade-disk-shroud structural system is complex and highly coupled, it is often impossible to isolate the response of a single structural mode. The results are confined to location of the boundary of neutral stability, rather than quantitative measurements of damping on either side of the boundary. Although there are semiempirical procedures for the correlation of such three-dimensional flutter data, there is no three-dimensional flutter theory.

The purpose of this investigation is to develop techniques by which quantitative parametric aeroelastic damping data can be extracted from a device operating in a working turbomachine environment. The methods developed can be applied to any of the stability boundaries, and to forced vibration in the stable interior of the map. Included in the present work are both a description of a new technique and the application of that technique to the MIT Rotor [9]. The result is one of the first direct measurements of damping in a transonic compressor.

Computation of Aerodynamic Forces Acting on the Blades

Among the data commonly acquired in rotating rig aeroelastic tests are the deflections of the blades relative to the disk, as can be extracted from simple strain gauge data. The quantity of interest to the aeroelastician is the net aerodynamic force acting on the blade. These aerodynamic forces might be due to perturbations in the flow arising outside the blade row which cause forced vibration, or they might be due to the motion of the blades, in which case they are thought of as aerodynamic stiffness, damping, and inertial terms. These motion-dependent aerodynamic forces are the key to the stability problem. A method for the measurement of these forces, which focuses on the structural response of the entire blade disk system and is based on the use of multiblade or modal coordinates, will be presented.

The underlying concept is that given the blade displacements, the structural dynamic equations of motion can be solved inversely to determine the aerodynamic forces acting on the blades. As an example, let the model equation of motion for the bladed disk be of the form

$$m\ddot{\mathbf{q}} + \mathbf{k}\mathbf{q} = \mathbf{F}(t) \quad (1)$$

where \mathbf{q} is a vector of the generalized blade displacements and \mathbf{F} of the generalized forces, and \mathbf{m} and \mathbf{k} are the mass and stiffness matrices. Only the inertial and elastic effects have been included in the left hand side of equations. The generalized force contains components due to structural

damping, aerodynamic damping, as well as aerodynamic disturbance forces, which arise from stall, surge, and passage in the proximity to upstream and downstream stators.

The conventional problem statement based on equation (1) is: given an arbitrary force $F(t)$, find the response of $q(t)$. However, in the case of a rotor the response of the blading is known. The desired unknowns are the external aerodynamic forces acting on the blading. The inverse problem statement is: given an arbitrary response q (and \dot{q}), find the force $F(t)$ which would produce that response. The mathematical formulation of the inverse problem is rigorous. The system defined by equation (1) is linear and the force $F(t)$ uniquely determined by q . Since $F(t)$ appears as a zeroth-order derivative in time, no initial conditions are necessary.

However, the practical application to the determination of aerodynamic damping raises many questions, including the selection of the proper structural dynamic model, the collection of "sufficient" data to characterize that model, the procedure for inverse solution of the equations to obtain the generalized forces, and the interpretation of those force results leading to the isolation of the aerodynamic damping. Each of these questions will now be addressed in detail.

Selection of the Structural Dynamic Model. The proper choice of a structural dynamic model depends on those aspects of the blade-disk participation important to the aeroelastic problem under investigation, and the nature of the bladed-disk system. For example, if the rotor under investigation has a thick, massive disk typical of many low aspect ratio research fans, and the aeroelastic phenomena involves the supersonic torsional flutter near the first torsional frequency of the blades, then an adequate structural dynamic model would include only the first torsional mode of the blades. If, on the other hand, the problem under investigation involved the broad band vibration of a rotor with a flexible disk, then the minimum structural dynamic model would contain the first several flexural and torsional modes of the blades coupled through the elasticity and inertia of the disk.

Consider the case of the flexural participation of N blades on a disk. If the motion of each of the blades and the segment of the disk to which it is attached are represented by M degrees of freedom, then the $M \times N$ coupled equations of motion are

$$\mathbf{m} \begin{bmatrix} \ddot{q}_1 \\ \vdots \\ \ddot{q}_{M \times N} \end{bmatrix} + \mathbf{k} \begin{bmatrix} q_1 \\ \vdots \\ q_{M \times N} \end{bmatrix} = \begin{bmatrix} F_1 \\ \vdots \\ F_{M \times N} \end{bmatrix} \quad (2)$$

Solution of the homogeneous part of equation (2) yields the

Nomenclature

a = amplitude of the sine mode	M = modal mass, number of circumferential degrees of freedom	Ω = frequency of rotation
A = modal force of the sine mode	n = number of nodal diameter	Subscripts
b = amplitude of the cosine mode	N = number of blades	b = blade
B = modal force of the cosine mode	q = displacement	d = disk
c = blade chord	Q = shaft force	h = hub
f' = force per unit length	r = radius	i = i th blade
F = force	α = angle of blade attachment to disk (Fig. 1)	m = m th circumferential mode
I = moment of inertia	β = interblade phase angle	n = n th diametrial mode
j = $\sqrt{-1}$	γ = mode shape	t = tip
k = stiffness	v = wavespeed	T = sum of blade and disk (total)
K = shaft stiffness	Φ = modal matrix	x = in the x -direction
m = mass, number of nodal circumferences	ψ_i = location of the i th blade	y = in the y -direction
	ω = natural frequency	θ = in the circumferential direction

$M \times N$ undamped natural frequencies and normal mode shapes of free vibration. The individual blade and disk displacements can be expressed as sums of the new modal or multiblade coordinates and the multiblade mode shapes as

$$\mathbf{q} = \Phi \begin{bmatrix} \mathbf{a}_{mn} \\ \vdots \\ \mathbf{b}_{mn} \end{bmatrix} \quad \begin{matrix} n=0,1, \dots, (N-1)/2 \\ m=0,1, \dots, M-1 \end{matrix} \quad (3)$$

where for a given multiblade mode, the subscript, m , now denotes the number of nodal circumferences and the subscript, n , denotes the number of nodal diameters.

Equation (3) represents a nonsingular linear similarity transformation between the individual blade-disk displacement form and the multiblade coordinate form, and can be inverted

$$\begin{bmatrix} \mathbf{a}_{mn} \\ \vdots \\ \mathbf{b}_{mn} \end{bmatrix} = \Phi^{-1} \mathbf{q} \quad (4)$$

Using the inverted form, the multiblade coordinates can be calculated if sufficient information about the individual blade and disk displacements is known.

The similarity transformation in equation (3) can be used to uncouple the governing equations of motion (2), by the standard technique of representing each displacement as the sum of contributions from the normal modes [10].

Substitution of equation (3) into equation (2), premultiplication by Φ^T , and enforcement of the orthogonality of normal modes will yield $M \times N$ uncoupled equations

$$\begin{aligned} M_{mn} \ddot{a}_{mn} + M_{mn} \omega_{mn}^2 a_{mn} &= A_{mn} \quad n=0,1, \dots, \frac{N-1}{2} \\ M_{mn} \ddot{b}_{mn} + M_{mn} \omega^2 b_{mn} &= B_{mn} \quad m=0,1, \dots, M-1 \end{aligned} \quad (5)$$

By using the normal or multiblade modes to transform the equations of motion to the type given in equation (5), the problem has been reduced to a set of single degree of freedom equations. Each can be solved inversely for the generalized modal force A_{mn} , B_{mn} , provided the modal coordinate (a_{mn} , b_{mn}), modal mass (M_{mn}), and frequency (ω_{mn}) are known. In general, the modal forces may recouple the normal equations of motion.

Definition of Sufficient Data. The need to determine accurately the multiblade modal coordinates (a_{mn} , b_{mn}) establishes the requirement for sufficient data collection to characterize the structural dynamic model. In general, for an N bladed disk, if the displacements of $M \times N$ multiblade modes are desired, then $M \times N$ independent transducers (e.g., strain gauges) measuring blade and disk displacements would be needed. The practical implication of this data collection requirement is to keep small the number of degrees of freedom and, therefore, modes in the structural dynamic model.

The formal relationship used to calculate the multiblade coordinates is given in equation (4). However, in some cases the rigorous requirement that $M \times N$ displacements be measured to resolve $M \times N$ modes can be relaxed. The natural modes of a bladed disk appear in families associated with m nodal circumferences (where $m=0,1, \dots, M-1$) and with a varying number of nodal diameters n (where $n=0,1, (N-1)/2$). The natural frequencies of the families with 2 different number of nodal circumferences are usually well separated. This frequency separation can sometimes be used to isolate the response of the different nodal families, if the response is primarily at or near the natural frequencies, as is the case for many flutter modes and free vibration response. If the circumferential nodal family frequencies are closely

spaced, or if the response of the system is not easily identifiable with a single particular mode, as would be the case in aerodynamically coupled bending-torsion flutter or broad band forced vibration, a full set of $M \times N$ transducers would be required to resolve the $M \times N$ modes.

Calculation and Interpretation of Modal Forces. Once each modal coordinate has been determined through a combination of time domain separation and use of equation (4), the modal force must be determined using equation (5). Several different approaches can be taken to extract the force information. If the original data is of high enough quality (in terms of signal to noise ratio, digitization resolution and sampling rate), the modal force can be solved for uniquely by substitution of the modal coordinates and their derivatives in equation (5), as demonstrated in [11]. If the data is not of high enough quality, techniques which examine the time average behavior of the system must be used. If the external force is linear viscous damping, as is the assumed form of aerodynamic damping, then transient decay methods can be used to determine the modal damping ratios. Among these methods are the random decrement method, and the observation of the free decay. The latter will be demonstrated.

Use of the modal amplitudes and equation of motion will yield information on the sum of the modal forces A_{mn} , B_{mn} . This sum contains at least three distinct components

$$A_{mn}^{\text{total}} = A_{mn}^{\text{aero}} + A_{mn}^{\text{disturbance}} + A_{mn}^{\text{structural damping}} \quad (6)$$

the unsteady aerodynamic aerodynamic forces due to blade motion, the unsteady aerodynamic forces due to upstream or downstream disturbances, and the structural damping.

Looking at the origins of each of the force components, the disturbance force includes effects of blade passage through stationary circumferential nonuniformities in the flow, such as inlet distortion, wakes from struts and guide vanes, influences from upstream and downstream stators, and nonuniformities in burner outflow in the case of a turbine. Also included would be unsteady aerodynamic loads not attributable to the rotation of the blades themselves, such as loads induced by surge and rotating stall.

The structural damping is best considered a modal force, since it is most easily measured for a particular blade-disk mode. If the modal structural damping can be expressed as a linear combination of the modal amplitude or velocity (i.e., hysteresis or equivalent viscous damping), this term can be moved to the left-hand side of equation (5) and considered a homogeneous term.

After the structural damping and disturbance forces have been sorted out, the remaining aerodynamic force is the one of most interest in the understanding of aerodynamic damping. The aerodynamic modal force of equation (6) represents exactly the quantity one calculates for each blade-disk mode in determining flutter boundaries; that is, the integrated effect along the blade spans over the disk mode of the damping forces. In the conventional calculation, this term is evaluated as

$$A_{mn}^{\text{aero}} = \sum_{i=1}^N \int_{r_h}^{r_i} f'_{i \text{ aero}}(r,t) \phi_{mn}(\psi_i, r) dr \quad (7)$$

where ϕ_{mn} represents the displacement of a blade section in a given mode, and f' is the unsteady aerodynamic force per unit span, found either from two-dimensional theory, or the results of cascade experiments.

The relation between this modal aerodynamic force and the conventional analytical expression of aerodynamic damping can be developed by expanding the unsteady aerodynamic

force on a typical two-dimensional blade section in its most general form

$$f'_i = f'_i(q_i, \dot{q}_i, \ddot{q}_i) + f'_{i+1}(q_{i+1}, \dot{q}_{i+1}, \ddot{q}_{i+1}) + f'_{i+2} + \dots + f'_{i-1}(q_{i-1}, \dot{q}_{i-1}, \ddot{q}_{i-1}) + f'_{i-2} + \dots \quad (8)$$

where the force acting on the i th blade section is dependent on the position, velocity and acceleration of all the blades in the cascade, as well as the aerodynamic parameters. In current analytical models for compressible and transonic aeroelastic interaction, the assumption is made that every blade in the cascade moves with a constant amplitude, frequency, and interblade phase angle. These assumptions reduce the functional dependence expressed by the infinite series of equation (8) to a dependence on just three parameters, the amplitude, reduced frequency ($\omega b/v$), and interblade phase angle, for any given aerodynamic operating point and cascade geometry.

With these assumptions, the displacement of a two-dimensional section of the i th blade of an n blade rotor located at ψ_i is given as

$$q_i = C e^{j(\omega t - n\psi_i)} \quad i = 1, 2, \dots, N \quad (9)$$

$$= C e^{j(\omega t - i\beta)}$$

with

$$\psi_i = \frac{2\pi i}{N} \beta = \frac{2\pi n}{N}$$

where β is the interblade phase angle, and n is the number of nodal diameters. By contrast, the structural problem is cast in terms of standing mode shapes. For any family of modes with m nodal circumferences, the displacements of two-dimensional sections of the blades are given as a sum of two standing waves of the disk

$$q_i = a_{mn} \sin n\psi_i + b_{mn} \cos n\psi_i \quad (10)$$

where a_{mn} and b_{mn} are the generalized coordinates of the n nodal diameter modes for the family of m nodal circumferences.

The relation between the two formulations can be seen by expanding the real part of equation (9)

$$q_i = C \cos(\omega t - n\psi_i) = C \cos \omega t \cos n\psi_i + C \sin \omega t \sin n\psi_i \quad (11)$$

By comparing this with equation (10), it can be seen that if $a_{m,n}$ and $b_{m,n}$ are sinusoidal and temporarily out of phase by 90 deg, they give rise to a traveling wave with interblade angle, β .

If the criteria that a_{mn} and b_{mn} are quasi-sinusoidal and 90 deg out of phase are met, then the response of the multiblade modes can be related directly to a specific interblade phase angle and reduced frequency. Further, the associated modal force is the net aerodynamic force acting on that mode and, in the absence of aerodynamic disturbances, is a measure of the aerodynamic damping associated with that particular interblade phase angle and reduced frequency.

A complete methodology to measure the net aerodynamic damping can now be outlined:

1 Develop the equations of motion of the blade disk system which adequately characterize the modes expected in the aeroelastic response. Experimentally verify the modal frequencies, shapes, and structural damping.

2 Instrument the rotor to gain sufficient data to identify the modal responses.

3 Run the aeroelastic experiment collecting data on every blade response and disk participation and analyze the data in the following manner:

(a) Identify by Fourier transform in time, the dominant frequencies of response, and the blade modes (first bending, etc.) with which they are associated.

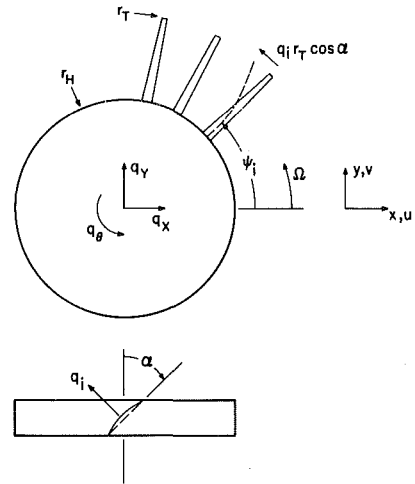


Fig. 1 Structural model of the MIT Rotor with flexible blades attached to a rigid disk, which possesses three in-plane degrees of freedom

(b) Narrow band pass filter the raw data to isolate each frequency of response.

(c) Use the modal relations and measured displacements to transform to multiblade coordinates.

(d) Use the amplitude data collected, together with the structural model, to calculate aerodynamic forces acting on the blades.

An example of the application of this method will now be given.

Structural Dynamics of the MIT Rotor

The first step in the proposed technique is to develop an adequate dynamic model of the rotor under investigation. The rotor chosen for the current experiments was the MIT Transonic Rotor, a 590-mm dia rotor with a hub-tip ratio of 0.5, and aerodynamic performance typical of current fans. In a structural arrangement typical of research rotors, 23 conventional, but somewhat stiff, unshrouded blades are mounted on a thick massive disk.

One characteristic of such research rotors is that the elastic deformations of the lower blade modes (first flex, second flex, first torsion) are coupled dominantly through the rigid body inertia of the disk, rather than the out-of-plane elastic deformation of the disk.

A structural dynamic model of the MIT Rotor has been developed and verified [12], which allows the disk two translational and one rotational in-plane degree of freedom (Fig. 1). Extending from a rigid disk which rotates at constant speed Ω are N blades located at angles $\psi_i = 2\pi i/N + \Omega t$. The blades are assumed to deflect with a single mode shape, γ , which has an amplitude of $q_i r_i$ at an effective stagger angle, α .

For uniform blades, the equations can be transformed to generalized multiblade coordinates, which for an odd number of blades N are

$$q_i = \sum_{n=1}^{\frac{N-1}{2}} a_n \sin n\psi_i + \sum_{n=1}^{\frac{N-1}{2}} b_n \cos n\psi_i + b_0 \quad (12)$$

With these assumptions, the equations of motion as expressed in multiblade coordinates are

$$I_T \ddot{q}_\theta / N + m_1 \cos \alpha \ddot{b}_0 + K_\theta q_\theta / N = Q_\theta$$

$$m_1 \cos \alpha \ddot{q}_\theta + m_0 \ddot{b}_0 + \bar{k}_i b_0 = B_0 \quad (13)$$

$$2M_T \ddot{q}_x / N - m_2 \cos \alpha \ddot{a}_1 + 2K_x q_x / N = Q_x$$

$$2M_T \ddot{q}_y / N + m_2 \cos \alpha \ddot{b}_1 + 2K_y q_y / N = Q_y$$

$$-m_2 \cos \alpha \ddot{q}_x + m_0 \ddot{a}_1 - 2\Omega m_0 \dot{b} + (\bar{k}_i - m_0 \Omega^2) a_1 = A_1$$

$$m_2 \cos \alpha \ddot{q}_y + m_0 \ddot{b}_1 + 2\Omega m_0 \dot{a} + (\bar{k}_i - m_0 \Omega^2) b_1 = B_1 \quad (14)$$

$$\left. \begin{aligned} m_0 \ddot{a}_n + \bar{k}_i a_n &= A_n \\ m_0 \ddot{b}_n + \bar{k}_i b_n &= B_n \end{aligned} \right\} n=2,3, \dots, (N-1)/2 \quad (15)$$

where the total mass, total moment of inertia, and inertial integrals are

$$M_T = M_d + NM_b \quad I_T = I_d + NI_b$$

$$\int dm = M_b \quad r_i^2 \int \gamma^2 dm = m_0$$

$$\int r^2 dm = I_b \quad r_i \int \gamma r dm = m_1$$

$$r_i \int \gamma dm = m_2 \quad (16)$$

where the limits of integration go from r_h to r_i . The effective blade stiffness is given by

$$\bar{k}_i = k_i + \Omega^2 \left[r_i^2 \int_{r_h}^{r_i} r \left(\frac{\partial \gamma}{\partial r} \right)^2 dr m dr - m_0 \cos^2 \alpha \right] \quad (17)$$

where the first term is the structural stiffness and the second is the centrifugal stiffening. The terms on the right-hand side of equation set (13-15) are the sought after modal forcing terms.

Transformation to the multiblade coordinates has greatly reduced the coupling of the structural dynamic equations. There are only two coupled sets and $N-3$ uncoupled equations. It can be seen from equation (13) that the average motion of the blades or the umbrella mode (b_0) couples only to the rigid body rotational degree of freedom of the disk. The $\sin 1\theta$ and $\cos 1\theta$ modes (a_1 and b_1) couple to translational motion of the disk, and to each other through gyroscopic terms (equation 14). All the higher modal diameter modes ($\sin 2\theta, \cos 2\theta, \sin 3\theta, \dots$) are completely uncoupled.

A complete set of vibration tests were carried out to determine the mass and stiffness properties of the MIT Aeroelastic Rotor. The blades were tuned to 374 ± 2 Hz for first bending and 1110 ± 30 Hz for second bending. Particularly in first bending, this represents a well tuned rotor. The structural damping of individual blades was measured in air and found to have an average log decrement of 0.015 (critical damping ratio of 0.0024). The combined material and structural damping only lightly damp the motion of the blades. While rotating in vacuum at the operating speed (10,000 rpm) the first bending frequency was 410 Hz, and the second bending frequency was 1150 Hz. As a result of bench and spin testing [12] it was verified that for any single blade mode, the simple inertially coupled model was adequate to characterize the dynamics of the MIT Rotor.

Apparatus and Instrumentation

The second step in the proposed test technique is to instrument the rotor so as to gain "sufficient" information about its structural response, and operate it under known aerodynamic conditions. Aeroelastic testing was conducted in the MIT Blowdown Compressor facility [13], providing quasi-steady flow conditions for a limited period of time. Prior to the test, a supply tank is filled to an initial pressure of 464 mm with a Freon-12 Argon mixture having a speed of sound 74 percent that of air, and a ratio of specific heats of 1.4. Downstream of an aluminum diaphragm which separates the supply tank from the test section, the rotor is driven to speed in a vacuum by a small electric motor. After diaphragm rupture and a start-up transient of approximately 60 ms, the flow becomes quasi-steady in the test section with the supply

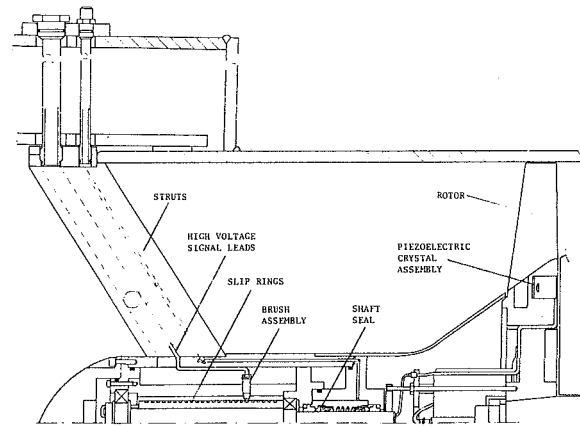


Fig. 2 Cut away view of the rotor, shaft and forward centerbody.

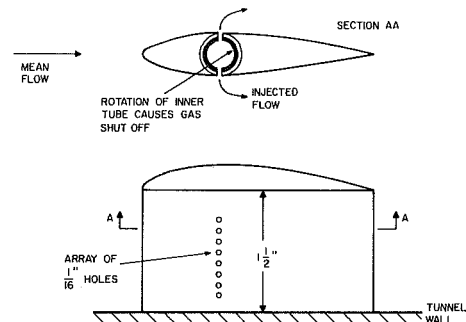


Fig. 3 Diagram of gas injector showing hole pattern and gas flow path

tank essentially behaving as a stagnation plenum. The mass flow is set by an orifice downstream of the stage which remains choked for about 150 ms. Although the rotor decelerates, the axial and tangential Mach numbers remain constant during the test and the steady aerodynamic performance of the stage can be determined from a number of wall static pressure transducers and a five-way pressure probe which traverses the flow during the test [14].

The Blowdown Facility has been adapted for use in aeroelastic studies by structural modification of the MIT Transonic Compressor Rotor, the geometry and performance of which are documented in [9]. The rotor operates at a tip Mach number of 1.2, an average pressure ratio of 1.66. The mass flow corrected to air at standard temperature and pressure is 35 kg/s at the design point. The rotor is cantilevered forward of a center body on which a fixed 48 blade stator is mounted, and which houses the drive motor and a 12 channel slip-ring assembly. In aeroelastic studies, these slip-rings are supplemented by a 24 channel slip-ring assembly housed in a centerbody supported by three struts ahead of the rotor (Fig. 2).

A time varying upstream disturbance was created by the interaction of the primary flow with a series of small jets injected normal to the surface of streamlined struts 120 mm upstream of the rotor face. The injection takes place through a 16-mm tube which extends 75 mm into the tunnel from the outer wall and is faired by an NACA 0012 airfoil. Two such assemblies were located 180 deg apart.

At 50 ms after diaphragm bursts, high-pressure Argon is vented to the hollow center of the injector (Fig. 3), and flows outward through two rows of twelve 1.6-mm dia holes (3.2 mm center to center) located on opposite sides of the injector, and is injected normal to the mean flow. In this way, the symmetric disturbance creates a region of velocity defect behind the injector, but imparts no mean swirl in the flow. The radial extent of the defect is about 40 mm. The distur-

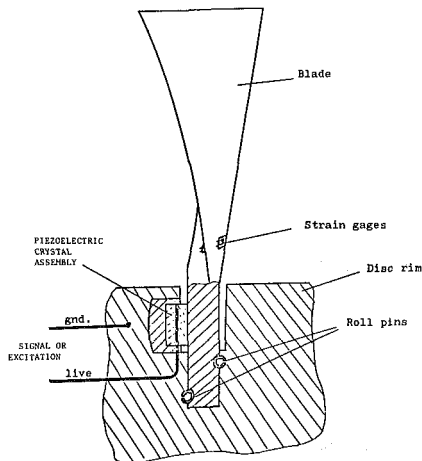


Fig. 4 Details of root attachment showing the location of the piezoelectric displacement transducer

bance is terminated at 100 ms after test start. The unique characteristic of this flow disturbance scheme is its ability to completely shut off flow within 1 ms, creating a well defined and sharp termination of the upstream disturbance.

The pertinent rotor instrumentation features are 23 piezoelectric crystals and 4 strain gauges for measuring blade response in bending. The disk incorporates a piezoelectric crystal into the root of each blade (Fig. 4). As transducers, the crystals give a signal which can be calibrated linearly against tip displacement for each of the natural modes of the blade. For frequencies above its RC rolloff point (about 30 Hz), the piezoelectric crystal is functionally identical to a strain gauge.

The on-rotor instrumentation thus provides one independent displacement measurement per blade. By the "sufficiency" criteria developed above, this is enough to resolve the multiblade modal response of the N blade-disk modes associated with one family of circumferential modes (e.g., the first flex family). If, however, the blade modes are well separated in frequency, the response of the first and second flex families can be determined. The free vibration response to imposed initial conditions is one instance where such frequency separation occurs.

Forced and Free Vibration Response

Since no aeroelastic stability boundaries were encountered within the performance map of the MIT Transonic Compressor Rotor, the response to forced vibration at the design point was investigated. The secondary flow injector system was used to create a stationary disturbance upstream of the rotor. After sharp termination of the disturbance, the subsequent free vibration ring down of the rotor served as a measure of the aerodynamic plus structural damping.

The aerodynamic response of the rotor to the upstream disturbance can be seen in a change in bow shock strength. Figure 5 shows the trace of the high frequency response wall static pressure transducer 0.1 chord upstream of the rotor at the 0 deg instrument location directly behind one of the injectors. An increase in the bow shock strength can be seen starting at about 55 ms and ending at 100–102 ms modulated near 70 ms by some remaining unsteadiness in the facility. During this entire period, a region of velocity defect is created behind the injector. As a blade passes through this region, its incidence increases, and with it the local shock strength. By comparison the unsteady pressure measured by a wall static transducer 72 deg from the injector shows no corresponding change in shock strength.

The individual response of all 23 blades is shown in Fig. 6. The blades are shown in their proper relative positions around

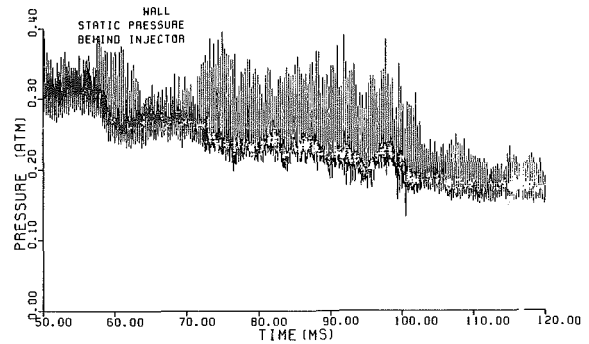


Fig. 5 Upstream wall static pressure measured 25 mm behind the injector

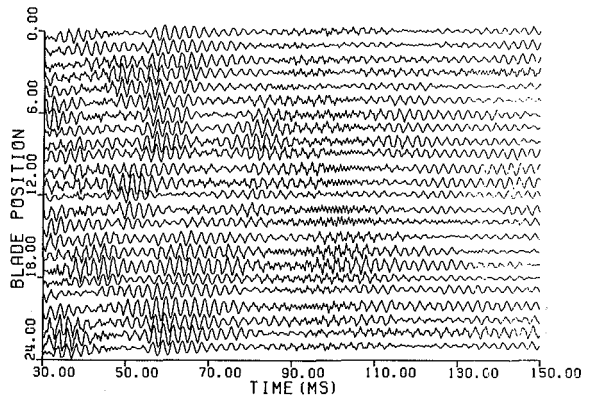


Fig. 6 Total response of the piezoelectric crystal for all blades. Each is shown in its proper relative location. Blade 23 is shown again as zero for reference.

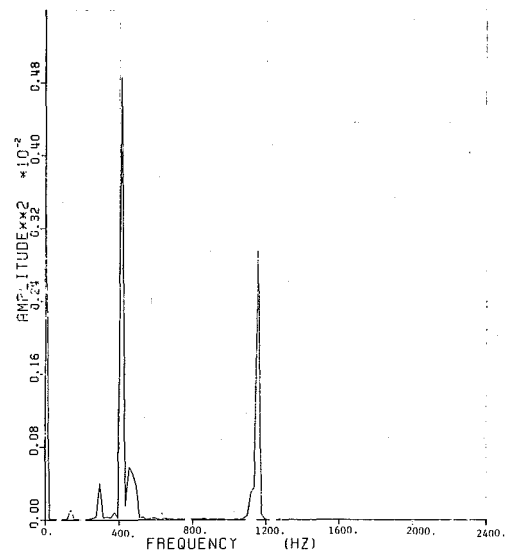


Fig. 7 Power spectrum density of Blade 3 response for the period from 100–150 ms.

the rotor. The signal from blade 23 is shown twice for reference, once at position zero and again at position 23. The reference time is that time when the diaphragm is commanded to burst. From this presentation of the data, some overall trends can be seen. At about 50 ms, the first bending frequency becomes dominant in a response which locally has some phase coherence. From 70 to 100 ms, the first bending mode appears to damp and a higher frequency grows, that of the second bending mode. After 100 ms, the second bending response decays and the first bending reemerges.

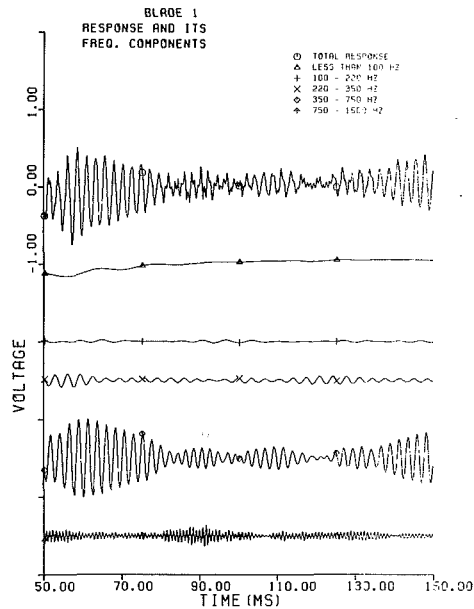


Fig. 8 Blade 1 response and its frequency components

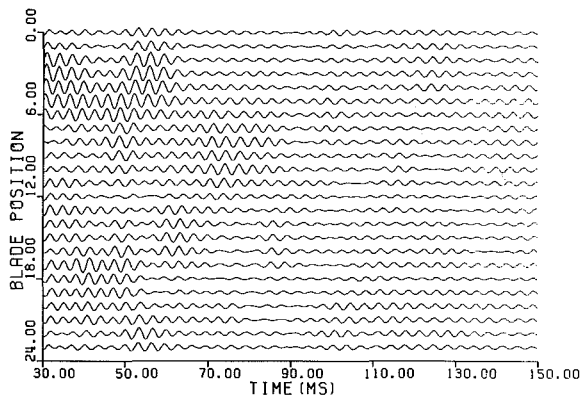


Fig. 9 Blade response in the range of 220-350 Hz. Each blade is shown in its proper relative position. Blade 23 is shown again as zero for reference (shown at 4 times the scale of Fig. 6).

The first step in reducing the data is to determine the frequency content of the response by performing Fast Fourier Transform in time of individual blade signals. Fourier transforms of blade 3 response is shown in Fig. 7 for the period of free response. The amplitude of response is concentrated in distinct frequencies; at low frequency less than 50 Hz, at about 150 Hz, at 300 Hz, in a band from 400 to 500 Hz, and a 1140 Hz. These spikes correspond to the low frequency response due to the blowdown transient, the first, second, and third rotor orders, and the second blade bending frequency at the eighth rotor order.

The next step in the data reduction is to narrow bandpass filter the total response of each blade to isolate each of the frequencies indicated. This is done digitally using a Nearly Equal Ripple digital filter [15]. The filter parameters typically used included a transition width at the edge of the pass band of 70 Hz and a loss outside of the pass band of 50 dB. Figure 8 shows the original data for blade 1, as well as its components derived from low pass filtering the raw data below 100 Hz, and in the ranges 100-220 Hz to isolate the first rotor order, 220-350 Hz to isolate the second rotor order, 350-750 Hz which contains the bulk of the first bending response, and 750-1500 Hz which contains the second bending response.

The bandpass filtered responses for the last three frequency ranges are shown for all the blades in Figs. 9, 10, and 11. The

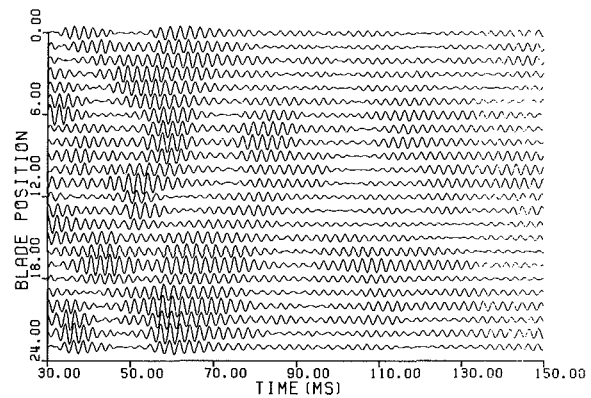


Fig. 10 Blade response in the range of 350-750 Hz (shown at the same scale as Fig. 6).

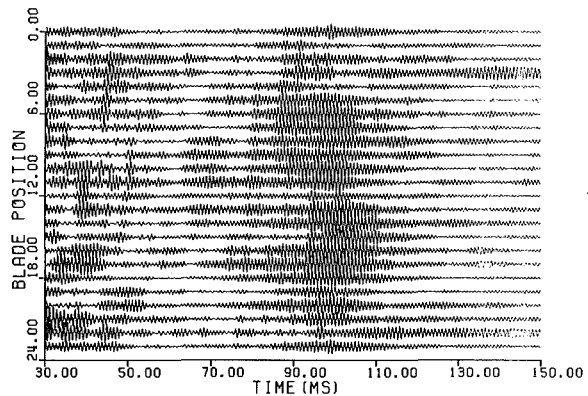


Fig. 11 Blade response in the range of 750-1500 Hz (shown at 3 times the scale of Fig. 6).

components of the blade displacement data at the second rotor order (Fig. 9) should show some sign of response to the flow injector since a two per revolution disturbance fixed in tunnel coordinates would be seen by the rotor at this frequency. While the amplitude of response is on average greater prior to 100 ms than after 100 ms, no clear pattern or phase relation emerges. In the response at first bending frequency (Fig. 10), certain "patches" of response have uniform amplitude and phase relation, such as the group of blades 1-8 from 50 to 70 ms and 16-22 from 60 to 80 ms. Again, no clear demarcation of the response before and after termination of the disturbance is evident. The response at second bending frequency (Fig. 11) does show a rise in amplitude prior to 100 ms and a decay thereafter for most blades, but no global pattern is evident.

The individual frequencies having been identified, the next step is to solve for the amplitudes of the multiblade modes using equation (4). In this case the values of the multiblade coordinates as described can be calculated from the individual blade displacements by performing at each instant in time a discrete Fourier transform in ψ such that

$$\begin{aligned}
 b_0 &= \frac{1}{N} \sum_{i=1}^N q_i \\
 a_n &= \frac{2}{N} \sum_{i=1}^N q_i \sin n\psi_i \\
 b_n &= \frac{2}{N} \sum_{i=1}^N q_i \cos n\psi_i
 \end{aligned} \quad (18)$$

In this way, the information contained in the displacements of

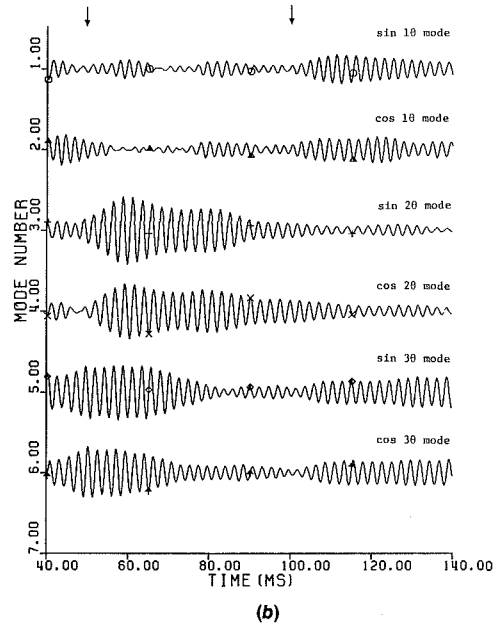
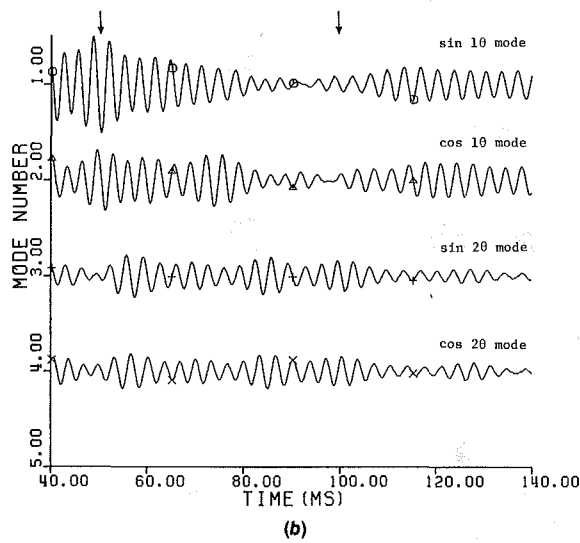
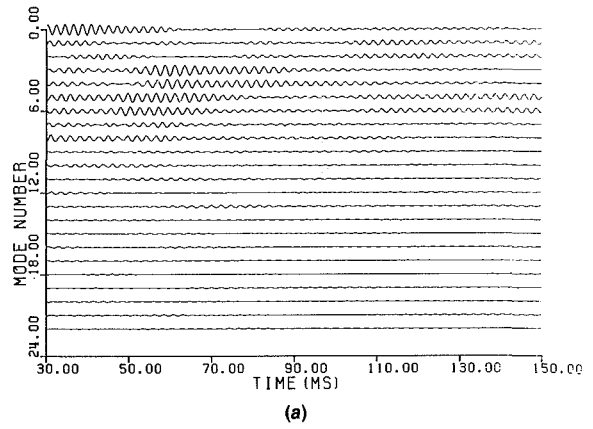
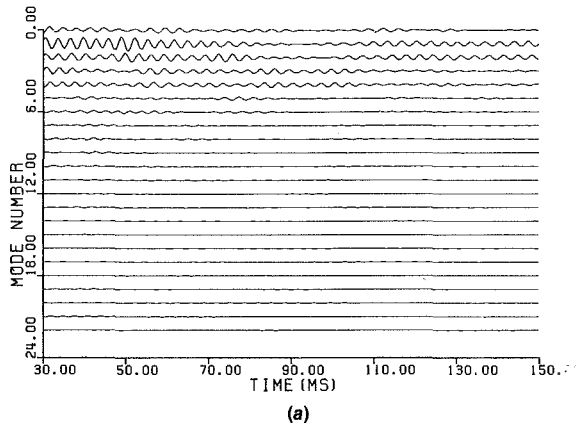


Fig. 12 Amplitude of the multiblade modes of the response in the range 220–350 Hz. Upstream excitation begins at 50 ms and ends at 100 ms, as shown by arrows¹

Fig. 13 Amplitude of the multiblade modes of the response in the range 350–750 Hz¹

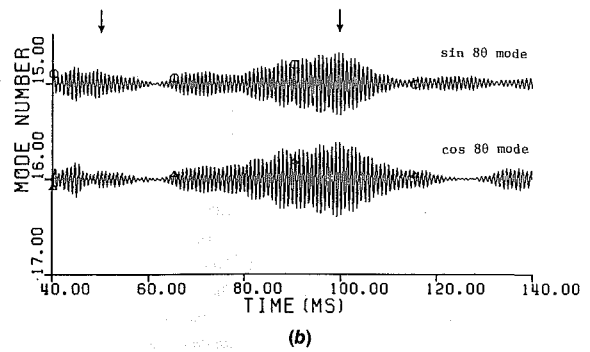
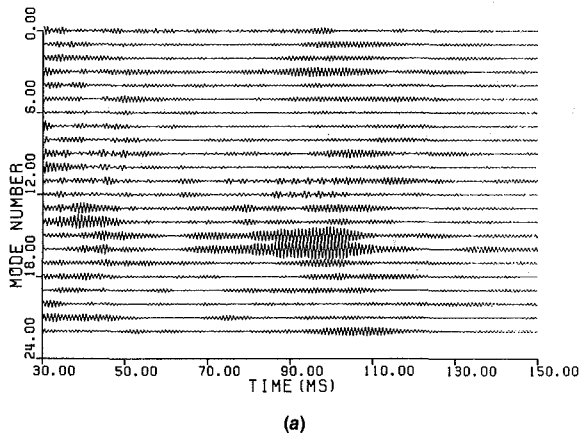


Fig. 14 Amplitude of the multiblade mode of the response in the range 750–1500 Hz¹

¹In Figs. 12–14, mode zero is the collective or umbrella mode, mode 1 is sin 1θ , 2 is cos 1θ , 3 is sin 2θ , 4 is cos 2θ , . . . , 21 is sin 11θ , and 22 is cos 11θ .

23 individual blades is transformed to the generalized coordinates of the average or collective mode (b_0), the 11 cosine modes ($\cos 1\theta, \dots, \cos 11\theta$) and the 11 sine modes ($\sin 1\theta, \sin 2\theta, \dots, \sin 11\theta$). The transformed data for the frequency ranges of interest corresponding to Figs. 9, 10, and 11 are shown in Figs. 12, 13, and 14. The global nature of the response is much more apparent from examination of the amplitudes of the multiblade modes. Figure 12 reveals that for the frequency range around second rotor order (220–350 Hz), the motion of the blades is primarily a superposition of the lowest seven modes; the collective mode (as shown as mode 0) and the $\sin 3\theta$ and $\cos 3\theta$ modes (shown as mode numbers 5 and 6) appear in bursts which are unrelated to the upstream excitation. However, the $\sin\theta$, $\cos\theta$, $\sin\theta$, and $\cos\theta$ modes (shown as modes 1–4 and again in Fig. 12(b)) clearly respond to the excitation. The two nodal diameter modes are the pair which should respond most strongly to the two per revolution disturbance, and this is seen to occur. Through the entire test time from 50 to 150 ms, the $\sin 2\theta$ and $\cos 2\theta$ have similar amplitude and are temporarily 90 deg out of phase.

The condition that the sine and cosine modes have the same amplitude and are 90 deg out of phase is synonymous with a traveling wave with a fixed amplitude and interblade phase angle. In the case of the $\sin 2\theta$ and $\cos 2\theta$ modes, the cosine mode lags the sine mode 90 deg. This translates to a rearward traveling wave in rotor coordinates, with an interblade phase angle

$$\beta = -\frac{2\pi n}{N} \quad (19)$$

where n is the number of nodal diameters. The wave speed of this travelling wave is

$$v = \pm \frac{\omega}{n} \quad (20)$$

which has a forward sense for a positive interblade phase angle and a rearward sense for a negative interblade phase angle.

The traveling blade displacement pattern given by the $\sin 2\theta$ and $\cos 2\theta$ modes has an interblade phase angle of -31.3 deg. Since the observed frequency is exactly twice the rotor speed, the wavespeed in rotating coordinates given by equation (20) is $-\Omega$. In rotor coordinates, the displacement pattern travels backward at Ω . Viewed by a stationary observer, this would be seen as a standing wave and is therefore the forced response to the fixed upstream disturbance. The observed response fluctuates in amplitude in the interval from 60 to 100 ms, but from 100 to 120 ms there is a smooth decay from a higher to a lower amplitude of response.

There is no resonance of the blade disk system at this frequency, so the continued response indicates some lower level two per revolution excitation must be present after 100 ms when the injector shuts off. The source of this disturbance is an innate 2θ nonuniformity of the flow in the facility. However, the smooth decay between two levels of excitation can be used to determine the total damping. With a knowledge of the structural damping, the aerodynamic damping for this

interblade phase angle and reduced frequency can be calculated. The numerical values of these parameters are listed in Table 1.

The response of the one nodal diameter mode ($\cos \theta, \sin \theta$) is also a backwards traveling wave disturbance with an interblade phase angle of -15.6 deg and a wave speed of -2Ω in rotor coordinates or $-\Omega$ as viewed by a fixed observer. This is therefore not the response to any fixed disturbance. The source of this excitation is the second rotor order excitation of the backward whirling mode of the blades and disk. Because of the coupled nature of this mode and the lack of information about the participation of the disk, no estimate of the damping can be made.

The amplitudes of the multiblade coordinates for the component of the response, which includes blade first bending frequency, is shown in Fig. (13). The lowest nine modes (collective, $\sin \theta, \dots, \cos 4\theta$) meet the criteria of significant amplitude of response, similar envelopes of response of the sine and cosine modes, and 90-deg phase lag of the cosine mode. While all nine show some response to the turn on or off of the injector, only the $\sin 3\theta$ and $\cos 3\theta$ modes (shown as mode numbers 5 and 6 and again in Fig. 13(b)) have a response from which a damping estimate can be made. This mode has an interblade phase angle of -47.0 deg, and again a wavespeed of $-\Omega$, giving a fixed pattern of blade deflection as viewed by a stationary observer. This is a forced response to a steady 3θ aerodynamic disturbance which has its origins in the interaction of a boundary layer bleed and three struts which support the forward centerbody. This response is present in every test, with or without the gas injector system present.

The interaction between the fixed 3θ disturbance and the controllable 2θ disturbance can be seen at two times in the test (Fig. 13(b)). Prior to 60 ms, the 3θ response is large. When the 2θ disturbance is turned on at about 55 ms, the three nodal diameter response diminishes sharply. When the injectors are turned off at 100 ms, the response grows. From this growth after 100 ms, the damping listed in Table 1 is calculated. The explanation of this response pattern is as follows. Prior to injector turn on, the three struts create wakes at 60, 180, and 300 deg locations. The third circumferential Fourier component of this distortion pattern is dominant, and the rotor sees an excitation at 3Ω (435 Hz). Since this is close to blade first bending frequency (410 Hz), there is a strong response. At 55 ms, the gas is injected and wakes created at 0 and 180 deg. If the wake production and aerodynamic response mechanisms were both linear, the structural response of the $\cos 3\theta$ and $\sin 3\theta$ modes would not change in response to the 2θ excitation. Obviously, the responses do interact such that the third circumferential Fourier component is reduced and the response at 3θ decreases. When the injector shuts off at 100 ms, the reverse process takes place and the 3θ component again dominates.

The response of the rotor at second blade bending frequency shows a completely different pattern in the response of the multiblade modes than the two frequency ranges already discussed. Figure 14 shows that only the eight nodal diameter modes ($\sin 8\theta, \cos 8\theta$ shown as mode numbers

Table 1 Measured values of damping

Blade mode	Interblade phase (β)	Frequency (Hz)	Tip reduced frequency ($\omega b/v$)	Critical damping ratio (ζ)	Re (C_{Lq}) based on 80% span	
					Measured	Adamczyk & Goldstein
1 bend	-31.3	290	.25	.045	-1.2	-.449
1 bend	-47.0	435	.38	.027	-1.1	-.501
2 bend	-125.0	1160	1.01	.011	-1.2	-.572

$$\text{Re}(C_{Lq}) = -\left(\frac{b\omega}{v}\right) \left(\frac{m}{\pi\rho b^2}\right) \zeta$$

15 and 16, and again in Fig. 14(b) respond to the disturbance created by the injector. It has an interblade phase angle of -125 deg and a wavespeed of $-\Omega$. Two injectors located 180 deg apart in the tunnel will create disturbances at all the even harmonics of the tunnel. The rotor will see the eighth harmonic at eight times rotor rotation speed or about 1160 Hz. Since this is very close to second blade bending, a large response in the eighth multiblade mode results. The response after 100 ms is a decaying free vibration which gives another measurement of aerodynamic damping. Notice also that a slight beating is evident due to the mistune of the $\sin 8\theta$ and $\cos 8\theta$ modes.

The techniques developed have been used to estimate three values of the damping for the operating point tested. They are summarized in Table 1. These are, in fact, measurements of the total modal damping: aerodynamic plus structural. Individual blade structural damping was found to have a log decrement of 0.015 in the first bending mode. Since this is 2 to 10 percent of the total damping, it can be assumed that the principal source of the measured damping is aerodynamic.

Discussion and Conclusions

A method has been demonstrated for the measurement of aerodynamic damping of a transonic rotor by an inverse solution of the structural dynamic equation of motion. The method is quite general and can be used in the analysis of forced vibration and damping of a rotor in that region of its performance map where the rotor is aeroelastically stable, as well as the behavior in regions of instability. It uses data which are available from conventional strain gauges. In damping studies, the final result is a direct measurement of the aerodynamic plus structural damping for a known point on the performance map as a function of the interblade phase angle and reduced frequency.

If two primary requirements are met, this method is applicable to any rotor in any facility. First, adequate instrumentation must be available to characterize the rotor response. This will usually include at least one strain gauge or tip displacement transducer per blade, and several per blade if the response of more than one blade mode is to be studied. The second requirement is that a controllable disturbance be created which can be terminated within one blade vibratory period in order to create a well defined initial condition to free response. This excitation could be created through the structure, but aerodynamic excitation is in general stronger. Ideally, the rotor could be excited by a controllable injector system, such that both forward and backward waves would be present. Alternatively a "white" excitation could excite all modes.

The current investigation was limited to only two controllable fixed upstream disturbances. The measured damping for these negative interblade phase angles (Table 1) indicates high levels of aerodynamic damping. For purposes of comparison, the levels of aerodynamic damping in translation have been calculated for these three values using the weak shock, zero back pressure, flat plate, two dimensional analysis of Adamczyk and Goldstein [16]. These results are also shown in Table 1. The "typical" section chosen was the 80 percent span, which has a gap to chord ratio of .905, a stagger angle of 56.5 deg, a mass ratio ($m/\pi\rho b^2$) of 120, and a relative Mach number of 1.22. The experimentally measured critical damping ratios have also been reduced to unsteady lift coefficients based on the 80 percent span section properties.

Comparison of analytic and experimental results show fair agreement, with a constant discrepancy of a factor of two. Similar discrepancies have been observed in comparison between cascade data and weak shock codes at Mach numbers around 1.2 and back pressure ratios in the vicinity of 1.6 [17]. Thus, the present experiment is in a sense consistent with such cascade measurements.

A useful application of the techniques developed would be to perform a series of experiments on a rotor known to have an aeroelastic stability boundary close to or within its normal operating map. A series of runs could then be made where the rotor was successively run first near, then at, then over, its stability boundary. The aerodynamic damping of the mode known to become unstable could be followed from positive to negative in value. In this way, a great deal of insight could be gained into the nature of aerodynamic damping in general, and its role in aeroelastic instabilities in particular.

Acknowledgments

This research was supported under grant NSG-3079 from NASA Lewis Research Center, with Dr. John Adamczyk serving as monitor. The author received fellowship support from the John and Fannie Hertz Foundation.

References

- 1 Adamczyk, J. J., "Analysis of Supersonic Stall Bending Flutter in Axial-Flow Compressors by Actuator Disk Theory," NASA Technical Paper 1345, 1978.
- 2 Dugundji, J., "Flutter Analysis of a Tuned Rotor With Rigid and Flexible Disks," MIT Gas Turbine and Plasma Dynamics Laboratory Report No. 146, July 1979.
- 3 Fleeter, S., et al., "An Experimental Determination of Unsteady Aerodynamics in a Controlled Oscillating Cascade," ASME JOURNAL OF ENGINEERING FOR POWER, Vol. 99, No. 1, Jan. 1977.
- 4 Fleeter, S., et al., "The Unsteady Aerodynamics of a Cascade in Translation," AGARD Symposium on Stress, Vibrations, Structural Integration and Engine Integrity (including Aeroelasticity and Flutter), AGARD CP 248, Apr. 1979.
- 5 Jones, W. H., et al., "Experimental Apparatus for Investigation of Fan Aeroelastic Instabilities in Turbomachinery," NASA TM-X-3508, June 1977.
- 6 Stargardter, H., "Subsonic Transonic Stall Flutter Study Final Report," NASA CR-165256, June 1979.
- 7 Lubomski, J. F., "Characteristics of Aeroelasticity Instability in Turbomachinery—NASA Full Scale Engine Test Results," NASA TM-X-79085, Apr. 1979.
- 8 Kerrebrock, J. L., "Flow in Transonic Compressors," 1980 Dryden Lecture, Paper AIAA-80-0124, Jan. 1980.
- 9 Durall, M., "Rotor Wake Behavior in a Transonic Compressor Stage and its Effect on the Loading and Performance of the Stator," MIT Gas Turbine and Plasma Dynamics Laboratory Report No. 149, Apr. 1980.
- 10 Crawley, E. F., "Measurements of Aerodynamic Damping in the MIT Transonic Rotor," MIT Gas Turbine and Plasma Dynamics Laboratory Report No. 157, Feb. 1981.
- 11 Crawley, E. F., Kerrebrock, J. L., and Dugundji, J., "Preliminary Measurements of Aerodynamic Damping of a Transonic Compressor Rotor," in *Measurement Methods in Rotating Components of Turbomachinery*, ASME 79-57425, Mar. 1980.
- 12 Crawley, E. F., "In Plane Inertial Coupling in Tuned and Severely Mistuned Bladed Disks," Paper No. 82-GT-288, 27th Gas Turbine Conference, ASME, London, Apr. 1982.
- 13 Kerrebrock, J. L., et al., "The MIT Blowdown Compressor Facility," JOURNAL OF ENGINEERING FOR POWER, Vol. 96, No. 4, Oct. 1974.
- 14 Kerrebrock, J. L., Epstein, A. H., and Thompkins, W. T., "A Mixture Miniature High Frequency Sphere Probe," *Measurement Methods in Rotating Components in Turbomachinery*, ASME 79-57425, Mar. 1980.
- 15 Kaiser, J. F. and Reed, A., "Data Smoothing Using Low-Pass Digital Filters," *Rev. Sci. Instrumentation*, Vol. 48, No. 11, Nov. 1977.
- 16 Adamczyk, J. J., and Goldstein, M. E., "Unsteady Flow in a Supersonic Cascade with Subsonic Leading-Edge Locus," *AIAA Journal*, Vol. 16, No. 12, Dec. 1978.
- 17 Riffel, R. E., and Rothrock, M. D., "Experimental Determination of Unsteady Blade Element Aerodynamics in Cascades, Translational Mode Cascade Final Report," NASA CR-165166, Dec. 1980.

In-Plane Inertial Coupling in Tuned and Severely Mistuned Bladed Disks

E. F. Crawley

Boeing Assistant Professor,
Department of Aeronautics and Astronautics,
Massachusetts Institute of Technology,
Cambridge, Mass. 02139

A model has been developed and verified for blade-disk-shaft coupling in rotors due to the in-plane rigid body modes of the disk. An analytic model has been derived which couples the in-plane rigid body modes of the disk on an elastic shaft with the blade bending modes. Bench resonance tests were carried out on the MIT Compressor Rotor, typical of research rotors with flexible blades and a thick rigid disk. When the rotor was carefully tuned, the structural coupling of the blades by the disks was confined to zero and one nodal diameter modes, whose modal frequencies were greater than the blade cantilever frequency. In the case of the tuned rotor, and in two cases where severe mistuning was intentionally introduced, agreement between the predicted and observed natural frequencies is excellent.

1 Introduction

In determining the response of a rotor to applied external forcing, and especially in determining the flutter boundaries of a stage, it is important to understand and characterize the coupled response of the blade-disk or blade-disk-shroud system. Previously, several authors have discussed the effects of blade-disk elastic coupling [1] and blade-disk-shroud elastic coupling [2] on the modal response of a tuned rotor. Other investigators have looked further into the effect that mistuning of blades has on the response of these systems [3].

These studies have focused primarily on the coupling of the flexural and torsional modes of the blades through out-of-plane elastic deflection of the disk. In these models, the hub or center of the disk is usually constrained from motion in or out of the plane. Therefore, the resulting coupling of blade modes into blade-disk modes, characterized by a number of nodal circles and diameters, is attributable solely to the elastic deformation of the disk. Even the very general model of Fabunmi [4] which allows for in-plane and out-of-plane motion of the disk imposes the boundary condition that the hub center remain fixed.

The hub of any real rotor is not perfectly constrained, but possesses six rigid body degrees of freedom which are elastically constrained by the stiffness of the shaft on which it runs. In the case of an isolated rotor on a shaft, the transverse deflection of the shaft allows two in-plane translation and two out-of-plane pitch modes of the disk. The single out-of-plane translational degree of freedom of the disk is resisted by the longitudinal stiffness of the shaft. The last of the six rigid body modes of the disk, in-plane rotation, is completely unconstrained by a shaft running on bearings.

Any of these rigid body degrees of freedom of the disk can couple the blades through the inertia of the rotor. In principle, all six should be considered in computing the coupled modes of the bladed disk. However, in the case of research rotors which tend to have thick, massive disks, the inertial effect of the relatively rigid disk can be the dominant source of blade disk coupling.

The importance of this inertial coupling is apparent in several ways. The inclusion of the motion of the disk and elastic restraint of the shaft shift the observed frequencies of the bladed disk. Depending on the ratio of the blade-on-disk frequencies to the disk-on-shaft frequencies, the observed modal frequencies can be either raised or lowered. When the effects of rotation are included, some of the modes of the bladed disk become gyroscopically coupled, leading to blade-disk-shaft whirl [5]. Such coupled whirl has three potentially important consequences on gas turbines, and fans in particular: First, the coupling causes whirl resonances to occur "far" from the nonrotating resonances, or from those resonances corrected for centrifugal stiffening. The presence of such a resonance could produce an unexpected forced vibration problem [6]. Second, the possibility of structural instability exists due to damping introduced in the rotor. Third, the possibility of whirl coupling with the unsteady aerodynamics introduces the possibility of whirl flutter, as was observed in some turboprop engines [7]. Fundamental to these whirl problems is an understanding of the role of inertial coupling in bladed disks.

This paper will deal with the question of in-plane inertial coupling as observed in the MIT Aeroelastic Rotor. In the next section, a model of the blade-disk-shaft system will be developed. In subsequent sections, the results of three sets of experiments are discussed in which the natural modes of the bladed rotor were found. In the first set of experiments, the

Contributed by the Gas Turbine Division of THE AMERICAN SOCIETY OF MECHANICAL ENGINEERS and presented at the 27th International Gas Turbine Conference and Exhibit, London, England, April 18-22, 1982. Manuscript received at ASME Headquarters December 22, 1981. Paper No. 82-GT-288.

blades were uniform and well tuned. In the latter two sets, different combinations of blades were weighted at the tips to produce a bladed disk system with extreme nonuniformity. The frequency results obtained from these experiments were found to correlate well with the proposed model.

2 Model of Blade-Disk Inertial Coupling

The proposed model of the blade-disk system is shown in Fig. 1. A solid disk extends from the center to the hub radius ($r = r_h$), and possesses two translational and one rotational in-plane degrees of freedom. Extending from the hub to the tip ($r = r_t$) are N blades located at angles ψ_i ($\psi_i = 2\pi i/N$). The blades deflect with a single mode shape, γ , which has an amplitude of $q_i r_i$. For every mode shape, the twisted blades deflect at an effective angle to the normal, so their in-plane component of deflection is $q_i r_i \cos \alpha$. With these assumptions, the deflections of a point on the blade are given as

$$\begin{aligned} u &= q_x - r q_\theta \sin \psi_i - \gamma r_i q_i \sin \psi_i \cos \alpha \\ v &= q_y + r q_\theta \cos \psi_i + \gamma r_i q_i \cos \psi_i \cos \alpha \\ w &= \gamma r_i q_i \sin \alpha \end{aligned} \quad (1)$$

Evaluating the kinetic energy of a single blade gives

$$\begin{aligned} T_i &= \frac{1}{2} \int_{r_h}^{r_t} (\dot{u}^2 + \dot{v}^2 + \dot{w}^2) dm \\ &= \frac{1}{2} \int_{r_h}^{r_t} (\dot{q}_x^2 + \dot{q}_y^2 + r^2 \dot{q}_\theta^2 + \gamma^2 r_i^2 \dot{q}_i^2 \\ &\quad + 2\dot{q}_\theta r [\dot{q}_y \cos \psi_i - \dot{q}_x \sin \psi_i] \\ &\quad + 2\dot{q}_i \gamma r_i \cos \alpha [\dot{q}_y \cos \psi_i - \dot{q}_x \sin \psi_i] \\ &\quad + 2\dot{q}_\theta \dot{q}_i \gamma r_i r \cos \alpha) dm \end{aligned} \quad (2)$$

Evaluating the mass integrals gives

$$\begin{aligned} T_i &= \frac{1}{2} M_b (\dot{q}_x^2 + \dot{q}_y^2) + \frac{1}{2} I_b \dot{q}_\theta^2 + \frac{1}{2} m_0 \dot{q}_i^2 \\ &\quad + \dot{q}_\theta S_b [\dot{q}_y \cos \psi_i - \dot{q}_x \sin \psi_i] \\ &\quad + \dot{q}_i m_2 \cos \alpha [\dot{q}_y \cos \psi_i - \dot{q}_x \sin \psi_i] \\ &\quad + \dot{q}_\theta \dot{q}_i m_1 \cos \alpha \end{aligned} \quad (3)$$

where the integrals are defined as

$$\begin{aligned} \int dm &= M_b \quad r_t^2 \int \gamma^2 dm = m_0 \\ \int r md &= S_b \quad r_t \int \gamma r dm = m_1 \\ \int r^2 dm &= I_b \quad r_t \int \gamma dm = m_2 \end{aligned} \quad (4)$$

where the limits of integration go from r_h to r_t . The integrals in equation (4) are, respectively, the contribution of the blade to the system mass (M_b), static imbalance (S_b), and moment of inertia (I_b), the blade modal mass (m_0), and the consistent mass terms of the coupling of the blade with the rotation (m_1) and translation (m_2) of the disk.

The kinetic energy of a uniform disk reduces to

$$T_d = \frac{1}{2} (\dot{q}_x^2 + \dot{q}_y^2) M_d + \frac{1}{2} \dot{q}_\theta^2 I_d \quad (5)$$

If the center of the disk is restrained by translational and rotary springs, the potential energy is

$$U_d = \frac{1}{2} K_x q_x^2 + \frac{1}{2} K_y q_y^2 + \frac{1}{2} K_\theta q_\theta^2 \quad (6)$$

and each blade has a potential energy

$$U_i = \frac{1}{2} k_i q_i^2 = \frac{1}{2} m_0 \omega_0^2 q_i^2 \quad (7)$$

where ω_0 is the cantilevered natural frequency.

Substitution of equations (3), (5), (6), and (7) into Lagrange's equation yields the equations of motion as expressed in individual blade coordinates.

$$\begin{aligned} M_T \ddot{q}_x + K_x q_x - \sum_{i=1}^N \{ \ddot{q}_\theta S_b \sin \psi_i + \ddot{q}_i m_2 \cos \alpha \sin \psi_i \} &= 0 \\ M_T \ddot{q}_y + K_y q_y + \sum_{i=1}^N \{ \ddot{q}_\theta S_b \cos \psi_i + \ddot{q}_i m_2 \cos \alpha \cos \psi_i \} &= 0 \\ I_T \ddot{q}_\theta + K_\theta q_\theta + \sum_{i=1}^N \{ S_b (\ddot{q}_y \cos \psi_i - \ddot{q}_x \sin \psi_i) \\ &\quad + \ddot{q}_i m_1 m_1 \cos \alpha \} = 0 \end{aligned}$$

Nomenclature

a = amplitude of the sine multiblade mode
 b = amplitude of the cosine multiblade mode
 i = blade index
 I = moment of inertia
 k = stiffness
 K = shaft stiffness
 m = mass
 M = modal mass
 n = number of nodal diameter
 N = number of blades
 q = displacement
 r = radius
 S = static imbalance
 T = kinetic energy
 u = displacement in x -direction
 U = strain energy
 v = displacement in y -direction
 w = displacement in z -direction
 α = angle of blade attachment to disk
 γ = mode shape
 σ = see equation (17)

ψ_i = location of the i th blade
 ω = natural frequency
 Ω = frequency of rotation

Subscripts

A = assumed mode of the unweighted blade
 B = assumed mode of the weighted blade
 b = blade
 d = disk
 h = hub
 i = i th blade
 IP = in phase assumed mode
 m = m th multiblade mode
 n = n th multiblade mode
 OP = out of phase assumed mode
 t = tip
 T = sum of blade and disk (total)
 w = of the weighted blade
 x = in the x -direction
 y = in the y -direction
 θ = in the circumferential direction

$$m_0 \ddot{q}_1 + m_2 \cos \alpha [\ddot{q}_y \cos \psi_i - \ddot{q}_x \sin \psi_i] + \ddot{q}_\theta m_1 \cos \alpha + k_i q_i = 0 \quad i = 1, 2, \dots, N \quad (8)$$

where

$$M_T = M_d + \sum_i M_b$$

$$I_T = I_d + \sum_i I_b \quad (9)$$

Note that the translational and rotational equations are coupled through the combined imbalance of the blades and the motion of the blades. The blade motions do not couple to each other directly, but through the inertial coupling of the disk represented by the $m_1 \cos \alpha$ and $m_2 \cos \alpha$ terms. Note that the angle α which controls the inertial coupling is the angle formed by the effective axis about which the blade bends.

The equations of motion as expressed in equation (8) are very general. They will be used in simplified form to examine the cases of extreme mistune of the disk. The equations are highly coupled through the disk rigid body modes, making them difficult to work with. For uniform blades, the equations can be simplified considerably by transforming to the generalized multiblade coordinates, which for an odd number of blades N are

$$q_i = \sum_{n=1}^{N-1} a_n \sin n \psi_i + \sum_{n=1}^{N-1} b_n \cos n \psi_i + b_0 \quad (10)$$

Substitution of this expression for q_i into set (8), and manipulation of the equations (by premultiplication of the last N by successive values of $\cos m \psi_i$ and $\sin m \psi_i$, and summation over i) yields

$$\begin{bmatrix} M_T - \frac{N}{2} m_2 \cos \alpha \\ -\frac{N}{2} m_2 \cos \alpha & \frac{N}{2} m_0 \end{bmatrix} \begin{Bmatrix} \ddot{q}_x \\ \ddot{a}_1 \end{Bmatrix} + \begin{bmatrix} K_x & 0 \\ 0 & \frac{N}{2} k_i \end{bmatrix} \begin{Bmatrix} q_x \\ a_1 \end{Bmatrix} = 0$$

$$\begin{bmatrix} M_T & \frac{N}{2} m_2 \cos \alpha \\ \frac{N}{2} m_2 \cos \alpha & \frac{N}{2} m_0 \end{bmatrix} \begin{Bmatrix} \ddot{q}_y \\ \ddot{b}_1 \end{Bmatrix} + \begin{bmatrix} K_y & 0 \\ 0 & \frac{N}{2} k_i \end{bmatrix} \begin{Bmatrix} q_y \\ b_1 \end{Bmatrix} = 0$$

$$\begin{bmatrix} I_T N m_1 \cos \alpha \\ N m_1 \cos \alpha & N m_0 \end{bmatrix} \begin{Bmatrix} \ddot{q}_\theta \\ \ddot{b}_1 \end{Bmatrix} + \begin{bmatrix} K_\theta & 0 \\ 0 & N k_i \end{bmatrix} \begin{Bmatrix} q_\theta \\ b_0 \end{Bmatrix} = 0$$

$$\left. \begin{aligned} m_0 \ddot{a}_n + k_i a_n = 0 \\ m_0 \ddot{b}_n + k_i b_n = 0 \end{aligned} \right\} n = 2, 3, \dots, \frac{N+1}{2} \quad (11)$$

where the equations have been simplified by the trigonometric summations valid for n, m , such that $n, m \neq N/2, N, 3N/2, \dots$, namely

$$\sum_{i=1}^N \cos m \psi_i \cos n \psi_i = \sum_{i=1}^N \sin m \psi_i \sin n \psi_i = \begin{cases} N/2 & m = n \\ 0 & m \neq n \end{cases}$$

$$\sum_{i=1}^N \sin m \psi_i \cos n \psi_i = 0 \quad (12)$$

Transformation to multiblade coordinates has reduced the completely coupled set of (8) to three sets of two coupled equations each and $N-3$ simple single degree of freedom equations. It can be seen that the $\sin \theta$ and $\cos \theta$ modes (a_1 and b_1) couple to the translational rigid body modes of the disk. The mode which represents the average or collective motion of the blades (b_0) couples only to the rotational degree of freedom of the disk. All higher modes ($\sin 2\theta, \cos 2\theta, \sin 3\theta, \dots$) are not coupled through the disk.

It remains to be shown that this disk inertial coupling model is sufficient to characterize the dynamics of the MIT Rotor. The next sections describe the methods used to determine the constants in equation (11) using a well-tuned rotor. Then, two experiments will be discussed in which severe mistuning was introduced to check and verify the model.

3 Experiments With a Tuned Rotor

A series of tests was performed on the tuned MIT Aeroelastic Rotor to determine its mass and stiffness properties and compare its resonant modes with those predicted by the proposed model. The rotor was mounted to a short steel shaft, machined with the same taper and keyway as the shaft on which the rotor was mounted in the Compressor Facility. This short shaft was then mounted directly to the head of a Ling Model 420 electromagnetic shaker designed to produce a peak force of 100 pounds. Excitation of the rotor to determine resonances was sometimes achieved by the shaker through the mounting shaft. In other cases, a loud speaker was used to acoustically excite the blades directly. Amplitudes of response were monitored with the rotor strain gauges and piezoelectric crystals and with blade and disk mounted accelerometers.

First, the mass properties of the rotor as defined by equations (4) and (9) were determined. The dimensions of the aluminum rotor and blades were carefully measured using calipers. These dimensions were used to calculate the mass and rotary moment of inertia (M_T and I_T) of the rotor. As a check, the calculated mass agreed to within 2 percent of the measured mass, which is well within the accuracy of the measurement. The blade mass properties (m_0, m_1, m_2) were based on the measured dimensions and holographic measurements of the first bending mode made while the rotor was not rotating. The dimension and mass properties for the blade first bending mode are summarized in the Appendix.

One more required constant can be estimated from the rotor geometry: the angle between the plane of the disk and

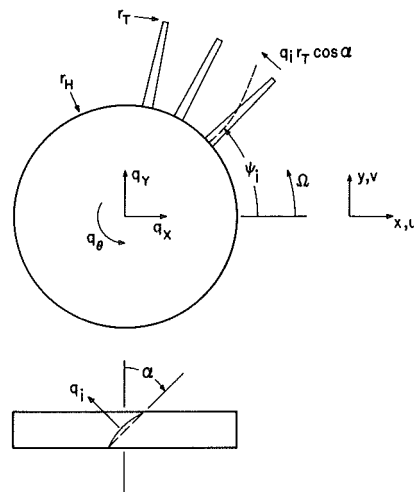


Fig. 1 Structural model of the MIT Rotor with flexible blades attached to a rigid disk, which possesses three in-plane degrees of freedom

the normal to the camber line (Fig. 1). For the blades of the MIT Rotor, this angle varies from about 30 deg at the root to 60 deg at the tip. The effective angle around which the blade flexes must lie between these limiting values. Reference [8] cites the normal to the chord at 20 percent span height outboard of the root attachment as the effective flexural axis of such blades in first bending mode. A value of 36 deg was measured for this location and will be used in further calculations.

The remaining constants to be determined were the stiffness of the hub restraint (K_x, K_y, K_θ) and blade (k_i). Rather than measure these directly, a search was made for the resonances suggested by the model and the stiffness calculated using the mass properties and observed frequencies.

Before any resonance tests were performed, the rotor was tuned in much the same way as a stringed instrument. In designing and installing the piezoelectric crystal assembly (Fig. 2), it was observed that by selectively tightening a bolt (not shown) which retains the assembly, a variation of about 6 Hz could be achieved in the frequency of the blade's first bending mode. It was impossible to simply tune any given blade due to the participation of all the other blades through the disk coupling. To isolate a given blade, all the other blades in the rotor were weighted at the tip by a 2-in. "C" clamp, which lowered the resonance of the weighted blades well below 200 Hz. The resonance of the single unweighted blade could then easily be identified and adjusted. In this way, the blades were tuned to 378 ± 2 Hz.

With the rotor thus tuned, scans were made for overall blade-disk resonances and their modal patterns. Using the shaker and acoustic excitation, a strong resonance was found at 374.5 Hz with no distinct modal pattern, a "counterrotating" mode at 417-418 Hz, a weak "corotating" mode around 40 Hz, a "countertranslating" mode at 390-394 Hz, and a weak "cotranslating" mode around 300 Hz.

The translating modes are the ones associated with the first two equations of set (11). In this mode the tip displacement pattern was observed to go as $\sin\theta$. At the upper frequency the disk moves counter to the sense of the tip motion, and in the lower mode the disk moves with the tips. From the upper frequency, K_x is calculated to have a value of 44×10^6 N/m to 51×10^6 N/m. Similarly the rotating modes are associated with the third equation of set (11). From the upper rotational frequency a K_θ of 2.0×10^4 Nm/rad is found.

The strong resonance at 374.5 Hz was found to be the true blade cantilever natural frequency, as given by the last $N-3$ equations of set (11). However, when the blades were tuned

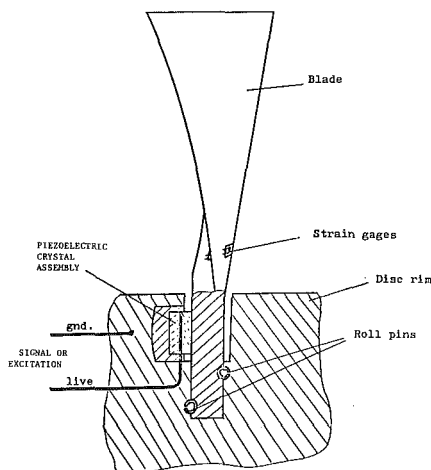


Fig. 2 Details of root attachment showing the location of the piezoelectric displacement transducer

individually, they resonated at an average frequency of 378 Hz. This difference of 3.5 Hz is associated with the participation of the disk. When the blades were tuned only one blade was excited at a time and the disk participated in the motion. This observed natural frequency was not based on the modal mass of the blade, but on the reduced mass of the blade-disk system. With all the blades free to vibrate, some combination of the higher modes ($\cos 2\theta, \cos 3\theta, \dots$) was excited; the disk did not participate and the real blade cantilever frequency was observed. In section 5, the difference between the blade modal mass and blade-disk reduced mass will be shown to lead to a difference of 3.5 Hz in first bending frequency.

4 Severely Mistuned Rotor With Several Blades Participating

In the process of tuning each blade of the rotor, weights were clamped to the tips of all the other blades. This process can be thought of as introducing a severe mistuning into the rotor, in this case to isolate the resonance of a single blade. This method of creating a severe mistuning was used in two additional ways. In one case, two blades were left unweighted and their natural frequencies were determined as a function of the angle that separated them. These results will be described in section 5. In the second case, between one and twenty-three adjacent blades were left unweighted. A study was made of how the observed frequency changed with an increasing number of participating blades.

Each blade was weighted by a 2-in. steel "C" clamp near the tip. Between the contact points of the clamp and the metal surface of the blade was a piece of 1/8-in. thick hard rubber mat to prevent the clamp from slipping or chattering. With this weighting, the blades were observed to have a very well damped resonance in the range of 160 to 180 Hz, well below the unweighted resonance of 374 Hz.

When only one blade was unweighted, its single natural frequency was near that to which the blades were tuned, 378 Hz. When two or more consecutive blades were unweighted, two strong resonances were found. At the blade cantilever frequency of 374 Hz, the blades moved without any noticeable phase relation. At a higher frequency, the blades were observed to move in phase. This natural frequency was found at 381 Hz for two consecutive unweighted blades and monotonically increased with increasing number of unweighted blades. As the number of consecutive unweighted

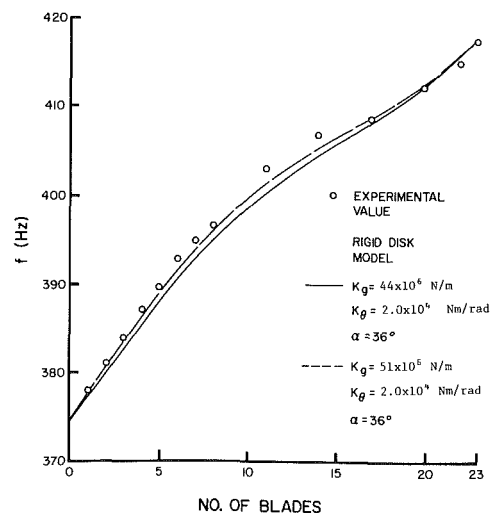


Fig. 3 Frequency of the highest observed (in phase) mode versus the number of blades participating

blades approached 23, the observed frequency approached the counterrotating mode of the tuned rotor at 418 Hz. The trend of the highest resonant frequency versus participating blades can be seen from the experimental data in Fig. 3.

This highest resonant mode of the mistuned rotor can be modeled by assuming two modes for the blade displacements whose amplitudes are q_A and q_B . The J unweighted blades respond at equal amplitude and in phase and are symmetrically distributed about $\psi = 0$ deg such that a blade at $\psi_i = 2\pi i/N$, the displacement is

$$q_i = q_A \quad i = \frac{1-J}{2}, \frac{1-J}{2} + 1, \dots, \frac{J-1}{2} - 1, \frac{J-1}{2} \quad (13)$$

The remaining K weighted blades respond in phase at equal amplitude and are symmetrically distributed about $\psi = 180$ deg such that

$$q_i = q_B \quad i = \frac{J-1}{2} + 1, \frac{J-1}{2} + 2, \dots,$$

$$N - \frac{J-1}{2} - 2, N - \frac{J-1}{2} - 1 \quad (14)$$

where

$$J + K = N$$

To derive the equations of motion for this untuned case, the two assumed modes q_A and q_B are substituted into equation set (8). The summations in the first three equations and over the last N equations are divided into sums over the K weighted and J unweighted blades. The resulting equations are

$$\begin{aligned} M_T \ddot{q}_x + K_x q_x &= 0 \\ M_T \ddot{q}_y + K_y q_y - \sigma S_w \ddot{q}_\theta - \sigma \ddot{q}_B m'_2 \cos \alpha + \sigma \ddot{q}_A m_2 \cos \alpha &= 0 \\ I_T \ddot{q}_\theta + K_\theta q_\theta - \sigma S_w \ddot{q}_y + K \ddot{q}_B m'_1 \cos \alpha + J \ddot{q}_A m_1 \cos \alpha &= 0 \\ J m_0 \ddot{q}_A + \sigma m_2 \ddot{q}_y \cos \alpha + J m_1 \ddot{q}_\theta \cos \alpha + J k_i q_A &= 0 \\ K m'_0 \ddot{q}_B - \sigma m'_2 \ddot{q}_y \cos \alpha + K m'_1 \ddot{q}_\theta \cos \alpha + K k_i q_B &= 0 \end{aligned} \quad (15)$$

where the blades have been assumed to be uniform except for the presence of the weights at the tips. The mass properties of the weighted blades are given in a form similar to equation set (4) as

$$\begin{aligned} r_i^2 \int \gamma^2 dm &= m'_0 & r_i \int \gamma dm &= m'_2 \\ r_i \int \gamma r dm &= m'_1 & M_w r_w &= S_w \end{aligned} \quad (16)$$

the last term representing the contribution to the static imbalance by a weight of M_w at radius r_w . The total rotor mass and inertia terms must also reflect the addition of weights at the tips. The term σ is defined as the partial sum

$$\sigma = \sum_J \cos \psi_i \quad (17)$$

where the summation over the J blades represents the indices in equation (13). It can be shown that

$$-\sigma = \sum_K \cos \psi_i \quad (18)$$

where the summation is over the K blades of the indices in equation (14). Note that since the displacements were assumed to be symmetric about the x -axis, the x equation has uncoupled from the remaining four.

The solution to the last four equations of set (15) is shown in Fig. 3 for the range of experimentally determined elastic constants. The agreement between the experimental results and those predicted by the model for this assumed mode are excellent. In particular, note that the model reproduces the dip in the resonance curve in the range of 15 to 20 blades unweighted. The lower end point for zero blades is the true

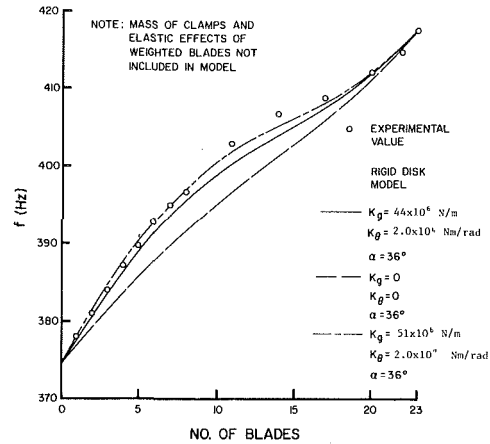


Fig. 4 Frequency of the highest observed (in phase) mode versus the number of blades participating

cantilever frequency of the blade, and the upper end point with all 23 blades unweighted is that of the in-phase mode found for the perfectly tuned rotor. In the range of 1 to 5 blades participating, the trend is nearly linear. When the first blade is unweighted, the reduced mass effect of the disk causes an increase in the observed resonance of about 3 Hz. As the next few adjacent blades are unweighted, the effective modal mass of the blades increases, growing closer to that of the disk. This increases the reduced mass effect and the increment in frequency. Once the participating blades subtend a large angle, the translational coupling begins to be reduced such that each additional blade causes a smaller increase in frequency, and the slope of the curve decreases.

A simplification can be made to equations (15) if the weighted blades are simply ignored; that is, they are assumed not to participate in the motion, and that the additional mass of the weights at the tips is not significant. With these assumptions, the last of the five equations of set (15) is removed, q_K and S_w are set to zero, and the remaining three equations are less highly coupled. Solutions of this simplified set of equations for the in-plane resonance are shown in Fig. 4. This agreement is also quite good. In this case, simply ignoring the mass of the weights and participation of the weighted blades still gives reasonable results.

5 Severely Mistuned Rotor With Two Blades Participating

In this second set of experiments with severe mistuning, two blades were left unweighted. The angle subtended by the two blades was varied so that the blades were first adjacent, then separated by one weighted blade, then two and so on until the unweighted blades were on opposite sides of the rotor.

For each location of the two blades, two distinct resonances were found: one in which the blades moved in phase, and one in which they moved out of phase. When the blades were adjacent, the out-of-phase mode was found at the true cantilever frequency of the blades (374 Hz). The out-of-phase motion of the blades cancelled the participation of the disk. The in-phase mode was found at about 381 Hz, 7 Hz above the cantilever frequency. This difference is just twice the increase in observed natural frequency caused by the reduced mass effect of the disk acting on a single blade. As the spacing of the two active blades increases, the two observed frequencies tend to coalesce as shown in Fig. 5. The error bars in the data represent several different pairs of blades tested for each angular separation.

Once again, this mistuning can be modeled by assuming two modes for the displacement of the two blades. As in the simplified analysis at the end of section 4, the weighted blades

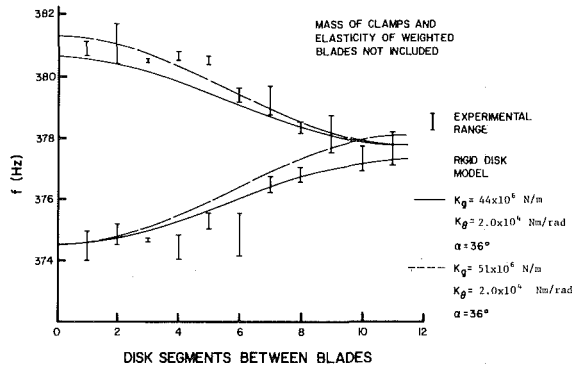


Fig. 5 The two observed frequencies of a system with two blades free to participate versus the angular separation between blades. (For a 23 bladed rotor, 11.5 corresponds to 180 deg.)

will be assumed to have no displacement and the mass of the clamps will be ignored. Then the displacement of the two blades participating in the motion at plus ψ_i and minus ψ_i can be given as the sum and difference of an in-phase and out-of-phase mode

$$q_i = \frac{q_{IP} + q_{OP}}{2} \text{ at } +\psi_i$$

$$q_i = \frac{q_{IP} - q_{OP}}{2} \text{ at } -\psi_i \quad (19)$$

where ψ is one/half the angle subtended by the two blades.

Substitution of the displacements expressed above into equations (8) gives

$$M_T \ddot{q}_x + K_x q_x - \ddot{q}_{OP} m_2 \cos \alpha \sin \psi = 0$$

$$M_T \ddot{q}_y + K_y q_y + \ddot{q}_{IP} m_2 \cos \alpha \cos \psi = 0$$

$$I_T \ddot{q}_\theta + K_\theta q_\theta + \ddot{q}_{IP} m_1 \cos \alpha = 0$$

$$m_0 \ddot{q}_{IP} + k_i q_{IP} + 2 \ddot{q}_y m_2 \cos \alpha \cos \psi + 2 q_\theta m_1 \cos \alpha = 0$$

$$m_0 \ddot{q}_{OP} + k_i q_{OP} - 2 \ddot{q}_x m_2 \cos \alpha \sin \psi = 0 \quad (20)$$

The symmetry of the in- and out-of-phase modes about the x -axis has caused an uncoupling of the equations of motion. It can be seen that the first and last of set (20) completely determine the out-of-phase resonance and lead to the lower curve of Fig. 5. The middle three equations are coupled and determine the in-phase resonance responsible for the upper curve of Fig. 5.

Within the uncertainty concerning the disk restraint stiffness, the agreement with experimental results is again excellent. Both branches of the response and their coalescence are predicted correctly. Examination of equations (20) shows the origin of this coalescence. The first and last equations are coupled through a term expressing the translational coupling which depends on $\sin \psi$. For adjacent blades, ψ is near zero and the true cantilever frequency is observed. As ψ moves towards 90 deg, the equations are increasingly coupled with a resulting upward shift in resonance. The middle three equations are coupled through translational terms which depend on $\cos \psi$ and rotational terms which have no ψ dependence. At small values of ψ both are present. As ψ approaches 90 deg the translational terms go to zero, reducing the coupling, but the rotational coupling still keeps the observed resonance above the cantilever frequency. If the magnitude of the translational and rotational coupling are the same, as they are in the MIT Rotor, the two frequencies tend to coalesce as ψ approaches 90 deg.

6 Conclusions

A structural model has been developed and demonstrated in

which the coupling of the blade motion is caused by the in-plane inertia of the disk. The model correctly predicts the resonances of the MIT Rotor even in the case of severe mistuning. This inertial coupling dominates the elastic coupling of the disk in the case of the MIT Rotor, which is typical of mid to low aspect ratio research rotors with thick disks. However, this rigid body coupling is present in all bladed disk systems. Detailed finite element analysis should take into account the flexibility of the shaft and rigid body motion of the disk in calculations of blade disk coupled frequency.

Acknowledgments

This research was supported under grant NSG-3079 from NASA Lewis Research Center, with Dr. John Adamczyk serving as monitor. The author received fellowship support from the John and Fannie Hertz Foundation.

References

- Ewins, D. J., "Vibration Characteristics of Bladed Disk Assemblies," *Journal of Mechanical Engineering Science*, Vol. 15, No. 3, 1973.
- Carta, F. O., "Coupled Blade-Disk-Shroud Flutter Instabilities in Turbojet Engine Rotors," *ASME Journal of Engineering for Power*, Vol. 89, July 1967.
- Ewins, D. J., "Vibration Modes of Mistuned Bladed Disks," ASME Paper No. 75-GT-14, Apr. 1975.
- Fabunmi, J. A., "Forced Vibration of a Single Stage Axial Compressor Rotor," *ASME Journal of Engineering for Power*, Vol. 102, No. 2, Apr. 1980.
- Coleman, R. P., and Feingold, A. M., "Theory of Self-Excited Mechanical Oscillations of Helicopter Rotors with Hinged Blades," NACA Report 1351, 1958.
- Crandall, S. H., and Dugundji, J., "Forced Backward Whirling of Aircraft Propeller-Engine Systems," *Proceedings of the Second International Conference on Vibrations in Rotating Machinery*, The Institution of Mechanical Engineering, Churchill College, Cambridge, England, Sept. 1980.
- Reed, W. H., III, "Review of Propeller Rotor Whirl Flutter," NACA TR R-264, July 1967.
- Adamczyk, J. J., "Analysis of Supersonic Stall Bending Flutter in Axial-Flow Compressor by Actuator Disk Theory," NASA Technical Paper 1345, Nov. 1978.

APPENDIX

Mass Properties of the MIT Rotor

The following are the overall and blade mass properties for all blades unweighted and for J blades unweighted (see equations 4, 9 and 16 for definitions).

	All blades unweighted	J blades unweighted
M_d (Kg)	11.6	---
M_b (Kg)	0.085	---
M_w (Kg)	---	0.113
M_T (Kg)	13.5	$13.5 + (N - J) 0.113$
I_T (Kg)	0.286	$0.286 + (N - J) 0.00815$
m_0 (Kg m ²)	0.00142	0.00640
m_1 (Kg m ²)	0.00229	0.00866
m_2 (Kg m)	0.00961	0.0334

Blade dimensions and first bending mode shape:

	138.	167.	192.	217.	243.	268.	294.
r (mm)	138.	167.	192.	217.	243.	268.	294.
chord (mm)	66.8	69.3	68.6	73.4	77.5	79.8	80.5
thickness (mm)	8.15	8.15	6.60	5.41	4.50	2.79	2.10
area (mm ²)	545.	481.	317.	278.	244.	156.	119.
γ (mode shape)	0.00	0.0693	0.168	0.311	0.489	0.714	1.00

An Improved Method for Calculating Critical Speeds and Rotordynamic Stability of Turbomachinery

B. T. Murphy

Weyerhaeuser Fellow.

J. M. Vance

Professor.

Mechanical Engineering,
Texas A&M University,
College Station, Texas

A number of the computer programs for rotordynamic stability and critical speed prediction in common use during recent years have been based on the works of Myklestad, Prohl, and Lund. Programs of this type, called transfer matrix programs, employ complex variables when damping or cross-coupling are included in the model. Most use an iteration scheme which at times fails to converge with sufficient accuracy on some critical speeds, and has been known to completely miss critical speeds on occasion. It is shown in this paper that by rearranging the calculations performed in a transfer matrix program, one can derive the characteristic polynomial for a complex rotor-bearing system with no loss in generality. The modeling procedures are identical for the rotor and bearing/foundations, including the effects of gyroscopics, damping, and any or all destabilizing influences which are linearized in the usual manner. With the characteristic polynomial known, critical speeds can be estimated and stability predicted with greater efficiency and with no fear of missing any modes. Such a program has been written, and a complete comparison between the two types of programs is shown.

Introduction

For years, linear transfer matrix programs have been used by rotating machinery engineers for estimating critical speeds and predicting stability of complex rotor-bearing systems. The basic idea behind the workings of these programs was first put forth by Holzer [1] as a way of finding natural frequencies of torsional systems. This method was later adapted by Myklestad [2, 3] to calculate the natural frequencies of airplane wings coupled in bending and torsion. At about the same time Prohl [4] showed how this method could be applied to rotor-bearing systems, complete with gyroscopic moments. The next significant advancement in the method was made by Lund [5, 6]. Using complex variables, Lund shows how it can be applied to much more general rotor-bearing systems. By developing a more general formulation of bearing forces, Lund shows how system damping can be accounted for as well as self-exciting influences such as oil whip and/or internal friction. It was with these latest developments that the method took on the full use of the general theory known as the "Linear Transfer Matrix Method."

One other item first introduced by Lund, and central to the subject of this paper, is a rather ingenious iteration scheme used to converge on the system eigenvalues. It is a Newton-Raphson approach and involves taking the derivatives of all

equations used in the program. When programmed for a digital computer, this technique works very nicely for many problems but runs into trouble on others. One such pitfall is that it fails to converge with sufficient accuracy on some eigenvalues and has been known to completely miss one or more eigenvalues in some applications.

It is shown in this paper that by rearranging the calculations performed in a Lund-type program [6], one can calculate the coefficients of the characteristic polynomial for the rotor-bearing system. The system natural frequencies, combined with their corresponding logarithmic decrements, are the roots of this polynomial. The logarithmic decrement provides the criteria for establishing system stability. With the polynomial known, these roots can be found and divided out in a more straightforward and efficient manner. Convergence can always be obtained and no critical speeds will be missed.

The roots, or eigenvalues, are found in an iterative manner by both types of programs, but the polynomial program performs transfer calculations for the rotor-bearing system only one time in order to derive the characteristic polynomial. The iterations are then performed on the polynomial to find the roots. The number of iterations required to find a root is typically 5 to 10 (rarely more than 11) to achieve an accuracy of six digits. The Lund-type program also requires about the same number of iterations per root. However, all transfer calculations for the rotor-bearing system must be redone four times for each individual iteration. This difference accounts for a significant increase in computational efficiency for the polynomial program.

Contributed by the Gas Turbine Division of THE AMERICAN SOCIETY OF MECHANICAL ENGINEERS and presented at the 27th International Gas Turbine Conference and Exhibit, London, England, April 18-22, 1982. Manuscript received at ASME Headquarters December 28, 1981. Paper No. 82-GT-294.

Procedure

The rotor-bearing system is modeled in exactly the same manner as for the usual transfer matrix program (see [5]). The rotor is represented by concentrated masses connected by massless shafts (see Fig. 1). Bearings and foundations are modeled as forces acting on the masses at the appropriate axial locations. The masses have the inertia properties of rigid circular cylinders and the shafts behave according to the Euler bending and Timoshenko shear formulas. A shaft "station," see Fig. 2, is normally considered to consist of a mass plus the shaft section immediately to its right.

With the rotor-bearing system modeled as a connection of shaft stations, one assigns degrees of freedom (coordinates) at the junctions between the stations (i.e., at each concentrated mass). The linear differential equations are then written for each station and are arranged in matrix form. Since the equations are linear and homogeneous the problem becomes an eigenvalue problem. Using the Laplace Transform, the matrices of differential equations are transformed into matrices of linear algebraic equations expressing the displacements and forces at the right end in terms of the displacements and forces at the left end [6]. The elements of these "transfer matrices" (or coefficients of the equations) are not constant but are actually polynomials in the system eigenvalue.

By definition, a transfer matrix "transfers" displacements and forces from one end of the station to the other. If the transfer matrices for two adjoining shaft stations are multiplied together using standard matrix multiplication, one obtains a single transfer matrix which fully represents the two stations. Since the elements of the two original matrices were polynomials so will be the elements of the new matrix (and of correspondingly larger degree). Following this logic one can multiply together all the transfer matrices for the system and obtain a single transfer matrix which fully represents the entire system. The degree of the polynomial elements that make up this overall transfer matrix will be determined by the number of stations in the original model.

Holzer [1] shows that the system eigenvalues can be found from the overall system transfer matrix by realizing that the forces at the shaft ends go to zero when the shaft vibrates at one of its natural frequencies. Thus, the determinant must vanish for the portion of the system transfer matrix that relates the forces at the right end to the displacements at the left end. Only at the natural frequencies can one have zero forces at the right end of the shaft even when the displacements are nonzero at the left end. Formulating the determinant of this sub-matrix yields the characteristic polynomial for the rotor-bearing system.

To illustrate the procedure, consider the N -inertia, rotor-bearing system shown in Fig. 1, with symmetric bearing supports ($k_{nx} = k_{ny}$, $c_{nx} = c_{ny}$). The transfer matrix for critical speeds across the n th mass ($n = 1, 2, \dots, N$), from left to right, is

$$\begin{Bmatrix} X'_n \\ \theta'_n \\ V'_n \\ M'_n \end{Bmatrix} = \begin{bmatrix} 1 & 0 & 0 & 0 \\ 0 & 1 & 0 & 0 \\ -M_n(s) & 0 & 1 & 0 \\ 0 & -J_n(s) & 0 & 1 \end{bmatrix} \begin{Bmatrix} X_n \\ \theta_n \\ V_n \\ M_n \end{Bmatrix} \quad (1)$$

where

$$\begin{aligned} M_n(s) &= m_n s^2 + c_n s + k_n \\ J_n(s) &= (T_n - P_n) s^2 \end{aligned}$$

The transfer matrix across the n th shaft section, from left to right, is

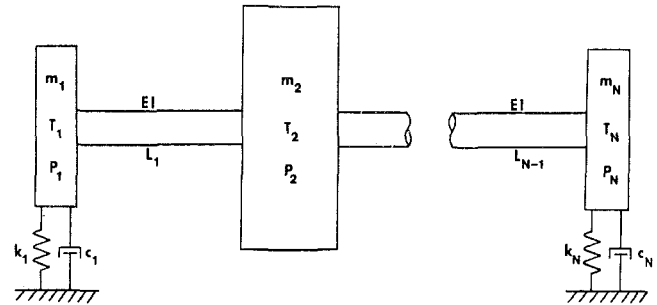
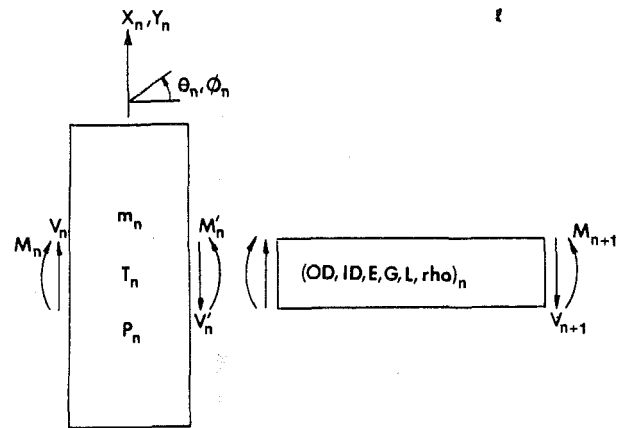


Fig. 1 An N -inertia rotor bearing system



Concentrated Mass Properties

m - amount of concentrated mass
 T - transverse (diametral) moment of inertia
 P - polar (axial) moment of inertia

Shaft Properties

OD - outside diameter
 ID - inside diameter
 E - Young's Modulus
 G - Shear Modulus
 ρ - mass density
 L - shaft length

Fig. 2 A single shaft station with displacements X and Y , rotations θ and ϕ , shearing forces V , and bending moments M

$$\begin{Bmatrix} X_{n+1} \\ \theta_{n+1} \\ V_{n+1} \\ M_{n+1} \end{Bmatrix} = \begin{bmatrix} 1 & l_n & l_n^3/6EI & l_n^2/2EI \\ 0 & 1 & l_n^2/2EI & l_n/EI \\ 0 & 0 & 1 & 0 \\ 0 & 0 & l_n & 1 \end{bmatrix} \begin{Bmatrix} X'_n \\ \theta'_n \\ V'_n \\ M'_n \end{Bmatrix} \quad (2)$$

Substitution of the left end boundary conditions, $V_1 = M_1 = 0$, and successive multiplication of the transfer matrices from left to right will yield

$$\begin{Bmatrix} V'_N \\ M'_N \end{Bmatrix} = \begin{bmatrix} d_{11} & d_{12} \\ d_{21} & d_{22} \end{bmatrix} \begin{Bmatrix} X_1 \\ \theta_1 \end{Bmatrix} \quad (3)$$

where the d_{ij} are polynomials in the eigenvalue s . In any contemporary computer program based on the Lund method, s will be assigned a numerical (complex) value for each iteration of the algorithm. Therefore, the d_{ij} will become complex numbers, and the coefficients of the polynomial are lost.

In the polynomial program, the algorithm is written so as to preserve the coefficients of the polynomial, and the iteration is then performed using the polynomial equation

$$D(s) = d_{11} * d_{22} - d_{12} * d_{21} = 0 \quad (4)$$

the roots of which are the complex eigenvalues. It should be pointed out that the characteristic polynomial given by equation (4) is exact and not an analytical approximation by way of additional simplifying assumptions.

The degree of the characteristic polynomial depends on the complexity of the formulation (degrees of freedom per element) and the number of stations the shaft is divided into. The usual formulation has two displacements and two rotations per station, and thus the degree of the polynomial is eight per station (i.e., 72 deg for a nine station shaft model). It was originally thought that finding the roots of such large order polynomials might be extremely sensitive to even the slightest computation errors in the coefficients. This was found not to be a problem and it can be shown analytically [7] that this situation is confined to only the higher modes. This seems reasonable since if one were to change, say, one of the masses by even a very small amount this could cause a large change in the 100th critical speed but certainly not in the first or second critical speeds.

As a method for finding the roots of the polynomial the Newton-Raphson approach was tried first. This method was found to work well requiring on the average six to eight iterations per pair of conjugate roots. Another method which was tried is the Bairstow method [8] of quadratic factoring. The advantage of this method is that it finds a pair of roots at a time and the roots appear in conjugate pairs. The Bairstow method executes in less than half the time of the Newton-Raphson and so is presently used in the program.

Results of Comparison

A complete comparison has been made of the polynomial type program with a Lund-type program written directly from reference [6]. The initial purpose of the comparison was to test the accuracy of the polynomial program against the Lund-type program. It should be pointed out, however, that both the Lund and polynomial programs calculate eigenvalues for the same set of linear differential equations. Thus, in the absence of any significant numerical difficulties (i.e., round-off error), the two programs should generate roots which are exactly equal for the number of significant digits obtained. This comparison was done using the Space Shuttle Hydrogen Turbopump as a model [9]. The model used, Fig. 3, consists of nine stations and contains asymmetric bearing stiffnesses, destabilizing cross-coupling at three axial locations due to the pump interstage seals, and the aerodynamics of the turbines. With the cross-coupling coefficients used, the first forward mode will be unstable.

All roots were found to an accuracy of six digits in both programs and a direct comparison shows all corresponding roots to be identical within the limits of this accuracy (i.e., first six digits are the same). The comparison illustrates a considerable improvement by the polynomial program in efficiency of execution time. To find eight modes the Lund-type program required 27.6 s of execution time on a Prime 750 digital computer. Performing the same tasks and giving the same results, the polynomial program took just 5.4 s. Also, since the model has nine stations it has 72 possible roots (36 conjugate pairs). The Lund-type program did not find all these roots since convergence breaks down for the higher modes. The polynomial program found all roots, requiring only one additional second of execution time. Thus, using the polynomial method one can find all the roots, be certain that none are missed, and for very little extra cost. It is felt that this is the greatest advantage of the polynomial program.

The Space Shuttle model of Fig. 3 can be considered to be of minimum complexity while still giving reasonably accurate results. The system is divided into just nine stations: one station for each disk (pump and turbine stages), one station for each bearing and for each portion of overhung shaft. This "minimum number of stations" modeling philosophy is used by some engineers because of its inherent simplicity. Another modeling philosophy that is widely used is to divide the rotor into many small stations in order to improve accuracy. To test

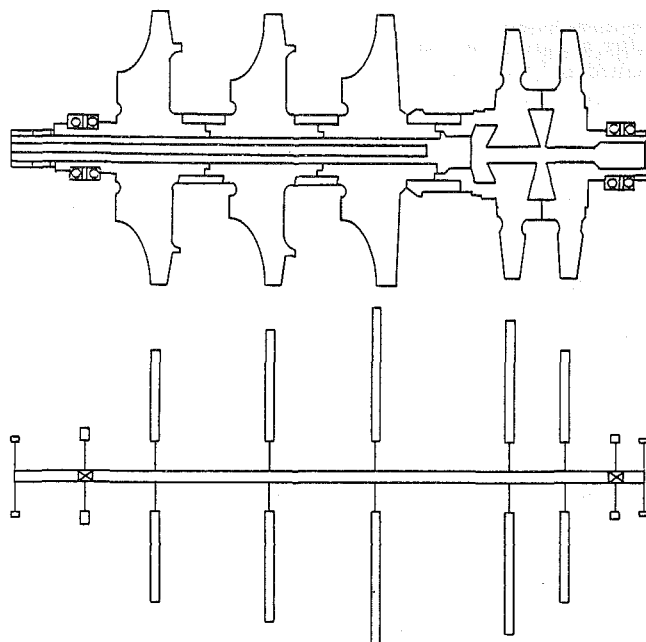


Fig. 3 Space shuttle rotor and computer model

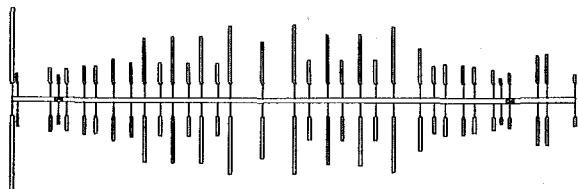


Fig. 4 35-station rotor model for eight stage centrifugal compressor

the performance of the polynomial program on this type of model another comparison was made using an eight-stage centrifugal compressor typical of the petrochemical industry. This machine, weighing 1400 lbs, is supported on two tilt-pad bearings with a bearing span of 80.7 in. and is 103 in. in length overall. There are also a coupling and thrust collar overhung at the shaft ends. The rotor is modeled (see Fig. 4) as 35 stations supported in two flexible and damped bearings at stations 4 and 32. Both the Lund-type program and polynomial program were executed to find the first eight modes. As for the Space Shuttle case the results are identical within the precision obtained (six digits). The Lund-type program required 72.5 s to execute and the polynomial program required 34.3 s (26 of these seconds to derive the polynomial). Since the model has 35 stations, there are 280 possible roots (140 conjugate pairs). The Lund-type program could not find all these roots but the polynomial program did requiring an additional 30 s.

As indicated above, the polynomial program executes faster than the Lund-type program. To investigate this further, a study was conducted using models of a uniform shaft supported in symmetric flexible bearings. Some of the results of this study are shown in Figs. 5 and 6. Figure 5 shows the ratio of execution times for finding roots for the two programs against the number of stations in the model and the number of roots found. It is seen that as more and more roots are sought the polynomial program gets better and better. This advantage is diminished by increasing the number of stations. Figure 5 also shows one of the problems sometimes encountered when running a Lund-type program. The erratic nature of two of the curves shown ($N=9$ and 12) is caused by the inability of the Lund-type program to converge on the higher modes. The program is attempting to iterate to a convergence accuracy of six significant digits. If an accuracy

of 4 or 5 digits is obtained but does not continue to improve after a chosen number of additional iterations, the search is halted and then continues on to the next root. This condition was encountered on the higher modes when using the Lund-type program and causes the curves of execution time to behave erratically in some instances.

Figure 6 shows why the advantage in execution time diminishes with the number of stations. The execution time of a Lund-type program increases rather linearly with the number of stations. Figure 6 shows that the time required to find the characteristic polynomial increases roughly with the square of the number of stations. For models with many stations, this is most (well more than half) of the total required execution time. If the model does have many stations and only a few roots are sought, then it is possible that the Lund program will require less execution time. The number of stations required to make the programs equal on execution time increases roughly linearly with the number of modes sought. As an example, if just 10 modes are required the model must have more than 115 stations for the Lund-type program to execute faster.

Another important difference was noted between the two types of programs while performing the above comparison. The Lund-type program was found at times to calculate roots in a rather random order. This condition can necessitate the calculation of many additional roots to assure that the first 3, 4 or 5 have been found. On the other hand, the polynomial program finds roots in a much more orderly fashion. Starting with the lowest root, the roots were almost always generated in order, and were never more than one or two roots out of place.

As for mode shapes, the two programs calculate mode shapes in the same manner with the polynomial program coming out ahead on execution time by about a factor of 2.75 (roughly constant). However this result may be of small significance since the time required to find the mode shapes is only in the range of 10 percent of the total time required to run the program.

Using the Program

Due to its faster execution time and reliable identification of all the eigenvalues, the polynomial program is especially well-suited for the type of parameter studies that are often necessary for effective rotordynamic stability analysis.

Many of the destabilizing forces which produce rotordynamic instability have not been quantitatively measured, and cannot be accurately predicted at present [10, 11, 12, 13]. Therefore the most productive method of analysis for troubleshooting often is to vary the undetermined coefficients in repeated runs of the computer program until the field-observed critical speeds, the stability threshold speeds, and the instability frequencies are reasonably well simulated by the program. Subsequently, the program can be used to investigate the effect of changes in the design parameters which are known and which can be practically modified (e.g., bearing or seal stiffness and damping).

As an example, consider the eight-stage centrifugal compressor described under Results of Comparison above. This type of machine (multistage, high discharge pressure, high speed, with centrifugal impellers) has a history of costly rotordynamic instability problems, difficult to diagnose and cure. There is a considerable body of experimental evidence [10, 11, 13] which suggests that large destabilizing forces are produced by the dynamics of the working fluid around the impellers.

The forces on each impeller can be modeled in the program as linearized stiffness and damping, including cross-coupled terms, originally formulated by Lund and described in reference [6]. Destabilizing effects from the working fluid

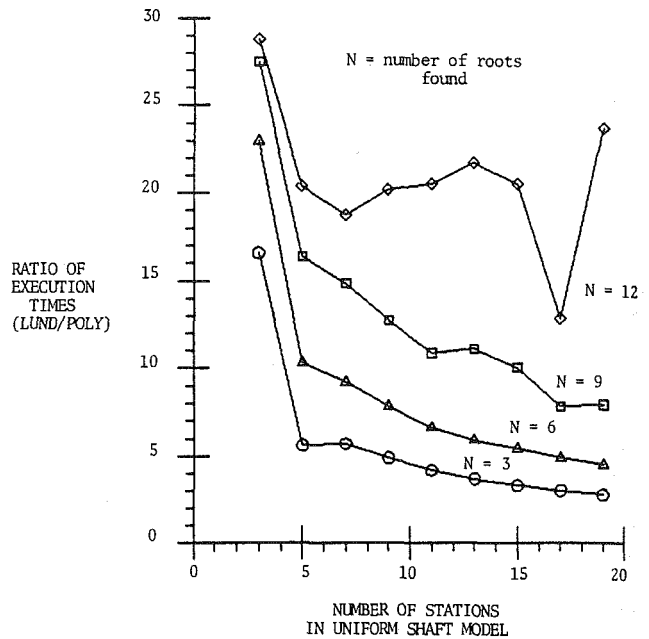


Fig. 5 Comparison of execution time required for finding roots

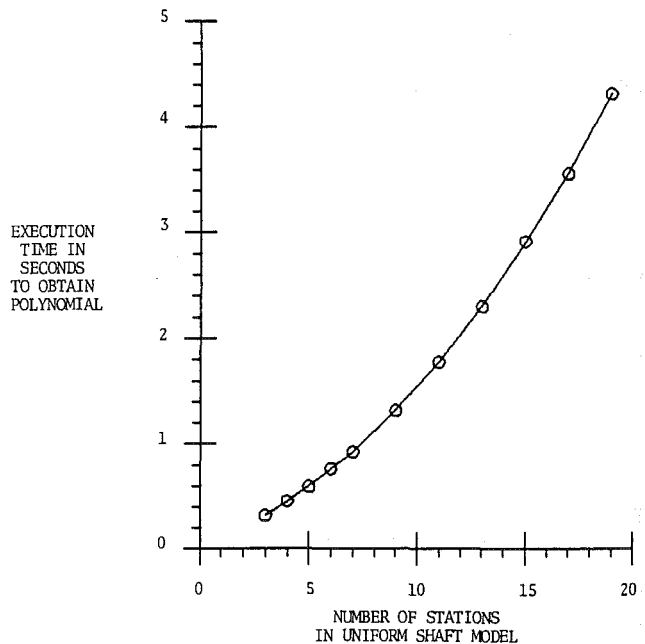


Fig. 6 Time required to find polynomial versus number of stations

often can be modeled using the cross-coupled stiffness coefficients $k_{xy} = -k_{yx}$. Figure 7 shows how the logarithmic decrement (stability indicator) for the 3090 cpm mode of the compressor varies with the coefficient k_{xy} over a range from 100 lb/in. to 10,000 lb/in. The data for this curve was generated by the polynomial program in 514 s of computer time. The Lund program required 1090 s to generate the same data.

Changing the design parameters in a compressor sometimes results in a shift of the instability from one mode to another [13]. In such a case, the greatest advantage of the polynomial program is that the "new" unstable modes and frequencies would not be missed by a failure to converge.

Conclusions

For stability and damped critical speed calculations on

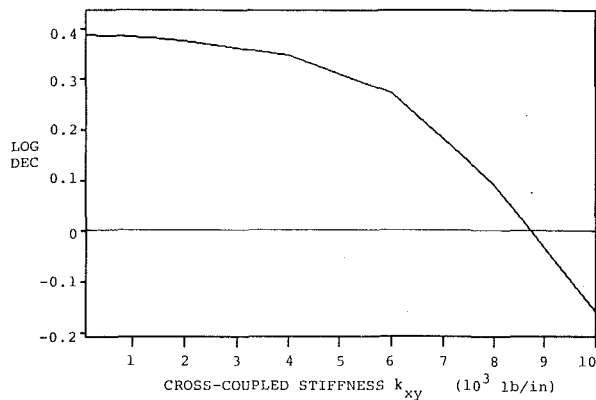


Fig. 7 Stability curve for first forward mode when shaft speed equals operating speed

rotor-bearing systems, the polynomial program can perform the same tasks and give the same results as a Lund-type program while offering a significant savings in cost of execution. The polynomial program can also find all the system's eigenvalues for only a very small additional cost (the Lund-type program is really not capable of finding all the eigenvalues at any cost). This capability eliminates the problem of sometimes missing eigenvalues and their associated modes.

The advantage of faster execution increases as more roots are sought and diminishes as more stations are used.

The polynomial program is also much faster at finding mode shapes than the Lund-type program. However, this may be of little significance since the execution time required to find mode shapes is only a small part of the total time.

The polynomial program is especially well suited for the type of parameter studies that are often necessary for effective

rotordynamic stability analyses, requiring repeated computer runs to determine the effective destabilizing forces acting in a machine.

References

- 1 Holzer, "Die Berechnung der Drehschwingungen," Springer-Verlag, Berlin, 1921.
- 2 Myklestad, N. O., "A New Method of Calculating Natural Modes of Uncoupled Bending Vibration of Airplane Wings and Other Types of Beams," *Journal of Aeronautical Sciences*, Vol. 11, No. 2, Apr. 1944, pp. 153-162.
- 3 Myklestad, N. O., "New Method of Calculating Natural Modes of Coupled Bending-Torsion Vibration of Beams," *Transactions of the ASME*, January 1945, pp. 61-67.
- 4 Prohl, M. A., "A General Method for Calculating Critical Speeds of Flexible Rotors," *ASME Journal of Applied Mechanics*, Vol. 12, Transactions of the ASME, Vol. 67, 1945, pp. A-142-A-148.
- 5 Lund, J. W., Orcutt, F. K., "Calculations and Experiments on the Unbalance Response of a Flexible Rotor," *ASME Journal of Engineering for Industry*, Vol. 89, No. 4, Nov. 1967, pp. 785-796.
- 6 Lund, J. W., "Stability and Damped Critical Speeds of a Flexible Rotor in Fluid-Film Bearings," *ASME Journal of Engineering for Industry*, Vol. 96, No. 2, May 1974, pp. 509-517.
- 7 Forsyth, G. E., Malcolm, M. A., and Moler, C. B., *Computer Methods for Mathematical Computations*, Prentice Hall, Englewood Cliffs, N. J.: Prentice Hall, 1977, pp. 17-19.
- 8 Carnahan, B., Luther, H. A., and Wilkes, J. O., *Applied Numerical Methods*, John Wiley and Sons, Inc., New York, 1969.
- 9 Barret, L. E., Gunter, E. J., Allaire, P. E., "The Stability of Rotor-Bearing Systems Using Linear Transfer Functions," School of Engineering and Applied Science, University of Virginia, Charlottesville, Virginia, Report No. UVA/464761/ME76/133, Dec. 1976.
- 10 Wachel, J. C., "Nonsynchronous Instability of Centrifugal Compressors," *ASME Paper No. 75-PET-22*, Petroleum Mechanical Engineering Conference, Tulsa, Oklahoma, Sept. 21-25, 1975.
- 11 Vance, J. M., and Laudadio, F. J., "Nonsynchronous Instability of Centrifugal Compressors—Are all the Excitations Understood," *ASME Journal of Engineering for Power*, Apr. 1981, Vol. 103, pp. 288-293.
- 12 Fowle, D. W., and Miles, D. D., "Vibration Problems with High Pressure Centrifugal Compressors," *ASME Paper No. 75-PET-28*, Petroleum Mechanical Engineering Conference, Tulsa, Oklahoma, Sept. 21-25, 1975.
- 13 Wachel, J. C., "Case Histories of Rotor-Dynamic Instabilities in the Field," *Short Course on Rotordynamics of Turbomachinery*, Texas A&M Turbomachinery Laboratories, May 18-20, 1981.

Comparison of Two- and Three-Dimensional Flow Computations With Laser Anemometer Measurements in a Transonic Compressor Rotor

R. V. Chima

A. J. Strazisar

NASA Lewis Research Center
Cleveland, Ohio 44135

Two- and three-dimensional inviscid solutions for the flow within a transonic axial compressor rotor at design speed are compared to laser anemometer measurements at maximum flow and near stall operating points. Computational details of the two-dimensional axisymmetric stream function solution and the three-dimensional full Euler solution are described. Upstream of the rotor, the two and three-dimensional solutions for radial distribution of relative Mach number and total pressure agree well with the data. Within the bow wave system and the blade row, the axisymmetric two-dimensional solution shows only qualitative agreement with the data.

Introduction

Computational and experimental techniques for the study of flows in turbomachinery are evolving concurrently and are mutually supportive. Experiments provide data for empirical correlations of phenomena that cannot yet be computed such as turbulence. Experimental data may also be used to verify direct computations of flow phenomena. Computational methods can solve for thermodynamic quantities that cannot be measured by optical techniques. Computational methods are also becoming important tools for the development of advanced turbomachine components and may be used to screen new designs before resorting to more costly experiments.

Advances in both computational and experimental fluid mechanics have been paced largely by advances in electronics, particularly in digital data acquisition and processing. In a 1958 NACA report [1], tip static pressure were measured in a transonic compressor rotor using oscilloscope traces of signals from four pressure transducers embedded in the shroud. Experimenters now rely on digital data acquisition and reduction systems coupled with traversing pressure and temperature probes for pitchwise averaged flow measurements upstream and downstream of rotors [2]. Two-dimensional throughflow analysis codes like [3] are the computational counterparts of these probe measurements. Current data processing equipment coupled with electro-optical sensors allows the experimenter to make detailed maps of the core flow in rotating compressors, [4, 5]. Three-dimensional analysis codes like [6] are the computational

counterparts of current laser anemometer measurements. Experimenters are just beginning to take measurements inside the viscous layers on blade rows. Similarly, computational methods are now being developed to analyze two-dimensional viscous flows in cascades [7]. It seems likely that the latest generation of supercomputers and continuing advances in instrumentation will allow both computational and experimental work to progress even further, and that the resulting gains in understanding will lead to improvements in turbomachinery performance.

It is important to note that the early experimental and analytical work is still extremely important. In fact, this paper relies heavily on all of references [1-6] mentioned previously. Before going into the details of the present work, it may be of interest to review current literature comparing optical measurements and computations of flows in turbomachinery.

Optical techniques that have been used for flow measurements in turbomachinery include holographic interferometry [8], the gas fluorescence technique [9], the laser-two-focus technique (L2F, also called laser transit anemometry or LTA) [10, 11], and laser anemometry (LA, also called laser Doppler velocimetry or LDV) [4, 5]. The LA technique reported in [5] was used in the present work.

Computational methods used to calculate flows in turbomachinery include two-dimensional through flow codes [3, 12, 16], two-dimensional steady, blade-to-blade codes [13, 14] two-dimensional unsteady, blade-to-blade codes [15 and 16], quasi-three-dimensional codes [6, 17]. The two-dimensional throughflow code in [3] and the three-dimensional code in [6] were used in the present work.

The following references compare optical measurements and computations of flows in turbomachinery. Several

Contributed by the Gas Turbine Division of THE AMERICAN SOCIETY OF MECHANICAL ENGINEERS and presented at the 27th International Gas Turbine Conference and Exhibit, London, England, April 18-22, 1982. Manuscript received at ASME Headquarters December 29, 1981. Paper No. 82-GT-302.

references have compared computations to L2F measurements in a transonic rotor designed and tested at DFVLR. Reference [12] compares these measurements with throughflow calculations at a full-speed operating point. Reference [13] compares them with a quasi-three-dimensional solution at a subsonic part-speed operating point, and reference [16] compares them with a quasi-three-dimensional, time-marching solution at three transonic operating conditions. A fully three-dimensional solution for transonic flow in the DFVLR rotor is presented in [17]. Comparisons between LTA measurements and steady blade-to-blade solutions of the flow in a low-speed, four-stage GE research rotor are given in [14]. Reference [15] gives an early comparison between LA measurements and a steady blade-to-blade solution in a GE transonic fan. Reference [18] compares gas fluorescence measurements with a three-dimensional, time-marching solution for a NASA low aspect ratio transonic fan.

The present work compares conventional probe measurements, LA measurements, two-dimensional throughflow computations, and three-dimensional Euler computations of transonic flows in a NASA-designed core compressor inlet rotor. These comparisons are made at design speed at two operating points, a maximum flow point and a near stall point. Comparisons between measured and computed data are made for total pressures and relative Mach numbers along grid lines, for nominal relative Mach numbers on the blade surfaces, for contour plots of relative Mach numbers and flow angles on grid planes, for shock locations and strengths, and for mass flows and total pressure ratios. These comparisons are intended to demonstrate the capabilities of the analysis codes for predicting two widely different flow conditions in an actual machine.

In [8] similar comparisons were made between LA data and a three-dimensional Euler solution of the maximum flow operating point for this rotor. Good comparisons were found near the tip, but the computed shock structures at midspan and near the hub were incorrect. Bow waves were poorly resolved. Several improvements over [8] have been made in the present work. First, bow wave resolution has been improved by increasing the grid size and by clustering the grid around the leading edge. Second, shock structures have been improved by replacing measured exit hub static pressure input to the code with values calculated using a two-dimensional throughflow code. The procedure used to calculate appropriate boundary values is described in detail later. Third, the near stall results presented here may be of more interest to designers since these results are more representative of a typical compressor design point.

Experimental Apparatus

Compressor Rotor. Rotor 33 was designed at NASA Lewis Research Center as an inlet rotor for a core compressor. The flowpath consists of a constant radius hub and a converging tip. At the inlet, the tip radius is 254 mm (10 in.), and the hub/tip radius ratio is 0.7. The rotor has 52 blades with a tip chord of 44.5 mm (1.75 in.) and a tip solidity of 1.48. At the design speed of 16,100 rpm the tip speed is 426 m/s (1398 ft/s).

The rotor was tested without inlet guide vanes or stators, thereby eliminating any circumferential variations that would be introduced by stationary blade rows. Radial surveys of total pressure, total temperature, flow angle, and static pressure were taken upstream and downstream of the blade row using conventional probes [2]. The upstream and downstream measurement stations, designated stations one and two, were located one chord upstream and one-half chord downstream of the rotor, respectively.

Data for this paper were taken at design speed at two throttle settings, a wide open maximum flow setting, and a partially closed near stall setting. At maximum flow the rotor pressure ratio was 1.49 and the mass flow was 208 kg/s/m² (42.40 lbm/s/ft²). Mass flows were measured using a calibrated orifice located far upstream. Inlet relative Mach numbers at maximum flow ranged from 1.14 near the hub to 1.35 near the tip. Near stall the rotor pressure ratio was 1.66 and the mass flow was 191 kg/s/m² (39.12 lbm/s/ft²). Inlet relative Mach numbers near stall ranged from 1.05 near the hub to 1.32 near the tip.

Laser Anemometer. The fringe type laser anemometer (LA) [4] is a single-channel, dual-beam system with on-axis backscatter light collection. A dedicated minicomputer, a disk storage system, and a CRT display were used for real time data acquisition and processing. The minicomputer was also connected to a large central computer for additional data processing and graphical output.

A window fabricated from commercial window glass provided optical access to the compressor. The window conformed to the outer endwall contour and measured 102 mm axially by 51 mm in circumference (11 deg arc by 3-mm thick).

Seed particles consisted of spray-atomized rhodamine 6G dye dissolved in a solution of benzyl alcohol and ethylene glycol. The particles were injected into the flow 460 mm upstream of the rotor. Exposed to laser light, the seed particles fluoresce orange. An orange-pass optical filter placed in front of the photomultiplier selectively removed unwanted green laser light reflected from the hub and blades. The seed particle diameter was determined by equating the particle velocity lag measured downstream of the rotor passage shock to that predicted by a one-dimensional Stokes drag model and solving for the unknown particle diameter. The particle diameter found by this procedure was 1.2-1.5 micrometers [5].

An efficient data acquisition system made it possible to map the blade-to-blade distribution of a velocity component at a given axial and radial position very quickly. Whenever a seed particle crossed the probe volume the particle velocity and the rotor shaft angular position were recorded as a data pair. Approximately 30 measurements were made at each of 1000 different shaft positions distributed as 50 positions per blade passage over 20 consecutive blade passages. The 30 velocities and flow angles at each shaft position were averaged to give time-averaged velocity distributions over 20 consecutive passages. The time-averaged distributions were analyzed to detect variations between individual passages [5]. The 20 time-averaged velocity distributions were spatially averaged to yield the velocity distribution across an average passage. A typical run consisting of 30,000 measurements at a single axial and radial position took between 15 and 45 s.

Errors in the LA measurements arise from a number of sources. The sources of error and the corresponding error magnitudes have been discussed in detail in [5] and will only be summarized here. Passage-to-passage velocity variations were on the order of 5 percent for most runs. Spatial averaging of data obtained across 20 blade passages improves the statistical accuracy of the data. Compressor speed drift during a run was on the order of 0.3 percent, and the repeatability of a given run was 1 percent. The error in velocity and flow angle measurements which encompassed 95 percent of the data was generally 5 percent or less, except in regions immediately downstream of shocks where speed particle velocity lag was the dominant error. The observed lag distance required for the seed particles to achieve 95 percent of the post-shock gas velocity was found to be 13 percent of chord for the maximum flow case at 15 percent span from the tip. The LA data has not been corrected for particle lag since

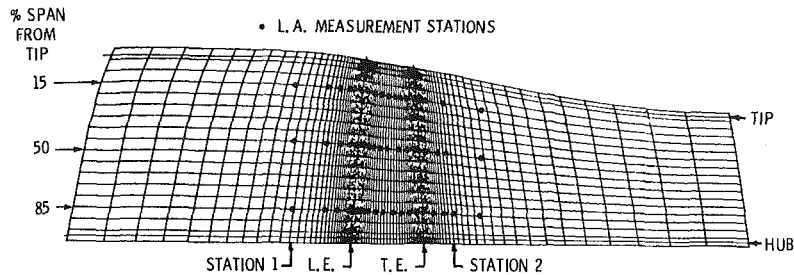


Fig. 1 Meridional view of the computational grid showing L.A. measurement stations and conventional probe measurement stations

velocity variations due to particle lag cannot in general be distinguished from those occurring due to the compression process.

Figure 1 shows the LA measurement stations and probe survey stations superimposed on the finite difference grid used with the three-dimensional code. Typically 22 measurement stations lie along each of three design streamlines located at 15, 50, and 85 percent span from the tip with 12 of the axial stations within the blade row. The three radial locations lie within 1 percent span of the grid lines shown. At the near stall operating point LA measurements were only taken at 15 percent span from the tip.

Computational Methods

Two-Dimensional Throughflow Code MERIDL. The throughflow analysis code used in the present work is the MERIDL code [3]. The code solves an axisymmetric inviscid momentum equation for a stream function along a mid-channel hub-shroud stream surface. The stream function is defined to satisfy continuity identically, and is differentiated numerically to find individual velocity components. Thermodynamic quantities are found from isentropic relations. Rotation, passage convergence, blade row turning, and blockage are all accounted for in the formulation. A successive overrelaxation finite difference technique is used to solve the nonlinear stream function equation. An orthogonal finite difference grid with 10 points radially and 40 points axially (10 points upstream and downstream, 20 within the blade row) was used for the present calculations. While the grid is not shown here, it had the same extent as the three-dimensional grid shown in Fig. 1. Input to MERIDL consists of blade, hub, and tip geometry, mass flow, upstream total conditions, up and downstream whirl (rV_θ) distributions, and axial and radial distributions of total pressure loss. Upstream total conditions were input as constants radially, and the upstream whirl was set to zero. The exit whirl was taken as a smooth curve fit through the measured probe data, excluding points obviously in the endwall boundary layers.

Three-Dimensional Euler Code BLADE3D. The three-dimensional analysis code used in the present work is the BLADE3D code described in [6]. Only a brief description is given here. The equations solved are the inviscid unsteady Euler equations written in cylindrical coordinates and in nonconservative form. The equations include the continuity equation, the axial, radial, and circumferential momentum equations, and the energy equation, which are solved for the density, three velocity components, and total energy. Pressure is found from the ideal gas law. Blade row rotation is specified.

MacCormack's explicit time-marching finite difference method in split operator form [19] is used to advance the unsteady solution in time from an initial guess to a converged steady solution. The method is second-order accurate and

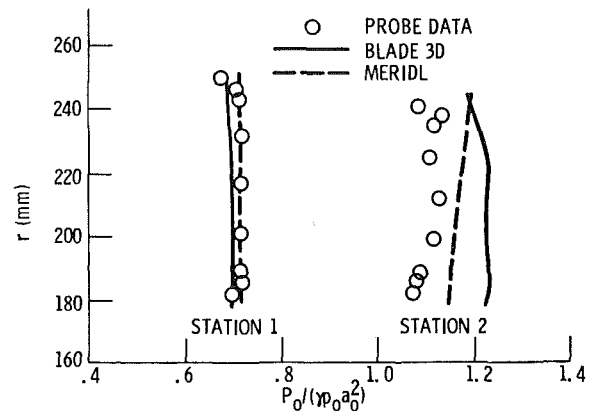


Fig. 2 Radial distribution of circumferentially averaged total pressure, maximum flow point

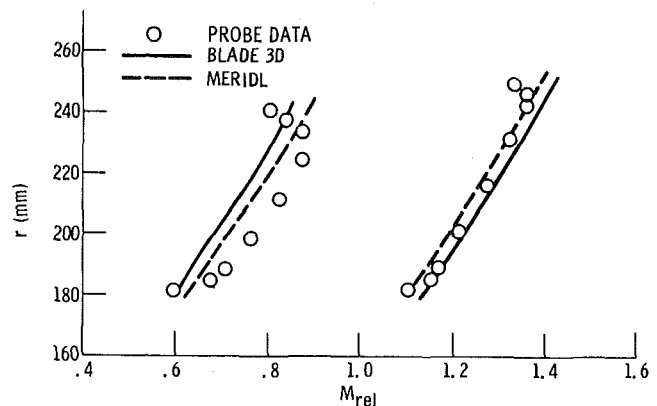


Fig. 3 Radial distribution of circumferentially averaged relative Mach number, maximum flow point

conditionally stable. Shocks are captured automatically and smeared over several grid points. Artificial viscosity terms are added to improve stability near shocks, but they also increase shock smearing.

Algebraic mappings are used to transform the complex flow path geometry into a rectangular computational domain. The computational mesh had 100 axial points (32 points upstream and downstream, 34 within the blade,) 17 circumferential points, and 18 radial points. Axially, the grid points were clustered around the leading and trailing edges to improve resolution of bow and shock waves. Points were stretched upstream and downstream to allow imposition of axisymmetric far field conditions. Radially, and circumferentially the points had constant spacing. A sheared blade-to-blade grid was used. Figure 1 shows a meridional view of the grid.

At the inlet grid plane the flow is assumed to be axisymmetric and is matched to desired conditions at upstream infinity, where total conditions are specified, the radial

Table 1 Comparison of measured and computed mass flows and total pressure ratios, maximum flow point

	\dot{m} (kg/s/m ²)	\dot{m} (lbm/s/ft ²)	tot.pres.ratio
LA	208.	42.6	1.49
BLADE3D	218.	44.6	1.71
MERIDL	208. ^a	42.6 ^a	1.64

^aMass flow is set explicitly as an input to MERIDL.

velocity is zero, and the whirl is specified (here also zero.) The nonreflective inlet boundary condition is based on the one-dimensional method of characteristics. The desired axial velocity and static temperature at upstream infinity are combined to form a single variable, the value of the downstream-running characteristic. This value may be computed from the desired mass flow or upstream Mach number using isentropic relations, or from MERIDL output. Although the BLADE3D solution is sensitive to the input characteristic value, all methods of computing that value give consistent results. The intersection of the specified downstream-running characteristic and the computed upstream-running characteristic at the inlet determine the inlet static temperature and axial velocity. Thus the mass flow is computed as part of the solution and may not necessarily match the measured value.

At the exit grid plane the flow is also assumed to be axisymmetric and the radial velocity is set to zero. The exit circumferential velocity, density, and downstream-running characteristic are extrapolated from within the flow field. Only one boundary value is specified, the hub static pressure at the exit of the computational domain. A radial equilibrium equation is integrated from hub to tip at the exit to determine the radial pressure distribution, which supplies the final unknown at the exit.

Other boundary conditions used in the BLADE3D code include periodicity up-and downstream of the blade row, tangency on the hub, shroud, and blade surfaces, and a Kutta condition specifying constant static pressure across the blade trailing edge.

Exit Pressure Specification. Euler codes typically require that the exit static pressure be specified as a boundary condition when the exit flow is subsonic. This input variable controls the computed mass flow and shock structure, and must be specified correctly to produce reasonable solutions. Experience with the BLADE3D code has shown that use of measured values of exit hub static pressures tends to produce solutions with higher mass flows and stronger shocks than those measured. This appears to be due to the neglect of viscous blockage and losses. Without these viscous effects, the BLADE3D code predicts higher mass flows for a given static pressure rise, or conversely, predicts a higher static pressure rise for a given mass flow than would be found in a viscous flow. Hence, to compute a case with a given mass flow, a designer must input an exit static pressure somewhat higher than measured. That exit pressure can be varied iteratively to match the desired mass flow, but computational times may become prohibitive.

Since the desired mass flow is an input variable for the MERIDL code and static pressures are included in the output, and since a MERIDL solution can be run in about a minute of computer time, the MERIDL code can be used effectively to estimate exit hub static pressures for the BLADE3D code.

Measured values of mass flow, upstream total conditions, and inlet and exit whirl are input to MERIDL as described earlier. One piece of input remains to be described, the axial and radial distributions of total pressure loss. Since MERIDL is incapable of predicting either shock or viscous losses, the amount of loss specified can make a MERIDL solution compare well with either measured data or a BLADE3D solution. For best comparison with measured data, measured

losses must be input. But for best comparison with a BLADE3D solution, only shock losses must be input.

The axial distribution of the loss has little or no effect on the exit static pressure, so losses may be distributed evenly within the blade row. Radial distributions of shock losses in rotor 33 were calculated as part of the probe data reduction using the Miller-Hartmann model described in [1]. The model estimates shock losses to be those occurring across a single normal shock standing near the passage entrance. The Mach number ahead of the shock is taken as the average of the inlet relative Mach number and a somewhat higher value on the suction surface near the shock intersection.

At the near stall operating point rotor 33 has a single shock system like the one in the Miller-Hartmann model, but at the maximum flow point it has a two shock system that is not modeled correctly. Overall the BLADE3D near stall solution compares better with the LA data than the maximum flow solution does. Much of this is attributed to the better fit of the near stall shock structure to the Miller-Hartmann model.

Computational Details. Initial conditions for the maximum flow case assumed constant upstream velocity based on a specified inlet Mach number, velocity variations within the blade row based on blade turning, and constant velocity downstream. Solutions were run on an IBM 3030 AP computer. The time set used ranged from 75 to 90 percent of the stability limit. Convergence to a steady state was determined by monitoring the trailing edge pressure distribution which reflects the Kutta condition and the blade loading. Trailing edge pressures were converged to the fourth significant figure.

The maximum flow case took approximately 12 CPU hrs (4500 time steps) to converge. The near stall case was calculated as the time-accurate response of the maximum flow case to a 9.6 percent increase in exit hub static pressure and a change in inlet conditions which resulted in an inlet Mach number drop of 0.06. This case took nearly twice as long to converge as the maximum flow case did because of the additional time necessary for the downstream pressure rise to travel upstream against a high subsonic flow. Starting from the nearly constant initial conditions described earlier, the near stall case converges about as fast as the maximum flow case. Thus, when only a steady solution is desired, it is often computationally more efficient to start with a simple initial guess than with a converged solution for a different flow.

The computer times quoted above are large. It should be noted that they were accumulated over many runs by restarting the code. Computer times can be reduced substantially by reducing grid size and grid clustering.

Results and Discussion

Maximum Flow Operating Point. Since mass flow is computed by BLADE3D and pressure ratio is computed by both BLADE3D and MERIDL, these global parameters are of particular interest. Table 1 shows that the mass flow calculated by BLADE3D is 4.8 percent higher than the measured orifice value. This is a substantial error at this operating point. Nevertheless, other aspects of the BLADE3D solution agree reasonably well with the LA data. Total pressure ratios calculated by both codes are high; BLADE3D is 14.8 percent high and MERIDL is 10.0 percent high. Differences between the BLADE3D and MERIDL solutions are attributed to differences in shock losses calculated by BLADE3D and by the Miller-Hartmann model.

Radial distributions of circumferentially averaged total pressure and relative Mach number are compared to probe measurements upstream and downstream of the rotor in Figs. 2. and 3. Axial locations labeled station 1 and station 2 are

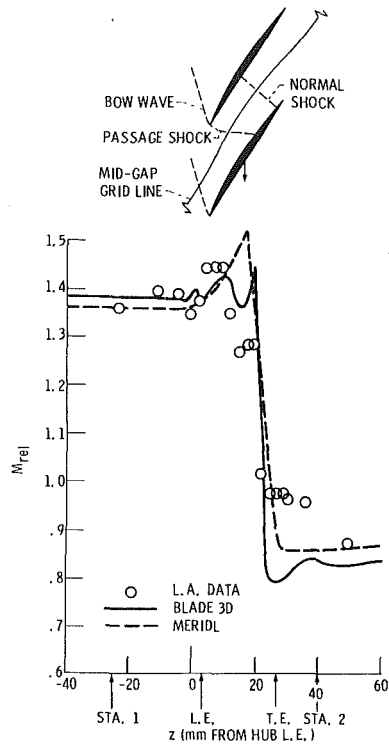


Fig. 4 Axial distribution of relative Mach number, 15 percent span from the tip, mid-gap, maximum flow point

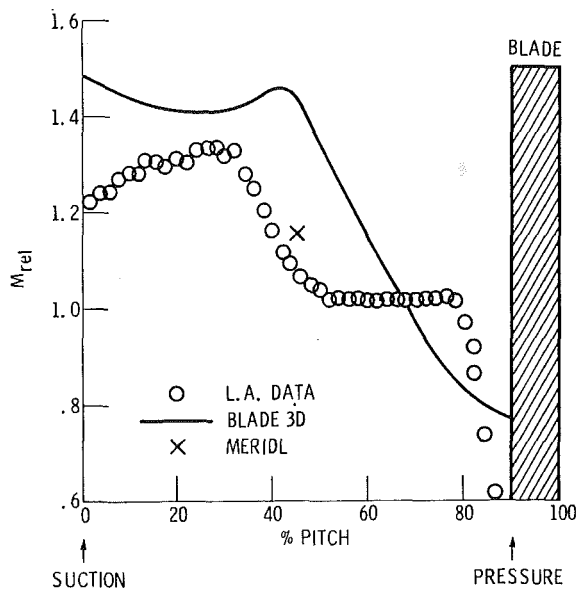


Fig. 5 Circumferential distribution of relative Mach number, 15 percent span from the tip, 78 percent chord (through the rear shock), maximum flow point

shown in Fig. 1. Upstream (station 1) the calculations and measurements are in good agreement, except for the error due to the high BLADE3D mass flow. Downstream (station 2) the high total pressures calculated inviscidly are evident. Endwall boundary layer effects that cannot be predicted inviscidly are evident in the probe measurements, especially at the tip of station 2.

Axial distributions of relative Mach number at 15 percent span from the tip are compared in Fig. 4. The MERIDL calculations are, of course, axisymmetric. The BLADE3D and LA results are shown along a mid-gap line. The MERIDL results show little upstream influence of the blades, while the

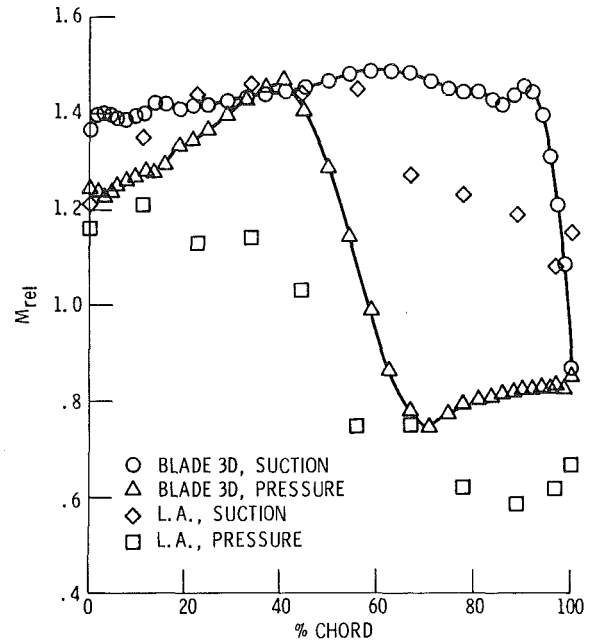


Fig. 6 Axial distribution of relative Mach number on the blade surfaces, 15 percent span from the tip, maximum flow point

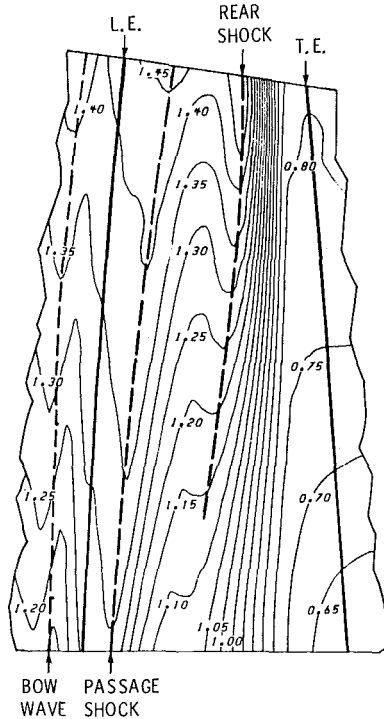
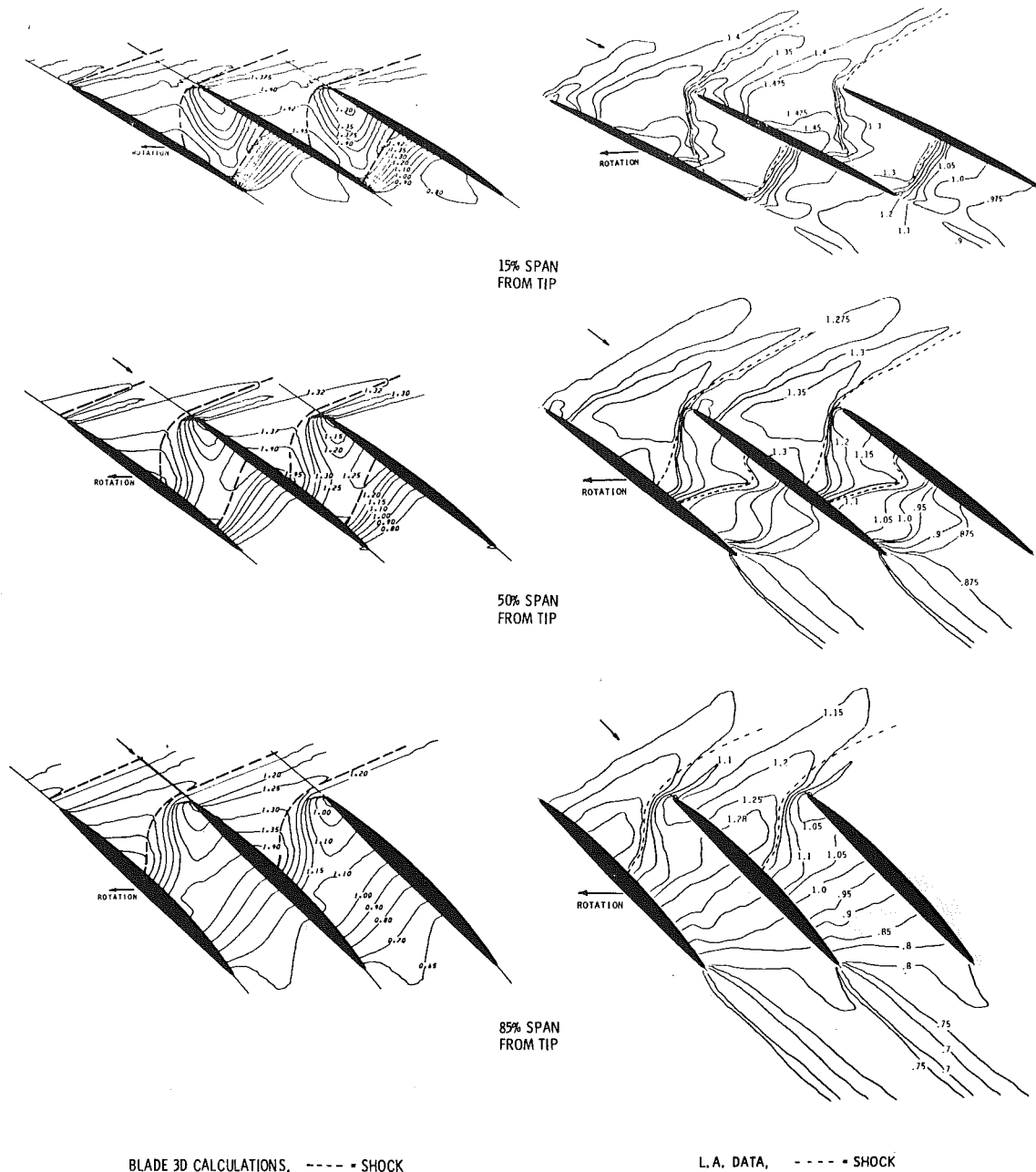


Fig. 7 Computed relative Mach number contours on a mean flow surface at midchannel, maximum flow point

BLADE3D and LA results show relative Mach number fluctuations due to a bow wave system. The computed bow wave is weaker than that measured. Within the blade row, the measured and BLADE3D computed flows accelerate slightly, decelerate across an oblique passage shock, and finally decelerate sharply across a normal shock near the trailing edge. The calculated normal shock is stronger than the measured shock, possibly due to the error in the computed mass flow or to the neglect of viscous blockage. Discrepancies between the shock jumps shown and the normal shock tables are due to the inclination of the rear shock relative to the line along which the results are shown. The MERIDL results show



BLADE 3D CALCULATIONS, - - - - SHOCK

L.A. DATA, - - - - SHOCK

Fig. 8 Blade to blade contours of relative Mach number, maximum flow point

surprising agreement inside the blade row, but the agreement is coincidental. The initial acceleration in the MERIDL results is due to blade blockage. The rapid deceleration that appears to be a shock is due to rapid turning of the flow to match the specified downstream whirl. Downstream of the blade row both computed flows reaccelerate slightly due to tip convergence.

Circumferential distributions of relative Mach number at 15 percent span from the tip and at 78 percent chord (through the rear shock) are shown in Fig. 5. The abscissa of the plot showing percent gap is measured from the suction surface of a leading blade to the suction surface of the following blade. At this axial location the flow near the suction surface (left) is upstream of the rear shock but the flow near the pressure surface (right) has passed through the shock. It is possible that the measured drop off in Mach number near the pressure surface is caused by shock-boundary layer interaction. The

shock location is clearly defined in both the LA measurements and the BLADE3D calculations as an abrupt drop in Mach number near mid-gap. Shock smearing evident in the LA measurements is due to seed particle lag; and shock smearing in the BLADE3D calculations is due to artificial viscosity. Blade boundary layer effects may be evident in the measurements. MERIDL results look reasonable as an axisymmetric average. MERIDL results are omitted from the remaining maximum flow results.

Blade surface relative Mach number distributions along the design streamline at 15 percent span from the tip are shown in Fig. 6. LA measurements of surface relative Mach number were taken from plots like Fig. 5 as the first circumferential point for which a statistically significant number of measurements was taken (at least 20 measurements.) At a tip chord Reynolds number of about 6×10^5 , an unseparated turbulent blade boundary layer thickness would be of the

Table 2 Comparison of measured and calculated shock loss parameters, rear shock, mid-gap, maximum flow point

% Span from tip	LA				BLADE3D			
	M _{rel}	β _{rel}	α	ω _s	M _{rel}	β _{rel}	α	ω _s
15	1.28	52.0	10.	.0037	1.323	50.5	14.	.0101
50	1.37	56.8	5.	.0118	1.387	56.0	7.	.0162
85	1.45	61.6	0.	.0235	1.426	60.9	2.	.0229

order of the measurement point spacing; so it is felt that the first statistically significant point should be near the edge of the core flow. Nevertheless, viscous effects may be present in the data. The calculations and measurements show only a qualitative agreement in shock location and the rearward blade loading.

Figure 7 shows contours of computed relative Mach number on a mean flow surface at midchannel, and is included to show the three-dimensional nature of the solution. Most of the upstream and downstream regions have been omitted. Dashed lines indicate shocks. The rear passage shock is slightly curved from hub to tip. Near the hub it is difficult to distinguish whether there is rear shock or just a diffuse compression.

Computed and measured blade-to-blade relative Mach number contours are compared side by side at the three spanwise locations in Fig. 8. Shocks are shown by dashed lines. Computed shock locations were determined from axial plots of relative Mach number like Fig. 4 as grid points with maximum Mach numbers before rapid drops. These grid points were located on the blade-to-blade plots and fit with a smooth curve. Experimental shock locations were determined similarly, except that circumferential plots like Fig. 5 were used. At 85 percent span from the tip the computations and measurements are in excellent agreement. Both show a bow wave with an exit Mach number of 1.2. The calculations show a stronger suction surface acceleration than the data. Both also show a forward passage shock with similar exit Mach numbers and small sonic regions on the pressure surface near the leading edge. Finally both show a diffuse compression to subsonic with no obvious rear shock. The calculated flow exits at a considerably lower Mach number than the measured flow. At midspan the comparison is similar except that here both show a definite rear shock. The measured rear shock is forward in the passage relative to the calculated shock, and may even be a reflection of the front shock. At 15 percent span from the tip the LA measurements show a stronger bow wave and passage shock than the BLADE3D solution. The calculations and measurements both show very strong rear shocks attached to the trailing edge. These results show improved bow wave resolution and rear shock location over the results in reference [8] due to grid refinement and adjustment of the exit hub static pressure.

Shock angles and total pressure loss coefficients for the forward passage shock at the three spanwise locations and at mid-gap are tabulated in Table 2. The shock inclination angle, α, is measured from the axial direction. The shock loss coefficient is defined in [1] as

$$\omega_s = (1 - P_2/P_1)/(1 - p_1/P_1)$$

where upper and lower case letter *p* refer to total and static pressure, respectively. The total pressure ratio P_2/P_1 is obtained from the normal shock relations using the component of relative Mach number ahead of and normal to the shock. There is some disagreement between the LA and BLADE3D shock loss coefficients, especially at the hub. Part of the disagreement is due to small discrepancies ahead of the shock; part is due to shock inclination in the meridional plane; but most is due to difficulties in determining the shock angle from shock locations found as described earlier.

Table 3 Comparison of measured and calculated mass flows and total pressure ratios, near stall point

	m(kg/s/m ²)	m(lbm/s/ft ²)	tot.pres.ratio
LA	191.	39.1	1.66
BLADE3D	188.	38.5	1.866
MERIDL	191. ^a	39.1 ^a	1.864

^aMass flow is set explicitly as an input to MERIDL

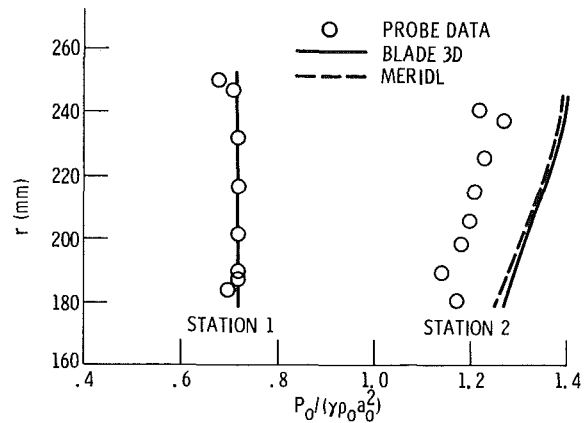


Fig. 9 Radial distribution of circumferentially averaged total pressure, near stall point

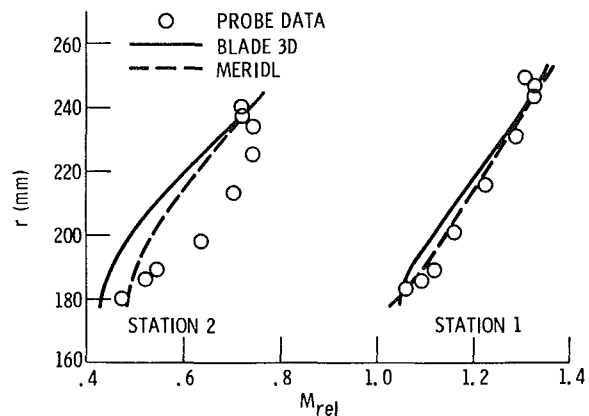


Fig. 10 Radial distribution of circumferentially averaged relative Mach number, near stall point

Near Stall Operating Point. Mass flow and total pressure ratio for the near stall case are compared in Table 3. The BLADE3D mass flow is 1.5 percent low, and the BLADE3D and MERIDL total pressure ratios are both 12.4 percent high, probably due to neglect of viscous losses and blockage.

Radial distributions of circumferentially-averaged total pressure and relative Mach number shown in Figs. 9 and 10 are similar to the maximum flow case except that here the BLADE3D and MERIDL results are in better agreement.

Axial distributions of relative Mach number at 15 percent span from the tip are shown in Fig. 11. The BLADE3D Mach numbers show good agreement with the LA measurements in the strong bow wave system and in location of the passage shock. The passage shock jump is over predicted, again

Table 4 Comparison of measured and calculated shock loss parameters, passage shock, mid-gap, near stall point

% Span from tip	LA				BLADE3D			
	Mrel	β_{rel}	α	ω_s	Mrel	β_{rel}	α	ω_s
15	1.40	62.5	28.0	.061	1.45	62.1	28.	.078

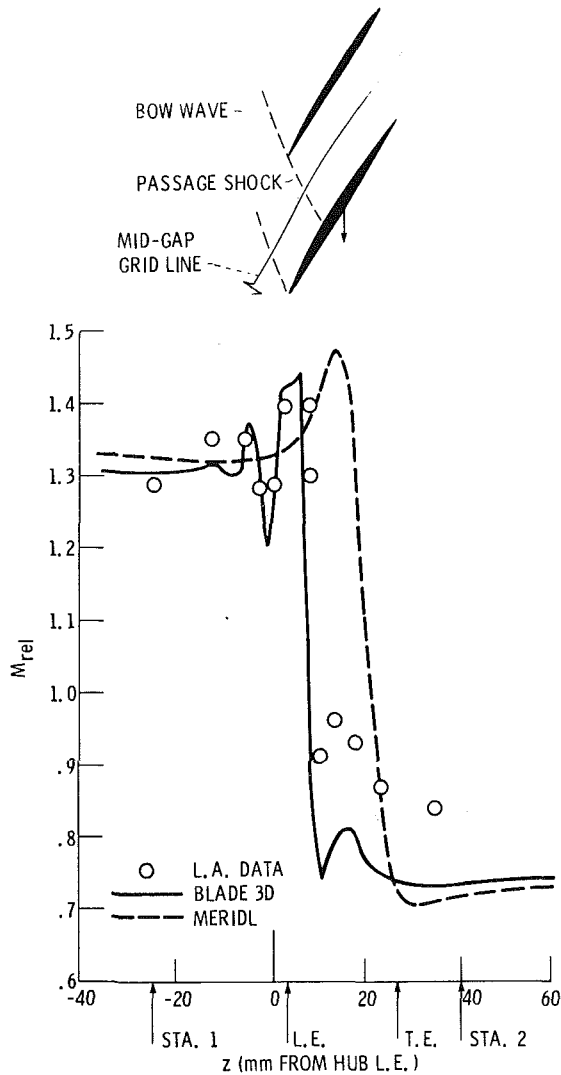


Fig. 11 Axial distribution of relative Mach number, 15 percent span from the tip, mid-gap, near stall point

possibly due to the neglect of viscous blockage. The MERIDL results behave as before, showing an initial acceleration due to blockage followed by a rapid compression due to turning. MERIDL cannot capture the upstream wave system or the passage shock, yet the MERIDL results agree fairly well outside the blade row.

Circumferential distributions of relative Mach number at 15 percent span from the tip and at 23 percent chord (through the passage shock) are shown in Fig. 12. At this axial location the flow near the suction surface (left) is upstream of the passage shock but the flow near the pressure surface (right) has passed through the shock. The Mach number distributions show slight discrepancies in shock location and strength. MERIDL results agree with flow conditions on the upstream side of the shock. MERIDL results are omitted from the remaining near stall results.

Figure 13 compares computed and measured blade surface relative Mach numbers at 15 percent span from the tip.

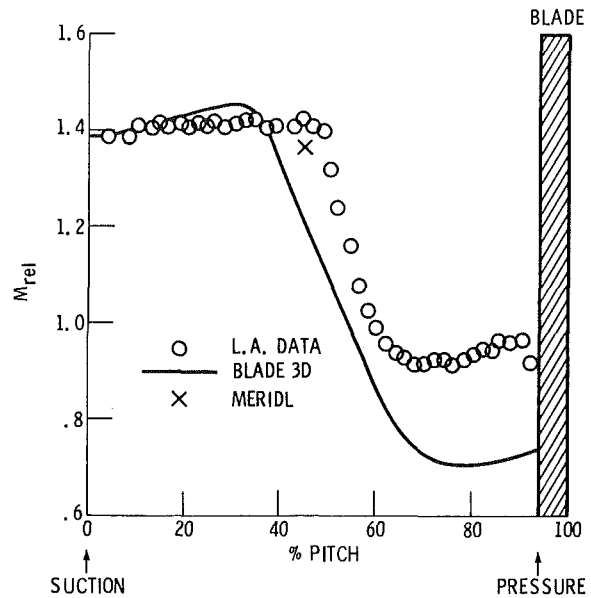


Fig. 12 Circumferential distribution of relative Mach number, 15 percent span from the tip, 23 percent chord (through the passage shock), near stall point

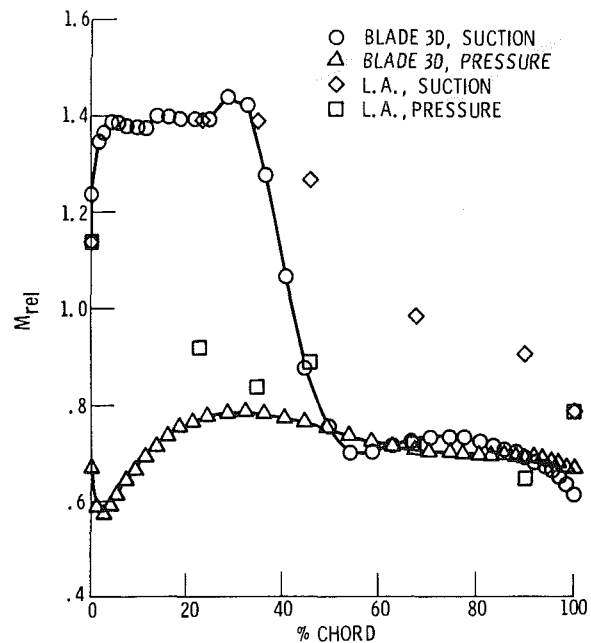


Fig. 13 Axial distribution of relative Mach number on the blade surfaces, 15 percent span from the tip, near stall point

Suction surface shock locations agree to within the measurement spacing. The computed near stall blade loading is dramatically shifted to the front of the blade compared to the maximum flow solution in Fig. 6.

Computed relative Mach number contours on a midchannel mean-flow surface in Fig. 14 show a complete change in shock structure from the maximum flow solution in Fig. 7. In the near stall solution the bow wave and passage shock are

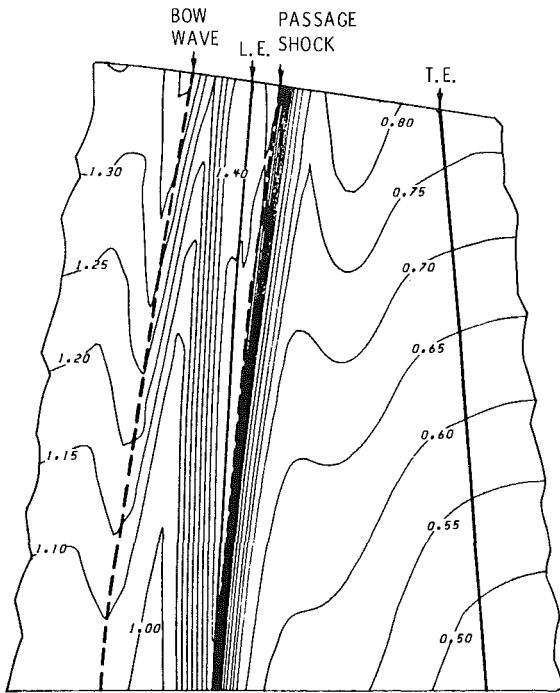


Fig. 14 Computed relative Mach number contours on a mean-flow stream surface at mid channel, near stall point

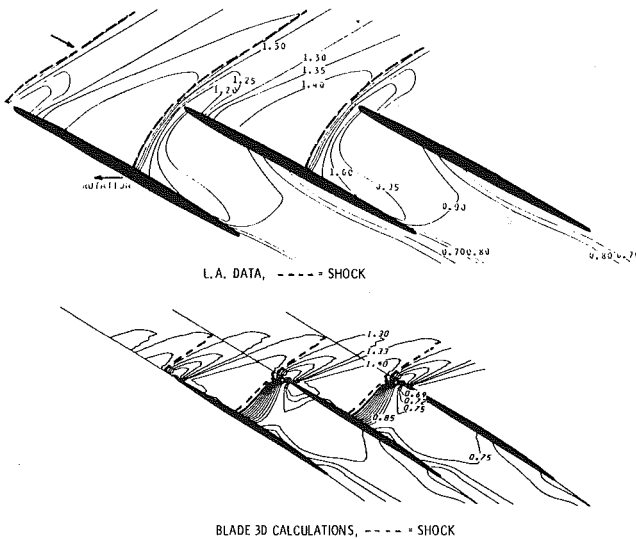


Fig. 15 Blade to blade contours of relative Mach number, 15 percent span from the tip, near stall point

stronger and straighter than in the maximum flow solution. The rear passage shock has been eliminated.

The shock structure at 15 percent span from the tip is shown in Figs. 15 and 16 which compare computed and measured contours of relative Mach numbers and flow angles. Unlike the tip Mach number contours for the maximum flow case in Figure 8, Figure 15 shows a pronounced bow wave and passage shock system with excellent agreement between the BLADE3D and LA results. Computed relative Mach numbers leaving the shock are low, however. The wakelike contours leaving the trailing edges in the computed results show an inviscid trailing edge slip line. Relative flow angle contours in Fig. 16 show an upstream angle of 68 to 69 deg. The suction surface metal angle at the leading edge is about 64 deg. The high incidence incoming flow turns smoothly through ex-

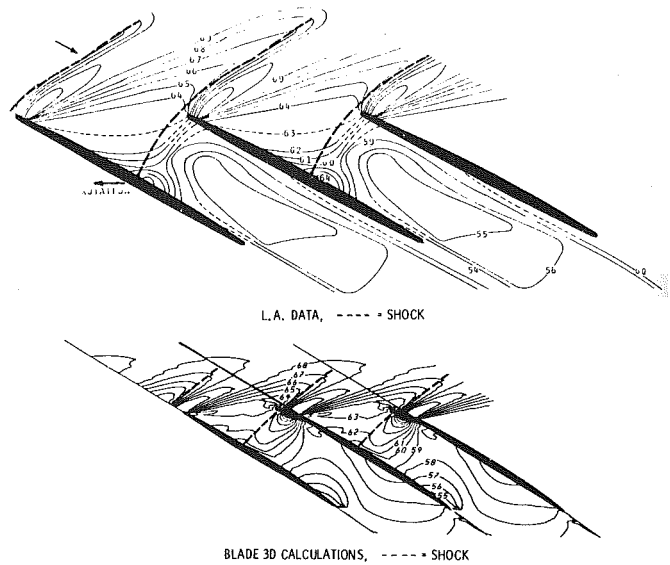


Fig. 16 Blade to blade contours of relative flow angle in degrees, 15 percent span from the tip, near stall point. Lightly dashed lines indicate uncertainty in the L.A. contours.

pansion fans originating one or two blade away to become well aligned with the suction surface at the leading edge.

Table 4 compares the measured and computed shock loss parameters. Since the passage shock is well defined in this case, the shock location and angle are relatively easy to determine. Slight discrepancies in flow conditions ahead of the shock account for a small disagreement in the shock loss parameters.

Concluding Remarks

Current laser anemometer (LA) measurements are of sufficient accuracy for verification of inviscid codes. Shock smearing in the LA measurements due to seed particle lag is of roughly the same magnitude as numerical shock smearing, and both need to be reduced. Either a better method of estimating boundary layer edge velocities or a means of directly measuring blade surface pressures is needed. More detailed measurements of blade and endwall boundary layers will be needed for verification of viscous codes.

Inviscid calculations from an axisymmetric throughflow code (MERIDL) and a three-dimensional Euler code (BLADE3D) compared well with probe data upstream of the blade row. Downstream, total pressures are high and relative Mach numbers are low due to the neglect of viscous effects. Within the blade row, the axisymmetric solutions agree only qualitatively with the other results.

The BLADE3D code accurately predicted Mach number and flow angle distributions and shock structure within an axial compressor rotor at maximum flow and near stall operating points. The near stall solution agree better with LA measurements than the maximum flow solution does. This is probably because most of the flow turning in the near stall case occurs across a forward passage shock away from viscous effects. But in the maximum flow case a second normal shock near the blade trailing edge (where viscous effects would be greatest) controls the blade row pressure rise. Present results for the maximum flow case have improved on the earlier results given in [8]. Bow wave resolution was improved through grid clustering, and rear shock structure was improved by adjusting the exit hub static pressure.

Downstream pressure boundary conditions typically needed by Euler codes are difficult to specify. Measured downstream pressures produce erroneous mass flows and shock structures because measured pressures contain viscous losses not ac-

counted for in inviscid codes. Computational times may prohibit iterating on boundary conditions. An axisymmetric throughflow code like MERIDL may be used as a consistent and computationally efficient tool for choosing downstream boundary values. MERIDL input includes upstream total conditions, mass flow, and whirl, and downstream whirl, all input as measured. Shock losses must be specified and may be estimated using the Miller-Hartmann model along with measured probe data. Loss distribution through the blade row does not significantly effect the computed up-or downstream solution. Downstream pressures calculated in this manner are higher than measured pressures but are appropriate boundary values for Euler codes, producing the best agreement between mass flows and shock structures measured in a viscous flow and computed inviscidly. In future three-dimensional viscous codes, the measured downstream pressure should suffice.

References

- 1 Miller, G. R., Hartmann, M. J., "Experimental Shock Configuration and Shock Losses in a Transonic Compressor Rotor at Design Speed," NACA RM E58A14b, June 5, 1958.
- 2 Moore, R. D., Lewis, G. W. Jr., and Osborn, W. M., "Performance of a Transonic Fan Stage Design for a Low Meridional Velocity Ratio," NASA TP-1298, 1978.
- 3 Katsanis, T., and McNally, W. D., "Revised FORTRAN Program for Calculating Velocities and Streamlines on the Hub-Shroud Midchannel Stream Surface of an Axial-, Radial-, or Mixed-Flow Turbomachine or Annular Duct, I, - User's Manual," NASA TN D-8430, Mar. 1977.
- 4 Powell, J. A., Strazisar, A. J., and Seasholtz, R. G., "Efficient Laser Anemometer for Intra-Rotor Flow Mapping in Turbomachinery," ASME JOURNAL OF ENGINEERING FOR POWER, Apr. 1981, pp. 424-429.
- 5 Strazisar, A. J., and Powell, J. A., "Laser Anemometer Measurements In a Transonic Axial Flow Compressor Rotor," ASME JOURNAL OF ENGINEERING FOR POWER, Apr. 1981, pp. 430-437.
- 6 Thompkins, W. T., Jr., "A FORTRAN Program for Calculating Three-Dimensional Inviscid Rotational Flows with Shock Waves in Axial Compressor Rotors," NASA CR3560, June 1982.
- 7 Steger, J. L., Pulliam, T. H., and Chima, R. V., "An Implicit Finite Difference Code for Inviscid and Viscous Cascade Flow," AIAA Paper No. 80-1427, July 1980.
- 8 Strazisar, A. J., and Chima, R. V., "Comparison Between Optical Measurements and a Numerical Solution of the Flow Field Within a Transonic Axial-Flow Compressor Rotor," AIAA Paper No. 80-1078, June 1980.
- 9 Epstein, A. H., "Quantitative Density Visualization in a Transonic Compressor Rotor," ASME JOURNAL OF ENGINEERING FOR POWER, July 1977, pp. 460-474.
- 10 Schodl, R., "On the Development of a New Optical Method for Flow Measurements in Turbomachines," ASME Paper 74-GT-157, 1974.
- 11 Schodl, R., "A Laser-Two-Focus (L2F) Velocimeter for Automatic Flow Measurements in the Rotating Components of Turbomachines," in *Measurement Methods in Rotating Components of Turbomachinery*, edited by B. Lakshminarayana, and P. Runstadler, Jr., ASME, New York, 1980.
- 12 Dunker, R. J., Strinning, P. E., and Weyer, H. B., "Experimental Study of the Flow Field Within a Transonic Axial Compressor Rotor by Laser Velocimetry and Comparison With Through-Flow Calculations," ASME JOURNAL OF ENGINEERING FOR POWER, Vol. 100, No. 2, April, 1978, pp. 279-286.
- 13 Dunker, R. J., and Strinning, P. E., "Flow Velocity Measurements Inside of a Transonic Axial Compressor Rotor by Means of an Optical Technique and Compared with Blade-to-Blade Calculations," Third International Symposium on Airbreathing Engines, Munich, Germany, Mar. 1976.
- 14 Smart, A. E., Wisler, D. C., and Mayo, W. T. Jr., "Optical Advances in Laser Transit Anemometry," ASME JOURNAL OF ENGINEERING FOR POWER, Apr. 1981.
- 15 Wisler, D. C., "Shock Wave and Flow Velocity Measurements in a High-Speed Fan Rotor Using the Laser Velocimeter," ASME Paper 76-GT-49, Mar. 1976.
- 16 McDonald, P. W., Bolt, C. R., Dunker, R. J., and Weyer, H. B., "A Comparison Between Measured and Computed Flow Fields in a Transonic Compressor Rotor," ASME Paper 80-GT-7, 1980.
- 17 Denton, J. D., and Singh, U. K., "Time Marching Methods for Turbomachinery Flow Calculations, Part I: Basic Principles and Two-Dimensional Applications, Part II: Three-Dimensional Flows," in *Application of Numerical Methods to Flow Calculations in Turbomachines*, von Karman Institute for Fluid Dynamics Lecture Series, April 23-27, 1979.
- 18 Haymann-Haber, G., and Thompkins, W. T., Jr., "Comparison of Experimental and Computational Shock Structure in a Transonic Compressor Rotor," ASME JOURNAL OF ENGINEERING FOR POWER, Vol. 103, Jan., 1981, pp. 78-88.
- 19 MacCormack, R. W., "Computational Efficiency Achieved by Time Splitting of Finite Difference Operators," AIAA Paper 72-154, 1972.

H. D. Nelson

Mechanical and Aerospace
Engineering,
Mem. ASME

W. L. Meacham

Engineering Sciences.

Arizona State University,
Tempe, Ariz. 85287

D. P. Fleming

National Aeronautics and Space
Administration,
Mem. ASME

A. F. Kascak

Propulsion Laboratory,
U.S. Army Research and Technology
Laboratories.

Lewis Research Center,
Cleveland, Ohio 44135

Nonlinear Analysis of Rotor-Bearing Systems Using Component Mode Synthesis

The method of component mode synthesis is developed to determine the forced response of nonlinear, multishaft, rotor-bearing systems. The formulation allows for simulation of system response due to blade loss, distributed unbalance, base shock, maneuver loads, and specified fixed frame forces. The motion of each rotating component of the system is described by superposing constraint modes associated with boundary coordinates and constrained precessional modes associated with internal coordinates. The precessional modes are truncated for each component and the reduced component equations are assembled with the nonlinear supports and interconnections to form a set of nonlinear system equations of reduced order. These equations are then numerically integrated to obtain the system response. A computer program, which is presently restricted to single shaft systems has been written and results are presented for transient system response associated with blade loss dynamics, with squeeze film dampers, and with interference rubs.

Introduction

The dynamic analysis of multiple shaft rotor-bearing systems generally requires the assembly and solution of large order sets of ordinary differential equations which, when justified, are linearized in the neighborhood of an operating point. For many situations, however, a linearized model is not satisfactory for simulating realistic system dynamic behavior. Only a few analysts have dealt with nonlinear rotor dynamics for large scale systems, and a considerable amount of activity in this area exists at the present time.

The large order system of equations, which are generated for linear and/or nonlinear simulations are usually time consuming to set up and costly to solve in terms of computation time and storage. This is particularly important in design studies which require a completely new system assembly and solution for each new set of system parameters. For most linear transient analyses and for all nonlinear analyses, numerical integration is required, causing cost and accuracy of the analysis to be strongly dependent on the order of the system equations.

The method of component mode synthesis (CMS) allows for substantial reduction in the size of the overall system equations while still retaining the essential dynamic characteristics and offers promise as a method of decreasing analysis time and cost for some types of problems. This paper presents a method of formulation and solution for nonlinear

rotor dynamic systems with examples illustrating its use and accuracy. It is a revision of Nelson and Meacham's paper [2] which dealt with linear transients utilizing the same method.

The dynamic characteristics of linear rotor-bearing systems have been successfully analyzed by many researchers using a variety of methods. The two most prevalent methods are the state vector-transfer matrix approach covered most recently in the works of Lund [3, 4, 5] and the direct stiffness approach as presented by many including Gasch [7], Dimarogonas [8], Childs [6], Adams [9], Nelson and McVaugh [10], Li and Gunter [11], Dennis, Eriksson, and Seitelman [12], and others. Some of these methods have been applied directly in terms of physical coordinates while others have successfully utilized various types of modal transformation.

Several authors have presented successful techniques for the general analysis of nonlinear phenomena in rotor-bearing systems. Of particular note are the works of Dennis, Eriksson, and Seitelman [12], Kirk and Gunter [13], Adams [9], and Adams, Padovan, and Fertis [14], and Kascak [15]. Dennis et al. used a normal mode expansion in terms of the undamped symmetric modes and treated damping, gyroscopic, and nonlinear terms as pseudoexternal loads. Kirk and Gunter utilized a modified Myklestad-Prohl method while Adams et al. have made use of existing finite element codes with the addition of new component element software to model engine nonlinear phenomena. Kascak directly integrates the system equations and illustrates its effectiveness by simulating a blade loss with interference rubs.

The approach utilized in this paper is an extension of the work of Glasgow and Nelson [1] and a revision of the paper

Contributed by the Gas Turbine Division of THE AMERICAN SOCIETY OF MECHANICAL ENGINEERS and presented at the 27th International Gas Turbine Conference and Exhibit, London, England, April 18-22, 1982. Manuscript received at ASME Headquarters December 29, 1981. Paper No. 82-GT-303.

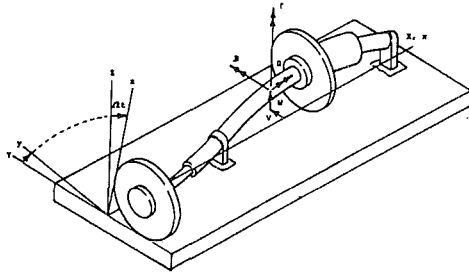


Fig. 1 Typical rotating component

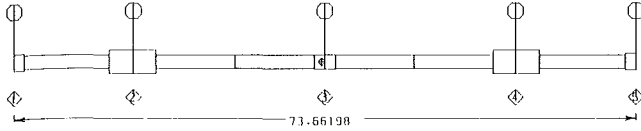


Fig. 2 Rotor 1: model schematic

by Nelson and Meacham [2], allowing for nonlinear support characteristics and for specified base motion and various forms of applied forces. The method utilizes a direct stiffness philosophy for formulating the rotating assembly component equations, a modal decomposition of the linear rotating assembly using complex component modes with truncation, assembly of the reduced component equations with the linear and/or nonlinear supports to form the system equations, and subsequent numerical integration. This work was sponsored by NASA LeRC under Grant NAG 3-6 and details relating to the mathematical formulation, associated digital computer program, and example analyses are contained in references [17-19].

Analytical Development

Physical Coordinates. The equation of motion of a

typical linearized rotor dynamic component, illustrated in Fig. 1, is of the form

$$\begin{bmatrix} \mathbf{M} & \mathbf{M}_2 \\ \mathbf{M}_3 & \mathbf{M}_4 \end{bmatrix} \begin{Bmatrix} \ddot{\bar{X}} \\ \ddot{\bar{X}}_S \end{Bmatrix} + \begin{bmatrix} \mathbf{C} & \mathbf{C}_2 \\ \mathbf{C}_3 & \mathbf{C}_4 \end{bmatrix} \begin{Bmatrix} \dot{\bar{X}} \\ \dot{\bar{X}}_S \end{Bmatrix} + \begin{bmatrix} \mathbf{K} & \mathbf{K}_2 \\ \mathbf{K}_3 & \mathbf{K}_4 \end{bmatrix} \begin{Bmatrix} \bar{X} \\ \bar{X}_S \end{Bmatrix} = \begin{Bmatrix} \bar{F}_S \\ \bar{F} \end{Bmatrix} \quad (1)$$

The physical coordinates in equation (1) are absolute in that they are observed from a fixed reference system.

The bearing support points on the rigid frame have specified motion and are related to specified frame motion by the rigid body constraint equation

$$\bar{X}_S = \mathbf{D}_f \bar{X}_f \quad (2)$$

where

$$\bar{X}_f = \begin{Bmatrix} V_f \\ W_f \\ B_f \\ \Gamma_f \end{Bmatrix} \quad (3)$$

The transformation of coordinates

$$\begin{Bmatrix} \bar{X} \\ \bar{X}_S \end{Bmatrix} = \begin{bmatrix} \mathbf{I} & \boldsymbol{\pi} \\ \mathbf{O} & \mathbf{I} \end{bmatrix} \begin{Bmatrix} \bar{x} \\ \bar{X}_S \end{Bmatrix} \quad (4)$$

with $\boldsymbol{\pi} = (-\mathbf{K}^{-1} \mathbf{K}_2)$, is introduced into equation (1) to transform the component equation of motion to physical coordinates which are observed relative to the rigid frame. The matrix, $\boldsymbol{\pi}$, is a constraint matrix which relates the ab-

Nomenclature

\mathbf{A}, \mathbf{B} = state vector matrices, physical coordinates
 \mathbf{G}, \mathbf{B} = state vector matrices, generalized coordinates
 \mathbf{C} = component damping matrix
 \mathbf{D}_f = rigid frame geometric constraint matrix
 e_3 = cg eccentricity of disk at station 3
 \bar{F} = component force vector, physical coordinates
 \bar{F}_f, \bar{F}_b = component forward and backward unbalance force vectors, physical coordinates
 \bar{G} = component unbalance force vector, physical coordinates
 \bar{h} = component state vector, physical coordinates
 \bar{H}_s = system state vector force, generalized coordinates
 \bar{H}_f, \bar{H}_b = system forward and backward unbalance force vectors, generalized coordinates
 \mathbf{K} = component stiffness matrix
 \bar{L} = linear force vector, physical coordinates
 \mathbf{M} = component mass matrix

N = number of system complex modes
 \bar{N} = nonlinear force vector, physical coordinates
 N_p = number of retained forward and backward component precessional modes
 \bar{P} = component state vector force, generalized coordinates
 \bar{q} = component principle coordinate state vector
 \bar{Q} = component state vector force, physical coordinates
 V, W = absolute displacements in Y, Z -directions
 \bar{x} = component relative displacement vector
 \bar{X} = component absolute displacement vector
 \bar{X}_f = rigid frame absolute displacement vector
 \bar{y} = component state vector, physical coordinates
 \bar{y}_s^B = assemblage of component boundary coordinates
 \mathbf{Y}, \mathbf{Z} = matrix of component right and left vectors transformation matrix

β = system eigenvalue
 $\mathbf{B}, \mathbf{\Gamma}$ = absolute rotations about Y, Z -axes
 $\boldsymbol{\gamma}$ = connectivity matrix
 $\boldsymbol{\Delta}$ = component coordinate transformation matrix
 \bar{X}_s = system state vector, generalized coordinates
 $\boldsymbol{\pi}$ = constraint mode matrix (absolute rigid frame coordinates)
 $\boldsymbol{\Psi}$ = constraint mode matrix (relative component coordinates)
 Ω = spin speed

Subscripts

b = backward
 c = cosine
 f = forward
 R = retained subset
 s = sine (or system)
 S = specified

Superscripts

B = boundary
 I = internal

solute motion of the rotating assembly to the rigid base. The procedure requires that the rotating assembly be adequately supported by a sufficient number of linear supports. If an adequate number of supports do not actually exist, then the procedure requires that artificial linear supports be added to provide a nonsingular \mathbf{K} matrix. The value of the artificial supports is arbitrary and their effect is subtracted from the model during the solution of the system equations.

The first row of the transformed equations gives

$$\begin{aligned} \mathbf{M} \ddot{\bar{x}} + \mathbf{C} \dot{\bar{x}} + \mathbf{K} \bar{x} &= \bar{G} - (\mathbf{M} \pi + \mathbf{M}_2) \mathbf{D}_f \ddot{X}_f \\ &- (\mathbf{C} \pi + \mathbf{C}_2) \mathbf{D}_f \dot{X}_f + \bar{N} \\ &= \bar{L} + \bar{N} \end{aligned} \quad (5)$$

The force vector, \bar{G} , includes rotating unbalance and such fixed frame forces as gravity and lateral gear loads. The second and third terms on the RHS provide the equivalent force terms due to maneuver loads. The usual application of these terms is to simulate either translational base acceleration or angular base turning maneuvers. The vector \bar{L} denotes all linear forces and \bar{N} contains the nonlinear forces which act on the rotating assembly.

First-Order Form. The displacement vector of equation (5) is partitioned into boundary and interior coordinates as

$$\bar{x} = \begin{Bmatrix} \bar{x}^B \\ \bar{x}^I \end{Bmatrix} \quad (6)$$

with related state vector

$$\bar{h} = \begin{Bmatrix} \dot{\bar{x}}^B \\ \dot{\bar{x}}^I \\ \bar{x}^B \\ \bar{x}^I \end{Bmatrix} \quad (7)$$

The component equation of motion, equation (5), in first order form is

$$\begin{bmatrix} \mathbf{O} & \mathbf{M} \\ \mathbf{M} & \mathbf{C} \end{bmatrix} \dot{\bar{h}} + \begin{bmatrix} -\mathbf{M} & \mathbf{O} \\ \mathbf{O} & \mathbf{K} \end{bmatrix} \bar{h} = \begin{Bmatrix} \bar{O} \\ \bar{L} \end{Bmatrix} + \begin{Bmatrix} \bar{O} \\ \bar{N} \end{Bmatrix} \quad (8)$$

It is convenient to reorder the component state variables into boundary and interior subsets by applying the transformation

$$\bar{h} = \mathbf{a} \bar{y} \quad (9)$$

with

$$\bar{y} = \begin{Bmatrix} \bar{y}^B \\ \bar{y}^I \end{Bmatrix} = \begin{Bmatrix} \dot{\bar{x}}^B \\ \bar{x}^B \\ \dot{\bar{x}}^I \\ \bar{x}^I \end{Bmatrix} \quad (10)$$

to equation (5) to give

$$\mathbf{A} \dot{\bar{y}} + \mathbf{B} \bar{y} = \bar{Q} \quad (11)$$

Equation (11), in partitioned form, is

$$\begin{bmatrix} \mathbf{A}^{BB} & \mathbf{A}^{BI} \\ \mathbf{A}^{IB} & \mathbf{A}^{II} \end{bmatrix} \begin{Bmatrix} \dot{\bar{y}}^B \\ \dot{\bar{y}}^I \end{Bmatrix} + \begin{bmatrix} \mathbf{B}^{BB} & \mathbf{B}^{BI} \\ \mathbf{B}^{IB} & \mathbf{B}^{II} \end{bmatrix} \begin{Bmatrix} \bar{y}^B \\ \bar{y}^I \end{Bmatrix} = \begin{Bmatrix} \bar{L}^B \\ \bar{L}^I \end{Bmatrix} + \begin{Bmatrix} \bar{N}^B \\ \bar{O} \end{Bmatrix} \quad (12)$$

and is ready for component mode development. The analysis restricts the nonlinear forces to be present only at rotating assembly boundary points.

Component Mode Synthesis. The procedure used in this work for component mode synthesis is presented in [1], so will not be repeated in detail here. In summary, however, the rotating assembly motion is represented as the superposition of two types of modes which appear in the transformation

$$\bar{y} = \begin{Bmatrix} \bar{y}^B \\ \bar{y}^I \end{Bmatrix} = \begin{bmatrix} \mathbf{I} & \mathbf{O} \\ \mathbf{\Psi} & \mathbf{Y} \end{bmatrix} \begin{Bmatrix} \bar{q}^B \\ \bar{q} \end{Bmatrix} = \Delta \bar{p} \quad (13)$$

The columns of $\mathbf{\Psi}$ describe the displacement and velocity of the component interior coordinates due to the absolute motion of the component boundary coordinates. The columns of \mathbf{Y} are complex right vectors (modes) which generate the displacement and velocity of the component interior coordinates relative to fixed boundary points. The elements of \bar{q} are time dependent generalized coordinates associated with the complex modes of \mathbf{Y} .

Reduction of order for the system model is realized by truncating a number of modes in the product $\mathbf{Y} \bar{q}$ and retaining a selected subset. The usual selection technique would be to retain the lower frequency modes with the cutoff frequency dependent on the type of excitation to be analyzed. The truncated form of equation (13) with a retained subset of complex modes is

Table 1 Rotor 1: physical properties^a

Station number	Subelement number	Length (cm)	Radius (cm)	Mass (kg)	Diametral inertia (kg-cm ²)	Polar inertia (kg-cm ²)
1	1	1.245	1.0035	2.921	0.	0.
	2	10.135	0.7940			
	3	2.845	1.3970			
2	1	2.667	1.3970	3.393	143.2	281.7
	2	9.335	0.7940			
	3	9.334	0.7940			
	4	1.270	0.8435			
3	1	1.270	0.8435	0.848	0.	0.
	2	9.334	0.7940			
	3	9.335	0.7940			
	4	2.667	1.3970			
4	1	2.845	1.3970	3.393	143.2	281.7
	2	10.135	0.7940			
	3	1.245	1.0035			
5				2.785	0.	0.

^a $E = 20.69 \times 10^6 \text{ N/cm}^2$

$\rho = 0$ for subelements

$$\dot{y} = \begin{bmatrix} \mathbf{I} & \mathbf{O} \\ \Psi & \mathbf{Y}_R \end{bmatrix} \begin{Bmatrix} \dot{y}^B \\ \dot{q}_R \end{Bmatrix} = \mathbf{A}_R \dot{p}_R \quad (14)$$

The generalized forces, compatible with the \dot{p}_R coordinates, are obtained by the transformation

$$\dot{P}_R = \begin{bmatrix} \mathbf{I} & \Psi^T \\ \mathbf{O} & \mathbf{Z}_R^T \end{bmatrix} \begin{Bmatrix} \dot{Q}^B \\ \dot{Q}^I \end{Bmatrix} \quad (15)$$

where \mathbf{Z}_R is the matrix of retained left vectors.

The introduction of the transformation of coordinates, equation (14), and the transformation of forces, equation (15), into equation (11) gives

$$\mathbf{A} \dot{p}_R + \mathbf{B} \dot{p}_R = P_R \quad (16)$$

which is the component equation in terms of constraint modes and a retained set of constrained (fixed boundary) complex modes. The order of equation (16) is dependent on the extent of truncation and is equal to twice the number of boundary coordinates plus the number of retained complex modes. The state force vector, \dot{P}_R , contains all the applied system forces and the nonlinear support forces.

System Equation Assembly. With the reduced order equations developed for each rotating assembly, as typified by equation (16), the system equation of motion can then be assembled. The state vector for the i th typical component is written as

$$\dot{p}_R^{(i)} = \begin{Bmatrix} \dot{y}_i^B \\ \dot{q}_R^{(i)} \end{Bmatrix} \quad (17)$$

A system state vector consisting of an assemblage of all the component boundary coordinates \dot{y}_i^B into \dot{y}_s^B and all of the retained complex generalized coordinates for each component is defined as

$$\dot{\eta}_s = \begin{Bmatrix} \dot{y}_s^B \\ \dot{q}_R^{(1)} \\ \dot{q}_R^{(2)} \\ \vdots \\ \dot{q}_R^{(N)} \end{Bmatrix} \quad (18)$$

The state vector coordinates for each component, equation (17), are related to the system state vector by a set of simple geometric constraint relations written in the matrix form

$$\dot{p}_R^{(i)} = \gamma_i \dot{\eta}_s \quad (19)$$

The columns of γ_i , consist of ones and zeros and equation (19) can be considered as an equation of coordinate compatibility which assures the connectivity of the system.

The assembly procedure follows the customary direct stiffness approach. A typical component equation of motion, given by equation (16) with index, i ,

Table 2 Rotor 1: component whirl mode frequencies

Mode number	Frequency (rpm)	
	Backward	Forward
1	1,256	1,866
2	4,967	5,278
3	11,153	12,857
4	13,080	18,538
5	18,111	21,578

$$\mathbf{A}_i \dot{p}_R^{(i)} + \mathbf{B}_i \dot{p}_R^{(i)} = \dot{P}_R^{(i)} \quad (16b)$$

is assembled into the system equation

$$\mathbf{A}_s \dot{\eta}_s + \mathbf{B}_s \dot{\eta}_s = \dot{H}_s \quad (20)$$

through the summations

$$\mathbf{A}_s = \Sigma \gamma_i^T \mathbf{A}_i \gamma_i \quad (21a)$$

$$\mathbf{B}_s = \Sigma \gamma_i^T \mathbf{B}_i \gamma_i \quad (21b)$$

$$\dot{H}_s = \Sigma \gamma_i^T \dot{P}_R^{(i)} \quad (21c)$$

Equation (20) is a nonlinear system equation of motion with the nonlinearities contained in the force vector, \dot{H}_s .

For systems with only linear supports, the usual options of free and forced vibration analysis exist and are discussed in [1, 2]. A digital computer program for analyzing linear and nonlinear rotor dynamic systems using component modes has been developed and information pertaining to its use is included in [18]. Analysis options include whirl speed/stability analysis, steady maneuver load response, blade loss dynamics, and transient response due to specified base motion and/or specified forces. Nonlinear support properties are included in the program by means of user supplied subroutines.

Numerical Examples

Example 1. The first example reproduces the results presented by Buono et al. [16] of United Technologies Corporation in their study of transient blade loss dynamics of a flexible rotor with squeeze films. A schematic of the rotor cross section is shown in Fig. 2. Detailed information on the rotor physical properties are contained in [16] and reproduced in Table 1.

The rotor is modeled with four finite elements (5 stations) with four degrees of freedom per station. Some of the elements contain several subelements as presented in Table 1. The rotor is supported by identical linear supports at station 1 and 5 with an isotropic stiffness coefficient of 4,450 N/cm and an isotropic damping coefficient of 0.65 N-s/cm. Squeeze film dampers with the properties:

Radius	= 5.715	cm
Length	= 1.270	cm
Radial clearance	= 0.02286	cm
Viscosity	= 0.0150	N-s/m ² stn 1
	0.0137	N-s/m ² stn 5

act in parallel with the linear supports at stations 1 and 5.

This particular rotor possesses four constraint modes due to the presence of a translational support at the two stations 1 and 5. Thus, the rotor possesses four constraint modes which are identical to rigid body modes since the number of constraints equals the number of rigid body modes. Sixteen fixed boundary point precessional modes (8 backward and 8 for-

Table 3 Rotor 1: linear system whirl speeds (rpm)

Mode	N_p			
	8	2	1	0
1B	1188	1188	1188	2452
1F	1571	1571	1570	2452
2B	2879	2896	3011	3013
2F	2937	2937	3156	3157
3B	3375	3402	3402	----
3F	4266	4311	4313	----
4B	5723	5771	----	----
4F	6709	6719	----	----
.	.	----	----	----
.	.	----	----	----

^aE = 20.69 10⁶ N/cm²

$\rho = 0$ for subelements

ward) exist for the rotating assembly. The frequency of the first five backward and forward component modes are displayed in Table 2 for a spin speed of 2950 rpm.

The linear system modes were determined as a function of the number of retained component modes to obtain some insight

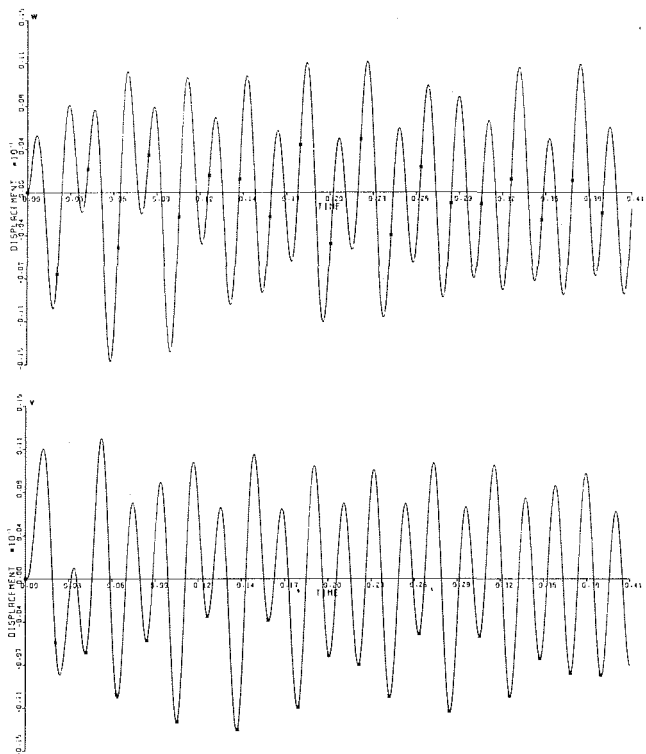


Fig. 3(a) Component mode synthesis analysis

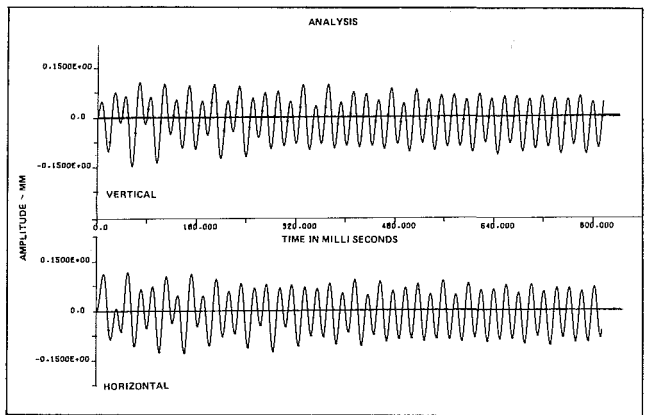


Fig. 3(b) Reproduction of [15], Fig. 48

Fig. 3 Rotor 1: time plots for station 2-2950 rpm 27.65 gm-cm unbalance at station 2

into the error introduced due to component mode truncation. The results of this study are displayed in Table 3.

The retention of all eight component mode pairs in Table 3 is equivalent to a direct analysis of the system, and a retention of zero component modes is equivalent to treating the rotating assembly as a rigid rotor. By retaining two component mode pairs, the first four system backward and forward modes are predicted within an accuracy of 1 percent when compared with a direct 20 degree of freedom analysis. For the blade loss simulation with squeeze films at 2950 rpm, two component mode pairs were retained. The results of this simulation are displayed in the time plot of Fig. 3(a) and compare very closely with the results presented by Buono et al. [16] and reproduced in Fig. 3(b). In addition, the transient response converged to a centered circular orbit as verified by an independent steady state analysis.

Example 2. The second example utilizes the same rotor used by Kascak [15] in his simulation of blade loss dynamics with squeeze film dampers and interference rubs. A schematic of the rotor cross section is shown in Fig. 4. Detailed information on the rotor physical properties are contained in [13] and reproduced in Table 4.

The rotor is modeled with six finite elements (seven stations) with four degrees of freedom per station. The rotor is supported by identical linear supports at stations 2 and 6 with an isotropic stiffness coefficient of 16,640 N/cm and an isotropic damping coefficient of 3.5 N-s/cm. Squeeze film dampers with the properties:

- Radius = 3.9370 cm
- Length = 0.7390 cm
- Radial clearance = 0.0064 cm
- Viscosity = 0.0330 N-s/m²

act in parallel with the linear supports at stations 2 and 6. An interference rub is simulated at stations 1, 4, and 7 with a stiffness of 176,772 N/cm and a radial clearance of 0.0051 cm. A coulomb coefficient ranging from 0.1 to 0.4 was used for various interference rub simulations. Several cases are presented below.

This example is considerably different from that of example 1 in that the number of constraints is larger. Rotor 2 possesses ten constraint modes due to the presence of a translational support at stations 2 and 6 and a translational rub at stations 1, 4, and 7. As a result of these large number of constraints, the 18 fixed boundary point precessional modes (9 backward and 9 forward) are of very high frequency. Table 5 contains a listing of the component whirl frequencies for a spin speed of 9500 rpm.

As for the previous example the linear whirl frequencies were determined at a spin speed of 9500 rpm as a function of the number of component modes retained with the results shown in Table 6. In this particular case, the retention of zero component modes provides excellent correlation with the system modes as predicted by a separate direct analysis up through the third forward and backward modes. The fourth

Table 4 Rotor 2: physical properties^a

Station number	Subelement number	Length (cm)	Radius (cm)	Mass (kg)	Diametral inertia (kg-cm ²)	Polar inertia (kg-cm ²)
1	1	6.223	0.953	0.400	19.541	39.082
2	2	12.075	1.270	0.262	0.	0.
3	3	12.075	1.270	0.	0.	0.
4	4	12.075	1.270	0.400	19.541	39.082
5	5	12.075	1.270	0.	0.	0.
6	6	6.233	0.953	0.262	0.	0.
7				0.400	19.541	39.082

^aE = 20.69 10⁶ N/cm²

ρ = 7915 kg/m³

Table 5 Rotor 2: component whirl mode frequencies

Mode number	Frequency (rpm)	
	backward	forward
1	59,889	62,051
2	91,883	94,043
3	122,031	139,907

Table 6 Rotor 2: linear system whirl speeds (rpm)

Mode	Np	Whirl speeds (rpm)			
		9	2	1	0
1B		7183	7185	7191	7191
1F		7246	7246	7255	7255
2B		9039	9041	9041	9052
2F		9244	9246	9246	9251
3B		10872	10879	10880	10880
3F		11447	11449	11450	11450
4B		31345	31824	31824	33701
4F		34918	35011	35011	38170

Table 7 Synchronous orbit radii (cm), $\mu = 0.3$

Station	9500 rpm	11,000 rpm
1	0.002440	0.0027
2	0.000828	0.0006
4	0.005266	0.0054
6	0.001867	0.0017
7	0.005144	0.0053

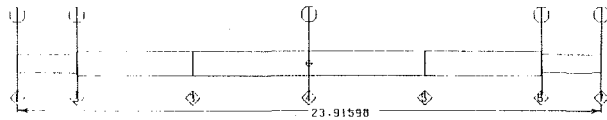


Fig. 4 Rotor 2: model schematic

forward and backward modes are predicted with less than 10 percent error. When the rotor makes contact with the interference rubs the system whirl speeds increase, so it is concluded that the retention of zero component precessional modes is adequate for this simulation.

The undamped critical speeds of the system were calculated to be 7208, 9266, and 11,542 rpm. Balde loss transients with the squeeze film dampers in operation at stations 2 and 6 and the interferences rubs at stations 1, 4, and 7 are shown below for the speeds of 9500 rpm and 11,000 rpm. A 0.0127-cm step change in cg eccentricity at station 7 was used for these simulations.

Figure 5 shows the transient response of the system at stations 1, 4, and 7 for a blade loss at 9500 rpm and an interference rub coulomb coefficient of 0.3. Station 7 displacement increases and makes initial contact with the interference rub at approximately 0.60 cycles. Station 4 displacement lags the motion of station 7 due to time required for a displacement wave to travel down the shaft and it makes initial contact with the interference rub at approximately 1.25 cycles. Station 1 displacement lags station 7 by a larger time interval and for this case never contacts the interference rub. There is very little radial movement of the disks after contact with the rub and the system converges very rapidly to a centered circular synchronous orbit of radii listed in Table 8.

Figure 6 shows the same information as Fig. 5, except for a rub coefficient of 0.4. For this case the motion is identical to that of the previous case until interference rub contact is made at station 7. The motion is quite similar in general character to the $\mu = 0.3$ case up until approximately 6.75 cycles. Then station 4 starts into a backward whirl with the other stations also whirling backward soon after. Station 7 finally goes into

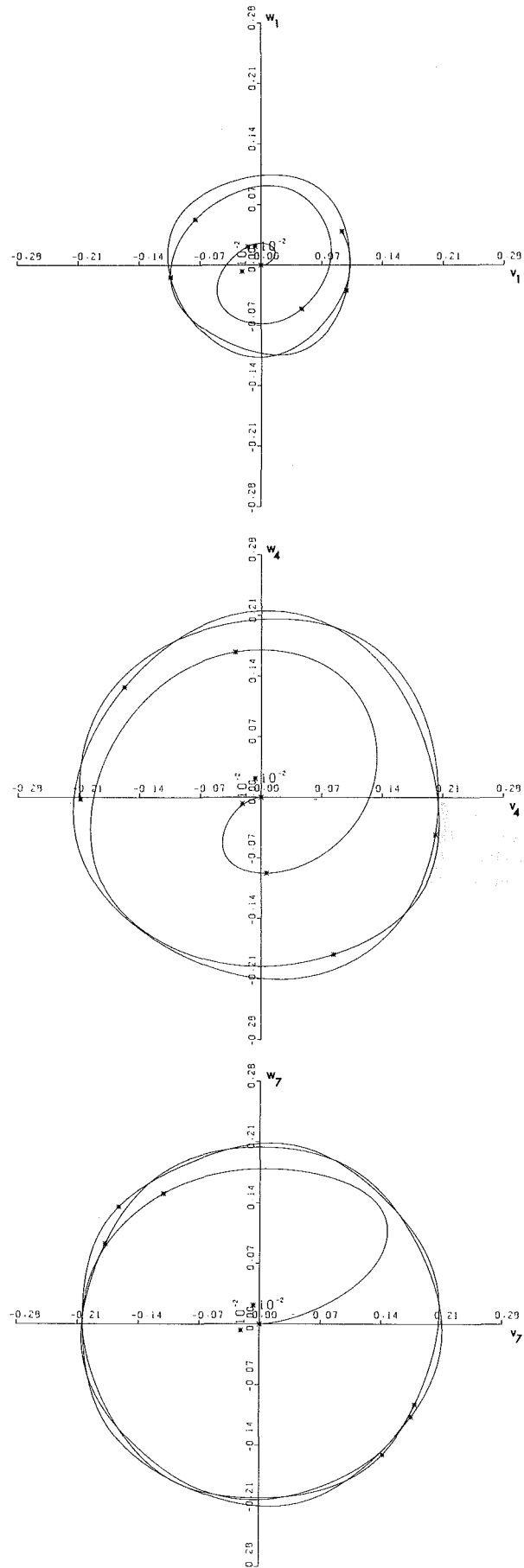


Fig. 5 Rotor 2: blade loss transient at 9500 rpm, $\mu = 0.3$

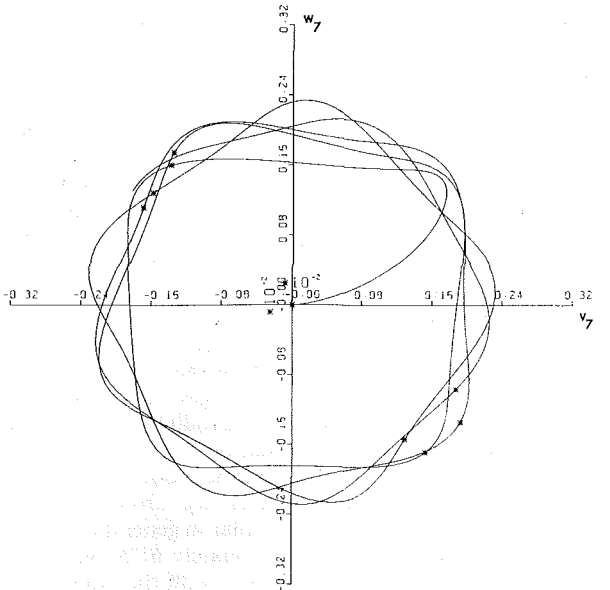
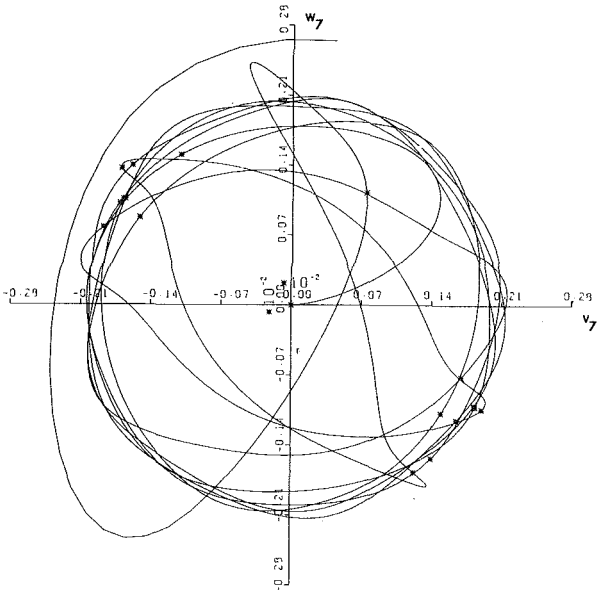
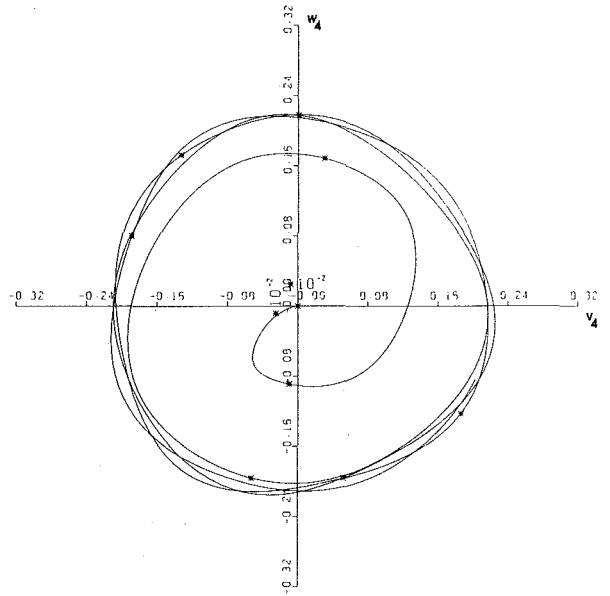
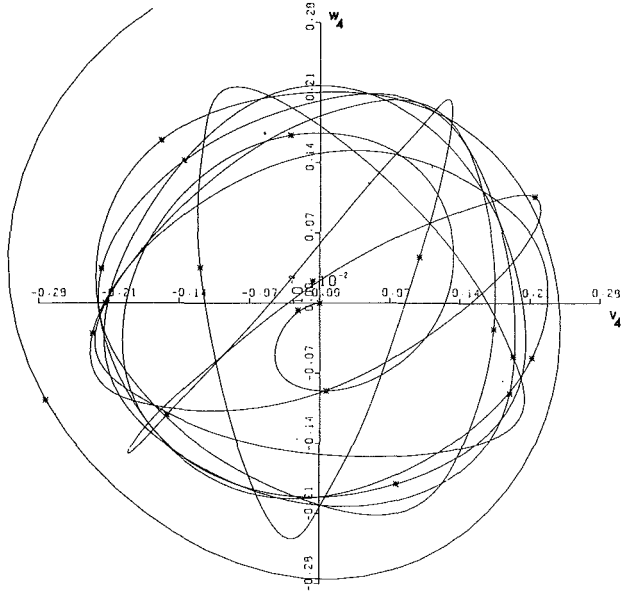
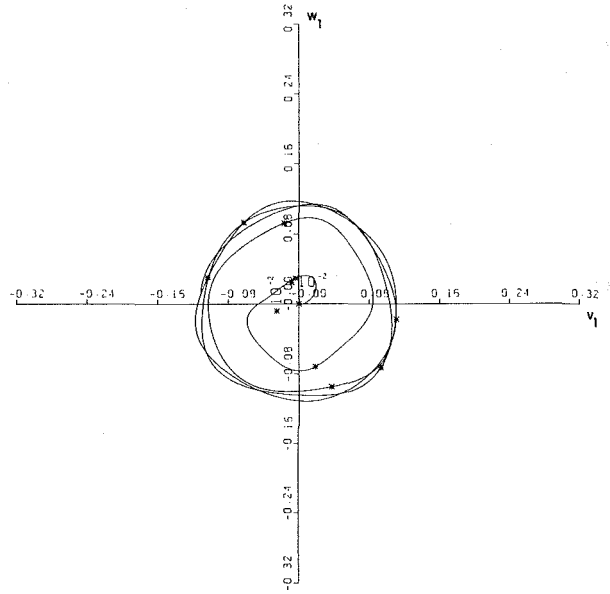
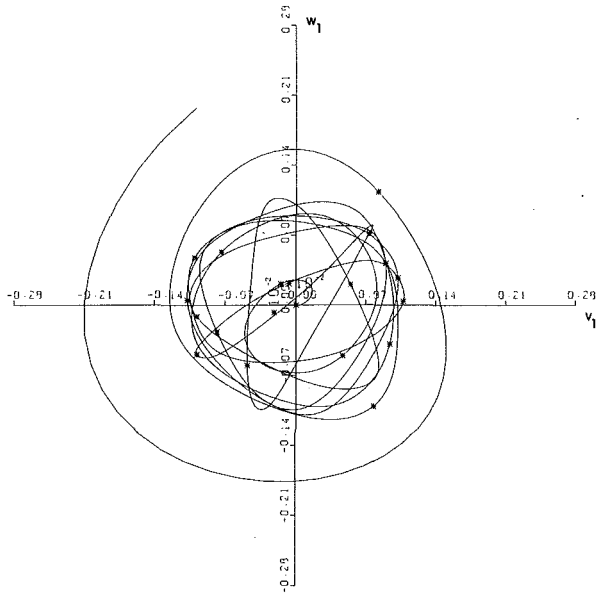


Fig. 6 Rotor 2: blade loss transient at 9500 rpm, $\mu = 0.4$

Fig. 7 Rotor 2: blade loss transient at 11,000 rpm, $\mu = 0.3$

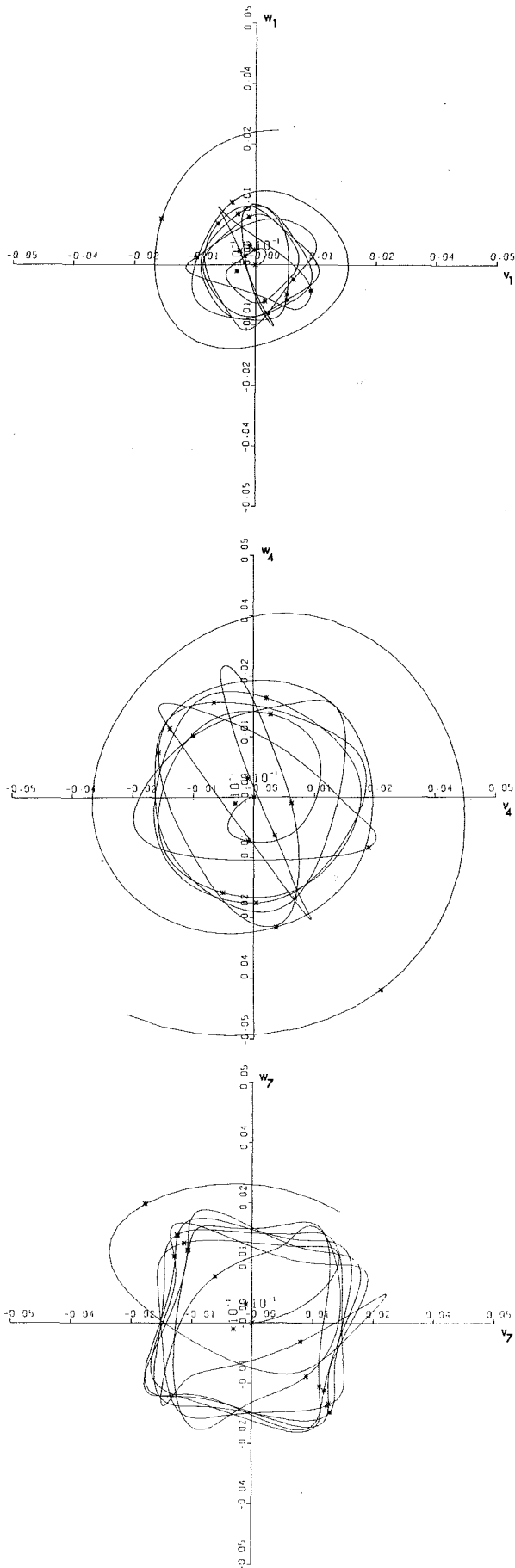


Fig. 8 Rotor 2: blade loss transient at 11,000 rpm, $\mu = 0.4$

a backward whirl at approximately 8.75 cycles and the amplitude of the system then increases very rapidly.

Figure 7 shows the rotor response at a spin speed of 11,000 rpm due to the same step change in unbalance and for a coulomb rub coefficient of 0.3. The behavior is similar to that of Fig. 5, except that disks 7 and 4 bounce off the interference rub approximately four times per cycle. This case also converges to a centered circular synchronous orbit but at a slower rate than the case of Fig. 5. After ten cycles the estimated steady-state radii are as listed in Table 7.

Figure 8 displays the blade loss transient response at 11,000 rpm for a rub coefficient of 0.4. As for the similar case of 9500 rpm (Fig. 6), this motion also goes into a backward whirl. The motion is initially similar to that of Fig. 7 in that disks 7 and 4 bounce off the rubs several times at a rate of approximately 4 times per cycle. At approximately 5.65 cycles station 4 initiates a backward whirl with station 7 starting backward at about 7.15 cycles. As for the previous unstable case, the amplitude then builds very rapidly.

Summary and Conclusions

The method of Component Mode Synthesis was developed to simulate nonlinear rotor dynamic behavior and a general purpose computer code, ARDS (Analysis of Rotor Dynamic Systems) was written. ARDS is a user-oriented code, which allows for the linear and nonlinear, steady and transient analysis of single shaft rotor systems. It is presently being expanded to multishaft capability. The user may supply subroutines to model whatever type of support characteristics are desired for the purpose of analyzing transient rotor dynamics.

Two example rotor systems were analyzed, using ARDS, to determine their dynamic characteristics due to blade loss. Both rotors contained squeeze film dampers which were modeled in closed form by short bearing theory and the second rotor also included interference rubs which were modeled as a nonlinear support with a radial clearance, linear radial stiffness, and a coulomb tangential friction force.

The results indicate that a high accuracy simulation is possible with the retention of a small number of component modes. The specific number to be retained for high accuracy depends on the particular application and requires a preliminary study of the systems natural whirl modes. All the numerical integrations in this paper were performed using a fixed-step, fourth-order Runge-Kutta algorithm with a step size equal to 1 percent of the spin period. Larger step sizes were used successfully; however, an extensive study of required minimum time increment to assure numerical stability has not been performed to date.

Several integration step sizes were used for those simulations that predicted unstable behavior to determine if the instability was due to the numerical instability process or to physical phenomena. No evidence of numerical instability was detected in these studies, and it is concluded that the mathematical model simulates realistic system behavior. In addition, the results presented here are similar to those obtained by Kascak [15] using an entirely different mathematical model and numerical procedure.

The examples were analyzed on an Amdahl 470 and required approximately 4.4 CPU per spin cycle for Rotor 1 and 5.6 CPU per spin cycle for Rotor 2.

Acknowledgment

The work reported in this paper was sponsored by NASA Lewis Research Center under NASA Grant NAG 3-6.

References

- 1 Glasgow, D. A., and Nelson, H. D., "Stability Analysis of Rotor-Bearings Systems Using Component Mode Synthesis," *ASME Journal of Mechanical Design*, Vol. 102, No. 2, Apr. 1980, pp. 352-359.
- 2 Nelson, H. D., and Meacham, W. L., "Transient Analysis of Rotor Bearing Systems Using Component Mode Synthesis," ASME Paper No. 81-GT-110, 1981 Gas Turbine Conference, Houston, Texas, Mar. 1981.
- 3 Lund, J. W., and Orcutt, F. K., "Calculations and Experiments on the Unbalance Response of a Flexible Rotor," *ASME Journal of Engineering for Industry*, Vol. 89, No. 4, Nov. 1967, pp. 785-796.
- 4 Lund, J. W., "Stability of Damped Critical Speeds of a Flexible Rotor in Fluid Film Bearings," *ASME Journal of Engineering for Industry*, Vol. 96, 1974, pp. 509-517.
- 5 Lund, J. W., "Modal Response of a Flexible Rotor in Fluid Film Bearing," *ASME Journal of Engineering for Industry*, Vol. 96, No. 2, May 1974, pp. 525-533.
- 6 Childs, D. W., "The Space Shuttle Main Engine High-Pressure Fuel Turbopump Rotordynamic Instability Problem," *ASME JOURNAL OF ENGINEERING FOR POWER*, Vol. 100, No. 1, Jan. 1978, pp. 48-57.
- 7 Gasch, R., "Vibration of Large Turbo-Rotors in Fluid Film Bearings on Elastic Foundation," *Journal of Sound and Vibration*, Vol. 47, No. 1, 1976, pp. 53-73.
- 8 Dimaragonas, A. D., "A General Method for Stability Analysis of Rotating Shafts," *Ingenieur-Archiv*, Vol. 44, 1975, pp. 9-20.
- 9 Adams, M. L., "Nonlinear Dynamics of Flexible Multi-Bearing Rotors," *Journal of Sound and Vibration*, Vol. 71, No. 1, 1980, pp. 129-144.
- 10 Nelson, H. D., and McVaugh, J. M., "The Dynamics of Rotor-Bearing Systems Using Finite Elements," *ASME Journal of Engineering for Industry*, Vol. 98, No. 2, May 1976, pp. 593-600.
- 11 Li, D., and Gunter, E. J., "Component Mode Synthesis of Large Rotor Systems," ASME Paper No. 81-GT-147, 1981 Gas Turbine Conference, Houston, Texas, Mar. 1981.
- 12 Dennis, A. J., Eriksson, R. H., and Seitelman, L. H., "Transient Response Analysis of Damped Rotor Systems by the Normal Mode Method," ASME Paper No. 75-GT-58, Gas Turbine Conference, Houston, Texas, Mar. 1975.
- 13 Kirk, R. G., and Gunter, E. J., "Nonlinear Transient Analysis of Multi-Mass Flexible Rotors—Theory and Application," NASA CR-2300, Sept. 1973.
- 14 Adams, M. L., Padovan, J., and Fertis, D. G., "Finite Element for Rotor/Stator Interactive Forces in General Engine Dynamic Simulation, Part I: Development of Bearing Damper Element," NASA CR 165214, Oct. 1980.
- 15 Kascak, A. F., "The Response of Turbine Engine Rotors to Interference Rubs," AVRADCOM TR 80-C-14, June 1980.
- 16 Buono, D. F., et al., "Transient Dynamics of a Flexible Rotor with Squeeze Film Dampers," NASA CR-3050, Sept. 1978.
- 17 Nelson, H. D., Russell, S. J., and Meacham, W. L., "Transient Response of Rotor-Bearing Systems Using Component Mode Synthesis, Part I—Mathematical Development," ERC-R81016-1, Arizona State University, Tempe, Ariz., March 1981.
- 18 Nelson, H. D., Meacham, W. L., and Alam, M., "Transient Response of Rotor-Bearing Systems Using Component Mode Synthesis, Part II—Digital Computer Manual for Program ARDS," ERC-R81030, Arizona State University, Tempe, Ariz., May 1981.
- 19 Nelson, H. D., and Meacham, W. L., "Transient Response of Rotor-Bearing Systems Using Component Mode Synthesis, Part III—Example Analyses," ERC-R81031, Arizona State University, Tempe, Ariz., July 1981.

The Effect of Temperature Ratios on the Film Cooling Process

P. J. Loftus

T. V. Jones

University of Oxford,
Department of Engineering Science,
Oxford OX1 3PJ, England

Film cooling experiments have been conducted at conditions which realistically simulate the gas turbine environment. Heat transfer has been measured using a short duration wind tunnel. Mainstream injection and wall temperatures have been varied independently in order to conduct a systematic investigation of the injection process. A model of the film cooling process based on the principle of superposition is used to interpret the experimental results. The effect of gas to wall temperature ratio on heat transfer to an uncooled plate has also been investigated.

Introduction

Film cooling is an important method of protecting components in gas turbine engines and a review of experimental and analytical investigations of this cooling technique is given by Goldstein [1]. In this method of cooling, relatively cold gas is usually injected onto the blade surface through rows of holes forming a cold film. It is important to be able to predict the heat-transfer rate to the blade under these conditions for a range of coolant, wall, and freestream temperatures. The variation of heat transfer with these parameters is compared with that predicted by a temperature superposition model.

The experiment employs a short duration wind tunnel to produce hot mainstream flows and coolant and wall temperatures are varied. Heat transfer is measured using a transient technique which allows accurate instantaneous heat-transfer rates to be found. The effects of property variations and varying surface temperature distributions are also examined.

The Superposition Model of Film Cooling

The concept of superposition in a turbulent boundary layer arises from the linearity and homogeneity of the simplified boundary layer differential equations and is an accepted method of dealing with problems of varying surface temperature (see for example Kays and Crawford [2] and Crawford, Kays and Moffat [3]). When film cooling through rows of small holes takes place the injected gas usually remains close to the wall, and the assumption in the proposed model is that the same simplified boundary layer differential equations hold true. The boundary layer velocity and temperature profiles will be distorted considerably compared to those for a boundary layer without injection, but it is assumed that superposition can be applied to determine the temperature field, assuming constant fluid properties.

In Fig. 1, the temperature boundary conditions for film cooling are sketched for a given "injection rate." These are shown for a two-dimensional situation, but the result deduced also applies to the three-dimensional case. The temperature profile of the injected gas is assumed to be self-similar with a

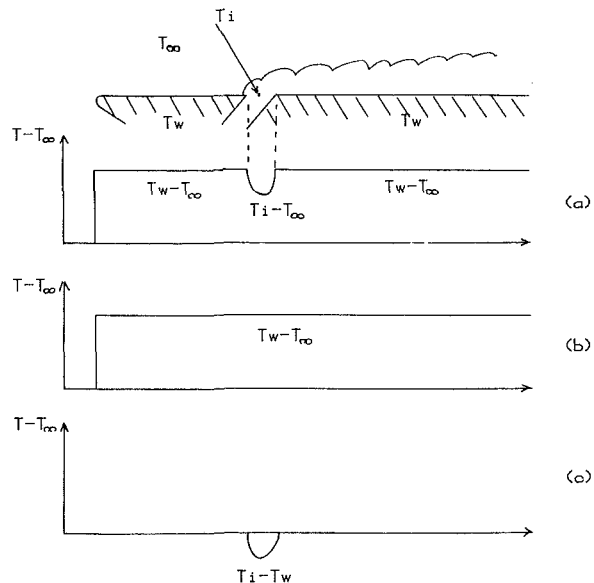


Fig. 1 Temperature boundary conditions for film cooling

value T_w at the wall and T_i on the centreline of the injection holes. Referencing all temperatures to the freestream value allows wall temperature profiles to be superimposed while still satisfying the freestream temperature boundary condition. Thus the temperature field required (a) is seen to be the sum of that for cases (b) and (c) in Fig. 1, and these in turn may be expressed as that for a unit temperature difference multiplied by the relevant temperature difference. Thus the heat-transfer rate, q , given by the flow temperature gradient at the wall, may be derived as

$$q(x) = q_1(x)[T_w - T_\infty] + q_2(x)[T_i - T_w] \quad (1)$$

where q_1 is for a unit temperature difference between wall and freestream, the coolant being at the wall temperature, and q_2 is for a wall temperature equal to the freestream value and a unit temperature difference between coolant centreline and wall. q_1 and q_2 are primarily dependent on the freestream Reynolds number and the coolant "injection rate." The term "injection rate" is used to imply similarity of the injection process.

Contributed by the Gas Turbine Division of THE AMERICAN SOCIETY OF MECHANICAL ENGINEERS and presented at the 27th International Gas Turbine Conference and Exhibit, London, England, April 18-22, 1982. Manuscript received at ASME Headquarters December 29, 1981. Paper No. 82-GT-306.

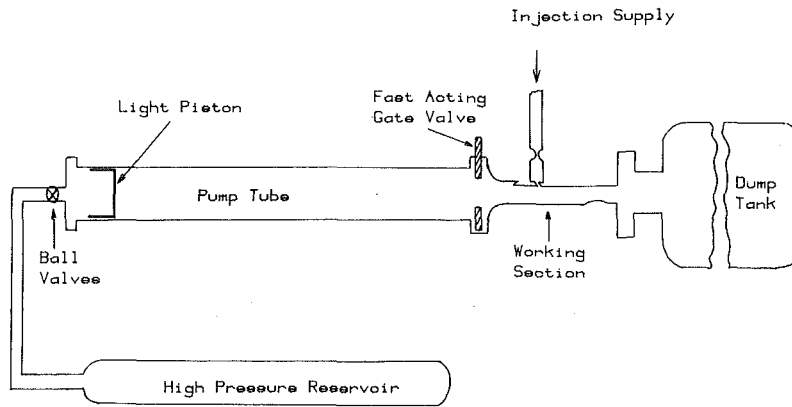


Fig. 2 Schematic of isentropic light piston tunnel

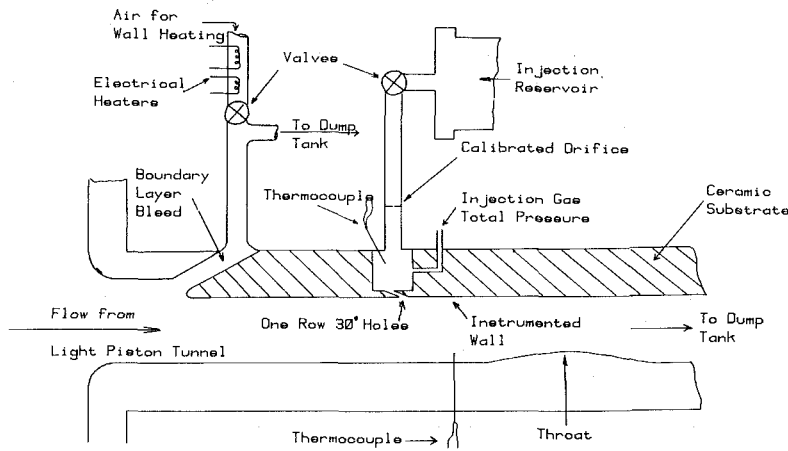


Fig. 3 Schematic of test section

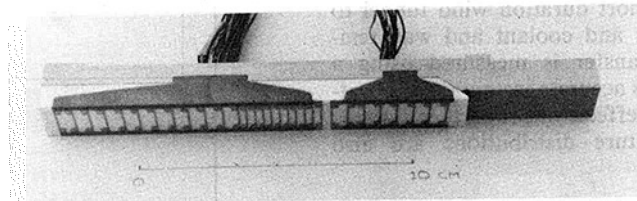


Fig. 4 Instrumented liner

The Test Facility

The facility used for this film cooling investigation was an Isentropic Light Piston Tunnel, which provides a steady hot flow for a duration of typically 300 ms. Correct full-scale engine Reynolds numbers, Mach numbers, and gas, wall, and coolant temperature ratios were simulated in order to examine the film cooling process at representative conditions. The operation of this type of facility is fully described in reference [4]. Briefly, test gas is compressed and heated by a free piston to the desired conditions in less than 1 s and then allowed to

pass through the working section when the fast acting gate valve is opened (see Fig. 2).

The working section is sketched in Fig. 3. The instrumented surface forms the top wall of a rectangular channel with a sonic throat at the downstream end. The inlet boundary layer is bled off upstream of the test surface, which is manufactured from a machineable glass ceramic (Corning MACOR). The instrumented liner is shown in Fig. 4. Provision was made for heating the instrumented wall prior to running the tunnel. This was accomplished simply by passing air from a regulated

Nomenclature

c = specific heat capacity, J/kg K
 h = heat transfer coefficient, W/m² K
 k = thermal conductivity, W/m K
 Nu = Nusselt number
 Pr = Prandtl number

q = spanwise averaged heat transfer rate, W/m²
 Re = Reynolds number
 St = Stanton number
 T = temperature, K
 x, y, z = coordinates, m
 ρ = density, kg/m³
 μ = viscosity, kg/m s

ϵ = distance, m

Subscripts

cp = constant properties
 i = injection
 0 = no injection
 w = wall
 ∞ } = free-stream total condition
 gas }

high pressure supply through a 3-kW electrical heater and into the working section via the boundary layer bleed slot at the leading edge. This heating air was then exhausted to the atmosphere via the dump tank. In this manner it was possible to vary the wall temperature between 290 and 350 K.

Injection Air Supply

In order to monitor accurately the rate of flow of the injection gas and to ensure repeatability of injection conditions from run to run, a constant mass flow supply system was used. The injection gas was fed from a high-pressure reservoir to the injection plenum via a calibrated sonic orifice. This system required some modification because of the mode of operation of the tunnel. In order to prevent ingestion of hot mainstream gas at the beginning of the run, a constant pressure supply is initiated 10 ms before the main gate valve is opened, the constant pressure being chosen to be equal to or slightly greater than the expected plenum pressure during the run. This supply is switched off and a constant mass flow system initiated as the main gate valve is opened.

Provision was also made for heating of the injection gas. This was done by enclosing a portion of the supply pipes in a jacket through which steam was passed. It was only necessary to heat a section of piping as only a small volume of injection gas is used during the tunnel run. Thus, it was possible to perform experiments at two different constant injection temperatures, varying the wall temperature in each case.

Instrumentation

Heat transfer rates were measured using conventional thin film gauge techniques (see reference [51]). By passing a constant current through the thin film gauge a signal proportional to the surface temperature change may be obtained. This is converted to a heat transfer signal using a heat-transfer analogue circuit. By plotting the heat transfer rate against the surface temperature change as the run progresses, a linear relation is obtained which can be extrapolated to zero time to give the heat-transfer rate for an isothermal wall [6]. It is because of this extrapolation process that great care is necessary in initiating the injection flow.

The total temperatures of mainstream and injection flows were determined using microminiature thermocouple probes (wire dia 0.0005 in.). Very small probes were needed to give an adequate frequency response.

Quartz piezo-electric pressure transducers were used to measure the pressures of interest – the tunnel total pressure, working section static pressure and injection total pressure. Semiconductor differential transducers were also used for greater accuracy in determining small pressure differences.

All data were recorded by an on-line minicomputer via a system of signal conditioning amplifiers. The data collected was subsequently analysed by the same dedicated computer. The complete data acquisition and processing system used is described in reference [6].

Experimental Investigation of Gas to Wall Temperature Ratio Effects

In order to be able to carry out careful and accurate film cooling measurements, certain preliminary experiments were necessary. One of these was an investigation of the effect of gas-to-wall temperature ratio on turbulent heat transfer. This was necessary as one of the effects of injection of cooling air is to change the gas to wall temperature ratio, thus any measurements of the dependence of the heat-transfer coefficients on injection would incorporate this effect. Accordingly, a series of tests were performed prior to drilling the injection holes in the instrumented liner.

The first experiments were performed at the following conditions: Reynolds number = $2.7E7$ per m, Mach number

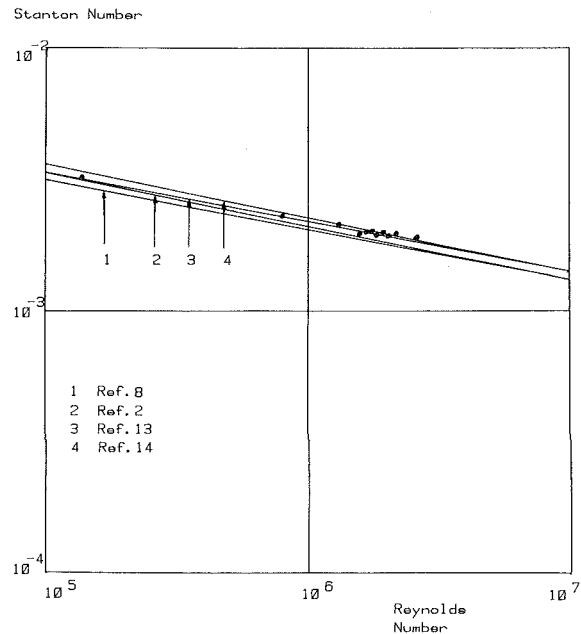


Fig. 5 Turbulent heat transfer – comparison of experimental results and correlation

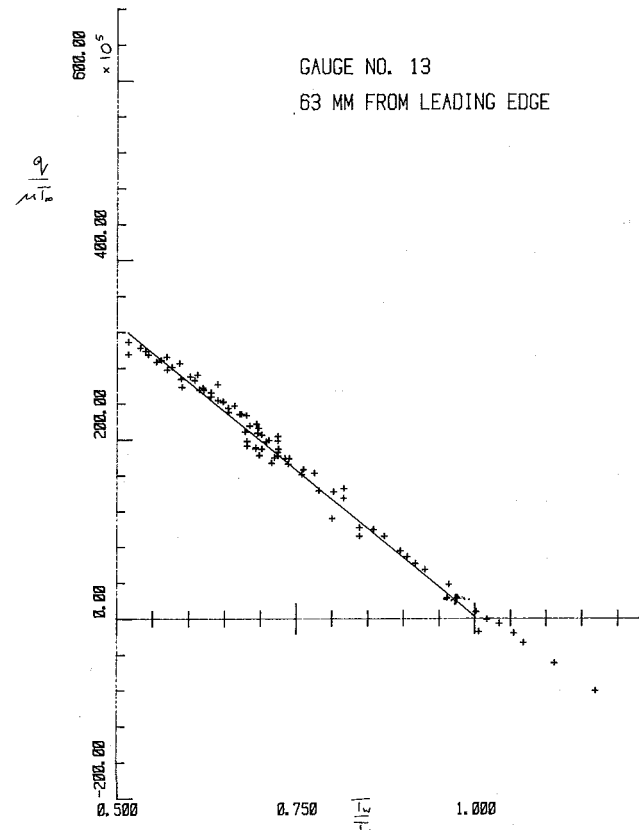


Fig. 6 Effect of temperature ratio on heat transfer

= 0.55, total temperature = 432 K, wall temperature = 290 K.

These initial experiments showed that there was a well behaved turbulent boundary layer on the test plate, and the results obtained showed good agreement with established turbulent boundary layer correlations, the difference between the experimental results and the correlations being of the same order as the difference between the correlations themselves. Figure 5 shows the heat-transfer results from one run together

with some correlations plotted as Stanton number versus Reynolds number.

Subsequently, experiments were performed at the above Reynolds and Mach numbers but varying the mainstream temperature from 300 to 570 K and the wall temperature from 290 to 350 K. For each of five total temperatures, the wall temperature was varied in the range specified, producing data over a range of gas-to-wall temperature ratio from 0.85 to 2.0.

At any temperature ratio the Nusselt number may be written:

$$Nu = Nu_{cp} f\left(\frac{T_w}{T_\infty}\right) f'(Re) \quad (2)$$

where Nusselt and Reynolds numbers are evaluated at freestream static conditions. f and f' represent the functional dependence of the Nusselt number on temperature ratio and Reynolds number, respectively. Thus

$$\frac{q}{kT_\infty} = \frac{Nu_{cp}}{x} f'(Re) f\left(\frac{T_w}{T_\infty}\right) \left(1 - \frac{T_w}{T_\infty}\right) \quad (3)$$

Figure 6 shows the data plotted in this form for a constant Reynolds number. There is no significant effect of gas-to-wall temperature ratio on the Nusselt number for the range of temperatures investigated. The small amount of relevant literature reports, in general, an increase of Stanton number with increasing gas to wall temperature ratio, for $T_w/T_\infty > 1$. In a recent review, Kays [2], comments that little evidence is available for the case reported here for $T_w/T_\infty < 1$, but suggests that there is indeed no variation. This is entirely consistent with the results reported here.

Recent computations by Brown [7] of flat plate heat transfer show an increase of Stanton number with temperature ratio for $T_w/T_\infty < 1$, as do the turbulent heat-transfer charts presented by Neal and Bertram [8] based on the Spalding and Chi method.

Kelnhofner and Rotta [9] have measured a significant decrease in the Stanton number as T_w/T_∞ is increased from 1.0 to 1.74. This data for $T_w/T_\infty > 1$, falls outside the temperature range investigated in the present study and support the recommendation of Kays [2].

Experimental Verification of Turbulent Boundary Layer Superposition

Some experiments were performed with a nonuniform wall temperature, the wall being hottest at the leading edge. In this case the heat transfer rate at a downstream location will be enhanced because of the hot upstream wall. A typical wall temperature profile is shown in Fig. 7.

Heat-transfer results for one position on the flat plate with such wall temperature profiles are shown in Fig. 8, plotted against ($T_{gas} - T_{wall}$) where T_{wall} refers to that position. They happen to fall on a straight line due to the form of the wall temperature profiles used. When extrapolated, the line does not pass through the origin, as would be expected had there been no wall temperature profile. The effect of a known wall temperature distribution on the heat transfer from a turbulent boundary layer can readily be calculated using superposition (see for example Kays [2]). At a given position, it is possible to determine the heat-transfer rate for a wall at a uniform temperature equal to the temperature at this position. This is shown in Fig. 9, where it can be seen that the results now fall on a straight line through the origin as expected. Thus superposition has been shown to be applicable to the present experiment.

Heat Transfer With Film Cooling

The temperature of the injected gas was monitored during the tunnel run using a microminiature thermocouple positioned in the plenum behind the injection holes. Prior to

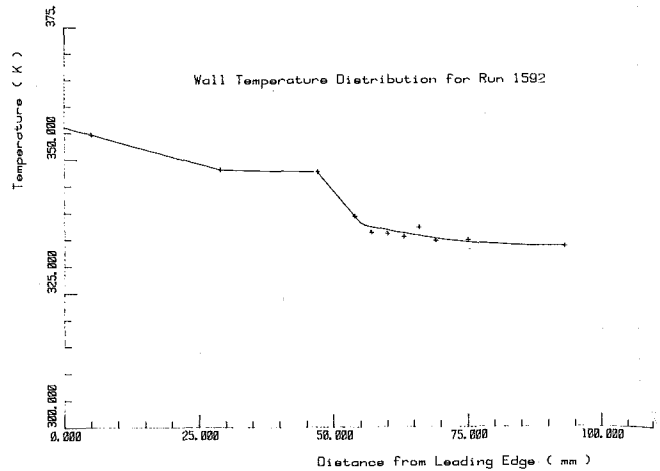


Fig. 7 Typical wall temperature profile in uncooled superposition tests

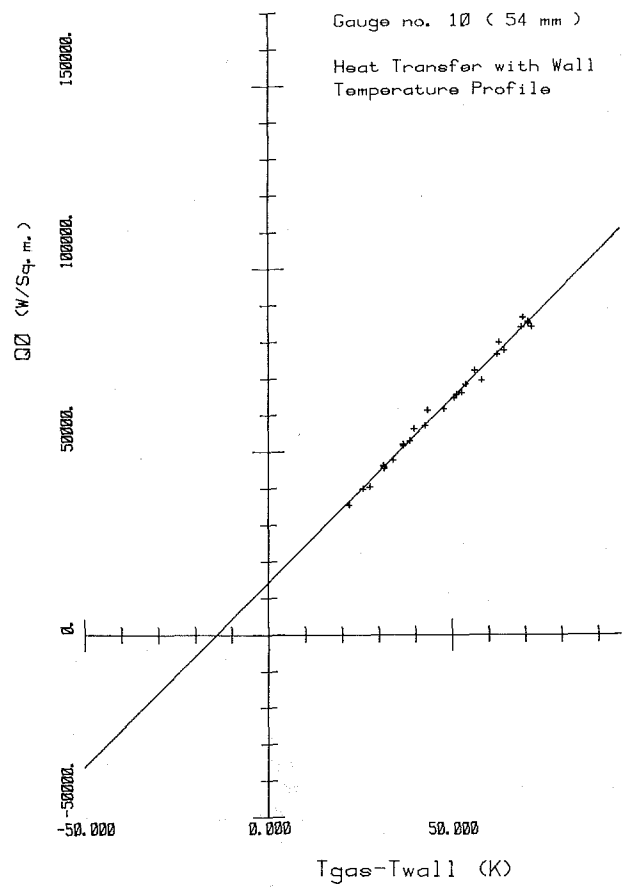


Fig. 8 Uncooled heat transfer

performing any injection tests a series of checks was made to determine any heat loss or gain by the injection gas between the plenum and the hole exit. These tests were done both for hot (375 K) and cold (295 K) injection gas and over the range of wall temperatures used. A noticeable temperature profile was observed in the jet, but for all mass flow rates and wall temperatures the centreline value was equal to that measured in the plenum.

The injection holes were 0.50 mm in dia, inclined at an angle of 30 deg to the flow direction and spaced at 2.5 dia between hole centers. The injection experiments were per-

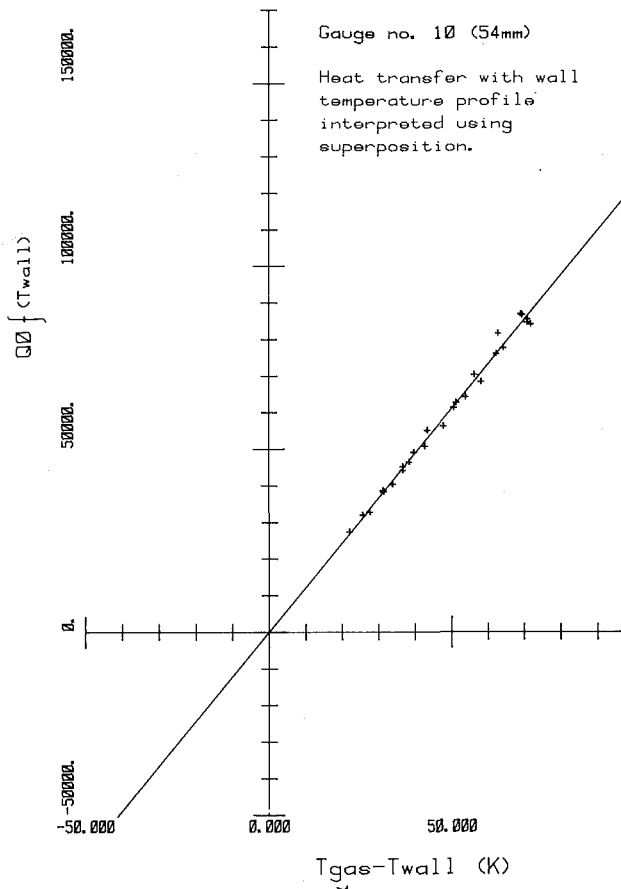


Fig. 9 Uncooled heat transfer

formed in the same manner as the uncooled tests: for constant mainstream and injection conditions the wall temperature was varied in the range 290 to 350 K. It was important to vary the wall temperature for constant injection temperature rather than vice versa in order that the flow field was not changed at all as the variation of heat transfer rate was investigated. Five injection rates were tested at each injection temperature and the measured heat transfer rates are shown in Figs. 10 and 11 for various downstream positions. The test conditions were as follows:

freestream Re	2.7E7 per m
freestream Mach no.	0.55
total temperature	365 K
injection temperatures	295 K and 375 K
wall temperature	290 K and 350 K

blowing rate $\frac{\rho_i u_i}{\rho_\infty u_\infty}$	0.30 to 1.45
--	--------------

Discussion of Injection Results

The above injection results may now be examined in the light of the superposition model already described. If it is assumed that the mass flux ratio determines similarity of injection, then it is evident from equation A that for a given injection rate the curves for hot injection should be displaced by a constant amount from those for cold injection, the displacement being a function of injection rate. Within experimental scatter this is seen to be true for all injection rates and downstream positions (see Figs. 10 and 11). Further, the heat-transfer rate is essentially a linear function of the wall temperature, a result again in keeping with the superposition model. If momentum ratio was chosen to define the injection

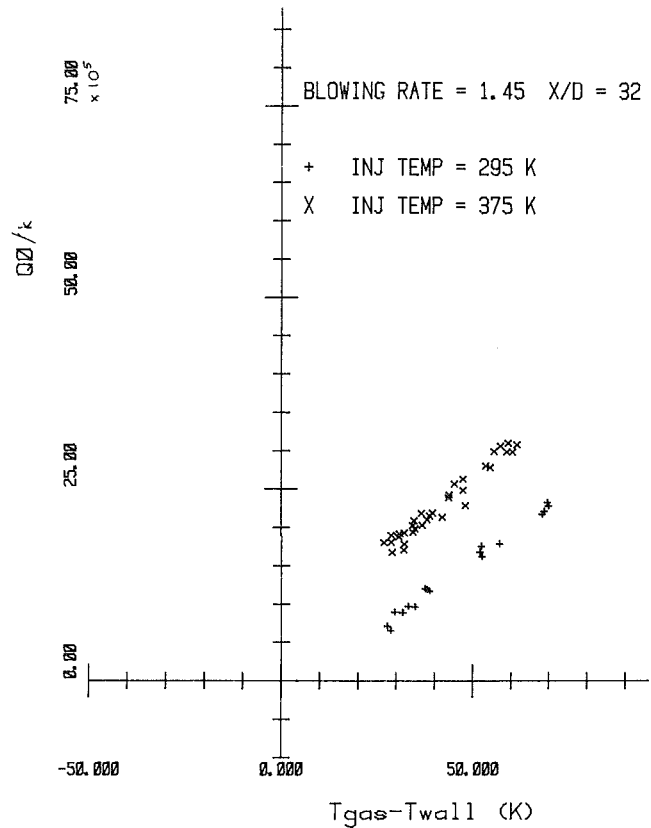


Fig. 10 Heat transfer with injection

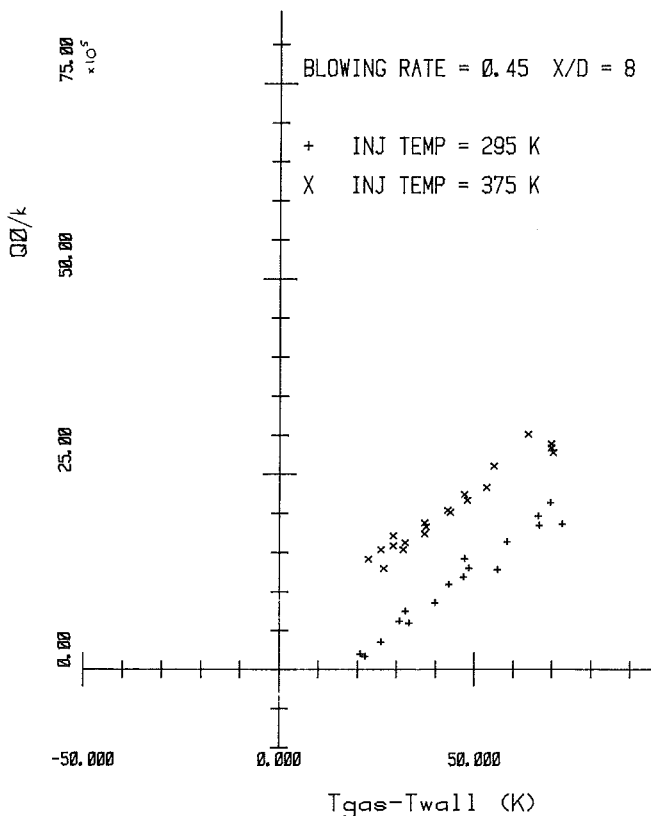


Fig. 11 Heat transfer with injection

rate, the conclusions above would not be significantly changed for the coolant temperature range investigated.

Conclusion

Several conclusions may be drawn from the experimental results presented. Firstly, the effect of gas-to-wall temperature ratio on a flat plate is found to be small for the case $T_w/T_\infty < 1$. Also, temperature superposition may be used to determine the effects of varying wall temperatures for the case of a flat plate boundary layer at the flow conditions used. Finally, the linearity predicted by a superposition model of film cooling has been demonstrated for conditions representative of gas turbines.

The importance of injection parameters (mass flux ratio, momentum flux ratio, etc.) is to be investigated in further analysis of the data already acquired and in future experiments exploring a wider range of temperature of the coolant and freestream flows.

Acknowledgment

The authors gratefully acknowledge the support of Rolls-Royce Ltd. and Ministry of Defence (PE) who funded the work reported here.

References

- 1 Goldstein, R. J., "Film Cooling," in *Advances in Heat Transfer*, Vol. 7, Academic Press, 1971.
- 2 Kays, W. M. and Crawford, M. E., *Convective Heat and Mass Transfer*, McGraw Hill, (1980).
- 3 Crawford, M. E., Kays, W. M., and Moffat, R. J., "Full Coverage Film Cooling," ASME Paper No. 80-GT-43, 1980.
- 4 Jones, T. V., Schultz, D. L., and Hendley, A. D., "On the Flow in an Isentropic Light Piston Tunnel," A.R.C. Reports and Memoranda No. 3731, 1973.
- 5 Schultz, D. L. and Jones, T. V., "Heat Transfer Measurements in Short Duration Hypersonic Facilities," A.G.A.R.D. AG-165, 1973.
- 6 Oldfield, M. L. G., Jones, T. V., and Schultz, D. L., "On-Line Computer for Transient Cascade Instrumentation," *IEEE Transactions on Aerospace and Electronic Systems*, Vol. AES-14, No. 5, 1978.
- 7 Browne, L. W. B., "Flat Plate Heat Transfer in High Speed Flow," Private Communication, 1979.
- 8 Neal, L. and Bertram, M. H., "Turbulent Skin Friction and Heat Transfer Charts Adapted from the Spalding and Chi Method," NASA TN-3969, 1967.
- 9 Kelnhofer, W. J., and Rotta, "Wall Temperature Effects on Subsonic Gas Flow," AVN-Bericht 67-A-26, 1967.
- 10 Crabtree, I. F., Dommet, R. L., and Woodley, J. G., "Estimation of Heat Transfer to Flat Plates, Cones and Blunt Bodies," RAE TR 65137, 1965.
- 11 Whitaker, S., in *Fundamental Principles of Heat Transfer*, Pergamon Press Inc., 1977.

J. T. Halkola

A. H. Campbell

Solar Turbines Incorporated,
San Diego, Calif. 92138

D. Jung

Naval Sea Systems Command,
Washington, D.C. 20362

RACER Conceptual Design

The Rankine Cycle Energy Recovery (or RACER) is an unfired waste heat recovery system designed for use aboard U.S. Navy gas turbine powered ships. The system converts waste heat from the exhaust of the main propulsion gas turbines into useful shaft horsepower and is currently planned for installation aboard the new DDG-51 class of ships. The design philosophy used in determining an overall system concept to minimize manning yet maximize availability, reliability and fuel savings is discussed. The paper also describes the trade-off analyses made to size the system in relation to overall fuel saving and gives a brief summary of the test programs to verify the system prior to ship installation.

Introduction

The recent commitment of the U.S. Navy to gas turbine propulsion aboard ships combined with rising fuel prices over the recent years has made more attractive the converting of the waste energy (or heat) from these engines into useful shaft power resulting in substantial fuel savings [1, 2]. The Naval Sea Systems Command awarded contracts in December 1979 to develop a conceptual design of a new generation of waste heat recovery systems to provide a 25 percent minimum improvement in ship propulsion fuel consumption and increase the ship's operating range by 1000 nautical miles.

As a result of this effort, the Rankine Cycle Energy Recovery (or RACER) system was developed as an unfired waste heat recovery system designed for use aboard Navy gas turbine ships to convert waste heat from the exhaust of the LM 2500 main propulsion gas turbines into useful shaft horsepower. RACER is considered a nonmission critical system whose primary function is to save fuel aboard gas turbine ships.

Systems Design Philosophy

As a fuel savings system, RACER must not affect the safety or the mission capability of the ship. It must also be compatible with the unique and desirable characteristics of the gas turbine engine, that is, simple operation, fast startups, high reliability and availability. Thus the overriding design goal for the entire RACER system is simplicity. Simplicity must be the goal in construction, operation, and maintenance to provide the maximum energy recovery, reliability, and availability with minimum impact on current gas turbine ship operations. It is also desirable to have a system which has as many similarities as possible with a commercially marketable system to provide a production base.

The RACER system has been designed to meet not only the needs inherent with operation behind a gas turbine engine but also the generic requirements of the U.S. Navy. These design criteria require that the unit:

- Be a slave to the LM 2500 gas turbine unit and not adversely affect either the safety or mission capability of the ship
- Be virtually invisible to the ship operator in terms of control
- Have high reliability
- Have low maintenance (no more than 50 additional man-hours per week)
- Have high availability
- Have low makeup feedwater requirements (less than 10 gal [38 L] per day as a goal)
- Have compact modular components which are quickly replaceable
- Be inherently safe
- Have high response
- Require minimal system support logistics
- Possess low volume

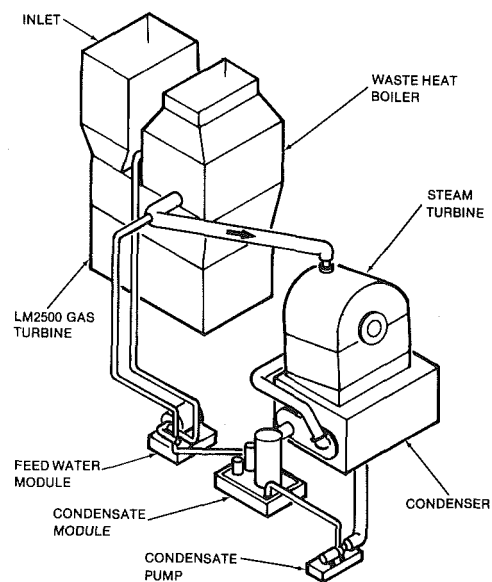


Fig. 1 Racer modular components

Contributed by the Gas Turbine Division of THE AMERICAN SOCIETY OF MECHANICAL ENGINEERS and presented at the 28th International Gas Turbine Conference and Exhibit, Phoenix, Arizona, March 27-31, 1983. Manuscript received at ASME Headquarters December 20, 1982. Paper No. 83-GT-50.

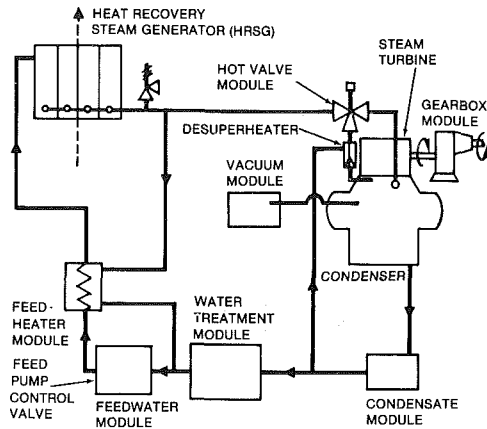


Fig. 2 Baseline schematic

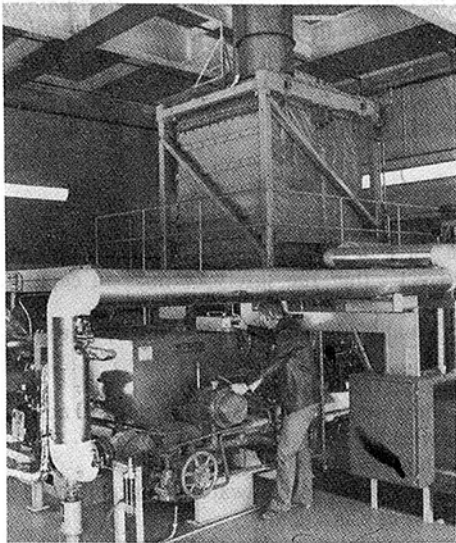


Fig. 3 Full-size industrial boiler

- Be capable of rapid startups
- Be capable of extended dry operation in the exhaust stream with no water flow
- Have low specific weight (lb/hp)

A review of conventional steam practices and systems reveal that they could not guarantee achieving the foregoing criteria; therefore, a new system, incorporating innovative design approaches, was necessary.

Figure 1 shows the modules or building blocks which comprise the RACER system, and Fig. 2 shows the baseline schematic. From the system's sizing point of view the dominant component is the waste heat boiler. The controls, water treatment subsystem, steam turbine, condenser, and feed pumps are essential, but have a lesser impact on the overall systems sizing.

Central to the development of the steam system is the choice of boiler concepts. Solar Turbines Incorporated has, for the past ten years, performed research and development of a new type of waste heat boiler for small industrial combined cycle equipment that is well matched to the criteria of RACER. As a result of completing more than two years of full-scale test and evaluation, both in the test cell and in the field, there exists a high degree of confidence in the compact once-through boiler (Fig. 3). The boiler uses corrosion-resistant materials as a keystone of the entire system design concept. The high efficiency and small size of the boiler minimizes material requirements; hence, more sophisticated corrosion-

resistant materials can be used without incurring substantial cost penalties.

The proven boiler concept makes it possible to design around traditional steam system problems and to use logical design principles in combination with advanced water treatment practices and latest materials knowledge to develop an advanced type of steam system that can meet all of the RACER's criteria. Many of the "new" items contained in the RACER are actually an adaptation of current nuclear and European practice, modified and applied to meet the goals and objectives of the system.

Thus, the system design philosophy can be summarized as identifying the problems and designing the system specifically to overcome each one. The overall concept is to provide a simple, reliable, safe, and easily maintainable system which can be accomplished through use of:

- Once-through boiler
- Passive water treatment, using the latest state-of-the-art deionization for feedwater and makeup water treatment
- Corrosion-resistant materials throughout the system which are compatible with the water treatment
- Condenser hotwell deaeration, eliminating the need for a separate deaerator
- Nearly total elimination of dynamic penetrations of the system to eliminate water/steam leakage
- Maximum integration and modularization of all components with all major components capable of being removed through the intake stack
- Titanium-tubed condenser with titanium-clad, double-tube sheets to eliminate sea water seepage or air leakage while minimizing weight and volume
- Single valve anticipatory control of waste heat boiler output conditions
- Safety enhanced by small boiler water inventory
- Use of all-welded tubular boiler, designed for maximum reliability and modular for easy repairability
- No special layup provisions, because of the materials used throughout the system and the self draining of the boiler

Some of the special design features of the RACER components are briefly discussed below.

Condensate Pump. The condensate pump is a canned motor unit to eliminate shaft seals and reduce leakage.

Boiler. The once-through boiler paces the system design philosophically. By proper design of the boiler and selection of materials, it is possible to greatly simplify the water treatment system and to make it a minor maintenance issue in the RACER design. It allows the incorporation of a passive water treatment system requiring only solids removal and no addition of chemicals. Industry has successfully utilized a similar type of water treatment in nuclear and supercritical utility power plants for years.

The use of an all-tubular boiler with no connections other than the inlet water and outlet steam headers makes a long-term, zero-leakage boiler practical by eliminating steam drums, water drums, drains, blowdowns, rolled tube-to-header connections, tube-to-drum connections, handhole, and manhole covers and gaskets. At the same time, inherent safety is provided because of the low water inventory and containment of all water and steam in the high structural integrity of the all-tubular design. Corrosion associated with crevices and dissimilar materials is eliminated, with water coming in contact only with a single corrosion-resistant material.

Since all joints and crevices have been eliminated in an all-welded tubular boiler which requires only a single valve to control its performance, a similar philosophy may be applied with confidence for the remainder of the system to minimize leakage from the system.

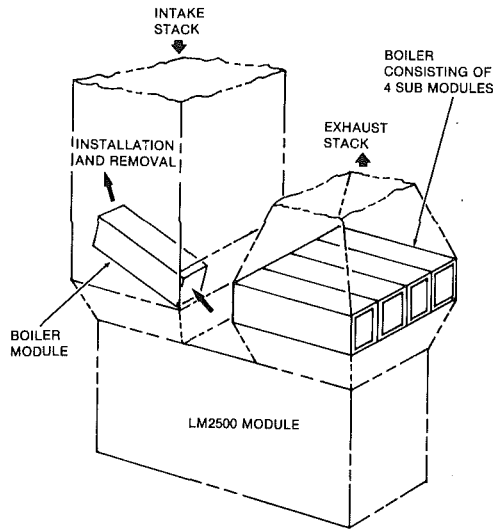


Fig. 4 Boiler installation and removal concept

Hot Valve. Steam generated by the boiler is piped to the modular hot valve which is an integrated, compact unit incorporating three basic functions: safety relief, steam turbine bypass, and steam turbine trip and throttle valves. This valve is actuated by fluid pressure from the feedpump, and is designed to fail in the safe position in the event of pressure loss. The safety relief or bypass valves directs the steam back to the condenser, which is designed to accept full-load dump flow conditions. The bypass is used during startups and shutdowns to prevent water or saturated steam from entering the steam turbine. The valve also controls the amount of steam flow to the steam turbine during startup, as well as provides a means of emergency shut-off of steam to the turbine.

The all-hydropneumatic dump valve provides the same function as the standard pilot operated safety valve. If steam pressure were to increase above the system set point, the pilot dump valve opens fully and stays open until system pressure falls to a prescribed value prior to allowing the valve to be closed. This all hydropneumatic overpressure safety system is a backup for an electric solenoid quick dump valve that would open at pressure levels lower than mechanical safety valve.

The same electric quick-dump valve is used as steam turbine overspeed protection by rapidly shutting the steam throttle and bypassing the boiler output to the condenser in case the steam turbine exceeds a prescribed rpm.

Steam Turbine. The steam turbine is a compact high-efficiency unit designed for floating pressure operation. The turbine drives from the LP end. The design precludes feed-water contamination by lube oil and all water drains are returned to the condenser to conserve and reduce the quantity of makeup water required.

Condenser. The use of titanium tubing will permit higher seawater velocity in the condenser tubes, substantially reducing the potential for fouling or plugging. An electrolytic chlorinator will also provide assurance against biological growth from plugging the condenser or degrading its performance. This concept will eliminate maintenance associated with condenser tube cleaning.

Component Removal. Since modern naval warships have developed a simple and effective technique to remove main propulsion engines through their respective stack, a similar criterion was used for RACER system components and has been incorporated in the design as illustrated in Fig. 4.

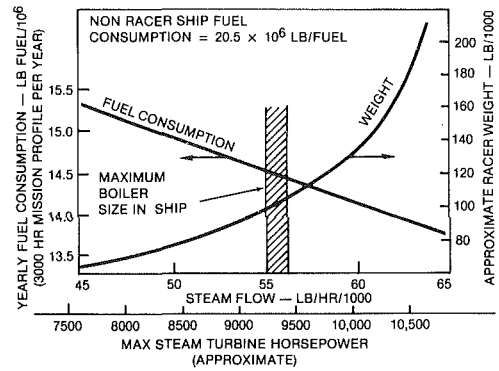


Fig. 5 Racer size effects on weight and fuel consumption

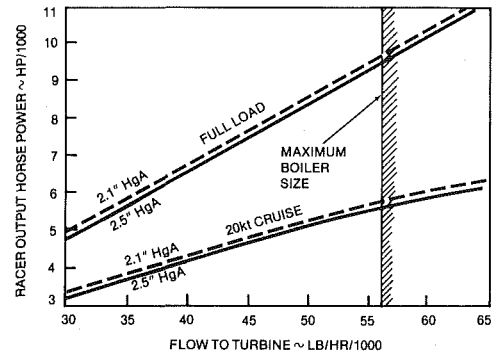


Fig. 6 Racer power output as a function of steam flow

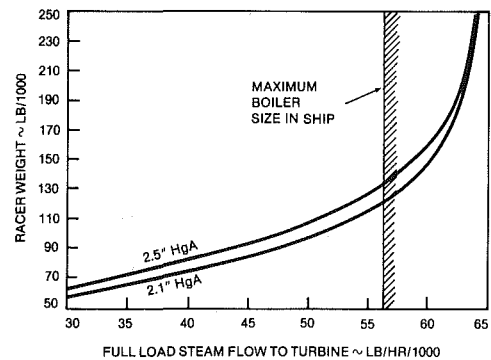


Fig. 7 Weight as a function of steam flow

Maintenance. All maintenance items have been designed for maximum simplicity so that unskilled operators can provide such routine maintenance as replacement of filter elements and deionization resins. Controls are fully automatic and require essentially no interface with the gas turbine controls. Only the simplest operator intervention is necessary (selector switch—off/standby/run). In addition, the microprocessor system controller can perform self and system diagnostic functions.

System Optimization

The size of the RACER system is governed by two basic criteria: the need to conserve fuel, and ship weight and volume constraints. As shown in Fig. 5, the greater the steam flow to the steam turbine, the larger the system and the greater the fuel savings. However, for the RACER system to be compatible with a naval combatant, minimum weight and volume must also be a major system design goal. Therefore, the final RACER design must be a trade-off between fuel savings and system weight and volume.

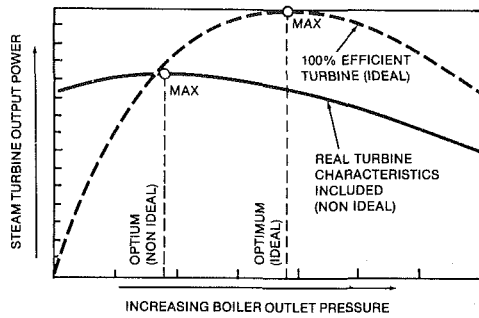


Fig. 8 Racer cycle optimization

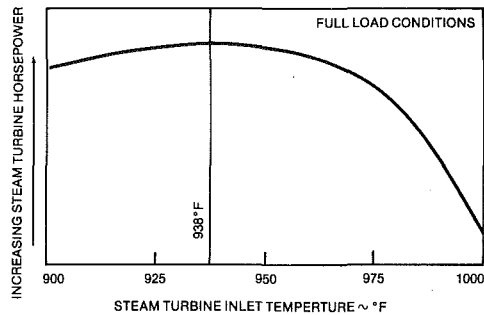


Fig. 9 Output horsepower as a function of inlet steam temperature

During the initial system sizing each component in the system is completely flexible with respect to size. That is, the size can be changed to meet the requirements of a particular ship. Thus, the system presented herein has been optimized for a given ship and engine room space.

Boiler. To maximize the system output power, it is desirable to increase the output steam flowrate as much as possible within the volume constraints of the ship's engine room. Output shaft power can be more easily increased by varying boiler steam output rather than by increasing turbine efficiency or increasing condenser vacuum. Thus, the boiler is the key in governing the system output power and the design is based on the largest boiler compatible with the space and weight constraint. The boiler sizing then determines the sizing of the remaining components in the system.

The primary limitation on boiler size is a ship constraint which limits the maximum boiler size to about $12 \times 12 \times 9$ ft ($3.7 \times 3.7 \times 2.7$ m). Using the same design concepts and the once-through boiler developed for industrial gas turbines, a modified design was developed for the RACER requirements of minimum weight and maximum output. The boiler differs only in tube diameters, fin heights, and support structure, but it retains the same concepts of a once-through boiler which provides for an efficient cross counterflow heat transfer matrix.

A once-through boiler was chosen over a conventional drum boiler because of its obvious advantages. These advantages include minimum weight and volume, rapid response capability, inherent simplicity, and much greater safety. The once-through boiler is much lighter than a conventional boiler and is much smaller for equivalent steam generation. Because of its smaller size it can respond much faster to load changes. Additionally, the once-through boiler has a much smaller water volume and is therefore much safer in the event of a tube failure.

The once-through boiler also greatly reduces the make-up feedwater requirements by eliminating the requirement for boiler blowdowns. This, in turn, eliminates the need for sophisticated feedwater treatment and allows for the passive feedwater treatment system selected.

The once-through boiler is also much simpler to control as

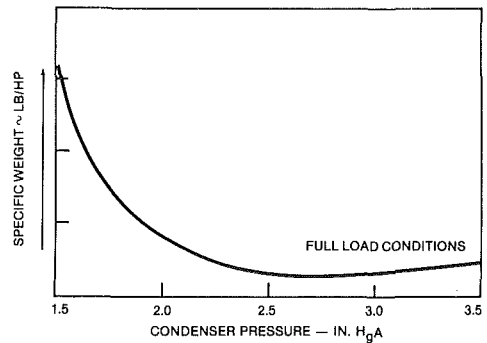


Fig. 10 System specific weight as a function of condenser vacuum

there are no drum level controls and no recirculation controls and pumps. Therefore, unmanned operation is readily achieved.

Steam Turbine. Since the maximum fuel usage during the given 3000 to 3500 hr yearly mission occurs around the cruise speeds, it is desirable to have the maximum turbine efficiency occur around the same point. To accomplish this, the steam turbine is designed for overpeaking to maximize the performance at the cruise condition while still maintaining high efficiencies up to full power.

The steam turbine must be designed to efficiently convert all the steam produced by the boiler into useable ship horsepower. Figure 6 shows that the output power from the steam turbine is a direct function of the flowrate. Also, slightly higher output power is attained for a given flow rate if a lower condenser pressure is used. The consequences of the higher output powers are shown in Fig. 7 as RACER weight increases rapidly above steam flow of 55,000 lbs/hr (25000 kg/hr). As seen from the curve, weight approaches an asymptote at around 63,500 pounds per hr (28,800 kg/hr) and weights are increasing extremely rapidly. The performance, however, is constrained by the maximum boiler size shown on the figures.

After the boiler size has been determined it then becomes necessary to optimize the pressure level at which steam is to be generated to obtain maximum steam turbine shaft output.

For a Navy combatant, such as cruiser and destroyer type ships, the important design points are at full and nominal cruise power. Thus the optimization was done for both full load and cruise conditions.

Figure 8 depicts the full load relationship between ideal steam turbine shaft output and operating steam pressure for the steam generator size chosen. Ideal (100 percent) steam turbine efficiency is utilized in order not to obscure the pure cycle effect sought. The characteristic dome shape of the curve shown is due to the fact that steam generator efficiency for single pressure waste heat recovery systems decreases with increasing pressure, whereas the internal rankine cycle efficiency increases with increasing pressure.

The foregoing would have constituted the complete pressure optimization if it were not for the fact that turbine efficiencies are not ideal (i.e., not 100 percent), that they also depend much upon pressure levels due to size effects (nozzle/blade heights, aspect ratios, blade tip clearances, etc.) and moisture effects. Figure 8 also shows how the optimum pressure and output power are lowered appreciably when these effects are included.

The thermodynamic advantage of operating the RACER plant in a floating pressure mode is clearly evident from analyses of this type at both full and cruise conditions. Both full load and cruise optimum operating points have the same relationship to the maximum SHP points—this would not have been the case for a constant pressure system. That is, designing for optimum conditions at full load will also give

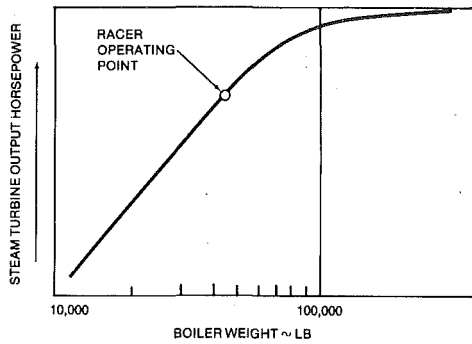


Fig. 11 Steam turbine horsepower as a function of boiler weight

near optimum performance at the cruise condition in a floating pressure system.

Outlet Steam Temperature. With a given size boiler, the outlet steam temperature must be optimized to maximize output power. Figure 9 shows the sensitivity of output power as a function of steam turbine inlet temperature for the selected boiler. The optimum inlet temperature appears to be around 938°F (500°C), but the curve is fairly flat and operation at high temperatures will allow for heat loss and degradation beyond the design conditions without affecting performance. Therefore, the 950°F (510°C) outlet temperature was chosen for the present system.

Condenser. Having defined the boiler size, steam flow rates, and steam turbine performance, the necessary system parameters have been defined to a point where the condenser sizing trade-offs can be made. As the condenser pressure is changed from the baseline value, the steam turbine, condenser, and vacuum subsystem weights also change. The minimum specific weight occurs at a condenser pressure of about 2.6 in. HgA (8.78 kPa) at full load conditions as shown in Fig. 10. However, the curve is fairly flat at the minimum, and a condenser pressure of 2.5 in. HgA (8.44 kPa) would provide more output power, hence fuel savings, with very little weight penalty. Further reduction in condenser pressure would result in a much greater condenser and steam turbine weights without corresponding increases in power.

The condenser sizing can now be performed assuming 75°F (23.9°C) cooling water and 2.5 in. HgA (8.44 kPa) condensing pressure at full load. Titanium tubes and titanium clad tube sheets were chosen to reduce weight by more than 4500 lbs (2040 kg) over a conventional copper-nickel tubed condenser. Titanium condenser tubes also allow the use of higher tube water velocities to prevent biological contamination. Thus, 12 ft/s (3.66 m/s) was chosen for the condenser design.

To increase system reliability, double tube sheets are used to offset the possibility of contaminating the RACER system water with sea water, a casualty which calls for shutdown of any steam system.

The condenser is also designed to take full dump steam flow for immediate transfer of steam from the steam turbine to the bypass mode of operation. This is a safety feature to allow power shedding, that is, to drop 90 percent of the shaft power within 10 s and 100 percent in less than two min.

Feedwater Heater. A direct contact feedwater heater has advantages over a tube and shell-type feedwater heater, primarily because of simplicity of operation, lower weight and volume, and higher operational efficiency, although the system will function with either. Both are currently being designed on a parallel development program for RACER.

Pumps. Since a major RACER system goal is simplicity,

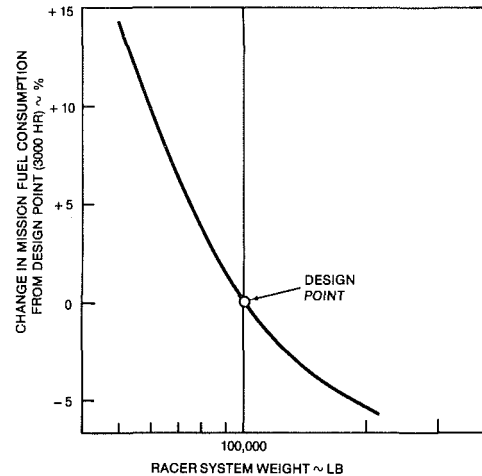


Fig. 12 Mission fuel consumption as a function of racer system weight

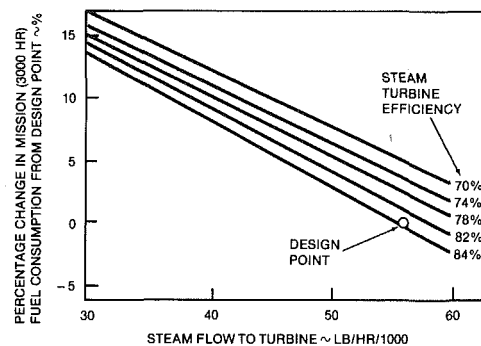


Fig. 13 Mission fuel consumption as a function of steam flow and steam turbine efficiency

single rather than duplex pumps and other auxiliaries have been used to reduce system weight and volume. System reliability goals can be achieved without duplexing, thereby making redundancy an unnecessary complication. This feature applies modern marine diesel engine and gas turbine philosophy (i.e., single readily replaceable lube pumps and fuel pumps) to the steam system design.

The condensate pump is a canned motor centrifugal pump and as such contains no dynamic penetrations to lose feedwater. The size range of the main feedpump precludes the use of readily available canned motor type pumps and, therefore, uses a high-speed centrifugal pump with a double mechanical seal to prevent excessive feedwater loss. A minor amount of feedwater leakage is anticipated with this type of sealing arrangement.

Vacuum Subsystems. The goal of simplicity for the RACER system precludes the use of standard steam ejectors for condenser air removal. With a floating pressure system, their operation is highly variable, more difficult to automate, and leakage of process fluid is more difficult to control.

A mechanical liquid ring vacuum pump was chosen for RACER because:

- It does not depend on system parameters for operation.
- It is electrically powered and can be immediately turned on and off.
- It provides for faster startups because it does not depend upon steam to initiate hogging.
- It is simple and adds a minimum of components which leads to increased system reliability and maintainability.
- It has a minimum of water loss from the system.

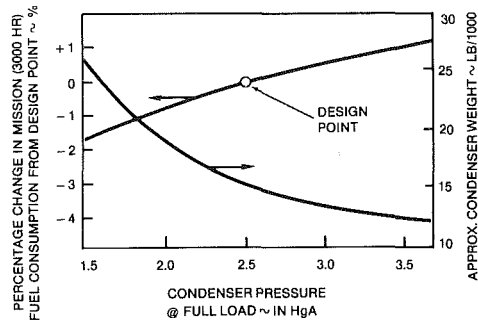


Fig. 14 Mission fuel consumption as a function of condenser pressure (full load)

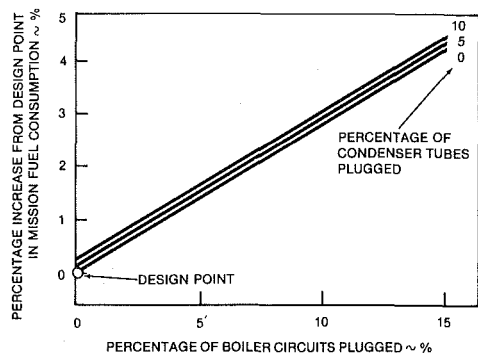


Fig. 15 Mission fuel consumption as a function of condenser pressure (fixed boiler and steam turbine)

System Sensitivity

The following discussion presents the system performance sensitivity to changes in various parameters.

The maximum full load steam turbine horsepower is shown in Fig. 11 as a function of boiler weight. As can be seen, above 70,000 lbs (31,750 kg) boiler weight, the curve starts to flatten out as it approaches an asymptote. Therefore boilers larger than this are definitely on the diminishing returns side of the curve. Smaller or larger boilers can be constructed to give lesser or greater outputs if required to meet the requirements of a specific installation. The point shown for the RACER operating condition represents the largest boiler that could advantageously be placed in the current ship.

The resultant fuel consumption over the 3000-hr mission is shown in Fig. 12 as a function of RACER system weight. The figure shows that, to satisfy the contract requirements of maximum fuel savings, the largest system compatible with ship constraints is indicated.

The sensitivity of the mission fuel consumption to variations in both the steam turbine full load efficiency (assuming the same efficiency curve shape with over peaking as used in RACER performance), and steam flow provided by the boiler is shown in Fig. 13.

The sensitivity of mission fuel consumption to condenser sizing, for a fixed boiler and steam turbine, is shown in Fig. 14.

Under certain circumstances it could become necessary to plug either some of the boiler circuits or condenser tubes

rather than replace the entire unit or repair it. The effects on overall fuel consumption of plugging up to 15 percent of the boiler circuits and up to 10 percent of the condenser tubes are shown in Fig. 15. The effect of plugging 10 percent of the condenser tubes varies from a slight amount to one-half of one percent fuel consumption over the 3000-hr mission profile. In contrast, an increase of 2.8 percent in mission profile fuel consumption is caused by plugging 10 percent of the boiler tubes.

The maximum horsepower developed is reduced by slightly less than a one-to-one ratio: 10 percent plugged boiler circuits equates to about a 9 percent reduction in steam flow and output horsepower, because the lower heat load yields a slightly lower condenser pressure resulting in a slight off-setting increase in output power. It was assumed that flow per circuit remained constant where in reality this could be increased slightly. However, this would tend to be offset by lower steam turbine efficiencies based on slightly lower volumetric flow rates.

Test Programs

The risk areas of concern will be addressed in more detail during the proposed test programs. The RACER system concept certainly does not hinge on any one of these areas. For instance, if leakage is increased from 10 gal per day (38 L/d) to 1 percent, or 1600 gal per day (6060 L/d), no change in the design is necessary. Low leakage enhances system reliability, but is by no means absolutely necessary.

A series of test programs will demonstrate and verify the proposed RACER technology issues. The current testing envisioned includes:

- 1 Closed-loop subscale module testing for about 15,000 hrs, primarily to verify the water side material interactions, including water chemistry upset conditions. Performance and some gas side fouling corrosion information will also be obtained. Bench scale tests will also be performed to screen materials.

- 2 A full-scale module test composed of one of the four RACER boiler modules will be used with full-size valving, etc. Gas side and water side conditions will be simulated as closely as possible (10,000-15,000 hrs).

- 3 Full-scale tests using an LM 2500 engine will be performed at NAVSSES, Philadelphia (1000 hrs) [3].

- 4 At sea, testing aboard the MSC chartered *Admiral Callaghan* is planned as is a land-based test facility of the complete propulsion system of the DDG-51, a NAVSSES Philadelphia.

The purpose of the subscale and the full-scale module tests are to accumulate a larger number of hours and provide further proof of the validity of RACER design parameters.

References

- 1 Miller, C. L., and Marron, H. D., "RACER—An Energy Conserving System for Ship Propulsion," *Proceedings of the 16th IECEC*, 1981, Atlanta, Ga.
- 2 Mattson, W. S., "Shipboard Energy Savings With the RACER System," *Naval Engineers Journal*, Feb. 1982.
- 3 Cipolla, R. F., and Collins, D. J., "The RACER System," *Proceedings of the 17th IECEC*, 1982, Los Angeles, Calif.

Investigation of F/A-18A Engine Throttle Usage and Parametric Sensitivities

C. L. Hall

Lead Engineer, Technology-Propulsion.

R. W. Hathaway

Engineer, Technology-Propulsion.

McDonnell Aircraft Company,
McDonnell Douglas Corporation,
St. Louis, Mo. 63166

S. M. Coté

Aerospace Engineer,
Naval Air Development Center,
Warminster, Pa.

Projection of realistic engine usage is essential for advanced tactical fighter aircraft to avoid significant durability problems and associated high weapon system costs. Previous engines such as the TF41 and F100 experienced durability deficiencies because actual field usage was more severe than initial projections. Thus, MCAIR developed systematic prediction procedures to provide improved usage estimates for preliminary design. These procedures based on digital flight simulation models were used to investigate throttle usage for peacetime training flights of the Navy F/A-18A aircraft with F404-GE-400 engines. The purpose was to identify major contributors to engine damaging usage and provide an early assessment of anticipated F/A-18A field utilization. Data are presented for individual mission throttle cycles and time histories as well as composite engine duty cycles. The prediction procedures were validated demonstrating excellent agreement by comparing results with flight data from the contractor phase of the Navy's Accelerated Service Test (AST) at Patuxent River Naval Air Station (NAS). Engine usage was projected for F/A-18A transitional training at Lemoore NAS, the first deployment site. Results indicate that the severity of cycles and hot time at Lemoore will be comparable to that for AST. The ground attack, air combat, and air intercept missions were found to contribute the most to usage. Sensitivities were also evaluated parametrically for F/A-18A aircraft performance and mission parameter variations. Usage was found to be most sensitive to aircraft thrust to weight, and insensitive to store drags. The results provide valuable insight into how missions, maneuvers, and aircraft performance parameters affect usage which is important for cost effective design of durable, high-performance engines.

1 Introduction

Definition of realistic duty cycle requirements early in the design phase is critical to providing superior performance and durability for cost effective advanced tactical aircraft engines. Overly stringent requirements result in increased weight and reduced performance. Inadequate requirements result in deficient durability with reduced readiness or costly maintenance, repair, and replacement plus component improvement retrofit programs. Comprehensive, systematic procedures have been developed by McDonnell Aircraft Company (MCAIR) for predicting engine usage based on digital flight simulation programs and a significant flight data base. These procedures have been applied to various CTOL and V/STOL designs and have successfully demonstrated the ability to calculate engine usage comparable to that measured in flight test, training programs, and field operations. The procedures have an advantage over other techniques which

rely on correlations of limited historical data for specific applications since aircraft/engine performance, advanced weapon systems and delivery tactics, missions, and basing are all taken into account. Further, they can readily be used to evaluate the impact of changes in performance and other parameters on usage without requiring expensive factory or flight testing.

This paper describes results from throttle usage analyses of the F/A-18A aircraft with F404-GE-400 engines conducted by MCAIR under sponsorship of the Naval Air Development Center (NADC) [1] and through Internal Research and Development studies. Significantly, F/A-18A engine usage predicted with MCAIR's analytical models described in section 3 agreed very well with flight data from the F404 engine Accelerated Service Test (AST) discussed in sections 4 and 5. Usage was also projected in section 6 for F/A-18A initial transitional training of Navy and Marine pilots at Lemoore NAS *before* flight data were available, illustrating the value of the procedures. Usage sensitivities to critical aircraft performance and mission variables were evaluated in section 7 using significant missions at Lemoore as a baseline. Conclusions drawn from this study are summarized in section 8.

Contributed by the Gas Turbine Division of THE AMERICAN SOCIETY OF MECHANICAL ENGINEERS and presented at the 28th International Gas Turbine Conference and Exhibit, Phoenix, Arizona, March 27-31, 1983. Manuscript received at ASME Headquarters December 21, 1982. Paper No. 83-GT-64.

2 Background

In 1975, the Navy selected an F404 powered F/A-18A to meet its new strike fighter requirement. The F404 engine, an evolutionary change from the flight verified YJ101 engine, was developed to satisfy F/A-18A mission performance requirements such as range, acceleration, and carrier suitability. The changes included: improved SFC, increased thrust, increased airflow, increased bypass ratio, improved thrust response, and the addition of an approach power compensator for carrier landings.

Other fighter aircraft turbofan engines at the time were experiencing serious reliability and durability problems with attendant shortages of spare parts. Thus, the Navy propulsion community had serious concerns that F404 reliability and durability might be less than predicted upon entering service. Consequently, Naval Air Systems Command (NAVAIR) expended considerable effort to define the expected engine usage of the F404 so that durability could be more accurately assessed and design changes could be identified as early as possible. The Operational Mission Environment (OME-II) engine power usage definition which resulted was characterized by nine mission profiles. Its purpose was to define expected power excursions which normally occur in peacetime training as well as during carrier deployment and was used for the 750-hr Simulated Mission Endurance Test (SMET) of the F404 engine. OME-II was also used as an engine duty cycle model for the specification durability requirements.

Later in the engine development program, the Navy reevaluated engine power usage related to the engine Accelerated Service Test (AST) in which two engines were to fly 1000 hrs in a "fleet leader" test to determine reliability and maintainability. In this reevaluation, six missions representing landbased training were defined for the AST program. The AST missions were task oriented whereas the OME-II missions were engine power usage oriented, i.e., the pilots performed the prescribed missions, and engine power usage was a fall-out. AST was completed in September 1982.

Analysis of the AST data has shown that the severity of engine usage was considerably higher than was anticipated in the OME-II mission definition. This result has an impact on projected engine durability and on engine parts usage predictions. Since the F404 engine has now moved into high production release, the Navy has a definite need to determine whether engine usage at Lemoore NAS and beyond will be as severe as indicated by AST, or more similar to OME-II which was the basis for durability, maintainability and reliability estimates. The answer will provide guidance in engine component improvement programs aimed at improving engine durability, etc., and will result in more efficient and effective provisioning of engine spare parts throughout the life of the F/A-18A program.

3 Usage Prediction Procedures

As mentioned, digital flight simulation models were applied to represent flight data and engine parameter time histories for peacetime missions. The detailed procedures are described in [1, 2, 3]. Complete missions defined from takeoff to landing were input considering tactics, maneuvers, training range constraints and aircraft performance, as illustrated in Fig. 1. Two MCAIR prediction models, the Generalized Engine Throttle Usage Program (GETUP) and the Multiple Opponent Air Battle Simulation Program (MOABS), were used along with a third program, Count, to analyze and summarize throttle excursions within the mission profiles.

GETUP simulates aircraft flight using three degree of freedom equations of motion assuming a point mass aircraft. Vector steering logic consists of resolving the aircraft velocity vector with the vector required to achieve the final conditions

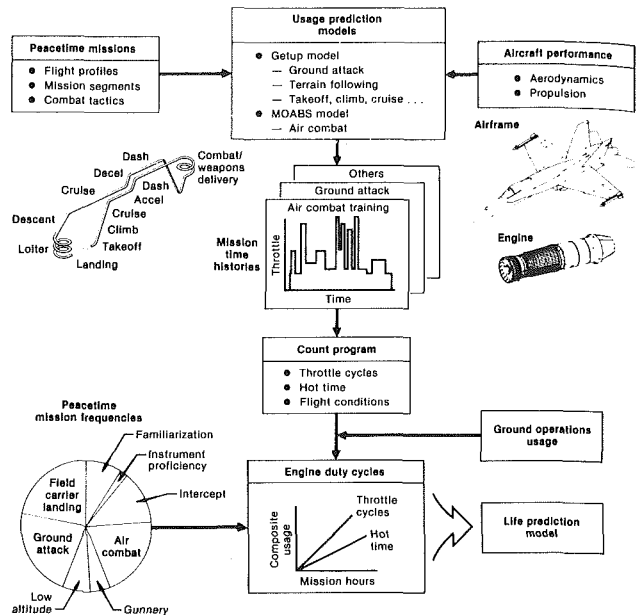


Fig. 1 MCAIR engine usage procedure

specified for each maneuver. The realistic predefined maneuvers available in GETUP were formulated based on flight test data, manned simulations, and pilot descriptions. These maneuvers are linked together in sequence from takeoff to landing. Mission segments represented include takeoff, climb, descent, cruise, aerial refueling, acceleration, deceleration, aerobatics, terrain following, air combat training, ground attack, and landing. Segments can be modified as required to represent more relaxed or demanding flights such as tighter loops, steeper climbs, higher g-loads, etc.

Performance data, including aerodynamic and propulsion characteristics, are input to represent each aircraft configuration in detail. Propulsion performance (thrust, fuel flow, power setting, engine response time, and other engine parameters) is determined using engine cycle decks and data provided by the engine companies. Aerodynamic performance is computed using MCAIR's Computerized Aircraft Design Evaluation program (CADE) for representing lift coefficients and drag polars. Configuration/store drags, weights, roll rates, maximum normal load factors, etc., are specified as inputs for each configuration.

MOABS is used to simulate air combat training for two to eight aircraft when more than predefined basic fighter maneuvers are required. MOABS utilizes the same equations of motion as GETUP, but the maneuvers are computed deterministically with established tactics based on relative position and energy. Starting conditions including Mach, altitude, separation distance, force ratio, and heading are specified for each engagement. The aircraft then maneuver automatically based on positional advantage, comparative performance, and weapons capabilities of the adversaries. Typically, air combat training is represented by averaging results from about 100 engagements chosen to simulate the variety of conditions encountered in actual practice. Air combat segments from MOABS are then combined with takeoff, landing, and cruise segments simulated in GETUP to form a complete combat mission.

Altitude, airspeed, and throttle time histories were computed for each simulated mission. A sample time history generated for ground attack training at Lemoore Naval Air Station (NAS), discussed in section 6, is presented in Fig. 2. The plot indicates the detail represented for each segment

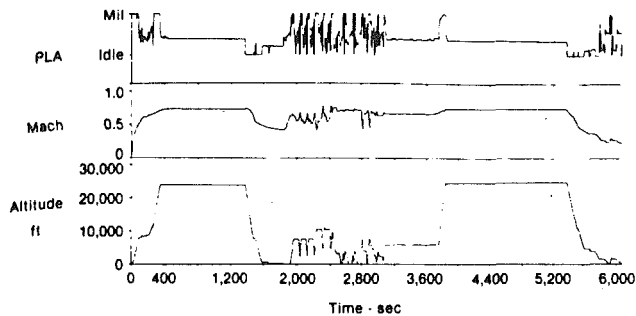


Fig. 2 Sample flight simulation time history F/A-18A ground attack training mission

including takeoff, the long distance cruise segments, repeated weapon deliveries, and touch and go landing practice.

Throttle time histories produced with GETUP and MOABS are analyzed using MCAIR's Count program. A rainflow counting technique is applied in Count using closed hysteresis loops as described in [4] to determine throttle cycles and hot time accumulations.

Engine duty cycles defining the average number of life limiting events that occur in normal operations are computed accounting for ground operations and average frequencies of missions flow. This composite usage provides a summary of the overall effects representing a mix of transitional and operational training. The throttle/mission time histories can be used by engine companies to assess operating severity and predict engine life.

4 AST Engine Usage

A study was conducted sponsored by NADC [1] to determine the capability of MCAIR's engine usage prediction models to simulate throttle usage from actual flight test data. Flight data were obtained from the F/A-18A Accelerated Service Test (AST) which was a 1000-hr, in-service evaluation in an instrumented F/A-18A aircraft to test engine durability. It was designed to duplicate the expected peacetime usage of the General Electric F404-GE-400 turbofan engines. Six well-defined mission profiles were used: (i) familiarization, (ii) instrument/cross country, (iii) air-to-air intercept, (iv) air combat, (v) navigation/low level, and (vi) air-to-ground attack. Each of these profiles was specified as a series of predetermined maneuvers selected to simulate field training. A detailed discussion of the AST missions is presented in [1].

The principal engine usage parameters tracked in the AST are defined in Table 1. Stress cycles define the amount of low-cycle fatigue damage to an engine. The throttle transients identified by General Electric as thermally and dynamically damaging transients that affect engine life include Low Cycle Fatigue (LCF), Full Thermal Cycles (FTC), and Other Major Thermal Cycles (OMTC). Hot time defines the damage due to creep and erosion in life-limited engine parts. Hot time is engine operating time spent at or near the maximum rated turbine inlet temperature (TAMP).

The AST engine usage was computed for each of the six mission profiles separately to compare with engine data recorded in-flight by the Navy-supplied Continuous Recording Data System (CRDS). The CRDS tape continually recorded existing aircraft flight conditions and engine parameters obtained from the aircraft FM-Multiplex Data Bus. Individual mission comparisons provided a better means of evaluating usage projections than that used in a previous study [3], where F-15/F100-PW-100 throttle usage data were only available for an overall engine duty cycle.

A mission analysis was conducted to identify the exact training range routes, restrictions, and maneuvers flown in the AST. The actual F/A-18A engine usage flight data, [5], were acquired during the second part of the AST contractor

Table 1 AST General Electric engine throttle cycle definitions

Description	Power setting variation (PLA)	Alternate definition
Cycles		
LCF: Low cycle fatigue cycle	0° - 80° - 0°	Type I (off-mil-off)
FTC: Full thermal cycles (includes LCF cycles)	40° - 80° - 40° ⁽¹⁾	Type III + Type I (idle-mil-idle)
OMTC: Other major thermal cycles	40° - 78° - 40° 40° - 75° - 40° 50° - 80° - 50° 50° - 78° - 50° 50° - 75° - 50°	Partial cycles
Hot time		
Time at military power (TAMP)	PLA > 92% MIL (80°)	Time at and above mil power

Note: (1) For F/A-18A F404 engine
Idle = 28° - 34°
Military = 84° - 89°

GP23-0756-2

Table 2 AST F/A-18A engine usage results (simulation compared to flight test data)⁽¹⁾

Missions	Mission frequency Percent		Flight time (hr)				Cycles per mission				Hot time per mission				A/B lights/flight	
					FTC-LCF ⁽²⁾		OMTC ⁽³⁾		TAMP ⁽⁴⁾		A/B time (min)					
	Sim	Act	Sim	Act	Sim	Act	Sim	Act	Sim	Act	Sim	Act	Sim	Act	Sim	Act
Familiarization	9	7.4	1.2	1.2	7.5	8.3	6.0	4.2	13.6	16.1	4.2	3.0	5.0	3.8		
Instrument/cross country	9	7.4	1.8	1.9	4.0	5.4	2.0	6.2	8.1	7.2	0	1.5	0	0.6		
Intercept/CAP	21	17.4	1.5	1.5	7.4	6.1	5.2	4.1	12.2	13.6	0.4	0.4	0.3	0.7		
Air combat	27	22.3	1.2	1.4	12.0	11.3	7.9	6.9	16.7	18.9	2.9	1.0	8.0	4.8		
Navigation/low level	7	5.8	1.3	1.4	4.0	4.9	1.0	3.8	1.7	3.2	0	0.3	0	1.2		
Air-to-ground	27	22.3	1.3	1.4	12.0	9.5	5.0	7.2	5.0	7.7	1.7	2.0	2.0	2.5		
Miscellaneous	—	17.4	—	1.1	—	6.9	—	4.3	—	8.9	—	1.2	—	1.7		
Composite	100	100	1.35	1.34	9.3	8.2	5.4	5.6	10.5	11.8	1.7	1.2	3.2	2.5		

Notes:

- (1) Actual data based on averaging L/H and R/H engine usage
- (2) FTC-LCF = Full Thermal Cycles minus Low Cycle Fatigue cycles
- (3) OMTC = Other Major Thermal Cycles
- (4) TAMP = Time At Military Power and above

GP23-0756-3

Table 3 F/A-18A AST engine duty cycle (162 flight hrs)

	Flight test data ⁽¹⁾	Simulation ⁽²⁾	Δ (percent)
Number of sorties	121	120	-1
Cycles			
Low cycle fatigue (LCF)	99	98	-1
Full Thermal (FTC)	1,093	1,214	11
Other Major Thermal (OMTC)	678	648	-4
Hot time			
Time at military power (TAMP)	23.7 hr	21.0 hr	-11
A/B time	2.5 hr	3.4 hr	36
A/B lights	297	384	29

Notes:

- (1) Based on GE's "F404 Accelerated Service Test II Demonstration Report", 21 October 1981
- (2) Based on composite simulation

phase (ASE-II) conducted at Patuxent River Naval Air Station (NAS) from May through October 1981. Data from a total of 121 flights and 162 flight hours were included in the analyses.

The results shown in Table 2, indicate good agreement between actual AST throttle usage and the MCAIR digital simulations. Slightly more cycles were projected than were indicated by flight data, whereas hot time was slightly underpredicted. In general, the results show the capability of the usage models to simulate realistic throttle usage in individual peacetime missions. In both the actual data and the simulation, more throttle transients were found to occur in the Air Combat and Air-to-Ground sorties than in the other missions. Also, the largest amount of hot time was found to occur in the Air Combat mission. The Navigation/Low Level mission was determined to be least damaging to the engine.

The composite usage shown in Table 2 represents the average cyclic and hot time accumulations per flight, established by frequency weighting the six missions. This composite can be used to represent an overall engine duty cycle of damaging events as shown in Table 3 for 162 flight hours. The composite simulation agreed very well with the cycles (LCF, FTC, and OMT) and hot time (TAMP) recorded in flight. Projected afterburner lights and afterburner hot time differed more from flight data due to both pilot variations and distinct deviations from planned operations. Note that normally at least one LCF cycle would occur per sortie. However, there were fewer in AST because ground operations at Patuxent River NAS including hot refueling, with both engines running at idle during refueling between sorties. This reduces the number of engine shut downs, i.e., LCF cycles. Such ground operations are readily modeled with MCAIR's engine usage procedure, Fig. 1. A more detailed discussion of the F/A-18A AST usage analysis is presented in [1].

5 AST Mission Segment Comparisons

MCAIR's simulations were further compared with flight data for selected mission segments to evaluate the modeling of specific maneuvers. Sample flight data time histories provided by General Electric for each of the six AST mission categories were used. The data recorded include power lever angle (PLA), Mach, altitude, spool speeds, exhaust gas temperature, and aircraft normal acceleration. The selected maneuvers presented here are a pop-up weapon delivery segment from the Navigation/Low Level mission and a touch and go, or field carrier landing practice (FCLP), from the Air-to-Ground mission. These segments were clearly identifiable in the sample time history traces.

A pop-up weapon delivery consists of a low-level, high-speed ingress to the target area, a rapid climb to acquire the target, a steep dive to deliver a conventional weapon, and a hard pull-up to egress the target area. The maximum altitude of a pop-up varies but is typically kept as low as practical while acquiring the target, to increase survivability.

The pop-up simulation is compared in Fig. 3 to the sample AST data: altitude, airspeed, normal load factor, and power setting. The maneuver was simulated with two different maximum altitudes, 7000 ft to match the sample AST altitude profile, and 4000 ft selected for good survivability. The 7000 ft pop-up matched the flight data very well with engine hot time in close agreement. However, the normal load factor on recovery from the dive of the actual flight data was higher than the simulation. This occurred since the simulation normal load factor after weapon release had to be low (1.25g) to avoid pulling out of the dive at a weapon release point much higher than the actual data to duplicate the actual altitude path. This suggests that in the sample case, the pilot was not concerned about hitting a specific target.

The low altitude 4000 ft pop-up simulation was found to take only half the time of the 7000 ft maneuver (as shown in Fig. 3), which reduced engine hot time significantly.

Power lever angle time histories for a touch-and-go landing practice segment are compared in Fig. 4. Both gear down and gear retracted were represented in the digital simulations. The aircraft gear and flaps remained down during go around for the flight data which is the typical procedure for Navy and Marine pilots. The gear down power setting simulation was found to agree closely with the flight data. No FTC cycles occurred in the segment since power was not reduced to idle. Less than 10 s was spent at military power in the climbout.

For the simulation with gear and flaps retracted during the climb, which is typical Air Force procedure, one FTC cycle was predicted. The throttle reached idle due to the airspeed restrictions and lower drag with gear up. Throttle cycling

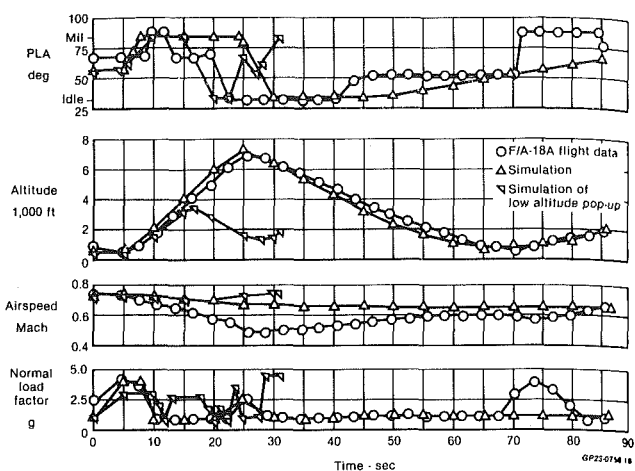


Fig. 3 AST pop-up weapon delivery comparison

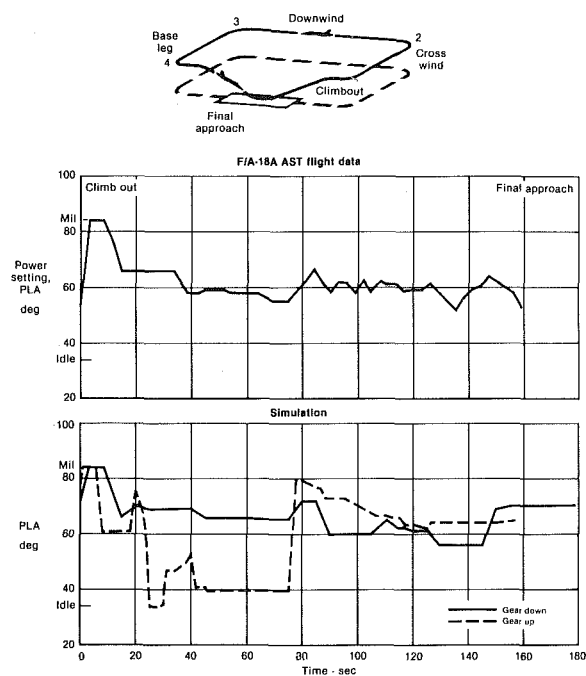


Fig. 4 AST touch and go landing segment comparison

associated with gear retraction would be more damaging to the engine in repeated landings.

These mission segment comparisons emphasize the importance of representing training maneuvers realistically. They demonstrate the capability and flexibility of MCAIR's engine usage tools in simulating training maneuvers to accurately predict engine usage. Also, MCAIR's digital simulation provides valuable insight into how alternate maneuvers affect throttle usage.

6 Projected F/A-18A Transitional Training Engine Usage

An engine duty cycle was projected for transitional training at the first F/A-18A base, Lemoore NAS, prior to initial deployment [1]. Such an early duty cycle projection provides valuable information that, along with engine life predictions, can be factored into a component improvement program, or used to improve service resource allocations and maintenance planning. An accurate, early definition of service usage is essential in achieving superior durability for advanced

engines, as acknowledged by engine manufacturers, such as by General Electric in [6]. This is important, both in the design process and in predicting life, after component durability characteristics are established to produce better engines at lower program cost.

Nine nominal missions and associated frequencies were identified to represent F/A-18A transitional training based on the syllabus planned for Lemoore NAS. These nine missions include: (i) familiarization, (ii) instrument training, (iii, iv) intercept training with and without aerial refueling, (v) air combat, (vi) aerial gunnery, (vii) low-altitude tactics (navigation), (viii) ground attack, and (ix) field carrier landing practice (FCLP). Three of the missions are not included in the AST missions: intercept training with refueling, aerial gunnery, and FCLP. Also, there are substantial differences for the other six mission profiles between Lemoore and AST even though the missions have the same labels. The principal differences are the longer cruise distances at Lemoore, illustrated in Fig. 2, the airframe configuration with external fuel tank at Lemoore, and training against actual adversary aircraft at Lemoore, whereas AST performed basic maneuvers against imaginary threats. The nominal configuration for Lemoore NAS has wing tip mounted AIM-9L missiles and a 315 gal centerline tank required to assure adequate training time, since all of the military operating areas are over 100 nautical miles away. A detailed discussion of other mission differences is included in [1].

The resulting throttle cycles and hot time accumulations projected for the nine Lemoore mission profiles are presented in Table 4. A composite usage is also presented which was computed based on relative mission frequencies from the Lemoore NAS training syllabus.

The Aerial Gunnery mission was projected to accumulate the most throttle cycles per mission due to repeated weaving passes at a banner towed in straight runs. However, the ground attack and air combat missions contribute more throttle cycles to the composite usage since their mission frequencies are higher. The field carrier landing and instrument missions have the least number of major throttle transients. The air combat, familiarization, and gunnery missions accumulate the most hot time per mission, whereas the air combat, ground attack, and familiarization missions contribute the most total hot time, respectively, to the composite mission. The intercept with refueling, low altitude, and FCLP missions contribute the least to the composite mission hot time.

A comparison of a 1000 mission hr engine duty cycle for the AST and the Lemoore NAS engine usage is presented in Table 5. The engine duty cycles are based on the composite usage presented in Table 2 for the AST missions and Table 4 for Lemoore transitional training. The Lemoore duty cycle, based on nine missions, was projected to have 3 percent more Full Thermal Cycles (FTC) and 33 percent more Other Major Thermal Cycles (OMTC) than the AST flight data, primarily due to increased throttle cycling in training. Lemoore was projected to have slightly less hot time (time spent above a PLA setting of 80 deg) with 8.2 percent versus 10.6 percent hot time due to the long cruise legs at Lemoore. The average Lemoore mission length was similar to AST, because the short duration FCLP mission offset the long cruise times.

For a more direct comparison, an alternate engine duty cycle at Lemoore was projected based on only the six Lemoore nominal missions most similar to the six AST missions, using AST mission frequencies. The resulting Lemoore duty cycle has fewer sorties and throttle cycles, but more hot time, as shown in Table 5. The major factor causing differences between these duty cycles is the average mission cruise lengths. The 2.05-hr average mission time for the six mission Lemoore duty cycle reflects the long cruise distances to Lemoore's training areas. The 1.88-hr average mission time

Table 4 Projected F/A-18A transitional training (Lemoore) engine usage

Missions	Frequency Percent	Flight Time (hr)	Cycles			Hot time		A/B lights
			LCF(1)	FTC(2)	OMTC(3)	TAMP(4) (min)	A/B (min)	
Familiarization	9	1.54	1.1	10.1	9.0	16.3	0.5	1.0
Instrument	2	2.16	1.0	6.0	2.0	6.3	0.0	0.0
Intercept								
With refueling	2	1.68	1.0	8.0	4.0	3.9	0.7	2.0
Without refueling	11	1.52	1.0	11.0	7.0	6.5	0.4	1.0
Air combat	20	1.26	1.0	9.0	11.0	18.1	8.1	16.0
Gunnery	5	1.73	1.0	33.0	20.0	15.7	0.0	0.0
Low altitude	7	1.58	1.0	8.0	1.0	4.1	0.0	0.0
Ground Attack	22	1.73	1.0	13.0	9.0	8.0	0.0	0.0
Field carrier landing	22	0.77	1.0	2.0	3.0	2.0	0.0	0.0
Composite	100	1.38	1.01	9.71	7.61	9.25	1.69	3.37

Notes:

- (1) LCF - Low Cycle Fatigue cycles
- (2) FTC - Full Thermal Cycles
- (3) OMTC - Other Major Thermal Cycles
- (4) TAMP - Time At Military Power and above

GP23-0756-5

Table 5 AST versus Lemoore engine duty cycle comparison⁽¹⁾ (1000 mission hours)

	AST		Lemoore ⁽²⁾ (9 mission profiles)	Δ ⁽³⁾ (percent)	Lemoore ⁽⁴⁾ (6 mission profiles)	Δ ⁽³⁾ (percent)
	sim ⁽⁵⁾	(actual)				
Number of Sorties	540	543	532	-2.0	488	-10.1
Average mission length	1.85 hr	1.84 hr	1.88 hr	2.2	2.05 hr	11.4
Cycles						
Low cycle fatigue	544	545	537.0	-1.5	492	-9.7
Full thermal	5,542	5,011	5,166.0	3.1	5,006	-0.1
Other major thermal	2,916	3,047	4,049.0	32.9	3,870	27.0
Time at military power	94.8 hr	106.4 hr	82.0 hr	-22.9	86.9 hr	-18.3
A/B time	15.3 hr	11.2 hr	15.0 hr	33.9	19.0 hr	69.6
A/B lights	1,728.0	1,329.0	1,793.0	34.9	2,255.0	69.7

Notes:

- (1) Assume 30 minutes ground time per sortie.
- (2) A Lemoore engine duty cycle based on the Lemoore training syllabus.
- (3) Percent Δ compared to actual AST values.
- (4) A Lemoore NAS engine duty cycle using the 6 Lemoore mission profiles comparable to the AST missions and using the simulation AST frequency.
- (5) Simulation revised to account for engine ground check and PLA vs PLAP difference.

GP23-0756-18

for the nine mission Lemoore duty cycle is reduced due to the effect of the significant (22 percent) FCLP training.

The F/A-18A duty cycle projected for Lemoore is comparable to that estimated in [7] for other Navy aircraft, including the F-4J, A-4M, and A-7E, although there are generally more cycles and less hot time associated with the F/A-18A transitional training. LCF cycles for these aircraft vary within 10 percent, FTC range up to 20 percent higher than the projected F/A-18A, and hot time compares within 4 percent of total operating time.

To summarize, the AST duty cycle approximates the average operational usage projected for transitional training at Lemoore NAS. The long cruise distances at Lemoore which reduce the average throttle cycles and percent hot time due to long mission times are offset by the short FCLP mission. As noted in [6] the severity of engine usage for AST in terms of thermal cycles, hot time, and afterburner lights is somewhat higher than for the design OME-II duty cycle. Average transitional training usage therefore may also be high, depending on the actual mission frequencies and operating procedures.

The detailed Lemoore simulations provide valuable insight into the relative severity of planned missions on engine usage. Applying this information, F404 engine life may be extended by modifying training procedures as required to reduce engine damaging events, thus reducing program costs.

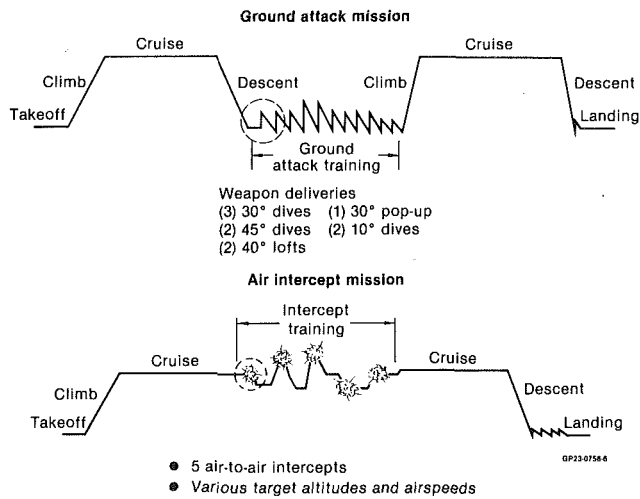


Fig. 5 Selected mission profile definitions

7 Parametric Sensitivities

MCAIR's usage prediction tools were applied parametrically to evaluate the effects of aircraft performance and mission parameters on engine throttle usage. Previous studies [2, 3] have shown that usage can be substantially affected by these parameters. It is important to quantify the sensitivities, so that engine durability can be properly considered in the design and operation of the weapon system. This was readily and economically accomplished using MCAIR's systematic analysis procedures. Similar analyses of sensitivities for fighter aircraft, engines, and missions are being conducted by MCAIR under contract to the Air Force [8].

Sensitivities were computed for the F/A-18A aircraft with F404 engines, wing-tip-mounted AIM-9L missiles, and a centerline fuel tank. Missions were selected from the projected training at Lemoore NAS discussed in Section 6. Aircraft design parameters investigated included thrust to weight ratio (T/W), wing loading (W/S), and store drags. Thrust loading was varied over a range of ± 10 percent about the baseline representing performance increments typical for a growth engine and a deteriorated engine. Wing loading was varied over a range of ± 10 lb/ft² by changing the wing reference area about the baseline of 400 ft². The selected store drag configurations which include wing tip AIM-9L missiles, inboard wing pylons, and a centerline tank represent nominal F/A-18A configurations projected for peacetime training at Lemoore.

Usage sensitivities were determined for the Ground Attack and Air Intercept training missions at Lemoore, since they contribute much to the overall usage, as noted in Section 6. Profiles for these missions are summarized in Fig. 5. A time history plot of the simulated ground attack mission is shown in Fig. 2. Mission sensitivities to the aircraft parameters are presented in Fig. 6. Accumulated hot time was found to decrease with increasing T/W for both missions. Less time and energy were required with higher thrust in the weapon delivery climbs for ground attack, and less was required to catch the same target aircraft for air intercept segments. Full Thermal Cycles (FTC) remained fixed for the ground attack mission and decreased only one cycle with increased thrust in the air intercept mission as a lower power setting was required. The reduced throttle excursion caused the FTC to become an Other Major Thermal Cycle (OMTC), as defined in Table 1.

Hot time was found to be insensitive to wing loading in the ground attack mission, whereas it increased with higher wing

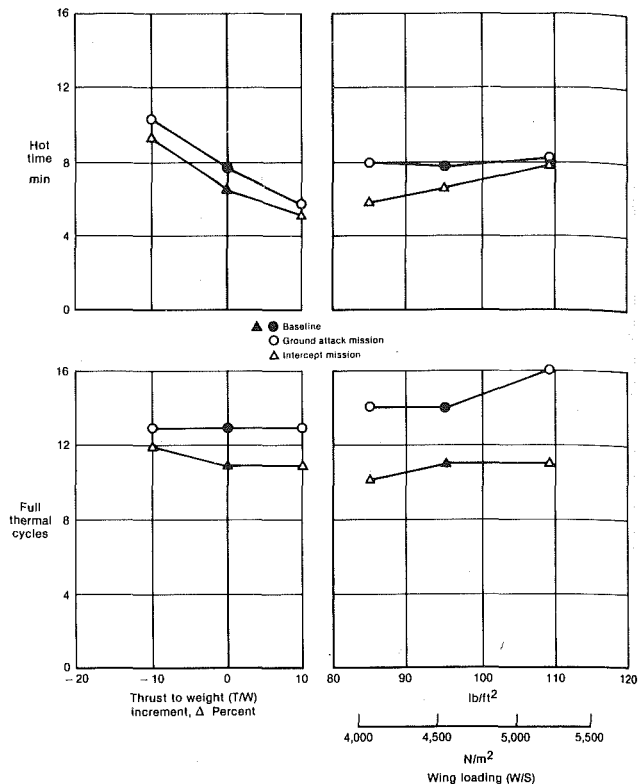


Fig. 6 Mission sensitivities to aircraft parameters

Baseline maneuver description	Number of training events	Usage per segment		Percent of composite usage	
		Full thermal cycles	Hot time (sec)	Full thermal cycles	Hot time
Dive pattern — 30° dive angle — 8,000 ft pattern altitude	7	2	15	31.5	4.2
Intercept — Altitude: 20,000 ft / 20,000 ft — Airspeed: 440 kts / 320 kts — Heading: 0° / 175° Interceptor → Target	7	3	130	18.9	8.4
Air combat engagement — Head on pass — Mach 0.9/30,000 ft co-altitude — 4 NM initial separation — Threat F/A-18 restricted to military power Fair fight starting condition Biased starting conditions	5	2	50	29.8	23.0
Total				80.2	35.6

Fig. 7 Mission segment impact on composite usage

loadings for air intercept. As wing loading increased, maneuverability was decreased, requiring more time turning in intermediate power to intercept the target. FTC cycles increased slightly with wing loading as shown in Fig. 6. For the ground attack, the lower drag of the high wing loading aircraft necessitated reducing the power setting down to idle in the two 10 deg dive passes which increased the number of FTC and reduced the OMTC cycles. Similarly, for air intercept, more FTC cycles are counted with increased wing loading as fewer OMTC cycles occur. The altitudes, airspeeds, and normal load factors selected to represent the maneuvers throughout each mission influence the usage results as much as the cycle definitions. Thus, it is important to model the actual training procedures as closely as possible.

Usage sensitivities to performance were further investigated for critical mission segments from the ground attack, air

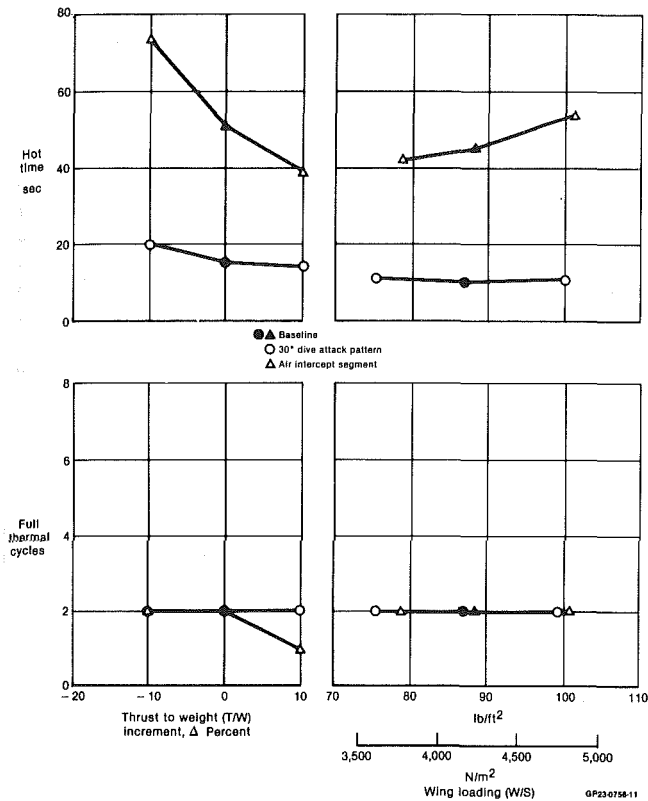


Fig. 8 Mission segment sensitivities to aircraft parameters

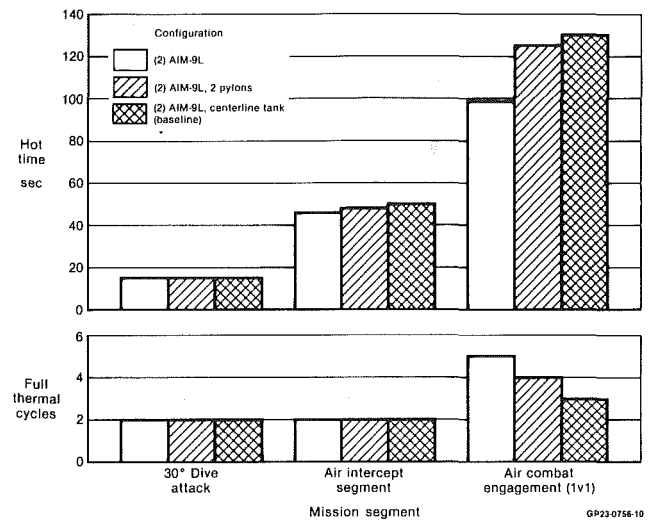


Fig. 9 Mission segment sensitivities to store drag

intercept, and air combat missions. The segments include (i) a 30 deg ground attack dive pattern, (ii) an air-to-air intercept, and (iii) an air combat engagement. These segments are significant because they are projected to contribute 80 percent of the full thermal cycles and one-third of the total hot time at Lemoore, as noted in Fig. 7. The baseline dive is a tight racetrack pattern with a 30 deg dive weapon delivery followed by a hard turning climb to a pattern altitude of 8,000 ft. The baseline air intercept is a forward sector co-altitude intercept against another F/A-18A simulating a bomber with limited speed and maneuvering capability. The baseline air combat engagement represents a head-on, one aircraft versus one aircraft (1v1) neutral setup against an F/A-18A threat restricted to military power.

Resulting sensitivities to aircraft T/W and W/S for the 30

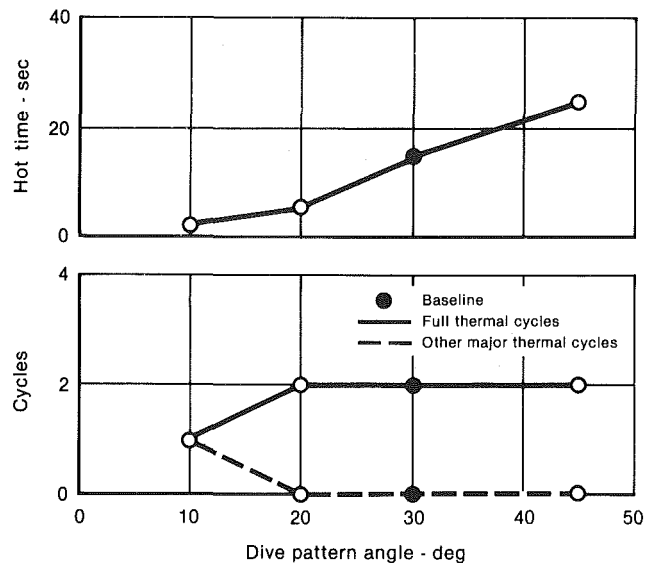


Fig. 10 Simulation engine usage sensitivity to changing dive pattern (variations in dive angle, pattern altitude, and initial airspeed)

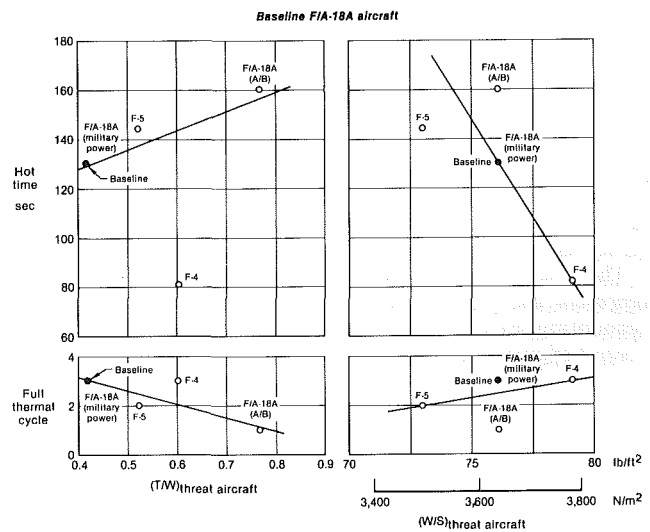


Fig. 11 Air combat engagement mission usage sensitivity to threat aircraft performance

deg dive and air intercept mission segments are shown in Fig. 8. The same trends for hot time accumulated during a mission can also be seen for the mission segments. The hot time accumulated during the air intercept mission segment was found to be more sensitive to changing T/W or W/S than in the ground attack segment. Throttle cycles were insensitive to thrust and wing loading for these mission segments.

Usage sensitivities to selected store drag configurations were also determined for the critical mission segments. As shown in Fig. 9, changing aircraft store drag configurations at a constant aircraft weight had no engine usage impact for the ground attack and air intercept segments. In the air combat engagement, as store drag was increased, the accumulated hot time was projected to increase and FTC cycles decrease. This sensitivity to store drag is caused by a shift from offensive to defensive tactics as drag is increased.

Sensitivities to mission parameters were computed for the F/A-18A aircraft by changing mission segment descriptions. These sensitivities indicate the effects of pilot variations and training scenarios on usage. They also establish how critical the assumptions are in modeling missions. Pattern altitude,

normal load factors, airspeeds, dive angle, and dive pattern type were independently varied to determine engine usage sensitivities in the ground attack segment. Target heading, altitude, and airspeed were varied in the air intercept segment. Initial separation distance, relative bearing, engagement time, and type of threat aircraft were varied in the air combat engagement. These results were reported in [1].

Changes due to pilot variability, such as airspeed or normal load factor, were found to have little impact on engine usage throttle cycles and only limited effect on hot time for the given mission segments. However, engine usage was found to be more sensitive to variations in training procedures. For example, accumulated hot time increased substantially with dive pattern angle, for different ground attack weapon delivery patterns, as shown in Fig. 10. This occurred because the bombing pattern altitude increased with dive angle and more energy was required to climb back to the pattern altitude.

Another example of the impact of changing training scenarios on usage is presented in Fig. 11. Engine usage associated with engaging various threat aircraft including the F-4, F-5, and F/A-18A in air combat segments was determined as a function of the threat aircraft's thrust loading at 0.9 Mach and 20,000 ft and as a function of wing loading. The threat aircraft's initial air combat weight was used to compute thrust to weight ratio and wing loading. In general, the baseline F/A-18A spent more time at high power settings against increased T/W threats resulting in increased hot time and fewer FTC cycles. The exception to this was the F-4 engagement. The high F-4 wing loading explains the lower hot time required. This resulted because hot time decreased, whereas cycles increased with a higher wing loading threat, as shown in Fig. 11. MOABS effectively represents air combat engine usage since the built-in tactics automatically accommodate these changes in threat aircraft performance.

The sensitivities described above emphasize the need to represent the actual training missions as closely as possible, accounting for changes in aircraft performance to accurately project engine throttle usage.

8 Conclusions

MCAIR's engine usage prediction procedures have been applied to the F/A-18A aircraft considering the effects of performance and mission parameters. The engine usage predicted for the F/A-18A F404 Accelerated Service Test agreed well with the actual AST flight data. Previous comparisons of predicted throttle usage to actual flight data were available only for composite or average usage. The AST data provided means to compare MCAIR's detailed engine usage predictions for individual mission throttle usage. The results show that MCAIR's procedures provide a powerful and reliable tool for evaluating usage which is essential in the design, analysis, and testing of durable advanced fighter engines. Realistic usage projections early in the development

process of an engine contribute to proper balance between performance and life with consequent lower acquisition or support costs.

The F/A-18A F404 engine duty cycle projected for Lemoore NAS indicates that peacetime transitional training will be as severe as the AST in terms of low cycle fatigue and full thermal cycles. The long cruise distances at Lemoore NAS which reduce throttle cycles and hot time due to long mission times are offset by the short field carrier landing practice flight time. Furthermore, when several more F/A-18A squadrons are established and they begin to co-locate at NAS Fallon and NAS Yuma, the long cruise effect may be negated. Depending on the missions, frequencies and aircraft configurations employed, usage potentially could increase beyond the severity of AST.

The engine usage sensitivities computed for variations in F/A-18A aircraft performance parameters show that thrust-to-weight ratio and wing loading significantly affect throttle cycles and hot time for ground attack dives, air intercept, and air combat mission segments. Usage was found to be insensitive to the store drag variations considered for the ground attack and air intercept mission segments. However, for air combat segments, usage varied with the alternate store drags. Mission parameters representing significant changes in training scenarios, such as ground attack dive angle and air combat against different threat aircraft, were found to strongly influence usage.

Further study is required to determine other key aircraft, engine, and mission parameters affecting engine usage, such as engine deterioration, ambient temperature, and the impact of advanced technologies for reduced observables. Also, enhanced procedures should be developed for utilizing the usage time histories to predict the impact on engine life and cost so that advanced design trades can be made between performance and durability.

References

- 1 Hall, C. L., and Hathaway, R. W., "Navy Engine Throttle Usage Analysis and Validation," Report No. NADC-81150-60, June 1, 1982.
- 2 Dietrick, C. C., and Schuppan, K. I., "Engine Usage Prediction for Advanced Fighter Aircraft," AIAA Paper No. 81-1367, July 27-29, 1981.
- 3 Osmer, J. G., and Dietrick, C. C., "Life and Utilization Criteria Identification in Design (LUCID), AFWAL-TR-81-2101, Vol. 11, Oct. 1981.
- 4 Dowling, N. E., "Fatigue Failure Predictions for Complicated Stress-Strain Histories," *Journal of Materials*, JMLSA, Vol. 7, No. 1, Mar. 1972, pp. 71-87.
- 5 General Electric Aircraft Engine Group, "F404 Accelerated Service Test II Demonstration Report," Contract No. N0019-76-C-0261, No. 81-MSS-37, October 21, 1981.
- 6 Rapp, G., "The F404 Development Program—A New Approach," AIAA Paper 82-1180, June 21-23, 1982.
- 7 Cote, S. M., and Byers, J. L., "Operational Environment of Naval Aircraft Gas Turbines," *Journal of Aircraft*, Vol. 16, No. 10, Article No. 78-1088R, Oct. 1979.
- 8 "Engine Usage Sensitivity Study and Procedure Validation," AFWAL/POTA Contract No. F33615-82-C-2200, Dec. 1981.

The Feasibility of Water Injection Into the Turbine Coolant to Permit Gas Turbine Contingency Power for Helicopter Application

G. J. Van Fossen

National Aeronautics and
Space Administration,
Lewis Research Center,
Cleveland, Ohio 44135

A system which would allow a substantially increased output from a turboshaft engine for brief periods in emergency situations with little or no loss of turbine stress rupture life is proposed and studied analytically. The increased engine output is obtained by turbine overtemperature; however, the temperature of the compressor bleed air used for hot section cooling is lowered by injecting and evaporating water. This decrease in cooling air temperature can offset the effect of increased gas temperature and increased shaft speed and thus keep turbine blade stress rupture life constant. The analysis utilized the Navy NASA Engine Program or NNEP computer code to model the turboshaft engine in both design and off-design modes. This report is concerned with the effect of the proposed method of power augmentation on the engine cycle and turbine components. A simple cycle turboshaft engine with a 16:1 pressure ratio and a 1533 K (2760° R) turbine inlet temperature operating at sea level static conditions was studied to determine the possible power increase and the effect on turbine stress rupture life that could be expected using the proposed emergency cooling scheme. The analysis showed a 54 percent increase in output power can be achieved with no loss in gas generator turbine stress rupture life. A 231 K (415° F) rise in turbine inlet temperature is required for this level of augmentation. The required water flow rate was found to be 0.0109 kg water per kg of engine air flow. For a 4.474 MW (6000 shp) engine this would require 32.26 kg (71.13 lbm) of water for a 2.5 min transient. At this power level, approximately 25 percent of the uncooled power turbine life is used up in a 2 1/2-min transient. If the power turbine were cooled, this loss of stress-rupture life could be reduced to zero. Also presented in this report are the results of an analysis used to determine the length of time a ceramic thermal barrier coating would delay the temperature rise in hot parts during operation at elevated temperatures. It was hoped that the thermal barrier could be used as a scheme to allow increased engine output while maintaining the life of hot section parts during short overtemperature transients. The thermal barrier coating was shown to be ineffective in reducing blade metal temperature rise during a 2.5-min overtemperature.

Introduction

Power from a helicopter engine at levels greater than the maximum rating may be desirable in several emergency situations. One scenario might be: a large twin engine helicopter with a full load loses one engine, the pilot requires increased power for a brief period from the remaining engine to land safely. This is the one engine inoperative (OEI) case. Another situation might be a hot day at high altitude where a power level greater than the 5 to 15 min maximum power rating is required for a short duration to insure a safe takeoff.

Contributed by the Gas Turbine Division of THE AMERICAN SOCIETY OF MECHANICAL ENGINEERS and presented at the 28th International Gas Turbine Conference and Exhibit, Phoenix, Arizona, March 27-31, 1983. Manuscript received at ASME Headquarters December 21, 1982. Paper No. 83-GT-66.

Copies will be available until January 1984.

Semple et al. [1] analyzed combat loss data for twin-engine helicopters. They found that 90 percent of power losses involved only one engine. They claim that if the remaining engine would have been capable of emergency power levels greater than fifty percent of the maximum power rating then power loss mishaps could have been reduced from 13.3 per 100,000 hours to 5.9 per 100,000 hours.

In [1] it was also found that emergency power capability in the OEI situation would also benefit commercial helicopter operation. Current gross weight capacity is limited by OEI capability. A 24 percent emergency power increase relative to maximum power rating would allow the load for the Boeing model 107 to be increased from six to twenty passengers on a 38° C (100° F) day.

Methods of augmentation with OEI were studied in [2]. The main conclusions reached were that a combination of water/alcohol injection into the inlet and over-temperature/overspeed could provide adequate emergency power. With this method of obtaining emergency power, hot section life is reduced to hours. Hot section replacement would thus be required after emergency power application. It is pointed out in [2] that to comply with present FAA regulations, emergency power must be demonstrated in a daily preflight check. This limits the use of overtemperature because of damage to hot section parts.

Dugas [3] studied many different possible augmentation systems. He defined two different levels of emergency power; one was hot day, high altitude augmentation. The engine would be required to produce the same power as at sea level standard day for five min with no loss of engine life. The second level of augmentation would be at sea level standard day conditions with OEI. The remaining engine would be required to produce 90 percent of the total installed power of both engines for one min without regard to engine life. The preferred methods of augmentation involved compressor inlet water injection and/or turbine overtemperature with fuel cooling of turbine cooling air.

Brooks [4] investigated the effects on engine operating conditions of power augmentation levels of 10, 20, and 50 percent relative to intermediate rated power (IRP) for a 2 1/2-min transient. In all cases, the method of augmentation was overspeed/overtemperature and, in addition, for the 50 percent power augmentation level water injection into the compressor inlet was used. He assumed that the 10 percent augmentation level would require no specific maintenance but the higher level would require post inspection and repair as necessary. The conclusion was that the 10 and 20 percent levels would be feasible and would not adversely affect the engine design by increasing size, weight, SFC, etc. Augmentation levels in excess of 20 percent are expected to be limited by compressor surge and local hot spots which would cause corrosion and/or adversely affect hot component life.

In 1977, while the author was conducting a literature survey on the application of liquid cooling to gas turbines [5], a scheme which would allow water cooling to be applied to the contingency power problem was conceived. Initial calculations showed the scheme had promise and in 1978 more detailed calculations were made using the NNEP computer

code [6]. The purpose of this report is to document the results of the feasibility study which analytically investigated the maximum possible level of augmentation with constant gas generator turbine stress rupture life as a constraint.

In the proposed emergency power augmentation scheme, the increased engine output is obtained by turbine over-temperature, however, the temperature of the compressor bleed air used for hot section cooling is lowered by injecting and evaporating water. This decrease in cooling air temperature can offset the effect of increased gas temperature and thus keep turbine blade stress rupture life constant. As in [1, 2, 4], 2 1/2-min was used as the length of time for which contingency power would be required.

It is important to note that liquid water is not allowed to come into contact with the turbine blades. Liquid cooling research performed in the 1950s at Lewis showed that the thermal shock of sudden water application had the potential to fracture turbine blades [7]. The coolant in the proposed scheme consists of compressor discharge air mixed with superheated steam.

The NNEP computer code was used to model a typical turboshaft engine of the type in use for helicopter propulsion. The engine selected had a 16:1 overall pressure ratio and a turbine inlet temperature of 1533 K (2760° R). The gas generator turbine was cooled while the power turbine was not. The criterion used to judge the success of the method was whether the gas generator turbine blade stress-rupture life could be maintained the same with application of emergency power. Stress-rupture life is the time required to produce failure in a constant load, elevated temperature environment. The results of the computer analysis of the engine were used along with a stress rupture analysis to determine the maximum level of augmentation possible with the proposed scheme. Also determined from the study were the required water usage rate and power turbine life fraction used for various levels of augmentation.

Also included in this report are the results of a transient heat conduction analysis to determine the length of time a ceramic thermal barrier coating would delay the temperature rise in cooled turbine blades during operation at elevated temperatures. It was hoped that the thermal barrier could be used to allow increased engine output while maintaining the life of hot section parts during short overtemperature transients.

Nomenclature

C = blade chord
 C_p = specific heat at constant pressure
 C_d = discharge coefficient for nozzle
 f = life fraction
 g_c = gravitational conversion factor (1.0 for metric units)
 H = enthalpy
 h = heat transfer coefficient
 J = mechanical equivalent of heat (1.0 for metric units)
 k = thermal conductivity
 M = Mach number
 m = molecular weight
 N = shaft speed
 PR = pressure ratio
 p = pressure
 R = universal gas constant
 T = temperature
 t = time
 U = blade speed

V = velocity in absolute frame of reference
 W = velocity in relative frame of reference
 \dot{w} = mass flow rate
 γ = ratio of specific heats
 ϕ = dimensionless wall blade wall temperature defined by equation (5)
 Δ = difference
 δ = ratio of inlet total pressure to standard pressure
 θ = ratio of inlet total temperature to standard temperature
 ϵ = function of specific heat ratio
 Ω = shaft speed
 σ = normal stress
 μ = viscosity
 η = efficiency

Subscripts

B = blade
 ca = cooling air
 cr = critical conditions
 D = design conditions
 g = hot gas
 H_2O = water
 in = inlet
 OD = off design
 out = outlet
 R = rotor
 ref = reference
 S = stator
 SR = stress-rupture
 T_c = evaluated at cooling air temperature
 u = tangential component
 x = axial component

Superscripts

($'$) = total absolute conditions
($''$) = total relative conditions

The Proposed Method

A schematic diagram of a turboshaft engine utilizing the proposed emergency power augmentation system is shown in Fig. 1. When emergency power is required, the fuel flow rate to the burner is increased. This causes an increase in the gas temperature, resulting in increased power output for both gas generator and power turbines. Gas generator shaft speed (and thus cycle pressure ratio) increases slightly, further adding to power output.

Unless something is done to keep the turbine blades and other hot parts cool, their temperature will rise with increasing gas temperature until their stress rupture life is completely used up and they fail. To prevent this from happening, it is proposed that the temperature of the compressor bleed air used for turbine cooling be lowered by injecting and evaporating water.

During the application of contingency power, the turbine coolant would be composed of air and saturated steam. Both the rotor and stator are cooled with this mixture. It is theoretically possible to lower the temperature of the cooling air to the saturation temperature of the injected water without having any liquid water left over. The saturation temperature is a function of the pressure. It is thought to be important that no liquid water be allowed to come into contact with hot metal parts. The vast difference in cooling rates between liquid water and air may cause turbine blade failure by thermal shock as demonstrated in [7].

Analysis

The proposed emergency cooling scheme was analyzed by using the NNEP computer code to model the thermodynamic performance of a typical helicopter turboshaft engine in both the design and off design modes. To study the effectiveness of the proposed emergency power scheme, the burner temperature was raised above the design value by a small amount and water was mixed and evaporated in the turbine coolant at the rate which produced saturation. The increased gas generator speed and gas temperature were used in a stress-rupture model to determine the blade metal temperature required to give constant stress rupture life. A correlation of coolant flow and dimensionless average blade wall temperature was used to calculate the required coolant temperature. This required coolant temperature was compared to

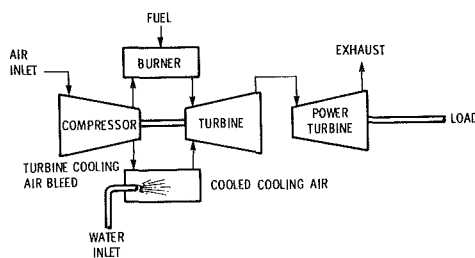


Fig. 1 Schematic diagram of a gas turbine engine utilizing the proposed emergency cooling system

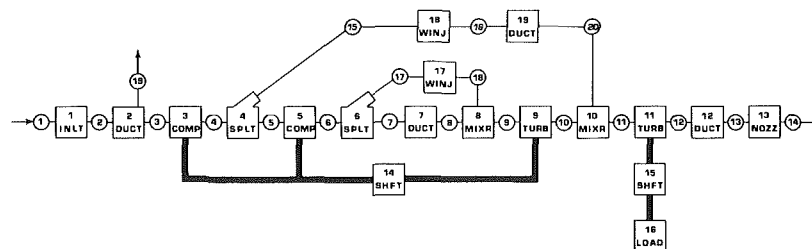


Fig. 2 Schematic diagram of arrangement of components used in NNEP model

the temperature of the saturated steam-air coolant mixture and if it was higher, the burner temperature was raised further and the analysis repeated. This was continued until the required and saturated (minimum) coolant temperatures were equal. This was considered to be the point of maximum emergency power for the system with the constraint of constant gas generator turbine stress rupture life.

The analysis will be divided into three sections: the NNEP computer model of the turboshaft engine studied, the stress rupture model, and the thermal barrier-transient conduction model.

The NNEP Engine Model. Figure 2 is a diagram showing the arrangement of components used to model the engine in this study. The square boxes represent individual components and lines between boxes represent flow path. The circled numbers represent stations where flows and pressures were balanced. Heavy dark lines represent shafting between components. Numbers in the boxes are component numbers corresponding to the numbers in Table 1, which is a summary of each component at the design condition. All calculations were performed at sea level static conditions. At design, the engine has a 16:1 overall pressure ratio. The compressor is split into two parts to allow turbine rotor cooling air to be bled off at a lower pressure. Compressor off-design performance is determined from the flow and efficiency maps shown in Figs. 3(a) and 3(b). These maps represent no particular compressor but were formulated to be representative of the type of compressor used in a helicopter engine. The same map is applied to both compressors shown in Fig. 2. At the design condition, the turbine inlet temperature was 1533 K (2760° R). Stator cooling air was mixed in with mainstream hot gas ahead of the gas generator rotor and allowed to do work in the turbine. Rotor cooling air was mixed downstream of the gas generator turbine and does work only in the power turbine. The flow and efficiency maps for both gas generator and power turbine are shown in Figs. 3(c)-3(f). As with the compressor maps they are generic in nature and represent no particular helicopter engine. The water injectors mix water with the turbine cooling air at the proper rate to obtain saturation, thus the coolant temperature is the lowest theoretically possible for all off design cases studied.

Stress Rupture.

Gas Generator Turbine. To calculate an allowable design point stress for the example turbine, several assumptions had to be made. Coolant flow rates were assumed to be 6.85 percent for the stator and 4.80 percent (both based on air flow rate at station 3) for the rotor. These values are reasonable for a modern turbine engine operating at the conditions considered here. To calculate the rotor relative gas temperature for heat transfer, the following assumptions were made:

Stator turning angle = 70 deg

Stator exit critical velocity ratio = 0.85

Mean rotor blade speed = 488 m/s (1600 ft/s).

The stator exit critical velocity was then calculated from

$$V_{cr} = \sqrt{\frac{2\gamma}{\gamma+1} \frac{R}{m} T_9} \quad (1)$$

The subscript on the temperature refers to the station number on Fig. 2. For the combustion products, the ratio of specific heats, γ , and the molecular weight, m , were taken from [8]. The stator exit absolute velocity, V , was then calculated as

$$V = 0.85 V_{cr} \quad (2)$$

From the stator exit velocity triangle shown in Fig. 4 it can be seen that the rotor relative inlet velocity is

$$W = \sqrt{W_x^2 + (V_u - U)^2} \quad (3)$$

The rotor relative total temperature is then given by [9]

$$T_9'' = T_9' - \frac{V^2 - W^2}{2g_c J C_p} \quad (4)$$

The specific heat of the combustion products was also taken from [8].

A curve fit of data given in Fig. 9 of [10] was used to obtain an expression which correlates blade wall temperature data over a wide range of temperatures and coolant flows. The correlation is

$$\phi = \frac{T_9'' - T_B}{T_9'' - T_{ca}} = \frac{1}{1 + 0.13 \left(\frac{\dot{w}_g}{\dot{w}_{ca}} \right)^{0.7}} \quad (5)$$

Given the coolant and main gas stream flow rates, \dot{w}_{ca} and \dot{w}_g respectively, and the relative gas temperature T_9'' and relative coolant temperature, T_{ca} , this expression allowed the calculation of blade average metal temperature, T_B .

In order to calculate an allowable design stress, a blade material, B1900, was selected as typical of nickel base superalloys for stress rupture properties. The stress rupture properties of this alloy can be described by [11]

$$T_B(20 + \log_{10} t) \times 10^{-3} = 3.081 + 33.08 (\log_{10} \sigma) - 5.111 (\log_{10} \sigma)^2 \quad (6)$$

The design point stress rupture life was taken as 1000 hrs and a factor of safety of 2.5 was used as a multiplier giving

$$t = 2500 \text{ hrs} \quad (7)$$

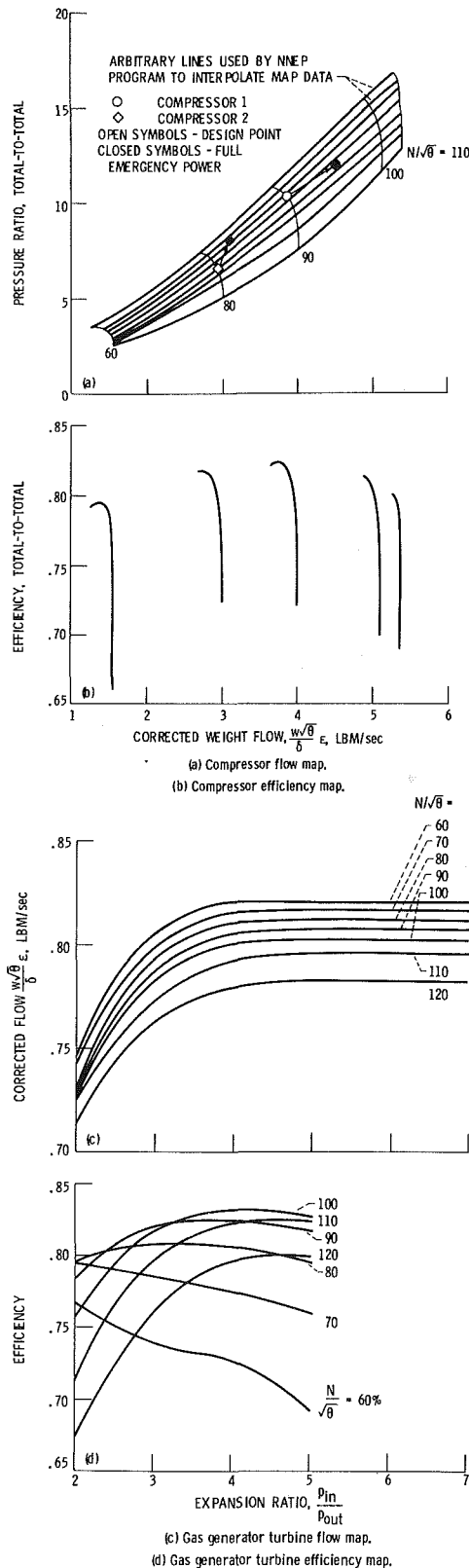


Fig. 3 Performance map for compressor and turbines

Table 1 Summary of engine components in NNEP model

Component No.	Type	Characteristics at Design Point
1	Inlet	exit pressure/ram pressure = 1.0
2	Duct	$ap/p = 0.01$; split off IPS bleed air
3	Compressor	$\eta = 0.81$; PR = 12:1; surge margin = 10.7 percent
4	Splitter	4.80 percent of flow at station 3 split off for rotor cooling; $ap/p = 0.05$ cooling flow stream
5	Compressor	$\eta = 79.5$ percent; PR = 1.33:1; surge margin = 14 percent
6	Splitter	6.85 percent of flow at station 3 split off for stator cooling; $ap/p = 0.05$ cooling flow stream
7	Duct (Burner)	burner efficiency = 99 percent; $ap/p = 0.05$; outlet temperature = 1533° K (2760° R)
8	Mixer	mix stator cooling flow with main stream
9	Turbine	PR = 4.63; $\eta = 0.832$ gas generator turbine
10	Mixer	mix rotor cooling flow with main stream
11	Turbine	PR = 3.108; $\eta = 0.87$ power turbine (uncooled)
12	Duct	no losses
13	Nozzle	$C_d = 0.85$; overall pressure ratio = 1.045 inlet total to exit static
14	Shaft	gas generator turbine to compressor; no losses
15	Shaft	power turbine to load; no losses; speed 20,000 RPM
16	Load	shaft power to gear box, etc.
17	Water Injector	spray water into cooling air; not used at design
18	Water Injector	spray water into cooling air; not used at design
19	Duct	$ap/p = 0.71$; drop pressure to match rotor relative pressure

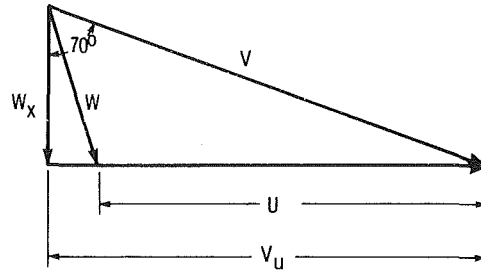


Fig. 4 Velocity triangle assumed for gas generator stator exit

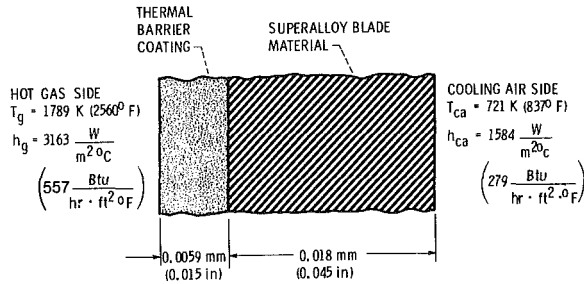


Fig. 5 Cross section of thermal barrier coated turbine blade used in transient model

With the life and calculated metal temperature, T_B , the quadratic formula was applied to equation (6) and the allowable design stress, σ_D , was calculated.

The off-design blade stress, or stress during application of emergency cooling, was calculated from

$$\sigma_{OD} = \sigma_D \left(\frac{\Omega_{OD}}{\Omega_D} \right)^2 \quad (8)$$

Ω_{OD} and Ω_D are the off-design and design shaft speeds, respectively. The value of σ_{OD} was then used in equation (6) to find the required blade metal temperature, T_B , for constant stress rupture life ($t = 2500$).

The off-design mean blade speed was calculated from the equation

$$U_{OD} = U_D \left(\frac{\Omega_{OD}}{\Omega_D} \right) \quad (9)$$

Equations (3) and (4) were used to calculate the new relative total temperature, T_9'' .

The dimensionless wall temperature expression (equation (5)) was then used again to find the required coolant temperature

$$T_{ca} = T_9'' - \frac{T_9'' - T_B}{\phi} \quad (10)$$

The dimensionless wall temperature calculated from equation (5) reflected an increased coolant flow due to the water injection and increased air flows at off-design. Air properties were used for the coolant; the thermal property changes of the coolant due to steam mixing were ignored. This is thought to be conservative since the thermal properties of steam are more favorable for heat transfer than those of air.

Power Turbine. The power turbine in this example engine was uncooled. The proposed scheme to lower coolant temperature thus has no effect on the power turbine and its life can be expected to be shortened due to increased temperature. If a cooled power turbine were utilized, its stress-rupture life could also be preserved by injecting water into its cooling air.

For the present analysis, the fraction of power turbine life used per application of emergency power was estimated using

a method similar to that in [12]. For the power turbine the blade stress remains constant because the rotor speed was held constant. This analysis assumes that the increased bending stresses due to increased blade gas loading are negligible compared to the centrifugal stress. The right-hand side of equation (6) is thus constant. The fraction of power turbine life used during a 2.5-min application of emergency power was calculated as

$$f = 2.5/t_{SR} \quad (11)$$

where t_{SR} is the time-to-stress rupture in minutes at the elevated temperature. t_{SR} was calculated from equation (6) with σ given and T_B assumed to be equal to the hot gas stream temperature at station 11.

Water Flow Rates. At the maximum theoretical level of emergency power, the water-air coolant mixture will contain saturated steam. At power levels less than the theoretical maximum, the coolant stream will contain air and superheated steam. All of the off-design NNEP calculations were carried out using the maximum water flow rate—the rate that makes the mixed coolant stream saturated. The water flow rates calculated in this section are estimates of the actual required water flow rate based on the temperature of coolant necessary to maintain constant stress rupture life. The water flow required to obtain this temperature was calculated from a simple energy balance on the mixing water and air streams. Assuming 100 percent water evaporation this gives an expression for the water flow rate into the rotor cooling air

$$\dot{W}_{H_2O,R} = \dot{W}_{ca,R} \left(\frac{H_{ca,in} - H_{ca,T_c}}{H_{H_2O,T_c} - H_{H_2O,in}} \right) \quad (12)$$

$\dot{W}_{ca,R}$ is the rotor cooling air mass flow rate, $H_{ca,in}$ and H_{ca,T_c} are the enthalpies of the cooling air before and after mixing, respectively. H_{H_2O,T_c} and $H_{H_2O,in}$ are the enthalpies of the water after and before mixing, respectively.

The total water flow rate was then calculated by assuming that the ratio of water to air mass flows remains the same in the stator coolant stream as that required in the rotor coolant stream. The total water flow rate was found from

$$\dot{W}_{H_2O} = \dot{W}_{H_2O,R} \left(1 + \frac{\dot{W}_{ca,S}}{\dot{W}_{ca,R}} \right) \quad (13)$$

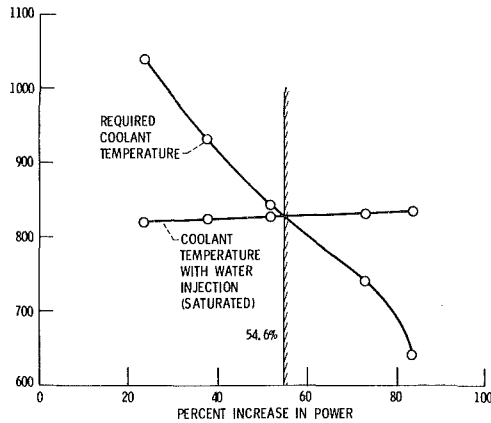


Fig. 6 Required and obtainable coolant temperatures for given power increase

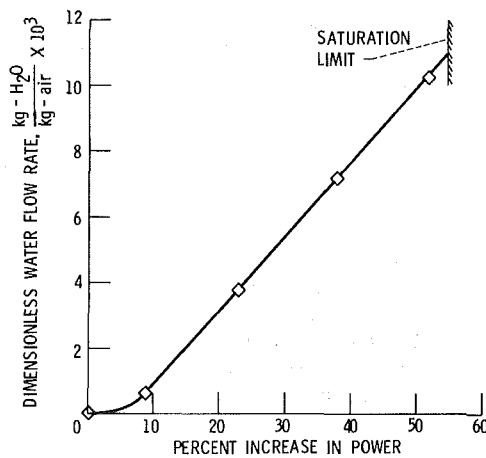


Fig. 7 Water flow rate required to maintain constant gas generator turbine life

where \dot{w}_{H_2O} is the total water mass flow rate required by rotor and stator, $\dot{w}_{ca,s}$ is the stator cooling air mass flow rate.

Thermal Barrier Coating. The ability of a thermal barrier coating to delay the rise in cooled blade metal temperature during an emergency power transient was assessed analytically. A thermal barrier of zirconia 0.038-cm (.015-in.) thick was assumed to be applied to the exterior of the blade. A transient heat conduction computer code was used to compare the rise in blade average metal temperatures for both coated and uncoated blades subjected to a sudden rise in gas temperature. The heat conduction code uses the method of solution described in [13].

The following assumptions were made in order to determine a representative value for gas-to-blade heat transfer coefficient:

Blade average surface Mach number, $M = 0.6$

Blade chord, $C = 5.72$ cm (2.25 in.)

Pressure, $p'' = 1.46$ kPa (212 psia)

Relative total gas temperature, $T_g'' = 1422$ K (2560 R)

The gas side heat transfer coefficient was then calculated from [14]:

$$h_g = \frac{0.0325}{C} k_g \left[\frac{p'' M \sqrt{\frac{\gamma T_g''}{R/m}} C}{\mu T_{ref} \left(1 + \frac{\gamma-1}{2} M^2\right)^{(3\gamma-1)/(2(\gamma-1))}} \right]^{.8} \quad (14)$$

The gas properties were taken from [8] and the reference temperature, T_{ref} , was the average between wall and hot gas temperatures.

The coolant side air temperature was assumed to be 721 K (1297 R) and average blade metal temperature was assumed to be 1089 K (1960 R). At the average coating temperature, the thermal properties of the thermal barrier coating material were assumed to be [15]:

$$\text{Thermal conductivity} = 1.506 \frac{w}{m - ^\circ C} \left(0.87 \frac{\text{Btu}}{\text{hr} - \text{ft} - \text{R}} \right)$$

$$\text{Density} = 4636 \frac{\text{kg}}{\text{m}^3} \left(289.4 \frac{\text{lbm}}{\text{ft}^3} \right)$$

$$\text{Specific heat} = 0.16 \frac{\text{cal}}{\text{gm} - \text{K}} \left(0.16 \frac{\text{Btu}}{\text{lbm} - \text{R}} \right)$$

The thermal properties of the blade wall material were taken as representative of B 1900 superalloy [16].

$$\text{Thermal conductivity} = 22.50 \frac{w}{m - \text{K}} \left(13 \frac{\text{Btu}}{\text{hr} - \text{ft} - ^\circ \text{F}} \right)$$

$$\text{Density} = 7753 \frac{\text{kg}}{\text{m}^3} \left(484 \frac{\text{lbm}}{\text{ft}^3} \right)$$

$$\text{Specific heat} = 0.11 \frac{\text{cal}}{\text{gm} - \text{K}} \left(0.11 \frac{\text{Btu}}{\text{lbm} - \text{R}} \right)$$

A simple one-dimensional energy balance on the element of blade wall shown in Fig. 5 then gave the coolant side heat transfer coefficients necessary to maintain the average wall temperature of 1089 K (1960 R). For the cases studied these were

$$1584 \frac{W}{\text{m}^2 - \text{K}} \left(279 \frac{\text{Btu}}{\text{hr} - \text{ft}^2 - ^\circ \text{F}} \right) \text{ for the coated blade and}$$

$$3163 \frac{w}{\text{m}^2 - \text{K}} \left(557 \frac{\text{Btu}}{\text{hr} - \text{ft}^2 - ^\circ \text{F}} \right) \text{ for the uncoated blade.}$$

The application of emergency power was simulated by a 256 K (460 R) step temperature rise in turbine inlet temperature. Coolant and gas side heat transfer coefficients as well as coolant temperature were assumed constant during the transient. These assumptions were thought to be accurate enough to assess the value of thermal barrier coating in delaying metal temperature rise during a transient.

Results and Discussion

A scheme has been proposed which will allow increased power from a turboshaft engine in emergency situations without decreasing gas generator turbine life. Emergency power is derived by increasing turbine inlet temperature, and the turbine is protected by lowering its cooling air temperature with water injection and evaporation. An analysis was conducted to determine the level of increased power possible using the proposed coolant water injection scheme. The performance of a modern turboshaft engine was simulated in both design and off-design modes with the NNEP computer code. An analysis was also conducted to determine if any significant delay in turbine blade metal temperature rise during an overtemperature transient could be obtained by using a thermal barrier coating.

Maximum Power. The maximum power obtainable using the proposed scheme can be determined from Fig. 6. Shown on the figure are the required coolant temperature versus percent power increase. This curve was obtained from the NNEP and stress rupture analysis as explained in the

ANALYSIS section. The near horizontal line on the figure shows the lowest possible coolant temperature obtainable using water injection and evaporation. Any increase in power where the required coolant temperature curve is higher than the minimum obtainable coolant temperature is thus possible. The point where the two curves cross is the theoretical maximum increase in power for constant gas generator turbine life. For the engine studied the maximum power increase possible was found to be 54.6 percent.

Water Flow Rate. The water flow rate required to maintain constant gas generator turbine life can be determined from Fig. 7. The figure shows dimensionless water flow rate as a function of percent power increase. The water flow rate was made dimensionless by dividing by the air flow rate at station 3 (see Fig. 2). As an example of how much water would be required for a helicopter engine in an emergency situation consider a 4.474 MW (6000 shp) engine operating at the temperatures and pressure ratio previously described (turbine inlet temperature = 1533 K (2760 R), pressure ratio 16:1). For a 54.6 percent increase in power to 6.92 MW (9276 shp) the air flow at station 3 would be 19.73 kg/sec (43.5 lbm/s). The weight of water required for a 2 1/2-min application of emergency power at this level would be

$$\left(10.9 \times 10^{-3} \frac{\text{kg} - \text{H}_2\text{O}}{\text{kg} - \text{air}}\right) \left(19.73 \frac{\text{kg}}{\text{s}}\right) \left(60 \frac{\text{s}}{\text{min}}\right) (2.5 \text{ min})$$

$$= 32.26 \text{ kg} - \text{H}_2\text{O} (71.13 \text{ lbm} - \text{H}_2\text{O}).$$

Power Turbine Life. The fraction of power turbine life used during a 2.5-min application of emergency power is shown versus percent power increase over the design value on Fig. 8. At the maximum value of 54.6 percent increased power, the power turbine would use up approximately 25 percent of its total stress rupture life. This is a less than desirable situation but it must be remembered that the power turbine in this study was uncooled. The proposed scheme could be applied to a cooled power turbine and no loss of turbine stress rupture life would occur.

Thermal Barrier Coating. The results of the transient heat conduction analysis on the segment of turbine blade wall shown in Fig. 5 are given on Fig. 9. The figure shows blade average wall temperature (temperature of the superalloy not the thermal barrier coating) as a function of time from the beginning of the transient step in gas temperature. The coolant side heat transfer coefficients were selected to give the same metal temperature for both coated and uncoated blades. It can be seen from the figure that the thermal barrier coating only has an effect for about 6 s. It can be concluded that the thermal barrier coating is of virtually no value in keeping blade metal temperature transients at acceptable levels for a 2.5 min overtemperature.

Summary of Results

An analytical investigation into the feasibility of using water injection and evaporation into the turbine cooling air to allow increased power output from a turboshaft engine has been conducted. The power increase is obtained by turbine overtemperature. The feasibility of using a thermal barrier coating on the blade to delay the rise in blade metal temperature during an overtemperature was also investigated analytically. The results of the study can be summarized as follows:

- 1 The theoretical maximum power increase possible was found to be 54.6 percent.
- 2 A dimensionless water flow rate of 0.0109 kg water per kg of engine airflow would be required to maintain constant gas generator turbine stress rupture life at the maximum power increase of 54.6 percent. It was shown that a 4.474 MW (6000 shp) engine would require 32.26 kg (71.13 lbm) for a 2.5-min application of emergency power at the maximum level.
- 3 Approximately 25 percent of the uncooled power turbine stress-rupture life is used up during a 2.5-min over-

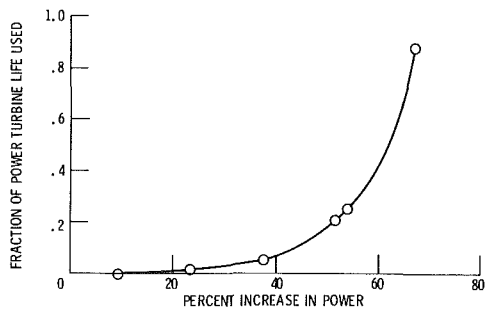


Fig. 8 The effect of increased power on power turbine life fraction used during a 2.5 min application of emergency power

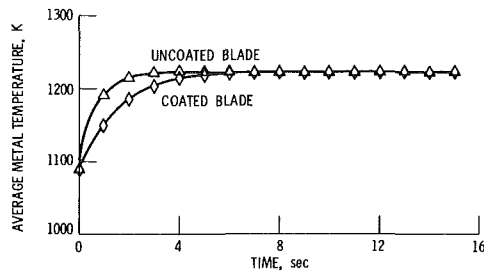


Fig. 9 Transient thermal response of coated and uncoated turbine blades to a 256 K (460°F) step in gas temperature

Table 2 Summary of major component parameters

Component	Design				Off-design			
	Pressure ratio	Efficiency, percent	Surge margin, percent	Speed, percent	Pressure ratio	Efficiency, percent	Surge margin, percent	Speed, percent
Compressor 1	12.00	81.00	10.68	100.00	14.68	79.29	12.61	106.6
Compressor 2	1.33	79.5	13.54	100.00	1.407	81.30	5.65	106.6
	Rotor relative mixed inlet temperature, (°R)	Pressure ratio	Efficiency, percent	Coolant* fraction, percent	Rotor relative mixed inlet temperature, (°R)	Pressure ratio	Efficiency, percent	Coolant fraction* (inc. water) percent
Gas generator turbine	2665	4.63	83.20	4.80	2946	4.72	83.21	5.31
Power turbine	1964	3.11	87.00	0	2185	3.84	85.15	0

*Based on air flow at station 3

temperature. This could be reduced to zero if the power turbine were cooled.

4 The thermal barrier coating was shown to be of no value in reducing the blade metal temperature rise during a 2.5-min transient.

Concluding Remarks

While the analysis has shown promising potential for the proposed emergency power augmentation system, the reader should be cautioned that this is a theoretical maximum value. The actual level of power increase obtainable with this system will be somewhat lower for several reasons: the main reason being the efficiency of evaporation. If the water flow rate required for this level of power increase cannot be fully evaporated, liquid water will spill over into the coolant stream. Liquid coming into contact with hot turbine parts could be disastrous. Thus, a lower water flow rate may be required to obtain a safety margin.

Another source of trouble could be the compressor operating point. As the power level is increased, the compressor is driven toward surge. This can be seen on Fig. 3(a); the open symbols are the design points and the closed symbols are the maximum emergency power operating points for compressors 1 and 2. As shown in Table 2, the surge margin for compressor 2 goes from 13.54 percent at the design point to 5.65 percent at the maximum power point. This was pointed out in [4].

Finally, the analysis does not consider other hot components in the engine. It was assumed that shrouds, combustor liners, etc. would be designed to withstand the required temperature transients. In [4], Brooks also warns that overtemperature can lead to local hot spots that could decrease turbine life through increased corrosion.

References

- 1 Semple, R. D., et al., "Emergency Power Benefits to Multi-Engine Helicopters," *Journal of the American Helicopter Society*, Vol. 22, No. 3, July 1977, pp. 27-33.
- 2 Yost, J. H., "Research Requirements for Emergency Power to Permit Hover-One-Engine-Inoperative Helicopter Operation," NASA CR-145115, Dec. 1976.
- 3 Dugas, R. E., "Gas Turbine Power Augmentation and Emergency Rating," USAAVLABS TR-68-12, General Electric Co., Lynn, Mass., Apr. 1968.
- 4 Brooks, A., "The Impact of Contingency Ratings on Advanced Turboshaft Design," Presented at the Helicopter Propulsion System Specialists Meeting, Southeast Region of the American Helicopter Society, Washington, D.C., November 1979.
- 5 Van Fossen, G. J., and Stepka, F. S., "Review and Status of Liquid-Cooling Technology for Gas Turbines," NASA RP 1038, 1979.
- 6 Fishbach, L. H., and Caddy, M. J., "NNEP—The Navy NASA Engine Program," NASA TM X-71857, Dec. 1975.
- 7 Freche, J. C., and Hinkel, R. O., "Turbojet Engine Investigation of Effect of Thermal Shock Induced by External Water-Spray Cooling on Turbine Blades of Five High-Temperature Alloys," NACA RM E55J17, Dec. 1955.
- 8 Pofnerl, D. J., Svehla, R. A., and Lewandowski, K., "Thermodynamic and Transport Properties of Air and the Combustion Products of Natural Gas and of ASTM-A-1 Fuel With Air," NASA TN D-5452, Oct. 1969.
- 9 Glassman, A. J., *Turbine Design and Application*, Vol. 1, NASA SP-290, 1972.
- 10 Yeh, F. C., Gladden, H. J., and Gauntner, J. W., "Comparison of Heat Transfer Characteristics of Three Cooling Configurations for Air-Cooled Turbine Vanes Tested in a Turbojet Engine," NASA TM X-2580, Oct. 1972.
- 11 Dreshfield, R. L., "Rupture Strength of Turbine Alloys," NASA Lewis Internal Memorandum, April 1975.
- 12 Miner, M. A., "Cumulative Damage in Fatigue," *Journal of Applied Mechanics*, Vol. 12, No. 3, Sept. 1945, pp. A159-A164.
- 13 Chapman, A. J., *Heat Transfer*, 2d ed., The Macmillan Company, New York, 1967.
- 14 Colladay, R. S., "Analysis and Comparison of Wall Cooling Schemes for Advanced Gas Turbine Applications," NASA TN D-6633, Jan. 1972.
- 15 Liebert, C. H., Personal Communication, June 1977.
- 16 Anon, "High-Temperature, High-Strength Nickel Base Alloys," 2d ed., Internal Nickel Company, Inc., 1968.

Inertia Effects on the Dynamics of a Disk Levitated by Incompressible Laminar Fluid Flow

D. K. Warinner

Mechanical Engineer,
Argonne National Laboratory,
Argonne, Ill. 60439

J. T. Pearson

Associate Professor,
School of Mechanical Engineering,
Purdue University,
West Lafayette, Ind.

This paper develops a nonlinear ordinary differential equation (O.D.E.) of motion for a disk parallel to a flat plate and levitated by incompressible laminar flow of fluid supplied from a central orifice. The fluid's inertia, reflected in high mass flow rates, is accounted for. The transient flow velocity and pressure field are found by iterative integration of the Navier-Stokes equation to determine the O.D.E. for the time-dependent height of the disk (or fluid film thickness). The film thickness is found by not only numerically integrating the O.D.E., but also by linearizing the equation to obtain a closed-form solution. The results of this combined squeeze-film, source-flow case compare favorably with experimental data presented which span cases from negligible inertia (viscous dominance) to cases of inertia dominance. Fortunately, the closed-form solution differs only slightly from the numerical solution; this provides relatively accurate expressions for the frequencies and damping coefficients in terms of the geometry, load (or weight of disk), mass flow rate, and the fluid properties.

Introduction

Devices such as circular hydrostatic bearings, disk valves, radial nozzles, diffusers, hydraulic-oil control-valves, radial-flow viscometers, and air micrometers have radial fluid flow between parallel disks and relative motion of one disk normal to the other. The designs of these devices are complicated by the transient, nonlinear behavior of the devices. A trial-and-error design might well be necessary when the mass flow rates in the film exceed those rates characterized by "viscous domination" (negligible fluid inertia). The design approach for viscous-dominated radial flow devices is well established; indeed, the technology is well developed.

The significance of fluid inertia on the steady-state film thickness was illustrated in [1]. Also, the effects of fluid inertia in the dynamic case, seen in the disk's frequency and damping characteristics, were found experimentally [2]. Indeed, such effects can be predicted by the magnitude of certain dimensionless parameters as shown in [3].

The objective of this investigation is to predict the dynamic behavior of a disk, levitated by laminar fluid flow supplied from a central orifice, for high mass flow rates. In particular, the objective is to predict this motion by ascertaining the height of the disk as a function of time when the disk is perturbed from its equilibrium position by a forcing function. Beginning with the Navier-Stokes equations, casting out the unimportant terms, and solving for the transient pressure field, we determine the time-varying, load-carrying capability

of the fluid film. Although this approach differs considerably from the lumped parameter approach for circular bearings [4-7], we anticipate that the linearized results here may help further the lumped-parameter approach for application to this type of problem. Thus, we seek a closed-form solution for the time-varying film thickness or disk height to simplify the design process.

The dynamics of a gas-lubricated, circular, aerostatic thrust bearing was studied extensively by Weber [8], Roudebush [9], Licht [10, 11], and others [2, 12, 13]. Although those studies included both incompressible [2, 12, 13] and compressible [8-11] flows, the assumed flows for the development of solutions were laminar and viscous-dominated (creeping flow).

Ishizawa's [14-16], full and sophisticated solution for the velocity profile and pressure distribution between disks separated by an arbitrarily time-varying gap with no source flow must be combined with his solution for source flow between fixed disks. Also, the source-flow solution is in two parts: a difference-method solution for the upstream region and an asymptotic solutions using Pohlhausen's parameter and a shape factor for the downstream region. Since the two solutions must be joined whenever the Reynolds number is changed, the practicality of obtaining a closed-form solution for the disk's dynamics are nil for Ishizawa's results.

Several studies of squeezing flow [17-22] include inertial effects; we will use these to check our results for the limiting case of no source flow.

Analysis

Assumptions and Governing Equations. We assume radial,

Contributed by the Gas Turbine Division of THE AMERICAN SOCIETY OF MECHANICAL ENGINEERS and presented at the 28th International Gas Turbine Conference and Exhibit, Phoenix, Arizona, March 27-31, 1983. Manuscript received at ASME Headquarters, December 27, 1982. Paper No. 83-GT-149.

incompressible laminar flow between the two parallel plates shown in Fig. 1. The case of no recess is considered for simplicity and brevity. (From the results of this paper, one can easily derive the equation for the dynamics of a recessed bearing or similar device by following the steps outlined in [1].) Only vertical (normal to the disk's face) motion of the disk is considered. Whitney [23], Licht and Kaul [24], and Ausman [25] have shown that oscillations about a horizontal axis (rocking) was heavily damped and can be neglected in comparison with the vertical motion. Also, the results should be valid for rotations where $\Omega \ll q_e/2\pi a^2 h \rho$ [3, 26].

The momentum and continuity equations that describe the fluid mechanics of the problem are shown by an order-of-magnitude analysis [3, 26] to reduce to the "boundary-layer equations" form

$$\frac{\partial u}{\partial t} + u \frac{\partial u}{\partial r} + w \frac{\partial u}{\partial z} = -\frac{1}{\rho} \frac{\partial p}{\partial r} + \nu \frac{\partial^2 u}{\partial z^2} \quad (1)$$

and

$$\frac{\partial ru}{\partial r} + \frac{\partial rw}{\partial z} = 0 \quad (2)$$

for radial, isothermal, incompressible laminar flow of a Newtonian fluid. Rotational symmetry ($\partial/\partial\theta = 0$) is assumed and the viscosity is constant for a perfect gas.

The integral continuity equation

$$\int_{\text{Control Surface}} \rho \mathbf{V} \cdot d\mathbf{A} = -\frac{\partial}{\partial t} \int_{\text{Control Volume}} \rho dV \quad (3)$$

applied to the control volume in Fig. 2 becomes

$$2 \int_0^h u dz = \frac{q}{\pi \rho r} - r \dot{h} \quad (4)$$

where h is the instantaneous film thickness, and q is the orifice mass flow rate. We first find the radial velocity, u , from equations (1) and (2) and then find the radial pressure distribution through equation (4); the motion of the oscillating disk is described simply by applying Newton's second law of motion to that member. This yields

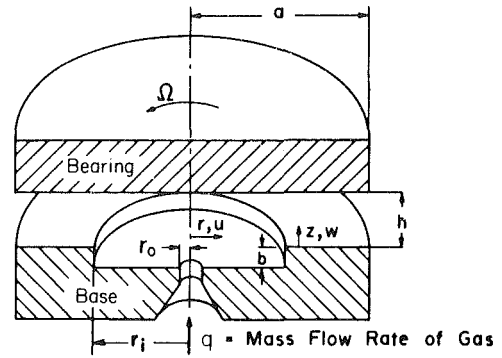


Fig. 1 Circular hydrostatic thrust bearing geometry

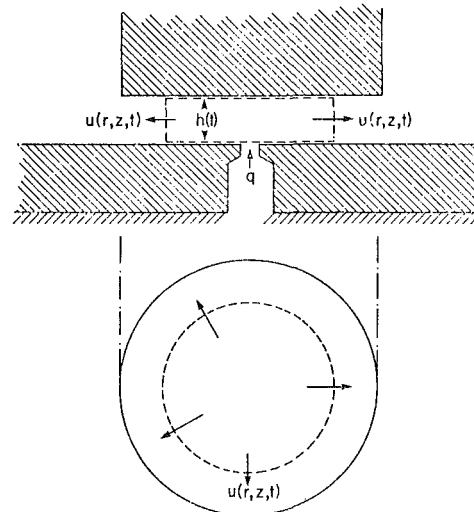


Fig. 2 Illustration of control volume for application of integral continuity equation

Nomenclature

- a = radius of disk or bearing
 A = surface area of control volume
 b = recess depth or mass flow rate parameter
 B = mass flow rate parameter;

$$B \equiv bh_e/q_e \equiv \frac{h_e \Delta q_e}{q_e \Delta h_e}$$

- c = second mass flow rate parameter
 d = orifice diameter
 $e; E$ = vertical displacement from equilibrium condition, $e \equiv h - h_e$; $E \equiv e/h_e \equiv H - 1$
 F = force, N (lb_f) or nondimensional angular frequency of vertical oscillation of disk, $F \equiv 2\pi/T_1$
 g = gravitational constant, taken as 32.16 ft/s² (9.802 m/s²) for experiments conducted at Stony Brook, N.Y.
 $h; H$ = film thickness; $H_e \equiv h/a$, $H \equiv h/h_e$
 H = half-life of vertical oscillation of disk; $\equiv t_1 \sqrt{3g/h_e} / \ln(e_i/e_1)$
 L = load supported by fluid lubricant
 m = mass of bearing or disk
 N = dimensionless load parameter, $N \equiv \rho L / 3\mu^2$

- N_{mr} = ratio of film lubricant mass to mass of bearing, $N_{mr} \equiv \rho \pi a^2 h_e / m = 3\beta \text{Re}_h H_e^3 / 4$
 $p; P$ = pressure; $P \equiv p/P_a$
 $q; Q$ = mass flow rate of fluid through central orifice; $Q \equiv q/q_e$
 Q_e^* = dimensionless mass flow rate of gas through central orifice at equilibrium condition, $Q_e^* \equiv 3\mu q_e / \rho m g a$
 r, θ, z = cylindrical coordinates
 Re = Reynolds number, $\text{Re} \equiv (\text{mean velocity})(\text{hydraulic diameter})/(\text{kinematic viscosity})$
 Re^* = reduced Reynolds number, $\text{Re}^* \equiv h_e \text{Re} / 2r$
 Re_h = squeezing Reynolds number, $\text{Re}_h \equiv \rho a \sqrt{3gh_e} / \mu$
 Re_h^* = reduced squeezing Reynolds number, $\text{Re}_h^* \equiv h_e \text{Re}_h / 2a$
 S = Strouhal number, $S \equiv \omega d / \bar{u}$ for orifice, $S \equiv \omega_n a / \bar{u}$ for disk
 S^* = modified Strouhal number for orifice or nozzle, $S^* \equiv \omega (A/\Omega)^{1/2} / V$
 $t; T$ = time; $T \equiv t / (h_e/3g)^{1/2}$
 u, v, w = velocity composite in radial, angular, and axial directions (r, θ, z)
 \bar{u} = average radial velocity, $\bar{u} \equiv q_e / 2\pi \rho h r$
 U = radial velocity at center line, $z = h/2$
 V = velocity or volume

$$m\dot{h} = 2\pi \int_{r_0}^a (p - p_a) |_{z=h} r dr + \pi r_0^2 (p_0^0 - p_a) - mg - F(t) \quad (5)$$

where $F(t)$ is the axially applied forcing function, p_0^0 is the total pressure at $r = r_0$, and p_a is the atmospheric pressure. (The superscript "0" denotes stagnation conditions; the subscript "0" indicates that the variable is evaluated at $r = r_0$, the radius of the central orifice.) Equation (5) also includes the assumption of negligible external damping effects, except for those that could be included in $F(t)$.

The initial and boundary conditions for these equations are

$$t = 0 \quad h(0) = h_i; \dot{h}(0) = \dot{h}_i \quad (6a)$$

$$z = 0 \quad u(r, 0, t) = w(r, 0, t) = 0 \quad (6b)$$

$$z = h \quad u(r, h, t) = 0; w(r, h, t) = \dot{h} \quad (6c)$$

$$r = a \quad p(a, t) = p_a \quad (6d)$$

To obtain $h(t)$, we must find the pressure as a function of the radius, r . (Since the order-of-magnitude analysis of [3] shows $\partial p / \partial z \approx 0$, we assume that $p = p(r, t)$.)

Pressure Distribution. Equation (1), a parabolic partial-differential equation, affords the possibility of an iterative, or successive-approximation, solution. The mathematical model for this unsteady, incompressible laminar-flow problem then becomes

$$\frac{\partial^2 u_j}{\partial z^2} = \frac{1}{\mu} \frac{\partial p_j}{\partial r} + \frac{1}{\nu} \frac{Du_{j-1}}{Dt} \quad (1)$$

$$0 = \frac{\partial p_j}{\partial z}$$

$$\frac{\partial ru_j}{\partial r} + \frac{\partial rw_j}{\partial z} = 0 \quad (2)$$

$$2 \int_0^h u_j dz = \frac{q}{\pi \rho r} - r\dot{h} \quad (4)$$

and

$$m\dot{h} = 2\pi \int_{r_0}^a (p_j - p_a) |_{z=h} r dr + \pi r_0^2 (p_0^0 - p_a) - mg - F(t) \quad (5)$$

with the initial and boundary conditions given by equation (6). The subscript, j , denotes the iteration number.

For our first approximation of u and w , we let $Du/Dt = 0$; the linear equation for viscous-dominated flow remains. Reference [12] shows the zeroth-iteration velocities for viscous-dominated flow to be

$$u_0 = \frac{3}{h^3} \left(\frac{q}{\pi \rho r} - r\dot{h} \right) (hz - z^2) \quad (7a)$$

and

$$w_0 = -\frac{\dot{h}}{h^3} (2z^3 - 3hz^2). \quad (7b)$$

(In 1874, Stefan [27], assuming a fully developed velocity profile, showed that $u = -3r\dot{h}(hz - z^2)/h^3$ for radial flow between disks solely due to squeezing action (no source flow). In 1917, Rayleigh [28], again assuming fully developed flow, showed that $u = 3(q/\pi\rho r)(hz - z^2)/h^3$ for pure source flow between fixed disks. Since equation (1) is linear when $u_j \partial u_j / \partial x_j$ is zero, its solution must equal the sum of these results, equation (7a).

For the second approximation, we use u_0 and w_0 to evaluate Du_0/Dt (r, z, t) and substitute it into equation (1). Integrating twice with respect to z , we have

$$u_1 = \frac{1}{2\mu} \frac{\partial p_1}{\partial r} (z^2 - hz) + \frac{1}{\nu} \left[\frac{1}{4h^3} \left(\frac{\dot{q}}{\pi \rho r} - r\dot{h} \right) (2hz^3 - z^4 - zh^3) - \frac{3}{20h^6} \left(\frac{q^2}{\pi^2 \rho^2 r^3} - r\dot{h}^2 \right) (5h^2 z^4 - 6hz^5 + 2z^6 - zh^5) + \frac{\dot{h}}{10h^6} \left(\frac{q}{\pi \rho r} - r\dot{h} \right) (4z^6 - 12hz^5 + 15h^2 z^4 - 10h^3 z^3 + 3h^5 z) \right]. \quad (8)$$

The pressure gradient is found by satisfying equation (4), integrating, and solving for $\partial p_1 / \partial r$, which gives

Nomenclature (cont.)

\mathbf{V} = vector velocity
 β = parameter occurring in damping coefficients, $\beta \equiv \pi \mu a^4 / 4mgh_e^2 (h_e/3g)^{1/2}$
 $\Gamma \equiv [\zeta + \sqrt{(\zeta^2 - 1)}] \omega_n$
 $\Gamma^* \equiv [\zeta - \sqrt{(\zeta^2 - 1)}] \omega_n$
 δ = logarithmic decrement, $\delta \equiv \ln(e_i/e_1)$
 ζ = damping ratio, defined by form of equation (24); $\zeta \equiv \delta / \sqrt{(4\pi^2 + \delta^2)}$ for calculation from experimental data
 μ = coefficient of viscosity
 ν = kinematic coefficient of viscosity
 ξ = functional coefficient, equation (12)
 ρ = density of fluid film
 ϕ = phase angle in sinusoidal solution
 ω = vertical oscillatory frequency of disk, rad/s (nondimensional $\omega_d \equiv F_d$); frequency of imposed pressure field
 ω_n = natural frequency of disk
 Ω = rotational velocity of bearing, rad/s; solid angle of nozzle

Subscript

a = atmospheric or at $r = a$
 d = damped value

e = equilibrium condition (for h and q) or exit ($r = a$) condition
 h = squeezing, based on velocity, $\sqrt{3gh_e}$
 i = initial condition, $t = 0$
 j = index 1, 2, 3
 mr = mass ratio
 0 = condition at $r = r_0$, zeroth iteration or condition at $z = 0$
 nt = nonlinear theory

Superscript

\dot{x}, \ddot{x} = time derivatives of x : dx/dt and d^2x/dt^2 , respectively
 \dot{X}, \ddot{X} = nondimensional time derivatives of X : dX/dT and d^2X/dT^2 , respectively
 x^0 = variable x at total or stagnation conditions

Mathematical Operator

$\frac{D}{DT}$ = substantial derivatives,
 $\frac{Du}{Dt} \equiv \frac{\partial u}{\partial t} + u \frac{\partial u}{\partial r} + \frac{v}{r} \frac{\partial u}{\partial \theta} - \frac{v^2}{r} + w \frac{\partial u}{\partial z}$
for cylindrical coordinates

$$\frac{\partial p_1}{\partial r} = \frac{6\mu\dot{h}}{h^3} - \frac{6\mu}{h^3} \frac{q}{\pi\rho r} - \frac{3}{5} \frac{\rho}{h} \left(\frac{\dot{q}}{\pi\rho r} - r\dot{h} \right) + \frac{27}{70} \frac{\rho}{h^2} \frac{q^2}{\pi^2\rho^2 r^3} + \frac{24}{35} \frac{\rho\dot{h}}{h^2} \frac{q}{\pi\rho r} - \frac{15}{14} \frac{\rho\dot{h}^2}{h^2} \quad (9)$$

Integrating equation (9) with respect to r , with $p(a, t) = p_a$, we obtain

$$p_1 - p_a = \frac{3\mu\dot{h}}{h^3} (r^2 - a^2) - \frac{6\mu}{h^3} \frac{q}{\pi\rho} \ln(r/a) + \frac{24}{35} \frac{\dot{h}}{h^2} \frac{q}{\pi} \ln(r/a) - \frac{15}{28} \frac{\rho\dot{h}^2}{h^2} (r^2 - a^2) - \frac{3}{5} \frac{\rho}{h} \frac{\dot{q}}{\pi\rho} \ln(r/a) + \frac{3}{10} \frac{\rho}{h} \dot{h} (r^2 - a^2) - \frac{27}{140} \frac{q^2}{h^2\pi^2\rho} \left(\frac{1}{r^2} - \frac{1}{a^2} \right), \quad (10)$$

in which the subscript (1) indicates that equation (10) is the first iterative solution. The first and second terms on the right-hand side of equation (10) are those obtained in [12] for the viscous-dominated case; the first term results from the squeezing motion of the disk, and the second term results from the viscous shear flow from the central orifice. The remaining terms are corrections for unsteady and convective inertial effects of the flow. Although equation (10) is only the second approximation, [26] shows that the results from the third approximation (being the second iteration) only differ insignificantly while being much more cumbersome ($\partial p_2/\partial r$ equals 32 terms). Also, equation (10) may be compared with previous results obtained by other investigators by considering the limiting cases of squeezing flow and of steady flow.

For steady state ($\dot{h} = \dot{q} = 0$), equation (10) reduces to

$$p - p_a = -\frac{6\mu}{h^3} \frac{q}{\pi\rho} \ln(r/a) - \frac{27}{140} \frac{q^2}{h^2\pi^2\rho} \left(\frac{1}{r^2} - \frac{1}{a^2} \right) \quad (11)$$

This result was obtained by Peube [29], Jackson and Symmons [30], Savage [31], and Ramanaiah [32] by approaches of varying sophistication. Moller's [33] equation differs only in the second term, where his constant is 6.7 percent less. Jackson and Symmons and Ramanaiah used an iterative procedure, Peube and Savage each used a series approach, and Moller used a correction factor on a parabolic velocity profile, i.e.,

$$\frac{u}{U} = 4 \frac{z}{h} \left(1 - \frac{z}{h} \right) + \xi \frac{z}{h} \left(1 - 2 \frac{z}{h} \right)^3, \quad (12)$$

in which ξ was left to be determined in an elegant solution.

We can compare equation (10) with other works by setting all source-flow terms equal to zero, i.e., omitting the central orifice by setting $q = \dot{q} = 0$. This leaves

$$p - p_a = (r^2 - a^2) \left(\frac{3\mu\dot{h}}{h^3} + \frac{3}{10} \frac{\rho\dot{h}}{h} - \frac{15}{28} \frac{\rho\dot{h}^2}{h^2} \right) \quad (13)$$

which is identical to Kuzma's [21] result in his study of squeeze films. Jackson's [20] study of squeezing flow yields

$$p - p_a = (r^2 - a^2) \left(\frac{3\mu\dot{h}}{h^3} + \frac{3}{10} \frac{\rho\dot{h}}{h} - \frac{24}{35} \frac{\rho\dot{h}^2}{h^2} \right) \quad (14)$$

which differs from equation (13) in the last term only: 15/28 versus 24/35 (22 percent difference). However, one easily traces this difference to Jackson considering only $u \partial u/\partial r$ as an important convective inertia term, whereas both $u \partial u/\partial r$ and $w \partial u/\partial z$ were considered for equation (10) and thus for equation (13). (Reference [3] shows that when one includes $\partial u/\partial t$, then $w \partial u/\partial z$ must also be included for consistency.)

The equations for these two limiting cases, equation (11) and (13), agree well with the experimental data obtained by Moller [33], Kuzma [21], and Morgan and Saunders [34]. These checks on equation (10) clearly demonstrate the credibility of the equation (for the assumptions stated); we will show that the resulting disk-dynamics equation predicts the observed dynamics of a gas-levitated disk fairly well, in spite of what appear to be rather stringent constraints imposed in the derivation. This degree of agreement might arise from compensating errors and the importance of compressible and/or turbulent flow in the inner radii only, the load area concerned being small (area $\sim r^2$).

The pressure on the disk in the vicinity of the central orifice inlet is difficult to predict. To apply it to the disk's dynamics, we simply propose that this pressure is merely the total pressure of the incoming fluid and that inlet losses are negligible. Vohr [35] proposes a loss coefficient which should be used if the orifice were not rounded. Thus,

$$p_0^0 = p(r, h) |_{r < r_0} = P_{r_0} + \rho \frac{\bar{u}_{r,0}^2}{2} \quad (15)$$

in which $\bar{u} = q/(2\pi\rho rh)$ is the instantaneous, local mean radial velocity.

The Disk-Dynamics Differential Equation. Substituting equation (15) into equation (5) gives

$$m\dot{h} = 2\pi \int_{r_0}^a (p - p_a) |_{z=h} r dr + \frac{q^2}{8\pi\rho h^2} + \pi(r_0^2 p_{r_0} - a^2 p_a) - mg - F(t), \quad (16)$$

an equation now amenable to direct substitution of equation (10) and subsequent integration. Thus, with $T \equiv \sqrt{3g/h_e} t$, ($*$) $\equiv d/dT$, $H \equiv h/h_e$, $Q \equiv q/q_e$, $Re_e \equiv q_e/(\pi\mu a)$, $Re_h \equiv \rho a \sqrt{3gh_e}/\mu$, $H_e \equiv h_e/a$, $Re_h^* \equiv Re_h H_e/2$, and $\beta \equiv \pi\mu a^4/[4\mu gh_e^2 \sqrt{h_e/3g}]$, equation (16) becomes, in dimensionless form

$$H^3 \dot{H} + \frac{2}{5} \beta Re_h^* H^2 \dot{H} (1 - R_0^4) + \frac{5}{7} \beta Re_h^* H \dot{H}^2 \left(\frac{8}{15} R_0^4 - 1 \right) - \frac{8}{3} \beta Re_e^* H \dot{H} Q \left(\frac{13}{140} R_0^2 - \frac{12}{35} \right) - \frac{4}{5} \beta Re_e^* H^2 \dot{Q} (1 - R_0^2) - 2\beta \dot{H} (R_0^4 - 1) - \frac{2}{63} \frac{Q_e^* Re_e^*}{H_e^3} Q^2 H \left(\frac{27}{10} \ln R_0 + \frac{7}{8} \right) + \frac{Q_e^*}{3H_e^3} Q (R_0^2 - 1) + \frac{H^3}{3} + \frac{F(t)}{3mg} H^3 = 0 \quad (17)$$

with initial conditions $\dot{H}(0) = 0$ and $H(0) = H_i$ corresponding to equation (6).

When R_0^2 is much less than unity, equation (17) becomes

$$\left(H^3 + \frac{2}{5} \beta Re_h^* H^2 \right) \dot{H} + \frac{5}{7} \beta Re_h^* H \dot{H}^2 + \frac{32}{35} \beta Re_e^* H \dot{H} Q - \frac{4}{5} \beta Re_e^* H^2 \dot{Q} + 2\beta \dot{H} - \frac{2}{63} \frac{Q_e^* Re_e^*}{H_e^3} Q^2 H \left(\frac{27}{10} \ln R_0 + \frac{7}{8} \right) - \frac{Q_e^*}{3H_e^3} Q + \frac{H^3}{3} + \frac{F(t)H^3}{3mg} = 0 \quad (18)$$

We find the equilibrium film thickness, H_e , by setting $H = Q = 1$ and $\dot{H} = \dot{H} = \dot{Q} = F(t) = 0$; i.e., with $N \equiv \pi Re_e/Q_e^*$,

$$NH_e^3 - \pi Re_e^2 \left(\frac{9}{70} \ln R_0 + \frac{1}{24} \right) H_e - \pi Re_e = 0 \quad (19)$$

A nearly identical equation was presented in 1972 [1].

$Re_h^* \ll 1$ characterizes the viscous-dominated case. When we assume Re_h to be of the same order of magnitude as Re_e or less, then $Q_e^* = H_e^3$, Rayleigh's [28] steady-state solution for viscous-dominated flow, results. Also, equation (18) for $Re_e^* \ll 1$ and $F(t) = 0$ reduces to

$$H^3 \ddot{H} + 2\beta \dot{H} + \frac{1}{3} (H^3 - Q) = 0 \quad (20)$$

This equation, derived for the viscous-dominated case [13], provides another check on the present work.

Solving equation (19) for H_e (assuming the equilibrium mass flow rate, q_e , is known) and substituting into equation (18) completes the solution, except for the determination of Q as a function of time. We now seek $Q(t)$.

The Transient Mass Flow Through the Orifice. In a previous investigation [13], the instantaneous mass flow rate was approximated by the linear relation

$$q = bh + c \quad (21a)$$

wherein b was experimentally determined. The disk was levitated and the change in the steady-state mass flow rate was noted for a corresponding ten percent increase and decrease of the disk's clearance, h , from h_e . Equation (21a) may be rationalized by using a Taylor-series expansion for $q(t) = q[h(t)]$, viz.,

$$q[h(t)] = q_e + \frac{dq}{dh}\bigg|_e (h - h_e) + \frac{d^2q}{dh^2}\bigg|_e \frac{(h - h_e)^2}{2!} + \dots \quad (21b)$$

If $q[h(t)]$ were approximated by the first two terms, equation (21b) in dimensionless form would become

$$Q[h(t)] = 1 + B(H - 1) \quad (21c)$$

in which $B = h_e/q_e \, dq/dh|_e$, the coefficient tabulated by Pearson. This equation uses steady-state flow data to describe transient flow phenomena. Schultz-Grunow [36] conducted theoretical and experimental investigations of pulsating flow through orifices and gave criteria for which instantaneous flow rates could be evaluated from steady-flow equations.

Others have pursued similar investigations. In particular, Elrod [37], Chiang et al. [38], and Deckker and Chang [39] investigated the validity of using steady-state pressure/flow-rate relations for orifices and nozzles with unsteady-state conditions. They found that when the modified Strouhal number, $S^* = \omega(A/\Omega)^{1/2}/V$ (becoming $S = \omega D/V$ when Ω , the solid angle of the nozzle, equals 60 deg), is less than 0.1, the phase angle and amplitude variations from quasi-steady flow are negligible; when $S^* < 1$, compressible-flow behavior is nearly identical to that of incompressible flow. (Chiang et al. [38] found that when their frequency parameter is small (i.e., $\omega R/a_0 < 0.01$), the quasi-static relationship between pressure and mass-flux fluctuations is valid (ω = frequency, R = fictitious radius from point sink to where the Mach number equals unity, and a_0 is the stagnation speed of sound.)

The "Strouhal number" of the disk ($S_{\text{disk}} = \omega_n a/u$) must be of 0(1) to even retain the unsteady terms [3, 26]. Therefore,

$$\begin{aligned} S_{\text{disk}} &= \frac{\omega_n a}{\bar{u}} = \omega_n a \frac{\rho 2\pi r_0 h_e}{q} \frac{r_0}{r_0} \\ &= \frac{\omega_n d}{V} \frac{a h_e}{r_0^2} \\ &= S_{\text{nozzle}} \frac{a h_e}{r_0^2} \end{aligned}$$

in which there is no recess ($d = 2r_0$), V is the nozzle or orifice mean-velocity and \bar{u} is the maximum radial-mean-velocity. When $S_{\text{disk}} = 0(1)$ —actually, it is found that the data with which the theory is compared to be much less than 0(1)—

$$S_{\text{nozzle}} = \frac{\omega_n d}{V} = 0(1) \frac{r_0^2}{a h_e}$$

and easily satisfies the $S < 0.1$ criterion for nearly any reasonable orifice or nozzle angle. Thus, the use of the coefficient B , measured or derived, is justified.

The Linearization of the Disk-Dynamics Differential Equation. Equation (18) was solved numerically on a CDC 6500 digital computer using a MIMIC routine and on an IBM 360/370 digital computer using a CSMP (Continuous System Modelling Program) routine. Each solution routine used 4th-order Runge-Kutta numerical integration. In all solutions, $F(t)$ was set equal to zero for a freely levitated disk. (Adams and Shapiro [7] outline a very simple computational procedure applied to their viscous-dominated-flow equation for rectangular bearings, a nonlinear differential equation closely resembling equation (20). That procedure, among many others, is probably valid for the solution of equation (18).) Although we may draw conclusions from these solutions, the linearization of equation (18) provides a closed-form solution which yields expressions for the frequency and damping characteristics in terms of the parameters H_e , Re_e , Q_e^* , and β that are, in turn, functions of the geometry, load, mass flow rate, and fluid properties.

For cases where $|H - 1| \ll 1$, we may define $E = H - 1$, substitute into equation (19), and cast out higher-order terms, while also assuming $|E| \ll 1$. This gives, with $Q = 1 + BE$,

$$\begin{aligned} \left(1 + \frac{2}{5} \beta Re_h^*\right) \ddot{E} + \left(\frac{32}{35} Re_e^* - \frac{4}{5} Re_e^* B + 2\right) \beta \dot{E} \\ + \left[1 - \frac{1}{63} \frac{Q_e^* Re_e}{H_e^2} \left(\frac{27}{10} \ln R_0 + \frac{7}{8}\right) (2B + 1) - \frac{B}{3} \frac{Q_e^*}{H_e^3}\right] E \\ - \frac{1}{63} \frac{Q_e^* Re_e}{H_e^2} \left(\frac{27}{10} \ln R_0 + \frac{7}{8}\right) - \frac{Q_e^*}{3H_e^3} + \frac{1}{3} = 0 \quad (22) \end{aligned}$$

Substituting equation (19) into equation (22) results in

$$\begin{aligned} \ddot{E} + \frac{\frac{32}{35} Re_e^* - \frac{4}{5} Re_e^* B + 2}{1 + 2\beta Re_h^*/5} \beta \dot{E} \\ + \frac{\frac{1}{3} \left[\frac{Q_e^*}{H_e^3} (B + 1) - 2(B - 1) \right]}{1 + 2\beta Re_h^*/5} E = 0 \quad (23) \end{aligned}$$

We now obtain the previously derived linear result for the viscous-dominated case [13], recalling that $Q_e^* = H_e^3$, $Re_e^* \ll 1$, and $0(Re_h) \leq 0(Re_e)$ for viscous domination. This gives the linearized ordinary differential equation [13]

$$\ddot{E} + 2\beta \dot{E} + \left(1 - \frac{B}{3}\right) E = 0 \quad (24)$$

Comparing equations (23) and (24) reveals that including the inertia terms (echoed in the Re_e^* terms) in the Navier-Stokes equations increases the damping ratio of the system, because B is usually less than unity. The solution to equation (23), with the initial conditions of equation (6), is readily found to be

$$E = E_i \csc \phi e^{-\zeta \omega_n T} \sin [(1 - \zeta^2)^{1/2} \omega_n T + \phi] \quad (25)$$

for $\zeta < 1.0$ where

$$\omega_n^2 = \frac{\frac{1}{3} \left[\frac{Q_e^*}{H_e^3} (B + 1) - 2(B - 1) \right]}{1 + 2\beta Re_h^*/5} \quad (26)$$

Transient Response for Run 04

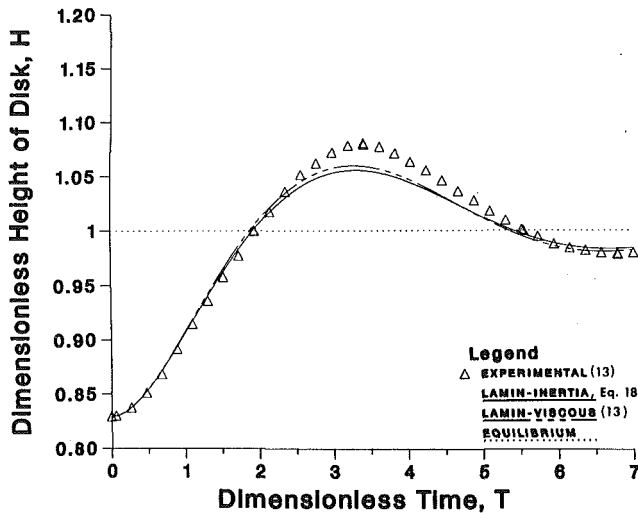


Fig. 3 Dynamic film thickness (disk height) versus time for disk no. 1 with nitrogen, group 4 ($m = 0.3572$ kg, $r_0 = 0.203$ mm, $Re_e^* = 0.0521$, $Q_e^* = 26.5 \times 10^{-9}$); very low fluid inertia

Transient Response for Run 08

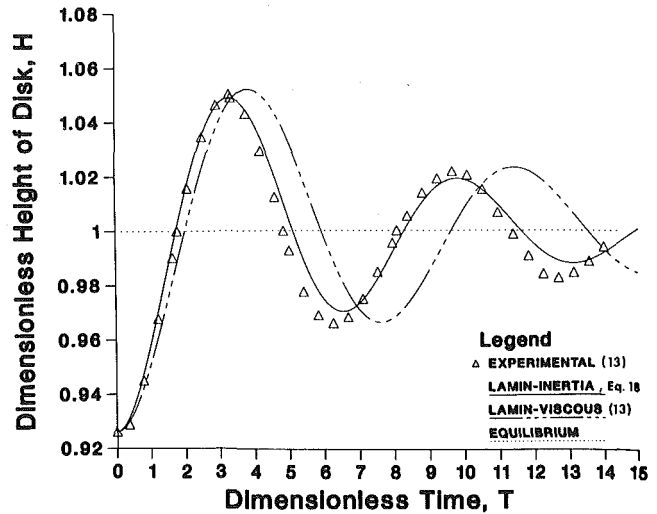


Fig. 5 Dynamic film thickness (disk height) versus time for disk no. 2 with nitrogen, group 8 ($m = 0.3509$ kg, $r_0 = 0.660$ mm, $Re_e^* = 0.316$, $Q_e^* = 108 \times 10^{-9}$); moderately low fluid inertia

Transient Response for Run 16

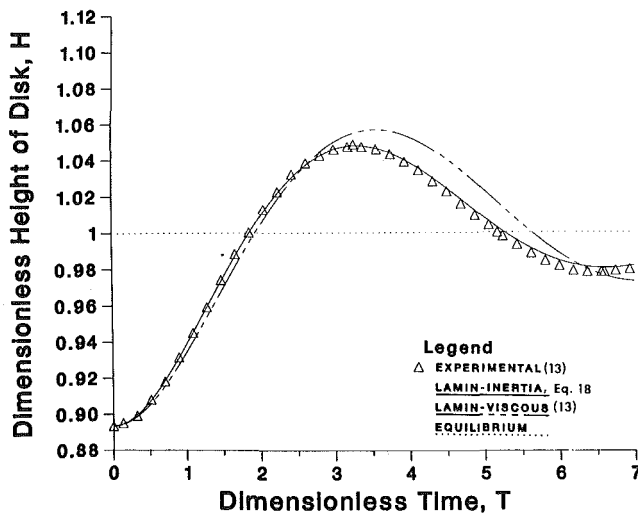


Fig. 4 Dynamic film thickness (disk height) versus time for disk no. 3 with argon, group 16 ($m = 0.11619$ kg, $r_0 = 0.495$ mm, $Re_e^* = 0.282$, $Q_e^* = 260 \times 10^{-9}$); moderately low fluid inertia

Transient Response for Run 12

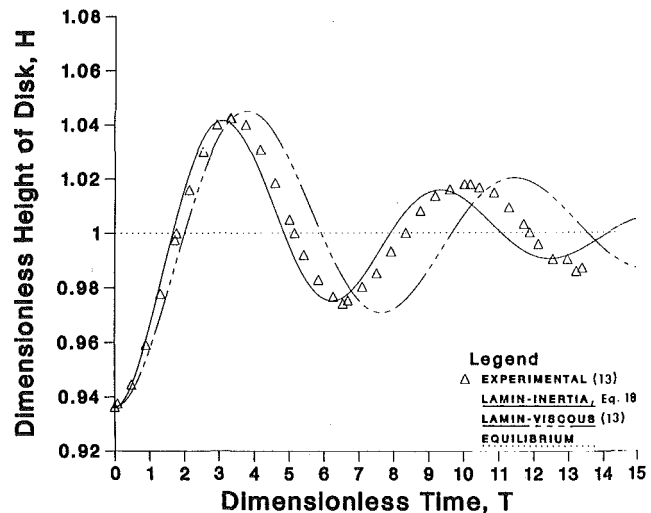


Fig. 6 Dynamic film thickness (disk height) versus time for disk no. 2 with argon, group 12 ($m = 0.3509$ kg, $r_0 = 0.660$ mm, $Re_e^* = 0.386$, $Q_e^* = 148 \times 10^{-9}$); moderate fluid inertia

$$\zeta = \frac{\frac{32}{35} Re_e^* - \frac{4}{5} Re_e^* B + 2}{1 + 2\beta Re_e^*/5} \beta/2\omega_n \quad (27)$$

and

$$\phi = \arccot [\zeta/\sqrt{1-\zeta^2}] \quad (28)$$

For $\zeta = 1$, we have

$$E = \left[E_i + \left(\frac{\dot{E}_i}{\omega_n} + E_i \right) \omega_n T \right] e^{-\omega_n T} \quad (29)$$

for $\zeta > 1.0$, we have the overdamped response

$$E = \frac{E_i}{\Gamma - \Gamma^*} (\Gamma e^{-\Gamma^* T} - \Gamma^* e^{-\Gamma T}), \quad (30)$$

in which $\Gamma = [\zeta + \sqrt{(\zeta^2 - 1)}] \omega_n$, and $\Gamma^* = [\zeta - \sqrt{(\zeta^2 - 1)}] \omega_n$.

ω_n . Including a forcing function results in a set of slightly more complicated equations, but since equations (25), (29), and (30) are written in standard form, the form of the solutions may be found in standard texts on vibrations [40, 41].

Comparison of Theory With Existing Experimental Data

In a previous investigation [2], the dynamic data were obtained by first levitating a disk at the desired equilibrium mass flow rate. A steel shot or piston was dropped through a glass tube so that it struck a boss on top of the disk and perturbed it. The shot bounced away, was deflected, and trapped, and an oscilloscope was triggered as the disk started its downward motion. The disk then underwent a free transient motion and, at the same time, the display on the oscilloscope was recorded photographically on Polaroid film.

Transient Response for Run 20

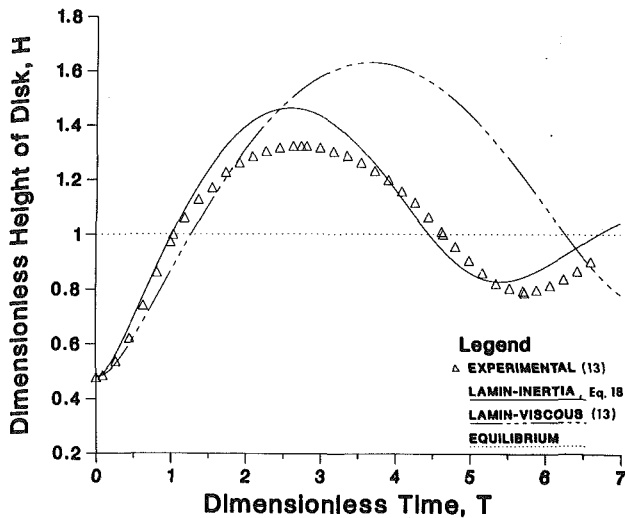


Fig. 7 Dynamic film thickness (disk height) versus time for disk no. 3 with argon, group 20 ($m = 0.11619$ kg, $r_0 = 0.495$ mm, $Re_e^* = 0.615$, $Q_e^* = 519 \times 10^{-9}$); moderately high fluid inertia

Transient Response for Run 18

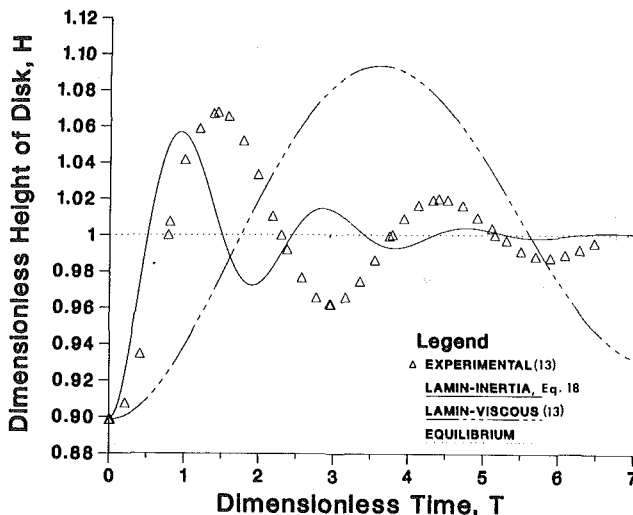


Fig. 8 Dynamic film thickness (disk height) versus time for disk no. 3 with argon, group 18 ($m = 0.11619$ kg, $r_0 = 0.495$ mm, $Re_e^* = 1.26$, $Q_e^* = 1242. \times 10^{-9}$); high fluid inertia

Two gases, nitrogen and argon, and three disks, each having diameters of 3 in., were used. Disks Nos. 1 and 2 are over three times as massive as disk No. 3, while the orifice radii of disks Nos. 2 and 3 are about three times that of disk No. 1.

The equilibrium mass flow rate, a primary known quantity in the experiments, was used in the solutions of the derived differential equations as the "given" quantity along with the mass and geometry of the disk, the temperature of the source-flow gas, and the atmospheric pressure and temperature. The equilibrium film thickness was then calculated by equation (19). With $H = h/h_e$ and $T = \sqrt{3g/h_e}t$, an error in predicting the equilibrium film thickness, h_e , is reflected in the dynamic case, since $H_e = h_e/a$ in equations (17) and (19).

Figures 3-8 show six representative sets of displacement data [2] for the three disks along with the solutions for viscous-dominated and laminar flows.

The dynamic traces shown for the viscous-dominated case in Figs. 3-8 differ from those shown in [2]. This is so because

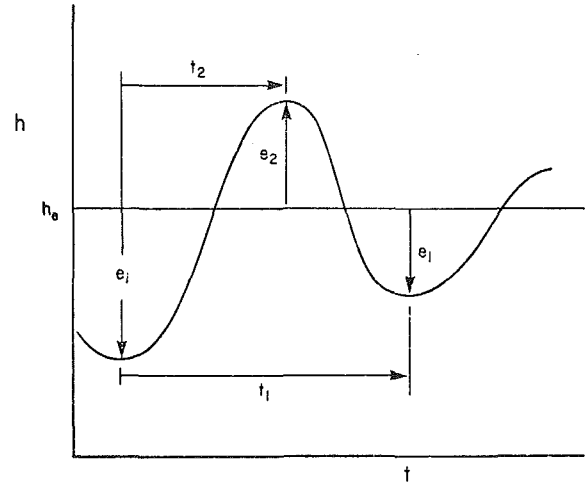


Fig. 9 Definitions of quantities used in the determination of frequency and logarithmic decrement

in the calculation of the damping coefficient, β , equation (20) uses the theoretical equilibrium film thickness, $H_e = Q_e^{*1/3}$, whereas [2] used the experimental film thickness.

Throughout this discussion "viscous-dominated" implies a fully laminar film with neglected inertia; "laminar" implies that the inertial terms are accounted for.

The very low mass flow rate for the trace shown in Fig. 3 gives a reduced exit Reynolds number of 0.0521. According to the equations developed, $Re_e^* = 0.0521$ should give nearly identical results for the laminar and viscous-dominated theories. Figure 3 shows this. The theory underpredicts the overshoot of the disk by about 30.0 percent and very closely models the general nature of the motion. The viscous-dominated theory, therefore, is quite adequate to predict the behavior for this low value of Re_e^* .

The flow field for the case presented in Fig. 3 is interesting. The minimum flow area is initially the annulus area, $2\pi r_0 h$ (being less than the orifice area πr_0^2), but becomes the orifice area as the disk rises and, depending on the amount of separation at the entrance, could possibly become the annular area at the end of one cycle and return again to be the orifice area as the motion is damped out. This minimum flow area oscillation apparently has very little effect on the dynamics of the disk. The equilibrium minimum area of πr_0^2 might account for the measured value of the parameter B being zero for this case. This appears to be substantiated by the fact that this is the only case in the experimental data for which the orifice area is the minimum flow area and in no other case is $B = 0$; most have $B > 0.5$.

Figures 4-6 correspond to $0.28 \leq Re_e^* \leq 0.39$. Figure 6 corresponds to a mass flow rate nearly six times that for Fig. 3, and the reduced exit Reynolds number is now 0.386, which does not quite satisfy the criterion of $Re_e^* \ll 1$ for viscous-dominated flow. Even so, Figs. 4-6 show that the results for viscous-dominated flow (equations (20) and (24)) is still a fair approximation and would give the frequency and damping characteristics with less than 20 percent error. The laminar theory more closely approximates the experimental trace and predicts the frequencies within 4 percent; the error in predicting the damping characteristics is minute. (According to [1], turbulence would now exist (theoretically) on 8.4 percent of the disk surface area for the steady-state film.)

Figure 7, for $Re_e^* \approx 0.6$, illustrates that the laminar theory is far preferable as the character of the flow changes from viscous dominated to inertial flow.

The dynamic trace for the highest mass flow rate available, over 8 times that for Fig. 6 and 47 times that for Fig. 3, is shown in Fig. 8. This corresponds to a reduced exit Reynolds number of 1.26 and a laminarization radius of 0.507 of the

Normalized Damped Frequencies

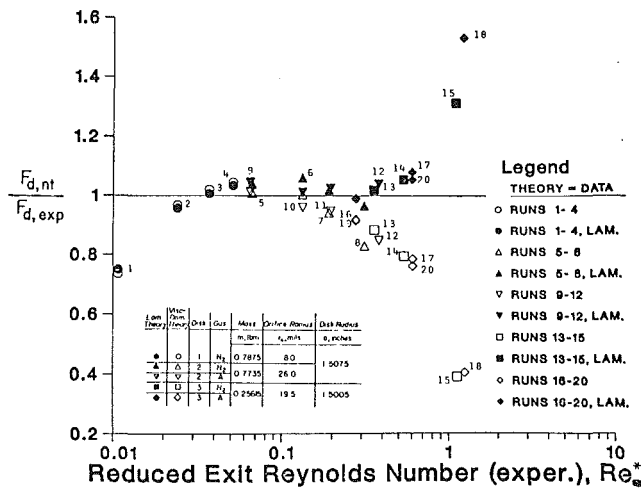


Fig. 10 Normalized damped frequency of disk versus reduced exit Reynolds number, laminar and viscous-domination theories

Normalized Logarithmic Decrements

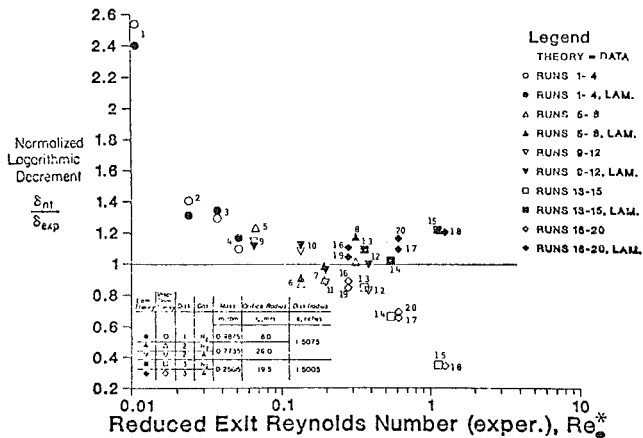


Fig. 11 Normalized logarithmic decrement versus reduced exit Reynolds number, laminar and viscous-domination theories

disk radius [1]. The viscous-dominated-flow theory is not expected to hold as, indeed, Fig. 8 illustrates. The laminar theory approximates the trace fairly well, particularly upon noting that not only does turbulence exist on 25.7 percent of the area, but also choked flow probably exists—although the radial flow would limit the region of supersonic flow to a very small area [26].

The traces for the viscous-dominated theory differ from those presented in [2, 13] because, for cases of high inertia, experimental values of h_e differ from the calculated values of β . The equilibrium film thickness prediction, 104 percent overpredicted by Rayleigh's equation and 22 percent underpredicted by equation (19) for the trace of Fig. 8, is manifested in the dynamics by similar errors.

The damped frequency, logarithmic decrement, and half-life were calculated for the nonlinear equation by the standard damped sinusoid method employed in [2] so that any theory-data comparison is consistent. Thus,

$$F_d = \frac{2\pi}{T_1} = \frac{2\pi\sqrt{h_e/3g}}{t_1} \quad (31)$$

$$\delta = \ln(e_i/e_1) = \ln(E_i/E_1) \quad (32)$$

$$H = \frac{T_1 \ln 2}{\delta} = \frac{t_1 \ln 2}{\sqrt{h_e/3g} \ln(e_i/e_1)} \quad (33)$$

in which t_1 , e_1 , and e_i are defined by the representative sketch

in Fig 9. Strong damping occurring in groups 1, 2, and 9 required the use of t_2 and e_2 .¹ The coordinates T_1 , E_1 and T_2 , E_2 were given in the MIMIC and CSMP solutions of the nonlinear differential equations and subsequently used in equations (31–33).

The experimental data are used as “absolute” with which to compare the theory so that Fig. 10 is the normalized damped frequency plotted versus the experimental reduced exit Reynolds number. First, note groups 1–4, which are for disk No. 1 and nitrogen. The laminar and viscous-dominated theories predict the behavior equally well, Re_e^* being less than 0.06. The discrepancy between theory and experiment is 5 percent or less, except for group 1 which has over 20 percent error. Even so, [13] gives total uncertainties of 10.4, 1.92, 1.46, and 1.44 percent for the frequencies, F_d , of groups 1, 2, 3, and 4, respectively. Also, the difficulty in taking the measurements under such strong damping conditions is noted in [2]. ζ for group 1 is calculated from the experimental data to be 0.728 and theoretically predicted to be ~ 0.93 . Note that ζ rarely exceeds 0.7 for most mechanical systems.

Next, the results for groups 5–8, being for disk No. 2 and nitrogen, agree with the data well, except for group 8. The laminar theory underpredicts the frequency for group 8 by 3.5 percent; the viscous-dominated theory underpredicts it by 17 percent (an error again to be expected in the viscous-dominated case since $Re_e^* = 0.317$).

The remainder of the data, groups 9–20, are predicted well by the laminar theory, all within 8 percent except for groups 15 and 18, which have discrepancies of 31 and 53 percent, respectively. The viscous-dominated theory underpredicts the frequency more and more as the reduced exit Reynolds number increases, giving 60 percent error for the highest mass flow rate groups, 15 and 18.

Figure 11 shows the damping characteristic, the logarithmic decrement, δ . The laminar theory overpredicts δ by as much as 22 percent, disregarding groups 1–5. Note that although the laminar theory reasonably predicts the damping for group 15, it overpredicts the frequency by 31 percent. Again, the viscous-dominated theory underpredicts the damping for larger Re_e^* by as much as 65 percent for $Re_e^* = 1.26$.

Figures 12–15 show the general behavior of the oscillatory motion of the disks. Figures 12 and 13 show how the data compare with equation (20), the previously derived nonlinear theory [12, 13], and the present laminar theory, equation (17), respectively. Note that if theory and experiment agreed perfectly, all points would lie on the quarter-circle line; therefore, the vertical distance from the line indicates the discrepancy for a given value of the damping ratio, ζ . Thus, upon again disregarding groups 1, 15, and 18, the laminar theory predicts the overall performance with less than 15 percent error. If group 2 were disregarded, this figure would drop to 6 percent. Figures 14 and 15 show the half-life, H , plotted versus $\omega_n \zeta$ for the linearized equations ($\omega_n \zeta$ equals β for the viscous-dominated case). The theory for viscous-dominated flow overpredicts the half-life, except for groups 1–4, particularly for smaller values of β . The linearized laminar theory predicts the half-life fairly well except for groups 1–5, 15, 18, and 20. We don't expect the experimental half-life for group 20 to agree with H from the linearized theory since $E_i = 0.508$, which does not initially satisfy the linearization criterion, $|E| \ll 1$. Group 19, however, has $E_i = 0.530$, but yet the half-life is predicted well. $Re_e^* = 0.281$ for group 19 and 0.615 for group 20, and equation (18), for example, contains the coefficient βRe_e^* for the nonlinear

¹This can, of course, be misleading. The computer results show that the frequencies for group 1 based on T_1 and T_2 are 0.46 and 0.33, respectively, producing an error of 27 percent when using T_2 and E_2 for the calculations. Groups 2 and 9 did not show a large discrepancy; T_1 , E_1 and T_2 , E_2 gave almost identical results.

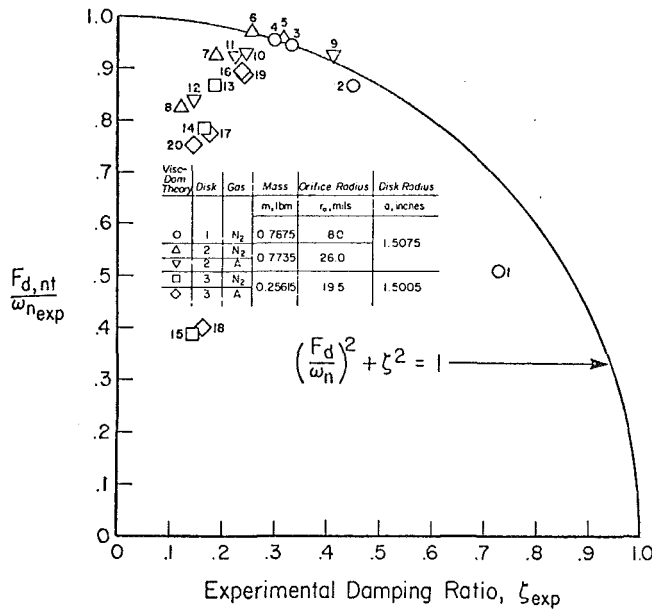


Fig. 12 Ratio of theoretical damped frequency to experimental natural frequency versus experimental damping ratio, viscous-domination

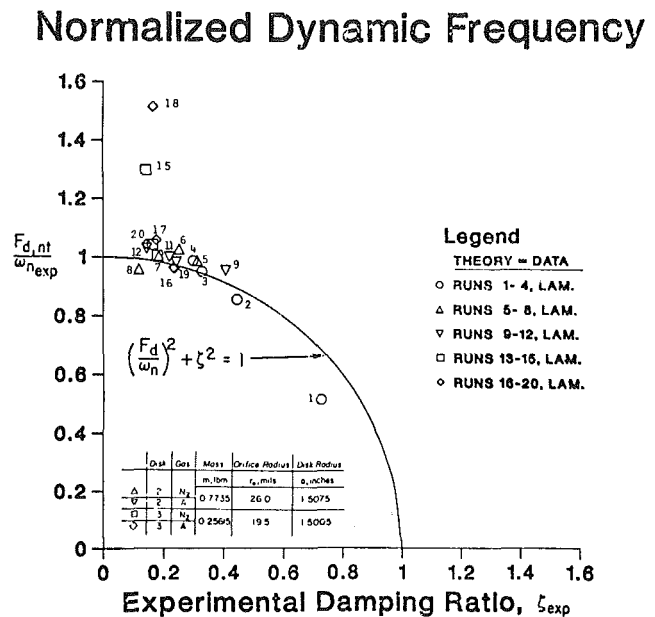


Fig. 13 Ratio of theoretical damped frequency to experimental natural frequency versus experimental damping ratio, laminar (inertial)

Table 1 Comparison of (a) experimental data,* (b) nonlinear laminar theory (equation (17)), and (c) linearized laminar theory (equation (23))

Group	F_d , damped frequency			ζ , damping parameter			H , half-life		
	(a)	(b)	(c)	(a)	(b)	(c)	(a)	(b)	(c)
1.	0.441	~0.33	0.409	0.728	~0.93	0.905	1.48	~0.82	0.796
2.	0.836	0.800	0.809	0.448	0.551	0.556	1.65	1.31	1.28
3.	0.889	0.895	0.891	0.331	0.429	0.427	2.22	1.63	1.65
4.	0.909	0.940	0.934	0.301	0.347	0.351	2.42	2.00	1.98
5.	0.702	0.730	0.731	0.315	0.380	0.377	2.97	2.31	2.33
6.	0.791	0.839	0.839	0.254	0.233	0.236	3.33	3.44	3.40
7.	0.882	0.898	0.897	0.187	0.185	0.188	4.13	4.10	4.03
8.	0.995	0.960	0.960	0.122	0.143	0.146	5.68	4.99	4.88
9.	0.669	0.700	0.703	0.411	0.450	0.445	2.30	1.97	1.98
10.	0.814	0.824	0.824	0.245	0.274	0.276	3.36	2.95	2.94
11.	0.866	0.887	0.887	0.222	0.214	0.217	3.52	3.56	3.52
12.	0.970	1.01	1.01	0.148	0.148	0.151	4.78	4.60	4.52
13.	0.982	1.00	1.00	0.183	0.201	0.206	3.78	3.37	3.29
14.	1.10	1.16	1.16	0.167	0.171	0.176	3.72	3.44	3.34
15.	2.24	2.94	2.95	0.145	0.177	0.182	2.11	1.31	1.27
16.	0.959	0.950	0.947	0.235	0.260	0.265	2.99	2.71	2.67
17.	1.12	1.21	1.21	0.179	0.196	0.203	3.39	2.87	2.78
18.	2.14	3.28	3.28	0.168	0.202	0.208	1.91	1.03	0.995
19.	0.946	0.936	0.947	0.239	0.250	0.265	2.98	2.87	2.67
20.	1.10	1.16	1.21	0.148	0.173	0.203	4.20	3.40	2.78

*Pearson [13]

terms HH and H^2 . We suggest that the criterion $|E_i| \ll 1$ for linearization is more stringent for higher values of Re_e^* .

Finally, the linearized equation, which gives a most useful closed-form solution, is shown to give rather accurate results by inspection of Table 1. The reader is also referred to the traces shown in [2] and [13]. The generality of the linearized, laminar disk-dynamics theory was tested [26] to show the variation of the damped frequency, logarithmic decrement, and half-life with increasing values of E_i , the initial displacement from the equilibrium film thickness. The dependence of all three parameters on the initial displacement was apparent so that the criterion of $|E_i| \ll 1$ is fairly stringent. This criterion becomes less important for lower values of Re_e^* and vice versa. The parameter B was varied in $Q = 1 + BE$ and an arbitrary time lag was introduced to test the sensitivity of the results to the quasi-steady flow approach. The results show that reasonable values of $0 \leq B \leq 1.3$ produce sufficiently accurate results [26].

Table 2 Comparison of errors involved when using (a) viscous-dominated and (b) laminar nonlinear disk dynamics theories.

Group	Re_e^*	Frequency		Percent error		Half-life	
		(a)	(b)	(a)	(b)	(a)	(b)
13	0.362	-11.7	2.10	-15.0	9.74	33.2	-10.7
14	0.547	-20.6	5.65	-33.3	2.38	88.3	-7.72
15	1.13	-60.9	31.9	-64.8	22.0	728.	-38.9

Groups 13-15 were chosen for Table 2 to compare the error in the results obtained for noninertial and inertial laminar flows. A cursory inspection of Table 2 shows the overriding importance of the fluid's inertia since the laminar theory predicts the behavior much better than the viscous-dominated theory for these moderate-to-high values of Re_e^* . The laminar

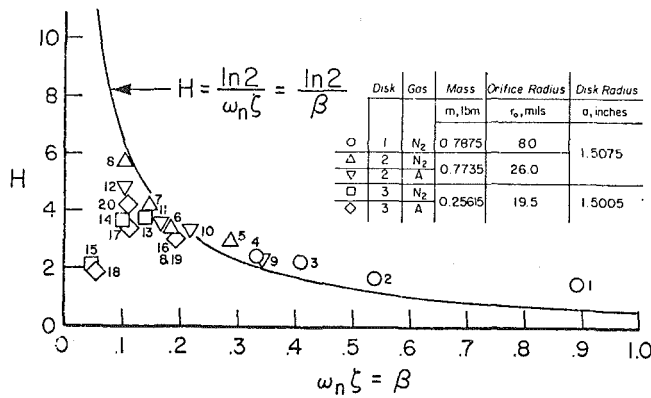


Fig. 14 Experimental half-life of disk's vertical oscillation versus damping coefficient, $(\omega_n \zeta = \beta)$

Damping Characteristics

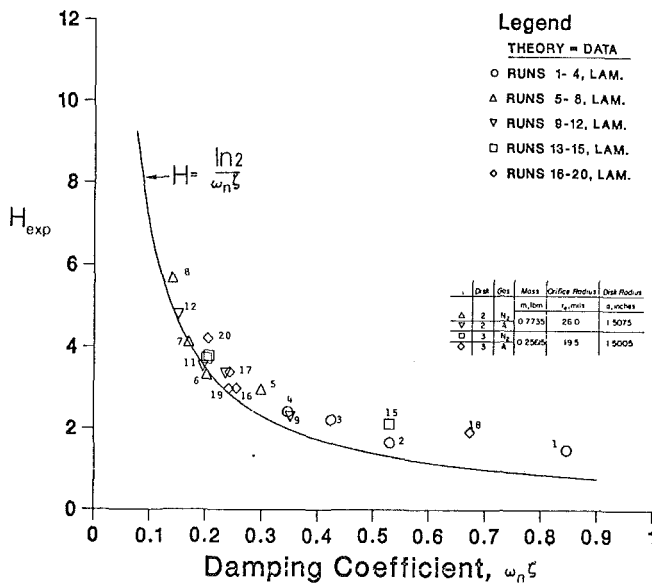


Fig. 15 Experimental half-life of disk's vertical oscillation versus damping coefficient, $\omega_n \zeta$: laminar

theory (viscous-inertial) predicts the dynamic behavior of the disk with sufficient accuracy until Re_d^* exceeds about 0.6. A review of [1] shows that this is consistent with the equilibrium film thickness predicted by the laminar theory.

In conclusion, it has been shown that the laminar theory (equation (17)) accurately predicts the dynamic behavior of the disk for $Re_d^* \leq 0.6$. It has been further shown that a closed-form solution of the linearized equation (equation (25)) will give reasonably good results for moderate-to-high values of Re_d^* when $|E_i| \ll 1$. Equation (25) may also be used when $Re_d^* \ll 1$ and $|E_i|$ is not $\ll 1$.

Acknowledgments

Portions of this were performed under a grant from the National Science Foundation and under the auspices of the U.S. Department of Energy. We appreciate the careful assistance of Eileen Johnson.

References

1 Warinner, D. K., and Pearson, J. T., "Laminar and Turbulent Film Thickness Relation for Circular Hydrostatic Thrust Bearings," ASME Gas Turbine and Fluids Engineering Conference, San Francisco, 1972, Paper No. 72-FE-38.

2 Pearson, J. T., and Bradfield, W. S., "Experimental Study of a Gas Levitated Disk," ASME Journal of Applied Mechanics, Vol. 38, 1971, pp. 651-658.

3 Warinner, D. K., and Pearson, J. T., "Fluid-Inertia Effects in Radial Flow Between Oscillating, Rotating Parallel Disks," ASME Journal of Lubrication Technology, Vol. 103, Jan. 1981, pp. 144-149.

4 Wilcock, D. F., "Externally Pressurized Bearings as Servomechanisms," ASME Journal of Lubrication Technology, Oct. 1967, pp. 418-424.

5 Brown, G. M., "The Dynamic Characteristics of a Hydrostatic Thrust Bearing," Int. J. Mach. Tool Des. Res., Vol. 2, 1961, pp. 157-171.

6 Stowell, T. B., "Pneumatic Hammer in a Gas Lubricated Externally Pressurized Annular Thrust Bearing," ASME Journal of Lubrication Technology, Vol. 93, Oct. 1971, pp. 498-503.

7 Adams, M. L., and Shapiro, W., "Squeeze Film Characteristics in Flat Hydrostatic Bearings With Incompressible Flow," ASLE Transactions, Vol. 1, 1969, pp. 183-189.

8 Weber, R. R., "An Investigation of the Dynamic Response of Hydrodynamic Gas Bearings," M.S. thesis, University of California, Los Angeles, 1952, p. 48.

9 Roudebush, W. H., "An Analysis of the Effect of Several Parameters on the Stability of an Air-Lubricated Hydrostatic Thrust Bearing," NACA Tech. Note 4095, July 1957.

10 Licht, L., "An Analytical and Experimental Study of the Stability of Externally Pressurized, Gas-Lubricated Thrust Bearings," Ph.D. thesis, Columbia University, 1961.

11 Licht, L., "Axial, Relative Motion of a Circular Step Bearing," ASME Journal of Basic Engineering, Vol. 81, June 1959, pp. 10-17.

12 Pearson, J. T., and Bradfield, W. S., "Time-Dependent Pressure Field Beneath a Gas-Levitated Disk," ASME Journal of Applied Mechanics, Vol. 38, 1971, pp. 276-277.

13 Pearson, J. T., "Dynamics of a Gas Levitated Disk," Ph.D. thesis, State University of New York at Stony Brook, Mar. 1967, pp. 180.

14 Ishizawa, Shingo, "The Axisymmetric Laminar Flow in an Arbitrary Shaped Narrow Gap," Bulletin JSME, Vol. 9, No. 1, 1966, pp. 86-103.

15 Ishizawa, Shingo, "Unsteady Laminar Flow Between Two Parallel Discs With Arbitrarily Varying Gap Width," Bulletin JSME, Vol. 9, No. 35, Aug. 1966, pp. 533-550.

16 Ishizawa, Shingo, "On the Momentum-Integral Method of Solution for the Laminar Disk," ASME Journal of Applied Mechanics, Vol. 93, 1971, pp. 651-658.

17 Terrill, R. M., "The Flow Between Two Parallel Circular Disks, One of Which is Subject to a Normal Sinusoidal Oscillation," ASME Journal of Lubrication Technology, Vol. 91, Jan. 1969, pp. 126-131.

18 Kuhn, E. C., and Yates, C. C., "Fluid Inertia Effect on the Film Pressure between Axially Oscillating Parallel Circular Plates," Trans. ASLE, Vol. 7, 1964, pp. 299-303.

19 Hunt, J. B., "Pressure Distribution in a Plane Fluid Film Subjected to Normal Sinusoidal Excitation," Nature, Sept. 1966, pp. 1137-1139.

20 Jackson, J. D., "A Study of Squeezing Flow," Appl. Sci. Res., Sec. A, XI, 1962, pp. 148-152.

21 Kuzma, D. C., "Fluid Inertia Effects in Squeeze Films," Appl. Sci. Res., Vol. 18, No. 1, Aug. 1967, pp. 15-20.

22 Tichy, J. A., and Winer, W. O., "Inertial Considerations in Parallel Circular Squeeze Film Bearings," ASME Paper No. 70-Lub. S-9, 1970.

23 Whitney, W. M., "Theory of the Air-Supported Puck," American Journal of Physics, Vol. 32, No. 1, 1964, pp. 306-312.

24 Licht, L., and Kaul, R. K., "Effects of Misalignment on a Circular Externally Pressurized, Gas-Lubricated Bearing," ASME Journal of Applied Mechanics, Vol. 31, No. 1, 1964, pp. 141-43.

25 Ausman, J. S., "Gas Squeeze Film Stiffness and Damping Torque on a Circular Disk Oscillating about Its Diameter," ASME Journal of Lubrication Technology, Vol. 89, No. 2, 1967, pp. 219-221.

26 Warinner, D. K., "The Dynamics and Gas Dynamics of a Circular Aerostatic Thrust Bearing," Ph.D. thesis, Purdue University, West Lafayette, Indiana, May 1973, pp. 189.

27 Stefan, J., "Versuche uber die scheinbare Adhasion," Akademie d. Wissenschaften (Wien), Mathnaturw. Kl, Sitzungsberichte Abt. II Mathematik, LXIX, January-May, 1874, pp. 713-735.

28 Rayleigh, L., "A Simple Problem in Forced Lubrication," Engineering, Dec. 14, 1917.

29 Puebe, J. L., "Sur l'écoulement Radial Permanent d'un Fluid Visqueux Incompressible entre Deux Plans Paralleles Fixes," Journal de Mecanique, Vol. 2, No. 4, 1963, pp. 377-395.

30 Jackson, J. D., and Symmons, G. R., "An Investigation of Laminar Radial Flow Between Two Parallel Discs," Appl. Sci. Res., Sec. A, XV, 1965, pp. 59-75.

31 Savage, S. B., "Laminar Radial Flow Between Parallel Plates," ASME Journal of Applied Mechanics, Vol. 31, No. 4, 1964.

32 Ramanaiyah, G., "Inertia Effects in Hydromagnetic Lubrication, Part I: Externally Pressurized Bearing," Appl. Sci. Res., Vol. 17, 1967, pp. 296-304.

33 Moller, P. S., "Radial Flow without Swirl between Parallel Discs," Aeronautical Quarterly, Vol. 14, May 1963, pp. 163-186.

34 Morgan, P. G., and Saunders, A., "An Experimental Investigation of Inertial Effects in Viscous Flow," Int. J. Mech. Sci., Vol. 2, 1969, pp. 8-12.

35 Vohr, J. H., "An Experimental Study of Flow Phenomena in the Feeding Region of an Externally Pressurized Gas Bearing," Mechanical Technology, Inc. Report MTI-65 TR47, July 21, 1966.

36 Schultz-Grunow, F., "Durchflussmessverfahren für Pulsierende Strömungen," *Forschung auf dem Gebiete des Ingenieurwesens*, Vol. 12, 1941, pp. 117-126.

37 Elrod, H. G., Jr., "The Theory of Pulsating Flow in Conical Nozzles," *ASME Journal of Applied Mechanics*, Vol. 30, Mar. 1963, pp. 1-6.

38 Chiang, T., et al., "Analysis of Pulsating Flows in Infinite and Finite Conical Nozzles," ASME Paper No. 69-APM-16, 1969.

39 Deckker, B. E. L., and Chang, Y. F., "Transient Effects in the Discharge of Compressed Air from a Cylinder through an Orifice," *Trans. ASME, Journal of Basic Engineering*, XC(D) Sept. 1968, pp. 333-342.

40 Steidel, R. F., Jr., *An Introduction to Mechanical Vibrations*, New York, John Wiley and Sons, 1971.

41 Thomson, W. T., *Vibration Theory and Applications*, Englewood Cliffs, N.J., Prentice-Hall Inc., 1965.

R. F. Tape

Rolls-Royce, Inc.,
Atlanta, Ga.

W. R. Hartill

Rockwell International,
Los Angeles, Calif.

Lt. S. Curry

Aero-Propulsion Laboratory,
Wright-Patterson AFB, Ohio

T. J. Jones

Rolls-Royce Limited,
Bristol, England

Vectoring Exhaust Systems for STOL Tactical Aircraft

An analytical study has been performed to investigate the performance and application of four exhaust nozzle concepts with the potential to enhance the short takeoff and landing capabilities of advanced tactical aircraft for the 1990s. The exhaust system concepts include side and rear exhaust thrust vectoring systems with axisymmetric and nonaxisymmetric nozzles. To investigate the application of the nozzle concepts, advanced tactical aircraft have been configured which will operate from 700 or 1000 foot fields. Four different propulsion system configurations were used, each producing glide slope equilibrium in a different way. The characteristics of these STOL aircraft are compared with those of a CTOL aircraft designed to perform the same mission. The results show that the short field performance can be achieved with little aircraft TOGW or LCC penalty. The study also identifies promising configurations for STOL tactical aircraft.

Introduction

There is widespread appreciation of the need to reduce the dependence of future tactical aircraft on long runways because of the latter's vulnerability to damage by enemy airstrikes. One solution to runway denial is to use short takeoff and landing (STOL) aircraft, which can either continue to operate from the undamaged sections of a bombed airfield or use the more plentiful shorter bases [1].

Addressing the problems of achieving STOL performance in tactical aircraft, it becomes apparent that, with the thrust-to-weight ratios typical of current and projected vehicles, there is generally little difficulty in achieving a short takeoff ground roll. The landing, however, becomes the field sizing parameter. To reduce landing ground roll, the aircraft must approach and touch down at lower velocities and be able to decelerate faster once on the ground. Two problems associated with the reduced dynamic pressure at low approach speed are the losses of aerodynamic lift and control forces. One way of supplementing the aerodynamic lift generated at low speed is to use some of the engine thrust to provide a lift component. The ability to maintain adequate aircraft stability and control can, however, still limit the minimum approach speed for an aircraft with conventional aerodynamic control surfaces. Lower approach speeds would require some form of reaction control system or blowing to supplement the aerodynamic control surfaces.

Advanced exhaust system concepts, predicted to enhance

the takeoff and landing performance of advanced tactical aircraft, are being investigated in the STOL Exhaust Nozzle (STOLEN) Concepts program sponsored by Air Force Wright Aeronautical Laboratories, Aero-Propulsion Laboratory, under Contract F33615-81-C-2002. This is a three-year analytical and experimental program. The first phase consisted of analytical definition and performance prediction of four STOL exhaust system concepts. Tactical aircraft configurations employing these concepts were synthesized and their characteristics compared with those of a conventional takeoff and landing (CTOL) aircraft designed to the same mission. Subscale model static and wind tunnel tests will be performed during the second phase in late 1983 to validate the predicted internal and installed performance and expand the data base for STOL nozzle performance predictions.

This paper presents some results of the Phase 1 study and the integration of the STOL exhaust system concepts into aircraft configurations to achieve 700 and 1000 foot field lengths. In this study the use of thrust vectoring to achieve the mission maneuvering requirements was not used and the minimum airspeeds for approach were selected to avoid the need for engine air bleed for reaction controls or control surface blowing.

CTOL Baseline Configuration

The design and alternate missions and flight performance requirements are summarized in Fig. 1. The design mission is defensive counterair (DCA) with a radius of 250 nautical miles, and the alternate mission is an air-to-ground role for close air support (CAS) or combat zone interdiction (CZI). A 100 nautical mile leg from base to FEBA (Forward Edge of Battle Area) is specified, with the penetration range at sea level beyond the FEBA, a fallout.

The CTOL baseline configuration for this study, shown in Fig. 2, had basic aerodynamic characteristics derived from Rockwell HiMat technology. An all-movable, flapped, close-

¹ Conversion to S.I. units:

1 nautical mile	= 1.852 km
1 ft	= .3048 m
1 lbm	= .4536 kg
1 lbf	= 4.448 N
1 lb/ft ²	= 47.88 Pa
1 knot	= .5144 m/s

Contributed by the Gas Turbine Division of THE AMERICAN SOCIETY OF MECHANICAL ENGINEERS and presented at the 28th International Gas Turbine Conference and Exhibit, Phoenix, Arizona, March 27-31, 1983. Manuscript received at ASME Headquarters January 4, 1983. Paper No. 83-GT-212.

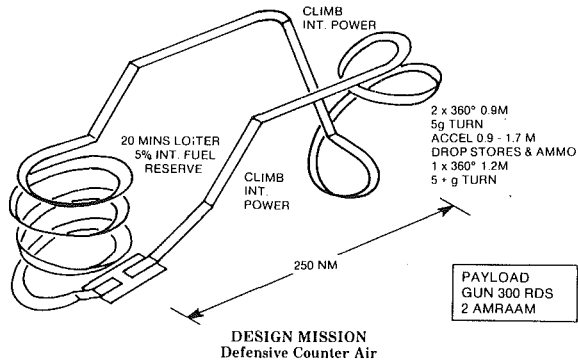


Fig. 1 Study missions

coupled canard was used, with a 15 percent design instability in pitch. A speed brake and a drag chute were included and sized to give a conventional landing distance within 1,500 feet. A single mixed flow turbofan engine was used with a fixed five degree ramp inlet and an axisymmetric C-D nozzle. A bypass ratio trade study for the engine in the CTOL baseline aircraft was performed which resulted in an optimum bypass ratio of 0.6 being used.

CTOL aircraft primary vehicle and performance characteristics are also summarized in Fig. 2. The vehicle sizing study determined the minimum TOGW to be 23,717 pounds, with the 5 g maneuver at Mach 0.9, 30,000 ft being the critical sizing requirement.

STOL Requirements

A parametric analysis of takeoff and landing characteristics was made to define STOL requirements. The landing results, Fig. 3, show that landing approach speeds of 80 and 100 knots are required to achieve 700 and 1000 foot landing distance respectively, using conventional braking and typical levels of thrust reversing.

The takeoff results of Fig. 3 indicate that with T/W of around 1.0 there should be little difficulty in achieving the required lift-off velocities within the required distance of 700 ft.

Nomenclature

ABDT = aero balanced deflected thrust
 CTOL = conventional takeoff and landing
 C_D = drag coefficient
 C_L = lift coefficient
 CRD = counter-rotating duct
 CG = center of gravity
 \bar{c}_w = mean aerodynamic wing chord
 FRL = fuselage reference line
 JBDT = jet balanced deflected thrust

LGR = landing ground roll
 P_s = specific excess power
 q = free-stream dynamic pressure
 STOL = short takeoff and landing
 TOGW = takeoff gross weight
 TRBPN = thrust reversing balanced piston nozzle
 VACS = vectored axisymmetric convergent side nozzle
 VFT = vectored fan thrust
 VTT = vectored total thrust

CD = convergent-divergent nozzle

Greek

α = aircraft angle of attack
 δ = control surface deflection angle
 θ = thrust deflection angle relative to aircraft centerline
 γ = glideslope angle
 Δ = increment

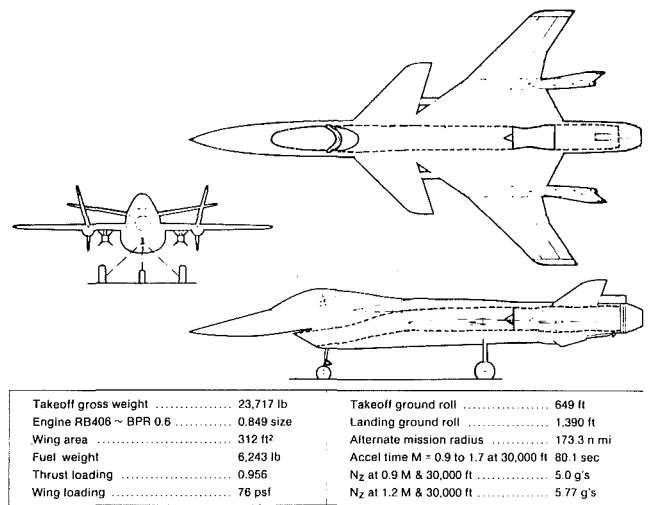


Fig. 2 CTOL baseline configuration

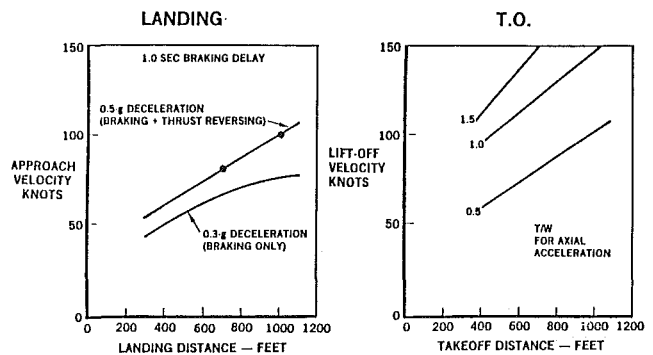


Fig. 3 STOL parametrics

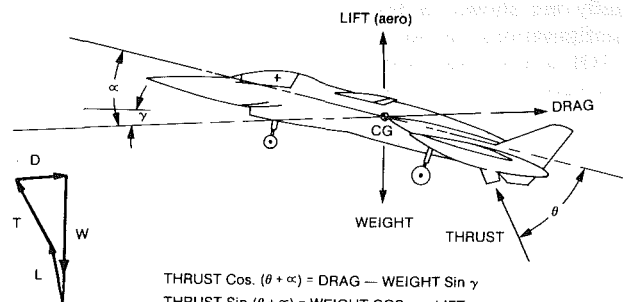


Fig. 4 Glide slope force equilibrium

With touchdown speeds of 100 knots or less, a considerable amount of additional "lift" is required beyond that generated

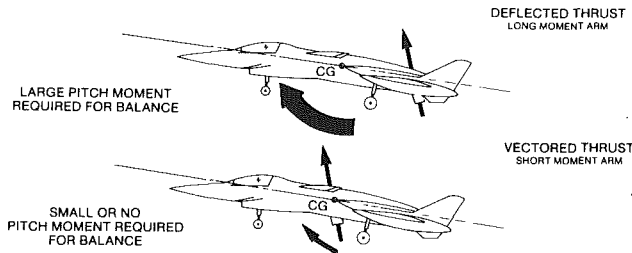


Fig. 5 Glide slope pitch moment equilibrium

by the aerodynamic lifting surfaces of a typical tactical aircraft. To provide this additional lift, the engine thrust can be vectored to a position where the net lift, drag, thrust, and weight vectors are in equilibrium, as shown in Fig. 4. Since the thrust component required along the line of flight is generally small at the approach velocities being considered, and the lifting thrust component required is large, large thrust vector angles are necessary to achieve equilibrium.

One consequence of vectoring the engine exhaust to provide a lifting thrust component is the inherent pitching moment generated when the engine thrust line acts away from the aircraft center of gravity. It is the ability to provide suitable forces to maintain the aircraft attitude and control in pitch which is critical to the achievement of the short field performance.

For stability, therefore, either a large counterbalance pitch moment must be produced or the thrust line must be moved close to the aircraft center of gravity, Fig. 5. Both these approaches to achieving pitch moment equilibrium have been investigated. The former (designated Deflected Thrust) used either aerodynamic or jet reaction forces to generate the balancing moment, and the latter (designated Vectored Thrust) used side vectoring nozzles in combination with either a rear vectoring nozzle or a rear nonvectoring nozzle.

The four STOL powerplant configurations analyzed in this study are shown in Fig. 6. For the two Deflected Thrust configurations, the same mixed flow turbofan as used in the CTOL aircraft was used, again with a bypass ratio of 0.6. The Vectored Thrust configurations required an unmixed flow engine cycle with the bypass flow exhausting through a pair of side nozzles and the core flow exhausting through a single rear nozzle. A trade study identified the optimum bypass ratio for this engine cycle as 1.3.

STOL Exhaust Nozzle Concepts

Four exhaust systems were investigated: two for the side installation on the Vectored Thrust configurations, and two for the rear nozzle on the Deflected Thrust configurations. All four nozzle concepts were designed with a technology level compatible with a mid-1990's Initial Operating Capability (IOC).

Vectoring Axisymmetric Convergent Side Nozzle (VACS). This exhaust system consists of a pair of side-mounted elbow ducts with variable-area nozzles mounted on the downstream end. The elbow duct rotates on a bearing at the forward flange which enables the exhaust to be directed at any angle from rearward through vertically downward to forward for thrust reverse. The engine carcass at the bearing position is a plenum chamber into which the bypass air from the low-pressure compressor is exhausted. Within this plenum, bypass air can be burned to augment the thrust (i.e., PCB). The nozzle is fully vectorable both dry and with PCB. Figure 7(a) shows the basic installation of the nozzle and elbow duct on one side of the engine.

The convergent nozzle has a number of flaps and seals to form a flow contraction with the flaps pivoted at the upstream

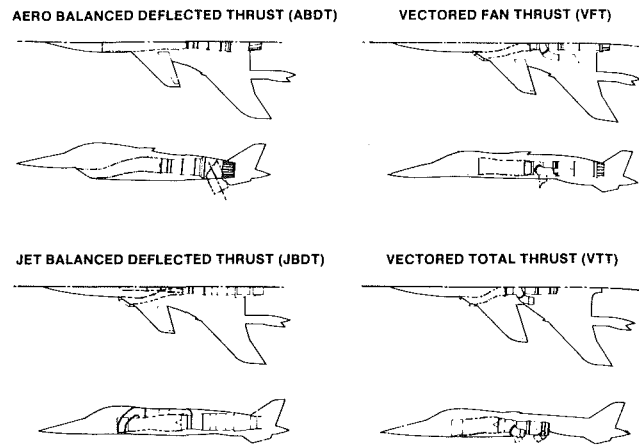


Fig. 6 STOL powerplant configurations

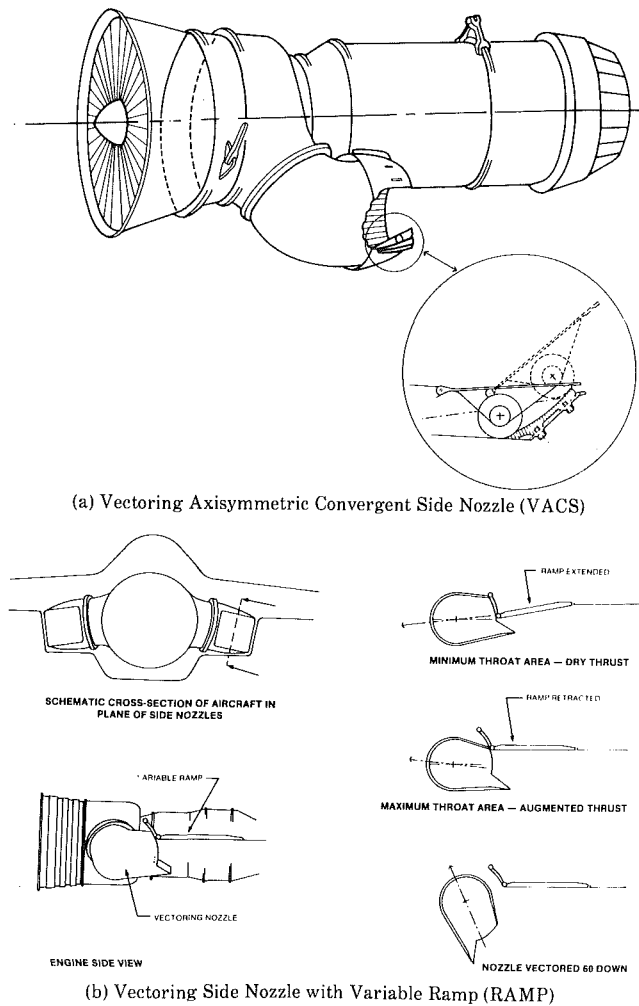
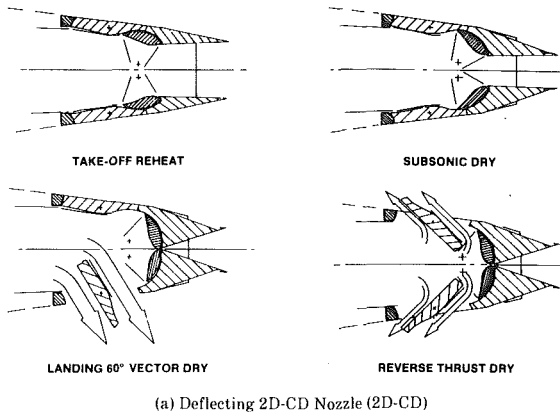


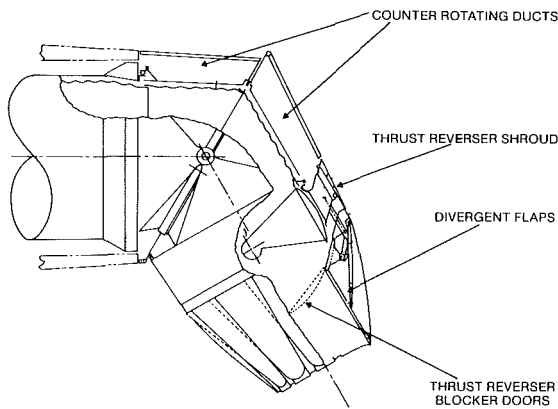
Fig. 7 Vectoring nozzle concepts

end to a translating annular ring. Each flap carries a roller on the rear face which moves in static axial tracks, cam profiled to vary the nozzle throat area as the annular ring is translated axially. The forward facing area of the annular ring acts as a pressure piston and is sized, and the cam track profiled to minimize the resultant loads on the actuation system.

Vectoring Side Nozzle With Variable Ramp (RAMP). The second side nozzle concept, shown in Fig. 7(b), consists of an



(a) Deflecting 2D-CD Nozzle (2D-CD)



(b) Counter-Rotating Duct (CRD)

Fig. 8 Deflecting nozzle concepts

elbow duct with a fixed area contraction at its downstream end. The elbow duct rotates on a bearing at the upstream end in the same manner as the previous concept. The elbow duct can rotate through 180 deg to provide thrust reverse on landing and the bypass air can be burned to augment the thrust by plenum chamber burning. Nozzle area variation is achieved by deploying a ramp, which is integrated into the aircraft underwing surface, to progressively block the nozzle exit until at maximum deployment a minimum throat area is achieved.

The downstream edge of the nozzle adjacent to the ramp is contoured to accommodate sealing and to enable movement of both ramp and elbow duct to vary the nozzle exit area and ramp divergence angle. This latter feature enables some 10–15 deg of vectoring and ramp angle optimization while retaining the area variation capability. Beyond this point the nozzle is always at maximum area.

Deflecting Two-Dimensional-CD Nozzle (2D-CD). This nozzle concept, shown in Fig. 8(a), has facility for thrust vectoring up to 70 deg and thrust reversing. The gas path has a transition from axisymmetric at the engine exhaust plane to square at the nozzle entry plane. The nozzle consists of static side walls with two moveable plates forming each of the upper and lower surfaces. The upstream pair of plates are pivoted and form a flow contraction at their downstream edge. They are mechanically coupled such that any movement is symmetrical and the downstream edges can meet to block completely the gas flow through the rear of the nozzle. The downstream pair of plates form a two-dimensional divergent passage and can also provide a limited range of thrust deflection.

Upstream of the convergent plates are two deflector doors

⊙ BASELINE STOL CONFIGURATION		STOL POWERPLANT CONFIGURATION			
		UNMIXED TURBOFAN		MIXED FLOW TURBOFAN	
EXHAUST NOZZLE CONCEPTS		VECTORED FAN THRUST (VFT)	VECTORED TOTAL THRUST (VTT)	AERO BALANCED DEFLECTED THRUST (ABDT)	JET BALANCED DEFLECTED THRUST (JBDT)
	VECTORED AXISYMMETRIC CONVERGENT SIDE NOZZLE (VACS)		⊙ D729-10		
	VECTORED SIDE NOZZLE WITH VARIABLE RAMP (RAMP)	⊙ D729-9			
	DEFLECTING 2D-CD (2D-CD)				⊙ D729-11
	COUNTER ROTATING DUCT & THRUST REVERSING BALANCED PISTON NOZZLE (CRD TRBPN)			⊙ D729-8	

Fig. 9 STOL configurations matrix

in the upper and lower surfaces which serve two functions. First, by progressively rotating the door in the lower surface and closing the convergent plates, thrust deflection can be achieved up to 70 deg; second, by further rotating of the lower door and opening the upper door, reverse thrust for landing deceleration can be achieved.

Counter-Rotating Duct (CRD). The deflecting system, shown in Fig. 8(b), is located upstream of a nozzle/reverser system, and allows up to 70 deg of thrust vector. Two scarfed ducts are mounted on large diameter lightweight bearings to allow counter rotation during deflection. Major loads are carried by horizontal center line trunnion mounts which also guide the nozzle in a vertical plane during deflection. Integrated external fairing provides a clean external flow path around the entire deflection system and rotate with the scarfed engine ducts via a support structure.

Downstream of the CRD is an axisymmetric variable area con-di nozzle. The convergent section consists of flaps mounted to a balance piston on hinges. Rollers on each flap ride in the stationary cam tracks to provide variable throat area and transmit gas pressure loads back to the static structure. The piston is axially positioned by actuators, thus varying nozzle throat area as the rollers follow the cam track contours. The divergent section consists of flaps hinged to the convergent flaps, and the nozzle exit area is controlled by struts which provide a scheduled exit area ratio at any nozzle throat area setting.

The integral reverser system consists of two clamshell blockage doors, which pivot to close and seal at the nozzle throat. An annular reverse flow passage is formed by conical forward and aft static structure walls, and an external translating shroud serves as a sealing door for the reverse thrust passage and balance piston cavity air.

STOL Configurations and Landing Analysis

Each of the four nozzle concepts described above was used in each of the four power plant configurations from Fig. 6 to configure advanced tactical aircraft which could achieve field lengths of less than 700 or 1000 feet.

Configuration Matrix. The combinations of nozzle concepts and power-plant configurations are shown in the matrix in Fig. 9. Early analysis concluded that it was not possible to achieve the 700 ft field length with the Deflected Thrust configurations; therefore, these were designed to the 1000 ft STOL requirement, while the two Vectored Thrust concepts achieved the 700 ft requirement.

A survey was made to determine dispersion allowances for the STOL landing distance. Study analysis estimated an actual miss distance of ± 75 ft at 100 knots and ± 50 ft at 80

knots (99 percent of occurrences). To this was added a margin of 25 feet at each end of the ground roll to allow for sighting error, gusts, and ground turning space. This converts to ground roll targets of 800 and 550 ft, respectively, for the 1000 and 700 ft field lengths.

Configuration Aerodynamics. The aerodynamic planform used for all the STOL configurations was a statically unstable, blended arrow wing with a close-coupled canard [2]. These features were developed to meet the maneuver design points at Mach 0.9 and Mach 1.2, 30,000 ft. A variable camber system was used to provide artificial longitudinal stability and control, camber optimization to maximize lift-to-drag ratio, and high lift. The variable camber elements included leading and trailing edge devices on the wing, and canard variable incidence with a trailing edge device.

A static longitudinal instability produced moment characteristics which favorably influenced the variable camber scheduling. Higher maximum lifts, increased buffet limits, and lower trimmed drags resulted from this control integration. The target low-speed static margin was -10 percent \bar{c}_{w} . Twin boom-mounted vertical tails gave very good directional stability characteristics at high angle of attack and for high dynamic pressure supersonic flight. The landing gear flotation requirements were 200 passes on California Bearing Ratio (CBR) 6 (sod field). A suite of avionics were defined compatible with 1995 IOC and appropriate weight and volume allowances made in the aircraft design.

The CTOL baseline and Aero Balanced Deflected Thrust aircraft used a single bottom-mounted inlet located on the forward underside of the fuselage. The inlet has a 5 deg fixed ramp with a diffuser following a smooth gradual "S" curve to connect with the engine face. The other STOL configurations used a side-mounted bifurcated inlet that is designed to the same characteristics as the bottom inlet. Performance characteristics of the two inlets were assumed to be the same.

Propulsion Systems. Two Rolls-Royce defined engine cycles were used, the selection of which was a function of the nozzle installation concept. The RB406-03 is a two-spool low-bypass ratio turbofan with the bypass stream and core exhaust mixed and ejected through a single exhaust nozzle. The mixed streams may be burned for thrust augmentation so that nozzle throat area variability is required during afterburner operation to rematch the engine to the required operating lines.

The RB420-02 is a two-spool military turbofan with a bypass stream exhausting into two thrust vectoring nozzles tucked behind the fan while the core stream is exhausted through a single rear nozzle. Thrust augmentation of the bypass air is available using plenum chamber burning (PCB) and the engine core thrust is also augmented by an afterburner.

The installed thrust of each engine was modified by application of a gross thrust coefficient appropriate to each exhaust system concept. The external drag for each concept was also estimated for use in the aircraft performance analysis and interference effects between the exhaust and aircraft surfaces were included in the predictions.

Landing Analysis. Preliminary analysis has indicated that the approach and landing condition essentially determines the STOL operation runway length. In adapting the baseline configuration to integrate the nozzle concepts and achieve STOL operation, the changes were mainly driven by the need to maintain equilibrium on the approach glide slope. Therefore, the STOL configurations and landing analyses are interrelated and are considered together.

The minimum approach speed of 80 knots at sea level was determined to ensure that the landing distances would be

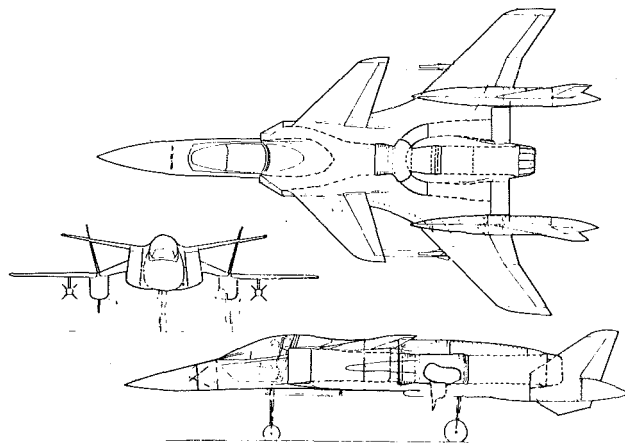


Fig. 10 Vectored fan thrust configuration 9

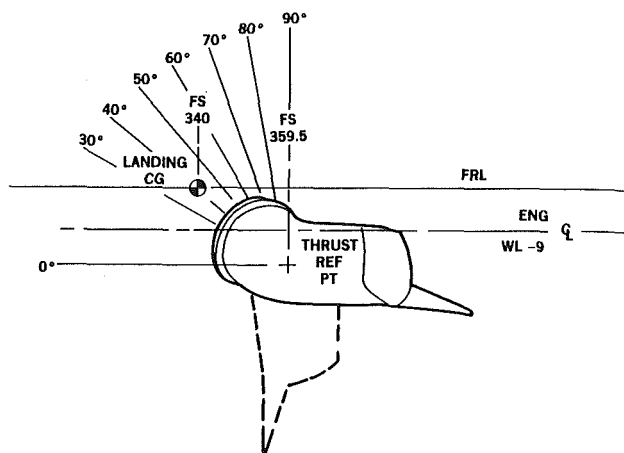


Fig. 11 Side nozzle thrust vectors 9

within the target range, and conventional roll and pitch controls are probably at their limiting speed. A maximum speed of 100 knots was considered the upper range for satisfying landing distances. A nominal flight path angle of -3 deg was used for the landing approach, with no-flare descent rates on runway contact of around 8 ft per second provided reasonable sink rates for nominal landing conditions. As much aerodynamic lift as possible, consistent with an angle of attack constraint determined by adequate over-the-nose vision, was used so that the lowest value of propulsive input was required thereby allowing greater thrust margins for aborted landings.

Flight at low speeds with highly deflected jets has its own unique aerodynamic characteristics which must be taken into account in a performance and/or stability and control analysis [3]. Interference effects of the nozzle jets on the basic aerodynamic characteristics were estimated and involved jet interference effects on the fuselage, wing, and canard for lift and pitching moment. In all cases, the lift interference effects resulted in substantial losses, and neglecting these effects would have produced optimistic results. Similarly, pitching moment interference effects substantially alter the basic aircraft pitching moment.

Considerations of the direct thrust forces resulted in relocation of the engine from the baseline case to minimize adverse effects on pitching moment for each candidate aircraft. Considerable levels of thrust were required for STOL operations to produce adequate lift force; therefore, inlet momentum effects were sizable, especially ram drag. Since the nozzles were deflectable, ram drag was not included in thrust data as is usually done for conventional aircraft data. The

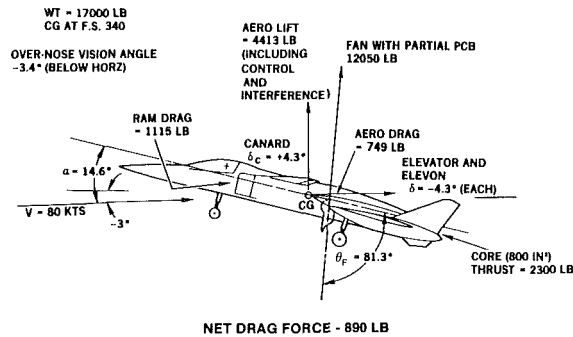
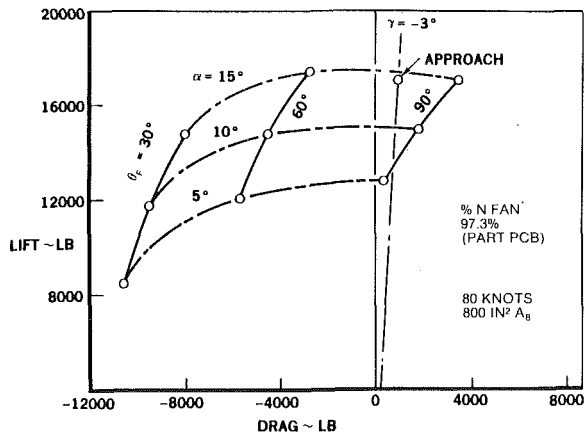


Fig. 12 Approach characteristics 9

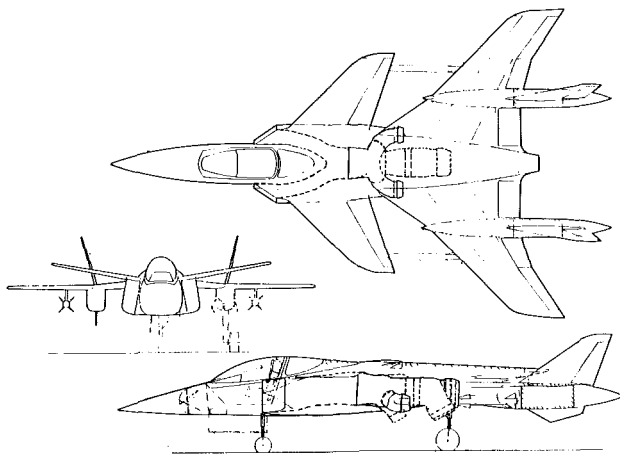


Fig. 13 Vectored total thrust configuration 10

inlet momentum effects were applied at the effective duct axis.

Vectored Fan Thrust. This configuration, shown in Fig. 10, consists of vectoring side ramp nozzles and a fixed core nozzle. STOL operation required that the fan nozzles operate with partial plenum chamber burning (PCB) to produce the necessary propulsive lift. For the landing approach, the core nozzle area was increased in order to reduce the aft nozzle thrust to maintain the required force along the stability axis. Figure 11 shows the fan nozzles thrust line in relation to the aircraft's landing CG. A forward shift of the engine from the baseline location was required to reduce the pitch-down moment produced at high nozzle deflections.

The lift-drag relationship is shown in Fig. 12 at the approach speed of 80 knots and with the fan nozzle producing 76 percent of maximum thrust. Aborted landings can be accomplished by simply deflecting the fan nozzles to ap-

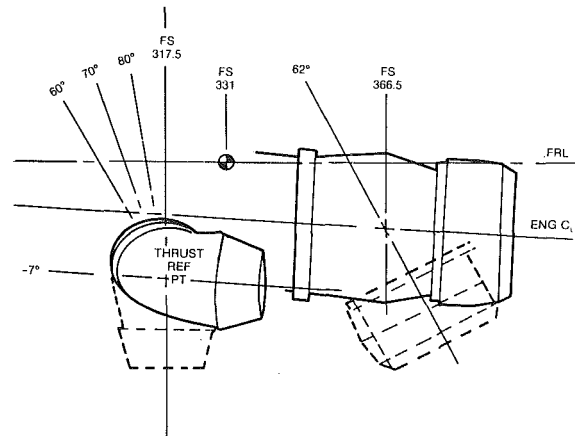


Fig. 14 Nozzle thrust vectors 10

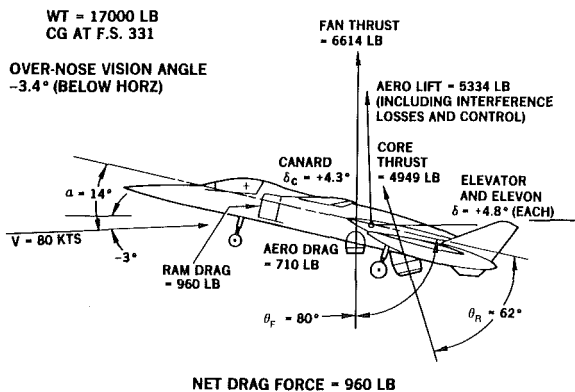
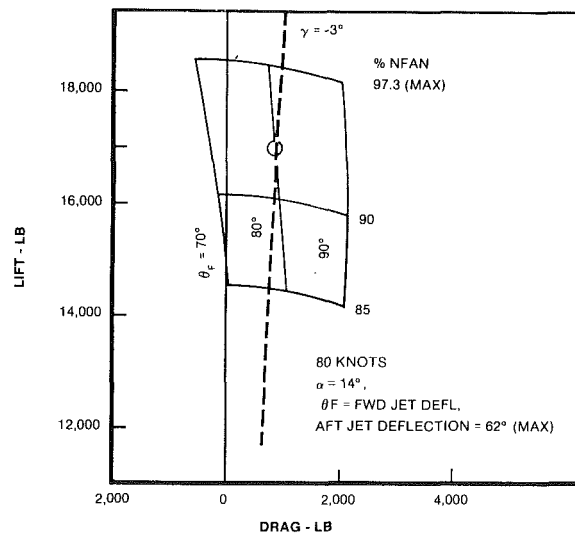


Fig. 15 Approach characteristics 10

proximately 60 deg. In addition, of course, the fan nozzle and core nozzle thrust can be increased.

Figure 12 also presents the approach trimmed on a -3 deg glide slope and shows the aerodynamic and propulsive force components. The pitch control employed for trimming the pitching moment is approximately 21 percent of the total pitch-up deflection and is considered satisfactory. A fan nozzle angle of 81.3 deg is required to produce the proper level of net drag for the -3 deg glide slope.

Vectored Total Thrust. This configuration, shown in Fig. 13, uses the Vectoring Axisymmetric Convergent Side nozzles and a vectoring rear nozzle. STOL operation requires that the

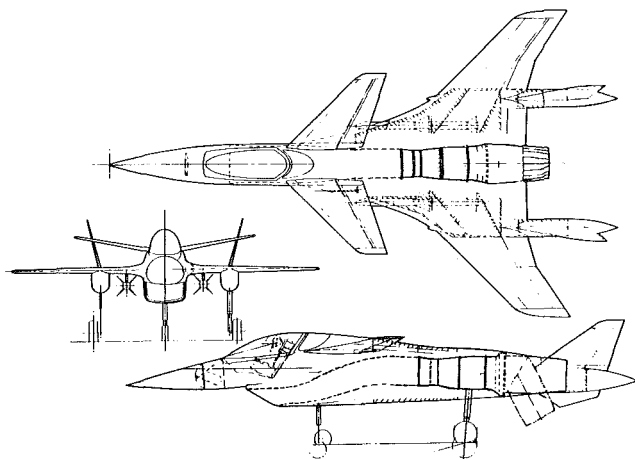


Fig. 16 Aero balanced deflected thrust 8

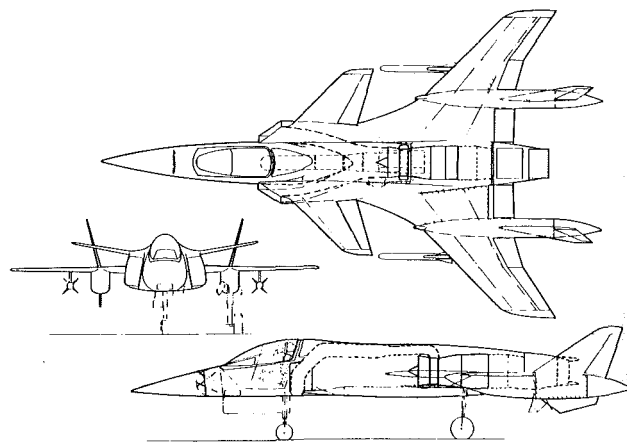


Fig. 18 Jet balanced deflected thrust 11

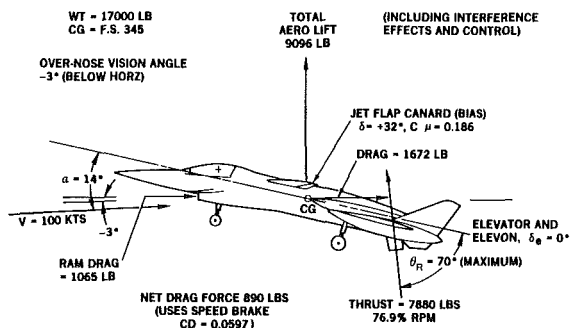
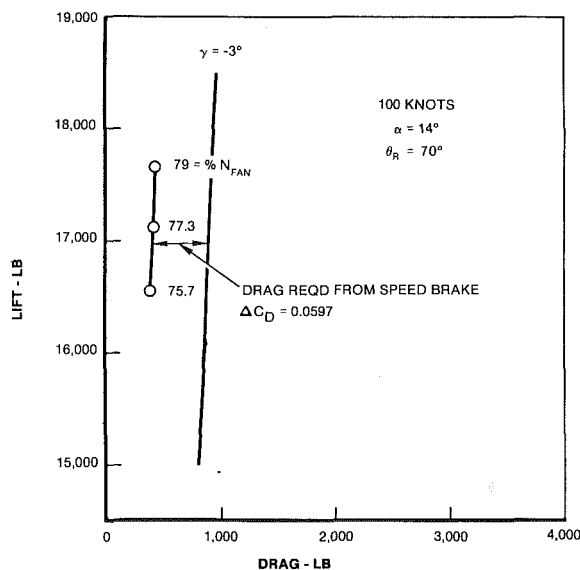


Fig. 17 Approach characteristics 8

side nozzles operate with PCB plus core burning to produce the necessary propulsive lift. Figure 14 shows the fan and core nozzle thrust lines in relation to the aircraft landing CG. The location of fan nozzle relative to the CG gave a desired pitch-up moment.

The lift-drag relationship is shown in Fig. 15 at the approach speed of 80 knots and with the fan nozzle producing 56.5 percent of maximum thrust. Aborted landings can be accomplished by simply deflecting the fan nozzles to approximately 70 deg. With the available increase in thrust, a safe go-around can be accomplished.

Figure 15 also presents the approach trimmed on a -3 deg glide slope and shows the aerodynamic and propulsive force

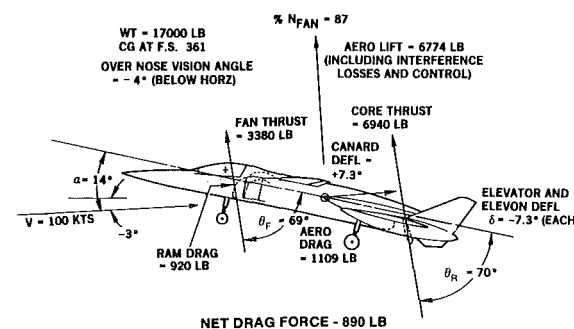
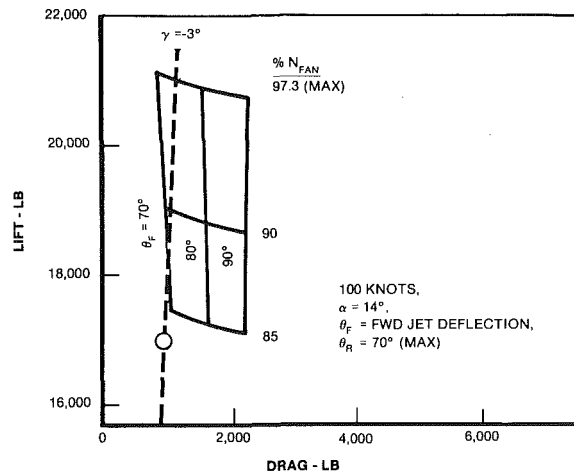


Fig. 19 Approach characteristics 11

components. The pitch control employed for trimming the pitching moment is approximately 24 percent of the total pitch-down deflection and is considered satisfactory. The fan nozzle thrust deflection of 80 deg is required to produce the proper level of net drag force for the -3 deg glide slope.

Aero Balanced Deflected Thrust. This configuration is shown in Fig. 16 and embodies the Counter Rotating Duct System with the axi con-di TRBPN nozzle. In order to operate at an approach speed that will satisfy the landing distance requirement, a blown flap canard with a 46 percent increase in size was chosen to produce the necessary pitch-up moment. The flap is blown using engine high-pressure bleed air and the canard flap deflects as a function of exhaust nozzle deflection.

Since the engine exhaust nozzle has a maximum deflection of 70 deg, achieving the proper drag force on the approach could not be accomplished by nozzle deflection with the high

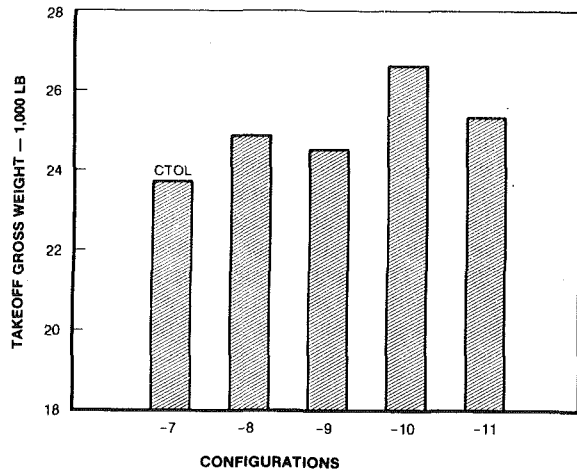


Fig. 20 Takeoff gross weight

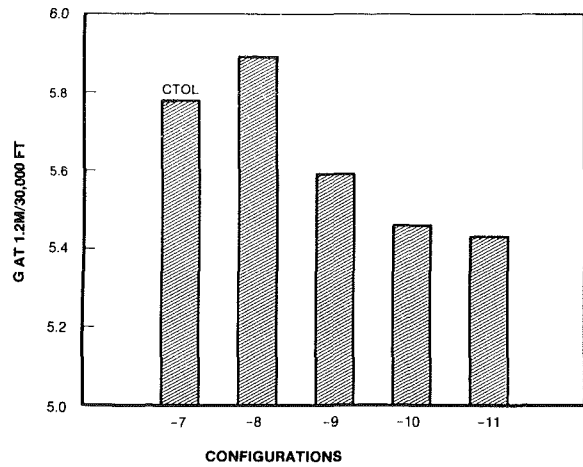


Fig. 23 Sustained load factor at Mach 1.2

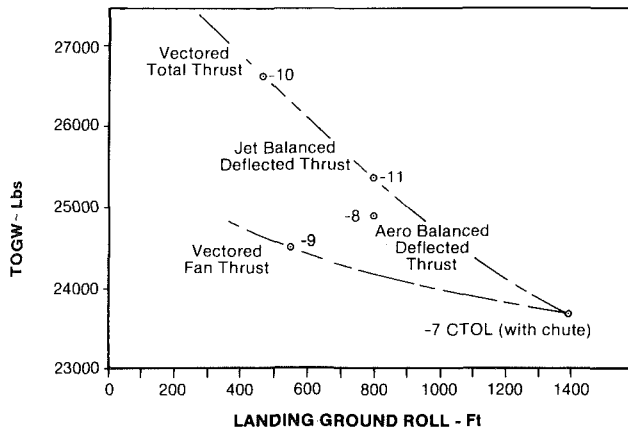


Fig. 21 Landing ground roll versus TOGW

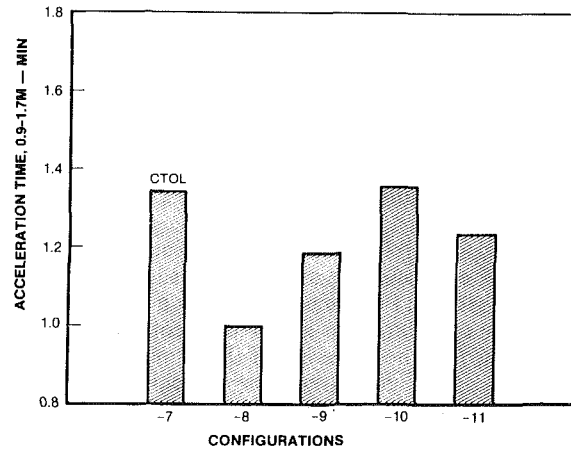


Fig. 24 Transonic acceleration time

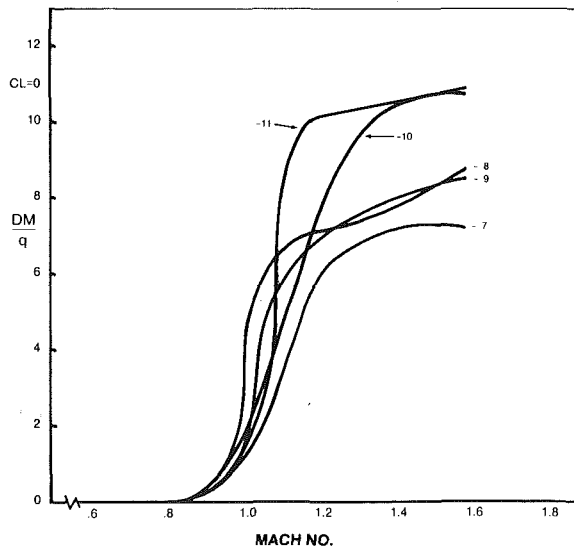


Fig. 22 Wave drag comparison

thrusts required. Therefore, a speed brake with a drag coefficient of 0.0597 was necessary at the 100 knot approach speed. Due to the aft location of the engine exhaust nozzle, a large interference pitch-up moment was produced which relieved the direct thrust moment somewhat.

Figure 17 presents the lift-drag relationship for the approach condition and illustrates the required speed-brake drag. Figure 17 also shows the approach trim condition with a relatively low power setting of approximately 77 percent. The

canard jet flap deflection of 32 deg provides a pitch-up moment and operates as a function of engine exhaust nozzle deflection. The pitch control is arbitrarily set at neutral at the approach condition. For this configuration, a go-around can be accomplished by advancing power, reducing the engine nozzle deflection, and closing the speed brake. In conventional flight and for take-offs, it is assumed engine bleed air is not used to blow the canard flap.

Jet Balanced Deflected Thrust. This configuration, shown in Fig. 18, employs the Deflecting two-dimensional-CD nozzle and a fixed pitch pipe nozzle for trim. During a landing approach, the aft nozzle is passing only the engine core flow and is at the maximum deflection to minimize the thrust component in the axial direction. The bypass flow is ducted forward to the pitch pipe nozzle mounted immediately behind the crew station to provide a pitch up moment and lifting force. The flow is unburned to avoid the weight and complexity of an additional burner and fuel system in the pitch pipe duct. The core thrust level is more than twice that of the bypass flow diverted through the pitch pipe, thereby creating a net nose-down moment.

The lift-drag characteristic for this configuration is shown in Fig. 19 at the approach speed of 100 knots. Less than 85 percent of the maximum thrust fan speed is required for the trim point and this condition requires only 7.3 deg of canard flap and elevator/elevon deflection. Both of these requirements provide a good control margin for an aborted landing. Figure 19 also shows the aerodynamic and thrust components for trimmed approach at 100 knots along a -3 deg flight path. The pitch pipe nozzle angle was optimized at 69 deg for this condition.

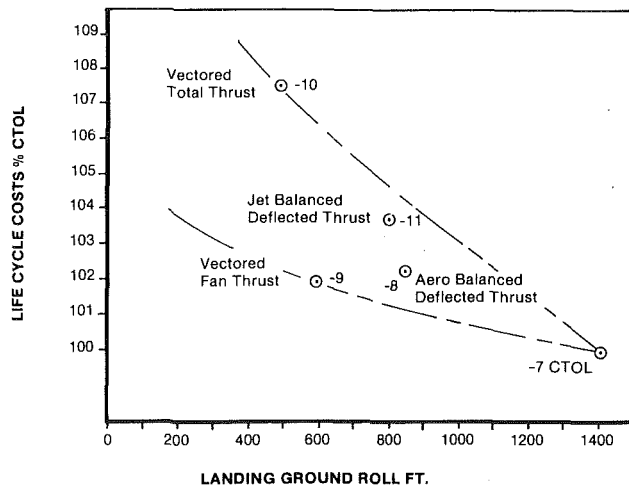


Fig. 25 Life cycle cost versus landing ground roll

Takeoff and Landing Ground Rolls. The landing ground roll analysis assumed a 1.0 s delay after touchdown for application of brakes and thrust reversing, and a braking coefficient of 0.3 for a dry concrete runway. The landing weight assumed 20 percent fuel remaining and with full armament. The effects of varying runway conditions were also analyzed by computing ground rolls with a range of braking coefficients.

Takeoff ground roll for all configurations was calculated by using the estimated C_L and untrimmed drag polars. An angle of attack of 14 deg was used giving a maximum C_L of 1.12. All the configurations achieved takeoff ground rolls of less than 700 ft without the use of thrust vectoring. Possible reduction in takeoff ground roll may be achieved with the use of thrust vectoring but was not investigated in this study.

STOL Configuration Characteristics

The STOL configurations were sized to the design mission by cross plotting performance restraints on a thrust and wing loading parametric analysis. In all cases, the 5 "g" turn at Mach 0.9, 30,000 feet was a sizing parameter with landing ground roll also identifying the vehicle size for some configurations. The resultant thrust and wing loadings are given below:

Configuration	-8	-9	-10	-11
Thrust/weight	1.078	1.015	1.087	1.078
Weight/wing area lb/sq ft	85.3	79.8	80.0	85.3

The performance for the sized STOL configurations was then computed and the results are shown relative to those of the CTOL configuration in Figs. 20–24.

The vehicle takeoff gross weights (TOGW), Fig. 20, show that the lightest STOL aircraft was 1.9 percent heavier than the CTOL and the heaviest was 13.8 percent heavier. The takeoff ground rolls calculated for a conventional takeoff, i.e., no thrust vector, varied between 600 and 650 feet for the CTOL and STOL configurations. The landing ground roll (LGR) was shortest for the Vectored Total Thrust configuration at 465 ft. The Vectored Fan Thrust configuration was sized at 550 ft and the two deflected thrust configurations sized at 800 ft.

Figure 21 shows the reduced landing ground rolls relative to the CTOL aircraft cross plotted against vehicle TOGW. This demonstrates the low weight penalty and good field performance of the Vectored Fan Thrust configuration.

Because of the reduced fineness ratio of the STOL configurations, they all have higher wave drag than the CTOL, as

shown in Fig. 22. Also, the side nozzle location of the Vectored Total Thrust and the pitch pipe ducting of the Jet Balanced Deflected Thrust give unfavorable area distributions.

The side nozzle propulsion system does not necessarily result in a high Mach dependent drag. In fact, the Vectored Fan Thrust configuration (-9) had the lowest predicted wave drag of the STOL configurations at the top speed.

The combat maneuver at Mach 0.9 sized all the STOL vehicles. The resulting load factor at $P_s=0$, Mach 1.2 are shown in Fig. 23. The Aero Balanced Deflected Thrust was slightly better than the CTOL and the rest were slightly worse. The transonic acceleration time from Mach 0.9–1.7 are compared in Fig. 24, and the STOL configuration performance either matched or was better than the CTOL performance. The low altitude subsonic penetration on the alternate mission showed little variation ranging from 72 to 81 miles for the STOL vehicles compared with the CTOL at 73 miles.

An incremental life cycle cost (LCC) analysis was performed for the STOL vehicles relative to the CTOL aircraft. The results of this analysis are shown in Fig. 25. All the STOL configuration costs were higher than the CTOL and ranged from 102 percent CTOL for the Vectored Fan Thrust to 108 percent for the Vectored Total Thrust configuration.

Conclusions

Phase 1 of this study has demonstrated that it is possible to achieve STOL (1000 or 700 ft.) performance with an advanced tactical aircraft for very little penalty in weight and cost and with no loss in mission capability.

General.

- Landing is the critical STOL mission element for a tactical aircraft. With vectored thrust, the specific requirement is to achieve equilibrium on the approach glide slope of the thrust, lift, weight, and drag forces, and to maintain stability in pitch.

- For propulsive lift during the landing approach, high vector angles are required, both to reduce axial thrust and to provide maximum lift.

- Low-speed stability and control characteristics can either limit minimum touchdown speed or dictate the use of control augmentation.

STOL Aircraft Configurations.

- The best 700 ft field length aircraft (Vectored Fan Thrust) was 3.3 percent heavier in TOGW than CTOL and 2.0 percent higher in life-cycle cost. This was also recommended as the best STOL configuration overall.

- The best 1000 ft field length aircraft (Aero Balanced Deflected Thrust) was 4.9 percent heavier in TOGW than the CTOL and 2.3 percent higher in life-cycle cost.

- The use of a side nozzle propulsion configuration did not necessarily result in high aircraft wave drag. In fact, the STOL configuration (-9) with the lowest predicted supersonic wave drag was a side nozzle configuration.

- The Vectored Total Thrust configuration achieved the shortest landing ground rolls, thereby demonstrating its superiority for ultra-STOL operation.

References

- 1 Byrnes, J. M., "Technology Solutions to the Runway Denial Problem," AIAA 80-1821, 1980.
- 2 Gloss, B. B., "Effects of Wing Planform and Canard Location and Geometry on the Longitudinal Aerodynamics of a Close-Coupled Canard Wing Model at Subsonic Speeds," NASA TN D-7910.
- 3 "V/STOL Handling Qualities Criteria," AGARD No. 577, Pt. 2, June 1973.

F-14 Aircraft and Propulsion Control Integration Evaluation

W. J. Davies

Pratt and Whitney Aircraft,
Government Products Division,
West Palm Beach, Fla. 33402

C. A. Hoelzer

Grumman Aerospace Corporation,
Bethpage, N. Y.

R. W. Vizzini

Naval Air Propulsion Center,
Trenton, N. J.

Since 1976, the U.S. Navy in conjunction with Pratt and Whitney Aircraft (PWA) has been actively engaged in developing the technology base for an engine, dual redundant, fault tolerant, full authority digital electronic control (FADEC) systems with the capability of aircraft control integration for application to the next generation Navy aircraft. Navy contracts were awarded in 1981 to PWA and Grumman Aerospace Corporation (GAC) to identify the operational benefits of the F-14 Aircraft with a dual-redundant FADEC interfaced to an Advanced Fuel Management Systems (AFM) and integrated with the F-14 aircraft control system. This paper presents the FADEC/F-14 integration evaluation performed by PWA and discusses the benefits of the FADEC/F-14 integrated system. These include improvements in reliability, mission abort, survivability, maintainability, cruise fuel consumption, engine weight, diagnostics and fault recording, inlet and engine air flow matching and propulsion control accuracy.

Introduction

The Navy/PWA advanced propulsion control programs (Fig. 1) are a systematic approach to identify the technology base of fault tolerant, dual redundant, full authority digital electronic control (FADEC). Control programs, sponsored by the Naval Air Systems Command and directed by the Naval Air Propulsion Center (NAPC), have successfully demonstrated single and dual-channel FADEC fault tolerant systems through design, development and engine tests. The success of these tests has led to an aircraft-propulsion control integration evaluation to demonstrate the benefits of a dual-redundant FADEC configuration and advanced fuel management system.

This paper presents the FADEC/F-14 system integration evaluation performed by PWA with highlights from the GAC evaluation [1]. The use of an integrated electronic flight and propulsion control system provides long-term advantages and benefits which may be demonstrated in a flight test program.

From a long-term viewpoint, government and industry research programs have repeatedly projected substantial life cycle cost benefits for electronic control systems. The cost, weight, reliability, and maintainability aspects of the FADEC systems were reevaluated and are discussed.

The many benefits which would be demonstrated in the F-14 flight test range from engine performance improvements to reduction in system maintenance requirements as presented in Table 1.

The recommended F-14/TF30/FADEC flight test configuration is shown schematically in Fig. 2. It retains the present F-14 propulsion system on the right side of the aircraft and incorporates the TF30 FADEC system and other interface

and display electronics changes on the left side of the aircraft. The flight test configuration has the following features:

- Maintains left/right propulsion system independency
- Includes redundant FADEC controls
- Incorporates fiber optics data bus (MIL-STD-1553B format)
- Incorporates electrical data bus (MIL-STD-1553B)

Table 1 FADEC/F-14 – flight test benefits

- Flight/propulsion control system integration
- No trim propulsion control system
- Fail operational FADEC system
- Propulsion control accuracy
- Diagnostics and fault recording
- Alternative fuels
- Stall detection and recovery
- No throttle movement restrictions
- Inlet and engine air flow matching
- Improved cruise fuel consumption

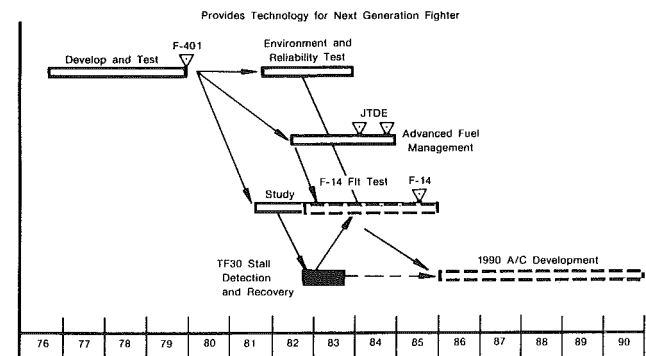


Fig. 1 Navy/PWA FADEC program

Contributed by the Gas Turbine Division of THE AMERICAN SOCIETY OF MECHANICAL ENGINEERS and presented at the 28th International Gas Turbine Conference and Exhibit, Phoenix, Arizona, March 27-31, 1983. Manuscript received at ASME Headquarters January 12, 1983. Paper No. 83-GT-234.

Table 2 FADEC/AFM system payoffs

	Current technology	Advanced system goals	Improvement factor
System failure rate	1400/10 ⁶ EFH	1/10 ⁶ EFH	1400X
MTBF	100 hr	550 hr	5.5X
Maintenance	100 \$/EFH	10 \$/EFH	10X
Cost	Base	0.75	25%
Weight	Base	0.67	33%

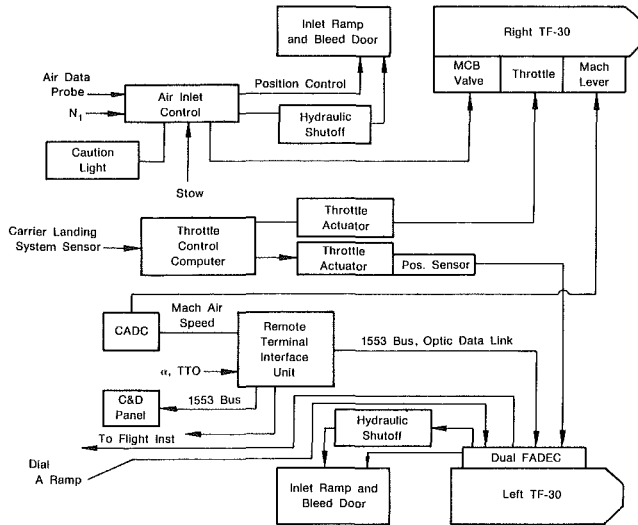


Fig. 2 Proposed F-14/TF30/FADEC flight test configuration

- Uses digital display I/O for engine control
- Integrates air inlet/engine controls (left side only)
- Incorporates midcompressor bleed function into FADEC
- Incorporates approach power control into FADEC
- Incorporates Mach lever function into FADEC

This control integration evaluation establishes the technology to be verified by a F-14 flight test program. Although this FADEC hardware will be configured to operate with the TF30-P-414 engine in the F-14 aircraft, the technology is generic to any advanced V/STOL, STOL or CTOL integrated aircraft.

FADEC/AFM System

The FADEC/AFM control system is designed to provide significant improvements in control reliability, cost, and weight for future Navy aircraft where the propulsion control system will be integral part of the total weapon system

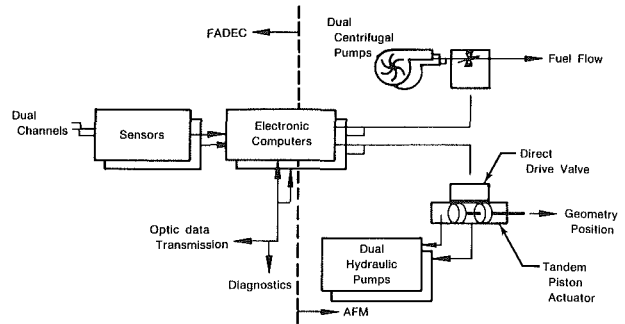


Fig. 3 FADEC/AFM

control, Table 2. The FADEC/AFM substantially improves the system failure rate and component MTBF for advanced aircraft applications. Maintenance will be improved because of more reliable control components and simplified troubleshooting.

Careful design of the control system architecture avoids the cost and weight penalty one might expect with a dual channel system. For example, fail-operational fuel pumping is achieved with only two pumps. Today's systems use two pumps, each with a special purpose, and therefore they cannot be used as backup for each other.

The FADEC/AFM control system for the F-14 flight test consists of dual FADEC digital electronic controls, redundant AFM direct drive actuators, dual centrifugal pumps, and a dual hydraulic system, Fig. 3.

The cost, weight, reliability, and maintainability aspects of the FADEC/AFM control system components have been evaluated as part of the FADEC and Full Authority Fault Tolerant Electronic Engine Control (FAFTEEC) Programs, [3, 4]. In addition GAC evaluated the reliability of the FADEC/AFM hardware, to establish the impact on the air inlet control system. This work consisted of gathering field failure and abort mission rates from the F-14 program reliability files for existing equipment. For new equipment, GAC or PWA reliability projections were obtained and biases applied to reflect field usage, lack of production maturity, and environmental stresses. Results showed that the

Nomenclature

- PWA = Pratt & Whitney Aircraft
 FADEC = Full Authority Digital Electronic Control
 AFM = Advanced Fuel Management
 NAPC = Naval Air Propulsion Center
 GAC = Grumman Aerospace Corporation
 V/STOL = Vertical/Short Take Off and Landing
 STOL = Short Take Off and Landing
 CTOL = Conventional Take Off and Landing
 MIL-STD-1553B = Aircraft Internal Time Division Command/Response Multiplex Data Bus
 I/O = Input/Output
 AGARD = Advisory Group for Aerospace Research and Development

- IR&D = Industrial Research and Development
 EAROM = Electrically Alterable Read Only Memory
 LVPT = Linear Variable Phase Transformer
 IACS C&D = Integrated Avionic Control System Control and Display
 FAFTEEC = Full Authority Fault Tolerant Electronic Engine Control
 LRU = Line Replaceable Unit
 A/B = Afterburner
 Mo = Mach number
 AOA = Angle of Attack
 MCB = Mid Compressor Bleed

FADEC/AFM system has the potential for improving the integrated control system (including engine inlet and aircraft components) reliability and mission abort rates in a prototype application on an F-14. The predicted abort rates are reduced from about 9 to 4 per 1000 missions, [1].

Flight/Propulsion Control System Integration

The key benefit to be demonstrated in the F-14 flight test program is the integration of the flight and propulsion control systems. Future STOL, V/STOL, and CTOI aircraft are being configured to take advantage of the advances in digital electronics. These advanced control systems will work in unison to provide the aircraft with capabilities beyond those of current weapon systems. These new aircraft configurations require that the propulsion control system be as reliable as the flight control system and be capable of communicating with the aircraft. The reliability aspects are being addressed in programs such as AFM and FAFTEEC and have established that a dual channel propulsion control system has the potential to meet the reliability requirements of an integrated system, Fig. 4. The flight test of the F-14 will address the requirements for communication between aircraft and engine. MIL-STD-1553B provides the best current method to implement this link and will be used in the flight test for transmission of both inlet control and cockpit display information.

No Trim Propulsion Control System

The propulsion control will operate the TF30-P-414 engine to an engine pressure ratio schedule for the flight test. In this mode of operation engine pressure sensors, inside of FADEC, measure the pressure ratio across the engine and maintain a constant performance level at any point in the F-14 flight envelope. The elimination of control trim requirements would save approximately 1.5 million dollars per year for 300 F-14 aircraft. This would break down into about 1 million in fuel and 500,000 dollars in maintenance man hours. For the flight test program the engine control system would not require trim during installation on the F-14.

Inlet and Engine Airflow Matching

The requirements and feasibility of providing improved inlet performance and inlet-engine stability throughout the F-14 flight envelope using FADEC were reviewed. An assessment of the F-14 inlet performance and inlet-engine stability that presently exists was made, and the appropriate levels quantified. The potential for improvement in performance and stability was then identified for the various speed ranges of the aircraft. Methods for providing this improvement by rescheduling variable inlet geometry and engine corrected airflow demand, as well as through the scheduling of new functions within the engine and inlet were studied.

The effects of TF30-P-414 engine afterburner transients, either lighting or retard from max A/B, significantly reduce high angle of attack (AOA) operation at the higher altitudes, at subsonic conditions. At the low Mach numbers, $M_0 = 0.30$, the A/B lighting restriction precludes stable operation at above 30 deg AOA at 15,000 ft and above 20 deg AOA at 30,000 ft. At the higher Mach number, $M_0 = 0.60$, the inlet-A/B lighting compatibility is somewhat better.

Inlet instabilities (buzz) have been reported from during fleet operations. The present inlet ramp schedule has been selected to minimize any potential buzz situations. However, it is possible that with the ramp positioning, engine airflow control tolerances, and variations in ambient air temperature buzz may occur. Using FADEC, the inlet control system will be restructured to provide a better variation of ramp and

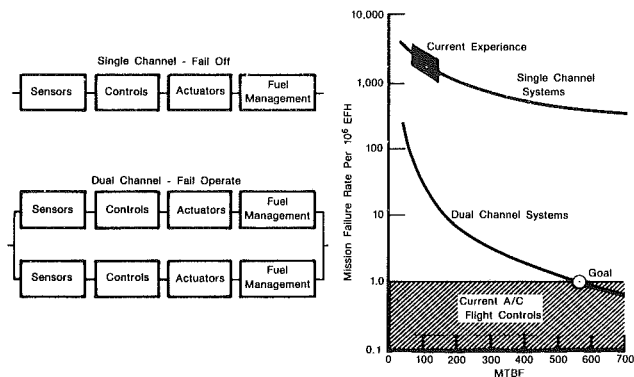


Fig. 4 Dual channels provide large improvement in mission failure rate

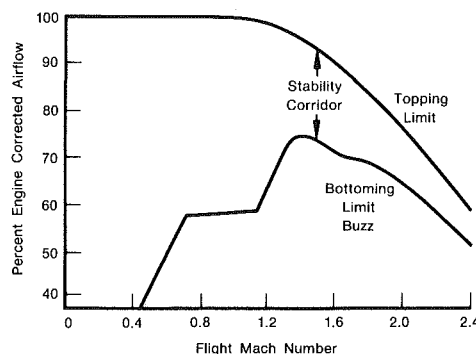


Fig. 5 F-14A inlet design limits - corrected airflow

bleed exit door positions with engine corrected weight flow. This would allow a significant increase in the stability corridor shown in Fig. 5, as well as almost eliminating any potential for inlet buzz.

High-speed flight, above $M_0 = 2.00$, is characterized by relatively high turbulence. Providing efficient inlet-engine matching for high supersonic flight as a means to ensure subcritical inlet operation using the FADEC system will be demonstrated during the proposed flight test program by including engine corrected airflow as one of the control parameters for determining the inlet ramp positions.

Stall Detection and Recovery

The use of a FADEC control, coupled with a high-speed fuel and airflow management system, may be effective in the detection and recovery from engine stall. A characteristic of engine stall would be a rapid drop in burner pressure. This rate of decay exceeds 300 percent psi/s (normal maximum rate is approximately 100 percent/s). The FADEC control senses burner pressure and can be programmed to take the appropriate corrective action. The FADEC/AFM control system would manipulate gas generator fuel flow and/or airflow, via the air bleeds or exhaust nozzle area, until the TF30-P-414 returned to normal operation. The FADEC engine protection functions constantly monitor the engine to insure that no temperature limits would be exceeded during the stall or attempted recovery.

Improved Cruise Fuel Consumption

The F-14 performance can be improved with an integrated control system through the coupling of aircraft status information to FADEC and then taking appropriate engine control action. An example of this type of operation would be the variation of TF30-P-414 nozzle geometry in areas of low inlet distortion flight. During the cruise phase of several

typical F-14 missions the aircraft may spend up to one hour in straight and level, nonafterburning flight. At this time, with an integrated control system, the pilot may manually send a signal to FADEC that he is in straight and level flight and wishes to go to a reduced fuel consumption operating mode. The FADEC response to this command would reduce the exhaust nozzle area to a new fixed position while holding engine thrust to a constant value. The ultimate result of this action is a reduction in fuel flow coupled with a reduction in engine surge margin. The new exhaust nozzle area would be sized such that the surge margin reduction was that allocated for inlet distortion only. The FADEC controls would sense the start of an aircraft maneuver or engine transient and return the TF30-P-414 to normal surge margin. Normal update times for the FADEC is less than 20 milliseconds compared to the approximately 100 milliseconds required for engine or aircraft response to a transient command. It should be noted that the current TF30-P-414 exhaust nozzle is closed to a mechanical stop at intermediate power. To demonstrate this mode of operation during the flight test would require modification or rerigging of the current exhaust nozzle.

Allocation of surge margin in the TF30-P-414 may be considered as shown in the bar chart of Fig. 6. This figure shows the allocation of surge margin available at a typical cruise flight condition for the F-14. The 9 percent reduction in surge margin at this point results in approximately 1 percent reduction in cruise fuel flow at a constant thrust.

The impact of this reduced surge margin or fuel consumption may be shown as an improved thrust specific fuel consumption, Fig. 7. The reduced surge margin may also, of course, be used to provide a small increase engine thrust at a constant fuel flow.

Fail Operational FADEC System

The FADEC electronic controls, propulsion system actuators, fuel and hydraulic pumps would be redundant for the F-14 flight test. The FADEC/AFM system would operate in a dual active mode, Fig. 8. In this mode of operation both FADEC units are in control of the all hydromechanical control devices at the same time, with equal authority. The dual active channel system eliminates switching transients which might occur in a master-standby system and also eliminates the possibility of transfer to a nonoperative secondary channel. During dual active operation, each channel's input is trimmed by the balancer logic until the outputs are equal. The gains of both channels are set equal and both channel requests send drive signals to the dual wound torque motors. The position of the AFM actuators is measured by a linear variable phase transformer, (LVPT) and fed back to the FADEC units.

A system failure is detected when the trim value between the two FADEC units exceeds a preset limit. At this time, the system will use internal self-checking routines to establish which unit has failed and transfer engine control to the healthy FADEC.

Diagnostics and Fault Recording

The FADEC/AFM System gives improved propulsion system diagnostic capability through the use of the built-in test capability and the ability to record fault information on the FADEC electrically alterable read only memory (EAROM). The fault identification logic incorporated in the controls will be capable of identifying the faulty component to the level of a line replaceable unit (LRU), whether it is the electronic control, a sensor, or an actuator.

The FADEC control will communicate the identification of a faulty LRU and engine status information to the line mechanic via an independent digital data link which could be read out on an aircraft maintenance panel or on the F-14

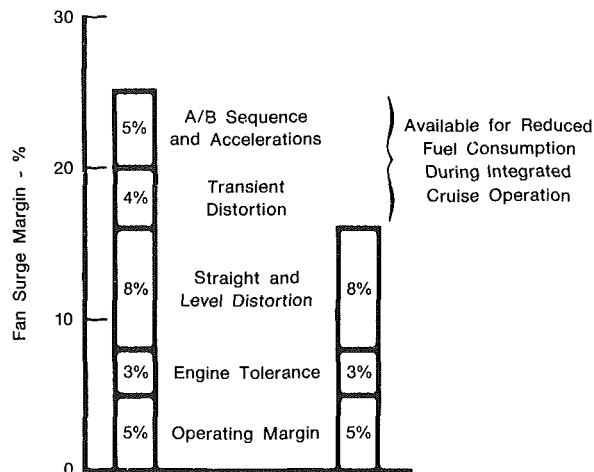


Fig. 6 Fan surge pressure ratio margin

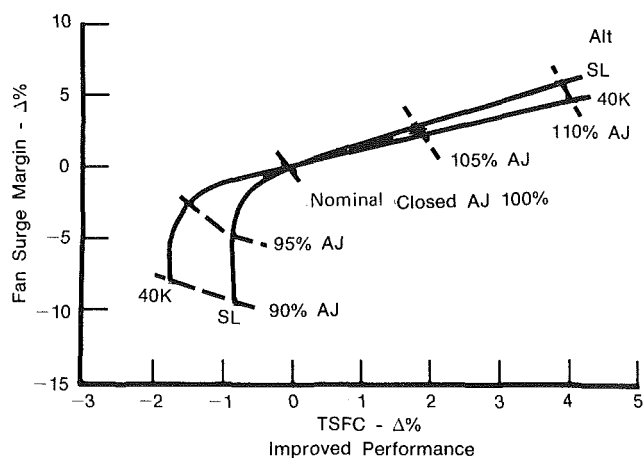


Fig. 7 TF30-P-414 performance exhaust nozzle effects

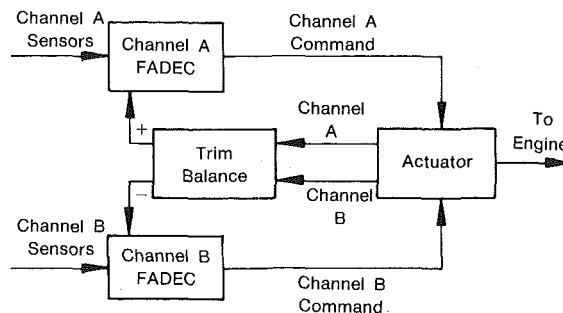


Fig. 8 FADEC/AFM fail operational control

aircraft cockpit display via the MIL-STD-1553B data bus. This procedure will minimize removal of suspect LRU's which, in fact, have not failed.

Use of Alternative Fuels

The FADEC/AFM System uses dual redundant centrifugal fuel pumps to supply both the gas generator and afterburner fuel systems. The independent FADEC/AFM hydraulic systems mean that the fuel pumps are not required to provide highly filtered fluid to any of the system servo valves. Centrifugal pumps provide the high reliability required to operate as part of the integrated control system. They also have the ability to work with antimisting and other alternative low lubricity fuels. Antimisting fuel has an affinity for contamination which can plug and collapse the fine filters

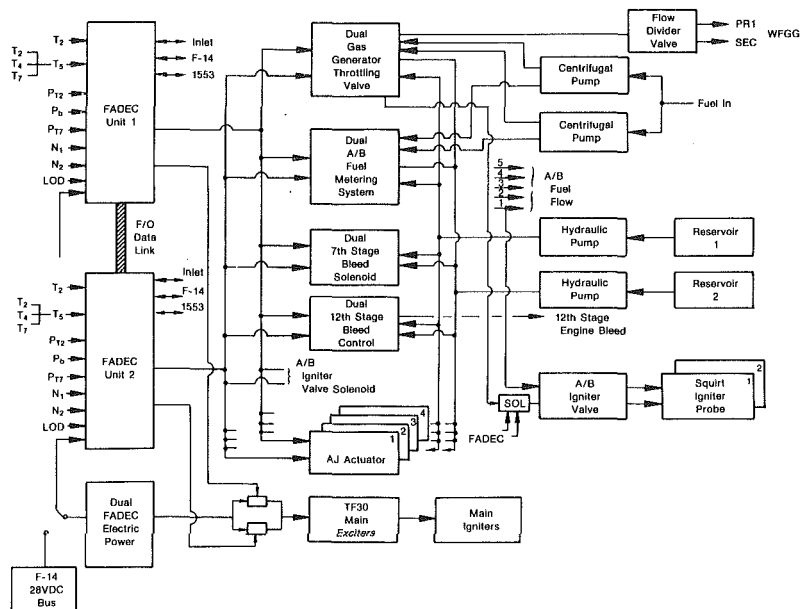


Fig. 9 FADEC/TF30-P-414 system

required for gear and vane fuel pumps. The centrifugal pumps do not have the wear problems of these pumps, and thus do not require this fine filtration. Similarly, the low lubricity fuels, such as those derived from shale oil, work well in centrifugal pumps which do not have the lubrication requirements of other pump types.

Air Start Envelope Expansion

In the event that the engine shuts down in flight the FADEC/AFM system integrated with the F-14 offers the potential to increase the operating envelope where a spooldown restart may be attempted. This is achieved through the FADEC awareness of both the aircraft and engine operating condition. The probability of a successful spooldown restart is enhanced by high airspeed, high engine RPM, and low engine turbine temperatures. All of these parameters exist in the FADEC for use in normal operating modes. The FADEC/AFM system can monitor these conditions and set an appropriate starting engine fuel flow. Hydromechanical controls operate with a fixed minimum fuel flow which limits the envelope where a spooldown restart may be attempted. In addition, the FADEC automatically protects the engine from hung or hot starts thus reducing the pilot workload during this critical operating phase.

Propulsion Control Accuracy

The use of the FADEC controls will provide a system capable of accurate control of the TF30-P-414 engine at any point in the flight envelope.

Digital electronic computations can, in general, be made as accurate as required and can easily reach a level of performance that contributes insignificant error to a control system. However, hydromechanical computation accuracy depends on manufacture, assembly, and calibration tolerances. These close tolerances are limited by allowable production cost.

No Throttle Movement Restrictions

A nonintegrated control system places limitations on the pilot's ability to make throttle movements due to the possibility of engine stall. The FADEC system integrated with the F-14 flight control system allows unrestricted movement

of the engine throttles throughout the flight envelope. The FADEC response to a throttle transient would increase or decrease fuel flow at a rate appropriate to the F-14 operating condition. In the event of engine stall or rapid increase in engine turbine temperature the FADEC would take recovery action or delay the transient until it was safe to continue.

FADEC/AFM Propulsion Control System

The FADEC/AFM engine control system was designed to perform four basic functions: provide safe stable operation of the TF30-P-414 engine, communicate with the F-14 aircraft, control the left engine inlet, and finally to provide benefits to the weapon system which can be measured and verified during flight test. This technology demonstration system for control of the TF30-P-414 in the F-14 is shown diagrammatically in Fig. 9.

The hardware for the flight test engine control system was derived from programs currently under way at PWA: FADEC, FAFTEEC, AFM, and IR&D. The FADEC electronic controls were derived from concepts developed in the Navy FADEC Program which has been an ongoing effort at PWA since 1976. The FADEC program established the dual fault tolerant control configuration, the use of EAROM's closed loop control modes, and aircraft integration system for use in the F-14 flight test program.

The AFM actuators operate the TF30-P-414 exhaust nozzle and modulate gas generator and augmentor fuel flows with direct drive actuators powered by dual wound, direct-drive torque motors. Each actuator has two, electrically independent LVPT feedback devices: one for each FADEC.

The AFM hydraulic system contains two isolated, gearbox-driven wobble plate, variable displacement hydraulic pumps which operate at 3000 psi. This hydraulic system will power all of the fuel flow and exhaust nozzle control actuators on the TF30-P-414 engine. Use of a separate, high-pressure, hydraulic system which does not use fuel pressure for actuation, permits the use of reliable dual redundant centrifugal fuel pumps.

Flight/Propulsion System Integration

The primary goal of the F-14 Aircraft and Propulsion Integration Evaluation was to configure a control system which would demonstrate the benefits of integrated control

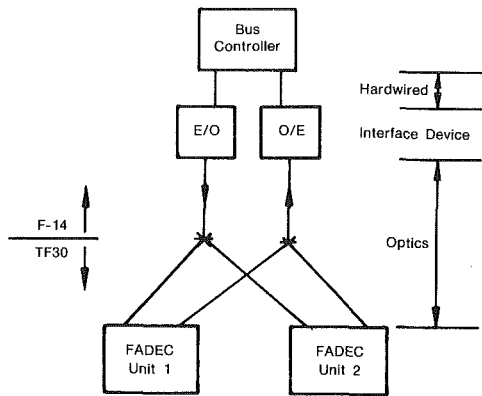


Fig. 10 FADEC/F-14 1553 data bus structure

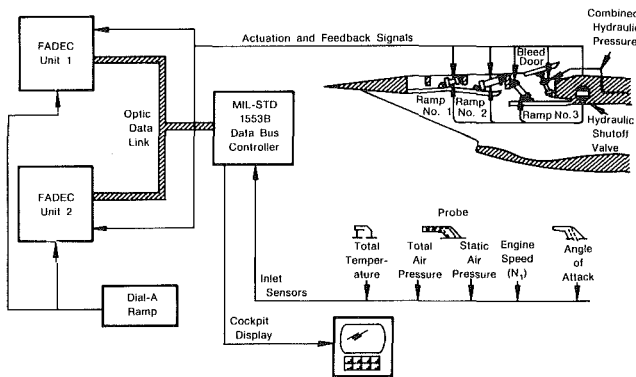


Fig. 11 FADEC/F-14 system integration

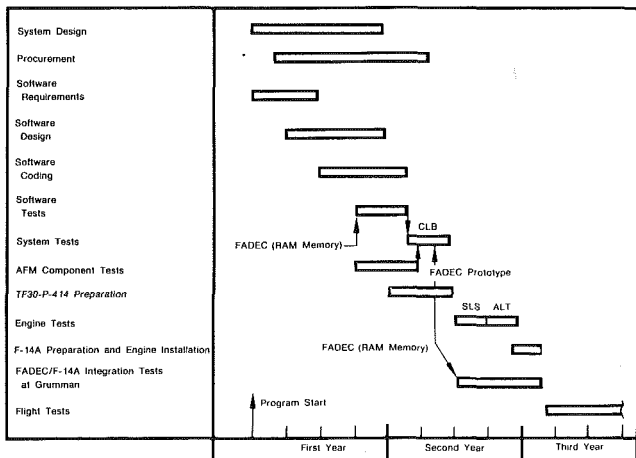


Fig. 12 FADEC/F-14A propulsion test schedule

systems. The control system for the F-14 flight test will address integration on two levels:

- Air inlet control
- Diagnostic and engine performance information

The link pins in this integrated control system are the dual FADEC units communicating with the F-14.

The FADEC units will communicate with the F-14 using both optic and hardwired links. The primary communication for information transfer between FADEC and the left inlet will be an optic MIL-STD-1553B format data bus, Fig. 10. Fiber optics are employed in this Navy application due to its superior electromagnetic interference and isolation characteristics.

A MIL-STD-1553B data bus operates asynchronously in a

Table 3 FADEC/F-14 control and display

Function
Mode and submode selection
Engine parameter readout selection and display
BIT diagnostic selection and readout
Failure simulation and readout
Aircraft parameter readout
"Dial a ramp/door" position commands

command/response mode. In this serial system, the FADEC units will act as remote terminals (RT) which transmit and receive data on command from the bus controller. This bus control function will be handled by a GAC designed remote terminal interface unit.

The FADEC controls will perform all of the computations required to position the left air inlet. Integration of the air inlet system with FADEC will be accomplished as shown in Fig. 11. Inlet sensor information will be processed in the F-14 and transmitted to FADEC on the MIL-STD-1553B optic data link. FADEC will perform the inlet calculations using ramp and bleed door schedules provided by Grumman. The increased computational power of FADEC will allow the use of angle of attack and corrected engine airflow, in addition to mach number, to position the inlet ramps and bleed door. The drive signals to the ramp and bleed door torque motors are hardwired from FADEC to each individual actuator. It should be noted that the ramp and bleed door LVDT excitation and position feedback functions will also be accomplished in FADEC.

The integrated flight and propulsion control system will provide engine and control operating and diagnostic data to the digital cockpit displays in the F-14. The use of FADEC as a remote terminal on the aircraft MIL-STD-1553B data bus would permit the aircraft, with preestablished programming, to have access to any of the parameters or calculations resident in the engine control. The preferred approach for the flight test program would use the F-14 Integrated Avionic Control System Control and Display (IACS C&D). This unit will provide digital readout capability, flexibility, and growth capability, and the existing IACS C&D in MIL-STD-1553B data bus compatible when used with a remote terminal unit. Table 3 shows a preliminary list of the type of functions being considered for display on an integrated FADEC and IACS C&D.

Summary

- Implementation of the FADEC/AFM system into the F-14/TF30 provides performance, reliability, and maintainability improvements that would be demonstrated in a flight test program.
- The FADEC/AFM hardware design is available from ongoing PWA programs to configure a system to control the TF30-P-414 and provide integration with the F-14 inlet.
- The schedule for the flight test program, Fig. 12, allows for demonstration before design of the next generation Navy fighter.

References

- 1 Nufer, W. H., "Configuration/Flight Test Definition for an Integrated F-14 Full Authority Digital Electronic (FADEC) TF30 Engine Control System Aircraft Test Program," Grumman Aerospace Corporation, May 1982.
- 2 Hoelzer, C. A., Nufer, W. H., and Vizzini, R. W., "Potential Benefits of a Full Authority Digital Electronic Control (FADEC) Installed on a TF30 Engine in an F-14 Flight Test Demonstration Aircraft," AGARD Lecture Series 1982.
- 3 Lenox, T. G., "Full Authority Digital Electronic Control Phase I Final Report," Pratt & Whitney Aircraft, Vol. I and II, FR-8652, June 1978.
- 4 Davies, W. J., McGlone, M. E., Miller, R. J., Peak, W., and Smith, T. B., "Full-Authority Fault Tolerant Electronic Engine Control Systems for Variable Cycle Engines," AFWAL-TR-81-2121, Dec. 1981.
- 5 Davies, W. J., and Miller, R. J., "FADEC-F-14 Flight Test Study, Final Report," Pratt & Whitney Aircraft, Dec. 1982.

LMFBR Operational and Experimental In-Core, Local-Fault Experience, Primarily With Oxide Fuel Elements^{1,2}

D. K. Warinner

Mechanical Engineer,
Magnetohydrodynamics Project and Reduced
Enrichment
Research and Test Reactors Program,
Argonne National Laboratory
Argonne, Ill. 60439
Mem. ASME

Case-by-case reviews of selective world experience with severe local faults, particularly fuel failure and fuel degradation, are reviewed for two sodium-cooled thermal reactors, several LMFBRs, and LMFBR-fuels experiments. The review summarizes fuel-failure frequency and illustrates the results of the most damaging LMFBR local-fault experiences of the last twenty years, beginning with BR-5, and including DFR, BOR-60, BR2's MFBS and Mol-loops experiments, Fermi, KNK, Rapsodie, EBR-II, and Treat-D2. Local-fault accommodation is demonstrated and a need to more thoroughly investigate delayed-neutron and gaseous-fission-product signals is highlighted in view of uranate formation, observed blockages, and slow fuel-element failure-propagation.

Introduction

The intent of this paper is to survey fuel-element behavior, primarily oxide endurance, (i) while operating in various liquid-metal-cooled, fast neutron breeder nuclear reactors (LMFBR's) around the globe, (ii) during LMFBR experiments and fuels testing in prototypes, and (iii) during experiments in thermal reactors with LMFBR-design fuels in an epithermal neutron flux (e.g., BR2/Mol 7B). This survey of experience with oxide fuels, primarily, and with carbide and metals fuels to a much lesser extent, is intended to help guide the research and development (R&D) remaining to ensure safe and clean LMFBR operation through the fulfillment of the LMFBR lines-of-assurance (LOAs) discussed in the companion paper, reference [1].

This paper focuses on fuel failure and fuel degradation as subsets of local faults. To improve the fuel design, we must not only gauge where the fuel has fallen short of the design expectation, but also note how design changes, and change from pellet to vibratory-packed (vipak) fuel, might have affected the operating performance of the fuel. Reference [1] tabulates some of these results. We cannot provide such definitive design-change results here, but we can review the operation of some reactors and experiments and leave impressions of how the fuel performed.

Although the conceptual-design-study (CDS) fuel has yet to be selected, certain weaknesses of (and less testing of and operation with) the attractive carbide fuels strongly suggest that we will drive the first-generation commercial breeders with the familiar oxide fuel. Metal fuels successfully drove Fermi and Dounreay Fast Reactor (DFR), and continue to drive EBR-II, but safety considerations have left this choice a distant runner for selection in a commercial LMFBR. Nitrides are too new and unfamiliar to designers to be serious candidates for the CDS fuel in the foreseeable future. Thus, a fuel akin to that chosen for the Clinch River Breeder-Reactor Plant (CRBRP) deserves our primary attention in a performance review, even though carbide and metallic fuels may perform better than oxide fuels with respect to such factors as breeding ratio, transient behavior, power density, and sodium bonding.

Reference [1] set the framework within which we are dealing through (i) a brief review of the LMFBR lines-of-assurance, (ii) a review, history, and definition of local faults, (iii) a description of the fuel designs and major reactor-design parameters in decommissioned, operating, and planned reactors, (iv) a summary of what the United States and other nations expect for fuel-design performance, and (v) a review of failed-fuel detection. Finally, the conclusions call for a review of operational experience so that one could determine what trends appear to possibly meet the design goal and what R&D remains to ensure that the lines-of-assurance goals are met.

To recapitulate the conclusions of reference [1] and prepare for the review following, a summary of out-of-pile experiments and analyses (coupled with previously published summaries) showed that [1, 2]:

¹Work performed under the auspices of U.S. Department of Energy while the author was with the Sodium Loop Safety Facility Program of ANL's Reactor Analysis and Safety Division.

²The submitted manuscript has been authored by a contractor of the U.S. Government under contract No. W-31-109-ENG-38.

Contributed by the Nuclear Engineering Division of American Society of Mechanical Engineers and presented at the Century 2 Nuclear Engineering Conference, San Francisco, California, August 19-21, 1980. Manuscript received at ASME Headquarters April 4, 1980. Paper No. 80-C2/NE-21.

Table 1 Statistics on irradiated oxide fuel pins in sodium-cooled fast reactors [3]

Reactor	Number of irradiated pins	Number of failed fuel	Fuel-failure rate, %
BR-5, BOR-60	4,600	150	3.3
DFR ^a	~1,000	~50	5.0
Rapsodie	25,000	24	0.1
Phenix	>30,000	~10	0.03
EBR-II, SEFOR	1,500	10	0.7
GfK-program	209	30	14.5
	~62,300	274	0.44

^aNaK-cooled**Table 2 Oxide fuel pins irradiated in FBR's [4] (based on information available Dec. 1973)**

Country	Reactor	Irradiated fuel	~ Failure rate, %	Total
USSR	BR-5	~2,490	<0.5	~61,600
	BR-10	~1,520		
	BOR-60	11,400		
	BN-350	~46,200		
France	DFR	41	10	44,650
	Rapsodie-Core 1	4,305	<0.2	
	Rapsodie-Fortissimo	~17,300		
	Phenix	23,002		
		(>40,000) ^a	<0.01	
USA	SEFOR	648		~2,450
	EBR-II	~1,800		
UK	DFR	~1,000	10	~1,000
DEBENELUX ^b	Rapsodie	73	10	181
	DFR	108		
Other				~150
				~110,000

^aFrom IWGFR-24-3 (April 1978), not included in total^bDEBENELUX refers to a joint program between West Germany (Deutschland), Belgium, The Netherlands, and Luxemburg; Luxemburg has since become inactive and the program is now referred to as "DEBENE."

- Rapid FEFP has been deemed extremely unlikely, if not impossible
- Slow FEFP should be (i) detectable, and (ii) self-limiting
- Slow blockage propagation is unlikely
- Slow blockage growth appears nonmechanistic from within and highly unlikely even for external debris
- In-core planar blockages can be ruled out as a credible local fault
- Molten-fuel release is very improbable, but even given a small release, resultant failure propagation or subassembly damage is unlikely
- Although pin distortion and vibration, wire-wrap breakage, and other faults are possible – indeed, likely – the basic conclusions from the analyses and out-of-pile studies appear to be relatively insensitive to such perturbations

Again, these conclusions ignored the reactor experience; indeed, Warinner and Cho [2] went on to review in-pile experience and experiments and altered these conclusions somewhat in view of the operational experience.

Whether the consequences of an in-core local fault will always be contained within the subassembly (S/A) will remain in question until many years of prototypic operating experience have been witnessed. The conclusions, based on analyses and prototypic out-of-pile experiments, often with a critical parameter or characteristic bounding, can be challenged to be conjectures. However, the in-reactor experience summarized here lends credence to these conclusions.

In-Reactor Operating-Experience and Experiments

To illustrate the basic conclusion of S/A containment of local faults, we limit our case-by-case review to selective multipin experience (or experiments) with fuel failures that had appeared to have some credible path to whole-core involvement. (This excludes many valuable single-capsule tests in GETR, SILOE, and FR-2; to include effects of adjacent pins and to illustrate fuel-element failure-propagation (FEFP), or lack thereof, requires a pin bundle.) Our review includes the following reactors and experiments: Sodium Research Experiment (SRE), Hallam, BR-5, Fermi, Dounrey Fast Reactor (DFR), Transient Reactor Test (TREAT), BR2 (Manufacture-Franco Belge-au-Bauche-Sodium (MFBS) and Mol 7 Series), KNK, Rapsodie, BOR-60, and EBR-II Run Beyond Cladding Breach (RBCB). This includes the planar blockage inserted into the DFR during decommissioning and MOL 7B, 7C/1, and 7C/2 summarized below; Mol 7C/3 results should be available this year. These studies have shown that such given blockages can be accommodated. Although we have no reason to believe that these in-pile results would not apply to a wire-wrap spacer design, to convince others of this is not without complications.³ However, the reactor experience covers a broad range of many parameters as listed in Tables 3 and 4 of reference [1].

The reactor experience for oxide fuel, tabulated through

³Results from ANL Sodium Loop Safety Facility P4 Experiment planned and designed by the author and run in August and September of 1981 should provide such information.

1976 in Table 1 from [3], provides a birds-eye view of the overall behavior.

However, this table appears to have underestimated the oxide irradiation considerably. Table 2 from an earlier report [4], shows that by the end of 1976, the USSR alone would have irradiated at least 61,600 pins. Also, experience such as that in PFR is not included.

These two tables illustrate a need for a comprehensive, continued tabulation that includes a screening process so that experiments, different cladding materials, differing pin diameters, etc., can be sorted to reveal that true failure rate for prototypes with a given linear power, fluence, and burn-up. This will not be done here; rather a case by case approach will illustrate the behavior of the fuel elements.

Local Faults in Sodium-Cooled Thermal Reactors. The 1959 SRE fuel-failure accident is included because it presents one extreme of many conditions, was sodium cooled, and had cylindrical metal (and later oxide) fuel elements on a triangular pitch with wire-wraps spacing 7-pin clusters. Further similarity to a U.S. LMFBR prototype ceases there, however (viz, SRE was a 20-MWt sodium-graphite thermal-breeder reactor with NaK bonded uranium metal fuel 1.83-m long, 19.1-mm in diameter, clad by 0.25-mm thick 304 SS and spaced 2.34 mm). After eight to thirty eight L of oil (Tetralin) leaked into the sodium and deposited on the fuel pins, the oil was “stripped” with nitrogen, only to possibly nitride the SS and zirconium and contribute to later fuel and moderator failures. Although the oil accumulated for thirteen months and its effects were detected over eight months with temperature anomalies and unexpected reactor behavior persisting, the reactor was repeatedly recovered from various scrams until repeated checks of a S/A showed the elements to have lost all freedom of motion. The reactor was finally shut down after reaching 14-MWt, scrambling, returning to 3–5 MWt, scrambling, and so on several times during its last run of ~14 days. (During this eight month period, several potential accidents were logged: failure of automatic scram, loss of secondary coolant flow, loss of auxiliary primary flow, fast periods, and seemingly runaway behavior.) The post-accident analyses strongly suggest repeated voiding of blocked channels. Yet, although the exit temperature had exceeded 760°C (nominal ~500°C) and a steel-uranium eutectic had formed, the cladding melted in but 10 of 43 assemblies; the melting was severe enough to separate the top and bottom halves of the fuel pins. Thompson [5] comments in his description of the accident, “one can postulate that there was a reactivity interaction between channels and that voiding in one led to heating and voiding in others and so on.” Even with this serious accident, the reactor had two more core loadings of different designs and finally attained 45-MWt with UO₂ fuel before it was shut down in 1964. All involved in nuclear safety, from safety analysts to utility managers, should periodically review the nearly forgotten SRE experience to learn from this incident of malfunction and poor judgement. As of January, 1979, the SRE decommissioning was “nearing completion” [6]. Finally, the oil leak, which can be regarded “external debris,” has appeared in other reactors (e.g., 27 L in Phenix, 10 L in BOR-60, and small amounts of Fluorolube in Fermi) as a potentially severe local-fault that can seriously damage the fuel. (It is interesting to note that the SRE supplied 6 MWe into the Southern California Edison Corporation grid.)

The Hallam Nuclear Power Facility (HNPf or “Hallam”), an outgrowth of the SRE and similarly designed as another sodium-cooled thermal-reactor, operated from 1962 to 1964. The reactor was troubled with many component failures; the relevance to local faults lies in the failure of, and sodium permeation of, some SS clad graphite moderator elements (such failures encouraged the use of the vented-fuel-to-

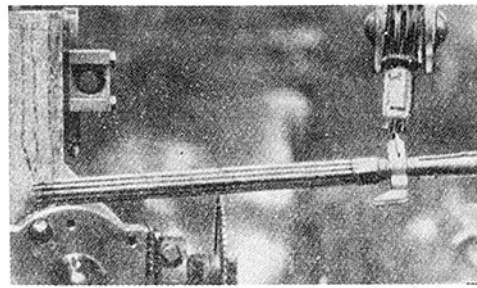


Fig. 1(a) Nineteen-pin subassembly

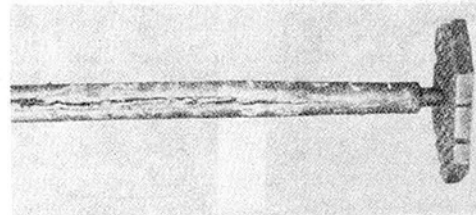


Fig. 1(b) The failed central pin

Fig. 1 BR-5 19-pin bundle of PuO₂ at 6.1 percent burnup with only central pin failed [8] (by permission of Plenum Publishing)

coolant concept, thought to prevent FEFP), difficulty of carbon-content control, and coolant flow maladjustment partly due to subassembly inlet sodium dioxide deposition. The Na₂O deposition has recurred in other reactors (e.g., Rapsodie).

Early Fast Reactor Experience with Oxide Fuels: BR-5. The Soviet BR-5 had PuO₂ fuel designed for 2 percent heavy atom burnup (b.u.) as its first charge in 1959. Significant activity registered at 2.4 percent b.u. and worsened beyond 137 Cs-activity detection at 3.2 percent b.u. The reactor was not shut down until ~5 percent b.u. (September 1961) when 18 of the 81 S/As were found to leak fission gas (gaseous fission products, GFP) badly. In early 1962, UO₂ S/As replaced the outer 20 percent of the PuO₂ 19-pin S/As. The PuO₂, rearranged in the central zone, had 4.85 percent max. b.u. and included leakers. The reactor then operated for three years with up to 6.5 percent b.u. until a major increase in the GFP activity gave BR-5 its lifetime maximum xenon activity on November 1, 1964. From [7], “In seven years of continuous monitoring of the BR-5 reactor, only once did an emergency fuel-element leakage [with PuO₂ fuel] occur [November 1, 1964]. Various signs indicated that more than ten fuel elements started leaking in 1 min. The rapidly worsening dosimetric conditions made it essential to reduce the power to 10 percent nominal within 6 hrs, and after another 2 hrs to shut the reactor down altogether. On recharging the packs, no melted fuel elements were found, although every fifth pack contained a leaking element. The recharging itself involved no difficulties.” Twenty-seven of 59 centrally located PuO₂ S/As were found to contain failed pins a month after discharging the fuel; 17 PuO₂ S/As with >5.1 percent b.u. had been defective for 2 1/2 years. Four months after reactor shut-down, the gas activity (primarily ⁸⁵Kr) from these S/As was from 10 to 1000 times higher than the background from leak tight S/As. BR-5 was restarted in May, 1965, charged with UC fuel except for four ~6 percent b.u. PuO₂ S/As, two ~1 percent b.u. PuO₂ S/As, and two ~1 percent b.u. UO₂ S/As. A delayed neutron monitor (DNM) had been installed in 1964. Two S/As were found to contain the first failed pins in August, 1965. Figure 1 shows one reported investigation of a BR-5 19-pin bundle of PuO₂ at 6.1 percent b.u.; all pins exhibited high swelling, *but only the center pin failed—quite*



Fig. 2(a) 5.0 percent b.u.



Fig. 2(b) 6.8 percent b.u.

Fig. 2 DFR oxide pin failure showing natural development of failure [9] (by permission of British Nuclear Energy Society)

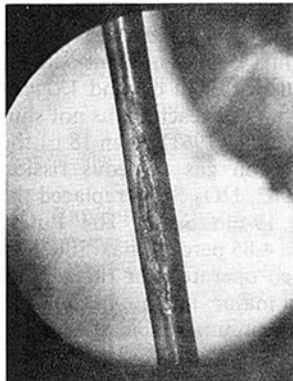


Fig. 3(a) Upper defect, pin G 24

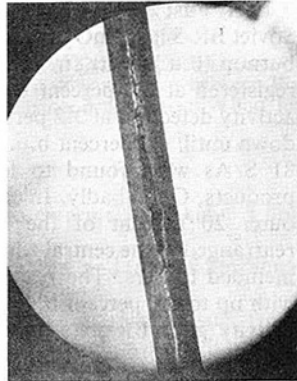


Fig. 3(b) Lower defect, pin G 24

Fig. 3 Two failures in DFR-435 test [12] (by permission of IAEA)

badly. The cladding had cracked along the *entire length on opposite faces*; the bundle had been irradiated in BR-5 for about 5 1/2 years [8]. Although we are not aware of whether transients initiated fuel failure or degraded the fuel, this BR-5 experience with close-to-prototypic geometry demonstrates that no propagation occurred (not even to an adjacent pin in the above case) while operating (i) with failed fuel much longer than our projected refueling cycle, (ii) with highly embrittled and swollen fuel, and (iii) at contamination levels not permitted for a prototype LMFBR. Having irradiated PuO_2 to a maximum of 6.7 percent b.u. with 3×10^{22} n/cm² fluence over 468 actual operating days by 1971, BR-5 was upgraded, received a third loading of PuO_2 intended for 10 percent b.u. and 10 MWt in 1972, and renamed BR-10. BR-10 ran at powers much less than 10 MWt from March 1973 through 1978; extensive structural irradiation prevented higher-power operation. Too little information on BR-10 fuel-failure has been received to include in this review. It is

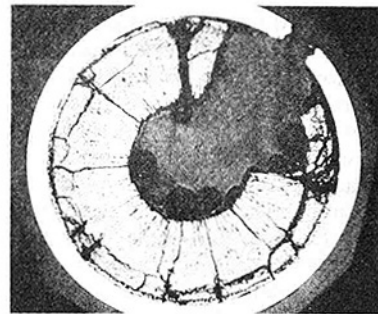
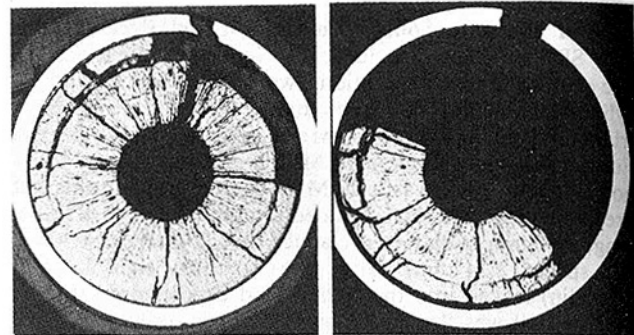
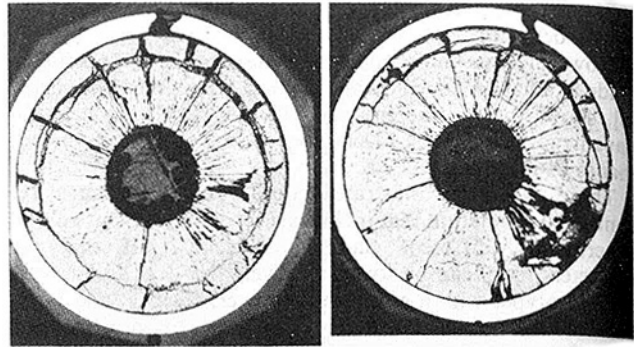


Fig. 4 Cross sections of failed pin in DFR-435 [13, 14]

interesting to note that BR-5 had an estimated 38 g of ^{235}U in the primary circuit coolant in 1969 [7].

The Fermi Subassembly Meltdown. The 1966 Fermi incident illustrates a degree of coolability, although the geometry, fuel, and cladding were unlike any projected prototype. This, the then largest FBR (200 MWt) and sodium cooled, had an inlet blockage affecting the flow through about four core S/As (144 fuel elements per S/A, 105 core S/As total). Ironically, the inlet blockage was a zirconium plate that had been added for safety, not operational, purposes. Three years after it went critical and during a rise to power (at ~34 MWt), at least one S/A voided, the fuel melted in two S/As (dispersed radially and slumped slightly), and two adjacent S/As were slightly damaged (deformation but no melting). The reactor-power increase was stopped, but the reactor was not immediately scrammed; a post-accident analysis suggests that the fuel melted a hole in the square SS wrapper and then the S/As were cooled (at that low power) by sodium flowing through the hole and exiting the most severely damaged S/A, hardly a case of S/A-to-S/A propagation to the whole core. While being mindful of the low power at which the accident occurred, this accident suggests favorable inherent behavior even in the most severe local-fault case of an inlet blockage. Indeed, the accident was so attenuated that repairs were possible; four years later the reactor returned to full power following an intense technical and government investigation, only to be decommissioned in 1972. Finally, the reference subassembly inlet design (e.g., for CRBRP and

FFTF) has been significantly altered so as to effectively preclude an inlet flow blockage.

The DFR Fuel Irradiation Tests. The 60-MWt DFR, unique for its combined NaK primary coolant, coolant downflow, N₂ cover gas, fuel-pin spacer grids, and vented-fuel-to-coolant design, went critical in 1959 and, except for jammed elements in 1965, ran remarkably trouble-free through decommissioning in 1977. It served beautifully as a fast-flux materials-test reactor; the operating experience, per se, adds optimism to local-fault issues. The O₂ level was held to about 6–8 ppm or less after about 1970. As early as 1964 and 1965, nucleate-boiling detectors and S/A-outlet temperature-noise monitors were installed, both intended to detect the presence of a S/A blockage (in anticipation of increasing the number of test rigs beyond 30 and therefore increasing the probability of blockage formation). The three basic pin irradiations were conducted in (i) reactor center S/As, (ii) core periphery mini-S/As, and (iii) single-pin or trefoil test rigs replacing driver fuel pins. The descriptions of selected DFR tests will be brief reminders of those that had operated with encapsulated mixed-oxide fuel; photographs will illustrate the results where possible. All failed pins ran for some time beyond failure because the DFR vented-fuel design precluded the use of an effective DNM.

Although failures have been relatively infrequent, some naturally failed pins (noticed during startup) were left at power for over 100 days to study the effect of Na₃(U, Pu)O₄ with no resultant gross deterioration; Fig. 2 illustrates the development of one failure [9]. However, more serious effects may be masked because NaK hinders sodium uranate formation and the potassium reacts to form a higher density compound than sodium uranate. Thus, the pin damage might be far less than it would in a Na-cooled reactor. Perhaps the worst failure rate of a prototypic bundle in DFR was with the Mk-VIIA 60-pin S/A in which 90 percent of the fuel failed while the reactor was operating at ~60 kW/m up to 9.0 percent b.u. Although the high-failure-rate cause is unknown, this bundle differed from others by having wire-wrap spacers, 30 and 40 percent Pu, and all vibrocompacted fuel [10]. Yet, the bundle retained its original shape with no sign of overheating. Before this, the most extensive failures had been twenty two failures in a 77-pin bundle; the failures were signaled by radon release into the blanket gas during the rise to full power, where the reactor remained for 30 hrs without developing a hazardous situation [11].

DFR-324/2 was a trefoil irradiated for ~1 1/3 years (~57 MWd/kg) at 44.0 kW/m maximum. A “massive fracture” of “not-obvious cause” occurred at the top of the fuel column (the cold end) and was not “associated” with the breeder region [12]. The experiments cite high fission-product content as the only unusual feature in the failure region; this suggests Cs migration to the lower-temperature regions and subsequent reaction with the fuel and axial-blanket, and/or cladding attack. Irradiation continued without propagation.

DFR-350 was a 30-pin bundle of 86.4 percent-enriched U_{0.80}Pu_{0.20}O_{1.98} fuel irradiated to 52 MWd/kg at 45.0 kW/m maximum with no failures, although 18 pins with one of two cladding types were badly swollen. The 21 pins with little swelling were then included in the DFR-435 trefoil series for further irradiation at ~40 kW/m. All seven failures occurred between 64 and 90 MWd/kg (9.7 percent b.u.). The two trefoils with the highest b.u. had either two or three of the three pins fail; although the experimenters do not cite propagation positively, it appears clearly possible that an initial failure caused others (particularly given the failure locations in the number seven trefoil and the thirty one shutdowns it experienced). Also, fuel was released and Na₃(U, Pu)O₄ was formed, but no further damage was reported. Figure 3 illustrates two of the failures [12]; Bagley et al.

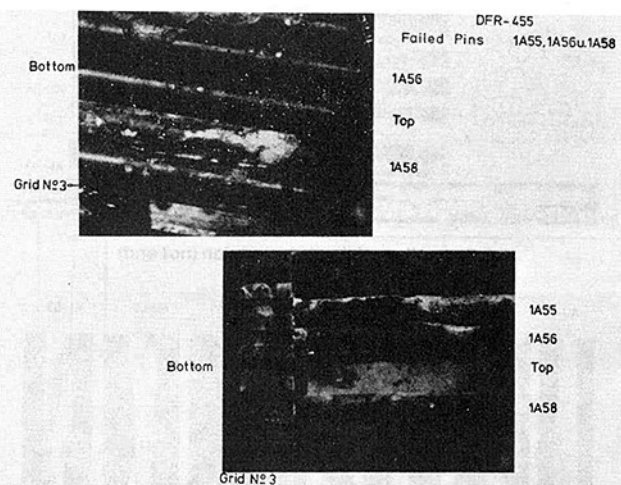


Fig. 5 Bundle damage in DFR-455 [12] (by permission of IAEA)

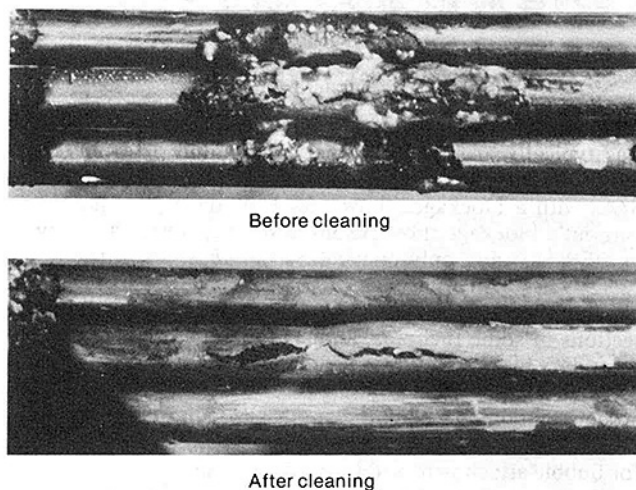


Fig. 6 BR2 Mol-7A (MFBS-5) experiment; Fuel pin damage between spacer grids 7 and 8 [20]

postulated the upper defect to possibly result from gas entrainment which created an overheated zone. Figure 4 shows cross sections of a failed pin; the cladding fissure and fuel-flushing zone are clearly shown as are the tiny particles separated by fissure zones [13, 14].

DFR-455, a 60-pin bundle of 93 percent enriched U_{0.70}Pu_{0.30}O_{1.95-1.98} irradiated from February 1973 to February 1974 at 49 kW/m, maximum, to 50 MWd/kg with failed fuel since ~5 MWd/kg [12]. Three cladding types and the spacer-grid, tie-rod design were used. Most of the seven failures have been attributed to “a single fabrication batch where some impurities causing heavy internal corrosion remained in the pins during fabrication” [15]. Although “fuel particles were released . . . and distributed within the assembly, . . . neighboring pins were [not] damaged even [around] severe failures” [12]. Again, such a severely damaged bundle remained cooled for months with no threat to the S/A wall. Figure 5 illustrates the damage.

The DFR-522, -528, -536, -539, and -540 series were the most severe DFR experiment series, entitled DFR Special Experiments, conducted, logically, during decommissioning. A series of prolonged (i.e., hours) boiling runs without and with a thin steel plate in place to simulate a 70 percent local heated-zone blockage provided a “proof test” for the mixed-oxide fuel. The CW M 316 SS cladding contained either

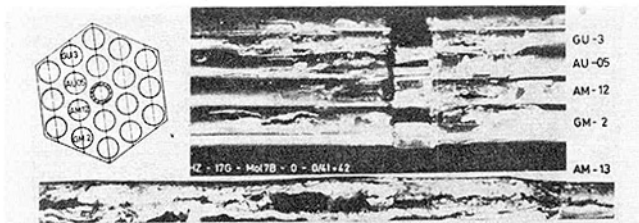


Fig. 7(a) View of the defect region (hot end)

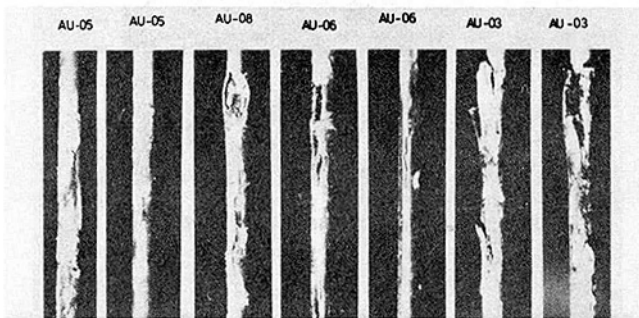


Fig. 7(b) Some pins of Mol-7B with bigger defects

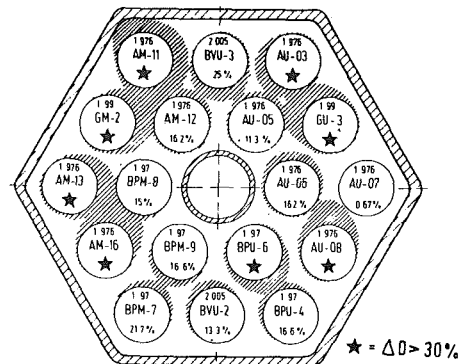
Fig. 7 Bundle and pin damage in Mol 7B with Na_3UO_4 blockage [21]

pellets or vipak fuel with from 0 to 10 percent b.u. The power was typically around 32 kW/m, maximum. The pins, contained in trefoils, mini-S/As without blockage, and mini-S/As with a blockage, show very little damage. Those tests without a blockage showed some swelling, significant bowing in DFR-528, and only one failure in 528/1 with little or no fuel loss or melting. The local-blockage tests exhibited blanketing by trapped vapor, several failures, loss of complete sections of some fuel pins, and cladding melting; even so, no secondary blockages formed and no fuel melted. These results are remarkable because boiling times ranged from minutes to a day, the boiling remaining stable throughout [16–19]. The down-flowing coolant should provide a worst-case scenario for bubble attachment and vapor blanketing.

The reactors or experiments discussed so far had no effective DN detection capability, except for BR-5 after 1964 and Fermi after 1970. Although the DNM information will not always be discussed with the following tests, to recognize which reactors and/or experiments can and did provide DN data is important [1].

Experiments in the BR2. Like the Engineering Test Reactor (ETR), the BR2 in Mol, Belgium, provides an epithermal flux with a cadmium filter on the test loop [20]. Several BR2 experiments bear directly on fuel failure, FEFP, blockages, and their accommodation.

Mol 7A (MFBS-5), a $\text{U}_{0.80}\text{Pu}_{0.20}\text{O}_{1.99}$ -fueled seven-pin test, ran from September 1968 to September 1969 at 59 KW/m (maximum) to 44 MWd/kg with three cladding types. One pin had severe melting of fuel and cladding (of unknown cause, probably fabrication defect [15]); no other failures were reported. This is illustrated in Fig. 6 [20]. This appears even more unusual upon considering that an earlier test, MFBS-4, ran from April 1968 to November 1968 with similar fuel (three pins) at 70 kW/m maximum to 28 MWd/kg with molten fuel, but without a failure (as in TREAT D1 and D2, discussed below). MFBS-6, a key test run from January 1970 to December 1972 at 57 kW/m maximum (and 650°C maximum cladding temperature) to 95 MWd/kg, had nine pins with pellets and five with either SOL-GEL or vipak fuel. Two SOL-GEL pins failed severely and might have propagated to at least two pins with pellets [12]. The other failed pin contained vipak fuel. Although the pin failures could be due to propagation (particularly with the extremely



Defect Size and Orientation

Fig. 8 Schematic of Mol 7B bundle showing regions of blockage and failed pins [21]

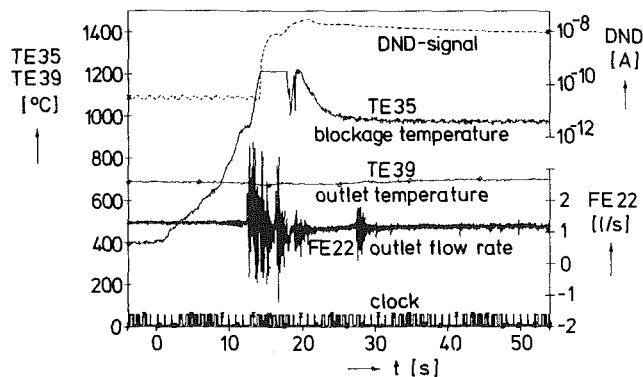


Fig. 9 Typical signals of the in-pile blockage experiment Mol-7C/1 [26] (courtesy of W. Kramer, KfK)

high fission-gas pressures present), the postulated propagation was limited and the S/A accommodated the faults.

The Mol 7B fuels irradiation experiment was the next BR2 test of significant importance to the LOA-2 accommodation topic discussed in reference [1]. This test irradiated 18 pins of 70 percent enriched $\text{U}_{72.5}\text{Pu}_{27.5}\text{O}_2$ from July 1972 to February 1974 at SNR-300 hot-channel temperatures and high power (700°C and 50 kW/m, maximum). Sixteen pins contained sintered pellets; two were vipak. The first failure was detected at 38 MWd/kg (~5.3 percent b.u.) after which a simple DNM was installed. The bundle was irradiated to 81 MWd/kg (~11.3 percent b.u.). Although only one fuel failure was reported initially [15], postirradiation examination (PIE) revealed that all pins had failed and a local 38 percent blockage had formed at one axial location (Figs. 7 and 8; note the central dummy pin [12, 13, 21, 22]), $\text{Na}_3(\text{U}, \text{Pu})\text{O}_4$ formed and the fuel swelled extensively – effects enhanced by the 16 reactor shutdowns experienced and the ~50 ppm O_2 present. Weimar [21] concluded, “a bundle running beyond failure will show the first blockage in the colder outer sub channels.” The pressure drop across the S/A was not held constant, but the Na flow rate was.

One should carefully note that the above MFBS and Mol experiments were fuels irradiation tests (as were the DFR tests) and were not intended for eventual interpretation with regard to safety (i.e., local faults).

We progress from the blockage formed in Mol 7B to the midplane, 24-channel, 40-mm-long porous SS blockage (of 0.5 mm SS spheres) inserted into the 37-pin bundle Mol 7C series (May 1977 and March 1978); Mol 7C/3, run successfully on Oct. 29, 1980 [23, 24], was identical except the blockage had 10- μm chromium-plated 93 percent enriched

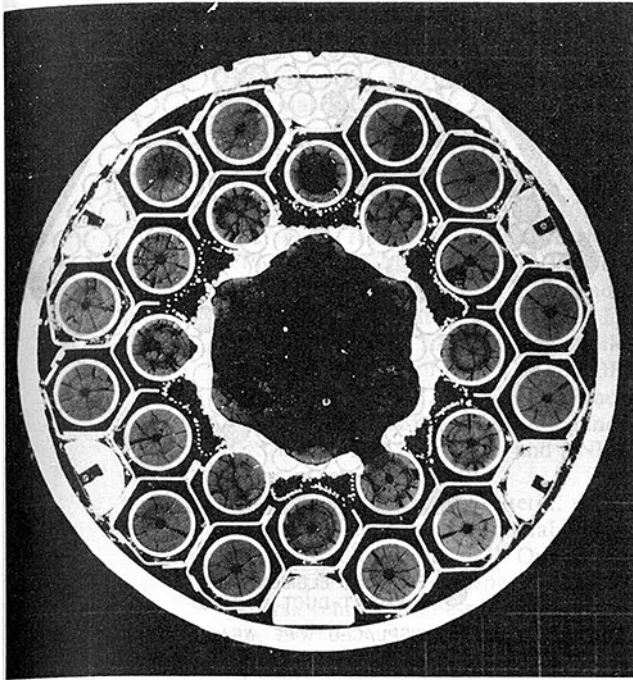


Fig. 10 PIE of Mol-7C/1: blocked region [26] (courtesy of W. Kramer, KfK)

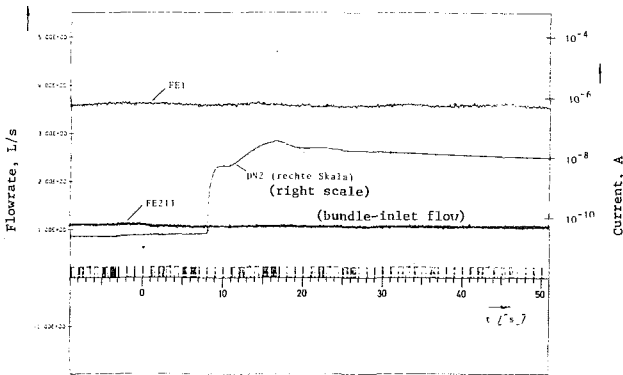


Fig. 11 Trace of signals from total flowmeter, bundle-inlet flowmeter, and delayed-neutron detector for 1 min during Mol 7C/2 transient (courtesy of W. Kramer, KfK)

fuel spheres, and Mol 7C/N will repeat this except the fuel pins will be irradiated. For 7C/1 and /2, the experimenters ran BOL 65-90 percent enriched UO₂ fuel at 40 kW/m maximum to 2.5 MWd/kg, halved the flow, interrupted the local cooling of the blockage (via flow through a central tube), and continued at power for 49 min (Mol 7C/1) and 6 min (Mol 7C/2). At least six pins failed (detected quickly by DND as shown in Fig. 9 [26]) and secondary blockages formed in Mol 7C/1; preliminary PIE showed no Na₃UO₄ formation and all failures to be between the blockage and the next spacer grid downstream [26, 27]. Figure 10 beautifully illustrates the bundle condition of Mol 7C/1. Mol 7C/2 was more mild. Two of the conclusions drawn were [28]:

- 1 At continued power production, local cooling disturbance with enforced pin failures do not lead to a fast pin-to-pin failure propagation.
- 2 Even at a strong destruction of the original fuel element geometry, integral cooling is guaranteed over a long time at full reactor power.

Figure 11 illustrates the signal responses in Mol 7C/2; a striking result is shown in Figure 12 where the DN responses

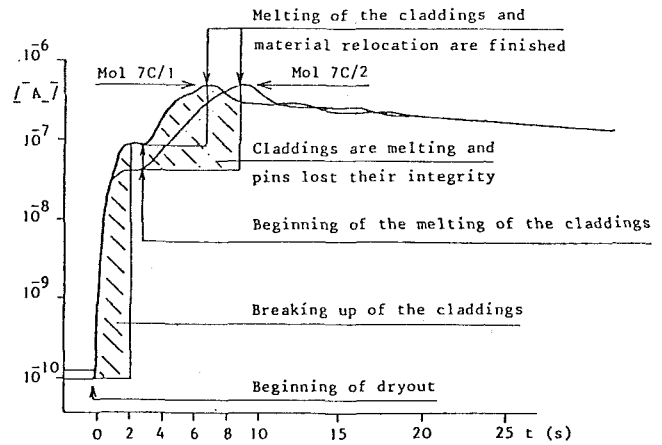


Fig. 12 Ionization chamber current, I , of the logarithmic DND channel DN-2 for Mol 7C/1 and Mol 7C/2 [27]

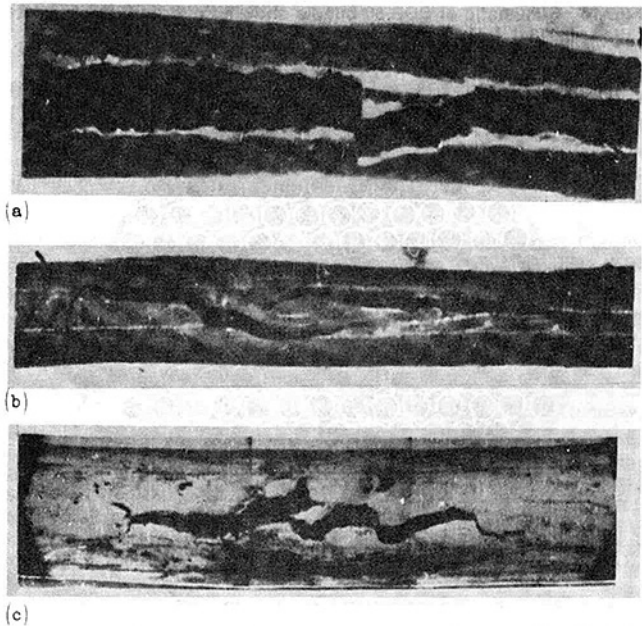


Fig. 13 BOR-60 breached pins with (a) all fuel lost, and (b) little and (c) no fuel loss [34]

are nearly identical for Mol 7C/1 and /2 [27]. The Mol 7C experimenters anticipated similar responses from Mol 7C/3 and 7C/N [29, 30]. Indeed, the Mol 7C/3 DN response was lower [24].

Differences between the Mol-7C bundle and a prototype U.S. LMFBR include the pin length, six dummy SS rods, one dummy central oversized coolant-filled SS tube, and low flow, besides the aforementioned items. Most non prototypicalities appear conservative for bundle coolability. We anxiously await the Mol 7C/3 results for a blockage of highly enriched UO₂. The Mol 7C/3 results for a blockage of highly enriched UO₂ should be available after July 1981. Later, Mol 7C/N will investigate an identical blockage accident with a bundle of preirradiated fuel.

From the drama of what would appear to be bounding experiments in DFR and BR2, we retreat to experience that includes local faults other than "age-old" failures and appears more mundane (as we hope all operating experience will be).

Miscellaneous Fuel-Failure Experience and Other Local Faults. In 1973, the KNK reactor at Karlsruhe experienced an unexplained transient partial blockage of one subassembly

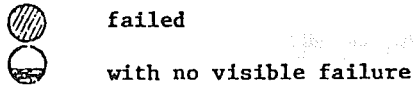
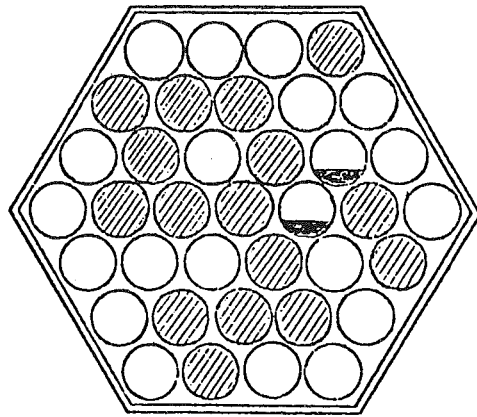


Fig. 14 Schematic of BOR-60 bundle showing distribution of twenty failed pins [34]

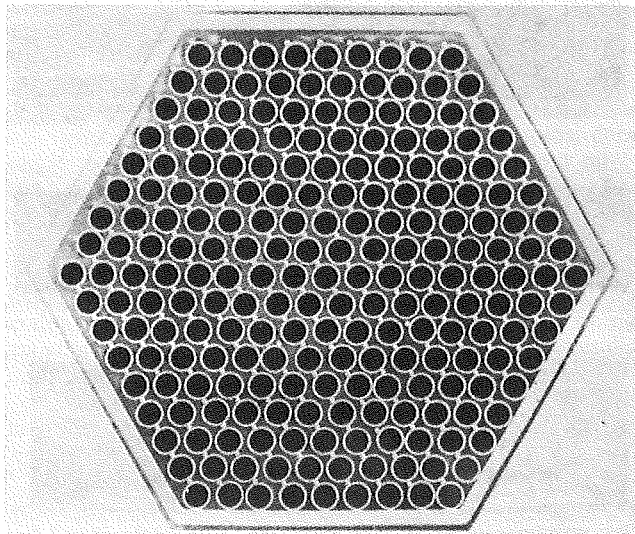


Fig. 15 Phenix subassembly cross section after 6.6 at . percent burnup: photograph of potted subassembly [37, 38]

(~35 percent reduction of flow, again during startup), apparently with no damage [31]. (Recent KNK-II experience with fuel-failure detection and location has been addressed by Jacobi [30].)

The Rhapsodie subassembly, Capricorn Ib, had a fuel failure on rise to power (at 20 percent full power) detected by DND, acoustic, TC, and other signals. The cause is attributed to the dislocation of a temp plug holder; two pins failed and released small amounts of fuel (> 5g) into the sodium [32].

TREAT D1 and D2 were seven-pin tests run with fresh 20 percent (peripheral) and 26 percent (central) enriched UO_2 of FFTF design except for shorter fuel length (348.3 mm). The center pin in each had a short "enrichment-error" section (38.7 mm fully enriched) to provide power ~2.1 times that of the 26 percent enriched portion (i.e., 140 kW/m in D2). The 0.38 mm cladding did not fail, even though ~58 percent areal average and ~75 percent areal maximum of the overenriched fuel melted and relocated axially in D2, the more severe test with power increased 71 percent over D1 [33].

Like DFR, BOR-60 has provided more evidence of the behavior of severely failed fuel; it has operated with up to 1 percent failed fuel. The experience of interest to our subject is that found upon investigation of >150 37-pin S/As, with

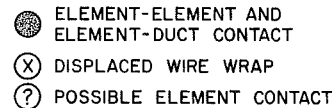
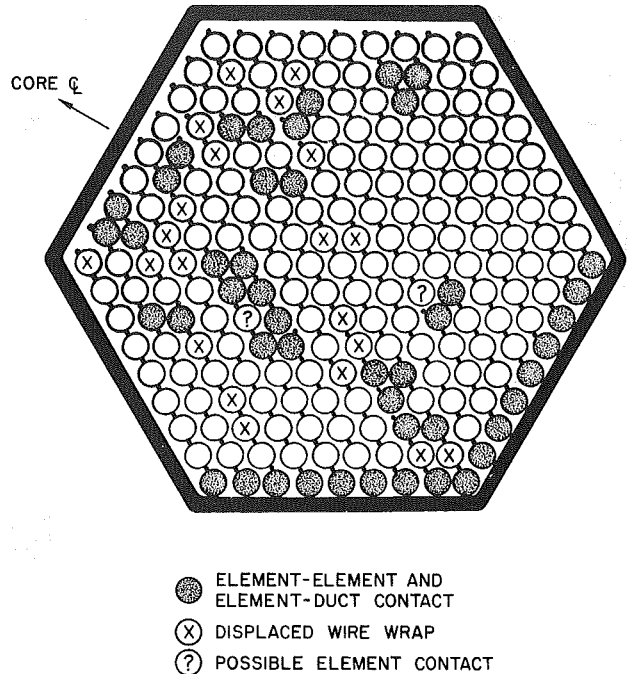


Fig. 16 Phenix subassembly cross section after 6.6 at . percent burnup: photograph of potted subassembly reversed to illustrate fuel-pin deformation

≥10 percent b.u. irradiated from 1970 to mid-1974. The UO_2 -fueled pins were of annular pellet (50 kW/m) and vipak (59 kW/m) designs. Eleven S/As contained failed fuel; failures were registered in one "at 2 percent b.u., another at 7.7 percent b.u. and the remaining . . . at 9 percent and higher burnup" [34]. The pellet-fueled 7.7 percent b.u. failed-pin remained in the reactor for a month and "the fuel . . . was not found at all." Three emergency shutdowns during the failure period and the wide longitudinal breach shown in Fig. 13 infer why all fuel was lost. The pin (at top) is difficult to see because the view is of a "cavity" or "black hole." A 37-pin S/A (A-89) with 10 percent b.u. had twenty failures with less damage to the four of 18 peripheral pins (see Fig. 14). The failure mechanism suggested is fuel swelling that exhausted cladding ductility for initial failures and subsequent failures stimulated by the presence of those failed pins (slow FEFP). Finally, an "essential fuel loss was observed in a pin from the subassembly EB-158" (b.u. not cited, although S/As were irradiated to 13 percent b.u. without pin failure [34]. Aristarkhov et al. [35] provide more information; S/A EB-158 is cited to have 8.45 percent b.u.

EBR-II RBCB-1 had sixteen 10.8 percent b.u. pins mixed with twenty one 2.0 percent b.u. pins in a reconstituted 37-pin S/A. After five days, a high b.u. pin failed and the S/A was stored in a basket for six months. The S/A was returned for further irradiation, and after five days of nearly full-power steady-state irradiation, the highly sensitive DNM exceeded the 800 cps limit with a DN spike which terminated the test. The results were minor compared to those seen in the more severe foreign tests discussed above. The center of the longitudinal crack in the 10.8 percent b.u. pin faced a "cladding stain;" although this would appear to be a case of the classical self-limiting FEFP, the stain is attributed to line pin-to-pin contact (a case of wire-wrap loosening) [36]. This domestic result alarmed some, but we can see from the foreign experience that such alarm was unwarranted.

Indeed, information on bowing and deformation has been obtained at EBR-II with instrumented subassemblies; so far these cases have been of benign nature. In addition to the above foreign experience, we have a recent report [37, 38]

which contains photographs of a potted cross section of a Phenix subassembly after 6.6 h.a percent burnup. One photograph, shown in Fig. 15, illustrates (i) wire-wrap movement from the nominal location, (ii) fuel pin contact with the subassembly wrapper, and (iii) contact between two and possibly three fuel pins. Upon photographic "reversal" and shading the involved fuel pins, one can clearly see the abnormal (bowing and deformation) regions (see Fig. 16).

Prototypic fuel failure results from BR-10 (e.g., reference [39] which includes FPM and DNM traces), BN-350, and Phenix have shown the failures to be benign and readily detected in a large reactor with very little background DN signals. However, if the U.S. operates LMFBRs with failed fuel, we must better understand the meaning of DN and GFP signals. (The reader is referred to [15, 40, 41] for more detailed information on some GETR, EBR-II [including more recent RCB tests], DFR, BR2, FR-2, Rapsodie, and KNK II tests.)

To satisfy the DOE LMFBR LOA-1 and -2 criteria, we are faced with the question, "Can subassembly coolability be maintained under severe local-fault conditions?" Our reactor operating and in-reactor experimental evidence, more extensive than one might first venture a guess, is highly supportive of an affirmative answer and reinforces conclusions drawn from out-of-pile tests and analyses.

Conclusions

Reference [1] briefly outlined the LMFBR LOA's to show the constraints of fuel-pin design. It also reviewed local faults, summarized fuel designs and reactor parameters, and discussed the requirements of the fuel and failed-fuel detection. LMFBR operating experience and experiments are summarized here with several "worst-case" occurrences reviewed.

An immense amount of information is available on LMFBR operations and experience, but a simple tabulation of failed fuel elements does not suffice to provide the designer with proper feedback. The operating history, etc., as cited in cases here, must be taken into account as well as the cladding type, fluence, power density, and so on. In each case of extensive fuel-failure, one can attribute it to such nonprototypic factors as high O₂ content, high power, reconstituted bundles, vibratory-packed fuel, and high b.u. Thus, the conclusions of references [1] and [2], cited above, appear valid for prototypic operations of an LMFBR.

The fuel-failure data, incoming now at an ever-increasing rapid pace, must be screened to determine the behavior of fuel under prototypic, off-normal transient, and upset conditions. The fuel-failure rate in Phenix is reported to be less than 1 in 10⁴ fuel pins irradiated. This is indeed impressive.

Acknowledgments

This work was performed under the auspices of the U.S. Department of Energy. My thanks go to D. H. Cho, L. W. Deitrich, H. K. Fauske, D. H. Thompson, and J. I. Sackett of ANL; R. G. Brown of SAI; and D. F. Giessing of DOE/RRT for valuable discussions and for alerting me to portions of the literature. Marsh Reinke's typing and assistance are very much appreciated, as is the typing of Velma Scott.

References

- Warinner, D. K., "The LMFBR Fuel-Design Environment for Endurance Testing, Primarily of Oxide Fuel Elements with Local Faults," ASME paper 80-C2/NE-25, presented at the Nuclear Engineering Conference of the ASME Century-2 Emerging Technology Conferences, San Francisco, Calif., Aug. 10-21, 1980.
- Warinner, D. K., and Cho, D. H., "Status and Needs of Local-Fault

Accommodation in LMFBR's," in *Proceedings of ANS/ENS International Meeting on Fast Reactor Safety Technology*, Seattle, Wash., Aug. 19-23, 1979.

3 Plitz, H., "Defektab- und Storfalleexperimente für den SNR," *Reactoragung*, Mannheim, Mar. 29-Apr. 1, 1977, p. 506.

4 Wolfe, W. B., "Compilation of Monthly Reports by the U.S. Representative to the German LMFBR Facility, November 1972-December 1973," U.S. Atomic Energy Commission, TID-26530, 1974.

5 Thompson, T. J., and Beckerley, J. G., eds, *The Technology of Nuclear Reactor Safety*, V. 1 (*Reactor Physics and Control*), MIT Press, Cambridge, Mass., 1964.

6 *Nuclear Engineering International*, Jan. 1979, p. 24.

7 Efimov, I. A., Mamaev, L. I., and Filonov, V. S., "Testing the Hermeticity (Air Tightness) of Fuel Elements in the BR-5 Reactor," *Soviet Atomic Energy*, Vol. 31, No. 6, 1971, pp. 1351-1355.

8 Kazachkovskii, O. D., Votinov, S. N., Lebedev, I. G., Kuz'min, V. I., Syuzev, V. N., Sytov, L. I., Vyskubov, V. P., Ilyasov, V. M., Prokhorov, V. I., Balashov, V. D., Ostrovskii, Z. E., and Tuchnin, L. M., "Investigation of a Working Fuel Element Bundle from the BR-5 Reactor with Plutonium Dioxide Fuel," *Soviet Atomic Energy*, Vol. 24, 1968, pp. 164-171.

9 Bishop, J. F. W., "Performance Development of the PFR Fuel and the Use of PFR as a Fuel Development Facility," in *Fast Reactor Power Stations, Proceedings of the International Conference Organized by the British Nuclear Energy Society*, London, Mar. 11-14, 1974.

10 Swanson, K. M., Sloss, W., and Batey, W., "UK Irradiation Experience Relevant to Advanced Oxide Fuel Concepts for LMFBR's," in *ANS Topical Meeting Proceedings Advanced LMFBR Fuels*, Tucson, Ariz., Oct. 10-13, 1977.

11 Bagley, K. Q., Edmonds, E., Powell, H. J., Bellamy, R. G., Paris, R. G., and Horspool, J. M., "Fuel Element Behavior Under Irradiation in DFR," in *Proceedings Symposium on Fuel and Fuel Elements for Fast Reactors*, Vol. 1, International Atomic Energy Agency, Vienna, 1974, July 2-6, 1973.

12 Mayer, H., "Summary on Fuel Pin Failures and Theoretical Approach," in *Summary Report of International Working Group on Fast Reactors, Meeting of Specialists on Fuel Failure Mechanisms*, Seattle, Wash., May 12-16, 1975, International Atomic Energy Agency (IWGFR/5).

13 Schultheiss, G. F., "Analysis of the Formation of Local Coolant Blockages in Sodium-Cooled Fast Breeder Reactors," EURFNR-1394 (KfK 2331) Karlsruhe, Germany (1976), and in *Nuclear Engineering Design*, Vol. 43, 1977, pp. 329-341.

14 Geithoff, D., "Brennstoff-Ausschwemmungen aus defekten UO₂/PuO₂-Mischoxid-Brennstäben," *Reaktortagung*, Apr. 1975, p. 458.

15 Kummerer, K. R., "The German Oxide Fuel Pin Irradiation Test Experience for Fast Reactors," in *Proceedings of International Conference on Fast Breeder Reactor Fuel Performance*, American Nuclear Society, Monterey, Calif., Mar. 5-8, 1979.

16 Smith, D. C. G., Bagley, K. Q., Gregory, C. V., Leet, G. O., and Tait, D., "DFR Special Experiments," in *Proceedings of International Symposium on Design, Construction, and Operating Experience of Demonstration LMFBRs*, Bologna, Italy, Apr. 10-14, 1978 (IAEA-SM-225/49).

17 Gregory, C. V., "A Brief Summary of Rig Operation During the DFR Special Experiments Programme," U.K.A.E.A. Memorandum, ND-M-290(D), Mar. 1978.

18 Dale, W. B., "Review of Safety Developments for CDFR, March-May, 1978," UKAEA Memorandum, ND-M-383(R), May 1978.

19 Dale, W. B., "Review of Safety Developments for CDFR: October 1977-February 1978," UKAEA Memorandum, ND-M-273 (revision 1) (R), Feb. 1978.

20 Kummerer, K., Geithoff, D., and Weimar, P., "Auslegung, Bestrahlung und Nachuntersuchung des UO₂-PuO₂-Brennstab-Bundels Mol-7A," KfK report 1522, GmbH, Nov., 1972.

21 Weimar, P., "Experimental and Theoretical Evaluation of Defect Growth of Fuel Pin Cladding by Chemical Fuel-Sodium Interaction," in *Proceedings of the Fourth Structural Mechanics in Reactor Technology (SMiRT) Conference*, Division C, Paper C-4/6, San Francisco, Calif., 1977.

22 Kleykamp, H., "Das Chemische Verhalten Defecter Mischoxid-Brennstäbe unter Bestrahlung," *Reaktortagung*, Mannheim, Mar. 29-Apr. 1, 1977, p. 510.

23 Letter, S. Jacobi to D. Warinner, Oct. 30, 1980.

24 Personal Communication with W. Kramer, June 12, 1981.

25 Kramer, W., and Vanmassenhove, G., "In-Pile Investigation of Local Cooling Disturbances in LMFBR's (Mol 7C)," in BR-2 Reactor Review Meeting, MOL, Mol, Belgium, June 1, 1978.

26 Kramer, W., Schleisiek, K., Schmidt, L., Vanmassenhove, G., and Verwimp, A., "In-Pile Experiments 'Mol 7C' Related to Pin Failure Propagation," in *Proceedings ANS/ENS International Meeting on Fast Reactor Safety Technology*, Seattle, Wash., Aug. 19-23, 1979.

27 Letter, W. Kramer and K. Schleisiek to D. K. Warinner, "In-Reacto Blockage Experiments," private communication, Jan. 31, 1979.

28 Kramer, W., Schleisiek, K., Schmidt, L., Vanmassenhove, G., and Verwimp, A., "Investigation of Local Cooling Disturbances in an In-Pile Sodium Loop in BR-2," in *Proceedings of ENS/ANS International Topical Meeting on Nuclear Power Reactor Safety*, Paper Log No. 25, Brussels, Oct. 1978.

29 Jacobi, S., and Schmitz, G., "Delayed Neutron Signals from Failed Pins and Bundles and their Relation to Safety Problems," *op. cit.*, reference [26].

30 Personal Communication with S. Jacobi, April 17, 1980.

31 Brudermuller, G., Finke, G., Guthmann, E., Hendl, G., and Marth, W.,

"Operating Experience with the KNK Reactor and Preparations for a Fast Mixed Oxide Core (KNK II)," in *Fast Reactor Power Stations, Proceedings of the International Conference Organized by the British Nuclear Energy Society*, London, Mar. 11-14, 1974.

32 Chalony, A., Chantoin, P., Cauvin, J. C., and Pages, J. P., "Fuel Failure on the Rapsodie Subassembly 'Capricorn 1.b'," in Summary Report of International Working Group on Fast Reactors, Meeting of Specialists on Fuel Failure Mechanisms, Seattle, Wash., May 12-16, 1975, International Atomic Energy Agency (IWGFR/5).

33 Palm, R. G., Deitrich, L. W., Murphy, W. F., Stanford, G. S., and Stahl, D., "TREAT Mark-II-Loop Tests National Laboratory Report, ANL-8100, Argonne, Ill., May 1974, 85 pp.

34 Davydov, E. F., Kuzmin, V. I., Lebedev, I. G., and Syuzev, V. N., "Experimental Study of Fast Reactor Fuel Pin Performance," in Summary Report of International Working Group on Fast Reactors, Meeting of Specialists on Fuel Failure Mechanisms, Seattle, Washington, May 12-16, 1975, International Atomic Energy Agency (IWGFR/5).

35 Aristarkhov, N. N., Bets, N. I., Efimov, I. A., Filonov, V. S., Kevrolev, V. P., and Rybakov, V. N., "Detection of Packets with Non-Hermetic Fuel Elements on Sodium-Cooled Fast Reactors," *op. cit.*, [9].

36 Washburn, D. F., Almasy, M. Y., Langstaff, D. C., Lambert, J. D. B., and Strain, R. V., "Mixed-Oxide Run-Beyond-Cladding-Breach Tests in EBR-II," in Proc. of *International Conference on Fast Breeder Reactor Fuel Per-*

formance, American Nuclear Society, Monterey, Calif., Mar. 5-8, 1979.

37 Marbach, G., Millet, P., Blanchard, P., and Hulberg, R., "Behavior of a Bundle of Phenix Fuel Rods Under Irradiation," International Meeting on Irradiation Behavior of Metallic Materials for Fast Reactor Core Components, Ajaccio, Corsica, France, June 4-8, 1979.

38 Letter, J. F., Koenig, "Photographs of Potted Phenix Subassemblies," July 29, 1980.

39 Efimov, I. A., Zhilkin, A. S., Mamaev, L. I., Mczentsev, A. N., Shestopalov, E. V., and Shipilov, A. E., "Leakage of Fission Products from Defective Fuel Elements of the BR-10 Reactor at High Plutonium Oxide Burnup," Presented at the US-USSR Seminar, Moscow, Oct. 1979.

40 Crawford, R. M., Marr, W. W., Padilla, A. Jr., and Wang, P. Y., "The Safety Consequences of Local Initiating Events in an LMFBR," ANL 75-73, Argonne National Laboratory, Dec. 1975.

41 Leggett, R. D., Heck, E. N., Levine, P. J., and Hilbert, R. F., "Steady-State Irradiation Behavior of Mixed Oxide Fuel Pins Irradiated in EBR-II," in *Proceedings of International Conference on Fast Breeder Reactor Fuel Performance*, American Nuclear Society, Monterey, Calif., Mar. 5-8, 1979.

42 Warinner, D. K., "Preliminary Report on Local Faults," ANL/RAS 81-3, Argonne National Laboratory, Dec. 16, 1980, 109 pp.

43 Warinner, D. K., "Objectives and Requirements for Sodium Loop Safety Facility In-Reacto Experiment P4 (SLSF-P4)," ANL/RAS 80-32, Dec. 1, 1980, 77 pp.

The LMFBR Fuel-Design Environment for Endurance Testing, Primarily of Oxide Fuel Elements With Local Faults^{1,2}

D. K. Warinner

Mechanical Engineer,
Magneto-hydrodynamics Project and
Reduced Enrichment
Research and Test Reactors Programs,
Chemical Engineering Division,
Argonne National Laboratory
Argonne, Ill. 60439
Mem. ASME

The U.S. Department of Energy LMFBR Lines-of-Assurance are briefly stated and local faults are given perspective with an historical review and definition to help define the constraints of LMFBR fuel-element designs. Local-fault-propagation (fuel-element-failure propagation and blockage propagation) perceptions are reviewed. Fuel pin designs and major LMFBR parameters affecting pin performance are summarized. The interpretation of failed-fuel data is aided by a discussion of the effects of nonprototypicalities. The fuel-pin endurances expected in the United States, USSR, France, UK, Japan, and West Germany are outlined. Finally, fuel-failure detection and location by delayed-neutron and gaseous-fission-product monitors are briefly discussed to better realize the operational limits.

Introduction

The intent of this paper is to set the framework within which we deal in the design of fuel elements to withstand expected local faults through (i) a brief review of the liquid-metal-cooled fast-neutron breeder nuclear-reactor (LMFBR) lines-of-assurance, (ii) a review, history, and definition of local faults, (iii) the fuel designs and major reactor-design parameters in decommissioned, operating, and planned reactors, (iv) a summary of what the United States and other nations expect for fuel-design performance, and (v) a review of failed-fuel detection. The companion paper [1] reviews international testing and operating experience with cases of the most serious local faults encountered.

These papers focus on fuel failure and fuel degradation as subsets of local faults, although cases of other local faults are also reviewed. To improve the fuel design, we must not only gauge where the fuel has fallen short of the design expectation, but also note how design changes, such as increased diameter, fuel-chemistry change, and change from pellet to vibratory-packed fuel, might have affected the operating performance of the fuel, particularly in the presence of local faults. We cannot provide such definitive design-change results here, but we can review the operation of some reactors and experiments [1] and leave impressions of how the fuel performed; one can then ascertain in a gross sense what trends

appear to possibly meet the design goal and what research and development remains to ensure that the lines-of-assurance goals are met. Reference [2] provides a more step-by-step review of the fuel-element design process.

The LMFBR Lines-of-Assurance (LOA)

An explanation of the LOA concept used by the U.S. Department of Energy (DOE) to guide LMFBR safety research and development will help our understanding of the ultimate constraints of fuel design (see references [3] and [4] for more thorough explanations of the LOA approach). The use of LOA's also ensure proper interpretation of our use of the words "incredible" and "highly unlikely" by defining these terms in a context that can be scientifically accepted. The LOA's are divided into the following groups with their associated assigned (not expected) frequencies per reactor year of full-power operation for LOA-1 and frequencies per challenge for LOA-2, -3, and -4.

LOA-1	Prevent accidents (prevent any event leading to substantial fuel melting and/or cladding breach)	$\leq 10^{-6}$
LOA-2	Limit core damage (maintain in-place coolability; no damage to primary containment even if an accident were to occur)	$\leq 10^{-2}$
LOA-3	Control accident progression (mitigate severity in case of damage to primary containment, and control radioactive releases to environment)	$\leq 10^{-2}$
LOA-4	Attenuate radiological consequences (in case containment systems fail to control radioactive releases)	$\leq 10^{-2}$

¹Work performed under the auspices of U.S. Department of Energy while the author was with the Sodium Loop Safety Facility Program of ANL's Reactor Analysis and Safety Div.

²The submitted manuscript has been authored by a contractor of the U.S. Government under contract No. W-31-109-ENG-38.

Contributed by the Nuclear Engineering Division of the American Society of Mechanical Engineers and presented at the Century 2 Nuclear Engineering Conference, San Francisco, Calif., August 19-21, 1980. Manuscript received at ASME Headquarters March 4, 1980, Paper No. 80-C2/NE-25.

Figures 1 and 2 show the work breakdown structures (WBS's) of LOA's 1 and 2; the areas relevant to this paper are underlined.

The LOA's are structured independently so that the health and safety of the public are assured a probability of at least $1 - 10^{-12}$ per reactor year of full-power operation. For a potentially damaging coolant blockage, we could assume an occurrence and damage probability of $\leq 10^{-8}$ if the blockage were deemed incredible. This suffices to define "highly unlikely" for the purpose of this paper.

The impact of the LOA approach on fuel behavior is seen when LOA-1 is interpreted in the strictest sense of having the necessary design goal of a cladding breach occurring with a probability of $\leq 10^{-6}$ per reactor year of full-power operation throughout the residence time of the fuel pin. This can be changed to another number as long as LOA-1 and LOA-2 combined can be ensured to be $\leq 10^{-8}$ (for local faults only). Thus, LOA-1 could be assigned, say, 10^{-3} , and LOA-2 assigned 10^{-5} . Even so, this interpretation would allow a cladding breach, per se, to be called an "accident."

Review of Local Faults

To put the local-fault problems into better focus, we define a local fault and pin-to-pin and blockage propagation, and summarize the findings of analyses and out-of-pile studies completed on local faults. The companion paper, reference [1], reviews the in-pile experiments and operating experience. Reference [5] presents a status of local faults, and proposes the research and development needed to resolve the remaining issues, at least for oxide fuel. The subject, ill-defined to many as an accident initiator, needed to be placed in perspective; this was the goal of [5]. The members of the International Working Group on Fast Reactors (IWGFR), specialists on fuel-failure mechanisms, last met in 1975 and were to document a state-of-the-art review on fuel-element failure-propagation (FEFP) studies and experience [6]—the task addressed by [7], although [1, 5, 8, 9, 10] largely fulfill this piecemeal. In 1976, Fauske et al. [11] summarized analyses and reasoned why rapid local-fault propagation could be ruled out. During the past five years, more analyses and in- and out-of-pile work have been reported. Upon reviewing this recent information in concert with an overall review of LMFBR oxide-fuel and local-fault experience, Warinner and Cho [5] suggest that we can be more comfortable with previous statements made about the unlikelihood of widespread core-damage from local faults. One key statement was that a necessary (but not sufficient) result for serious consequences from normal operations with local faults is contact between liquid coolant and molten fuel; however, to even deliberately design molten-fuel release into the LMFBR coolant is no easy task. It appears that the plausible intuitive hypothesis of small causes producing small effects is again at work.

A Brief Look at Two Local Faults and Pin-to-Pin and Blockage Propagation. Since neutron flux irradiation embrittles stainless steel, one could (quite simplistically) imagine that closely spaced LMFBR fuel-pins might bow, fail mechanically, strike the neighboring pin and cause it to bow, and so on; one could envision such a process to march, dominolike, across the subassembly (S/A) rapidly. Similarly, it has been postulated that a pin with a high inventory of gaseous fission products (GFP) might burst and eject a gas jet that blankets an adjacent pin which in turn might burst; the process is postulated to continue or cascade through the S/A [12, 13]. The first process, presented here only to more easily envision FEFP, is unrealistic; the second process, more complex, can be dismissed. To postulate FEFP (in this case rapid) to be a natural safety issue which deserved attention

must have seemed only reasonable. Coolant-channel blockages reared their heads as possibly posing a safety threat because the closely packed LMFBR-bundle appears as an effective filter for the primary-circuit coolant during normal operation. Blockage accidents (e.g., in Fermi and the Sodium Research Experiment (SRE) reviewed in [1]) made the issue more difficult to dismiss. (We have often spoken of FEFP and blockage propagation synonymously.) Indeed, Argonne National Laboratory's (ANL's) first in-reactor attempt to address this issue began with the Fuel-Element Failure-Propagation Loop (FEFPL) project, now called the Sodium-Loop Safety-Facility (SLSF) program. In 1972, the Atomic Energy Commission listed nine priority research and development issues: fuel-failure thresholds and FEFP ranked 2 and 3 after "criteria, codes, and standards." The complete list follows [14] (emphasis added):

"The current priority considerations in the LMFBR safety research and development program are:

- 1 criteria, codes and standards;
- 2 fuel failure thresholds and margins from normal conditions;
- 3 propagation of fuel element failure;
- 4 sodium voiding dynamics;
- 5 fuel behavior under accident conditions;
- 6 molten fuel-coolant interactions;
- 7 anomaly detection and safety instrumentation;
- 8 accident definition and analysis; and
- 9 post-accident heat removal."

However, while the FEFPL of SLSF was being built, domestic out-of-pile research (at Oak Ridge National Laboratory (ORNL) and ANL), foreign research (British and West German), and more operating experience with failed fuel (French and Soviet) had begun to dismiss aspects of FEFP in the early 1970s. This progress was striking. A blockage or fuel-failure test, scheduled to be the first SLSF test (and later the focus of the Belgian-West German Mol 7C series), was postponed while analyses and out-of-pile experimental results here and abroad indicated that FEFP was not only of less consequence than once believed, but also perhaps entirely benign. However, doubters remain while residual issues linger. Without a complete in-pile program to not only add credibility to the out-of-pile work and analyses completed, but also to address the residual issues, the challenge to stand before an LMFBR licensing board and assert that either rapid propagation cannot occur, or would be accommodated if it could occur, remains.

Has slow propagation ever been observed? Possibly, in Manufacture-Franco Belge-au-Bouche-Sodium (MFBS)-6, Mol 7B, EBR-II Run-Beyond-Cladding-Breach (RBCB)-1 and -2, BOR-60, and DFR, for examples; however, we will cite only the experimenters' conclusions as such. In each possibly observed case of FEFP, the conditions were extreme and, in RBCB-1 and 2, the additional failure would be called self-limiting if one could call it propagation. (It is noteworthy that "propagation," used alone, has recently taken a new meaning with respect to fuel failure—crack propagation or extension.)

The following sections present (i) a definition and summary of local faults (the generic term given to FEFP initiators, blockages, and other S/A anomalies), (ii) a review of local-fault perceptions, (iii) a review of fuel and reactor designs, (iv) design expectations, and (v) failed-fuel detection. The companion paper [1] presents the status of analyses and out-of-pile experiments and prototypic fuel-failure experience and in-pile experimental results (e.g., from DFR, BR2 Mol 7 series, and ERB-II RBCB program).

Definition of Local Faults. For the purposes of this paper, local faults are those off-design conditions at the

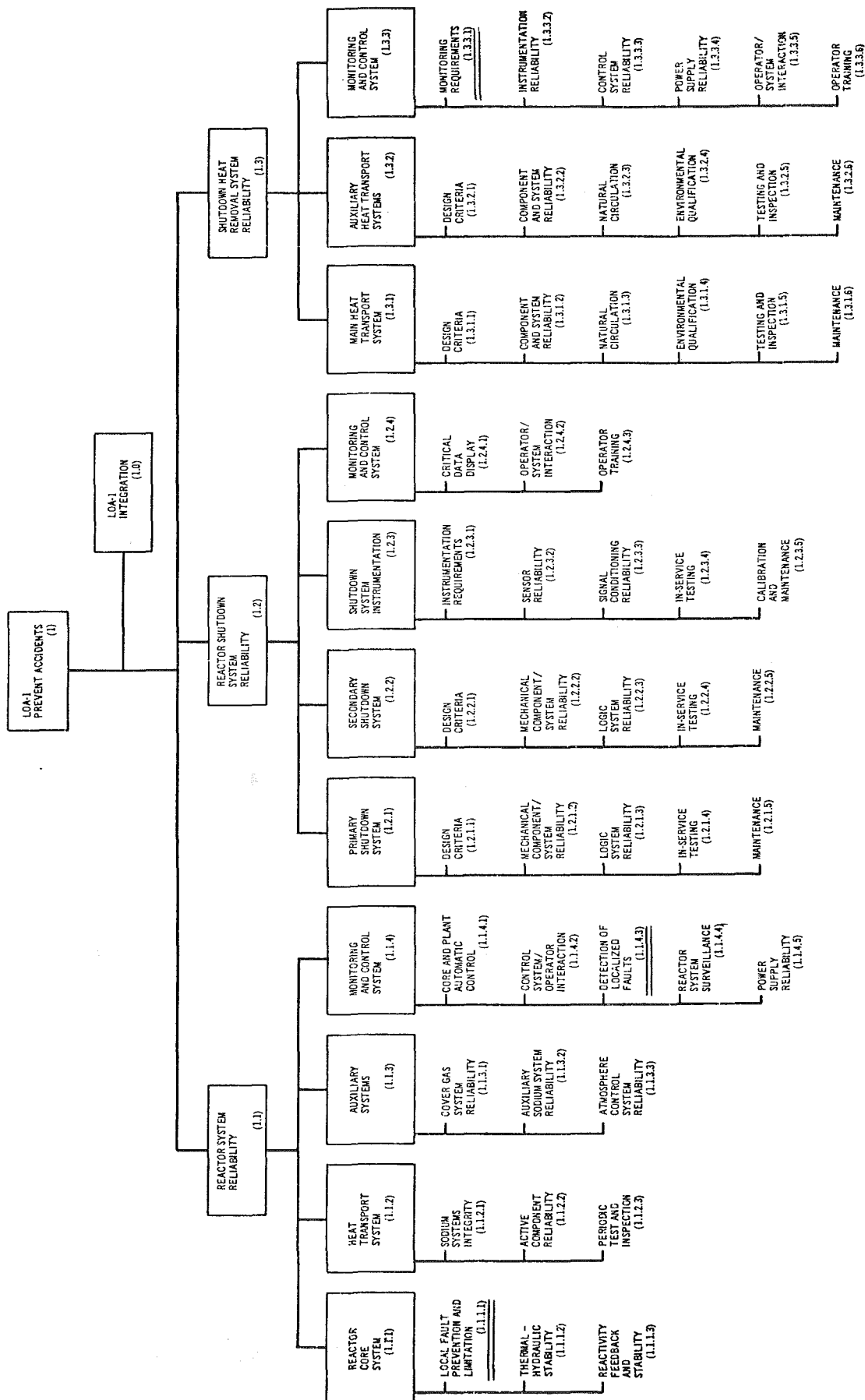


Fig. 1 LOA-1 work breakdown structure

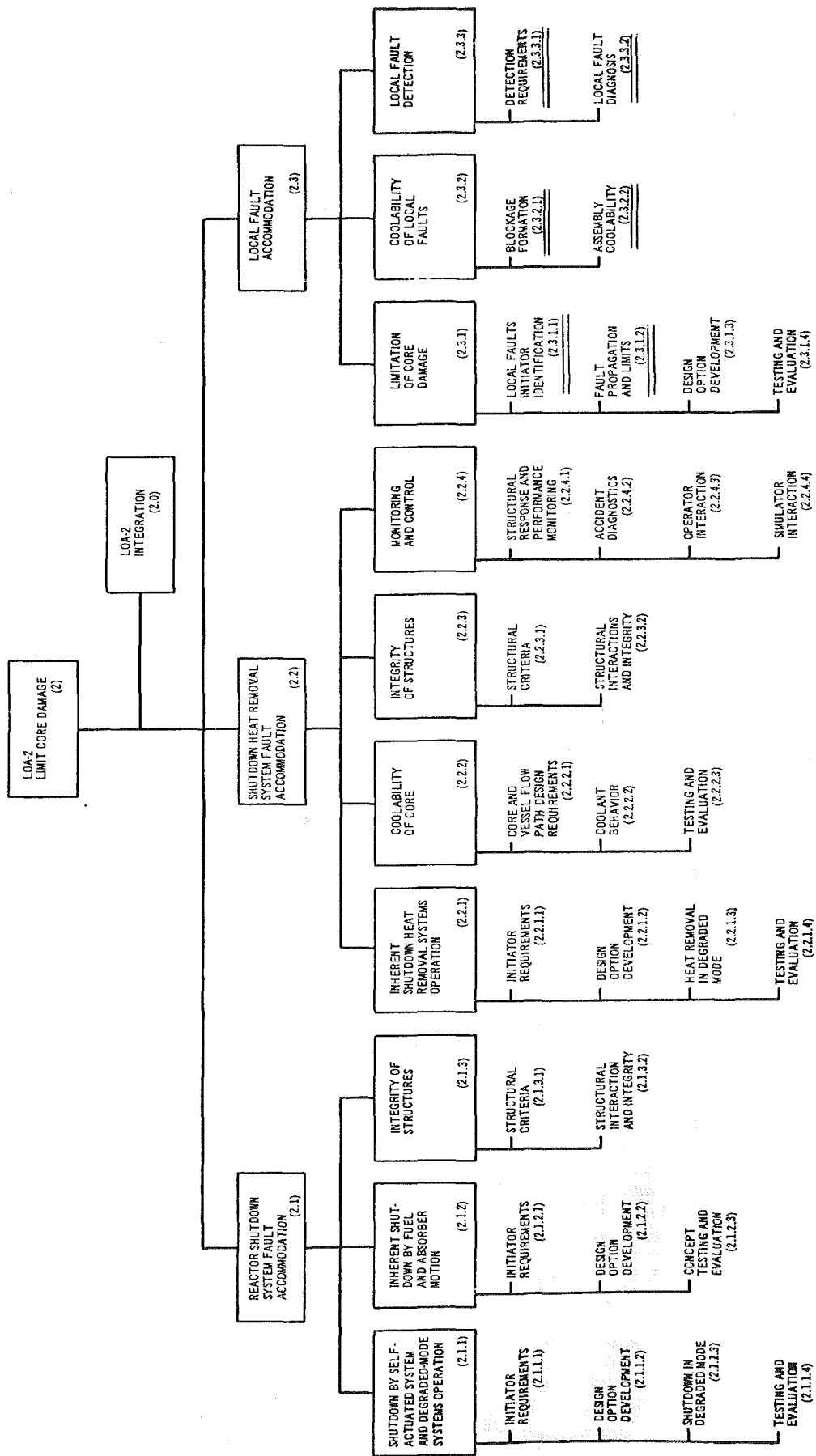


Fig. 2 LOA-2 work breakdown structure

Table 1 Possible LMFBR local faults and their consequences

Local fault (Initiator)	Consequence (Phenomena)	Operational status
Cladding defect	fuel failure	observed
Cladding swelling	fuel failure	observed
Local over-enrichment	fuel failure (with possible molten fuel ejection)	observed (not observed)
Inert coolant-channel blockage	fuel failure	observed
S/A inlet blockage	S/A-to-S/A propagation	observed
Loose spacer wire	fuel failure (local line hot spot)	observed
Broken spacer wire	benign	observed
Pin bowing	local hot spots, fuel failure	observed
Pin distortion	local hot spots,	observed
Excess Na oxygen	fuel failure local blockages	observed

Table 2 Possible local-fault consequences and end state(s)

Consequences	Further Consequences and end state(s)	Operational status
fuel failure	severe breach, loss of fuel, damage of adjacent pin, $\text{Na}_3(\text{U,Pu})\text{O}_4$ formation, blockage formation	observed
Molten fuel ejection	e.g., mild FCI, mechanical failure of other pins, and overheating to saturation if flow halted long enough	not observed ^a
Local heat-generating blockages	fuel failure, et seq. or, much less likely, molten fuel ejection, et seq.	either nor observed or not reported ^a
S/A-to-S/A propagation	whole-core involvement; meltdown beyond initiated S/A's	not observed

^aThese effects may have resulted in the Mol 7C/3 and the SLSF P4 experiments.

entrance and within a subassembly that could potentially cause core damage, i.e., those operational or constructional divergences which alter the intended geometry or material distribution to such a degree that they can be (or have been) considered possible *initiators* for structural, hydraulic, thermal, and neutronic *consequences (phenomena)* which could possibly result in either a damaged core or unacceptable contamination. To have a damaged core (i.e., cause more than mere fuel failure with in-situ fuel-deterioration) implies that the local accident might have involved some degree of power/flow mismatch to cause local events analogous to those involved in a core-wide accident.³ The question is, Will this local event remain localized or will it (perhaps when coupled with an upset transient) spread or cascade to involve the whole core? This cascading is generally termed FEFP (although some call it "auto-catalytic pin-failures") and S/A-to-S/A propagation. All consequences of local faults should result in, if any damage at all, localized (self-limiting) damage, except possibly for certain faults with a concurrent transient. Even then, the neighboring subassemblies should not be affected. To explain this conclusion, credible local faults and a history of FEFP, the most oft-cited consequence, are set forth. (In some cases "credible" means the fault has

been taken seriously enough to warrant treatment in either the Fast-Flux Test-Facility Final Safety-Analyses Report (FFTF-FSAR), the Clinch River Breeder Reactor Plant (CRBRP) - Preliminary Safety-Analyses Report (PSAR), or elsewhere in the open literature sometime during the past fifteen years.) These local faults and possible consequences are listed in Tables 1 and 2.

Fuel failure severity, and thus fuel performance, depends on the local fault. With effective quality control, a random failure will more likely occur near EOEC or end of life (EOL) than near beginning of life (BOL). This EOL case with high fission-gas pressure would have damage potential from gas-blanketing or pin deflection causing FEFP. However, such cases have been shown to be highly unlikely [12]; the pin's natural period exceeds the minimum thrust time from fission-gas exhaust by three orders of magnitude. It has also been shown that sudden emission of gas from a lower plenum, sufficient to fully surround a pin, would not raise the coolant temperature enough to cause another failure [16].

Cladding swelling has been negligible except in cases where the fuel failed with concomitant sodium ingress, uranate formation increasing the breach severity, and so on.

Historical Perceptions of Local Faults. To review the status of FEFP is interesting and instructive; this helps place the problem in perspective and thereby helps to focus our attention on further needs.

Many expressed skepticism early about the fuel-pin integrity, and properly so, given the lack of operating experience. Yet, others who closely studied FEFP concluded

³Some in the LMFBR safety community prefer the following definition of "local fault" [10]: "A local fault is generally defined to be any condition which results in a localized mismatch of power generation and coolant flow outside the bounds considered in normal design evaluations. This power/flow imbalance may either be a local effect which influences only a small region within the pin bundle, or it may be a subassembly-wide condition in which the performance of every pin in the bundle is affected."

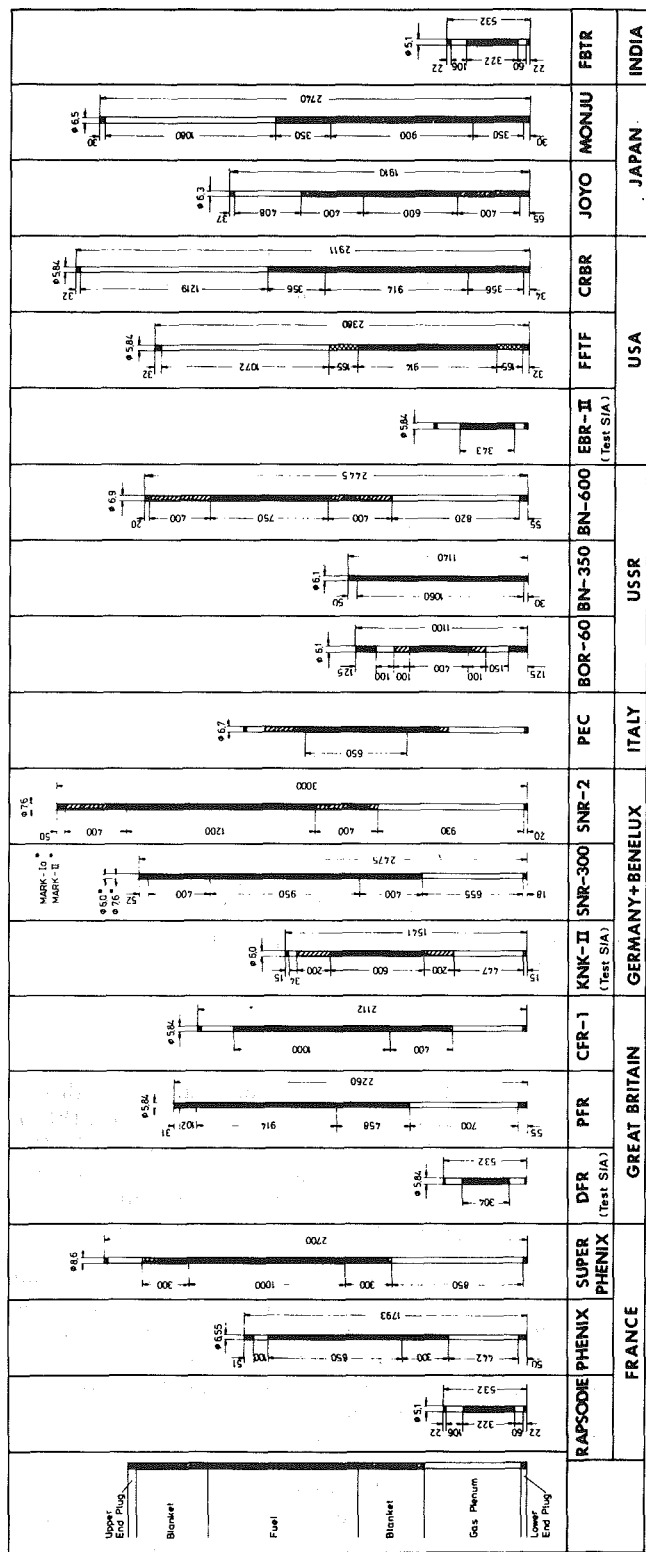


Fig. 3 Fast reactor fuel pins – synopsis of the different designers [2]

early on that no problem existed. The 1965 Fast Reactor Conference was marbled with both pessimism and optimism about FEFP [17]. Several papers presented studies on vented fuel to coolant, a concept clearly pursued primarily to avoid FEFP. Gas-Cooled Fast Reactors (GCFRs) were highlighted on ability to view a local fault (versus opaque sodium systems); shorter doubling time and “voided” channels added incentive.

Although the 1966 British Nuclear Energy Society (BNES) Conference was less FEFP-oriented, the discussions reveal many striking statements about FEFP. Examples are [18]:

“We regard the propagation of subassembly faults as the *most pressing problem* facing the fast reactor designer today as far as core design is concerned, and we have assumed that we cannot detect certain types of faults, . . .” [emphasis added], and

“ . . . Our biggest concern is the rate of propagation of the fault. This is the big uncertainty in subassembly behavior at the present time.” [Also, we find;] . . . and the safety system must be capable of detecting the onset of any local fault and shutting the reactor down before any serious propagation has occurred.”

This reasoning and cautionary tone also appears in the 1974 BNES conference on Fast Reactor Power Stations [19, 20] and in the CRBR-PSAR which states,

“It will be shown that pin-to-pin failure propagation would be very remote in CRBRP for an initiating event such as stochastic fuel pin failure or even for the postulated event of a small release of molten fuel or a postulated local flow blockage in the fuel assembly.”

Many pages of the CRBR-PSAR and the FTF-FSAR are devoted to FEFP blockages (e.g., [21]).

Later, to detect true concern requires a keener eye. The results of reactor experience, out-of-pile studies, and analyses have been reassuring (with regard to public safety) and have alerted us to potential problems (in the areas of operational safety and contamination). Overall, the results for oxide fuel can be judged to be encouraging, indeed, impressive, particularly in the reactors in which the pins were not driven hard during tests (e.g., 0.03 percent fuel failure in Phenix versus 5.0 percent in DFR [1]). Even so, we find that a decade after the aforementioned FEFP caution, fuel-failure propagation and formation of blockages or blockage propagation are still feared by some. Examples are:

1 “Under these conditions the calculation, very conservative, shows that a faulty pin should preferably be left in place *no longer than a week* if its burn-up is more than 20,000 MWd/t, or *no longer than a day* if its burn-up exceeds 40,000 MWd/t. However, these periods are certainly very much underestimated and, it is probably quite safe to leave defective pins in place for a week,” [22] [emphasis added].

2 “With these values, the ‘clean-reactor’ operating option can be respected. This decision is extremely important from the accident prevention viewpoint since plugging risks are considerably reduced if reactor operation with cladding failures is prohibited,” and (Discussion) “it is preferable to devote effort to developing a fuel clad which permits high fuel burn-up without failure. This also gives a wide margin against subassembly blockage by plugging, which enhances safety,” [23].

3 (Mol-7B experiment) “The blockage in that axial position was about 38 percent,” “ . . . One cannot neglect the possibility of blockages in a defect bundle. We propose to remove the defective bundle within the first week after discerning a pin failure,” [24].

4 “Important and mostly unavoidable abnormal operation conditions for fuel elements in power stations can be: coolant blockage in a fuel bundle.

“ . . . The objectives for the fuel pin performance in normal operation are that:

No gross propagation from a blockage coolant channel region to the whole bundle” [25].

The first two quotes above imply pessimism with regard to public safety for operation with failed fuel. Kummerer, who also cites limited experience with failed-fuel operation, refers to a blockage problem. The natural question is: Are the above views warranted based on analyses, out-of-pile experiments,

Table 3 Major LMFBR design parameters affecting fuel-element performance

	BR-5	BR-10	RAPSODIE	EBR-II*	BOR-60	DFR*	JOYO	FFTF	PFR	PHENIX	BN-350	MONJU	SNR-300	CRBRP	SUPER	BN-600
Date critical	1959	1973	1967	1963	1970	1959	1977	1980	1974	1973	1972	1985?	?	?	1983?	1980
Power, MWt	5	7.5	40	62.5	60	60	100	400	559	563	650 ^v	714	736	975	3000	1470
Coolant	Na	Na	Na	Na	Na	Na ^k	Na	Na	Na	Na	Na	Na	Na	Na	Na	Na
Pool/loop	Loop	Loop	Loop	Pot	Loop	Loop	Loop	Loop	Pool	Pool	Loop	Loop	Loop	Loop	Pool	Pool
Core length, mm	280	320	340	343	400	304	600	914	914	850	1060	900	950	914	1000	750
Spacer	Wire	Wire	Wire	Wire	Wire	Grid	Wire	Wire	Grid	Wire	Wire	Wire	Grid ^d	Wire ^c	Wire	Wire
Spacer pitch or interval, mm						100	209	305	102	150	307	150	150	305	180	180
No. core S/As	81				80	77	91	73	78	103	211	196	195	198	364	369
No. S/A pins	19	19	37	61	37	77	127	217	325	217	169	169	169	217	271	127
Pitch o.d., mm	5.0	5.0	5.72	5.84	6.1	5.84	6.3	5.84	5.84	6.55	6.1	6.5	6.0 ^e	5.84	8.6	6.9
Peak linear power, kW/m	25.0	25.0	46	46.0	56.0	43.5	40.2	42.5	46.0	45.0	44.0	46.5	46.0	47.5	48.0	53.0
Inlet temp., °C	430	230	410 ^g	372	340	230	370	316	400	400	280	390	377	388	395	375-410
Exit temp., °C	500	440	495 ^g	483	615	450	500	459	600	560	410 ^f	540	546	535	545	545-580
Peak flux, 10 ¹⁵ n/cm ² s	1	1.9	3	3	3.7	3.8	5	7	8.5	7.2	8.0	4 ^g	8	8	10	10
Local max. b.u., MWd/kg		60		80	100	100	60	80	75	75	50	72	90	150	70	100
Peak fluence, 10 ²³ n/cm ²					0.75											
Cladding type	321		316	316	316	M316	316	316	M316	316L	2.2	316	1.4970	316	316	3.5
Cladding wall, mm	0.4	0.4	0.45	0.40	0.38	0.35	0.38	0.38	0.45	0.45	0.35	0.47	0.38	0.38	0.4	0.4
Max. O ₂ ppm	3			20	40			10			30					
Max. C ₁ ppm				40						43	40					
Shear density, % T.D.	50	85		85.5	73.5		80	85.5	80	80	73.5	79	80	85.5		77

*For test fuel only; the driver fuel not considered

^aAverage

^b1.0-4.8 m/s downflow vs. ~7.5 m/s upflow for PFR, for example

^cAdvanced cores planned to be gridded as of 1974

^dWire spacer for radial blanket elements; wire spacers likely for future cores

^eTo be increased to 7.6 mm with 205 fuel S/As

^fDesigned for 1000 MWt and 500 °C exit temperature

^gTemperatures for initial 20 MWt nominal design.

Table 4 Characteristics of variables and effects of results from failed-fuel experience

Characteristics which might be nonprototypic	Examples, values; test or facility	Results conservative? comments
<u>Coolant</u>		
Downflow	DFR	Yes; fuel-failure due to gas blanketing or entrained gas bubbles.
NaK	DFR	No; for blockage formation No; less Na ₃ (U,Pu)O ₄ formation than for Na. Yes; surface bubbles tend to form.
High O ₂ content	Varies; high in Mol 7B	Yes; more O ₂ available for Na ₃ (U,Pu)O ₄ formation; NaO ₂ blockages have formed.
High impurity content	Varies	Yes; could affect results depending on impurity (e.g., carburize cladding or begin local blockage).
High velocity	Varies	Yes; for cladding wastage. No; for blockage formation.
High temperature	Varies	Yes; infers clad temperature.
Low pressure at midcore	Varies	Yes; higher pin to coolant ΔPs and lower coolant saturation point.
High axial dT/dz	Varies	Yes; indicates higher power/flow mismatch.
<u>Pin design</u>		
<u>Fuel</u>		
UO ₂	Mol 7C, some BR-5 S/As, . . .	No; less O ₂ produced through fissioning to be available for uranate formation.
PuO ₂	BR-5	Yes; more O ₂ available.
Higher %Pu in (U, Pu)O ₂	Varies ~ 15 to 40%	Yes; Pu variation probably negligible for impact on local faults (as are many of these parameters) except above ~ 25%
High O/M	Varies	Yes; Na ₃ (U,Pu)O ₄ formation.
Annular pellets	e.g., BOR-60 and DFR and GETR tests	No; low smear density.
Dished-end pellets	Fairly standard	No.
Vibrocompacted (vipack) fuel	DFR tests (preferred in U.K.)	Results nonconservative before failure, may be conservative after failure.
Small gas-bond gap (fabricated)	Varies	Yes; more FCMI.
Large pellet o.d.	Varies	Yes.
Low smear density	BR-5	No.
Short active core length	Mol-7, EBR-II, and DFR tests	No; except for impedance to plenum gas flow.
<u>Cladding</u>		
Long overall pin length	Varies (see Fig. 3)	Yes; for sweepout.
Fuel vented to coolant	DFR	No; for pin-to-pin propagation.
High fill pressure	Varies	Yes.
Fill gas other than helium (and purity)	Rare	Yes; any other fill gas (argon or xenon) conservative.
Pin-plenum space and location(s)	Varies (see Fig. 3)	Smaller plenum more conservative (higher internal pressure).
S.S. other than 20% C.W. 316	In USSR and West Germany	Effect differs for each material. Ti-stabilized preferred in U.K.
Cladding o.d.	Varies little	Has increased 1.9 mm in 20 years in USSR.
Thinner cladding	Fairly standard at ~0.38 mm	Yes; results should be fairly sensitive as thickness decreases to reduce number of grains; irradiation embrittlement and swelling more severe.

Table 4 cont.

Characteristics which might be nonprototypic	Examples, values; test or facility	Results conservative? comments
Subassembly (or pin-bundle) design		
Smaller pin pitch	Varies little	Yes
Fewer number of pins per bundle than 217 for U.S. design	Varies from single pin to trefoil to 19 pins, etc.	Yes; little difference down to ~ 19 pins; difficult to infer effect with smaller bundle.
Nonuniform enrichment distribution	Varies (e.g., high variation for Mol 7C)	Yes; for high radial variation of enrichments (adverse effects of radial fuel motion).
Grid instead of wire-wrap spacers	In U.K. and Germany (DFR and Mol series)	Yes; for blockage formation in upflow (natural barrier). No; for pin deformation (bowing and distortion).
Reconstituted bundles	EBR-II RBCB and DFR series	Yes; results require careful interpretation.
Dummy central tube with coolant flow	Mol 7C series	Results require careful interpretation.
Dummy pins (e.g., S.S.)	Mol 7C series	Results require careful interpretation
Reactor design and operation		
Irradiation history with many startups	Varies	Yes; important to determine effect of sodium ingress.
Number of S/As	Varies	Important for impurity distribution, for example.
Small sodium volume	20 L in Mol 7B and C	Affects impurity concentration and DN signals.
Flat radial power-profile	Usually flat in S/A	Conservative for radially graded enrichments.
High average pin power	Varies	Yes
High max/ave. power (axial)	Varies	Yes; more Cs migration
High fluence	Varies	Yes; high displacement per atom (dpa) on cladding.
Low fluence-to-b.u. ratio	Varies	No
Neutron flux spectrum	Varies	Effects on cladding and fuel differ for high thermal-flux vs. high fast-flux
Failure Characteristics		
Higher linear pin-power at time of failure	Varies	Yes
High burnup at failure	Varies	Yes
Neighboring pins failed, if any (location and time of such failures)	MFBS-6, Mol 7B	Yes
High b.u. (and dpa) before failure removed	Mol 7B	Yes
Nature of failure (size, shape, location) or other local fault	BOR-60, BR-5, DFR-435	Important to recognize

and finally, in-pile experience? To answer this question requires an extensive review of reactor experience; let us first review the designs from which the conclusions were drawn and the designs to which the conclusions would be applied.

Fuel Designs and Major Reactor-Design Parameters

The Soviets and French have led in LMFBR implementation of the wire-wrap hexagonal, oxide-fuel assemblies now favored in the United States, U.S.S.R., and France; the design has passed the test of time beginning with the BR-5, in the 1950s and continuing with Rapsodie, Phenix, BOR-60, and BN-350, in the 1970s. We see no reason why this success should not continue with FFTE, CRBR, BN-600, and Super-Phenix in the foreseeable '80s. Great Britain and West Germany have chosen to alter this somewhat by replacing the wire-wrap spacers with grid spacers. Table 3 summarizes the pertinent reactor-design parameters which influence fuel performance. Figure 3 summarizes the fuel designs for several reactors [2].

All reactors except DFR used upflowing sodium as the primary coolant. It is important to keep DFR's downflowing NaK in mind while reviewing the DFR test data. Although the

in-pile experience covers a broad range of such parameters as stoichiometry, smear density, and linear pin power, enough anomalies with this experience exist to be open to criticism if the results were applied directly to a reference U.S. design. Even some aspects of the experience gained in the primary U.S. fuels test-bed, EBR-II, could be challenged. Table 4 lists the major nonprototypicalities.

Table 4, lengthy as it is, probably omits some non-prototypicalities. The broad range of parameters involved will caution us to more properly interpret the fuel failures observed. The section on historical perceptions has indicated the cautious French and German positions on failed fuel. We now turn to the United States and the USSR to help round out, but not complete, the picture; some nations have yet to take a firm position on permissible fuel-failure.

Expectations of the Designed Fuel Elements

While the fuel provides the power, it must also meet the LOA criteria which concentrate on preventing accidents. Primarily, then, the fuel must not degrade to the point of initiating a course of events endangering public safety. This means that a flow blockage must not form to threaten FEFP

or blockage propagation. Further, operational safety must be ensured; e.g., plant contamination must be minimized. Thus, ideally, no fuel element should lose hermeticity. However, this is not practical for economic operation of LMFBR's.

In comparison to other country's practices for their LM-FBR prototypes, the United States has imposed the most stringent criteria on the CRBRP fuel to demonstrate safe and economic benefits. The following is excerpted from the CRBRP-PSAR:

"In the first core loading the fuel rods are limited to a peak pellet burnup to 80,000 megawatt days per metric ton on heavy metal (MWd/T.) For later cores the peak burnup increases to 150,000 MWd/T with an average burnup of 100,000 MWd/T The duration of the first cycle is 128 full power days (FPD), and the second cycle is 200 FPD. . . . For all operating cycles after the first two, the cycle length is increased to 274 FPD and the maximum fuel assembly residence time is subsequently increased to three cycles Maintenance of fuel rod structural integrity is a design basis should an Unlikely Fault occur during the fuel residence time."

Although the CRBRP-PSAR cites the cleanup systems to be capable of handling the failure of 1 percent of the fuel pins, the failure limit allowed is not clear (although a consensus existed in the DOE LOA local-faults committee that 0.1 percent should be the permissible limit for DN-receipt failures). Operation with failed fuel is permitted, but the permissible degree of sodium contact with fuel remains to be established. The French have established a DND sensitivity of 0.1-0.2 cm² equivalent exposed fuel area and scram on a DND signal of 2.5 cm² equivalent area (for pure recoil). DN signal amplification (sometimes up to 100 times that for pure recoil), as seen by United States, Soviet, German, British, and Japanese researchers, render the 2.5 cm² to have a rather ambiguous meaning. Further research is required in this area.

The Soviets allow only 5.8 percent b.u. in the BN-350; even this is a recent increase [26]. The failure limit (limited to loss of hermeticity in this case) is 400 pins in the BN-350 (~1 percent of the reactor's fuel pins) and they shut down the reactor upon receipt of a delayed-neutron (DN) signal indicative of sodium contact with fuel [27]. The BN-600 will be permitted ≤ 0.1 percent fuel failure. As experimental facilities, BR-5 and BOR-60 were allowed much higher b.u. and much higher failure rates. In view of this and the historical review of local faults, the U.S. appears to hold the most liberal view on failed-fuel operation and b.u. limit. (It should be noted that the French and Soviets differentiate between "failures" and "gas-leakers;" sodium must contact the fuel before they consider that to be a fuel-element failure.) A hint of West Germany's approach comes from the KNK-II fuel permitted to operate to 80 MWd/kg with up to 43.5 kW/m [28]. The British approach is as stringent as the French; PFR has each S/A monitored for DN's, and six TC's are installed at the exit of each S/A to detect such anomalies as blockages. As of 1974, Japan planned to add individual S/A flow meters to monitor for blockages, but West Germany did not have a definite arrangement for the fuel failure detection system, and location techniques were in the "thinking" stage. The official posture of each country is not clearly defined, perhaps because the technology is evolving.

The detection of failed fuel by GFP and DN monitors, key elements in the philosophy of failed-fuel operating, is discussed next.

Failed-Fuel Detection

A discussion of fuel-failure detection may well begin with why such detection is needed. Besides structural integrity, impervious cladding is required to prevent coolant con-

tamination and fuel-coolant chemical reactions. As a cladding failure develops, the fission gas is first released to the coolant; this gas may be tagged with a unique xenon- or krypton-isotope blend to help locate the detected failure. (The detection time is usually on the order of tens of minutes whereas location requires hours or days without a sophisticated location system.) As the failure worsens or conditions become such that fuel daughters (DN precursors) enter the coolant stream, a downstream monitor detects the emitted DN's within tens of seconds (thirty seconds is commonly cited). This can produce the unexpected results of a high DN signal burst from fission gas carrying DN emitters from a not-visible-to-the-naked-eye pinhole failure and a low DN signal for particulate fuel washed by the coolant (as would be the case in a particulate blockage) because of the dependence of the DN signal on temperature. The results must be carefully interpreted, particularly when a "background" or "noise" DN signal exists from several previously failed pins. Reference [29] reports some interesting experience with failed fuel in the BR-10. The DNM is sensitive to many variables, including coolant transit time (from the failure site to the monitor), exposed-fuel temperature, fuel type, porosity of exposed fuel, failure geometry (size, shape, and location), sodium "rinsing" of hot fuel, burnup, and linear pin-power. Data indicated that DN signals from a blockage would be very low whereas the DN signal from a breached pin would be quite high [30].

Briefly, the DN and tag-gas detection and location techniques permitted the increase of not only the irradiation, but also the operating temperatures and total specific powers. We might be expecting too much from our present systems, however. Although we have hoped to be able to depend on the DNM for early warning of potentially serious events, we need much more research and development to realize that goal. We also have less hope on gas tagging as a fast, reliable failed-fuel locator when operating with failed fuel. (The United States is seriously considering the Soviet off-line location-technique of capping an individual S/A, pressurizing it to lower the Na level and gas-blanket the S/A pins, and sniffing to detect a failure within that S/A [26-34].) Although the DN receipt in Mol 7C has provided valuable information, translating the loop DN receipt to what a global monitor would receive in a prototype LMFBR does not appear easy. Finally, to infer that such a signal would always be seen in a prototype remains to be demonstrated (or reported) (see reference [36-38] for more thorough discussions on failed-fuel detection).

Conclusions

Warinner and Cho [5] concluded from their summary of out-of-pile experiments and analyses (coupled with previously published summaries) that:

- Rapid FEFP has been deemed extremely unlikely, if not incredible
 - Slow FEFP should be (i) detectable, and (ii) self-limiting
 - Slow blockage propagation is unlikely
 - Slow blockage growth appears nonmechanistic from within and highly unlikely even for external debris
 - In-core planar blockages can be ruled out as a credible local fault
 - Molten-fuel release is very improbable, but even given a small release, resultant failure propagation or subassembly damage is unlikely
 - Although pin distortion and vibration, wire-wrap breakage, and other faults are possible—indeed, likely—the basic conclusions from the analyses and out-of-pile studies appear to be relatively insensitive to such perturbations
- These conclusions ignored the reactor experience; indeed, Warinner and Cho [5] went on to review in-pile experience

and experiments and altered these conclusions somewhat in view of the operational experience.

Whether the consequence of an in-core local-fault will always be contained within the S/A will remain in question until many years of prototypic operating experience have been witnessed. The conclusions, based on analyses and prototypic out-of-pile experiments, often with a critical parameter or characteristic bounding, can be challenged to be conjectures. However, the in-reactor experience summarized in reference [1] lends credence to these conclusions.

The LMFBR LOA's have been briefly outlined to show the constraints of fuel-pin design, local faults reviewed, fuel designs and reactor parameters summarized, requirements of the fuel discussed, and failed-fuel detection reviewed. Outstanding are the trends toward larger pin diameter for economic benefit and titanium-stabilized 20 percent C.W. 316 S.S. cladding, the many parameters affecting fuel failure, and the stringent constraints set by the United States in comparison with other countries (e.g., 150 MWd/kg b.u. and ≤ 0.1 percent failure). Whether that goal will be met, with confidence of detecting all other safety hazards with such a high DN-signal background, remains to be seen.

Acknowledgments

This work was performed under the auspices of the U.S. Department of Energy. I thank D. H. Cho, L. W. Deitrich, H. K. Fauske, J. I., Sackett, D. H. Lennox, J. H. Tessier, and D. H. Thompson of ANL; R. G. Brown of SAI; R. Tilbrook of WARD; and D. F. Giessing of DOE/RRT for valuable discussions and for alerting me to portions of the literature. Marsha Reinke's typing and assistance are very much appreciated, as is the typing of Velma Scott.

References

- 1 Warinner, D. K., "LMFBR Operational and Experimental Local-Fault Experience, Primarily with Oxide Fuel Elements," ASME paper 80-C2/NE-21 presented at the Nuclear Engineering Conference of the ASME Century-2 Emerging Technology Conferences, San Francisco, Calif., Aug. 10-21, 1980.
- 2 Kummerer, K., "General Characteristics of Fast Reactor Fuel Pins," *Progress in Nuclear Energy, Nuclear Energy Maturity, Proceedings of the European Nuclear Conference*, Paris, Apr. 21-25, 1975.
- 3 Gavigan, F. X., and Griffith, J. D., "The Application of Probabilistic Methods of Safety R&D and Design Choices," in *Proceedings of International Conference on Nuclear Systems Reliability Engineering and Risk Assessment*, Gatlinburg, Tenn., June 20-24, 1977.
- 4 Griffith, J. D., Avery, R., Graham, J., Greebler, P., Lancet, R., and Simpson, D. E., "U.S. Approach to LMFBR Risk and Safety R&D Cost Benefit Assessment," in *Proceedings of ENS/ANS International Topical Meeting on Nuclear Power Reactor Safety*, Brussels, Belgium, Oct. 16-19, 1978.
- 5 Warinner, D. K., and Cho, D. H., "Status and Needs of Local-Fault Accommodation in LMFBRs," in *Proceedings ANS/ENS International Meeting on Fast Reactor Safety Technology*, Seattle, Wash., Aug. 19-23, 1979.
- 6 "Summary Report of International Working Group on Fast Reactors," Meeting of Specialists on Fuel Failure Mechanisms, Seattle, Wash., May 12-16, 1975, International Atomic Energy Agency (IWGFR/5), p. 14.
- 7 Warinner, D. K., "Preliminary Report on Local Faults," ANL/RAS 81-3, Argonne National Laboratory, Dec. 1980.
- 8 Fauske, H. K., "Liquid Metal Fast Breeder Reactor Safety Technology," Chapter VIII, *Local Core Accidents* (Northwestern University Course notes, May 2-6, 1977).
- 9 Schleisiek, K., "Local Cooling Disturbances in Subassemblies of Sodium Cooled Reactors," CSNI Group of Senior Experts on LMFBR Safety R&D, Status Reports on LMFBR Safety Research, IRE, KfK, GmbH, Feb. 1978.
- 10 Brown, R. B., Chang, S. A., and Kadambi, N. P., "Status of LMFBR Safety Technology, I. Fission Gas Release in Reactor Safety," CSNI Report No. 40, Nuclear Safety Division, OECD Nuclear Energy Agency, Nov. 1979.
- 11 Fauske, H. K., Grolmes, M. A., and Chan, S. H., "An Assessment of Fuel Failure Propagation in LMFBRs," in *Proceedings of International Meeting on Fast Reactor Safety and Related Physics*, Oct. 5-8, 1976, Chicago, IL.
- 12 Van Erp, J. B., Chawla, T. C., Wilson, R. E., and Fauske, H. K., "Pin-to-Pin Failure Propagation in Liquid-Metal-Cooled Fast Breeder Reactor Fuel Subassemblies," *Nuclear Safety*, Vol. 16, No. 3, May-June 1975.
- 13 Crawford, R. M., Marr, W. W., Padilla, A. Jr., and Wang, P. Y., "The Safety Consequences of Local Initiating Events in an LMFBR," ANL 75-73, Argonne National Laboratory, Dec. 1975.
- 14 Kintner, E. E., "Engineering of U.S. Fast Breeder Reactors for Safe and Reliable Operation," in *Proceedings of Engineering of Fast Reactors for Safe and Reliable Operation*, GmbH, Karlsruhe, 1973.
- 15 Bleich, H. H., "Dynamic Interaction Between Structures and Fluid," *Proceedings of the First Symposium on Naval Structural Mechanics*, edited by J. N. Goodier and N. J. Heff, Pergamon Press, 1960.
- 16 Freslen, H., Fauske, H. K., and Eggen, D. T., "Local Flow Starvation in an LMFBR Subassembly Due to Fission Gas Release," *Transactions American Nuclear Society*, Vol. 16, 1973, pp. 197-198.
- 17 Okrent, D., ed., *Proceedings of the Conference on Safety, Fuels, and Core Design in Large Fast Power Reactors*, Oct. 11-14, 1965, Argonne, Ill., ANL-7120 pp. 910.
- 18 Evans, P. V., ed., "Fast Breeder Reactors," *Proceedings of the London Conference on Fast Breeder Reactors Organized by the British Nuclear Energy Society*, May 17-19, 1966, Pergamon Press, London, 1967.
- 19 Bohaboy, P. E., McWethy, L., Spalaris, C. N., Horst, K. M., and Craig, C. N., "Performance of Failed Fuel in Fast Reactors, in *Fast Reactor Power Stations, Proceedings of the International Conference Organized by the British Nuclear Energy Society*, Mar. 11-14, 1974, London.
- 20 Gryazev, V. M., Krasnoyarov, N. V., Kevrolev, V. P., Kondrat'ev, V. I., Nechaev, B. N., and Smirnov, A. M., "Four Years Operating Experience on the Experimental BOR-60 Nuclear Power Station," in *Fast Reactor Power Stations, Proceedings of the International Conference Organized by the British Nuclear Energy Society*, Mar. 11-14, 1974, London.
- 21 Clinch River Breeder Reactor Plant PSAR - Docket 50537, Section 15.4, "Local Failure Events."
- 22 Gatesoupe, J. P., and Perret, F., "Kinetic Study of Fuel Failure Due to Manufacturing Faults," *op. cit.* reference [6].
- 23 Megy, J. M., Cravero, M., Leduc, J., and Noel, H., "The Consequences of Safety Prescriptions for Fast Breeder Reactor Design in France," in *Optimization of Sodium Cooled Fast Reactors, Proceedings of the International Conference Organized by BNES*, London, Nov. 28-Dec. 1, 1977, pp. 9-13.
- 24 Weimar, P., "Experimental and Theoretical Evaluation of Defect Growth of Fuel Pin Cladding by Chemical Fuel-Sodium Interaction," in *Proceedings of the Fourth Structural Mechanics in Reactor Technology (SMIRT) Conference*, Division C, Paper C-4/6, San Francisco, Calif. 1977.
- 25 Kummerer, K. R., "The German Oxide Fuel Pin Irradiation Text Experience for Fast Reactors," in *Proceedings of International Conference on Fast Breeder Reactor Fuel Performance*, American Nuclear Society, Monterey, Calif., Mar. 5-8, 1979.
- 26 Alekhin, L. A., Demin, A. A., and Kiselev, G. V., "Operation of the BN-350 Reactor in Power Generation," presented at US-USSR Seminar, Moscow, Oct. 1979.
- 27 Batalin, Yu. D., Vasilenko, K. T., Zemtsev, B. V., Samarkin, A. A., Skorikov, N. V., Tsurukin, Yu. P., and Yurchenko, D. S., "Radiation Conditions and Condition of Coolant in the First Circuit of the BN-350 Reactor," presented at US-USSR Seminar, Moscow, Oct. 1979.
- 28 *Nuclear Engineering International*, Apr. 1979, p. 10.
- 29 Efimov, I. A., Zhilkin, A. S., Mamaev, L. I., Mezentsev, A. N., Shestopalov, E. V., and Shipilov, A. E., "Leakage of Fission Products from Defective Fuel Elements of the BR-10 Reactor at High Plutonium Oxide Burnup," presented at US-USSR Seminar, Moscow, Oct. 1979.
- 30 Sackett, J. I., ANL/EBR-II, personal communication, September 16, 1980.
- 31 Report of the USA Nuclear Power Reactor Delegation Visit to the USSR, ERDA 76-60, June 1975.
- 32 Aristarkhov, N. N., Bets, N. I., Efimov, I. A., Filonov, V. S., Kevrolev, V. P., and Rybakov, V. N., "Detection of Packets with Non-Hermetic Fuel Elements on Sodium-Cooled Fast Reactors," *op. cit.* [20].
- 33 Yurchenko, D. S., Vasilenko, K. T., Pomerantsev, G. B., Samarkin, A. A., and Timofeev, A. E., "Summary of Operating Experience of the BN-350 Reactor," presented at US-USSR Seminar, Moscow, Oct. 1979.
- 34 Letter, J. I. Sackett (ANL/EBR-II) to F. X. Gavigan (DOE/RRT), USSR/US Trip Report on Breached Fuel Experience, Nov. 21, 1979.
- 35 Efimov, I. A., Kulakovskii, M. Va., Filonov, V. S., "Principles of Controlling Damage to Fuel Elements of Fast Reactors According to the Activity of Sodium and Gas," ERDA-tr-63, of *Printsipy Kontrolya Razrusheniya TVEL Energeticheskikh Reaktorov* . . . , 19 pp., 1972.
- 36 Braid, T. H., et al., "Delayed Neutron Detection in the Sodium Loop Safety Facility," in *Proceedings ANS/ENS International Meeting on Fast Reactor Safety Technology*, Seattle, Wash., Aug. 19-23, 1979.
- 37 Kramer, W., et al., "In-Pile Experiments "Mol 7C" Related to Pin Failure Propagation," *ibid.*
- 38 Jacobi, S., and Schmitz, G., "Delayed Neutron Signals from Failed Pins and Bundles and their Relation to Safety Problems," *ibid.*

Design Concept and Development of a Heavy-Duty Truck Diesel Engine for Better Fuel Economy

A. Kobayashi
Chief of Section.

M. Ozawa
Assistant Chief.

M. Noda
Engineer.

K. Kikuchi
Engineer.
Hino Motors, Ltd.,
Tokyo, Japan

Due to the increasing price of fuel, demands for fuel economy of heavy-duty trucks become severer year by year, and many efforts, such as reduction of air drag of vehicle, optimization of transmission and engine performance, improvement of engine combustion, etc., have been taken to meet these demands. However, requirements for the reduction of fuel consumption are expected to become even more critical, so the authors have studied a new design concept for heavy duty truck diesel engines to satisfy these requirements. The basic idea for getting a fuel-economic engine is to make the engine as small as possible and also to apply higher boost turbocharging for obtaining a sufficiently high output. However, measures to improve the undesirable problems which conventional turbocharged engines possess, such as lack of acceleration response and low-speed torque, increase of thermal and mechanical loads, shortage of engine brake torque, poor cold start ability, etc., should also be pursued. A chassis-mounted air-to-air intercooler, inertia-charged air induction system, highly backward-curved impeller of turbocharger, electronically controlled fuel injection timing device, etc., have been applied. And a new design technique as well as new material and construction have also been applied. This engine was installed to a long-haul truck with a gross weight of around 20,000 kg (44,000 lbs) and got better fuel mileage, as expected.

Introduction

With the successive oil crises, the demands for improving fuel economy of the heavy-duty truck diesel engine became stronger. Diesel engines used for these trucks in the United States mostly employ turbocharging or turbocharging with an intercooler. These engines have a reduced maximum engine speed as well as an increased torque back-up for improving fuel economy, and some good results have been announced [1, 2, 3]. These engines are usually connected with a transmission of 7 to 13 speeds and with a high-speed type differential gear. This combination is mostly suited to such running conditions where the engine is kept around a rather high speed and load.

On the other hand, Japanese heavy-duty trucks with a gross weight of around 20,000 kg (44,000 lbs) are mainly equipped with naturally aspirated engines, while turbocharged versions occupy only about 15 percent of the total production. These engines are usually combined with a 6-speed transmission instead of 7 to 13 speeds. The main reason for such combination is that, even for the heavy-duty truck, the Japanese traffic conditions require a high frequency of acceleration and deceleration due to the mixture of city road and highway running and also frequent uphill and downhill driving. This

causes the engine to run over a wide speed range with a minimum of gear changing.

So a flat torque curve without a steep decrease of low engine speed torque is necessary, and the naturally aspirated engine is suitable for it. Thus, improvement of the combustion of the naturally aspirated engine has been the main aim for improving fuel economy. In order to improve the combustion, a specially shaped intake air port which produces stronger turbulence was applied to promote the mixing of fuel droplets and compressed air in the cylinder. This is known as HMMS (Hino Micro Mixing System) [4, 5]. In the case of a naturally aspirated engine, combustion improvement combined with optimum selection of the transmission and application of the aerodynamic cabin have reduced fuel consumption about 15 to 20 percent.

However, the demands for fuel economy from the market are expected to become severer, and the authors decided to meet these demands by establishing a new design concept for the engine. Although their main object was to pursue fuel economy, they also aimed at a better engine response and a sufficient engine brake force to meet the frequent acceleration and deceleration, as well as uphill and downhill driving.

The design concept as well as the development results are described in detail in the following sections.

Design Concept of the Fuel-Economic Engine and the Related Problems to be Solved

Basic measures to improve the fuel consumption are to

Contributed by the Diesel and Gas Engine Power Division of The American Society of Mechanical Engineers and presented at the Diesel and Gas Engine Power Conference and Seminar, Nashville, Indiana, October 3-5, 1982. Manuscript received at ASME Headquarters June 11, 1982. Paper No. 82-DGEP-3.

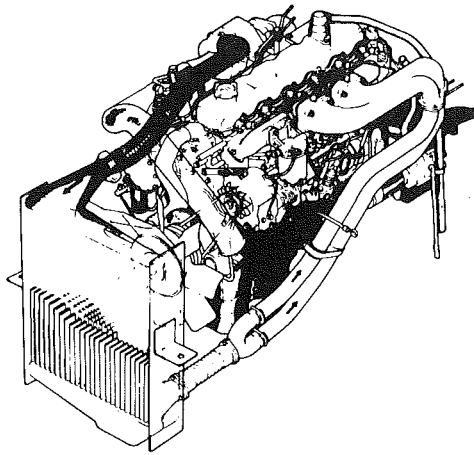


Fig. 1 EPI00 engine three-quarter view

reduce the loss of exhaust gas energy and loss of cooling and also to reduce friction. To collect the exhaust gas energy the turbocharging is popularly applied, and an idea to reduce the cooling loss by using ceramics around the combustion chamber in order to recover the exhaust gas energy has been reported by some researchers [6]. The authors, however, consider that it is too early to apply such an idea to the existing commercial vehicles because of problems in reliability, accessibility, maintenance, and production cost, etc. Therefore, they aimed at reducing the engine friction.

Usually, engine friction increases with the increase of engine speed as well as engine swept volume. In the United States a reduction of the rated speed has been pursued to improve the fuel consumption of diesel engines. On the other hand, the Japanese truck drivers have asked for a wider range of engine operating speed, whereas the authors intended to reduce the engine swept volume. That is to say, they aimed at a minimum swept volume with sufficiently high output, and this can be regarded as a very simple and clear design concept.

With this concept, the authors decided to apply turbocharging and intercooling. They also realized they must solve the following problems in order to meet the requirements of the Japanese markets:

- 1 Wider operating speed range and flat torque characteristics
- 2 Prevention of steep reduction of low-speed torque
- 3 Enough engine brake force to satisfy the frequent deceleration and downhill driving
- 4 Better cold starting and white smoke level (the same as that of the naturally aspirated engine)
- 5 Durability
- 6 Compliance with the exhaust gas and noise emission regulations of Japan

For higher turbocharging, the intercooling is effective in reducing the intake air temperature and increasing the air density. It is also effective in reducing the thermal load as well as the nitric oxide (NO_x) emission [7]. And to get a higher cooling capacity even at a low speed and light load, the authors selected the chassis-mounted air-to-air intercooler.

This newly developed engine is called the EP100. Figure 1 shows the three-quarter view of the engine, and Table 1 shows its specification compared with that of the predecessor (a naturally aspirated engine called the EK100).

Turbocharger, Inertia-Charging and Intercooler. Basically, the turbocharged engine is not suitable for a wide range of operating speeds and flat torque characteristics. The turbocharger, being a fixed size tur-

Table 1 Specification of the new high-boost turbocharged engine and the naturally aspirated engine

Engine type	EP100	EK100
Aspiration	TI*	NA*
Cylinder arrangement-number	L-6	L-6
Bore × Stroke mm	120 × 130	137 × 150
Swept volume dm ³	8.821	13.267
Maximum output (JIS) kW/rps (ps/rpm)	210/38.3 (285/2300)	199/38.3 (270/2300)
Maximum torque (JIS) N·m/rps (kg·m/rpm)	961/23.3 (98/1400)	932/23.3 (95/1400)
BSFC g/kW·h (g/ps·h)	201 (148)	216 (159)
Dry weight kg	862	965
Specific output kW/l (ps/l)	23.8 (32.3)	15.0 (20.4)
Specific weight kg/kW (kg/ps)	4.10 (3.02)	4.85 (3.57)
Maximum BMEP kPa (kg/cm ²)	1370 (14.0)	880 (9.0)

*TI: Turbo-charged Intercooled
NA: Naturally Aspirated

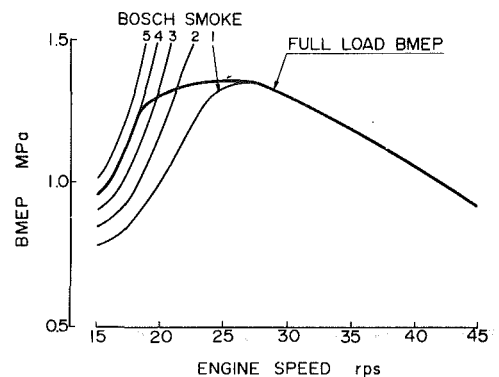


Fig. 2 Smoke concentration of turbocharged engine

bomachinery, is limited in optimum matching range with the diesel engine, which is a reciprocating machine.

This results in a lack of intake air, especially at the lower engine speed range, and thus reduces the torque. In order to solve this problem, the turbocharger should be modified to produce higher efficiency over a wide speed range and also the inertia-charging system, which was effectively developed to produce high volumetric efficiency, should be utilized. A study to combine the inertia-charging system with turbocharging was reported [8, 9, 10], but it usually requires a large damping volume which presents some difficulties with regard to accessibility to the vehicle engine. The authors pursued the air quality necessary for combustion and found that the inertia-charging system of the turbo-charged engine should be tuned for low speed. They decided to accomplish this system without a damping chamber, the theory of which was established by Shimamoto [11].

In addition, the air-to-air intercooler can, through improvement of the low-speed air charging, promote the low-speed torque because the intercooler works effectively even at low-engine speed.

Combustion Tuning and Electronically Controlled Fuel Injection Timing Device. The authors tried analysing the combustion characteristics of the turbocharged engine: namely, with this engine, the high compression temperature

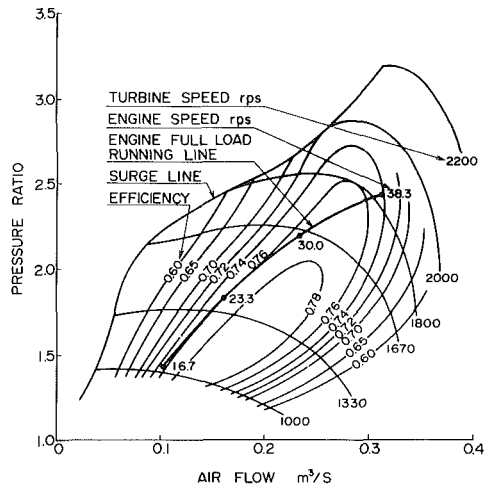


Fig. 3 Compressor map of UBCI turbocharger

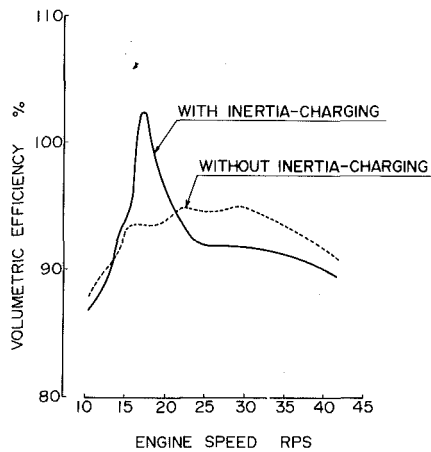


Fig. 4 Effect of inertia-charging on volumetric efficiency

and pressure allow excessively short ignition delay at high engine speed, and this induces diffusion burning.

However, at low engine speed, the compression temperature and pressure are almost the same as the naturally aspirated engine and accordingly the combustion was thought to be similar to the naturally aspirated engine, i.e., ignition delay is relatively long and there is a premixed combustion followed by diffusion burning. The authors decided to apply their specially shaped intake air port which acts effectively for improving the combustion of the naturally aspirated engine (HMMS as mentioned before).

For the purpose of getting a better fuel economy, authors tried controlling the fuel injection timing according to each engine speed and load. They decided to apply the newly developed electronically controlled fuel injection timing device (ET control).

Engine Swept Volume. The engine speed for the United States long-haul trucks is generally kept within a very narrow range, so the response is considered mainly with regard to engine load. For the authors, however, the response concerning the engine speed is more essential. Reduction of the turbocharger inertia moment is a basic requirement for this problem but the exhaust gas energy which accelerates the turbocharger itself is also important. And the selection of the engine swept volume is also thought to be important.

Cold Start and White Smoke. With a highly turbocharged engine, a low compression ratio is normally selected in order

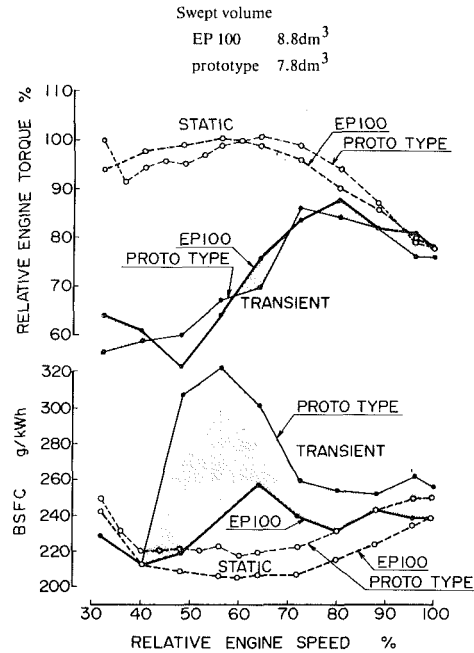


Fig. 5 Transient and static performance of EPI00 engine compared with prototype engine

to reduce the thermal and/or mechanical load, and this induces the cold start problem and white smoke. One of the authors previously studied the combustion characteristics of the engine under cold starting conditions [12, 13]. Combustion at low ambient temperature is quite different from the normal operation, and the fuel injection timing acts quite sensitively for the ignition and the succeeding combustion.

Therefore, the authors decided to apply the ET control to improve the cold starting. They also applied the electric intake air heater, which is commonly applied to the naturally aspirated engine.

Engine Brake. A small swept volume was selected mainly to reduce the engine friction, but this reduces the engine brake force as well. Accordingly, the authors intended to improve the exhaust brake system.

Development of the Turbocharged Fuel-Economy Engine

Low-Speed Torque and Acceleration Response. In order to meet the Japanese domestic usage, the engine full load torque should be flat even for the turbocharged engine. For this purpose, the low speed torque should be over 95 percent of the maximum torque. However, if the peak torque brake mean effective pressure is above 1.3~1.4 MPa with the conventional turbocharged engine, the full load torque usually drops below 20 rps. The main reason for this poor low-speed torque is a decrease of fuel input to suppress the smoke level caused by a lack of inlet air quantity. The smoke concentration is shown in Fig. 2. To keep the smoke level below the acceptable limit, the torque at low speed should be reduced by reduction of the fuel supplied.

Therefore, the first target for getting adequate low-speed torque is the air inlet quantity, and improvement of the turbocharger itself and application of inertia-charging, as well as an intercooler, have been studied. In addition, the selection of engine swept volume and the optimization of combustion have also been studied.

Turbocharger. The straight blade radial compressor wheel applied to the conventional turbocharger has a rather

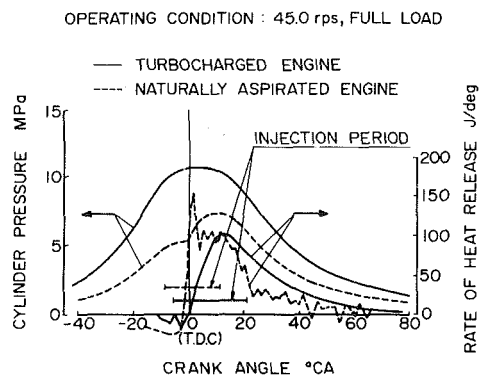


Fig. 6(a) Comparison of combustion characteristics: turbocharged engine versus naturally aspirated engine (high speed)

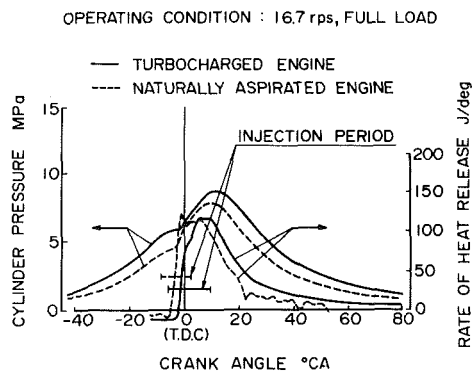


Fig. 6(b) Comparison of combustion characteristics: turbocharged engine versus naturally aspirated engine (low speed)

high efficiency in the range of large flow quantity and high pressure ratio. However, if it is applied to a wide speed range of operation, it shows signs of surging at low speed as well as poor efficiency at high speed.

The authors decided to apply an extremely backward-curved impeller, and the design of the turbocharger was intended to maintain high efficiency at low engine speed and light load. Backward curve is 40 deg and, in order to recover the boost pressure, the diameter of the wheel is increased about 8 percent compared with the conventional design.

Figure 3 shows the compressor map of the turbocharger. In order to get enough strength with such a large diametral compressor wheel, even under the maximum operation speed of 2200 rps, stress analysis using the finite element method (FEM) is widely applied, and a newly developed aluminum alloy is also utilized.

Intercooler. An intercooler is usually applied to highly turbocharged engines to reduce the inlet air temperature.

The intercooler is also effective in reducing exhaust gas emission of the engine especially NO_x. Precisely, the reduction of the combustion temperature and pressure is effective for NO_x reduction, and when considering the Japanese 6-mode test, the intercooler should have a cooling capacity even at low engine speed and light load.

The authors selected the air-to-air type chassis-mounted intercooler for this reason. This intercooler serves to increase the low-speed air, thus boosting the low-speed torque too.

Inertia-Charging. Over the past 10 years, the authors have developed and applied their own inertia-charging system for the naturally aspirated engine. In the case of the naturally aspirated engine, the matching point of the system lies at a

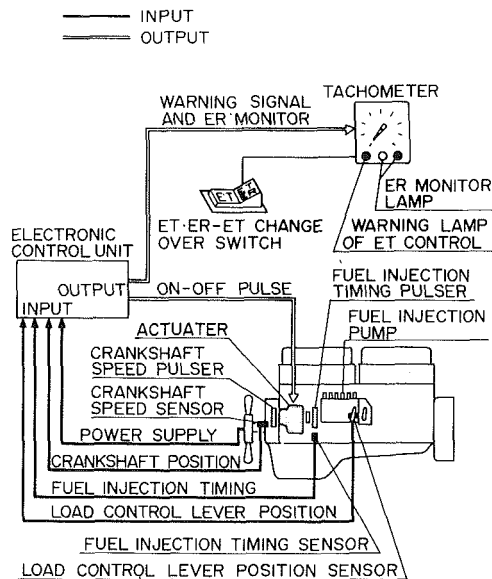


Fig. 7 Block diagram of ET-control system

rather high speed in order to get higher volumetric efficiency around engine rated speed. However, with the turbocharged engine, inlet air at rated speed is too great so the matching point of the inertia-charging system should be aimed at low engine speed.

The matching point was selected around 17 rps and in addition to the effect of the intercooler, inlet air quantity could be kept sufficient at the low speed. Figure 4 shows the effect of the inertia-charging, as well as the intercooler and the increase of low-speed air quantity. It moves the smoke limit line to improve the low-speed torque.

Selection of the Engine Swept Volume. As mentioned before, the authors can get flat torque characteristics under static operation. However, in the case of vehicle acceleration which occurs frequently in the Japanese traffic conditions, such static flat torque characteristics cannot usually be kept, and the shortage of inlet air due to a delay of turbocharger speed during acceleration reduces the torque because of poor combustion. Such tendency is thought to become severer for an engine with smaller swept volume even if it has enough static torque.

For the purpose of studying such effect on acceleration, the authors tried operating the engine while measuring the instantaneous change of engine torque and fuel consumption from idling position to rated speed. This simulated the normal operation when starting with the transmission at second gear.

Figure 5 shows a comparison of the two kinds of swept volume concerning the abovementioned two characteristics. The engines accelerate from idling to rated speed within about 5 s. The figure shows that the shortage of instantaneous torque as well as excessive fuel consumption are improved with a larger swept volume (8.8 dm³), inertia-charging, and the turbocharger having highly backward-curved impeller.

Optimization of Combustion. From the point of view of smoke limit, combustion of the turbocharged engine at higher engine speed is not so difficult because there is excessive air. However, with regard to the combustion at the low-speed range, combustion tuning should be considered more carefully to utilize the air to get enough low-speed torque.

This brings into importance of the fuel-air mixture formation using the specially shaped intake port which produces higher turbulence.

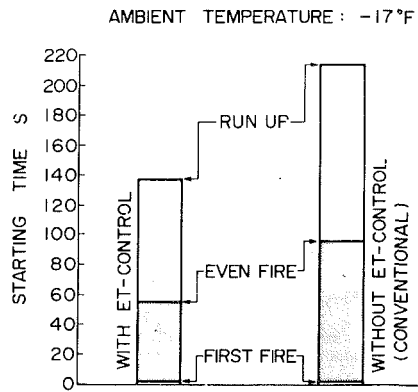


Fig. 8 Comparison of startability with and without ET-control

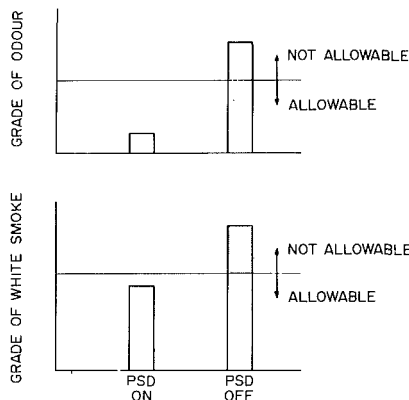


Fig. 9 Improvement of white smoke and odour by partial shut down system (PSD system)

The injection system is another important item. At higher engine speed the fuel injection period should be short enough to keep the combustion period as the essential factor for better fuel economy. Atomization of the fuel at lower engine speed is also important in order to keep the smoke level as low as possible, i.e., to keep the low-speed torque as high as possible.

Figures 6(a) and 6(b) show the cylinder pressure diagram and the heat release curve of both turbocharged and naturally aspirated engines. At higher engine speeds, the difference between the types of engines is very clear, but at lower engine speeds, the heat release curve of the turbocharged engine looks very close to that of the naturally aspirated engine. Therefore, a highly turbulent intake port and a multihole injection nozzle were selected.

Another improvement concerning the combustion is the application of ET control, the details of which will be presented by a colleague of the authors. This device selects an optimum compromise of fuel injection timing for better fuel economy, low exhaust emission, low combustion noise, and high reliability, etc. The device also works effectively in the cold start condition mentioned later. Figure 7 shows a block diagram of the system.

Cold Starting. Low compression ratio and small cylinder size have a disadvantage concerning the cold startability. A large capacity electric intake air heater and a high torque starting motor are applied to solve the problem. Namely, the intake heater and the starting motor assist the initial ignition of the injected fuel, but the engine speed sometimes falters during the next period, and this results in a long starting time.

The reason for this lies in comparing the change of engine

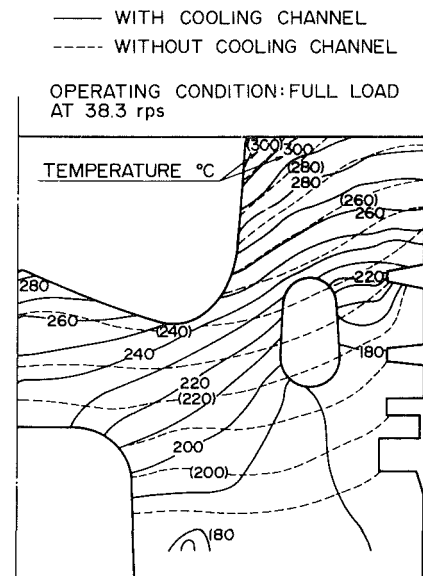


Fig. 10 Improvement of temperature distribution by piston cooling channel

speed and the ignition delay [12, 13]. In such a faltering condition, if the engine speed increases due to sufficient combustion pressure, an ignition delay relative to crank angle cannot keep up with this change and the ignition timing moves from before-top dead center to after-top dead center. The combustion pressure tends to weaken versus an increase in engine speed. Therefore, if the authors can select a fuel injection timing to offset the increase of ignition delay relative to the engine speed, they can reduce the cold starting time. Figure 8 shows the improvement of the cold starting time with the application of ET control.

Another problem to be considered with the lower compression ratio engine is white smoke and odor. For this purpose, the authors developed the partial shutdown system (PSD system). In an idling condition at low ambient temperature, the fuel to the injection pump is limited to three cylinders instead of six, which doubles the fuel input per cylinder to increase the temperature of the combustion chamber wall and reduces the white smoke emission and the odor. Figure 9 shows that PSD system keeps the white smoke and the odor within the allowable levels which is empirically established.

Thermal and Mechanical Loading. The thermal loading of this highly turbocharged engine is about 25 percent higher than that of the naturally aspirated engine. The fuel input per piston surface area for every cycle is about 25 percent greater for this turbocharged engine than for the naturally aspirated engine with the same output. Combustion pressure is about 12 MPa compared to 7 and this makes, for example, the combustion force acting on the connecting rod about 30 percent larger. The authors paid much attention to the engine components which relate to the thermal and/or mechanical load mentioned above.

Cylinder Head. The cylinder head is a single piece of alloy cast iron. FEM is widely applied to cylinder head, especially for the place around the fuel injection nozzle, intake valve, and exhaust valve. Specially cast alloy iron which contains molybdenum, chromium, nickel, etc., was examined and supplied for the durability tests.

Piston. Piston material is cast aluminum alloy with a solid body. Positive cooling by lubricating oil was considered from the first stage of development, and a piston with a

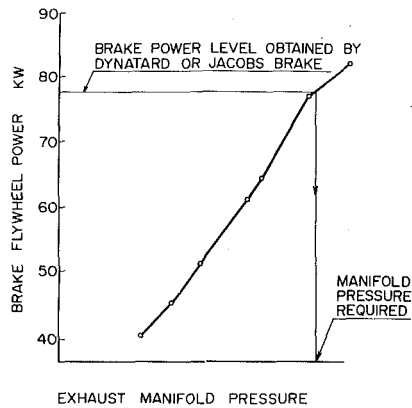


Fig. 11 Exhaust brake performance at various manifold pressure (26.6 rps)

cooling channel into which the oil jet from a separate oil hole is injected has been applied. The structure of the piston is also analyzed using FEM and the three-dimensional photoelasticity method. Figure 10 shows the effect of the cooling channel, and when considering the temperature of the piston crown around the combustion bowl and the top ring groove, there is a reduction of about 50 K and 20 K, respectively, compared to the piston without the cooling channel.

Exhaust Brake. In typical Japanese traffic conditions, about 15 percent of the total running time is taken up by uphill and downhill driving, and the engine brake force is normally required to be 70 to 80 percent of the rated horsepower at the rated speed. Since the EP100 engine is designed to reduce the engine friction, the engine has about 75 percent of the friction compared to the naturally aspirated engine of the same horsepower.

Next, measures to increase the engine brake force were studied. Such systems of brakes as the Jacobs [14] or Dynatard [15] brake can be expected to produce sufficient brake torque. These brakes release the compression gas pressure around the piston top dead center and thus produce brake force. An exhaust brake system which has a mechanism to shut-off the exhaust pipe to increase the pumping loss has also been studied.

The authors compared both types of brake systems with regard to construction, production cost, etc., and reached a conclusion to apply the exhaust brake system. Figure 11 shows the relation of exhaust manifold pressure and brake power. The authors found out that if they could get a sufficient back pressure, the resultant brake force would be satisfactory.

The structure of the shut-off valve was surveyed, and the Guillotine type (sliding valve) instead of the conventional butterfly type was finally selected.

Test Result on Actual Truck

Figure 12 shows the engine performance map which includes full load torque characteristics and brake-specific fuel consumption.

This newly developed turbocharged and intercooled engine, EP100, was equipped to a heavy-duty truck having gross vehicle weight of about 20,000 kg (44,000 lbs). Figure 13 shows the improvement of the fuel mileage both for combined route and highway running. The new type of truck equipped with the EP100 engine, which is called as Dolphin Turbo 8.8, improves mileage about 30 percent on the highway and 20 percent on city roads compared to the predecessor with naturally aspirated engine of the nearly same output. Fuel

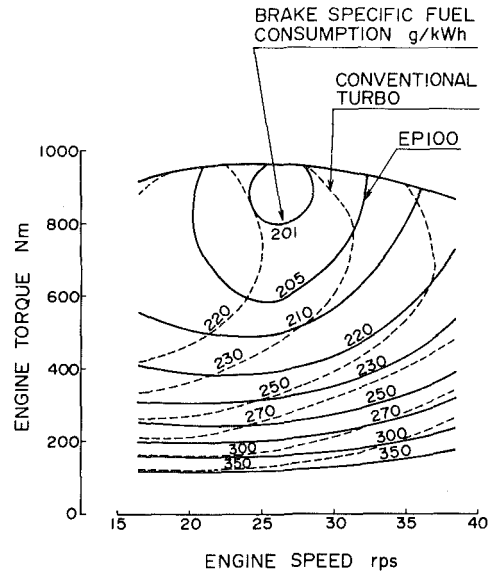


Fig. 12 Engine performance map

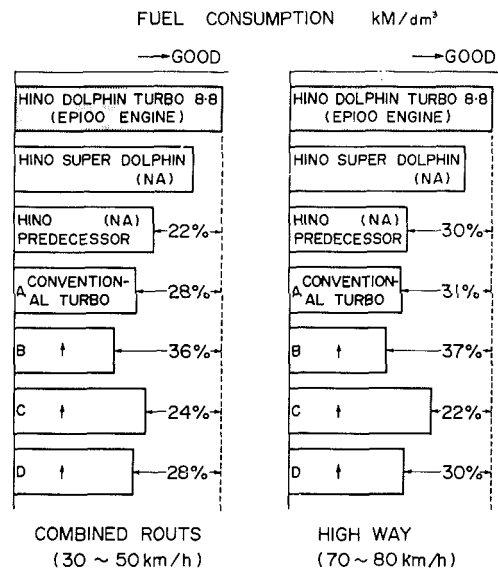


Fig. 13 Actual fuel consumption of trucks

mileage of the same new type of truck, but equipped with a naturally aspirated engine, is shown as the Super Dolphin. The figure also shows the comparison of the fuel mileage between the new truck with the EP100 engine and the competitive truck with conventional turbocharged engines, defined as conventional turbo A, B, C, and D in the figure.

Other performance factors, such as acceleration and engine brake, were also confirmed to be better than the naturally aspirated engine.

Conclusion

The authors have described the design concept and development results of their EP100 engine. They applied this engine to long-haul trucks, and it is getting a good reputation in the market.

Acknowledgment

The authors wish to thank the many cooperating companies

and academic circles who contributed to this study and development work. The authors are also thankful to their colleagues who assisted the work and to the directors of Hino Motors, Ltd. for their permission to publish this paper.

References

- 1 "DDA Introduces Its Total Value Package," *Diesel Equipment Superintendent*, Apr. 1980, pp. 46.
- 2 "Caterpillar's Family of 1600-rpm Engines Saves Fuel," *Commercial Car Journal*, Dec. 1980, pp. 88-89.
- 3 "Cummins Announces New 1600-rpm Fuel Economy Engine," *Commercial Car Journal*, Apr. 1981, pp. 256.
- 4 Suzuki, T., and Shiozaki, T., "A New Combustion System for the Diesel Engine and Its Analysis via High Speed Photography," SAE Paper 770674, 1977.
- 5 Shiozaki, T., Suzuki, T., and Shimoda, M., "Observation of Combustion Process in D.I. Diesel Engine via High-Speed Direct and Schlieren Photography," SAE Paper 800025, 1980.
- 6 Kamo, R., and Bryzik, W., "Cummins-TARADCOM Adiabatic Turbocompound Engine Program," SAE Paper 810070, 1981.
- 7 Suzuki, T., Kobayashi, A., and Fujii, T., "Controlling Exhaust Emission from the Turbocharged Automotive Diesel Engine," *FISITA*, May 1976, pp. 2.81-2.92.
- 8 Cser, G., "Some Results of Combined Charging Application," *Proceedings of the Institute of Mechanical Engineers*, 1978, pp. 127-132.
- 9 Brands, M. C., Helmholtz Tuned Induction System for Turbocharged Diesel Engine," SAE Paper 790069, 1979.
- 10 Zürner, H., "Entwicklung von Aufgeladenen M.A.N. - Fahrzeug — Dieselmotoren in Sechszylinder - Reihenbauart," *MTZ*, Vol. 41, No. 2, Feb. 1980, pp. 41-46.
- 11 Shimamoto, Y., Oka N., and Tanaka, Y., "Research on Inertia Charging Effect of Multi-Cylinder Engines," *Transaction of the Japan Society of Mechanical Engineers*, Vol. 43, No. 371, July 1977, pp. 2766-2737. (Japanese)
- 12 Kobayashi, A., Suzuki, T., and Nakajima, J., "Combustion Analysis of the High-Speed Diesel Engine in Cold Starting Condition via High Speed Photography," *13th CIMAC Congress*, D70, May 1979, pp. 1-26.
- 13 Kobayashi, A., Suzuki, T., and Nakajima, M., "Combustion Analysis of the Vehicular Diesel Engine in Cold Starting Condition via High-Speed Photography," *ASME 80-DGP-7*, Feb. 1980, pp. 1-7.
- 14 Morce, W. H., and Rife, J. M., "Compression Engine Brake Performance with Turbocharged Diesel Engines," SAE Paper 790769, Aug. 1979, pp. 1-7.
- 15 Greathouse, J. F., Gibson, R. B., and Pekar, F. J., "Mack's V-8 Maxidyne Diesel with Dynatard Engine Brake," *Diesel and Gas Turbine Progress*, July 1971, pp. 22-24.

Some Aspects of Constant Pressure Turbocharged Marine Diesel Engines of Medium and Low Speed

T. Azuma

Manager,
Diesel Engine Research Department,
Kawasaki Heavy Industries, Ltd.,
Kobe, Japan

T. Yura

Lecturer,
Osaka Institute of Technology,
Osaka, Japan

Y. Tokunaga

Diesel Engine Research Department,
Kawasaki Heavy Industries, Ltd.,
Kobe, Japan

The constant pressure turbocharge system is widely used in marine diesel engines because of its high thermal efficiency. This study has been made to establish a simulation system for exhaust gas pulsation of the constant pressure turbocharge system and to clarify its characteristics. The previous paper reported that the pressure fluctuations measured on test units and some engines agreed very well with those simulated by the scheme developed in this study. The study used the characteristic method for solving the differential equations of unsteady flow. This report will first discuss the high thermal efficiency of this turbocharge system in the range of high mean effective pressure, then it will show the advantages of the two-step Lax-Wendroff's method in solving the unsteady flow equations in comparison with the characteristic method. Furthermore, it will present some characteristics of the pulsation and the unique pulsation resonance in this turbocharge system.

Introduction

The constant pressure turbocharge system is of higher thermal efficiency than the pulse turbocharge system in the range of higher mean effective pressure. This is why the system has been increasingly adopted in marine diesel engines of medium and low speed, since energy savings became an urgent problem as described in the previous report [1].

Because of the very large volume of the exhaust pipe, the amplitude of the exhaust gas pulsation is supposed to be negligibly small in this system, and this is considered to be one of its features.

However, there is actually pulsation of some amplitude which is extremely complicated in its shape, with adverse effect on some engines. The complicated pulsation is due to the fact that many cylinders are connected with one common exhaust pipe.

On the other hand, one to three cylinders are connected to one exhaust pipe in the pulse turbocharge system. This enables it to obtain the exhaust systems in which only cylinders with certain minimum ignition intervals exhaust into the same pipe and thus to avoid the adverse effect of the exhaust gas pulsation. The pulse turbocharge system has long been in dominant use because of the advantage mentioned above and other preferable characteristics.

Early in the 1960s, however, the constant pressure turbocharge system came into practical use in large-bore, two-cycle engines for marine use which were about $0.7 \sim 0.8$ MN/m² in the mean effective pressure at that time. The advent of the system was because of the higher thermal efficiency in the range of higher mean effective pressure, simple

construction of the exhaust systems, and some other features of the system.

As the examples of the adverse effect of the pulsation, it has since been experienced that cylinder pressure at the beginning of compression can be largely different among cylinders (especially in two-cycle engines), that inlet ports can be fouled by back flow of exhaust gas into cylinders [2], and that pulsation of extremely large amplitude can occur in some engines to give adverse effect on engine performance [3].

It was difficult, however, to take effective countermeasures against the adverse effect caused by the pulsation. This was because no systematic study on the exhaust gas pulsation in the constant pressure turbocharge system had been made and accordingly its characteristics had remained unclarified.

In the previous report [1] a comparison of the simulation with the measurement on two experimental units and on some engines was presented. Some characteristics of the pulsation were also discussed.

In order to confirm the value of this study it is important and useful to make clear why the constant pressure turbocharge system is of higher thermal efficiency than the pulse turbocharge system in the range of high mean effective pressure. In this report, therefore, this subject will be discussed first.

Furthermore, in order to carry out the second plan of this study, i.e., the study on the interaction between the pulsation and engine performance, it is required to modify the simulation system so that it may include the process in cylinders which was not included in the previous simulation system. In the new simulation system, the accuracy of the simulated gas flow quantity is also important because air consumption is one of the most important factors of engine performance, while pressure fluctuation in the exhaust pipe was the main concern in the previous simulation system.

Contributed by the Diesel and Gas Engine Power Division of THE AMERICAN SOCIETY OF MECHANICAL ENGINEERS and presented at the Diesel and Gas Engine Power Conference and Seminar, Nashville, Indiana, October 3-5, 1982. Manuscript received at ASME Headquarters June 11, 1982. Paper No. 82-DGEP-4.

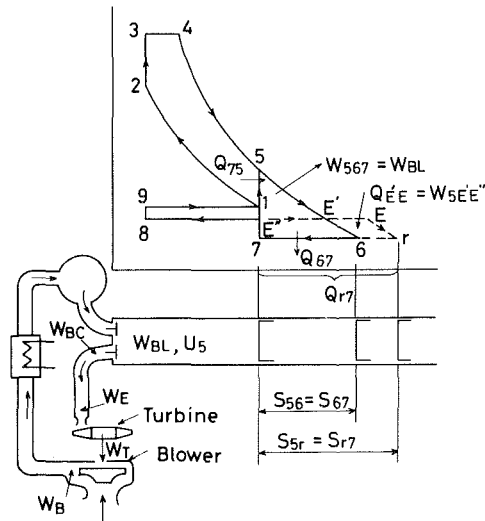


Fig. 1 Theoretical cycle of exhaust gas turbocharged diesel engines (four-cycle engine)

In the second subject of this report, it will be shown that more accurate simulation of gas flow quantity and shorter computational time can be obtained by using the two-step, Lax-Wendroff's method instead of the characteristic method used so far, $0 \rightarrow a$, as the numerical solution of the unsteady flow equations.

In the third subject of this report, some characteristics of the pulsation will be further presented. These are (i) the characteristic of gas flow at the branch in the exhaust system; (ii) a consideration on experimental unit for the pulsating flow; (iii) the characteristics of pressure waves at an orifice at the end or halfway in the exhaust pipe; and (iv) effect of orifices for damping pulsation.

In the last subject, a consideration on the unique mechanism of the pulsation resonance in the exhaust pipe of multicylinder engines shall be presented. This will be done by assuming a model of pressure pulsation in the exhaust pipe. Also, a simulation shall be presented to justify the consideration on the mechanism of the pulsation resonance.

In the constant pressure turbocharge system, the volume of the scavenging air manifold is so large that in fact there is no pressure fluctuation in the air manifold of medium and low speed engines. Therefore, the discussion about the pulsation is concerned only with that in the exhaust pipe in this report.

Thermodynamical Characteristics

By using computer simulation, Horst Zapf and Helmut Pucher [4] made a detailed analysis of thermal efficiency of the constant pressure and pulse turbocharge systems to show why the former is of higher thermal efficiency than the latter in the range of higher mean effective pressure.

In this report, however, not a detailed but a broad analysis and consideration on the fundamental factors will be made on the subject.

Nomenclature

a = acoustic speed	n = rotational speed of engine	v = specific volume
D = diameter	P = absolute pressure	W = mechanical work
F = cross-sectional area	P_{atm} = atmospheric pressure	z = number of cylinders
f = coefficient of friction loss	P_{me} = mean effective pressure	ζ = coefficient of loss at curvature
L_E = geometrical length of exhaust pipe	R = gas constant	κ = specific heat ratio
L_{eq} = equivalent length	T = absolute temperature	η = efficiency
m = mass	t = time	ρ = density
	u = velocity	

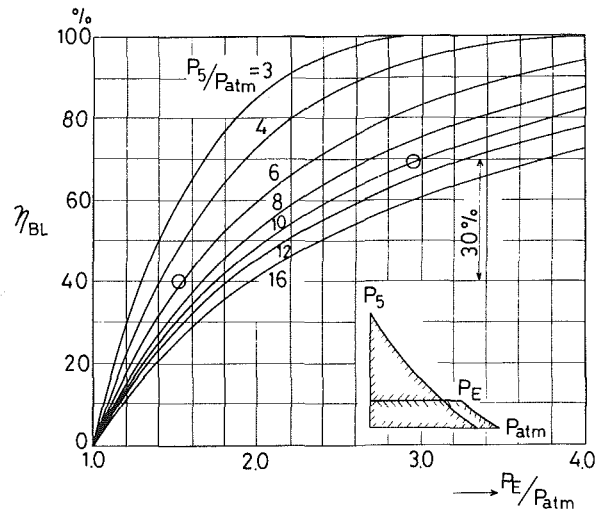


Fig. 2 Blow-down efficiency of constant pressure turbocharge system

Blow-down Energy and Factors Affecting its Utilization Efficiency. Figure 1 shows the concept of blow-down energy, W_{BL} , along with its transferred and transported value, W_{BC} , W_E , W_T and W_B .

Suppose that the engine is at the timing of exhaust open (EO) and the working fluid in the cylinder contains internal energy, U_5 , as shown in Fig. 1

We shall define blow-down energy, W_{BL} , as the theoretically available work, W_{567} . This is contained in the working fluid in the cylinder as shown in the figure. W_{BC} and W_E shall be defined as the available energy in the working fluid at the cylinder outlet and in front of the exhaust gas turbine, respectively. W_{BC} is usually smaller than W_{BL} depending on the types of blow-down. We shall call W_E available exhaust gas energy. W_T is net output of the turbine, and W_B that of the blower.

Furthermore, we shall define the efficiencies concerned as follows:

- η_{uE} = utilization efficiency of blow-down energy
- η_{BL} = blow-down efficiency
- η_{TP} = transport efficiency of exhaust pipes
- η_T = turbine efficiency
- η_{Bad} = adiabatic efficiency of blowers

As the relation between the factors mentioned above, we have

$$\eta_{uE} = \frac{W_{BC}}{W_{BL}} \cdot \frac{W_E}{W_{BC}} \cdot \frac{W_T}{W_E} \cdot \frac{W_B}{W_T} = \eta_{BL} \cdot \eta_{TP} \cdot \eta_T \cdot \eta_{Bad} \quad (1)$$

The fundamental factors concerned with the thermal efficiency of the type of the turbocharge systems are η_{BL} , η_{TP} , and η_T . Therefore, these factors shall be discussed in the following section.

Blow-down Efficiency. In the pulse turbocharge system all the blow-down energy, W_{BL} , is assumed to be transferred into

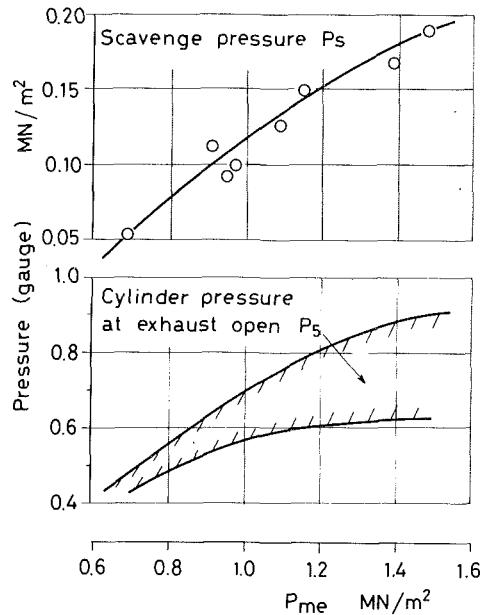


Fig. 3 An example of historical development of scavenge pressure and cylinder pressure at exhaust open in relation to mean effective pressure (data from some different two-cycle engines)

kinetic energy at the cylinder outlet and accordingly η_{BL} to be 100 percent in this type of turbocharging.

In the constant pressure turbocharge system, however, all the expansion work $W_{5E'E}$ is assumed to be changed into heat $Q_{E'E}$ at the cylinder outlet as shown in Fig. 1. Then, $Q_{E'E}$ heats the working fluid under the constant exhaust pressure, P_E , to make it expand over E'E. The process, Er, is adiabatic expansion.

With the assumptions described above, the blow-down efficiency of the constant pressure turbocharge system η_{BL} is obtained as follows

$$\eta_{BL} = \frac{\frac{1}{\kappa-1} \left\{ \frac{P_5}{P_{atm}} - 1 \right\} - \frac{\kappa}{\kappa-1} \left\{ \frac{1}{\kappa} \frac{P_5}{P_E} \left(\frac{P_E}{P_{atm}} \right)^{\frac{1}{\kappa}} + \frac{\kappa-1}{\kappa} \left(\frac{P_E}{P_{atm}} \right)^{\frac{1}{\kappa}} - 1 \right\}}{\frac{1}{\kappa-1} \left\{ \frac{P_5}{P_{atm}} - 1 \right\} - \frac{\kappa}{\kappa-1} \left\{ \left(\frac{P_5}{P_{atm}} \right)^{\frac{1}{\kappa}} - 1 \right\}} = f(P_5/P_{atm}, P_E/P_{atm}) \quad (2)$$

Figure 2 shows the calculated result of η_{BL} as function of P_E/P_{atm} and P_5/P_{atm} . As is shown, the blow-down efficiency η_{BL} of the constant pressure turbocharge system is very low in the range of lower P_E/P_{atm} . It also shows that η_{BL} rapidly increases and approaches that of the pulse turbocharge system, $\eta_{BL} = 100$ percent with increase of P_E/P_{atm} , if P_5/P_{atm} is kept constant.

Figure 3 shows a plot of data obtained on some two-cycle engines. It shows how P_s and P_5 have actually increased in relation to P_{me} . In the constant pressure turbocharge system, P_E is approximately equal to the scavenging pressure P_s . Therefore, P_5/P_{atm} can approximately be used instead of P_E/P_{atm} in Fig. 2.

Applying the smallest and the largest value of P_5/P_{atm} , respectively, to Fig. 2, we know that the blow-down efficiency increased by about 30 percent corresponding to the increase of P_{me} from 0.7 ~ 1.5 MN/m² in the case of two-cycle engines as shown in the figure.

Summarized Review Over Thermal Efficiency. Gas speed in the exhaust pipe is assumed to be zero in the constant pressure turbocharge system in the model shown in Fig. 1. Therefore, there is no loss of kinetic energy in the exhaust pipe in this

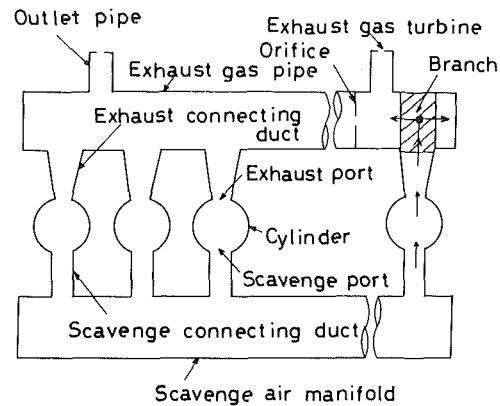


Fig. 4 Model of engine gas flow systems

system, while some loss is inevitable in the pulse turbocharge system. As a result, η_{TP} is greater in the constant pressure turbocharge system than in the pulse turbocharge system. An example of measured η_{TP} is reported to be 55 ~ 68 percent depending on the types of the branch [5]; straight pipe, three-way, or four-way branch.

As is well known, the turbine efficiency η_T is also greater in the constant pressure turbocharge system. This is because energy loss in the exhaust turbine is greater in the pulse turbocharge system due to partial admission and pulsating flow.

In conclusion, the higher thermal efficiency of the constant pressure turbocharge system in the range of higher mean effective pressure is due to the better blow-down efficiency of the system in the higher range than in the lower range of mean effective pressure.

This chapter presented the thermodynamical features of the constant pressure turbocharge system. It is required, however,

to optimize engine parameters in order to incorporate the features into actual engines. For example, longer effective stroke can incorporate the higher utilization efficiency of blow-down energy in improving thermal efficiency of engine plants.

Performance Simulation System

Engine Model and Flow Equation. A performance simulation system of high accuracy is an effective tool not only for the study on the interaction between engine performance and pulsation but also for fine optimization of engine parameters.

As shown in Fig. 4, a two-cycle engine of the constant pressure turbocharge system type is assumed to consist of the following five elements:

- 1 Pipe :exhaust and scavenge pipe, connecting ducts, outlet pipes
- 2 Nozzle :scavenge and exhaust ports, and exhaust gas turbine
- 3 Throttle:orifice in pipe
- 4 Branch :junction point of pipes
- 5 Volume:cylinders

Four-cycle engines can also be represented by the model of Fig. 4, replacing ports with valves.

Mathematical models are required for all the aforementioned elements, including those for the processes of compression, combustion, expansion and gas exchange in cylinders. The mathematical models for gas flow were presented in the previous report in detail and those for the events in cylinders are the familiar ones, used in performance simulation such as the energy equation, Eicherberg's equation for heat transfer, Wiebe's formula for heat release, and so forth. Therefore, only the equation of the unsteady flow is needed to be presented here in relation to the following discussion.

$$\frac{\partial}{\partial t} \begin{pmatrix} \rho \\ \rho u \\ e \end{pmatrix} + \frac{\partial}{\partial x} \begin{pmatrix} \rho u \\ \rho u^2 + P \\ \frac{\rho u^3}{2} + \frac{\kappa}{\kappa-1} P u \end{pmatrix} = \begin{pmatrix} X \\ Y \\ Z \end{pmatrix} \quad (3)$$

where

$$e = \frac{\rho u^2}{2} + \frac{1}{\kappa-1} P$$

$$X = -\frac{\rho u}{F} \frac{\partial F}{\partial x}$$

$$Y = -\left(\frac{\rho u^2}{F} \frac{\partial F}{\partial x} + \rho \Delta P \right)$$

$$Z = \rho q - \frac{1}{F} \frac{\partial F}{\partial x} \left(\frac{\rho u^3}{2} + \frac{\kappa}{\kappa-1} u p \right)$$

q = rate of heat generation in unit time

ΔP = (friction loss) + (loss at curvature)

$$= \Delta p_f + \Delta p_c = \left(\frac{4f}{D} + \zeta \right) \frac{\rho |u|}{2}$$

Improving Accuracy of Simulation. As described already, the accuracy of predicted gas flow quantity is important in the simulation of engine performance.

By using the characteristic method in our new system modified for the simulation of engine performance, it was noticed that gas flow quantity per engine cycle was not necessarily equal at each cross section of a flow path, although it gave a correct prediction of pressure fluctuation. Also, it required rather too much computational time. Therefore, the former difficulty must be overcome above all in order to establish a simulation system for the engine performance, including the analysis of unsteady flow.

An observation of the two-step, Lax-Wendroff's method, a method of difference calculus, hints towards a possibility of overcoming the former difficulty encountered in the characteristic method, because it keeps the style of the integral of the conservation form equations of fluid dynamics in its computational procedure as described below. Furthermore, the two-step, Lax-Wendroff's method has been proved to save computational time in comparison with the characteristic method [6], and, therefore it can be expected that the method may overcome the two difficulties just above. In the simulation system using the two-step Lax-Wendroff's method, the characteristic method is also used at the boundaries.

Equation (3) itself is expressed in the conservation form which is represented in a general form as

$$\frac{\partial \mathbf{U}}{\partial t} + \frac{\partial \mathbf{F}}{\partial x} = \mathbf{B} \quad (4)$$

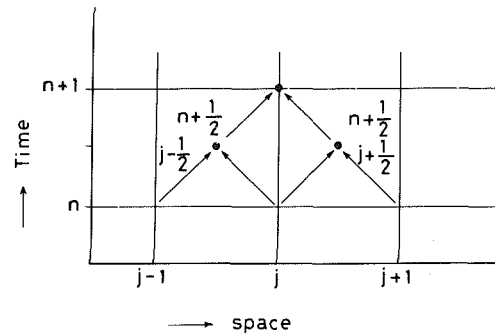


Fig. 5 Two-step Lax-Wendroff's method

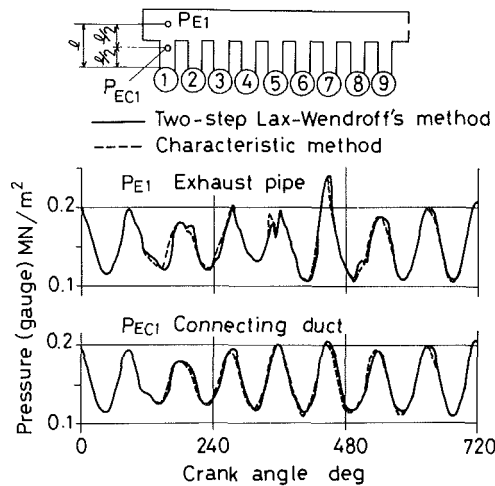


Fig. 6 Comparison between simulated pulsations

where \mathbf{U} is the vector of such components as mass, ρ , momentum, ρu , and energy e , per unit volume, and \mathbf{F} the function of \mathbf{U} or $\mathbf{F} = \mathbf{F}(\mathbf{U})$, and \mathbf{B} the vector of such terms as friction, heat transfer and area change.

By integrating the homogeneous equation of the formula (4), i.e., $\partial \mathbf{U} / \partial t = -\partial \mathbf{F} / \partial x$, from x_1 to x_2 along the flow path and manipulating the result, we have

$$\frac{d\mathbf{S}}{dt} = \mathbf{F}(x_1) - \mathbf{F}(x_2) \quad (5)$$

where

$$\mathbf{S} = \int_{x_1}^{x_2} \mathbf{U} dx \quad (6)$$

The term \mathbf{S} is the vector of total amounts of mass, momentum, and energy, respectively, in a slab from x_1 to x_2 , and $d\mathbf{S}/dt$ its time derivative. $\mathbf{F}(x_1)$ and $\mathbf{F}(x_2)$ are, therefore, flow rates at points x_1 and x_2 , respectively.

Thus, the integral of the equation (5) over one engine cycle must be equal to zero, and we have

$$\int_t^{t+T} \frac{d\mathbf{S}}{dt} dt = 0$$

Then, we have

$$\int_t^{t+T} \mathbf{F}(x_1) dt = \int_t^{t+T} \mathbf{F}(x_2) dt \quad (7)$$

where T is the time for one engine cycle.

Equation (7) shows that integral of flow rate over one engine cycle is equal at every cross section of a flow path in the periodical solution of the conservation form equation.

The result implies that a method which keeps the style of the

Table 1 Comparison of simulated gas flow quantity per engine cycle: Lax, two-step Lax-Wendroff's method; Char, characteristic method

Engine	Two-cycle		Four-cycle			
	10 cylinders		12 cylinders		9 cylinders	
Method of calculation	Lax	Char	Lax	Char	Lax	Char
$m_{ZE}/\text{kg cycle}$	3.89	4.13	0.269	0.273	0.422	0.421
$m_{TC}/\text{kg cycle}$	3.90	3.68	0.270	0.268	0.416	0.416
Measurement kg/cycle	3.92		0.266		0.421	
Ratio of computational time	1.0	1.3	1.0	1.6	1.0	1.4

$m_{ZE}; m_{TC}$; gas flow quantity per engine cycle through exhaust ports and exhaust turbines respectively

integral of the conservation form equation in its computational procedure may give better agreement among calculated gas flow quantities per engine cycle at different points along a flow path than the characteristic method.

The two-step, Lax-Wendroff's method is proved to keep the style of the integral of the conservation form equation (7).

It is obtained from Taylor's series of $U(x, t + \Delta t)$ and finally represented as

$$U_{j+1/2}^{n+1/2} = \frac{1}{2} (U_{j+1}^n + U_j^n) - \frac{\Delta t}{2\Delta x} \{F(U_{j+1}^n) - F(U_j^n)\} \quad (8a)$$

$$U_j^{n+1} = U_j^n - \frac{\Delta t}{\Delta x} F(U_{j+1/2}^{n+1/2}) - F(U_{j-1/2}^{n+1/2}) \quad (8b)$$

where subscripts j refer to space and superscripts n to time in the grid of $x-t$ space.

In this method, U_j^{n+1} is calculated based on the information at points $n + 1/2$ and $j \pm 1/2$, as shown in Fig. 5, and it is of second-order accuracy while the characteristic method is usually of first-order accuracy. The equation (6) shall be approximated by

$$S^n = \sum_{j=j_1}^{j_2} U_j \Delta x \quad (9)$$

Thus, in place of the equation (8b), we have

$$\frac{S^{n+1} - S^n}{\Delta t} = F(U_{j_1-1/2}^{n+1/2}) - F(U_{j_2+1/2}^{n+1/2}) \quad (10)$$

which shows that the computational procedure of the two-step, Lax-Wendroff's method correctly keeps the style in the integral of the conservation form equation of fluid dynamics.

As in the case of the periodical solution (7) for the differential equation, we have

$$\sum_n F(U_{j_1-1/2}^{n+1/2}) \Delta t = \sum_n F(U_{j_2+1/2}^{n+1/2}) \Delta t \quad (11)$$

(one cycle) (one cycle)

Figure 6 shows a comparison between the calculated pressure fluctuation by the two-step, Lax-Wendroff's method and that by the characteristic method. It shows good agreement between them.

Table 1 shows a comparison between the simulated gas flow quantities per engine cycle by the two-step, Lax-Wendroff's method and those by the characteristic method in a two-cycle and a couple of four-cycle engines. m_{ZE} and m_{TC} refer to the gas flow quantities per engine cycle at exhaust ports and exhaust gas turbines, respectively. For the two-cycle engine, the calculated flow quantities m_{ZE} and m_{TC} agree more ac-

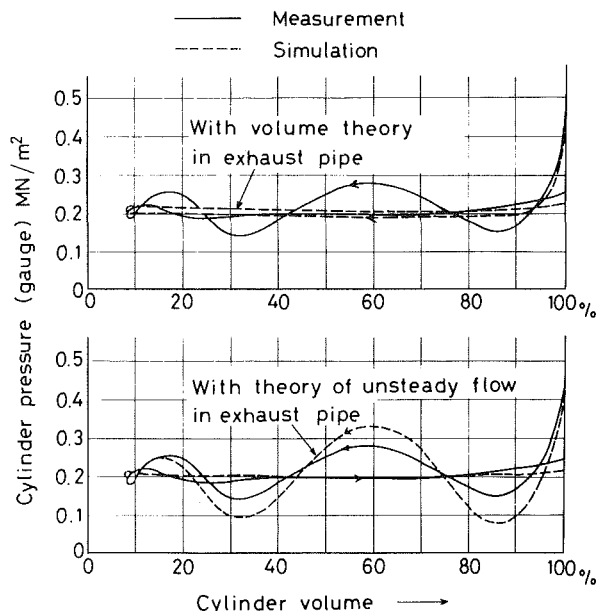


Fig. 7 A comparison of measurement with simulations of PV-diagram (four-cycle engine)

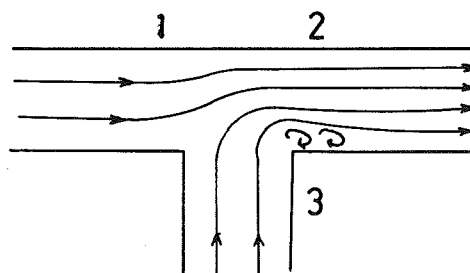


Fig. 8 An example of branch flow

curately with the two-step, Lax-Wendroff's method. In the case of the four-cycle engines, however, m_{ZE} and m_{TC} agree very well not only in the simulation by the two-step, Lax-Wendroff's method but also in that by the characteristic method.

In our experience the characteristic method produces calculated flow rate per engine cycle equal enough at every point of a flow path in isentropic systems, for example, in the simulations of motoring. On the other hand, the characteristic method sometimes brings about some discrepancy among calculated flow rates at different points of a flow path in the simulations of actual engine cycle.

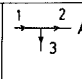
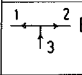
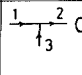
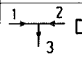
This is probably because the characteristic method originally pursues propagation of pressure waves very well, but it does not follow the transfer of fluid elements with enough accuracy.

The result also shows that the computational time is shorter by 30 ~ 60 percent by using the two-step Lax-Wendroff's method.

In conclusion, the two-step, Lax-Wendroff's method has made it possible to predict the unsteady flow with enough accuracy in a simulation system for engine performance. Therefore, the new system using the two-step Lax-Wendroff's method shall be used in the study hereafter.

The performance simulation system is so constructed that the event in the exhaust pipe can be simulated not only by the filling and emptying method but also by the theory of unsteady flow. The former method, also called volume theory,

Table 2 Pressure drop at branch (Benson's momentum theory)

Flow type		Pressure drop
Separating flow	 A	$\Delta P_{12} = P_1 - P_2 = C_1(\rho_2 u_2^2 - \rho_1 u_1^2)$ $\Delta P_{13} = P_1 - P_3 = C_2 \rho_3 u_3^2$
	 B	$\Delta P_{12} = P_1 - P_2 = C_3(\rho_2 u_2^2 - \rho_1 u_1^2)$ $\Delta P_{13} = P_1 - P_3 = -C_3 \rho_1 u_1^2$
Joining flow	 C	$\Delta P_{12} = P_1 - P_2 = C_4(\rho_2 u_2^2 - \rho_1 u_1^2)$ $\Delta P_{13} = P_1 - P_3 = 0$
	 D	$\Delta P_{12} = P_1 - P_2 = 0$ $\Delta P_{13} = P_1 - P_3 = C_6 \rho_3 u_3^2$
		$C_1 = 0.3 \quad C_2 = 0.6 \quad C_3 = 0.75 \quad C_4 = 0.9 \quad C_6 = 0.85$

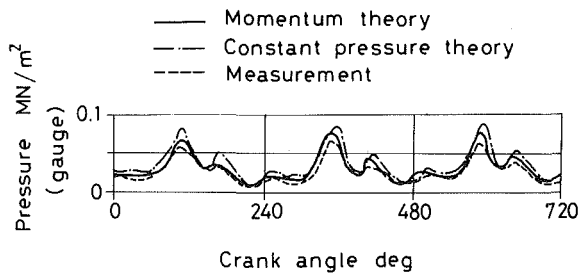


Fig. 9 A comparison of exhaust pulse simulations with measurement (simulated at half load; 93 KW/cyl, 750 rpm)

neglects flow process in pipes and observe them as volume. The latter method shall be called the "precise method" for convenience.

Figure 7 shows a measured PV-diagram with two simulations by the method mentioned above. It shows that the simulation by the precise method reproduces the pressure pattern in the cylinder very well. The simulation by the volume theory is, however, very different from the measurement.

As a result, a system for simulating interaction between the exhaust pulsation and engine performance has been established.

Characteristics of Pulsating Flow

Characteristics of Flow at Branch. In the analysis of unsteady flow in the exhaust system of the constant pressure turbocharged engines, the simplest mathematical model at the branch, i.e. the constant pressure theory can be used [1]. Thus, we have $p_1 = p_2 = p_3$ in Fig. 8.

It was briefly described in the previous report that the constant pressure theory at the branch is one of the features of the pulsating flow of the constant pressure turbocharge system and that Benson's momentum theory makes it possible to attribute the feature to the large area ratio $(D_E/d_E)^2$ where D_E is the diameter of the exhaust pipe and d_E that of the connecting duct.

Benson's momentum theory (8), calculates pressure drop at the branch by using the formulas shown in Table 2 in the case of the pulse turbocharge system. He confirmed that the theory produced a good result when applied to an experimental unit consisting of pipes of 41.6-mm dia and pulse generator. In the simulation, the factors $C_1 \sim C_6$ shown in Table 2 were used which were obtained in the experimental unit under steady flow.

Figure 9 shows a comparison between pressure fluctuation measured in a pulse turbocharged four-cycle medium size engine of 560 kW at 750 rpm with six cylinders, as shown in

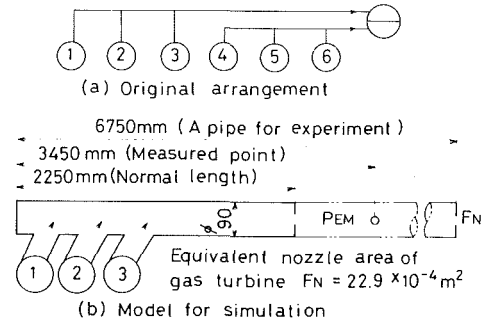


Fig. 10 Exhaust system of a pulse turbocharged four-cycle engine R6V 22/30ATL 560KW, 750rpm

Fig. 10(a), and simulations on the same engine using Benson's momentum theory and the constant pressure theory at the branch, respectively. The measurement and the simulations were made for the half-load of the engine, and the pulsation in Fig. 9 is the one at the point P_{EM} in an exhaust pipe for experiment as shown in Fig. 10(b). Figure 9 shows that the simulation using Benson's momentum theory is in closer agreement with the measurement.

As a result, it has been confirmed that Benson's momentum theory using the factors $C_1 \sim C_6$ in Table 2 reproduces unsteady flow at the branch very well as measured in actual engines. In this section, therefore, the characteristic of flow at the branch will be discussed in more detail based on Benson's momentum theory, presenting some analytical data.

Figure 11 shows simulated fluctuation of gas velocity, u , and density of gas ρ , at the branch in front of the No. 3 cylinder in the exhaust pipe shown in Fig. 10.

The simulation was made for both turbocharge systems where the constant pressure turbocharge system is simply an assumed modification of the pulse turbocharge system shown in Fig. 10(b), i.e., a three-cylinder engine. This was achieved by making the cross-sectional area of its exhaust pipe nine times larger.

Figure 11(a) shows that during blow-down in the pulse turbocharge system the gas velocities at the branch are $u_1 = -100$, $u_2 = 230$, and $u_3 = 300$ m/s, where u_1 and u_2 are the velocities upstream and downstream in the exhaust pipe at the branch, respectively, and u_3 the velocity in the connecting duct as shown in the figure. Thus, the flow during blow-down is of type B as shown in Table 2.

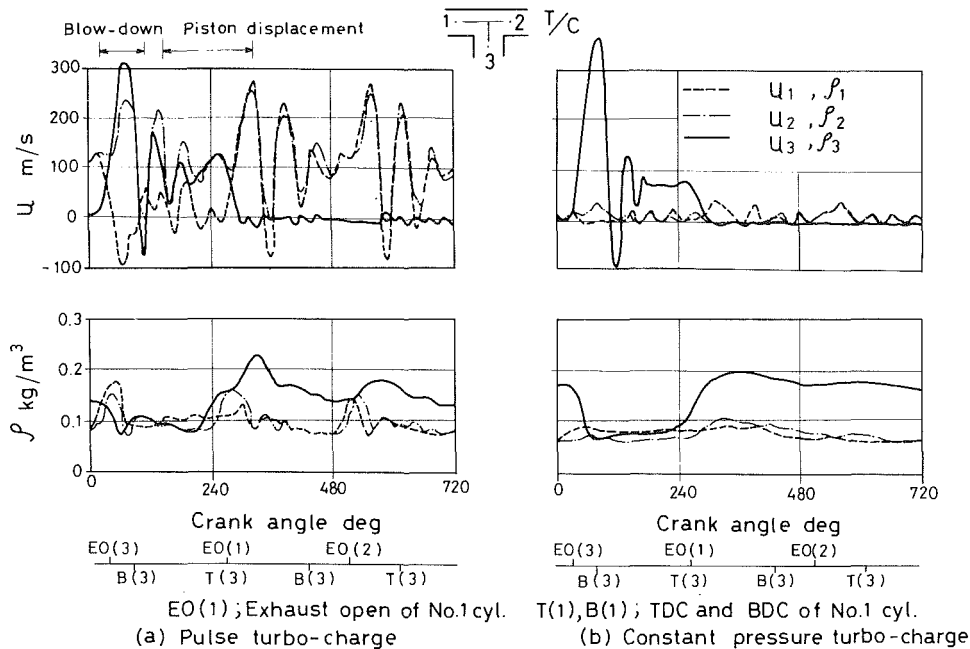
Just after blow-down is finished, the gas in the connecting duct flows backwards to the cylinder to result in flow type A, which continues, however, for a negligible period.

Then, the displacement stroke of the piston follows and the gas in the connecting duct again flows downwards to the branch, with the result that the flow is of type C throughout the whole period following blow-down.

As a whole, the flow at the branch in the pulse turbocharge system can be considered to be of type B during blow-down and of type C during the following period.

Based on observation of Fig. 11(b), it can be approximately regarded that the flow at the branch is of type C over one engine cycle in the constant pressure turbocharge system.

Figure 12 shows a calculated result of pressure drop, ΔP , at the branch over one engine cycle in both turbocharge systems. It shows that the pressure drop cannot be negligible in the pulse turbocharge system because $|\Delta P_{12}|$ and $|\Delta P_{23}|$ range from 0.01 ~ 0.03 MN/m², covering approximately one engine cycle. In the constant pressure turbocharge system, however, ΔP is so small that it can be negligible, although $|\Delta P_{13}|$ and $|\Delta P_{23}|$ are about 0.02 MN/m² or less during a very short period just after blow-down. The simulation shown in Fig. 12(b) was made for the six-cylinder engine of the



EO(1); Exhaust open of No.1 cyl. T(1),B(1); TDC and BDC of No.1 cyl.
 (a) Pulse turbo-charge (b) Constant pressure turbo-charge

Fig. 11 Fluctuation of gas velocity and density at a branch (three-cylinder engine)

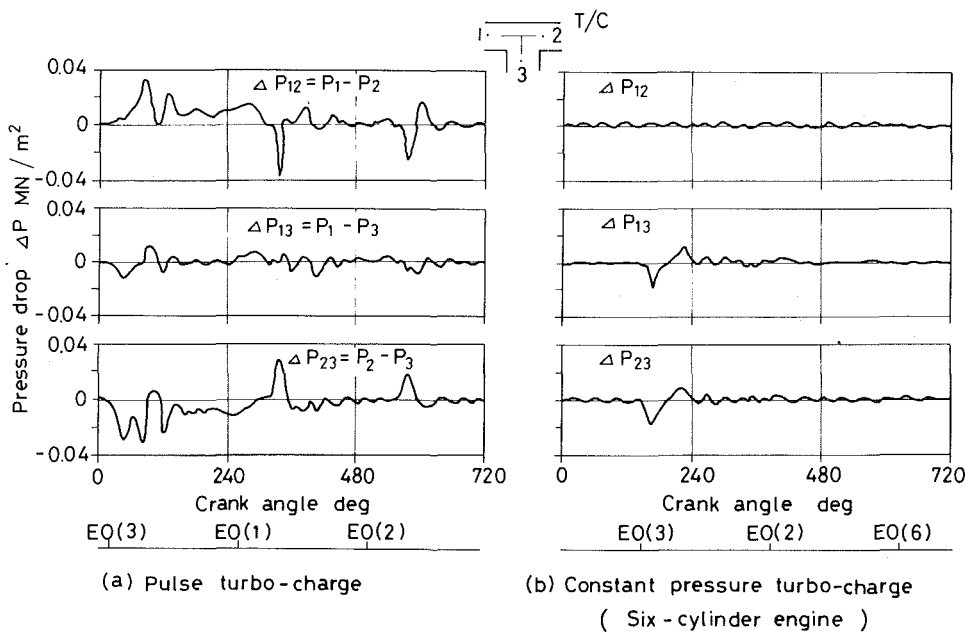


Fig. 12 Simulated pressure drop at a branch

constant pressure turbocharge system modified from the pulse turbocharged engine shown in Fig. 10(a), while the simulation shown in Fig. 11(b) was made for the three-cylinder engine as already described.

As another characteristic of the pulsating flow in the constant pressure turbocharge system, the pressure drop at the branch can be regarded as being not directly dependent on the gas velocity in the connecting duct. This is because the flow in the duct is approximately of flow type C over one engine cycle and because the pressure drop of flow type C is represented by the formula $\Delta P = C(\rho_2 u_2^2 - \rho_1 u_1^2)$ where C is an experimental coefficient.

On the other hand, the above formula shows that the flow in the connecting duct theoretically has effect on ΔP through its effect on the momentum $\rho_1 u_1^2$ and $\rho_2 u_2^2$. This is,

however, actually negligible because a flow of high speed in the connecting duct is slowed down so considerably in the exhaust pipe that it has no effect upon the velocities u_1 and u_2 and the densities ρ_1 and ρ_2 in the exhaust pipe as shown in Fig. 11(b). That is, the flow in the connecting duct has no effect upon the momentum $\rho_1 u_1^2$ and $\rho_2 u_2^2$. This is due to the large area ratio $(D_E/d_E)^2$ where D_E and d_E are the diameters of the exhaust pipe and the connecting duct respectively.

In conclusion, it has been demonstrated, based on Benson's theory, that the pressure drop at the branch is negligible in the constant pressure turbocharge system and that this is due to the large area ratio $(D_E/d_E)^2$ in this system.

A Consideration on Experimental Units. As described in the previous report, two experimental units are used in this

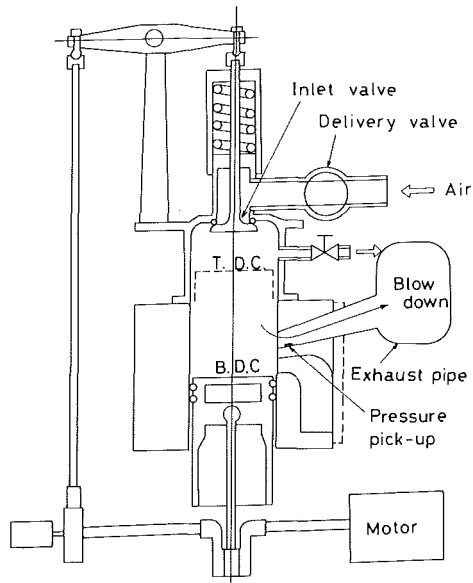


Fig. 13 Experimental unit for continuous blow-down

study. One of them, called a one-dimensional unit, is constructed of pipes of 53-mm dia and generates continuous blow-down with three rotary valves. The other one which is a half-scale model of a two-cycle engine is constructed of an exhaust pipe of 550-mm dia and a cylinder of aluminum casting, in which pulsation is generated by a single blow-down from the cylinder.

As a preparatory test for the experiment to be presented in the following section, an investigation was made to clarify whether the pulsation generated by a single blow-down is fundamentally the same as that by a continuous one.

Figure 13 shows the experimental unit for continuous blow-down modified from the test unit for a single blow-down. The inlet valve which is governed by the cam mechanism is open and supplies compressed air to the cylinder while the piston moves from T.D.C. to the point about 30 millimeters above the exhaust ports. Figure 14 shows the cross section of the cylinder and the points where pressure fluctuations were measured during blow-down.

Figure 15 is a measurement [1] in the experimental unit for a single blow-down, while Fig. 16 is a measurement in the unit for continuous blow-down. As shown in the figures, the pattern of the pressure fluctuation in Fig. 15 is fundamentally the same as that in Fig. 16 and, therefore, experimental study on the characteristics of pulsating flow in the constant pressure turbocharge system can be made on the unit for a single blow-down.

Characteristics of Waves at an Orifice in Pipe-End or Halfway in Flow Path of the Pipe. Figure 17 shows an exhaust pipe whose cross-sectional area is F_E . The term F_N is the area of an orifice in the end of the pipe which shall be called a nozzle, an equivalent of an exhaust gas turbine, while F_0 in Fig. 17 is the area of an orifice located halfway down the exhaust pipe. The area ratios β_N and β_0 shall be defined as $\beta_N = F_N/F_E$ and $\beta_0 = F_0/F_E$, respectively, as shown in Fig. 17.

An experimental study by Yamada et al. [9], reports that a pipe-end nozzle with $\beta_N \geq 1/2$ can be regarded as an open end and that with $\beta_N \leq 1/6$ a closed end. Between $\beta_N = 1/6 \sim 1/2$, there is a value of β_N where there occurs almost no reflection of pressure wave. This is found to be $\beta_N \doteq 1/4$, which means that a pipe with the nozzle of $\beta_N \doteq 1/4$ can be regarded as one of infinite length.

This study by Yamada et al. was made on an experimental

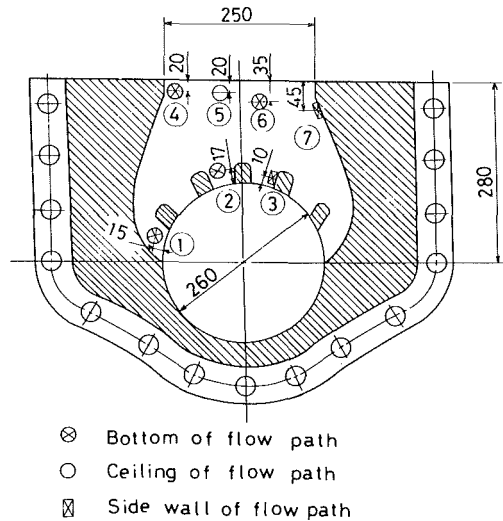


Fig. 14 Detailed cross-sectional view of the cylinder model and measured points

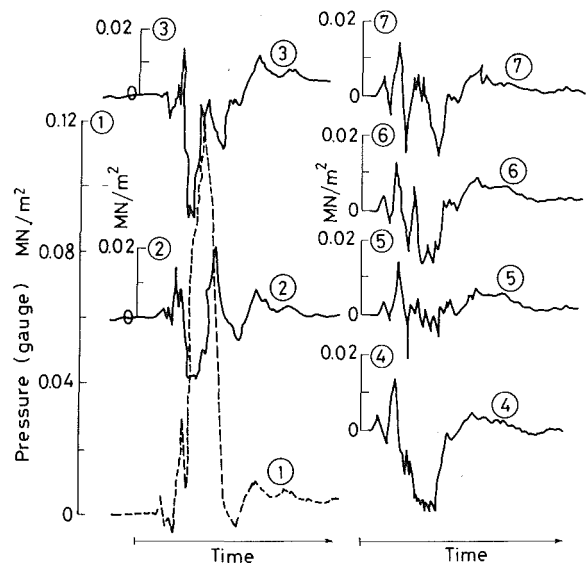


Fig. 15 Pulsation in the experimental unit for single blow-down

unit in which L_E/D_E , or the ratio of the length to the diameter of the pipe is quite large, i.e., $L_E/D_E \doteq 180$ with the diameter being 41.6 mm. However, the diameter of the exhaust pipe in the constant pressure turbocharge system is much larger, while L_E/D_E is much smaller than those mentioned above. For example, $D_E \doteq 550$ mm and $L_E/D_E \doteq 30$ in a model four-cycle engine to be referred to later.

In order to confirm, therefore, whether the aforementioned experimental result also applies to the pulsation in the exhaust pipe of the constant pressure turbocharge system, an experiment was made on the test unit which is a half-scale model of the exhaust system of a two-cycle engine and generates a single blow-down [1].

Figure 18 shows an experimental result on the characteristics of the pressure wave at a pipe-end nozzle with $L_E/D_E \doteq 10$. It shows that the nozzle of $\beta_N \geq 0.5$ can be regarded as an open end because the reflected negative waves are almost the same in magnitude in both cases of $\beta_N = 0.5$ and 0.65 . It also shows that reflection is negligible with $\beta_N = 0.25$.

In another experiment where the characteristics of pressure wave at an orifice halfway down the flow path were investigated, the area ratio of nozzle was kept constant at $\beta_N =$

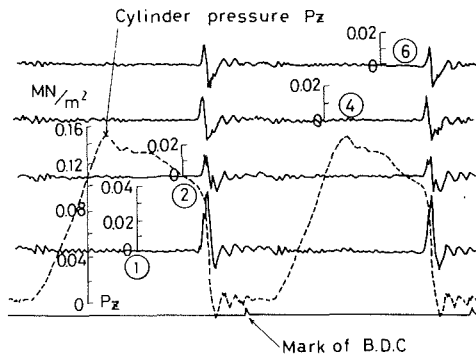


Fig. 16 Pulsation in the experimental unit for continuous blow-down

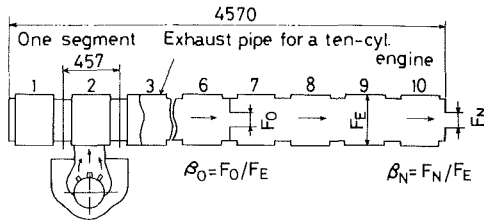


Fig. 17 Test unit for a single blow-down (half-scale model of a two-cycle engine)

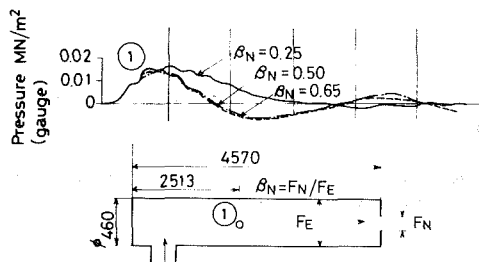


Fig. 18 Wave reflection at pipe end (experimental result)

0.25 so that the exhaust pipe might be an equivalent of the one of infinite length. Figure 19 shows the results for $\beta_0 = 0.1$, 0.25, etc. It shows that the wave passes through without any damping with $\beta_0 \geq 0.5$, while it is damped to about half in magnitude with $\beta_0 = 0.25$ and down to about one-tenth with $\beta_0 = 0.10$. The result hints also that an orifice to be inserted in the exhaust pipe for damping pulsation must be such a one with $\beta_0 < 0.5$.

Figure 20 and 21 are the simulations for the similar cases in Figs. 18 and 19, respectively, which produce the same result as the experiment.

The results in Figs. 18 ~ 21 leads to the first conclusion that the experimental result shown by Yamada et al. on the characteristics of pressure wave at a pipe-end nozzle applies

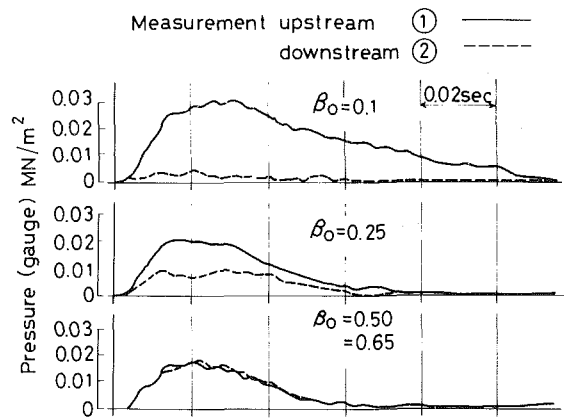


Fig. 19 Damping of pressure wave through an orifice in pipe (experimental result)

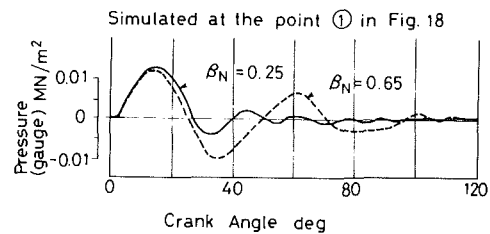


Fig. 20 A simulation of wave reflection at pipe end

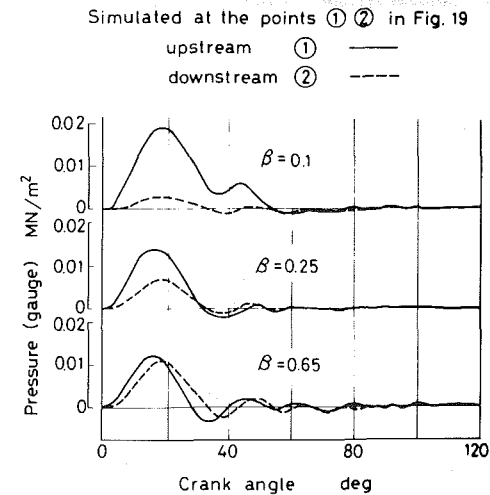


Fig. 21 Damping of pressure wave through an orifice in pipe (calculated result)

also to the exhaust system of the constant pressure turbocharged diesel engines and the second conclusion that the system developed in this study to analyze pulsating flow simulates the events at boundaries very well.

In the actual exhaust system of the constant pressure turbocharged engines, the exhaust turbine is considered to act only as a closed end because β_N is usually small enough, i.e., $\beta_N \leq 1/6$ in this system, while a nozzle is regarded as an open

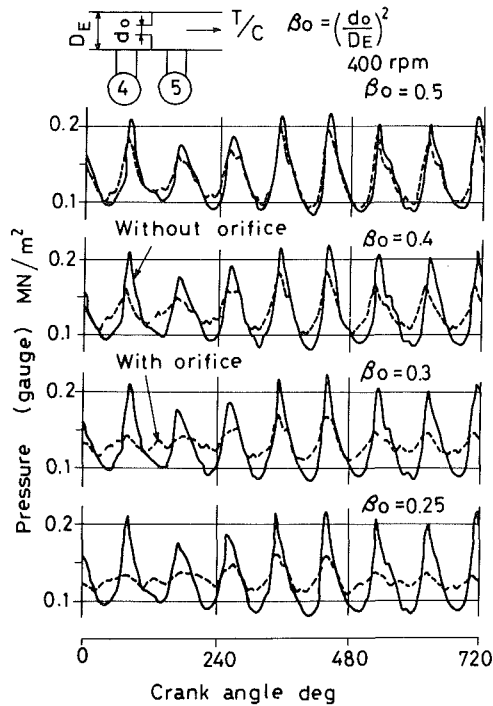


Fig. 22 Pulsation with or without an orifice in pipe (in front of turbine)

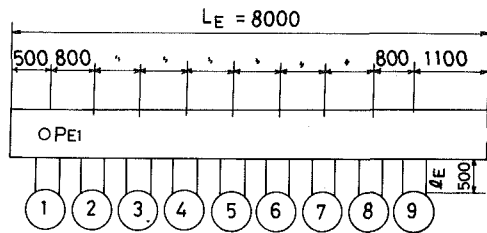


Fig. 23 Exhaust system of a four-cycle engine with nine cylinders

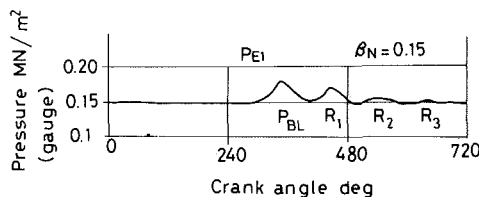


Fig. 24 A simulation of pulsation by a single blow-down from No. 1 cylinder of nine-cylinder engine (constant pressure turbo-charge)

end with $\beta_N \geq 0.5$ and it shows the mixed characteristics of closed and open end with $1/6 < \beta_N < 1/2$.

Damping Effect of Orifices. Such unfavourable results as described in the introduction are brought about by pulsation of unexpectedly large amplitude, unfavourable pattern of the pulsations or both. In such case orifices are inserted in the exhaust pipe to damp the pulsations. The loss caused by the orifice is not clarified yet. However, inserting orifices has brought about favourable results as a whole. We have an experience that fuel consumption was slightly improved by damping the resonant pulsation with the orifice.

An example was already reported in which the simulated damping effect agreed very well with the measured damping [1].

Figure 22 shows a comparison between simulated pulsations without an orifice and those with a orifice between

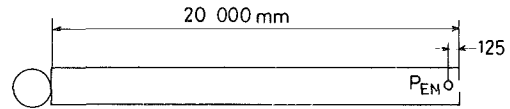


Fig. 25 Model of exhaust system (one-cylinder engine)

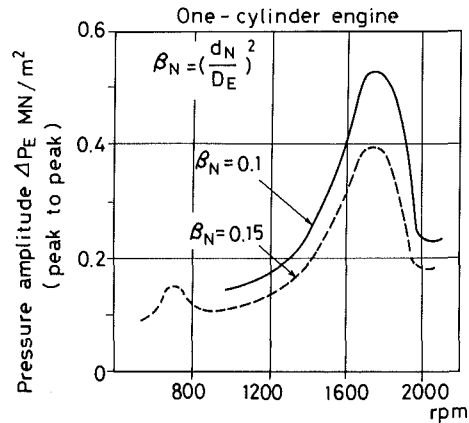


Fig. 26 Effect of area ratio on resonance (in front of turbine)

No. 4 and No. 5 cylinder in the model exhaust system at engine speed $n = 400$ rpm. The model four-cycle engine is shown in Fig. 23. The simulation was made for $\beta_0 = F_0/F_E = 0.25, 0.30, 0.40$, and 0.50 , where F_0 and F_E are the area of the orifice and the exhaust pipe, respectively.

Figure 22 shows that the orifice effectively damps the pulsation without any effect upon the pattern of pressure fluctuation in the range of β_0 covered by the simulation. It also shows, however, that the orifice has no damping effect on the pulsation with $\beta_0 \geq 0.5$.

The foregoing simulation agrees very well with the experiment just described, where the pressure wave passed through an orifice with $\beta_0 \geq 0.5$ without being damped, while it was damped through an orifice with $\beta_0 < 0.5$.

Therefore, orifices with $\beta_0 < 0.5$ must be used in order to damp the pulsation. However, too small orifices should be avoided so that they may not adversely affect engine performance.

Pulsation Resonance in Multicylinder Engines of Medium and Low Speed

Fundamental Features of Pulsation. Many cylinders are connected with one common exhaust pipe in the constant pressure turbocharge system, in which a unique pulsation resonance sometimes occurs.

Based on simulation, we shall discuss (i) basic features related to the pulsation resonance in the constant pressure turbocharge system and (ii) the unique mechanism through which pulsation resonance is caused in the exhaust pipes of multicylinder engines.

The exhaust system of multicylinder engines shall be represented by the model shown in Fig. 23.

Figure 24 shows a simulated pulsation at the point P_{EI} shown in Fig. 23 which is caused by a single blow-down from No. 1 cylinder. We shall call it an element pulsation which consists of the pressure wave P_{BL} and the reflected waves R_j ($j = 1, 2, 3, \dots$) as shown in the figure. The wave P_{BL} is the one that is generated during blow-down and shall be called blow-down wave.

The simulation was made under normal conditions of the model engine, that is, $n = 450$ rpm and $\beta_N = 0.15$.

Figure 24 shows that the element pulsation in the model

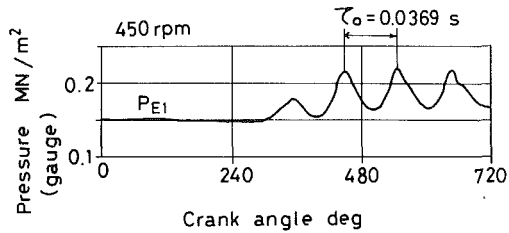


Fig. 27 A simulated element pulsation with both ends closed ($\beta_N = 0.0$)

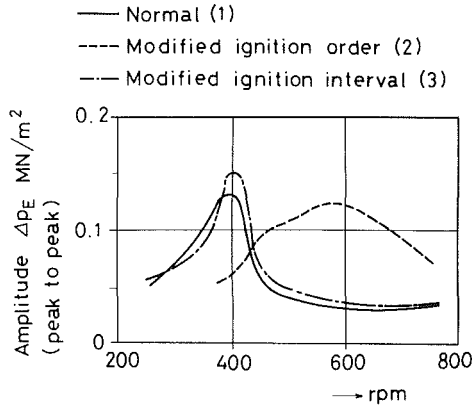


Fig. 28 Effect of some factors on pulsation resonance (in front of turbine)

four-cycle engine is damped after every reflection and eventually vanishes in a little more time than half the engine cycle, i.e., in crank angle of 410 deg. This is because some of the energy contained in a wave flows out through the nozzle every time it reaches the nozzle.

In the constant pressure turbocharge system of medium and low-speed engines, therefore, the pulsation of a certain cycle usually has no effect upon that of the following cycles. This is because the pulsation caused by a blow-down is completely damped with three or four reflections at the nozzle and because the time of one cycle is long enough for the reflections to occur that many times in these engines.

We shall first consider pulsation resonance in the exhaust system of a hypothetical one-cylinder engine shown in Fig. 25. In this case resonance is caused by superposition of the blow-down wave of a cycle on the reflected wave of the previous cycle.

Let f_E be the frequency of the engine and f_0 the natural frequency of the gas column vibration in the exhaust system. Then, the pulsation resonance occurs at $f_E = f_0$ with superposition of P_{BL} on the first reflection R_1 . On the other hand, the resonance at $f_E = f_0/2$ occurs with superposition of P_{BL} on the second reflection R_2 . However, the resonance by P_{BL} and R_2 is expected to be very weak because R_2 is much weaker than R_1 as shown in Fig. 24.

In order to confirm the above consideration, a simulation was made on the hypothetical one-cylinder engine shown in Fig. 25 at various engine speeds under a constant load. Full amplitude of pressure fluctuation ΔP_E at the nozzle is plotted against the engine speeds in Fig. 26.

In every case of the simulation, the exhaust gas temperature T_E and specific heat ratio κ are approximately estimated to be $T_E \doteq 750$ K and $\kappa \doteq 1.33$, respectively, which gives acoustic speed $a = \sqrt{\kappa R T_E} \doteq 535$ m/s, with $R = 287$ J/kg·K. Accordingly, natural frequency of the gas column vibration is approximately calculated to be $f_0 = a/2L_E \doteq 13.4$ Hz and $n = 120 f_0 \doteq 1608$ rpm, which approximately agrees with the resonance speed $n \doteq 1700$ rpm in Fig. 26.

Table 3 Three cases of simulation (Nine-cylinder engine)

Case	Normal	Modified ignition order	Modified ignition interval
Item	(1)	(2)	(3)
Ignition order	1-3-5-7 9-8-6 4-2-1	1-9-2-6 7-5-4-3 8-1	Normal
Ignition interval	Equal 80 deg.	Equal 80 deg.	Unequal See Note 1

Note 1

Ignition order 1 3 5 7 9 8 6 4 2 1
 Ignition interval 90 70 90 70 90 70 90 70 80
 (deg)

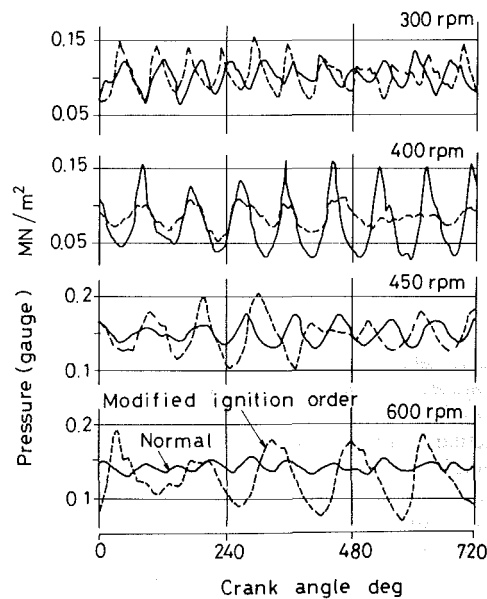


Fig. 29 Pulsation with normal and modified ignition order (in front of turbine)

As expected, the resonance by the second reflection R_2 is so weak that it may be neglected for practical purposes.

It should also be noticed that the pulsation resonance occurs at the same speed $n \doteq 1700$ rpm in both cases with $\beta_N = 0.10$ and 0.15 , which confirms that a nozzle at a pipe-end can be regarded as a closed end with $\beta_N \leq 1/6$, as referred to in the previous chapter.

The foregoing investigation has proved that exhaust pulsation of a certain cycle usually has no effect upon those of the following cycles in the constant pressure turbocharged marine diesel engines of medium and low speed and that the resonance by those reflections other than the first reflection can practically be neglected in these engines.

As a preparation for the discussion in the following section, we shall consider equivalent length L_{eq} of piping systems.

In the foregoing, the natural frequency of gas column vibration in an exhaust pipe with both ends closed was calculated with the formula $f_0 = a/2L_E$ where L_E is simply

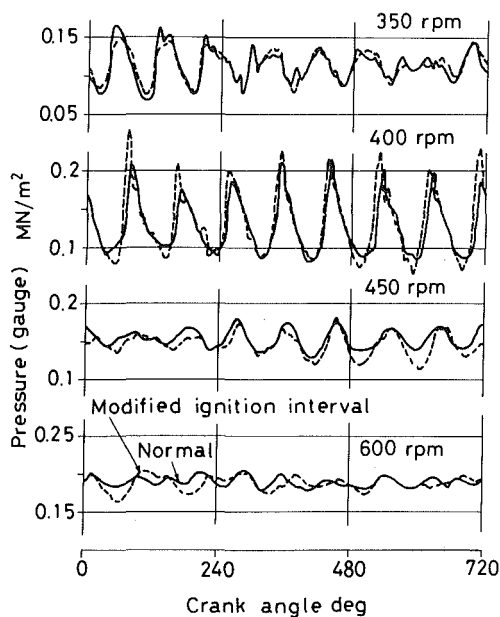


Fig. 30 Pulsation with normal and modified ignition interval (in front of turbine)

the geometrical length of the pipe. For analysis of higher precision, however, it is reasonable to use L_{eq} instead of L_E .

L_{eq} is obtained experimentally by measuring f_0 and the gas temperature t_E to calculate acoustic speed $a = \sqrt{\kappa RT_E}$. Thus, we have

$$L_{eq} = \frac{a}{2f_0} \quad (12)$$

In the model exhaust system shown in Fig. 23, L_{eq} is considered to be mainly affected by the length and volume of the connecting ducts, and the accuracy of the average gas temperature, T_E , which actually fluctuates throughout the engine cycle.

In actual engines it is very difficult to determine L_{eq} experimentally. However, the simulation system developed in this study simulates events in the exhaust system very well as described hitherto. Therefore, L_{eq} is assumed to be estimated by simulation in this study.

Figure 27 shows a simulated element pulsation at 450 rpm with both ends closed. The simulation gives $f_0 \doteq 1/\tau_0 \doteq 27.0$ Hz and $T_E \doteq 750$ K, or $a \doteq 535$ m/s with the result $L_{eq} \doteq a/2f_0 = 9.91$ m, where τ_0 is the natural period of the gas column vibration as shown in the figure.

The pressure wave of the element pulsation with $\beta_N = 0.15$ as shown in Fig. 24 is damped and deformed after every reflection at the nozzle, and makes it difficult to estimate the natural frequency based on it. This is why the element pulsation with both ends closed as shown in Fig. 27 is simulated to estimate f_0 .

Pulsation Resonance in Multicylinder Engines. As previously described, the strongest pulsation resonance in the case of one-cylinder engine is the one which occurs at $f_0 = f_E$.

On the other hand, the speed of medium size engines ranges from 400 ~ 600 rpm and that of large size ones from 100 ~ 200 rpm. Let it be that T_E and κ are 750 K and 1.33, respectively, in both types of engines, and that length of the exhaust pipe L_{eq} is represented with $L_E = 10$ m in the medium-size and $L_E = 15$ m in the large-size engines. Then, the natural frequency of the gas column vibration is approximately calculated to be $f_0 = 26.8$ Hz for the medium and $f_0 = 17.8$ Hz for the large-size engines.

As a result, resonance speed n at $f_0 = f_E$ is estimated to be

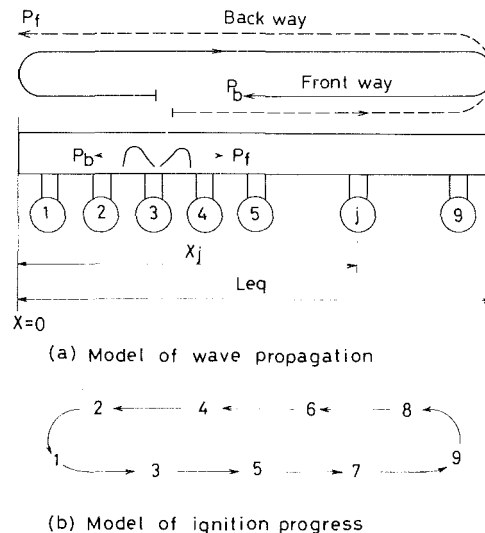


Fig. 31 Model of wave propagation and ignition progress

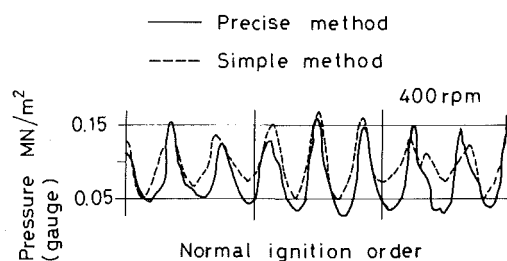


Fig. 32 Comparison between pulsations simulated by different methods

$n \doteq 2500$ rpm in the medium and $n \doteq 1000$ rpm in the large size engines, which are, however, far above the ordinary speeds of these engines. Pulsation resonance at $f_0 = f_E$, therefore, does not take place in the normal operation of these engines.

However, in the range of ordinary speeds, pulsation of unusually large amplitude actually takes place in some of the constant pressure turbocharged engines of medium and low speed [3]. The large amplitude and the pattern of the pulsations suggest those pulsations may be a kind of resonance.

On the model engine shown in Fig. 23, a simulation was made under a constant load for three cases as shown in Table 3; (i) the case of normal condition of the engine, (ii) that of the modified ignition order and (iii) that of unequal ignition interval.

Figure 28 shows a plot a full amplitude of the simulated pressure fluctuation at the nozzle ΔP_E against engine speed, n . Figures 29 and 30 show the pressure fluctuations for the cases of the modified ignition order and the modified ignition interval in comparison with those of normal ignition order.

Figure 28 shows peaks of amplitude at $n = 400$ and 600 rpm, and we shall call the pulsation at these speeds resonance hereafter.

As shown in Figs. 28 and 29, the resonance speed, n and the pattern of pressure fluctuation are highly affected by the ignition order, while they are not affected by unequal ignition interval as shown in Figs. 28 and 30.

Before considering the mechanism of the pulsation resonance, a model for wave propagation and that for the progress of ignition order shall be assumed.

Figure 31 (b) is a model of how the ignition order progresses

making a loop in the case of the normal ignition order. Furthermore, as shown in Fig. 31 (a), two pressure waves, P_b and P_f , are formed by a blow-down and the latter propagates in the same direction as that of ignition order, while the other travels in the opposite direction. P_b and P_f shall be called backward and forward wave, respectively. These waves travel along the exhaust pipe and reflect at the pipe ends.

Replacing the reflection by the U-type turn as shown in the figure, a wave can be assumed to travel in a loop-type way. We shall call it a loop model of wave propagation.

We shall now examine the mechanism of the pulsation resonance at 400 rpm with the normal ignition order, beginning with some calculations for the discussion.

The mean acoustic speed is $a = 535$ m/s and the equivalent length of the exhaust pipe is $L_{eq} = 9.91$ m in the model engine as already estimated. The time δt for one ignition interval is calculated to be $\delta t = 120/n \cdot z = 120/(400 \times 9) = 0.0333$ s.

In an ignition interval, therefore, a pressure wave travels the distance $S_0 = a \cdot \delta t = 17.8$ m $= 2L_{eq} - 2.02$ m $= 2L_{eq} - 2(L_{eq}/z)$, where z is the number of cylinders. Thus, in an ignition interval δt a pressure wave caused by the blow-down of a certain cylinder travels through the exhaust pipe and reaches the point about two cylinders away from where it was generated. As a result, superposition of the blow-down from the cylinder of the neighboring ignition order on the propagating wave can take place.

As shown in the example in Fig. 31, P_b of No. 3 cylinder comes to No. 5 cylinder in δt with the result of superposition of P_b on the blow-down in coherence, while P_f comes to No. 1 cylinder where it may be out of any coherent superposition. This suggests that only the backward waves cause the pulsation resonance at 400 rpm with the normal ignition order.

In the mechanism described above, the backward wave P_b travels round the exhaust pipe eight times in a cycle at 400 rpm and resonant pulsation of eighth order occurs, i.e., eight waves are observed at the pipe ends in a cycle. The event mentioned above is, therefore, a kind of resonance because the blow-down is superposed on the reflected wave in coherence as a driving force of vibration. Furthermore, this is a unique event which is observed in multicylinder engines.

The mechanism of the pulsation resonance in multicylinder engines can be analyzed approximately in the same way as above consideration, including that at 600 rpm with the modified ignition order. However, it is very difficult to predict the shape of pressure fluctuations based on the procedure described above.

In this section, the mechanism through which pulsation resonance occurs in the range of ordinary revolution speed in medium and large size engines of the constant pressure turbocharge system has been examined. Also, it has been demonstrated that the pulsation resonance which is caused at $f_0 = f_E$ is far outside the ordinary operation of these engines.

A Simple Mathematical Model for Pressure Fluctuation and Some Simulations. Exhaust gas pulsation can now be predicted with high accuracy by the simulation system described hitherto, which shall be called a precise simulation system or a precise method as against a simple method to be described in the following.

Simulation by the precise method requires computers of high performance together with much computational time and cost. On the other hand, prediction of only the pressure fluctuation by any simple method of reasonable accuracy, if not of high accuracy, is often required in practice in order to get information about interference of pulsation with gas exchange beforehand.

A simple mathematical model for pressure fluctuation in the exhaust pipe shall be presented, based on the assumptions described below.

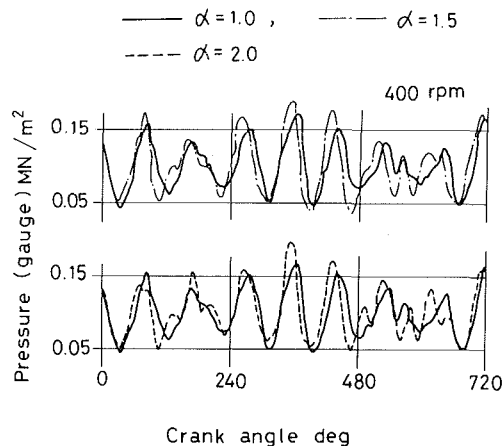


Fig. 33 Effect of α on pulsation (simple method)

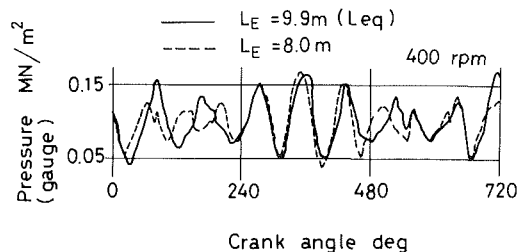


Fig. 34 Effect of the length of exhaust pipe on pulsation (simple method)

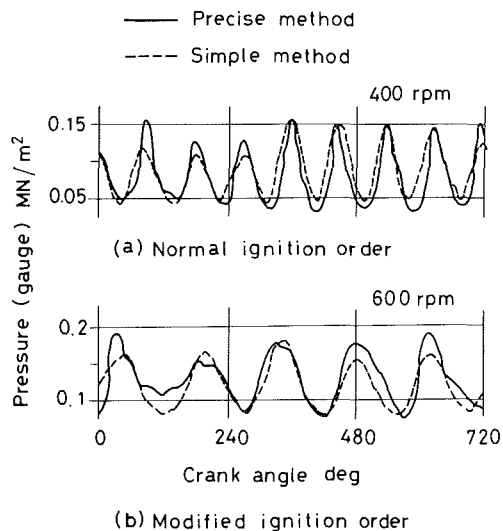


Fig. 35 Pulsations simulated by the simple method using backward waves

1 Pressure waves can be obtained by superposing individual waves.

2 Reflection of the waves occurs at pipe ends without any loss or deformation. However, the pulsation is damped in proportion to the distance travelled.

3 The mean acoustic speed, a , the mean exhaust pressure, P_E , and the equivalent length of the exhaust pipe, L_{eq} , are given. If not given, they can be obtained by the precise method.

Those waves which are propagating in a group occupying a definite space are called a wave packet $f(\phi)$. Both the forward and backward waves are assumed to have the same wave pattern $f(\phi)$, where ϕ is the phase angle of the wave packets

with the beginning of the blow-down as the starting point, $\phi = 0$.

Let it be that θ_j is the blow-down timing of No. j cylinder and x_j the distance between pipe end and No. j cylinder as is shown in Fig. 31. Then, the pressure $P(\theta, x)$ at crank angle θ and at the position x can be represented as follows in the case of four-cycle engines (refer to Appendix).

$$P(\theta, x) = \sum_j^z e^{\frac{\lambda a(\theta - \theta_j)}{12nL_{eq}}} \times \sum_m \{f(\phi_{ff}^m) + f(\phi_{bj}^m) + f(\phi'_{ff}^m) + f(\phi'_{bj}^m)\} \quad (13)$$

where

- m = the number of times that the waves travel through the exhaust pipe
- b, f = suffixes for backward or forward wave
- n = engine speed (rpm)
- z = number of cylinders
- λ = damping factor
- ϕ' = phase angle along the back way as shown in Fig. 31

By the front way in Fig. 31 (a) is meant one-half or the lower half of the loop-type way to be travelled by the forward and the backward waves, while by the back way the other half.

If a wave has the wave length of $2L_{eq}$, then its phase angle is represented as

$$\begin{aligned} \phi_{ff}^m &= \frac{\pi}{L_{eq}} \left\{ \frac{a}{6n} (\theta - \theta_j) - (x - x_j + 2mL_{eq}) \right\} \\ \phi_{bj}^m &= \frac{\pi}{L_{eq}} \left\{ \frac{a}{6n} (\theta - \theta_j) - (x_j - x + 2mL_{eq}) \right\} \\ \phi'_{ff}^m &= \frac{\pi}{L_{eq}} \left\{ \frac{a}{6n} (\theta - \theta_j) - (2L - x - x_j + 2mL_{eq}) \right\} \\ \phi'_{bj}^m &= \frac{\pi}{L_{eq}} \left\{ \frac{a}{6n} (\theta - \theta_j) - (x_j + x + 2mL_{eq}) \right\} \end{aligned} \quad (14)$$

The shape of the wave packets are influenced by many factors such as intensity of blow-down, geometry of exhaust ports, engine speed, and so on. For simplicity, $f(\phi)$ is assumed to be described as

$$f(\phi) = \begin{cases} A \{1 - \cos(\alpha\phi)\} & 0 < \alpha\phi < 2\pi \\ 0 & \alpha\phi \leq 0 \text{ or } \alpha\phi \geq 2\pi \end{cases} \quad (15)$$

$$\alpha = \frac{2L_{eq}}{a\Delta t} = \frac{12nL_{eq}}{a\Delta\theta}$$

where

- A = amplitude
- Δt = period of blow-down in time, s
- $\Delta\theta$ = period of blow-down in crank angle

Parameters such as A , α , and λ can be determined based on the simulation of a single blow-down by using the precise method.

Figure 32 shows a comparison of the simulation by the simple method with the one by the precise method. They agree fairly well as is shown. Figures 33 and 34 show the effect of α and L_{eq} on the simulated pulsation. They show that the effect of α is weak while that of L_{eq} seems to be very strong. As is shown, the simple method can be applicable to practical use by using the reasonable parameters.

In order to confirm whether the mechanism of pulsation resonance considered in the previous section is reasonable or not, a simulation was made for the resonant pulsation. It was made by combining only the backward waves P_b 's. The result is shown in Fig. 35 in comparison with the one by the precise method. As is shown, the resonant pulsation is well represented by a combination of only the backward waves to show that the mentioned mechanism of pulsation resonance is reasonable.

As described, the discussion in this chapter is based on the characteristics of the exhaust gas pulsation in the constant pressure turbocharged engines which have been made clear in this study.

They are very different from the characteristics of the pulsation in pulse turbocharged engines. Therefore, it is not advisable to apply the above discussion to the pulse turbocharged engines, for example, to the high speed engines of small size now in use.

Conclusion

Based on a broad analysis by ordinary thermodynamical calculation, this report showed that higher thermal efficiency of the constant pressure turbocharge system in the range of higher mean effective pressure is due to higher blow-down efficiency in that range than in the lower range of mean effective pressure.

Furthermore, the result of the study has made it possible to simulate not only the exhaust gas pulsation but also the gas flow quantity in the constant pressure turbocharge system. This can be done with higher accuracy and with shorter computational time by using the two-step, Lax-Wendroff's method instead of the characteristic method. Therefore, a simulation system for engine performance with analysis of the pulsations has been established.

As to the characteristics of the pulsating flow in the constant pressure turbocharge system, the following has been clarified in addition to that reported previously [1]: (i) the pressure drop at the branch is negligible, based on Benson's momentum theory concerning the pressure drop at the branch; (ii) in general, the exhaust gas turbine of the constant pressure turbocharge system can be regarded as a closed end; (iii) in order to damp the pulsation by inserting orifices in an exhaust pipe, an orifice with $\beta_0 = F_0/F_E < 0.5$ must be used where F_0 is the area of the orifice and F_E the cross-sectional area of the exhaust pipe. This is because an orifice with $\beta_0 \geq 0.5$ allows the pulsation to pass through it without any damping; (iv) when an orifice with $0.25 \leq \beta_0 < 0.5$ is used for damping, the original pattern of the pressure fluctuation is kept almost unchanged, although the amplitude of the pulsation becomes smaller.

As the last subject a consideration on the mechanism of the pulsation resonance was presented. A simple mathematical model for pressure fluctuation was proposed and simulation by the model showed that the consideration on the mechanism of the pulsation resonance was reasonable.

A simulation system for engine performance including analysis of the pulsation has been established and many of the fundamental features of the pulsation of the constant pressure turbocharge system have been clarified. Therefore, a study on the interaction between the pulsation and cylinder process will be reported in the near future.

Acknowledgments

We should like to express our heartiest thanks to Professor Dr. Mizumachi of Tokyo University, Professor Dr. S. Ohigashi of Kyoto University and Professor Dr. M. Ohmi of Osaka University for their useful advice.

Also, the Ship Building Research Association of Japan is gratefully acknowledged for its financial aid.

References

- 1 Azuma, T., Tokunaga, Y., and Yura, T., "Characteristics of Exhaust Gas Pulsation of Constant Pressure Turbo-Charged Diesel Engines," ASME JOURNAL OF ENGINEERING FOR POWER, Vol. 102, Oct. 1980, pp. 827-835.
- 2 Vormstein, and Pleimling, "Valve Timing and Its Effect on the Performance of Medium-Speed Diesel Engines," Proceedings of the International Council on Combustion Engines, (CIMAC), B25, Tokyo, 1977.
- 3 Fujimori, T., and Kasai, H., "Kawasaki-M.A.N Medium Speed Diesel Engines," Journal of the Marine Engineering Society in Japan, Vol. 13, No. 1, Jan. 1978, pp. 19-26.
- 4 Zapf, H., and Pucher, H., "Abgasenergie-Transport und Nutzung für Stoss und Stau-Aufladung," Hansa, Vol. 114, Nr. 14, 1977, pp. 1321-1326.
- 5 Akashi, G., "On the Utilization of Exhaust Gas Energy and the Control Valve of Exhaust Gas in Turbo-charged Two-cycle Engines," Kawasaki Review, Vol. 12, Apr. 1957, pp. 31-38.
- 6 Maclaren, J. F. T., et al., "A Comparison of Numerical Solutions of the Unsteady Flow Equations Applied to Reciprocating Compressor Systems," Journal Mechanical Engineering Science, I. Mech. E., Vol. 17, No. 5, 1975, pp. 271-279.
- 7 Richtmyer, R. D., and Morton, K. W., Difference Methods for Initial-Value Problems 2nd ed., Interscience, 1967, pp. 300-308.
- 8 Benson, R. S., Woollatt, D., and Woods, W. A., "Unsteady Flow in Simple Branch System," Proceedings Instn Mech Engrs 1963-64, Vol. 178, pt. 31, (iii), pp. 24-49.
- 9 Yamada, S., and Ohtani, I., "Damping of Pulsation with Orifice and Arrangement of Air Vessels in π -Type," JSME Transactions, Vol. 34, No. 268, Dec. 1968, pp. 2139-2145.

APPENDIX

Suppose that a pressure wave, Δp , caused by a blow-down at x_j or j -cylinder is propagating along in a pipe of infinite length. Then Δp is represented as

$$\Delta p = e^{-\mu \Delta t} f(a \Delta t - \Delta l) \quad (\text{A1})$$

where

- Δl = the distance travelled by the pressure wave
- Δt = time after the blow-down occurred at x_j
- μ = damping factor of the wave.

Instead of the pipe of infinite length, let the pipe be of length L_{eq} and that waves reflect at the pipe ends without any loss or deformation, as assumed in the text.

Then, depending whether the wave is in the front or the back way, shown in Fig. 31 (a), Δl traveled by the forward wave of j -cylinder is represented in two equations

$$\Delta l_f = x - x_j + 2mL_{eq} \quad (\text{A2})$$

$$\begin{aligned} \Delta l_{f'} &= x - x_j + 2mL_{eq} + 2(L_{eq} - x) \\ &= 2L_{eq} - x - x_j + 2mL_{eq} \end{aligned} \quad (\text{A3})$$

$(m = 0, 1, 2, \dots)$

where the subscripts f and f' show that the wave is in the front and the back way, respectively. Furthermore, m shows how many times the wave has traveled round the loop-type way of the exhaust pipe.

As the result, a pulsation P_{ff} formed by the forward wave that is caused by the blow-down of j -cylinder is represented as

$$\begin{aligned} P_{ff} = e^{-\mu \Delta t_j} \sum_m \{ & f\{ a \Delta t_j - (x - x_j + 2mL_{eq}) \} \\ & + f\{ a \Delta t_j - (2L_{eq} - x - x_j + 2mL_{eq}) \} \} \end{aligned} \quad (\text{A4})$$

The pulsation P_{bj} caused by the backward wave can be obtained in the same way as described above.

On the other hand, we have the following relations

$$\tau_0 = 2L_{eq}/a \quad (\text{A5})$$

$$\mu = \frac{\lambda}{\tau_0} = \frac{a\lambda}{2L_{eq}} \quad (\text{A6})$$

$$\Delta t_j = (\theta - \theta_j)/6n \quad (\text{A7})$$

where

- τ_0 = the natural period of the gas column vibration
- λ = the logarithmic attenuation coefficient
- θ_j = the crank angle at which the blow-down of j -cylinder occurs.

The Equation (13) can be obtained by incorporating equations (A6) and (A7) into equation (A4).